Proceedings of the International Congress of the Mexican Hydrogen Society XIV, Ciudad de México, México, 2018

September 18th -September 21st, 2018
In Honor of Dr. Nicolas Alonso Vante

INFORMACIÓN LEGAL
PROCEEDINGS OF THE INTERNATIONAL CONGRESS OF THE MEXICAN HYDROGEN SOCIETY DERECHOS DE AUTOR Y DERECHOS CONEXOS, **Año 5, No. 5, 2018**, es una publicación anual editada por la Sociedad Mexicana del Hidrogeno A. C., Calle Monte Bello No. 108, Col. Colinas del Padre, C.P. 98085, Zacatecas, Zacatecas, México, Teléfono (614) 4394815, Editor responsable: Alejandro López Ortiz., **ISSN: 2448-7120**, otorgado por el Instituto Nacional del Derecho de Autor.
Responsable de la última actualización de este Número, Dr. Alejandro López Ortiz, Cordillera de Guanacaste, 6435, Frac. Cordilleras, C.P. 31124, Chihuahua, Chihuahua, México, teléfono (614) 4394815, correo electrónico lalejan@gmail.com, fecha de última modificación, 8 de Septiembre 2016.

Topics

This conference will address important aspects of the hydrogen technologies, from fundamentals, applications, policies and environmental aspects.

Topics will include but are not limited to:

1. Nanostructured materials
2. Hydrogen production, storage and applications
3. Direct Oxidation Fuel Cells
4. Fuel Cells components and stacks
5. Modelling and design
6. Renewable energy systems
7. Control and power conditioning
8. Policies, economy and market strategies
9. Codes, standards and safety issues
10. Environmental aspects

Committee

SMH Commitee

President Dr. Alejandro López Ortiz (CIMAV)

Vice-president Dra. Beatriz Ruiz Camacho (UGto)

Treasurer Dra. Virginia Collins Martínez (CIMAV)

Secretary Dra. Ivonne Alonso Lemus (CINVESTAV Saltillo)

Local Committee

- Dra. Rosa de Guadalupe González Huerta (ESIQIE-IPN), Coordinator
- Dr. Omar Solorza Feria (CINVESTAV)
- Dr. Juan Manuel Sandoval Pineda (ESIME-IPN)
- Dr. Miguel Tufiño Velázquez (ESFM-IPN)
- Dr. Miguel Ángel Oliver Tolentino (UPIBI-IPN)
- Dr. Jorge Roberto Vargas García (CNMNT-IPN)
- Dra. Claudia Alicia Cortés Escobedo (CIITEC-IPN)
- Dr. Fray de Landa Castillo (ESFM-IPN)
- Dr. Guadalupe Ramos Sánchez (UAM-I)
- Dr. Prospero Acevedo Peña (CICATA-Legaria)
- Dr. Daniel Ramírez Rosales (ESFM-IPN)
- PhD student. Natasha Arellano Ahumada (ESFM-IPN)
- PhD student Juvencio Vázquez Samperio (CICATA-IPN)
- Masters student Carlos Enrique Moreno Crespo (ESFM-IPN)

Scientific Committee

- Dra. Claudia Alicia Cortes Escobedo (CIITEC-IPN), Coordinator
- Dr. Nicolás Alonso Vante (Universidad de Poitiers)
- Dr. Vicente Compañ (Universidad de Valencia)

- M.C. Luana F. Vieira (Universidade do Extremo Sul Catarinense)
- Dr. Marcos Marques da Silva Paula (Universidade Federal do Amazonas)
- Dr. Mariano Bruno (National Council of Scientific and Technical Research - CONICET)
- Dr. Fernando Godinez (Texas State University)
- Dr. Agustín Medina Valera (Universidad de Cardiff, UK)
- Dr. Miguel Valenzuela Zapata (ESIQIE-IPN)
- Dra. Martha Leticia Hernández Pichardo (ESIQIE-IPN)
- Dra. Silvia Patricia Paredes (ESIQIE-IPN)
- Dr. Arturo Manzo Robledo (ESIQIE-IPN)
- Dra. Beatriz Ruiz Camacho (UGTO)
- Dra. Beatriz Escobar Morales (CICY-Mérida)
- Dr. Romeli Gliserio Barbosa Pool (UQroo)
- Dra. Karina Suarez Alcántara (IIM_UNAM)
- Dr. Javier Rodríguez Varela (CINVESTAV)
- Dr. Alejandro López Ortiz (CIMAV)
- Dra. Virginia Collins Martínez (CIMAV)
- Dra. Ivonne Liliana Alonso Lemus (CINVESTAV Saltillo)

General Program Congress

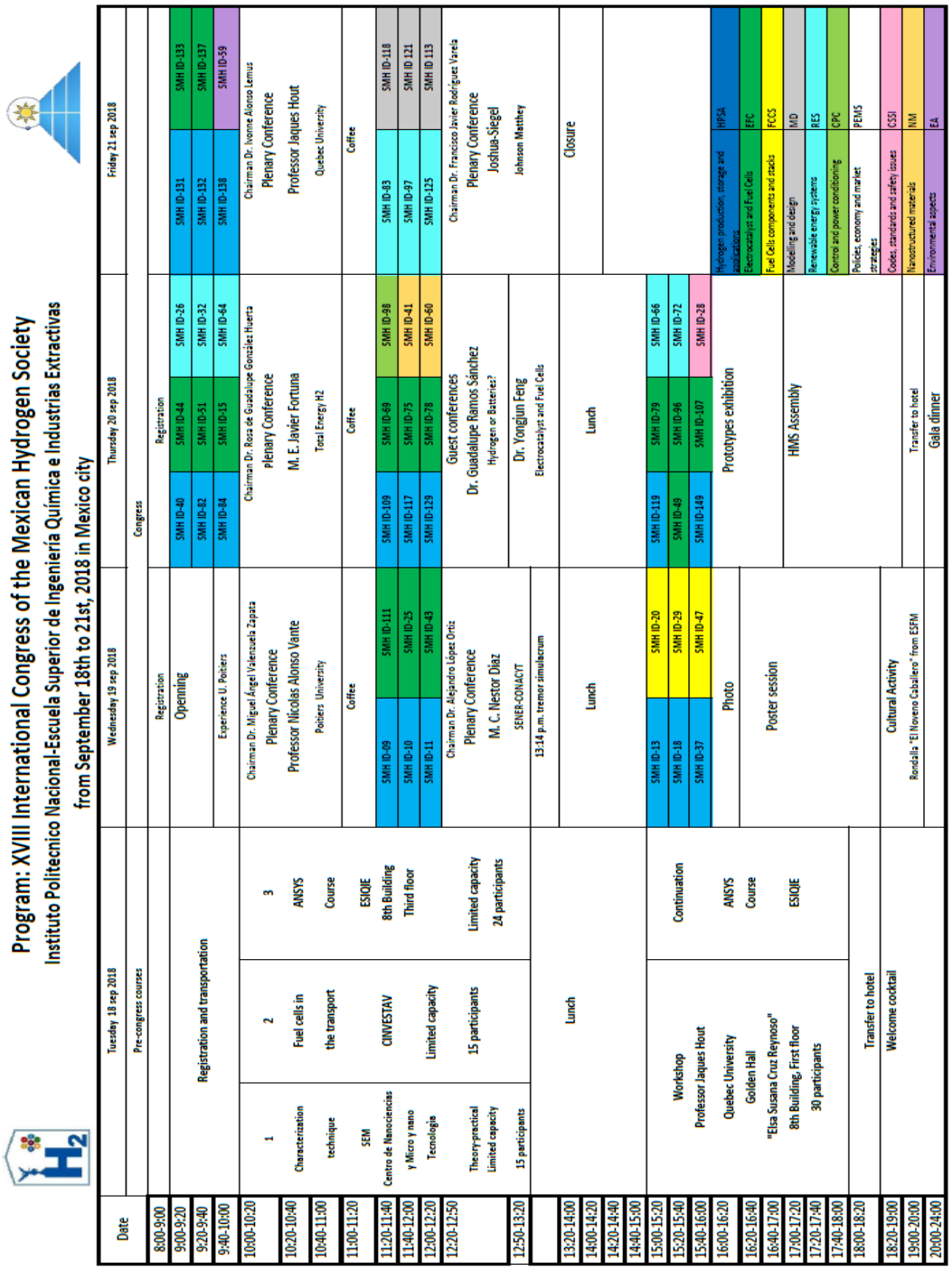

Program: XVIII International Congress of the Mexican Hydrogen Society
Instituto Politecnico Nacional-Escuela Superior de Ingeniería Química e Industrias Extractivas
from September 18th to 21st, 2018 in Mexico city

Date	Tuesday 18 sep 2018			Wednesday 19 sep 2018	Thursday 20 sep 2018			Friday 21 sep 2018		
	Pre-congress courses			Congress						
8:00-9:00				Registration	Registration					
9:00-9:20	Registration and transportation			Openning	SMH ID-40	SMH ID-44	SMH ID-26	SMH ID-131	SMH ID-133	
9:20-9:40					SMH ID-82	SMH ID-51	SMH ID-32	SMH ID-132	SMH ID-137	
9:40-10:00				Experience U. Poitiers	SMH ID-84	SMH ID-15	SMH ID-64	SMH ID-138	SMH ID-59	
10:00-10:20	1	2	3	Chairman Dr. Miguel Ángel Valenzuela Zapata	Chairman Dr. Rosa de Guadalupe González Huerta			Chairman Dr. Ivonne Alonso Lemus		
10:20-10:40	Characterization	Fuel cells in	ANSYS	Plenary Conference	plenary Conference			Plenary Conference		
10:40-11:00	technique	the transport	Course	Professor Nicolas Alonso Vante	M. E. Javier Fortuna			Professor Jaques Hout		
11:00-11:20	SEM	ESIQIE		Poiters University	Total Energy H2			Quebec University		
11:20-11:40	Centro de Nanociencias	CINVESTAV	8th Building	Coffee	Coffee			Coffee		
11:40-12:00	y Micro y nano		Third floor	SMH ID-09	SMH ID-111	SMH ID-109	SMH ID-69	SMH ID-98	SMH ID-83	SMH ID-118
12:00-12:20	Tecnología	Limited capacity		SMH ID-10	SMH ID-25	SMH ID-117	SMH ID-75	SMH ID-41	SMH ID-97	SMH ID 121
12:20-12:50	Theory-practical	15 participants	Limited capacity	SMH ID-11	SMH ID-43	SMH ID-129	SMH ID-78	SMH ID-60	SMH ID-125	SMH ID 113
	Limited capacity		24 participants	Chairman Dr. Alejandro López Ortiz	Guest conferences			Chairman Dr. Francisco Javier Rodríguez Varela		
	15 participants			Plenary Conference	Dr. Guadalupe Ramos Sánchez			Plenary Conference		
12:50-13:20				M. C. Nestor Díaz	Hydrogen or Batteries?			Joshua-Siegel		
				SENER-CONACYT	Dr. Yongjun Feng			Johnson Matthey		
				13:14 p.m. tremor simulacrum	Electrocatalyst and Fuel Cells					
13:20-14:00	Lunch			Lunch	Lunch			Closure		
14:00-14:20										
14:20-14:40										
14:40-15:00										
15:00-15:20	Workshop			SMH ID-13	SMH ID-20	SMH ID-119	SMH ID-79	SMH ID-66		
15:20-15:40	Professor Jaques Hout	Continuation		SMH ID-18	SMH ID-29	SMH ID-49	SMH ID-96	SMH ID-72		
15:40-16:00				SMH ID-37	SMH ID-47	SMH ID-149	SMH ID-107	SMH ID-28		
16:00-16:20	Quebec University	ANSYS		Photo	Prototypes exhibition			Hydrogen production, storage and applications	HPSA	
16:20-16:40	Golden Hall	Course						Electrocatalyst and Fuel Cells	EFC	
16:40-17:00	"Elsa Susana Cruz Reynoso"			Poster session				Fuel Cells components and stacks	FCCS	
17:00-17:20	8th Building, First floor	ESIQIE			HMS Assembly			Modelling and design	MD	
17:20-17:40	30 participants							Renewable energy systems	RES	
17:40-18:00								Control and power conditioning	CPC	
18:00-18:20	Transfer to hotel							Policies, economy and market strategies	PEMS	
18:20-19:00	Welcome cocktail			Cultural Activity				Codes, standards and safety issues	CSSI	
19:00-20:00				Rondalla "El Noveno Caballero" from ESFM	Transfer to hotel			Nanostructured materials	NM	
20:00-24:00					Gala dinner			Environmental aspects	EA	

Daily Program

19-sep

8:00 - 9:00		REGISTRATION
		Auditorium
9:00 - 9:40		OPENING
9:40 - 10:00		Experience U. Poitiers (Dra. Yadira Gochi)
10:00 - 11:00		Poitiers University (Dr. Nicolas Alonso Vante)
11:00 - 11:20		COFFEE
		Auditorium
11:20 - 11:40	SMH ID-9	Towards double metal alanates
11:40 - 12:00	SMH ID-10	Low-cost charging station for hydride hydrogen storage tanks-II
12:00 - 12:20	SMH ID-11	Production of sustainable NaAlH4 for hydrogen storage
		Golden Hall "Elsa Susana Cruz Reynoso"
11:20 - 11:40	SMH ID-111	Residual biomass-based hydrogen production: Potencial and posible uses in Ecuador
11:40 - 12:00	SMH ID-25	Electrochemical Studies of Ruddlesden-Popper Oxides (Sr,Ln)n+1(Fe,Co)nO3n+1 for IT-SOFC Cathode Applications
12:00 - 12:20	SMH ID-43	Electrocatalytic effect of bimetallic nanoparticles AuM (M: Ag, Pt & Pd) in the sorbitol electro-oxidation in alkaline medium
		Auditorium
12:20 - 13:20		SENER-CONACYT (M. en C. Nestor Diaz)
13:20 - 15:00		LUNCH
		Auditorium
15:00 - 15:20	SMH ID-13	Low-cost Sieverts machine for the study of hydriding/dehydriding reactions
15:20 - 15:40	SMH ID-18	Statistical optimization of biohydrogen production from waste diapers
15:40 - 16:00	SMH ID-37	Biohydrogen production from acid hydrolizates of fruits-and-vegetables wastes and corn stover: effects of inoculum/substrate ratio and sugar concentration
		Golden Hall "Elsa Susana Cruz Reynoso"
15:00 - 15:20	SMH ID-20	Design of polymer nanocomposites based on polypropylene, carbon nanotubes and carbon nanofibers for application in bipolar plates
15:20 - 15:40	SMH ID-29	The space charge effect on the grain boundary conduction of
15:40 - 16:00	SMH ID-47	Effect of the sulfonation in the properties of poly(styrene-co-butyl acrylate) for proton exchange membrane fuel cells
16:00 - 16:20		PHOTO
16:20 - 18:20		Poster session
18:20 - 20:00		Cultural activity (Rondalla "El Noveno Caballero" from ESFM)

20-sep

		Auditorium
9:00 - 9:20	SMH ID-40	Evaluation of Electrochemical Hydrogen Production Using
9:20 - 9:40	SMH ID-82	Flexible solar cells coupled to aeration system for a photobioreactor hydrogen generator
9:40 - 10:00	SMH ID-84	A closer look at how a TiFe hydride doped with ZrV2 is affected globally by its primary and secondary phase behavior.
		Golden Hall "Elsa Susana Cruz Reynoso"
9:00 - 9:20	SMH ID-44	Oxygen reduction reaction on PtBi and PdBi alloys for PEMFC
9:20 - 9:40	SMH ID-51	Platinum sulfide: Synthesis, characterization and performance towards ORR
9:40 - 10:00	SMH ID-15	Pt3Fe/C bimetallic alloy nanoparticules as electrocatalysts whit improved activity for the oxygen reduction reaction
		Multipurpose room
9:00 - 9:20	SMH ID-26	Biological synthesis of iron nanoparticles from anaerobic consortia
9:20 - 9:40	SMH ID-32	Electrofermentation for production of value-added compounds and its Integration to biorefineries: an overview
9:40 - 10:00	SMH ID-64	Dilute phosphoric acid hydrolysis of stem of faba bean for reducing sugar production
		Auditorium
10:00 - 11:00		The hydrogen in the Mexican industry (Ing. Javier Fortuna)
11:00 - 11:20		COFFEE
		Auditorium
11:20 - 11:40	SMH ID-109	Hydrogen production from methanol decomposition using copper-
11:40 - 12:00	SMH ID-117	Design proposal for a hydrogen production plant from the hydrolysis of aluminum waste coupled to a PEM fuel cell
12:00 - 12:20	SMH ID-129	Design and manufactured of alkaline membrane electrolyzer
		Golden Hall "Elsa Susana Cruz Reynoso"
11:20 - 11:40	SMH IS-69	High surface area N-doped porous carbon from Sargassum spp. for oxygen reduction reaction in alkaline media
11:40 - 12:00	SMH ID-75	Thin film CuBi2O4 as a p-type photoelectrode for solar water reduction
12:00 - 12:20	SMH ID-78	Palladium carbon-supported electrocatalyst for oxygen reduction reaction (ORR)

		Multipurpose room
11:20 - 11:40	SMH ID-98	A New Two-Level Power Sharing Control Strategy for a Multi-Stack Fuel Cell System
11:40 - 12:00	SMH ID-41	Support Interaction Effect of Platinum Nanoparticles on Non-, Y-, Ce-Doped Anatase and Its Implication on the ORR in Acid and Alkaline Media
12:00 - 12:20	SMH ID-60	Synthesis and characterization of Au@Pd core-shell nanoparticles
		Auditorium
12:20 - 12:50		Hydrogen or Batteries? (Dr. Guadalupe Ramos Sánchez)
12:50 - 13:20		Electrocatalyst and Fuel Cells (ORR) SMH ID-31 (Dr. Yongjun Feng)
13:20 - 15:00		LUNCH
		Auditorium
15:00 - 15:20	SMH ID-119	OBD2 monitoring and control system for hydrogen generator used as complementary fuel on internal combustion vehicles
15:20 - 15:40	SMH ID-49	Effect of nitrogen precursors on graphene-doping and electrochemical evaluation as an active electrocatalyst for oxigen reduction reaction
15:40 - 16:00	SMH ID-149	Sustainable and efficient off-grid production of Hydrogen. Demo project on-going in Spain
		Golden Hall "Elsa Susana Cruz Reynoso"
15:00 - 15:20	SMH ID-79	Effect of the Transition Metal Oxides (WO3-ZrO2) as a support for Oxygen Reduction Reaction
15:20 - 15:40	SMH ID-96	Low Pt-Loading Electrocatalysts Supported On Ordered Mesoporous Carbon Hollow Spheres With High Performance for Oxygen Reduction Reaction
15:40 - 16:00	SMH ID-107	Theoretical study of hydrogen adsorption on graphyne doped with N and transition metal atoms: the quest for novel singles atom catalysts
		Multipurpose room
15:00 - 15:20	SMH ID-66	Hydrogen, energy storage technology for marine renewable energies
15:20 - 15:40	SMH ID-72	Graphene oxide as catalyst in plant-microbial fuel cells
15:40 - 16:00	SMH ID-28	Measurement of pollutant emissions for an engine gasoline internal combustion enriched system with oxyhydrogen
16:00 - 17:00		Prototypes exhibition
17:00 - 19:00		HMS Assembly
19:00 - 20:00		Transfer to hotel
20:00 - 24:00		Gala dinner

21-sep

		Auditorium
9:00 - 9:20	SMH ID-131	Photocatalytic hydrogen production from glycerol reforming using highly active CuO@TiO2 core-shell catalysts
9:20 - 9:40	SMH ID-132	Au/CeO2 and Au/CexZr1-xO2 Sol-Gel Catalysts for Hydrogen Production via Partial Oxidation of Methanol
9:40 - 10:00	SMH ID-138	Performance diesel engine enrichment with oxyhydrogen and the
		Golden Hall "Elsa Susana Cruz Reynoso"
9:00 - 9:20	SMH ID-133	Effect of the Oam/Oac ratio in the synthesis, characterization, and performance of Ni-Pt nanoparticles employed as catalysts for the Oxygen Reduction Reaction in PEM fuel cells.
9:20 - 9:40	SMH ID-137	Pd-CeO2-NR/C Nanocatalyst With High Catalytic Activity and Stability for the Electrooxidation of Etanol in Alkaline Media
9:40 - 10:00	SMH ID-59	Microbial fuel cell to heavy metals removal from acid mine drainage
		Auditorium
10:00 - 11:00		Dr. Jackes Hout
11:00 - 11:20		COFFEE
		Auditorium
11:20 - 11:40	SMH ID-83	Sodium polyacrylate inhibits fermentative hydrogen production from a cellulosic substrate
11:40 - 12:00	SMH ID-97	Molecular characterization of microbial consortia in a hydrogen based biorefinery
12:00 - 12:20	SMH ID-125	Effect of fermentation time/hidraulic retention time in a UASB reactor
		Golden Hall "Elsa Susana Cruz Reynoso"
11:20 - 11:40	SMH ID-118	Model of a fixed bed catalytic reactor to produce H2 by Ethanol steam reforming with a Ni-Co/Al2O3 catalyst
11:40 - 12:00	SMH ID-121	Kinetic modeling of the gasification of the palm kernel shell for the production of hydrogen
12:00 - 12:20	SMH ID-113	Reconstruction of stochastis materials for energy applications
		Auditorium
12:20 - 13:20		Universidad de Quebec (Joshua-Siegel)
13:20 - 14:20		CLOSURE

Invited speakers

Dr. Nicolás Alonso Vante

University of Poitiers, France.

Nicolas Alonso-Vante, from Ixtepec, Oaxaca (Istmo de Tehuantepec), studied ESIQIE-IPN (1970-1974) in Mexico City. After a short activity period at the rubber Industry in Mexico City, he undertook Master's studies with the specialty in Physical-Chemistry at the CINVESTAV in Mexico City (1976-1978). This research center opened his eyes to pursue doctoral studies abroad in Strasbourg, France, where he obtained the degrees of Docteur Troisième Cycle (1981), and Doctorat d'Etat (1984) from the University of Strasbourg. During the years in Strasbourg, he had the opportunity to interact with Professors JM Lehn, and JP Sauvage. Both Nobel Prize winners in 1987 and 2016, respectively. In Germany working with Prof. H. Tributsch, where he later worked as a senior scientist in the department of solar energy until August 1997. He moved to France, in September 1997, as Professor of Chemistry at the University of Poitiers (LACCO UMR-CMRS 6503), now since 2012, IC2MP UMR-CNRS. Prof. N Alonso-Vante has developed materials in the nanodivided scale based on transition metal and chalcogenides in metallic and semiconducting form to oxygen reduction reaction process, an important technological reaction in low temperature fuel cells. He is the author of over 200 publications, book chapters, editor of a two-volume e-book on electrochemistry in Spanish and holds 2 US, 2 German, and 2 French patents; his work has been widely cited. He has received the awards of the National Polytechnic Institute-Mexico as a R&D distinguished graduate, and of the Mexican Council of Technology SNI-III recognition as a Mexican researcher working outside Mexico, and has been awarded the NM Emanuel Medal from the Russian Academy of Science. Part of his activities have been devoted to teach many young scientists (from Mexico, China, India, Brazil, etc.) who spend from several months to several years doing master, doctoral and postdoctoral studies under his direction.

He is also a member of the International Society of Electrochemistry, the Electrochemical Society, the Bunsengesellschaft für Physikalische Chemie, and of the International Academy of Electrochemical Energy Science (IAOEES) and member of the Editorial board of Fuel Cells Journal.

Ing. Javier Fortuna Espinosa

Total Energy

Mexican, born in Minatitlan, Veracruz, with studies at the Instituto Tecnológico de Toluca of industrial electromechanical engineering, 1987.

WORK EXPERIENCE

From 1985 to 1986. AEROQUIP Mexicana (PARKER). Shift supervisor, tool sharpening workshop, maintenance.

From 1986 to 1990. HYDRO-CHEM Processing of México. Projects division, for new and refurbished plants of generation of hydrogen type elecrolytic and steam methane reforming, spare parts and services sales specialist.

From 1990 to 2003. Panamerican Enterprises INC, management of Latin America operations, for steam methane reforming type, hydrogen generation plants, projects, sales of spare parts, technical services and representations.

From 2003 to this date. As a physical person, with business and professional activities. Consulting services for companies that produce, store and compress hydrogen. Consulting services for companies that require to acquire equipment, spare parts, catalysts related to hydrogen generation and handling.

Training courses, related to operation, maintenance and safety in hydrogen handling.

Services of mechanical assembly of process equipment, as a contractor, for installations of hydrogen, natural gas and propane.

Representation services in Latin America to foreign companies, related to hydrogen technologies.

Process, control and instrumentation, mechanical and thermal services engineering.

Active member of the Sociedad Mexicana del Hidrógeno, A.C. since 2000.

Founder member of the Red Nacional del Hidrógeno, A.C. 2005

President of the Sociedad Mexicana del Hidrógeno, A.C. 2008-2010 period.

Responsible of the Committee of the Link with Industry and International Associations of the SMH, in the year 2010.

Participation in 3 books, related to hydrogen technologies, published by the Sociedad Mexicana del Hidrógeno, A.C. with other institutions.

Member of the Consultative Committee of the Mexican Society of Hydrogen, A.C.

M. en C. Nestor L. Díaz Ramírez

Director de Desarrollo Tecnológico at CONACYT

Director de Desarrollo Tecnológicon at CONACYT from 2012 to current day.
In this Direction, sectoral energy funds are administered:

- Sener- CONACYT hydrocarbons
- Sener- CONACYT- sustainability and the CFE

Graduated from the ESIQIE-IPN 1976 - 1979
ESIQIE-IPN PROFESSOR, from 1974 to 2012.
He was Director of the Escuela Superior de Ingeniería Química e Industrias Extractivas - Instituto Politécnico Nacional, from 2001 to 2007
Master's degree ESIQIE-IPN
Academic Chemical Engineering

Dr. Jacques Hout

University of Québec

Since 2004, Dr. Jacques Huot is professor of the Department of Chemistry, Biochemistry and Physics, in Université du Québec à Trois-Rivières (UQTR) Québec, Canada. Also, he is Member of the Hydrogen Research Institute. His Ph. D. studies were performed in Université Laval (Canada), then he perform his first post-doc in the National Institute of Materials and Chemical Research, Tsukuba, Japan and a second post-doc in Chemical Engineering Department, Texas A & M University, Texas, USA. He has developed in the last 2 years other professional activities such as editor of the book Neutron Scattering and Other Nuclear Techniques for Hydrogen in Materials. Neutron Scattering Applications and Techniques. 2016: Springer International Publishing. VIII, 413. Author of the book Enhancing Hydrogen Storage Properties of Metal Hybrides, 2016: Springer International Publishing. VI, 39, among other. From 1995 to 2004 Professor Huot was a researcher at Hydro-Québec where he studied magnesium-based nanocrystalline alloys for hydrogen storage. His expertises are solid-gaz interactions, metal hydrides, and material characterization. He has been invited researcher at the Institute for Energy Technology (Norway), Federal University of São Carlos (Brazil), National Institute of Advanced Industrial Science and Technology (Japan), Université de Bordeaux (France), Institut NÉEL (France), et Max Plank Institut fur Kohlenforschung (Germany). He published 158 papers, is co- inventor of 10 patents, and belongs to the Editorial Board of the Journal of Alloys and Compounds (Elsevier).

Joshua Siegel

Johnson Matthey

Joshua Siegel is the Global Commercial Leader, Structured Catalyst for Johnson Matthey, located in Oakbrook Terrace, Illinois. He is presently responsible for ensuring that Johnson Matthey's CATACELJM SSR product and services meets the global needs of the marketplace. Josh has been with Johnson Matthey for 9 years, where he previously held roles as Regional Account Manager and Technical Service Manager. He has over 20 years' experience in the refinery catalyst industry where he has worked with Hydroprocessing, FCC and Polyolefin catalyst. Prior to joining Johnson Matthey, Josh has held various responsibilities from manufacturing, quality manager, technical service and sales. Josh graduated with a BS in Forensic Chemistry from Ohio University in 1993 and an MS in Analytical Chemistry from Governors State University in Illinois in 2000.

Sponsors

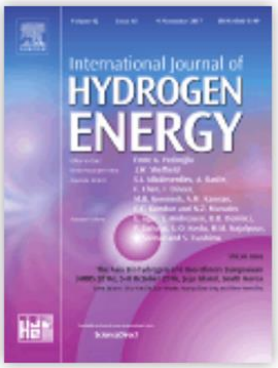

Metrohm México

SAIDE

Generatoris S.A. de C.V.

ISASA® INSTRUMENTACION

nanociencias de México

JM Johnson Matthey
Inspiring science, enhancing life

Princeton Applied Research

solartron analytical

GrupoSSC

Index

Hydrogen production, storage and applications

ID	Title	Autor(s)	Abstract page	Full paper page
141	Photocatalytic activities of BaTiO3/Ba4Ti2O27 mixtures towards efficient hydrogen production (water splitting reaction)	M.A. Escobedo Bretado, M.A González Lozano, R.H. Lara, V. Collins Martínez, M. J. Meléndez Zaragoza and A. López Ortiz	43	-------
143	Scope of fuel cells in current transport with hydrogen as fuel	José Juan Alvarado Flores, María Liliana Ávalos Rodríguez, Jaime Espino Valencia and Jorge Víctor Alcaraz Vera	44	298
149	Sustainable and efficient off-grid production of Hydrogen. Demo project on-going in Spain	Edgar Bueno, Lorién Gracia and Pedro Casero	45	307
150	Hydrogen production by the reaction between water and the intermetallic AlLi activated by mechanical milling	Diana Laura Álvarez Acosta and José Luis Iturbe García	46	316
152	Design of an oxy-hydrogen system to be implemented in internal combustion engines of motorcycle	U. Maza Nájera, J. M. Sandoval Pineda, R. González Huerta and M. Rico Cortez	47	326
154	Computational Design of an Oxyhydrogen Gas Burner	R. Moreno Soriano, R. de G. González Huerta, J. M. Sandoval Pineda, F. Soriano Moranchel	48	335
155	Evaluation of NiWO4 as an oxygen carrier for the hydrogen storage by chemical looping.	P.E. González Vagras, M. J. Meléndez Zaragoza, J. M. Salinas Gutiérrez, V. Collins Martínez, A. López Ortiz	49	346
156	Thermodynamic Evaluation and process simulation of the production of Hydrogen-Syngas Using Mixed Fe-based oxides with Methane.	J. F. Cazares Marroquín, J. M. Salinas Gutiérrez, M. J. Meléndez Zaragoza, V. Collins Martínez, A. López Ortiz	50	356
157	Synthesis, Characterization And Photocatalytic Evaluation Of Niwo4 For The Production Of H2 By Water Splitting	Ma. G. Joaquín Morales, A. F. Fuentes, S. M. Montemayor, W.J. Pech Rodríguez, M. J. Meléndez Zaragoza, J. M. Salinas Gutiérrez, A. López Ortiz, V. Collins Martínez	51	375

ID	Title	Autor(s)	Abstract page	Full paper page
158	Photo-Assisted Synthesis of GO/ZnO Nanocomposites for the Production of Photocatalytic Hydrogen	B.C. Hernández Majalca, E. J. Núñez Murillo, S.A. Victor Chávez, J. L. Dominguez Arvizu, J. Jiménez Miramontes, J. C. Pantoja Espinoza, M. J. Melendez Zaragoza, J. M. Salinas Gutiérrez, A. López Ortiz, V. Collins Martínez	52	388
159	Synthesis of Carbon-Based Support for Ruthenium Electrocatalyst for ORR Formed by Graphite and Asphalt Carbon Pyrolyzed	P. E. González Vargas, M. J. Meléndez Zaragoza, J. M. Salinas Gutiérrez, V. Collins Martínez, A. López Ortiz	53	398
160	Synthesis and Characterization of NiTiO3 Nanoparticles and AgCl/Ag/NiTiO3 Nanocomposites for Improvement of the Photocatalytic Hydrogen Production	J. C. Pantoja Espinoza, M. J. Meléndez Zaragoza, J. M. Salinas Gutiérrez, J. L. Dominguez Arvizu, J. Jiménez Miramontes, C. Hernández Majalca, A. López Ortiz, V. H. Collins Martínez	54	-------
161	ZnFe2O4 Synthesis Method Effect on its Photocatalytic Properties towards Hydrogen Production via Water Splitting	J. L. Dominguez Arvizu, M. J. Meléndez Zaragoza, J. Jiménez Miramontes, B. C. Hernández Majalca, J. C. Pantoja Espinoza, J.M. Salinas Gutiérrez, A. López Ortiz, V. Collins Martínez	55	-------

Electrocatalyst and Fuel Cells

ID	Title	Autor(s)	Abstract page	Full paper page
14	Synthesis and characterization of IrRuOx/TiO2 electrocatalysts for the oxygen evolution reaction in acidic medium	A. Martínez Séptimo, M. A. Valenzuela, Zapata and R. de G. González Huerta.	57	410
15	Pt3Fe/C bimetallic alloy nanoparticles as electrocatalysts with improved activity for the oxygen reduction reaction	M. M. Téllez Cruz, M. A. Padilla Islas, H. Cruz Martínez, H. M. Alfaro López, M. G. Salinas Juárez and O. Solorza Feria	58	-------

ID	Title	Autor(s)	Abstract page	Full paper page
58	Synthesis and Evaluation of Nanostructured NiPt Catalysts for the Hydrogen Evolution Reaction	A. Velázquez Osorio, J. L. Reyes Rodríguez and O. Solorza Feria	72	-------
63	Methanol electro-oxidation on Ag and Pt supported in carbon Vulcan catalyst in alkaline condition	J. Mateos Santiago, V. Silva Castro, L. P. A. Guerrero Ortega, J. Soto Hernández, C. R. Santiago Ramírez, M. Luna Trujillo, T. Poznyak and A. Manzo Robledo	73	-------
67	Synthesis and Characterization of Pt3Ni doped with Co Alloy Nanoparticles for the Oxygen Reduction Reaction	H. M. Alfaro López, M.M. Téllez Cruz, M. A. Padilla Islas, H. Cruz Martínez, M. G. Salinas Juárez and O. Solorza Feria	74	-------
68	Synthesis and characterization of N-doped carbon nanofibers modified with Co, Ni and Fe as electrocatalysts for the Oxygen Reduction Reaction in Alkalyne media.	D. Gómez Cholula, R. Ojeda López and G. Ramos Sánchez	75	-------
69	High surface area N-doped porous carbon from Sargassum spp. for oxygen reduction reaction in alkaline media	K. Pérez Salcedo, B. Escobar Morales, I. Alonso Lemus and R. Barbosa	76	-------
71	Development of Pt and Pt-Ru nanocatalysts supported on N-doped Ordered Mesoporous Hollow Carbon Spheres for the Methanol and Ethanol Oxidation Reactions	J.H. Serna Mata, J.A. Díaz Guillén, M. Salazar Oropeza, J. Escorcia García, I.L Alonso Lemus and F. J. Rodríguez Varela	77	-------
75	Thin film CuBi2O4 as a p-type photoelectrode for solar water reduction	Manuel Rodríguez Pérez, Ingrid Rodríguez Gutiérrez, Alberto Vega Poot, Rodrigo García Rodríguez, Geonel Rodríguez and Gattorno Gerko Oskam	78	-------
76	Electrochemical Comparative Study of PtCo/MNC and PtCo/rGO in Methanol Electro-oxidation in Acid Medium	D. Macias Ferrer, J. A. Melo Banda, R Silva Rodrigo, M. Lam Maldonado, J. Y. Verde Gómez, U. Páramo García, P. Del Ángel Vicente and M.A. Meraz Melo	79	-------
78	Palladium carbon-supported electrocatalyst for oxygen reduction reaction (ORR)	J. Soto Hernández, C. R. Santiago Ramírez, E.Y. Cervantes Aspeitia, J. Vera Iturriaga, J. Mateos Santiago, M.L. Hernández Pichardo, T. Poznyak, A. Manzo Robledo	80	-------

ID	Title	Autor(s)	Abstract page	Full paper page
133	Effect of the Oam/Oac ratio in the synthesis, characterization, and performance of Ni-Pt nanoparticles employed as catalysts for the Oxygen Reduction Reaction in PEM fuel cells.	J.L. Reyes Rodríguez and O. Solorza Feria	92	-------
134	Qualities of Mn3+ sites in Nickel-based layered double hydroxides throughout methanol electro-oxidation in alkaline media	Stephany N. Arellano Ahumada, Miguel A. Oliver Tolentino, Guadalupe Ramos Sánchez, Carlos E. Moreno Crespo, Juvencio Vazquez Samperio, Arturo Manzo Robledo, Ariel Guzmán Vargas and Daniel Ramírez Rosales	93	-------
135	Study of the synthesis, characterization, and performance of polyhedral Ni-Pt nanocatalysts and their application as cathodes in PEM fuel cells.	L. Reyes Rodríguez and O. Solorza Feria	94	-------
137	Pd-CeO2-NR/C Nanocatalyst With High Catalytic Activity and Stability for the Electrooxidation of Etanol in Alkaline Media	P.C. Meléndez González, M.E. Sánchez Castro, I.L. Alonso Lemus, R. Pérez Hernández and F.J. Rodríguez Varela	95	-------
151	Electrochemical Measurements: Is It Easy to Work in Alkaline Medium?	C.A. Campos Roldán, R.G. González Huerta and N. Alonso Vante	96	-------

Fuel Cells components and stacks

ID	Title	Autor(s)	Abstract page	Full paper page
20	Design of polymer nanocomposites based on polypropylene, carbon nanotubes and carbon nanofibers for application in bipolar plates	C. A. Ramírez Herrera, J. Pérez González, O. Solorza Feria, H. Martínez Gutiérrez, A. Flores Vela and J. G. Cabañas Moreno	98	455
29	The space charge effect on the grain boundary conduction of GdBaCo2O5+δ	C. I. Ramos Villegas and H. J. Ávila Paredes	100	-------
47	Effect of the sulfonation in the properties of poly(styrene-co-butyl acrylate) for proton exchange membrane fuel cells	L. Francisco Vieira, E. Cuara Diaz, R. Benavides and D. Morales Acosta	101	464
50	Computational Characterization of Solid Polymer Electrolyte for Polysufide retention in Li-S Batteries	Y. A. Peña Castañeda and Perla B Balbuena	102	-------

ID	Title	Autor(s)	Abstract page	Full paper page
104	Effect of the calcination temperature on the purity of GdBaCo2O5+δ synthesized by a sol-gel method	D. A. Jurado Ferral, C. I. Ramos Villegas and H. J. Ávila Paredes	103	473
108	Effect of the synthesis method on the ionic conductivity of zirconate-based solid electrolytes on views to their use in SOFC	K. A. Gonzalez García, D. Rentería, S.M. Montemayor, J.A. Díaz Guillén, M. Salazar Zertuche, M. E. Bazaldúa Medellín, O. Burciaga Díaz and A.F. Fuentes	104	-------
130	Construction and electrochemical characterization of a microtubular solid oxide fuel cell at intermediate temperatures	R. Guzmán Salinas, C. I. Ramos Villegas and H. J. Ávila Paredes	105	480
136	Environmentally friendly low-cost membranes for micro and meso-scale bioelectrochemical systems	M.J. González Pabón, F. Figueredo, DC Martínez Casillas and E Cortón	106	487
139	Fuel cell design up to 50 W	A. T. Rodríguez Victoria, J. M. Sandoval Pineda R de G. González Huerta and M. Rico Cortez	107	497

Modelling and design

ID	Title	Autor(s)	Abstract page	Full paper page
52	A suitable designed-cell for testing the catalyst performance applied towards hydrogen evolution reaction	R. Zenteno López, A. Martínez Séptimo, L. A. Estudillo Wong and R. de G. González Huerta	109	508
90	Simulated annealing optimization heuristic algorithm for modelling PEM fuel cell)	Edumis Viera, Martin G. Martínez, Alina Martínez and Sergio Serna	110	-------
113	Reconstruction of stochastic materials for energy applications	Abraham Misraim Rios Cano, Jaime Silverio Ortegón Aguilar, and Gliserio Romeli Barbosa Pool	111	-------
118	Model of a fixed bed catalytic reactor to produce H2 by Ethanol steam reforming with a Ni-Co/Al2O3 catalyst	I. F. Martínez, J. L. Contreras, G. Pérez, J. Salmones, B. Zeifert and L. Nuño	112	517
121	Kinetic modeling of the gasification of the palm kernel shell for the production of hydrogen	J Acevedo, J. Durán, F Posso and E. Arenas	113	-------

ID	Title	Autor(s)	Abstract page	Full paper page
148	Ab initio study of the graphene structure doped with iron and its interactions with chemical species to improve the oxygen reduction reaction in fuel cells	Ernesto López-Chávez, Alberto Díaz-Góngora, Alberto Garcia-Quiroz, Lucy J. Jiménez González Góngora and Yesica A. Peña-Castañeda	114	-------

Renewable energy systems

ID	Title	Autor(s)	Abstract page	Full paper page
18	Statistical optimization of biohydrogen production from waste diapers	P. Sotelo Navarro, S. Turpin Marion and H. Poggi Varaldo	116	-------
26	Biological synthesis of iron nanoparticles from anaerobic consortia grown in anaerobic fluidized bed reactors from biohydrogen-based biorefineries	Leticia Romero Cedillo, Héctor Mario Poggi Varaldo, Yasuhiro Matsumoto Kuwuabara, Teresa Ponce Noyola, Luz Bretón Deval, Carlos Escamilla Alvarado and Miguel García Rocha	117	-------
32	Electrofermentation for production of value-added compounds and its Integration to biorefineries: an overview	H. M. Poggi Varaldo and E. Hernández Correa	119	-------
64	Dilute phosphoric acid hydrolysis of stem of faba bean for reducing sugar production	J. C. Gómora Hernández, M. del C. Carreño de León, S. M. Fernández Valverde	120	526
66	Hydrogen, energy storage technology for marine renewable energies	Jorge Olmedo González, Guadalupe Ramos Sánchez and Rosa de Guadalupe González Huerta	121	-------
72	Graphene oxide as catalyst in plant-microbial fuel cells	M.G. Salinas, Juárez, M.M. Téllez Cruz, M.A. Padilla Islas, H. Cruz Martínez, H.M. Alfaro López and O. Solorza Feria	122	-------
77	Photocatalytic performance of NaTaO3-C applied in the photoreduction of CO2 to produce formaldehyde	J. M. Mora Hernández, Ali M. Huerta Flores and Leticia M. Torres Martínez	123	-------
83	Sodium polyacrylate inhibits fermentative hydrogen production from a cellulosic substrate	P. Sotelo Navarro, S. Turpin Marion, H. M. Poggi Varaldo	124	-------
85	The effect of hydrophobic chain length of co-absorbent to improve dye sensitized solar cell performance	Luciano da Silva, Hammad Cheema, Roberto Benavides Cantu and Harold Freeman	125	-------

ID	Title	Autor(s)	Abstract page	Full paper page
87	Tetrazole as anchoring group for dye-sensitized solar cells	Luciano da Silva, Hammad Cheema, Roberto Benavides Cantu and Harold Freeman	126	-------
97	Molecular characterization of microbial consortia in a hydrogen based biorefinery	Carlos Alfredo Amaro Aponte, Leticia Romero Cedillo, Héctor Mario Poggi Varaldo, Daniel A. Estrada Bárcenas, Édgar Baldemar Sepúlveda García, Dulce María Delgadillo Álvarez, Teresa Ponce Noyola and José Tapia Ramírez	127	-------
122	Hydrogen production by anaerobic digestion from Agave lechuguilla hydrolysates	Leopoldo J. Rios González, Thelma K. Morales Martínez, Gabriela G. Hernández Enríquez, José A. Rodríguez De la Garza and Mayela Moreno Dávila	128	536
125	Effect of fermentation time/hidraulic retention time in a UASB reactor for hydrogen production using surface response methodology.	Ileana Mayela María Moreno Dávila, Emma Berenice Herrera Ramírez, José Antonio Rodríguez de la Garza, Leopoldo Javier Ríos González and Yolanda Garza García	129	549

Control and power conditioning

ID	Title	Autor(s)	Abstract page	Full paper page
98	A New Two-Level Power Sharing Control Strategy for a Multi-Stack Fuel Cell System	A. Macias, M. Kandidayeni, L. Boulon and H. Chaoui	131	-------

Policies, economy and market strategies

ID	Title	Autor(s)	Abstract page	Full paper page
145	The need for a strategic plan for the effective use of hydrogen as an alternative energy in Mexico	María Liliana Ávalos Rodríguez, José Juan Alvarado Flores and Jorge Víctor Alcaraz Vera	133	557

Codes, standards and safety issues

ID	Title	Autor(s)	Abstract page	Full paper page
28	Measurement of pollutant emissions for an engine gasoline internal combustion enriched system with oxyhydrogen	Santos Fernández M., Hernández Hernández M., Contreras López L. F. and Cortés Escobedo C. A.	135	567

Nanostructured materials

ID	Title	Autor(s)	Abstract page	Full paper page
39	Synthesis of MoCoW as a transition metal oxides electrocatalyst for oxygen reduction reaction in alkaline medium	J. E. G. Béjar, M. Guerra Balcázar, L. Álvarez Contreras, L.G. Arriaga and N. Arjona	137	-------
41	Support Interaction Effect of Platinum Nanoparticles on Non-, Y-, Ce-Doped Anatase and Its Implication on the ORR in Acid and Alkaline Media	Luis A. Estudillo Wong and Nicolás Alonso Vante	138	-------
60	Synthesis and characterization of Au@Pd core-shell nanoparticles	Eduardo Y. Cervantes Aspeitia, Martha L. Hernández Pichardo, Rosa G. González Huerta and Paz del Ángel	139	-------
65	Electrochemical and Photoelectrochemical Properties of TiO2 Nanotubes Arrays Modified with Coordination Polymers for Hydrogen Generation	Kevin Rosas Barrea, Julio Andrés Pedraza Avella, Edilso Reguera and Próspero Acevedo Peña	140	-------
100	Transport properties of dense graphene oxide – polyvinyl chloride composite membranes for H2 /CO2 separation	U. Hernández Castellanos, H. J. Ávila Paredes and A Godínez García	141	-------
101	Methanol oxidation using Pt /graphene-carbon as electrocatalyst in acid media	J.A Palafox Segoviano, B. Ruiz Camacho, A. Medina Ramírez, C. Martínez Gómez and C. M. López Badillo	142	588
102	Synthesis of Pt/nanozeolite- graphene oxide composite and its electrochemical evaluation for formic acid electrooxidation	V.K. González Rodríguez, A Medina Ramírez, L. K. Arellano Ariza and B. Ruiz Camacho	143	595

ID	Title	Autor(s)	Abstract page	Full paper page
110	Silicon Doped Carbon with Low Pt as electrocatalysts for the ORR	O.G. Mejía Ramírez, Zeferino González, L. A. Romero Cano, A. M. Valenzuela, Muñiz and Y. Verde Gómez	144	-------
115	Synthesis and characterization of nanosize cobalt-doped nickel ferrite obtained for hydrogen production by thermochemical cycles	Mario Aldahir Mar Torres, Ana Lidia Martínez Salazar, Margarita García Hernández, Marco Antonio Cornel García and José Aarón Melo Banda	145	-------
116	Photocatalytic behaviour of TiO2, ZnO and CuO modified SBA-15 in hydrogen production	J. C. Espinoza Tapia, F. A. Duran, A. K. Medina, Mendoza, C. R. Tapia Medina, J.L. Contreras Larios I. Hernández Pérez J. C. García Martínez and J. A. Colín Luna	146	603
142	Immobilization of Glucose oxidase on glutathione capped Carbon or CdTe Quantum Dots for use in biosensors and biofuel cells	Jairo Daniel Lozano López, Marisol Galván Valencia Ricardo Escalona Villalpando and Sergio M. Durón Torres	147	577
144	Structural and optical properties of nanostructured CeO2 thin films obtained by spray pyrolysis	Mario Fidel García Sánchez, Inti Zumeta Dubé, Issis Claudette Romero Ibarra, José Manuel García Rangel, José Francisco Malagón García and Ernesto Espinoza Hernández	148	-------
146	Green synthesis of Ni-Co nanoparticles for their use as anodic catalyst in urea fuel cells.	B. Rojas de Soto, M. Galván Valencia, A. Cervantes Villagrana and S. Durón Torres	149	613
147	Ru, Sn and Sb based catalyst for Oxygen Evolution Reaction synthetized by one step method	N. J. Pérez Viramontes, I. L. Escalante García, M. Galván Valencia and S. M. Durón Torres	150	620

Environmental aspects

ID	Title	Autors	Abstract page	Full paper page
24	Photocatalytic Activity of Layered Perovskite Oxides Sr2.7-xCaxLn0.3FeO7-δ for MB Degradation	L.E. Verduzco, R. García Díaz, J. Oliva, A.I Martínez, C. Gómez Solís, C.R. García, A. F. Fuentes and K. P. Padmasree	152	629
59	Microbial fuel cell to heavy metals removal from acid mine drainage	L. S. Vélez Pérez, G. Hernández Flores, O. Solorza Feria, O. Talavera Mendoza, H. M. Poggi Varaldo and J. A. López Díaz	153	-------
127	Residual power in portable energy storage electrochemical devices: an experimental collection approach.	C. M. Bautista Rodríguez, A. Horta Mendez, M. Maldonado Santoyo, B. Ruiz Camacho and Richard R. Lindeke	154	638
162	Synthesis and characterization of Bi2O3:Gd for hydrogen production under visible light.	Durvel de la Cruz Romero, David Salazar Marín, V. Collins-Martinez, M. J. Melendez-Zaragoza Srinivas Godavarthi	---------	650

Abstract

September 18 to 21, 2018 in Mexico City, Mexico

Hydrogen production, storage and applications

September 18 to 21, 2018 in Mexico City, Mexico

Towards double metal alanates

J.R. Tena-Garcia[1], A. Flores-Jacobo[1], K. Suarez-Alcantara[1,*]

[1] Morelia Unit of the Materials Institute Research of the National Autonomous University of Mexico
Antigua carretera a Patzcuaro 8701, Ex-Hacienda de San José de La Huerta, 58190 Morelia, Mich.
* 5623-7300 ext 37889. karina_suarez@iim.unam.mx

ABSTRACT

Alanates are interesting materials for hydrogen storage. In particular sodium alanate ($NaAlH_4$) is interesting due to its hydrogen charge/discharge reversibility when appropriately catalyzed. However, the high hydrogenation pressures and low practical hydrogen storage (3-5 wt. %, almost never reaching the theoretical value of 5.6 wt. %), incentive the research on new kind of alanates. At the borohydride family ($M^x(BH_4)_x$), the formation of double cation materials such as $NaSc(BH_4)_4$ or $NaZn_2(BH_4)_5$ resulted in the tailoring of $NaBH_4$ properties. Similar studies of the formation of double metal alanates have not being performed to the best of knowledge of the authors. Thus we prepared and characterized mixtures of NaH-TiH_2-Al or NaH-ZrH_2-Al at several molar proportions as precursors for Na-Ti or Na-Zr alanates ($NaM_y(AlH_4)_x$, M=Ti or Zr). The mixtures were prepared by mechanical milling in two different mills, a planetary mill or an N_2-liquid-cooled mill (cryomill). The samples were characterized by X-ray diffraction and scanning electron microscope to determine the most suitable structural characteristics for hydrogenation. The mixtures were tested for hydrogenation, reaching about 0.6 wt.%. Improvement of the hydrogenation conditions is under research to increase the hydrogen uptake.

Acknowledgment: *Ciencia Básica-CONACyT 251347: Alanatos no convencionales para almacenamiento de hidrógeno a baja temperatura*

XVIII International Congress
of the Mexican Hydrogen Society

Low-cost charging station for hydride hydrogen storage tanks-II

J.R. Tena-Garcia[1], E.P Armenta-Garcia[1], K. Suarez-Alcantara[1,*]

[1] Morelia Unit of the Materials Institute Research of the National Autonomous University of Mexico
Antigua carretera a Patzcuaro 8701, Ex-Hacienda de San José de La Huerta, 58190 Morelia, Mich.
* 5623-7300 ext 37889. karina_suarez@iim.unam.mx

ABSTRACT

A hydrogen charging station was designed and constructed. The station is used for characterizing the tanks constructed by the research group. The tanks were constructed on the basis of different hydrogen storage materials, thus several P-T conditions must be met. The station consists of inert gas and hydrogen pipes for hydrogen charging/ discharging; and, pressure, temperature and flow meters. The determination of the hydrogen storage/ release is based on the careful measurement of gas flow during programmed heating under a fixed initial pressure. The gas flow measures are translated to hydrogen release or storage in wt.% by means of real gas state equations and suitable mass balance. An analysis of heat-transfer outside the tank was performed for safe installation and operation. The station is solving a specific need of the research group: a reliable and low-cost equipment for the characterization of hydrogen storage tanks and it constitute the prototype for bigger hydrogen charging stations.

Acknowledgment: The present work was supported by the UNAM-DGAPA-PAPPIT IA100817 Estudio del comportamiento masivo de $NaAlH_4$ como material de almacenamiento de hidrógeno obtenido a partir de Al reciclado

Keywords: hydrogen storage, charging station, hydrogen tanks

XVIII International Congress
of the Mexican Hydrogen Society

Production of sustainable $NaAlH_4$ for hydrogen storage

Juan Rogelio Tena-García[1], Ricardo Guerrero-Ortíz[1], Karina Suárez-Alcántara[1,*]

[1] Unidad Morelia del Instituto de Investigaciones en Materiales de la Universidad Nacional Autónoma de México. Antigua Carretera a Pátzcuaro No. 8701, Col. Ex Hacienda de San José de la Huerta, C.P. 58190, Morelia, Michoacán, México.
* Corresponding author: (+52) 443 1477889, karina_suarez@iim.unam.mx

ABSTRACT

Currently, hydrogen is considered the most promising option to replace hydrocarbons as the main energy vector. However, an adequate storage system is necessary to extend the use of hydrogen. $NaAlH_4$ is prospected up to now as the best hydrogen storage material. Even more, as we prove, the $NaAlH_4$ could be produced in a sustainable way using recycled aluminum cans. Recycling residues such as Al-cans is a problem on developing countries like Mexico. Additionally, the purchasing of fine and high purity metal powders such as Ti, Al, Na or Mg, i.e. the precursors of hydrogen storage materials, is facing increasing restrictions and cost. Thus, the research group decided to deal both problems by using Al from cans as recycled material.
Aluminum cans at 10 wt.% stoichiometric excess, NaH and a catalyst (5 wt %) were milled together for a period of 15 hours. The samples were tested at 3 cycles of hydrogenation/dehydrogenation in a pressure range of 30-100 bar of hydrogen and at 100, 125 and 150 °C by means of PCT (Pressure-Composition-Temperature) isotherm. The milled and hydrogenated samples were characterized by Scanning Electron Microscopy (SEM) and X-Ray Diffraction (XRD). Fourier-transform infrared spectroscopy (FT-IR) was used for the hydrogenated samples. The produced material can store about 3.0 wt% (reversible). Thus we produce sustainable $NaAlH_4$.

Acknowledgment: The present work was supported by the UNAM-DGAPA-PAPPIT IA100817 Estudio del comportamiento masivo de $NaAlH_4$ como material de almacenamiento de hidrógeno obtenido a partir de Al reciclado

Keywords: Hydrogen storage; Recycled Al; Sodium alanate

XVIII International Congress
of the Mexican Hydrogen Society

Low-cost Sieverts machine for the study of hydriding/dehydriding reactions

K. Suarez-Alcantara[1*]

[1]Unidad Morelia del Instituto de Investigaciones en Materiales de la Universidad Nacional Autónoma de México. Antigua Carretera a Pátzcuaro No. 8701.Col. Ex Hacienda de San José de la Huerta C.P. 58190, Morelia, Michoacán, México

* * Corresponding author: E-mail: karina_suarez@iim.unam.mx

ABSTRACT

The design and construction of infrastructure for the study of hydriding/dehydriding reactions at different materials are presented. This is a Sieverts type machine where small amount (0.2-1 gram) of solid hydrogen storage materials can be characterized. The machine combines the features of double (sample and reference) branches, to eliminate small thermal effects on the reservoir volumes, with a $\Delta p=\Delta p_{sample}-\Delta p_{ref}$ approach, to eliminate the need of a differential pressure transducer and to reduce costs. This machine can work from -1 to 100 bar hydrogen pressure and up to 500°C. The collected data of pressures, temperature and volume are transformed by a real gases equation state and mass balance to hydrogen uptake or release in %wt. Characterization of typical hydrogen storage materials such as Mg was performed and presented to validate the good performance of the machine.

Acknowledgment: The present work was supported by the UNAM-DGAPA-PAPPIT IA100817 Estudio del comportamiento masivo de $NaAlH_4$ como material de almacenamiento de hidrógeno obtenido a partir de Al reciclado

Keywords: hydrogen storage, charging station, hydrogen tanks

XVIII International Congress
of the Mexican Hydrogen Society

Hydrogen adsorption depending of temperature on surface (110) of $Mg_{1-x}M_x$ alloys (M = Al, Ni, Zn; 0.0≤ x ≤ 0.10)

O. Ramírez-Rodríguez [1], G. Ramírez-Dámaso [1], F. Caballero [2], F. L. Castillo-Alvarado [3, 4], J. Roberge [1, 5], D. Romo–Rico[1] and A. Ortiz-Ubilla [1].

[1] Escuela Superior de Ingeniería y Arquitectura "Unidad Ticomán" del Instituto Politécnico Nacional, Av. Ticomán No. 600, Col. San José Ticomán, C. P. 07340, Del. Gustavo A. Madero, CDMX, México.
[2] Carrera de Ingeniería Química, Facultad de Estudios Superiores Zaragoza C. II UNAM, Batalla 5 de Mayo s/n, Col. Ejército de Oriente, C.P. 09320, Iztapalapa CDMX, México.
[3] Escuela Superior de Física y Matemáticas del Instituto Politécnico Nacional, Av. I. P. N. s/n, Unidad Profesional Adolfo López Mateos, Edificio 9, col. Lindavista, Del. Gustavo A. Madero, C. P. 07738, CDMX, México.
[4] Becario COFAA, EDD Instituto Politécnico Nacional.
5 Becaria COFAA, EDI Instituto Politécnico Nacional.
* Corresponding author: fitoram_omarod@live.com.mx

ABSTRACT

In this work, the adsorption energies for temperatures of 100, 300, 500 and 700 K, were compared with concentration of magnesium of 1.0, 0.98, 0.96, 0.94, 0.92 and 0.90 in magnesium-aluminum, magnesium-nickel and magnesium-zinc alloys respectively. Magnesium is one of the best metals to store hydrogen, with about 7.6 % in weight of H2. In order to compare our results with experimental results of pure magnesium, these temperatures were selected based on previous works which reported the range of adsorption and desorption temperatures for hydrogen on magnesium were between 300 and 500 K. The calculations were done with the Dmol3 module from the molecular simulation program Materials Studio.

Keywords (Maximum 4 words): Hydrogen adsorption, magnesium-aluminum alloy, magnesium-nickel alloy, magnesium-zinc alloy.

---

1. Introduction

The problem in using hydrogen as a fuel resource is its storage, because hydrogen is a diatomic gas with a very low density of 0.0899 Kg/m^3, at standard temperature and pressure (-273.15 K, 1 atm). This means that we can store about 90 g of H_2 in 1 m^3, therefore making it complicated to store in gaseous state, as it would require very large containers. So, the hydrogen

XVIII International Congress
of the Mexican Hydrogen Society

Hydrogen isotope separation in metal organic frameworks

C. Rodríguez-Castellanos[a,b*]; J. Toledo-Marín[c]; A. Valderrama-Zaldívar[c]; Y.Divó-Matos[b]

[a]Universidad de La Habana. San Lázaro y L. Vedado. La Habana 10400. Cuba.
[b]CICATA- Legaria. Instituto Politécnico Nacional. Legaria 664. Ciudad de México 10400. México
[2]Universidad Nacional Autónoma de México. Ciudad Universitaria. Ciudad de México 04510, México
* 52+5534388872; rodriguez.carlos1950@gmail.com

ABSTRACT

Separation of H_2, D_2 and T_2 from gaseous mixtures is important for many practical applications, but available separation technologies are expensive and energy consuming. The new methods of quantum sieving and quantum selective adsorption in nanoporous materials show a great potential. These techniques exploit mass differences through their influence on the de Broglie wavelength and the zero point oscillation energy of adsorbed molecules. Progress in quantum sieving has been modest, but recent contributions show high quantum selectivity during adsorption of H_2 and D_2 mixtures on MOFs with open metallic centers. Here a lattice model is proposed to describe the adsorption and diffusion of a H_2, and D_2 mixture in a nanoporous crystalline solid. The temperature dependent separation coefficient is calculated and its relation with the difference of adsorption enthalpies is derived. The contribution of different molecular degrees of freedom is discussed. The influence of pressure and weak adsorption sites is also studied. Atomistic simulations for MFU-4l – X (X= Cu, Ni, Fe, Co) give the necessary information to predict the separation coefficient. Isotopic exchange during adsorption is discussed with the aid of MC simulations of diffusion. Quantitative criteria for D_2/H_2, selectivity of a sorbent are given.

Keywords: Hydrogen isotope separation, MOF, adsorption, diffusion

XVIII International Congress
of the Mexican Hydrogen Society

Transition Phases in the Structure of Calcium Hydride

W. Ramírez-Carbellido[1], F. de L. Castillo-Alvarado[1], T. Ramírez-Rodríguez[1,*]

[1]Instituto Politécnico Nacional, Av. Luis Enrique Erro S/N, Unidad Profesional Adolfo López Mateos, Zacatenco, Delegación Gustavo A. Madero, C.P. 07738, Ciudad de México; México.
* Corresponding author: 044 (55) 4352 0891, teresa.ramirez7715@gmail.com

ABSTRACT

It is thought that hydrogen is a clean energy alternative for transportation applications in a stationary manner. Calcium hydride is a light metal hydride being among the promising materials for the storage of hydrogen. It requires a practical storage of hydrogen and there are still several technological challenges to be solved. It is important to have a database of the fundamental structures and properties of hydride materials as an aid to improve the design of materials for hydrogen storage. A detailed study of the structure and properties of calcium hydride that shows how these properties change with destabilization by characterizing the local bonding potentials associated with hydrogen is of great importance.
The vibratory properties of calcium hydride and its crystalline structure have been determined in the space groups Pnma, $P6_3mmc$ and P6mmm. The calculations of the electronic structure were made using the pseudopotential plane wave within the theory of the functioning of the density, as well as for the calculation of the vibratory modes in linear response, the vibrational modes to environmental conditions of the calcium hydride have been assigned for the calculations in the space group Pnma. The Materials Studio software has been used, the Generated Gradient Approach (GGA) has been used for the exchange correlation potential within the parametrization of Perdew Burke Ernzerhof (PBE), the rules conservation scheme has been used to generate the pseudopotentials for the calcium and hydrogen atoms.
The calculation of the phonons based on the optimized structure reproduces the density of calcium hydride states in the spatial groups Pnma, $P6_3mmc$ and P6mmm of reported works.

Keywords: calcium hydride; vibrational properties; first principles calculation

XVIII International Congress
of the Mexican Hydrogen Society

Biohydrogen production from acid hydrolizates of fruits-and-vegetables wastes and corn stover: effects of inoculum/substrate ratio and sugar concentration

Santiago Rodríguez-Valderrama[1], Jean-Pierre Magnin[2], Pasiano Rivas-García[1], Refugio Bernardo García-Reyes[1], Idania Valdez-Vázquez[3], Elvira Ríos-Leal[4], Carlos Escamilla-Alvarado[1,*]

[1] Universidad Autónoma de Nuevo León, Faculty of Chemical Sciences, Engineering and Sustainable Bioprocesses Group, Av. Universidad S/N Ciudad Universitaria, San Nicolás de los Garza, NL, 66455, México.
[2] Laboratory of Electrochemistry and Physico-chemistry of Materials and Interfaces, Martin d'Hères, France.
[3] Laboratory for Research on Advanced Processes for Water Treatment, Instituto de Ingeniería, Unidad Académica Juriquilla, Universidad Nacional Autónoma de México, México.
[4] Environmental Biotechnology and Renewable Energies R&D Group, Department of Biotechnology and Bioengineering, CINVESTAV-I.P.N. Mexico City, México
* Corresponding author: Tel: +521 55 27 31 6440. E-mail address: cea_escamilla@yahoo.com.mx

ABSTRACT

Biohydrogen can be produced from renewable sources such as fruits-and-vegetables wastes (FVW) and corn stover (CS) by bioprocess like dark fermentation. The aim of this work was to evaluate the effect of inoculum/substrate ratio and sugar concentration in biohydrogen production from acid hydrolizates.

The acid hydrolysis pretreatment was carried out with a general factorial experiment design 5X2. The factors were the combination of co-substrates (0:100, 25:75, 50:50, 75:25, 100:0, FVW:CS $\%_{dry\ base}$) and the acid catalyst (HCl and H_2SO_4, 0.5 % v/v). Reducing sugars, monomeric sugars and inhibitory compounds, such as 5-hydroxymethylfurfural, furfural and total phenolic compounds, were quantified. Afterwards, a 3^2 experimental design was developed for hydrogen production in serological bottles at 35 °C; the factors were the inoculum/substrate ratio (0.8, 1.0 and 1.2 g $SV_{inoculum}$ g $SV_{substrate}^{-1}$) and the initial concentration of reducing sugars (10, 13 and 16 g L^{-1}) respectively.

The effect of the acid catalyst and the combination of co-substrates was significant in terms of reducing sugars and conversion of sugars. The best catalyst acid was HCl for the ratio 75:25 FVW:CS. For such combination, the concentration of monomeric sugars was (g L^{-1}): 10.02, 3.67 and 2.93 for glucose, xylose and arabinose, respectively. The liquid hydrolysates thus obtained were pretreated to eliminate inhibitory compounds. The accumulated hydrogen production was observed through the modified Gompertz model: the maximum production of hydrogen was 8.08 mmol H_2 and the maximum rate of hydrogen production was 0.34 mmol H_2 h^{-1} for initial concentration of 13 g L^{-1} and inoculum/substrate ratio of 1.2. The metabolites produced were butyric acid, acetic acid, propionic acid and ethanol.

In conclusion, acid hydrolysis favored the production of fermentable sugars; moreover, an indirect relationship between the initial concentration of reducing sugars and the accumulated hydrogen production was established.

Keywords: dark fermentation, dilute acid hydrolysis, liming pretreatment.

September 18th to 21st, 2018 in Mexico City, Mexico.

XVIII International Congress
of the Mexican Hydrogen Society

Evaluation of Electrochemical Hydrogen Production Using Electrodeposited AISI/SAE 304 Stainless Steel Expanded Mesh under different conditions

Maria I. Jaramillo-Gutiérrez[1*], Carlos A. Ramírez-González[1]
Sonia M. Sierra-González[1], Julio E. Pedraza-Rosas[1], Julio A. Pedraza-Avella[1]

[1]Grupo de Investigaciones en Minerales, Biohidrometalurgia y Ambiente - GIMBA, Universidad Industrial de Santander - UIS, Sede Guatiguará, Transv. Guatiguará, Calle 8N No. 3W-60, Barrio El Refugio, C.P. 681011, Piedecuesta (Santander), Colombia
* Corresponding author: (+57) 317 5203921
maria.jaramillo@correo.uis.edu.co

ABSTRACT

Hydrogen is considered an attractive alternative to solve the current energy problem, because it can be obtained by clean processes taking water from the medium and separating it into its components, hydrogen and oxygen, through electrochemical processes. For this reason it is essential to search for materials with catalytic properties capable of reducing the overpotential of hydrogen production reactions and thus achieve an improvement in the performance of electrolytic processes.
In this work was evaluated the effect of the time, potential and concentration of Ni + 2 in the nickel electrodeposition on stainless steel meshes; which are used as a cathode in the electrolytic production of hydrogen. First of all, it was made an electrochemical characterization of the Watts bath system - stainless steel mesh, in which was identified the potential who had a pair reduction in the Ni^{+2} / Ni^{0} (0.70V vs Ag / AgCl). Afterwards, the electrodeposition process of nickel was evaluated under different experimental conditions, keeping constant the temperature, agitation and distance between electrodes conditions. After that it was made the microelectrolyte and macroelectrolyte evaluation for the production of hydrogen by electrolysis of water, in which an increase in the production of hydrogen was detected under the use of nickel-plated cathodes in comparison with uncoated cathodes. The highest hydrogen production was 507ppm and it was obtained using an electrodeposited specimen at 2.3 V for 20 min, with an intermediate concentration of Ni^{+2} in Watts electrolyte. Finally this test tube was characterized by electro-microscopy scanning and scattered energy spectroscopy hence was identified a thickness lining average of 46.92 µm and a nickel composition of 99.29%.

Keywords: Electrolysis; Hydrogen energy; Electrochemistry; Nickel

September 18th to 21st, 2018 in Mexico City, Mexico.

XVIII International Congress
of the Mexican Hydrogen Society

Kinetic study of biohydrogen production from cheese whey using *Klebsiella pneumoniae*

B.L. Gamero Enríquez[1], R.M. Soto Meraz[1], A.M. López Rodríguez[1], R.H. Lara[1], D.M. Nuñez Ramírez[1], O. La llave Leon[2], S.V. Reyes Aguilera[1], C.M. Pérez Carranza[1], M.A. Escobedo Bretado[1,*]

[1]Facultad de Ciencias Químicas, Universidad Juárez del Estado de Durango, Av. Veterinaria s/n, Circuito Universitario, Durango, Dgo., 34120 México.
[2]Instituto de Investigación Científica, Universidad Juárez del Estado de Durango, Avenida Universidad esq. con Volantín. Zona centro, Durango, Dgo., 34000 México.
* M.A. Escobedo Bretado: phone number: +52 618 1301120, e-mail: miguel.escobedo@ujed.mx

---

ABSTRACT

Dark fermentation is a promising approach to produce hydrogen (H_2) from industrial waste. Microbial consortia are commonly used to evaluate fermentation. Establishing operating parameters is fundamental for achieving the theoretical values of gas production. However, the contribution of each hydrogen-producing strains integrating the consortium is usually unknow, making difficult to get the optimal biohydrogen production. Our goal was to analyze the growth kinetics of the previously reported hydrogen-producing bacteria *Klebsiella pneumoniae,* using as a substrate the cheese whey raw locally produced at the dairy industry (Regalet from Durango, Mexico), evaluating the composition of biogas generated. Once *K. pneumoniae* was isolated and identified by conventional biochemical tests and PCR analysis of 16S-23S internal transcribed spacer; fermentation was performed using a mechanically-stirred 1 L reactor (Aplikon). Cell growth was monitored by measuring the OD 645 using a UV-VIS spectrophotometer (DR5000; Hach Company, USA), while biogas produced was monitored through the Agilent 7820A Gas Chromatograph. After 7 h of fermentation we got the higher biogas volume. 40.6% H_2 with 29.9% CO_2 without methane formation was obtained with the following conditions: rpm = 200, pH = 5.5, T = 37°C, Vol. = 0.4 L, organic load = 2 g lactose, atm = N_2 in a batch system. The highest hydrogen ratio was 0.42 mol H_2/mol lactose. *K. pneumoniae* as an excellent candidate for biohydrogen production and our results can be used to scale up bioprocess optimizing condition and operation factors to get highest rate production.

Keywords: cheese whey; *K. pneumoniae*; biohydrogen

XVIII International Congress
of the Mexican Hydrogen Society

Production of Hydrogen by Pt-Pd/γ-Al_2O_3-Nd_2O_3 bimetallic catalysts.

M. Caballero-Díaz[a, *]; G. del Ángel Montes[a]; V. Tostado-Ramirez[a]

[a] Universidad Autónoma Metropolitana-Unidad Iztapalapa, Departamento de Química, Área de Catálisis, Av. San Rafael Atlixco No. 186, C.P. 09340, A.P 55-534. México D. F. México.
* Corresponding author: 55-20032433 and e-mail: marcabdi@yahoo.com.mx

ABSTRACT

Hydrogen can be used for energy purposes, or used as a chemical reagent in industrial processes. The quantify of energy produced during the combustion of hydrogen is higher than that obtained by any other fuel. The advantages of hydrogen as an energy source is that it represents an abundant raw material and the combustion doesn't produce CO_2, only water vapor, which is the ideal candidate for the reduction of the "greenhouse effect".

Three Pd-Pt catalysts supported on γ-Al2O3 and γ-Al2O3-Nd2O3 at 1 and 10% by weight were synthesized, was made using the support in the ball flask with a small amount of water while making a solution of the precursor salt ($H_2PtCl_6 \cdot 6\ H_2O$ and $PdCl_2$) for a content of 1% of the metals, dissolved in the minimum amount of water and this is added in the same flask where the support is and it is left stirring for 3 hours in the rotary evaporator, and it is evaporated using a water bath at 60 ° C; the solids are dried in an oven at 120 ° C for 12 hours, then calcined at 500 ° C with air flow at 60 mL / min for 5 hours and finally the catalysts are reduced in a flow of 60 mL/min. H_2 at 500 ° C for 5 hours.

The decomposition reaction of methane is carried out in a batch or intermittent flow system in a temperature range of 400 to 750 ° C with a previous activation with nitrogen (30 mL/min at 200 ° C) and the flow of the Reagent (methane) will be 2 mL/min. To accomplish this an electric furnace with a tubular reactor made of quartz with a porous plate inside will be used to hold the catalyst (50 mg).

The product from the reaction will be analyzed by gas chromatography, for detecting output gases from the reactor, which will prove that hydrogen is actually being produced.

Hydrogen was obtained from the decomposition of methane.

It was determined that the best catalyst for the production of hydrogen is Pt-Pd Y-alumina (without neodymium).

Keywords: hydrogen, chromatography, synthesis, methane.

XVIII International Congress
of the Mexican Hydrogen Society

Production of hydrogen, from the decomposition of methane over Pd catalysts supported on alumina doped with neodymium.

M. Caballero Diaz[a,*]; G. del Ángel Montes[a].

[a] Universidad Autónoma Metropolitana-Unidad Iztapalapa, Departamento de Química, Área de Catálisis, Av. San Rafael Atlixco No. 186, C.P. 09340, A.P 55-534. México D. F. México.
* Corresponding author: 55-20032433 and e-mail: marcabdi@yahoo.com.mx

ABSTRACT

In this work we study the effect of the addition of neodymium on Pd-containing catalysts in the dehydrogenation reaction of CH_4 at temperatures between 400 and 750 ° C in a fixed bed reactor. The γ-Al_2O_3 and γ-Al_2O_3 doped supports with 1 and 10% by weight neodymium were synthesized. Once the supports were prepared, the Pd/γ-Al_2O_3 and Pd/γ-Al_2O_3-Nd catalysts were obtained by wet impregnation method. The catalysts were characterized by BET areas, X-Ray Diffraction, Infrared Fourier Tranform (FTIR) of pyridine adsorption and TEM microscopy.
For the analysis of the reaction products, a gas chromatograph Shimadzu GC-2014 was used. Experiments were conducted using a quartz tubular reactor, electric oven, a type K thermocouple and a mass of 0.05 g of catalyst was employed, γ-Al_2O_3 support was prepared from Boehmita Catapal B. Firstly the Boehmite was dried to 120° C for 12 hours, then the solid was calcined in air flow of 60 mL/min for 24 h using a ramp of temperature from 25°C to 650°C. The γ-Al_2O_3-Nd_2O_3 (loaded with 1 and 10 wt% neodymium) mixed oxides, were prepared by wet impregnation of the Boehmite with the necessary quantity of $Nd(NO_3)_3 \cdot 6H_2O$, the mixture was maintained in stirring for 3h. Then, the solids were dried in an oven to 120°C for 12 h, after that, samples were calcined at 650°C in airflow for 24 h. The catalysts Pd/γ-alumina and Pd/γ-alumina-Nd al (1 and 10%) were impregnated with solution of $PdCl_2$ at a pH of approximately 1, with the appropriate amount for obtain 1% by weight of Pd in each catalyst.
The catalysts showed high activity and hydrogen production at 750°C, with conversions around 63-80 %vol and hydrogen production over 33,100, 32,900, 22,800 ppm for PdANd1, PdANd10 and PdA catalyst respectively. It is remarkable that a possible electronic interaction between Pd and Nd could be controlling the activity and selectivity, which could explain this results.
The best catalyst was the Pd/γ-Al_2O_3Nd1, since at 63% conversions at 750 °C, it had the highest hydrogen production, followed by the catalyst Pd/γ-Al_2O_3Nd10, since it had the same production of hydrogen but less selectivity to this.

Keywords: palladium; RDX; hydrogen; pyridine

XVIII International Congress
of the Mexican Hydrogen Society

Ruthenium catalysts supported on γ-Al_2O_3 from different precursors for the Hydrogen production.

M. Caballero Diaz[*1]; G. Alicia del Ángel Montes[2]; R. Mendoza Serna[1]; A. J. Chong Santiago[1]

[1] Facultad de Estudios Superiores Zaragoza, UNAM, Carrera de Ingenieria Quimica, Batallón 5 Mayo s/n esq. Prol. Plutarco Elías Calles, Col. Ejercito de Oriente, Ciudad de México, C.P. 09230.
[2] Universidad Autónoma Metropolitana-Unidad Iztapalapa, Departamento de Química, Área de Catálisis, Av. San Rafael Atlixco No. 186, C.P. 09340, A.P 55-534. México D. F. México.
(*) corresponding author: marcabdi@yahoo.com.mx

ABSTRACT

The Preparation of γ-Al_2O_3 from Boehmite catapal B, Alumina (Merck) and Aluminum Secbutoxide, the precursor was placed in a crucible and dried for 12 hours at 120 ° C with a ramp of 2 ° C/min, then were calcined at 650 °C in air flow of 60 mL/min for 24 hours, using a heating ramp with a speed of 2 °C/min, after calcination, the system was cooled to room temperature with air flow. Wet Impregnation Method for the preparation of Ru/γ-Al_2O_3, the support is placed in a ball flask with a small amount of water, while the amount of $RuCl_3.3H_2O$ required for a content of 1% by weight is dissolved in the minimum amount of water, this solution is added to that of the support and left in agitation for 3 hours in a rotavapor at 30 rpm, the water is evaporated using a water bath at 60 ° C and a vacuum of 0.072 bar, later the solids are dried in an oven at 120 °C, for 12 hours. The catalyst is introduced in a quartz reactor with a fixed bed to be calcined at 500 °C in an air flow of 60 mL/min for 5 hours, using a heating ramp with a speed of 2 °C/ min; starting from the ambient temperature at 120 °C, keeping it there for 1 hour, when this time passes, the temperature increases to 500 °C, a temperature that is maintained for 5 hours. Finally, the catalysts were reduced in H_2 flux of 60 mL/min at 500 °C for 5 hours, at a heating rate of 2 °C/min. Reaction by catalytic decomposition of methane: 50 mg of catalyst was deposited in a U-type quartz reactor, inerted with 30 ml/min of N_2 for 15 min at 200 ° C. 2 ml/min of CH_4 were passed at 400 °C, 500 °C, 600 °C, 700 °C and 750 °C per 6 min. The catalyst by Boehmite Catapal B and Alumina (Merck) obtained the highest production of H_2 at 700 ° C, as well as the highest conversion of CH_4, while the catalyst by Aluminum Secbutoxide obtained an almost constant H_2 production between 500 ° C and 700 ° C, as well as its conversion of CH_4.
The catalyst by Boehmite Catapla B obtained the highest production of H_2 at 700 ° C compared to the other two, although the catalyst by Aluminum Secbutoxide obtained the best H_2 productions at different temperatures.

Keywords: boehmite; Secbutoxide; Alumina.

XVIII International Congress
of the Mexican Hydrogen Society

Synthesis of WO_3 nanoparticles included in TiO_2, surface modification with metallic nanoparticles; photoelectrochemical study and its role in the photocatalytic hydrogen production

David Ramírez-Ortega[1], Diana Guerrero-Araque[1], Próspero Acevedo-Peña[2], Juan Carlos Duran-Alvarez[1], Rodolfo Zanella[1,*]

[1]Instituto de Ciencias Aplicadas y Tecnología, Universidad Nacional Autónoma de México, Circuito Exterior S/N, Ciudad Universitaria, P.O. Box 70–186, Coyoacán, 04510, Mexico City, Mexico
[2]CONACyT-Centro de Investigación en Ciencia Aplicada y Tecnología Avanzada-Unidad Legaria, IPN, 11500 Mexico City, Mexico
* Corresponding author: Rodolfo Zanella, Tel: +52 55 56228601, e–mail: rodolfo.zanella@ccadet.unam.mx

ABSTRACT

WO_3 and TiO_2 have been investigated perhaps more thoroughly than any other metal oxide. Semiconductors with narrow band gap such as WO_3 are able to absorb visible light and effectively overcome disadvantages of single-semiconductor photocatalysts in the aspect of low use rate of solar power. In this way, composite nanoparticles were synthesized with WO_3/TiO_2 using a sol-gel method, in order to form inclusion nano-WO_3 with TiO_2 nanoparticles and improve the separation of photogenerated charge carriers. These (e^--h^+) play key roles in the reduction and oxidation process in photocatalytic hydrogen production; however, even if the (e^--h^+) are separated, the reaction cannot happen without proper active sites. So, co-catalysts are needed to improve the reduction and oxidation process on the surface of a photocatalyst.

WO_3/TiO_2 composites with surface modification with metallic nanoparticles (co-catalyst) were characterized by X-ray diffraction (XRD), scanning electron microscopy/energy dispersive spectroscopy (SEM/EDS), transmission electron microscopy (TEM) and cyclic voltammetry (CV). Their photoelectrochemical properties were characterized by open circuit potential (OCP) measurements and electrochemical impedance spectroscopy (EIS). The modification with nanoparticles of Cu, Au and Pd improve the photocatalytic hydrogen production, obtained the best photocatalyst with WO_3/TiO_2/Pd explained with the electrochemical and photoelectrochemical tests.

Keywords:; sol-gel method; co-catalyst; photocatalysis; photo/electrochemistry

September 18th to 21st, 2018 in Mexico City, Mexico.

XVIII International Congress
of the Mexican Hydrogen Society

The rol of metallic nanoparticles (Au, Ag) on ZnO-TiO_2 structure in the photocatalytic hydrogen production

David Ramírez-Ortega[1], Diana Guerrero-Araque[1], Prospero Acevedo-Peña[2], Juan Carlos Durán-Álvarez[1], Rodolfo Zanella[1]*

[1]Instituto de Ciencias Aplicadas y Tecnología, Universidad Nacional Autónoma de México, Circuito Exterior S/N, Ciudad Universitaria, P.O. Box 70–186, Coyoacán, 04510, Mexico City, Mexico
[2]CONACyT-Centro de Investigación en Ciencia Aplicada y Tecnología Avanzada-Unidad Legaria, IPN, 11500 Mexico City, Mexico
* Corresponding author: Rodolfo Zanella, Tel: +52 55 56228601, e–mail: rodolfo.zanella@ccadet.unam.mx

ABSTRACT

The production of clean and renewable hydrogen through photocatalytic hydrogen production has received much attention due to the increasing global energy demand. TiO_2 is the most widely used due to its low toxicity, high resistance photocorrosion and low cost. However, this semiconductor has some limitations due to the high recombination rate of photogenerated electron-hole pairs. Therefore, to improve its photocatalytic activity, TiO_2 have been coupled with other semiconductors for to promote the electron-hole pair separation or it have been supported metal nanoparticles, such as Ag or Au that acts as cocatalysts.

In this work, Ag/ZnO-TiO_2 and Au/ZnO-TiO_2 materials were synthesized with different of metal content. Initially, ZnO-TiO_2 mixed oxide (6 mol % of ZnO) was obtained by means of sol-gel method. Later, silver and gold nanoparticles were deposited on ZnO-TiO_2 employing deposition-precipitation method. These materials were evaluated in the photocatalytic hydrogen production and the charge transfer processes were studied. The optimal silver and gold content were 2 and 3 wt%, respectively. The results shows that the Au nanoparticles have the best activity associated to that these acts as electron tramps and are more efficient in the electron transference.

Keywords: Photocatalytic hydrogen production; metallic nanoparticles; charge transfer process; electron traps.

XVIII International Congress
of the Mexican Hydrogen Society

Composite materials (MOFs @ graphene oxide) for hydrogen storage.

N Torres-Figueredo[1,2,*]; J. A. Galicia-Apolinar[1]; L. F. Desdín-García[2], E. Reguera[1].

[1] Centro de Investigación en Ciencia Aplicada y Tecnología Avanzada, Unidad-Legaria. Legaria No. 694 Col. Irrigación, Del. Miguel Hidalgo, C.P. 11500, Ciudad de México, México.
[2]Centro de Aplicaciones Tecnológicas y Desarrollo Nuclear (CEADEN). Calle 30 y 5ta Ave. Miramar, C.P 11300, La Habana, Cuba.
* Corresponding author: +52-1-5529074048, neiltorres84@yahoo.es

ABSTRACT

The search for materials with structural characteristics that allow for proper adsorption for either greenhouse gases (CO_2, CH_4), or energy carrier gases (H_2) is nowadays one of the main research lines in the scientific community. This contribution reports the synthesis, evaluation and characterization of Fe-BTC @ graphene oxide composite for hydrogen storage.
The Fe-BTC lattice shows promising features to achieve the stated objective, they present large surface area for the capture and storage of gases in order of 500 - 1500 m^2/g, also the structures having a pore volume accessible between 25 and 45 % of the total volume. Another important feature is its high chemical and thermal stability. The graphene oxide (GO) by its characteristics has been candidates for gas adsorption studies. The GO employed is purchased from Sigma Aldrich. Fe-BTC @ graphene oxide composite was obtained by solvothermal synthesis.
The composite obtained with combination of these structures not present an increase expected in surface area, achieving the increase pore size and decreased the micropore volume, but the most interesting feature is the strong interactions with hydrogen. Furthermore, the structure of MOF was not disturbed by graphene oxide incorporation. The aim of this work is the exploration of the possible synergy between MOFs and GO. Therefore, this study included: a) Obtaining by solvothermal synthesis a composite material, b) obtaining information on the adsorbate-adsorbent interactions, and c) determining the maximum adsorption capacity for considered gas.

Keywords: Hydrogen storage; Fe-BTC; MOFs composite; graphene oxide

XVIII International Congress
of the Mexican Hydrogen Society

Bulk Nanostructured Magnesium Alloys for Hydrogen Storage: Preliminary Experiments

J. G. Cabañas Moreno[1*], R. Hernández Jiménez[2], O. Hernández Silva[1], C. Casas Quesada[3], J.M. Cabrera[3], A. Tejeda Ochoa[4,5], J. M. Herrera-Ramírez[4], F. Cruz-Gandarilla[6], Y. Todaka[5]

[1]CINVESTAV-IPN, Programa de Nanociencias y Nanotecnología, Cd de México, México
[2]ESIQIE-IPN, Depto. de Ing. Metalúrgica y de Materiales, Cd de México, México
[3]Departamento de Ciencia de Materiales e Ingeniería Metalúrgica, Universitat Politècnica de Catalunya, Barcelona, España
[4]CIMAV, Chihuahua, Chihuahua
[5]Toyohashi University of Technology, Toyohashi, Japan
[6]ESFM-IPN, Cd. de México, México
* Corresponding author: 55-57473800 ext. 6785, jcabanasm@cinvestav.mx

---

ABSTRACT

Hydrogen storage in the form of MgH_2 has several potential advantages, including high gravimetric and volumetric densities, as well as wide availability and nontoxic nature of magnesium, and complete reversibility of the corresponding hydriding reaction. In addition, for many years it has been known that nanostructured powders and nanoparticles display considerable improved hydriding and dehydriding kinetics. However, the performance of the Mg-MgH_2 system may degrade rapidly because of unwanted reactions with water vapor, oxygen and carbon dioxide, particularly when the materials are used as fine and/or nanostructured powders. In the present work, we aim to avoid the high surface area exposed by fine powders without relinquishing the advantages imparted by nanostructuring, with the fabrication of bulk nanostructured Mg alloys of a composition optimized for hydrogen storage. In this way, Mg alloys containing Ni, Nb_2O_5 and multiwalled carbon nanotubes have been processed by severe plastic deformation in order to fabricate bulk nanostructured Mg alloys. The hydrogen storage properties of the bulk alloys have been compared to those of milled mixtures of the same composition. The preliminary results of these experiments seem to indicate that the bulk nanostructured alloys do show better characteristics as hydrogen storage materials, but after a number of cycles we observe in them a tendency to lose their integrity and become pulverized. A strategy to include a certain amount of porosity is being implemented as a means to lower the effects of volume changes on the consolidation of the bulk nanostructured alloys.

Keywords: hydrogen storage, magnesium hydride, nanostructured Mg alloys, hydriding kinetics

XVIII International Congress
of the Mexican Hydrogen Society

Flexible solar cells coupled to aeration system for a photobioreactor hydrogen generator

Hernández Hernández M.-[1], Cortés Luqueño R. I. [1], Gómez Alvarado R. R. [1] Cortés Escobedo C. A. [1], López Hernández, J. A.[1]

[1] Instituto Politécnico Nacional, CIITEC
* rafa_kingston@hotmail.com, phone number: +5217751212555
* godofwar438@gmail.com, phone number: +525513558837

ABSTRACT

In this work design, and structural and electronic construction of solar cells system used to start an aeration pump for a photobioreactor hydrogen generation is presented, in such a way that the orientation of cells is appropriate to the position of the sun and efficiently provides the current and voltage demanded by the pump.

The use of solar cells, allows the assurance of the use of clean energies, being this solar energy, properly said, so that, the complete photobioreactor system has the capacity to be self-sustaining in energy terms. With the importance of the proper position, developing a brief study of the site for the placement of this system, power supply, in such a way that could take full advantage of solar energy during the day was made.

The objective of this project is to provide technological improvements and energy use to a photobioreactor for the final production of hydrogen as an energy source. The position, efficiency and durability of the cells are studied, in such a way that the results favor the production of hydrogen through microalgae.

The design of the base structure for the solar cells started from the geometry of the same; for the control stage, the electrical characteristics of the cells were contemplated, allowing considering the adequate electrical and electronic materials for a higher performance, such obtaining sufficient voltage and current for the fulfillment of the main objective. An improvement in efficiency of the voltage generated was achieved by modifying an integrated circuit in its external components. As a final result, the control of the electric power generating system was obtained, capable of satisfying the needs of the photobioreactor.

Keywords: solar cells, photobioreactor, control.

September 18th to 21st, 2018 in Mexico City, Mexico.

XVIII International Congress
of the Mexican Hydrogen Society

A closer look at how a TiFe hydride doped with ZrV_2 is affected globally by its primary and secondary phase behavior.

E. Ulate-Kolitsky[1*], P. Lv[2], J. Cubero-Sesín[1*], J. Huot[2].

[1] Centro de Investigación y Extensión en Materiales, Escuela de Ciencia e Ingeniería de los Materiales, Instituto Tecnológico de Costa Rica, Cartago, 159-7050, Costa Rica
[2] Hydrogen Research Institute, Université du Québec à Trois-Rivières, 3351 des Forges, Trois-Rivières, Québec G9A 5H7, Canada
*(+506)8343 9100, elenaulatekolitsky@gmail.com, (506)25502704, jcubero@itcr.ac.cr

---

ABSTRACT

The improvement of first hydrogenation kinetics is one of the main focuses when studying TiFe hydrides. Doping with transitional metals and rare-earth metals has proven to be a good option to improve this property. Morphologically, the addition of these elements to TiFe alloy enables the formation of a two-phase system. The differences in the behavior of the doped alloy are a response to the nature of the doping element and the phases formed within the alloy. The information each phase has to offer could be a great way to understand and redesign the way doping elements are selected and how two phase systems could eventually perform together.

For TiFe+12wt.% ZrV_2 the presence of the secondary phase greatly improves the kinetics; however, the reversibility is negatively affected by the same reason. Therefore, the focus of the study was to synthesize both a primary phase-like alloy and a secondary phase-like alloy. The primary phase was assumed to have a similar capacity to TiFe. Surprisingly, this was not the case. Although Zr and V were present in very small fractions, their influence was significant. The secondary phase presented a higher capacity than expected and was not able to desorb at RT. X-Ray diffraction showed that stable hydrides formed during activation.

The results for each phase show that for this two-phase system (50-50 vol.%) each phase contributed to half of the hydrogen capacity, and the secondary phase does not activate completely which allows the alloy to desorb at RT. In conclusion, this study demonstrates how H capacity and activation kinetics are specifically affected by each component's properties and to what extent the components characteristics alter when they work together.

Keywords: TiFe alloy, Doping, Hydrogenation properties, Hydrogen storage.

XVIII International Congress
of the Mexican Hydrogen Society

Parameters analysis for hydrogen continuous production control by aluminum corrosion in aqueous acid solution.

Erick Arellano Domínguez[1*], Ana Lidia Martínez Salazar[1], Pedro Martín García Vite[1], Marco Antonio Coronel García[1].

[1]Centro de Investigación en Petroquímica (ITCM Campus 3), Prol. Bahía del Aldair, Av. de las Bahías, Parque Industrial Tecnia, Altamira, Tamaulipas, México
* Corresponding author: Tel.: +52 (833) 1090128; E-mail: erick.ad.14@gmail.com.

ABSTRACT

Throughout the last decades several studies have been made about in situ hydrogen production by the corrosion of aluminum in aqueous solution to supply PEM fuel cell systems in transport systems. However, main issue is that processes have been developed as batch type systems in which hydrogen production is limited to a short period of time. Another crucial point has been the use of alkaline aqueous systems using sodium or potassium hydroxides as the main corrosion medium which usually have low hydrogen production rates, as well as aluminum surface could be passivated easily by metal sub products by $Al(OH)_3$ which inhibit the hydrogen evolution. This research presents specific analysis of real variables involved to generate a continuous hydrogen production rate by aluminum alloys reaction in an aqueous acid solution, using sodium molybdate as a promoter. To obtain continuous hydrogen production, different parameters that affect the hydrogen evolution reaction were analyzed and evaluated, controlling initial temperature at 75 °C, and acid aqueous solution pH at 2. Aluminum alloy composition (Al/Si and Al/Mn), amount of aluminum (1 to 5 g) and promoter per gram of aluminum were varied according to hydrogen production rate demanded. The results obtained through this analysis were favorable for demand requested by a 100W PEM fuel cell stack. Achievement of requested flow hydrogen with desired continuous production makes it a promising alternative system to be use in higher demand equipment. This could be the first step of hydrogen production in situ technology for electric vehicles based on hydrogen fuel.

Keywords: Hydrogen; generator; fuel cell; aluminum corrosion

XVIII International Congress
of the Mexican Hydrogen Society

Coal Gasification Obtained from the Pyrolysis of *Quercus* Pellets to Produce Hydrogen with CO_2 Capture

V.D. Nuñez Retana[1], A. Carrillo Parra[1], R.H. Lara[3], V. Collins Martínez[2], A. López Ortiz[2], S.V. Reyes Aguilera[3], M.A. Escobedo Bretado[3,*]

[1]Instituto de Silvicultura e Industria de la Madera, Universidad Juárez del Estado de Durango, Av. Veterinaria s/n, Circuito Universitario, Durango, Dgo., México, 34120.
[2]Departamento de Ingeniería y Química de Materiales, Centro de Investigación en Materiales Avanzados, S.C., Miguel de Cervantes 120, Chihuahua, Chih., México, 31136.
[3]Facultad de Ciencias Químicas, Universidad Juárez del Estado de Durango, Av. Veterinaria s/n, Circuito Universitario, Durango, Dgo., México, 34120.
* M.A. Escobedo Bretado: phone number: +52 618 1301120, e-mail: miguel.escobedo@ujed.mx

ABSTRACT

The objective of this research was to study the gasification of coal obtained by pyrolysis of pellets of the *Quercus* species for the production of hydrogen under the absorption enhanced steam reforming (AESR) concept using calcined dolomite (CaO*MgO) as CO_2 absorbent. Operating conditions of the pyrolysis were studied by themogravimetry (TGA) using heating rates of 5, 10, 15 and 20 °C/min, a particle size of 150 ≥ dp ≥ 425 µm and a N_2 flowrate of 50, 100 and 150 cm^3/min. Coal gasification was studied in a steel reactor fed with vaporized water by means of a syringe pump. To evaluate the AESR system a NiO/Al_2O_3 catalyst was synthesized by the impregnation technique, while dolomite was calcined at 900 °C for 4h, finally the materials were characterized by XRD, SEM and BET surface area. Results of pyrolysis indicate that at 400 °C a maximum condensable volatile matter of 54% W can be obtained along with 43.4% W of solid carbon, while only 2.6% W of ash was produced. The reduced catalyst resulted in Ni/Al_2O_3 crystalline phases with 125 m^2/g of surface area. Whereas, Dolomite ($CaCO_3$*$MgCO_3$) calcination produced only the CaO*MgO crystalline phase along with 8.5 m^2/g of surface area. The thermodynamic analysis of the AESR system with a carbon feedstock obtained from the pyrolysis in a steam/carbon/CaO*MgO feed molar ratio = 6/1/2 indicates that it is possible to reach the maximum gas concentration of 97.6% H_2 at a temperature of 600 °C free from carbon oxides. Finally, experimental results of this system under a flowrate of 100 cm^3/ min of N_2 at a temperature of 600 °C, allow to achieve a maximum gas concentration of 80% H_2, 10% CO and 10% CO_2 on a dry basis. These results show the great potential of the use of *Quercus* biomass towards the production of H_2 under the AESR scheme.

Keywords: Biomass gasification; *Quercus sp*; hydrogen; CO_2 capture

XVIII International Congress
of the Mexican Hydrogen Society

Characterization and Analysis of an Alkaline Reactor and Photovoltaic Panel for Hydrogen Production.

J. A. Melo-Máximo[1*], R. G. Gonzáles-Huerta[2].

[1]Universidad Politécnica de Cuautitlán Izcalli, CP. 54760, Edo de Mex.
[2]Instituto Politécnica Nacional ESIQIE, Laboratorio de Electroquímica y Corrosión, UPALM, CP. 07738, CDMX.
*jorgemelomaximo@hotmail.com

ABSTRACT

Limited Fossil fuels reserves are expected that in 2030 we have been consumed more than 80% of the natural resource of petroleum. In another hand, the pollution by the greenhouse effect is growing, and the researchers are looking for new clean and renewable alternatives. Consequently, hydrogen generation offers the possibility of reducing the negative impact generated with the use of fossil fuels expelled to the environment.
Hydrogen production electrolysis has two principal generation ways, alkaline electrolysis (AE) and PEM electrolysis. Electrolysis provide a sustainable solution to produce hydrogen, and is well suited to couple with energy sources such as wind, sun and ocean. Alkaline electrolysis is the technology used in the project, because of it is mature development, easy manipulation and the less cost. But due to low demand in electrolytic hydrogen in the last decade, little research has been done on AE with many challenges still unexplored.
The alkaline electrolysis system is composed by a stack of 24 stainless steel electrodes that are in contact with a 5% w NaOH solution. Electrolyzer performance was made in test module. Polarization curves and efficiency were obtained, we used 20 different arrangement. The electrodes were connected in series-parallel (two negative poles, the first one was fixed and the second one had changed of positions; positive pole was fixed too) each arrangement was operating from 1 A to 50 A.
The arrangement (1,13-24) showed the best performance when it was integrated with the solar panel (270 W). The system generated 0.5 SL/min of H_2 with just 35 V-15 A, in this point the potential of the photovoltaic panel was enough to power the reactor.
The obtained results attended the necessary parameter of operation for the equipment, and ensure that is viable have a photovoltaic system to power the electrolyzer. These results support the use of renewable energies to decrease the usage of fossil fuels.

Keywords: Electrolysis; Hydrogen Cell; Electrolyte; Stainless Steel Electrode.

September 18 to 21, 2018 in Mexico City, Mexico

XVIII International Congress
of the Mexican Hydrogen Society

Tropical Woody Biomass Pyrolysis to Obtain Bio-Oil and Experimental Hydrogen Production with CO_2 capture

J.D. García Quezada[1], A. Carrillo Parra[1], R.H. Lara[3], D.M. Nuñez Ramírez[3], V. Collins Martínez[2], A. López Ortiz[2], S.V. Reyes Aguilera[3], M.A. Escobedo Bretado[3,*]

[1]Instituto de Silvicultura e Industria de la Madera, Universidad Juárez del Estado de Durango, Av. Veterinaria s/n, Circuito Universitario, Durango, Dgo., México, 34120.
[2]Departamento de Ingeniería y Química de Materiales, Centro de Investigación en Materiales Avanzados, S.C., Miguel de Cervantes 120, Chihuahua, Chih., México, 31136.
[3]Facultad de Ciencias Químicas, Universidad Juárez del Estado de Durango, Av. Veterinaria s/n, Circuito Universitario, Durango, Dgo., México, 34120.
* M.A. Escobedo Bretado: phone number: +52 618 1301120, e-mail: miguel.escobedo@ujed.mx

---

ABSTRACT

The objective of the present research is to determine the pyrolysis performance of tropical wood biomass to obtain bio-oil, identify the compounds present in this and experimentally evaluate the production of hydrogen under the absorption enhanced steam reforming (AESR) concept using a bio-oil/steam gaseous mixture and solid sodium zirconate (Na_2ZrO_3) as a CO_2 absorbent. Operating conditions of the pyrolysis were studied by thermogravimetric analysis (TGA) employing heating rates of 5, 10, 15 and 20 ° C/ min, a particle size of 150 ≥ dp ≥ 425 µm and a N_2 flowrate of 50, 100 and 150 cm^3/min. The bio-oil was obtained in a tubular steel reactor and the identification of compounds was achieved by GC/MS. Hydrogen production evaluation used a NiO/Al_2O_3 catalyst prepared by incipient impregnation, while the Na_2ZrO_3 was synthesized by the solid state method, finally the materials were characterized by XRD, SEM and BET surface area. TGA results for 10 wood species present moisture content between 1.9-4.4 wt%, volatile matter 56.8-67.9 wt%, fixed carbon 26.5-36.5 wt% and ash content 2.5-3 wt%. Pyrolysis results from the steel reactor indicate that at 400 °C a maximum of 45% W of condensable volatile matter (CVM) and 55% W of solid carbon can be obtained. The synthesized and reduced catalyst present Ni/Al_2O_3 crystalline phases with 125 m^2/g of surface area, while the CO_2 absorbent showed only the Na_2ZrO_3 phase along with 1.8 m^2/g of surface area. Results of H_2 production using a bio-oil/steam/Na_2ZrO_3 feed molar ratio of 1/6/6, a temperature of 600 °C and flowrate of 100 cm^3/min of N_2 indicate that it is possible to reach a maximum dry-gas composition of 80% of H_2, 10% CO, 5% CO_2 and 5% CH_4. These results show the great potential of tropical wood bio-oil from Mexico for the production of hydrogen.

Keywords: Bio-oil; tropical wood; hydrogen; CO_2 capture

XVIII International Congress
of the Mexican Hydrogen Society

Hydrogen production by α-cellulose gasification over hydroxyapatite supported Nickel-Molybdenum carbide catalysts

Jonathan Jesús Malpica Malpica[1], José Aaron Melo Banda[1], Ana Lidia Martínez Salazar[1] Margarita García Hernández[1].

[1] Centro de Investigación en Petroquímica, Instituto Tecnológico de Ciudad Madero, Prol. Bahía del Aldair, Av. de las Bahías. Parque Industrial Tecnia, Altamira, Tamaulipas, México, 89608.
*833-261-13-32, jonathan-jesus15@hotmail.com

ABSTRACT

Catalytic gasification of cellulose was studied using supported catalysts of molybdenum carbide doped with nickel over hydroxyapatite as a support. Several works Suggest that molybdenum carbide has catalytic properties similar to those noble metals in some reactions, making it an attractive catalyst to gasification reaction. Moreover, molybdenum carbide has excellent mechanical and thermal stability.

In this research we show the hydrogen production in a fluidized-bed reactor at two different reaction temperatures (1073.15 K and 1173.15 K). Also, the load of nickel varies from 0 to 25 wt%. The composition of gases produced by the reaction was analyzed with chromatographic gas.

The synthesis of Ni-Mo2C was prepared employing temperature-programmed reaction method using ammonium heptamolybdate tetrahydrate and nitrate of nickel hexahydrate as precursor salts and sucrose as carbon source.

The extraction of hydroxyapatite from bovine bones was made by thermal treatment under an inert atmosphere of nitrogen.

Finally, the impregnation of Ni-Mo_2C in the hydroxyapatite was done by incipient humidity.

The samples of these catalytic materials were characterized by Fourier Transform Infrared Spectroscopy (FTIR), Scanning Transmission Electron Microscopy (STEM) X-Ray Diffraction (XRD) and physical adsorption of nitrogen at 77 K.

Keywords: Hydrogen Production, Molybdenum Carbide, Hydroxyapatite, Supported Catalysts.

XVIII International Congress
of the Mexican Hydrogen Society

Hydrogen generation by aluminum alloys corrosion in aqueous acid solutions promoted by sodium molybdate

Julia Guadalupe Salazar Barrera[1*], Ana Lidia Martínez Salazar[1], Margarita García Hernández[1], José Aarón Melo Banda[1], Marco Antonio Coronel García[1], Ulises Páramo García[1].

[1] Centro de Investigación en Petroquímica, Instituto Tecnológico de Ciudad Madero, Prol. Bahía del Aldair, Av. de las Bahías. Parque Industrial Tecnia, Altamira, Tamaulipas, México, 89608.
* Corresponding author: 833 4 602457, juliasalazarb@outlook.com

---

ABSTRACT

The aluminum alloys corrosion system was studied for hydrogen production in aqueous acid solutions using sodium molybdate as promoter. Aluminum alloys has been considerate as the most promising material to hydrogen generation in corrosion reaction due to its amphoteric behavior, high electron density, volumetric energy density, low cost and high abundance. There were so far no studies on the use of molybdates to hydrogen production. Nevertheless, sodium molybdate at low concentration has been reported as a corrosion accelerator for aluminum in hydrochloric acid, therefore it is a good promoter to increase the hydrogen production.
In the present study a sustainable and economic system of hydrogen production is carried out in a batch reactor with different concentration of sodium molybdate (0.008 – 0.044 M) at low temperature (333 K); employing aluminum alloys waste, seawater and hydrochloric acid as aqueous acid solution. Promoter corrosion efficiency in different hydrochloric acid concentrations (1.25M and 1.5M) was studied by potentiodynamic polarisation curves. Gas composition produced during the reaction was analyzed by gas chromatography.
Sodium molybdate particles were synthesized via sonochemical precipitation method based on the reaction between ammonium heptamolybdate tetrahydrate and sodium nitrate in water. The structural and morphological properties were characterized by techniques such as Fourier Transform Infrared Attenuated Total Reflection Spectroscopy (FTIR-ATR), Scanning Transmission Electron Microscopy (STEM) and X-Ray Diffraction (XRD).
Main gas product generate in aluminum alloys corrosion was hydrogen. Besides this, an improvement of hydrogen production rates and yields was observed using sodium molybdate as promoter material and varying aluminum alloys composition.

Keywords: hydrogen production; corrosion; sodium molybdate.

September 18th to 21st, 2018 in Mexico City, Mexico.

XVIII International Congress
of the Mexican Hydrogen Society

H_2 production by dry reforming of CH_4 in Ni-Pt/CeO_2 catalysts.

Diana G. Arcos[1], Antonio Gómez-Cortes[1]*, Daniel G. Araiza[1], Gabriela Díaz[1]

[1]Instituto de Física, Universidad Nacional Autónoma de México (UNAM), Circuito de la Investigación Científica Ciudad Universitaria, C.P. 04510 Ciudad de México, México
* Corresponding author: 52 (55) 56225112 and e-mail: gomez@fisica.unam.mx

ABSTRACT

The constant emission of greenhouse gases to the atmosphere like CO_2 and CH_4 is one of the reasons of the global warming. An approach to decrease the concentration of these compounds can be achieved by using them as reactants in a catalytic reaction like the dry reforming of methane to produce syngas ($CH_4 + CO_2 \rightarrow 2CO + 2H_2$). The H_2 produced from this reaction is intended to be used as feed of fuel cells. The selectivity to hydrogen can be increased either by modifying the CH_4/CO_2 ratio and/or by improving the catalyst performance. Nevertheless, due to the endothermic nature of this reaction (ΔH_{298K} = +247 kJ/mol) high temperatures (> 700 °C) are required to reach competitive yields. Under these conditions, the catalyst exhibits deactivation due to sintering or to the blocking of catalytic sites by carbon deposits. In this work, a study of the effect of the metallic composition of Ni-Pt/CeO_2 catalysts on their catalytic properties is carried out, particularly the effect on the deactivation of the materials is explored. The use of CeO_2 as catalytic support is related to its well redox behavior, a feature that could help to remove the carbon deposits, the main drawback in this reaction. For this study, a series of Ni-Pt catalysts supported in CeO_2 at different atomic concentrations were prepared. Characterization of materials was performed using various analysis physical and chemical techniques. The catalytic behavior was determined as a function of the reaction temperature and time-on-stream. A good performance of the Ni-Pt/CeO_2 catalysts is observed. Notably, a marked resistance to the deactivation of bimetallic catalysts Pt50Ni50 and Pt25Ni75 is exhibited as well as a higher H_2 selectivity during 24 hours of reaction.

Keywords: hydrogen production; dry reforming; Ni-Pt/CeO_2; catalysts

XVIII International Congress
of the Mexican Hydrogen Society

Hydrogen production from methanol decomposition using copper-based bimetallic catalysts

Daniel G. Araiza[1,*], Antonio Gómez-Cortés[1], Gabriela Díaz[1]

[1]Instituto de Física, Universidad Nacional Autónoma de México, Circuito de la Investigación Científica s/n, Cd. Universitaria, Ciudad de México 04510, México
* Corresponding author: +(52) 55 56225077 ext. 2221, araiza@ciencias.unam.mx

ABSTRACT

Methanol decomposition is considered as one of the simplest reactions for producing hydrogen from a renewable source. Copper-based catalysts have been extensively used in reactions involving methanol, specifically in methanol decomposition, copper has been typically supported over ZnO; however, some drawbacks related to the use of this system have not been overcome yet (e.g. low selectivity and deactivation issues related with coke deposition). Among many strategies to solve the above mentioned, two are considered in the present work: i) the first is related to the use of CeO_2 as support, which due to its high oxygen storage capacity, could increase the catalyst stability by improving the removal of carbon deposits; ii) the second one is associated with addition of a second metal (Ni, Pd, Pt) to the copper-ceria system; bimetallic catalysts usually exhibit better catalytic performances, compared to monometallic systems. In this framework here we present results concerning a series of bimetallic Cu-M/CeO_2 catalysts (where M = Ni, Pd, Pt) prepared by co-impregnation method at different metal loadings, while keeping copper as the most abundant metal. Catalysts were studied in the methanol decomposition reaction ($CH_3OH \rightarrow 2H_2 + CO$) as a function of reaction temperature (100-450 °C) and as a function of reaction time (350 °C, 24 h). Materials were characterized by XRD, N_2 adsorption, EDS-SEM, HRTEM, Raman spectroscopy, H_2-TPR and CO-DRIFTS. Results show that activity boosts after addition of small quantities of the second metal (Ni, Pd or Pt) and that in bimetallic catalysts the coke formation is inhibited. In the bimetallic systems, reduction properties are improved by the second metal, which could explain their better catalytic performance.

Keywords: Bimetallic, Copper-based, Methanol

September 18th to 21st, 2018 in Mexico City, Mexico.

XVIII International Congress
of the Mexican Hydrogen Society

Residual biomass-based hydrogen production: Potential and Possible Uses in Ecuador

F. Posso[1*], J. Siguencia[2], Ricardo A. Narváez C.[3]

[1]Universidad de Santander. Campus Lagos del Cacique. Calle 70 N° 55-210. Bucaramanga. 68003. Colombia
[2]Universidad de Cuenca. Campus Central. Av. 12 de Abril y Av. Loja. 010104. Cuenca. Ecuador
[3]Instituto Nacional de Eficiencia Energética y Energías Renovables (INER), Iñaquito N35-37. Quito. 170507. Ecuador
* Corresponding author: (57)3016696647. e-mail: faustopossorivera@gmail.com

ABSTRACT

In this paper, the residual biomass sources available in Ecuador (livestock, forestry and agricultural waste) are evaluated as prime matter for hydrogen production. The analysis is performed out of the official cropping information available per provinces (jurisdictional division of Ecuador). In addition, the parameters considered for the energy assessment are availability, conversion yield and physicochemical properties. In such context, the hydrogen production methods to be assayed consider thermochemical and electrochemical paths initially, as well as the projected yield of each technology. Results show that the total hydrogen potential of biomass waste in Ecuador is 1 646 598 ton H_2/ yr and the H_2 production density is 6.71 ton/yr-km^2. This scenario projected the combination of thermochemical processes and the most abundant types of agricultural waste. In such conditions, H_2 potential of this combination reached shares above 86.2% of the total amount. Besides this issue, it is mentioned that the H_2 potential distribution per province demonstrates that Esmeraldas, Guayas and Los Rios contribute with 69% of the total national potential.
Regarding the potential H_2 end-uses, the analysis of the energy sector shows that 46% of the national energy demand in 2016 could be covered by biomass waste-based hydrogen. Moreover, the specific energy demand of transport, industry or residential sector could be fulfilled in 78%, 188% and 278%, correspondingly. Other stakeholders such as the local petrochemical industry is also assessed, since the only petrochemical complex in Ecuador is located in Esmeraldas which contributes with 33% of the national H_2 potential.
This work aims to contribute to the assessment of the renewable sources-based H_2 in Ecuador and present this choice as a sustainable alternative in the near future.

Keywords: residual biomass; hydrogen; energy consumption; thermochemical processes

XVIII International Congress
of the Mexican Hydrogen Society

Hydrogen by Ethanol Steam Reforming using Ni, Co- hydrotalcite-like compounds as catalysts

J. L. Contreras[1]*, B. Zeifert[2], J. Salmones[2], J.A. Colin[1], G.A. Fuentes[3], T. Vázquez[2], and L. Nuño[1]

[1]Universidad Autónoma Metropolitana-Azcapotzalco, México, D.F.,02200, México
[2]Instituto Politécnico Nacional, ESIQIE, Mexico,D.F. U.P. López Mateos, Zacatenco, México 3 Universidad
[3]Autónoma Metropolitana-Iztapalapa. México,D.F, 09340, México
* Corresponding author: 5591911047 and jlcl@correo.azc.uam.mx

---

ABSTRACT

Ni-Co-Hydrotalcite-like oxides promoted with WOx showed high activity and stability in the ethanol steam reforming (ESR) producing H_2, CH_4, CO_2, and CO. The presence of Ni and Co in the bimetallic catalysts changed the products selectivity observed respect to the selectivity of the monometallic catalysts. The bimetallic catalysts of Ni-Co showed higher selectivity to H_2 than the selectivity of the monometallic Ni catalyst. The surface area in the Ni and Co catalysts was inversely proportional to the metals concentration. Metal oxides of Ni and Co in the bimetallic catalysts interacted with the hydrotalcite-like oxides obtained after calcination at 450°C, causing a partial blockage of pores, resulting in a decrease of pore volume. The peaks located between 275 to 450°C in the ATG-DSC analysis, were attributed to dehydroxylation and decarbonation of the hydrotalcite structure. The particles on the bimetallic catalysts showed a semi-cubic shape observed instead of laminar shape typical of hydrotalcites. By X-ray diffraction (XRD), $MgNiO_2$, periclase (MgO), κ-Al_2O_3 and bunsenite (NiO) were identified. The reduction by TPR of the Co-catalyst showed two peaks in 300-480°C and 560-700°C attributable to the oxides of Co_3O_4 and CoO respectively.The Ni catalyst showed a single peak located at 720°C due to the presence of $MgNiO_2$ or $NiAl_2O_4$. The bimetallic catalysts of Ni-Co-hydrotalcite-WO_X showed high selectivity to H_2 and total conversion of ethanol. The bimetallic catalysts did not produce CO.
Key words: Ni-Co-hydrotalcite-WOx, catalysts, Hydrogen, ESR.

Keywords: Ni-Co-Hydrotalcite-like-oxides, Hydrogen, Ethanol, Steam Reforming,

.

XVIII International Congress
of the Mexican Hydrogen Society

Modification of the Kinetics of Hydrogen Production in Alkaline Water Electrolysis by Forced Polarity Conditions

Julio C. Villalobos, H. J. Vergara-Hernández*, Gerardo M. Chávez-Campos, Mario M. Machado-López, Octavio Vázquez-Gómez.

División de Estudios de Posgrado e Investigación, Instituto Tecnológico de Morelia, Avenida Tecnológico #1500, Col. Lomas de Santiaguito. Morelia, Mich.
* Corresponding author: hvergarah@yahoo.com

ABSTRACT

Currently, the search for new renewable energies is the principal goals of developed and sub-developed countries. It is necessary to use economically competitive, technologically feasible and clean alternative energy sources for the environment; hydrogen is an alternative. However, the main challenge at present is to produce, store and transport it in a safe and efficient way. One of the main forms of industrial production of hydrogen is through the electrolysis of alkaline water (NaOH) and using Ni and Pt as electrodes for the water electrolysis process for its high efficiency, but these materials are very expensive. In substitution 316L stainless steels have been used due to its low price compared with Ni and Pt and high corrosion resistance. In this work, we report the study of the hydrogen evolution reaction (HER) in stainless steel electrodes 316L, in different electrolytic solutions concentration: 0.5, 1.0 and 1.5 M NaOH. The electrochemical study of the stainless steels in alkaline media was performed by cyclic voltammetry, and potentiodynamic curves to determine the HER efficiency at room temperature by Tafel slopes. In addition, the circuit was excited electrically by applying polarity changes in the order of seconds for a hydrogen production time of two hours. Tafel curves were obtained at the beginning and at the end of the hydrogen production process to verify the sensitivity to catalytic activity of the electrodes subjected to polarity change and without polarity changes.

Keywords: Hydrogen evolution reaction, stainless steel, forced polarization

XVIII International Congress
of the Mexican Hydrogen Society

Design proposal for a hydrogen production plant from the hydrolysis of aluminum waste coupled to a PEM fuel cell

A. Arturo Osorio-Sandoval[1]; Romeo Moreno-Flores[2]; Félix Loyola-Morales[3*]; Alberto A. Alvarez-Gallegos[1]; P. J. Sebastian[2]

[1]Centro de Investigación en Ingeniería y Ciencias Aplicadas, Av. Universidad 1001, Col. Chamilpa, Cuernavaca, Morelos, C.P. 62210, México
[2]Instituto Energías Renovables-UNAM, Priv. Xochicalco S/N, Col. Azteca, Temixco, Morelos, C.P. 62580, México
[3]Instituto Nacional de Electricidad y Energías Limpias, Reforma 113, Palmira, Cuernavaca, Morelos C.P. 62490, México
* Corresponding author: +52 (777) 362 3811 and felix.loyola@ineel.mx

ABSTRACT

In this work, the results of the design of a laboratory scale pilot plant for the production of hydrogen from the exothermic reaction of aluminum hydrolysis, coupled to a proton exchange membrane fuel cell (PEMFC) are presented. The raw material fed to the process consists of a solution of sodium hydroxide and pieces of aluminum from used cans. Sodium hydroxide allows removing the oxide layer that passivates the metal, a technique known as alkaline activation. The design of the plant is based on the analysis of the mass and energy balance, its experimental verification and the fuel requirements of the PEMFC, additionally the use of the heat released by the reaction through the Seebek effect was considered. The plant consists of a container that supplies sodium hydroxide solution to a batch reactor, which delivers the gas produced to a NaOH adsorption column. The three components function as a temporary gas storage system, while hydrogen is delivered on demand and under regulated pressure to the PEMFC. The 0.45 L container stores a 2.13 M solution sufficient to react 10 g of aluminum that will produce 12 L NTP of hydrogen. The 2.1 L reactor has the shape of a rectangular prism to couple to its surface Peltier plates that function as heat converters to electricity. The pilot plant proposal will be built using stainless steel at laboratory scale to evaluate its overall energy efficiency.

Keywords: PEM fuel cells; Hydrolysis of aluminum; hydrogen production plant; Sebeek effect

September 18th to 21st, 2018 in Mexico City, Mexico.

XVIII International Congress
of the Mexican Hydrogen Society

OBD2 monitoring and control system for hydrogen generator used as complementary fuel on internal combustion vehicles

G. Macias-Bobadilla[1*], D. Becerra-Ruiz[1], A. Amaro-Reyes,[2] J.N. Gracida-Rodriguez[2,]

[1]Facultad de Ingeniería, Universidad Autónoma de Querétaro, Cerro de las Campanas S/N, Col. Las Campanas, Querétaro, Qro. México. C.P. 76010
Facultad de Ingeniería, Universidad Autónoma de Querétaro, Cerro de las Campanas S/N, Col. Las Campanas, Querétaro, Qro. México. C.P. 76010
* Corresponding author: (+52)4421921200 ext. 6016 and gonzalo.macias@gmail.com

ABSTRACT

OBD2 systems on modern vehicles allow the possibility to access a large amount information related to speed, load, fuel level injection and air to internal combustion system of vehicles, this system on modern vehicles also allows the possibility to supervise gas exhaust system and advise to driver if something is wrong or if the vehicle is ready to be verified for an authorized control pollution center. At this respect, this work presents a human-machine interphase made whit Arduino and Bluetooth connection OBD2 standard connector compatible with all modern cars to supervise driving condition to activate and deactivate a hydrogen generator used as complementary fuel on internal combustion vehicles, the interphase includes algorithms to determine the ideal moment to activate the hydrogen generator to optimize fuel efficiency. Results include graphs of improvement of exhaust systems gas emission of an experimental vehicle using the developed human-machine interphase and its respective comparative without the use of this interphase.

Keywords: OBD2 human-machine interphase; Bluetooth Arduino communication; exhaust system gas emission.

September 18th to 21st, 2018 in Mexico City, Mexico.

XVIII International Congress
of the Mexican Hydrogen Society

Modelling and simulation of an alkaline water electrolyser

Valeria Juárez Casildo[1], Rosa de Guadalupe González Huerta[1*], Rogelio Sotelo Boyás[2]

[1]ESIQIE-IPN, Lab. Electroquímica y Corrosión, UPALM, CP 07738, Ciudad de México.
* rosgonzalez_h@yahoo.com.mx
55 57296000 ext 54246

ABSTRACT

Very promises perspectives exist for the use of hydrogen as a fuel, it is known that hydrogen production with renewables is suitable and environmentally friendly. Today, alkaline water electrolysis has become in a mature technology due to de many studies made in whole world in order to improve efficiency and performance.

Many studies made in this topic has focused in develop modelling and simulation due to the advantages which it has in comparison with experimental analysis. In fact the currently technology computing condition allows solve complex models which describes this kind of multiphysics system, for instance, it is possible save money because of the prototypes are not built. Developing modelling and simulation is easy to understand the alkaline water electrolysis behaviour, determinate the dimensions of process equipment and it could be possible to do a redesign of it.

This paper is a mini-review of the modelling and simulation works in order to analyses the state of the art in this topic and identify the most often phenomena modelling and which are the commercial software most often use for simulate this electrochemical system.

This information will be a tool for a future modelling and simulation study in order to understand the relation between gas separator and alkaline electrolyser. According with this review, the commercial software more used is MATLAB-Simulink® and it is thought this is because develops their studies considering the electrochemical system as an electrical circuit.

Keywords (Maximum 4 words): modelling, simulator, alkaline water electrolysis system.

XVIII International Congress
of the Mexican Hydrogen Society

The photo electrochemical effect of Boron and Cerium incorporation in TiO_2 nano-structures

A.A. Flores-Caballero[1, 2], N. Alonso-Vante[2], A. Manzo Robledo[1,*]

[1]Instituto Politécnico Nacional. Laboratorio de electroquímica y corrosión. Departamento de Ingeniería Química. Escuela Superior de Ingeniería Química e Industrias Extractivas (ESIQIE)-IPN, Distrito Federal, México, 07300.
[2]IC2MP- UMR-CNRS 7285, University of Poitiers, 4 rue Michel Brunet, F-86022 Poitiers Cedex, France.
*Corresponding author: 01(55) 5729600 ext. 54246. Email: amanzor@ipn.mx

ABSTRACT

The depletion of fossil fuels to obtain energy from natural gas, coal, electricity, oil and by-products suggest the development of renewable energy systems based on alternative sources that provide benefits to the environment at low costs. Technologies are focused on materials based on semiconductors, such as titanium dioxide (TiO_2), which have been studied toward the photolysis of water using photo-electrocatalytic methods to form H_2 and O_2. In this way, photo-electrochemical analysis in acid conditions was carried out to study the interaction between boron and cerium species (2 %at) at TiO_2 nanoparticles synthesized by sol-gel method and calcinated during 4h at 400 °C. X-ray Diffraction (XRD), Scanning Electronic Microscopy (SEM), Brunauer-Emmett-Teller (BET), diffuse reflectance (DRS), Surface photoelectron spectroscopy (XPS), and photo electrochemical analyses were employed. The photo electrochemical stability of drop-casted oxide layers onto SnO_2: F (Solems) supports, in H_2SO_4 + CH_3OH solutions, was studied. The incident photon to current efficiency (IPCE) and the MeOH/H_2O ratio revealed UV highest photo activity and low photo generated electron-hole pairs recombination on TiO_2-B sample in MeOH containing electrolytes. Boron ions substitutional for O sites and interstitial effects were confirmed by XPS analysis, observing a decrement on the recombination rate to promote the highest photo current density (μA/cm^2). The surface chemistry of this material, as revealed by XPS, promote and important displacement in the negative direction (electrochemical scale) of the flat band potential (V_{FB}) level. This phenomenon favors the reducing power of the photo generated electrons. The photo electrochemical activity of boron and cerium species incorporated in TiO_2 follows the trend: TiO_2-B > TiO_2 > P25 > TiO_2-Ce.

Keywords: Oxide semiconductor; photo-electrochemistry, Surface chemistry, adsorption phenomena.

XVIII International Congress
of the Mexican Hydrogen Society

Enhance Photoactivity of Hydrogen production using photocatalysis and TiO_2-NiO as semiconductor

Alejandro Pérez-Larios[1*], R. Gomez[2], R. Zanella[3], J. Bedia[4], C. Belver[4].

[1]Universidad de Guadalajara, Centro Universitario de los Altos, Depto. Ingenierias, Carretera a Yahualica km. 7.5, Tepatitlán de Morelos, Jalisco, México. 47600.
[2]Universidad Autónoma Metropolitana-Iztapalapa, Depto. de Química, Área de Catálisis, Av. San Rafael Atlixco No 189, Ciudad de Mexico, Mexico, 09340.
[3]Instituto de Ciencias Aplicadas y Desarrollo Tecnológico, Universidad Nacional Autónoma de México (UNAM), Ciudad Universitaria, Cd. Mexico, México. 04510
[4]Seccion de Ingenieria Quimica, Facultad de Ciencias, Universidad Autónoma de Madrid, Campus Cantoblanco, E-28049 Madrid, Spain.

(*) alarios@cualtos.udg.mx

ABSTRACT

The most studied processes at the present for the hydrogen production are electrochemical, steam reforming of alcohols or hydrocarbons and water splitting. Thus, the water splitting using semiconductors materials had recently acquired great relevance because of the low cost for the hydrogen production. The principle of this technique is based on the photoexcitation of the semiconductor using a UV or visible light sources. The electrons-hole pairs formed are capable to split water molecules into gaseous oxygen and hydrogen[1].
Titanium dioxide doped with Nickel (1.0, 3.0, 5.0 and 10.0 % wt) by sol-gel method were obtained. The solids were characterized by nitrogen adsorption using adsorption isotherm (BET) and porosity (BJH) method, XRD patterns and UV-Vis spectroscopy. The photoactivity was evaluated using a Pyrex reactor of 200 ml using a solution Methanol-Water (1:1) and 0.1 g of catalyst. A high pressure Hg lamp (with a λ=254 nm, I_o = 2.2 mW/cm^2) encapsulated in a quartz tube was used as source of energy.
The results showed materials with specific surface area among 100 to 180 m^2/g and mesopority characteristics. The XRD patterns show the formation of the crystalline anatase phase. The band gap energy (Eg) for the materials were obtained with UV-Vis spectroscopy, the Eg values were lower than 3.2 eV. In the water splitting evaluation a maxim in the efficient was found at Ni at 10 wt.%. The hydrogen produced was 3000 µmol, this is a value comparable to that obtained with Pt-TiO_2[1].

Keywords: Photocatalysis, Energy, mixed oxide, semiconductor, hydrogen production

XVIII International Congress
of the Mexican Hydrogen Society

Design and manufactured of alkaline membrane electrolyzer

F. A. Soriano-Moranchel[1*], J. M. Sandoval-Pineda[1], R. de G. Gonzalez-Huerta[2]

[1]ESIME UA -Instituto Politécnico Nacional, Sección de Posgrado, Av. De las Granjas 682, C.P. 07738 Ciudad de México, México
[2]ESIQIE- Instituto Politécnico Nacional, Laboratorio de Electroquímica, UPALM, C.P. 07738, Ciudad de México, México
* Ing.froylan_soriano@outlook.com, 5571696278

ABSTRACT

Alkaline water electrolysis is one of the easiest methods for hydrogen production, offering the advantage of simplicity. The challenges for widespread use of water electrolysis are to reduce energy consumption, cost and maintenance and to increase reliability, durability and safety. A basic water electrolysis unit consists of an anode (+), a cathode (-), power supply and an electrolyte (NaOH).

The main objective of this study is to develop alkaline electrolyzer stacks for high volume oxyhydrogen production (1 – 2 sL/min) and investigate operating parameters for a higher efficiency. It was established a small-scale manufacturing process for alkaline electrolyzers using Advanced Product Quality Planning (APQP) methodology, which can offer security in design, installation, and operation of alkaline electrolyzer, it includes Engineering process to optimize the relationship between design function, easy manufacture and assembly. The application will be in an open combustion process to reduce pollutants in ovens and burners. Alkaline membrane electrolyzer model AME-01-500 was established, which allow us generate Hydrogen and Oxygen in individual containers, this electrolyzer is constituted by two electrolytic cells connected in series.

The electrolyzer stack prototype is made up of 3 plated electrodes (with a thin layer of nickel, 20 µm, with matte finish was deposited on stainless steel surfaces), 6 acrylic electrolyte container (10 mm thickness) and 2 Stainless steel support endplates (1.2 mm). All the elements such as Stainless steel endplates, nickel plated electrodes, serial electrodes and current collector plates, were designed and machined in house. The energy consumption ranged from 75 Wh to 750 Wh, which corresponds to 45−65% of efficiency.

Keywords: Design, Manufacturing, alkaline, Electrolyzer, Membrane, Hydrogen, Production

XVIII International Congress
of the Mexican Hydrogen Society

Photocatalytic hydrogen production from glycerol reforming using highly active CuO@TiO_2 core-shell catalysts

S.P. Ramírez[1], J.A. Wang[1,*], M.A. Valenzuela[1], A. Dalai[2]

[1] Laboratorio de Catálisis y Materiales, ESIQIE-Instituto Politécnico Nacional, 07738 Ciudad de México, Mexico.
[2] Department of Chemical Engineering, University of Saskatchewan, Saskatoon S7N 5A9, Canada.
* Corresponding author: Tel: 52 55 57296000 ext. 55276; email: jwang@ipn.mx

ABSTRACT

Hydrogen production from the photocatalytic reforming of glycerol was performed on several core-shell nanostructured catalysts under simulated solar light. The catalysts were prepared by modified sol-gel method and characterized by powder X-ray diffraction (XRD), UV-Vis diffuse reflectance spectroscopy (UV–Vis DRS), scanning electron microscopy (SEM), transmission electron microscopy (TEM), and nitrogen physisorption isotherms. The band gap energy was 3.25 eV for pure TiO_2, 3.19 eV for NiO@TiO_2, and 3.11 eV for CuO@TiO_2. The catalysts containing TiO_2 as a shell showed much higher activity compared with those formulated with bared Cu or Ni oxides. The highest rate of hydrogen production obtained with the CuO@TiO_2 catalyst was as high as 153.8 $\mu mol \cdot g^{-1} \cdot h^{-1}$, which was 29.0, 24.8, 11.2 and 3.2 times greater than that obtained on CuO@NiO, NiO@CuO, TiO_2 P25, and NiO@TiO_2 catalyst, respectively. For the high active CuO@TiO_2 catalyst, after activation with solar light, the conduction band electrons in TiO_2 can transfer to CuO through the heterojuctiion structure of the core-shell interfaces which led to CuO gradually reducing to Cu_2O and Cu, favoring the reduction of proton to hydrogen.

Keywords: Core-shell structure; Photocatalysis; Hydrogen production; Glycerol

1. Introduction

In the photocatalytic reactions, synthesis method of the photocatalyst takes key role. In recent years, the preparation and exploration of core–shell nanoparticles have been demonstrated to possess improved physical and chemical properties for electronics, magnetism, optics, catalysis, and other applications. Numerous studies have shown that the nanoparticles with core–shell unique structure improve their catalytic activity and selectivity. In photocatalytic H_2 evolution, the catalysts with core-shell structure play an important role in the charge separation. For example,

XVIII International Congress
of the Mexican Hydrogen Society

Au/CeO_2 and $Au/Ce_xZr_{1-x}O_2$ Sol-Gel Catalysts for Hydrogen Production via Partial Oxidation of Methanol

E. Hernández[1], J.A. Wang[1,*], L.F. Chen[1], M.A. Valenzuela[1], R. Azargohar[2], A.K. Dalai[2]

[1]ESIQIE, Instituto Politécnico Nacional. Zacatenco, 07738 Ciudad de México, Mexico.
[2]Department of Chemical Engineering, University of Saskatchewan, Saskatoon - S7N 5A9, Canada
* Corresponding author: Tel: 525557296000 ext. 54276; e-mail: jwang@ipn.mx

ABSTRACT

Catalytic activity of Au/CeO_2 and $Au/Ce_xZr_{1-x}O_2$ catalysts in the partial oxidation of methanol for hydrogen production under different pretreatment conditions was investigated. ZrO_2 addition to Au/CeO_2 catalyst led to formation of $Ce_xZr_{1-x}O_2$ solid solution that promoted the formation of Au^{n+} nanoclusters and improved the reducibility of surface oxygen of the support. The pretreatment of the catalysts played a key role, influencing the catalytic activity and product selectivity. Under reductive condition, the catalysts exhibited better catalytic activity and higher hydrogen selectivity than that obtained under oxidative condition. Generally the $Au/Ce_xZr_{1-x}O_2$ catalyst exhibited higher catalytic activity and H_2 selectivity.

Keywords: Au/CeO_2; $Au/Ce_xZr_{1-x}O_2$; Partial oxidation of methanol; Hydrogen production.

1. Introduction

Recently, hydrogen received great attention because it is regarded as a clean fuel related to the global-concerned issues of environmental pollution control, climate change and energy crisis. Hydrogen has a wide spectrum of applications in fuel cell technology and petrochemicals industries, and many other areas [1]. There are a number of approaches or processes for hydrogen production, for instance, the catalytic decomposition of natural gas, steam reforming, photocatalytic decomposition of water, and biomass gasification, partial oxidation of methanol (POM) [2–8]. The POM reaction is considered as a structure-sensitive reaction as the selectivity of the products is greatly dependent of the configuration of the surface atoms and the structure character of the catalyst. This reaction can lead to several products, like H_2, CO, CO_2 and CH_4 etc, strongly influenced by the catalyst composition, reaction temperature, and methanol conversion degree. A variety of catalysts such as iron and copper oxides catalysts have been

XVIII International Congress
of the Mexican Hydrogen Society

Performance diesel engine enrichment with oxyhydrogen and the analysis of its gases emission

I. Trujillo-Olivares[1*], J. M. Sandoval-Pineda[1], R. de G. Gonzalez-Huerta[2],

[1]Instituto Politécnico Nacional, ESIME-Azc., SEPI, Av. de las Granjas 682, Col. Santa Catarina, CP 02250, CDMX
[2]Instituto Politécnico Nacional, ESIQIE, Laboratorio de Electroquímica y Corrosión, UPALM, CP 07738, CDMX
Tel: +52 1 (55) 57296000 ext 64503; e-mail: masey5310class@gmail.com

ABSTRACT

Internal combustion engine (ICE) vehicles are an important source of pollution gases; therefore several works have been published in recent years, where systems to reduce hydrocarbon emissions are implementing, for example diesel engine enrichment with alternative fuels such as hydrogen and others have been considered.

In this experimental study, the mixtures of diesel with oxyhydrogen gas (HHOG) were used as additional fuel in an ICE. For this, a single-cylinder 406 cm^3 diesel engine was adapted, monitoring the power and fuel consumption, enriching it with a theoretical 10% based on the calorific value of the main fuel (diesel). The oxyhydrogen reactor (HHOR) was designed and manufactured, where stainless steel with a nickel coating of 20 µm thickness was used as the material of the electrodes, for its resistance to corrosion and with an effective area of 77.55 cm^2 for each face of the electrodes. The optimum performance of HHOR was found using two anode and one cathode with a 5% NaOH solution, producing up to 3 NL_{HHO}/min. Using the HHOR, four experimental cases were performed. In the first case it was diesel fuel without HHOG; the second case is with addition of 1 NL_{HHO}/min, the third case is with 2 NL_{HHO}/min and the four case with 3 NL_{HHO}/min. The effects with the different enrichments of the HHO fuel in relation to the diesel-only engine operations were investigated between speeds from 800 to 3400 rpm and were expressed in values as; fuel consumption and exhaust emissions such as; NOx, CO_2, CO and HC. The results showed that with the addition of HHOG, the flux more effective to improve the performance of the diesel engine was the 2 NL_{HHO}/min, with an increase in speed of more than 50 rpm and 10% less diesel fuel consumption in the ICE, in addition, on average 10% and 16% reduction in emissions of NOx, CO_2, CO and HC were observed.

Keywords: oxyhydrogen reactor; gases emission, diesel engine, internal combustion engine

September 18th to 21st, 2018 in Mexico City, Mexico.

XVIII International Congress
of the Mexican Hydrogen Society

Dielectric Barrier Discharge for hydrogen production out of intermediate molecular weight hydrocarbons

M. A. Segura[1]*, M. Nieto Perez[2], R. G. González Huerta[3]
[1]Centro Mexicano para la Producción más Limpia, Instituto Politécnico Nacional, C.P. 07738, México, CDMX
[2]Centro de Investigación en Ciencia Aplicada y Tecnología Avanzada, Instituto Politécnico Nacional, 76090 Querétaro, Qro
[3]Escuela Superior de Ingeniería Química e Industrias Extractivas, Instituto Politécnico Nacional C.P. 07738, México, CDMX
* Corresponding author: miguel.segura@correo.nucleares.unam.mx

ABSTRACT

In this paper an atmospheric dielectric barrier discharge is proposed as an alternative solution to production, transportation and storage of hydrogen for mobility applications. One of the features of plasmas is its electron temperature, up to 5eV, which is enough to break molecular bonds and generate reactive species. The aim of the study is to probe the possibility of hydrogen production using intermediate weight hydrocarbons (naphta) as precursors, opening the possibility of producing the hydrogen from gasoline on board of the vehicle; different mixes of heptane (0 octane rating) and iso-octane (100 octane rating) were used to simulated average fuel. A two-component/two phase characterization as a benchmark for chemical conversion efficiency of the plasma in the hydrogen production is presented. By means of this technology, a cheaper way of producing hydrogen, compared with nowadays most popular form (SMR), can be achieved for vehicular applications, solving also the transportation and storage problem by *in situ* production.

Keywords: Hydrogen, plasma, dielectric barrier discharge, hydrocarbon reforming.

XVIII International Congress
of the Mexican Hydrogen Society

Photocatalytic activities of $BaTiO_3/Ba_4Ti_2O_{27}$ mixtures towards efficient hydrogen production (water splitting reaction)

M.A. Escobedo Bretado[1,*], M.A Gonzalez Lozano[1], R.H. Lara[1], V. Collins Martínez[2], M.J. Meléndez Zaragoza[2], A. López Ortiz[2]

[1]Facultad de Ciencias Químicas, Universidad Juárez del Estado de Durango, Av. Veterinaria s/n, Circuito Universitario, Durango, Dgo., México, 34120.
[2]Departamento de Ingeniería y Química de Materiales, Centro de Investigación en Materiales Avanzados, S.C., Miguel de Cervantes 120, Chihuahua, Chih., México, 31136.
* M.A. Escobedo Bretado: phone number: +52 618 1301120, e-mail: miguel.escobedo@ujed.mx

---

ABSTRACT

Barium titanates (BT) have shown a great potential in photocatalytic water splitting for hydrogen evolution. The aim of the present study is to determine the effect of PbO and BaO during the synthesis of BT, in order to evaluate their photocatalytic activity towards the efficient hydrogen production. The photocatalysts were obtained from a mixture of TiO_2, Al_2O_3, H_3BO_3, K_2CO_3, $Ba(NO_3)_2$ and PbO. The following relationships were considered during experiments: TiO_2:Al_2O_3:B_2O_3:K_2O:XPbO:YBaO = 38:16:13:9:X:Y (Mmol %) where X = 0.5, 1.5, 2.5, 3.5, 4.5 and Y = 23.5, 22.5, 21.5, 20.5, 19.5, which were designated as VC1, VC2, VC3, VC4 and VC5, respectively. These mixtures were treated at 400 °C/0.5 h., followed by subsequent process at 1350 °C/2 h. The molten mixtures were cooled at ambient temperature in order to induce a secondary treatment at 680 °C/2 h until recrystallization. Materials were characterized by XRD, BET, SEM and UV–Vis. All treated samples exhibited a solid solution among $BaTiO_3$ and $Ba_4Ti_2O_{27}$ phases with a specific surface area and morphology. Band gap energies of these titanates fell within the electromagnetic spectrum from 3.0 eV for (VC1), (VC2) and (VC3), 2.9 eV (VC4) and 2.7 eV (VC5). Maximum hydrogen production was achieved by (VC5) with 113.1 µmol H_2/gcat, followed by (VC2) = 112.2 µmol H_2/gcat, while the lowest production was observed for sample (VC1) with 96.3 µmol H_2/gcat at 8 hours of irradiation. VC3 and VC4 samples did not show activity. From these results, the crystals of barium titanates exhibited high photocatalytic activity for water splitting and they can be considered as potential photocatalysts for hydrogen production.

Keywords: hydrogen production; water splitting; barium titanates.

XVIII International Congress
of the Mexican Hydrogen Society

Scope of fuel cells in current transport with hydrogen as fuel

José Juan Alvarado Flores[1*], María Liliana Ávalos Rodríguez[2], Jaime Espino Valencia[3], Jorge Víctor Alcaraz Vera[4]

[1] Instituto Tecnológico del Valle de Morelia, Tecnológico Nacional de México, Km. 6.5 Carretera Morelia Salamanca, Nardo S/N Morelia, Michoacán, México.
[2] Escuela Nacional de Estudios Superiores, Universidad Nacional Autónoma de México, Antigua Carretera a Pátzcuaro No. 8701, Morelia, Michoacán, México.
[3] Facultad de Ingeniería Química, Universidad Michoacana de San Nicolás de Hidalgo, Francisco J. Mújica S/N, Col. Felicitas del Rio, C.P. 58040, Morelia, Michoacán, México
[4] Instituto de Investigaciones Económicas y Empresariales, Universidad Michoacana de San Nicolás de Hidalgo, Francisco J. Mújica S/N, Col. Felicitas del Rio, C.P. 58040, Morelia, Michoacán, México.

* Corresponding author: doctor.ambientalista@gmail.com

ABSTRACT

In recent years, the increase in oil prices has increased by more than 150%. At present, and in the society in which we live, it is difficult to imagine what would happen if in a very short period of time the price of a barrel of oil would grow to levels not tolerable for most economies. Renewable energy sources, which are distributed with greater or lesser abundance throughout the planet, have as an intrinsic characteristic, the fact that they are temporary and not completely storable. The electricity that can be produced from them cannot be stored in appreciable quantities either. For all these reasons, an element or vector is necessary to allow its transitory accumulation. Hydrogen has the energy power per unit mass almost three times higher than gasoline, and its storage, transportation and distribution are also feasible, which would allow its application to any segment of the demand, such is the case of the automotive industry. In this way hydrogen as a fuel has to be considered in the framework of a complete energy system. In this paper we compare some of the most important properties that the various fuel cells must have using hydrogen as a fuel for transportation use.

Keywords: Fuel cells; energy; motor vehicle; hydrogen technology

September 18th to 21st, 2018 in Mexico City, Mexico.

XVIII International Congress
of the Mexican Hydrogen Society

Sustainable and efficient off-grid production of Hydrogen. Demo project on-going in Spain

Edgar Bueno[1*], Lorién Gracia[1], Pedro Casero[1]

[1]Parque Tecnológico Walqa, Ctra N330a, km 556, 22197 Huesca, España
* Corresponding author: +34 974 215 258; ebueno@hidrogenoaragon.org

ABSTRACT

Work presented in this abstract is part of the Ely4Off Project, European FCH-JU, contract number 700359, whose objective is to demonstrate the viability of a system that integrates renewable energy and hydrogen produced by water electrolysis, in a completely off-grid and autonomous way. The system to generate green hydrogen is formed by a PEMWE (Polymer Electrolyte Membrane Water Electrolyser) industrial prototype of 56 kW that will be directly linked to track the solar photovoltaic power source producing over 1.5 tonnes of hydrogen per year for different end uses ensuring cold start and rapid response to changes. It will be managed by an autonomous Communication and Control system with a backup energy system formed by a fuel cell and batteries to supply during no radiation periods.

The off-grid situation and the impact of the photovoltaic source due to the variation in daily radiation should be taking into account to estimate communications and control protocols, hydrogen production and strategies to follow to achieve higher efficiencies. To determine them, several simulations and sensitivity analysis were done on a computer model.

The main achievements accomplished by now are:

- First assessment of thin membranes was carried out, showing low hydrogen diffusion properties, and good efficiency levels.
- A detailed reengineering design of the electrolyser plant is underway to maximize the available power for electrolysis, by improving the efficiency of the balance of plant. By now, a large-scale reduction of kilowatt hours required for frost protection has been achieved.
- An in-depth assessment of the best options available for the DC/DC conversion linking the PV plant with the stack has been conducted. One prototype module has been built for testing.
- Most of the overarching control signals are clear and the communication protocols with the micro-grid equipment have been defined.
- Several energy storage architectures have been assessed. The following elements will be part of this system: 96 kWh lead acid batteries to supply safety loads up to 20 hours, 4.5 kW stationary low temperature PEM fuel cell to cover safety loads when the lead acid batteries are discharged, and a H2 capacity of 7 kg at low pressure tank (20 bar), and 23 kg at high pressure tank (350 bar).

September 18th to 21st, 2018 in Mexico City, Mexico.

XVIII International Congress
of the Mexican Hydrogen Society

Hydrogen production by the reaction between water and the intermetallic AlLi activated by mechanical milling

Diana Laura Álvarez Acosta[1,2] , José Luis Iturbe García[1*]

[1] Departamento de Química, Instituto Nacional de Investigaciones Nucleares, Carretera México-Toluca s/n, la marquesa, C.P. 52045, Ocoyoacac, Estado de México, México
[2] Facultad de Química, Universidad Autónoma del Estado de México, Paseo Colón y Tollocan s/n, CP 50000, Toluca, Estado de México, México.
*Corresponding Author: 53297200 ext. 12274: joseluis.iturbe@inin.gob.mx

---

ABSTRACT

Hydrogen is the most abundant and simplest element in the universe and is considered as a possible clean and reliable alternative in its use as a fuel that can reduce the emission of greenhouse gases and environmental deterioration, however, the main limitation is the lack of availability to obtain hydrogen from renewable energy sources. In this work the results of hydrogen production are presented from the direct reaction between the AlLi compound and water at normal conditions of pressure and temperature. Activation of the compound was performed by mechanical milling in a spex-type high energy mill in a 80:20 percentage ratio for Al and Li respectively with an Ar atmosphere, where the modified parameter was the milling time from 0.5 to 10 hours. The reaction was carried out from 20-100 mg of compound by adding distilled water. The quantification of hydrogen was performed with a graduated cylinder by liquid displacement. Compounds activated by mechanical milling as well as obtained after the reaction were characterized by X-ray diffraction (XRD) to determine the phases that contributed effectively in the production of hydrogen. The milling time of 3 hours was the most favorable to carry out the reaction between AlLi material and water. The volume of hydrogen obtained was 1700 mL/g. This value is greater than that obtained only by the hydrolysis of Li, therefore, the Al has a significant contribution in the volume of hydrogen produced. Consequently, the compound (AlLi)-water reaction is a promising method for hydrogen generation in a simple way and in relatively short times compared with other hydrogen production methods.

Keywords: AlLi compound, mechanical milling, XRD, hydrolisis, hydrogen generation.

September 18th to 21st, 2018 in Mexico City, Mexico.

XVIII International Congress
of the Mexican Hydrogen Society

Design of an oxy-hydrogen system to be implemented in internal combustion engines of motorcycle

U. Maza-Nájera[1*], J. M. Sandoval-Pineda[1], R. González-Huerta[2], M. Rico-Cortez[3]

[1]Instituto Politécnico Nacional, ESIME-Azc., SEPI, Av. de las Granjas 682, Col. Santa Catarina, CP 02250, CDMX
[21]Instituto Politécnico Nacional, ESIQIE, Laboratorio de Electroquímica y Corrosión, UPALM, CP 07738, CDMX
[31]Instituto Politécnico Nacional, ESIME, SEPI, Edificio 5 tercer piso, UPALM, CP 07738, CDMX
* 5564107134 ulisesmaza94@gmail.com

ABSTRACT

The oxy-hydrogen production capacity of an electrolyzer (NL/min) is an important parameter for judging the performance of an electrolyzer. According to the need of energy or hydrogen, electrolyzers of different scales are designed to meet the varying needs of the end users. An electrolyzer can vary from the several W to several kW in terms of power consumption. Considering the volume of the electrolyzer (L_E) and the H_2 production rate, the unit of NL_{H2}/(L_E kWh min) symbolizes the mobility, energy consumed and capacity of the electrolyzer. From the safety point of view, the wide range of the flammability limits of H_2/O_2 mixture demands careful design of the system configurations. Leakage of the electrolyte is also a safety issue. Due to the corrosive nature of the electrolyte, the leakage is more likely to occur at the connections and the seals.

The present research work shows the design of an Oxy-hydrogen system to be implemented in internal combustion engines of motorcycle. The Quality Function Deployment (QFD) methodology was used in order to design of the electrolyzer and its components. The durability is also an important criterion for electrolyzers. Materials for system construction determine the electrolyzer lifetime, the selection of materials was carried out through the CES Edupack® software and the Ashby methodology. Based on the results obtained from the application of the QFD methodology, three design alternatives are proposed, which were modeled with the help of the SOLIDWORKS® Software. The virtual final design is presented, which consists of a deposit for four electrolysis cells, with square spirals electrodes connected in series. The operating condition will be 10 A-12 V to obtain an Oxyhydrogen production of 0.546 NL/min.

Keywords: Alkaline Electrolysis; Automotive Vehicles; Electrolyzer Design

September 18th to 21st, 2018 in Mexico City, Mexico.

XVIII International Congress
of the Mexican Hydrogen Society

Computational Design of an Oxyhydrogen Gas Burner

R. Moreno Soriano[1], R. de G. González-Huerta[2], J. M. Sandoval-Pineda[1], F. Soriano-Moranchel[1]

[1]Instituto Politécnico Nacional – ESIME – Azc, SEPI, Av. De las Granjas, No 682, Azcapotzalco, CP 02250, México
[2]Instituto Politécnico Nacional – ESIQIE, Laboratorio de Electroquímica y Corrosión, UPALM, CP 07738, México
* Corresponding author: 5568780642, beto.mec@outlook.es

ABSTRACT

The energy stored in hydrogen can be converted to useful energy through either fuel cells to directly produce electricity or combustion to produce power. The use of H_2 in combustion systems is attractive because it has a very wide flammability range, it is easy to ignite, and has a large flame propagation velocity and small quenching distance. The flame propagation velocity in a mixture of hydrogen and air is very large in comparison to that of hydrocarbons. This is due primarily to the faster reaction rates of the H_2/O_2 system. The large diffusion coefficient of H_2 also plays a role in the large flame speed because of the enhanced transport of radicals and heat ahead of the flame. Hydrogen also has a higher heat of combustion relative to hydrocarbon fuels on a per unit mass basis. At 298K and 1 atm the heat of combustion (lower heating value) of H_2 is about 120 MJ/kg while that of methane is 45 MJ/kg, however, that on a per unit volume basis the lower heating value for H_2 is about a factor of four less than CH_4.

The design of a pre-mixed burner for a gas flow of 2 (L/ min) is presented, using oxy-hydrogen as fuel gas. The design was based on a methodology available in the literature from hydrocarbons, p. e. CH_4. The flow velocity and pressure drop in the main areas of the burner were evaluated. Dimensions and geometry of the injector was varied, according to the operating conditions and considering the phenomena of takeoff and flashback of the flame. Primary air intake ports, some diameter, orientation and location of the same along the mixer were analyzed. The modeling and simulation of the obtained geometry was performed by means of computational tools, evaluating the mixing of the gases (hydrogen-oxygen) and the distribution of velocities and pressures of the gas flow through the different zones of the burner, emphasizing the velocities and pressures developed in the burner output ports, comparing the theoretical values of the laminar combustion speed for the hydrogen-oxygen mixture according to the percentage of primary aeration.

Keywords: Burner, oxy-hydrogen, combustion, flame speed

XVIII International Congress
of the Mexican Hydrogen Society

Evaluation of $NiWO_4$ as an oxygen carrier for the hydrogen storage by chemical looping.

P.E. González-Vargas; M.J. Meléndez-Zaragoza; J.M. Salinas-Gutiérrez; V. Collins-Martínez; A. López-Ortiz *

Centro de Investigación en Materiales Avanzados, S.C., Miguel de Cervantes 120, Complejo Industrial Chihuahua Chihuahua, Chih. México. C.P. 31136
* Tel: +52 6144394815; e-mail: alejandro.lopez@cimav.edu.mx

ABSTRACT

Chemical looping process (CL) have recently been used for various purposes, one of which is the hydrogen storage using metal oxides (MeO) as the only source of oxygen (oxygen carriers) to produce water ($MeO + H_2 = Me + H_2O$) and regenerating the metal oxide with a steam oxidizing atmosphere for the hydrogen release ($Me + H_2O = MeO + H_2$). It is important that these oxygen carriers have certain characteristics to be used for this purpose, such as thermal stability and the ability to store and release the lattice oxygen to the cyclic reaction conditions. In order to evaluate the nickel tungstate ($NiWO_4$) for this purpose, it was thermogravimetrically tested (TGA) in three accelerated redox cycles using a mixture of 5 v% of H_2/Ar as a reducing atmosphere and a mixture of 5 v% H_2O/Ar gas stream as the oxidizing atmosphere. Characterization made to the material before and after the redox cycles were performed by XRD, BET surface area, and SEM and have shown its favorable potential as an oxygen carrier when testing its thermal and reactive stability after three consecutive redox cycles. TGA tests revealed an oxidation mechanism of the reduced metals (Ni + W) that follows a reaction path, which consists in the formation of WO_3 by the oxidation of W with steam, followed by the formation of $NiWO_4$. This reaction path was confirmed by thermodynamic calculations that indicate that the oxidation of Ni, WO_3 and steam is presumably the rate-determining step.

Keywords: $NiWO_4$; redox reaction; chemical hydrogen storage; chemical looping.

September 18th to 21st, 2018 in Mexico City, Mexico.

XVIII International Congress
of the Mexican Hydrogen Society

Thermodynamic Evaluation and process simulation of the production of Hydrogen-Syngas Using Mixed Fe-based oxides with Methane

J.F. Cazares-Marroquin[1,2], J. M. Salinas-Gutierrez[2], M. J. Melendez-Zaragoza[2], V. Collins-Martinez[2], A. Lopez-Ortiz[2*]

[1]ESIQIE-Instituto Politécnico Nacional, Unidad Profesional Adolfo López Mateos, Edificio 8, Ciudad de México
[2]Departamentode Ingeniería y Química de Materiales, Centro de Investigación en Materiales Avanzados, S.C. Miguel de Cervantes 120, Chihuahua, Chih., 31136, México
*Alejandro López Ortiz: 6144394815, alejandro.lopez@cimav.edu.mx

---

ABSTRACT

Hydrogen-syngas production is one of the actual and continuous problem in the petrochemical and refining industry, whereas a process that exhibits an optimal industrial efficiency and usage is needed. The use of mixed metal oxides ($FeMO_4$, $FeMoO_4$, $Fe2ZnO_4$, Fe_2MnO_4) as oxygen carriers is proposed to minimize the disadvantages of the current partial oxidation of methane. The objective of the present work is to identify oxides that help the production of syn-gas and are able to regenerate through favorable conditions. This is accomplished by simulating an arrangement of two reactors. The main reduction reaction is carried out in the first reactor: $CH_4 + Fe_2MO_4 = H_2 + CO + Fe + M$. While in the second reactor the following reaction is carried out: $Fe + M + H_2O = Fe_2MO_4 + H_2$. Results indicate that It is possible for the oxide to be completely regenerated, while optimal reaction parameters were obtained for each reactor observing that the material were completely regenerated while not affecting the hydrogen. $FeMoO_4$ produced syn-gas at 750 ° C. However, it was possible not regenerate at favorable conditions. Otherwise, Fe_2ZnO_4 produced syn-gas at 730 ° C and regeneration was feasible at 440 °C. Finally, Fe_2MnO_4 produced syn-gas at 640 °C with regeneration at 600 °C, being the one with the best operating conditions among the studied materials. Simulation results of the different oxides are presented using Aspen-Plus©.

Keywords: Fe2MnO4; syn-gas; Hydrogen; reduction

XVIII International Congress
of the Mexican Hydrogen Society

SYNTHESIS, CHARACTERIZATION AND PHOTOCATALYTIC EVALUATION OF $NiWO_4$ FOR THE PRODUCTION OF H_2 BY WATER SPLITTING

Ma. G. Joaquín-Morales[1], A. F. Fuentes[1], S. M. Montemayor[2], W.J. Pech-Rodríguez[3], M. J. Meléndez Zaragoza[4], J. M. Salinas Gutiérrez[4], A. López Ortiz[4], V. Collins-Martínez[4]*

[1]CINVESTAV, Unidad Saltillo, C.P. 25900, Ramos Arizpe, Coah. México, [2]Centro de Investigación en Química Aplicada, Blvd. Enrique Reyna No. 140, Col. San José de los Cerritos, 25294 Saltillo, Coah. México, [3]Universidad Politécnica de Victoria, departamento de Ingeniería Mecatrónica. Av. Nuevas Tecnologías 5902, Parque Científico y Tecnológico de Tamaulipas, C. P. 87138 Ciudad Victoria, Tamps. Mexico.[4]Centro de Investigación en Materiales Avanzados S. C., Miguel de Cervantes 120, C. P. 31136, Chihuahua, Chih. México.
virginia.martinez@cimav.edu.mx

ABSTRACT

This work describes the synthesis through precipitation, characterization and photocatalytic evaluation of nickel tungstate ($NiWO_4$) under visible light irradiation for the production of H_2 by the water splitting reaction. This photocatalyst was obtained at room temperature by a dissolution-precipitation reaction between the corresponding Ni^{+2} and $(WO_4)^{-2}$ ions. The precipitation reaction was carried out with the addition of oleic acid (AO, 0.1 and 1%V) using two stirring methods: magnetic (AM) and shear stress (TU) stirring, each performed separately. Characterization was carried out by TGA, XRD, BET, SEM and UV-Vis spectroscopy. Photocatalytic evaluation under visible light irradiation was followed by GC analysis. The thermal behavior of the samples (TGA) revealed the physical and chemical absorption of the OA on the surface of $NiWO_4$, reflected in the increase of the weight loss as a consequence of the increase in AO content. XRD patterns confirmed the crystalline phase of the wolframite structure, with a crystallite size around 22 nm for AM and 22-25 nm for UT for 0.1 and 1% AO. The BET surface area of the samples were 22.43, 24.25 m^2/g and 27 and 18 m^2/g for AM and UT in both percentages of AO, respectively. UV-Vis diffuse reflectance characterization of the samples revealed that these materials present an indirect transition of Eg ~ 2 eV, which is favorable for their photoactivation under visible irradiation of the electromagnetic spectrum. The photocatalytic evaluation for sample 1% AO under UT resulted in a production of 6.5 µmol $H_2/g*h$, resulting in a sevenfold increase compared to WO_3.

Keywords: Photocatalysis, N_iWO_4, water splitting, visible light.

XVIII International Congress
of the Mexican Hydrogen Society

Photo-Assisted Synthesis of GO/ZnO Nanocomposites for the Production of Photocatalytic Hydrogen

B. C. Hernández-Majalca[1], E.J. Núñez-Murillo[2], S.A. Victor-Chavéz[3], J. L. Dominguez-Arvizu[1], J. Jiménez-Miramontes[1], J. C. Pantoja-Espinoza[1], M.J. Melendez-Zaragoza[1], J.M. Salinas-Gutiérrez[1], A. López-Ortiz[1], V. Collins-Martínez[1]*

[1] Departamento de Ingeniería y Química de Materiales, Centro de Investigación en Materiales Avanzados, S.C., Miguel de Cervantes 120, Chihuahua, Chih., 31136, México.
[2] Universidad Autónoma de Chihuahua, Facultad de Ingeniería, Circuito Número I s/n, Nuevo Campus Universitario II, 31100 Chihuahua, Chih.
[3] Instituto Tecnológico de Chihuahua, Avenida Tecnológico 2909, Colonia 10 de Mayo Chihuahua, Chihuahua, México
*virginia.collins@cimav.edu.mx

ABSTRACT

In this study, zinc oxide was synthesized by the precipitation method. Graphene oxide (GO) was prepared by oxidation of graphite powder using a microwave pretreatment. This GO was used for the modification of the photocatalytic properties of ZnO. Fixation of particles was carried out using a photoassisting technique by visible light irradiation. Characterization of the material consisted in morphology, crystalline structure and optical properties and these were performed by XRD, SEM, BET and UV-Vis spectrometry, respectively. Photocatalytic evaluation of the material towards the water splitting reaction was followed by gas chromatography, using a metal halide lamp of 250W as a light source in a quartz-sealed photocatalytic reactor, obtaining a production of 1,200 μmolH_2/g, showing an enhanced photocatalytic activity compared to ZnO.

Keywords: *graphene oxide, photo-anchoring, hydrogen production, ZnO/graphene oxide*

XVIII International Congress
of the Mexican Hydrogen Society

Evaluation of $NiWO_4$ as an oxygen carrier for the hydrogen storage by chemical looping.

P.E. González-Vargas; M.J. Meléndez-Zaragoza; J.M. Salinas-Gutiérrez; V. Collins-Martínez; A. López-Ortiz *

Centro de Investigación en Materiales Avanzados, S.C., Miguel de Cervantes 120, Complejo Industrial Chihuahua Chihuahua, Chih. México. C.P. 31136
* Tel: +52 6144394815; e-mail: alejandro.lopez@cimav.edu.mx

ABSTRACT

Chemical looping process (CL) have recently been used for various purposes, one of which is the hydrogen storage using metal oxides (MeO) as the only source of oxygen (oxygen carriers) to produce water ($MeO + H_2 = Me + H_2O$) and regenerating the metal oxide with a steam oxidizing atmosphere for the hydrogen release ($Me + H_2O = MeO + H_2$). It is important that these oxygen carriers have certain characteristics to be used for this purpose, such as thermal stability and the ability to store and release the lattice oxygen to the cyclic reaction conditions. In order to evaluate the nickel tungstate ($NiWO_4$) for this purpose, it was thermogravimetrically tested (TGA) in three accelerated redox cycles using a mixture of 5 v% of H_2/Ar as a reducing atmosphere and a mixture of 5 v% H_2O/Ar gas stream as the oxidizing atmosphere. Characterization made to the material before and after the redox cycles were performed by XRD, BET surface area, and SEM and have shown its favorable potential as an oxygen carrier when testing its thermal and reactive stability after three consecutive redox cycles. TGA tests revealed an oxidation mechanism of the reduced metals (Ni + W) that follows a reaction path, which consists in the formation of WO_3 by the oxidation of W with steam, followed by the formation of $NiWO_4$. This reaction path was confirmed by thermodynamic calculations that indicate that the oxidation of Ni, WO_3 and steam is presumably the rate-determining step.

Keywords: $NiWO_4$; redox reaction; chemical hydrogen storage; chemical looping.

XVIII International Congress
of the Mexican Hydrogen Society

SYNTHESIS AND CHARACTERIZATION OF $NiTiO_3$ NANOPARTICLES AND AgCl/Ag/$NiTiO_3$ NANOCOMPOSITES FOR IMPROVEMENT OF THE PHOTOCATALYTIC HYDROGEN PRODUCTION

J. C. Pantoja-Espinoza[1], M. J. Meléndez-Zaragoza[1], J. M. Salinas-Gutiérrez[1], J. L. Dominguez-Arvizu[1], J. Jiménez-Miramontes[1], C. Hernández-Majalca[1], A. López-Ortíz[1], V. H. Collins-Martínez[1*]

[1]Departamento de Ingeniería y Química de Materiales, Centro de Investigación en Materiales Avanzados, S. C., Miguel de Cervantes 120, Chihuahua, Chih., 31136, México.

* e-mail: virginia.collins@cimav.edu.mx

ABSTRACT

At present, the environmental pollution caused by the burning of fossil fuels have triggered to look for a sustainable and renewable source of energy to replace these fuels. Hydrogen is considered as an important energy carrier for the future, showing a number of advantages. Hydrogen can be produced through different methods. Hydrogen production through photocatalytic water splitting is a current challenging research area that requires high catalytic activity materials. The objective of the present work, is to prepare highly active photocalysts in order to enhance the water splitting hydrogen production. $NiTiO_3$ nanoparticles and AgCl/Ag/$NiTiO_3$ nanocomposites were prepared by sol-gel and chemical deposition-photoreduction methods, respectively. $NiTiO_3$ powders were synthesized by both the sol–gel and autocombustion reaction techniques. Chemicals used for the sol-gel technique were citric acid, titanium (IV) isopropoxide, nickel nitrate, acetic acid and ethylene glycol. While, chemicals employed for the autocombustion route were citric acid, titanium (IV) n-butoxide and nickel nitrate. The AgCl/Ag/$NiTiO_3$ nanocomposite was prepared with $NiTiO_3$ (synthesized by sol-gel and autocombustion) silver nitrate and hydrochloric acid. Synthesized powders were characterized by thermo-gravimetric analysis (TGA), X-ray diffraction (XRD), Brunauer–Emmett–Teller (BET) surface area and UV–vis diffuse reflectance spectroscopy. XRD measurements were carried out to determine the crystalline structure of the calcined samples. UV–vis diffuse reflectance spectra were measured on a UV–vis spectrophotometer equipped with an integrating sphere. Spectra were collected in the range of 190–1100 nm. Band gap energies were determined by constructing Tauc plots for an indirect semiconductor from the calculated Kubelka-Munk functions of their corresponding diffuse reflectance spectra. The band gap energies were estimated by extrapolation of the absorption edge to the energy axis of the Tauc plot. In this research, samples were calcined at 650 °C for 4 hours. XRD study confirms the rhombohedral crystal structure and dense $NiTiO_3$ formation. BET surface areas found were 22 and 34 m^2/g and band gap energies were 2.2 and 2.1 eV for synthesized powder by sol-gel and autocombustion, respectively. Photocatalytic activity preliminary results indicated an enhancement in $NiTiO_3$ nanoparticles and AgCl/Ag/$NiTiO_3$ nanocomposites towards the photocatalytic hydrogen production.

Keywords: $NiTiO_3$; AgCl/Ag/$NiTiO_3$; hydrogen production; photocatalysis

September 18th to 21st, 2018 in Mexico City, Mexico.

XVIII International Congress
of the Mexican Hydrogen Society

$ZnFe_2O_4$ Synthesis Method Effect on its Photocatalytic Properties towards Hydrogen Production via Water Splitting

J. L. Dominguez-Arvizu, M. J. Meléndez-Zaragoza, J. Jiménez-Miramontes, B. C. Hernández-Majalca, J. C. Pantoja-Espinoza, J. M. Salinas-Gutiérrez, A. López-Ortiz, V. Collins-Martínez*

Departamento de Ingeniería y Química de Materiales, Centro de Investigación en Materiales Avanzados, S. C., Miguel de Cervantes 120, Chihuahua, Chih., 31136, México.

*virginia.collins@cimav.edu.mx

ABSTRACT

At present, photocatalysis for hydrogen production via water splitting, is a research area, which needs the development of active materials under visible light irradiation. Spinel-type transition metal ferrites (MFe_2O_4), unlike the well-known TiO_2, show remarkable activity under the visible electromagnetic spectrum, which makes them promising candidates for future applications on photocatalytic water splitting. In the present research, nanoparticles of $ZnFe_2O_4$ were synthesized by a solid-state reaction and Pechini's method and their synthesis, characterization and photocatalytic evaluation towards H_2 production by the water splitting reaction are compared. Both materials were characterized by TGA, BET Surface area, XRD, SEM and UV/Vis spectroscopy in order to obtain the structural, morphological, textural and optical properties of the $ZnFe_2O_4$ photocatalyst. Furthermore, photocatalytic activity for hydrogen production was evaluated by gas chromatography by measuring the amount of hydrogen at each hour up to a total period of 8 h. A quartz reactor with a solution of 2% methanol as a sacrificial agent and a 250 Watts metal halides lamp as source of radiation were employed. The comparison between the two synthesis routes of the $ZnFe_2O_4$ photocatalyst was performed.

Keywords: $ZnFe_2O_4$; water splitting, Visible light photocatalysis, hydrogen production

Electrocatalyst and Fuel Cells

September 18 to 21, 2018 in Mexico City, Mexico

XVIII International Congress
of the Mexican Hydrogen Society

Synthesis and characterization of $IrRuO_x/TiO_2$ electrocatalysts for the oxygen evolution reaction in acidic medium

A. Martínez-Séptimo[1,2], M.A.Valenzuela Zapata[1], R. de G. González Huerta[2*]

[1]Lab.Catálisis y Materiales, ESIQIE-Instituto Politècnico Nacional. Zacatenco, 07738, CDMX
[2]Laboratorio de Electroquímica y Corrosión, ESIQIE-Instituto Politècnico Nacional, Ed. Z-5, 3er piso, UPALM, C.P. 07738, México DF
Mail: abissaid@hotmail.com

ABSTRACT

Currently hydrogen is proposed as a viable energy vector considering its high energy density per unit mass compared and the by-products of its combustion do not generate an environmental impact.The most efficient and clean method for producing high purity hydrogen is the PEM electrolysers, however, it involves very high costs because the catalytic layer of the cathode and anode where the evolution of hydrogen and oxygen is carried out, respectively is made up of scarce and high cost metals, such as Pt, Ru and Ir. Therefore, there is a need to obtain electrocatalysts with a lower charge of precious metals or, in contrast, with other noble metal-free compounds. In this research work $IrRuO_x$ supported on TiO_2 ($IrRuO_x/TiO_2$) was obtained by the impregnation method followed by an oxidative heat treatment using of $RuCl_3$, $IrCl_3$ as Ru sources. The studied electrocatalysts contained nominal 50% mixed metallic phase (Ru 40% wt. and Ir 10% wt) supported on 50% wt of TiO2 (Degussa P25). The prepared electrocatalysts were chemical and structurally characterized by means of XRF, XRD and SEM analyses. A typical cyclical and linear voltammetry was carried out by anodic scanning in a potential range of 0 to 1 V(NHE) and 1 to 1.68 V (ENH) in acid medium, respectively. $IrRuO_x/TiO_2$ electrocatalyst showed electrochemical stability practically equal to that of the commercial RuO_2-IrO_2 (3:1). Mass activity experiments were obtained at E= 1.6 V(NHE), showing values of 89 mA/mg_{metal} for $IrRuO_x/TiO_2$, which was higher than that obtained with the commercial electrocatalyst (60 mA mg_{metal}). These results were explained in terms of a higher and homogeneous dispersion of Ir and Ru oxides onto TiO_2 support.

Keywords: oxygen evolution reaction; ruthenium oxide; iridium oxide, anodic electrocatalysts

XVIII International Congress
of the Mexican Hydrogen Society

Pt_3Fe/C bimetallic alloy nanoparticles as electrocatalysts with improved activity for the oxygen reduction reaction

M. M. Tellez-Cruz[1*], M. A. Padilla-Islas[1], H. Cruz-Martinez[2], H. M. Alfaro-López[1], M. G. Salinas-Juarez[1], O. Solorza-Feria[1]

[1] Departamento de Química, CINVESTAV, Av. Instituto Politécnico Nacional 2508, Cuidad de México, C.P. 07360, México
[2] Programa de Doctorado en Nanociencias y Nanotecnología, CINVESTAV, Av. Instituto Politécnico Nacional 2508, Cuidad de México, C.P. 07360, México
* Corresponding author: +52 (55) 5747 3800. Ext. 4473, mtellez@cinvestav.mx

ABSTRACT

The synthesis of octahedral and octopods nanocatalysts of Pt_3Fe for oxygen reduction reaction (ORR) in acid media is presented. Catalysts were prepared through chemical reduction with the correct amount of oleylamine, oleic acid, and precursor salts ($Pt(acac)_2$ and $Fe(acac)_3$). In one of the two syntheses, we use dibenzyl ether and tungsten hexacarbonyl ($W(CO)_6$) as the solvent and reducing agent respectively. Subsequent, both catalysts were dispersing in a carbon matrix (Vulcan Carbon) previously thermally treated. The presence of the alloy Pt_3Fe in the nanoparticles was proved by XRD. STEM micrographs showed the morphology of the nanoparticles with an average 7-9 nm for octahedral and 12-14 nm in size for octopods. The electrochemical performance of Pt_3Fe/C was evaluated by cyclic voltammetry, CO stripping and rotating disk electrode in $HClO_4$ as the electrolyte. Octopods of Pt_3Fe/C nanocatalyst showed the best catalytic activity regarding mass activity and specific activity than commercially available 20-wt% Pt /C-Etek® catalyst. Therefore, this finding suggests a methodology for producing a carbon supported octopods nanocatalyst, which could be used as a cathode electrode in a PEM fuel cell.

Keywords: Pt_3Fe alloy; nanocatalyst; ORR; PEMFCs

XVIII International Congress
of the Mexican Hydrogen Society

Nanocatalyst of CuNiPt alloy, supported on reduced graphene oxide

Miguel Adrian Padilla-Islas [1*], Miriam Marisol Tellez-Cruz [1], Maria Guadalupe Salinas-Juarez [1], Hilda Margarita Alfaro-Lopez [1], Omar Solorza-Feria[1].

[1] Departamento de Química, CINVESTAV, Av. Instituto Politécnico Nacional 2508, Col. San Pedro Zacatenco, Delegación Gustavo A. Madero, México D.F. Código Postal 07360.

* 5535784453, adrianmapi@gmail.com

ABSTRACT

Controllable synthesis of non-noble alloys remains a significant challenge. Among core-shell nanoparticles of various combinations, those made of an inexpensive metal core and a noble metal shell has received particular attention.

The cores obtained with phases (111) which facilitate coverage at the same stage by the platinum which greatly favors the oxygen reduction reaction.

Nano-catalyst of NiCu is synthesized by two steps; reduction of non-noble metals as nuclei and decoration of platinum (shell) by galvanic displacement. New synthesis of catalysts for the reduction reaction of oxygen by the adequate amount of oleylamine and oleic acid and precursor salts of non-noble metals, Cu (acac)2 and Ni(acac)2 , and using morpholine borane as a reducing agent, and supported on a reduced graphene oxide matrix which confers electronic density to the catalyst. The prepared NiCu@Pt octahedral core-shell were characterized by TEM, octahedral nanoparticles have narrow size distribution, with a measured average edge length of 30 ±5 nm. The EDX analysis by elemental mapping show that three elements were found homogeneously distributed throughout nanoparticles. The XRD pattern shows characteristic peaks, it suggests that CuNi is decorated whit Pt. The metallic core inherits the crystal structure of its composing elements, i.e., the face-centered-cubic (FCC) structure. The diffraction peaks at can be assigned to (1 1 1), (2 0 0), (2 2 0) and (311) crystallographic planes, respectively, which correspond to FCC phase. The electrochemical performance of NiCu decorate with Pt/C was evaluated by cyclic voltammetry, CO stripping and rotating disk electrode in HClO4 as electrolyte. NiCu@Pt/C shows better catalytic activity in terms of mass activity 311mA/cm2 and specific activity, which is 246 mA/cm2 , respect to commercially available 20-wt% Pt/C-Etek® with mass activity of 105 mA/cm2 and specific activity of 184 mA/cm2

Keywords: nanocatalyst; ORR; PEMFCs nanoalloy.

XVIII International Congress
of the Mexican Hydrogen Society

NiPdPt trimetallic electrocatalysts towards the oxygen reduction reaction

H. Cruz-Martínez[1, *], M. M. Tellez-Cruz[2], C. A. Ramírez-Herrera[1], M. G. Salinas-Juárez[2], P. Calaminici[2], O. Solorza-Feria[2]

[1]Programa de Doctorado en Nanociencias y Nanotecnología, CINVESTAV, Av. Instituto Politécnico Nacional 2508, San Pedro Zacatenco, Gustavo A. Madero, C.P. 07360, Ciudad de México, Mexico
[2]Departamento de Química, CINVESTAV, Av. Instituto Politécnico Nacional 2508, San Pedro Zacatenco, Gustavo A. Madero, C.P. 07360, Ciudad de México, Mexico
* Corresponding author: hcruzm@cinvestav.mx

ABSTRACT

In this study, the synthesis and characterization of NiPdPt (60:20:20 wt. %) nanoparticles are analyzed towards the oxygen reduction reaction (ORR) in acid medium. We report a novel trimetallic nanocatalyst produced by a synthetic chemical route by reacting chemical reagents in oleylamine and oleic acid. The physical characterization of the synthesized nanoparticles was performed by X-ray diffraction (XRD), energy disperse X-ray spectroscopy (EDS) and scanning transmission electron microscopy (STEM). The presence of Ni, Pd, and Pt in the nanoparticles was confirmed by EDS and XRD. From STEM micrographs, a size distribution of nanoparticles in a range of 30-52 nm was obtained. In the electrocatalyst research, cyclic voltammetry (CV), CO stripping, and rotating disk electrode (RDE) were used for electrochemical characterization of the synthesized nanoparticles in acid medium. The NiPdPt/C nanocatalyst showed superior mass and specific activity compared to the commercial Pt/C towards the ORR in acid medium.

Keywords: NiPdPt nanoparticles; Nanocatalysts; Mass activity; Specific activity; Oxygen reduction reaction; PEM fuel cell technology

XVIII International Congress
of the Mexican Hydrogen Society

Comparative Study Of The Catalytic Activity Of Carbon Hollow Spheres And Chicken Manure-Derived Biocarbon As Metal-Free Electrocatalysts For The ORR In Acid Media

M. Salazar-Oropeza[1], B. Escobar-Morales[2], E. Reguera[3], J. Escorcia-García[4], F.J Rodríguez-Varela[1], I.L Alonso-Lemus[5*].

[1]Sustentabilidad de los Recursos Naturales y Energía, Cinvestav Unidad Saltillo, Av. Industria Metalúrgica 1062, Parque Industrial Saltillo-Ramos Arizpe, C.P. 25900, Ramos Arizpe, Coah., México.
[2]CONACyT, Centro de Investigación Científica de Yucatán (CICY), Unidad de Energía Renovable, Calle 43 No. 130 Col. Chuburná de Hidalgo, Mérida, Yucatán, C. P. 97200, México.
[3]Centro de Investigación en Ciencia Aplicada y Tecnología Avanzada-Unidad Legaria, Instituto Politécnico Nacional, Ciudad de México, Distrito Federal, México.
[4]CONACYT-CINVESTAV del IPN, Unidad Saltillo, Av. Industria Metalúrgica 1062, Parque Industrial, Ramos Arizpe 25900, Coahuila, México.
[5]CONACYT, Sustentabilidad de los Recursos Naturales y Energía, Cinvestav Unidad Saltillo.

* Corresponding author: ivalemus@gmail.com

ABSTRACT

One effective strategy to decrease the cost of Polymer Electrolyte Membrane Fuel Cells (PEMFCs) is the development of metal-free electrocatalysts. In recent years, carbon-based cathode materials have demonstrated a high catalytic activity for the Oxygen Reduction Reaction (ORR) in acid and alkaline media, aiming to avoid the use of expensive metals such as Pt and Pd. However, most of metal-free carbon-based electrocatalyst have poor performance in acid electrolytes. In this work, the evaluation of the catalytic activity of metal-free electrocatalysts for ORR is evaluated. Ordered mesoporous carbon hollow spheres (OMCHS) have been synthesized by the silica template method, while a second type of electrocatalysts has been obtained from the pyrolysis of chicken manure (ChMB). Both electrocatalysts have been submitted to functionalization with methanol by the intermittent microwave heating method (OMCHS-f and ChMB-f samples, respectively). The results obtained by the Rotating Ring-Disk Electrode (RRDE) technique in 0.5 mol L^{-1} H_2SO_4 show onset potential of the ORR of 0.5, 0.77, 0.75 and 0.65 V/RHE at ChMB, ChMB-f, OMCHS and OMCHS-f respectively. Meanwhile, functionalized electrocatalysts show an increase in current density from -1.24 to -1.62 mA cm^{-2} at 0.1 V / RHE (ChMB vs. ChMB-f) and from -3.55 to -4.07 mA cm^{-2} (OMCHS vs. OMCHS-f) at 0.1 V / RHE. Interestingly, the production of hydrogen peroxide (H_2O_2) ranges between 10-21 % for ChMB-f, which is higher than 2-11 % for OMCHS-f. Moreover, the number of electrons transferred has been determined between 3.5 and 3.9 for both functionalized metal-free electrocatalysts, close to the $4e^-$ transfer mechanism expected. Therefore, the functionalization

with methanol using the microwaves technique has a positive effect on the catalytic activity for the ORR of these metal-free cathode materials. Overall, OMCHS vs. OMCHS-f show an enhanced catalytic activity for the ORR, compared to ChMB and ChMB-f. Both metal-free electrocatalysts are cheap alternatives to Pt and Pd based cathodes for PEMFCs applications.

Keywords: Ordered mesoporous carbon hollow spheres, chicken manure, Oxygen Reduction Reaction, Metal-free electrocatalysts.

XVIII International Congress
of the Mexican Hydrogen Society

Electrochemical Studies of Ruddlesden-Popper Oxides $(Sr,Ln)_{n+1}(Fe,Co)_nO_{3n+1}$ for IT-SOFC Cathode Applications

K.P. Padmasree[1,2*], Ke-Yu-Lai[2] and A. Manthiram[2]

[1]Cinvestav Unidad Saltillo, Parque Industrial, Ramos Arizpe, Coahuila, 25900, México
[2]Materials Research Institute, The University of Texas at Austin, Austin, Texas, 78712, USA
* Corresponding author: phone number: 8444389600 (8521), e-mail: padmasree@cinvestav.edu.mx

ABSTRACT

A solid oxide fuel cell (SOFC) is an electrochemical device for the direct conversion of chemical energy to electrical energy with high efficiency, low emission of pollutants and excellent fuel flexibility at high operating temperatures around 1000 °C. The high operating temperatures leads to a number of problems such as thermal expansion compatibility, high cost, interface reaction between cell components etc. Therefore, reducing the operating temperature to an intermediate temperature (IT) around 600-800 °C is one of the main objective to increase the life time and decrease the overall SOFC cost. Two main problems associated with lowering the operating temperature is a decrease in ionic conductivity of the electrolyte and an increase in the polarization resistance of the electrodes. Therefore, current efforts have thus focused on developing new electrode materials with mixed ionic-electronic conductivity and electrolyte materials with high ionic conductivity for the intermediate temperature operation of SOFCs. For IT-SOFC cathode materials, mixed ionic-electronic conducting (MIEC) oxides have shown a great interest owing to their high electrocatalytic activity for the oxygen reduction reaction. In this context the Ruddlesden-Popper oxides with MIEC properties have attracted much attention as an alternative cathode material for the intermediate temperature operation of SOFCs. In this work we present a comparative study of the Ruddlesden-Popper phases $(Sr,Ln)_{n+1}(Fe,Co)_nO_{3n+1}$ (where n = 2, 3 and ∞, and Ln = La and Pr) to analyze their ability as cathodes for intermediate-temperature solid oxide fuel cells. As the value of n increases the overall electrical conductivity increases in the intermediate temperature range. Similarly, the symmetric cell studies show the polarization resistance decreases in the order n= ∞, 2 and 3. Comparing the different phases studied, n = 3 phase exhibited an enhanced performance and considered as a promising cathode material among the Ruddlesden-Popper series for IT-SOFC applications.

Keywords: solid oxide fuel cells; cathode; Ruddlesden-Popper oxides; electrochemical properties

September 18th to 21st, 2018 in Mexico City, Mexico.

XVIII International Congress
of the Mexican Hydrogen Society

Design and Synthesis of Cobalt-based Electrocatalysts for Oxygen Reduction Reaction

Yongjun Feng*, Haihong Zhong, Xiaoman Gong, Shuwei Zhang, Jing Wang

State Key Laboratory of Chemical Resource Engineering, Beijing University of Chemical Technology, No. 15 Beisanhuan East Road, Beijing, China, 100029
* Corresponding author: +86 10 6443 6992, yjfeng@mail.buct.edu.cn

ABSTRACT

Oxygen reduction reaction (ORR) plays a crucial role in alternative energy harvesting technologies, conversion and storage systems such as fuel cells and rechargeable metal-air batteries, which require the highly active and stable catalysts to make it feasible. Pt-based noble-metal catalysts are the state-of-art catalyst for ORR. However, some demerits containing high cost, limited availability, poor stability and detrimental environmental impacts block the development of electrochemical energy. Cobalt–based electro catalysts with excellent intrinsic activity and sufficient stability are seemed as a promising alternative to these precious metals. In addition, their structural diversity makes Co-based electro catalysts more concerned. Here we summarize the research currently available concerning the cobalt–based electro catalysts including oxides/chalcogenides and Co-N_x/C, and the synthesis methods with the corresponding impact factors of ORR performance, such as ligand effect, particle size effect, crystal structure, nanostructure, defects and active centers. Besides these, low cost and high performance are also being considered. However, it remains a great challenge to fabricate cobalt-based ORR electrocatalysts with comparable high performance.

Keywords: electrocatalysis; oxygen reduction reaction; cobalt chalcogenide; Co-Nx; synthesis method

XVIII International Congress
of the Mexican Hydrogen Society

Effect of Pd/C, PdMn/C, PdFe/C and PdZn/C synthesized using ionic liquids in the electro-oxidation of crude glycerol in alkaline media

I. Velázquez-Hernández[1], V. Lair[2], L. Álvarez-Contreras[3], M. Guerra-Balcázar[4], y N. Arjona[1,*].

[1]Centro de Investigación y Desarrollo Tecnológico en Electroquímica, Sanfandila, Pedro Escobedo, Qro., C.P. 76703, México.
[2]Institut de Recherche de Chimie Paris, CNRS-Chimie ParisTech, 11 rue Pierre et Marie Curie,75005 Paris, France.
[3]Centro de Investigación en Materiales Avanzados S.C., Complejo Industrial Chihuahua, Chihuahua Chi., C. P. 31136, México. Facultad de Ingeniería, División de Investigación y Posgrado.
[4]Universidad Autónoma de Querétaro, Querétaro, Qro., C. P. 76010, México.
* Corresponding author: +52(442 211 60 00 EXT 7874) wvelazquez@cideteq.mx

---

ABSTRACT

Crude glycerol as waste from the synthesis of biodiesel has been used in fuel cells to obtain electrical energy employing mainly Pt-based electrocatalysts. In the present work, nanoparticles of Pd/C, PdMn/C, PdFe/C and PdZn/C were synthesized and tested in the electro-oxidation reaction of crude glycerol. The synthesized materials were characterized by X-ray diffraction (XRD), X-ray fluorescence (XRF), thermogravimetric analysis (TGA), high-resolution transmission electron microscopy (HR-TEM) and cyclic voltammetry. On the other hand, crude glycerol was prepared by transesterification reaction in alkaline medium and temperature with edible vegetable oil, KOH and methanol. In addition, Pd, PdMn, PdFe and PdZn were synthesized and supported on Vulcan® carbon via green chemistry using the 2-hydroxyethylammonium formate ionic liquid. The composition obtained by XRF revealed the composition of $Pd_{82}Mn_{18}$, $Pd_{84}Fe_{16}$ and $Pd_{88}Zn_{12}$. The electrocatalytic evaluation were performed by cyclic voltammetry at 0.1, 0.5, 1 and 2 M of glycerol and crude glycerol in KOH 0.3M. Raman spectrum of crude glycerol showed bands of methanol, soaps and glycerol, and the Raman spectrum of purified glycerol exhibited the characteristically signals of analytical glycerol. On the other hand, PdMn/C exhibited a lower peak oxidation potential (0.0889 V vs. NHE) than the rest of the materials, this means PdMn/C required less energy to electro-oxidize glycerol resulting in a higher current density (8.1901 mA cm^{-2}) with respect to PdZn/C and PdFe/C at a concentration of 0.5M analytical glycerol. In summary, PdMn/C can be used as an alternative to Pt-based electrocatalysts for the efficient usage of crude glycerol as fuel for energy conversion applications.

Keywords: Pd/C; PdMn/C; PdZn/C; PdFe/C; crude glycerol; electrocatalyst.

XVIII International Congress
of the Mexican Hydrogen Society

Bioethanol as a sustainable energy source for fuel cell applications: the effect of polyaniline in Pd/carbon paper electrodes for bioalcohol oxidation

K. Perez-Flores[1], I. Velázquez-Hernández[1], V. Lair[2], M. Cassir[2], J. A. Bañuelos[3], L. Álvarez-Contreras[4], M. Guerra-Balcázar[5], and N. Arjona[1]*

[1]Centro de Investigación y Desarrollo Tecnológico en Electroquímica, Sanfandila, Pedro Escobedo, Qro., C.P. 76703, México.
[2]Institut de Recherche de Chimie Paris, CNRS-Chimie ParisTech, 11 rue Pierre et Marie Curie,75005 Paris, France.
[3]Centro de Innovación Aplicada en Tecnologías Competitivas, Departamento de Investigación y Posgrado, Omega 201, Fraccionamiento Industrial Delta, C.P. 37545, León, Guanajuato, México
[4]Centro de Investigación en Materiales Avanzados S.C., Complejo Industrial Chihuahua, Chihuahua Chi., C. P. 31136, México. Facultad de Ingeniería, División de Investigación y Posgrado.
[5]Universidad Autónoma de Querétaro, Querétaro, Qro., C. P. 76010, México.
* Corresponding author: wvelazquez@cideteq.mx;
Tel: +52 (442) 211 60 00 ext. 7874

ABSTRACT

Bioethanol was synthesized from Salicornia Bigelovii (a salt-tolerant plant) and because its nature, this plant was watered with seawater, converting it in an interesting sustainable energy source. Pani was growth electrochemically on carbon paper (Pani-T) for the further electrodeposition of Pd on both, carbon paper (T) and Pani-T. Physicochemical characterization was performed by XRD, TEM, EDX mapping, and XPS. Pani promoted shifts in binding energies of Pd because the formation of a metal/support interaction. Electrocatalytic evaluation of Pd/Pani-T for EOR resulted in a maximum current density of 295.88 mA cm^{-2} and, an oxidation potential of -0.41 V vs. NHE at 5 M ethanol, being this current almost 110 mA cm^{-2} higher than that found for the control. Pd/Pani-T presented also the highest current density for BioEOR (146.41 mA cm^{-2} at 3M bioethanol).

Keywords: Surface-enhance Raman spectroscopy; bioethanol; polyaniline; carbon paper.

XVIII International Congress
of the Mexican Hydrogen Society

Electrocatalytic effect of bimetallic nanoparticles AuM (M: Ag, Pt & Pd) in the sorbitol electro-oxidation in alkaline medium

L. J. Torres-Pacheco[1], L. Álvarez-Contreras[2], M. Guerra-Balcázar[3*], and N. Arjona[1]

[1]Centro de Investigación y Desarrollo Tecnológico en Electroquímica S. C., Parque Tecnológico Querétaro, Sanfandila, Pedro Escobedo, C.P. 76703, Querétaro, México.
[2]Centro de Investigación en Materiales Avanzados S. C., Complejo Industrial Chihuahua, Chihuahua, C. P. 31136, México.
[3]Facultad de Ingeniería, División de Investigación y Posgrado, Universidad Autónoma de Querétaro, Querétaro, C. P. 76010, México.
* Corresponding author: minbalca@yahoo.com.mx
Tel: +52 (442) 1921200 ext 65421

ABSTRACT

Sorbitol is a polyol that has driven much attention in the last years due to facility of producing it from biomass. Being considered among the 12 most important building blocks obtained from biomass, it's vastly used in the food, pharmaceutical and cosmetic industry. However, few works have been published in the last 20 years regarding the sorbitol electro-oxidation reaction (SOR), and those works were mainly focused on platinum alone material (mono and polycrystalline) in acid medium. As a first approach to understand the SOR and direct future works to the develop of more efficient electro-catalysts for alkaline fuel cells, we synthetized bimetallic AuM (M: Ag, Pt, & Pd) nanoparticles and tested them in a range of 10-1000 mM sorbitol, complemented by the effect of the electrolyte temperature 20-60 °C in the SOR. The nanoparticles where characterized by XRD, XRF, HR-TEM, TGA, and electrochemical tests. The synthetized nanocatalysts showed mean particles sizes ranging from 6 to 14 ± 1 nm, with metallic loadings around 20 %, which were used normalize the current values. The XRD patterns showed metallic face-centered cubic (fcc) structures for all the catalysts, and the electrochemical tests confirmed the presence of the metallic catalyst. The addition of platinum to the catalyst lowered the peak potentials to 0.14 V/NHE, while adding palladium increased the current densities up to 113 mA/cm^2, almost 3 times bigger than gold alone. These upgrades are believed to be to a synergic effect between the two metals in the adsorption mechanism of sorbitol and the oxidation/desorption of the SOR by-products.

Keywords: Sorbitol electro-oxidation, Alkaline media, Naparricles, Electrocatalysis

XVIII International Congress
of the Mexican Hydrogen Society

Oxygen reduction reaction on PtBi and PdBi alloys for PEMFC

O. X. Guerrero-Gutiérrez[1,*], M. A. Padilla-Islas[1], O. Solorza-Feria[1], P. B. Balbuena[2]

[1] Departamento de Química. Centro de Investigación y de Estudios avanzados, CINVESTAV-IPN. Av. IPN 2508, Zacatenco. México D.F.
[2] Artie McFerrin Department of Chemical Engineering, Texas A&M University, College Station, TX, USA
* Corresponding author: xguerrero@cinvestav.mx

ABSTRACT

Fuel Cells are a very promising alternative for clean energy production but commercializing them has been slowed down in great part by the high cost and instability of the catalysts. Pt is among the best catalyst for fuel cells because of its high activity towards the oxygen reduction reaction (ORR) and high stability. Preparing materials with less Pt content by alloying with different transition metals has shown to increase the electrocatalytic activity in some cases. This work focuses on evaluating the effect of Bi on Pt and Pd catalysts. Since Mexico is one of the largest Bi producers, it is also our objective to add value to this metallic national product. In this work, BiPt and BiPd nanoparticles were synthesized via chemical reduction and supported on a mesoporous carbon to evaluate their catalytic activities. The structure of the materials was characterized by XRD and TEM. Catalytic activities were measured via a thin film on a rotating disk electrode, getting the kinetic current generated at 0.9 V in acidic media and then compared with commercially available Pt nanoparticles. Cyclic voltammograms results show a non-Pt-like behavior. The results were also compared with theoretical density functional theory (DFT) calculations to examine the geometric and electronic structure to further explain the electrochemical behavior. Calculations were based on a slab model were adsorption energies for oxygen and density of states (DOS) analysis were performed for all adsorption sites. We show the changes in the descriptors of catalytic behavior d-band center and adsorption energy in respect to the Bi content.

Keywords: electrocatalyst; ORR; fuel cell; DFT

XVIII International Congress
of the Mexican Hydrogen Society

Effect of nitrogen precursors on graphene-doping and electrochemical evaluation as an active electrocatalyst for oxygen reduction reaction

N.M. Sánchez-Padilla[1], R. Benavides[1]*, E. De-Casas[2], J.A. Mercado[2], S. Fernández[2], D. Morales-Acosta[1]*

[1]Departamento de Procesos de Transformación de Plásticos, Centro de Investigación de Química Aplicada
[2]Laboratorio Nacional de Materiales Grafénicos, Centro de Investigación de Química Aplicada
Blvd. Enrique Reyna No. 140, Col. San José de los Cerritos, Saltillo, 25290; Coahuila, México.
*E-mail: roberto.benavides@ciqa.edu.mx, diana.morales@ciqa.edu.mx

ABSTRACT

Metal-free oxygen reduction reaction (ORR) catalysts are needed to have more available alkaline fuel cell technologies. In this study nitrogen-doped reduced graphene oxides (N-rGO) were obtained by hydrothermal reaction of graphene oxide with urea or amitrole. Graphene oxide (GO) was synthetized by Tour's method and simultaneously doped and reduced under hydrothermal process. N-rGO$_{urea}$ and N-rGO$_{amitrole}$ were characterized by XRD, TGA, Raman and FT-IR techniques. The electrocatalytic activity toward the ORR was evaluated in alkaline media by rotating disk electrode linear sweep voltammetry (RDE-LSV) at different rotating speeds. XRD, TGA and FT-IR results confirm the reduction of GO (rGO) while Raman spectra for N-rGO$_{amitrole}$ and N-rGO$_{urea}$ show a displacement of the G band located in ~1590 cm^{-1} confirming the successful doping of rGO. The LSV curves show a higher onset potential for N-rGO$_{amitrole}$ than N-rGO$_{urea}$ with (0.9 V vs 0.85 V) and a higher current density (4.6 mA cm^{-2}). Koutecky-Levich analysis indicated that N-rGO$_{amitrole}$ catalyze the ORR by a 4-electron pathway while N-rGO$_{urea}$ follows a 2-electron pathway.

Keywords: N-doped graphene, oxygen reduction reaction, fuel cells.

XVIII International Congress
of the Mexican Hydrogen Society

Platinum sulfides: Synthesis, characterization and performance towards ORR

A. Sigüenza Orozco[1*], G. Alonso-Núñez[2], M.T. Oropeza-Guzmán[3], Y. Gochi-Ponce[3]

[1]Instituto Tecnológico de Oaxaca, 68030, Oaxaca, Oax., México
[2]Centro de Nanociencias y Nanotecnología-UNAM, 22860, Ensenada, B.C., México
[3]Centro de Graduados e Investigación en Química. Instituto Tecnológico de Tijuana, 22000, Tijuana, B.C., México

* adriana.siguenza@gmail.com (+52) 951-119-1530

ABSTRACT

Proton exchange fuel cells (PEMFC) are an important alternative for clean energy generation, being the electrocatalyst a key component in this devices, however PEMFC performance is limited by the cathodic oxygen reduction reaction (ORR), since this reaction is slower than the anodic oxidation of hydrogen, platinum supported on electrically conductive carbon is the most widespread electrocatalyst used to this aim, however Pt is a rare precious metal which translates in high costs of electrocatalysts, therefore, it is desirable to decrease the Pt content of electrocatalyst materials by combining with another element, such as platinum chalcogenides which have been reported as efficient catalysts towards ORR, the aim of this work is to evaluate the physical and electrochemical characteristics of platinum sulfides synthesized by different methods.

Platinum sulfides were synthesized by solvothermal reaction (PtS/N-CNT O), N-CNT supported platinum sulfuration (PtS/N-CNT U) and chemical reduction at 1:1 and 1:3 stoichiometric ratio (PtS1:1/N-CNT and PtS1:3/N-CNT, respectively), N-doped carbon nanotubes (N-CNT) were used as support, the platinum content in these materials was calculated to be 20% versus 80% of N-CNT support. Physical characteristics of these materials were analyzed by X-Ray diffraction (XRD), scanning electron microscopy (SEM) and transmission electron microscopy (TEM), it was found that the cooperite phase of platinum sulfur were formed accompanied by crystalline platinum, it was also found that particle dispersion of catalyst synthesized by solvothermal method (PtS/N-CNT O) was optimal.

The electrochemical behavior of materials was analyzed in acidic media by cyclic voltammetry (CV) and linear sweep voltammetry (LSV) techniques under inert atmosphere and oxygen saturated atmosphere, respectively. CV indicates that PtS/N-CNT O material presents the best

electrocatalytic response. LSV analysis showed a lower response of PtS/N-CNT U when compared to other materials, it was also found that by varying the stoichiometric ratio of Pt and S in materials PtS1:1/N-CNT and PtS1:3/N-CNT the electrocatalytic behavior is affected, finally it was confirmed that PtS/N-CNT O shows the best electrocatalytical behavior towards ORR.

Keywords: Catalyst, ORR, PEMFC.

XVIII International Congress
of the Mexican Hydrogen Society

Synthesis and Evaluation of Nanostructured NiPt Catalyst for the Hydrogen Evolution Reaction

A. Velazquez-Osorio[1,*]; J.L. Reyes-Rodriguez [2]; O. Solorza-Feria [2]

[1]Instituto Politecnico Nacional – ESFM, Av. Instituto Politecnico Nacional SN, Edificio 9, Col. San Pedro Zacatenco, Gustavo A. Madero, 07738, Mexico
[2]Centro de Investigación y Estudios Avanzados del Instituto Politecnico Nacional – CINVESTAV, Av. Instituto Politécnico Nacional 2508, San Pedro Zacatenco, Gustavo A. Madero, 07360, Mexico
* Corresponding author: +52-55-5747-3800 ext. 4473, contact@adrianvelazquez.com

ABSTRACT

Fuel cells are an attractive technology to produce efficient renewable energy; however, their use requires the constant feed of high-purity oxygen and hydrogen gases as fuel. Most of the hydrogen currently produced worldwide is obtained from gas reformation and cryopurification, processes which are highly contaminant and energy intensive. Water electrolysis is an attractive way to simultaneously produce hydrogen and oxygen gas for use fuel cells. In order to efficiently operate, an electrolyzer requires the use of catalytic materials to accelerate the decomposition of water into gas molecules.

This work explored the synthesis of NiPt catalysts with characteristic morphologies (e.g. spherical, core-shell), as well as, their performance for the hydrogen evolution reaction. The catalysts were prepared through the hot-injection method from Ni and Pt precursors with a variation of temperature and organic stabilizer concentration as important factors in the morphology of the synthesized material. The resulting particle possessed sizes ranging from 20-50 nm. The catalysts were subjected to physiochemical evaluation through SEM, TEM, XRD, linear and cyclic voltammetry. A 0.1M KOH solution was used as electrolyte. The catalytic properties of each nanostructured material were compared against each other and against commercial Pt-Etek.

Keywords: nanoshapes, electrolysis, NiPt

XVIII International Congress
of the Mexican Hydrogen Society

Methanol electro-oxidation on Ag and Pt supported in carbon Vulcan catalyst in alkaline condition

*J. Mateos Santiago, V. Silva Castro, L.P.A. Guerrero Ortega, J. Soto Hernández, C. R. Santiago Ramírez, M. Luna Trujillo, T. Poznyak, A. Manzo-Robledo**

Escuela Superior de Ingeniería Química e Industrias Extractivas (ESIQIE), Instituto Politécnico Nacional (IPN), Ciudad de México, 07738, México.
*e-mail: amanzor@ipn.com

ABSTRACT

Methanol is a promising fuel for direct methanol fuel cells in portable devices. A deeper understanding of its electro-oxidation is needed for evaluating electrocatalytic performance and catalyst design. In this work, nanoparticulate and clusters-like materials based on silver and platinum (Ag-Pt) were synthesized by impregnation method and the carbonyl chemical route, respectively. Sodium hexachloroplatinate and silver nitrate were employed as precursors. The as-prepared materials were supported in a carbon vulcan matrix and used as electro-catalyst for the methanol oxidation reaction (MOR) in alkaline condition. The structural and morphological characterization by X-ray powder diffraction and scanning electron microscopy (SEM) showed the formation of agglomerates in the nanometric scale. X-ray photoelectron spectroscopy analysis showed the different species of silver and platinum. The i-E profiles obtained by cyclic voltammetry technique in the monometallic indicated redox process attributed only to platinum, as expected. Whereas in the bimetallic material process associate with silver and platinum were observed. It was found that as-prepared Ag-Pt/C showed enhanced activity for the MOR and superior electron transfer ability compared to Pt/C. The interaction between Pt-CO_{ads} and Ag-OH_{ads} increase the current obtained in the electro-oxidation of methanol, having an important effect during MOR for applications in fuel-cell systems.

Keywords: Fuel cells, electro-catalysis, Ag nano-particles

XVIII International Congress
of the Mexican Hydrogen Society

Synthesis and Characterization of Pt_3Ni doped with Co Alloy Nanoparticles for the Oxygen Reduction Reaction

H.M. Alfaro- López[1], M.M. Tellez-Cruz[1], M.A. Padilla-Islas[1], H. Cruz-Martínez[2], M.G. Salinas-Juárez[1], O. Solorza-Feria[1].
*

[1]Departamento de Química, CINVESTAV, Av. Instituto Politécnico Nacional 2508, Col. San Pedro Zacatenco, Delegación Gustavo A. Madero, México D.F. C.P. 07360, México D.F. C. P. 07360. *Tel: +52 (55) 5747 3800, ext. 4473; e-mail: mtellez@cinvestav.mx

[2] Programa de Doctorado en Nanociencias y Nanotecnología, CINVESTAV, Av. Instituto Politécnico Nacional 2508, Col. San Pedro Zacatenco, Delegación Gustavo A. Madero.

ABSTRACT

With the industrial revolution began the development of transport. In the middle of the 18th century, the use of fuels increased the carbon dioxide emissions in the atmosphere, although at that time electric batteries had been an alternative, irreversibility was a limiting factor. Currently, fuel cells offer a potentially more efficient and cleaner source of energy due to their high efficiency as a result of the chemical energy converted directly to electrical energy with low emissions, compared with internal combustion engines. However, two significant technical gaps limit their commercialization: cost and reliability. The primary challenge in the widespread of fuel cell technology is to decrease the content of Pt in catalysts without losing their performance.
The synthesis of Pt_3Ni doped with Co nanocatalyst for oxygen reduction reaction (ORR) in acid media presented. The catalyst prepared through chemical reduction with the correct amount of oleylamine, oleic acid and precursor salts ($Pt(acac)_2$, $Ni(acac)_2$, $Co(acac)_2$ or $Co_6(CO)_2$), for subsequent dispersion in a carbon matrix (Vulcan Carbon) previously thermally treated. XRD proved the presence of the alloy Pt_3Ni doped with Co in the catalyst.TEM micrographs showed the morphology of the nanoparticles. Cyclic voltammetry evaluated the electrochemical performance of Pt_3Ni doped Co/C, CO stripping and rotating disk electrode in $HClO_4$ as the electrolyte. Pt_3Ni doped with Co/C nanocatalyst showed the best catalytic activity concerning mass activity and specific activity than commercially available 20 wt% Pt /C-Etek® catalyst. Therefore, this finding suggests a methodology for producing a carbon supported nanocatalyst which could use as a cathode electrode in a PEM fuel cell.

Keywords: Pt_3Ni doped with Co alloy; ORR catalyst; fuel cells.

XVIII International Congress
of the Mexican Hydrogen Society

Synthesis and characterization of N-doped carbon nanofibers modified with Co, Ni and Fe as electrocatalysts for the Oxygen Reduction Reaction in Alkalyne media.

D. Gómez-Cholula[1], R. Ojeda-López[2], G. Ramos-Sánchez [1,*]

[1]Departamento de Química, Área de Electroquímica, Universidad Autónoma Metropolitana-Iztapalapa, Avenida San Rafael Atlixco 186, Vicentina, 09340, Iztapalapa, CDMX, México.
[2]Departamento de Química, Área de Fisicoquímica de Superficies, Universidad Autónoma Metropolitana-Iztapalapa, Avenida San Rafael Atlixco 186, Vicentina, 09340, Iztapalapa, CDMX, México.
* Corresponding author: 55 519591115, gramossa@conacyt.mx

ABSTRACT

The search for low cost/high performance electrocatalysts for the oxygen reduction reaction (ORR) in fuel cells is crucial for fuel cells large scale utilization. It is essential the development of non-precious metal catalysts with high performance to reduce costs; in this regard, the active phases and support can be combined in a single phase with the presence of active sites, large area and porous structure to allow the transport of species. In a previous work, Carbon nanofibers (CNF) have been modified with inclusion of nitrogen as dopant leading to a single-phase material possessing good properties as support (high area, good electrical conductivity and transport of species) while the presence of Nitrogen lead to enhanced catalytic activity towards the ORR. In the present work, it is proposed a new electrocatalyst, which consists of carbon nanofibers doped with Co-N, Ni-N and Fe-N, aiming to improving the catalytic activity towards the ORR in fuel cells. These modified electrocatalysts are synthesized in-situ by the addition of the corresponding M-Phthalocyanines during the nanofiber formation, then they are calcined under N_2 at 800°C. The as obtained powders are analyzed by SEM and N_2 adsorption/desorption experiments as well as by cyclic voltammetry and rotating disc electrode experiments. The inclusion of the metals causes the diminishment of the specific surface area however it leads to an increase towards the ORR in comparison to N-doped fibers. This performance can be attributed to the modification of the electronic structure by the presence of both N and M doped sites.

Keywords: electrocatalyst, oxygen reduction reaction, carbon nanofibers, non-noble metal catalysts, Nitrogen doped materials.

This work was financially supported by the Project SECITI/080/2017

XVIII International Congress
of the Mexican Hydrogen Society

High surface area N-doped porous carbon from *Sargassum spp.* for oxygen reduction reaction in alkaline media

K. Pérez-Salcedo[1]; B. Escobar Morales [1,*]; I. Alonso Lemus[2], R. Barbosa[3]

[1] Centro de Investigación Científica de Yucatán. Carretera Sierra Papacal– Chuburná Puerto, Km. 5, Sierra Papacal, Mérida, 97302, México.
[2] Grupo de Sustentabilidad de los Recursos Naturales y Energía. CINVESTAV Unidad-Saltillo, Ramos Arizpe, Coahuila, 25900, México.
[3] Universidad de Quintana Roo, Boulevard Bahía S/n, Chetumal, C.P 77019, Quintana Roo, México

* Phone number: +529999300760 ext. 1203; e-mail: beatriz.escobar@cicy.mx

ABSTRACT

N-doped porous carbon (NPC) is a potential candidate as low cost metal-free electrocatalyst for oxygen reduction reaction (ORR) and catalyst support for low temperature fuel cells. *Sargassum spp.* is an algae that grows in the Sargasso Sea. In recent years, seaweed blooms have become a serious economic threat as well as an environmental disaster due to seaweed very fast growing.

In the present study, high surface area NPC catalysts were synthesized by thermochemical treatments (pyrolysis, activation and doping) from *Sargassum spp*. The raw sample (RS) was activated with KOH (SKPH) and doped with N_2H_4 (SKPHD). Electrocatalysts physicochemical properties were determined by nitrogen adsorption analysis by the Brunauer-Emmett-Teller method (BET), scanning electron microscopy (SEM), elemental analysis (CHNS), Raman spectroscopy, X-ray spectroscopy (XPS) and X-ray diffraction (XRD). SKPH and SKPHD possess high surface area (2289 and 1961 $m^2\ g^{-1}$, respectively).

Electrochemical experiments were performed in a conventional three-electrode test cell at room temperature in 0.5 M KOH and compared with commercial Pt/C catalyst. ORR was performed using rotary disk electrode (RDE) technique at 5 mV s^{-1} scan rate in O_2 saturated electrolyte at 200, 400, 800, 1200, 1600 and 2000 RPM rotation rates. SKPHD delivers a higher current density (j=6.1 mA cm^{-2}) compared with commercial 20% Pt/C (j=5.6 mA cm^{-2}) with the best onset potential (0.838 V) while SKPH shows a four-electron-transfer pathway which demonstrates the great potential of NPC as a low cost alternative for widespread fuel cells commercialization and as an alternative for disposal of seaweed in the Mexican Caribbean.

Keywords: N-doped porous carbon; *Sargassum spp.*; oxygen reduction reaction; KOH activation

XVIII International Congress
of the Mexican Hydrogen Society

Development of Pt and Pt-Ru nanocatalysts supported on N-doped Ordered Mesoporous Hollow Carbon Spheres for the Methanol and Ethanol Oxidation Reactions

J.H. Serna-Mata[1], J.A. Díaz-Guillén[1], M. Salazar-Oropeza[2], J. Escorcia-García[3], I.L Alonso-Lemus[4], F.J Rodríguez-Varela[2,*]

[1]Instituto Tecnológico de Saltillo, 25280-Saltillo, Coahuila, México
[2]Sustentabilidad de los Recursos Naturales y Energía, Cinvestav Unidad Saltillo, Av. Industria Metalúrgica 1062, Parque Industrial Saltillo-Ramos Arizpe, C.P. 25900, Ramos Arizpe, Coah., México.
[3]CONACYT-CINVESTAV del IPN, Unidad Saltillo.
[4]CONACYT, Sustentabilidad de los Recursos Naturales y Energía, Cinvestav Unidad Saltillo.
*javier.varela@cinvestav.edu.mx

The synthesis and characterization of Pt and Pt-Ru nanoparticles supported on N-doped Ordered Mesoporous Hollow Carbon Spheres (N-OMHCS) is presented. N-OMHCS have been synthesized by template method; first, silica spheres are obtained from tetraethyl orthosilicate (TEOS) by the Stöber method, followed by addition of cetyltrimethylammonium chloride (CTAC) and pyridine as carbon and nitrogen precursor respectively. The solution is then hydrothermally treated at 100°C for 24 hours, washed and dried. The resulting material is subjected to carbonization at 1000°C for 4h. Afterwards, the silica template is removed from the powder by leaching in HF solution. The obtained N-OMHCS are functionalized with methanol by intermittent microwave heating. The Pt/N-OMHCS and Pt-Ru/N-OMHCS nanocatalysts have been synthesized by the microwave-assisted polyol method. Their catalytic activity for the Methanol and Ethanol Oxidation Reactions (MOR and EOR) in acid media is compared to those of conventional Vulcan-supported Pt/C and Pt-Ru/C.

Keywords: N-doped Ordered Mesoporous Hollow Carbon Spheres, Pt/N-OMHCS and Pt-Ru/N-OMHCS nanocatalysts, Methanol and Ethanol Oxidation Reactions, Direct Alcohol Fuel Cells.

XVIII International Congress
of the Mexican Hydrogen Society

Thin film $CuBi_2O_4$ as a p-type photoelectrode for solar water reduction

Manuel Rodríguez-Pérez[1,*], Ingrid Rodríguez-Gutiérrez[2], Alberto Vega-Poot[2], Rodrigo García-Rodríguez,[2] Geonel Rodríguez-Gattorno[2], Gerko Oskam[2]

[1]Facultad de Ingeniería, Universidad Autónoma de Campeche, Campus V, Colonia Ex Hacienda Kála, San Francisco de Campeche, Campeche, Cam. 24085, México
[2]Departamento de Física Aplicada, CINVESTAV-IPN, Ant. Carr. a Progreso km 6, Mérida, Yuc. 97310, México
* Dr. Manuel Rodríguez Pérez: +529991716884 and mjrodrig@uacam.mx

ABSTRACT

Photoelectrochemical (PEC) water splitting is a promising approach to provide a clean and storable chemical fuel (e.g. hydrogen) directly from sunlight. However, it is crucial to identify new PEC materials that produce a high photocurrent density and provide a large photovoltage. One material that may be able to meet both of these requirements is $CuBi_2O_4$; this is a recently developed p-type metal oxide semiconductor with a spinel-type structure that has been studied for its magnetic, dielectric, optical and electrical properties. With a bandgap energy of 1.6-1.8 eV and a photocurrent onset potential near 1 V vs RHE and a high photoactivity, this material is interesting for the water reduction reaction in photoelectrochemical applications.

In this work, we present the synthesis of $CuBi_2O_4$, the structure, morphology; composition and optical light absorption properties, which were characterized by X-ray diffraction, SEM and UV-Vis spectrophotometry, respectively. Photoelectrochemical characterization was performed in a three-electrode system under illumination using a solar simulator. We show that this material has spherical particles with a good connectivity and porous films on FTO on a glass substrate with bandgap of 1.8 eV generate photoelectrons from the blue and visible part of electromagnetic spectrum. Current potential curves under chopped illumination shown that this material acts mainly as a p-type semiconductor and a cathodic photocurrent corresponding to water reduction is observed, however, an anodic photocurrent can also be obtained at potentials sufficiently positive. Intensity-modulated photocurrent spectroscopy measurements shown that an unfavorable balance of the rate constants for charge transfer and recombination limits the efficiency of the photoelectrode.

Keywords: Photoelectrochemistry; Water splitting; $CuBi_2O_4$ thin film

XVIII International Congress
of the Mexican Hydrogen Society

Electrochemical Comparative Study of PtCo/MNC and PtCo/rGO in Methanol Electro-oxidation in Acid Medium

D. Macias-Ferrer[1*], J.A. Melo-Banda[1], R. Silva-Rodrigo[1], M. Lam Maldonado[1], J.Y. Verde Gomez[2], U. Páramo García, P. Del-Ángel-Vicente[3], M.A. Meraz-Melo[4]

[1]TecNM/Instituto Tecnológico de Cd. Madero, Centro de Investigación en Petroquímica, Avenida de las bahías, Prolongación bahía Aldahir S/N, Altamira, Tamps., México
[2]TecNM/Instituto Tecnológico de Cancún, División de Estudios de Posgrado, Cancún, Quintana Roo, 77500, México
[3]Instituto Mexicano del Petróleo, Laboratorio de Caracterización de Materiales Naturales y Sintéticos, Ciudad de México, 07730, México
[4]Departamento de Ingeniería, TecNM/Instituto Tecnológico de Iztapalapa III, 09630, Ciudad de México, México
* Corresponding author: +52 (1) 833-3248014, maestro_macias@hotmail.com

---

ABSTRACT

PtCo/MNC and PtCo/rGO (20% wt Pt loading) electrocatalysts have been prepared by non sequential impregnation method and chemical reduction route by citric acid, ethanol and Ar-H_2 atmosphere. Micro/nano structured (MNC) sample was synthesized via nanocasting process using SBA-15 as hard template and refined sugar as carbon source. Graphene oxide (GO) was synthesized by modified Hummers method using graphite as carbon precursor. The prepared materials were characterized by means of N_2 physisorption analysis, X-ray diffraction (XRD), X-ray Photoelectron Spectroscopy (XPS), Fourier transform infrared spectroscopy (FTIR), Raman spectroscopy, scanning electron microscopy (SEM), energy-dispersive X-ray spectroscopy (EDS) and high resolution transmission electron microscopy (HRTEM). The performance of electrocatalysts for methanol oxidation reaction (MOR) was measured by cyclic voltammetry (CV), chronoamperometry (CA) and electrochemical impedance spectroscopy (EIS). The electrochemical characterization techniques revealed that the mass activity of PtCo/MNC, PtCo/rGO and of the commercial electrocatalyst Pt/C were 474, 323 and 182 mA/mg_{Pt} respectively as well as the total electron transfer resistance for these catalysts were 0.0825, 0.1416 and 0.4794 kΩ respectively. Therefore, Pt/MNC and Pt/GO exhibit better electrocatalytic performance and a best resistance to the electron transfer in electrode-electrolyte interface during methanol electro-oxidation.

Keywords: Platinum, Cobalt, Methanol Electro-oxidation

XVIII International Congress
of the Mexican Hydrogen Society

Palladium carbon-supported electrocatalyst for oxygen reduction reaction (ORR)

J. Soto-Hernandez[1]; C. R. Santiago-Ramirez[1,2]; E.Y. Cervantes-Aspeitia[1,2]; J. Vera-Iturriaga[2]; J. Mateos-Santiago[1]; M.L. Hernandez-Pichardo[2]; T. Poznyak[3]; A. Manzo-Robledo[1]

[1]Instituto Politécnico Nacional-ESIQIE, Laboratorio de Electroquímica y Corrosión, UPALM, 07738 México CDMX., México
[2]Instituto Politécnico Nacional-ESIQIE, Laboratorio de Nanomateriales Sustentables, UPALM, 07738 México CDMX, México.
[3]Instituto Politécnico Nacional-ESIQIE, Laboratorio de investigación en Ingeniería Química Ambiental, UPALM, 07738 México CDMX, México.
amanzor@ipn.mx

ABSTRACT

The development of catalysts in nanometric scale for enhancing the electrocatalytic activity and stability of materials used in fuel cells is a key factor to solve the energy and environmental problems that have become prevalent in our society. This situation still represents a major challenge due to the high cost and limited resources of noble metals such as platinum. Recent efforts have focused on the synthesis of palladium-based materials for oxygen reduction reaction (ORR). In this work, the catalytic activity of a homemade Pd (10 wt%) and PdCu (Pd 5wt%-Cu5wt%) carbon-supported catalysts as well as Pd/C (10 wt%) from commercial source has been studied for the ORR in alkaline media. Palladium and copper nanoparticles were supported on carbon vulcan (90 wt%) by impregnation method at 80°C for 3h. The synthetized electrocatalysts (Pd/C and PdCu/C) were characterized by scanning electron microscopy (SEM), X-ray diffraction (XRD) and X-ray Photoelectron Spectroscopy (XPS). Also, the electrocatalytic activity was monitored by cyclic and linear voltammetry. While electrochemical surface area (ECSA) was obtained from CO-stripping reaction. A crystallite size of ca. 5 and 12 nm, and ECSA values of 93.8 and 65.3 $m^2 g_{Pd}^{-1}$ for PdCu/C and PdC, were calculated. It was found that PdCu catalyst exhibit a better activity and enhanced stability for ORR than monometallic Pd/C, with an onset potential of 0.946 V/RHE and a half-wave potential of 0.81 V/RHE. These results are similar to those obtained from commercial Pd/C catalyst. The enhancement effects should be attributed to synergic effect of copper with palladium, crystallite size and higher ECSA. These results are promising for the designs of catalysts with lower noble-metals content to improve the activity of several energy-related electrochemical reactions.

Keywords: *Bi-metallic catalysts*, electrocatalysis, oxygen reduction reaction, interfacial reactions, fuel cells.

XVIII International Congress
of the Mexican Hydrogen Society

Effect of the Transition Metal Oxides (WO_3-ZrO_2) as a support for Oxygen Reduction Reaction

C. R. Santiago-Ramirez[1,2]; J. Soto-Hernandez[2]; J. Mateos-Santiago[2]; E.Y. Cervantes-Aspeitia[1,2]; O.A. Rodriguez-Alvarez[2]; A. Manzo-Robledo[2]; P. del Angel[3]; M.L. Hernandez-Pichardo[1, *]

[1]Instituto Politécnico Nacional-ESIQIE, Laboratorio de Nanomateriales Sustentables, UPALM, 07738 México CDMX, Mexico
[2]Instituto Politécnico Nacional-ESIQIE, Laboratorio de Electroquímica y Corrosión, UPALM, 07738 México CDMX., Mexico
[3]Instituto Mexicano del Petróleo, Dirección de Investigación y Posgrado, Eje Central L. Cárdenas 152, 07730 México CDMX., Mexico
* +5215557296000, mhernandezp@ipn.mx

ABSTRACT

Fuel cells generally use platinum-based electrocatalysts for the anode (hydrogen oxidation) and cathode (oxygen reduction) reactions. Recent efforts have focused on the development electrocatalysts with a small amount of this metal, or even platinum free. In this regard, it has been found that metal oxides electrocatalysts are promising materials for clean energy application. In this work, a nanostructured WO_3-ZrO_2 support (ZWC) composed by Vulcan carbon (60 wt. %), WO_3 (35 wt. %) and ZrO_2 (5 wt. %) was synthetized by coprecipitation method. Subsequently, platinum nanoparticles were added by impregnation method (10 wt. % Pt). For comparison a Pt/C (10 wt. %) reference sample was also synthesized by the same method. The electrocatalysts were characterized by nitrogen physisorption, scanning electron microscopy (SEM), high resolution transmission electron microscopy (HR-TEM) and X-ray diffraction (XRD). The catalytic activity was evaluated using Rotating Disc Electrode (RDE). In addition, electrochemically active surface area was determined by the CO stripping technique. The results show that the electrocatalysts are stable in alkaline media under experimental conditions employed. The Pt/ZWC material exhibited the higher electrocatalytic activity for the oxygen reduction reaction (ORR), in comparison to reference Pt/C material and Pt-Etek catalyst from commercial source. The higher catalytic activity could be attributed to the presences of the mixed metal-oxide support (WO_3-ZrO_2-C) such as high population of hydroxyl groups and hydrated state ($W(OH)_6$) promoting a bronze type formation on the surface during cathodic polarization. Furthermore, the bronze sites induce a faster electron transfers associated with spillover mechanisms, transferring protons and the formation of free Pt active sites.

Keywords: Metal-oxide-supports, Oxygen-reduction reaction, Pt nanoparticles

XVIII International Congress
of the Mexican Hydrogen Society

Photocatalysts Derived from Nitroprussides of Transition Metals for Hydrogen Evolution Reaction.

A. Diaz Lujan[1*]; P. Acevedo Peña [2]; M. Gonzalez-Montiel[2], J. Vazquez Samperio[1] and E. Reguera[1].

[1] Centro de Investigación en Ciencia Aplicada y Tecnología Avanzada Unidad Legaría IPN, 11500. Ciudad de México, México.
[2] CONACyT-Centro de Investigación en Ciencia Aplicada y Tecnología Avanzada Unidad Legaría IPN, 11500. Ciudad de México, México.

** Corresponding author: +52 5548118147 lujanalfred@icloud.com*

ABSTRACT

The responsibility and commitment of Latin American countries, like Mexico, to generate up to 35% of electricity through the use of renewable energy increases every day. In a quest to develop sustainable energy conversion processes, many research groups have attempted water splitting using sunlight. Among the different compounds, Nitroprussides (Np) presents high potential catalysts for hydrogen evolution reaction and quite promising for artificial photosynthesis systems.
It is important to study the catalytic activity of different materials, especially when using sustainable and cheaper semiconductors for photoactivated water oxidation. In this work, the synthesis, characterization and evaluation of photocatalysts for Oxygen Evolution Reaction (OER) derived from nitroprusside as new materials for this purpose, is presented. Nitroprussiates *(Np) M [Fe (CN)$_5$ NO]* where *M= Fe^{2+}, Mn^{2+}, Co^{2+} and Ni^{2+},* were synthesized by precipitation with drip systems and controlled agitation. These transition metals offer a variety of crystalline structures and compositions, characteristics that make these materials highly attractive to be employed as photocatalysts. The morphology of *Np* was characterized by SEM and the crystal structure by XRD. The spectroscopic characterization of the materials was carried out by FT - IR, Raman and UV-Vis. This characterization was performed before and after the photocatalytic evaluation, to determine the stability of the materials.
The photocatalytic activity of the Np for visible-light driven OER was examined in a reaction using a reactor what containing $[Ru(bpy)_3]^{2+}$ (bpy = 2,2'-bipyridine) as a sensitizer and $Na_2S_2O_8$ as an electron acceptor, respectively. The photo-irradiation was made with two 35W Xe, to characterize the response of materials. The transition metal determined the performed of the photocatalysts derived from the nitroprussides.

Keywords: Nitroprussides; Photocatalysts; Hydrogen Evolution Reaction (HER)

XVIII International Congress
of the Mexican Hydrogen Society

Green synthesis of platinum nanoparticles and nitrogen doped carbon from *Sargassum spp.* for electrochemical applications

D. Rosas[1], B. Escobar[2,*]

[1]Centro de Investigación Científica de Yucatán, A.C. Calle 43 No. 130, Col. Chuburná de Hidalgo, C.P. 97200, Mérida, Yucatán, México.
[2]Centro de Investigación Científica de Yucatán, A.C. Calle 43 No. 130, Col. Chuburná de Hidalgo, C.P. 97200, Mérida, Yucatán, México.
* 9993514293 beatriz.escobar@cicy.mx

ABSTRACT

The aim of this paper is the development of a new carbon based with platinum nanoparticles catalyst for PEM fuel cells, obtained through a process of pyrolysis of the waste biomass Sargassum spp. then adding the previously green synthesized platinum nanoparticles with the same waste biomass, the final product is a carbon based catalyst with 1% load of platinum in form of nanoparticles. Given the troublesome waste biomass deposited in the Caribbean beaches Sargassum spp. which generates tons of organic decomposing material thus affects the tourist sector and the ecosystem so it seems imperative the proper use of this waste. The nanoparticles were synthesized with a sample of Sargassum spp. through a process of drying, milling and sieve through a number 100 mesh, then boil 5gr of sample in 100ml of deionized water for 10min, filter the extract and then put 5ml of it in reaction with 95ml of a 1mM PtCl4 solution at 60°C for 2 hours in stirring, then the formation of nanoparticles was confirmed with a UV-vis analysis, later the sample was dried out in a hot plate and put in a tubular oven at 400°C for 2 hours, then the crystal formation was confirmed with a DRX analysis. Aside a sample of 10gr of the milled and sieved Sargassum spp. was activated with 20gr of KOH in 500ml of deionized water in stirring for 4 hours, after it was filtered through a no.1 Whatman filter and then pyrolyzed at 700°C in presence of nitrogen for 2 hours at a temperature rate of 10°C/min, the resulting carbon will be characterized to know the given surface area and porous size.

Keywords: Platinum nanoparticles; electrocatalyst; waste biomass; Sargassum spp.

XVIII International Congress
of the Mexican Hydrogen Society

Low Pt-Loading Electrocatalysts Supported On Ordered Mesoporous Carbon Hollow Spheres With High Performance for Oxygen Reduction Reaction

E. Garza-Durán[a], P.C. Meléndez-González[b], M. Salazar-Oropeza[a], J.H. Serna-Mata[c], I.L. Alonso-Lemus[d], F.J. Rodríguez-Varela[a,b,*]

[a] Sustentabilidad de los Recursos Naturales y Energía, Cinvestav Unidad Saltillo, Av. Industria Metalúrgica 1061, Parque Industrial Ramos Arizpe. Ramos Arizpe, Coahuila, C.P. 25900, México.
[b] Nanociencias y Nanotecnología, Cinvestav Unidad Saltillo, Av. Industria Metalúrgica 1061, Parque Industrial Ramos Arizpe. Ramos Arizpe, Coahuila, C.P. 25900, México.
[c] Instituto Tecnológico de Saltillo, Blvd. V. Carranza 2400, Saltillo, Coahuila, C.P.25280, México.
[d] CONACYT, Sustentabilidad de los Recursos Naturales y Energía, Cinvestav Unidad Saltillo, ,Av. Industria Metalúrgica 1061, Parque Industrial Ramos Arizpe. Ramos Arizpe, Coahuila, C.P. 25900, México.

* javier.varela@cinvestav.edu.mx 52 +844 438-9600 (Ext. 8526)

ABSTRACT

In this study, 5 wt. % Pt-based electrocatalysts supported on Ordered Mesoporous Carbon Hollow Spheres (OMCHS) were synthesized by the Polyol and Bromide Anion Exchange (BAE) methods and labeled as Pt/OMCHS-P and Pt/OMCHS-B, respectively. Their catalytic activity for the Oxygen Reduction Reaction (ORR) was evaluated in 0.5 M KOH by the Rotating Disk Electrode (RDE) technique and compared with that of a commercial 20 wt. % Pt/C electrocatalyst. FE-SEM analysis showed the porous morphology of the CHS, with an average diameter close to 260 nm. The chemical composition of Pt/OMCHS-P and Pt/OMCHS-B determined by SEM-EDS approached the nominally expected. The evaluation of catalytic activity indicated that both Pt/OMCHS-P and Pt/OMCHS-B have a higher catalytic activity than Pt/C for the ORR. The polarization curves showed that Pt/OMCHS-B and Pt/OMCHS-P have an onset potential of the ORR close to 1.0 V vs. RHE and current densities of -2.44 mA cm^{-2} and -2.19 mA cm^{-2} at 0.9 V vs RHE, respectively. According to Koutecky-Levich plots, the mechanism of the ORR at the low Pt-loading electrocatalysts proceeded via a $4e^-$ transfer. Moreover, the mass catalytic activity of the electrocatalysts supported on OMCHS was significantly higher than that of Pt/C. Therefore, these novel electrocatalysts showed enhanced catalytic activity for the ORR than commercial Pt/C, due their unique morphological and structural characteristics, that improve the mass and

electron transfer during the reaction. These results suggested that OMCHS are a promising support for Pt-based cathodes for Anion Exchange Membrane Fuel Cell applications.

Keywords: Ordered Mesoporous Carbon Hollow Spheres (OMCHS), Pt-based electrocatalysts, Oxygen Reduction Reaction (ORR) in alkaline media.

XVIII International Congress
of the Mexican Hydrogen Society

Preparation of Pt and Pt-Ag nanostructured catalysts for alcohol oxidation reaction

Cano – Reséndiz O.[1*], Ruíz – Camacho B.[1], Fuentes – Ramírez R.[1], Galindo – Esquivel R. I.[1]

[1]Department of Chemical Engineering, Division of Natural and Exact Sciences, University of Guanajuato
Noria Alta S/N, Guanajuato, Guanajuato, CP 36000, México
* Phone: 4731443870, e – mail: o_cano_resendiz@hotmail.com

ABSTRACT

The search for new catalytic materials for direct alcohol fuel cells is the aim of this work. One of the main challenges presented by fuel cells is to have adequate catalytic material dispersed on a substrate to enhance its catalytic activity. We have synthesized by the ultrasound technique nanostructured electrocatalysts of Pt and Pt – Ag supported on Vulcan carbon (CV) and carbon nanotubes (NTC) with the goal of studying the effect of the properties of the substrate as electrical conductivity for the oxidation of methanol (MeOH). Particle size and metal dispersion were evaluated by transmission electron microscopy (TEM) and X-ray diffractometer (XRD) technique was used to determine the crystalline structure. Cyclic voltammetry (VC) and chronoamperometry (CA) were performed in acid and alkaline medium. Preliminary results show the Pt and Pt – Ag nanoparticles were successfully synthesized by the ultrasound method. The method is simple, economical and easy to control, and the time spent is relatively little. By means a greater dispersion of the metallic phase was observed in monometallic catalysts compared with bimetallic catalysts due to the tendency of the Ag to agglomerate. The synthesized materials catalyze the oxidation reaction of methanol (MOR), however, the presence of Ag and the substrate used play a key role in the oxidation of methanol. When using Vulcan carbon as a substrate, the Pt-Ag / C shows the highest oxidation peak of methanol (5.1 mA cm^{-2}) with respect to Pt / C (4.4 mA cm^{-2}). When using NTC, it was observed that the bimetallic material Pt-Ag / NTC presents a lower intensity of the peaks of oxidation and electro-oxidation of methanol.

Keywords: Fuel cells, Catalysts, ultrasound

XVIII International Congress
of the Mexican Hydrogen Society

Study of the electrochemical performance of heteroatom-doped carbon nanostructures as cathodes of alkaline fuel cells

C.J. Parga-Marruffo[1], J.A. Díaz-Guillén[1], J. Escorcia-García[2], M.Z. Figueroa-Torres[3], A. Fernández-Fuentes[4] FJ Rodriguez-Varela[5], I-L Alonso-Lemus[6,*]
,*

[1]Instituto Tecnológico de Saltillo. Blvd. Venustiano Carranza 2400 Tecnológico, Saltillo Coahuila 25280
[2]CONACYT-CINVESTAV del IPN, Unidad Saltillo, Av. Industria Metalúrgica 1062, Parque Industrial, Ramos Arizpe 25900, Coahuila, México.
[3]Facultad de Ingeniería Civil, Universidad Autónoma de Nuevo León, Av. Universidad s/n, Ciudad Universitaria, San Nicolás de los Garza, Nuevo León, C.P. 66451, México
[4]Ingeniería Cerámica. Cinvestav Unidad Saltillo
[5]Sustentabilidad de los Recursos Naturales y Energía, Cinvestav Unidad Saltillo
[6]CONACYT Sustentabilidad de los Recursos Naturales y Energía. CINVESTAV, Unidad Saltillo,

* Corresponding author: 01 (844) 438 9626 ivalemus@gmail.com

ABSTRACT

Global energy demand is constantly increasing, which requires alternative forms to produce energy that does not depend on fossil fuels. Promising alternatives to fossil fuels and common batteries are fuel cells. Fuel cells are electrochemical devices that use hydrogen and oxygen producing energy with high efficiency and low/zero emissions. One of the biggest difficulties for these technologies scalability is the use of noble metals as platinum as catalyst in the inner reactions. A promising alternative to replace noble metal is the development of novel heteroatom-doped carbon materials as metal-free electrocatalysts. The main objective of this project is to synthesize, characterize and evaluate the electrochemical performance of graphenes and nanofibers doped with heteroatoms such as N and S, as cathodes of alkaline fuel cells.
Graphenes were synthesized by mechanical milling 8 hours using graphite as carbon precursor and aluminum powder as exfoliating agent. After that; graphenes were doped by microwave assisted doping using pyridine as nitrogen precursor (N-graphene) and dimethyl sulfoxide (DMSO) as sulfur precursors (S-graphene). Moreover, carbon nanofibers (CNF) were obtained by electrospinning using polyvinylpirrolidone (PVP) as carbon source and DMSO and pyridine as sulfur and nitrogen precursors respectively. Polymeric nanofibers then were thermally stabilized at 250°C for 24 hours before being pyrolyzed at 700°C during 90 minutes in N2 atmosphere. The metal-free electrocatalysts were labeled as N-CNF and S-CNF. Physicochemical

characterization will be performed by field-emission scaning electron microscopy, Raman and X-ray photoelectron spectroscopy. Electrochemical performance of the metal-free electrocatalysts will be performed by rotating ring-disc electrode (RRDE) technique in order to evaluate the catalytic activity for the oxygen reduction reaction in alkaline electrolyte.

Keywords: heteroatom-doped graphene; heteroatom-doped nanofiber; metal-free electrocatalyst; microwave assisted doping.

XVIII International Congress
of the Mexican Hydrogen Society

Theoretical study of hydrogen adsorption on graphyne doped with N and transition metal atoms: the quest for novel singles atom catalysts

Christian A. Celaya[1*], Jesús Muñiz[2,3], Luis Enrique Sansores[1]

[1]Departamento de Materiales de Baja Dimensionalidad, Instituto de Investigaciones en Materiales, Universidad Nacional Autónoma de México, Apartado postal 70-360, Ciudad de México, 04510, México.
[2]Instituto de Energías Renovables, Universidad Nacional Autónoma de México, Priv. Xochicalco s/n, Col. Centro, Temixco, Morelos CP 65580, México.
[3]CONACYT-Universidad Nacional Autónoma de México, Priv. Xochicalco s/n, Col. Centro, Temixco, Morelos CP 65580, México.
* Corresponding author: Tel.: 5545478526; E-mail: acelaya@iim.unam.mx

ABSTRACT

In this theoretical work, we present the results from Dnsity Functional Theory (DFT) calculations on novel system formed by graphyne-γ (GY-γ) with defects and doped with N and transition metal atoms (M). Systems with vacancy defects present a widening on the band gap. We found that the properties of the GYM family may be tuned, from a semiconducting to a metallic character. This may be due to the presence of N atoms in acetylenic linkages. The adsorption of metallic atoms in the GY-substrates is very favorable for the Pt atom. The system with vacancy defects presents high values in the adsorption energy (-6.84 eV) of the Pt atom. All the M@GY-complexes shown to generate thermodynamically stable system with different electronic properties, which can be further confirmed by *ab initio* Molecular Dynamics simulations. The catalytic character of the series of Pt@GY-complexes under study was tested by assessing the capability to absorb the H_2 molecule on the M@GY-complexes (single atom catalysts). It was discovered that the Pt@GYN-β complex represent the model that was able to absorb the H_2 molecule (-0.80 eV) onto the surface, due to the modified electronic structure after the N and Pt-doping. The minimum energy path (MEP) was also studied, in order to find the energy barriers in the dissociation of H_2O molecule. Such M@GY complexes represent potential candidates to be implemented as catalysis in devices such as fuel cell materials. All calculations were made using the Quantum-Espresso 6.1 computer code.

Keywords: Density Functional Theory, Fuel Cells, Energy storage.

XVIII International Congress
of the Mexican Hydrogen Society

EFFECT OF EPITAXIAL GROWTH OF BIMETALLIC NANOCRYSTALS ON THE ACTIVITY OF ELECTROCATALYSTS IN THE OXYGEN REDUCTION REACTION

F. F. Tello Casas[1], R. de G. González Huerta[1], M. L. Hernández [2], P. del Ángel Vicente[3]

[1] ESIQIE-IPN, Laboratorio de Electroquímica y Corrosión, Ed. Z-5, 3er piso, C.P. 07738, México D.F.
[2] ESIQIE-IPN, Laboratorio de Investigación de Nanomateriales, Ed. Z-5, 2er piso, C.P. 07738, México D.F.
[3] IMP, Laboratorio de Microscopia Electrónica de transmisión, C.P. 07730, México D.F.
Mail: f.tello_99@hotmail.com

ABSTRACT

The use of renewable energy is the best solution to stop the global warming and exhaustion of fossil fuels. The advantages of fuel cells are: high efficiency, do not generate pollutant emissions, low maintenance costs and wide ranges of energy.
However, the high cost of noble metals has limited the application of fuel cells. To overcome this problem, the use of bimetallic nanoparticles has been proposed.
The interaction of two or more metals at the nanometric level can form alloys, metal aggregates, core-shell nanoparticles with properties different from monometallic particles.

In this work, bimetallic nanoparticles Pt-Pd were synthesized by surface oxide-reduction reactions and evaluated catalytically towards oxygen reduction reaction. Physicochemical characterization was performed, using analysis techniques such as X-ray diffraction, transmission electron microscopy (HRTEM and STEM), and Raman spectroscopy. In the analyzes obtained the bimetallic nanoparticles well dispersed on carbon Vulcan, and with morphology truncated octahedrons. There was catalytic activity towards ORR, it was obtained a current density of 5 mA cm^{-2} in 0.7 V to 1600rpm. With well-defined plateaus and one Tafel slope 65mV dec^{-1}.

Keywords: oxygen reduction reaction; surface oxide-reduction reactions; bimetallic nanoparticles

XVIII International Congress
of the Mexican Hydrogen Society

Mexican contributions for the improvement of electrocatalytic properties for the oxygen reduction reaction in PEM fuel cells

H. Cruz-Martínez[1, *], M. M. Tellez-Cruz[2], O. X. Guerrero-Gutiérrez[2], C. A. Ramírez-Herrera[1], M. G. Salinas-Juárez[2], A. Velázquez-Osorio[2], O. Solorza-Feria[2]

[1]Programa de Doctorado en Nanociencias y Nanotecnología, CINVESTAV, Av. Instituto Politécnico Nacional 2508, San Pedro Zacatenco, Gustavo A. Madero, C.P. 07360, Ciudad de México, Mexico
[2]Departamento de Química, CINVESTAV, Av. Instituto Politécnico Nacional 2508, San Pedro Zacatenco, Gustavo A. Madero, C.P. 07360, Ciudad de México, Mexico
* Corresponding author: hcruzm@cinvestav.mx

ABSTRACT

Like the rest of the world, Mexico faces severe environmental challenges due to its energy dependence on fossil fuels, for that reason Mexican researchers have conducted studies related to the development of renewable energy technologies. In this sense, different research groups have contributed top quality results in the design, synthesis, characterization, and evaluation of the performance of electrocatalysts for the oxygen reduction reaction (ORR) in proton exchange membrane fuel cells (PEMFC). This work describes Mexican contributions to the design of new nanocatalysts for the cathodic reaction in fuel cells. Two categories of nanocatalysts are discussed, those based on Pt and those which are Pt-free, with special attention given to Pd and Ru-based materials, whose catalytic activities are noteworthy. Mexican scientific groups have published more than 100 articles on the ORR in the last 20 years, with over 50% of those publications focused on the performance of Pt-based catalytic compounds which have shown high active and stable surface area, and low catalyst loading. The remaining publications address Pt-free nanoparticles that present catalytic activity for the ORR.

Keywords: Pt-based nanocatalysts; Pt-free nanocatalysts; Mass activity; Specific activity; Oxygen reduction reaction; PEM fuel cell technology

XVIII International Congress
of the Mexican Hydrogen Society

Effect of the Oam/Oac ratio in the synthesis, characterization, and performance of Ni-Pt nanoparticles as catalysts for the Oxygen Reduction Reaction in PEM fuel cells.

J.L. Reyes-Rodríguez[1,*], O. Solorza-Feria[2]

[1]Departamento de Química, Centro de Investigación y de Estudios Avanzados del I.P.N., Av. IPN 2508, Col. San Pedro Zacatenco, 07360, Ciudad de México, México.
* Corresponding author: (55) 3084 9664 ; jreyes@cinvestav.mx

ABSTRACT

Recent research has focused on the control of the shape of nanoparticles to improve the catalytic activity for the oxygen reduction reaction (ORR) in PEM fuel cells. The use of organic reagents such as oleylamine (Oam) and oleic acid (Oac) during a thermo-chemical reduction synthesis allows the production of nanoparticles with characteristic morphologies. This work studied the effect of the Oam:Oac ratio in the size, morphology, and catalytic activity of synthesized Ni-Pt nanomaterials. Electrochemical tests using rotating disk electrode techniques were used to evaluate the catalytic activity towards the ORR in acid media. HRTEM, SEM, EDS, and XRD were performed to study the physical properties of the nanocatalysts. Additionally, material stability and H_2O_2 formation were also evaluated. From the synthesis and characterization results, the best-performing nanomaterial was chosen and applied as a cathode in single-cell performance evaluation. Later, a PEMFC prototype composed of six single-cells was constructed and tested. Experimental results revealed that the use of Oam and Oac favored the synthesis of nanomaterials that presented a polyhedral morphology and Pt segregation to the edges of the nanoparticles; the exclusive use of oleylamine during the synthesis resulted in particles with the best catalytic activity for ORR. On the other hand, an increase of oleic acid content during the synthesis resulted in nanoparticles smaller in size and variations in the morphology, namely, a transition of well-defined polyhedral to spheres, bi-pyramidal or amorphous shapes. Greater oleic acid content also causes a decrease in Ni content through the formation of a Ni-carboxylate complex and a lower catalytic activity. Electrochemical stability tests showed the formation of cavities on the faces of the nanoparticles after of 10,000 cycles of voltammetry degradation. Despite degradation, the Ni-Pt nanomaterial synthesized exclusively with Oam was able to perform with a specific activity that was 7 times higher than Pt/C-ETEK, and a mass activity 1.5 times greater, respectively.

Keywords: Polyhedral Ni-Pt nanoparticles, Oxygen reduction reaction, Fuel cell prototype

XVIII International Congress
of the Mexican Hydrogen Society

Qualities of Mn^{3+} sites in Nickel-based layered double hydroxides throughout methanol electro-oxidation in alkaline media

Stephany N. Arellano-Ahumada[1*], Miguel A. Oliver-Tolentino[2], Guadalupe Ramos-Sánchez[3], Carlos E. Moreno-Crespo[1], Juvencio Vazquez-Samperio[4], Arturo Manzo-Robledo[5], Ariel Guzmán-Vargas[5], Daniel Ramírez Rosales[1]

[1]Instituto Politécnico Nacional, ESFM-Departamento de Física, UPALM Edif. 9 Zacatenco, GAM CdMx 07738, Mexico.
[2]Instituto Politécnico Nacional, UPIBI, GAM CdMx 07340, Mexico.
[3]Universidad Autónoma Metropolitana-Iztapalapa, Departamento de Química, CdMx 09340, Mexico.
[4]Centro de Investigación en Ciencia Aplicada y Tecnología Avanzada Unidad Legaría IPN, 11500. CdMx
[5]Instituto Politécnico Nacional, ESIQIE, UPALM Edif. 7 Zacatenco, GAM CdMx 07738, Mexico

* torchynsnat@yahoo.com.mx

ABSTRACT

In the context of global environmental problems, triggered from the use of fossil fuels, new electrochemical devices capable to carry out direct transformations of plentiful raw materials into energy, arises as an ecofriendly and cost-effective process. This means the impulse of other sources of energy taking into account the depletion of conventional sources e.g. petroleum, carbon, etc.

Ni-based layered double hydroxides (LDHs), or hydrotalcite-like materials (HTs), were synthetized through coprecipitation at constant pH (NiAl and NiMg) and urea hydrolysis (NiMn) methods, and they were tested in the electrochemical methanol oxidation (MOR). The physicochemical properties were explored by using techniques such as X-ray diffraction, FT-IR spectroscopy, as well as electron paramagnetic resonance. In addition, correlation between active site arrangements and electrocatalytic activity was evidenced by density functional calculations.

Specific site m(Ni_2Mn-OH) showed the lowest proton energy removal at approximately 3.6 eV and the NiMn LDH sample containing a higher proportion of this site exhibited the best performance for the MOR process, with an enhancement factor of 5.16, which is attributed to limited deactivation of Ni during the reaction. CO_2 production was detected by differential electrochemical mass spectrometry to be on the order of ten times greater than O_2.

Keywords: electrochemical methanol oxidation, LDH

September 18th to 21st, 2018 in Mexico City, Mexico.

XVIII International Congress
of the Mexican Hydrogen Society

Study of the synthesis, characterization, and performance of polyhedral Ni-Pt nanocatalysts and their application as cathodes in PEM fuel cells.

J.L. Reyes-Rodríguez[1,*], O. Solorza-Feria[2]

[1]Departamento de Química, Centro de Investigación y de Estudios Avanzados del I.P.N., Av. IPN 2508, Col. San Pedro Zacatenco, 07360, Ciudad de México, México.
* Corresponding author: (55) 3084 9664 ; jreyes@cinvestav.mx

ABSTRACT

This work encompasses a study that addresses the synthesis, characterization, and performance evaluation of Ni-Pt polyhedral nanocatalysts for their application as cathodes in PEM fuel cells. The main objective of the study was the construction of a low-power fuel cell prototype; each stage involved in its construction, from the synthesis of catalysts to the preparation of membrane electrode assemblies (MEA's) is discussed. As a first stage, NiPt catalytic materials were synthesized by a thermo-chemical reduction route using the hot injection technique of the metal precursors in oleylamine (Oam) and/or oleic acid (Oac) as reaction agents. A synthesis optimization was achieved by exploring the effect that some variables like temperature, ratio of Oam:Oac, and variation of metallic composition had on the size, morphology, and catalytic properties of the nanoparticles. On a second stage, the synthesized catalysts were evaluated electrochemically to determine their stability and catalytic activity towards the oxygen reduction reaction (ORR). From those tests, the best material was chosen for use in the preparation of membrane electrode assemblies. On a third stage, a six monocell prototype was built. This prototype employed the best synthesized catalyst as cathode and was electrochemically characterized to measure its performance. This work resorted to several characterization techniques such as TEM, SEM, EDS, XRD, and electrochemical evaluations using RDE. Results revealed that the best polyhedral nanocatalyst for the ORR was synthesized by using only oleylamine as a reagent. The synthesized catalyst presented specific and mass activities greater than commercial Pt/C-Etek by a factor of 7 and 1.5, respectively. Nanomaterials synthesized with oleic acid possessed diminished catalytic activity. Single-fuel cell tests revealed that the chosen cathode nanocatalyst achieved a current density of 770 mA cm^{-2} and a power density of 308 mW cm^{-2} at 0.4 V.

Keywords: Polyhedral Ni-Pt nanoparticles, Oxygen reduction reaction, Fuel cell prototype.

XVIII International Congress
of the Mexican Hydrogen Society

Pd-$CeO_{2\text{-}NR}$/C Nanocatalyst With High Catalytic Activity and Stability for the Electrooxidation of Etanol in Alkaline Media

P.C. Meléndez González[1], M.E. Sánchez-Castro[1,2], I.L. Alonso-Lemus[3], R. Pérez-Hernández[4], F.J. Rodríguez Varela[1, 2*]

[1] Programa de Nanociencias y Nanotecnología, Cinvestav Unidad Saltillo, Av. Industria Metalúrgica 1062, Parque Industrial Ramos Arizpe. Ramos Arizpe, Coahuila, C.P 25900, México.
[2] Programa de Sustentabilidad de los Recursos Naturales y Energía, Cinvestav Unidad Saltillo.
[3]CONACYT, Sustentabilidad de los Recursos Naturales y Energía, Cinvestav Unidad Saltillo.
[4]Instituto Nacional de Investigaciones Nucleares, Carr. México-Toluca. S/N. La Marquesa, Ocoyoacac, Edo. de México, C. P. 52750, México.
*E-mail: javier.varela@cinvestav.edu.mx

ABSTRACT

Alkaline Direct Ethanol Fuel Cells (A-DEFCs) are considered efficient clean energy technologies with low environmental impact. A-DEFCs offer several advantages, such as the use of renewable ethanol, with easy handling of the liquid fuel. However, in order to reach a commercial status, it is necessary to overcome some scientific-technological challenges. For example, to increase their performance, highly active catalysts must be developed. Also, in order to reduce the fuel cell costs, the precious metal (Pt, Pd) content has to be minimized. Both issues can be addressed by using a suitable low-cost co-catalyst, such as CeO_2.
In this study, 20% Pd-$CeO_{2\text{-}NR}$/C (cerium oxide nanorods) nanocatalysts have been synthesized by the polyol method. Their catalytic activity for the ethanol oxidation reaction (EOR) is evaluated in 0.5 M KOH and the results compared to those of a Pd/C catalyst prepared by the same procedure. EDS analysis of the nanocatalysts indicates a chemical composition similar to the nominally expected. XRD results show crystalline catalysts having a crystallite size of 11.8 and 7.9 nm (Pd-$CeO_{2\text{-}NR}$/C and Pd/C, respectively). The polarization curves of the EOR show a peak mass current density of 697.70 mA mg_{Pd}^{-1} generated by Pd-$CeO_{2\text{-}NR}$/C (at 0.84 V/RHE) higher than the 663.66 mA mg_{Pd}^{-1} obtained from Pd/C (at 0.93 V/RHE). Meanwhile, the specific current density at Pd-$CeO_{2\text{-}NR}$/C (3.55 mA cm^{-2}) is about 2.4 compared to that of Pd/C. It has been determined that after accelerated degradation test (ADT, 2000 cycles between 0.05 and 1.2 V/RHE), the ECSA loss of Pd-$CeO_{2\text{-}NR}$/C is about 10 % (22 % in the case of Pd/C). Nevertheless, the current density of the EOR delivered by Pd-$CeO_{2\text{-}NR}$/C after ADT increases by 38.9 % compared to that before, which suggest an important activation of the nanocatalyst. The results shown in this work suggest that Pd-$CeO_{2\text{-}NR}$/C is a promising candidate for the A-DEFCs applications.

Keywords: Cerium Oxide nanorods as co-catalyst; Pd nanocatalysts; Ethanol Oxidation Reaction; A-DEFCs.

September 18th to 21st, 2018 in Mexico City, Mexico.

XVIII International Congress
of the Mexican Hydrogen Society

Electrochemical Measurements: Is It Easy to Work in Alkaline Medium?

C.A. Campos-Roldán,[1,2] R.G. González-Huerta,[2] N. Alonso-Vante [1]*

[1]IC2MP, UMR-CNRS 7285, University of Poitiers, 4 rue Michel Brunet, 86022 Poitiers, France

[2]Instituto Politécnico Nacional-ESIQIE, Laboratorio de Electroquímica y Corrosión, UPALM, 07738, CDMX, México

* Corresponding author: nicolas.alonso.vante@univ-poitiers.fr

---

ABSTRACT

This work revises the essentials of electrocatalytic electrochemical measurement done in alkaline electrolytes. The hydrogen oxidation reactions (HOR) and the oxygen reduction reaction (ORR) were considered as a baseline to understand some key critical factors in a half-cell system. The material considered herein was essentially the carbon supported platinum nanoparticles as the benchmark material. The main electrochemical techniques considered were cyclic voltammetry (CV) and the rotating disk electrode (RDE). The critical factors considered were the electrochemical cell, reference electrode, nature of the cation in the alkaline electrolyte, and ohmic drop correction.

Our results reveal the importance to not underestimate the aforementioned experimental factors, since the chemical glass etching at contact with alkaline solutions, the instability of many widely used reference electrodes, the iR compensation for kinetic parameters determination, and the interaction of the alkaline cation in the solution impact strongly the *measured performance* of the benchmark Pt/C material. Regardless the reaction, we suggest the use of Teflon electrochemical cells and the Hg/HgO reference electrode as a standard system for alkaline measurements and the iR compensation must be done. However, the interaction between the alkaline cation in the solution depends on the nature of the reaction: we suggest the use of KOH for oxygen reactions, meanwhile for hydrogen reactions there is not an significant effect.

Even though the development of novel materials, which are non-precious catalytic centers, are able to catalysts the ORR or the HOR in alkaline medium, it is crucial to make sure that experimental measurements (at least for the benchmark material) were carried out in a reproducible, comparable way.

Keywords: Alkaline fuel cells; experimental methods; HER/HOR; ORR

September 18th to 21st, 2018 in Mexico City, Mexico.

Fuel Cells components and stacks

September 18 to 21, 2018 in Mexico City, Mexico

XVIII International Congress
of the Mexican Hydrogen Society

Design of polymer nanocomposites based on polypropylene, carbon nanotubes and carbon nanofibers for application in bipolar plates

C. A. Ramírez-Herrera[a,*]; J. Pérez-González[b]; O. Solorza-Feria[c]; H. Martínez-Gutiérrez[d]; A. Flores-Vela[e]; J. G. Cabañas-Moreno[a]

[a]Programa de Doctorado en Nanociencias y Nanotecnología, CINVESTAV, Av. Instituto Politécnico Nacional 2508, Cd. de México, C.P. 07360, Mexico.
[b]Departamento de Física, Escuela Superior de Física y Matemáticas, Instituto Politécnico Nacional, Av. Instituto Politécnico Nacional s/n, Cd. de México, C.P. 07738, Mexico.
[c]Departamento de Química, CINVESTAV, Av. Instituto Politécnico Nacional 2508, Cd. de México, C.P. 07360, Mexico.
[d]Centro de Nanociencias y Micro y Nanotecnologías, Instituto Politécnico Nacional, Av. Luis Enrique Erro s/n, Ciudad de México, C.P. 07738, Mexico.
[e]Centro Mexicano para la Producción más Limpia, Instituto Politécnico Nacional, Av. Acueducto s/n, Cd. de México, C.P. 07340, Mexico.
* Corresponding author: 8331289066, caramirezh@cinvestav.mx

ABSTRACT

Compared to the internal combustion engines, proton exchange membrane fuel cells (PEMFCs) have attracted particular attention as alternative power devices in transportation applications due to their high efficiency, low operating temperature, and zero emissions; however, the manufacturing costs of fuel cell stacks are relatively high and limit their current commercial viability. Bipolar plates constitute a key component of PEMFCs concerning their cost and weight; therefore, one of the major challenges in the production of economical PEMFCs is the development of materials for bipolar plates which can be readily manufactured and have high electrical conductivity and adequate mechanical strength. In this sense, polymer nanocomposites filled with carbon-based nanofillers have shown several advantages as suitable materials for bipolar plates. In this work, polypropylene (PP) nanocomposites using multiwalled carbon nanotubes (MWCNT) alone or in combination with carbon nanofibers (CNF) have been prepared by melt mixing using different loadings of MWCNT and CNF. The nanocomposites obtained were molded by compression for subsequent characterization. The maximum in-plane electrical conductivity for the nanocomposites with a MWCNT content of 20 wt.% was around 3 S/cm, whereas for the nanocomposites combining 15 wt.% MWCNT and 15 wt.% CNF was about 8 S/cm. The addition of CNF to form hybrid PP/MWCNT/CNF nanocomposites allowed to increase to 30 wt.% the total content of nanofiller incorporated in the PP matrix and higher conductivities could be thus obtained. Moreover, the incorporation of 20 wt.% MWCNT in the PP matrix enhanced the tensile strength of the nanocomposites by 56% compared to the unfilled polymer, while the combined additions of 15 wt.% MWCNT and 15 wt.% CNF yielded an improvement of 63%. Similarly, the microhardness and elastic modulus of the nanocomposite

with 20 wt.% MWCNT increased by about 69% and 47%, respectively, whereas in the hybrid nanocomposite the increases were around 63 and 45%, respectively, compared to the PP matrix. In general, the results show a positive effect of the combination of both nanofillers on the electrical conductivity, strength, and stiffness of the nanocomposites.

Keywords: bipolar plates; polymer nanocomposites; MWCNT; CNF; electrical properties; mechanical properties

XVIII International Congress
of the Mexican Hydrogen Society

The space charge effect on the grain boundary conduction of $GdBaCo_2O_{5+\delta}$

C. I. Ramos-Villegas, H. J. Ávila-Paredes*

Departamento de Ingeniería de Procesos e Hidráulica, Universidad Autónoma Metropolitana, Unidad Iztapalapa, Av. San Rafael Atlixco186, Col. Vicentina, C.P. 09340, Ciudad de México, México.
*(52) 55 5804 4600 ext. 1243; hjap@xanum.uam.mx

ABSTRACT

Among the cathodic materials for Intermediate Temperature Solid Oxide Fuel Cells, $GdBaCo_2O_{5+\delta}$ has been recently proposed as a promising candidate based on its high mixed ionic-electronic conductivity values and compatibility with ceria based electrolytes. Generally, grain boundaries of ceramic conductors offer a blocking effect to oxygen ion conduction, either because of secondary phases or the space charge effect, while electronic conduction is enhanced. Regarding the space charge effect, a depletion of the oxygen vacancies concentration in the vicinity of the grain boundary cores, which have an excess of positive charges, causes that the grain boundaries behave as a barrier to ionic transport. In this contribution, the grain boundary resistivities of $GdBaCo_2O_{5+\delta}$ samples were characterized as a function of grain size. Impedance spectroscopic measurements were performed for the electrical characterization of the samples in the temperature range of 100 to 700 °C under air. The grain boundary characteristics will be discussed in the context of the space charge effect.

Keywords: grain boundary resistance; space charge effect; ceramic mixed ionic-electronic conductors.

XVIII International Congress
of the Mexican Hydrogen Society

Effect of the sulfonation in the properties of poly(styrene-co-butyl acrylate) for proton exchange membrane fuel cells.

L. Francisco-Vieira, E. Cuara-Diaz, R. Benavides*, D. Morales-Acosta*

Centro de Investigación de Química Aplicada, Blvd Enrique Reyna No. 140, Col. San José de los Cerritos, 25290. Saltillo, Coahuila, México
*Tel: +52844-4389830 E-mail: roberto.benavides@ciqa.edu.mx; diana.morales@ciqa.edu.mx

ABSTRACT

Proton exchange (PEMFC) and direct methanol (DMFC) electrolytic membranes for fuel cells are focused for portable and transport devices and this work is relates with the development of novel sulfonated aromatic hydrocarbon polymers for PEMs as alternatives to conventional perfluorinated polymers. **S**tyrene-butyl acrylate (St:BuA) copolymer with 90:10 (St:BuA) comonomer composition was obtained by mass copolymerization via free radical reaction, using BPO as initiator. St:BuA copolymers with different degree of sulfonation (50, 100 and 150%) were considered in order to evaluate their potential for fuel cell application. The sulfonated copolymers presented good solubility in common solvents. Membranes were prepared from sSt-BuA copolymers through casting method. NMR ^{1}H and GPC were used for characterization of the prepared copolymers. The sSt-BuA degree of sulfonation (DS) and the ion-exchange capacity (IEC) were determinated by titration, while thermal properties were evaluated by thermogravimetric analysis (TGA).
NMR ^{1}H spectroscopy confirmed the chemical composition of St-BuA copolymer, the molecular weight by GPC was Mw= 215,308 g·mol^{-1}. FT-IR and TGA results confirmed the successful sulfonation as well as a good thermal stability under 350 °C. The IEC of sSt-BuA membranes was found to be in the range of 0.55 to 1.09 meq·g^{-1}, depending of the concentration of the sulfonic groups. Degree of sulfonation varied from 12 to 27%. Results demonstrated that these copolymers are promising materials to be used as low cost membranes in fuel cells applications.

Keywords: Proton exchange membranes, styrene-co-butyl acrylate, fuel cells

XVIII International Congress
of the Mexican Hydrogen Society

Computational Characterization of Solid Polymer Electrolyte for Polysufide retention in Li-S Batteries

Y A Peña Castañeda[1], Perla B Balbuena[2,*]

[1]College of Science and Technology Universidad Autonoma de la Ciudad de Mexico, Dr. Garcia Diego 168, Doctores Cuauhtemoc 06720 Ciudad de Mexico, Mexico
[2]Department of Chemical Engineering, Texas A&M University, College Station, Texas 77843, United States
* Corresponding author: 979.845.3375 and balbuena@tamu.edu

ABSTRACT

The need for developing better energy-storage devices has been increased due to the excessive demand by the current society. The lithium-sulfur battery appears as a promising chemistry because of their component properties, such as low cost and high theoretical capacity. However, their practical implementation has various challenges. among them, a major issue is the migration from cathode to anode of the long-chain soluble lithium polysulfides (PS) causing instability and low capacity in the battery. Retention strategies include coating the cathode with special materials able to retain these molecules, or developing membranes that could be incorporated into the separator with the same purpose. The selection of the solid polymer electrolyte is a key for the performance of the battery, either the minimization of the shuttle process or PS retention mechanisms depend on it. In this work, we investigate solid polymer electrolyte systems that have a suitable chemical backbone in order to facilitate the lithium polysulfide retention. These materials will act as separator in contact with the electrolyte solution including the PS species, solvents, and salts. We use density functional theory and classical molecular dynamics to evaluate the PS retention properties of these polymer electrolytes.

Keywords: Solid Polymer Electrolyte; energy storage systems; MD; shuttle Polysulfide

September 18th to 21st, 2018 in Mexico City, Mexico.

XVIII International Congress
of the Mexican Hydrogen Society

Effect of the calcination temperature on the purity of $GdBaCo_2O_{5+\delta}$ synthesized by a sol-gel method

D. A. Jurado Ferral[1], C. I. Ramos Villegas[1], H. J. Ávila Paredes[1]*

Departamento de Ingeniería de Procesos e Hidráulica, Universidad Autónoma Metropolitana, Unidad Iztapalapa, Av. San Rafael Atlixco186, Col. Vicentina, C.P. 09340, Ciudad de México, México.
*(52) 55 5804 4600 ext. 1243; hjap@xanum.uam.mx

ABSTRACT

Solid oxide fuel cells (SOFC´s) are energy conversion devices that can operate with hydrogen as a fuel, with efficiencies higher than those for the thermo-power generation systems. In order to prevent the issues that conventional SOFC´s present due to the high operating temperatures, Intermediate Temperature (500 - 700 °C) SOFC´s are under development. When the operating temperature is below 800 °C, the catalytic activity of conventional cathodic materials is reduced, so that new materials need to be developed or found. Recently $GdBaCo_2O_{5+\delta}$ has been proposed as a promising cathodic material for SOFC´s based on its high mixed conductivity values at intermediate temperatures. The most commonly used synthesis method for $GdBaCo_2O_{5+\delta}$ is solid state reaction, however this method offers disadvantages such as high temperature synthesis (> 500 °C), non-uniform particle sizes and formation of secondary phases. On the other hand, the sol-gel method allows obtaining uniform and small particle sizes, and a lower synthesis temperature (< 300 °C). The present work focuses on determining the effect of the calcination temperature on the purity of $GdBaCo_2O_{5+\delta}$ synthesized by a sol-gel method. The synthesized materials were characterized by x-ray diffraction, scanning electron microscopy and energy dispersive x-ray spectroscopy.

Keywords: Solid Oxide Fuel Cells; Cathodic materials; Sol-gel method; $GdBaCo_2O_{5+\delta}$.

XVIII International Congress
of the Mexican Hydrogen Society

Effect of the synthesis method on the ionic conductivity of zirconate-based solid electrolytes on views to their use in SOFC

K.A. Gonzalez-García[1], D. Rentería[1], S.M. Montemayor[2], J.A. Díaz-Guillén[1*], M. Salazar-Zertuche[1], M.E. Bazaldúa-Medellín[3], O. Burciaga-Díaz[1], A.F. Fuentes[3]

[1]Tecnológico Nacional de México, Instituto Tecnológico de Saltillo, 25280-Saltillo, Coahuila, México
[2]Centro de Investigación en Química Aplicada, Blvd. Enrique Reyna Hermosillo 140, 25294-Saltillo, Coahuila, México
[3]CINVESTAV Unidad Saltillo, Av. Industria Metalúrgica 1062, Parque Industrial 25900-Ramos Arizpe, Coahuila, México.
José Alonso Díaz Guillén: Tel. (+52) 844-4389500, Ext. 1203, *jadiaz@itsaltillo.edu.mx

---

ABSTRACT

In this research we analyze the effect of three different synthesis methods on the electrical properties of solid electrolytes based on $Gd_2Zr_2O_7$, an oxygen ion conductor, on views to be used in the Solid Oxide Fuel Cells (SOFC) technology, and looking to overcome some issues related to this technology. Selected methods to obtain this zirconate were the traditional ceramic method (solid state synthesis (SSS)), mechanical milling (MM) and a sol-gel derived method (SG), starting from high purity oxides (for SSS and MM) or nitrates (SG) of the involved elements. Characterization of synthesized samples was made by XRD. This method was also used to analyze the evolution of structure in synthesized samples (MM and SG) with temperature.
After characterization, $Gd_2Zr_2O_7$ powders were then uniaxally pressed by using a hydraulic press and a steel die, to obtain pellets, which were sintered at 1200 and 1500°C during 6 hours.
Ionic conductivity and activation energies for oxygen ion diffusion were determined in these sintered pellets by impedance spectroscopy, as a function of temperature and frequency. Results show that these materials can be successfully synthesized by these methods and their structural arrangement is related to the synthesis method and temperature of sintering. Two different cubic structural arrangements are presented by these materials, anion deficient fluorite or pyrochlore. Results of electrical properties reveal that these materials (synthesized by all methods) show good electrical properties, similar to those obtained for ionic conductors, making these complex oxides interesting candidates to be used as solid electrolytes in Solid Oxide Fuel Cells.

Keywords: SOFC, zirconates, fluorites, pyrochlores, ionic conductors.

XVIII International Congress
of the Mexican Hydrogen Society

Construction and electrochemical characterization of a microtubular solid oxide fuel cell at intermediate temperatures

R. Guzmán Salinas[1], C. I. Ramos Villegas[1], H. J. Ávila Paredes[1]*

Departamento de Ingeniería de Procesos e Hidráulica, Universidad Autónoma Metropolitana, Unidad Iztapalapa, Av. San Rafael Atlixco186, Col. Vicentina, C.P. 09340, Ciudad de México, México.
*(52) 55 5804 4600 ext. 1243; hjap@xanum.uam.mx

ABSTRACT

Solid oxide fuel cells (SOFC´s) are electrochemical devices that convert the chemical energy of fuels, e.g. hydrogen, into electrical energy, with efficiencies close to 60 %. Conventional SOFC´s operate at temperatures near 1000 °C. However, under these conditions there are some drawbacks like components degradation and the restriction of the type of materials to be used as interconnectors and supports, which increases the cost of these devices. Hence, there is a current trend in terms of research to develop SOFC´s that operate at intermediate temperatures (500 - 700 °C).Traditionally, SOFC´s applications are in stationary power generation systems, but recently research has been focused on the development of micro-cells, for portable applications. Microtubular SOFC´s have recently attracted much attention due to their lower operating temperature, higher tolerance to thermal cycles, faster start-up capacity and higher volumetric power densities compared to conventional tubular SOFC´s. In the present work the results of the performance evaluation, in terms of the electric power density, of a Ni-GDC ($Ce_{0.8}Gd_{0.2}O_{2-\delta}$) / GDC / LSCF ($La_{0.8}Sr_{0.2}Co_{0.2}Fe_{0.8}O_3$) prototype are presented. The electrical characterization was performed by linear voltammetry and the performance of the cells was evaluated from polarization curves in the 500 - 700 °C range; cell was operated with air and water saturated hydrogen.

Keywords: Energy Conversion; Solid Oxide Fuel Cells.

XVIII International Congress
of the Mexican Hydrogen Society

Environmentally friendly low-cost membranes for micro and meso-scale bioelectrochemical systems

MJ González-Pabón[1], F Figueredo[1], DC Martínez-Casillas[2], E Cortón[1*]

[1] Laboratory of Biosensors and Bioanalysis (LABB), Departamento de Química Biológica (IQUIBICEN-CONICET), Facultad de Ciencias Exactas y Naturales, Universidad de Buenos Aires, Ciudad Autónoma de Buenos Aires 1428, Argentina.
[2] Instituto de Energías Renovables, Universidad Nacional Autónoma de México, Priv. Xochicalco s/n, Col. Centro, 62580 Temixco, Morelos, México.
* eduardo@qb.fcen.uba.ar. TEL/FAX: INT + 54-11-4576-3342.

ABSTRACT

Microbial fuel cells (MFCs) and microbial electrolysis cells (MECs) are well known bio-electrochemical systems (BESs) that can be used to produce electricity, and hydrogen respectively, by means of microbial metabolic activity. Nonetheless, new strategies for constructions, start up, operation and maintenance are required to improve BESs efficiency and commercial feasibility. At that point, BESs manufacturing materials (electrodes and membranes) represent the main bottleneck for industrial use and scalable real-world applications. Then, one of the challenges to make MFCs and MECs a viable technology is to obtain low cost and environmentally sound materials to fabricate them. In this work we synthesized membranes by a simple procedure: using solution casting and solvent evaporation technique, involving low price and biodegradable materials such as poly (vinyl alcohol) (PVA), chitosan (CS) and PVA:CS, all cross-linked with sulfuric acid. The synthesized membranes were characterized by SEM and EIS, as well as their water uptake, oxygen diffusion and MFC performance, and compared to Nafion® 117, as our reference/control membrane. Conductivity values of the three synthesized membranes were lower than Nafion® 117. However, PVA and PVA:CS show lower oxygen permeability in comparison to Nafion® 117 membranes, a strong advantage in order to maintain anaerobic conditions in the anodic compartment of MFCs. Membranes were first studied in a typical meso-scale H-Type MFCs with LB medium containing *E. coli* (OD = 1). Our results show that CS membrane has the best current output performance (76.1 ± 11.9 mA/m^2). On the other hand, PVA:CS membranes outperform Nafion® 4 times (power production, 20.8 ± 2.9 mW/m^2) while being 75 times more economic. Furthermore, the best membrane in terms of power generation (PVA:CS) were used to made disposables paper-based micro-scale devices (16 µL), were power production was 10.5 ± 0.7 $\mu W/cm^3$. PVA:CS membranes presented here can be useful to fabricate miniaturized and biodegradable MFC, for analytical uses as biosensors, and meso-systems capable to produce energy in a sustainable mode.

Keywords: green technology; low cost membrane; oxygen permeability; micro-scale MFC; meso-scale MFC; PEM substitute.

XVIII International Congress
of the Mexican Hydrogen Society

FUEL CELL DESIGN UP TO 50 W

A. T. Rodríguez-Victoria[1]; J. M. Sandoval Pineda[1], R de G. González-Huerta[2], M. Rico-Cortez[3]

[1]Instituto Politécnico Nacional, ESIME-Azc., SEPI, Av. de las Granjas 682, Col. Santa Catarina, CP 02250, CDMX
[2]Instituto Politécnico Nacional, ESIQIE, Laboratorio de Electroquímica y Corrosión, UPALM, CP 07738, CDMX
[3]Instituto Politécnico Nacional, ESIME, SEPI, Edificio 5 tercer piso, UPALM, CP 07738, CDMX
*Mail: ale_tona@icloud.com

ABSTRACT

The concept of H_2 as an energy carrier is often discussed. This concept can best be described in the context of H_2 produced directly from water using electrolysis. While this process is not economically attractive at current costs, if the electricity required to convert H_2O to H_2 is provided by wind, ocean or solar power, then the H_2 is produced without creating any CO_2. Given the intermittent nature of renewables power sources, surplus energy produced during very windy, big waves or bright sunny days could be used to produce H2 that is stored for later use. The energy stored in hydrogen can be converted to useful energy (electricity) through of fuel cells.
In this research work we present the design of a fuel cell stack based on APQP methodology, a virtual prototype with the capacity to generate up to 50 W of power for lighting applications was developed. The virtual design of the flow fields of the bipolar plates, which are a key component in this device, was made. The bipolar plates connects each cell electrically, while flow fields the supplies reactive gases to the anode and the cathode, and eliminates the reaction products of the cell. The novel promise that is proposed in this work, is the design and machining of the flow fields of radial type, 3 design alternatives are proposed based on the Fibonacci sequence, the objective is to observe the effect of orientation of the flow through of the radial configuration, in order to understand and evaluate the effects of these configurations on the fuel cell behavior. As a result, a comparative analysis of these configurations was obtained evaluating the gases dispersion throughout the complete active area. It has been found that the gases dispersion uniformity depends to a large extent on the design of the flow channels.

Keywords: *Stack, fuel cell, flow fields, hydrogen, Fibonacci.*

September 18th to 21st, 2018 in Mexico City, Mexico.

Modelling and design

September 18 to 21, 2018 in Mexico City, Mexico

XVIII International Congress
of the Mexican Hydrogen Society

A suitable designed-cell for testing the catalyst performance applied towards hydrogen evolution reaction

R. Zenteno-López*, A. Martínez-Séptimo, L. A. Estudillo-Wong, R. de G. González-Huerta

ESIQIE-IPN, Laboratorio de Electroquímica y Corrosión, UPALM, 07738, México, Ciudad de México.
*Corresponding author: 5537167728 and e-mail: zenteno_ricardo@outlook.com

ABSTRACT

Nowadays, it is possible to produce energy from different sources such as coal, natural gas, wood, wind and solar. However, some of these technologies have contributed with the greenhouse. In this context, fuel cells devices have more developed in order to generate less polluting gases. This device use hydrogen and oxygen gas in order to produce energy. Instead of oxygen gas, hydrogen has received an increasing attention due to its high contained energy. Nevertheless, we need to produce hydrogen gas through different technologies. One of the most promising technologies for approaching this challenge, is the electrolysis of water into the proton exchange membrane electrolyzer (PEME). Therefore, the efficiency and stability have to be improved, based on the design such as gas diffuser (porous titanium plate), plates (titanium current collector) and the material used as anode in the electrolyzer. For this propose, a new PEME design was developed. Thus, different loadings of iridium and ruthenium oxides were tested and compered with preliminary PEME. Chronoamperometry was used as electrochemical method for testing the performance. We observed a better performance with the new PEME design.

Keywords: Design PEME, porous titanium plate, titanium current collector.

XVIII International Congress
of the Mexican Hydrogen Society

Simulated annealing optimization heuristic algorithm for modelling PEM fuel cell)

Edumis Viera[1], Martin G. Martínez[2], Alina Martínez[3], Sergio Serna[1*]

[1]CIICAP-UAEM, Cuernavaca, Morelos México, Av. Universidad 1001, C.P62209
[2] FC-UAEM, Cuernavaca, Morelos México, Av. Universidad 1001, C.P62209
[3] Cuernavaca, Morelos México, Av. Universidad 1001, C.P62209
* Corresponding author: 5555-3297039 e-mail: aserna@uaem.mx

ABSTRACT

The oil and natural gas reserves continue to decrease and due global warming the hydrogen economy seems to be an alternative solution to this problematic energy condition. Fuel cells are the key support of the hydrogen economy as they deliver clean and sustainable energy maintaining a healthy environment. Polymer electrolyte membrane (PEM) offers relatively high efficiency and power density as the main candidate to replace the internal combustion engine in transportation applications. Even though PEM fuel cells have an excellent potential to meet the economic and technical targets, considerable challenges are still facing the PEM industry an optimization of PEM fuel cells parameters is clearly necessary for making this technology competitive among others.

As an open and demanding problem, accurate modeling of polarization curve in PEM fuel cell has become the main issue of various researches. In recent years, because of their great potentials, metaheuristic optimization algorithms have represented good performances in identification of the unknown parameters of the proton exchange membrane fuel cell model, but there is the possibility to obtain more accurate results with more capable algorithms.

In the literature, many heuristic optimization algorithms have been developed based on natural phenomena. However, there are still some possibilities to devise new ones. In this paper, simulated annealing has been regarded, and the intelligent behavior to avoid local solutions and to achieve global solutions. Moreover, in this paper, the whole unknown parameters of the model, even dimensional parameters, are included in the identification process. The proposed algorithm is used to optimize an already constructed PEM fuel cell. Simulation results reveal the superior performance of optimized PEM fuel cell.

Keywords: PEM fuel cell, heuristic, simulated annealing, modelling.

XVIII International Congress
of the Mexican Hydrogen Society

Reconstruction of stochastic materials for energy applications

Abraham Misraim Rios Cano[1], Jaime Silverio Ortegón Aguilar[2],Gliserio Romeli Barbosa Pool[3]

[1] Universidad de Quintana Roo. 1620811@uqroo.mx
[2] Universidad de Quintana Roo. jortegon@uqroo.edu.mx
[3] Universidad de Quintana Roo. romelix1@gmail.com

ABSTRACT

The reconstruction of stochastic materials is a topic of interest for researchers in energy because it allows the study of the properties of materials from two-dimensional images of them. In this proposal, it starts with the classification of phases: solid and empty. A set of 3 correlation functions is used to evaluate its behavior: pore size (PS), two points (TP) and linear path (LP). The reconstruction process starts from a volume generated with PS-based spheres; continuing through simulated annealing and the iterative evaluation of TP and LP of each phase. One of the advantages of the system is a decimation process prior to reconstruction, which reduces the image by preserving the correlation functions by 98%. Simulated annealing uses the sum of the errors in the correlation functions, exchanging two pixels of different phases in each iteration. The updating of the correlation functions is done only for the pixels exchanged. Additionally, the minimum temperature is established based on the size of the image after the decimation, adapting to the complexity. The decimation, the updating of the functions and the selection of the minimum temperature generates a reduction in the processing time of an image with an accuracy of 98% with respect to the original image.

Keywords: reconstruction; materials; simulated annealing

XVIII International Congress
of the Mexican Hydrogen Society

Model of a fixed bed catalytic reactor to produce H_2 by Ethanol steam reforming with a Ni-Co/Al_2O_3 catalyst

I.F. Martínez[1], J. L. Contreras[1]*, G. Pérez[1], J. Salmones[2] B. Zeifert[2], L. Nuño[1]

[1]Universidad Autónoma Metropolitana-Azcapotzalco, México, D.F.,02200, México
[2]Instituto Politécnico Nacional, ESIQIE, Mexico,D.F. U.P. López Mateos, Zacatenco, México 3 Universidad
[3]Autónoma Metropolitana-Iztapalapa. México,D.F, 09340, México
* Corresponding author: 5591911047 and jlcl@correo.azc.uam.mx

ABSTRACT

A mathematical model has been developed to predict the conversion profiles and temperature in axial and radial form of a fixed-bed catalytic reactor using a spherical catalyst of Ni-Co / Al_2O_3 with a particle diameter of 1/8 in. A reactor tubular with a diameter of ¾ in and with a length of 13 cm was used. The operating conditions of the reactor were: operating pressure of 1 atm, water / ethanol mole ratio of 4, feed temperatures of 450, 480, 510 and 540 ° C, the construction material of the reactor was stainless steel 316. After applying a differential balance of mass and energy, the solution of the differential equations were discretized by a variant of the implicit methodology of Crank-Nicholson. The values of the transport properties were obtained from the literature such as: the effective diffusivity and the effective thermal conductivity, as well as the reaction rate equation. For the numerical solution, physically reasonable conditions have been introduced in the model and, in this way, establish initial and border conditions that delimit the problem. The Wolfram Mathematica® software has been applied to calculate the phenomena present in the reactor of ethanol steam reforming towards the production of hydrogen. For the validation of the model, the conversions and the calculated temperatures were compared with the experimental ones. This study shows that the implemented program was reliable to simulate an integral fixed bed catalytic reactor.

Key Words: Model, Hydrogen, Integral Reactor, Reform-Ethanol-Water.

.

XVIII International Congress
of the Mexican Hydrogen Society

Kinetic modeling of the gasification of the palm kernel shell for the production of hydrogen

J. Acevedo[1,*], J. Durán[1], F. Posso[2], E. Arenas[3]

[1]Universidad de Santander, Grupo Eureka UDES, Avenida 4 10N-61 Cúcuta. 540003. Colombia.
[2]Universidad de Santander. Grupo Nuevas tecnologías. Calle 70 N55-210. Bucaramanga. 680003. Colombia
[3]Universidad Pontificia Bolivariana, Grupo Energía y Termodinámica, Circular 1 70-01 Medellín. 050031. Colombia.
* Corresponding author: +57 313 8290852, jua.acevedo@mail.udes.edu.co

ABSTRACT

The use of biomass as a source of renewable energy is already contributing between 10-14% of the world's energy supply, with an important growth projection. One way of exploiting biomass is to obtain new energy vectors, such as hydrogen which production from residual biomass is technically and economically feasible. The biomass generated in the oil extraction process from the african palm (*Elaeis guineensis*) is attractive for the production of hydrogen by thermochemical processes, due to its high calorific value. Thus, in a research in progress, whose advances are presented, it is intended to determine the type and characteristics of the chemical reactions of the kinetic gasification model by thermogravimetric analysis coupled with mass spectrometry (TGA-MS) from the palm kernel shell (PKS), determining the conversion and the reaction rate during the thermal process. Applying the Arrhenius equation, we will obtain the kinetic parameters and the kinetic model with better adjustments to the PKS gasification process. It also seeks to identify the ideal heating curve to obtain the highest hydrogen production, the lowest content of tars and other unwanted materials. With regard to the TGA-MS analysis, a sample of 20 mg with a size of 250 µm of PKS will be used and N_2 flow of 50 ml/min. As variable conditions, the effect of: gasifying agents CO_2 and steam, heating rates of 15 and 30 °C/min, temperature (750, 850, 950 °C) on the PKS gasification will be determined.

At this time the main properties of the residual biomass from the palm oil process have already been obtained, such as the real density (1.20 g/cm³), higher heating value (20.36 MJ/Kg) and proximate analysis (moisture: 6.98 %, volatile matter: 69.4 %, fixed carbon: 22.1 %, ash: 1.52 %), finding values such as higher heating value and fixed carbon that profile to PKS as a feedstock technically viable for the production of hydrogen by catalytic gasification.

Keywords: gasification; kinetic modeling; palm kernel shell; TGA-MS analysis.

September 18th to 21st, 2018 in Mexico City, Mexico.

XVIII International Congress
of the Mexican Hydrogen Society

Ab initio study of the graphene structure doped with iron and its interactions with chemical species to improve the oxygen reduction reaction in fuel cells

Ernesto López-Chávez[1], Alberto Garcia-Quiroz[1*], Lucy J. Jiménez-González[2], José A. I Díaz-Góngora[3], Yesica A. Peña-Castañeda[1]

[1]College of Science and Technology, Autonomous University of Mexico City (UACM). Av Fray Servando Teresa de Mier 92-110. Centro Histórico, Cuauthémoc, 06080 Ciudad de Mexico, México.
[2]COBO Computational Bio-Organic Chemistry Bogotá. Department of Chemistry. Universidad de los Andes. Carrera 1 N° 18A - 12 Bogotá, Colombia.
[3]CICATA-Legaria-IPN Cento de Investigación en Ciencia Aplicada y Tecnología Avanzada del Instituto Politécnico Nacional de México. Calz Legaria 694, Col. Irrigación, 11500 Ciudad de México, México.
* Celular: 04455-43838313, email: albertogaqa@hotmail.com, alberto.garcia@uacm.edu.mx

---

ABSTRACT

Structural studies of graphene doped with iron (Fe-G) in conjunction with investigations on their interaction with chemical species such as O, O2, OOH, OH. They were taken into account in order to find the most suitable structure to improve the chemical kinetics of the reaction of reduction of oxygen, ORR. Using density functional theory, DFT, we could study the molecular boundary orbitals, Mulliken atomic charges, molecular geometry optimization processes and thermochemical studies. By this means, we were able to determine the oxygen reduction reaction on Fe-G. We correlated the results obtained at the quantum level with the macroscopic parameters, such as, rate constant, activation energies, energies of adsorption, catalytic activity, that describe the chemical kinetics of the reaction. Finally, we compared our results with those reported by other authors for different systems .
Some of our conclusions were that the adsorption energy of the the oxygen atom, O*, for the proposed Fe-G was found to be 1.7534 eV, while for platinum have been reported to be 1.57 eV, so our material could substitute catalytic Pt in PEM-fuel cells. We found that the presence of water does not affect substantially either the stability or the adsorption energy of O* on Fe
the presence of water reduces the HO* adsorption energy and therefore its stability, at last, the free energy profiles showed that for potential cell of U=0 V the hydrogenation of O* is the limiting step. We also found for this potential cell that the intermediate ORR steps are strongly exothermic. Moreover, for equilibrium potential cell U=1.23 V, the removal of HO* is the limiting step and both electron/proton-transfer steps, that is the HO* removal the limiting ORR step and both $O^* + H^+ + e^- \rightarrow HO^*$ and $HO^* + H^+ + e^- \rightarrow H_2O + *$ electron/proton-transfer steps are endothermic.

Keywords: oxygen reduction reaction, ORR, DFT, density functional theory, adsorption energy, Mulliken charges, Fe-G, graphene.

September 18th to 21st, 2018 in Mexico City, Mexico.

Renewable energy systems

September 18 to 21, 2018 in Mexico City, Mexico

XVIII International Congress
of the Mexican Hydrogen Society

Statistical optimization of biohydrogen production from waste diapers

P. Sotelo-Navarro[1]; S. Turpin-Marion[1]; H. Poggi-Varaldo[2,*]

[1] Department of Energy, Sustainable Technologies Laboratory, UAM-A, México, D. F. Av. San Pablo #180 Col. Reynosa Tamaulipas,Ciudad de México, D. F., C. P. 02200.
[2] Environmental Biotechnology and Renewable Energies Group GBAER-EBRE, Dept. of Biotechnol. & Bioeng., CINVESTAV del IPN, P.O.Box 14-740, Mexico City D.F., 07000, México.
* Corresponding author: 57473800 ext. 4321; r4cepe@yahoo.com

ABSTRACT

In Mexico, waste diapers (WD) are typically disposed of in landfills and dumping sites with no previous treatment at all. In the open literature it has been reported experiments with WD composting, degradation by lignocellulolytic fungi, and anaerobic co-digestion of WD and biological sludge. Yet, information on bioH_2 from WD is still scarce.

The purpose of this work was to statistically optimize the biological production of H_2 (Y') from WD using the response surface (RS) methodology. The factors were the ratio C/N (30,40 g/g) and the initial total solids (TS_i) (15, 25%). Two RS were run, one at 37ºC and the second at 55°C. The core design was based on a factorial 2^2 with central and axial points. The response variables were Y', concentrations of organic acids and solvents of low molecular weight, lactic acid, ratio acetic acid-to-butyric acid A/B, the ratio organic acids-to-solvents. H_2 and CH_4 contents in the bioreactors headspace were routinely determined, concentrations of metabolites in the fermented solids were determined at time 0 and at the end of incubation.

The maximum Y' at 37 ºC (2.48 mmolH_2/gTS_i) corresponded to values of 40 and 15% for C/N and TS_i, respectively. At 55 ºC the maximum Y' was less than half, 0.83 mmol H_2/gTS_i, and corresponded also to 40 and 15% of C/N and TS_i, respectively. The corresponding values of Y' predicted by the equations of RS for the best treatments were in good agreement with the experimental values, although slightly lower, 2.23 and 0.78 mmol H_2/gTS_i at 37 and 55 ºC, respectively.

Both factors C/N and TS_i had significant effects on Y' at 37 ºC as well as the interaction ($p < 0.05$). However, neither factor nor their interaction exhibited significant effects on Y' at 55 ºC. It is advantageous that mesophilic maximum Y' resulted higher than the thermophilic one: the energy expenses at 37 ºC are much lower than those at 55 ºC and consequently, the net energy gain due to bioH_2 production will be considerably higher. In summary, the hydrogenogenic mesophilic batch fermentation of WD seems to be a technically feasible option.

Keywords: biohydrogen production, optimization, response surface, waste diapers

September 18th to 21st, 2018 in Mexico City, Mexico.

XVIII International Congress
of the Mexican Hydrogen Society

Biological synthesis of iron nanoparticles from anaerobic consortia grown in anaerobic fluidized bed reactors from biohydrogen-based biorefineries

Leticia Romero-Cedillo[1]; Héctor Mario Poggi-Varaldo[2*]; Yasuhiro Matsumoto-Kuwuabara[1]; Teresa Ponce-Noyola[2]; Luz Bretón-Deval[3]; Carlos Escamilla-Alvarado[4]; Miguel García-Rocha[1]

[1]Nanoscience and Nanotechnology Program, CINVESTAV, P.O. Box 17-740, Mexico City, 07000, Mex.
[2]Environmental Biotechnology and Renewable Energies Group, CINVESTAV, P.O. Box 17-740, Mexico City, 07000.
[3] The Institute of Biotechnology, UNAM, Av. Universidad 2001, Chamilpa, CP 62210 Cuernavaca, Morelos.
[4] Faculty of Chemical Science, UANL, Av. Universidad s/n, Colonia Universidad 66455, San Nicolás de los Garza, N.L.

*Corresponding author: r4cepe@yahoo.com; leticia.romero@cinvestav.mx

---

ABSTRACT

Iron nanoparticles (Fe-NP) have been extensively used in bioremediation of soils and aquifers contaminated with a variety of pollutants. Fe-NP are usually produced by the use of chemical agents, toxic compounds and high energy consumption. An alternative route that allows to obtain Fe-NP, particularly magnetite, is based on the metabolism of iron reducing bacteria (IRB). The purpose of the present work was to synthesize Fe-NP using anaerobic consortia from the anaerobic fluidized bed reactors (AnFBR) that are part of a biohydrogen-based biorefineries. Two lab scale, mesophilic, AnFBR were fed with hydrolizates from the organic fraction of municipal solid waste (OFMSW). One AnFBR was dedicated to bioH2 production (AnFBR-H) whereas a second one produced CH_4 (AnFBR-M). The AnFBRs were loaded with granular activated carbon (GAC) as carrier medium. GAC particles were colonized by the corresponding anaerobic consortia leading to beds of bioparticles (BP) inside the AnFBRs. After 90 d, BPs were sampled and transferred to flasks containing either *(i)* ferric and ferrous chloride 0.25 M and 0.5 M, respectively or *(ii)* ferric citrate 2mM, plus hydrolyzate sufficient to give initial 10 g/L or 16g/L reducing sugars. This intended to decorate the BPs with Fe-NP; herein after the nano-decorated bioparticles are called bio-nano bioparticles (BNBP). After 7 d, the bioparticles were sampled and subjected to characterization. According to XRD pattern of BNBPH and BNBPM, the most prominent peaks for magnetite XRD were for planes (311) (400) (422) (440) and (442) at 35.4°, 43°, 53.4°, 62.5° and 67° 2θ, respectively. SEM analysis indicated an amorphous distribution of nanoparticles over the bioparticle. Analysis by EDS (Energy Dispersive Spectroscopy) showed consistent iron concentration in BNBPM extracted from the AFBR-M (54-64% iron), while iron concentration in BNBPH (extracted from AFBR-H) was lower in average (range 7.8-62%, depending on iron source.) These results are promising, because iron NP are commonly use in wastewater treatment of several polluting agents, such as the removal of

organo-chlorinated compounds. Finally, the biological production of BNBP coupled to a biohydrogen biorefinery is a potential environmentally friendly platform for nanomaterial synthesis.

Key words: biohydrogen; bioremediation; fluidized bed reactors; bioparticles, nano-decorated bioparticles

XVIII International Congress
of the Mexican Hydrogen Society

Electrofermentation for production of value-added compounds and its Integration to biorefineries: an overview

H. M. Poggi-Varaldo[1] *; E. Hernández-Correa[1]

[1]Environmental Biotechnology and Renewable Energies Group, CINVESTAV-IPN, P.O. Box 14-740, Mexico City, 07000, Mexico.

* Corresponding author: 5255 57473800 ext 4321; r4cepe@yahoo.com

---

ABSTRACT

Microbial electrosynthesis cells (*MESynC*) are a new technology that requires biocatalysts and electric power for enhanced production of value-added products (*VAPs*) as well as selected commodities, such as H_2. *MESynC* has received great attention in the last years as an alternative to chemical synthesis or conventional fermentation and can be coupled to biorefineries in sutainable approaches to chemicals production. Yet, the information is still disperse. The objective of this work is to critically review recent efforts on *MESynC*. The scope includes the following issues: (*i*) Principles of *MESynC* for chemicals´ production; (*ii*) *VAPs* and other products; (*iii*) energy efficiency and mass/energy balances; (*iv*) system analysis of *MESynC*; (*v*) *MESynC* and biorefineries; and *(vi)* Perspectives and conclusion.

*MESynC*s need to overcome barriers as economic costs, electrode materials, membranes, microorganisms, scale-up, etc. From the product point of view, there is more information on the bioelectrochemical production of CH_4 and H_2, although these biofuels are commodities (relatively low prices) , than on *VAPs*. Information on systemic evaluation of the *MESynC* that determine energy expenditures as well as environmental impacts is still scarce. Life cycle analysis (*LCA*) is an accepted method for evaluating these issues. Though in the last years have been published some studies, definitive incorporation of *LCA* and energy/mass balances to *MESynC R&D* is still lagging behind. Our Group has recently demonstrated that electrical energy is in the order of only 1% or less of the total energy required in the lab scale production of succinic acid by electrofermentation. Scale up will slightly increase the electrical energy percentage, because considering a scale factor *k* of volume increase, heating energy increases by just $k^{0.67}$ whereas the electrical energy increases by *k*. Yet, the electricity share will remain well below 5%. Therefore, low temperature electrofermentation should be a focus of future research. Finally, this work gives an overview of the advantages and advances of coupling of *MESynC* to biorefineries. This integration may lead to accelerated development of sustainable environmental technologies.

Keywords: biorefinery; electrofermentation; life cycle assessment; microbial electrosynthesis cells; value-added products

September 18th to 21st, 2018 in Mexico City, Mexico.

XVIII International Congress
of the Mexican Hydrogen Society

Dilute phosphoric acid hydrolysis of stem of faba bean for reducing sugar production

J. C. Gómora-Hernández[1,2], M. del C. Carreño de León[1], S. M. Fernández-Valverde[2,*]

[1]Depto. de Química, ININ, A.P. 18-1027, México D.F. C.P.11801, Mexico. Tel. 5553297200 ext 12277
[2]ITT, Avenida Tecnológico s/n, Fracc. La Virgen, Metepec, Edo Mex., México. C.P. 52149. Tel. 7222087200
* Corresponding author: 5553297200 ext. 12277, suilma.fernandez@inin.gob.mx

ABSTRACT

One of the most important agricultural harvests in State of Mexico is faba bean; this harvest reaches an annual production of 32,033 tons. After harvesting, some residues such as stems, leaves and husks are generated, among all these, stems are not metabolized by cattle and usually are disposed in open dumps contributing to soil erosion and environmental damage, thus, an adequately treatment or revalorization of this residue is necessary. Due to the high amount of carbohydrates, stem of faba bean has a great potential for its transformation by biological methods into many value add products such as hydrogen, however, a previous depolymerization of these carbohydrates into monomeric sugars is needed. The objective of the present work was to evaluate the efficiency of dilute phosphoric acid hydrolysis for reducing sugar production from stem of faba bean. For this, stems of faba bean were obtained from local crops located at State of Mexico, then they were dried and milled, particles with a size under 250 µm were taken and characterized. Acid hydrolysis was performed mixing into 20 mL vials, 1 g of raw stem of faba bean with 15 mL of three different acid solutions (0.58, 0.96 and 1.34 M) heated at three different temperatures (90, 100 and 110ºC) from 30 minutes to 300 minutes. After hydrolysis, phases were separated and liquor was taken to determine pH and the total amount of reducing sugars by 3-5 dinitrosalicylic acid method (DNS). The maximum sugar production was 21.20 g of sugar / 100 g of stem of faba bean observed at 110ºC, 1.34 M and after 270 minutes. The amount of sugar production increased with an increase in acid concentration and temperature. Some tests showed their maximum sugar production after 270 minutes, after this time the amount of sugars diminished due to thermal cracking of saccharides. Sugar production data was well fitted to Saeman and first order kinetic model. FTIR analysis showed a diminishing in amplitude and intensity of the main vibrational bands of hemicellulose and cellulose after hydrolysis. Sugars obtained from stem of faba bean are a potential substrate for fermentative biohydrogen production.

Keywords: Fermentative biohydrogen; Agricultural waste; fermentable sugars; acid treatment

XVIII International Congress
of the Mexican Hydrogen Society

Hydrogen, energy storage technology for marine renewable energies

J. Olmedo González[1*], Guadalupe Ramos Sanchez[2], Rosa de Guadalupe González Huerta[1]

[1]Instituto Politécnico Nacional, Escuela Superior de Ingeniería Química e Industrias Extractivas, UPALM, ZC 07738, Mexico City, Mexico
[2]Universidad Autónoma Metropolitana-Iztapalapa, Chemistry Department, ZC 09340, Mexico City, Mexico
* Corresponding author: +52 1 5527092864 jorgeolmedog@outlook.com

ABSTRACT

Marine renewable energy (MRE) can be considered a stochastic resource, technologies to harness the power of the seas are at an early stage of development. In general, ocean energy can be divided into six types of different origin and characteristics: ocean wave, tidal range, tidal current, ocean current, ocean thermal energy and salinity gradient. Renewable energies like MRE present different electrical energy production (EEP) problems which mainly depend on process control and the possibility of having control variables. These problems such as stability production, intermittence in short or seasonal periods, mismatch of electricity generation and load caused by the limited dispatch-ability requires electrical energy storage (EES) in order to increase their flexibility. According to the International Energy Agency (IEA) Road Map for Energy Storage Technologies, it is very important that variable renewable energies (VRE) are supported by energy storage technologies (EST).

EST have several classifications, they can be classified according to the application into three types, a) Conditioning or regulation of the produced energy, b) Storage energy capacity for post-consumption and c) Energy Storage for mobile applications. Hydrogen (H_2) is considered as an important and prominent EST due to high energy density, cycle efficiency, life time and energy capital cost. However, it is very important specify the range and the proper applications in relation with the different entries such as power density, energy density, rated power rating, cycle efficiency, response time, energy capital cost, influence on environment.

In this work is exposed a documentary research about the best suited applications for H_2 in MRE as EES. It was found that H_2 is not suitable for regulations due to low response time, but it is suitable for b and c applications. H_2 has a huge potential as EES but it will be depend on the proper applications and a correct energy management strategy.

Keywords: Energy storage technologies, Electrical energy storage, Marine renewable energies, Hydrogen.

September 18 to 21, 2018 in Mexico City, Mexico

XVIII International Congress
of the Mexican Hydrogen Society

GRAPHENE OXIDE AS CATALYST IN PLANT-MICROBIAL FUEL CELLS

M.G.Salinas-Juárez[1,*], M.M. Téllez Cruz[1], M.A. Padilla Islas[1], H. Cruz-Martínez[1], H.M. Alfaro López[1], O. Solorza-Feria[1]

[1] Departamento de Química, CINVESTAV, Av. Instituto Politécnico Nacional 2508, México D.F. AP: 14-740, 07000 México, D.F. Mexico
* Corresponding author: Tel: +52(55)5747 3800, maria.salinas@cinvestav.mx, maria.salinas@outlook.com

ABSTRACT

The reduced graphene oxide (rGO) is studied as catalyst for the oxygen reduction reaction that takes place at cathode in a plant-microbial fuel cell. Biological fuel cells are electrochemical devices integrating microorganisms and/or living beings with a fuel cell. Thus, it is possible to generate power taking advantage of the microbial activity of microorganisms with reduced greenhouse gas emissions. A plant-microbial fuel cell is a biofuel cell composed by a plant, whose roots are located at the anode. The roots discharge organic compounds which are oxidized by microorganisms at anode. Electrons, protons and CO_2 are released as a product of oxidation. Electrons are transferred to the cathode by means of an external electric circuit and protons pass through the medium to the cathode, where react with the electrons and oxygen to form water. Graphene oxide (GO) was synthesized under the improved Hummers method. GO is characterized by thermogravimetric analysis (TGA), X-ray photoelectron spectroscopy (XPS), by the measurement of its electrical conductivity, as well as, by energy-dispersive X-ray spectroscopy (EDS), by the specific surface area (BET) and by UV-vis. The reduction of GO is being carried out using ascorbic acid as reductant. The same parameters of characterization are used to analyze the reduced GO. Finally, the rGO is used as catalyst at cathode of a lab scale plant-microbial fuel cell in order to improve the oxygen reduction reaction and thus, the performance of the bio-fuel cell. The plant-microbial fuel cell is electrochemically characterized by means of linear and cyclic voltammetry to measure the anode and cathode potential as well as the cell voltage, which is about 370 mV with no addition of rGO.

Keywords: Reduced graphene oxide, Bio-fuel cells, Plant-microbial fuel cells, Electrocatalyst.

XVIII International Congress
of the Mexican Hydrogen Society

Photocatalytic performance of $NaTaO_3$-C applied in the photoreduction of CO_2 to produce formaldehyde

J.M. Mora-Hernandez[1*], Ali M. Huerta-Flores[2], Leticia M. Torres-Martínez[2]

[1]CONACYT - Universidad Autónoma de Nuevo León, UANL, Facultad de Ingeniería Civil, Departamento de Ecomateriales y Energía, Av. Universidad S/N Ciudad Universitaria, San Nicolás de los Garza, Nuevo León, C.P. 66455, México.
[2]Universidad Autónoma de Nuevo León, UANL, Facultad de Ingeniería Civil, Departamento de Ecomateriales y Energía, Av. Universidad S/N Ciudad Universitaria, San Nicolás de los Garza, Nuevo León, C.P. 66455, México.
* Corresponding author: jmmora@live.com.mx

ABSTRACT

A carbon doped $NaTaO_3$ photocatalyst was synthesized by the solvo-combustion method. The as-prepared material $NaTaO_3$-C was annealed at different temperatures (500 to 700 °C) in an air atmosphere, to study the crystallographic phases present in the samples, and to relate the morphological, physical and chemical properties of the carbon doped material to the photocatalytic activity to perform the CO_2 reduction. Several physicochemical characterization techniques and electrochemical measurements were employed to study the structural, morphological, optical, textural and electrical properties of the materials. The formation of a solid solution between the carbon and the perovskite, and the formation of a second phase, $Na_2Ta_4O_{11}$; was confirmed through XRD measurements. While it is true that both formations improve the photocatalytic activity of the $NaTaO_3$-C, an optimal carbon amount is a key parameter to reduce the bang gap value, and diminish the charge transference resistance by an improvement in the electrical conductivity of the sample. It is worth to mention that the ratio between the surface area and crystallinity of the sample is a key parameter to obtain the highest photocatalytic activity and. This optimal ratio was achieved by the $NaTaO_3$-C sample heat treated at 650°C. The high surface area and the crystallinity play an important role to explain an enhanced photocatalytic activity caused by a higher active surface and a lower recombination of the charges photogenerated. The photoelectrochemical evaluations revealed that the sample annealed a 650°C is the only material with a conduction band value below the potential required to perform the generation of formaldehyde from the photocatalytic reduction of CO_2. $NaTaO_3$-C annealed at 650°C presented the highest formaldehyde production (39 $\mu mol\, g^{-1}$); from this work, we can suggest that the appropriate combination and synergy of crystalline structure, light absorption and surface area properties of the samples are determinant steps in the photocatalytic activity of the $NaTaO_3$-C materials.

Keywords: Carbon doped perovskites, CO_2 photoreduction, based solar fuels.

September 18th to 21st, 2018 in Mexico City, Mexico.

XVIII International Congress
of the Mexican Hydrogen Society

Sodium polyacrylate inhibits fermentative hydrogen production from a cellulosic substrate

P. Sotelo-Navarro[1]; S. Turpin-Marion[1]; H. M. Poggi-Varaldo[2,*]

[1] Department of Energy, Sustainable Technologies Laboratory, UAM-A, México, Ciudad de México, D. F., C. P. 02200.
[2] Environmental Biotechnology and Renewable Energies Group GBAER-EBRE, Dept. of Biotechnol. & Bioeng., CINVESTAV del IPN, P.O.Box 14-740, Ciudad de México D.F., 07000, México.
* Corresponding author: 57473800 ext. 4306; r4cepe@yahoo.

ABSTRACT

The purpose of this work was to evaluate the inhibitory or toxic effects of sodium polyacrylate (SAP, a moisture absorbent used in diapers) on bioH_2 production in dark fermentation of a cellulosic model waste that resembles waste diapers. Three types of treatments were carried out: substrate bond paper and filter paper (P, substrate control with no SAP), only sodium polyacrylate (only SAP control, SAP is also known as hydrogel, HG), and paper-hydrogel (P-HG) were tested in hydrogenogenic batch bioreactors at 37 °C. All bioreactors were seeded with 10% v/w of a methanogenic solid substrate inoculum that received heat-shock treatment at 90 °C for 1 h previous to seeding. The cellulosic model substrate was intended to simulate the diaper composition.

It was found that the SAP hydrogel did not produce hydrogen. Units loaded with P-HG showed H_2 productions *ca.* 25% lower than that of bioreactors P loaded with only paper and no HG. The cumulative H_2 productions were 5.50 ± 0.89, 0.02 ± 0.005, and 4.22 ± 0.66 mmol $H2/gTS_{substrate}$ for the P, HG, and P-HG units, respectively. BioH_2 production was associated to predominance of the pathway that generates 1 mol butyric acid plus 2 moles H2 in the P and P-HG units, according to values of acetic acid-to-butyric acid A/B ratios; indeed A/B < 0.79 mg COD HAc/mg COD HBu in both cases.

To the best of our knowledge, this is the first time that there is a documented evidence of deleterious effect of SAP on the hydrogenogenic dark fermentation of cellulosic wastes. Yet, further experiments should be performed at different levels of SAP, to determine the half inhibition value of SAP (the amount of SAP that will exhibit half of the H_2 production of the non SAP control).

Keywords: cellulosic wastes, diaper-like, hydrogen, fermentation, sodium polyacrylate

XVIII International Congress
of the Mexican Hydrogen Society

The effect of hydrophobic chain length of co-absorbent to improve dye sensitized solar cell performance

Luciano da Silva[1*], Hammad Cheema[2], Roberto Benavides Cantu[3], Harold Freeman[4]

[1] Departamento de Química, Universidade Federal de Roraima, Brazil

[2] Department of Chemistry and Biochemistry, University of Mississippi, University, USA.

[3] Centro de Investigacion en Quımica Aplicada, Blvd. Enrique Reyna H. 140, Saltillo, Coahuila, 25294, Mexico.

[4] Department of Textile Engineering,, Fiber and Polymer Science Program, North Carolina State University.

* Corresponding author: + 55 48 996890600, lab.lapen@gmail.com

ABSTRACT

Dye sensitized solar cell (DSSC) are important compared to the conventional solar cells such as monocrystalline, polycrystalline, and even amorphous silicon; basically due to its low manufacturing cost. However, the DSSC consists of many anode/cathode interfaces, such as semiconductor to dye and dye to electrolyte and electrolyte to platinum catalyst at the cathode. Therefore, the effect of charge recombination at dye-electrolyte interface is the most important role to cell efficiency. One of major implementations to alleviate the recombination effect could be efficiently solved by adding a hydrophobic co-adsorbent to dye solution. Such molecule will be anchored to a titanium dioxide semiconductor like dye and can be the barrier to protect the interface of the triiodide, dye and mesoporous titanium dioxide (TiO2). In this study, N,N-diethyl-4-{[[4'-nitro-2'-tetrazoyl] phenyl]-diazenyl}aniline (SD-3) and 5- (4-octhyloxy phenyl) tetrazole (CPhTz) were synthesized and used as the co-adsorbent with HD-14 dye to prepare the photoanode for a dye-sensitized solar cell (DSSC), and its photovoltaic performance evaluated., The short-circuit current and the open-circuit voltage of the DSSC are increased for CPhTz with the co-adsorption and reduced for SD-3, comparing to deoxycholic acid (DCA) as co-adsorbent. The reason might be due to an observed negative direction shift in the conduction band (CB) for the co-absorbent CPhTz, not seen for SD-3. This can be associated to the ground state oxidation potential in SD-3, which is smaller than HD-14 while ground state oxidation potential in CPhTz is higher than HD-14. The energy conversion efficiency of the DSSC is 9.22 % to HD-14 - DCA, 9.21% to HD-14 - CPhTz and 7.49% to HD-14 - SD-3, on the TiO2 photoanode.

Keywords: DSSC, Co-adsorbent, dye, tetrazole.

XVIII International Congress
of the Mexican Hydrogen Society

TETRAZOLE AS ANCHORING GROUP FOR DYE-SENSITIZED SOLAR CELLS

Luciano da Silva[1*], Hammad Cheema[2], Roberto Benavides Cantu[3], Harold Freeman[4]

[1] Laboratório de Pesquisa em Materiais – Departamento de Química, Universidade Federal de Roraima

[2] Department of Chemistry and Biochemistry, University of Mississippi, University, USA.

[3] Centro de Investigacion en Quımica Aplicada, Blvd. Enrique Reyna H. 140, Saltillo, Coahuila, 25294, Mexico.

[4] Department of Textile Engineering, Fiber and Polymer Science Program, North Carolina State University.

* Corresponding author: +5548996890600, lab.lapen@gmail.com

ABSTRACT

The dyes used for dye-sensitized solar cells [DSSCs] require one or more chemical substituents acting as anchors, enabling their adsorption onto TiO2. Here we report structure-property relationships of phenyl-tetrazole unit for DSSC. These molecules containing tetrazole as anchorring group and a phenyl unit containing different donor group linked at 2-position. Such donnor groups are 1-naphtol [SD-1], 6-benzoylamine-1-naphtol-3-sulfonyl [SD-2] and N,N-diethylaniline [SD-3] linked through azo moieties to the 2-position on the 5-(5-nitrophenyl)tetrazole system. These donor groups were strategically chosen to determine the influence of steric effect between donor-π-acceptor [D-π-A] groups on the photovoltaic properties. All dyes showed similar redox potential. Incident photon to current conversion efficiency [IPCE] response higher than 30% at only 330 nm were exhibited by all dyes. Based on Nyquist plot of impedance measurements, it was concluded that Rd [diffusion impedance] for all dyes are smaller than Rct [charge transfer impedance], which is associated with the anchoring capacity of the TiO2 electrode. Despite having good donor groups attached to the anchoring group by pi chains, this results demonstrate the need to adjust the geometry and load transfer capacity to match ground state energies and excited state oxidation potentials, which play a crucial role in energy related applications.

Keywords: solar cells, sensitizer, tetrazole, anchoring groups.

September 18th to 21st, 2018 in Mexico City, Mexico.

XVIII International Congress
of the Mexican Hydrogen Society

Molecular characterization of microbial consortia in a hydrogen-based biorefinery from wastes

Carlos Alfredo Amaro-Aponte[1]; Leticia Romero-Cedillo[2]; Héctor Mario Poggi-Varaldo[1]*; Daniel A. Estrada-Bárcenas [3]; Édgar Baldemar Sepúlveda-García [4]; Dulce María Delgadillo-Álvarez [5]; Teresa Ponce Noyola [4]; José Tapia-Ramírez [5]

[1]Environmental Biotechnology and Renewable Energies Group, CINVESTAV; P.O.Box 14-740, CP 07000, Mexico City, Mexico
[2]Nanoscience and Nanotechnology Program, CINVESTAV, P.O. Box 14-740, CP 07000, Mexico City, Mexico
[3]National Collection of Microbial Strains and Cell Cultures, CINVESTAV, Mexico City, Mexico
[4]Department of Biotechnology and Bioengineering, CINVESTAV, P.O. Box 14-740, CP 07000, Mexico City, Mexico
[5]LANSE-CINVESTAV; P.O. Box 14-740, CP 07000, Mexico City, Mexico
* Corresponding author: phone number: 5747-3800 Ext. 4321. e-mail: r4cepe@yahoo.com

---

Molecular techniques used to characterize microbial communities in bioprocesses include denaturing or temperature gradient gel electrophoresis (DGGE or TGGE, respectively), Restriction Fragment Length Polymorfism (RFLP), among others. All of them require primer design with target regions that allow to amplify DNA fragments as well as to differentiate species. The objective of this work was to characterize and to identify the microbial species in consortia acting in the stages H-M-N from an HMZSN biorefinery.

An important consideration in TGGE is to design primers that would facilitate the implementation of nested PCR. So, the design of primers should exhibit novel features. Among the latter we highlight that the target of the first set of primers was the 16S gene in order to simultaneously include the domains archaea and bacteria, and that of the second pair of primers was to increase specificity in the V3 hypervariable region. Primers in this work were representative of the two groups: *(i)* methanogens, and *(ii)* H_2-producing bacteria. Isolation of strains was carried out in liquid culture media M_1 and M_2, one for promoting H_2 production and the seccond for methanization. Inocula were sampled from hydrogenogenic and methanogenic fluidized bed reactors, and a semi-continuous, complete mix Seed Methanogenic Reactor. Considering the 3 inocula, a total of 40 strains were isolated; 75% corresponded to methanogenic archaea (MA). From these, 12 strains (40% of the MA) grew in culture medium M_1 (glucose plus trace metals and vitamins) whereas 18 (60%) grew in M_2 (also glucose, although poorer in trace metals and vitamins, spiked with $NaHCO_3$). Up to 10 of the total isolated strains (25%) were H_2-producing bacteria; half of them were able to grow in both culture media. Interestingly, inoculum from the hydrogenogenic fluidized reactor only had H_2-producing bacteria. On the other hand, inoculum from the methanogenic reactors only exhibited CH_4-producing microorganisms. Bacterial genuses of some isolated strains corresponded to *Citrobacter, Rhodobacter, Rummelibacillus* and *Planomicrobium.* Work is on going to implement the method with TGGE and nested PCR to validate biological Fe(III) reduction for bionanoparticle synthesis and reductive dehalogenation of PCE using the primers.

Keywords: 16S gene; Hydrogen producing bacteria; Methanogens; Nested PCR; Temperature Gradient Gel Electrophoresis.

XVIII International Congress
of the Mexican Hydrogen Society

Hydrogen production by anaerobic digestion from *Agave lechuguilla* hydrolysates

Leopoldo J. Rios-González[1*], Thelma K. Morales-Martínez[1], Gabriela G. Hernández-Enríquez[1], José A. Rodríguez-De la Garza[1], Mayela Moreno-Dávila[1]

[1] Departament of Biotechnology, Faculty of Chemistry, Autonomous University of Coahuila. Saltillo, Coahuila, México.
* Corresponding author: phone number +52 1 8441077790
email: leopoldo.rios@uadec.edu.mx

ABSTRACT

The aim of the present work was to optimize the hydrogen production from enzymatic hydrolysates of *Agave lechuguilla* pretreated by autohydrolysis. The pretreatment was carried out in a high pressure reactor using a solid/liquid ratio of 1:6 (w/v) at 190 °C during 30 min at 200 rpm. The pretreated solids were enzymatically hydrolyzed and then digested with a treated mix consortia at different conditions using a Taguchi ($L_9(3^4)$) experimental array. The results showed that the xylan was solubilized in 65.17% during pretreatment and the glucan preserved was hydrolyzed in 77.52% obtaining a hydrolysate with 55 g/L of glucose. After anaerobic digestion of hydrolysates, the hydrogen production was significantly influenced mainly by the temperature (80.6%) and glucose concentration (15.1%). The best conditions were 40 ºC, glucose 20 g/L, inoculum 5% (v/v) and initial pH 7. Under optimal conditions, the hydrogen yield achieved was 3.48 mol H_2/mol glucose consumed at 120 h.

Keywords: *Agave lechuguilla*; autohydrolysis pretreatment; anaerobic digestion; hydrogen.

September 18th to 21st, 2018 in Mexico City, Mexico.

XVIII International Congress
of the Mexican Hydrogen Society

Effect of fermentation time/hidraulic retention time in a UASB reactor for hydrogen production using surface response methodology.

Ileana Mayela María Moreno Dávila[1*], Emma Berenice Herrera Ramírez[1], José Antonio Rodríguez de la Garza[1], Leopoldo Javier Ríos González[1], Yolanda Garza García[1].

[1] Departament of Biotechnology, Faculty of Chemistry, Autonomous University of Coahuila. Saltillo, Coahuila, México.
* Corresponding author: phone number +52 1 8443819485
email: imayelamorenod@hotmail.com

ABSTRACT

The aim of the present work was to study the fermentation time and also the hydraulic retention time effect using surface response methodology for hydrogen production using a synthetic media as sustrate. The inoculum used for biofilms was previously pretreated, the anaerobic sludge was heat (100°C, 30 min.) and after was subject to acid-basic procedures to selectively enrich the hydrogen producing mixed consortia. The reactor used 44 spheres with anaerobic biofilms developed in fiber ixtle for immobilization of anaerobic sludge and was operated at mesophilic temperatures and initial pH of 5.0. A factorial arrangement of 2^3 was carry out on MINITAB statistical program, the statistical analysis of the surface response methodology of the hydrogen production process during the development and growth of biofilms was carried out at 3 different hydraulic retention times (1,3,6 h), as well as three fermentation times, as response variables (40, 140 and 280 h). The analysis of variance given by the statistical program with respect to the two factors studied: hydraulic retention time and fermentation time showed that they are highly significant, but in the interaction between variables no significance was detected. A longer time of hydraulic retention (TRH = 6) as well as a longer fermentation time (280h) the hydrogen production is favored obtaining 4.34 moles, and no methane was detected.

Keywords: hydrogen, anaerobic biofilms, surface response methodology, hydraulic retention time***.***

Control and power conditioning

September 18 to 21, 2018 in Mexico City, Mexico

XVIII International Congress
of the Mexican Hydrogen Society

A New Two-Level Power Sharing Control Strategy for a Multi-Stack Fuel Cell System

A. Macias[1, *], M. Kandidayeni[1], L. Boulon[1], H. Chaoui[2]

[1]Hydrogen Research Institute, Université du Québec à Trois-Rivières, Quebec, Canada
[2]Department of Electronics, Carleton University, Ottawa, Ontario
* Corresponding author: +52 33 10 25 89 46 alvaro.omar.macias.fernandez@uqtr.ca

---

ABSTRACT

Control strategy design has a significant part in the maturity development of fuel cell technology by enhancing the performance and reliability of the system. This paper presents the design of a novel adaptive power splitting control strategy for a multi-stack fuel cell system (MFCS), which comprises four proton exchange membrane fuel cells (PEMFCs) and a battery pack. The proposed strategy has two operating levels. The first level is composed of an optimized fuzzy controller, which considers the demanded power from the system and the state of charge of the battery (SOC) as inputs and the required power from the PEMFCs as the output. The second level is mainly responsible for distributing the power among the four PEMFCs. To do so, a rule-based power sharing algorithm has been combined with a new maximum power point tracking (MPPT) method to distribute the power among the PEMFCs. The power sharing algorithm uses the minimum number of PEMFCs to supply the requested power in a particular sequence. It uses the first PEMFC until it reaches the maximum power, and then it activates the next PEMFC until the demanded power is met. Therefore, it can be stated that the power sharing algorithm performs well assuming that it has a priori knowledge about the maximum power of each PEMFC. However, fuel cell is a multi-physics system and its maximum power changes with respect to the variation of the operating conditions and degradation level. In order to adapt the power sharing algorithm to the mentioned performance drifts of the PEMFCs, a MPPT technique based on water cycle algorithm (WCA) has been used to determine the maximum power of each PEMFC at each moment and reconfigure them in an ascending order to be used by the power sharing method. The performance of the proposed control strategy has been compared with the equal distribution and Daisy Chain algorithms, which are two common methods for splitting the power in a MFCS, in Simulink environment of Matlab. The obtained results from the suggested strategy indicate promising hydrogen consumption reduction in the system.

Keywords: fuel cell system; control strategy; fuzzy logic control; power sharing; maximum power point tracking

September 18th to 21st, 2018 in Mexico City, Mexico.

Policies, economy and market strategies

September 18 to 21, 2018 in Mexico City, Mexico

XVIII International Congress
of the Mexican Hydrogen Society

The need for a strategic plan for the effective use of hydrogen as an alternative energy in Mexico

María Liliana Ávalos Rodríguez[1*], José Juan Alvarado Flores[2], Jorge Víctor Alcaraz Vera[3]

[1]Escuela Nacional de Estudios Superiores, campus Morelia, perteneciente a la Universidad Nacional Autónoma de México. Antigua carretera a Pátzcuaro 8701, sin nombre, INDECO, la Huerta. Morelia, Michoacán.
[2]Instituto Tecnológico del Valle de Morelia. Carretera Morelia-Salamanca, km. 6.5, Morelia, Michoacán.
[3]Instituto de Investigaciones Económicas y Empresariales, Universidad Michoacana de San Nicolás de Hidalgo, Francisco J. Mújica S/N, Col. Felicitas del Rio, C.P. 58040, Morelia, Michoacán, México.
* Corresponding author: 4434 09 59 44, lic.ambientalista@gmial.com

ABSTRACT

In Mexico, a public source of water that can be used and the use of hydrogen as an alternative source of energy is sold, in the sense that there is no legal backing that makes the extraction, storage, use and use of hydrogen feasible; that is why, the objective of the present research is, through a qualitative approach, to carry out an exploratory, descriptive and correlational study of the main legal systems at the federal and state levels that must consider hydrogen as an alternative source of energy, this with the purpose of a strategic plan for its effective use, which contributes to the attention of public policies that obey the environmental and energy problems that contribute to the development of sustainable development conditions in Mexico. It is appreciated that there is a broad environmental legal framework that has left aside the integration of hydrogen as an alternative source of energy; in addition, there are public energy policies that continue to bet on energy an oil base and new actions that have an incentive to renewable energies to the new paradigm of the hydrogen economy. Due to these circumstances, the viability of the hydrogen strategic plan is appreciated because to date there is no document that integrates social needs in energy matters, the scope of public policies and legal issues, highlighting the benefits of use and use of hydrogen, not only as an alternative energy, but as a promoter factor of environmental care and protection and the determining factor of development.

Keywords: *L*egal framework, public policies, strategic hydrogen plan, development

September 18th to 21st, 2018 in Mexico City, Mexico.

Codes, standards and safety issues

September 18 to 21, 2018 in Mexico City, Mexico

XVIII International Congress
of the Mexican Hydrogen Society

Measurement of pollutant emissions for an engine gasoline internal combustion enriched system with oxyhydrogen

Santos Fernández M.[1*], Hernández Hernández M.-[1], Contreras López L. F. [1], Cortés Escobedo C. A. [1]

[1] Instituto Politécnico Nacional, CIITEC
* marianna.s.f@hotmail.com, phone number: +9221991228

ABSTRACT

Description and analysis of a validation protocol for analytical methods applied to the measurement of emissions for combustion engine system enriched gasoline-oxyhydrogen reactor based on the EURACHEM Guide (The Fitness for Purpose of Analytical Methods – A Laboratory Guide to Method Validation and Related Topics) is presented.
The validation of the methodologies, together with other activities included in the control of quality assurance, allows to demonstrate to the laboratories that their analytical methods provide reliable results. However, there are no validated methodologies to determine the specifications of maximum permissible limits or analytical techniques with adequate detection limits for the measurement of polluting emissions in oxyhydrogen coupled systems.
The objective of this research is to analyze requirements for the validation of analytical methods satisfying the requirements of conformity assessment of measuring emissions oxyhydrogen coupled system, based on the EURACHEM guide.
The precision and robustness indicators suggested by the NMX-EC-17025-IMNC-2006 were studied, as well as the application criteria implemented by the Entidad Mexicana de Acreditación (EMA) AC.
Measurements were made in accordance with national and international standards corresponding to vehicle emissions internal combustion engine-oxyhydrogen coupled systems:

- Emissions of Vehicle Gases, Test FTP-75, Cold phase, Test HOT 505, carried out in the Vehicle Emissions Laboratory referenced in the NMX-AA-11-1993-SCFI standard.
- Vehicle emissions speciation, based on the method: Standard Test Method for Determination of Gaseous Organic Compounds by Direct Interface Gas Chromatography-Mass 1 ASTM D 6420- Spectrometry 99.
- Measurements of polluting emissions by infrared sensors or probes.

Results of concentration of total hydrocarbons, CO_2, O_2, CO and NO_x for a combustion engine coupled to an oxyhydrogen reactor, as well as without it. A slight decrease in the total hydrocarbons (0.065%) was found between the chromatographic results and the results of infrared spectrometry.

Keywords: methods validation, oxyhydrogen coupled systems, vehicular emissions.

Nanostructured materials

September 18 to 21, 2018 in Mexico City, Mexico

XVIII International Congress
of the Mexican Hydrogen Society

Synthesis of MoCoW as a transition metal oxides electrocatalyst for oxygen reduction reaction in alkaline medium

J. E. G. Béjar[1], M. Guerra-Balcázar[2], L. Álvarez-Contreras[3], L. G. Arriaga[1] and N. Arjona[1]*

[1]Centro de Investigación y Desarrollo Tecnológico en Electroquímica, Sanfandila, Pedro Escobedo, Qro., C.P. 76703, México.
[2]Facultad de Ingeniería, División de Investigación y Posgrado.
Universidad Autónoma de Querétaro, Querétaro, Qro., C. P. 76010, México.
[3]Centro de Investigación en Materiales Avanzados S.C., Complejo Industrial Chihuahua, Chihuahua Chi., C. P. 31136, México.
* Corresponding author:* wvelazquez@cideteq.mx

ABSTRACT

Fuel cells are limited by the cost of the membrane and catalysts. Therefore, it requires the design of highly active nanomaterials without using Pt as the base catalyst. There are many strategies followed for this purposes, including the use of carbides, nitrides, chalcogenides and others. However, other option is the mixture of transition metal oxides, due to they are highly stables in alkaline medium and, they can provide oxygenated species for the oxidation/reduction reaction. In this work, MoCoW was synthesized using a simple method that enables a high production rate of metal oxides. These MoCoW electrocatalyst was characterized by XRD, TGA, TEM, and XPS. The electrocatalytic evaluation for ORR indicated that, MoCoW need 200 mV more energy to carry the oxygen reduction reaction than commercial Pt/C. However, the stability tests performed during 1000 cycles demonstrated the superior stability of the metal oxides electrocatalyst.

Keywords: Electrocatalysis; transition metal oxides; MoCoW; ORR; HER.

XVIII International Congress
of the Mexican Hydrogen Society

Support Interaction Effect of Platinum Nanoparticles on Non-, Y-, Ce-Doped Anatase and Its Implication on the ORR in Acid and Alkaline Media

Luis A. Estudillo-Wong[1, 2], Nicolás Alonso-Vante[2,*]

[1] ESIQIE-IPN, Laboratorio de Electroquímica y Corrosión, UPALM, 07738, México, Ciudad de México.
[2]IC2MP, UMR-CNRS 7285 University of Poitiers 4rue Michel Brunet, 86022 Poitiers (France)
*Corresponding author: nicolas.alonso.vante@univ-poitiers.fr

ABSTRACT

Platinum nanoparticles (Pt NPs) were prepared by using the photo-assisted method and supported onto oxide-carbon composites synthesized through a modified sol-gel route (M:TiO_2-C, with M=Y and Ce). The physicochemical properties of these materials were investigated by transmission electron microscopy (TEM), X-ray diffraction (XRD) and X-ray photo- electron spectroscopy (XPS). Rietveld refinement was used to identify existing phases of electrocatalysts and to determine the crystallite size. Micro-strain and intrinsic stacking fault increased and decreased, respectively, as a function of crystallite size. Molecular probing via CO-stripping analyses assessed the selectively deposition of Pt NPs onto oxide domains of M:TiO_2-C (M=Y and Ce) supports. This phenomenon can be associated with the formation of the covalent bond at the heterojunction interface between Pt and oxide sites. As confirmed by DFT simulation, this phenomenon was related to the adsorption energy between Pt NPs and Y- or Ce-doped TiO_2. Turnover frequency evaluation revealed that, in acid medium, the strong Pt/oxide interaction promotes the oxygen reduction reaction activity by 1.7-fold, as compared to alkaline medium.

Keywords: Pt nanoparticles; ORR; Strong Metal-Support Interaction; metal doped-TiO_2

September 18th to 21st, 2018 in Mexico City, Mexico.

XVIII International Congress
of the Mexican Hydrogen Society

Synthesis and characterization of Au@Pd core-shell nanoparticles

Eduardo Y. Cervantes-Aspeitia[1], Martha L. Hernández-Pichardo[1,*], Rosa G. González-Huerta[2], Paz del Ángel[3]

[1]Laboratorio de Nanomateriales Sustentables, ESIQIE-Instituto Politécnico Nacional. Av. IPN s/n, Ciudad de México 07738.

[2]Laboratorio de Electroquímica y Corrosión, ESIQIE-Instituto Politécnico Nacional. Av. IPN s/n, Ciudad de México 07738.

[3]Caracterización de Materiales Sintéticos y Naturales, Instituto Mexicano del Petróleo. Eje Central L. Cárdenas 152, Ciudad de México 07730

* Corresponding author: +5215557296000, mhernandezp@ipn.mx

ABSTRACT

To achieve the commercialization of fuel cells the development of low-content or non-Pt catalysts is crucial. In this work, core-shell nanoparticles of Au-Pd were synthesized through a seed growth method and tested in oxygen reduction reaction (ORR). Two different bimetallic Au-Pd structures were obtained using diverse types of surfactants. A continuous coating of Pd over Au was obtained by using CTAB (Cetyltrimethylammonium Bromide), while small Pd particles growing over the surface of Au were obtained by using CTAC (Cetyltrimethylammonium Chloride).

The formation and the morphological changes were followed by different techniques of TEM/STEM. Thus, several analyzes with these methods were performed for each of the 3 steps of the synthesis to control the size and morphology. By using HAADF-STEM, Au@Pd core-shell nanoparticles with sizes between 95-100 and 60-70 nm (prepared by CTAB and CTAC respectively) were found. With this technique it was possible to observe different contrast, due to the atomic weight of the elements present in the sample. By XRD the FCC structure for both metals was found. Also, the electrochemical behavior of both structures was analyzed in order to know the effect of the morphology toward ORR. We found that by using CTAC as a surfactant we obtained an enhanced activity and higher stability with an onset potential of 0.93 V and a half-wave potential of 0.82 V. These results are comparable to those of the commercially available Pd/C catalyst. Thus, this work shows that through the growth of monometallic crystals it is possible to tailor the core of the particles for a later addition and formation of a defined shell, which allows to improve the activity toward the RRO.

Keywords: Core-Shell Nanoparticles; Surfactant, ORR.

XVIII International Congress
of the Mexican Hydrogen Society

Electrochemical and Photoelectrochemical Properties of TiO_2 Nanotubes Arrays Modified with Coordination Polymers for Hydrogen Generation

Kevin Rosas Barrea[1*], Julio Andrés Pedraza Avella[1], Edilso Reguera[2] and Próspero Acevedo Peña[3]

[1] Grupo de Investigación en Minerales, Biohidrometalurgia y Ambiente-GIMBA, Universidad Industrial de Santander-UIS, Sede Guatiguará, Piedecuesta, Colombia.
[2] Centro de Investigación en Ciencia Aplicada y Tecnología Avanzada-Unidad Legaria, Instituto Politécnico Nacional-IPN, Ciudad de México. México.
[3]CONACyT-Centro de Investigación en Ciencia Aplicada y Tecnología Avanzada-Unidad Legaria, Instituto Politécnico Nacional-IPN, Ciudad de México. México

*+52 55 7540 4315, klrosas@gmail.com

ABSTRACT

A source potentially clean and renewable for hydrogen fuel generation is the photoelectrochemical water splitting using sun light. In this work, we report the synthesis of TiO_2 nanotubes arrays obtained by electrochemical anodization of Ti foil. These nanostructures were successfully modified with different amount and type of coordination polymers by a pulse electrodeposition method. The structural characterization, morphology, elemental composition and light absorption capability of samples were characterized by XRD, RAMAN, FE-SEM, EDS and UV–Vis methods. Photoelectrochemical characterization was achieved through OCP, LSV, CA and EIS procedures in a three electrodes cell. It was found nanostructures modified with coordination polymers exhibits photo-potentials greater than those measured for unmodified materials. Furthermore, the linear sweep voltammetry of nanostructures modified showed current densities at lower overpotentials than bare TiO_2 nanotubes, evidencing the electrocatalytic effect of the coordination polymers.

Keywords: Electrocatalyst, Electrodeposition, photoelectrochemical cells, TiO_2 nanotubes

XVIII International Congress
of the Mexican Hydrogen Society

Transport properties of dense graphene oxide – polyvinyl chloride composite membranes for H_2/CO_2 separation

U. Hernández Castellanos[1], H. J. Ávila-Paredes[1], A. Godínez García[2,*]

[1] Departamento de Ingeniería de Procesos e Hidráulica, Universidad Autónoma Metropolitana, Unidad Iztapalapa, Av. San Rafael Atlixco186, Col. Vicentina, C.P. 09340, Ciudad de México, México.
[2] Departamento de Ciencias Básicas, Universidad Autónoma Metropolitana, Unidad Azcapotzalco, Av. San Pablo Xalpa 180, Col. Reynosa Tamapulipas, C. P. 02200, Ciudad de México, México.
* Corresponding author: (52) 5553189011, andgog007@gmail.com

ABSTRACT

Hydrogen separation from gaseous mixtures containing CO_2 by membrane permeation is a promising process under development. In the present contribution, a series of (0 - 30 w. %) graphene oxide (GO) – polyvinyl chloride composite membranes were prepared by a spray process coupled with a spin coating technique. The samples were characterized by FTIR, TGA, SEM, and transport properties (i.e. diffusion coefficient, solubility, permeability and selectivity) were determined by a conventional variable pressure – constant volume technique. Samples with a GO content lower than 30 w. % were fully dense. Due to the functional groups present on the surface of the GO particles, membranes with a higher GO content exhibited higher CO_2 diffusion coefficient and CO_2 permeability values. In contrast, sample with 10 w.% GO showed the highest H_2 diffusion coefficient and permeability values. Results show that this set of composites are promising candidates for H_2/CO_2 separation with membranes at relatively low pressures.

Keywords: hydrogen separation; transport properties; membrane permeation.

XVIII International Congress
of the Mexican Hydrogen Society

Methanol oxidation using Pt /graphene-carbon as electrocatalyst in acid media

J. A. Palafox Segoviano[1], B. Ruiz Camacho[1]*, A. Medina Ramírez[1], C. Martínez Gómez[1], C. M. López Badillo[2]

[1]Deparment of Chemical Engineering, Division of Natural and Exact Sciences, University of Guanajuato Noria Alta S/N, Guanajuato, Guanajuato, CP 36000, México

[2]Facultad de Ciencias Químicas, Universidad Autónoma de Coahuila, Blvd. V. Carranza y José Cárdenas, 25280, Saltillo, Coahuila, México

* Phone: 4731443870, e-mail:beatriz.ruiz@ugto.mx

ABSTRACT

Pt and Pd supported on carbon Vulcan are the most commonly catalysts used for methanol oxidation reaction. However, new support with more stability and higher dispersion are required in fuel cells systems. Recently, various studies has been focused in improved the stability of carbon support researching with different materials as carbon nanospheres, graphene, carbon nanotubes, ordered mesoporous carbon and graphene, graphene oxide and graphene reduced. In this work, Pt nanoparticles supported on graphene, carbon and graphene-carbon (1:2, 1:1, 2:1) were synthesized as electrocatalysts for methanol oxidation reaction (MOR) in order to investigate the effect of the support. The materials Pt/graphene, Pt/graphene-carbon and Pt/carbon were synthesized by ultrasound method and characterized by transmission electron microscopy (TEM) and X-Ray diffraction (XRD). Samples synthesized were electrochemically characterized by cyclic voltammetry (CV) and chronoamperometry (CA) techniques in acid media in presence and absence of methanol. Significates differences in the current intensity peak of methanol oxidation reaction were found it CV curves. The sample Pt/oxide-graphene (2:1) showed the higher electrochemical activity for MOR. The half-wave potential ($E_{1/2}$) and onset potential (E_{onset}) indicated that the Pt/oxide-graphene had the higher electrochemical activity for MOR compare to Pt/carbon > Pt/graphene. The test of stability indicated that materials synthesized on graphene are more stables than on carbon Vulcan. Last results are associated at the formation of fewer intermediaries (formaldehyde and formic acid) during the methanol oxidation reaction. The materials synthesized using graphene oxide exhibits electrochemical activity for MOR.

Keywords: fuel cell, electrocatalysts, graphene, Pt nanoparticles

September 18th to 21st, 2018 in Mexico City, Mexico.

XVIII International Congress
of the Mexican Hydrogen Society

Synthesis of Pt/nanozeolite- graphene oxide composite and its electrochemical evaluation for formic acid electrooxidation

V.K. González Rodríguez[1], A. Medina Ramírez[1*], L.K. Arellano Ariza[1], B. Ruiz Camacho[1]

[1]Departamento de Ingeniería Química, División de Ciencias Naturales y Exactas, Universidad de Guanajuato, Campus Guanajuato. Noria Alta s/n Z.P. 36050, Guanajuato, Guanajuato, Mexico
* Corresponding author: +55 01 473 7320006 adriana.medina@ugto.mx

ABSTRACT

The properties of the catalyst support in the direct formic acid fuel cells (DFAFC) influence the electrochemical response and the efficiency of the oxidation reactions of the formic acid. Particularly, the surface and structure of the support affect the size and morphology of the active specie and therefore its electrochemical performance. For these reasons in the present work the effect of distribution of the platinum nanoparticles on the nanozeolite-graphene oxide (GO) composite on the electrochemical evaluation was studied. EMC-2–type nanozeolite was synthesized by hydrothermal treatment and then the GO was incorporated to nanozeolite by ultrasound method. The electrocatalyts were obtained by incorporation of platinum to the supports using the ultrasound method. The nanozeolite, GO and composite were characterized by X Ray Difracttion, Transmission and Scanning Electronic Microscopies. The electrochemical activity of the nanomaterials was performed as electrocatalyst for formic acid electrooxidation in acid media using cyclic voltammetry and choronoamperometry. The results indicate that the EMC-2 nanozeolite was identified as crystalline phase of hexagonal morphology with a size of 20 nm. For nanozeolite-GO composite the nanocrystals of EMC-2 were located onto and between the graphene oxide sheets. The electrochemical behavior of the electrocatalysts evaluated indicated that the structure and dispersion of platinum affect the formic acid electro-oxidation reactions. The pathways of the electrical conductivity of the supports are enhanced by the hydrogen spillover through zeolite channels, the nature of the acid sites and the electrical conductivity of the graphene oxide. These results allow inferring that the Pt/nanozeolite-GO could be useful as electrocatalyst for direct formic fuel cells.

Keywords: nanozeolite; graphene oxide; DFAFC; platinum

XVIII International Congress
of the Mexican Hydrogen Society

Silicon Doped Carbon with Low Pt as electrocatalysts for the ORR

O. G. Mejía Ramírez[1], I. Zeferino-González[2], L. A. Romero Cano[2],
A. M. Valenzuela-Muñiz[3*], Y. Verde-Gómez[2]

[1]Universidad Autónoma de San Luis Potosí, Facultad de Ciencias, Av. Dr. Salvador Nava Martínez S/N Zona Universitaria, San Luis Potosí, S.L.P., México C.P. 78290
[2] TecNM/Instituto Tecnológico de Cancún, Departamento de Estudios de Posgrado e Investigación, Av. Kabah, Km. 3, Cancún, Quintana Roo, México C.P. 77500.
[3]CONACYT-TecNM/Instituto Tecnológico de Cancún, Departamento de Estudios de Posgrado e Investigación, Av. Kabah, Km. 3, Cancún, Quintana Roo, México C.P. 77500.

* Corresponding author: +(52) 998 8807432 ext.2018,2031 anavalenzuelam@yahoo.com

---

ABSTRACT

The outstanding properties of multiwalled carbon nanotubes (CNT) position them as an excellent option to be used as support of electrocatalysts. The insertion of heteroatoms in the graphitic carbon network can drastically change their characteristics. Recently it has been reported that CNT doped, have a great potential for catalytic applications in fuel cells, especially in the cathode where oxygen reduction reaction (ORR) takes place. However, despite the interesting behavior of the doped materials, the electrochemical surface area obtained when a metal is used in the electrocatalysts is still not achieved. In the present study, Si doped-CNT where synthesized by a modified chemical vapor deposition method, using toluene as carbon source, ferrocene as metal catalyst for the nanotubes growth and triphenylsilane as dopant. In addition low loading of Pt nanoparticles were added (1 and 5 wt%) in order to evaluate a possible synergetic interaction between the metal and the dopant. The physical and chemical properties of the obtained electrocatalysts were analyzed mainly by scanning electron microscopy (SEM), transmission electron microscopy (TEM), X ray diffraction (XRD) and Raman spectroscopy. In addition, in order to analyze the electrocatalytic behavior of the synthesized materials towards the ORR, studies were performed in a Rotating Disk Electrode. A normal three electrode cell was used with the Pt-SiCNT materials as working electrode (deposited in glassy carbon), Ag/AgCl (NaCl Sat) as reference, a Pt wire as counter electrode, and 0.5M H_2SO_4 as supporting electrolyte. The interesting results and discussion of the electrochemical studies will be presented at the conference.

Keywords: Low Pt electrocatalysts; Si-doped CNT; ORR

XVIII International Congress
of the Mexican Hydrogen Society

Synthesis and characterization of nanosize cobalt-doped nickel ferrite obtained for hydrogen production by thermochemical cycles

Mario Aldahir Mar Torres[1], Ana Lidia Martínez Salazar[1], Margarita García Hernández[1], Marco Antonio Cornel García[1], José Aarón Melo Banda[1].

[1] Centro de Investigación en Petroquímica, Instituto Tecnológico de Ciudad Madero, Prol. Bahía del Aldair, Av. de las Bahías. Parque Industrial Tecnia, Altamira, Tamaulipas, México, 89608.
* Corresponding author: 833 3 114908, oiram_aldahir_13@hotmail.com

ABSTRACT

Thermochemical cycles have been acquired great importance due to their capacity of dissociate water molecules, obtaining high purity hydrogen. Therefore, they do not generate secondary products such as greenhouse gases.
Non-volatile metal oxides are one of the leading thermochemical cycles families. In previous investigations, iron oxide shows 42% hydrogen production efficiency, carrying out reduction reaction at higher temperature than 2000 ºC and oxidation reaction at higher temperatures than 700 ºC. Energy consumption represents the main challenge on this innovating technology. According to literature, metal addition to iron oxides (mixed ferrites) achieve oxide-reduction process at lower temperatures. Nickel ferrite causes an endothermic reaction below 1200 °C. On the other hand, thermodynamic study developed, previous to this research work, shows theoretical capacity to carry out material oxidation at lower temperatures, adding a cobalt doping.
In this research work, $Co_{1-x}Ni_xFe_2O_4$ (x = 0.5) was synthesized by sol-gel method for its evaluation in water dissociation by thermochemical cycles.
The synthesis was carried out dissolving $Ni(NO_3)_2{\cdot}6H_2O$, $Co(NO_3)_2{\cdot}6H_2O$, $Fe(NO_3)_2{\cdot}9H_2O$ in alcohol with a chelating agent, the gel was heated at 110ºC for 24hrs. The powder obtained was subjected to a heat treatment at temperature range of 300-800ºC, taking samples every 100ºC. The formation of cubic spinel phase has been confirmed with characterized techniques such as X-Ray Driffraction (XRD), Scanning Transmission Electron Microscopy (STEM) and Fourier Transform Infrared Attenuated Total Reflection Spectroscopy (FTIR-ATR). The achieved phase has demonstrated, in investigations with similar materials, a water dissociation remarkable performance through thermochemical cycles at moderate temperatures and, therefore, a hydrogen production higher yield.

Keywords: hydrogen production; sol-gel; ferrite.

September 18th to 21st, 2018 in Mexico City, Mexico.

XVIII International Congress
of the Mexican Hydrogen Society

Photocatalytic behaviour of TiO2, ZnO and CuO modified SBA-15 in hydrogen production

J. C. Espinoza Tapia[1], F. A. Duran[1], A.K. Medina-Mendoza[2], C. R. Tapia-Medina1, J.L. Contreras-Larios[1], I. Hernández-Pérez[2], J. C. García-Martínez[1] , J. A. Colín-Luna[1,*]

[1]UAM-Azc, Departamento de Energía, Av. San Pablo 180, Col. Reynosa-Tamaulipas, 02200, CDMX, Méx.
[2]UAM-Azc, Departamento de Ciencias Básicas, Av. San Pablo 180, Col. Reynosa-Tamaulipas, 02200, CDMX, Méx.
* Corresponding author: (01)5553189044 and jacl@correo.azc.uam.mx

---

ABSTRACT

Photocatalytic water splitting is one of the cleanest and economic methods employed to produce hydrogen. In the literature is have reported TiO_2 can be used as photocatalysts in the photodegradation of many organic molecules as colorants. Although semiconductors show limitations due to the recombination of the electron-hole pair, the photocatalysts also have high bandgap and require the use of a source luminescent within the UV region. For this reason, it is important to implement materials with photocatalytic properties that improve efficiency in a heterogeneous photocatalysis process, suppressing the limitations in the production of hydrogen. Some recent researches have shown that other metal oxides such as ZnO or CuO, also present excellent properties as photocatalyst materials

The use of mesoporous materials SBA-15 of high specific area (> 600 m^2 / g) used as supports for semiconductors such as TiO_2, maximize photocatalytic properties due to that high surface area increases the active surface area of the catalyst, varying the pore geometry of the support, the catalyst can become size and shape selective. Finally, it is known that the photocatalytic characteristics are often increased by quantum size effects for nanometer-sized (<10 nm) semiconductor particles. Therefore, by confining the particles inside an ordered host material, narrow size distributions for quantum size particles can be attained. Although also to improve the response to solar light of photocatalysts has been used a hole scavenger, which reacts with photogenerated holes increasing the lifetime of the electrons in the conduction band, these sacrificial scavengers would allow the use of narrow band gap semiconductors.

In this work, is proposed to use semiconductors of TiO_2, ZnO, and CuO which improve their photocatalytic properties when incorporated into a mesoporous SBA-15 materials. By increasing the number of possible reaction sites, an improvement in the photocatalytic production of hydrogen will be obtained with the synthesized materials (supported); this in comparison with the metal oxides outside the support in the presence of a sacrificial molecule.

Keywords: SBA-15; water splitting; hole scavenger; cinc oxide; cupper oxide

XVIII International Congress
of the Mexican Hydrogen Society

Immobilization of Glucose oxidase on glutathione capped Carbon or CdTe Quantum Dots for use in biosensors and biofuel cells

Jairo Daniel Lozano-López[1], Marisol Galván-Valencia[1], Ricardo Escalona-Villalpando[2], Sergio M. Durón-Torres[1*]

[1]Unidad Académica de Ciencias Químicas, Universidad Autónoma de Zacatecas, Campus Siglo XXI, Carretera a Guadalajara Km. 6.0, Ejido la Escondida, Zacatecas, Zac. México, 98160.
[2]Centro de Investigación y Desarrollo Tecnológico en Electroquímica S.C. Sanfandila, Santiago de Querétaro, México, 76703.
* Tel: +524929256690 Ext. 4655; e-mail: serduro@yahoo.com

ABSTRACT

Enzyme immobilization on conductive materials is an actual research topic for the development of biosensors and biofuel cells. The most common anchoring methods (covalent binding, cross-linking or entrapment in gels and membranes) often interfere with enzymatic catalysis due to an occlusion of active sites, enzyme denaturation, or substrate diffusion issues. The use of quantum dots as a support matrix for enzyme immobilization, has been reported as a viable alternative for the macromolecules anchoring, diminishing in a great extent the above mentioned well-known problems.

In this work, a comparison between Graphene QD´s (GSH-CQD) and CdTe QD´s (GSH-CdTeQD) coated with glutathione is presented for the immobilization of the enzyme Glucose oxidase (GOx). The surface of graphite electrodes was modified, with 5,10,15,20-Tetrakis (1-methyl-4-pyridinium) Porphyrin, then a layer of QD was deposited to finally binds GOx. The modified electrodes were evaluated by cyclic voltammetry (CV) in PBS 0.1 M pH 7.4 at a scan rate of 50 mVs-1. The results obtained shown that GSH-CdTeQD modified electrodes have a greater enzyme immobilization capacity than those modified with GSH-CQD and non-modified graphite electrodes. Besides, the GSH-CdTeQD modified electrodes showed a higher current response for glucose oxidation.These results suggest that the use of CdTe QD´s could be exploited in the design of enzymatic electrodes for glucose biosensors and biofuels cells.

Keywords: biofuel cell, enzyme immobilization, quantum dots, glucose oxidase.

XVIII International Congress
of the Mexican Hydrogen Society

Structural and optical properties of nanostructured CeO_2 thin films obtained by spray pyrolysis

Mario Fidel García Sánchez[1,*], Inti Zumeta Dubé[1], Issis Claudette Romero Ibarra[1] José Manuel García Rangel[1], José Francisco Malagón García[2], Ernesto Espinoza Hernández[1]

[1] Unidad Profesional Interdisciplinaria en Ingeniería y Tecnologías Avanzadas. Instituto Politécnico Nacional, Av. I.P.N. 2580, Gustavo A. Madero, 07340, Ciudad de México, México.
[2] Instituto de Investigaciones en Materiales, U.N.A.M., A.P. 70-360, Coyoacán, C.P. 04510, Ciudad de México, México.
* Corresponding author: +(55)57296000 ext. 56860, mgarciasan@ipn.mx

ABSTRACT

In this work, nanostructured ceria thin films have been prepared by ultrasonic spray pyrolysis using cerium acetylacetonate as metalloorganic precursor dissolved in anhydrous methanol on silicon, glass and FTO cover glass substrates. The morphology, structure and optical properties were studied by scanning electron microscopy, X-ray diffraction (XRD), Raman spectroscopy, UVvis and impedance spectroscopy. The spray conditions were optimized for obtaining homogeneous nanocrystalline films with grains sizes smaller than 20 nm. By XPS were demonstrated the presence of Ce^{3+}. The Ce^{3+} concentration do not depend of the grown temperature. The variations in the flow rate modified the optimal temperature, the preferential orientation and the defects distribution in the films. The nanometric grain size increase the conductivity of samples. The films have potential applications in photocatalytic process in hydrogen production.

Keywords: ceria; nanostructured materials; spray pyrolysis; impedance spectroscopy

XVIII International Congress
of the Mexican Hydrogen Society

Green synthesis of Ni-Co nanoparticles for their use as anodic catalyst in urea fuel cells

B. Rojas de Soto[1]; M. Galván-Valencia[1]; A. Cervantes-Villagrana[1]; S. Durón-Torres[1,*]

[1]Universidad Autónoma de Zacatecas. Carretera Zacatecas-Guadalajara Km. 6, ejido "La Escondida", Ciudad Universitaria campus Siglo XXI, CP 98160, México.
* Corresponding author: 492 106 2933, serduro@yahoo.com

ABSTRACT

Nickel metallic nanoparticles exhibit electrochemical activity to oxidize biological substances such as urea and producing electrical energy in fuel cells (FC). The FC are used as an alternative in energy production with an associated decrease in environmental pollution. Additional advantages are achieved, if the synthesis of catalytic materials is obtained by "green chemistry" by exploiting the reducing properties of plant extracts to generate metallic nanoparticles from inorganic precursors.

In this study is presented the results of the electrochemical evaluation of Ni-Co bimetallic nanoparticles synthesized from the use of *Punica granatum* and *Eucalyptus globulus* reducing extracts that avoids the utilization of inorganic harmful compounds such as NaBH4. The synthesis was based on the reduction of a $NiCl_2.6H_2O$ / $CoCl_2.6H_2O$ solution by using aqueous extracts of the plants. The synthesis consisted in the addition of the extract to a 1% $NiCl_2$-$CoCl_2$ solution at an alkaline pH. Glassy carbon electrodes modified with catalytic inks were used to evaluate the presence of the Ni redox pair in 1M KOH solution by cyclic voltammetry (VC). Using the same technique the urea oxidation capacity was determined in a 0.33M / KOH 1M solution.

It was found that the reduced particles showed catalytic activity for the urea oxidation reaction (UOR). The electrochemical response for UOR obtained with the nanoparticles synthesized with green chemistry can be compared with those synthesized ~~with those~~ by conventional methods that use NaBH4 as reducing agent. The Ni-Co nanoparticles synthesized could be used as anodic catalysts in urea FC.

Keywords: nickel-cobalt; green synthesis; urea

XVIII International Congress
of the Mexican Hydrogen Society

Ru, Sn and Sb based catalyst for Oxygen Evolution Reaction synthetized by one step method

N. J. Pérez-Viramontes, I. L. Escalante-García, M. Galván-Valencia, S. M. Durón-Torres*

[1] Unidad Académica de Ingeniería Eléctrica, Doctorado en Ciencias de la Ingeniería, Universidad Autónoma de Zacatecas Campus SXXI, Carretera a Guadalajara km 6.0. Ejido La Escondida Zacatecas, Zacatecas, México.
* Phone number: +52 4939256690 e-mail: duronsm@prodigy.net.mx

---

ABSTRACT

Multimetallic oxide of Ru, Sn, and Sb was synthetized by simple thermal decomposition method of the chloride precursor $RuCl_3xH_2O$, $SnCl_4x5H_2O$, and $SbCl_3$ in ethanol. This material functions as electrocatalyst and support for the oxygen evolution reaction (OER) in Solid Polymer Electrolyte Water Electrolyser (SPEWEs). Four different proportions of $RuCl_3$ was used in the synthesis (10, 20, 30 and 40 at. %) of the catalyst support material. The effect of the ruthenium amount was evaluated on the electrocatalytic activity for OER by cyclic voltammetry (CV) and linear sweep voltammetry (LSV). Cyclic voltammetry shows the presence of ruthenium oxide, this is more evident as the increase of ruthenium atomic percent. The onset potential for OER was found close to 1.4 V vs NHE, which is less than Ir based catalyst synthetized by the same technique (previously reported). From the linear sweep voltammetry analysis was possible to obtain the Tafel slope which is close to 60 mV dec^{-1}. The obtained parameters for the metallic oxides make it attractive as electrocatalyst for OER in SPEWE.

Keywords: Ruthenium oxide, Electrocatalyst, Support, SPEWEs.

Environmental aspects

September 18 to 21, 2018 in Mexico City, Mexico

XVIII International Congress
of the Mexican Hydrogen Society

Photocatalytic Activity of Layered Perovskite Oxides $Sr_{2.7-x}Ca_xLn_{0.3}FeO_{7-\delta}$ for MB Degradation

L.E. Verduzco[1], R. Garcia-Diaz[2], J. Oliva[3], A.I Martinez[1], C. Gomez-Solis[4], C.R. Garcia[2], A. F. Fuentes[1] and K. P. Padmasree[1*]

[1]Cinvestav Unidad Saltillo, Parque Industrial, Ramos Arizpe, Coahuila, 25900, México
[2]CONACYT-Facultad de Ciencias Físico-Matemáticas, Universidad Autónoma de Coahuila, 25000, Saltillo, México
[3]CONACYT-Facultad de Ciencias Químicas, Universidad Autónoma de Coahuila, 25280, Saltillo, México
[4]Universidad de Guanajuato, Campus León, División de Ciencias e Ingenierías, 37150 León, Guanajuato, México
* Corresponding author: phone number: 8444389600 (8521), e-mail: padmasree@cinvestav.edu.mx

ABSTRACT

The semiconductor photocatalyst such as TiO_2, ZnO etc. are very efficient for the photocatalytic degradation of organic pollutants from water because of their excellent photocatalytic activity, ultraviolet absorbency, low cost and photochemical stability. However, these oxides absorb only a small portion of solar spectrum in the ultraviolet region which limits their practical applications. Therefore, the development of photosensitized degradation process by utilizing visible light has recently received much attention. Perovskite oxides have received significant attention because of their unique properties such as oxygen vacancy order, high conductivity, intrinsic oxygen reduction reaction activity etc. Many perovskite and perovskite-type oxides have been found to be suitable for photocatalytic degradation reaction. In this work we analyzed the photocatalytic activity of the layered perovskites belonging to n = 2 series of Ruddlesden – Popper oxides $Sr_{2.7-x}Ca_xLn_{0.3}FeO_{7-\delta}$ with x = 0 and 0.3 and Ln = La and Nd. The $Sr_{2.7-x}Ca_xLn_{0.3}FeO_{7-\delta}$ catalyst were synthesized by a solid-state reaction method and characterized by X-ray diffraction, scanning electron micrograph, diffuse reflectance UV-visible spectroscopy, reactive oxygen species generation etc. As the lanthanide size decreases, the absorption band in the US-VIS-NIR region increases. Similarly, the Ca-substituted sample exhibited a small decrease in absorption band. The band gap energy (E_g) value was obtained from the Kubelka-Munk plot. The photocatalytic activity of $Sr_{2.7-x}Ca_xLn_{0.3}FeO_{7-\delta}$ samples was analyzed by the degradation of MB at room temperature under solar and UV irradiation. An increased degradation of MB was shown by Nd samples compared to La samples because of the increased absorbance and low band gap values shown by Nd samples. The degradation rate was fast under solar irradiation (180 min) compared to UV irradiation (300 min). It suggests that the layered perovskite $Sr_{2.7-x}Ca_xLn_{0.3}Fe_2O_{7-\delta}$ could be a possible option for the degradation of contaminant dyes in water treatment plants under solar irradiation.

Keywords: Photocatalyst; layered perovskite; methylene blue; solar and UV irradiation

September 18th to 21st, 2018 in Mexico City, Mexico.

XVIII International Congress
of the Mexican Hydrogen Society

Microbial fuel cell to heavy metals removal from acid mine drainage

L.S. Vélez-Pérez[a]; G. Hernández-Flores[b, *]; O. Solorza-Feria[c]; O. Talavera Mendoza[a]; H.M. Poggi-Varaldo[d]; J.A. López-Díaz[a]

[a]Escuela Superior de Ciencias de la Tierra, Universidad Autónoma de Guerrero. Ex Hacienda s/n, San Juan Bautista, 40323, Taxco el viejo, Guerrero. Ex Hacienda San Juan Bautista S/N, Taxco el Viejo, Guerrero, México, C.P. 40323.
[b]CONACYT-Escuela Superior de Ciencias de la Tierra, Universidad Autónoma de Guerrero. Ex Hacienda s/n, San Juan Bautista, 40323, Taxco el viejo, Guerrero. Ex Hacienda San Juan Bautista S/N, Taxco el Viejo, Guerrero, México, C.P. 40323.
[c]Dept. of Chemistry, Centro de Investigación y de Estudios Avanzados del Instituto Politécnico Nacional, Av. Instituto Politécnico Nacional 2508, Col. San Pedro Zacatenco, Delegación Gustavo A. Madero, México, C. P. 07360.
[d]Environmental Biotechnology and Renewable Energies R&D Group, Dept. of Biotechnology and Bioengineering, Centro de Investigación y de Estudios Avanzados del Instituto Politécnico Nacional, Av. Instituto Politécnico Nacional 2508, Col. San Pedro Zacatenco, Delegación Gustavo A. Madero, México, C. P. 07360.
* Corresponding author: phone number +52 1 5521903883, e-mail: ghernandez@conacyt.mx

---

ABSTRACT

Acid mine drainage (*AMD*) represent an important source of pollution around the world with critical concern. The acidic pH and the high concentrations of heavy metals affect seriously the soil and water. Thus, the goals of this research were (*i*) to design a dual-chamber microbial fuel cell (*DC-MFC*) and (*ii*) to evaluate the heavy metals removal from *DAM* using a *DC-MFC*. The *DC-MFC* was built with a cylinder in Plexiglas and divided by a proton exchange membrane (*PEM*), Nafion® 117. The volume of the anodic and cathodic chambers was 64 cm^3. Graphite rods were used as anode and cathode. The anodic chamber was filled with wastewater and anaerobic sludge (collected from Wastewater Treatment Plant, Taxco de Alarcón, Guerrero), substrate and inoculum, respectively. On the other hand, actual *DAM* (collected from a mine located in Taxco de Alarcón, Guerrero) was used as catholyte (pH<3). The polarization data were obtained by linear sweep voltammetry at a scan rate of 0.5 mV/s. The internal resistance was determined by electrochemical impedance spectroscopy, using a frequency range of 100 kHz to 1 mHz with an alternating current signal of 10 mV pic-to-pic. Furthermore, the heavy metals concentration was analyzed by inductively coupled plasma-atomic emission spectra in the effluent of the catholyte. The cathodic material was analyzed by powder X-ray diffraction (XRD) and EDS to determine the chemical composition of deposited heavy metals. Finally, the topography of anode and cathode materials were analyzed by scanning electron microscopy (SEM).The removal heavy metals from *DAM* by *MFC* is an interesting proposal of bioremediation.

Keywords: acid mine drainage; bioelectricity; heavy metals removal; microbial fuel cells

XVIII International Congress
of the Mexican Hydrogen Society

Residual power in portable energy storage electrochemical devices: an experimental collection approach.

C. M. Bautista-Rodríguez[1*], A. Horta-Mendez[2], M. Maldonado-Santoyo[1], B. Ruiz-Camacho[3], Richard R. Lindeke[4].

[1] Centro de Innovación Aplicada en Tecnologías Competitivas (CIATEC). Dirección de Investigación y Posgrado, Omega 201, Fraccionamiento Industrial Delta, P.O. Box 37545, León, Guanajuato, México.
[2] Universidad Politécnica del Bicentenario. Ingeniería en Agrotecnología. Carretera Estatal Silao – Romita Km 2. Col. San Juan de los Durán, CP. 36283. Silao, Guanajuato, México.
[3] Departamento de Ingeniería Química, División de Ciencias Naturales y Exactas, Universidad de Guanajuato, Campus Guanajuato, Noria alta S/N, CP. 36050, Guanajuato, Gto. México.
[4] Professor Emeritus University of Minnesota Duluth, Volunteer Peace Corps Mexico at CIATEC.
[*] Corresponding author: + 52 (477) 710 0011, ext. 13003 ; cbautista@ciatec.mx

ABSTRACT

This document presents the results of an experimental program for appropriate handling of discarded domestic batteries (single-cells), including the next procedures: (1) collection, (2) classification, (3) parametric records, (4) temporal storage and (5) sending to reciclage processes. A statistical study was designed later at the collect, classification and record battery parameters, including residual voltage and residual current, present in discarded domestic single-cell batteries. The results showed that 55% of discarded batteries registered more than 70% of their nominal voltage and only 19% contained indicators of exhaustion, representing a significant energy waste by consumers. Of the collected AA cell batteries, more than 57% had residual voltage up of 1.0 V, and 29.5% more than 1.3 V, when compared to their nominal 1.5 V starting voltage. After comparing energy parameters (voltage and electrical current) between discarded and new batteries, we concluded that the incomplete use of stored energy is significant. We conclude then that measures of electrical current would be a better indicator of the energy level present in the domestic batteries rather than voltage, which is a characteristic of battery size, but not of the available energy.

Keywords. Energy, Cells, batteries, residual power, alkaline batteries.

Full Paper

September 18 to 21, 2018 in Mexico City, Mexico

Hydrogen production, storage and applications

September 18 to 21, 2018 in Mexico City, Mexico

XVIII International Congress
of the Mexican Hydrogen Society

Towards double metal alanates

J.R. Tena-Garcia[1], A. Flores-Jacobo[1], K. Suarez-Alcantara[1,*]

[1] Morelia Unit of the Materials Institute Research of the National Autonomous University of Mexico
Antigua carretera a Patzcuaro 8701, Ex-Hacienda de San José de La Huerta, 58190 Morelia, Mich.
* 5623-7300 ext 37889. karina_suarez@iim.unam.mx

ABSTRACT

Alanates ($M(AlH_4)_x$) are interesting materials for hydrogen storage. In particular sodium alanate ($NaAlH_4$) is interesting due to its hydrogen charge/discharge reversibility when appropriately catalyzed. However, the research on new kind of alanates is intense. At the borohydride family ($M(BH_4)_x$), the formation of double-cation materials such as $NaSc(BH_4)_4$ or $NaZn_2(BH_4)_5$ resulted in the tailoring of $NaBH_4$ properties. A similar approach can be applied to the alanates family. Thus we prepared and characterized mixtures of NaH-TiH_2-Al or NaH-ZrH_2-Al as precursors for double-cation alanates ($NaM_y(AlH_4)_x$, M=Ti or Zr). The mixtures were prepared by mechanical milling in two different mills, a planetary mill and an N_2-liquid-cooled mill (cryogenic mill or cryomill). The samples were characterized by X-ray diffraction (XRD) and scanning electron microscope (SEM) techniques to determine the most suitable structural characteristics for hydrogenation. The mixtures were tested for hydrogenation, reaching about 0.3 wt.%. Improvement of the hydrogenation conditions is necessary; however, the formation of an unknown phase after hydrogen exposure may lead to a wanted double-cation alanate.

Acknowledgment: *Ciencia Básica-CONACyT 251347: Alanatos no convencionales para almacenamiento de hidrógeno a baja temperatura*

Keywords: hydrogen storage, alanates, double cation

---

1. Introduction

Alanates ($M(AlH_4)_x$) are interesting materials for hydrogen storage. In particular sodium alanate ($NaAlH_4$) is interesting due to its hydrogen charge/discharge reversibility when appropriately catalyzed [1, 2]. Alanates are frequently synthesized by the reaction of metals or hydride metals (i.e. Na or NaH) with Al, H_2, and a catalyst in organic solvents such as toluene, hexane, n-octane, ether, diglyme, or THF [3, 4]. This method needs the use of moderate-high pressures of hydrogen (100-150 bar) and moderate temperatures (120-150°C). This method can be considered highly dangerous due to the mixture of organic solvents, metal hydride and Al with oxygen/ humidity is highly explosive. This production method needs steps of purification and drying.

As an alternative, mechanical milling can be used. Some alanates can be produced by the mechanical milling of the corresponding metal hydride and aluminum (precursor mixture) and further hydrogenation, i.e. the so-called “direct synthesis” method. The direct synthesis by mechanical milling procedure eliminated the need for organic solvents, purification and drying steps [5, 6]. Usually, the milling is performed in planetary mills or shaker mills at room temperature. Recently, the advance of mechanochemistry and its applications had led to the development of mills such as the magnetic mills or the cryogenic mills. Thus we explore the use of cryomilling for producing the precursor mixtures for double-cation alanates. Also, we explore different milling times in a conventional planetary mill and then compare with the cryogenic milling.

At the borohydride family ($M(BH_4)_x$), the formation of double-cation materials such as $NaSc(BH_4)_4$ or $NaZn_2(BH_4)_5$ resulted in the tailoring of $NaBH_4$ properties. Similar studies of the formation of double metal (or cation) alanates are rather scarce, and most of these studies are theoretical by means of first principles, ab-initio, etc. [7, 8, 9]. Thus, we propose the possible production of double cation alanates by the direct synthesis method, i.e by milling NaH-TiH_2-Al or NaH-ZrH_2-Al mixtures in two different mills and further hydrogenation.

2. Materials and Methods

2.1. Sample preparation

Samples of 0.5NaH-0.5TiH_2-4Al and 0.5NaH-0.5ZrH_2-4Al were produced by mechanical milling at two different mills; a planetary mill and a cryogenic mill. The reactives were purchased to Sigma-Aldrich and used without further purification. The Al was granular, with a particle size roughly of 1 mm and 99.7% purity. Meanwhile, the rest of the materials were fine powders of high purity. The milling was performed in batches of 1 gram of mixture as needed for performing reactions or characterization. The handling of materials was performed inside a glove box filled with high purity argon (10 ppm O_2 and H_2O).

2.1.1. Planetary milling: This milling was performed in an Across-International planetary mill, with the rotation frequency of the main plate of 40 Hz. Three total milling times were performed: 5, 25 and 50 hours, divided into periods of 1-hour milling and 10 minutes resting. In each cycle of milling-pause, the rotation direction of the planetary mill was inverted. The millings in the planetary mill were performed at room temperature. The different milling times were performed to study the structural changes in the samples induced by the ball milling. The milling vials were machinated in stainless steel 316L with an internal volume of 100 ml, with bolted lids. The ball to powder ratio

was 15:1. $YZrO_2$ balls were used. The samples obtained in the planetary mill are identified adding a *"–P"* to the sample name.
2.1.2. Cryo-milling: This milling was performed in a Retsch Cryomill. The samples were milled for 1 hour divided into 6 periods of 10 minutes of milling at 25 Hz of vibration and 2 minutes "resting" at 5 Hz of vibration. Cooling with liquid nitrogen was kept all the time. The milling vial was machinated in stainless steel 316L with an internal volume of 50 ml. The ball to powder ratio was 15:1. $YZrO_2$ balls were used. The samples obtained in the cryogenic mill are identified adding a *"–C"* to the sample name.

2.2. Hydrogenation.
Hydrogenation was performed in a PCT-fashion in an *isorb-100* equipment from Quantachrome. Samples were transferred from the glove box to the equipment without exposition to oxygen or humidity by means of a de-attachable sample-holder with an isolation valve. The samples were proper degasified at 150ºC in dynamic vacuum for 12 hours. Then the equipment was cooled to room temperature and it was carefully calibrated for void volume with ultra-high purity helium. Then the sample was heated to the testing temperature. The testing temperatures were 50, 100, 150, 200, 250, 300 and 350ºC. After an appropriate time for isothermal stability on all the equipment (sample-holder and manifold zones), hydrogen was allowed to enter the system. The hydrogen pressure was gradually increased along the experiment from 0.1 bar to 95 bar. The transition from one point to another was guided by the reaching of equilibrium in the solid-gas system; thus a curve collected at each temperature lasted between 7 to 10 days. After the end of the experiment, the sample was cooled down to room temperature. The remaining hydrogen of the void volume of apparatus was released, and the apparatus was charged with helium. Then, the sample-holder was transferred back to the glove box for recovering and characterization. The hydrogen-exposed samples are identified by adding a "*–HH"* to the sample name.

2.3. Characterization of the as-milled and hydrogenated samples.
The as-milled and dehydrogenated samples were characterized by SEM and XRD. SEM images were obtained in a JSM-IT300 microscope. Samples were dispersed on carbon tape and mounted in an appropriate sample-holder. Then they were transferred to the SEM chamber reducing the oxygen contact by means of a glove bag, even though partial oxidation could be possible. Unless otherwise indicated, SEM images were obtained by backscattered or secondary electrons and 10kV or 20kV of acceleration voltage. The conditions were dictated by each sample accordingly its own characteristics.
XRD was performed in a D2 Phaser diffractometer of Bruker. Cu Kα (1.540598Å) wavelength was used. The powders of as-milled and hydrogenated materials were compacted in a dedicated sample-holder, then they were covered with a Kapton foil for protection against ambient oxygen and moisture.

3. Results and Discussion
3.1 Characterization of as-milled materials
Fig. 1 present the milling progression at 5, 25 and 50 hours of the samples 0.5NaH-0.5TiH_2-4Al-P and 0.5NaH-0.5ZrH_2-4Al-P, milled in the planetary mill. The main effects are a reduction of the

particle size, a dispersion of the materials and the formations of irregularities and defects at the particles surface. Some of the milled particles reached values lower than 1μm. These three effects are wanted because, in principle, they would help kinetically the hydrogenation reaction. The bright spots at the 0.5NaH-0.5ZrH_2-4Al-P samples correspond to the ZrH_2.
Fig. 2 present the materials, 0.5NaH-0.5TiH_2-4Al-C and 0.5NaH-0.5ZrH_2-4Al-C, milled in the cryogenic mill. The morphology is quite astonishing for a milling time of 1 hour. First stand out the presence of two phases: a crystalline material inside an amorphous material. Second, some of the observed crystals sizes are well below 1μm. This level of particle size reduction is reached (or equivalent) by the planetary mill at 25 hours of milling. Thus the milling at the cryogenic mill can reduce milling times, i.e. to make efficient the milling process.

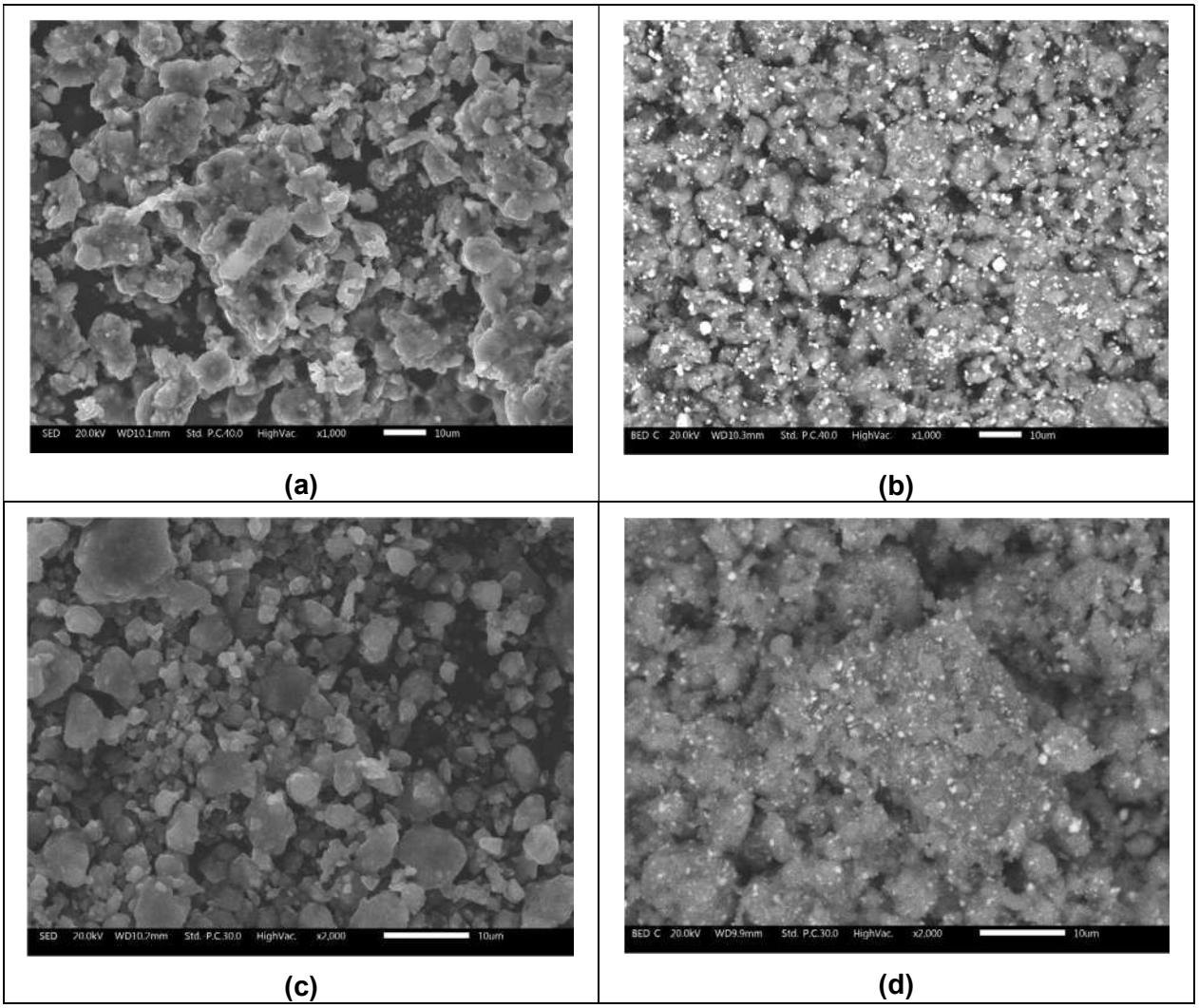

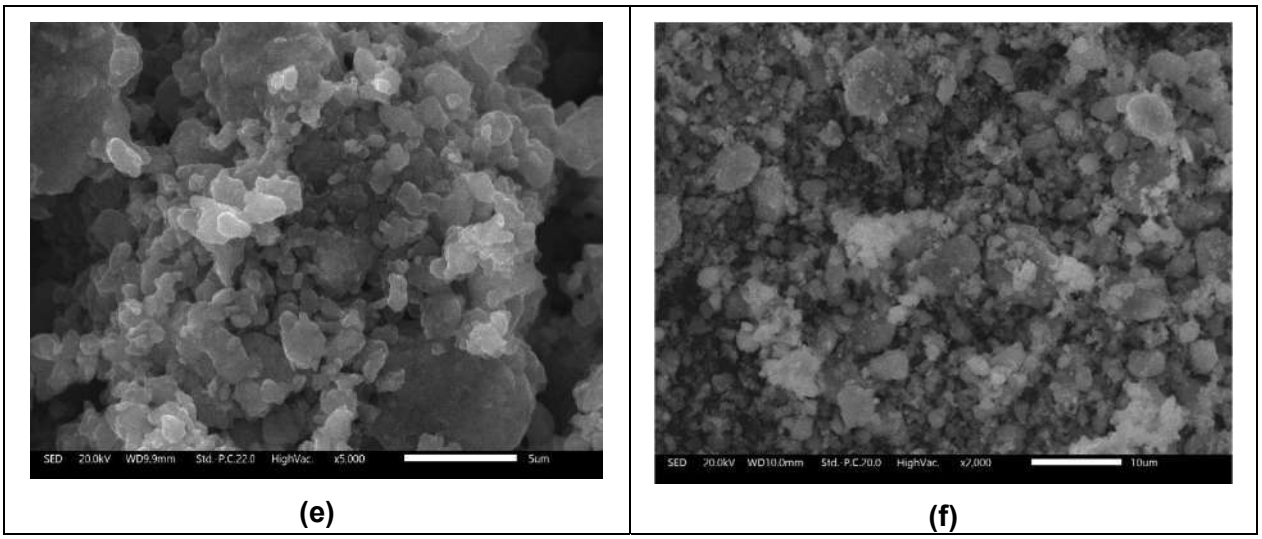

Fig. 1. SEM images of as-milled 0.5NaH-0.5TiH_2-4Al-P (left column) and 0.5NaH-0.5ZrH_2-4Al-P (right column). (a) and (b) 5 hours of milling. (c) and (d) 25 hours of milling. (e) and (f) 25 hours of milling.

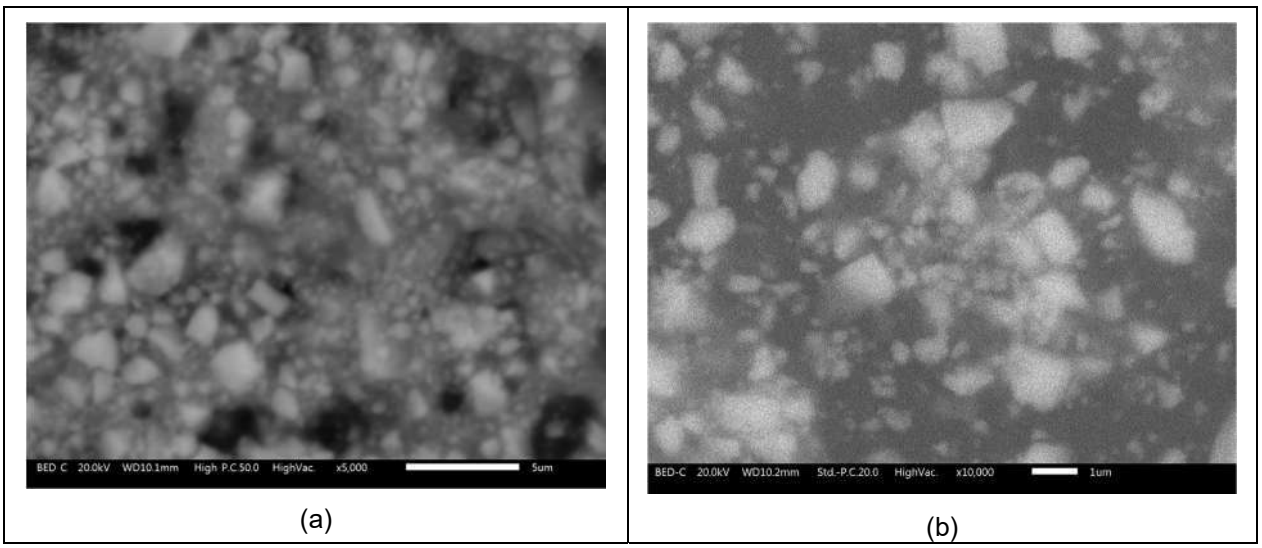

Fig. 2. SEM images of as-milled (a) 0.5NaH-0.5TiH_2-4Al-C and (b) 0.5NaH-0.5ZrH_2-4Al-C, 1 hour of milling.

Fig.3 presents the XRD patterns of the as-milled 0.5NaH-0.5TiH_2-4Al series. The patterns are dominated by the Al and TiH_2 peaks. The absence of NaH peaks indicates a complete amorphization of this material even in the early stages of milling. A Rietveld refinement was performed to obtain the crystal size and the deformations on the cell dimensions as the milling time progressed. In this regard, the milling of Al is a "tricky" process, due to the tendency to the cold-welding and formation of agglomerates rather than the reduction of particle size of Al. The inset of Fig. 3 presents the refined Al crystal size as a function of milling time at the two mills. The results are quite remarkable, 1 hour of milling in the cryo-mill is almost equivalent to 20 hours of milling in the planetary mill. Quite similar results were obtained with the 0.5NaH-0.5ZrH_2-4Al series (Fig. 4). In that series, the NaH peaks also are not present. Rietveld refinements of Al-crystal size indicate that the cryogenic milling time of 1 hour is equivalent to 25 hours of milling in the planetary mill (inset of Fig. 4). This confirms the findings of SEM characterization, evidence the improvement in the process of formation of precursor mixtures towards the synthesis of double-cation alanates, and indicates that the cryogenic milling can be the most recommended mixing process for producing precursor mixtures.

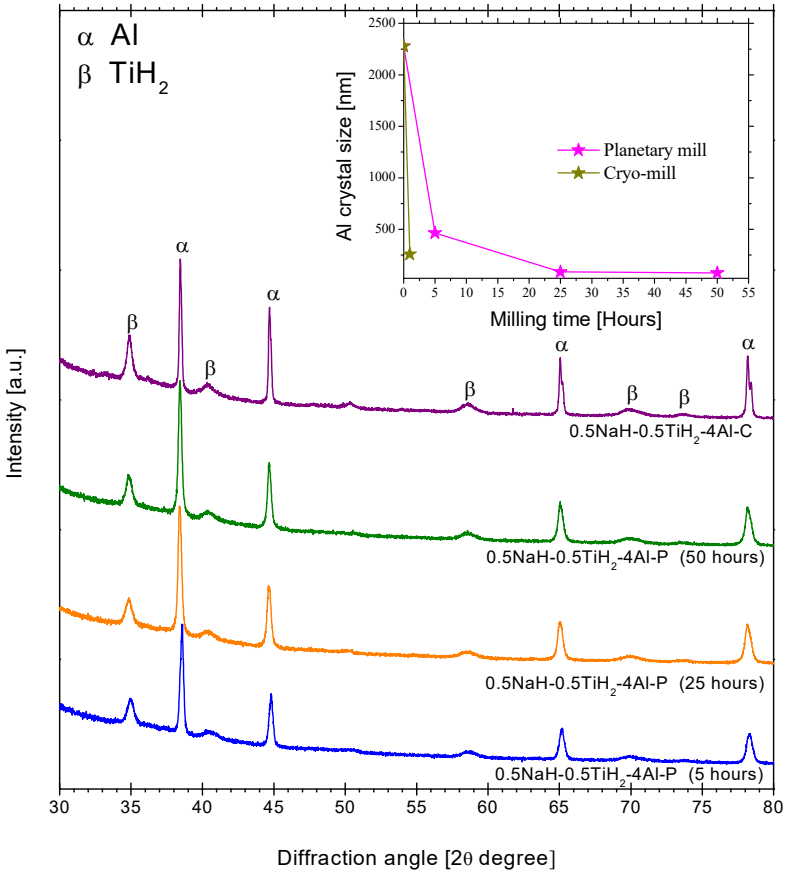

Fig. 3. XRD patterns of as-milled 0.5NaH-0.5TiH_2-4Al-series.

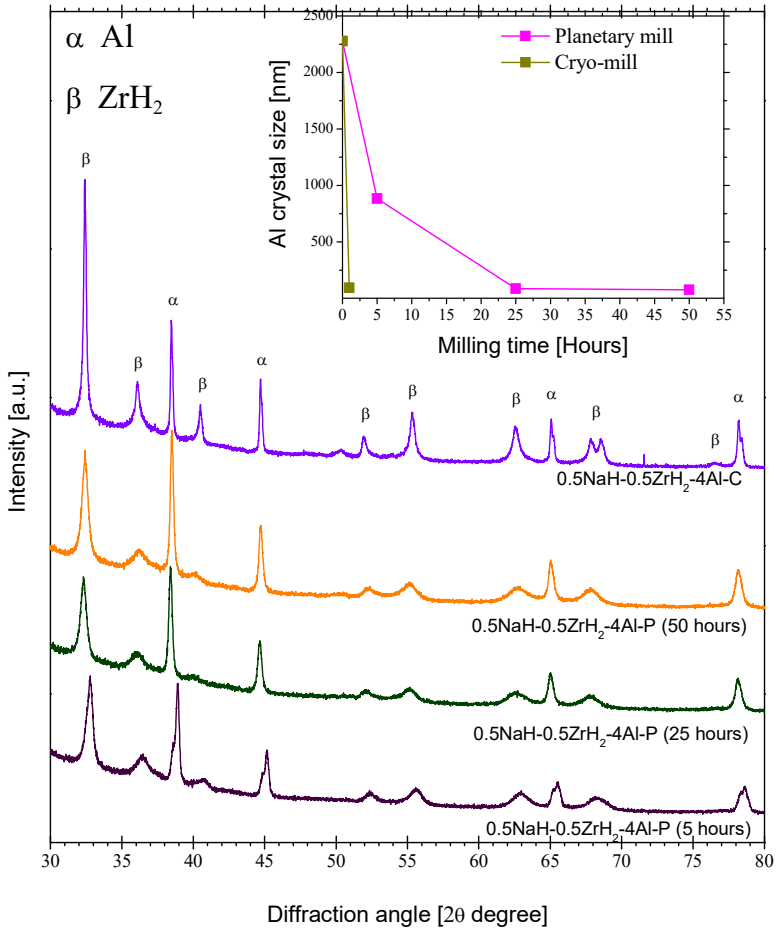

Fig. 4. XRD patterns of as-milled 0.5NaH-0.5ZrH_2-4Al-series.

3.2. Hydrogenation curves

Fig.5 collects the hydrogenation curves in a PCT mode. Due to the long time employed in each curve, only the materials milled for 50 hours in the planetary mill and the materials milled in the cryo-mill were tested. In general, the hydrogen storage is rather small, indicating the need for a suitable catalyst just as the pure hydrogenation of NaH+Al to give $NaAlH_4$ needs [1, 2]. However, as the title of the present work indicates, we are on the way towards double-cation alanates, and in this part of the work we established at a glance the most suitable hydrogenation conditions, these are 250°C-350°C and hydrogen pressure upper than 95 bar. The relatively high temperature of hydrogenation, compared with pure $NaAlH_4$, can be due to the high stability of TiH_2 and ZrH_2, as compared with NaH. Regarding the hydrogenation pressure, Fig. 5 indicates that the maximum hydrogen content was not achieved as a function of pressure, i.e. it can be expected a

better hydrogen uptake by increasing the pressure. However, the isorb-100 apparatus is limited to 100 bar of maximum pressure. On the other hand, the hydrogenation curves of Fig. 5 indicates that the materials milled at the cryogenic-mill are more prone to hydrogenation. In the second stage of this on-going research, the materials will be doped with catalyst and tested at the maximum pressure available in our apparatus.

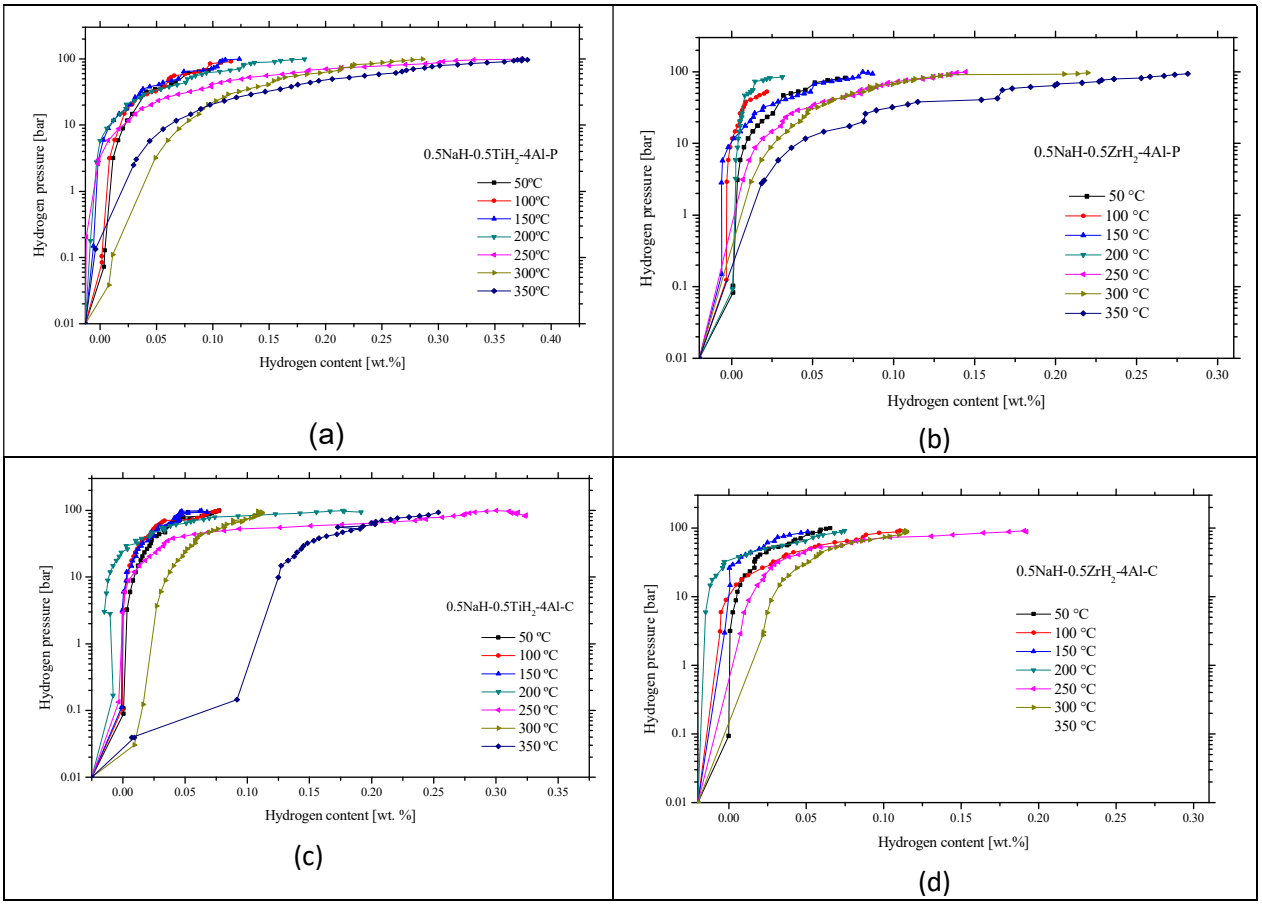

Fig. 5. PCT curves of (a) 0.5NaH-0.5TiH_2-4Al-P, (b) 0.5NaH-0.5ZrH_2-4Al-P, (c) 0.5NaH-0.5TiH_2-4Al-C and (d) 0.5NaH-0.5ZrH_2-4Al-C.

3.3. Characterization of hydrogenated materials

Fig. 6 present the characteristic SEM images of the hydrogenated samples. The main change, as compared to the as-milled materials, is the formation of protuberances at the surface of materials. These protuberances are common to hydrogenated materials, and it is believed that the nucleation and growing of hydrogenated phases start there. In a catalyzed material, these points of nucleation and growing usually correspond to the existence of a particle of a catalyst. In our materials, the

nucleation and growing points may correspond to TiH_2 or ZrH_2 particles. In general, the particle size did not change upon the long exposition to hydrogen pressure and temperature.

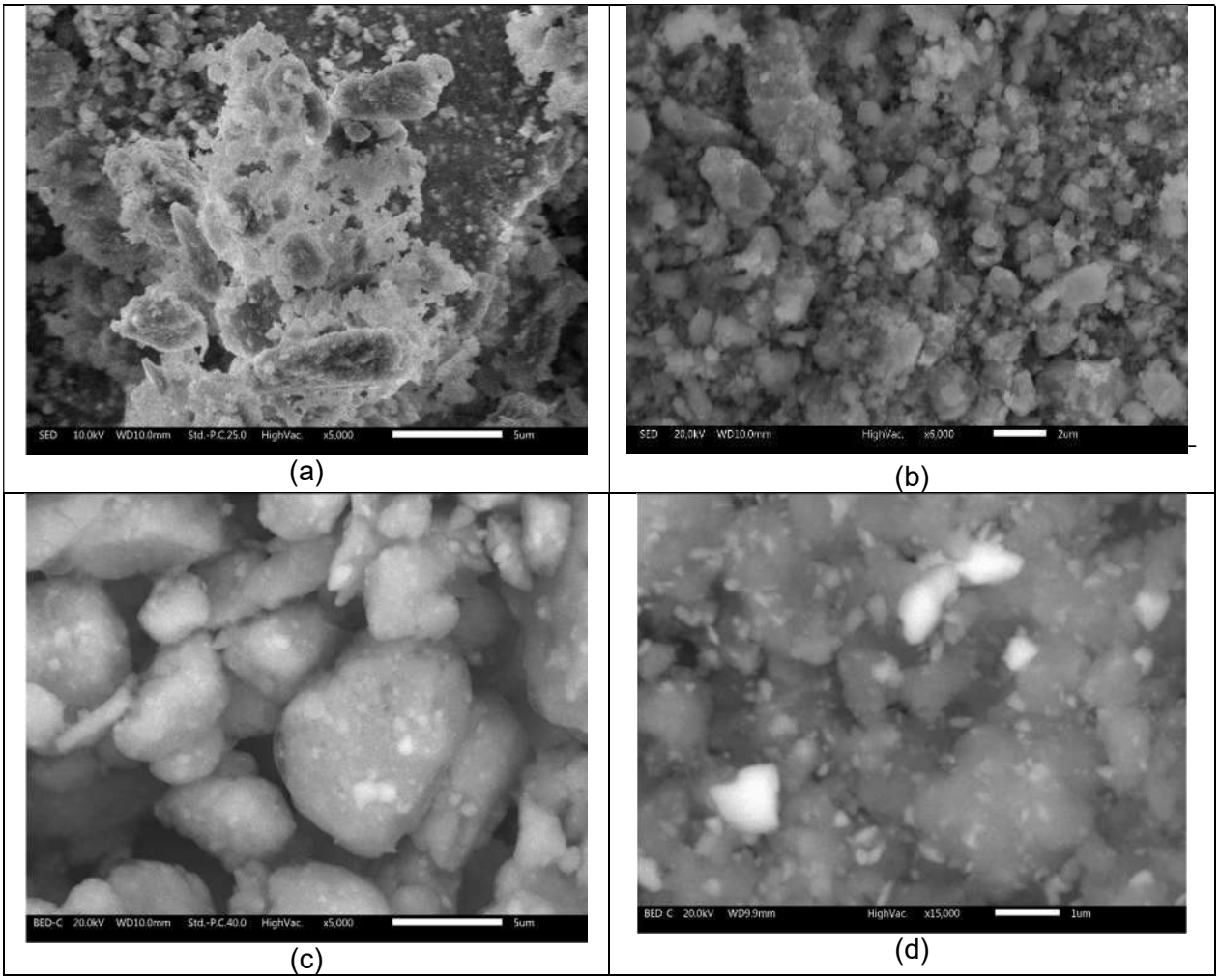

Fig. 6. SEM images of hydrogenated (-HH) (a) 0.5NaH-0.5TiH_2-4Al-P-HH, (b) 0.5NaH-0.5ZrH_2-4Al-P-HH, (c) 0.5NaH-0.5TiH_2-4Al-C-HH and (d) 0.5NaH-0.5ZrH_2-4Al-C-HH.

Fig. 7 presents the XRD patterns of the hydrogenated materials. The results confirm the observations after the PCT-curves, i.e. the limited formation of hydrogenation products. However, some differences can be highlighted. The first of them is that the materials with TiH_2 are more prone to hydrogenation than the materials with ZrH_2. The hydrogen exposed 0.5NaH-0.5TiH_2-4Al-P (HH) presents the formation of Al_5Ti_2 phase. The formation of Al-Ti phases had been recognized as a precursor of the formation of $NaAlH_4$ in NaH+Al catalyzed with Ti-compounds. This supports our statement about the need for a higher hydrogen

pressure for completing hydrogenation reactions. The hydrogen exposed 0.5NaH-0.5TiH_2-4Al-C (HH) presents the more interesting results. There, the formation of Al_5Ti_2 also can be observed. Stand out the formation of $NaAlH_4$ without the formation of Na_3AlH_6, i.e. the intermediary of formation of $NaAlH_4$. Even more, a set of peaks that were not identified at the COD and ICSD databases may correspond to the incipient formation of the wanted double cation alanate.

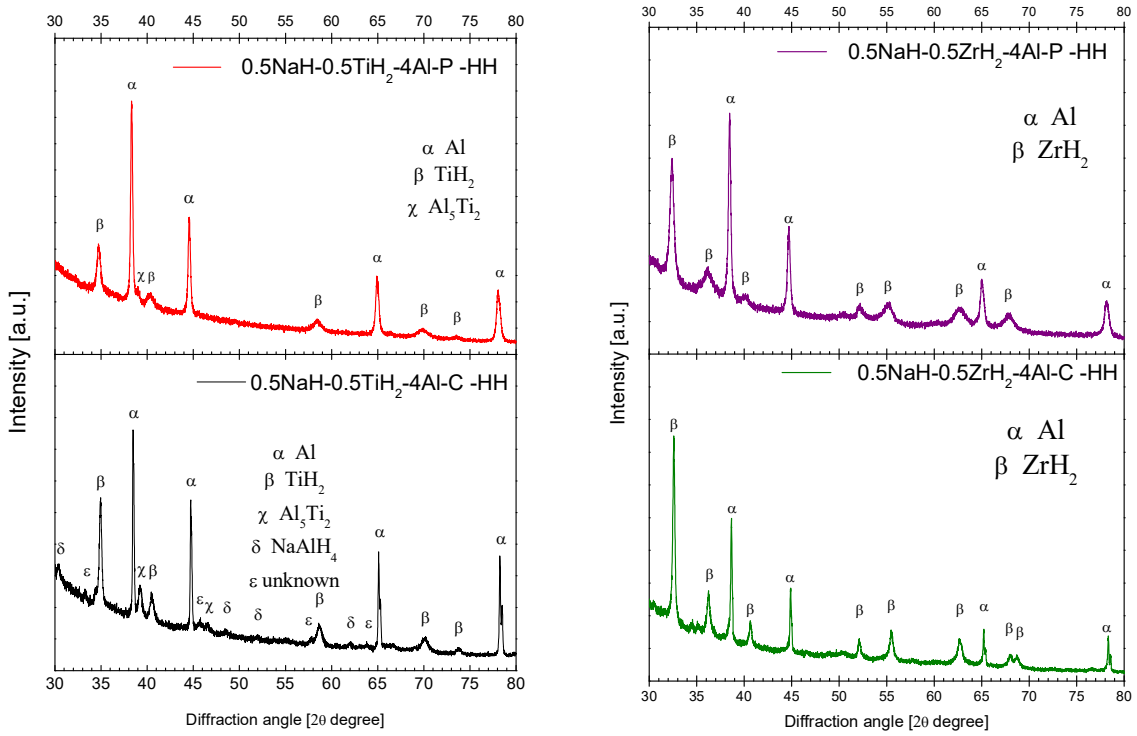

Fig. 7. SEM images of hydrogenated (-HH) (a) 0.5NaH-0.5TiH_2-4Al samples and (b) 0.5NaH-0.5ZrH_2-4Al-samples.

4. Conclusion

A series of 0.5NaH-0.5TiH_2-4Al and 0.5NaH-0.5ZrH_2-4Al-samples were produced by mechanical milling in two different mills, a planetary mill, and a cryogenic mill. The SEM and XRD characterization of as-milled materials indicate an important time-reduction, i.e. a more efficient preparation procedure of mixtures by the use of the cryogenic mill. Hydrogenation testing confirms that the materials milled in the cryogenic mill present a better tendency towards hydrogenation reaction and the formation of alanates. Also, the materials with TiH_2 present a better tendency towards hydrogenation than the samples with ZrH_2. Characterization of hydrogen exposed Ti-materials indicate the formation of Al_5Ti_2, which is considered as a precursor to the formation of alanates. The 0.5NaH-0.5TiH_2-4Al milled at the cryogenic mill presented the formation of sodium alanate and the formation of an unknown phase that can be the wanted double cation alanate.

Further research must focus on the 0.5NaH-0.5TiH_2-4Al sample added with a suitable catalyst and higher hydrogen pressure.

Acknowledgements

This research was founded by ***CONACyT*** proyect ***Ciencia Básica 251347: Alanatos no convencionales para almacenamiento de hidrógeno a baja temperatura.***

References

[1] Bogdanovic B, Schwickardi M. Ti-doped alkali metal aluminum hydrides as potential novel reversible hydrogen storage materials. J Alloys Compds. 1997: 253-254; 1-9.
[2] Gross KL, Majzoub E. US Patent 2003/0143154 A1
[3] Sanjeev L. Ethyl Corporation, US Patent 5,295,581, 22.03.1994, Gunner E.N. Ethyl Corporation, US Patent 4,790,985, 13.12.1988
[4] Ashby EC, Brendel OJ, Redman E. Direct synthesis of complex metal hydrides. Inorg. Chem. 1963: 2(3); 499–504.
[5] Bogdanovic B, Schwickardi M. US Patent 2003/0053948 A1
[6] Huot J, Ravnsbæk DB, Zhang J, Cuevas F, Latroche M, Jensen TR. Mechanochemical synthesis of hydrogen storage materials. Progress Mat. Sci. 2013: 58, 30-75.
[7] Loevvik OM, Swang O. Crystal structures and electronic structures of alkali aluminohexahydrides from density functional calculations. J. Alloys Compd. 2005: 404; 757 761.
[8] Liu DM, Qian ZX, Si TZ, Zhang QA. Synthesis, crystal structure and thermal decomposition of $LiCa(AlH_4)_3$. J. Alloys Compd 2012: 520, 202-206.
[9] Akbarzadeh AR, Wolverton C, Ozolins V. First-principles determination of crystal structures, phase stability and reaction thermodynamics in the Li-Mg-Al-H hydrogen storage system. Phys. Rev. B 2009: 79; 184102-1 184102-9.

XVIII International Congress
of the Mexican Hydrogen Society

Hydrogen adsorption depending of temperature on surface (110) of $Mg_{1-x}M_x$ alloys (M = Al, Ni, Zn; 0.0≤ x ≤ 0.10)

O. Ramírez-Rodríguez [1], G. Ramírez-Dámaso [1], F. Caballero [2], F. L. Castillo-Alvarado [3, 4], J. Roberge [1, 5], D. Romo–Rico[1] and A. Ortiz-Ubilla [1].

[1] Escuela Superior de Ingeniería y Arquitectura "Unidad Ticomán" del Instituto Politécnico Nacional, Av. Ticomán No. 600, Col. San José Ticomán, C. P. 07340, Del. Gustavo A. Madero, CDMX, México.
[2] Carrera de Ingeniería Química, Facultad de Estudios Superiores Zaragoza C. II UNAM, Batalla 5 de Mayo s/n, Col. Ejército de Oriente, C.P. 09320, Iztapalapa CDMX, México.
[3] Escuela Superior de Física y Matemáticas del Instituto Politécnico Nacional, Av. I. P. N. s/n, Unidad Profesional Adolfo López Mateos, Edificio 9, col. Lindavista, Del. Gustavo A. Madero, C. P. 07738, CDMX, México.
[4] Becario COFAA, EDD Instituto Politécnico Nacional.
5 Becaria COFAA, EDI Instituto Politécnico Nacional.
* Corresponding author: fitoram_omarod@live.com.mx

ABSTRACT

In this work, the adsorption energies for temperatures of 100, 300, 500 and 700 K, were compared with concentration of magnesium of 1.0, 0.98, 0.96, 0.94, 0.92 and 0.90 in magnesium-aluminum, magnesium-nickel and magnesium-zinc alloys respectively. Magnesium is one of the best metals to store hydrogen, with about 7.6 % in weight of H2. In order to compare our results with experimental results of pure magnesium, these temperatures were selected based on previous works which reported the range of adsorption and desorption temperatures for hydrogen on magnesium were between 300 and 500 K. The calculations were done with the Dmol3 module from the molecular simulation program Materials Studio.

Keywords (Maximum 4 words): Hydrogen adsorption, magnesium-aluminum alloy, magnesium-nickel alloy, magnesium-zinc alloy.

---

1. Introduction

The problem in using hydrogen as a fuel resource is its storage, because hydrogen is a diatomic gas with a very low density of 0.0899 Kg/m^3, at standard temperature and pressure (-273.15 K, 1 atm). This means that we can store about 90 g of H_2 in 1 m^3, therefore making it complicated to store in gaseous state, as it would require very large containers. So, the hydrogen

storing have been directed to store in metals (adsorption) and later extracted from the same material (desorption). The use of metal hydrides with applications in hydrogen fuel cells is one of the most important topic and one of the most studied by their use for hydrogen fuel cells.

Several experimental studies have been done on the storage of hydrogen in magnesium [1], magnesium-aluminum [2, 3], magnesium-nickel [4, 5], magnesium-zinc [3] and different structures of magnesium [6-10]. Experimental results reported that the pure magnesium can store about 7.6 wt. % of hydrogen, but, the low rate of absorption and temperatures near 600 K, makes its use difficult. Saluzka et. al. [1], found that a larger residence time of the magnesium powder into a ball mill, allowed a higher hydrogen adsorption rate. On the other hand, Andreasen A. [2] and Milanese et al. [3] reported that the magnesium-aluminum alloy allows to lowers the adsorption temperature of hydrogen, though with a minor capacity of adsorption. Schlapbach et al. [4] mentioned that nickel helps to dissociate the hydrogen molecule in the process of adsorption, and Saluzki et al. [5] mentioned that the magnesium-nickel alloy has an adsorption temperature of the order of 500 K (10 bars) and a desorption temperature of about 600 K (1 bar). Furthermore, the capacity of adsorption of magnesium-nickel alloy is of the order of 3.6 wt% of hydrogen. Finally, for the magnesium-zinc alloy, Milanese et al. [3] showed that an Mg0.70Zn0.30 alloy can possibly adsorb about 4.5 wt. % of hydrogen, but at temperature ~ 630 K.

Theoretical results of magnesium hydride were obtained by Liang et al. [6], who analyzed different simulations of the MgH2 alloy in bulk and in thin films. They concluded that by increasing the number of films, the enthalpy of formation; becomes similar to the enthalpy of formation of the bulk MgH2. Norskov et al. [7] computed the energy of activation produced by the adsorption of H molecules on the surface of magnesium and they found a value in the order of 0.5 eV.

Recently, works have been done on the adsorption of hydrogen on the surface (110) of MgAl alloy, for concentrations between 90 and 100 wt. % Mg [8-10]. Then, MgAl, MgNi and MgZn alloys, for concentrations between 80 and 100 wt. % Mg was also studied by Ramírez-Platón [11], which found that magnesium-aluminum is the best alloy for hydrogen adsorption, with concentrations between 6 and 8 wt. % of Al, for temperatures close to absolute zero; (the adsorption energies were calculated between 0.1 and 0.9 eV).

In this work, the main goal is to compare the results of adsorption energies of magnesium-aluminum, magnesium-nickel and magnesium-zinc alloys, for magnesium concentrations between 90 and 100 wt. % Mg, in order to find the biggest value of adsorption, as a function of temperature.

2. Materials and Methods

The first step is to construct a bimetallic alloy $Mg_{1-x}M_x$, with hexagonal closed packed (hcp) crystal structure, because the concentration of magnesium is higher than the concentration of M (aluminum, nickel, zinc). The building of magnesium crystal structure was done with CASTEP, from the program Materials Studio, a quantum mechanics program of molecular simulation. The setup parameters used for the building of the magnesium structure are presented in Table 1.

Table 1. Setup parameters in the CASTEP calculations.

	Final enthalpies calculation
Functional	GGA (PW91)
Basis Set	Plane waves
Core treatment	All electron
Hamiltonian integration accuracy	Fine
k-point separation (1 Å)	0.04 (fine)
SCF convergence	10^{-6}

The set of optimizations, considering concentrations of 100, 98… 90 wt. % Mg, provide the enthalpies of formation on the surface without hydrogen $Mg_{1-x}M_x$ (110), $Mg_{1-x}M_x$ with hydrogen and the supercell (2x1). These values are used to obtain average chemisorption energy (ΔE_{chem}) and repulsion energy (ΔE_{rep}) of H_2 on the MgAl alloy [12] :

$$\Delta E_{chem} = \frac{1}{2} E_{(2x1)\ H2\ on\ Mg1-xMx(110)} - \Delta E_{Mg1-xMx\ (110)} - \Delta E_{H2\ molecule} \quad (1)$$

And

$$\Delta E_{rep} = \frac{1}{2} E_{(2x1)\ H2\ on\ Mg1-xMx(110)} - E_{(1x1)H2\ on\ Mg1-xMx(110)} \quad (2)$$

3. Results and Discussion

In order for the hydrogen molecule to interact with the magnesium-nickel alloy we cleaved the surface in the direction of the plane (110). Figure. 1, shows the optimized structure of this cleaved surface, before it interacts with hydrogen molecule.

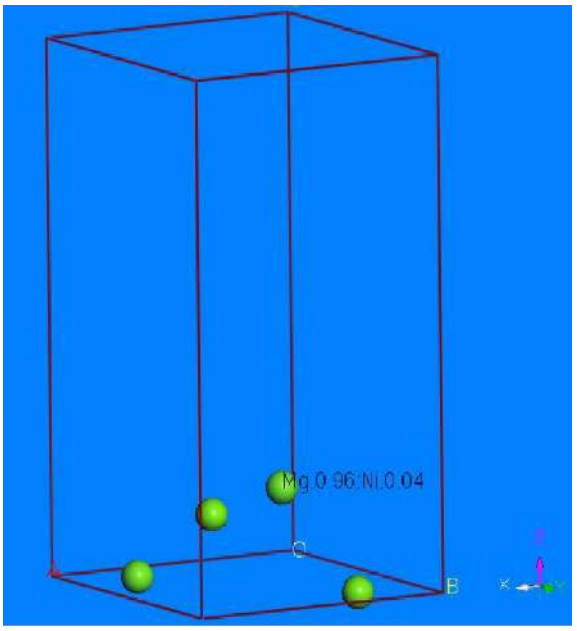

Fig. 1. Cleaved surface (110) of $Mg_{0.96}Ni_{0.04}$.

Once the surface is optimized, the hydrogen molecule can interact with MgNi alloy to build a supercell, as shown in figure 2.

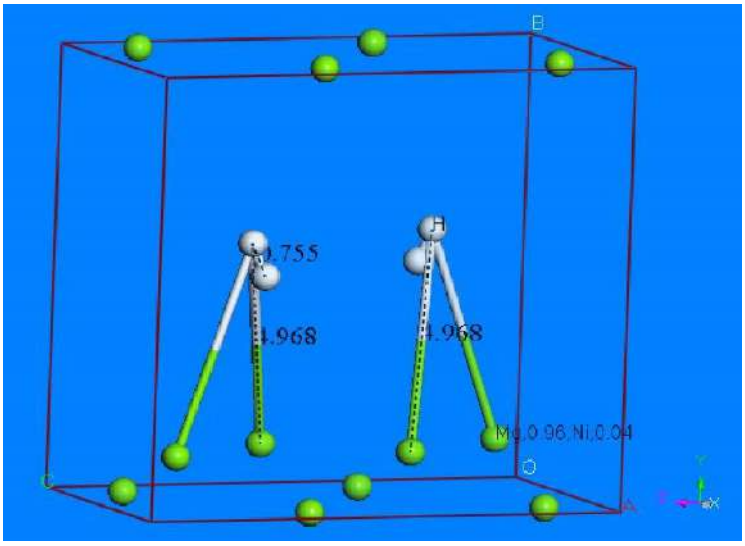

Fig. 2. Optimized supercell (2x1) of $Mg_{0.96}Ni_{0.04}$ alloy with hydrogen molecule on his surface.

This geometric optimization shows that H_2 molecule is not dissociated (d=0.755$\dot{A}$) and is maintained at a distance of 4.267$\dot{A}$ of the nearest atom of the metallic surface.

Finally, with the module DMol3, we obtain the chemisorption and repulsion energy of the hydrogen molecule on the surface of these metallic alloys as a function of the composition and temperature [13]. The resulting adsorption energies (Eads=Echem-Erep) from the interaction of hydrogen molecule with the surface of Mg1-xAlx at temperatures from 0 to 700 K are represented in figure 3.

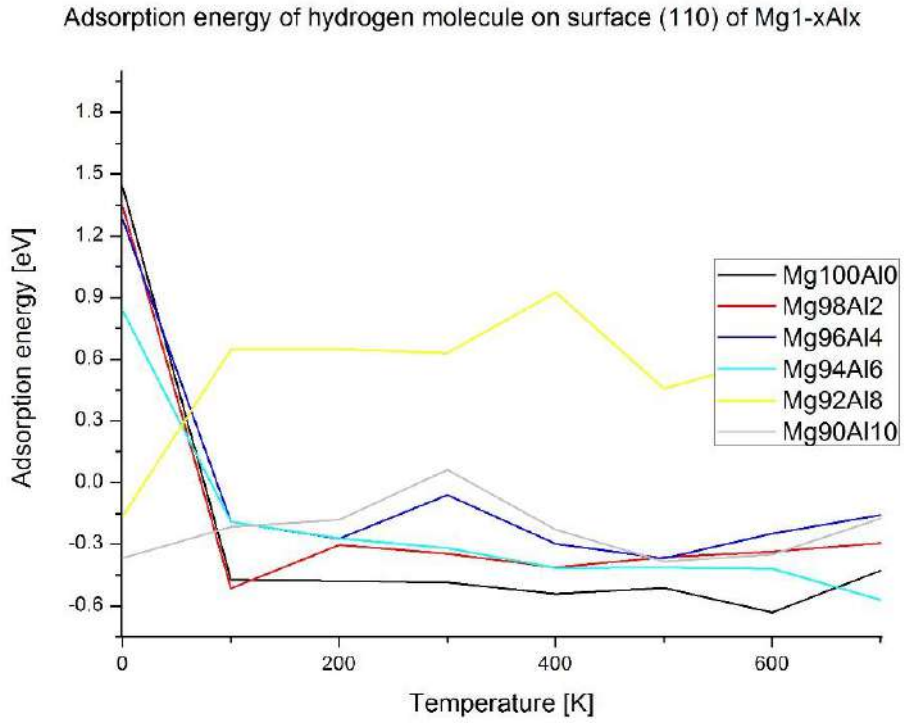

Fig. 3. Adsorption energies of $Mg_{1-x}Al_x$, $0 \leq T \leq 700$.

The best values of adsorption energies of magnesium-aluminum alloy, for 0 K, are $Mg_{0.92}Al_{0.08}$ and $Mg_{0.90}Al_{0.10}$. When the temperature increases, the hydrogen absorption capacity is improved, except for $Mg_{0.92}Al_{0.08}$. We also found that magnesium-aluminum alloy have the best values of adsorption energies, between -0.6 eV and –0.1 eV.

The results of hydrogen adsorption energy on the surface of magnesium-nickel alloy are presented in figure 4.

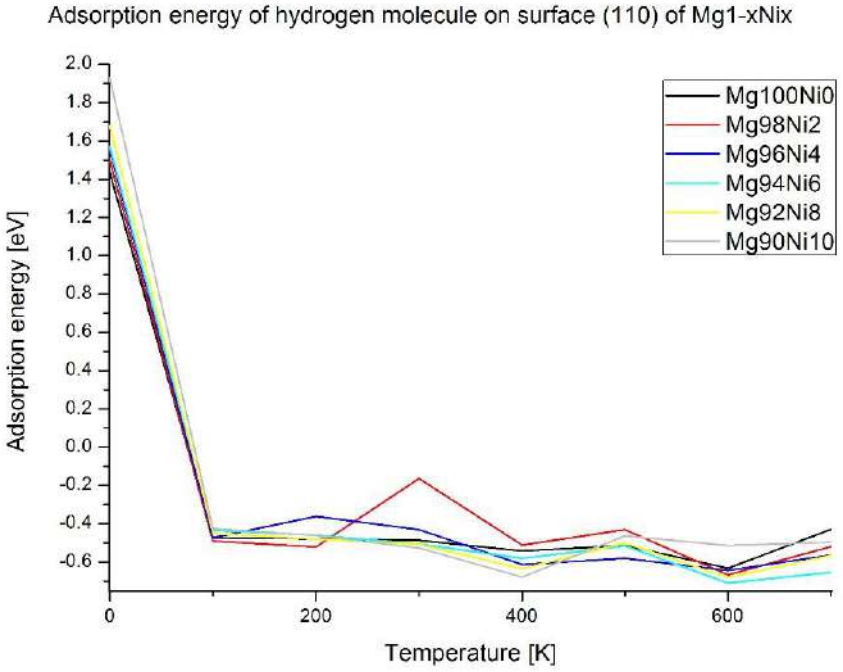

Fig. 4. Adsorption energies of $Mg_{1-x}Ni_x$, $0 \leq T \leq 700$.

At 0 K, the hydrogen adsorption is not good enough, but when the temperature increases, the adsorption capacity of the hydrogen molecule is improved.

Finally, in figure 5, we show the results of hydrogen adsorption on the magnesium-zinc alloy.

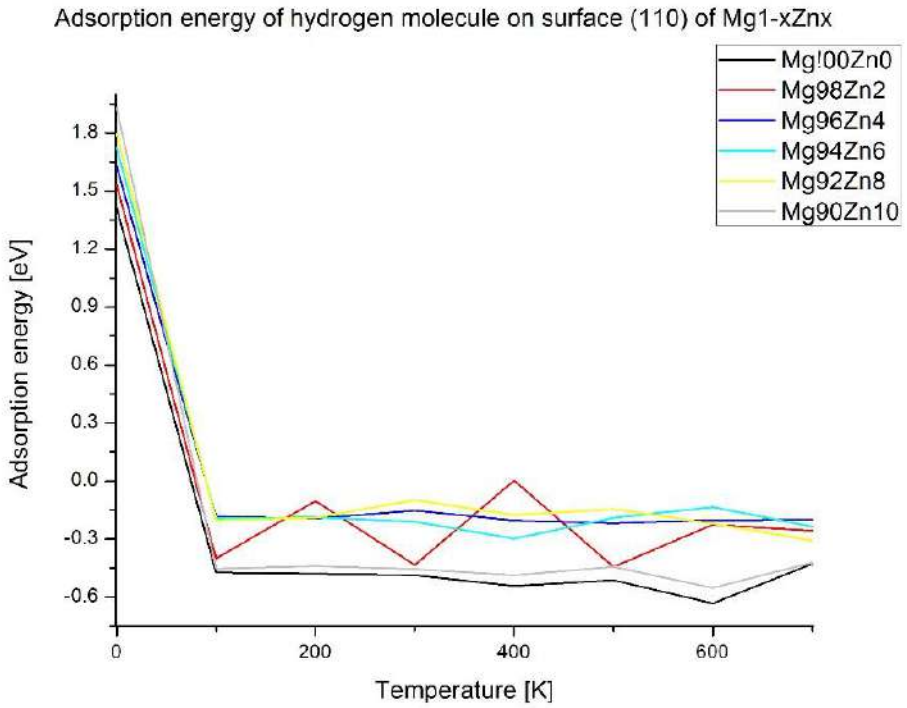

Fig. 5. Adsorption energies of $Mg_{1-x}Zn_x$, $0 \leq T \leq 700$.

The case of magnesium-nickel and magnesium-zinc are very similar, because the increase in temperature produce an increases in the adsorption energy of hydrogen on the metallic surface. For magnesium nickel the best concentration occurs for $Mg_{0.96}Ni_{0.04}$, and for magnesium-zinc the best adsorption occurs for $Mg_{0.92}Zn_{0.08}$. Our results are in good agreement with experimental results of enthalpies and adsorption energy of $Mg_{1-x}M_x$ reported by different authors [2, 6, and 7].

4. Conclusion

The values of adsorption energies of hydrogen on the surface (110) of $Mg_{1-x}M_x$ as a function of temperature let us conclude than the increment of temperatures is improved with the increment of concentrations of aluminum, nickel and zinc. The best temperature for the hydrogen adsorption energy is of 600 K for all three alloys. The effect of increasing the temperature stabilizes the hydrogen adsorption in magnesium-nickel and-magnesium-zinc alloys.

5. Acknowledgements

F. L. Castillo-Alvarado acknowledges the partial support provided by COFAA-Instituto Politécnico Nacional and EDD- Instituto Politécnico Nacional, MEXICO.

Julie Roberge acknowledges the partial support provided by COFAA-Instituto Politécnico Nacional and EDI- Instituto Politécnico Nacional, MEXICO.

G. Ramírez-Dámaso acnowledges the partial support provided trhough the project SIP-20170593, by Instituto Politécnico Nacional, MEXICO.

6. References

[1] Zaluska A., Zaluski L., Strom-Olsen J. O., Nanocrystalline magnesium for hydrogen storage, J. Alloys Comp. (1999) 288: 217–225.
[2] Andreasen A., Hydrogenation of Mg-Al alloys. International Journal of Hydrogen Energy 33 (2008) 7489-7497.
[3] Milanese C., Girella A., Bruni G., Berbenni V., Cofrancesco P., Marini A., Villa M., Matteazzi P., Hydrogen storage in magnesium–metal mixtures: Reversibility, kinetic aspects and phase analysis, Journal of Alloys and Compounds 465 (2008) 396–405.
[4] Schlapbach L., Seiler A., Stucki F. and Siegmann H. C., Surface effects and the formation of metal hydrides, Journal of the Less-Common Metals, 73 (1980) 145-160.
[5] Zaluski L., Zaluska A., Strom-Olsen J. O., Nanocrystalline metal hydrides, Journal of Alloys and Compounds 253–254 (1997) 70–79.
[6] Liang J, J. Theoretical insight on tailoring energetics of Mg hydrogen absorption/desorption through nano-engineering, Appl. Phys. A (2005) 80(1): 173–178.
[7] Norskov J. K., Houmoller A., Johansson P. K., and Lundqvist B. I., Adsorption and Dissociation of H2 on Mg Surfaces, Phys. Rev. Lett. Vol. 46, No. 4, 257-260, (1981).
[8] G. Ramírez-Dámaso, I.E. Ramírez-Platón, E. López-Chávez, F.L. Castillo-Alvarado, A. Cruz-Torres, F. Caballero, R. Mondragón-Guzmán, E. Rojas-Hernández, A DFT study of hydrogen storage on surface (110) of Mg1-xAlx (0 ≤ x ≤ 0.1), Int. J. Hydrogen Energy 41 (2016) 23388-23393.
[9] I. E. Ramírez-Platón et al, , Memory of the XVI International Congress of the Mexican Hydrogen Society, p. 206-5208, 2016.
[10] O. Ramírez-Rodríguez et al, Book of Proceedings of the XVII International Congress of the Mexican Hydrogen Society, p. 52-56, 2017.
[11] I. E. Ramírez-Platón, “Almacenamiento de Hidrógeno en Aleaciones $Mg_{1-x}M_x$ (M=Al, Ni, Zn) para $0 \leq x \leq 0.2$”, Master Degree Thesis, SEPI-ESIA TICOMAN, Instituto Politécnico Nacional, México (2016), in Spanish.
[12] Web page: www.accelrys.com.
[13] O. Ramírez-Rodríguez, “DEPENDENCIA DE LA TEMPERATURA PARA EL ALMACENAMIENTO DE HIDROGEBO EN HIDRUROS METALICOS $Mg_{1-x}M_x$ (M=Al, Ni, Zn, x= 0.00, 0.02,…, 0.20)”, Master Degree Thesis, SEPI-ESIA TICOMAN, Instituto Politécnico Nacional, México (2018), in Spanish.

XVIII International Congress
of the Mexican Hydrogen Society

Transition Phases in the Structure of Calcium Hydride

W. Ramírez-Carbellido[1], F. de L. Castillo-Alvarado[1], T. Ramírez-Rodríguez[1,*]

[1]Instituto Politécnico Nacional, Av. Luis Enrique Erro S/N, Unidad Profesional Adolfo López Mateos, Zacatenco, Delegación Gustavo A. Madero, C.P. 07738, Ciudad de México; México.
* Corresponding author: 044 (55) 4352 0891, teresa.ramirez7715@gmail.com

ABSTRACT

It is thought that hydrogen is a clean energy alternative for transportation applications in a stationary manner. Calcium hydride is a light metal hydride being among the promising materials for the storage of hydrogen. It requires a practical storage of hydrogen and there are still several technological challenges to be solved. It is important to have a database of the fundamental structures and properties of hydride materials as an aid to improve the design of materials for hydrogen storage. A detailed study of the structure and properties of calcium hydride that shows how these properties change with destabilization by characterizing the local bonding potentials associated with hydrogen is of great importance.
The vibratory properties of calcium hydride and its crystalline structure have been determine in the space groups Pnma, $P6_3mmc$ and P6mmm. The calculations of the electronic structure were made using the pseudopotential plane wave within the theory of the functioning of the density, as well as for the calculation of the vibratory modes in linear response, the vibrational modes to environmental conditions of the calcium hydride have been assigned for the calculations in the space group Pnma. The Materials Studio software has been used, the Generated Gradient Approach (GGA) has been used for the exchange correlation potential within the parametrization of Perdew Burke Ernzerhof (PBE), the rules conservation scheme has been used to generate the pseudopotentials for the calcium and hydrogen atoms.
The calculation of the phonons based on the optimized structure reproduces the density of calcium hydride states in the spatial groups Pnma, $P6_3mmc$ and P6mmm of reported works.

Keywords: calcium hydride; structural properties; first principles calculation

1. Introduction

Hydrogen is a clean energy alternative, light metal hydrides such as LiH, MgH_2 and CaH_2 are the most promising due to their high mass densities of hydrogen. However, adequate storage of hydrogen requires materials with low molecular weight, low operating temperature, fast kinetics, reversibility and low cost. [1, 2]. Hydrogen is one of the basic objects of science and many major discoveries have been made on the basis of atomic and molecular hydrogen. Under ambient pressure and low temperature. The hydrogen forms a molecular crystal whereas under high pressure, the hydrogen molecules dissociate and are transformed into a monotonic crystal called metallic hydrogen. The dissociation of hydrogen is a highly endothermic process, which in part justifies its low reactivity at room temperature. The hydrogen atom can acquire an electron thereby completing the structure $1s^2$ of Helium to form the hybrid ion H^-. This ion exists as such on the saline hydrides (KH and CaH_2) that form the most electropositive metals [3]. Metal hybrids have higher hydrogen-storage density. At moderate temperature and pressure, hydrogen can be stored in metal hydrides [4]. Bonding in metallic hydrides is closely related to the issue of the electronic make-up of hydrogen. The hydrides exhibit ionic bond. The alkali metal is easily ionized and loses its valence electron to form the hydride anion and the system is stabilized by its Madelung energy. CaH_2 is isomorphic to crystallize with orthorhombic lattice at low pressure and temperature below 600°C, exhibiting the Pnma space group [5-6].
In Wallace's research, the metal ions of CaH_2 are arranged in a slightly distorted cph structure of an orthohexagonal cell $b/a = \sqrt{3} = 1.73$. He also mentions that in the orthorhombic structure of CaH_2, the metal ions are displaced so that this ratio increases by approximately 10% to 1.89. Half of the hydride ions are located in tetrahedral interstices, but due to the peculiarities of the C29 structure, not all metal atoms are equidistant from the central H ion. The distances from Ca-H range between 2.24 and 2.28 Å. The remaining hydride ions have 5 Ca^{2+} ions as close neighbors of distances ranging from 2.38 to 2.63 Å. [7].
The anionic model states that an electron of the metal ion is transferred to the hydrogen atom; the protonic model contrary to the previous proposes that an electron is produced by hydrogen for the metallic band of the occupied third part. On the other hand, the covalent model implies that hydrogen atoms are bound to calcium covalently. The anionic model is more adequate to study the alkali-metal hydrides, which are typically ionic. Concerning CaH_2, is known as the most useful of the three light-metal hydrides (LiH, MgH_2, CaH_2) although it's ionic character resulting from the large electro negativities. The best way, allowing to understand completely the electronic properties of metal hydrides is proved to be by means of band-structure calculations. However because of the low orthorhombic symmetry, no calculation of band structure of CaH_2 has been undertaken in its real structure [8].

2. Materials and Methods

Under ambient conditions, CaH_2 crystallizes in a complicated orthorhombic phase of the $PbCl_2$ type, with space group 62 (Pnma) [9]. Also for the spatial groups 191 (P6/mmm) and 194 ($P6_3/mmc$), vibrational properties and crystalline structures were obtained based on the Density Functional Theory.

To obtain the theoretical calculations in this investigation, the Software Materials Studio was used. For the search of the electronic structure, the pseudo plane wave potential was used, as well as the linear response for the vibrational modes. With the focus on generalized gradient (GGA) for the potential for exchange correlation between the parameterization of Perdew, Burke and Ernzerhof (PBE), based on the rules of the conservation scheme to generate pseudo potentials for hydrogen and calcium atoms [10-14].
The cell contains four CaH2 molecules. This structure contains the crystalline parameters (a, b, c), six fractional coordinates (x(Ca), x(H1), x(H2), z(Ca), z(H1), z(H2)). The space groups Pnma, P6/mmm and $P6_3/mmc$ the positions of the occupied ions have been placed from what the literature suggests [15-17]. The hydrogen could be distributed over the available over the available sites, taking into account that the interatomic distance between two hydrogen ions should be larger than a minimum value. This condition could be satisfied with one arrangement only. The hydrogen positions satisfy Pnma, P6/mmm and $P6_3/mmc$ symmetries.

3. Results and Discussion

The optimization geometries were made from the data shown in Table 1. It was taken into account that the hydrogen atoms occupy two positions.

Table 1. Data to optimize the geometry of the crystals.

	Pnma(62) z=4 Orthohombic	**$P6_3/mmc$(194) z=2 Hexagonal**	**P6/mmm(191) z=1 Hexagonal**
a(Å)	4.535	3.634	3.030
b(Å)	3.606	3.634	3.030
c(Å)	6.087	4.762	1.80
V(Å)^3	147.157	54.462	14.3116
Ca(x)	0.240	2c	1a
Ca(z)	0.110		
1H(x)	0.356	2d	2d
1H(z)	0.427		
2H(x)	0.975	2a	
2H(z)	0.6765		

3.1 Structural properties

The symmetry principle in crystal chemistry **[18].** In crystal structures the arrangement of atoms reveals a pronounced tendency towards the highest possible symmetry. Counteracting factors due to special properties of the atoms may prevent the attainment of the highest possible symmetry. However, in most cases the deviations from the ideal symmetry are small (key-word pseudo-symmetry).

During phase transitions and solid state reactions which result in products of lower symmetry, the higher symmetry of the starting material is indirectly preserved by the formation of oriented domains and atoms of the same kind tend to occupy equivalent positions.

Mulliken atomic charge is defined based on orbitals. For each atom, all electronic charge contributions from orbital centered at than the atoms are summed up, and electronic overlap clouds between two atoms are divided equally to the two atoms. Mulliken charges should only be used as a quick and qualitative guild for the atomic charges in molecules.

Table 2 shows the population of Mulliken in the three different crystals. On the other hand, the density related charges. Another observable property which is closely related to atomic charges of a molecular system is the electron density of the system. Atomic charges in molecules serve to provide a simple picture of the electron density distribution of the molecule. It is also well known that the ground state properties of a many-electron system are uniquely determined by its electron density. Defining atomic charges from the system's electron density seem natural. Effect of isotropic compression of crystalline parameters a, b, and c (Å) on the charges of Ca and H, which are evaluated according to the Mulliken atomic charge.

Table 2. Mulliken atomic charges.

Pnma						
1Ca charge= 0.576	4 s	1.286				
	3 p	4.900				
	3 d	1.238				
2H charge= -0.277	1 s	1.239				
	2 p	0.038				
3H charge= -0.306	1 s	1.282				
	2 p	0.023				
$P6_3/mmc$			**P6/mmm**			spin
1Ca charge= 1.228	4s	0.083	1Ca charge= 0.657	3s	0.969	-0.007
	4p	0.140		3p	2.974	
	3d	0.163		3d	0.725	
2Ca charge= 1.228	4s	0.083	2H charge= -0.328	1s	0.670	0.042
	4p	0.140		2p	0.015	
	3d	0.163				
3H charge= -0.691	1s	0.841	3H charge= -0.328	1s	0.670	0.042
	2p	0.005		2p	0.015	
4H charge= -0.691	1s	0.841				
	2p	0.005				
5H charge= -0.537	1s	0.766				
	2p	0.002				
6H charge= -0.537	1s	0.766				
	2p	0.002				

Analysis of the Mulliken electronic population shows nature of bonding in CaH_2 (Pnma). The net charges on the calcium and the two non-equivalent hydrogens are 0.576|e|, -0.277|e| and -0.306|e|. The electrons in the orbitals for calcium in 3d, for 1H and 2H in 1s shows that they are more ionic in character, which supports the ionic nature in the crystal.
The following figures show the crystalline structures of calcium hydride with space group 62 (Pnma) in figure 1, 194 (P63/mmc) in figure 2 and 191 (P6/mmm) in figure 3. The Brillouin zone (BZ) is simply the primitive unit cell in reciprocal space. Typically, the unit cell is centered on zero. The path contains to coordinate of symmetry points in the Brillouin zone showing in Figures 2 and 3 that they represent the crystalline structures of the calcium hydride in their respective groups clear coincidences.

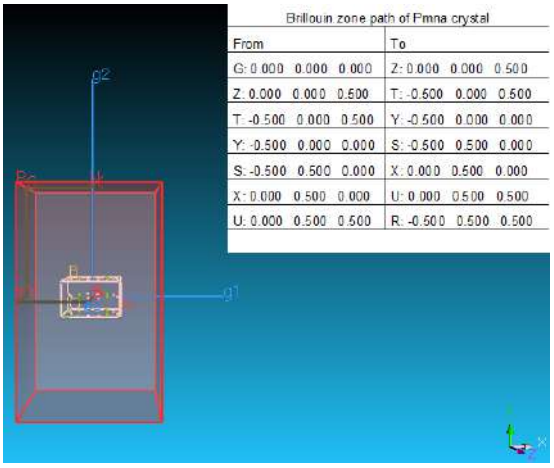

Fig. 1. Brillouin zone path of Pnma (62) crystal.

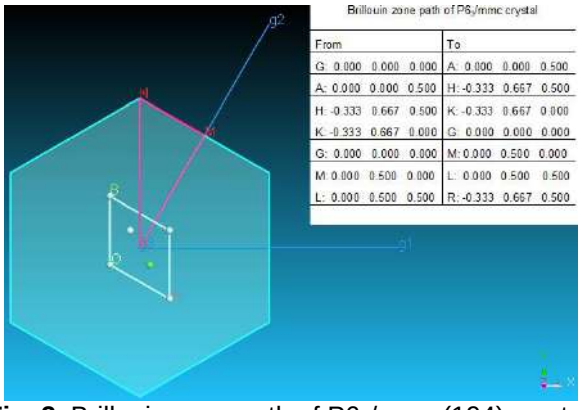

Fig. 2. Brillouin zone path of $P6_3/mmc$ (194) crystal.

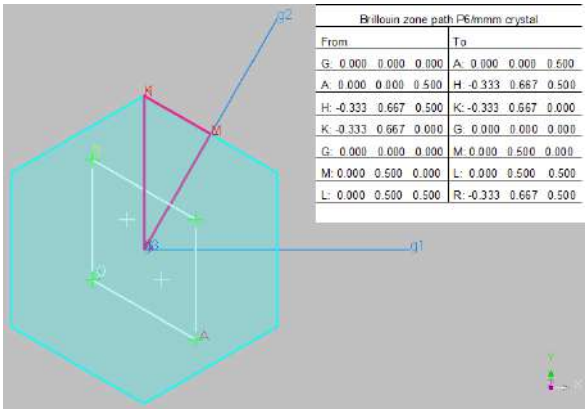

Fig. 3. Brillouin zone path of P6/mmm (191) crystal.

4. Conclusion

Hydrogen fuels are an attractive alternative energy source, as they are clean, non-toxic and renewable. However, the biggest challenge lies in the development of safe, compact, portable and cost-effective hydrogen storage systems with high energy densities for vehicular applications. Metal hydrides are promising candidates for the storage of solid state hydrogen. Calcium hydride of which we present in this work some result obtained in our research. Show the crystalline phases Pnma, P63/mmc and P6/mmm have been calculated on their crystalline properties has two ionic bonds between calcium and the two hydride ions, it is saline hydride, and that is, its structure is similar to salt. Its crystalline structure of Pnma is the same as lead chloride, which belongs to the orthorhombic crystal system. In this work we present the first part of the studies we have done on calcium hydride. The electrons in the orbitals for calcium in 3D, for 1H and 2H in 1s show that they are more ionic, which supports the ionic nature in the crystal.

References

[1] Wu, H., Zhou, W., Udovic, T. J., Rush, J. J., & Yildirim, T. (2007). Structure and vibrational spectra of calcium hydride and deuteride. *Journal of alloys and compounds*, *436*(1-2), 51-55.
[2] Rusman, N. A. A., & Dahari, M. (2016). A review on the current progress of metal hydrides material for solid-state hydrogen storage applications. *International Journal of Hydrogen Energy*, *41*(28), 12108-12126.
[3] COTTON, F. A. (1981). Química Inorgánica Avanzada. México: Limusa, S.A.
[4] Sakintuna, B., Lamari-Darkrim, F., & Hirscher, M. (2007). Metal hydride materials for solid hydrogen storage: a review. *International journal of hydrogen energy*, *32*(9), 1121-1140.
[5] Smith, G. S., Johnson, Q. C., Smith, D. K., Cox, D. E., Snyder, R. L., Zhou, R. S., & Zalkin, A. (1988). The crystal and molecular structure of beryllium hydride. *Solid state communications*, *67*(5), 491-494.

[6] Ofe, U., Onuu, M. U., & Udoimuk, A. B. (2014). Electronic and Structural Properties of CaH_2 Using GGA and GGA+ U Approximation with WIEN 2K Codes. *International Journal of Innovation and Applied Studies*, *7*(3), 1071.
[7] Wallace, W. E. (1982). Bonding of metal hydrides in relation to the characteristics of hydrogen storage materials. *Journal of the Less Common Metals*, *88*(1), 141-157.
[8] El Gridani, A., & El Mouhtadi, M. (2000). Electronic and structural properties of CaH2: an ab initio Hartree–Fock study. *Chemical Physics*, *252*(1-2), 1-8.
[9] Schäfer, H., Eisenmann, B., & Müller, W. (1973). Zintl-Phasen: Übergangsformen zwischen Metall-und Ionenbindung. *Angewandte Chemie*, *85*(17), 742-760.
[10] Seminario, J. M. (Ed.). (1996). *Recent developments and applications of modern density functional theory* (Vol. 4). Elsevier.
[11] Delley, B. (1996). Fast calculation of electrostatics in crystals and large molecules. *The Journal of Physical Chemistry*, *100*(15), 6107-6110.
[12] Perdew, J. P., Burke, K., & Ernzerhof, M. (1996). Generalized gradient approximation made simple. *Physical review letters*, *77*(18), 3865.
[13] Hammer, B. H. L. B., Hansen, L. B., & Nørskov, J. K. (1999). Improved adsorption energetics within density-functional theory using revised Perdew-Burke-Ernzerhof functionals. *Physical Review B*, *59*(11), 7413.
[14] McNellis, E. R., Meyer, J., & Reuter, K. (2009). Azobenzene at coinage metal surfaces: role of dispersive van der Waals interactions. *Physical Review B*, *80*(20), 205414.
[15] Verbraeken, M. C., Suard, E., & Irvine, J. T. (2009). Structural and electrical properties of calcium and strontium hydrides. *Journal of Materials Chemistry*, *19*(18), 2766-2770.
[16] Bergsma, J., & Loopstra, B. O. (1962). The crystal structure of calcium hydride. *Acta Crystallographica*, *15*(1), 92-93.
[17] El Gridani, A., & El Mouhtadi, M. (2000). Electronic and structural properties of CaH2: an ab initio Hartree–Fock study. *Chemical Physics*, *252*(1-2), 1-8.
[18] Müller, U. (2013). *Symmetry relationships between crystal structures: applications of crystallographic group theory in crystal chemistry* (Vol. 18). OUP Oxford.

XVIII International Congress
of the Mexican Hydrogen Society

Biohydrogen production from acid hydrolizates of fruits-and-vegetables wastes and corn stover: effects of inoculum/substrate ratio and sugar concentration

Santiago Rodríguez-Valderrama[1], Jean-Pierre Magnin[2], Pasiano Rivas-García[1], Refugio Bernardo García-Reyes[1], Idania Valdez-Vázquez[3], Elvira Ríos-Leal[4], Carlos Escamilla-Alvarado[1,*]

[1]Universidad Autónoma de Nuevo León, Faculty of Chemical Sciences, Engineering and Sustainable Bioprocesses Group, Av. Universidad S/N Ciudad Universitaria, San Nicolás de los Garza, NL, 66455, México.
[2] Laboratory of Electrochemistry and Physicochemistry of Materials and Interfaces, Martin d'Hères, France.
[3] Laboratory for Research on Advanced Processes for Water Treatment, Instituto de Ingeniería, Unidad Académica Juriquilla, Universidad Nacional Autónoma de México, México.
[4] Environmental Biotechnology and Renewable Energies R&D Group, Department of Biotechnology and Bioengineering, CINVESTAV-I.P.N. Mexico City, México
* Corresponding author: Tel: +521 55 27 31 6440. E-mail address: cea_escamilla@yahoo.com.mx

ABSTRACT

Biohydrogen can be produced from renewable sources such as fruits-and-vegetables wastes (FVW) and corn stover (CS) by bioprocess like dark fermentation. The aim of this work was to evaluate the effect of inoculum/substrate ratio and sugar concentration in biohydrogen production from acid hydrolizates.

The acid hydrolysis pretreatment was carried out with a general factorial experiment design 5X2. The factors were the combination of co-substrates (0:100, 25:75, 50:50, 75:25, 100:0, FVW:CS $\%_{dry\ base}$) and the acid catalyst (HCl and H_2SO_4, 0.5 % v/v). Reducing sugars, monomeric sugars and inhibitory compounds, such as 5-hydroxymethylfurfural, furfural and total phenolic compounds, were quantified. Afterwards, a 3^2 experimental design was developed for hydrogen production in serological bottles at 35 °C; the factors were the inoculum/substrate ratio (0.8, 1.0 and 1.2 g $SV_{inoculum}$ g $SV_{substrate}^{-1}$) and the initial concentration of reducing sugars (10, 13 and 16 g L^{-1}) respectively.

The effect of the acid catalyst and the combination of co-substrates was significant in terms of reducing sugars and conversion of sugars. The best catalyst acid was HCl for the ratio 75:25 FVW:CS. For such combination, the concentration of monomeric sugars was (g L^{-1}): 10.02, 3.67 and 2.93 for glucose, xylose and arabinose, respectively. The liquid hydrolyzates thus obtained were pretreated to eliminate inhibitory compounds. The accumulated hydrogen production was observed through the modified Gompertz model: the maximum production of hydrogen was 211.97 mL H_2 and the maximum hydrogen production rate was 8.83 mL H_2 h^{-1} for initial concentration of 13 g L^{-1} and inoculum/substrate ratio of 1.2. The metabolites produced were butyric acid, acetic acid, propionic acid and ethanol.

In conclusion, acid hydrolysis favored the production of fermentable sugars; moreover, an indirect relationship between the initial concentration of reducing sugars and the accumulated hydrogen production was established.

Keywords: dark fermentation, dilute acid hydrolysis, overliming pretreatment.

1. Introduction

The common sources for hydrogen production are the fossil fuels in processes such as steam reforming of natural gas (*ca.* 48%) and crude oil (*ca.* 30%), gasification of coal (*ca.* 18%) and water electrolysis (*ca.* 4%) [1]. These processes required high amounts of energy, furthermore emitting large amounts of oxides of carbon, sulfur, nitrogen as well as heavy metals [2]. Therefore bio-based energy arises as a promising alternative to avoid fossil fuel use. Biohydrogen production from biomass is a new area of technology that offers the potential use of hydrogen from different renewable sources, playing a double role when waste generation is reduced and energy is produced [3,4].

Hydrogen can be produced biologically through microbial electrolysis cells, photolysis, photofermentation and dark fermentation. Dark fermentation H_2 production has become a promising technology as it may be used to transform various organic wastes to hydrogen, furthermore, it does not require luminous energy, it has high hydrogen rates and its production may be maintained at non-aseptic conditions [5]. Many kinds of organic wastes have been used for hydrogen production such as organic fraction of municipal solid waste [6,7], corn stover [8,9], rice straw [10], sugarcane bagasse [11,12] and fruits and vegetables wastes [13–15]. However, duo to harsh microstructure of lignocellulosic feedstocks, pretreatments are required to hydrolyze the incorporated heterogeneous and crystalline structure, to facilitate the carbohydrates use in fermentation [16,17]. Cellulose and hemicellulose can be catalyzed to its constituents (*i.e.* glucose, xylose) by dilute acid hydrolysis; but sugar concentration after hydrolysis depend on the operational conditions (reaction time, temperature, acid concentration) and type of feedstock [5,12].

The hydrogen production by dark fermentation can be influenced by many factors like: type of inoculum, inoculum concentration, sugar concentration, inhibitory concentration, temperature and pH [17,18]. The inoculum/substrate ratio (ISR) expresses the initial amounts of inoculum and substrate fed in terms of volatile solids (VS) to experimental apparatus. At ISRs lower than 1/6, hydrogen production is inhibited due to an excessive amount of substrate that on the one hand increases osmotic pressure and hence inhibits hydrogen bacteria growth [18], and on the other promotes accumulation of volatile fatty acids (VFAs) that cause a pH decrease. Another type of inhibition occurs when partial pressure of hydrogen is increased as a consequence of the excessive accumulation of hydrogen in the headspace that results in acidogenic to solventogenic metabolic shift [12,17].

A mixture of wastes for different sources has contributed to increase hydrogen production and hydrogen yields, because mixing carbohydrates and nitrogen-rich substrates improves the nutrient content in fermentations [18,19]. The present study was therefore conducted to investigate the effects of inoculum/substrate ratio and initial sugar concentration in biohydrogen production from acid hydrolizates of a fruits-and-vegetables wastes (FVW) and corn stover (CS) mixture.

2. Materials and Methods

2.1. Co-substrates

The CS feedstock was obtained from Cuencamé, Durango, Mexico. CS was dried at 85 °C for 24 h. Subsequently, dried CS was grinded to a particle size of 180 µm by using a manual mill.

The pH of the CS was 7.54, the total solids were 94.59 %, volatile solids 89.78 $\%_{dry\ base}$ and 10.22 $\%_{dry\ base}$ of ashes. The main composition of volatile solids was 33.25 % cellulose, 24.35 % hemicellulose, 24.74 % lignin and 3.25 % protein. The elemental composition (CHON) of CS was C-43.84 %, H-15.74 %, O-39.98 % and N-0.44 %.

The FVW was collected from the university restaurant (Facultad de Ciencias Químicas of the Universidad Autónoma de Nuevo León, Nuevo León, México). FVW was ground and dried at 85°C for 24 h, then it was grinded to a particle size of 180 µm by using a mortar. Roughly, the FVW was a mixture (wet weight) of papaya peels (16.94 %), squash peels (15.57 %), potato peels (17.67 %), spinach stems (20.26 %); parsley stems (6.71 %), cucumber peels (5.72 %); melon peels (10.20 %) and apple(6.92 %). The pH of the FVW was 5.52; the total solids were 10.19 %, volatile solids 87.66 $\%_{dry\ base}$ and 12.34 $\%_{dry\ base}$ of ashes. The volatile solids contained 12.8% of cellulose, 23.4% of hemicellulose, 10.26% of lignin and 12.63% of protein. The elemental composition (CHON) of FVW was C-51.69 %, H-3.43 %, O-42.69 % and N-2.19 %.

2.2. Dilute acid hydrolysis pretreatment

The dilute acid hydrolysis was evaluated by general factorial experiment design 5X2. The factors were the mixture ratio of co-substrates (0:100, 25:75, 50:50, 75:25, 100:0, FVW:CS $\%_{dry\ base}$) and the acid catalyst type (HCl or H_2SO_4, 0.5 % v/v). The co-substrates hydrolysis was carried out by triplicate in a block digestor (DRB 200, HACH, U.S.A.); the co-substrates combination was put into HACH tubes at 6.6% of solid content. The hydrolysis time and temperature were set at 120 min and 120 °C according to Carrillo-Verastequi *et al.* [20]. After the hydrolysis pretreatment, solid residues were removed by centrifugation at 10 000 rpm for 10 min. Supernantant portion was used to sugar analysis (reducing and monomeric sugars) and degradation products (i.e., furfural, 5-hydroxymethyl-furfural (HMF), total phenolic compounds (TPC), formic acid, acetic acid, propionic acid, succinic acid and lactic acid).

2.3. Scaling of acid hydrolysis and overliming treatment

The dilute acid hydrolysis was scaled in 120 mL serum bottles. The combination of co-substrates was 75:25 FVW:CS $\%_{dry\ base}$ and the acid catalyst was HCl. 3.3 g of co-substrates was put into the serum bottles with 50 mL of HCl (0.5% v/v). Serum bottles were closed with silicone rubber stoppers and screw caps. The acid hydrolysis was carried out in autoclave at 121 °C for 120 min. Solid residue was separated by centrifugation. To remove inhibitory compounds (i.e. HMF, furfural, TPC) overliming treatment was applied according Chang *et al.* [10]. The pH of the hydrolyzates was adjusted to 10 by $Ca(OH)_2$ addition with stirring for an hour. The resulting precipitate was removed by centrifugation at 10 000 rpm, 15 min; supernatant was decanted and neutralized to pH 7 by 6 M HCl addition.

2.4. Inoculum and hydrogen production

Anaerobic inoculum was obtained from an anaerobic digester fed with FVW at 30 d of hydraulic retention time, started-up using the Poggi-Varaldo *et al*. [21] method. The methane content in biogas was 86%. To inhibit methane producing microflora, the anaerobic sludge was heat-shock treated in boiling water at 96 °C for 2 h [22].

The hydrogen production was evaluated by a 3^2 experimental design to analyze the inoculum/substrate ratio (ISR=g SV inoculum/g SV substrate) and initial sugar concentration effects (Table 1).

Batch dark fermentation experiments were carried out by duplicate at mesophilic (35 °C) conditions in 120 mL serum bottles with 70 mL fermentation volume. The initial RS concentration was adjusted by dilution of concentrated hydrolyzates (21.13 g L^{-1}) according to fermentation volume and ISR. The fermentation was supplemented with 0.4 mL of 200X mineral medium [23]. One liter of mineral medium contained (mg L^{-1}): $ZnCl_2$, 75; $MgCl_2 \cdot 6H_2O$, 100; $MnCl_2 \cdot 4H_2O$, 10.77; $FeCl_3 \cdot 6H_2O$, 25.97; $CuCl_2 \cdot 2H_2O$, 3.41; y $NiCl_2 \cdot 6H_2O$, 101.25. Phosphate buffer of K_2HPO_4 (3 g L^{-1}) and KH_2PO_4 (1.5 g L^{-1}) was used. After inoculation, each bottle was flushed with nitrogen for 3 min to promote anaerobic conditions and sealed with a rubber stopper and aluminum rings. The serum bottles were incubated in a controlled temperature incubator (PRENDO INO-650 M, México) with orbital agitation (150 rpm).

Table 1. Factors and levels in 3^2 experimental design.

Run	RS (g L^{-1})	ISR
1	10	1.2
2	13	1.2
3	16	1.2
4	10	1.0
5	13	1.0
6	16	1.0
7	10	0.8
8	13	0.8
9	16	0.8

2.5. Analytical methods

The pH of co-substrates was determined according to the proceedings described by NMX-AA-25-1984 [24] using a pH-meter Conductronic PC45 (Mexico). Total solids (TS), volatile solids (VS) and ashes were measured according standard methods [25]. Cellulose analysis was carried out by gravimetric method [26] after lignin and hemicellulose were removed using 1.25 mL of nitric acid (66.10 % v/v) and 17.5 mL of acetic acid (70 % v/v). Insoluble lignin was determined by carbohydrates solubilization by concentrated acid hydrolysis (H_2SO_4 72 % v/v) followed by mild acid hydrolysis; finally, the lignin was recovered by filtration and quantified by gravimetric method. The hemicellulose amount was determined by difference between holocellulose and cellulose content. Holocellulose was determined by lignin oxidation using NaHClO according to AOAC [26]. Elemental quantities of carbon, hydrogen, oxygen and nitrogen were determined by organic elemental analyzer (Thermo Scientific Flash 2000, U.S.A.).

The content of total reducing sugars (RS) in hydrolyzates was determined by 3,5-dinitrosalicylic acid method (dextrose as the standard) [27]. Monomeric sugars were quantified by high performance liquid chromatography (LDC Analytical, U.S.A.) with a Rezex RHM-Monosacharide (300mm X 7.8 mm) column and a refractive index detector (Varian Prostar, U.S.A.) with H_2O as mobile phase. The column temperature and mobile phase flow rate were 65 °C and 0.6 mL min^{-1}, respectively.

The total phenolic compounds (TPC) were determined by colorimetric method proposed by Blaninski *et al.* [28] using Folin Ciocalteu reactive (tannic acid as the standard). Secondary compounds such as furfural, HMF, formic acid, acetic acid, propionic acid, succinic acid and lactic acid were demined by gas chromatography in a gas chromatograph (Varian CP 3380, U.S.A.) equipped with a column (ZB-FFAP, 15m x 0.53 x 1 µm) and flame ionization detector (FID). The temperatures of the injector and the detector were 230 and 280 °C, respectively. The column was first heated to 90 °C for 3 min, then the temperature was raised gradually to 200 °C with the step rate of 20 °C min^{-1}, the temperature was maintained at 200°C for 3 min and finally raised to 250 °C at 30 °C min^{-1} which was then maintained for 4 min.

Hydrogen gas was sampled from the head space of the serum bottles using a chromatograph gas syringe. Hydrogen gas content was determined by using a gas chromatograph (Thermo Scientific Trace 1310, U.S.A.) equipped with a molecular sieve column (TG-BOND Msieve 5A, 30 m x 0.33 mm) and thermal conductivity detector. The temperatures of the oven, injector and detector were 100 °C, 150 °C and 200°C, respectively. Nitrogen gas was used as carrier gas with a flow rate of 3 mL min^{-1}. The amount of total gas produced was determined by alkaline displacement method (NaOH 1 N).

Volatile fatty acids composition in the liquid phase were determined using a gas chromatograph (Thermo Scientific Trace 1310, U.S.A.) equipped with a flame ionization detector. The temperatures of the injector and the detector were 250 and 250 °C, respectively. The capillary column (Nukol Fused silica, Supelco, 30 m x 0.25 mm, U.S.A.) was first heated to 120 °C for 1 min, then the temperature was raised gradually to 140 °C with the step rate of 20 °C min^{-1}, the temperature was maintained at 140 °C for 1 min and finally raised to 240 °C at 40 °C min^{-1}. Before analysis, liquid samples were centrifugated and filtrated (filter with porous size of 0.45 µm. After filtration, samples were acidified with 20 µL of H_3PO_4 (5 % v/v) per 100 µL of sample.

2.6. Kinetic analysis

The hydrogen cumulative hydrogen production was fitted by the modified Gompertz equation (Eq. 1), to estimate maximum H_2 volume, maximum H_2 production rate and lag time [29]:

$$H(t) = H_{max} \cdot \exp\left\{-\exp\left[\frac{R_{max} \cdot e}{H_{max}}(\lambda - t) + 1\right]\right\} \qquad (1)$$

where *H(t)* is the cumulative hydrogen gas volume (mL H_2) produced at any time *t*, H_{max} is the maximum H_2 volume (mL H_2), R_{max} is the maximum rate of hydrogen formation (mL H_2 h^{-1}), λ is the duration of the lag phase, *e* is 2.718 and *t* is time (h).

3. Results and Discussion

3.1. Diluted acid pretreatment of co-substrates

The highest concentrations of RS were obtained at 100:0 FVW:CS ratio, being 19.32 and 27.32 g L^{-1} for H_2SO_4 and HCl, respectively (Fig. 1a), probably as a consequence of a number ofg factors such as: a greater digestibility of FVW over CS, heterogenous composition of FVW, lower lignin content and minor degradation temperature [30,31]. The maximum RS obtained for co-substrate combinations were 24.69 and 17.99 g L^{-1} for HCl and H_2SO_4, respectively for co-substrate relation 75:25 FVW:CS.

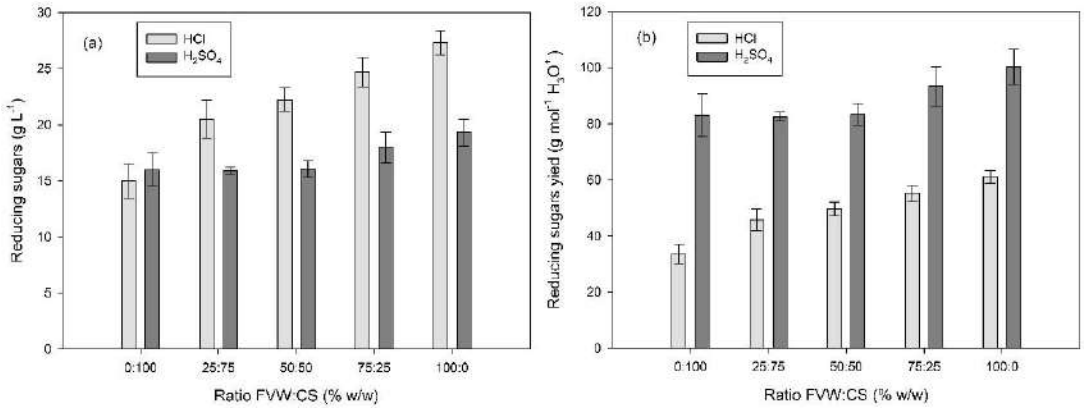

Fig. 1. (a) reducing sugars concentration and (b) reducing sugars yield

Comparing the H_2SO_4 0.5% (v/v) and HCl 0.5% (v/v) performance, HCl presented the best results at every combination, probably influenced by the concentration of hydronium ion, 2.32 times higher than H_2SO_4 treatments at the same volumetric concentration. The hydronium ion concentration affects the hydrolysis yields, this effect was described by Hilpmann *et al.* [32], hydronium concentrations lower than 0.1 present lower yields than 5% while hydronium concentrations higher than 0.1 promote yields close to 100%. On the other hand, H_2SO_4 is the most used catalyst in hydrolysis processes of lignocellulosic wastes, it has two available protons [H^+] to hydrolysis in comparison to HCl that only has one proton [33], moreover H_2SO_4 is less corrosive than another acids (HCl or HNO_3) [34]. The RS yield with H_2SO_4 was higher than HCl, achieving a yield of 100.33 g mol^{-1} H_3O^+ at 100:0 FVW:CS ratio, whereas for the same ratio, the RS yield was 61.13 g mol^{-1} H_3O^+ for HCl as shown in Fig. 1b.

RS yield was determined by comparing the experimental RS concentrations and the theoretical values based on holocellulose content. The maximum efficiency average was 96.74 % for 100:0 ratio, this corroborates the ease for the degradation of FVW; the main effects of RS efficiency can be seen in Fig. 2. According to ANOVA analysis to RS efficiency, the co-substrate ratios and acid catalyst were significant (table not shown). The R^2 and R^2_{adj} were 0.9591 and 0.9407, respectively. In the same way, at high content of FVW the sugar efficiency increase (Fig. 2a) and HCl presented the major efficiency than H_2SO_4 (Fig 2b). This proved that high content of FVW and HCl allowed to achieve high RS efficiency. The main effects were calculated according to Montgomery [35].

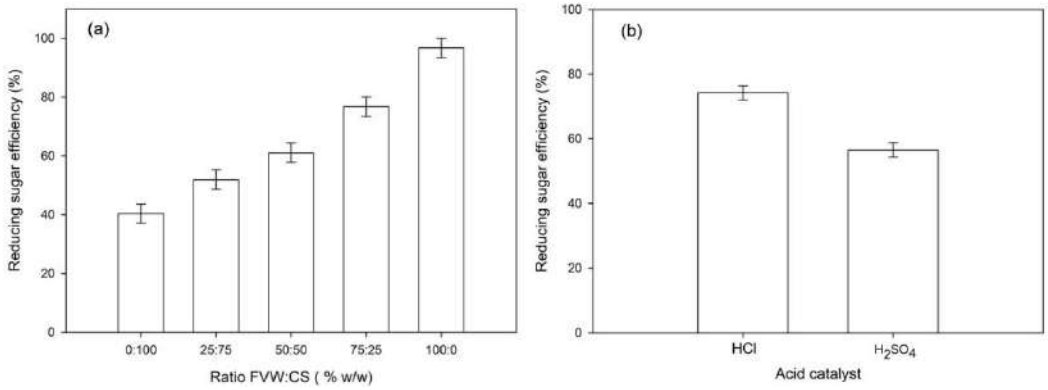

Fig.2. Main effects in RS efficiency: (a) FVW:CS ratio, (b) acid catalyst.

The maximum glucose concentration was 10.02 g L^{-1} for 75:15 FVW:CS ratio for HCl, as shown in Fig 3. This concentration is important as glucose is the main carbon source for microorganisms [36]. When CS content increased, glucose content diminished below to 1.44 g L^{-1} at 0:100 ratio for HCl. The ratios with higher CS concentration , presented high xylose concentrations as the hemicellulose hydrolysis is favored by CS content, whereas the cellulose is hardly hydrolyzed due to its rigid crystalline structure [37]. Considering that xylose is the main sugar from the hemicellulose, for 0:100 ratio high concentrations of xylose were obtained both for HCl and H_2SO_4 (7.03 and 7.65 g L^{-1}, respectively). Zu *et al.* [38] and Cao *et al.* [8] evaluated the CS hydrolysis with HCl and H_2SO_4 as acid catalysts and found xylose concentrations higher than glucose (20.44 g L^{-1} and 6.25 g L^{-1}, respectively), because hemicellulose is more easily solubilized than cellulose by acid catalyst.

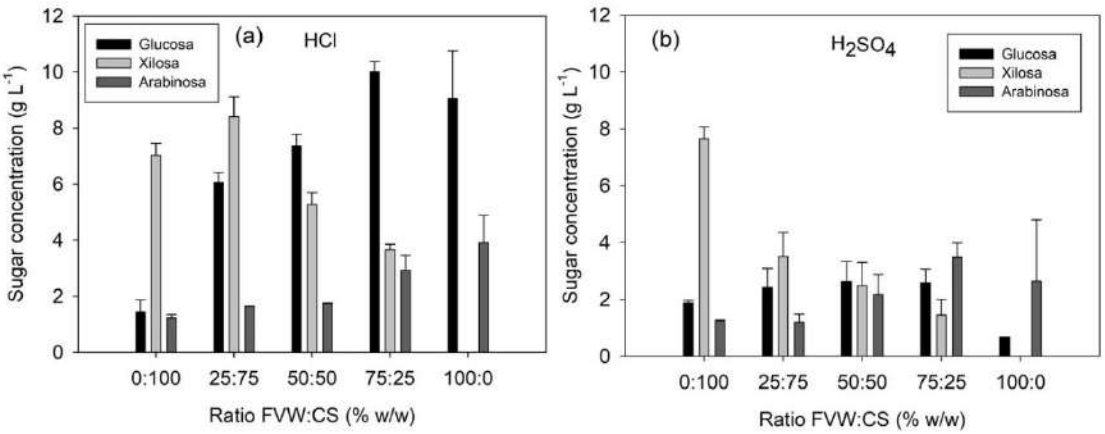

Fig. 3. Monomeric sugars in liquid hydrolizates.

In our experiment, although the yields of H_2SO_4 per mole of hydronium ion were higher, the highest yields were found for HCl. The use of H_2SO_4 in processes of acid hydrolysis has been taken with cautiously because it promotes the degradation of hydrolyzed carbohydrates and their conversion into inhibitory compounds such as HMF, as well as the release of acetic acid and the

degradation of lignin in phenolic compounds that also have negative effects on microbial cultures [33,39]. However, this premise could not be proven in our experiments, since the analysis of the secondary metabolites that formed during acid hydrolysis (Table 2) did not show a clear effect of the acid catalysts. The concentration of these compounds was found in the following intervals (g L^{-1}): 0.138-1.160 for HMF, 0.131-0.208 for furfural, 0.571-1.114 for TPC, 3.096-6.589 for formic acid, 0.447-0.788 for acid acetic, 0.746-4.266 for propionic acid (data no shown), 0.159-0.210 for succinic acid (data no shown) and 0.165-3.063 for lactic acid (data no shown). The presence of these metabolites in the liquid hydrolysates is an indication of the decomposition of pentoses and hexoses [32,40].

The highest concentrations of HMF, formic acid, propionic acid, succinic acid and lactic acid were found in the 100:0 ratio using both catalytic acids, while the furfural had a maximum concentration (0.208 g L^{-1}) in the 25:75 ratio with HCl. The concentrations of HMF, furfural, CFT and acetic acid (the main compounds inhibiting microbial growth) were lower than some of the inhibitory concentrations reported for dark fermentation and anaerobic digestion systems: 1.89 g HMF L^{-1}, 3.41 g furfural L^{-1}, 2.28 g TPC L^{-1} and 7.806 g acetic acid L^{-1} [16,41,42]. Still, Kumar *et al.* [43] found that at concentrations of 0.69 g HMF L^{-1} and 12 g formic acid L^{-1}, growth and hydrogen production were inhibited. On the other hand, Zheng *et al*. [44] reported that up to 4 g L^{-1} concentrations of HMF or furfural and 6 g acetic acid L^{-1} inhibited microbial metabolism. In general, it should be considered that initial concentrations of HMF greater than 1 g L^{-1} in hydrolyzates have reduced the yield in hydrogen production [39,45].

Table 2. Main acid hydrolysis secondary metabolites.

Ratio FVW:CS (% w/w)	HMF (g L^{-1})	Furfural (g L^{-1})	TPC (g L^{-1})	Formic acid (g L^{-1})	Acetic acid (g L^{-1})
0:100 HCl	0.138 ±0.002	0.143 ±0.003	0.627 ±0.011	6.131 ±0.071	0.742 ±0.157
0:100 H_2SO_4	0.154 ±0.000	0.170 ±0.001	0.578 ±0.022	5.799 ±0.490	0.772 ±0.078
25:75 HCl	0.469 ±0.020	0.208 ±0.008	0.788 ±0.019	5.369 ±0.303	0.835 ±0.239
25:75 H_2SO_4	0.266 ±0.057	0.139 ±0.009	0.571 ±0.112	3.096 ±0.861	0.447 ±0.089
50:50 HCl	0.149 ±0.126	0.172 ±0.002	0.769 ±0.016	3.422 ±0.872	0.513 ±0.090
50:50 H_2SO_4	0.447 ±0.037	0.143 ±0.010	0.650 ±0.020	4.285 ±0.436	0.461 ±0.072
75:25 HCl	0.654 ±0.015	0.138 ±0.001	0.898 ±0.037	4.017 ±0.152	0.532 ±0.012
75:25 H_2SO_4	0.558 ±0.013	0.131 ±0.000	0.826 ±0.122	3.826 ±0.381	0.478 ±0.030
100:0 HCl	1.160 ±0.012	0.149 ±0.008	1.114 ±0.034	6.296 ±0.724	0.788 ±0.117
100:0 H_2SO_4	0.850 ±0.137	0.140 ±0.008	0.871 ±0.008	6.589 ±0.575	0.771 ±0.189

In our experiments, the concentrations of TPC were 0.1 – 1.2 g L^{-1}, being the 100: 0 HCl ratio the one with the highest concentration: 1.114 g L^{-1}. Considering the results discussed, presumably these hydrolyzates could be used for dark fermentation and anaerobic digestion without any inconvenience [46]. It is important to note that in the 100:0 ratio, no xylose content was detected, most likely due to its degradation in furfural and subsequent transformation into formic acid, lactic acid and succinic acid, both for HCl and H_2SO_4 [47,48], in fact, the sum of these compounds was around 9.5 g L^{-1}, a concentration comparable to that obtained in xylose for the FVW:CS ratio of 25:75.

3.2. Dark fermentation of acid hydrolizates

The co-substrate ratio 75:25 FVW:CS and acid catalyst HCl showed the best monosaccharides distribution (i.e. glucose, xylose, arabinose) and high RS concentration; dark fermentation was

developed with liquid hydrolyzates from ratio 75:25 and HCl. The overliming treatment reduced the RS in 11.71% and the TPC in 27.07%. It can be considered that the reduction of RS was according to expected since it can be compared with the reduction of 9.1% in the RS reported by Chang *et al*. [10] when acid hydrolysates from rice husks using HCl as acid catalyst were overlimed. The TPC reduction exceeded the expectations of 20% that can be achieved with the treatment of overliming in acid hydrolysates according to Larsson *et al*. [49]; the same reduction value in HMF is also expected and it is not considered a decrease in the concentration of some organic acids present.

Fig. 4 depicts the cumulative hydrogen production for each ISR and initial RS concentration evaluated, while the parameters of Gompertz equation are shown in Table 3. According to Gompertz parameters, the best H_{max} (211. 97 mL H_2) and B_{max} (8.83 mL H_2 h^{-1}) were obtained for ISR=1.2 and initial RS= 13 g L^{-1}. Comparing the cumulative hydrogen production is complicated due to the different operation conditions using in literature. For mixed cultures, Datar *et al.* [41] reported a cumulative hydrogen volume of 4137.5 mL when used CS hydrolyzates (10 g L^{-1}) in dark fermentation by anaerobic sludge heat-treated (105 °C, 2h) in a 1250 mL CSTR. This production was comparable with the best experiment obtained in this study (ISR: 1.2/ RS 13 g L^{-1}), even though the cumulative hydrogen was 20 times higher than ours (211.97 mL H_2); their operational volume was also 18 times higher. Nevertheless, in their experiments the lag time was 38 h, due inhibitory compounds such as HMF and furfural were obtained under extreme hydrolysis conditions (acid steam-explosion 1.2 % H_2SO_4: 200 °C, 1 min). On the other hand, Escamilla-Alvarado *et al.* [6] achieved 331.4 mL H_2 from the organic fraction of municipal solid wastes from solid-state fermentation at 470 h (55 °C, operational volume 500 g) with anaerobic sludge as inoculum, whereas our maximum cumulative hydrogen was 211.97 mL obtained in 87 h. According to maximum hydrogen rates and lag times, at fermentation time of 87 h, the cumulative hydrogen calculated for solid-state fermentation would be 55 mL H_2, 70.3 % less than our best experiment (ISR 1.2 and RS 13 g L^{-1}), because at solid-state fermentation the microorganisms present low specific growth rates [50]. Due to the lower inoculum amounts and high substrate amounts, the experiment RS 16 g L^{-1} and ISR 0.8 presented the highest lag time (λ = 22.33 h), which was an indicative of a slower adaptation of hydrogen-producers to substrate [10].

Table 3. Gompertz parameters of experimental design 3^2

Experiment	H_{max} (mL H_2)	R_{max} (mL H_2 h^{-1})	λ (h)
10-1.2	179.95	6.70	16.52
13-1.2	211.97	8.83	15.35
16-1.2	207.72	6.92	17.00
10-1.0	179.88	6.19	15.23
13-1.0	200.87	6.13	16.08
16-1.0	202.71	7.61	17.33
10-0.8	196.20	7.03	16.55
13-0.8	199.64	6.34	16.06
16-0.8	201.33	7.52	22.53

Note: For all experiments, R^2 was greater than 0.99.

The model and initial RS concentration were significant according to the ANOVA (table not shown), however, the coefficient of determination and adjusted coefficient of determination were 0.42 and 0.30, respectively, showing that the model was not adequate to predict the cumulative hydrogen production. The ISR was not significant, although the results agreed with those reported by Ozmihci *et al.* [51], who observed increasing accumulated hydrogen as the ISR increased at constant substrate concentrations; this was remarkable for the concentrations evaluated in this study of 13 g L^{-1} and 16 g L^{-1}. Contrary to RS of 10 g L^{-1}, the accumulated hydrogen production decreased as the ISR increased, this was mainly because a high ISR the inoculum concentration was higher and there may be limitations of substrate by the formation of microbial flocs.

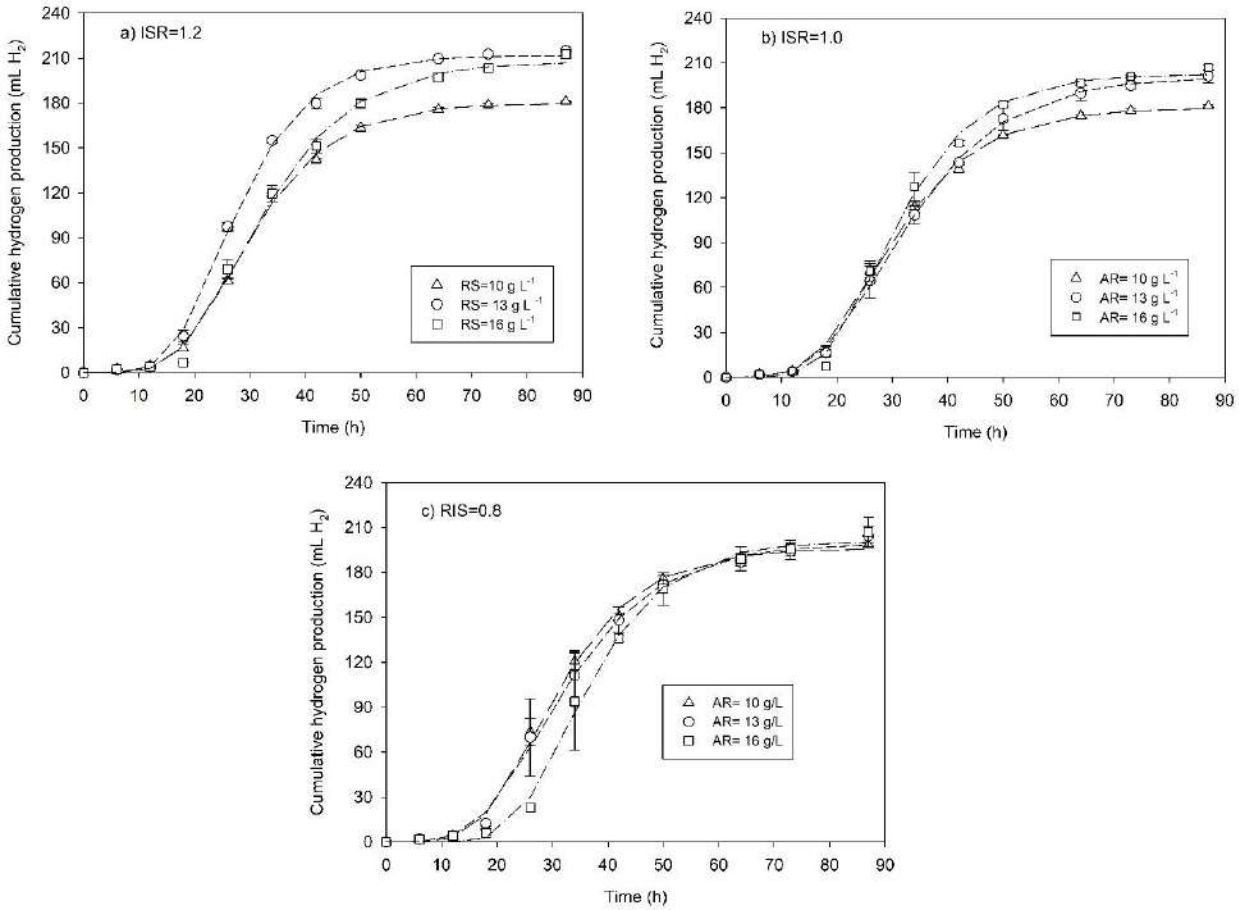

Fig. 4. Cumulative hydrogen production. (a) ISR=1.2, (b) ISR=1.0, (c) ISR=0.8.

The main effects (data no shown) of initial concentration of RS on the accumulate hydrogen production showed that when RS concentration was increased from 10 to 13 g L^{-1}, hydrogen production increased from 185.34 to 204.16 mL H_2 and subsequently had a slight decrease when the SR increased to 16 g L^{-1}. Similar behaviors have been found in the literature, as in the case of Fangkum *et al*. [12] who reported an increase in accumulated hydrogen production (42 to 91.98

mL H_2) when the initial concentration of fermentable sugars increased from 5 g L^{-1} to 10 g L^{-1}. However, when initial concentration of sugars in their experiments exceeded 10 g L^{-1}, cumulate hydrogen production decreased mainly due to the accumulation of organic fatty acids, this is reflected in a drop in pH; this causes inhibition in bacteria growth.

The pH and VFAs were also quantified at the end of fermentation, this can be seen in Table 4. The VFAs accumulation affected the fermentation pH, which decreased from 7 to 6 in most experiments, except for the experiments with initial RS of 16 g L^{-1} where the pH was reduced down to 5.3. The main metabolites were acetate, propionate, butyrate and ethanol; these metabolites are common in fermentations from hydrolizates containing glucose and xylose [9]. Indeed, butyrate was the most abundant metabolite, so the predominant metabolism in hydrogen production was butyrogenic [39]. The propionate average concentrations were lower in 89 and 94.33% than acetate and butyrate, respectively, which was advantageous since it may indicate low presence of propionogenic microorganisms that could cause negative effect on hydrogen production since they use H_2 as electron donor [52]. Low ethanol concentrations are attributed to a low partial pression effect, because in batch fermentations when the production of hydrogen is high, the variation in the partial pressure is significant and may change the route of metabolites production, solvents such as ethanol, acetone or butanol instead of VFAs [3,18,53].

The RS consumption at initial concentrations of 10 and 13 g L^{-1} was higher than 94%, while at concentration of 16 g L^{-1}, it was lower than 81%, except for the experiment with ISR=0.8 that presented a consumption near to 70%; this confirms the possible inhibition by excess of substrate, by concentration inhibitors, due to high substrate concentrations, the inhibitory concentrations (data not determined) or by VFAs accumulation [54]. Although the highest VFAs concentration (8.12 g L^{-1}) was presented for RS 13/ISR 1.2, possibly the VFAs concentration for the experiment RS 16/ISR 0.8 (VFA=4.74 g L^{-1}) affected the hydrogen production, since as the ISR decreased, the amount of microorganisms decreased and probably the diffusion of sugars through microorganisms is limited [51].

The highest molar yield (1.99 mol H_2 mol^{-1} glucose) was obtained when the SR concentration was 10 g L^{-1} and ISR was 0.8. These results were comparable to those found using pure cultures, as in the case of Pattra *et al*. [36] who reported 1.73 mol H_2 mol^{-1} glucose by *C. butyricum* when fermenting sugarcane acid hydrolyzates at higher concentration (20 g L^{-1}); or as in the case of Cao *et al*. [8] who obtained 2.24 mol H_2 mol^{-1} glucose by *T. thermosaccharolyticum* fermenting 12 g L^{-1} of sugars of corn hydrolyzates at thermophilic temperatures (60 °C) . This demonstrates that the use of FWV:CS hydrolyzates is an interesting alternative for hydrogen production by microbial consortia.

Table 4. Secondary metabolites from dark fermentation.

(RS-ISR)	Final pH	Ethanol ($g\ L^{-1}$)	Acetic acid ($g\ L^{-1}$)	Propionic acid ($g\ L^{-1}$)	Butyric acid ($g\ L^{-1}$)	TVFA ($g\ L^{-1}$)	Volumetric productivity ($mL\ H_2\ L^{-1}_{reactor}$)	SR consumption (%)	Y_{H2} ($mol\ H_2\ mol^{-1}$ glucose)
10-1.2	6.02	0.06	2.30	0.29	4.34	6.93	2473.54	95.36	1.82
13-1.2	5.94	0.06	2.42	0.41	5.29	8.12	2933.30	96.33	1.66
16-1.2	5.25	0.05	1.30	0.13	1.61	3.04	2904.59	80.38	1.34
10-1.0	5.96	0.04	1.92	0.29	3.78	5.99	2473.43	95.27	1.82
13-1.0	5.90	0.05	2.01	0.27	5.09	7.37	2747.38	95.94	1.55
16-1.0	5.26	0.07	2.00	0.12	3.16	5.28	2753.20	78.04	1.27
10-0.8	5.71	0.13	2.10	0.36	3.61	6.07	2711.90	95.33	1.99
13-0.8	5.67	0.06	2.09	0.30	5.37	7.76	2789.41	94.92	1.57
16-0.8	5.17	0.06	1.88	0.13	2.73	4.74	2826.77	69.96	1.30

Note: TVFA: Total volatile fatty acids measured as the sum of acetic, propionic and butyric acids.

4. Conclusion

According to the results obtained in the acid hydrolysis of the co-substrates, the FVW:CS ratio that shows the highest results in both RS and monosaccharides (i.e. glucose, xylose, arabinose) was 75:25 with HCl as acid catalyst. The effects of initial concentration of RS and ISR in hydrogen production were evaluated.

Indirect relationship between the initial concentration of RS and accumulated hydrogen production was established. The highest hydrogen production was 211.97 mL H_2, presented at ISR 1.2 and RS 13 $g\ L^{-1}$.

Acknowledgements

The authors express their gratitude to Dr. Eduardo Soto Regalado and Dr. Felipe Cerino Córdova for supporting the project (02-106534-PST-15/123), and to Dr. Margarita Loredo Cancino and Dr. Luis Humberto Alvarez Valencia for their advising and facilitating laboratory equipment. As well as the Mexican Hydrogen Society for the scholarship granted to Santiago Rodríguez Valderrama.

References

[1] Kothari R, Buddhi D, Sawhney RL. Comparison of environmental and economic aspects of various hydrogen production methods. Renew Sustain Energy Rev 2008;12:553–63.
[2] Rafa Ł, Ho I, Kucharska K, Glinka M, Rybarczyk P. Hydrogen production from biomass using dark fermentation 2018;91:665–94.
[3] Levin DB, Pitt L, Love M. Biohydrogen production: Prospects and limitations to practical application. Int J Hydrogen Energy 2004;29:173–85.
[4] Wang J, Wan W. Kinetic models for fermentative hydrogen production: A review. Int J Hydrogen Energy 2009;34:3313–23.
[5] Nissila ME, Lay C, Puhakka JA. Dark fermentative hydrogen production from lignocellulosic hydrolyzates-A review 2014;7.
[6] Escamilla-Alvarado C, Ponce-Noyola T, Ríos-Leal E, Poggi-Varaldo HM. A multivariable evaluation of biohydrogen production by solid substrate fermentation of organic municipal wastes in semi-continuous and

batch operation. Int J Hydrogen Energy 2013;38:12527–38.
[7] Chu CF, Li YY, Xu KQ, Ebie Y, Inamori Y, Kong HN. A pH- and temperature-phased two-stage process for hydrogen and methane production from food waste. Int J Hydrogen Energy 2008;33:4739–46.
[8] Cao G, Ren N, Wang A, Lee D, Guo W, Liu B. Acid hydrolysis of corn stover for biohydrogen production using *Thermoanaerobacterium thermosaccharolyticum* W16. Int J Hydrogen Energy 2009;34:7182–8.
[9] Zhang K, Ren N, Wang A. Fermentative hydrogen production from corn stover hydrolyzate by two typical seed sludges : Effect of temperature. Int J Hydrogen Energy 2015;40:3838–48.
[10] Chang ACC, Tu YH, Huang MH, Lay CH, Lin CY. Hydrogen production by the anaerobic fermentation from acid hydrolyzed rice straw hydrolysate. Int J Hydrogen Energy 2011;36:14280–8.
[11] Rai PK, Singh SP, Asthana RK, Singh S. Biohydrogen production from sugarcane bagasse by integrating dark- and photo-fermentation 2014;152:140–6.
[12] Fangkum A, Reungsang A. Biohydrogen production from sugarcane bagasse hydrolysate by elephant dung: Effects of initial pH and substrate concentration. Int J Hydrogen Energy 2011;36:8687–96..
[13] Akinbomi J, Taherzadeh MJ. Evaluation of Fermentative Hydrogen Production from Single and Mixed Fruit Wastes 2015;504:4253–72.
[14] Tenca A, Schievano A, Perazzolo F, Adani F, Oberti R. Bioresource Technology Biohydrogen from thermophilic co-fermentation of swine manure with fruit and vegetable waste : Maximizing stable production without pH control. Bioresour Technol 2011;102:8582–8.
[15] Singh A, Kuila A, Adak S. Utilization of Vegetable Wastes for Bioenergy Generation 2012;1:213–22.
[16] Rolly R, Sivagurunathan P, Parthiban A, Kim S. Optimization of substrate concentration of dilute acid hydrolyzate of lignocellulosic biomass in batch hydrogen production 2016;113:22–7.
[17] Ren N, Wang A, Cao G, Xu J, Gao L. Bioconversion of lignocellulosic biomass to hydrogen: Potential and challenges. Biotechnol Adv 2009;27:1051–60..
[18] Wong YM, Wu TY, Ching-Juan J. A review of sustainable hydrogen production using seed sludge via dark fermentation. Renew Sustain Energy Rev 2014;34:471–82.
[19] Wang W, Xie L, Chen J, Luo G, Zhou Q. Biohydrogen and methane production by co-digestion of cassava stillage and excess sludge under thermophilic condition. Bioresour Technol 2011;102:3833–9.
[20] Carrillo Verastegui Kenia, Ignacio CU, Escamilla-alvarado C. Hidrólisis ácida de resisuos agrícolas-GIBIOS 2017:1–12.
[21] Poggi-Varaldo HM, Valdés L, Esparza-García F, Fernández-Villagómez G. Solid substrate anaerobic co-digestion of paper mill sludge, biosolids, and municipal solid waste. Water Sci Technol 1997;35:197 LP-204.
[22] Zinatizadeh AA, Mirghorayshi M, Birgani PM, Mohammadi P, Ibrahim S. Influence of thermal and chemical pretreatment on structural stability of granular sludge for high-rate hydrogen production in an UASB bioreactor. Int J Hydrogen Energy 2017;42:20512–9.
[23] Cisneros-Pérez C, Etchebehere C, Celis LB, Carrillo-Reyes J, Alatriste-Mondragón F, Razo-Flores E. Effect of inoculum pretreatment on the microbial community structure and its performance during dark fermentation using anaerobic fluidized-bed reactors. Int J Hydrogen Energy 2017;42:9589–99.
[24] NMX-AA-25-1984. Norma Mexicana NMX-AA-25-1984. Protección al ambiente-Contaminación del suelo-residuos sólidos-determinación del pH-Método potenciométrico. Norma Mex 1992:4–5.
[25] APHA/AWWA/WEF. Standard Methods for the Examination of Water and Wastewater. Am Public Heal Assoc 2005.
[26] AOAC. AOAC Official Methods of Analysis. Assoc Off Agric Chem Washington, DC 1992;15th:136–8.
[27] Miller GL. Use of Dinitrosalicylic Acid Reagent for Determination of Reducing Sugar. Anal Chem 1959;31:426–8.
[28] Blainski A, Lopes GC, Palazzo de Mello JC. Application and Analysis of the Folin Ciocalteu Method for the Determination of the Total Phenolic Content from Limonium Brasiliense L. Molecules 2013;18:6852–65.
[29] Zwietering MH, Jongenburger I, Rombouts FM, van 't Riet K. Modeling of the Bacterial Growth Curve. Appl Environ Microbiol 1990;56:1875–81.
[30] Herrera Rosales DL. Hidrólisis de bagazo de agave pretratado con líquidos iónicos y su aplicación a cultivos microbianos. Instituto Tecnológico de Durango, 2016.
[31] Sluiter A, Hames B, Ruiz R, Scarlata C, Sluiter J, Templeton D. Determination of structural carbohydrates and lignin in biomass determination of structural carbohydrates and lignin in biomass. Natl Renew Energy Lab 2010.

[32] Hilpmann G, Becher N, Pahner FA, Kusema B, Mäki-Arvela P, Lange R, et al. Acid hydrolysis of xylan. Catal Today 2014;259:376–80.
[33] Hutomo GS, Rahim A, Kadir S. The Effect of Sulfuric and Hydrochloric Acid on Cellulose Degradation from Pod Husk Cacao. Int J Curr Microbiol Appl Sci 2015;4:89–95.
[34] Argun H, Onaran G. Glucose and 5-hydroxymethylfurfural production from cellulosic waste by sequential alkaline and acid hydrolysis. Renew Energy 2016;96:442–9..
[35] Montgomery DC. Diseño y análisis de experimentos. In: LIMUSA WILEY, editor. Segunda ed, 2004, p. 194–201.
[36] Pattra S, Sangyoka S, Boonmee M, Reungsang A. Bio-hydrogen production from the fermentation of sugarcane bagasse hydrolysate by Clostridium butyricum 2008;33:5256–65.
[37] Moniz P, Pereira H, Quilhó T, Carvalheiro F. Characterisation and hydrothermal processing of corn straw towards the selective fractionation of hemicelluloses. Ind Crops Prod 2013;50:145–53.
[38] Zu S, Li W zhi, Zhang M, Li Z, Wang Z, Jameel H, et al. Pretreatment of corn stover for sugar production using dilute hydrochloric acid followed by lime. Bioresour Technol 2014;152:364–70.
[39] Gonzales RR, Sivagurunathan P, Kim S-H. Effect of severity on dilute acid pretreatment of lignocellulosic biomass and the following hydrogen fermentation. Int J Hydrogen Energy 2016;41:21678–84.
[40] Hongqiang L, Hongzhang C. Detoxification of steam-exploded corn straw produced by an industrial-scale reactor 2008;43:1447–51.
[41] Datar R, Huang J, Maness PC, Mohagheghi A, Czernik S, Chornet E. Hydrogen production from the fermentation of corn stover biomass pretreated with a steam-explosion process. Int J Hydrogen Energy 2007;32:932–9.
[42] Lin R, Cheng J, Ding L, Song W, Zhou J, Cen K. Inhibitory effects of furan derivatives and phenolic compounds on dark hydrogen fermentation. Bioresour Technol 2015;196:250–5.
[43] Kumar G, Cheon HC, Kim SH. Effects of 5-hydromethylfurfural, levulinic acid and formic acid, pretreatment byproducts of biomass, on fermentative H2production from glucose and galactose. Int J Hydrogen Energy 2014;39:16885–90.
[44] Zheng Y, Lee C, Yu C, Cheng YS, Zhang R, Jenkins BM, et al. Dilute acid pretreatment and fermentation of sugar beet pulp to ethanol. Appl Energy 2013;105:1–7.
[45] Zyi C Van, Prior BA, Preez JC. Acetic acid inhibition of D-xylose fermentation by Pichia stipitis 1991.
[46] Quéméneur M, Hamelin J, Barakat A, Steyer JP, Carrre H, Trably E. Inhibition of fermentative hydrogen production by lignocellulose-derived compounds in mixed cultures. Int J Hydrogen Energy 2012;37:3150–9.
[47] Giuliano A, Poletto M, Barletta D. Process optimization of a multi-product biorefinery: The effect of biomass seasonality. Chem Eng Res Des 2016;107:236–52..
[48] Möller M, Shröder U. Hydrothermal production of furfural from xylose and xylan as model compounds for hemicelluloses. RSC Adv 2013;3:22253–60.
[49] Larsson S, Reimann A, Nilverbrant NO, Jönsson L. Comparison of Different Methods for the Detoxification of Lignocellulose Hydrolyzates of Spruce. Appl Biochem Biotechnol 1999;77:2273–89.
[50] Doelle HW, Mitchell DA, Rolz C. Solid Substrate Cultivation. vol. 49. 1993.
[51] Ozmihci S, Kargi F, Cakir A. Thermophilic dark fermentation of acid hydrolyzed waste ground wheat for hydrogen gas production. Int J Hydrogen Energy 2011;36:2111–7.
[52] Bundhoo MAZ, Mohee R. Inhibition of dark fermentative bio-hydrogen production: A review. Int J Hydrogen Energy 2016;41:6713–33.
[53] Hernández MA, Rodríguez Susa M, Andres Y. Use of coffee mucilage as a new substrate for hydrogen production in anaerobic co-digestion with swine manure. Bioresour Technol 2014;168:112–8.
[54] Elbeshbishy E, Dhar BR, Nakhla G, Lee HS. A critical review on inhibition of dark biohydrogen fermentation. Renew Sustain Energy Rev 2017;79:656–68. doi:10.1016/j.rser.2017.05.075.

XVIII International Congress
of the Mexican Hydrogen Society

Evaluation of Electrochemical Hydrogen Production Using Electrodeposited AISI/SAE 304 Stainless Steel Expanded Mesh under different conditions

Maria I. Jaramillo-Gutiérrez[1*], Carlos A. Ramírez-González[1]
Sonia M. Sierra-González[1], Julio E. Pedraza-Rosas[1], Julio A. Pedraza-Avella[1]

[1]Grupo de Investigaciones en Minerales, Biohidrometalurgia y Ambiente - GIMBA, Universidad Industrial de Santander - UIS, Sede Guatiguará, Transv. Guatiguará, Calle 8N No. 3W-60, Barrio El Refugio, C.P. 681011, Piedecuesta (Santander), Colombia
* Corresponding author: (+57) 317 5203921
maria.jaramillo@correo.uis.edu.co

ABSTRACT

In this work was evaluated the variables effect of the time, potential and concentration of Ni^{+2} in electroplating nickel on stainless steel meshes; which are used as a cathode in the electrolytic production of hydrogen. First of all, it was made an electrochemical characterization of the Watts bath system - stainless steel mesh, in which was identified the potential who had a pair reduction in the Ni^{+2} / Ni^{0} (0.70V vs Ag / AgCl). Afterwards, the electrodeposition process of nickel was evaluated under different experimental conditions, keeping constant the temperature, agitation and distance between electrodes conditions. After that it was made the microelectrolyte and macroelectrolyte evaluation for the production of hydrogen by electrolysis of water, in which an increase in the production of hydrogen was detected under the use of nickel-plated cathodes in comparison with uncoated cathodes. The highest hydrogen production was 507 ppm and it was obtained using an electrodeposited specimen at 2.3 V for 20 min, with an intermediate concentration of Ni^{+2} in Watts electrolyte. Finally this test tube was characterized by electro-microscopy scanning and scattered energy spectroscopy hence was identified a thickness lining average of 46.92 µm and a nickel composition of 99.29%.

Keywords: Electrolysis; Factorial experimental design; stainless steel expanded mesh, Factor nickel.

1. Introduction

Today, the energy demand in the world is mainly supplied by fossil fuels with about 86.3% of the primary energy production world, however, the impacts generated due to the dependence on

this type of fuel are generating the exhaustion of current reserves and environmental awareness. In this sense, finding energy sources that are friendly to the environment and capable of meeting current energy requirements is perhaps one of the main reasons why studies related to hydrogen energy are increasing and becoming more popular [1].

Hydrogen is considered a promising alternative to solve the current energy problem, since it can be obtained by clean processes taking water from the medium and separating it into its components, hydrogen and oxygen, through electrochemical processes. Water electrolysis, besides being a simple process and that does not generate by-products, is a very promising technology for the sustainable generation of hydrogen through renewable electric energy such as wind, water and solar energy [2],[3]. However, one of its main disadvantages are the costs associated with the electrochemical process, derived from the high overpotentials imposed by the materials used to carry out the water separation reaction. For this reason it is essential to search for materials with catalytic properties capable of reducing the overpotential of hydrogen production reactions and thus achieve an improvement in the performance of electrolytic processes [4], [5].

In the present work, nickel electroplating was carried out on stainless steel meshes, due to its relative low cost, chemical stability and catalytic properties that contribute to the reduction of the overpotential of hydrogen production in comparison with other transition metal [6]. This was carried out under various experimental conditions such as voltage, time and concentration of nickel in the electrolyte, while constant conditions of temperature, agitation and distance between electrodes were maintained.

In this way it was possible to fulfill the general objective of this work, which consisted in determining the effect of nickel electrodeposition variables in stainless steel meshes used as a cathode in the production of hydrogen by water electrolysis. For this, the appropriate parameters for the electrodeposition of nickel on stainless steel were established by means of electrochemical techniques, in the same way the influence of the potential, the concentration of the electrolyte and the time on the electrodeposition of nickel in stainless steel meshes were identified. Additionally was evaluated the production of hydrogen using coatings prepared under different conditions as the cathode.

2. Materials and Methods

2.1. *Pretreatment of the meshes of experimentation*

2.1.1. *Substrate material*. The support material on which the electrodeposition was made was expanded mesh with rhombic form of stainless steel AISI 304 (IMT -10) of 0,9 mm thickness and opening size 6,6 mm X 3,76 mm whose chemical composition, the mesh was cut into rectangles of 70 mm X 18 mm, with a total surface geometric area of 1405 mm^2, used as working electrodes or test specimens.

2.1.2. ***Preparation and cleaning of working electrodes***. Initially, a preliminary surface treatment was carried out on the experimental specimens. Previous studies have shown an increase in surface roughness when the surface is subjected to an initial treatment of Sand Blasting [14], thus allowing an increase in the adherence of the coating; therefore, the test tubes were subjected to this initial treatment at the company Procesadora del Cristal (Bucaramanga, Colombia). Subsequently, the specimens were subjected to an ultrasonic bath alternately in acetone and ethanol for 20 min in each solvent.

2.2. *ELECTROCHEMICAL CHARACTERIZATION OF THE WATTS BATH SYSTEM - STAINLESS STEEL MESH*

2.2.1. ***Watts Solution*.** The electrolyte was prepared, composed of $NiSO_4*6H_2O$ 0,87 M, $NiCl_2*6H_2O$ 0,21 M y H_3BO_3 0,49 M, with deionized water and using analytical grade reagents.

2.2.2. ***Cyclic voltammetry.*** The potential range at which the nickel reduction is presented was established by the cyclic voltammetry technique (CV), using a potenciostat - galvanostat controlled by the NOVA 1.11 software. A conventional electrochemical cell of three electrodes with a capacity of 75 ml was used, using the stainless steel specimens as a working electrode, as a reference electrode for Ag / AgCl (3 M KCl) and a high purity graphite bar (99 , 9995%) as counter electrode. The solution described above was used as an electrolyte. When initiating the measurements, the oxygen present in the electrolytic solution was removed by bubbling a stream of nitrogen for 10 minutes with constant agitation. The test was carried out by sweeping the potential between the open circuit potential (OCP), in a negative direction, up to a potential of -1.25 V vs. Ag / AgCl, where the potential is inverted up to 1.5 V vs Ag / AgCl.

2.3*. NICKEL ELECTRODEPOSITION*

2.3.1. ***Experimental system***. This process was carried out in a 100ml beaker, inside a Shaker with thermostated bath. As a cathode, pre-treated steel meshes were used, exposed to the electrolyte in an area of 803 mm^2; and as anode a high purity nickel bar.

2.3.2. ***Electrolytic solution used***. Three working electrolytes of high, medium and low concentration of nickel were prepared, maintaining the nickel chloride/nickel chloride ratio constant at a value of 3.91 as specified in Table 1. To these conditions the influence of the Nickel concentration in the electrodeposition process.

Table 1.Concentration of the working electrolyte.

Reagent concentration [g/L]	High	Medium	Low
$NiSO_4*6H_2O$	300,48	241,15	181,82
$NiCl_2*6H_2O$	76,85	61,67	46,50

The concentration of boric acid in each of the prepared baths was kept constant, at a value of 30.8 g / L according to [6]. In addition to what is reported in the literature, in this work sodium sulphate was added to the Watts solution, in order to improve the migration effects of the ions in the solution.

2.3.3. Design of experiments. As reported in literature[7] the most influential variables in the nickel plating process are: time, potential and composition of the electrolyte. The working values of these variables to perform the experimentation are presented in Table 2.

Table 2. Working conditions established for electrodeposition

Variable	Value established		
Potential (V)	1,7	2,0	2,3
Time (min)	10	15	20
Total concentration Ni^{+2} (g/L)	52,097	69,097	86,097

Once these variables and their experimental values were defined, a factorial design 3^3 was proposed using the Minitab 17 statistical software. With this design, the 27 experimentation tests were developed.The response variable evaluated was the variation of the weight gained by each test tube, once each electrodeposition test was performed.

On the other hand, it was decided to carry out a nickel coating on two stainless steel meshes in the company Niquelados Moreno (Bucaramanga), in order to make a comparison between the experimental coatings made in this work and the commercial ones.

2.4. HYDROGEN PRODUCTION

2.4.1. ***Microelectrolytic evaluation of nickel-plated electrodes.*** The overpotential required to carry out the production of hydrogen on the cathode was evaluated by electrochemical tests of linear voltammetry (LSV) in the negative direction; between the open circuit stabilization potential

(OCP) up to -2.0V vs Ag / AgCl, at a sweep speed of 10 mV s^{-1}, in a solution of 0.5 M Na_2SO_4 desagraded with nitrogen and constant agitation, for 10 min at room temperature and pressure.

2.4.2. Hydrogen production by conventional electrolysis. The electrolysis of water was carried out using a cylindrical cell designed in a previous study [16]. A 0.3 M NaOH solution was used as the supporting electrolyte, selected according to previous studies [15], as an anode of AISI 304 stainless steel mesh and as the cathode the already nickel-plated test tube. The submerged area of the two electrodes was kept constant and equal for both at a value of 401.51 mm2. According to the design of the electrolytic cell, the distance between electrodes was set at 2 cm, because according to reports [17], this is the distance at which a greater production of hydrogen and a low energy requirement is achieved. The voltage supplied to the process was 2.0 V, using a power supply with an adjustable current between 0 to 1A.

Defined the conditions to carry out the electrolysis of water, the H2 produced in the cathodic compartment was quantified using a hydrogen flow meter. The measurement was carried out for 30 minutes for each of the 27 resulting tests using, in each of these as a cathode, the already nickel-plated samples under the conditions of the experimental design. This value of 30 minutes of reaction corresponds to the minimum stabilization time of the detector.

2.5 CHARACTERIZATION OF NICKEL COATING

The morphological characteristics of the nickel-plated electrodes and their elemental composition were analyzed, in the Microscopy Laboratory of the Universidad Industrial de Santander, Guatiguará headquarters, by the techniques of scanning electron microscopy (SEM) and scattered energy spectroscopy (EDS) using a FEI Quanta 650 FEG microscope.

3. Results and Discussion

3.1 ELECTROCHEMICAL CHARACTERIZATION OF THE WATTS SOLUTION SYSTEM - STAINLESS STEEL MESH

In Figure 1 the obtained cyclic voltammogram is presented.

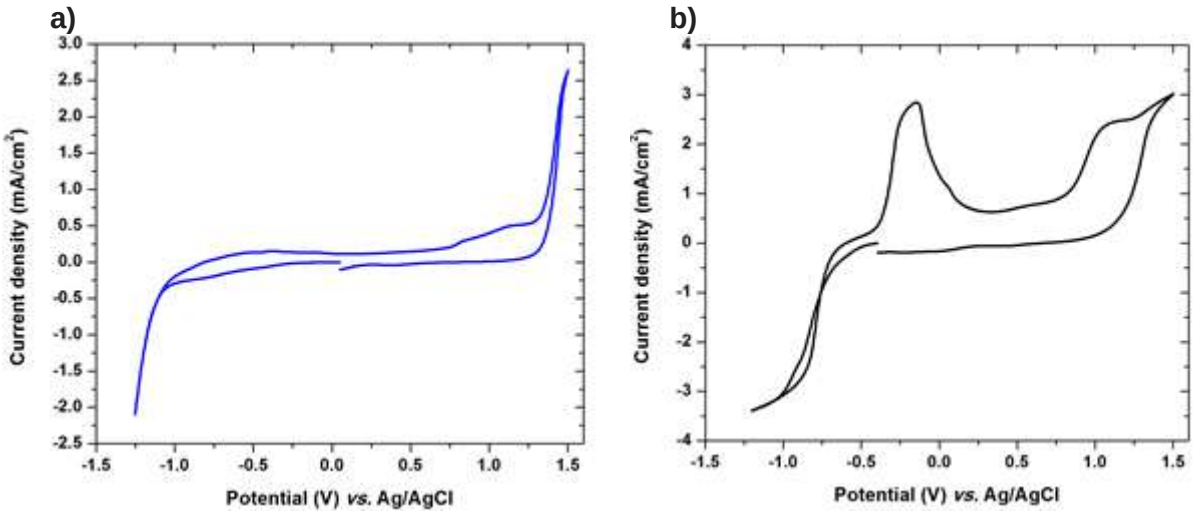

Figure 1. Cyclic voltammetry for solutions (a) 0.5 M Na2SO4 and (b) Watts solution, using a stainless steel electrode and with a scanning speed of 10mV / s.

In Figure 1 (b) it can be seen that after starting the potential sweep from the OCP (-0.39V vs Ag / AgCl) in negative direction a negative increase of the current is evidenced when reaching potentials close to -0, 70V vs Ag / AgCl (zone I). This potential is associated with the nickel reduction process through the reaction:

$$Ni^{2+}_{(ac)} + 2e^- \rightarrow Ni_{(s)} \quad (1)$$

Subsequently, when moving to more negative potentials of -1.1 V vs Ag / AgCl, the current continues to increase (Zone II). This process is associated with the reduction of H + ions in solution that is favored by nickel deposit, as shown in the following reaction:

$$2H^{+}_{(ac)} + 2e^- \rightarrow H_{2(g)} \quad (2)$$

When the potential sweep is reversed at -1.25V vs Ag / AgCl and when moving to more positive potentials, an increase in current is observed until an oxidation peak is reached at a current density value of 2.84 mA / cm2. a potential of -0.14 V vs Ag / AgCl (zone III), related to the oxidation of the nickel previously deposited during the reduction process:

$$Ni_{(s)} \rightarrow Ni^{2+}_{(ac)} + 2e^- \quad (3)$$

It is also possible to observe another oxidation process at a potential of 0.99 V vs Ag / AgCl and at a current density of 2.15 mA / cm2 (zone IV), which is associated with the oxidation of chlorine, according to:

$$2Cl^{-}_{(ac)} \rightarrow Cl_{2(g)} + 2e^- \quad (4)$$

The zone V presents an increase in the current density associated with the O2 evolution of the medium, as described in the following reaction:

$$2H_2O \rightarrow O_2 + 4\,H^+_{(ac)} + 4e^- \quad (5)$$

To corroborate that the zones I, III and IV present in the diagram of Figure 1b are characteristics of the processes of reduction and oxidation of the components present in the electrolytic solution used, a comparison pattern was made (Figure 1 (a)) where only the areas attributed to the hydrogen evolution reaction (zone I) and the oxygen evolution of the medium (zone II) are evidenced, which allows concluding that the potentials found in zone I and III are associated with the reduction and Nickel oxidation.

3.2 NICKEL ELECTROLYTIC DEPOSITION

Figure 2 shows the gain in mass of the already nickel-plated specimens.

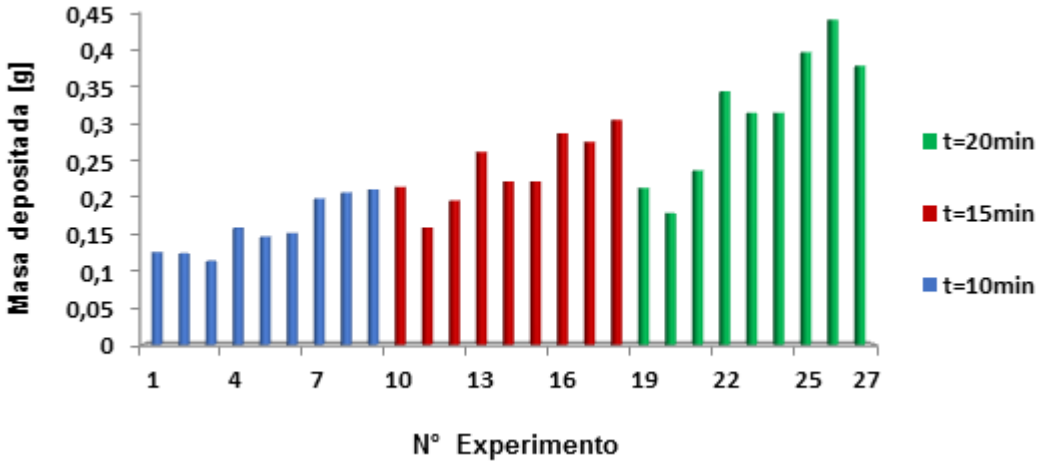

Figure 2. Nickel deposited in the experiments carried out.

In this figure we can observe the difference of nickel deposited at the same time, attributable to the variation of the potential and concentration conditions of nickel to which the different tests were carried out; therefore it is not possible to identify a clear trend of the influence that the electrodeposition time has on the amount of mass deposited. For this reason, using the Minitab 17 software, the graphs of Figure 6 were drawn, where the influence of each of the 3 variables on the variation of the weight gained in each test tube can be observed. In this figure, it can be seen that time is the variable that most influences the electrodeposition of nickel because when making variations between each of its ranges, the delta in the variation of the weight of the test pieces is greater than the other variables studied. As for the potential, it can be established that, like time, it generates considerable changes in the amount of mass deposited when making variations in its work values, achieving a greater deposit at 2.3V potentials. It is evident that when the concentration of Ni + 2 varies within the established ranges there is no significant change

in the nickel deposited in the substrates, however, it is shown that the highest nickel deposits were achieved when working with the highest concentrations.

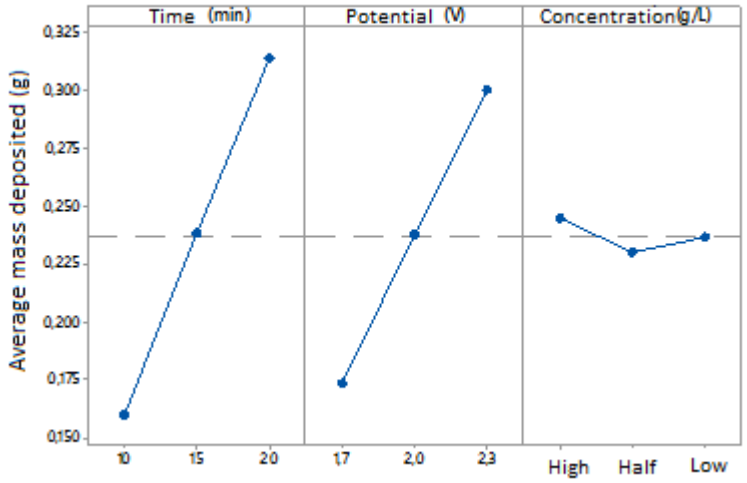

Figure 3. Main effects of time, potential and concentration of nickel in the electrodeposition

In accordance with the above, it was possible to identify that time and voltage are the variables that have the greatest effect on the amount of nickel deposited.

Like the main effects, the software also traced the interactions between the variables studied. These are presented in Figure 4.

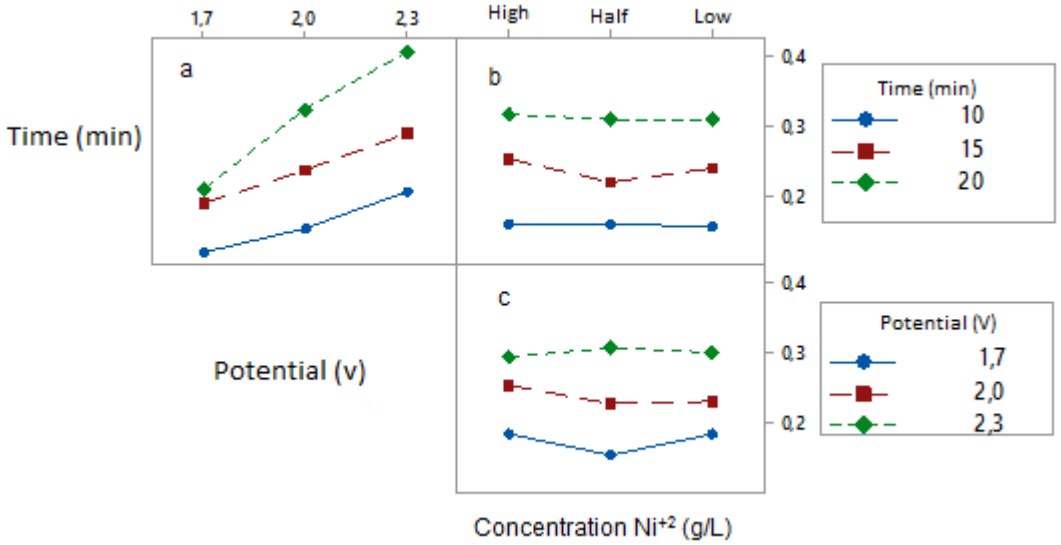

Figure 4. Effect of the interactions of time, potential and concentration on the deposited nickel mass

Figure 4 (a) shows that the interaction of time and potential have a considerable effect on the amount of deposited mass, since an increase in both time and potential, generates an increase in the amount of nickel deposited . A maximum nickel deposited of 0.41g was obtained at the highest values of potential and time, 2.3V and 20 min.

On the other hand, as shown in Figure 7 (b) and (c), the lines present an approximately horizontal tendency, with which it can be inferred that the effect on the nickel weight deposited by varying the nickel concentration is not significant when it interacts with the time and potential variables.

HYDROGEN PRODUCTION

Microelectrolytic evaluation of nickel-plated electrodes. Figure 8 shows the voltammograms obtained by using a stainless steel mesh without nickel coating (white), a nickel-plated mesh in the Niquelados Moreno company (commercial electrode) and the nickel-plated experimental mesh that required the lowest overpotential to initiate the evolution of the medium, of the 27 experiments performed; which was obtained by nickel-plating, at a concentration of Ni + 2 intermediate, a time of 20 min and a potential of 2.3 V.

In Figure 8 it is observed that for the experimental electrode the medium evolves to a lower overpotential (-0.8 V vs. Ag / AgCl) compared to the uncoated electrode and the commercial electrode, which do so at a potential of -1, 15 V and -0.95 V vs. Ag / AgCl, respectively. The decrease of the overpotential of hydrogen production in the commercial and experimental electrodes was achieved by the electrocatalytic action of the nickel coating deposited on the substrate, because this is a metal that has catalytic and conductive properties [5].

When comparing the commercial electrode with the experimental electrode, even though both have a nickel coating, it is evident that the evolution of the medium occurs at a lower overpotential in the experimental electrode; which could be attributed to the coating finish, since the commercial electrode has a bright surface while the experimental electrode was matte. Based on this, it can be concluded that the brightness in nickel coatings is a factor that contributes in a smaller proportion to the reduction of the hydrogen potential overpotential.

Figure 8. Linear voltammetry with negative polarization for an experimental electrode, uncoated and commercial.

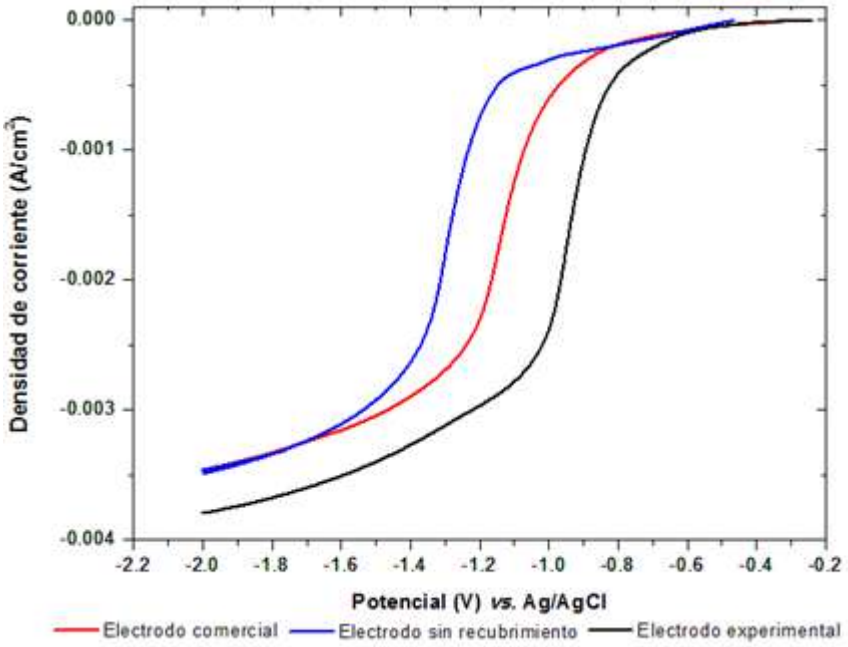

Hydrogen electrolyte production. By making a continuous record of the variation in hydrogen concentration, in order to identify the behavior that occurs once the electrolysis process has begun and up to 30 minutes, the curves presented in Figure 9 were obtained, which correspond to the concentration of hydrogen detected when a non-coated mesh is used as a cathode, one with a commercial coating, and the experimental one obtained under electrodeposition conditions of 2.3 V, 20 min and electrolyte with an intermediate concentration of Ni + 2, this being the one with the highest hydrogen concentration reported (507 ppm) at minute 30 (experiment 26).

Figure 9. Hydrogen detected from a 0.3 M NaOH solution.

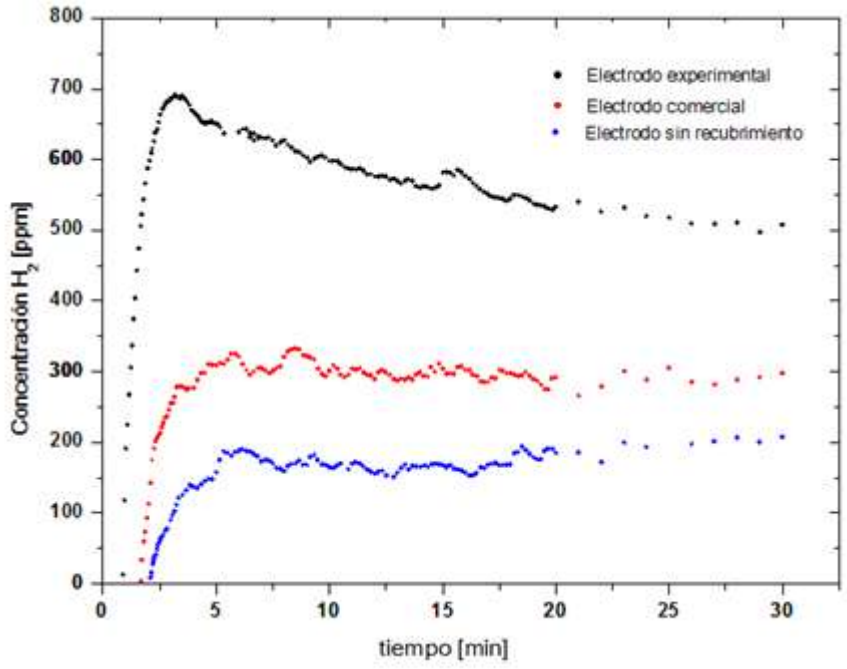

Figure 9 shows the influence of the nickel coating acting as a catalyst [5], since the experimental and commercial electrodes have higher concentration values (507 and 298 ppm) than the uncoated electrode (207 ppm). When comparing the values of the concentration of hydrogen for the experimental and commercial coating, there is an increase of 70% in the production with the experimental one, which can be attributed to the decrease in the value of the overpotential (Figure 8).

On the other hand, it is observed that the fact that the cathodes have a nickel coating means that the detector response time is shorter. This will be directly associated with the reduction of cell overpotential and therefore with a higher concentration of H + on the surface of the electrode, which diffusive phenomena are transported more rapidly from the electrolyte, favoring the generation of H2 and therefore which the detector registers to a shorter time this evolution.

3.4. CHARACTERIZATION OF NICKEL COATING

Using the scanning electron microscopy (SEM) technique, the commercially nickel-plated substrate surface was analyzed and that of the experimental one with the highest hydrogen production (2.3 V, 20 min and intermediate concentration of Ni + 2). The captured images are shown in Figure 11, taken at 100X and 500X magnification.

In Figure 11 (a), which shows the commercially nickel-plated substrate surface, it is evident to obtain a uniform and smooth-appearing surface, characteristic of a glossy coating; and that when the micrograph was taken at a greater magnification, it is appreciated that a large part of the substrate is discovered, which can be attributed to the poor adherence of the coating on the steel mesh, thus generating its detachment when subjected to a shear stress. The electrode that produced the highest hydrogen production was also subjected to a shear stress, however in the micrographs of Figure 11 (b) a granular, homogeneous and rough surface is observed, which allows inferring that the coating obtained with the Watts electrolyte of intermediate concentration of Ni + 2 showed a good adherence to the substrate. With the obtaining of rough surfaces in the deposition of Ni0 it is possible to increase the electrocatalytic power of the material due to the fact that there is a greater electroactive area that favors the hydrogen production reaction, agreeing with what was affirmed by Besoky and Won Kang [14].

Figure 11. SEM micrograph of coated electrodes: (a) Commercial and (b) Experimental

4. Conclusion

• From the electrochemical characterization, it was found that the reduction of the nickel present in the electrolytic bath composed of 0.87 M sodium sulfate, 0.21 M nickel chloride and 0.49 M boric acid, is carried out in a range of potential from -0.70 V to -0.90 V vs. Ag / AgCl.

• It was determined that the amount of nickel deposited in the metal substrates is influenced in a direct relation with the electrodeposition variables time and potential, while the nickel concentration in the electrolytic bath did not significantly influence the mass deposited. The maximum amount of nickel deposited on a 70 mm X 18mm substrate, with a total surface geometric area of 1405 mm2; was 0.41g with purity of 99.29% and average thickness of 46.92 µm, obtained at conditions of 2.3V and 20 min using the Watts bath as electrolyte.

• A decrease in the overpotential required to carry out the water electrolysis reaction was achieved through the use of nickel-plated specimens, and, with the use of experimentally nickel-plated samples as a cathode in electrolysis, an increase in hydrogen production was achieved of 145% with respect to a stainless steel cathode and 44% with respect to a commercially nickel-plated electrode.

Acknowledgements

This work has been carried out with the financial support of UIS (DIEF Ingenierías Fisicoquímicas, Project 1320) and Colciencias, project 1102-658-43664 (VIE code 8836). M.I. Jaramillo-Gutierrez thanks COLCIENCIAS for the studentship in the frame of the program a Colciencias Ph.D. scholarship.

References

[1] R. Boudries, “Techno-economic Assessment of Solar Hydrogen Production Using CPV-electrolysis Systems,” *Energy Procedia*, vol. 93, pp. 96–101, 2016.

[2] “Hydrogen production by photoelectrolysis of aqueous solutions of phenol using mixed oxide semiconductor films of Bi – Nb – M – O (M = Al , Fe , Ga , In) as photoanodes,” vol. 252, pp. 150–156, 2015.

[3] M. F. Kaya, N. Demir, M. S. Albawabiji, and M. Taş, “Investigation of alkaline water electrolysis

performance for different cost effective electrodes under magnetic field," *Int. J. Hydrogen Energy*, vol. 42, no. 28, pp. 17583–17592, Jul. 2017.

[4] A. Saraby-Reintjes and M. Fleischmann, "Kinetics of electrodeposition of nickel from watts baths," *Electrochim. Acta*, vol. 29, no. 4, pp. 557–566, 1984.

[5] T. Mimani, S. M. Mayanna, and N. Munichandraiah, "Influence of additives on the electrodeposition of nickel from a Watts bath: a cyclic voltammetric study," *J. Appl. Electrochem.*, vol. 23, no. 4, pp. 339–345, 1993.

[6] F. ezzahra Chakik, M. Kaddami, and M. Mikou, "Effect of operating parameters on hydrogen production by electrolysis of water," *Int. J. Hydrogen Energy*, vol. 42, no. 40, pp. 25550–25557, Oct. 2017.

[7] S. M. Kim, S. H. Jin, Y. J. Lee, and M. H. Lee, "Design of Nickel Electrodes by Electrodeposition: Effect of Internal Stress on Hydrogen Evolution Reaction in Alkaline Solutions," *Electrochim. Acta*, vol. 252, pp. 67–75, Oct. 2017.

XVIII International Congress
of the Mexican Hydrogen Society

Production of hydrogen on Pt-Pd/γ-Al_2O_3-Nd_2O_3 bimetallic catalysts.

M. Caballero-Díaz[a,b *]; G. Del Angel Montes[a]; V. Tostado-Ramírez

[a] Universidad Autónoma Metropolitana-Unidad Iztapalapa, Departamento de Química, Área de Catálisis, Av. San Rafael Atlixco No. 186, C.P. 09340, A.P 55-534. México D. F. México.
[b 2]Carrera de Ingeniería Química, UNAM, Facultad de Estudios Superiores Zaragoza, Batalla del 5 de Mayo, Colonia Ejército de Oriente, Iztapalapa, C.P. 09230 México, Ciudad de México.
* Corresponding author: 55-20032433 and e-mail: marcabdi@yahoo.com.mx

ABSTRACT

Hydrogen can be used for energy purposes or used as a chemical reagent in industrial processes. The amount of energy produced during the combustion of hydrogen is higher than that obtained by any other fuel. The advantages of hydrogen as an energy source is that it represents an abundant raw material and combustion does not produce CO_2, only water vapor, which is the ideal candidate to reduce the "greenhouse effect".
Three Pd-Pt catalysts supported on γ-Al_2O_3 and γ-Al_2O_3-Nd_2O_3 at 1 and 10% by weight were synthesized. The support was placed in the balloon with a small amount of water while a solution of the precursor salt was prepared (H_2PtCl_6 6 H_2O and $PdCl_2$) for a content of 1% of the metals, dissolved in the minimum amount of water and this was added in the same flask where the support was left and stirring for 3 hours in the rotary evaporator, and evaporated using a water bath at 60 ° C. The solids were dried in an oven at 120 ° C for 12 hours, then calcined at 500 ° C with air flow at 60 ml / min for 5 hours and finally the catalysts were reduced in a H_2 flow at 60 ml/min. and 500 ° C for 5 hours.
The decomposition reaction of the methane was carried out in a batch or intermittent flow system in a temperature range of 400 to 750 ° C with a previous activation with nitrogen (30 ml / min at 200 ° C) and the flow of the reagent (methane) was 2 ml / min. To achieve this, an electric furnace was used with a tubular quartz reactor with a porous plate inside to contain the catalyst (50 mg).
The product of the reaction was analyzed by gas chromatography to detect the gases leaving the reactor, which showed that hydrogen is actually being produced.
Hydrogen was obtained from the decomposition of methane.
It was determined that the best catalyst for the production of hydrogen is Pt-Pd γ-alumina (without neodymium).

Keywords: hydrogen, Pt-Pd catalysts, Al_2O_3-Nd supports, methane.

1. Introduction

With the increase in world population, industrialization and urbanization, the demand for energy is rapidly increasing. Currently, around 85% of the energy in the world is obtained from non-renewable resources such as coal, natural gas and oil; this contributes to environmental problems (global warming), economic problems and political crises. These resources are finite and their reserves around the world are running out, resulting in an increase in prices. The depletion of finite fossil fuels is a critical problem that must be overcome for a sustainable energy future. [1]

Hydrogen is abundant and is the most available renewable energy. In addition, only steam is produced from the combustion of hydrogen. Therefore, it is considered as the cleanest energy source [2]. It is also considered that hydrogen is the right solution to environmental problems if it is produced from renewable resources. The advantages of hydrogen are the zero emission of greenhouse gases if it is produced using renewable energy; high energy density between 120 MJ/kg (lowest heating value, LHV) and 142 MJ/kg (highest heating value, HHV) [3,4]. The feasibility and utilization of hydrogen requires evaluating, for example, storage capacities, versatility of energy density, transport and environmental impact.

Hydrogen can be produced from both renewable technologies and fossil fuels. The generation of hydrogen from fossil fuels can be through steam reforming, partial oxidation, autothermal oxidation and gasification. The generation of hydrogen from renewable sources can be through the gasification of biomass / biofuels and the division of water through solar or wind energy.
The obtaining of hydrogen from hydrocarbons (mainly natural gas) can be differentiated by three means of chemical reactions such as [5]:
1. Methane reforming (SMR),
2. Partial oxidation (POX)
3. Reformed autothermal (ATR).

All these processes to produce hydrogen have certain disadvantages such as the use of catalysts that are deactivated quickly, high operating conditions which generates a greater use of energy, in some cases using reagents such as oxygen that generates a great expense or steam that Likewise, it requires the use of energy, but above all, as we have discussed, they all produce carbon dioxide.
To economize all this has been proposed the thermal decomposition of methane.

Thermal decomposition of methane.
The application of methane thermal decomposition (TDM) to produce H_2 and solid carbon has been proposed as a potential technology for the period of transition to the H_2 economy [6]. An analysis of the life cycle of TDM and SMR carried out by Dufour et al. [7,8] have revealed that

TDM has lower fossil energy consumption and a better total environmental impact than SMR, even when carbon capture and storage (CCS) is coupled to SMR. In addition, a study of the entire energy system reveals that the H_2 economy where H_2 is produced by TDM and used in fuel cells assuming that natural gas leaks would be under control, can potentially reduce global equivalent CO_2 emissions by up to 27% compared to the current situation [9]. One benefit of TDM is the exploitation of the current natural gas infrastructure, and therefore, could provide a short-term solution for the production of less polluting H_2.

The decarbonisation of fossil fuels, and especially the treatment of natural gas by the thermal decomposition of methane (TDM), has been proposed as a potential technology in the transition to the H_2 economy [10]. The reaction equation for the endothermic TDM reaction is as follows [11]:

$$CH_{4(g)} \rightarrow C_{(s)} + 2\ H_{2(g)} \qquad (\Delta H^{\circ}_{r} = +\ 76\ KJ / mol)$$

2. Materials and Methods

Synthesis of Pt-Pd catalysts.

Three Pd-Pt catalysts supported on γ-Al_2O_3 and γ-Al_2O_3-Nd_2O_3 were synthesized at 1 and 10% by weight, the support (γ-alumina) was placed in the flask with a small amount of water while preparing a solution of the precursor salt (H_2PtCl_6 6 H_2O and $PdCl_2$) for a content of 1% of the metals, dissolved in the minimum amount of water and this is added in the same flask where the support is and it is left stirring for 3 hours in the Rotary evaporator is evaporated using a water bath at 60 ° C; the solids are dried in an oven at 120 ° C for 12 hours, then calcined at 500 ° C with air flow at 60 ml / min for 5 hours and finally the catalysts are reduced with an H_2 flow of 60 ml / min, at 500 ° C for 5 hours.

3. Results and Discussion

The reactions were carried out in a fixed bed U-type quartz micro reactor of the same material at atmospheric pressure, with a catalyst mass of 0.05 g. Before each reaction, the catalyst was activated with a N_2 flow of 30 ml min^{-1} for 15 min at 200 °C. After activation, the reaction was carried out at the set temperatures (400, 500, 600, 700 and 750 °C) with a N_2 flow of 2 ml min^{-1} of CH_4. The conversion of CH_4 and H_2 production as well as the other hydrocarbons such as CH_4, C_2H_4 and C_2H_6 were monitored in a gas chromatograph.

The dehydrogenation of methane was carried out at temperatures of 400, 500, 600, 700, 750 ° C with a methane flow of 2 ml min-1. Fig. 1 shows the conversion profiles of methane as a function of temperature, where the maximum conversion of the catalysts was at 750 ° C.
Fig. 2 shows the profiles of hydrogen production as a function of temperature; likewise the maximum production was presented at 750 ° C for the three catalysts.
The minimum conversion and production occurred at 400 °C for the different catalysts.

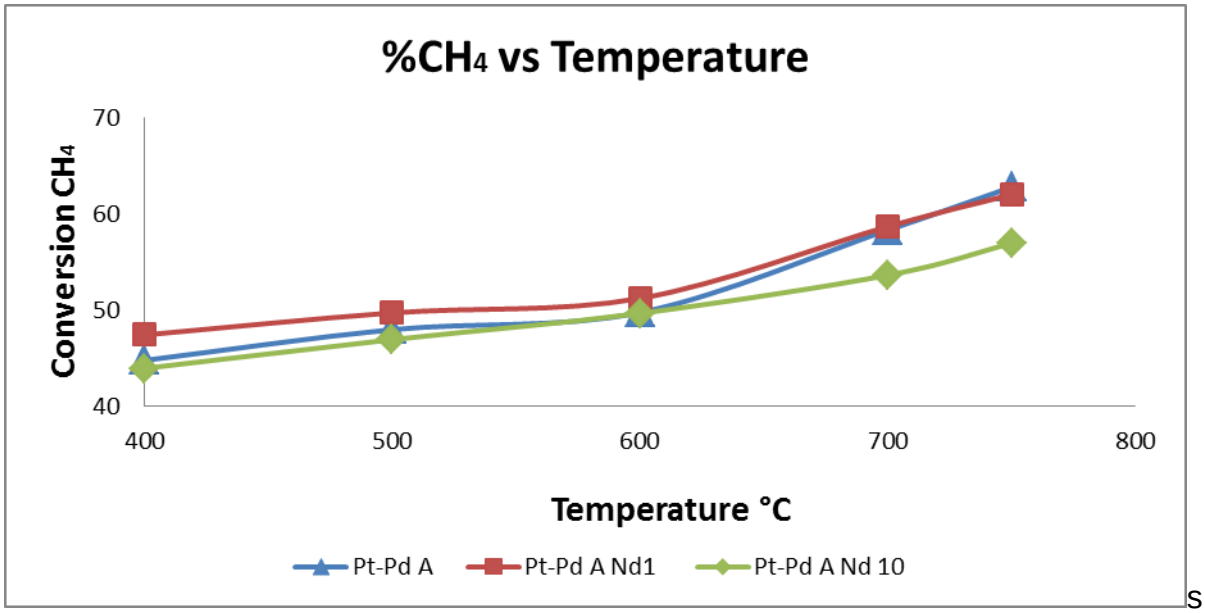

Figure 1. Temperature relationship with methane conversion.

The Pt-Pd/A catalyst generated the highest hydrogen production, since, as the neodymium was added to the catalysts (1 and 10 wt%), the H_2 production was decreasing to such a degree that the catalyst of Pt-Pd/ANd10% presented the lowest performance. Therefore it can be concluded that the addition of neodymium to the catalyst was detrimental to the process (in this case the use of a bimetallic catalyst). The interaction of the neodymium with the bimetallic particles was not favored, the fact of having bimetallic phases increases the probability of generate further interaction with the neodymium, showing greater carbon formation on the catalyst surface, which poisoned the metal active sites.

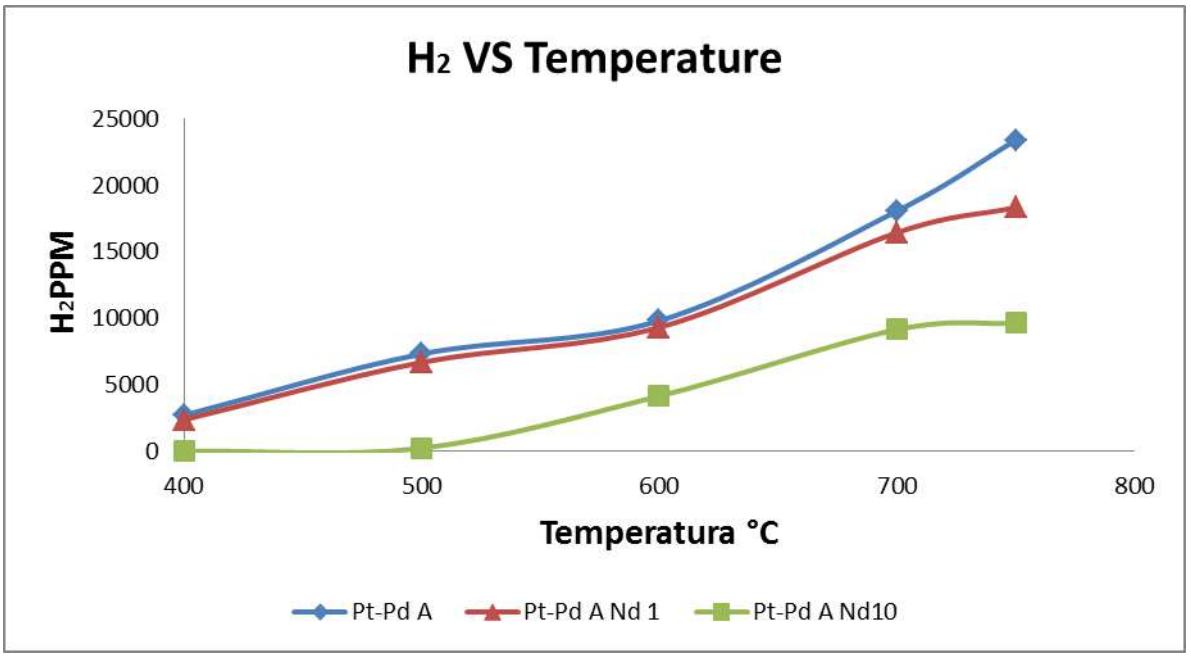

Figure 2. Relationship of the temperature with the production of hydrogen.

4. Conclusion

In the present work the effect of the addition of neodymium to the Pt-Pd catalyst was studied in order to obtain a greater selectivity to hydrogen.
1) The bimetallic Pt-Pd/A and of Pt-Pd/ANd1% showed higher conversion than the Pt-Pd/ANd10% catalyst. 2) Whereas, the highest hydrogen production was obtained on Pt-Pd/A catalyst. 3) The presence of Nd inhibit the selectivity towards hydrogen as the Nd increases (1 and 10 wt%). It is assumed that neodymium could interact stronger with the Pt-Pd bimetallic particles causing a high deposit of the coque on the metal sites, poisoning the active sites.

Acknowledgements

We acknowledge to CONACYT for the support provided to the project SEP-CONACYT CB-2013-01-220191 and Marina Caballero Diaz thanks to the CONACYT for the grant awarded No 387137/255851.

References

[1] M.H. Mahfuz,et al.Exergetic analysis of a solar thermal power system with PCM storage Energy Convers Manage, 78 (2014), pp. 486-492.

[2] T.M. Ivancic, et al.Discovery of a new Al species in hydrogen reactions of NaAlH4 J Phys Chem Lett, 1 (15) (2010), pp. 2412-2416.

[3] G Thomas. Overview of storage development DOE hydrogen program. Annu Rev; 2000.

[4] L.Z. Ouyang, et al.Excellent hydrolysis performances of Mg3RE hydrides
Int J Hydrogen Energy, 38 (7) (2013), pp. 2973-2978.

[5] D. Bradhurst, P. Heuer, G. Stolarski. Hydrogen production and storage; 1981.

[6] N.Z. Muradov, T.N. VeziroğluFrom hydrocarbon to hydrogen-carbon to hydrogen economy
Int J Hydrogen Energy, 30 (2005), pp. 225-237.

[7] J. Dufour, D.P. Serrano, J.L. Gálvez, J. Moreno, C. GarcíaLife cycle assessment of processes for hydrogen production. Environmental feasibility and reduction of greenhouse gases emissions Int J Hydrogen Energy, 34 (2009), pp. 1370-1376.

[8] J. Dufour, J.L. Gálvez, D.P. Serrano, J. Moreno, G. Martínez Life cycle assessment of hydrogen production by methane decomposition using carbonaceous catalysts Int J Hydrogen Energy, 35 (2010), pp. 1205-1212.

[9] L. Weger, A. Abánades, T. ButlerMethane cracking as a bridge technology to the hydrogen economy Int J Hydrogen Energy, 42 (2017), pp. 720-731.

[10] L. Weger, A. Abánades, T. ButlerMethane cracking as a bridge technology to the hydrogen economy Int J Hydrogen Energy, 42 (2017), pp. 720-731.

[11] N.Z. MuradovCO2-Free production of hydrogen by catalytic pyrolysis of hydrocarbon fuel Energy & Fuels, 12 (1998), pp. 41-48.

XVIII International Congress
of the Mexican Hydrogen Society

Production of hydrogen, from the decomposition of methane over Pd catalysts supported on alumina doped with neodymium.

M. Caballero Diaz[a,*]; G. del Ángel Montes[a].

[a] Universidad Autónoma Metropolitana-Unidad Iztapalapa, Departamento de Química, Área de Catálisis, Av. San Rafael Atlixco No. 186, C.P. 09340, A.P 55-534. México D. F. México.
* Corresponding author: 55-20032433 and e-mail: marcabdi@yahoo.com.mx

ABSTRACT

In this work we study the effect of the addition of neodymium on Pd-containing catalysts in the dehydrogenation reaction of CH_4 at temperatures between 400 and 750 ° C in a fixed bed reactor. The γ-Al_2O_3 and γ-Al_2O_3 doped supports with 1 and 10% by weight neodymium were synthesized. Once the supports were prepared, the Pd/γ-Al_2O_3 and Pd/γ-Al_2O_3-Nd catalysts were obtained by wet impregnation method. The catalysts were characterized by BET areas, X-Ray Diffraction, Infrared Fourier Tranform (FTIR) of pyridine adsorption and TEM microscopy.
For the analysis of the reaction products, a gas chromatograph Shimadzu GC-2014 was used. Experiments were conducted using a quartz tubular reactor, electric oven, a type K thermocouple and a mass of 0.05 g of catalyst was employed, γ-Al_2O_3 support was prepared from Boehmita Catapal B. Firstly the Boehmite was dried to 120° C for 12 hours, then the solid was calcined in air flow of 60 mL/min for 24 h using a ramp of temperature from 25°C to 650°C. The γ-Al_2O_3-Nd_2O_3 (loaded with 1 and 10 wt% neodymium) mixed oxides, were prepared by wet impregnation of the Boehmite with the necessary quantity of $Nd(NO_3)_3 \cdot 6H_2O$, the mixture was maintained in stirring for 3h. Then, the solids were dried in an oven to 120°C for 12 h, after that, samples were calcined at 650°C in airflow for 24 h. The catalysts Pd/γ-alumina and Pd/γ-alumina-Nd al (1 and 10%) were impregnated with solution of $PdCl_2$ at a pH of approximately 1, with the appropriate amount for obtain 1% by weight of Pd in each catalyst.
The catalysts showed high activity and hydrogen production at 750°C, with conversions around 63-80 %vol and hydrogen production over 33,100, 32,900, 22,800 ppm for PdANd1, PdANd10 and PdA catalyst respectively. It is remarkable that a possible electronic interaction between Pd and Nd could be controlling the activity and selectivity, which could explain this results.
The best catalyst was the Pd/γ-Al_2O_3Nd1, since at 63% conversions at 750 °C, it had the highest hydrogen production, followed by the catalyst Pd/γ-Al_2O_3Nd10, since it had the same production of hydrogen but less selectivity to this.

Keywords: palladium; RDX; hydrogen; pyridine

1. Introduction

Increasing environmental concerns has prompted the search for clean fuels to avoid emissions of greenhouse-gas (GHG) like COx, NOx, and SOx. Hydrogen has recently emerged as a clean energy, which is carbon free to replace the fossil fuels, resulting in the great demand of hydrogen production [1–3]. The energy produced by the combustion of hydrogen is 4 and 2.40 times more than the that of coal and natural gas combustion, respectively [4,5]. The generally used methods for H_2 production appear to be the reforming of methane (dry and steam), since CH_4 in its free form, is the rich source of hydrogen [6].
Currently, the hydrogen production by thermocatalytic decomposition of CH_4 ($CH_4 \leftrightarrow C+2H_2$) has received great attention due to numerous advantageous related to this single step technology, for instance: generating hydrogen with high purity, reducing greenhouse-gas emissions, low energy consumption and finally the production of stable
valuable carbon formed which is considerable essential for specific applications [5,7–9]. The energy needed for catalytic cracking of methane is almost half that is required for steam reforming per mole of decomposed methane.

2. Materials and Methods

The Pd catalysts were prepared by wet impregnation of the γ-Al_2O_3 and γ-Al_2O_3-Nd_2O_3 supports with the necessary quantity of $PdCl_2$ to obtain 1 wt% of Pd, at a pH of about 1 to dissolve palladium precursor salt. The solids were left in stirring for 3 h, and then, the water is evaporated using a vacuum evaporator bath. Subsequently the solids were dried in an oven at 120 °C, for 12 h. The catalysts were calcined at 500 °C under airflow for 5 h, finally reduced in H_2 flow at 500 °C for 5 h. The Pd real percentage on the catalysts was obtained by atomic absorption technique. Catalysts were labeled as: PdANdX%, where: Palladium, as Pd, alumina as A, neodymium as Nd, X% is the concentration of Neodymium in wt%, AR the catalysts after reaction and ST stability test.

3. Results and Discussion

The activity determinations were carried out at atmospheric pressure and a catalyst loading of 0.05 g. The reaction temperatures varied from 400 to 750 °C, with increases of 100 °C and only the last was 50 °C with a heating rate of 5 ° C min^{-1}. Fig. 1 shows the profiles of methane conversion as function of temperature. The PdANd10% catalyst showed the highest conversion of methane at all temperatures with respect to the other catalysts, with a maximum of 77.5% at 750 ° C, with increasing in reaction temperature up to 750 °C, increased the conversion, which could be explained by the endothermic nature of this process. The Table 1 shows the results of conversion, TOF, selectivity and yield for the dehydrogenation of methane on Pd catalysts at 750 ° C. The PdANd10% catalyst had a hydrogen selectivity of 100%, since there were no detected byproducts only unconverted methane.

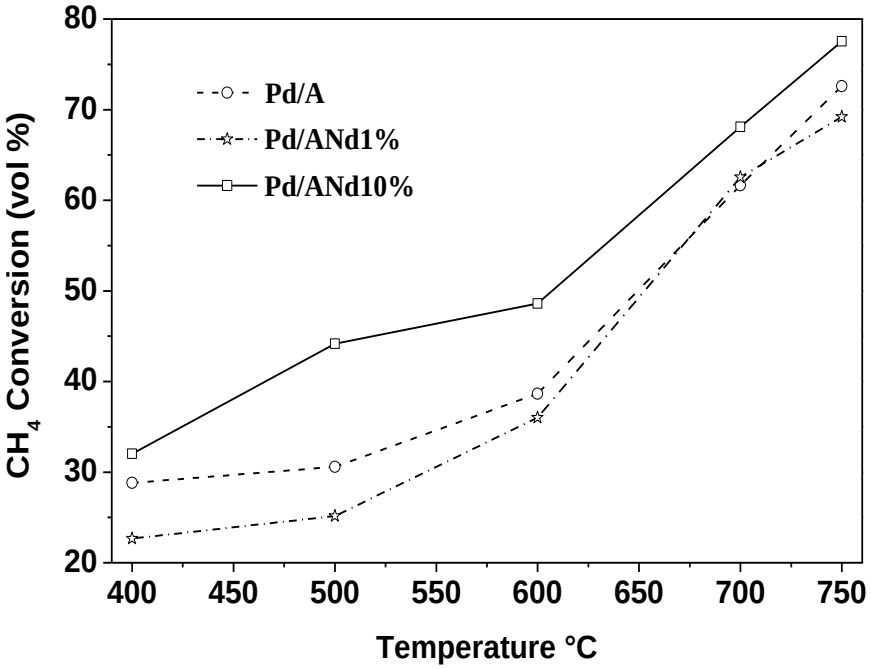

Fig. 1. Profiles of methane conversion as function of temperature for all catalysts.

Table 1. Conversion, TOF, selectivity and yield for the methane dehydrogenation on PdA and PdANdX% at 750 °C.

Catalyst	Conversion (%)	TOF (h^{-1})	Selectivity H_2 (%)	Yield (%)
PdA	72.6	39.2	100.0	72.6
PdANd1%	69.2	37.0	100.0	69.1
PdANd10%	77.5	50.3	100.0	77.5

4. Conclusions

A larger metal particle size, lower acidity and a surface rich on neodymium oxide of PdANd10% catalyst favored a high catalytic activity and long life for methane decomposition at reaction temperature of 750 °C. In particular, PdANd10% showed the highest hydrogen yield among all of the catalysts tested.
The PdANd10% catalyst had a hydrogen selectivity of 100%, since there were no byproducts only unconverted methane. It was observed in the output stream, traces of C_2H_4 and C_2H_6 (less than 1%) and unconverted methane over PdA and PdANd1% catalysts.

Acknowledgements

We acknowledge to CONACYT for the support provided to the project SEP-CONACYT CB-2013-01-220191 and Marina Caballero Diaz thanks to the CONACYT for the grant awarded No 387137/255851.

References

[1] Uddin MN, Daud WW, Abbas H F. Co-production of hydrogen and carbon nanofibers from methane decomposition over zeolite Y supported Ni catalysts. Energy Convers Manage 2015;90:218–29.
[2] Anjaneyulu C, Naresh G, Kumar VV, Tardio J, Rao TV, Venugopal A. Influence of La on reduction behavior and Ni metal surface area of Ni–Al_2O_3 catalysts for CO_x free H_2 by catalytic decomposition of methane. ACS Sustain Chem Eng 2015;3:1298–305.
[3] Abbas HF, Daud WW. Hydrogen production by methane decomposition: a review. Int J Hydrogen Energy 2010;35:1160–90.
[4] Bayat N, Rezaei M, Meshkani F. Hydrogen and carbon nanofibers synthesis by methane decomposition over Ni–Pd/Al_2O_3 catalyst. Int J Hydrogen Energy 2016;41:494–503.
[5] Pudukudy M, Yaakob Z, Mazuki MZ, Takriff MS, Jahaya SS. One-pot sol-gel synthesis of MgO nanoparticles supported nickel and iron catalysts for undiluted methane decomposition into CO_x free hydrogen and nanocarbon. Appl Catal B 2017;218:298–316.
[6] Keipi T, Hankalin V, Nummelin J, Raiko R. Techno-economic analysis of four concepts for thermal decomposition of methane: reduction of CO_2 emissions in natural gas combustion. Energy Convers Manage 2016;110:1–12.
[7] Ying Y, Meisheng C, Minglai L, Na Z, Zhiqi L, Yongxi S. Rare earth modified Ni-Si catalysts for hydrogen production from methane decomposition. J Rare Earths 2014; 32:709–14.
[8] Pudukudy M, Yaakob Z, Takriff MS. Methane decomposition into CO_x free hydrogen and multiwalled carbon nanotubes over ceria, zirconia and lanthana supported nickel catalysts prepared via a facile solid state citrate fusion method. Energy Convers Manage 2016;126:302–15.

[9] Nuernberg GDB, Fajardo HV, Foletto EL, Hickel-Probst SM, Carreño NL, Probst LF, et al. Methane conversion to hydrogen and nanotubes on Pt/Ni catalysts supported over spinel $MgAl_2O_4$. Catal Today 2011;176:465–469.

XVIII International Congress
of the Mexican Hydrogen Society

Ruthenium catalysts supported on γ-Al_2O_3 from different precursors for the Hydrogen production.

M. Caballero Diaz[*1]; G. Alicia del Ángel Montes[2]; R. Mendoza Serna[1]; A. J. Chong Santiago[1]

[1] Facultad de Estudios Superiores Zaragoza, UNAM, Carrera de Ingenieria Quimica, Batallón 5 Mayo s/n esq. Prol. Plutarco Elías Calles, Col. Ejercito de Oriente, Ciudad de México, C.P. 09230.
[2] Universidad Autónoma Metropolitana-Unidad Iztapalapa, Departamento de Química, Área de Catálisis, Av. San Rafael Atlixco No. 186, C.P. 09340, A.P 55-534. México D. F. México.
(*) corresponding author: marcabdi@yahoo.com.mx

ABSTRACT

The Preparation of γ-Al_2O_3 from Boehmite catapal B, Alumina (Merck) and Aluminum Secbutoxide, the precursor was placed in a crucible and dried for 12 hours at 120 ° C with a ramp of 2 ° C/min, then were calcined at 650 °C in air flow of 60 mL/min for 24 hours, using a heating ramp with a speed of 2 °C/min, after calcination, the system was cooled to room temperature with air flow. Wet Impregnation Method for the preparation of Ru/γ-Al_2O_3, the support is placed in a ball flask with a small amount of water, while the amount of $RuCl_3.3H_2O$ required for a content of 1% by weight is dissolved in the minimum amount of water, this solution is added to that of the support and left in agitation for 3 hours in a rotavapor at 30 rpm, the water is evaporated using a water bath at 60 ° C and a vacuum of 0.072 bar, later the solids are dried in an oven at 120 °C, for 12 hours. The catalyst is introduced in a quartz reactor with a fixed bed to be calcined at 500 °C in an air flow of 60 mL/min for 5 hours, using a heating ramp with a speed of 2 °C/ min; starting from the ambient temperature at 120 °C, keeping it there for 1 hour, when this time passes, the temperature increases to 500 °C, a temperature that is maintained for 5 hours. Finally, the catalysts were reduced in H_2 flux of 60 mL/min at 500 °C for 5 hours, at a heating rate of 2 °C/min. Reaction by catalytic decomposition of methane: 50 mg of catalyst was deposited in a U-type quartz reactor, inerted with 30 ml/min of N_2 for 15 min at 200 ° C. 2 ml/min of CH_4 were passed at 400 °C, 500 °C, 600 °C, 700 °C and 750 °C per 6 min. The catalyst by Boehmite Catapal B and Alumina (Merck) obtained the highest production of H_2 at 700 ° C, as well as the highest conversion of CH_4, while the catalyst by Aluminum Secbutoxide obtained an almost constant H_2 production between 500 ° C and 700 ° C, as well as its conversion of CH_4.
The catalyst by Boehmite Catapla B obtained the highest production of H_2 at 700 ° C compared to the other two, although the catalyst by Aluminum Secbutoxide obtained the best H_2 productions at different temperatures.

Keywords: boehmite; Secbutoxide; Alumina.

1. Introduction

The current need for energy is supplied by the combustion of non-renewable energy sources, that is, fossil fuels, and is associated with the release of large amounts of greenhouse gases (GHGs), especially carbon dioxide (CO_2) and other harmful gases released into the atmosphere. It is possible that one day hydrogen will replace fossil fuels in several applications such as automobiles and power plants [1]. However, hydrogen currently is produced mainly through fossil fuel reform. It's expected that fossil fuels remain as a significant source of long-term hydrogen [2]. Nowadays, hydrogen finds application as a chemical compound instead of a fuel in commercial operations, but if hydrogen is used to replace existing fuels, suitable methods must be developed for its large-scale production.
Hydrogen is the simplest element and the most abundant gas in the universe. However, hydrogen doesn't appear by itself in nature, but is combined with other elements such as oxygen and carbon, that is, water or hydrocarbons, so these substances must be decomposed / reformed to obtain H_2 [3].] To release the hydrogen, heat can be applied to the hydrocarbons, and to decompose the water molecules can be used thermo-chemical processes, by electrical charge (electrolysis) or a photolytic process.

2. Materials and Methods

Preparation of γ-Al_2O_3 from Boehmite catapal B, Alumina (Merck) and Aluminum Secbutoxide.

- The precursor was placed in a crucible and dried for 12 hours at 120 ° C with a ramp of 2 ° C/min.
- They were calcined at 650 °C in air flow of 60 mL/min for 24 hours, using a heating ramp with a speed of 2 °C/min.
- After calcination, the system was cooled to room temperature with air flow.

Wet Impregnation Method for the preparation of Ru/γ-Al_2O_3

- The support is placed in a ball flask with a small amount of water, while the amount of $RuCl_3.3H_2O$ required for a content of 1% by weight is dissolved in the minimum amount of water.
- This solution is added to that of the support and left in agitation for 3 hours in a rotavapor at 30 rpm.
- The water is evaporated using a water bath at 60 ° C and a vacuum of 0.072 bar, later the solids are dried in an oven at 120 °C, for 12 hours.
- The catalyst is introduced in a quartz reactor with a fixed bed to be calcined at 500 °C in an air flow of 60 mL/min for 5 hours, using a heating ramp with a speed of 2 °C/ min; starting from the ambient temperature at 120 °C, keeping it there for 1 hour,
- When this time passes, the temperature increases to 500 °C, a temperature that is maintained for 5 hours. Finally, the catalysts were reduced in H_2 flux of 60 mL/min at 500 °C for 5 hours, at a heating rate of 2 °C/min.

Reaction by catalytic decomposition of methane

- 50 mg of catalyst was deposited in a U-type quartz reactor, inerted with 30 ml/min of N_2 for 15 min at 200 ° C.
- 2 ml/min of CH_4 were passed at 400 °C, 500 °C, 600 °C, 700 °C and 750 °C per 6 min.

3. Results and Discussion

The following three Ruthenium catalysts supported on γ-Al_2O_3 at 1% by weight of the metal were synthesized by the wet impregnation technique from different precursors:

1. Ru / γ-Al_2O_3 by Boehmita Catapal B
2. Ru / γ-Al_2O_3 by Alumina (Merck)
3.-Ru / γ-Al_2O_3 by Aluminum Secbutoxide

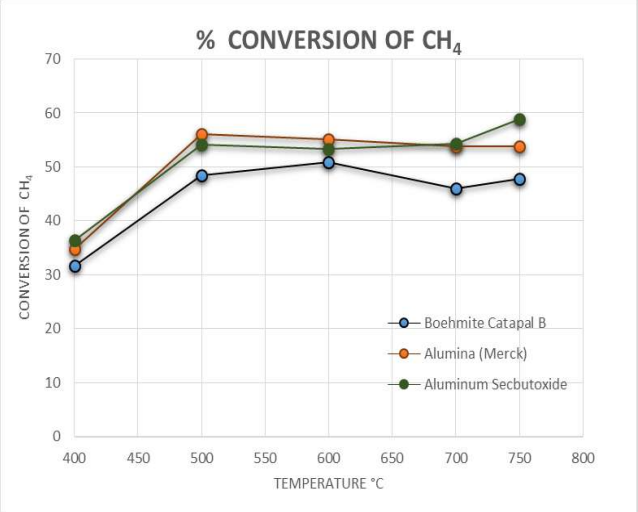

Fig. 1. Methane conversion

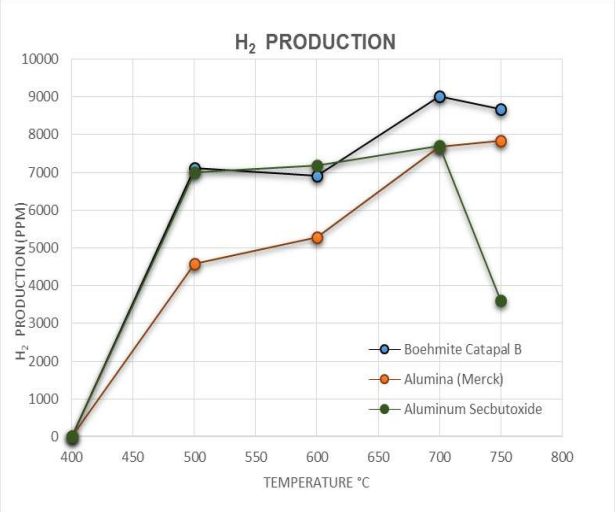

Fig. 2. Hydrogen production

4. Conclusions

The catalyst by Boehmite Catapal B and Alumina (Merck) obtained the highest production of H_2 at 700 ° C, as well as the highest conversion of CH4, while the catalyst by Aluminum Secbutoxide obtained an almost constant H_2 production between 500 ° C and 700 ° C, as well as its conversion of CH_4.

The catalyst by Boehmite Catapla B obtained the highest production of H_2 at 700 ° C compared to the other two, although the catalyst by Aluminum Secbutoxide obtained the best H_2 productions at different temperatures.

Acknowledgements

To the Support Program for Research Projects and Technological Innovation PAPIIT with Password: TA100518.

References

[1] Malaika A., Krzyzynska B., Kozlowski M., “Int J Hydrogen Energy”. 2010; 35:7470-5.
[2] Muradov N., “Int J Hydrogen Energy” 1993; 18:211-5.
[3] Abbas H., Daud W., “Int J Hydrogen Energy” (2010); 35:12268-76

XVIII International Congress
of the Mexican Hydrogen Society

Synthesis of catalytic material of Ni-Mo_2C over hydroxyapatite for application in hydrogen production by biomass gasification

Jonathan Jesús Malpica Malpica[1]*, José Aaron Melo Banda[1], Ana Lidia Martínez Salazar[1].

1 Centro de Investigación en Petroquímica, Instituto Tecnológico de Ciudad Madero, Prol. Bahía del Aldair, Av. de las Bahías. Parque Industrial Tecnia, Altamira, Tamaulipas, México, 89608.

*833-261-13-32, jonathan-jesus15@hotmail.com

ABSTRACT

Several works suggest that molybdenum carbide has catalytic properties similar to those noble metals in biomass reforming reactions, making it an attractive catalyst to gasification reaction. Moreover, molybdenum carbide has excellent mechanical and thermal stability. On the other hand, the nickel content in the molybdenum carbide catalysts increases the selectivity in the production of hydrogen in this type of reactions.

Hydroxyapatite was used as a support due its main constituent is CaO, which improve selectivity by CO adsorption capacity in the cases of hydrogen production processes with CO presence as a by product.

Ni-Mo2C synthesis was carried out employing temperature-programmed reaction method using ammonium heptamolybdate tetrahydrate and nickel nitrate hexahydrate as precursor salts and sucrose as carbon source. Hydroxyapatite extraction from bovine bones was made by thermal treatment under nitrogen inert atmosphere. Finally, Ni-Mo2C impregnation in hydroxyapatite was done by incipient humidity method.

Catalytic materials (Ni-Mo2C/Hydroxyapatite) samples were characterized by Fourier Transform Infrared Spectroscopy (FTIR), Scanning Transmission Electron Microscopy (STEM), X-Ray Diffraction (XRD) and physical adsorption of nitrogen at 77 K.

The catalyst Ni-Mo_2C supported on hydroxyapatite could be a very well option to be used in green processes for hydrogen production. The properties of active phase and the properties catalytic support make the catalytic material have excellent thermal and mechanical stability.

Keywords: Hydrogen Production; Molybdenum Carbide; Hydroxyapatite.

1 Introduction

The problems related to the contamination of the environment have been caused or associated to several factors, among them is the production, transformation and consumption of products derived from fossil resources in order to be used as sources of energy.

Currently, oil has become not only one of the most widely used sources of energy in the world, but it is also the basis of many products that are used in the daily life of the human being, and due to excessive consumption of crude oil worldwide reserves have decreased significantly, so it is necessary to find new forms of energy from alternative sources [1], [2].

The most used processes for the production of hydrogen involve the use of fossil resources as raw material; Nearly 96% of hydrogen production uses methane as a raw material [3], [4]. Currently, the most widely used process for the production of hydrogen is methane reforming [3], [5], [6], with wet methane reformation (equation 1) and methane dry reforming (equation 2) the most used at the industrial level.

$$CH_4 + H_2O \rightarrow CO + 3H_2 \qquad (Ec.1)$$
$$CH_4 + CO_2 \rightarrow 2CO + 2H_2 \qquad (Ec.2)$$

One of the most interesting topics that has been discussed over these years is the application of biomass to be used as raw material in processes for the production of hydrogen, because hydrogen is one of its main components, however, the amount of this element or some other type of elements can vary according to the type of biomass, origin and degree of decomposition of this. In general, the main products obtained from biomass are gases such as methane, carbon dioxide, hydrogen, among others (equation 3).

$$\alpha C_x H_y O_n + \beta\, H_2O \xrightarrow{\Delta} aH_2 + bCO + cCO_2 + dCH_4 + eC + f\, Tar \quad (Ec.3)$$

The catalytic activity of molybdenum carbide is attributed to the electronic structure induced due to the ligand effect in the carbon. The increase in molar ratio C / Mo causes the carbide species to be more stable due to the decrease in molybdenum activity caused by the transfer of electrons from molybdenum to carbon [7].
Likewise, other investigations [6], [8], [9] have succeeded in demonstrating a very significant increase in the selectivity towards the production of hydrogen in catalysts containing nickel.

On the other hand, hydroxyapatite extracted from bones is material that has not yet been studied to be applied in the field of catalysis. The study of the properties of this material [10–12] show a high thermal and mechanical stability, in addition, these studies show a high porosity of the hydroxyapatite extracted by thermal methods. In conclusion, the use of hydroxyapatite can be very useful in the catalytic material for the production of hydrogen through biomass.

2 Materials and Methods

2.1 Ni-Mo_2C synthesis

Ni-Mo_2C synthesis was done by solid-solid method using temperature programmed reaction. Ammonium heptamolybdate tetrahydrate, $(NH_4)_6Mo_7O_{24}{*}4H_2O$ (0.0674 M), was used as molybdenum source and nickel (II) nitrate hexahydrate, $Ni(NO_3)_2\ {*}6H_2O$ (0.2057 M), was used as nickel source. Sucrose (0.9440 M) was employed as carbon source to obtain Ni-Mo_2C catalysts. Ni-Mo_2C samples were prepared with 0, 10, 15 and 20 nickel weight percentage, maintaining C/Mo constant molar ratio of 2. Nickel solution was added to molybdenum solution keeping at constant stirring for 2 hours. After precursor salts homogenization in aqueous medium, they are placed in room temperature at 110 °C for 12 hours. Finally, sucrose solution was added to samples with constant stirring for 2 hours. Resulting samples were dried for 12 h at 110 °C.

To obtain Ni-Mo_2C, a reducing carburizing atmosphere at 900°C were flowed at 4 l/min through the samples during 2 hours. Carbon contained in samples develop Ni-Mo_2C compounds under this reducing atmosphere of pure hydrogen. After obtaining the carbides, these were placed in a sonicator bath for 5 hours using 25 ml of isopropanol as dispersing agent.

2.2 Hydroxyapatite extraction from bovine bone

Hydroxyapatite is a material which is found naturally in bone matrix of bones [13]. Hydroxyapatite extraction was carried out by thermal treatments. Bones were cleaned to eliminate excess fat content. Subsequently, particle sizes were reduced by physical means. Bovine bone powders were dried at 120 °C for 24 hours. The heat treatment of bone was carried out in 400 ml/min nitrogen flow in order to avoid oxidation of the material at three different temperatures (700 °C, 800 °C and 900 °C) for 2 hours.

2.3 Preparation of Ni-Mo_2C/hydroxyapatite

Nickel doped molybdenum carbides were impregnated over hydroxyapatite extracted at 900 °C with 20 weight percentage of metals content. Impregnation of hydroxyapatite support with metals was made by the incipient wetness method using 10 ml of isopropanol as dispersing agent. The mixture was kept under constant stirring for 2 hours. Isopropanol was removed by evaporation and the resulting samples were dried for 24 hours at 120 °C.

2.4 Catalyst characterization

Structural properties and phase identification of prepared catalyst were verified by X-ray diffraction, using a Buker D8 Advance diffractometer with a Cu-Kα-2 radiation source. For Ni-Mo_2C and Ni-Mo_2C/hydroxyapatite materials, 20-80° (2θ) scan range was made with 0.01° steps. For hydroxyapatite, 20-60° (2θ) scan range was made with 0.01º steps. Textural properties were determined by N_2 physisorption at 77 K, these measurements were performed by Quantachrome Autosorb-iQ equipment. Specific area was calculated by Brunauer-Emmet-Teller (BET) method, while distributions of pore sizes were obtained according to Barrett-Joyner-Halenda method (BJH). Scanning transmission electron microscopy images were collected on a JEOL JSM-7100F microscope operated at 1.3- 20.0 kv.

Hydroxyapatite FTIR spectroscopy analysis was performed in Perkin Elmer, Spectrum 100 model, spectrophotometer; analyses were carried out in middle infrared region (4000-380 cm^{-1}).

3 Results and Discussion

3.1 Ni-Mo_2C Properties

Figure 1 Shows X-ray diffraction patterns of Ni-Mo_2C samples with different nickel content from 0 to 25 wt%. This result exhibits characteristic peaks of Mo_2C, Ni_3C and graphite.

It can be in figure 1, crystallographic structure of Mo_2C correspond with hexagonal structure at molar ratio to C/Mo = 2, Ni_3C crystallographic structure correspond to trigonal structure. X-ray diffraction profiles show molybdenum carbide characteristic peaks at 34.65, 38.18, 39.72, 52.51, 62.11, 70.05 73.12 75.29 y 76.29° angle 2θ, correspond to crystallographic planes (100), (002), (101), (012), (110), (013), (200), (112) and (201) respectively. Also, X-ray diffraction profiles show characteristic peaks of nickel carbide at 42.03, 45.12, 59.16 y 71.97 ° angle 2θ, correspond to crystallographic planes (006), (113), (116) and (300) respectively.

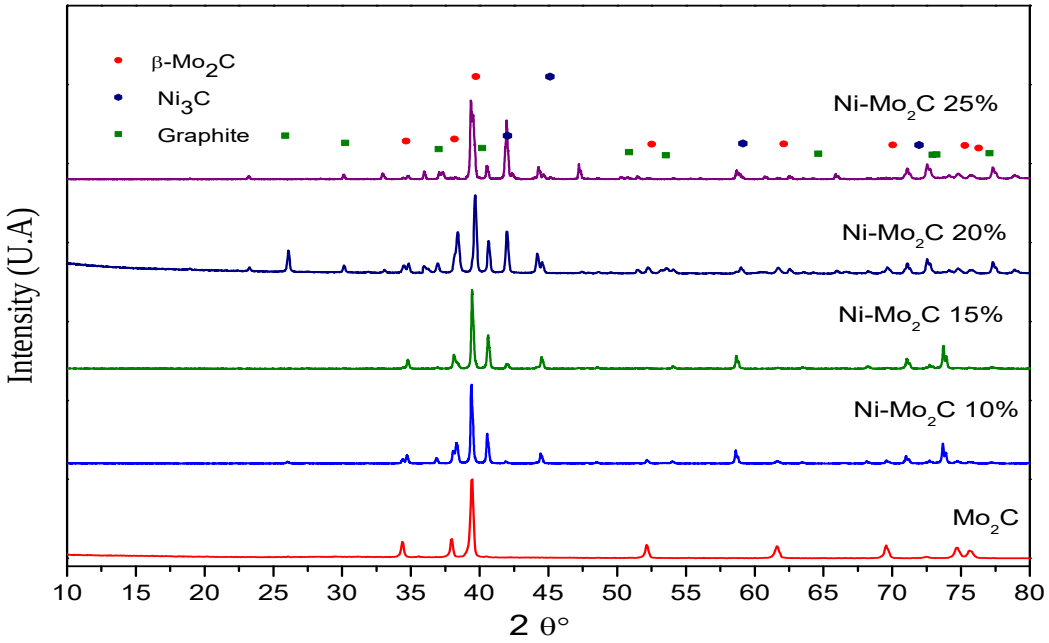

Figure 1 X-ray diffraction profiles corresponding to molybdenum carbide samples doped with different charges of nickel.

Table 1 shows textural properties of nickel-modified molybdenum carbide samples.
An increase in the surface area of Ni-Mo_2C materials is observed as nickel content increases. However, in the case of 20 wt % nickel content, the surface area is very low, this can be attributed to a possible material agglomeration and surface coating caused by nickel amount. Likewise, pore diameter decreasing behavior can be related to samples surfaces coating due to increasing nickel doping. According to X-ray diffraction results, intense and well-defined peaks of nickel carbide and graphite can be observed. Due to Ni_3C and C content over Mo_2C, it is possible to have a composites formation attributed to molybdenum carbide interstitial structure saturation.

Table 1. Textural Properties of Ni-Mo_2C samples.

Nickel content (wt %)	Superficial area (m^2/g)	Pore volume (cm^3/g)	Pore Diameter (Å)	**Cristallite size (nm)**
0	0.83	0.0082	393	33.69
10	1.8	0.0054	118	43.94
15	6.0	0.0099	67	45.10
20	0.25	0.0021	34	36.73
25	2.7	0.0055	83	26.02

Figure 2 shows STEM micrographs representative of Mo_2C and Ni-Mo_2C synthesized with geometric shapes of irregular parallelepipeds. As result, particles agglomeration could be observed on material surface, causing large particle sizes. On the other hand, it can be see that the surface of the sample without nickel content corresponds to the surface of synthetic graphitic carbon [14]. Besides, metallic particles (corresponding to Mo) can be observed on material surface.

Due to thermal treatment effect, pores can be seen in the surface of the material, these pores are caused by material sintering at high temperatures.
According to energy dispersion spectroscopy analysis, main composition of sample corresponds to carbon and molybdenum with C / Mo average molar ratio of 1.93.
A surface coating is shown in all Ni-Mo_2C samples, caused by molybdenum carbide interstitial structure saturation due to nickel content, confirming results of DRX and textural properties about the formation of composites in Ni-Mo_2C samples. Therefore, pores cannot be seen in the figures. Geometrical morphologies of irregular parallelepiped can be observed in 10 and 15 wt % nickel content samples. In addition, agglomerates of Ni-Mo_2C materials can be seen. On the other hand, in samples with 20 wt % nickel content, geometric shapes of irregular spherical

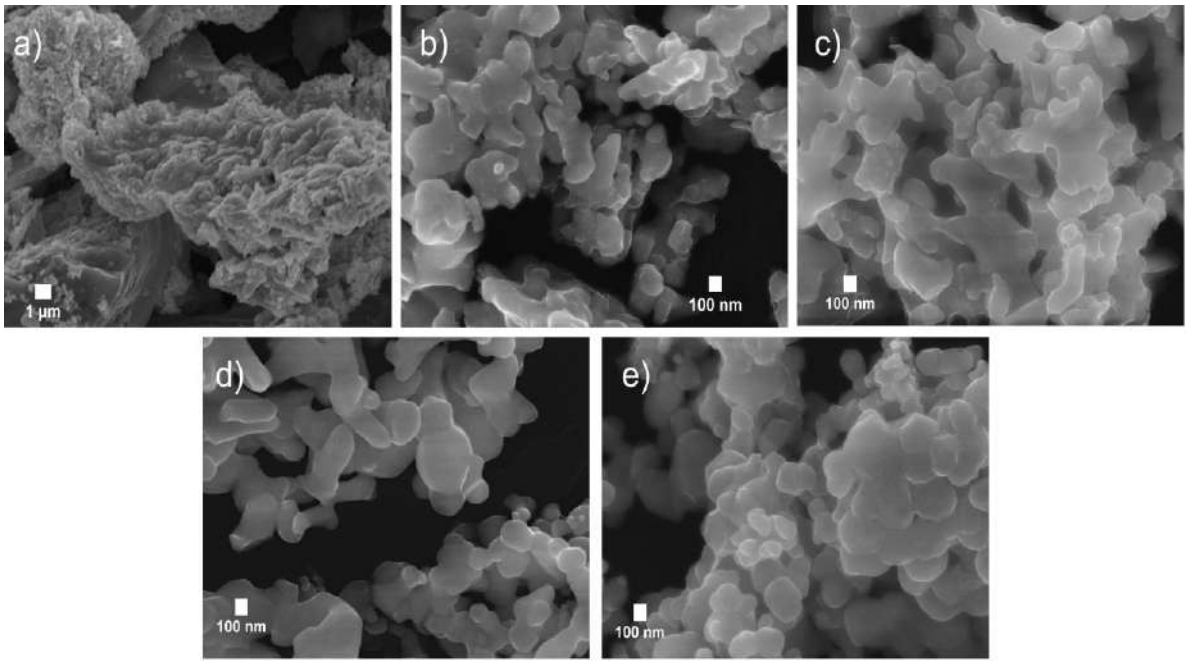

Figure 2. STEM micrograph of Ni-Mo_2C synthesized with a) 0 (4,000 x), b) 10 40,000 x), c) 15 (40,000 x), d) 20 (40,000 x) and e) 25 wt % (40,000 x) nickel content.

particles and irregular parallelepiped shapes can be noticed.

3.2 Hydroxyapatite properties

Hydroxyapatite (HA) X-ray diffraction profiles at 700, 800 and 900 ° C temperature range are shown in figure 3 at 20-60° (2θ) scan range. HA sample patterns show that crystalline activity corresponds mainly to hydroxyapatite crystals content presenting characteristic peaks at 25.47 °, 31.83 °, 39.95 °, 46.86 °, 48.83 ° and 53.28 ° angle 2θ, with planes (201), (211), (310), (222), (320) and (004) [15]. Diffraction patterns exhibit a hexagonal crystal structure [15] with network parameters of a = 9.4235 Å and c = 6.8852 Å. Figure 3 an increase in peaks height is show according temperature increases. As well, an increase in average width of the most intense peaks (FHWM) can be observed at 700 and 800 ºC so, it can be concluded that there is a decrease in crystallite sizes by bone sintering. There is a slight decrease in FHWM at 900 ºC, this is attributed to crystal agglomeration due to thermal treatment effect in hydroxyapatite extraction.

Figure 4 shows bovine bone IR spectra samples before and after thermal treatment, exhibiting characteristic bands of hydroxyapatite absorption in mid-infrared region [15, 16]. There are no significant differences observed in FTIR spectras of the samples after thermal treatment (700, 800 and 900 ºC) so, it can be concluded that this material is thermally stable, without phase changes.

It should be noted that inorganic matter signal ($PO4^{-3}$ groups) acquires greater intensity in samples after thermal treatment, this could be attributed to the elimination of organic matter and recrystallization of hydroxyapatite crystals.

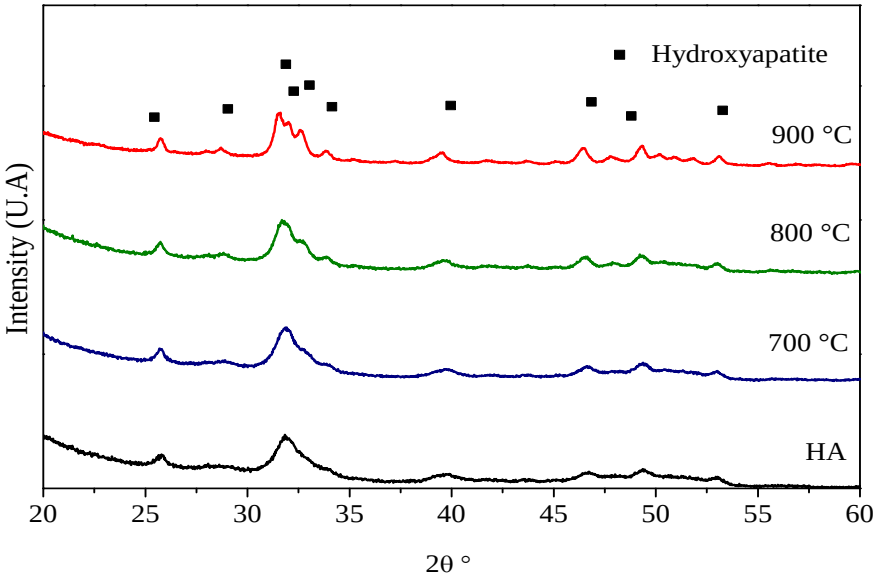

Figure 3 X-ray diffraction profiles corresponding to hydroxyapatite extracted from bovine bone.

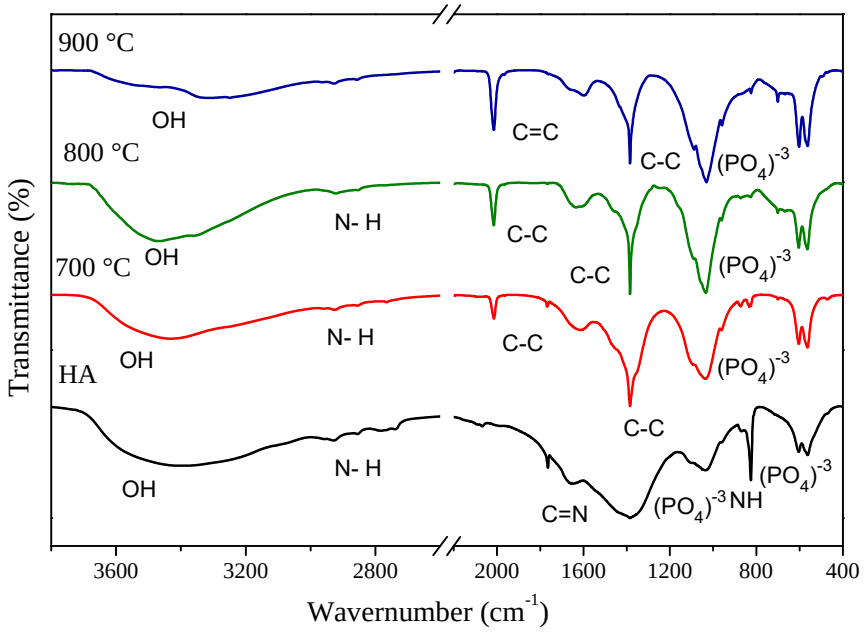

Figure 4 FTIR spectra of hydroxyapatite extracted from bovine bone.

Textural properties results (table 2) show a decrease in surface area according temperature increases due material sintering by exposure to high temperatures. Adsorption and desorption isotherms of hydroxyapatite at 700, 800 and 900 ºC are shown in figure 5, which display type III isotherms, according to IUPAC classification, which correspond to mesoporous solids of H3 type.

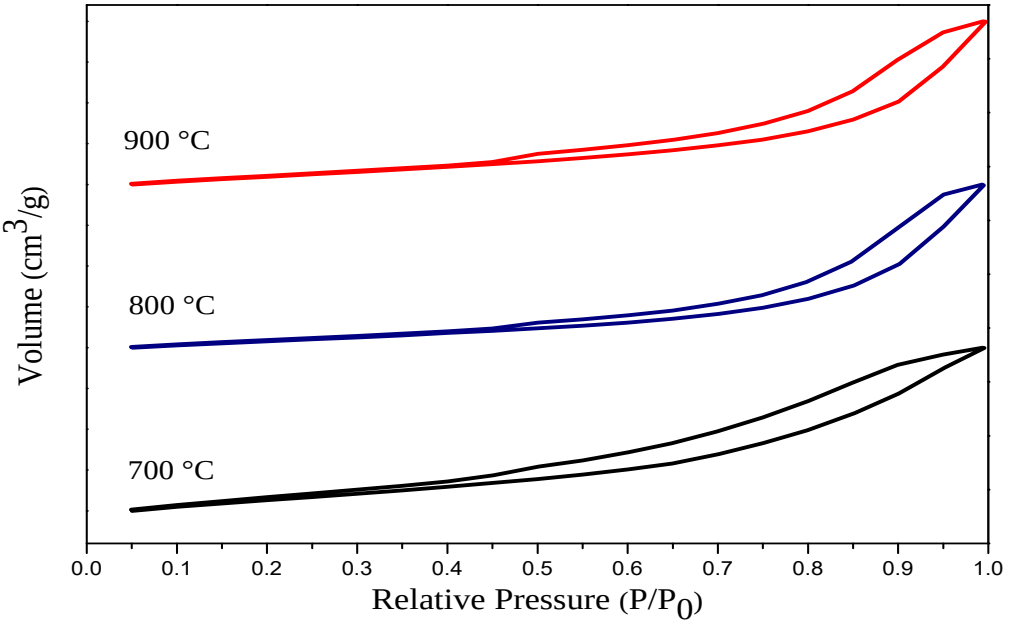

Figure 5 Adsorption-desorption isotherms of hydroxyapatite.

3.3 Ni-Mo_2C/HA Characterization

Figure 6 shows NHM catalysts diffraction profiles. It can be observed the presence of Ni_3C, Mo_2C, hydroxyapatite and carbon as catalysts components. In figure 9 d) a greater intensity in coal characteristic peaks can be observed, this is attributed to the need to maintain the molar ratio C / Mo = 2. Therefore, it is necessary to add an excess of sucrase in the synthesis of catalyst with nickel content 20 wt % to ensure molar ratio despite the increase of nickel in this sample.

Figure 7 shows STEM micrographs representative of NHM catalyst samples corresponding to 3,500 X magnification.

Characteristic morphology of hydroxyapatite at 900 °C can be observed, it is also observed that there are no apparent changes in the support morphology by nickel-molybdenum carbide compounds impregnation. However, Ni-Mo_2C materials are present on material surface and in hydroxyapatite pores according to XRD results (Figure 6).

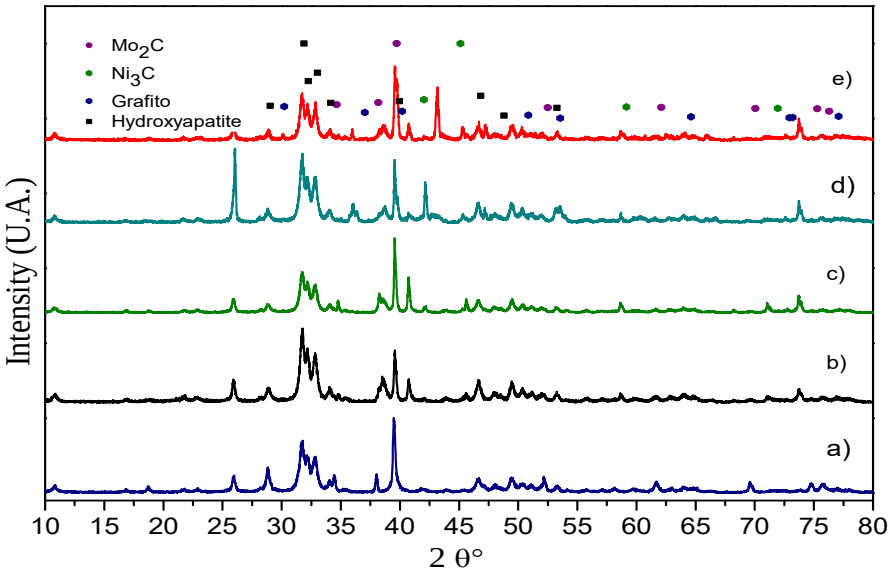

Figure 6 X-ray diffraction profiles corresponding to NHM catalyst samples doped with different charges of nickel a) 0, b) 10, c) 15, d) 20 and e) 25 wt %.

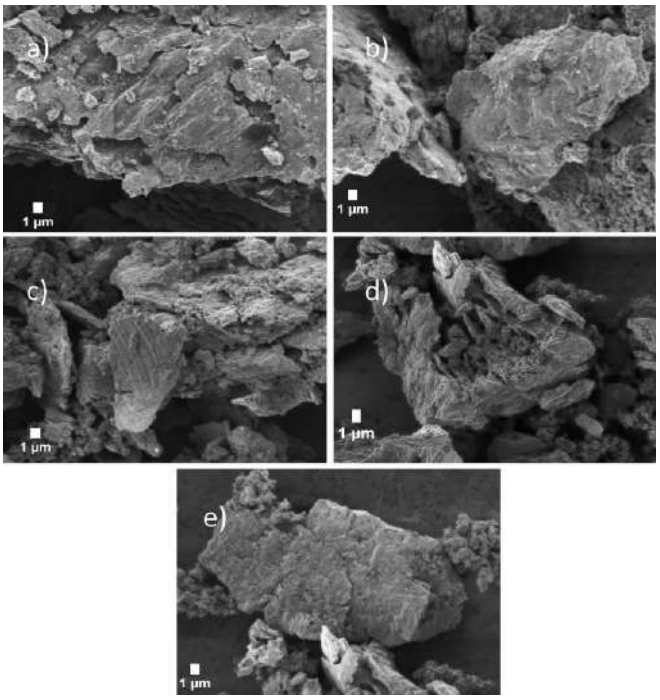

Figure 7. STEM micrograph representative of NHM catalyst doped with different charges of nickel a) 0, b) 10, c) 15 and d) 20 and e) 25 wt%.

4. Conclusion

In this work, molybdenum carbide catalytic materials doped with nickel were synthesized via alternative methodology for molybdenum carbide synthesis. Likewise, hydroxyapatite extraction from bovine bones was successfully achieved, increasing its porosity with the increase in temperature maintaining its structural stability. According to results obtained in Ni-Mo_2C materials synthesis it can be concluded that the method used is suitable for obtaining molybdenum carbide with hexagonal crystalline structure, which presents a catalytic activity similar to noble metals. However, particle sizes are too large for composites formation due to molybdenum carbide crystalline network saturation by the excess of nickel carbide and carbon deposits on material surface. On the other hand, it is possible to extract hydroxyapatite from bones via thermal treatments. Heat treatment causes bone matrix organic matter degradation; therefore, this causes the obtaining of porous materials ideal to be used as support for catalyst. However, results suggest an apparent hydroxyapatite degradation due to hydroxyl groups (OH^{-1}) elimination. According to elemental chemical composition analysis, Ca/P molar ratio is adequate for obtaining hydroxyapatite crystals.

References

[1] Y. Kalinci, A. Hepbasli, and I. Dincer, “Biomass-based hydrogen production : A review and analysis,” *Int. J. Hydrogen Energy*, vol. 34, no. 21, pp. 8799–8817, 2009.

[2] H. Balat and E. Kirtay, “Hydrogen from biomass - Present scenario and future prospects,” *Int. J. Hydrogen Energy*, vol. 35, no. 14, pp. 7416–7426, 2010.

[3] A. I. R. De Torre, I. Tecnológico, D. C. Madero, and J. M. Dominguez, “Hydrogen production by methane reforming with H2S using Mo , Cr / ZrO2 – SBA15 and Mo , Cr / ZrO2 – La2O3 catalysts ScienceDirect,” no. July 2016, 2015.

[4] F. Ausfelder and A. Bazzanella, “Hydrogen in the Chemical Industry,” *Hydrog. Sci. Eng. Mater. Process. Syst. Technol.*, vol. 1, pp. 19–39, 2016.

[5] J. D. Holladay, J. Hu, D. L. King, and Y. Wang, “An overview of hydrogen production technologies,” vol. 139, pp. 244–260, 2009.

[6] C. Shi, “In-situ synthesis of nickel modified molybdenum carbide catalyst for dry reforming of methane,” *CATCOM*, vol. 12, no. 9, pp. 803–807, 2015.

[7] P. Liu and a Rodriguez, “Catalytic properties of Mo carbide, nitride and phosphide a theoretical study ,” *Catal.Lett.*, vol. 91, no. December, p. 247, 2003.

[8] W. Chen *et al.*, “Hydrogen-Evolution Catalysts Based on Non-Noble Metal Nickel – Molybdenum Nitride Nanosheets ** Angewandte,” pp. 6131–6135, 2012.

[9] C. Shi *et al.*, “Ni-modified Mo2C catalysts for methane dry reforming,” *Appl. Catal. A Gen.*, vol. 431–432, pp. 164–170, 2012.

[10] C. Liao, F. Lin, K. Chen, and J. Sun, “Thermal decomposition and reconstitution of hydroxyapatite in air atmosphere,” vol. 20, pp. 1807–1813, 1999.

[11] M. Younesi, S. Javadpour, and M. E. Bahrololoom, “Effect of heat treatment temperature on chemical compositions of extracted hydroxyapatite from bovine bone ash,” *J. Mater. Eng. Perform.*, vol. 20, no. 8, pp. 1484–1490, 2011.

[12] “Processing and Properties of HAp Based Biomaterials for Use as Hard Tissue Replacement Implants,” no. July, 2017.

[13] S. Joschek, B. Nies, R. Krotz, and A. Göpferich, “Chemical and physicochemical characterization of porous hydroxyapatite ceramics made of natural bone,” *Biomaterials*, vol. 21, no. 16, pp. 1645–1658, 2000.

[14] M. Wissler, “Graphite and carbon powders for electrochemical applications &,” vol. 156, no. 2, pp. 142–150, 2006.

[15] B. O. Fowler, “Reference Material,” vol. 109, no. 6, pp. 553–568, 2004.

[16] C. Y. Ooi, M. Hamdi, and S. Ramesh, “Properties of hydroxyapatite produced by annealing of bovine bone,” *Ceram. Int.*, vol. 33, no. 7, pp. 1171–1177, 2007.

XVIII International Congress
of the Mexican Hydrogen Society

Hydrogen generation by aluminum alloys corrosion in aqueous acid solutions promoted by sodium molybdate

Julia Guadalupe Salazar Barrera[1*], Ana Lidia Martínez Salazar[1], Margarita García Herzandez[1], José Aarón Melo Banda[1], Marco Antonio Coronel García[1], Ulises Páramo García[1].

[1] Centro de Investigación en Petroquímica, Instituto Tecnológico de Ciudad Madero, Prol. Bahía del Aldair, Av. de las Bahías. Parque Industrial Tecnia, Altamira, Tamaulipas, México, 89608.
* Corresponding author: 833 4 602457, juliasalazarb@outlook.com

ABSTRACT

The aluminum alloys corrosion system was studied for hydrogen production in aqueous acid solutions using sodium molybdate as promoted Aluminum alloys has been considerate as the most promising material to hydrogen generation in corrosion reaction due to its amphoteric behavior, volumetric energy, density and low cost. There were so far no studies on the use of molybdates to hydrogen production. Nevertheless, sodium molybdate at low concentration has been reported as a corrosion accelerator for aluminum in hydrochloric acid, therefore it is a good promoter to increase the hydrogen production.
In the present study a sustainable and economic system of hydrogen production is carried out with different concentration of sodium molybdate at low temperature (333 K), employing aluminum alloys waste, seawater and hydrochloric acid as a aqueous acid solution. Promoter corrosion efficiency at 1.25M hydrochloric acid solution was studied by volumetric measurements. Gas composition produced during the reaction was analyzed by gas chromatography.
Sodium molybdate particles were synthesized via sonochemical precipitation method based on the reaction between ammonium heptamolybdate tetrahydrate and sodium hydroxide in water. The structural and morphological properties were characterized by techniques such as Fourier Transform Infrared Attenuated Total Reflection Spectroscopy (FTIR-ATR), Ultraviolet-visible spectroscopy (Uv-vis), Scanning Transmission Electron Microscopy (STEM) and X-Ray Diffraction (XRD).
Main gas product generate in aluminum alloys corrosion was hydrogen. Besides this, an improvement of hydrogen production rates and yields was observed using sodium molybdate as promoter material and varying aluminum alloys composition.

Keywords: hydrogen production; corrosion; sodium molybdate

September 18th to 21st, 2018 in Mexico City, Mexico.

1. Introduction

Hydrogen is the most abundant element in the universe, on Earth is chemically combined with other elements and substances as water and hydrocarbons. During the last 30 years the hydrogen has been attracted attention as a fuel alternative because of its abundance, energy-efficient and low polluting fuel. Nevertheless the 55% and 60% of the hydrogen in the world is produced by steam reformation of natural gas with the generation of CO_2 that is one precursor to produce greenhouse gases, acid rain and global climate change which induce health and environmental problems [1].

Up to now many researchers are working to develop attractive methods to generate hydrogen as a renewable fuel for the future. Water electrolysis is one the large-scale hydrogen generation not based on fossil fuels, but this method demands large amounts of power and the energy efficiency is very low, the advanced methods such as thermo chemical, photochemical and photo-electrochemical, have their own disadvantages as low efficient, storage and high cost [1,2]. Nowadays, active metals are studied to produce in real-time hydrogen by the hydrolysis with water under mild conditions. Aluminum has been identified as an ideal metal due to its low price, oxidation potential and high abundance, aluminum can also produce hydrogen directly in water and has been evaluated with the following reaction [3]:

$$2Al + 6H_2O \rightarrow 2Al(OH)_3 + 3H_2 \qquad (1)$$

The passive film ($2Al(OH)_3$) formed easily on the aluminum surface is the main disadvantage of hydrogen production via corrosion in water, however in a pH lower than 2 and higher than 11 the passive film is dissolved, and the bare aluminum matrix react releasing large amounts of hydrogen [2,4]. Considerable efforts have been made for minimizing the passivation, the reactions of commercial and aluminum alloys with different bases (e.g. KOH, NaOH and $NaAlO_2$) even in seawater have been studied showing an increase hydrogen production rate, but a diminishes free hydroxide concentration in aqueous solution caused of carbon dioxide from the air [5-7].

Therefore, this work proposes a hydrogen production method to generate clean energy using cans waste as source of aluminum in hydrochloric acid solution and seawater. Besides sodium molybdate is synthetized and evaluated as a promoter to reduce the passivation effect and develop renewable energy through a sustainable and economic corrosion system.

2. Materials and Methods

2.1 Promoter synthesis

Sodium molybdate was synthetized using ammonium heptamolybdate $(NH_4)_6Mo_7O_{24}{\cdot}4H_2O$ and sodium hydroxide NaOH as Na and Mo sources. Ammonium molybdate (AM) was previously treated for 3h at 873K to obtain MoO3. Following the reaction:

$$MoO_3 + 2NaOH + H_2O \rightarrow Na_2MoO_4 + 2H_2O \qquad (2)$$

In the procedure 1.39 g MoO_3 was dissolved in 50 ml of water and 0.77 g NaOH was dissolved in 50 ml distilled water. Then NaOH solution was added drop wise to the MoO_3 solution into a beaker glass under rigorous stirring at 363 K. Afterwards, the above solution was loaded into an ultrasonic bath system 4 h at 45kHz and 353K. The final solution was dried onto a hot plate 1h at 433 K and the Na_2MoO_4 powder was collected.

2.2 Experimental procedure

Aluminum cans wastes (3xxx alloy according to ASM International) were cut off both ends and disposed, the rest cans were sanded and cut into small stripes. Hydrochloric acid solution 1.25 M was prepared using hydrochloric acid (Fermont) and distiller water. The reaction was carried out into a büchner flask. 0.5 g of aluminum and 40 ml of acid solution were used in the all experiments at 333 K with different concentration (0.008-0.044M) of Na_2MoO_4.The hydrogen was collected into an upside down 1L graduated cylinder inside a container full of water to measure the hydrogen production.

3. Results and Discussion

3.1 Characterizations of the promoter

3.1.1 UV-visible

The UV-visible absorption spectra of sodium molybdate is shown in Fig. 1. The absorption spectrum was compared with commercial sodium molybdate showing the same absorptions at 210 and 235nm according with the $[MoO_4]^{2-}$ ion as the only specie in water [9].

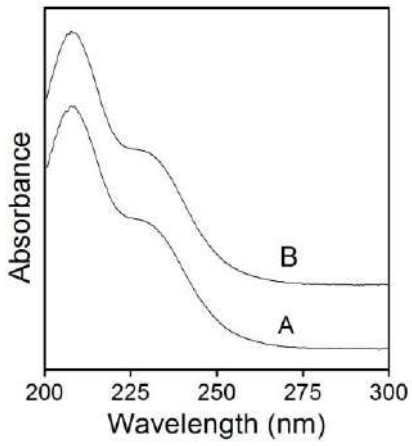

Fig. 1. UV-Visible spectra of sodium molybdate particles. (A) spectra of commercial sodium molybdate particles; (B) spectra od sodium molybdate particles synthesized.

3.1.2 Dynamic light scattering

Dynamic light scattering was carried out in methanol solution to avoid the Na_2MoO_4 dissolution. DLS reported an average hydrodynamic diameter size, showing a size distribution of particles with diameters ranging from 70 nm from 180 nm, obtained from the intensity-weighted distribution curve. Hence, the Na_2MoO_4 particles synthesized had an average diameter size of 150 nm.

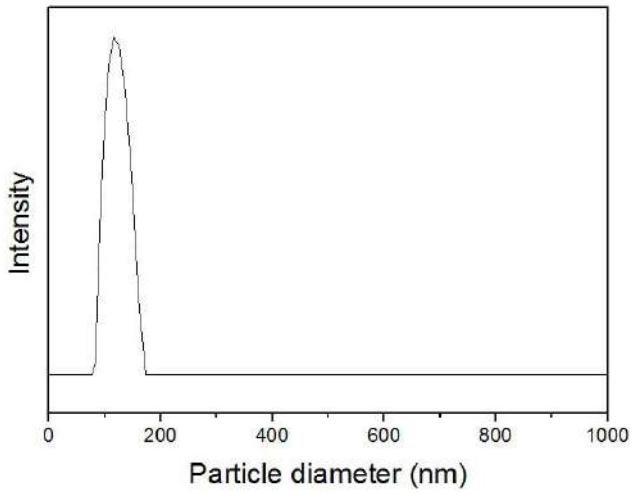

Fig. 2. Hydrodynamic diameter distribution plot

3.2 Hydrogen production

Once the Al added into contact with the acid solution, the hydrogen production was observed after a short time (<19 s), in all experiments the H_2 production rate was quite high at the first minutes of the experiment and decreased as Al was consumed. The hydrogen production was evaluated varying the Na_2MoO_4 concentration under identical conditions. In order to compare the rates and yields obtained, an experiment with 1.25 M HCl and 0.5 g of Al was carried out without promoter (see Fig. 3).

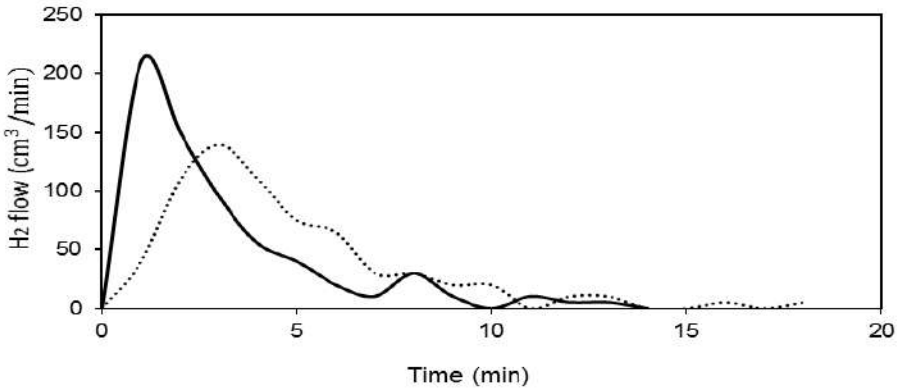

Fig. 3. H_2 production rate obtained from 0.5 g Al in 40 ml of acid solution, ····· flow rate obtained from reaction in absence of promoter, —— flow rate from reaction with 0.012M Na_2MoO_4 as promoter

During the measurement rates of the Na_2MoO_4 concentrations (0.008-0.044M), it was found that initial H_2 production yield using 0.012M Na_2MoO_4 is higher than the rest of the concentration, in the first minute the H_2 production rate of this concentration was 210 cm^3, 5 times higher than the reaction without promoter. Besides the use of seawater increased the production rate at 250 cm^3 (Fig. 4) this behavior results from the chlorine ions that accelerates the dissolution of the passivation layer. The total volume of hydrogen was measured (Fig. 5) showing the same volume production in reaction with 0.012M Na_2MoO_4 and without promoter.

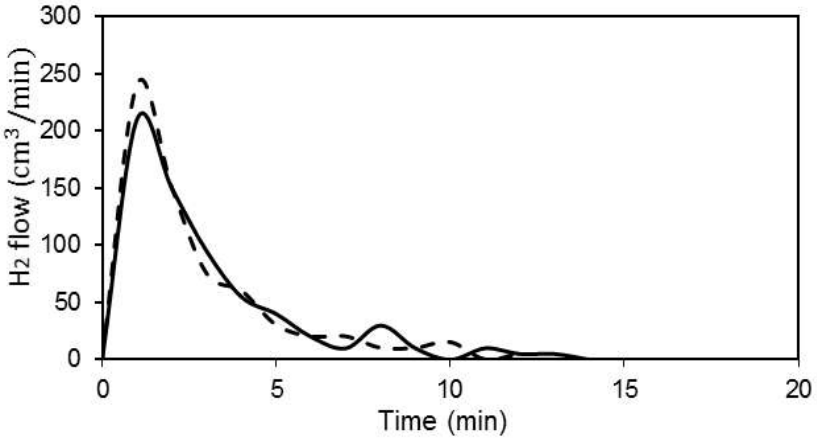

Fig. 4. The effect of seaware in the H_2 production with 0.012M Na_2MoO_4 (——) and (– – ·) with 0.012 Na_2MoO_4 in seawater

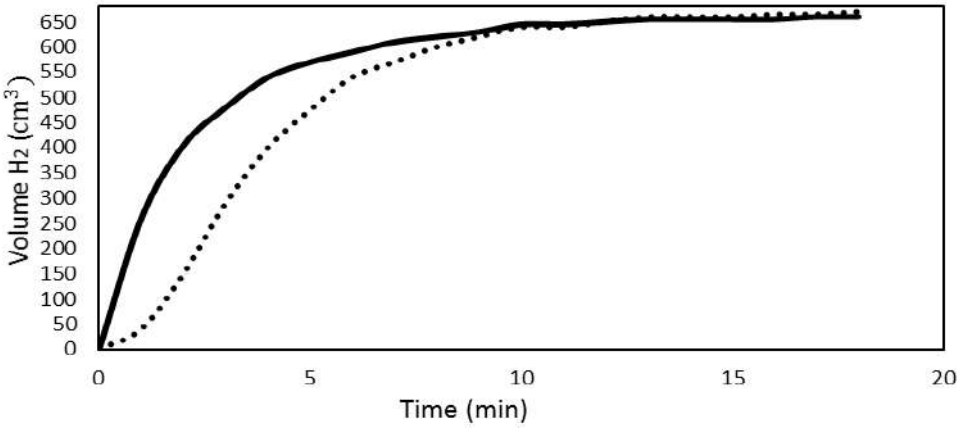

Fig. 5. Hydrogen production as a function of time, 0.012 Na_2MoO_4 (——) and (·····) without promoter

4. Conclusion

The comparison of flow rates reveals that it is possible to enhance H2 production using Na2MoO4 as reaction promoter to obtain better flows. Moreover, the total volume obtained using or not promoter doesn't increase the amount of H_2, but strongly accelerates H_2 production probably by the cathodic centers formation between Mo and Al. Otherwise, the use of seawater can be an advantage due to the increase of the production rate, making this system sustainable and economic.
The average size and size distribution of Na_2MoO_4 must be determined by transmission electron microscopy to have a measurement in dry state.

Acknowledgements

We want to acknowledge the Instituto Tecnológico de Ciudad Madero – Centro de Investigación en Petroquímica by resources and equipment provided for this research.

References

[1] Susana Silva Martínez, Wendy López Benítes, Alberto A. Álvarez Gallegos, P.J. Sebastián. Recycling of aluminum to produce green energy. Solar Energy Material & Solar Cells, 2005; 88, 237–243.
[2] A.A. El-Meligi. Hydrogen production by aluminum corrosion in hydrochloric acid and using inhibitors to control hydrogen evolution. International Journal Hydrogen Energy, 2011; 36, 10600-10607.
[3] Hanbo Zou, Shengzhou Chen, Zhaohui Zhao, Weiming Lin. Hydrogen production by hydrolysis of aluminum. Alloys and Compounds, 2013; 578, 380–384.

[4] Macanás J, Soler L, Candela AM, Muñoz M, Casado J. Hydrogen generation by aluminum corrosion in aqueous alkaline solutions of inorganic promoters: The AlHidrox process. Energy 2011;36:2493-501
[5] Lluís Soler, Angélica María Candela, Jorge Macanás, Maria Muñoz. Hydrogen generation from water and aluminum promoted by sodium stannate. International Journal of Hydrogen Energy, 35, 1038-1048. (2009).
[6] Lluís Soler, Jorge Macanás, Maria Muñoz, Juan Casado. Aluminum and aluminum alloys as sources of hydrogen for fuel cell applications. Journal of Power Sources, 2007; 169;144.149.
[7] Guang-Lu Ma, Hong-Bin Dai, Da-Wei Zhuang, Hai-Jie Xia, Ping Wang. Controlled hydrogen generation by reaction of aluminum/sodium hydroxide/sodium stannate solid mixture with water. International journal of hydrogen energy, 2012; 37, 5811-5816.
[8] Xianghong Li, Hui Fu. (2011). Sodium molybdate as a corrosion inhibitor for aluminium in H3PO4 solution. Corrosion Science, 2011; 53; 9; 2748-2753.
[9] Dr P.C.H. Mitchell. Speciation of molybdenum compounds in water. Report for the International Molybdenum Association.2009

XVIII International Congress
of the Mexican Hydrogen Society

Residual biomass-based hydrogen production: Potential and Possible Uses in Ecuador

F. Posso[1*], J. Siguencia[2], Ricardo A. Narváez C.[3]

[1]Universidad de Santander. Campus Lagos del Cacique. Calle 70 N° 55-210. Bucaramanga. 68003. Colombia
[2]Universidad de Cuenca. Campus Central. Av. 12 de Abril y Av. Loja. 010104. Cuenca. Ecuador
[3]Instituto Nacional de Eficiencia Energética y Energías Renovables (INER), Iñaquito N35-37. Quito. 170507. Ecuador
* Corresponding author: (57)3016696647. e-mail: faustopossorivera@gmail.com

ABSTRACT

In this paper, the residual biomass sources available in Ecuador (livestock, forestry and agricultural waste) are evaluated as prime matter for hydrogen, H_2, production. The analysis is performed out of the official cropping information available per provinces (jurisdictional division of Ecuador). In addition, the parameters considered for the energy assessment are availability, conversion yield and physicochemical properties. Hydrogen production methods to be assayed consider thermochemical, biochemical and electrochemical paths, as well as the projected yield of each technology. Results show that the total hydrogen potential of biomass waste in Ecuador is 1600000 ton H_2/yr and the H_2 production density is 6.71 ton/yr-km^2. This scenario projected the combination of gasification processes and the most abundant types of agricultural waste. In such conditions, H_2 potential of this combination reached shares above 86.2% of the total amount. Besides this issue, it is mentioned that the H_2 potential distribution per province demonstrates that Esmeraldas, Guayas and Los Rios contribute with 69% of the total national potential. Regarding the potential H_2 end-uses, the analysis of the energy sector shows that 46% of the national energy demand in 2016 could be covered by biomass waste-based hydrogen. Moreover, the specific energy demand of transport, industry or residential sector could be fulfilled in 78%, 188% and 278%, correspondingly. Using the residual biomass-based H_2 as one of the inputs of the only hydrotreatment process available in the oil refining facilities in the country is proposed. This proposal is focused on the province of Esmeraldas since this location could produce 33% of the national H_2 potential. Results show that 2.5% of the total amount of H_2 could fulfil the oil refining requirements of this input. This finding demonstrate that residual biomass-based H_2 could become a suitable source of this vector for energy and chemical uses in Ecuador. This work aims to contribute to the assessment of the renewable sources-based H_2 in Ecuador and present this choice as a sustainable alternative in the near future.

Keywords: residual biomass; hydrogen; energy consumption; thermochemical processes;

September 18th to 21st, 2018 in Mexico City, Mexico.

1. Introduction

The residual biomass obtained from agriculture, cattle husbandry and forestry has gained interest as hydrogen source for energy-related and manufacturing-related chemical processes such as oil refining. This is because residual biomass offers advantages related to its availability, geographical distribution, environmental benefits and suitability for H_2 transformation [1]. However, every non-fossil-related H_2 production path requires a primary estimation of the residual biomass availability and the theoretical H_2 amount that could be obtained when a given conversion process is applied to it. In such a context, the H_2 potential estimation gains relevance in order to assess residual biomass as starting point [2-4].

In Ecuador, the H_2 production potential of several renewable energy sources and municipal solid waste (MSW) has been assessed [5, 6]. However, residual biomass obtained from agriculture, cattle husbandry and forestry has not been yet evaluated as primary energy source for a H_2 production potential study. For this reason, the H_2 production based on residual biomass in Ecuador is evaluated in this paper. In addition, the H_2 production distribution was evaluated according to geographical considerations with the purpose of analyzing a non-centralized H_2 production scenario. This analysis is based on the official information of waste biomass generation in each one of the Ecuadorian provinces [7]. Moreover, the methodology reported in [6] is also adopted for this study. In such a context, H_2 production and H_2 production density are calculated per waste biomass type and province. These indicators are reported as the result of the H_2 production assessment stage.

The second stage aims to identify potential end-use applications for the residual biomass hydrogen. For this purpose, the local fulfilment of primary energy demand and the H_2 demand of locally identified stakeholders such as an oil refinery are considered. The estimation of local demand rates expects to establish specific links between local sources and consumers of waste biomass-based hydrogen.

The information presented in this paper expects to complete the assessment of renewable sources-based H_2 production in Ecuador [5, 6]. These results aim to become a contribution to the core information of further analysis related to the identification and subsequent development of local exploitation proposals of H_2.

2. Waste biomass potential in Ecuador

One of the primary information sources that were adopted for this research is the Bioenergy Atlas of Ecuador [7] which presents geolocation-related information for the main crops and cattle nursing facilities along the country. Regarding the residual agriculture biomass types, the main six products were selected in order to determine the amount of waste biomass generated in those activities. In addition, cattle husbandry waste was sorted by source (poultry, beef and pork cattle). The registered forestry waste information included in [7] was gathered from registered

plantations in order to be included in the database. Using this information source ensures the analysis is based in a proper dataset.

Table 1 summarises the waste biomass amounts considered for this research in each one of the provinces of Ecuador. It should be mentioned that information included in Table 1 intentionally skips non-significant amounts of waste biomass in certain provinces and reports its values as null. This consideration is adopted since a minimum biomass amount for feasible exploitation has been already reported [7].

Table 1. Waste biomass availability in Ecuador per location and activity

Province	Agriculture residues (t/yr)	Cattle husbandry residues (t/yr)	Forestry residues (t/yr)	Total residues (t/yr)	Residues location density (t/km² yr)
Azuay	7010	104101	0	111112	13
Bolívar	80682	40633	0	121315	37
Cañar	237177	54692	0	291869	75
Carchi	3639	47724	0	51364	14
Chimborazo	65962	74045	0	80642	15
Cotopaxi	175573	81561	36404	293539	45
El Oro	1542216	36191	0	1578407	264
Esmeraldas	4267607	26425	9638	4303671	289
Guayas	4094557	173215	19949	4287721	250
Imbabura	46806	33598	50123	130528	28
Loja	227017	48353	0	275371	25
Los Ríos	4340758	20786	45146	4406691	705
Manabí	587761	186878	4875	779515	42
MoronaS.	27742	21184	0	48926	2
Napo	25749	8148	0	33898	3
Orellana	402699	7203	0	409902	20
Pastaza	15352	26361	0	41713	1
Pichincha	772813	178886	28931	980630	103
Sta. Elena	6118	8130	0	14249	4
Sto. Domingo	659749	102608	21088	783446	187
Sucumbíos	48314	7004	0	55318	3
Tungurahua	0	130182	0	130182	39
Zamora	27429	21502	0	48932	5
TOTAL	**17603374**	**1439420**	**216157**	**19258952**	**77**

3. Residual biomass-based H_2 production

Residual biomass-based H_2 production methods can be sorted according to their nature (thermochemical, biochemical or electrochemical). Regarding the thermochemical paths, gasification, reforming and combustion can be considered amongst the available alternatives. In the case of biochemical methods, anaerobic digestion can be mentioned as the most

representative choice. In addition, electrolysis is the most relevant method in the case of electrochemical H_2 generation paths. In this study, three H_2 production methods are considered. The first one considers gasification purely. The second case combined combustion and electrolysis. The third one considers anaerobic digestion and biomethane reforming.

3.1 Gasification path

This H_2 production path has been assayed for lignocellulosic biomass mainly, moreover the typical reported conversion yield that can be considered is 0.075 kg H_2/ kg biomass dry-basis [4,8]. This figure was adopted in this study with the purpose of calculating the potential amount of H_2 that can be obtained from forestry and agriculture residues.
3.1 Producción de hidrógeno por gasificación

3.2 Combustion + electrolysis path

In this case, the considered H_2 production path is formed by two stages. The first stage is based on combustion since it is required during the thermal power generation (electricity). The second stage considers H_2 generation through water electrolysis powered by the electricity previously mentioned. For this calculation, the total amount of residual biomass that was identified is considered.

3.2.1 Electricity generation

Electrical power calculation was performed by using a power conversion factor of 19.91% since it considered a steam cycle as energy conversion mechanism [7]. Equation (1) was used for the power estimation.

$$E_{EE} = (M_R\ PCI\ F_C)/\ R_{GP} \quad (1)$$

E_{EE}= Electrical power generated (MWh/yr)
M_R = Residual biomass amount (t)
PCI = Net heating value for residual biomass (kcal/t)
F_C = Conversion factor (kcal/kwh)
R_{GP} = Power conversion factor

The electrical power estimation is presented in Table 2 for each one of the provinces.

Table 2. Electrical power generation per province in Ecuador– Steam cycle path

Province	Electrical power generation (MWh/yr)
Azuay	7010
Bolívar	80682
Cañar	237177

Carchi	3639
Chimborazo	65962
Cotopaxi	175573
El Oro	1542216
Esmeraldas	4267607
Guayas	4094557
Imbabura	46806
Loja	227017
Los Ríos	4340758
Manabí	587761
Morona S.	27742
Napo	25749
Orellana	402699
Pastaza	15352
Pichincha	772813
Sta. Elena	6118
Sto. Domingo	659749
Sucumbíos	48314
Tungurahua	3840
Zamora	27429
TOTAL	17603374

3.2.2 H_2 production

The calculation of the amount of hydrogen that could be obtained through electrochemical path considers an energy conversion factor of 75% of the high heating value (HHV) of H_2. In addition, an availability factor of 95% for a year is included [9]. The calculation model is shown in Equation (2).

$$P_{H2} = E_{EE}\, EFI\, F_D/HHV \quad (2)$$

P_{H2}: H_2 production (kg/yr)
EFI: Energy conversion efficiency (%)
F_D: Availability factor (%)
HHV H_2 = 39.4 kWh/kg

3.3. Anaerobic digestion + biomethane reforming path

The H_2 production path, in this case, considers the following stages: a. Biogas generation through anaerobic digestion - The calculation requires the volatile carbon content of residues and a methane conversion factor (0.2) that is based on the maximum methane emission as reported in [7]. b. Biomethane concentration - This calculation considers that the biomethane yield is the 87% of the initial methane amount that is contained in biogas [10]. c. H_2 production

through biomethane reforming – A conversion factor of 0.30 kg H_2/ kg biomethane is adopted for this calculation [10].

4. Results and discussion

According to the calculation considerations, the total amount of H_2 that was calculated is approximately 1 600 000 t/yr. Results are presented in Fig. 1. These figures show that gasification is the process that contributes the most to the H_2 generation amongst the production paths that were analysed. This finding can be justified due to the proportion of agriculture residues and the suitability of gasification as thermochemical H_2 production path.

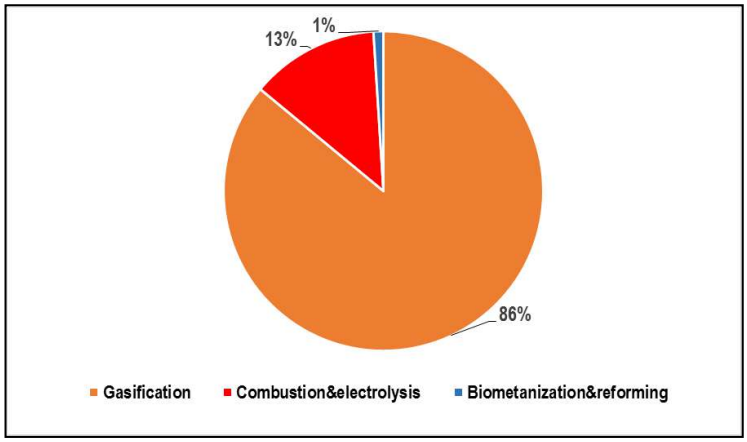

Fig. 1 H_2 production share

The geographical distribution of H_2 generation through gasification and its production density are shown in Fig. 2 and 3. It can be notice that the provinces located in the shore region have the most relevant potential in terms of H_2 production suitability.

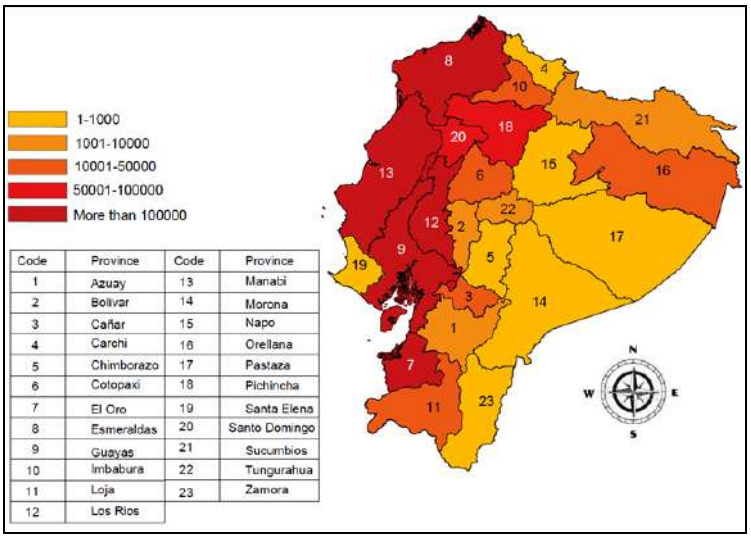

Code	Province	Code	Province
1	Azuay	13	Manabi
2	Bolivar	14	Morona
3	Cañar	15	Napo
4	Carchi	16	Orellana
5	Chimborazo	17	Pastaza
6	Cotopaxi	18	Pichincha
7	El Oro	19	Santa Elena
8	Esmeraldas	20	Santo Domingo
9	Guayas	21	Sucumbios
10	Imbabura	22	Tungurahua
11	Loja	23	Zamora
12	Los Rios		

Fig. 2 H_2 production per province (t/yr) – Gasification

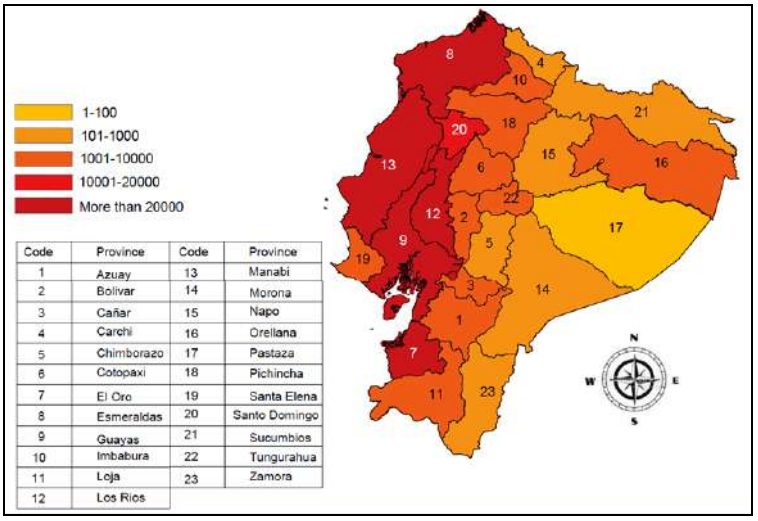

Code	Province	Code	Province
1	Azuay	13	Manabi
2	Bolivar	14	Morona
3	Cañar	15	Napo
4	Carchi	16	Orellana
5	Chimborazo	17	Pastaza
6	Cotopaxi	18	Pichincha
7	El Oro	19	Santa Elena
8	Esmeraldas	20	Santo Domingo
9	Guayas	21	Sucumbios
10	Imbabura	22	Tungurahua
11	Loja	23	Zamora
12	Los Rios		

Fig. 3. H_2 production density per province - Gasification (t/yr km^2)

The H_2 production estimation maps obtained for the remaining paths are not presented in this paper since further evaluation is required prior their presentation. However, it can be mentioned that their behaviour is similar to the one obtained for gasification. Results are shown in Table 3. Even if a feasibility study should select the most promising path for each geographical location, the main purpose is to present an overview of the overall potential of H_2

potential. In addition, results show that three provinces (Esmeraldas, Guayas and Los Rios) could contribute with the 72% of the national potential.

Tabla 3. H_2 production and H_2 production density of residual biomass in Ecuador

Province	H_2 production (t/year)	H_2 production density (t/year km^2)
Azuay	8.03E+02	9,65E-02
Bolívar	7.05E+03	1.79E+00
Cañar	2.16E+04	6.85E+00
Carchi	4.77E+02	1.26E-01
Chimborazo	7.75E+02	1.19E-01
Cotopaxi	1.91E+04	3.13E+00
El Oro	1.38E+05	2.40E+01
Esmeraldas	**3.83E+05**	2.43E+01
Guayas	**3.71E+05**	2.42E+01
Imbabura	9.40E+03	2.05E+00
Loja	2.11E+04	1.91E+00
Los Ríos	**3.91E+05**	5.43E+01
Manabí	5.23E+04	2.92E+00
Morona S.	2.47E+03	1.03E-01
Napo	2.22E+03	1.77E-01
Orellana	3.60E+04	1.66E+00
Pastaza	1.41E+03	4.77E-02
Pichincha	7.26E+04	7.61E+00
Sta. Elena	5.83E+02	1.58E-01
Sto. Domingo	6.16E+04	1.63E+01
Sucumbíos	4.12E+03	2.27E-01
Tungurahua	5.14E+02	1.52E-01
Zamora	2.40E+03	2.27E-01
TOTAL	**1.60E+06**	**6.49E+00**

The produced H_2 can also be used as energy vector or input in manufacturing/oil refining processes. In the first scenario, the H_2 potential availability generated through the gasification path could fulfil 46% of the total energy consumption in 2016 for Ecuador [11]. The differentiated consumption per sector is presented in Table 4. Results show that the energy demand of industrial and residential sector could be covered by residual biomass-derived hydrogen.

Table 4. H_2 potential participation in the energy demand fulfilment (2016)

Energy consumption sector (kboe)	H_2 coverage percentage (%)
Transport, (43538)	78
Industry (17840)	188
Residencial sector (12118)	278

Regarding the oil refining/manufacturing use proposal, the H_2 demand of diesel and heavy naphtha hydrotreating processes (HDS and HDT, correspondingly) of the Esmeraldas Refinery is considered. For both processes, the annual demand is 8341 t/yr, assuming a continuous operation of 8000 hours [12]. This amount would require 2.5% of the total H_2 potential of the province of Esmeraldas, in the gasification scenario. Hence, a more detailed analysis is required in this potential application.

4. Conclusion

The residual biomass in Ecuador shows a significant potential for H_2 production and its use in energy and manufacturing processes. The gasification-based path has been recognized as the one with the largest potential amongst the analysed alternatives. This is because its relative simplicity when comparing each one of the stages in the proposed paths, and also due to the waste valorisation implied in this proposal. This analysis aims to complete the renewable H_2 production assessment in Ecuador and also to open new insights for further studies related to its exploitation. In a wider sense, it is expected that such a type of studies contributes to the H_2 incorporation in the local economy and to the energy availability solutions in the near future

Acknowledgements

To Universidad de Santander for the financial and institutional support required for participating in this conference.

References

[1] Balat H, Kirtay E. Hydrogen from biomass - Present scenario and future prospects. Int. J. Hydrogen Energy 2010; 35: 7416-7426.
[2] Ahmad I, Athar S, Khan R. Green hydrogen production potential for developing a hydrogen economy in Pakistan. Int. J. Hydrogen Energy 2018; 43: 6011-6039.
[3] Levin D, Zhu H, Beland M, Cicek N, Holbein B. Potential for hydrogen and methane production from biomass residues in Canada. Bioresource Technology 2007; 98: 654–660.
[4] Sigal A, Leiva E, Rodríguez C. Assessment of the potential for hydrogen production from renewable resources in Argentina. Int. J. Hydrogen Energy 2014; 39:8204-8214.

[5] Posso F, Espinoza J, Sánchez J, Siguencia, J. Preliminary estimation of electrolytic hydrogen production potential from renewable energies in Ecuador. Int. J. Hydrogen Energy 2016; 41: 2326–2344
[6] Posso F, Narváez R, Siguencia J, Sánchez J. Use of Municipal Solid Waste (MSW)-derived Hydrogen in Ecuador: Potential applications for urban transportation". Journal Waste and Biomass Valorization. Springer. https://doi.org/10.1007/s12649-017-0161-1.
[7] Atlas Bioenergético del Ecuador. Instituto de Preinversión. Quito, 2014.
[8] Milbrandt A, Mann M. Hydrogen resource assessment. Technical Report. 2009. NREL/TP-560e42773.
[9] Posso F, Espinoza J, Sánchez J, Zalamea J. Hydrogen from hydropower in Ecuador: use and impacts in the transport sector. Int. J. Hydrogen Energy 2015; 40: 15432–15447
[10] Saur G, Milbrandt A. Renewable Hydrogen Potential from Biogas in the United States. Technical Report NREL/TP-5400-60283.
[11] Balance Energético Nacional 2016. Ministerio Coordinador de los Sectores Estratégicos. Ecuador
[12] Narváez J. "RV: caudal consumo de hidrógeno". Personal communication received by R. Narváez C., 8th January 2018.

XVIII International Congress
of the Mexican Hydrogen Society

Production of Hydrogen by Ethanol Steam Reforming using Ni-Co-hydrotalcite-like compounds as catalysts stabilized with tungsten

José L. Contreras[1]*, Beatriz Zeifert[2], José Salmones[2], José Antonio Colin[1], Gustavo A. Fuentes[3], Tamara Vázquez[2], Leticia Nuño[1]

[1] *Universidad Autónoma Metropolitana-Azcapotzalco, México, D.F.,02200, México*
[2] *Instituto Politécnico Nacional, ESIQIE, Mexico,D.F. U.P. López Mateos, Zacatenco, México*
[3] *Universidad Autónoma Metropolitana-Iztapalapa. México,D.F, 09340, México*
jlcl@correo.azc.uam.mx,

ABSTRACT

Ni-Co/Hydrotalcite-WOx catalysts showed high activity in the ethanol steam reforming (ESR) producing H_2, CH_4, CO_2, and CO. The presence of Ni and Co in the bimetallic catalysts changed the products selectivity observed respect to the selectivity of the monometallic catalysts. The bimetallic catalysts of Ni-Co showed higher selectivity to Hydrogen than the selectivity of the monometallic Ni catalyst. The surface area in the Ni and Co catalysts was inversely proportional to the metals concentration. Metal oxides of Ni and Co in the bimetallic catalysts interacted with the hydrotalcite structure, causing a partial blockage of pores, resulting in a decrease of pore volume. The particles on the bimetallic catalysts showed a semi-cubic shape observed instead of laminar shape typical of hydrotalcites. By X-ray diffraction (XRD), hydrotalcite, $MgNiO_2$, periclase (MgO), κ-Al_2O_3 and bunsenite (NiO) were identified. The bimetallic catalysts of Ni-Co-hydrotalcite-WO_X showed high selectivity to H_2 and total conversion of ethanol.

Keywords: **Ni-Co-hydrotalcite-WOx, Hydrogen, ethanol, steam-reforming**

1. Introduction

Ethanol has several advantages as a combustible, and can be stored easier than other fuels, without significant risk of handling and can be obtained in large quantities from biomass [1-2]. In order to produce H_2 by ethanol steam reforming (ESR), the catalysts must show high thermal stability, because the relative high operation temperatures at which reforming reactions take place, as well as high selectivity to H_2 production. Several studies have shown that supported

noble metals such as: Rh, Ir, Pt, Pd and Ru [3,4], or inexpensive metals such as Co [5-7], Ni [8], or bimetallic materials [9-10] are good options to catalyze the ESR reaction.

Several supports, such as: MgO, ZnO, SiO_2, Al_2O_3, La_2O_3 or CeO_2, among others, are the most commonly used to support the active metals [11].

We have chosen the so-called hydrotalcite-like compounds as supports, also known as layered double hydroxides (LDHs) [12]. LDHs are a family of lamellar materials derived from brucite layers, which are currently of academic and industrial interest [12-14]. These compounds contain Mg^{2+} and Al^{3+} metal cations. In this study, catalysts bimetallic of Ni-Co and hydrotalcite-like compounds were prepared by the coprecipitation method using four Ni/Co atomic ratios which were stabilized by the addition of WOx and then evaluated in the ESR reaction.

2. Materials and Methods

2.1.- Preparation of Catalysts.

The hydrotalcite support (HTA) was made by coprecipitation using two salt solutions as precursors. First, in a stirred reactor a salt solution of $Mg(NO_3)_2$ and $Al_2(NO_2)_3$ (J.T. Baker) with a molar ratio of 1.6:1 was prepared and a second solution of Na_2CO_3 (5%) and NaOH (pH = 10) (Carlo Erba) was also prepared. These two solutions were added simultaneously, drop by drop, to a third stirred reactor using water as solvent (60 drops/min) at 60°C maintaining an atomic ratio of Mg^{2+}/Al^{3+} of 1.65. In this step a solution of $(NH_4)_{12}W_{12}O_{41}\bullet 5H_2O$, (Aldrich) was added in order to get 0.5%wtW in the final catalyst.

A Ni monometallic catalyst with 10wt% (C-Ni) was prepared using $Ni(NO_3)_2$ (Aldrich) during the coprecipitation of the hydrotalcite. Also a Co monometallic catalysts with 18wt% (C-Co) was prepared using $Co(NO_3)_2$ (Aldrich). The bimetallic Ni/Co catalysts were prepared with the following atomic ratios: 2.23 (C-NiCo1), 0.836(C-NiCo2), 0.371(C-NiCo3) and 0.139 (C-NiCo4). The final suspension in the reactor was maintained at 70°C and pH of 11 with stirring for 18 h. The solid precipitated was washed, dried at 110°C during 18 h and calcined at 450°C for 5 h.

2.2.- Catalyst Characterization

The X-ray diffraction (XRD) of the samples calcined at 450°C was obtained in a Rigaku diffractometer (Phillips X´pert) fitted with a Cu anode tube (30kV, 20mA) using CuKα radiation. XRD patterns were made using angles of 2θ ~ 10 to 70°, with a step size of 0.02° and a counting time of 2 s. The identification of the different crystalline phases was performed by comparison with the corresponding JCDPS diffraction data cards.

Measurements of N_2 adsorption-desorption isotherms at -196°C (77K) were carried out in an ASAP-2000 (Micromeritics) equipment. The samples were previously outgassed at 300°C during 3 h under vacuum of $1x10^{-3}$ Torr. The surface area values were obtained by application of the BET equation. The micropore volume of the samples was calculated by means of the t-plot method. The calculation of the pore size was carried out by applying the BJH model to desorption branch of the isotherm, assuming cylindrical pore geometry.

The thermal gravimetric analysis (TGA) and differential thermal analysis (DSC) were made simultaneously using a SDTQ-600 equipment of TA Intruments, using α-alumina as reference. The experiments were made using 2-5 mg of sample and air flow of 30 cm^3/min with a heating rate of 5ºC/min from 25 to 800 ^oC. Both dried and deactivated catalysts were evaluated by TGA/DSC without pretreatment. The loss of weight and the derivative of the weight change with respect to temperature (%/°C) were measured in function of temperature.

Temperature programmed reduction (TPR) profiles of the calcined samples were obtained under H_2 flow (10 % H_2 in Ar) by using a commercial thermodesorption apparatus multipulse RIG model (from ISRI) equipped with a thermal conductivity detector (TCD). Samples of 30 mg and a gas flow rate of 25 cm^3/min were used in the experiments. The TPR profiles were registered by heating 30 mg of sample from 25 to 800°C at a rate of 10°C/min, and the rate of H_2 consumption was monitored by a TCD. The amount of H_2 consumed was obtained by the deconvolution and integration of the TPR peaks using the Peak Fit program. The calibration was done by measuring the change in weight due to a reduction in H_2 of 20 mg of CuO using an electrobalance Cahn-RG. The TPR signal of CuO was made and correlated with the stoichiometric H_2 consumption.

H_2 chemisorption experiments were carried out in a vacuum line by a volumetric method. The catalysts were reduced at 500°C for 2 h in H_2 atmosphere and evacuated at 500°C in the vacuum line. The sample weight was about 0.5 g and the H_2 adsorption was performed at room temperature. Gas pressure at adsorption equilibrium was about 550 torr. The dead volume of the apparatus was 16.942 cm^3, for the estimation of Co and Ni metal dispersion.

2.3.- Catalytic Activity

The catalytic reaction was made in a differential stainless steel fixed bed reactor charged with 0.5 g of catalyst having an average particle diameter of 0.147 mm (US mesh 100). In order to prevent the presence of diffusional effects during the evaluation of the catalysts, the best flow conditions and catalyst particle size were determined. The feed of the reactants consisted of ethanol (Aldrich), water and N_2 (Infra-Air Products) in gas phase and a space velocity WHSV of 4.8 h^{-1} was used. The mixture of H_2O and ethanol has a molar ratio of 4/1 in presence of a N_2 stream using two metal saturators. In order to activate the catalysts, the temperature of the catalyst was controlled at 450°C(±1°C) in flow of H_2 for 30 min to clean and activate the catalyst surface. After this step, a flow N_2 (30 cm^3/min) was introduced to remove the remaining gas inside the reactor.

After the activation step, four reaction temperatures were studied: 450, 500, 550 and 600°C. Each catalyst was held at the reaction temperature for 30 min in order to make three chromatographic analyses. Each analysis of the reactants and all the reaction products were carried out online by gas chromatography. Inside an automated injection valve, the sample was divided into two portions which were then analyzed in order to obtain a complete quantification of the reaction products. H_2, CO, CO_2 and CH_4 were identified using a thermal conductivity detector (TCD) with a column of silica gel 12 grade 60/80 mesh (18´x 1/8”) in a chromatograph Gow-Mac Model 550. Ethanol, acetaldehyde and ethylene were analyzed in a Varian (model 3800

chromatograph using a capillary column (Varian, VF-1ms, 15 m. 0.25mm, 0.25 µm) and a flame ionization detector (FID). Both, conversion and selectivity for each catalyst and reaction temperature were determined.

3.- Results and discussion

3.1.- Structure by XRD

The presence of patterns of hydrotalcite (HT) or layered double hydroxides (LDHs) were observed in all catalysts dried at 120° C. The reflections located in 2θ = 11.3, 23, 35, 38.8, 46, 60, 62 and 66° corresponded with well-defined peaks and pointed to a highly crystalline structure, typical of hydrotalcite like materials ((HT, JCPDS file 70-2151). This structure crystallizes in the hexagonal system- R3m space group. These diffraction peaks correspond to the sharp and symmetric peaks for the (003), (006), (009), (110) and (113) planes and broad an asymmetric peaks for the (102),(105) and (108) planes, all typical of clay mineral having a layered structure..

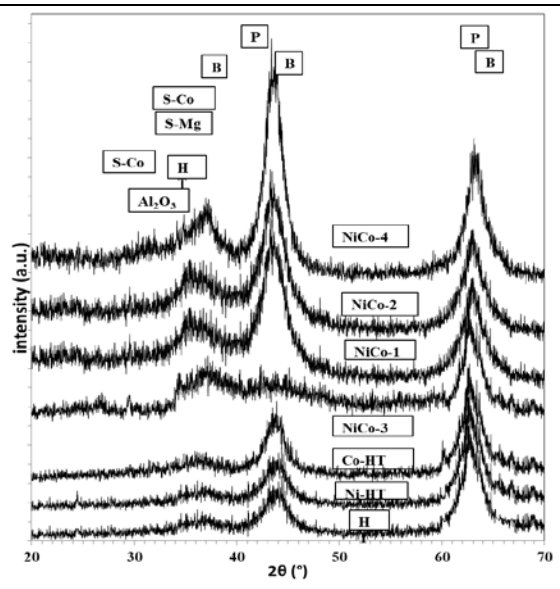

Fig. 1. XRD of calcined Ni-Co-Hydrotalcite catalysts

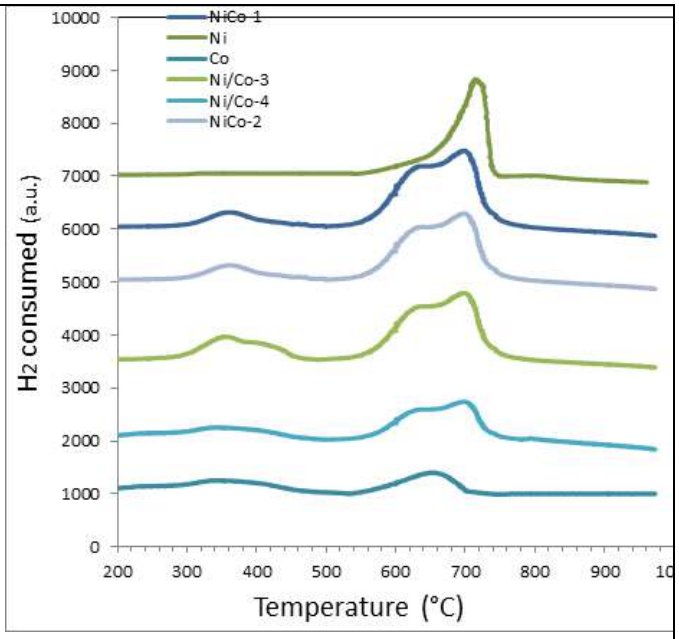

Fig. 2. TPR of the Ni-Co catalysts

The hydrotalcite-like oxides (ex-LDH) were analyzed after calcination at 450°C of the corresponding LDH-precursors. In Figure 1, XRD patterns of the ex-LDH oxides are shown, after calcination the layered LDH network is destroyed and several amorphous components were

formed such as spinels of Co (Co_3O_4) (S), MgO periclase (P), spinel of Mg ($MgAl_2O_4$)(S), $MgNiO_2$ (S), NiO Bunsenite (B) and κ-Al_2O_3.

It has also been reported in the literature, the formation of spinels of Co_3O_4 and MgO, [19]. On the other hand, it was observed that increasing the concentration of Co (sample NiCo-4), the intensity of reflection located at 2θ = 42° attributed to MgO (periclase) increased. This result suggests that the presence of Co atoms contribute to formation of amorphous MgO.

When the samples of LDH were calcined at 450°C, the intensity of the hydrotalcite reflections decreased and some disappeared, in Figure 1 three wide bands were located at 36.5, 44 and 62.5° which corresponded with the formation of spinels of Co (Co_3O_4) (S), [JCPDS file 80-1545] and MgO periclase (P), spinel of Mg ($MgAl_2O_4$)(S), NiO Bunsenite (B) and κ-Al_2O_3. The width of these reflections suggests (according to the Scherrer equation) the occurrence of nanometer size crystals and low ordered metal oxide phases.

3.2 Textural analysis

The samples showed the IV type hysteresis according to the IUPAC classification and this hysteresis cycle corresponds to a type B which is related with the structure of parallel plates typical of the hydrotalcites.

The isotherms exhibit slight adsorption at low relative pressure due to the presence of micropores. These isotherms show a sharp increase at high relative pressure originated from interparticle porosity, which seems to indicate that these samples consist mainly of non-porous nanoparticles within the nanometer range.

The high meso, macro and external specific surface area values show the non-microporous nanoparticle nature of the ex-LDH materials. These samples showed mesoporous and macroporous (Table 1) and exhibited high specific surface area values after calcination. All calcined samples having Mg as modifying cation show high surface area. This observation was made previously in another study in which the area of catalysts containing Mg showed the highest area compared with catalysts containing Zn and Cu [17].

Table 1. Characterization of Ni-Co-hydrotalcite-WOx catalysts prepared by coprecipitation.

Catalyst	Ni wt%	Co wt%	A_{BET} [m^2/g]	Dp [Å]	XRD[a] Compounds	SEM Particles	EDS Elements
HTA	0	0	226	578	H,P,A	20-55nm	Mg,Al
Ni-10	10	0	152	108	H,M,P,N,	20-70	Mg,Al,Ni
Co-18	0	18	220	64	H,P,A	30-66	Mg,Al,Co
Ni/Co-1	10	4.5	200	84	H,M,P,N,	20-45	Mg,Al,Co,Ni
Ni/Co-2	7.5	9	160	88	H,M,P,N,	20-65	Mg,Al,Co,Ni
Ni/Co-3	5	13.5	117	107	H,M,P,N,	-----	----
Ni/Co-4	2.5	18	142	84	H,M,P,N,	-----	----

a H=hydrotalcite, M=MgNiO2,P=Periclase(MgO),A=κ-Al2O3,N=Bunsenite(NiO).

3.3.- Thermogravimetry (TGA/DSC)

The thermogravimetric analysis of the catalysts prepared from NiCo-hydrotalcite is similar in all samples. In the dried sample NiCo-1 there are three areas of weight change. The first loss (peak-1 and 2) are narrow bands located at 25-100 °C present in all the samples and they can be attributed to the loss of non-structural water physisorbed on the external surface of the LDH crystallites. The second and third peaks (peaks 2 and 3) are located between 100 to 210°C. These peaks can be attributed to the losses of water differently bonded to the structure such as interlayer water co-intercaled with carbonate or chemisorbed water, among others. The peaks 4 and 5 located between 275 – 450°C are attributed to dehydroxylation and decarbonation of the LDH materials. In accordance with R. Guil López [17-19] this processes do not allow to differentiate between dehydroxylation and decarbonation.

3.4.- Temperature programmed reduction TPR

The catalyst for Ni (Ni-HT) showed a single peak located at 720° C (Figure 2) as it is reported in the literature [17-19]. This reduction peak does not correspond with the reduction of NiO bulk peak, which occurs at 380°C, however it has been shown that it corresponds to the reduction of species not strongly linked with oxides of Mg and Al matrix. It means that Ni^{2+} ions could be incorporated within the matrix of oxides containing Mg^{2+} - Al^{3+} [21] It has been reported that the reduction temperature is depending on the concentration of Ni, as Fang has demonstrated et to the. [18-19].

When the calcination temperature was 450°C, the reduction peak of Ni-HT catalyst was close to 700°C [R. Guy], while if the calcination rises between 500 and 800°C, the temperature reduction peak appears above of 827°C. In the latter case, the presence of $MgNiO_2$ and $NiAl_2O_4$ has been attributed despite the differences in the maximum temperature. The $MgNiO_2$ is very difficult to reduce (due its thermodynamically stability) and it could be measured a reduction only of 40% up to 850°C, however with the increase of the content of Al, the degree of reduction increased. These authors mentioned that these two compounds $MgNiO_2$ and $NiAl_2O_4$ require reduction temperatures above 850°C.

In the case of the reduction of the catalyst for Co-HT they were found two peaks (Figure 2). The first begins between 300°C and ends at 480°C and the second begins at 560°C and ends at 700°C. The first peak has been attributed to the reduction of the Co_3O_4 towards the formation of CoO [17] while the second peak has been attributed to CoO reduction towards the formation of Co metal Chica, A Sayas S.

In the case of Ni-Co catalysts, two peaks similar to the peaks of the catalyst for Co-HT were observed, however the second peak is the result of the fusion of two peaks, one due to the reduction of oxides of Ni^{2+} and the other to the reduction of the CoO. The studies of TPR of Guil López et al. [17] also showed the presence of two peaks for a calcined catalyst for Co-Hydrotalcite (687°C and 400°C) and a peak for the catalyst calcined of Ni-Hydrotalcite (702°C).

3.5.- H_2 Chemisorption

The calculation of the metal dispersion of the Ni catalyst took into account that all Ni^{2+} was reduced to Ni metal as observed in the TPR studies. By chemisorption of H_2, it was observed low dispersions of Ni (Figure 3). This could be explained by the presence of strong metal-support interactions between Ni metal and the matrix of Mg and Al oxides, such as it has been reported for the case of $NiTiO_2$, $NiAl_2O_3$, and to a lesser extent in very well-dispersed $NiSiO_2$ [20-21]. This phenomenon is apparently more pronounced in Ni than in Co, since total Co (expressed as oxides of Co^{3+} and Co^{2+}) the 18% was only reduced to metal Co, and the dispersion was 3.33%, being the highest of all catalyst dispersions. Other authors have also reported low levels of dispersion in Ni-hydrotalcite catalysts, J. Chen et al. [22]. reported a dispersing of 5.9% on a catalyst with atomic relations Ni/Mg/Al:9/66/25. In the case of bimetallic catalysts of Ni and Co, when the Ni concentration increases, (Figure 3), from 2.5% to 10%, it is observed a decrease in the Ni dispersion (with exception of the NiCo-1 catalyst). The increase in the dispersion of the bimetallic catalysts was determined by the increase in the concentration of oxides of Co (Figure 2), mainly the CoO.

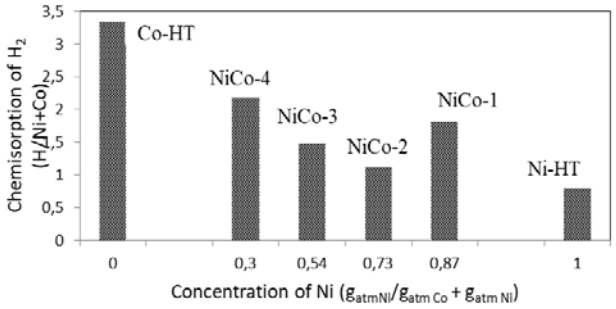

Figure 3. H_2 chemisorption of the Ni,Co and Ni-Co hydrotalcite catalysts.

3.6.- Catalytic Activity

The catalysts were evaluated at temperatures of 450, 500, 550 and 600°C, with the analyses performed in each temperature. The presence of H_2, CO_2, CH_4, CO was confirmed and ethanol was not detected in the reaction products because a total conversion was reached (Fig. 4 to 7).

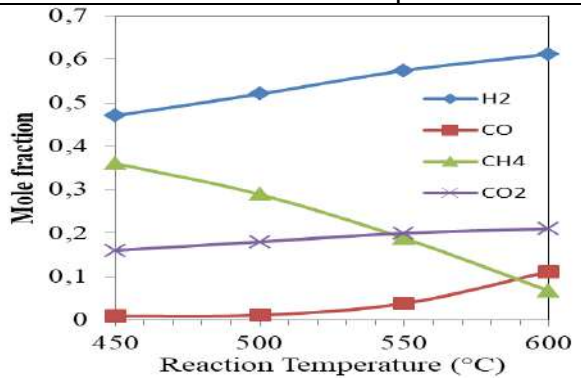

Fig. 4 Mole fraction of ESR for the Ni

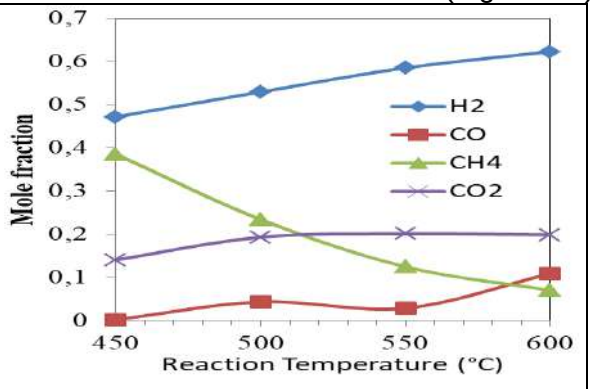

Fig. 5 Mole fraction of ESR for the Co

catalyst.	catalyst.
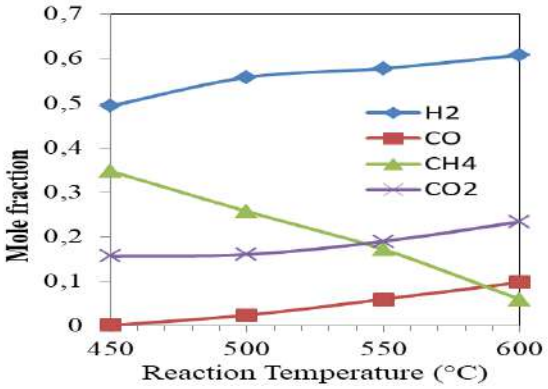	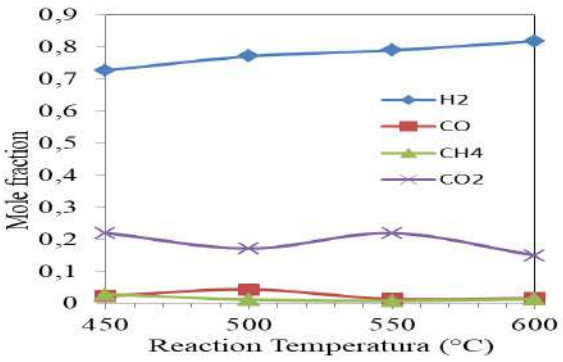
Figure 6 Mole fraction of ESR for the NiCo-1 catalyst.	Figure 7 Mole fraction of ESR for the NiCo-2 catalyst.

4. Conclusion

The bimetallic catalysts of Ni-Co-hydrotalcite-WO_X showed high selectivity to H_2 and total conversion of ethanol between 450 to 600°C. The hydrotalcite and the monometallic Ni catalyst produced CO, but in the bimetallic Ni-Co catalysts this product was absent. The best catalyst to produce H_2 was Ni/Co-1 having 10wt% Ni and 4.5wtCo. The monometallic Co catalyst did not produce CO and this fact could suggests that Co inhibits the production of CO on the Ni-Co bimetallic systems.

Acknowledgements

The authors are grateful for the financial support of this research to the Universidad Autónoma Metropolitana-Azcapotzalco.

References

[1] R.D. Cortright, R.R. Davda, J.A. Dumesic, Nature 418, 964(2002).
[2] J. Llorca,N.,Homs,J.Sales,J. L. G. Fierro and P. Ramírez de la Piscina, J. Catal. 222, 470-480(2004).
[3] J. L.Contreras, J. Salmones, L. A. García, A. Ponce, B. Zeifert and G.A. Fuentes, J. of New Materials for Electrochemical Systems 11, 109-117(2008).
[4] M. N.Barroso, M. F.Gómez, L.A.Arrúa,M. C.Abello, Appl. Catal. A:General 304, 116-123(2006).
[5] J. Llorca, N. Homs, J. Sales, and P. Ramírez de la Piscina, J. Catal. 209, 306-317(2002).
[6] K. Sing, D. Everett, R. Haul, L. Moscou, R. Pierotti, J. Rouquerol, and T. Siemieniewska, Pure Appl. Chem. 57, 603 (1985).
[7] L. D. Gelb, K. E. Gubbins, R. Radhakrishnan, and M. Sliwinska-Bartkowiak, Reports on Progress in Physics 62, 1573 (1999).

[8] S. Lowell, J. E. Shields, M. A. Thomas, and M. Thommes, Characterization of Porous Solid and Powders: Surface Area, Pore Size and Density, Kluwer Academic Publishers, (2004).
[9] M. del Arco, D. Carriazo, S. Gutiérrez, C. Martín and V. Rives, Inorg. Chem. 43, 375-384(2004).
[10] F. Basile, G. Fornasari, M. Gazzano, A. Vaccari, Appl. Clay. Sci. 16,185(2000).
[11]T.Shishido, M.Sukenobu, H.Morioka, R.Furukawa, H.lShirahase, K.Takehira, Catal. Lett.73, 21 (2001).
[12] C. Resini, T. Montenari, L. Barattini, G. Ramis, G. Busca, S. Presto, P. Riani, R. Marazza, M. Sisani, F. Marmottini, U. Costantino, Appl. Catal.A: General, 355, 83-93(2009).
[13] A. Bartecki and Dembicka, D. J. of Inorg. and Nuclear Chem.V.29,I.12, 2907-2916(1967).
[14] A. Iannibello, L. Villa, and S. Marengo, Gazzetta Chimica Italiana,109, 521(1979).
[15] R.C Reuel, C.H. Bartholomew, J. Catal. 85(1984)63.

[16] M.K. Niemela, L Backman, A.O.I. Krause, T.Vaara, Appl. Catal.A: Gen. 156(1997)319.

[17] R. Guil, R. Lopez, R.M. Navarro, M to Peña, JLG Fierro, International Journal of Hydrogen Energy, 36 (2011) 1512-1523].

[18] [M. Montañez, S.Moreno, International Journal of Hydrogen Energy, 39 (2014) 8225-8237

[19] W. Fang, Appl. Catal. B: Envirnomental 152-153 (2014) 370-382.

[20] C.H. Bartholomew , R.B. Pannell, J.L.Butler, Support and crystallite size effects in CO and hydrogenation on nickel. J. of Catal. [Vol. 65, Issue 2, 335-347 (1980)].

[21] F. Basile, L. Basini, M. Daoré, G. Fornasari, G. Guarinoni, D. Matteuzzi, J. of Catalysis 173, 2, (1998), 247-256.

[22] J.Chen, M.Tamura, Y.Nakagawa, K.Okumura, K. Tomishige, Appl. Catal. B: Environmental, 179 (2015) 412-421].

XVIII International Congress
of the Mexican Hydrogen Society

OBD2 monitoring and control system for hydrogen generator used as complementary fuel on internal combustion vehicles

G. Macias-Bobadilla[1*], D. Becerra-Ruiz[1], A. Amaro-Reyes,[2] J.N. Gracida-Rodriguez[2,]

[1]Facultad de Ingeniería, Universidad Autónoma de Querétaro, Cerro de las Campanas S/N, Col. Las Campanas, Querétaro, Qro. México. C.P. 76010
Facultad de Ingeniería, Universidad Autónoma de Querétaro, Cerro de las Campanas S/N, Col. Las Campanas, Querétaro, Qro. México. C.P. 76010
* Corresponding author: (+52)4421921200 ext. 6016 and gonzalo.macias@gmail.com

ABSTRACT

OBD2 systems on modern vehicles allow the possibility to access a large amount information related to speed, load, fuel level injection and air to internal combustion system of vehicles, this system on modern vehicles also allows the possibility to supervise gas exhaust system and advise to driver if something is wrong or if the vehicle is ready to be verified for an authorized control pollution center. At this respect, this work presents a human-machine interphase made whit Raspberry Pi 3 and Bluetooth connection OBD2 by using ELM327 standard connector compatible with all modern cars to supervise driving condition to activate and deactivate a hydrogen generator used as complementary fuel on internal combustion vehicles, the interphase includes algorithms to determine the ideal moment to activate the hydrogen generator to optimize fuel efficiency. Results include pictures from vehicle using the developed human-machine interphase working on Cayenne my Devices cloud services.

Keywords: OBD2 human-machine interphase; Bluetooth Arduino communication; exhaust system gas emission.

1. Introduction

The On Board Diagnostics System

The On Boar Diagnostics (OBD) system is a standard implemented in several modern vehicles to read and monitoring different parameter from the behavior of the systems installed into the vehicle, like motor, gears, cooler system, air intake, exhaust system, voltage generator and battery system, emission level and other electronic devices also can be monitored.

Since 1988 in California, USA, the California Air Resources Board (CARB) stablish that all modern vehicles sealed in USA must implement an OBD system to determine pollution levels from exhaust system of the vehicle and fuel / oxygen ratio used on real time by the motor. The most common indicator that implement OBD it was the Malfunction Indicator Lamp (MIL) also known as Service Soon Lamp or Check Engine. See Figure 01 for more details.

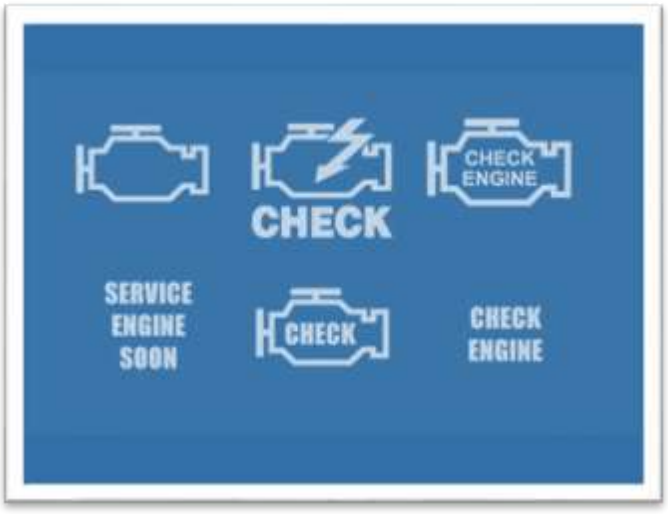

Figure 01.- Different form of MIL lamp stablished by CARB

OBD it was just the beginning, but few years' late standards stablished by CARB was increased in 1996 and OBD was not enough to accomplish the parameter of monitoring required by CARB, modern parameters require to monitoring chemical changes into the mechanical elements from the vehicle like the function of the catalytic converter, to do this OBD-II standard was created to include monitoring parameters from oxygen sensors at the input and output from the catalytic converter. This way not only mixes from fuel / oxygen could be monitored, also degradation from catalytic converter and also from oxygen sensors could be monitored.

Another advantage that can be useful from monitoring parameters by the OBD-II systems is check Revolution Per Minute (RPM) from main engine and the shift gear position, this could be useful to determine the level of effort or stress in the main engine and this is useful to determine in which moment is necessary to implement a kind of additive or increase the octane level from the fuel, in this case Hydrogen gas (HHO) is a good alternative to increase torque in the main engine depending of the speed and stress level or load level.

Different kind of modern tools and devices has been developed to monitoring and to communicate with the OBD-II in the vehicle, some of them uses Bluetooth and WIFI technology, allowing the possibility to communicate with the ECU (Electronic Computer Unit) to obtain all the main parameters from vehicle even using mobile device like Smartphones and Tablets, additionally if these devices have connection to internet this could be useful to send and receive information to and from the Cloud Services, an example of this function is the software focus on Internet of Things (IoT) called Cayenne.

Internet of Things using Cayenne to control Electrolyzers in a vehicle

Cayenne is a cloud service that allow send and receive parameters and instructions from a device connected to internet and to operate programing boards like Arduino and Raspberry Pi to control electrical and electronics devices added to an experimental vehicle (not OEM elements), like to turn on and turn off electrolyzers to produce Hydrogen Gas (HHO) to increase torque in the engine depending of monitored parameters like RPM and position of the Shift Gear.

To implement and control devices like Arduino and Raspberry Pi is mandatory to download and implement Cayenne agent in this programing boards, after that the Cayenne agent will allow the possibility to access to an Internet account from Cayenne web site to send and receive parameter and activate inputs and outputs from this programing boards using a Computer, Smartphone or Tablet connected to internet.

Figure 02 show the block diagram from control using IoT Cayenne services and a device connected to internet.

Figure 02.- Block diagram of IoT Cayenne interphase

2. Materials and Methods

For the experiments and element developed for this work, a Mitsubishi Galant 2011 LS 3.0L was ben used, this vehicle includes a OBD-II and it have a V6 engine with double catalytic converter and 4 oxygen sensors to determine pollution and mixes of fuel and oxygen, each catalytic converted is connected to the exhaust system from each 3 spark plug from engine due this motor is configured in “V” position.

OBD-II connector is disposed in this vehicle behind the direction wheel and down of the vehicle board, to connect with the ECU from this vehicle an ELM327 OBD-II Bluetooth interphase was ben used and connected to Raspberry Pi 3 running Raspbian Operative System. Raspberry Pi 3 used for this experiments also runs Cayenne agent to connect to Cloud Services of and active account of Cayenne website to send and receive data an instruction to activate and deactivate an electrolyzer to produce HHO gas and be introduced to vehicle engine via Intake System.

Figure 03 show a picture of Mitsubishi Galant LS – 2011 V6 3.0L used in this experiment, Figure 04 show vehicle board and Raspberry Pi 3 placed temporary at top of vehicle board, energized by cigarette power connector.

Figure 03.- Mitsubishi Galant LS – 2011 V6 3.0L

Figure 04.- Raspberry Pi 3 running Cayenne agent to activate relay for electrolyzer (left), Temperature Sensor for Electrolyzer (right). (Not final connection, just demonstrative picture)

Electrolyzer ON / OFF instruction can be configured and activated by a Smartphone connected to internet and running Cayenne Mobile App, Figure 05.- Show iOS interphase running into an iPhone SE, and with the option for manual activation and deactivation of HHO electrolyzer system.

Figure 05.- Developed Cayenne App on iOS (iPhone SE), show real time Temperature from Electrolyzer and HHO control button to activate manually the Electrolyzer.

3. Results and Discussion

The algorithm used for this experiment only determine the activation and deactivation by measuring RPM from engine, also the interphase have the possibility to measure other parameters like electrolyzer temperature to avoid overhead risk or serious electrolyzer cell damages.

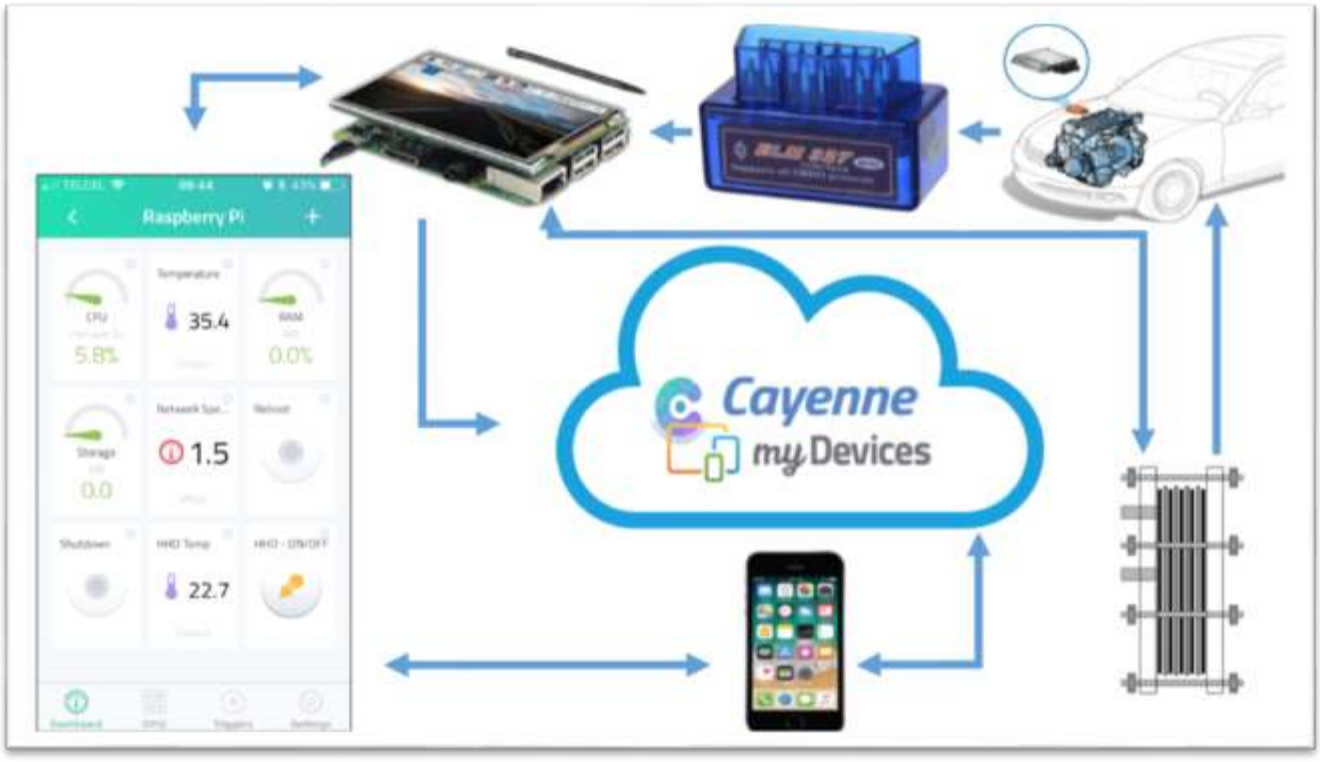

Figure 6.- Final App developed on Cayenne Cloud Services communication interphase controlled by iOS (iPhone SE) and Raspberry Pi 3 to activate and deactivate electrolyzer

4. Conclusion

Electrolyzer control system for activation and deactivation can be improved by analyzing another's parameters obtained from ECU in real time, like load sensor, shift gear system, engine motor temperature an electrolyzer temperature.

The system developed for this experiment only includes a ON/OFF control system for activation and deactivation by using a mechanical relay connected to electrolyzer. In this way a PI (Proportional and Integral), PD (Proportional Derivative) or full PID (Proportional Integral and Derivative) control system for activation and deactivation of electrolyzer can be implemented and controlling the energy supplied by a PWM (Pulse Wide Modulation) to avoid have unnecessary power losses by applying full power with the ON/OFF control system used in this experiment.

Another important improvement that can be implemented is the monitoring and control of temperature from electrolyzer, due low temperatures reduces HHO production and high temperatures degrade electrolyte used on the electrolyzer.

References

[1] Al-Hamamrea, Z., y J. Yaminb. 2013. The effect of hydrogen addition on premixed laminar cetylene–hydrogen–air and ethanol–hydrogen–air flames. International Journal of Hydrogen Energy 38:7499-7509.
[2] Al-Hasan, M. 2003. Effect of ethanol–unleaded gasoline blends on engine performance and xhaust emission. Energy Conversion and Management 44:1547- 1561.
[3] De Almeida, L. Q., L. C. M. Sales, y J. R. Sodré. 2015. Fuel consumption and emissions from a vehicle operating with ethanol, gasoline and hydrogen produced on-board. International ournal of Hydrogen Energy 40:6988-6994.
[4] Almselati, A. S. I., R. A. O. K. Rahmat, y O. Jaafar. 2011. An overview of urban transport in Malaysia. Social Sciences 6:24-33.
Amrouche, F., P. Erickson, J. Park, y S. Varnhagen. 2014. An experimental investigation of hydrogen-enriched gasoline in a Wankel rotary engine. International Journal of Hydrogen Energy 39:8525-8534.
[5] Apostolescu, N., y R. Chiriac. 1996. A study of combustion of hydrogen-enriched gasoline in a spark ignition engine.
[6] Changwei, J., y W. Shuofeng. 2009. Effect of hydrogen addition on the idle performance of a spark ignited gasoline engine at stoichiometric condition. International Journal of Hydrogen Energy 34:3546-3556.
[7] D'Andrea, T., P. Henshaw, y D. S. K. Ting. 2004. The addition of hydrogen to a gasoline-fuelled SI engine. Int J Hydrogen Energy 29:1541-1552.
[8] Dupont, V. 2007. Steam reforming of sunflower oil for hydrogen gas production. Helia 30:103-132. Eckermann, E. 2001. World History Of The Automobile. En: 371. Ilustrated. p. 1-72.
[9] Elfasakhany, A. 2013. Investigation on performance and emissions characteristics of an internal combustion engine fuelled with petroleum gasoline and a hybrid 81 methanol-gasoline fuel. Int J Eng Technol 13:24-43.
[10] Elfasakhany, A. 2014. The effects of ethanol-gasoline blends on performance and exhaust emission characteristics of spark ignition engines. Int J Automotive Eng 4:608-620.

XVIII International Congress
of the Mexican Hydrogen Society

Modelling and simulation of an alkaline water electrolyser

Valeria Juárez Casildo[1], Rosa de Guadalupe González Huerta[1*]

[1]ESIQIE-IPN, Lab. Electroquímica y Corrosión, UPALM, CP 07738, Ciudad de México.
* rosgonzalez_h@yahoo.com.mx
55 57296000 ext 54246

ABSTRACT

Very promises perspectives exist for the use of hydrogen as a fuel, it is known that hydrogen production with renewables is suitable and environmentally friendly. Today, alkaline water electrolysis has become in a mature technology due to de many studies made in whole world in order to improve efficiency and performance.
Many studies made in this topic has focused in develop modelling and simulation due to the advantages which it has in comparison with experimental analysis. In fact the currently technology computing condition allows solve complex models which describes this kind of multiphysics system, for instance, it is possible save money because of the prototypes are not built. Developing modelling and simulation is easy to understand the alkaline water electrolysis behaviour, determinate the dimensions of process equipment and it could be possible to do a redesign of it.
This paper is a mini-review of the modelling and simulation works in order to analyses the state of the art in this topic and identify the most often phenomena modelling and which are the commercial software most often use for simulate this electrochemical system.
This information will be a tool for a future modelling and simulation study in order to understand the relation between gas separator and alkaline electrolyser. According with this review, the commercial software more used is MATLAB-Simulink and it is thought this is because develops their studies considering the electrochemical system as an electrical circuit.

Keywords (Maximum 4 words): modelling, simulator, alkaline water electrolysis system.

1. Introduction

The energy condition of Mexico is not favourable, according on the statistics shown by the Secretariat of Energy, the demand for fuels is approximately double what is produced internally [1,2], therefore, our energy dependence to oil products is danger to energy security. This increase in consumption is due to the growing population and an irrational use of energy resources which damage the environment.

Within the development of alternative energies, hydrogen has seen a great opportunity as an energy vector that works as a complement to renewable energy sources. Based on this, "hydrogen technologies" have been developed that focus on finding different ways to produce, store and use it in a clean way, helping the environment.

Due to the cost of the electrolysis process, nowadays it is giving greater application to the hydrogen produced by alkaline electrolyser (AE). Depending on their manufacture, the AE can produce gases separately or generate a mixture of hydrogen and oxygen, because of the membrane absence, the latter case is called the Oxihydrogen Reactor (ROH2). AEs are a technology that can be adapted to different needs, given that they are modular systems and do not require the use of noble metals in their electrodes [3-6].

The principle of operation is as follows: a direct current (DC) is applied from the power supply, the electrons flow from the negative output to the cathode. A reduction reaction is carried out on the surface of the cathode where the water molecule receives the electrons breaking one of the O-H bonds, generating molecular hydrogen, as well as hydroxide ions (OH^-) that are incorporated into the alkaline solution. The hydroxide (OH-) anions dissolved in the solution diffuse to the anode surface where them adsorbs in the active sites and transfer their electron to the anode generating molecular oxygen and water, finally the electrons return to the positive terminal of the power supply. This operation mechanism is shown in [6,8] **Fig. 1**.

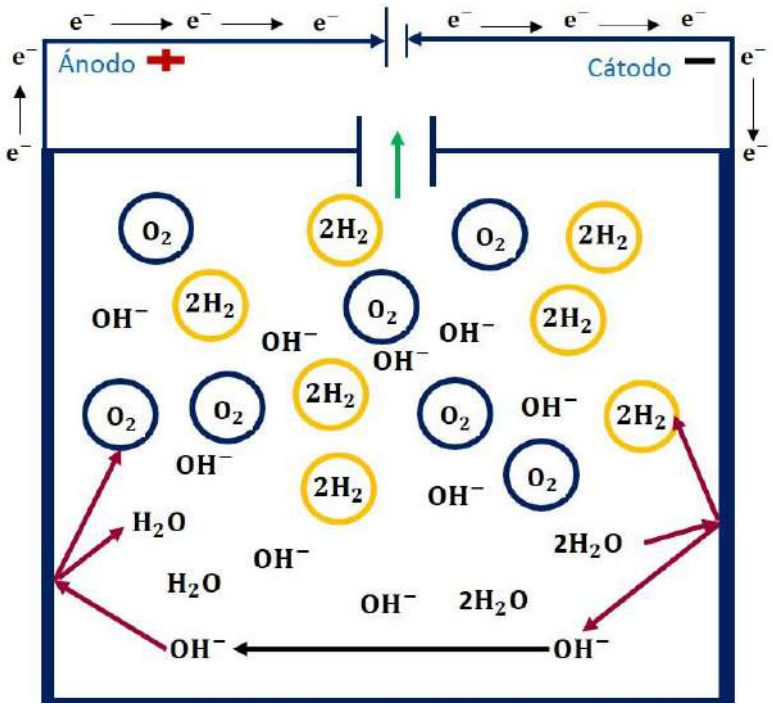

Fig1. Operation diagram of an alkaline water electrolizer without membrane.

The reactions that carried out in this process are as follow:

$$4H_2O + 4e^- \rightarrow 2H_2 + 4OH^- \quad E^0 = -0.83\ V \quad (1)$$

$$4OH^- \rightarrow O_2 + 2H_2O + 4e^- \quad E^0 = -0.40\ V \quad (2)$$

$$2H_2O_{(l)} \rightarrow H_{2(g)} + O_{2(g)} \quad E^0 = -1.23\ V \quad (3)$$

Those electrochemical reactors have some intrinsic particularities which is generated a low efficiency [5,6,8], for instance:

a) An electrical resistance due to the interconnection of the external circuit.
b) The resistance due to the gas bubbles produced on the surface of the electrodes.
c) The resistance due to ion transport in the electrolyte.
d) The electrode resistance is due to the over potentials required to overcome the activation energies of the reactions.

In these systems are involved: diffusion species, mass transfer, gradients thermal and fluidic problems which are linked with the resistance problems. Any strategy in order to improve the energy efficiency of water electrolysis and therefore, the performance of the system must involve the understanding of these physical phenomena in order to minimize intrinsic resistances.

In order to continue with the development of this technology many studies it has been made for decades in whole world, some of them are experimental evaluations but others are a theoretical analysis. The current computing technology condition allows evaluate this kind of processes without experiments and little time. Modelling and simulation of energetic systems is an excellent way for study rigorously all phenomena with a lot of precision.

2. Modelling in alkaline water electrolysis.

Currently, simulation in engineering is one of the most essential and powerful tools that engineers can use when designing and creating processes or products, which must be under the framework of energy efficiency. It is necessary to simulate the conditions under which the new design will be operated, this implies the consideration of the impact of the greater number of physical factors that occur simultaneously within the analysis system, such as structural dynamics, heat transfer, fluid flow, the non-linear behaviour of materials, the electromagnetic phenomenon, the transport of chemical species, etc.

2.1. Some statistics

The work in modelling of electrochemical systems emerges as a complement to experimental work due to the need to understand the multiphysical phenomena that occur in this

type of systems. The development of models for the description of electrolysis systems took boom since 1990, having an increase in publications from 2000-2016 as shown in **Fig 2**. [16].

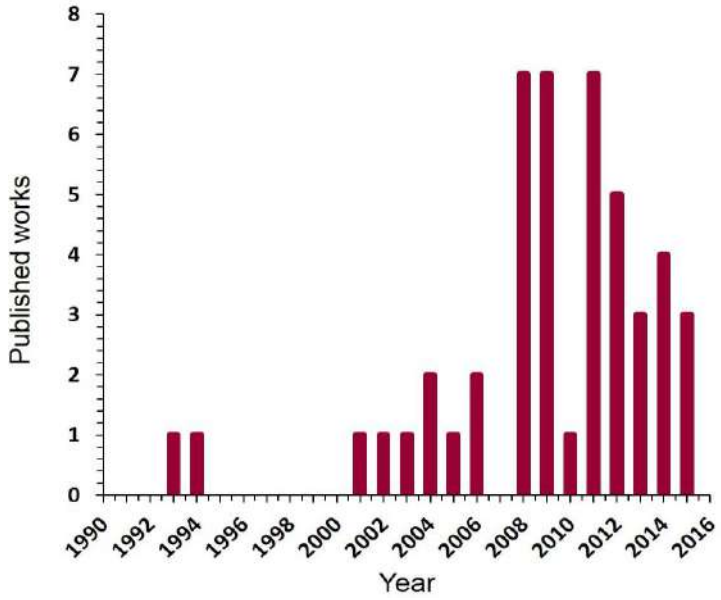

Fig2. Modelling statistics in alkaline electrolysis [16]

2.2. Modelling levels and physical domains.

As previously was mentioned, alkaline water electrolysis is a complex systems due to different phenomena which are involved in operation. This complexity induces some problems of conception and operation at different levels such as:

a) **Stack:** It is necessary to ensure a uniform current and temperature distribution, a good gas evacuation, good reactant diffusion to the electrodes active sites. It is important to have a good distribution of the interfaces (electrolyte electrode assemblies), deal with biphasic problems (bubbles), and ensure a good electrical response and a good flow distribution between the cells [16].
b) **System:** It is crucial ensure a good regulation of all reactor variables (reactor temperature, electrolysis voltage and liquid separator levels). This is possible with the presence of auxiliary elements. An electrolysis stack does not work without external equipment [3,12].

In order to classify the multiphysics behaviour in an alkaline electrolysis system, it is distinguished 4 physical domains (**Fig. 3**.), this classification is important for modelling aspects for stablish the phenomena boundaries. This is as follows:

a) **Electrical domain**: It studies the cell electrical response and evaluates the performance of the power electronic; also monitoring the electrical consumption of the auxiliary equipment such as pumps and converters according to the operating conditions [16, 18].

b) **Thermal Domain**: Modelling in this domain is responsible for describing the thermal behaviour of an electrolysis stack [8, 16].

c) **Electrochemical domain**: It studies the reactions and charge transfer between the electrodes and the electrolyte, evaluates the behaviour of the electrolyte (concentration and conductivity) [16, 20, 21, 22].

d) **Fluidic Domain**: Represents the hydraulic dynamic state that includes the mass flow and the behaviour of the pressures in the electrolysis system, particularly in the cell channels [16, 23].

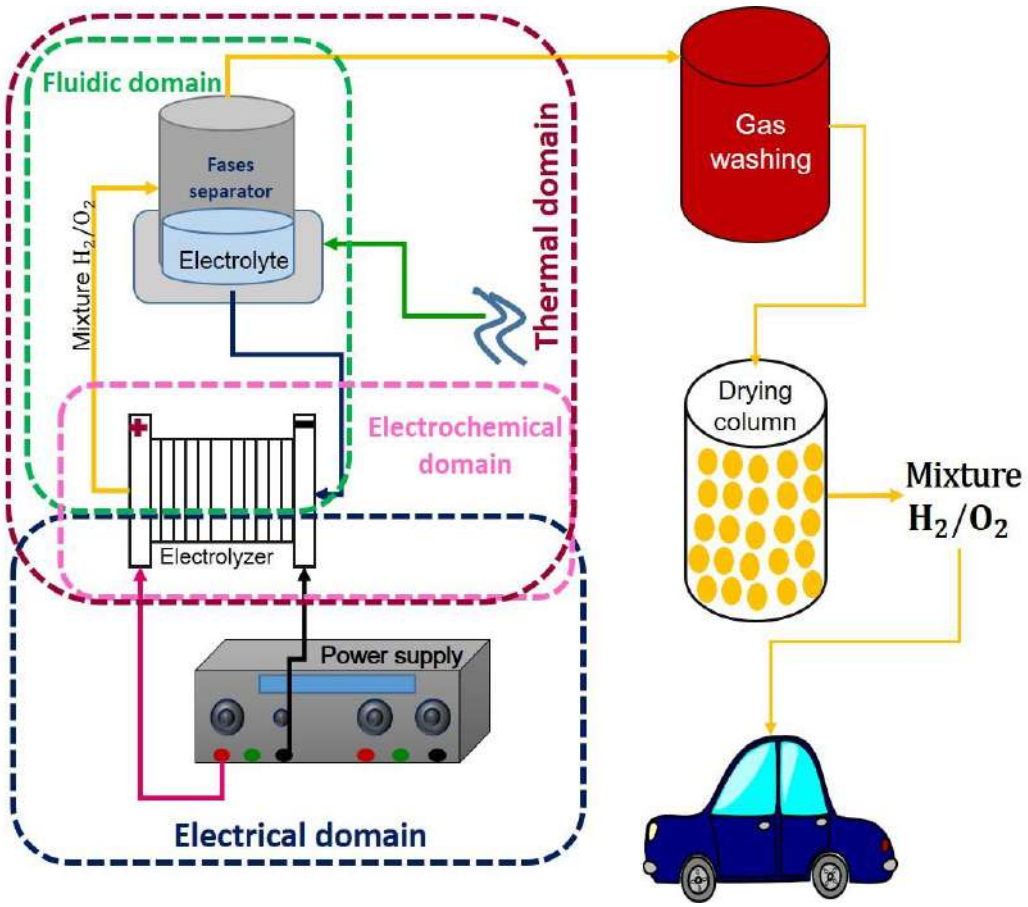

Fig3. Physical domains of an alkaline electrolysis system [3,16].

2.3. The most important models developed.

The alkaline electrolyser modelling has focused mainly on the prediction of the power demand or hydrogen production capacity. Ulleberg [6] developed a mathematical model that combines thermodynamics, heat transfer theory and empirical electrochemical relationships for the calculation of total cell voltage. The model is often used by other authors, for instance, Amores et al. [10] who adapted the Ulleberg model and extended it taking into account the concentration of electrolytes and the distance of the electrode. His model was able to predict the dynamic voltage characteristics of an electrolyser together with a solar energy supply with a maximum error of 3%.

Ursúa et.al. [18], analysed the stationary and transient behaviour of a commercial alkaline electrolyser with a production of 1 N m3 / h through the development of a complete and integrated dynamic-static electric model that can be applied to any commercial water electrolyser. The model is based on the effects and thermodynamic, activation, double layer and ohmic phenomena that take place in a real process of alkaline electrolysis. They validated the model in three different operating environments: in static operation through the characteristic curves of I vs V; to the dynamic operation by means of a sinusoidal current of several amplitudes and frequencies superimposed on a direct current; and by using two power supplies with different conversion topologies, the first free of harmonics and the other with a high content of harmonics. With this model, they were able to demonstrate with great precision the experimental electrical behaviour of an alkaline electrolyser.

Haug, et. al. [5], developed a model for predicting the purity of the gas in an a AE. For the estimation of the compositions of the gases, they considered the operating conditions, such as the current density, the electrolyte flow rate, the concentration and the temperature, as well as the possibilities of process management. The development of the model was based on a classic process engineering approach and represents the electrolysis cell through continuously coupled agitated tank reactors. In addition, the phenomena of mass transport between phases are considered by applying the Reynolds and Sherwood correlations. With this model, they found that the purity of the gas in the electrolysis of alkaline water is mainly affected by the mixing of the anodic and cathodic electrolyte cycles, which transport the dissolved electrolysis products to the compartments of the half of the opposite cell.

1. Simulation in alkaline electrolysis systems

As a result of this mini-review, it has been found that there are a different commercial simulators which are useful for alkaline water electrolysis simulation. The most often used are: MATLAB-Simulink, COMSOL Multiphysics, ANSYS, and TRNSYS. On the other hand there are many authors who developed their own simulators by solving a mathematical algorithm. In order to develop this paper as a mini-review, thirty references has been analysed in 7 of them built a mathematical model and simulated it using commercial software, 20 investigators only validated their models with experimental data.

It has been created a table (**Table 1**) where is register the work cited, the phenomena modelling, physical domain, software used and nationality. It is important to mention that in the cited literature only one paper about modelling and simulation of alkaline water electrolysis without membrane (ROH2).

Table1. Software used in simulation of alkaline water electrolysis

Author and country	Physical Domain	Study made	Modelling level	Software	Reference number
Q. Ulberg and O. Morner (USA)	Electrical	(PV) system-AWE Parametric studies for different climates. Power supply.	System	TRNSYS	19
P.M. Diéguez (Spain)	Thermal	Thermal performance	Stack	ANSYS	8
S. Tijani et al (Malaysia)	Electrochemical	I-V behaviour Energy consumption	Stack	MATLAB	20
A. Ursúa et. al. (Spain)	Electrochemical	I-V behaviour Activation and Ohmic effects	Stack	MATLAB-Simulink	18
Z. Abdin et. al. (Australia)	Electrochemical	I-V behaviour Electrolyser performance	Stack	Simulink	21
C. Henaeo (Canada)	Electrochemical	Electrical properties Thermodynamics	Stack	MATLAB-Simulink	22
E. Amores et.al. (Spain)	Fluidic Electrochemical Electrical	Behaviour cell powered by a PV system	System	COMSOL Multiphysics	23

In this paper it is seen that the most useful simulation software is MATLAB-Simulink, the authors, who used this simulator worked on the electrochemical domain at level stack. Might is because this software is specialised for electrical control, robotic, motor and power control, as well electrical signals; that enable to do a greater analytical capacity and with an adequate environment.

On the other hand ANSYS and COMSOL MULTYPHYSICS, both software allows simulation several phenomena of different domains, it is interesting the way in which Amores et al. used Comsol for simulate in tree different domains with only one simulation. Today the investigators have many powerful tools to develop their model simulations, the relevance of this is the criteria for selecting software, according with the table, choosing is linked with the investigation approach as well with the main of it
Finally, TRNSYS is a flexible graphically based software environment used to simulate the behaviour of transient systems. While the vast majority of simulations are focused on assessing the performance of thermal and electrical energy systems.

2. Conclusion

Care must be taken to choose the software in which you will simulate the mathematical model. It is necessary to understand the approach and objectives of modelling; for this, it is necessary to identify in detail the phenomenon to be described as well as the domain to which it belongs.

The software presented in this work are of scientific analysis rather than of the chemical industry, they focus on the detailed analysis of the physical phenomena that occur in the systems, it means, in transport phenomena; in chemical engineering, from the process point of view it is more appropriate to use simulators such as ASPEN and Pro II, where the analysis focuses on material and energy balances of the whole process without the need to solve equations as complex as when you need to analyse a problem that is too specific.

It is important to mention that the most appropriate software if the modeller has programming skills, the electrical domain is Simulink with MATLAB to have access to the multiple calculation libraries.

In general, especially for alkaline water electrolysis systems where several physical and chemical phenomena are involved, using COMSOL or ANSYS is the most appropriate because of the multiphysics tools; It is possible to do a complete characterization at stack or system level all domains.

Acknowledgements

Thanks to the financial support granted: IPN multidisciplinary project SIP-1820 (2018-2019**)**

References

[1] Alexandri, R. et al, (2017) .Prospectiva de las Energías Renovables 2017-2031. Recuperado, abril 2018, sener.gob.mx.
[2]Alexandri, R. et al, (2017) .Prospectiva de Petróleo Crudo y Petrolíferos 2017-2031. Recuperado, abril 2018, sener.gob.mx.
[3] Alexandri, R. et al, (2017). Prospectiva del Sector Electrico 2017-2031. Recuperado, abril 2018, sener.gob.mx.
[4] Horcasitas M., Sandoval J., Grunstein B., Terán L., González R., Design and Manufacture of ICE Test Module to Reduce Gasoline Consumption Using Oxyhydrogen Gas from an Alkaline Electrolyzer, Energy & Fuel (2016), vol. 30, pp. 6640
[5] Haug, P. et al. Process modeling of an alkaline water electrolysis. Journal of Hydrogen energy (2017), vol. 42, pp.15689-15707.

[6] Zeng K, Dongke Z, Recent progress in alkaline water electrolysis for hydrogen production and applications, J. Progress in Energy and Combustion Science (2010), vol. 36, pp. 307-326.
[7] Hammoudi M. New Multi-physics approach for modelling and desing of alkaline electrolyzer (2012), vol. 37, pp. 13895-13913.
[8] Smolinka T. et al. Fundamentals of PEM Water Electrolysis. *PEM electrolysis for hidrogen production principles and aplications,* New York, USA: Taylor and Francis group (2016), pp. 11-32.
[9] Diéguez P. Thermal performance of an alkaline water electrolyzer: Experimental study anda mathematical modelling. (2008), vol. 33, pp. 7338-7354.
[10] Amores E. Influence of operation parameters in the modelling of of alkaline water electrolyzers for hydrogen production (2014), vol.39, pp. 13063-13078.
[11] Flores D, Diseño y manufactura de un prototipo de electrolizador alacalino de hasta 20 sL/min de gas oxihidrógeno para ser empleado en embarcaciones marinas. Tesis de maestría ESIME Azcapotzalco-IPN. Ciudad de México (2017).
[12] González R., López E. y Velázquez B., Hidrógeno: *Introducción a la energía limpia, Ed. UACM,* Ciudad de Méxio: Biblioteca del estudiante (2009), pp 69-86.
[13] González R., Solorza O. y Valenzuela A., *Tecnologías del hidrógeno y celdas de combustible de fuentes renovables,* Ciudad de México: Editorial académica española (2012), pp. 51-68 .
[14] Grunstein B., Ruiz E., Meneses G., González R., Design, construction and implementation of electronic control module for the enrichment of hydrogen in combustion engines, XV International Congress of the MHS, CINVESTAV (2015).
[15] Kjartansdóttir, C. K., & Møller, P., Development of Hydrogen Electrodes for Alkaline Water Electrolysis. PhD thesis, DTU Mechanical Engineering (2014), pp. 100.
[16]Oliver P. et al. Low temperature electrolysis system: A Review (2017), vol. 78, pp. 280-300.
[17] Zeng K, Dongke Z, Recent progress in alkaline water electrolysis for hydrogen production and applications, J. Progress in Energy and Combustion Science (2010), vol. 36, pp. 307-326.
[18] Úrsua A. y Sanchis P. Static-dynamic modelliing of the electrical behavior of a commercial advanced alkaline water electrolyser, vol. 37, pp. 18598-18514.
[19] Q. Ulleberg and O Morner. TRNSYS simulation models for solar-hydrogen systems, Solar energy (1997), vol. 99, pp 271-279.
[20] S. Tijani. Mathematical modelling and simulation analysis of advanced alkaline electrolyser system for hydrogen production. Procedia Technology (2014), vol. 15, pp 798-806.
[21] Z. Abdin et. al. Modelling and simulation of an alkaline water electrolyser cell. Energy (2017), vol. 138, pp 316-331.
[22] C. Heaneo et. al. Simulation tool based on a physics model and an electrical analogy for an alkaline electrolyser. Journal of Power Sources (2014), vol. 250, pp 58-67.
[23] E. Amores et. al. Study of an Alkaline electrolyser powered by renewable energy. Comsol conference 2011.

XVIII International Congress
of the Mexican Hydrogen Society

Photocatalytic hydrogen production from glycerol reforming using highly active CuO@TiO_2 core-shell catalysts

S.P. Ramírez[1], J.A. Wang[1,*], M.A. Valenzuela[1], A. Dalai[2]

[1] Laboratorio de Catálisis y Materiales, ESIQIE-Instituto Politécnico Nacional, 07738 Ciudad de México, Mexico.
[2] Department of Chemical Engineering, University of Saskatchewan, Saskatoon S7N 5A9, Canada.
* Corresponding author: Tel: 52 55 57296000 ext. 55276; email: jwang@ipn.mx

ABSTRACT

Hydrogen production from the photocatalytic reforming of glycerol was performed on several core-shell nanostructured catalysts under simulated solar light. The catalysts were prepared by modified sol-gel method and characterized by powder X-ray diffraction (XRD), UV-Vis diffuse reflectance spectroscopy (UV–Vis DRS), scanning electron microscopy (SEM), transmission electron microscopy (TEM), and nitrogen physisorption isotherms. The band gap energy was 3.25 eV for pure TiO_2, 3.19 eV for NiO@TiO_2, and 3.11 eV for CuO@TiO_2. The catalysts containing TiO_2 as a shell showed much higher activity compared with those formulated with bared Cu or Ni oxides. The highest rate of hydrogen production obtained with the CuO@TiO_2 catalyst was as high as 153.8 $\mu mol \cdot g^{-1} \cdot h^{-1}$, which was 29.0, 24.8, 11.2 and 3.2 times greater than that obtained on CuO@NiO, NiO@CuO, TiO_2 P25, and NiO@TiO_2 catalyst, respectively. For the high active CuO@TiO_2 catalyst, after activation with solar light, the conduction band electrons in TiO_2 can transfer to CuO through the heterojuctiion structure of the core-shell interfaces which led to CuO gradually reducing to Cu_2O and Cu, favoring the reduction of proton to hydrogen.

Keywords: Core-shell structure; Photocatalysis; Hydrogen production; Glycerol

1. Introduction

In the photocatalytic reactions, synthesis method of the photocatalyst takes key role. In recent years, the preparation and exploration of core–shell nanoparticles have been demonstrated to possess improved physical and chemical properties for electronics, magnetism, optics, catalysis, and other applications. Numerous studies have shown that the nanoparticles with core–shell unique structure improve their catalytic activity and selectivity. In photocatalytic H_2 evolution, the catalysts with core-shell structure play an important role in the charge separation. For example,

Zhang et al. [1] reported that the coupling of CdS and TiO_2 nanorods has a beneficial role in improving charge separation and in the reduction of electron–hole recombination rate, due to the quick transferring of the excited electrons from CdS nanoparticles to TiO_2 nanorods and the extension of absorption spectrum into the visible region by TiO_2@CdS core–shell nanorods.

TiO_2 has been extensively studied as a promising candidate to support the future hydrogen economy due to its high photocatalytic activity, long-term photostability, strong oxidizing power, abundant availability, and environmentally friendly nature [2, 3]. However, it can be activated only under UV light irradiation (380 nm) due to its relatively big band gap energy (titania anatase 3.2 eV, rutile 3.0 eV). To extend its light absorption into the visible light spectrum and prevent the high recombination rate of photogenerated electron–hole pairs, a core-shell nanostructure can be used as an excellent option. Several semiconductors have been used as sensitizers in core-shell structures because they are capable to transfer electrons to large band gap semiconductors of TiO_2, for instance, Fe_3O_4@TiO_2 [4], Cu_2O@TiO_2 [5], WO_3@TiO_2 [6], CdS@TiO_2 [7], Fe_3O_4@ZnO@TiO_2 [8], ZnS@TiO_2 [9], and so on, showing good results for different applications.

Among low-cost transition metal oxide catalysts, copper and nickel oxide are two of the most efficient oxidation catalysts to substitute precious metals. The oxidation states of copper may vary between CuO, Cu_2O and Cu; while, nickel vary among Ni_2O_3, NiO and Ni, depending of temperature and hydrogen partial pressure. The oxygen defects in the crystalline structure and adsorbed oxygen species in these oxides are thought to be the reasons for their high activity and selectivity [10]. It is widely recognized that p-type CuO facilitates charge separation and acts as a water reduction site [11]; and it has also been regarded as a good active component for the reduction of water under sacrificial condition [12], because it can inhibit the recombination between photogenerated electrons and holes and can decrease the band gap energy. It can exist in several different forms on TiO_2, depending on the CuO content and catalyst pretreatment conditions. CuO alone is inactive for H_2 production under UV or visible light irradiation since the conduction band of CuO is more positive than that of the H_2O/H_2 redox potential. So this semiconductor has been coupled with TiO_2. On the other hand, NiO_x doping onto TiO_2 surface is effective for p-type (NiO_x)–n-type (TiO_2) heterojunction formation. Such NiO_x-doped TiO_2 catalysts were recently reported to show good performance in the photocatalytic degradation of organic compounds [13].

This work presents the results of CuO@TiO_2 and NiO@TiO_2 core-shell catalysts for an efficient photocatalytic hydrogen production where CuO or NiO (15wt%) were introduced as core and TiO_2 as shell. Their performance in photocatalytic H_2 production was evaluated using glycerol as a feedstock. The photocatalytic activity of all samples for hydrogen evolution under UV-Vis irradiation was then compared under the same operation condition.

2. Materials and Methods

2.1. Synthesis of CuO@TiO_2 and NiO@TiO_2 core-shell catalysts

TiO_2 shell was prepared via sol-gel process [28]. CuO nanoparticles (0.125 g) were dispersed in 5 mL absolute ethanol and this suspended solution was added in a mixture of 0.1 g

hydroxypropyl cellulose, 20 mL absolute ethanol and 0.125 mL of deionized water. This mixture was stirred for 30 min at 600 rpm, and then 1 mL titanium (IV) butoxide (TBOT) in 5 mL absolute ethanol was injected, using a syringe pump, into the above solution at a rate of 0.5 $mL \cdot min^{-1}$; while the mixture was stirring at 900 rpm and a milk-like solution was obtained. After injection, the temperature of the solution was increased to 85 °C under reflux and agitation condition for 90 min. The precipitate containing $CuO@TiO_2$ was centrifuged, washed three times with ethanol and redispersed in 5 mL absolute ethanol. The coating procedure was repeated three more times in order to increase thickness of the TiO_2 layer. Finally, the samples were dried and calcined at 400 °C (1ºC/min) for 3 h in an air atmosphere. The same procedure was followed for the preparation of $NiO@TiO_2$ core-shell nanoparticles but with NiO as core. A schematic representation of $CuO@TiO_2$ and $NiO@TiO_2$ nanostructures is shown in Fig.1.

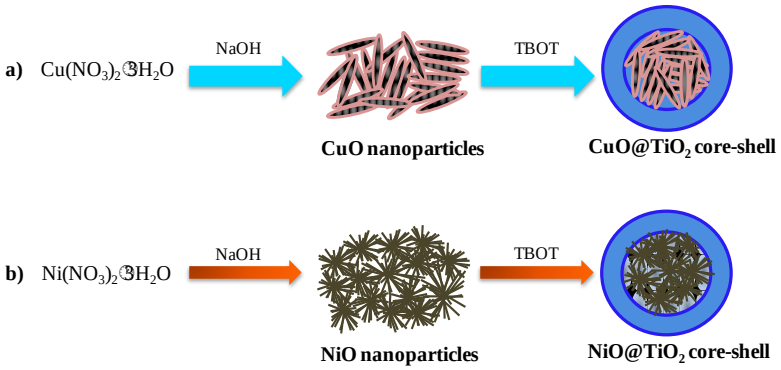

Fig. 1. Scheme of preparation process of core-shell catalysts.

a) $CuO@TiO_2$; b) $NiO@TiO_2$.

2.2. Characterization techniques

X-ray diffraction measurements were carried out on a Rigaku MiniFlex 600 X-ray diffractometer, using $CuK_{\alpha 1}$ radiation (λ=1.5406 Å). The accelerating voltage and the applied current were 40 kV and 15 mA, respectively. The 2θ angular regions from 10º to 100º were explored with a scanning speed of 0.1º in 0.01θ/min. The crystallite size of the samples was calculated using the Scherrer's formula.

UV–Visible spectroscopy measurements were performed on a UV-visible spectrophotometer GBC Cintra 20 and the UV-visible spectra were recorded over the range from 200 to 800 nm. The reflection data were converted to absorbance through the standard Kubelka– Munk method.

The textural properties were measured using nitrogen adsorption–desorption isotherms method at -196 °C using a Quantachrome NovaWin gas sorption system. Before the measurements, each sample was degassed at 200 °C for 2 h. Surface area determination was performed by using the Brunauer–Emmett–Teller (BET) method. The average pore size and pore volume were calculated by using the Barrett–Joyner–Halenda (BJH) method.

The X-ray photoelectron spectroscopy (XPS) was used to examine the surface properties about chemical valence and oxidation state of the metal elements after the catalytic test. XPS can detect signals within the upper 5–10 nm thickness on the surface. The measurements were carried out with a *K*-Alpha Thermo Scientific spectrometer equipped with a hemispherical electron analyzer and a monochromatic Al K_α X-ray source.

2.4. Photocatalytic test

The photocatalytic activity for hydrogen evolution was studied in a closed-gas circulation system connected to an autosystem XL Perkin Elmer gas chromatograph analyzer equipped with a Carbonxen 1006 PLOT capillary column and a thermal conductivity detector (TCD). The photocatalyst (15 mg) was added in a 20 mL clear glass vial at ambient temperature and atmospheric pressure containing 1.5 ml glycerol and 13.5 ml deionized water, and this was connected to a closed gas circulation system. The suspension was then exposed to a Hg-Xe Newport 66901 (solar simulator) 200 W irradiation lamp at a distance of 17 cm. Before each experiment the suspension was dispersed in an ultrasonic bath for 15 min then the photocatalytic cell was purged with nitrogen for 15 min to eliminate oxygen and other gases. The reaction was studied during 8 h with vigorous agitation (500 rpm) to ensure the uniform irradiation of the suspension. The photocatalytic cell is equipped with gas inlet/outlet lines and sealed with a silicone rubber septum to collect and transfer gaseous products to the analytical system for analysis.

3. Results and Discussion

3.1. Crystalline structure

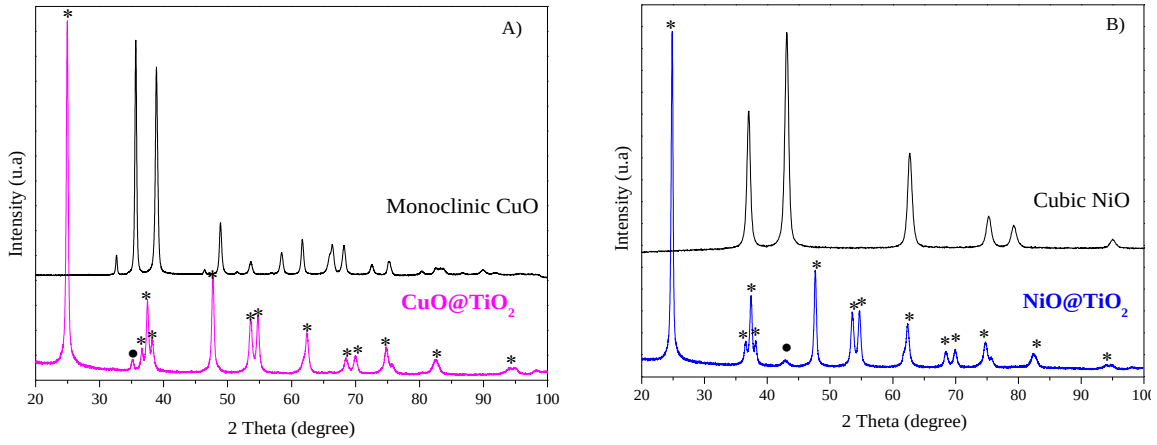

Fig. 2. X-ray diffraction patterns of core-shell catalysts calcined at 400 °C.

X-ray diffraction patterns of the pure CuO and CuO@TiO_2 core-shell catalyst are shown in Fig. 2A and the X-ray diffraction patterns of the pure NiO and NiO@TiO_2 are shown in Fig. 2B, respectively. All XRD peaks of copper oxide (2θ = 32.5°, 35.4°, 38.7°, 48.7°, 53.5°, 58.3°, 61.5°, 66.2°, 68.1° and 72.4°) match the monoclinic CuO phase (JCPDS No. 48-1548), demonstrating the formation of well-crystallized CuO nanoparticles. Pure NiO shows peaks at 2θ = 37.2°, 43.3°, 62.9°, 75.4° and 79.4° which can be well indexed to the cubic structure of nickel oxide (JCPDS No. 47-1049). Besides CuO and NiO characteristic peaks, no impurity peaks were detected. The average crystallite sizes estimated from the FWHM of NiO (2 0 0) and CuO (0 0 2) reflections using the Scherrer equation are 17.1 nm for pure CuO and 11.9 nm for NiO, respectively.

X-ray diffraction patterns of the NiO@TiO_2 and CuO@TiO_2 samples are dominated by anatase peaks; however, a small amount of CuO peak at 35.4° (0 0 2) and NiO peak at 43.3° (2 0 0) were also detected. In both XRD patterns, the peaks at 2θ = 25.3°, 36.6°, 37.8°, 38.6°, 48.0°, 53.9°, 55.1°, 62.7°, 68.8°, 70.3°, 74.1°, 82.2° and 94.2°, are indexed as anatase TiO_2 (21-1272 JCPDS card). The anatase TiO_2 crystallite size calculated from the most intense diffraction peak (1 0 1) at 2θ = 25.3° is 41.2 nm for NiO@TiO_2 and 44.8 nm for CuO@TiO_2. Because the loading of metal oxide NiO and CuO was asppproximately 15 wt.%, certainly above XRD detection limits, the very weak characteristic peak of NiO and CuO in both the NiO@TiO_2 and CuO@TiO_2 samples could be tentatively attributed to the formation of TiO_2 thick shell or coating [14]. Therefore, XRD analyses confirm that TiO_2 anatase was well coated on the outer of the CuO and NiO oxide cores.

3.2. UV–Vis DRS analysis

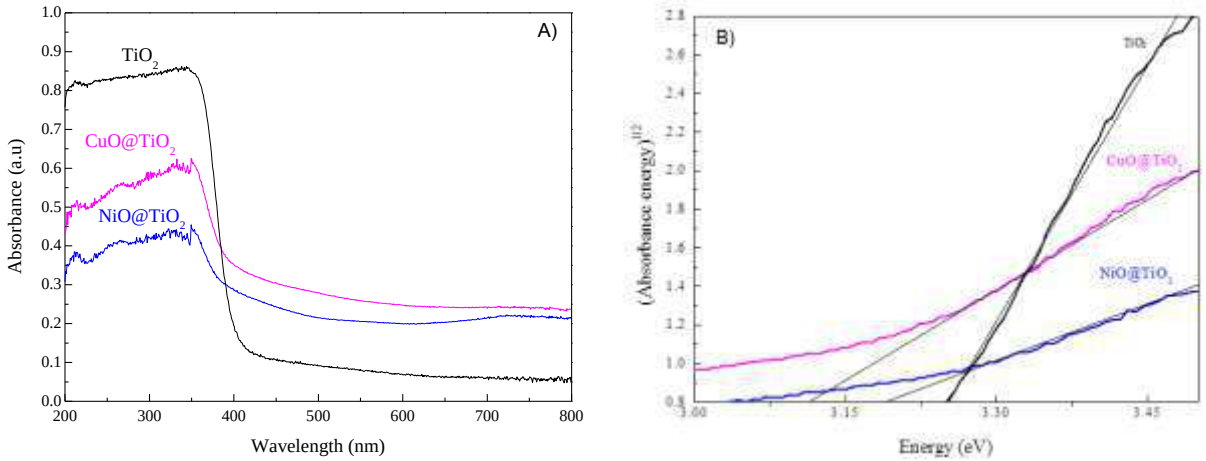

Fig. 3. A) UV-vis spectra measured for NiO@TiO_2, CuO@TiO_2 and TiO_2; B) Plot of (adsorbance· energy)$^{1/2}$ versus energy.

The optical properties of $NiO@TiO_2$ and $CuO@TiO_2$ photocatalysts were probed by the UV–Vis DRS technique and converted to the UV-Vis absorption edge energies by the Kubelka–Munk method, as shown in Fig.3A and Fig.3B. From Fig. 3A, the UV-vis-DRS of both $NiO@TiO_2$ and $CuO@TiO_2$ samples are very similar to the bare TiO_2 which indicates that the presence of NiO or CuO practically did not change the intrinsic properties of TiO_2. As seen in Fig. 3B, the band gap energy was estimated to be 3.25 eV for TiO_2, 3.19 eV for $NiO@TiO_2$, and 3.11 eV for $CuO@TiO_2$. Obviously, the presence of CuO caused greater absorption of photons in the visible region compared with NiO addition. It is reported that, the addition of Ag, Cu, Pt toTiO_2 causes changes in the band gap transition to larger values in the wavelength [15, 16]. Our results presented in Fig. 3 demonstrate that the stabilization of TiO_2 anatase would be encapsulating the CuO and NiO phases and results in a dramatic reduction in the band gap energy, with respect to that of bare TiO_2 (E_{BG}= 3.1-3.2 eV) [17].

3.5. Surface chemical analysis

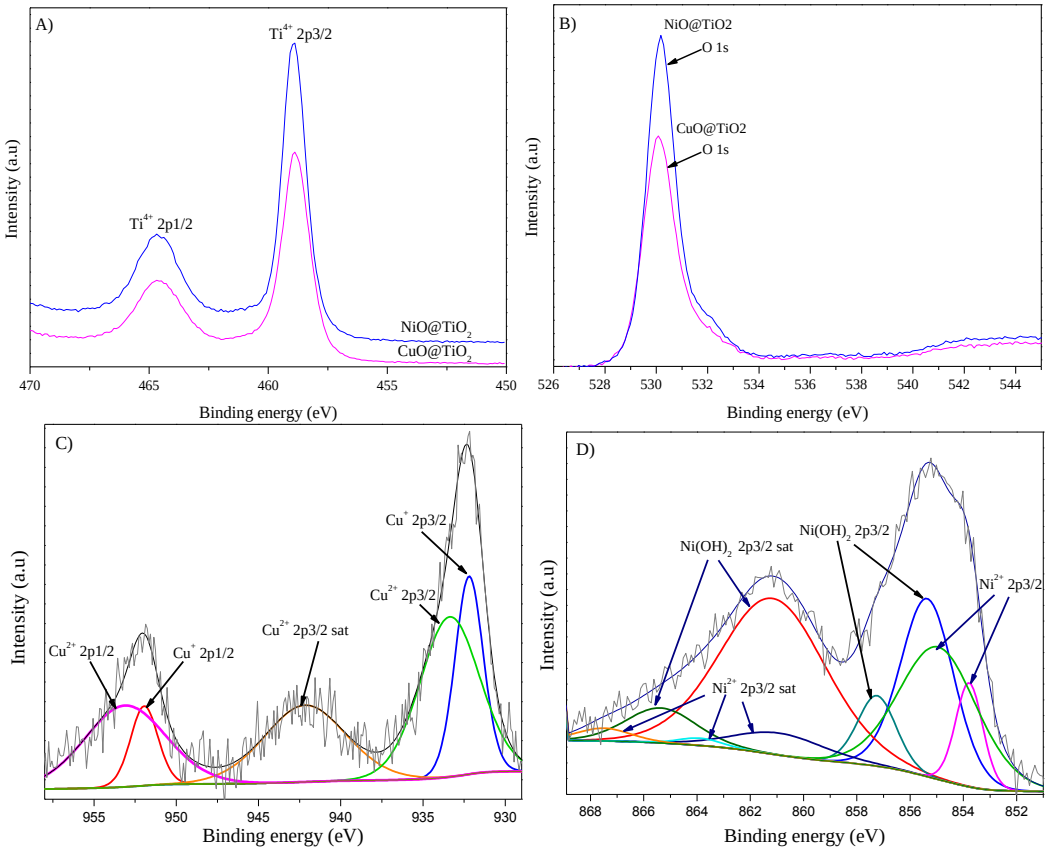

Fig. 4. The core levels of XPS spectra of $NiO@TiO_2$ and $CuO@TiO_2$ catalysts. A) Ti 2p; B) O 1s; C) Cu 2p; and D) Ni 2p.

The XPS spectra were recorded in the Ti 2p, O1s and Ni 2p regions for $NiO@TiO_2$ and in Ti 2p, O1s and Cu 2p for $CuO@TiO_2$ is shown in Fig. 4A. For Ti^{4+} ion, the binding energy values of Ti*2p* spectrum were 458.8 eV ($2p_{3/2}$) and 464.5 eV ($2p_{1/2}$) in both $NiO@TiO_2$ and $CuO@TiO_2$. These peaks have been assigned to Ti^{4+} in the crystalline structure of anatase TiO_2 [13].

For $NiO@TiO_2$ catalyst, the spectra of O_{1s} show (Fig. 4B) only one principal peak with binding energy 530.10 eV that corresponds to lattice O^{2-} in TiO_2 or /and O^{2-} ion NiO; while for $CuO@TiO_2$ the peak at 530.09 eV is attributed to lattice O^{2-} in TiO_2 or /and O^{2-} ion in CuO with literature values of 528.60-530.70 eV. One small peak at approximately 532.2 eV may indicate a small amount of adsorbed oxygen species in the samples. The Cu2p spectrum in Fig.4C shows the characteristic set of peaks at 952.7 eV ($2p_{1/2}$) and 932.7 eV ($2p_{3/2}$) of Cu^{2+} ion and a typical shake up satellite peak occurring at 943.1 ($2p_{3/2}$) eV characteristic of CuO [18]. The $Cu2p_{1/2}$ peak was fitted by two peaks at 951.9 eV and 953.1 eV assigned to CuO (Cu^{2+}) and Cu_2O (Cu^{+}), respectively. The broad $Cu2p_{3/2}$ peak was fitted for an energy binding of 933.3 eV and 932.1 eV that corresponds to CuO (Cu^{2+}) and Cu_2O (Cu^{+}), respectively. This result suggests that a certain amount of Cu^{2+} and Cu^{+} ions exist in the shell layer of TiO_2. Furthermore, Fig 4D shows Ni 2p core levels of XPS spectrum which can be fitted with spectral combinations of metal, oxide and hydroxide species [19]. A main peak at 855.4 eV (Ni 2p 3/2), and its satellite peak at 861.7 eV (2p 3/2 sat) corresponding to Ni^{2+} ion are observed [18].

3.6. Photocatalytic hydrogen production tests

The photocatalytic activity of four catalysts for H_2 production from glycerol-water mixtures (90 vol.% glycerol, 10 vol.% H_2O) was evaluated under simulated solar light at ambient temperature. As shown in equation 1, H_2 and CO_2 are the products. Results of the rates of evolution of H_2 and CO_2 are presented in Fig. 5. TiO_2 Degussa P25 was also tested as a reference for the photocatalytic hydrogen production.

$$C_3H_8O_3 + 3H_2O \xrightarrow{h\nu} 7H_2 + 3CO_2 \qquad (1)$$

When $CuO@TiO_2$ was used as catalyst, the maximum H_2 evolution rate was as high as 153.8 $\mu mol \cdot g^{-1} \cdot h^{-1}$ at 2 h of reaction. When $NiO@TiO_2$ was used as photocatalyst, the H_2 evolution rate was 48.1$\mu mol \cdot g^{-1} \cdot h^{-1}$. For the other catalysts like TiO_2 P25, NiO@CuO, and CuO@NiO, their H_2 evolution rate was 13.8, 6.2 and 5.3 .8 $\mu mol \cdot g^{-1} \cdot h^{-1}$, respectively. Because both CuO@NiO and NiO@CuO catalysts displayed very low photocatalytic activity for H_2 production, showing that pure CuO and NiO were not active for the photocatalytic hydrogen production under the test conditions. Therefore, TiO_2 serves as active phase in the test reaction. CuO core nanoparticles dramatically enhanced the rate of H_2 production.

The rate of CO_2 evolution was 20.1 $\mu mol \cdot g^{-1} h^{-1}$ for the $CuO@TiO_2$ catalyst. The molar ratio of H_2/CO_2 is approximately 7.65, which is much greater than the stoichiometric value 2.33. For the other catalysts, the molar ratio of H_2/CO_2 is 4.18 for $NiO@TiO_2$, 3.53 for CuO@NiO, 3.29 for TiO_2 P25, and 2.82 for NiO@CuO. The fact of all these actual H_2/CO_2 values greater than the stoichiometric value indicates that these catalysts may simultaneously catalyze the water spilling

reaction to generate hydrogen, apart from the glycerol reforming reaction. The amount of H_2 generated varied with the catalyst mass, Fig. 6. When the catalyst concentration varied from 0.5 to 1 g/L, the amount of H_2 generation significantly increased by approximately 3 times. However, catalyst concentration higher than 2g/L, the H_2 generation rate may not increase further due to the light scattering influence resulted from the catalyst particles in the suspended mixture.

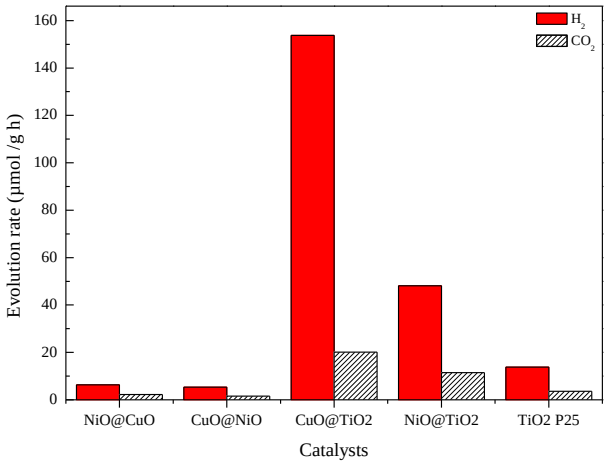

Fig.5. Evolution rate of H_2 and CO_2 with different photocatalysts using glycerol-water mixture under visible light irradiation at ambient temperature.

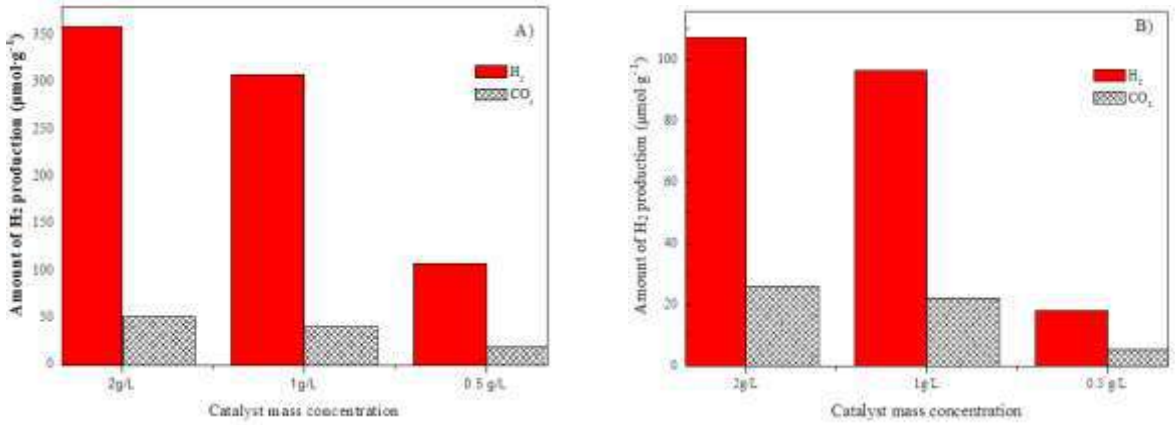

Fig.6. The amount of H_2 generation with different catalyst mass for 2 h of reaction.

A) $CuO@TiO_2$; B) $NiO@TiO_2$.

In the interface of CuO core and TiO_2 shell of the CuO@TiO_2 may form a heterojunction structure. When the heterojunction was initiated by a photon with energy higher than or equal to the bandgap of the catalyst, the photo-initiated electron-hole pairs in the TiO_2 shell are quickly separated: the electrons in the TiO_2 conduction band (CB) in the shell may flow to CuO. The accumulation of excess electrons in the conduction band of CuO caused a negative shift in the Fermi level of CuO to give the required energy for efficient water reduction. The holes in CuO may transfer to TiO_2 structure. Therefore, the migration of electrons and holes promoted the red-ox cycles of Cu^{2+}/Cu^{1+} couples and in return, the recombination of the photogenerated electrons and holes is effectively inhibited. Under solar light irradiation, Cu^{2+}/Cu^{+} together with TiO_2 with holes and electrons pairs served as a bridge for charge transfer and prolonged the lifetime of holes and electrons by effectively inhibition their recombination rate, and enhanced the photo efficiency of hydrogen production.

4. Conclusion

CuO@TiO_2 and NiO@TiO_2 core-shell catalysts were synthesized through a modified sol-gel method. The band gap energy was estimated to be 3.25 eV for pure TiO_2, 3.19 eV for NiO@TiO_2, and 3.11 eV for CuO@TiO_2. In the glycerol reforming reaction, hydrogen evolution rate was as high as 153.8 $\mu mol \cdot g^{-1} \cdot h^{-1}$ using CuO@TiO_2 core-shell catalyst, which is 29.0, 24.8, 11.2 and 3.2 times greater than that obtained on CuO@NiO, NiO@CuO, TiO_2 P25, and NiO@TiO_2 catalyst, respectively. A higher photocatalytic activity was obtained with the CuO@TiO_2 core-shell catalyst was explained in terms of electron transfer from photoexcitated TiO_2 to the conduction band of CuO in the heterojunction structure in the interface of TiO_2 shell and CuO core and in the oxidation-reduction cycles among Cu^{2+}/Cu^{+} couples and the inhibition of electron-hole recombination.

Acknowledgements

Financial support of this work was provided by Instituto Politécnico Nacional (Grant No. SIP-20181280). S.P. Ramírez thanks the financial support offered by CONACYT-Mexico for her doctoral thesis study and for investigation exchange in the University of Saskatchewan in Canada.

References

[1] Jia H, Hua Xu, Hu Y, Tang Y, Zhang L. TiO_2@CdS core–shell nanorods films: Fabrication and dramatically enhanced photoelectrochemical properties. Electrochem Commun 2007; 9:354–360.
[2] Zhang Y, Xu Y, Li T, Wang Y. Preparation of ternary Cr_2O_3–SiC–TiO_2 composites for the photocatalytic production of hydrogen. Particuology 2012; 10:46– 50.
[3] Kokporka L, Onsuratoom S, Puangpetch T, Chavadej S. Sol–gel synthesized mesoporous assembled TiO_2–ZrO_2 mixed oxide nanocrystals and their photocatalytic sensitized H_2

production activity under visible light irradiation, Mater Sci Semiconductor Processing 2013; 16:667–678.
[4] He Q, Zhang Z, Xiong J, Xiong Y, Xiao H. A novel biomaterial Fe_3O_4:TiO_2 core-shell nano particle with magnetic performance and high visible light photocatalytic activity. Optical Materials 2008; 31: 380–384.
[5] Su X, Zhao J, Li Y, Zhu Y, Ma X, Sun F, Wang Z. Solution synthesis of Cu_2O/TiO_2 core-shell nanocomposites . Colloids and Surf. A: Physicochem Eng Aspects 2009; 349: 151–155.
[6] Smith W, Zhao YP. Superior photocatalytic performance by vertically aligned core–shell TiO_2/WO_3 nanorod arrays. Catal Commun 2009; 10: 1117–1121.
[7] Meng HL, Cui C, Shen HL, Liang DY, Xue YZ, Li PG, Tang WH. Synthesis and photocatalytic activity of TiO_2@CdS and CdS@TiO_2 double-shelled hollow spheres. J Alloys and Compounds 2012; 527:30– 35.
[8] Wang F, Liu J, Wang X, Kong J, Qiu S. Synthesis of hollow Fe_3O_4 at ZnO at anatase TiO_2 core–shell structured spheres. Ceramics Int 2012; 38: 6899–6902.
[9] Vaidya S, Patra A, Ganguli AK. CdS@TiO_2 and ZnS@TiO_2 core–shell nanocomposites: Synthesis and optical properties. Colloids and Surfaces A: Physicochem Eng Aspects 2010; 363: 130–134.
[10] Radwan NRE, El-Shall MS, Hassan HMA. Synthesis and characterization of nanoparticle Co_3O_4, CuO and NiO catalysts prepared by physical and chemical methods to minimize air pollution. Applied Catalysis 2007; 331: 8–18.
[11] Chen WT, Jovic V, Sun-Waterhouse D, Idriss H, Waterhouse GIN. The role of CuO in promoting photocatalytic hydrogen production over TiO_2. Int J Hydrogen Energy 2013; 38:1503–1504.
[12] Wu J, Li C, Zhao X, Wu Q, Qi X, Chen X, Hu T, Cao Y. Photocatalytic oxidation of gas-phase Hg^0 by CuO/TiO_2. Appl Catal B Environ 2015; 176-177: 559–569.
[13] Liu R, Yoshida H, Fujita SI, Arai M. Photocatalytic hydrogen production from glycerol and water with NiO_x/TiO_2catalysts. Appl Catal B Environ 2014; 144:41– 45.
[14] Lee I, Joo JB, Yin Y, Zaera F. A yolk@shell nanoarchitecture for Au/TiO_2 catalysts. Angew Chem 2011; 50: 10208 –10211.
[15] Grabowska E, Zaleska A, Sorgues S, Kunst M, Etcheberry A, Colbeau-Justin C, Remita H. Modification of Titanium(IV) Dioxide with Small Silver Nanoparticles: Application in Photocatalysis, J Phys Chem C, 2013; 117:1955–1962.
[16] Kowalska E, Remita H, Colbeau-Justin C, Hupka J, Belloni J. Modification of titanium dioxide with platinum ions and clusters: application in photocatalysis. J Phys Chem C. 2008; 112:1124–1131.
[17] Luna AL, Valenzuela MA, Colbeau-Justin C, Vázquez P, Rodriguez JL, Avendaño JR, Alfaro S, Tirado S, Garduño A, De la Rosa JM, Photocatalytic degradation of gallic acid over CuO-TiO_2 mixtures under Vis-LED irradiation, Appl Catal A Gen 2016; 52: 140–148.
[18] Ranga Rao G, Meher SK, Mishra BG, P. Charan PK. Nature and catalytic activity of bimetallic CuNi particles on CeO_2 support. Catal Today 2012; 198:140– 147.
[19] Biesinger MC, Payne BP, Lau LWN, Gerson A, Smart RSC. X-ray photoelectron spectroscopic chemical state quantification of mixed nickel metal, oxide and hydroxide systems. Surf Interface Anal 2009; 41:324–332.

XVIII International Congress
of the Mexican Hydrogen Society

Au/CeO_2 and $Au/Ce_xZr_{1-x}O_2$ Sol-Gel Catalysts for Hydrogen Production via Partial Oxidation of Methanol

E. Hernández[1], J.A. Wang[1,*], L.F. Chen[1], M.A. Valenzuela[1], R. Azargohar[2], A.K. Dalai[2]

[1]ESIQIE, Instituto Politécnico Nacional. Zacatenco, 07738 Ciudad de México, Mexico.
[2]Department of Chemical Engineering, University of Saskatchewan, Saskatoon - S7N 5A9, Canada
* Corresponding author: Tel: 525557296000 ext. 54276; e-mail: jwang@ipn.mx

ABSTRACT

Catalytic activity of Au/CeO_2 and $Au/Ce_xZr_{1-x}O_2$ catalysts in the partial oxidation of methanol for hydrogen production under different pretreatment conditions was investigated. ZrO_2 addition to Au/CeO_2 catalyst led to formation of $Ce_xZr_{1-x}O_2$ solid solution that promoted the formation of Au^{n+} nanoclusters and improved the reducibility of surface oxygen of the support. The pretreatment of the catalysts played a key role, influencing the catalytic activity and product selectivity. Under reductive condition, the catalysts exhibited better catalytic activity and higher hydrogen selectivity than that obtained under oxidative condition. Generally the $Au/Ce_xZr_{1-x}O_2$ catalyst exhibited higher catalytic activity and H_2 selectivity.

Keywords: Au/CeO_2; $Au/Ce_xZr_{1-x}O_2$; Partial oxidation of methanol; Hydrogen production.

1. Introduction

Recently, hydrogen received great attention because it is regarded as a clean fuel related to the global-concerned issues of environmental pollution control, climate change and energy crisis. Hydrogen has a wide spectrum of applications in fuel cell technology and petrochemicals industries, and many other areas [1]. There are a number of approaches or processes for hydrogen production, for instance, the catalytic decomposition of natural gas, steam reforming, photocatalytic decomposition of water, and biomass gasification, partial oxidation of methanol (POM) [2–8]. The POM reaction is considered as a structure-sensitive reaction as the selectivity of the products is greatly dependent of the configuration of the surface atoms and the structure character of the catalyst. This reaction can lead to several products, like H_2, CO, CO_2 and CH_4 etc, strongly influenced by the catalyst composition, reaction temperature, and methanol conversion degree. A variety of catalysts such as iron and copper oxides catalysts have been

commercialized for hydrogen production [9,10]. In the last 15 years, it has been discovered that the nanosized gold catalysts exhibited extraordinarily high activity for hydrogen production via low temperature water-gas shift (WGS) reaction [11–13]. Unfortunately, the nano-gold catalysts used for POM reaction have not tensely investigated yet.

In the Au/CeO_2 catalysts, CeO_2 support had high oxygen storage/release capacity due to the high shift ability between oxidized and reduced states ($Ce^{4+} \leftrightarrow Ce^{3+}$) under the reaction condition. The surface oxygen vacancies in ceria played an important role in facilitating oxygen transfer. Woods et al. reported that CeO_2 was active during preferential oxidation of CO when it combined with Co; the conversion of CO reached 100 % [14]. Liu and coauthors concluded that Au/CeO_2 catalysts with interconnected networks of spherical voids favored the formation of highly dispersed Au nanoparticles, which positively affected the catalytic oxidation of HCHO [15]. It was reported that ZrO_2 addition could modify Au dispersion, acid/based properties, and catalytic activity [16].

In the present work, taking into account both the remarkable activity of nanosized gold catalysts in the WGS reaction for hydrogen production and the excellent oxygen storage/release ability of CeO_2 solid, two Au/CeO_2 and $Au/Ce_xZr_{1-x}O_2$ catalysts were synthesized using urea solution as precipitating agent. The catalytic behavior in the methanol partial oxidation was investigated and the effects of reaction temperature, pretreatment, and the ZrO_2-addition into CeO_2 on the catalytic activity were discussed.

2. Materials and Methods

Ceria and zirconia mixed oxides were synthesized by a sol-gel method. The pH of the hydrolyzing solution was set at 3.0 using 1M HNO_3. The molar ratios were as follows: H_2O/isopropoxide = 30, methanol/isopropoxide = 65, and acid/isopropoxide = 0.2. The total molar ratio of Zr/Ce was adjusted to 1:1. After the gelation step, the precipitates were obtained by solvent vaporization. The solid was washed and dried for 12 h at 100 °C and calcined at 550 °C for 4 h.

The Au loaded catalysts were prepared by depositing Au nanoparticles (corresponding to 3% wt. of Au) onto CeO_2 and $Au/Ce_xZr_{1-x}O_2$ solids via a deposition-precipitation (DP) method. A solution of $HAuCl_4$ (4.2×10^{-3} M) was prepared using $HAuCl_4$ as Au precursor. 3 g of support with 16 mL of urea solution (0.45 M) were added to the $HAuCl_4$ solution under stirring. The suspended mixture was heated to 80 °C with stirring for 11 h. And then the solids were washed with 150 ml deionized water for 4 times in order to remove Cl^- and NH_4^+ ions; the filtered materials were dried at 80 °C overnight. Part of the gold loaded catalysts were reduced under a reductive condition by using a H_2 flow of 25 ml·min^{-1} at 200 °C for 2 h. Other part of catalysts were thermally treated under oxidative condition by using an O_2 flow of 25 ml·min^{-1} at 200 °C for 2h. Thse $3wt\%Au/CeO_2$ and $3wt\%Au/Ce_xZr_{1-x}O_2$ catalysts are noted as 3%AuCe and 3%AuZrCe, respectively.

Textural properties of the catalysts were obtained using N_2 adsorption-desorption isotherms at -196 °C on an automated gas adsorption analyzer (ASAP 2020, Micrometirics, Instruments Inc., GA USA). 0.2g sample was degassed at 200 °C for 2h before the measurements.

Crystalline and phase compositions of the catalysts were analyzed X-ray diffraction technique (XRD) on a Bruckcer D8 Advance X-Ray Diffractometer with Cu Kα radiation (λ =1.54056 Å).

Surface oxygen reduction behavior of the catalysts was analyzed using temperature-programmed reduction of hydrogen (TPR– H_2) method on a Micromeritics 2920 AutoChem II. 50 mg catalyst was placed in a U-type glass reactor and was thermally treated at 300 °C for 60 min under a nitrogen flow. After the sample was cooled down to 50 °C, a gas mixture (5.5% H_2 in Ar) was allowed to pass through the catalyst bed with a flow rate of 25 ml·min^{-1}. The TPR signals were recorded by a thermal conductivity detector (TCD).

Catalytic properties of the catalysts were evaluated in the partial oxidation of methanol at atmospheric pressure. For each test, the catalyst loading was 50 mg. The O_2/CH_3OH ratio was 0.5 using air as oxygen supplier. The reactants were fed to the reactor with a space velocity (SV) 50,000 h^{-1}. The reaction temperature varied between 210 °C and 300 °C. In a typical run, CH_3OH was injected with a syringe pump, and then mixed with air into a pre-heater at 100 °C. The total injected flow was 75 ml·min^{-1}. The gas outlet was connected to a condenser in order to condense unreacted methanol. Finally, the liquid and gas reaction products were analyzed by the gas chromatography method. Liquid product was analyzed by flame ionization detector (FID); while gas products were analyzed by thermal conductivity detector (TCD) to determinate H_2, CO_2, CO, CH_4 composition and unreacted O_2. The methanol conversion was calculated according to the Eq. 1.

$$X_{CH_3OH} = \frac{n^{in}_{CH_3OH} - n^{out}_{CH_3OH}}{n^{in}_{CH_3OH}} \times 100\% \quad (1)$$

Where $n^{in}_{CH_3OH}$ and $n^{out}_{CH_3OH}$ were the mole number of methanol in the inlet and outlet stream, respectively. The selectivity of product *x* was calculated by excluding water on a dry-based gas composition (Eq. 2).

$$S_X = \frac{n^{out}_X}{\Sigma n^{out}_X} \times 100\% \quad (2)$$

Where, n^{out}_X was the mole number of product *x* in the outlet stream, and Σn^{out}_X was the sum of the mole number of all products.

3. Results and Discussion

3.1. Textural properties

Fig.1 showed the loops of N_2 adsorption-desorption isotherms of Au/CeO_2 and $Au/ Ce_xZr_{1-x}O_2$ catalysts. They corresponded to the IV type. However, Au/CeO_2 had a H2 type desorption branch associated to condensation and evaporation processes occurring in pores with narrow necks and wide bodies; whereas the $Au/ Ce_xZr_{1-x}O_2$ catalyst shows to a H3 type hysteresis loop. The $Au/Ce_xZr_{1-x}O_2$, Fig.2, showed a sharp and narrow monomodal pore size distribution with a

maximum value approximately 3 nm. The Au/CeO_2 catalyst had a relatively wide bimodal pore size distribution with a maximum value approximately 7 nm and a small shoulder at about 2.4 nm. The Au/CeO_2 catalyst had a larger BET surface area (89 $m^2 \cdot g^{-1}$) with larger pore volume of 0.22 $cm^3 \cdot g^{-1}$ and a bigger average pore size 14 nm in comparison with the $Au/Ce_xZr_{1-x}O_2$ catalyst which had surface area of 72 $m^2 \cdot g^{-1}$, pore volume of 0.10 $cm^3 \cdot g^{-1}$ and an average pore size of 6 nm. Obviously, zirconium addition into CeO_2 led to the surface area and pore volume smaller and pore diameter distribution narrower for the $Au/Ce_xZr_{1-x}O_2$ catalyst.

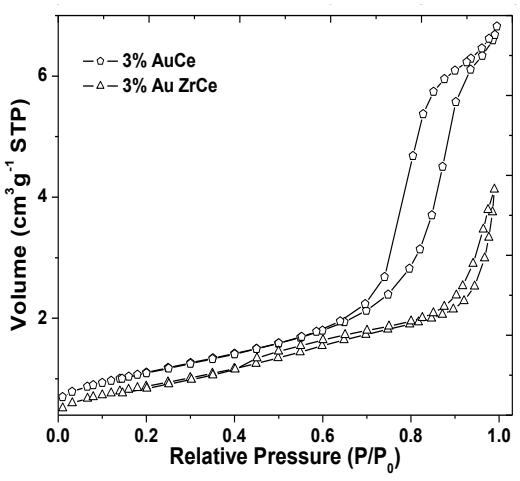

Figure 1. N_2 adsorption-desorption isotherms.

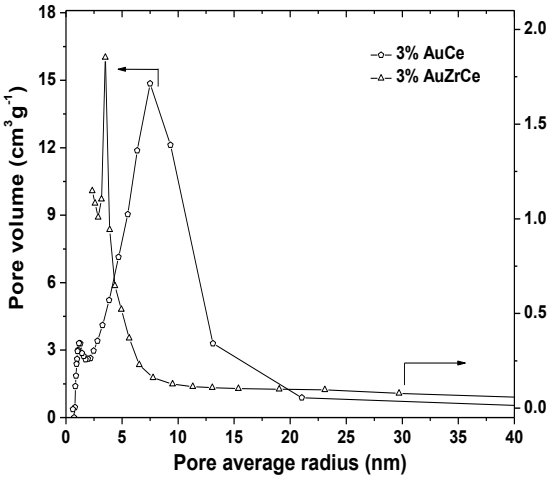

Figure 2. Pore radius distribution profiles

3.2. Crystalline structure and phase compositions

Powder X-ray diffraction patterns of the reduced Au/CeO_2 and $Au/Ce_xZr_{1-x}O_2$ catalysts were shown in Fig.3. The fluorite CeO_2 cubic phase was identified as indicated by the characteristic diffraction peaks at 2θ = 28.5°, 32.8°, 48.5 °, and 57.0 °, which corresponded to (111), (200) (220) (311) planes of the cubic CeO_2 crystals (JCPDS: 030394) [17]. Main diffraction peak of Au (111) (2θ = 38.2°) was not detected, suggesting a high dispersion of Au nanoparticles on the catalyst surface. The average particle size of CeO_2 was calculated on the basis of the main peak (111) by using the Scherrer equation. CeO_2 crystal size was approximately 8.2 nm. While ZrO_2-CeO_2 had an average crystallite size approximately 5.4 nm. On the basis of the results obtained from the N_2 adsorption-desorption isotherms and XRD analysis, we may conclude that ZrO_2 addition modified the crystalline structure, crystallite size, and textural properties of the CeO_2 support. The characteristic peaks in the XRD patterns corresponding to single CeO_2 and ZrO_2 crystals were not found in $Au/Ce_xZr_{1-x}O_2$ sample, indicating the formation of ($Ce_xZr_{1-x}O_2$) solid solution. This result was in good agreement with the results reported by Hosokawa et al. who

claimed that the Ce and Zr ions were homogeneously dispersed to form $Ce_xZr_{1-x}O_2$ solid solution which exhibited high oxygen release capacity [18].

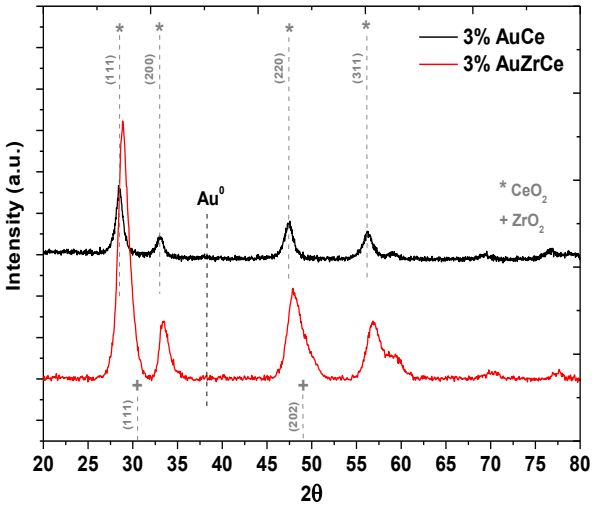

Figure 3. X-ray diffraction patterns of the reduced Au/CeO_2 and $Au/Ce_xZr_{1-x}O_2$ catalysts

3.3. Surface oxygen reduction properties

The reducibility of the catalysts was investigated by the TPR– H_2 method. The TPR–H_2 profiles were shown in Fig.4. For both catalysts, a strong and sharp peak with a temperature maximum at 105 °C was observed; it was attributed to the reduction of cationic Au^{n+} species to metallic phase (Au^0). The area of the peak at 105 °C for Au/CeO_2 was almost two times greater than that of $Au/Ce_xZr_{1-x}O_2$ catalyst, confirming that more Au^{n+} species were reduced in the former, similar to the results reported by Fonseca et al [19]. It was assumed that some Au^{n+} ions were bounded to the surface oxygen to form AuO_x with high dispersion on $Ce_xZr_{1-x}O_2$. Zirconium addition partially promoted the formation of AuO_x species that were just partly reduced; so the area of the TPR peak around 105 °C in $Au/Ce_xZr_{1-x}O_2$ catalyst was small.

H_2 consumption was also observed between 300 and 700 °C in $Au/Ce_xZr_{1-x}O_2$, indicating the reduction of surface oxygen in the ZrO_2-modified CeO_2 mixed oxide support [20]. The greater area under the TPR–H_2 curve in this temperature range evidenced that more available oxygen species on $Ce_xZr_{1-x}O_2$ than that in the CeO_2 surface were reduced. In the temperature range between 400 and 600 °C, the $Au/Ce_xZr_{1-x}O_2$ has a greater reducibility than Au/CeO_2, probably affecting methanol conversion and hydrogen selectivity in the methanol partial oxidation reaction. The H_2 consumption above 600 °C in Au/CeO_2 corresponded to the reduction of the bulk oxygen in CeO_2. The TPR–H_2 experiments confirmed that some defective AuOx nanoclusters probably existed in the $Au/Ce_xZr_{1-x}O_2$ after reduction at 200 °C and ZrO_2 addition

into CeO_2 could significantly improve the reducibility of the surface oxygen species of the support.

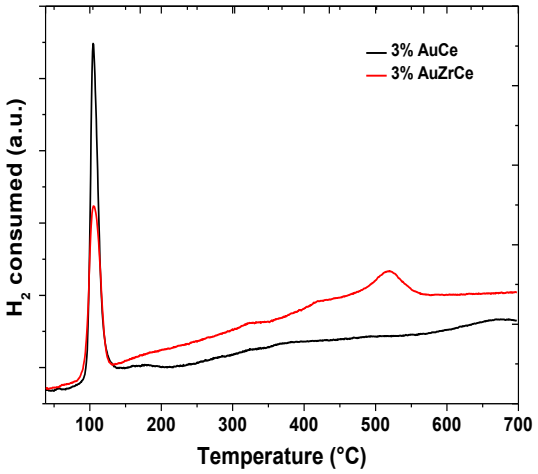

Figure 4. TPR–H_2 profiles of the Au/CeO_2 and $Au/Ce_xZr_{1-x}O_2$ catalysts.

3.4. Catalytic properties and discussion

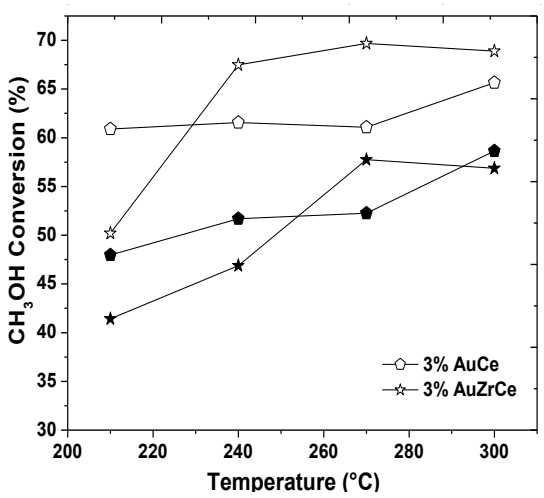

Figure 5. Partial oxidation of methanol over Au/CeO_2 and $Au/Ce_xZr_{1-x}O_2$. Empty icons: reductive pre-treatment condition; Full icons: oxidative pre-treatment condition. O_2/CH_3OH = 0.5.

Fig. 5 showed the catalytic activity of Au/CeO_2 and $Au/Ce_xZr_{1-x}O_2$ in the partial oxidation of methanol. These catalysts were pretreated under oxidative and reductive atmosphere condition,

respectively. The catalysts pretreated under the reductive condition showed a better catalytic activity for methanol conversion in comparison with the catalysts pretreated under oxidative condition. In the reaction temperature range between 210 and 270 °C, methanol conversion over the $Au/Ce_xZr_{1-x}O_2$ catalyst significantly increased with increasing of temperature, independent of the pretreatment condition. It was observed that at initial of reaction (210 °C), for the catalysts pretreated under reductive condition, methanol conversion over Au/CeO_2 catalysts was 11% greater than that achieved using $Au/Ce_xZr_{1-x}O_2$ catalyst. When the reaction temperature was above 210 °C, the catalytic activity of the $Au/Ce_xZr_{1-x}O_2$ was higher than the Au/CeO_2 catalyst. This seemed to indicate that at low reaction temperature more available surface oxygen species in the Au/CeO_2 than that in the $Au/Ce_xZr_{1-x}O_2$ catalyst participated in the POM reaction; and at higher reaction temperature, more active oxygen were formed in the $Au/Ce_xZr_{1-x}O_2$ than that in the Au/CeO_2 catalyst [21, 22]. The maximum methanol conversion was 69.6% over $Au/Ce_xZr_{1-x}O_2$ and 61% over Au/CeO_2 at 270 °C.

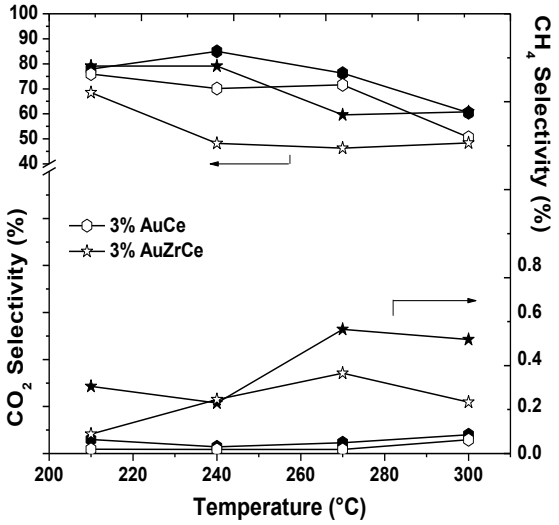

Figure 6. CO_2 and CH_4 selectivity over Au/CeO_2 and $Au/Ce_xZr_{1-x}O_2$ catalysts during POM reaction. Empty icons: reductive pre-treatment condition; Full icons: oxidative pre-treatment condition.

Fig. 6 showed the CO_2 and CH_4 selectivity during POM reaction. For the reductive pretreated Au/CeO_2, the CO_2 selectivity was about 73-75% in the temperature between 210 and 270 °C. However, it decreased from 75% at 270 °C to 50% at 300 °C. Similarly, after the oxidative pretreatment, the Au/CeO_2 catalyst showed stable CO_2 selectivity at temperature below 270 °C and it decreased at higher temperature. These results seemed to indicate that reversible water gas shift reaction probably took place at higher temperature, which led to CO_2 selectivity decrease (Eq. 3).

$$CO_2 + H_2 \rightarrow H_2O + CO \quad (3)$$

To the contrary, for the reductive pretreated $Au/Ce_xZr_{1-x}O_2$ catalyst, the CO_2 selectivity was decreased from 69 % at 210 °C to 50% at 240 °C, and then remained the almost same at higher temperature between 240 and 300 °C. Similar results were observed for the oxidative pretreated Au/ZrO_2-CeO_2 catalyst. These results seemed to indicate that over the $Au/Ce_xZr_{1-x}O_2$ catalyst, the water gas shift reaction took place at lower reaction temperature.

However, the above suggestion about CO_2 selectivity varying with temperature was not supported by the fact that CO was not detected in the whole temperature range for both catalysts pretreated under reductive or oxidative condition. On the other hand, it was observed that CH_4 was formed in the whole reaction temperature region between 210 and 300 °C. The Au/CeO_2 catalyst showed higher selectivity of CH_4 than that obtained over $Au/Ce_xZr_{1-x}O_2$ catalyst. Taking into account the fact of CO absence, we assumed that CH_4 was produced from methantion via CO and CO_2 reaction with hydrogen (Eqs. 4-5).

$$CO + 3H_2 \rightarrow CH_4 + H_2O \quad (4)$$

$$CO_2 + 4H_2 \rightarrow CH_4 + 2H_2O \quad (5)$$

Moreover, CO could be probably converted to CO_2 as the nano-gold catalyst was very active for CO oxidation.

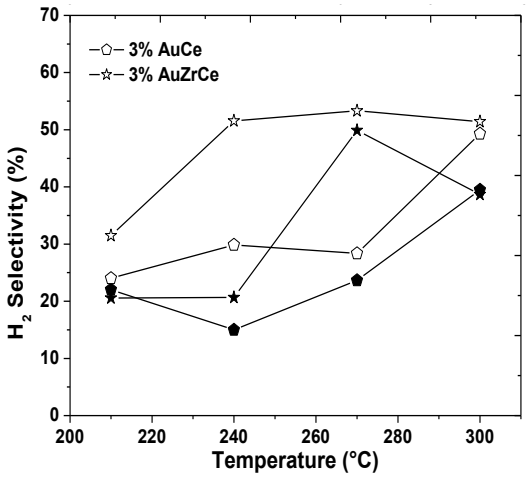

Figure 7. Hydrogen selectivity over Au/CeO_2 and $Au/Ce_xZr_{1-x}O_2$ catalysts during POM reaction. Empty icons: reductive pre-treatment condition; Full icons: oxidative pre-treatment condition.

Hydrogen selectivity was shown in Fig. 7. The highest hydrogen selectivity (52%) was achieved over $Au/Ce_xZr_{1-x}O_2$ at 270 °C. In addition, the reductive pretreatment could improve the hydrogen selectivity and methanol conversion as well. It was noted that the IR band at 3178 cm^{-1} disappeared at 300 °C (not shown). An increment of adsorbed methoxy groups (1050 cm^{-1}) and a decrease of the band of O-H (1637 and 3178 cm^{-1}) over $Au/Ce_xZr_{1-x}O_2$ were observed between

210 and 300 °C. These observations suggested that methoxy species reacted with O–H hydroxyls to yield hydrogen and formate at 300°C, which was opposite to lower temperature. Therefore, hydrogen selectivity was enhanced from 31.5 % at 210 °C to 51.5% at 300 °C. Methanol partial oxidation was complex as it involved in several different reactions: methanol oxidation, CO oxidation, water gas shift reaction, and methanation. In both conditions of reductive and oxidative pretreatment, the $Au/Ce_xZr_{1-x}O_2$ catalyst showed a better hydrogen selectivity and greater methanol conversion than that achieved on the Au/CeO_2 catalyst at reaction temperature above 210 °C. These may be related to the formation of surface foxygen defective AuO_x nanoclusters in the $Au/Ce_xZr_{1-x}O_2$ catalyst.

4. Conclusion

ZrO_2 addition into Au/CeO_2 could form $Ce_xZr_{1-x}O_2$ solid solution in the $Au/Ce_xZr_{1-x}O_2$ catalyst which promoted the formation of defective AuO_x nanoclusters and the surface oxygen reducibility of the support, favoring the improvement of catalytic performance. The catalyst pretreatment condition took an important role in the methanol partial oxidation. Under reductive treatment condition, the catalysts exhibited better catalytic activity and higher hydrogen selectivity than that obtained under oxidative treatment condition. The metallic Au^0 together with defective AuO_x nanoclusters were the active centers in the target reaction. In the products, H_2, CO_2 and a small amount of CH_4 were detected but CO, formaldehyde, formic acid, methyl formate, and dimethyl ether were not detected.

Acknowledgements

The authors would like to acknowledge the financial support from the projects SIP-20150553, SIP-20150554 and 20181280. E. Hernández also thanks CONACyT-Mexico for supporting him doctoral study and research exchange at the University of Saskatchewan in Canada.

References

[1] Larsson M, Mohseni F, Wallmark C, Grönkvist S, Alvfors P, Energy system analysis of the implications of hydrogen fuel cell vehicles in the Swedish road transport system. Int J Hydrogen Energy 2015; 40:11722–11729.
[2] Gosselink JW. Pathways to a more sustainable production of energy: sustainable hydrogen: a research objective for shell. Int J Hydrogen Energy 2002; 27(11–12):1125–9.
[3] Holladay JD, Hu J, King DL, Wang Y. An overview of hydrogen production technologies. Catal Today 2009; 139(4):244–60.
[4] Armor JN. The multiple roles for catalysis in the production of H_2. Appl Catal A: Gen 1999; 176(2):159–76.
[5] Song CS. Fuel processing for low-temperature and high temperature fuel cells: challenges, and opportunities for sustainable development in the 21st century. Catal Today 2002; 77(1–2):17–49.

[6] MuHugh K. Hydrogen production methods. MPR Associates Inc; 2005. pp. 41.
[7] Hoogers G. Fuel cell technology handbook. Boca Raton: CRC Press; 2003. pp. 23.
[8] Chum HI, Overend RP. Biomass and renewable fuels. Fuel Process Technol 2001; 71(1–3):187–95.
[9] Roselin LS, Liao LM, Ou YC, Chang FW. Hydrogen production by partial oxidation ethanol over gold supported on Fe_2O_3. J. Nanosci Nanotechnol 2014; 14(9):7215–23.
[10]. Yang HC, Chang FW, Selva Roselin L, Hydrogen production by partial oxidation of methanol over Au/CuO/ZnO catalysts, J Mol Catal A Chem 2007; 276: 184–190.
[11]. Gong JL, Structure and surface chemistry of gold-based model catalysts, Chem Rev. 2011; 153: 745–57.
[12]. Burch R, Gold catalysts for pure hydrogen production in the water–gas shift reaction:activity, structure and reaction mechanism, Phys Chem Chem Phys 2006**;** 8**:**5483–5500.
[13]. Zhang Y, Zhan Y, Chen C, Cao Y, Lin X, Zhang Q, Highly effect Au/ZrO_2 catalysts for low temperature waster-gas shift reaction: effect of pre-calcination temperature on ZrO_2. Int. J. Hydrogen Energy 2012; 37: 12292–12300.
[14]. Woods MP, Gawade P, Tan B, Ozkan US. Preferential oxidation of carbon monoxide on Co/CeO_2 nanoparticles. Appl Catal B Environ 2010; 97:28–35.
[15]. Liu B, Li C, Zhang Y, Liu Y, Hu W, Wang Q. Investigation of catalytic mechanism of formaldehyde oxidation over three-dimensionally ordered macroporous Au/Ce. Appl Catal B Environ 2012; 111– 112: 467–475.
[16]. Vindigni F, Manzoli M, Tabakova T, Idakiev V, Boccuzzi F, Chiorino A. Gold catalysts for low temperature water-gas shift reaction: Effect of ZrO_2 addition to CeO_2support. Appl Catal B Environ 2012; 125: 507–515.
[17]. Zhang J, Jin Y, Li C, Shen Y, Han L, Hu Z, Di X, Liu Z. Creation of three-dimensionally ordered macroporous Au/CeO_2 catalysts with controlled pore sizes and their enhanced catalytic performance for formaldehyde oxidation. Appl Catal B Environ 2009; 91:11–20.
[18]. Hosokawa S, Imamura S, Iwamoto S, Inoue M. Synthesis of CeO_2–ZrO_2 solid solution by glycothermal method and its oxygen release capacity. J Eur Ceram Soc 2011; 31:2463–2470.
[19]. Fonseca J, Royer S, Bion N, Laurence PR, Rangel MC, Duprez D. Preferential CO oxidation over nanosized gold catalysts supported on ceria and amorphous ceria–alumina. Appl Catal B-Environ 2012; 128:10–20.
[20]. Wu H, Wang L. Shape effect of microstructured CeO_2 with various morphologies on CO catalytic oxidation, Catal Commun 2011; 12:1374–1379.
[21]. Chang FW, Selva-Roselin L, Ou TC. Hydrogen production by partial oxidation of methanol over bimetallic Au–Ru/Fe_2O_3catalysts. Appl Catal A-Gen 2008; 334:147–155.
[22]. Li C, Shen Y, Jia M, Sheng S, Adebajo MO, Zhu H. Catalytic combustion of formaldehyde on gold/iron-oxide catalysts. Catal Commun 2008; 9:355–361.

XVIII International Congress
of the Mexican Hydrogen Society

Scope of fuel cells in current transport with hydrogen as fuel

José Juan Alvarado Flores[1,*], María Liliana Ávalos Rodríguez[2], Jaime Espino Valencia[3], Jorge Víctor Alcaraz Vera[4]

[1] Instituto Tecnológico del Valle de Morelia, Tecnológico Nacional de México, Km. 6.5 Carretera Morelia Salamanca, Nardo S/N Morelia, Michoacán, México.
[2] Escuela Nacional de Estudios Superiores, Universidad Nacional Autónoma de México, Antigua Carretera a Pátzcuaro No. 8701, Morelia, Michoacán, México.
[3] Facultad de Ingeniería Química, Universidad Michoacana de San Nicolás de Hidalgo, Francisco J. Mújica S/N, Col. Felicitas del Rio, C.P. 58040, Morelia, Michoacán, México
[4] Instituto de Investigaciones Económicas y Empresariales, Universidad Michoacana de San Nicolás de Hidalgo, Francisco J. Mújica S/N, Col. Felicitas del Rio, C.P. 58040, Morelia, Michoacán, México.

* Corresponding author: doctor.ambientalista@gmail.com

ABSTRACT

In recent years, the increase in petroleum prices has increased by more than 150%. At present, and in the society in which we live, it is difficult to imagine what would happen if in a very short period of time the price of a barrel of oil would grow to levels not tolerable for most economies. Renewable energy sources, which are distributed with greater or lesser abundance throughout the planet, have as an intrinsic characteristic, the fact that they are temporary and not completely storable. The electricity that can be produced from them cannot be stored in appreciable quantities either. For all these reasons, an element or vector is necessary to allow its transitory accumulation. Hydrogen has the energy power per unit mass almost three times higher than gasoline, and its storage, transportation and distribution are also feasible, which would allow its application to any segment of the demand, such is the case of the automotive industry. In this way hydrogen as a fuel has to be considered in the framework of a complete energy system. In this paper we compare some of the most important properties that the various fuel cells must have using hydrogen as a fuel for transportation use.

Keywords: Fuel cells; energy; motor vehicle; hydrogen technology

September 18th to 21st, 2018 in Mexico City, Mexico.

1. Introduction

Fuel cells are basically open thermodynamic systems. They operate based on present electrochemical reactions and reagents consumed from an external source [1-4]. They are favorable alternatives to conventional methods of electric power generation. Hydrogen and hydrocarbon fuels contain a significant amount of chemical energy compared to battery materials; In this sense, they have now been developed for numerous energy applications. The technology of fuel cells is a promising substitute for fossil fuels to provide energy to rural areas where there is no access to the public network or when the cost of wiring is huge, as well as the transfer of electricity. In addition, fuel cells can be used as a safe source of electrical power in uninterruptible power supplies (UPS), power generation stations and distribution systems. Table 1 shows a general comparison between fuel cell systems and other power generation systems [5-7].

Table 1 indicates that the highest performance is obtained in fuel cell systems, compared to conventional energy distribution systems. They have a simple design and also reliable operation. In addition, with the use of hydrogen as a reagent, these systems are friendly to the environment producing clean and silent energy [8-13]. Currently, fuel cell systems are widely used in small and large-scale applications, for example, in combined power and heat systems (Co-generation Heat Power/Combined Heat and Power, CHP), mobile power systems, laptops and military communication equipment.

Table 1. Comparison of fuel cells with other electric generation systems

	Alternative engine: diesel	Turbine generator	Photovoltaic	Wind turbine	Fuel cell
Capacity	500 kW – 50 MW	500 kW – 5 MW	1 kW – 1 MW	10 kW – 1 kW	200 kW – 2 MW
Efficiency	35%	29 - 42%	6 - 19%	25%	40 - 85%
Cost-capital ($/kW)	200 – 350	450 - 870	6600	1000	1500 - 3000
Operation-maintenance cost ($/kW)	0.005 - 0.015	0.005 - 0.0065	0.001 - 0.004	0.01	0.0019 - 0.0153

Despite all these advantages, there are some limitations in the use of fuel cells. For example, the useful life of the cells is shortened due to the voltage and impurities in both the flow of gases used, as well as in the materials that make up the elements of the cell, such as the anode-electrolyte-cathode of the cells. cells of solid oxides. Other challenges for the technological development of fuel cells are: optimizing the power density per unit volume, accessibility and durability of its components. It is worth mentioning that, although for several years no great progress was observed, the progress of these devices in recent years is evident.

2. Principle of operation of a fuel cell

The fuel cells generate electricity and heat through an electrochemical reaction that is actually an inverted electrolysis reaction. This happens between oxygen and hydrogen to form water. There are a variety of designs available for fuel cells, however, they all operate with the same basic principles. The main difference in the design of the cells is based on the chemical characteristics and the size of the electrolyte used in each one. Equation 1 shows the electrochemical reaction and figure 1 represents the operating principle of a fuel cell.

$$2H_2(g) + O_2(g) \rightarrow 2H_2O + energy \quad (1)$$

A fuel cell consists of four main parts: anode, cathode, electrolyte and the external circuit. At the anode, hydrogen is oxidized, resulting in protons and electrons, while at the cathode oxygen is reduced to oxide species, which react to form water. Depending on the electrolyte, protons or oxide ions are transported through an insulating ion conductor, while electrons travel through an external circuit to release electrical energy4. However, generally the fuel cells produce very small amounts of current, due to the small contact area between the electrodes, electrolyte and gas. Another problem that must be considered is the distance between the electrodes. To improve the efficiency of the cell and maximize the contact area, a thin electrolytic layer and high porosity electrodes are necessary for optimal gas penetration.

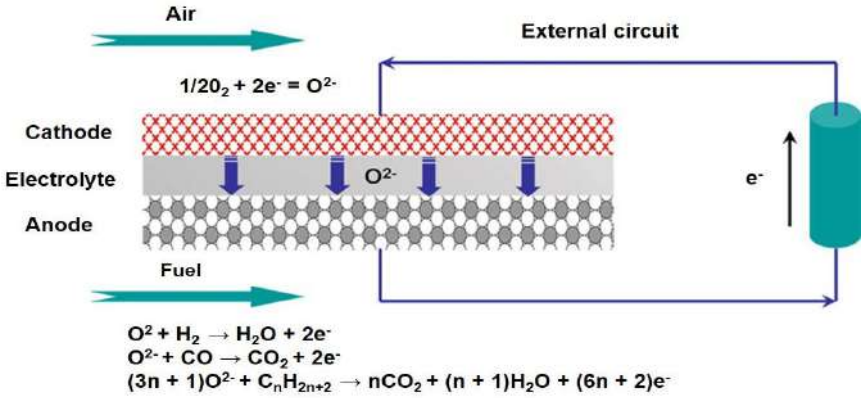

Fig. 1. Working principle of a solid oxide fuel cell.

The reaction between oxygen and hydrogen to generate electricity is different in the different types of fuel cells. In an acid electrolyte, the electrons and protons (H^+) are released from the hydrogen gas to the anodic electrode. The electrons generated pass through an external circuit and travel to the cathode while the protons pass through the electrolyte. This exchange releases electrical energy. Simultaneously, on the cathode side, water is formed as a result of the reaction

between the electrons of the electrode and the electrolyte protons. The reactions present at the anode and cathode are shown in equations 2 and 3:

$$Anode: 2H_2 \rightarrow 4H^+ + 4e^- \quad (2)$$

$$Cathode: O_2 + 4e^- + 4H^+ \rightarrow 2H_2O \quad (3)$$

Acid electrolytes and certain polymers that contain free H^+ ions are often called "proton exchange membranes". They are adequate and effective when used in proton functions, because they only allow H^+ ions to pass through them. In the event that electrons pass, the electric current is reduced [6].

3. Technical characterization of the fuel cells

The fuel cells can be classified according to their operating temperature, efficiency, applications and cost. As shown in table 2, in relation to the type of electrolyte are classified into six groups [14]: Alkaline Fuel Cell (AFC), Phosphoric Acid Fuel Cell (PAFC), Solid Oxide Fuel Cell (SOFC), Molten Carbonate Fuel Cell (MCFC), Proton Exchange Membrane Fuel Cell (PEMFC), Direct Methanol Fuel Cell (DMFC).

Table 2. Performance specifications in fuel cell technology

Fuel Cell	AFC	PAFC	SOFC	MCFC	PEMFC	DMFC
Electrolyte	KOH	H_3PO_4	YSZ	Molten carbonates	Nafion	Nafion
Anodic reaction	$2H_2+4OH^-\rightarrow 4H_2O+4e^-$	$2H_2\rightarrow 4H^++4e^-$	$O^{2-}(s)+H_2(g)\rightarrow H_2O(g)+2e^-$	$H_2O'+CO_3^{2-}\rightarrow H_2O+CO_2+2e^-$	$H_2(g)\rightarrow 2H^++2e^-$	$CH_3OH+H_2O\rightarrow CO_2+6H^++6e^-$
Cathodic reaction	$O_2+2H_2O+4e^-\rightarrow 4OH^-$	$O_2+4H^++4e^-\rightarrow H_2O$	$1/2O_2(g)+2e^-\rightarrow O^{2-}(s)$	$1/2O_2+CO_2+2e^-\rightarrow CO_3^{2-}$	$1/2O_2(g)+2H^++2e^-\rightarrow H_2O$	$3/2O_2+6e^-+6H^+\rightarrow 3H_2O$
Load carrier	OH^-	H^+	O^-	CO_3^-	H^+	H^+
Fuel	H_2 pure	H_2 pure	H_2, CO, CH_4, others	H_2, CO, CH_4, others	H_2 pure	CH_3OH
Oxidizer	O_2 (air)	O_2 (air)	O_2 (air)	O_2 (air)	O_2 (air)	O_2 (air)
Co-generation	No	Yes	Yes	Yes	No	No
Cell voltaje (V)	1.0	1.1	0.8 - 1.0	0.7 - 1.0	1.1	0.2 - 0.4

4. Fuel Cell Electric Vehicle (FCEV)

There are numerous applications of fuel cells. Each application demands its own requirements as well. Most applications of fuel cells can be classified as:

- High power applications: telecommunications, high technology facilities and data processing.
- Minimization or elimination of emissions: urban areas, industrial facilities, airports, cars, buses and regions with strict emission standards.
- Application in areas with limited access to the electricity supply network: portable uses and remote areas.
- Applicability in the management of biological waste gases: waste treatment plants.

Of all the applications of fuel cells, its use in a vehicle type FCEV, has attracted the most attention in recent years. Almost all vehicle manufacturers currently present research and development in FCEV vehicles. These, are a special type of electric vehicles built with a different structure to the internal combustion engine. In conventional vehicles with diesel fuel or gasoline, the energy is transmitted from the fuel from the engine to the wheels by a mechanical traction train; however, in a FCEV, the power of the train is obtained from electricity. Recent studies [15] indicate that a hybrid fuel cell car (FCEV) in combination of fuel cells and a battery system, provides in its entirety greater efficiency compared when only one FCEV is used. Therefore, the most important concern is to design and develop hybrid devices type FCEVs. To improve the efficiency of a vehicle by using a storage device, it is recommended to use a battery or an ultra capacitor "charge leveler". Another suggestion is to regenerate the braking power and use it for acceleration and on slopes or prolonged climbs.

Commonly, a stacking of PEMFC cells (Fig. 2) is used as the power source for a FCEV, due to its low operating temperature (about 80°C), power density, current, compact size, it is light, it presents fast initialization of the system and fast adjustment in the power output. Table 3 shows the car manufacturers involved in the research and development of FCEVs. It is noted that most manufacturers are using the PEMFC cell array.

Table 3. Automobile manufacturers involved in the research and development of FCEV

Company	Type of system	Fuel cell	Fuel
Daimler-Chrysler	Continuous fuel cell-hybrid battery	Direct-Indirect	Hydrogen-Methanol
Ford	Continuous fuel cell	Direct-Indirect	Hydrogen-Methanol
General Motors	Hybrid battery-battery cell	Direct-Indirect	Hydrogen-Methanol
Honda	Fuel cell-ultra hybrid capacitor	Direct-Indirect	Hydrogen-Methanol
Mazda	Fuel cell - hybrid battery	Direct	Hydrogen
Nissan	Fuel cell - hybrid battery	Indirect	Methanol
Renault	Fuel cell - hybrid battery	Direct	Hydrogen
Toyota	Fuel cell - hybrid battery	Direct-Indirect	Methanol
Volkswagen	Continuous fuel cell - hybrid battery	Direct-Indirect	Hydrogen-Methanol
ZeTech	Fuel cell - hybrid battery	Direct	Hydrogen

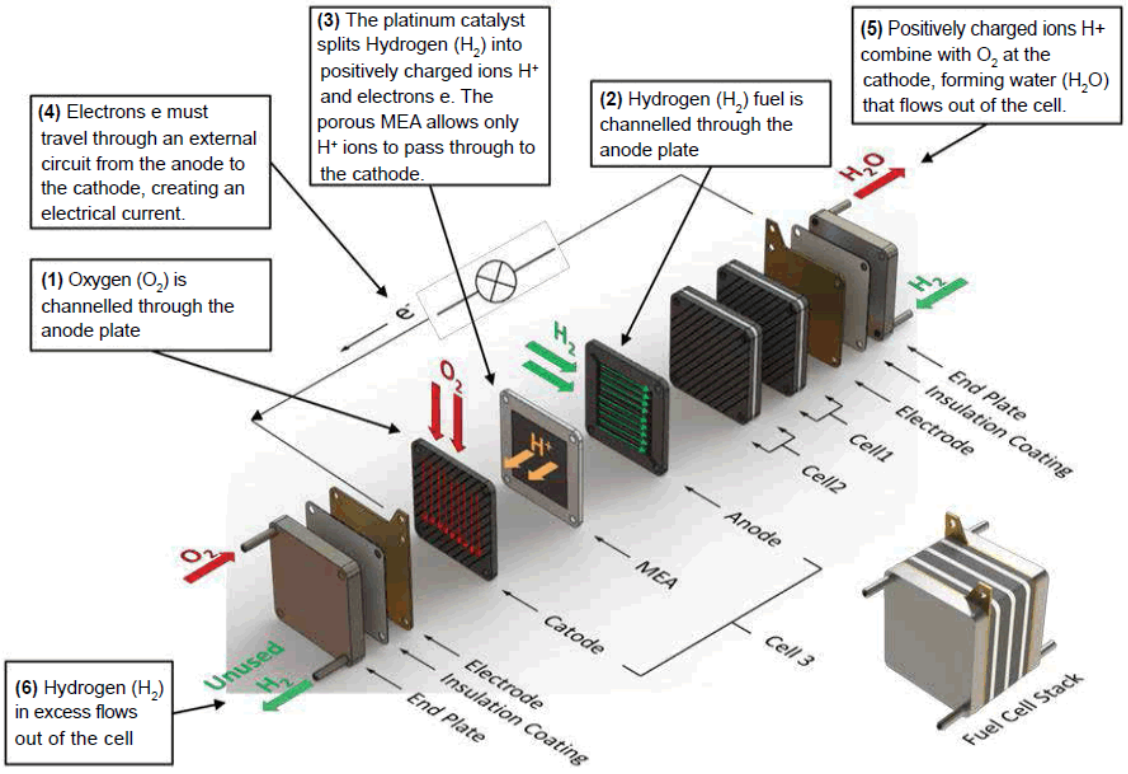

Fig. 2. Layout of a typical PEMFC stack.

5. Hydrogen fuel cell *vs* vehicles with internal combustion engine

In order to carry out the realization of the FCEV cars, the costly distribution of the infrastructure must be considered. The approximate cost of a hydrogen reformer in a cell is US $5000, while the cost of manufacturing a conventional engine is around US $3000. The cost of a hydrogen FCEV ranges from US $1500 to US $3000/kW, while the cost of an ICE is US $50/kW. In addition, the stations for the hydrogen service, require a high cost of capital to be built, approximately US $470,000. The modification of an average-sized gas station would cost around US $70,000. Therefore, the price of hydrogen FCEV vehicles must decrease and, in addition, other economic improvements are required to be able to carry out the commercial phase. The first FCEV car was presented by the Ford company. It was quite expensive, however, mass production helped significantly reduce costs [6]. Recent research mentions that, in Canada, the approximate cost of a car with a fuel cell is US $28,300 compared to US $21,700 for a car with an internal combustion engine. The results show up to 30% difference. Table 4 compares the price of the current ICEV vehicles with the FCEV cars. It is observed that the fuel cell contributes a very high cost to the total cost of the system. Although the cost of a FCEV car is greater than the ICEV, the costs of operation and maintenance seem to be convincing in the long term [16].

Table 4. Comparative costs between the conventional ICEV and FCEV

Propulsion system	**ICEV**	**FCEV**
Fuel	Gasoline	Hydrogen
Type of vehicle	Passenger	Passenger
Initial cost	US $21,717.65	US $21,717.65
Engine		
Credit by reduction of dimension		-US $6000.00
Fuel cell system		
Fuel cell		US $5195.04
Fuel tank		US $975.00
Electric motor		US $1558.51
Transmission of a stage		US $226.50
Battery		US $2597.52
Exhaust gases		-US $645.00
Vehicle		
Weight reduction		US $2400.00
Aerodynamics		US $225.00
Total cost of the vehicle	US $21,717.65	US $28,250.22

6. Conclusion

The comparison of the estimated capital costs between an ICEV and a FCEV shows that, although the latter is more expensive due to the costs involved with the modifications for the hydrogen system and infrastructure for its distribution, they are more convincing in the long term due to the operational and mechanical cost. Current fuel cell technologies need to be economically more accessible and overcome the advantages of existing technologies, so that they are more acceptable and therefore can be mass produced.

References

[1] Connihan MA. Dictionary of energy. Routledge and Kegan Paul; 1981.
[2] Fuel cell, Wikipedia, the free encyclopaedia. Available online at: http://en.wikipedia.org/wiki/Fuel cell [accessed 08.04.10].
[3] Cook B. An introduction to fuel cells and hydrogen technology. Vancouver, Canada: Heliocentris; 2001.
[4] Mark Ormerod R. Solid oxide fuel cells, the royal society of chemistry. Chem Soc Rev 2003; 32:17–28.
[5] Nahar G, Kendall K. Biodiesel formulations as fuel for internally reforming solid oxide fuel cell. Fuel Process Technol 2011; 92:1345–54.
[6] Larminie J, Dicks A. Fuel cell system explained. 2nd ed. United Kingdom: John Wiley & Sons; 2003.
[7] Winter M, Brodd RJ. What are batteries, fuel cells, and super capacitors? Chem Rev 2004; 104: 4245–69.
[8] Zhang X, Shen Z. Carbon fiber paper for fuel cell electrode. Fuel 2002; 81:2199–201.
[9] Larrosa-Guerrero A, Scott K, Head IM, Mateo F, Ginesta A, Godinez C. Effect of temperature on the performance of microbial fuel cells. Fuel 2010; 89:3985–94.
[10] Xu H, Kong L, Wen X. Fuel cell power system and high power dc–dc converter. IEEE Trans Power Electron 2004; 19:1250–5.
[11] DG Technologies. http://www.distributed-generation.com/technologies.html; 2005 [accessed 15.07.08].
[12] Rayment C, Sherwin S. Introduction to fuel cell technology. Notre Dame, IN, USA: Department of Aerospace and Mechanical Engineering, University of Notre Dame; 2003, May.
[13] Grove WR. On voltaic series and the combination of gases by platinum. Philos Mag J Sci 1839; XIV:127–30.
[14] Kirubakaran A, Jain S, Nema RK. A review on fuel cell technologies and power electronic interface. Renew Sustain Energy Rev 2009; 13:2430–40.
[15] Bitsche O, Gutmann G. Systems for hybrid cars. J Power Sources 2004;127 (1–2):8–15.

[16] Alvarado Flores, J. Estudio comparativo de las diferentes tecnologías de celdas de combustible. Bol Soc Esp Ceram V, 2013; 52 (3), 105-17.

XVIII International Congress
of the Mexican Hydrogen Society

Sustainable and efficient off-grid production of Hydrogen. Demo Project on-going in Spain

Rubén Galvéz[1*], Logan Lopéz[1], Estanis Oyarbide[1], Lorién Gracia[2], Pedro Casero[2], Edgar Bueno[2]

[1]Epic Power, Mariano Esquillor, Nave 3, Campus Río Ebro, 50018 Zaragoza, España
[2] Aragon Hydrogen Foundation, Parque Tecnológico Walqa, Ctra N330, km 556, 22197 Huesca, España
* Corresponding author: +34 665116331; rgalvez@epicpower.es

ABSTRACT

Work presented in this abstract is part of the Ely4Off Project, European FCH-JU, contract number 700359, whose objective is to demonstrate the viability of a system that integrates renewable energy and hydrogen produced by water electrolysis, in a completely off-grid and autonomous way. The system that generates green hydrogen is formed by a PEMWE (Polymer Electrolyte Membrane Water Electrolyser) industrial prototype of 56 kW that will be directly linked to track the solar photovoltaic power source producing over 1.5 tonnes of hydrogen per year for different end uses ensuring cold start and rapid response to changes. It will be managed by an autonomous Communication and Control system with a backup energy system formed by a fuel cell and batteries to supply during no radiation periods.
The off-grid situation and the impact of the photovoltaic source due to the variation in daily radiation should be taken into account to estimate communications and control protocols, hydrogen production and strategies to follow to achieve higher efficiencies. To determine them, several simulations and sensitivity analysis were done on a computer model.

Keywords (Maximum 4 words): PEM Electrolyser, Renewable Energy, off-grid, autonomous

1. Introduction

Nowadays, the adaptation of the electrolyser to the fully off-grid operation has still margin for improvement. PEM electrolysis is a very promising technology due to its dynamic response behaviour, an important parameter for renewable energy sources integration.

A direct coupling between the renewable source (photovoltaic in this study case) and the PEM electrolyser cannot reach the maximum power available. Thereby, we aim to design power

electronics that provides efficiency and flexibility in such a way the photovoltaic (PV) generation can present different sizes, in terms o power, to couple the same PEM electrolyser, considering literature. [1], [2], [3], [4].

The devices that are subject of this study are Direct Current to Direct Current (DC/DC) and include Maximum Power Point Tracker (MPPT) that extract the maximum power from the photovoltaic source in any moment through the correct control strategy, solving the issues of the direct coupling, as shown in **Fig.1**.

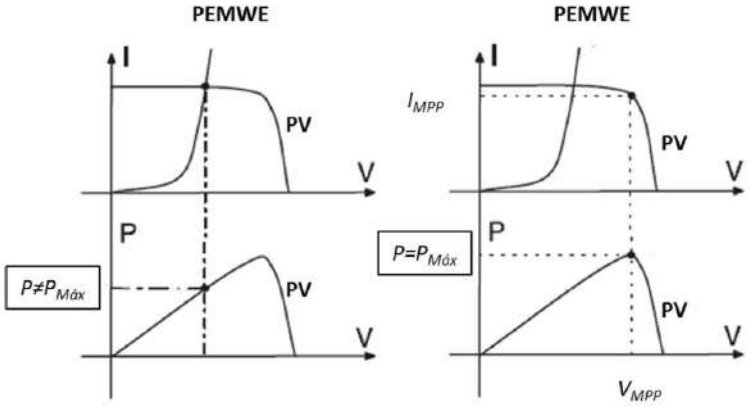

Fig. 1. Direct coupling (left) and DC/DC converter (right) configurations

In the de following document, the work developed to determine the behaviour of the DC/DC converters to operate in an efficient way coupling the photovoltaic energy to the required for the electrolyser is going to be detailed. The system has been modelled, simulated and tested in the laboratories.

Results show the designed converters with a reliable, robust, efficient, quick and dynamic response electronics, front the point of view of techno-economic criteria.

2. Analysis developed

In this section is going to be detailed the analysis carried out to evaluate the most promising configuration of the converters proposed. The main parameters that are objective of improvements and modifications are: Maximum Power Point Tracking (MPPT) efficiency, power sages chain efficiency, volume, weight, cost, control complexity and redundancy.

2.1 Power electronics architectures

The commercial architecture commonly used nowadays in applications such as this one is a solar inverter followed by an internal rectifier within the PEM electrolyser.

Different architectures have been analyzed. On the one hand, it would be useful to maintain the usual AC/DC rectifier located in the stack to supply the electrolyser from the grid; on the other hand, it is needed to simplify the supply chain and obtain the maximum production of

hydrogen. The analysis has been made taking into account these considerations and also the sensitive parameters mentioned before.

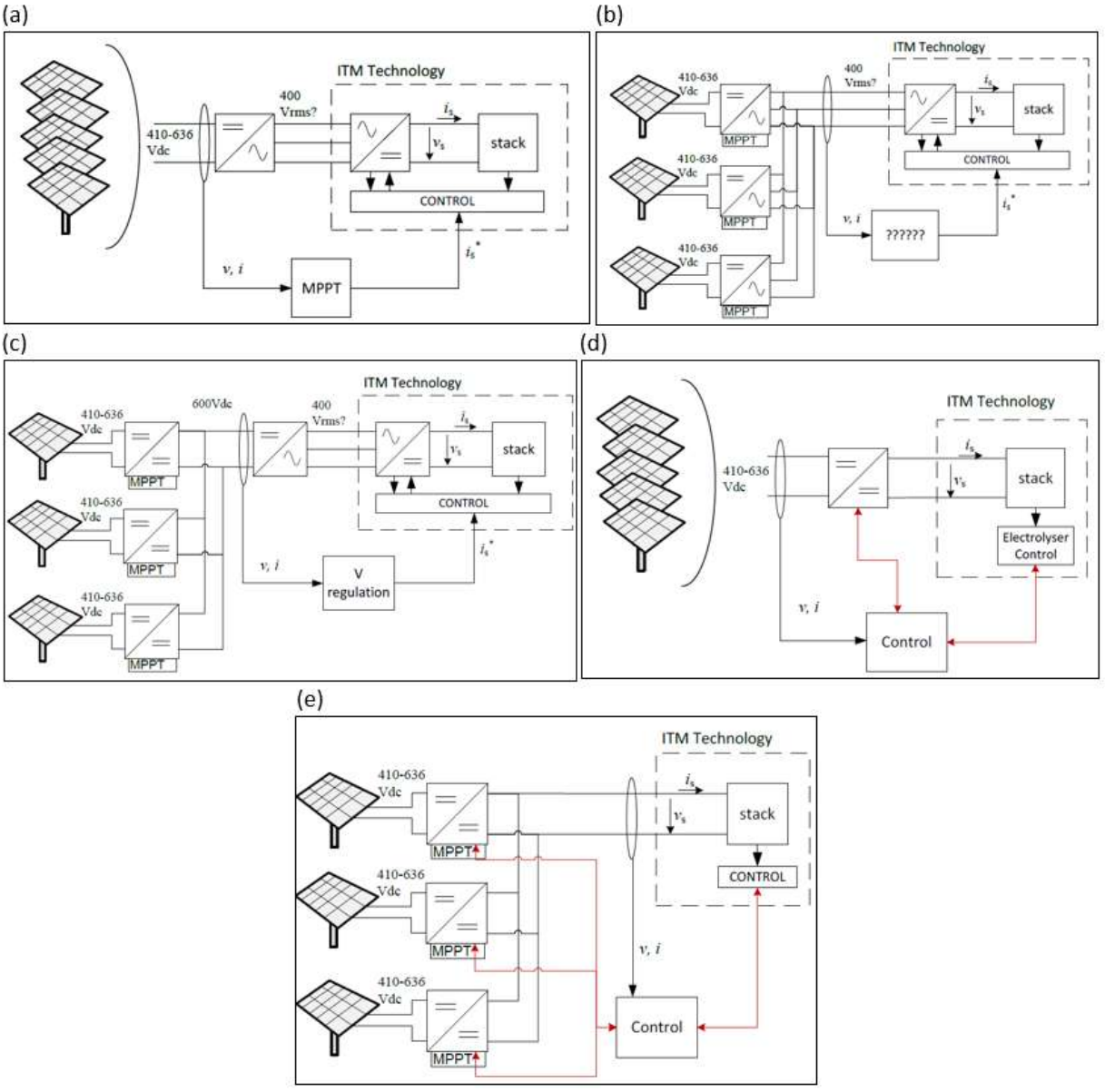

Fig. 2. Different architectures analyzed. (a) DC to AC and AC to DC architecture; (b) Parallelized DC to AC and AC to DC architecture; (c) DC to AC and AC to DC architecture with parallelized DC to DC; (d) DC to DC architecture; (e) Parallelized DC to DC architecture

Table 1. Technical analysis between architectures.

Architecture	MPPT efficiency	Power conversion efficiency	Volume	Weight	Architecture control complexity	Redundancy
a	Bad	Low	High	High	High	No
b	Good	Low	High	High	Very high	No
c	Good	Lowest	Highest	Highest	Very high	No
d	Bad	Good	Lower	Lower	Low	No
e	Good	Good	Lower	Lower	Low	Yes

After the analysis, the best solution is a parallelized DC to DC architecture, in order to obtain the maximum production of hydrogen and guaranteeing the operation of the electrolyser even if a converter fails, thanks to the redundancy of the architecture.

2.2 Topology section

The objective is to convert a high side of DC in the photovoltaic field bus into a low side DC bus in the electrolyser achieving high efficiency (>90%) and galvanic isolation as desired requirement.

Different topologies are analyzed in order to achieve these requirements:

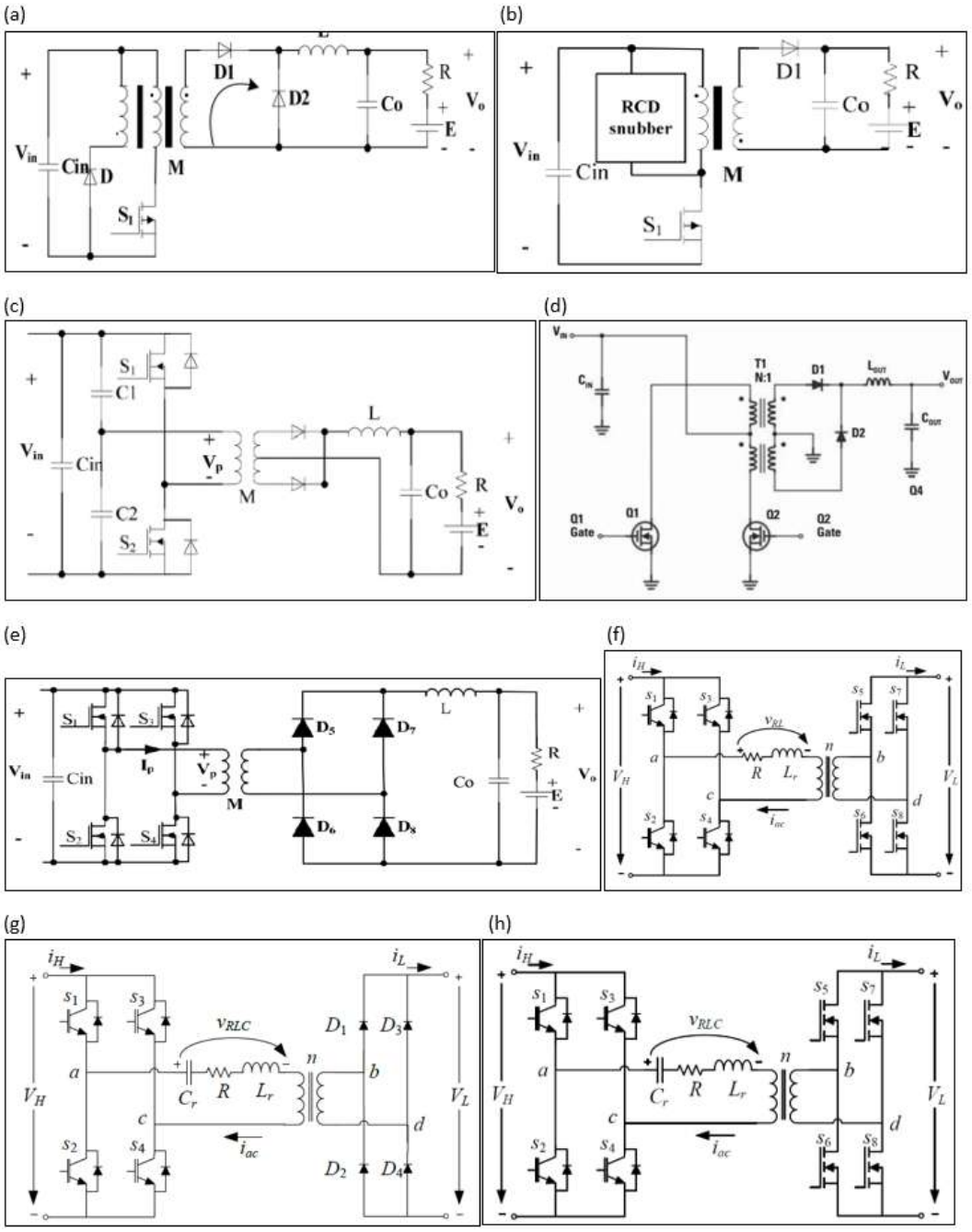

Fig. 3. Different topologies analyzed: (a) Forward; (b) Flyback; (c) Half bridge; (d) Push pull; (e) Full bridge; (f) Dual Activate Bridge (DAB); (g) Full Bridge LLC; (h) Dual Activate Bridge Series Resonant Converter (DAB-SRC)

Table 2. Techno-economic analysis between topologies

Topology	Device Stress	Power	Efficiency	Control	EMC/EMI	Cost
a	High	< 1 kW	Very low	Easy	Bad	High
b	High	< 1 kW	Low	Easy	Bad	Low
c	Medium	< 2 kW	Medium	Easy	Bad	High
d	High	< 6 kW	Low	Easy	Bad	Medium
e	Low	< 6 kW	Medium-High	Easy	Medium	Medium
f	Low	< 6 kW	Medium-High	Medium	Medium	Medium-High
g	Low	< 6 kW	High	High	High	High
h	Low	< 6 kW	Very High	High	High	High

The most suitable topology is a DAB-SRC converter as its efficiency is the best of all studied topologies and its devices are submitted to low stresses.

2.3 Efficiency improvement

The efficiency improvement is analyzed considering the proposed architecture of parallelized DC to DC and the proposed topology of DAB-SRC. Is well known that IGBT and MOSFET are the main transistor technologies used in this field, so the use of them is also included in the analysis.

Thereby, in order to increase the efficiency, both devices have been validated within the topology, including the two main parameters to be considered when analyzing switching losses: turn-off current and switching frequency.

Silicon Carbide (SiC) MOSFETs exhibits a much faster switching transient so the switching losses are drastically reduced. Hence, SiC MOSFETs are more promising to build high power converters with high power density. Although SiC materials have superior characteristics, the impact of SiC devices in systems must be carefully studied, given their higher cost.

A losses model is created to test the main characteristics of the device, and a large set of tests are carried out considering different turn-off currents, as shows the **Fig. 4.**

Using the losses model developed, it is possible to compute the improvement of power losses achieved by SiC technology under different operating conditions. Four stack voltages are studied (115V, 130V, 145V and 160V) and three power exchange levels are analysed (1200W, 2000W and 3600W). High side voltage is kept at 600V. **Fig. 4** shows the computed improvement of power losses in each case. The 115V/3600W case falls out of the operation range due to control mapping limitations.

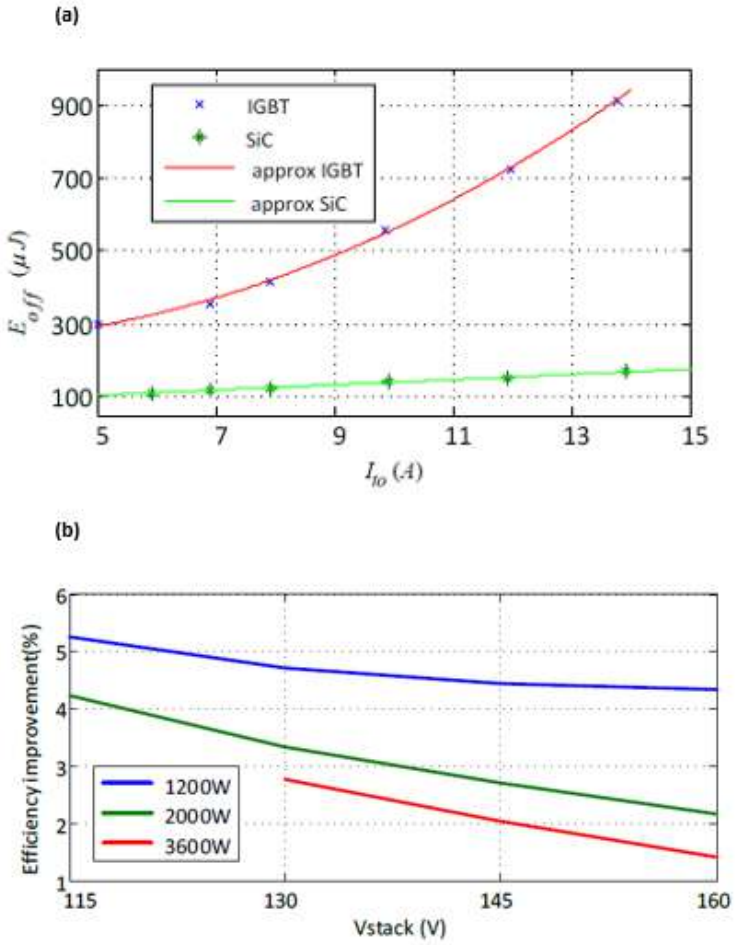

Fig. 4. (a) Measured and approximate turn-off losses for Vds=600V; (b) Estimated improvement of the efficiency

3. Results and discussion

As it can be observed in **Fig. 4**, thanks to the proposed control strategy combined with the SiC technology satisfactory efficiencies over 90% are obtained along all the operating range, or over 94% if only 1.2kW is converted.

SiC devices offer lower power losses than IGBT devices in some operation modes and ranges. So a simple IGBT-SiC replacement can improve the efficiency of the converter. Anyway, the impact of this advantage can be boosted if the design of the converter considers, in an a-priori basis, the use of SiC devices. Instead of balancing the power losses between the high-side IGBT and the low-side MOSFET devices, the control strategy seeks for minimum switching

losses at MOSFETs and concentrates the switching stress at IGBTs. Thus, the impact of the inclusion of SiC devices is magnified. The new DC/DC converter achieves efficiencies over 90% along almost all the operating range. The combination of the control strategy and the SiC devices leads to the possibility of non-stop permanent operation, which was not possible for an IGBT-based converter. Further efficiency improvement is still possible if two or more MOSFETS are parallelized.

The impact of the converters average efficiency is shown clearly if the production of hydrogen per year is analyzed, as it is shown in **Fig. 6**. The commercial solution needs two conversion stages, being reduced the general efficiency. For this solution, a commercial inverter from SMA Solar [5] has being considered and the internal rectifier of the electrolyser (confidential). Both devices operate most of the time over 90% efficiency, and below 96% [6] but adding together both stages the final efficiency is obviously lower than one single stage.

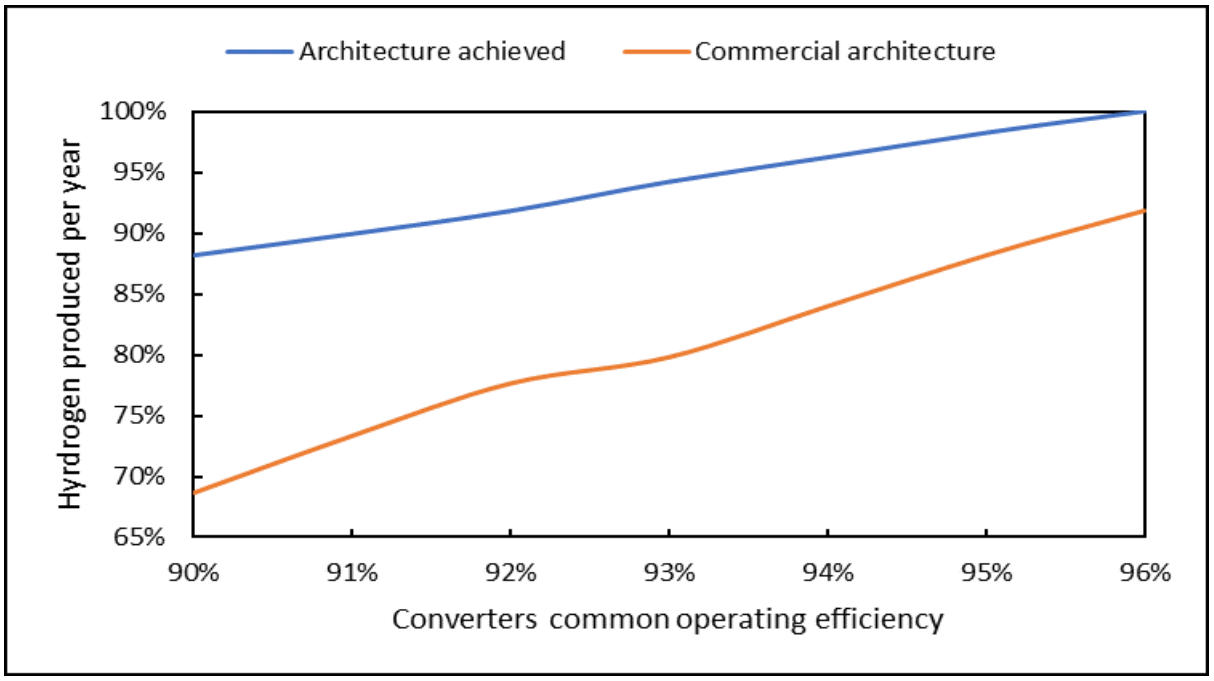

Fig. 5. The commercial architecture commonly used is based on commercial solar inverters and an internal rectifier of the PEM electrolyser, meanwhile the architecture achieved uses only one conversion stage of DC to DC. The architecture achieved (blue) shows how the production of hydrogen per year is higher because two conversion steps used in the commercial architecture is avoided (orange).

At the highest point of efficiency achieved (96%), the hydrogen produced at the end of the year is an 8,2% higher with the achieved solution than with the commercial one.

4. Conclusion

The new DC / DC converter achieves a series of objectives included in the project:

- An architecture that supplies the stack without the use of a rectifier and ensuring redundancy of the system when is coupled to photovoltaic strings.
- A topology that ensures efficiencies over 90% along almost all the operating range thanks to the combined use under a control strategy of IGBT and SiC MOSFETS.
- Quick response and use of Maximum Power Point Tracking to ensure the maximum power supply to the PEM Electrolyser.
- Higher green hydrogen production than with the commercial systems.

Acknowledgements

The project to which this study belongs has received funding from the Fuel Cells and Hydrogen 2 Joint Undertaking under grant agreement No 700359. This Joint Undertaking receives support from the European Union's Horizon 2020 research and innovation programme and Hydrogen Europe and N.ERGHY. The project is developed by five partners from different locations of Europe, being the main driver of this study the Spanish company Epic Power.

References

[1] Solmecke H, Just O, Hackstein D. Comparison of solar hydrogen systems with and without power electronic DC/DC converters. Renew Energy Jan-Feb 2000;19(1e2):333e8

[2] Maeda T, Ito H, Hasegawa Y, Zhou Z, Ishida M. Study on control method of the stand-alone direct-coupling photovoltaic e water electrolyzer. Int J Hydrogen Energy March 2012;37(6):4819e28.

[3] Paul B, Andrews J. Optimal coupling of PV arrays to PEM electrolysers in solarehydrogen systems for remote area power supply. Int J Hydrogen Energy, Jan 2008;33(2):490e8

[4] Garrigos A, Blanes JM, Rubiato J, Avila E, García CG, Lizan JL. Direct coupling photovoltaic power regulator for stand-alone power systems with hydrogen generation. Int J Hydrogen Energy Oct 2010;35(19):10127e37.

[5] SUNNY ISLAND 6.0H / 8.0H. SMA Power Technology

[6] Juwi Solar GmbH. Solar Stand-Alone Power and Backup Power Supply. SMA Power Technology

XVIII International Congress
of the Mexican Hydrogen Society

Hydrogen production by the reaction between water and the intermetallic AlLi activated by mechanical milling

D. L. Alvarez Acosta[1,2], J. L. Iturbe García[1,*]

[1]Departamento de Química, Instituto Nacional de Investigaciones Nucleares, Carretera México-Toluca s/n, La Marquesa, C.P. 52045, Ocoyoacac, Estado de México, México
[2]Facultad de Química, Universidad Autónoma del Estado de México, Paseo Colón y Tollocan s/n, C.P. 50000, Toluca, Estado de México, México
* Corresponding author: joseluis.iturbe@inin.gob.mx; Tel. 5553297200 ext.12274

ABSTRACT

Hydrogen is the most abundant and simplest element in the universe and is considered as a possible clean and reliable alternative in its use as a fuel that can reduce the emission of greenhouse gases and environmental deterioration, however, the main limitation is the lack of availability to obtain hydrogen from renewable energy sources. In this work the results of hydrogen production are presented from the direct reaction between the AlLi compound and water at normal conditions of pressure and temperature. Activation of the compound was performed by mechanical milling in a spex-type high energy mill in an 80:20 percentage ratio for Al and Li respectively with an Ar atmosphere, where the modified parameter was the milling time from 0.5 to 10 hours. The reaction was carried out from 20-100 mg of compound by adding distilled water. The quantification of hydrogen was performed with a graduated cylinder by liquid displacement. Compounds activated by mechanical milling as well as obtained after the reaction were characterized by X-ray diffraction (XRD) to determine the phases that contributed effectively in the production of hydrogen. The milling time of 3 hours was the most favorable to carry out the reaction between AlLi material and water. The volume of hydrogen obtained was 1700 mL/g. This value is greater than that obtained only by the hydrolysis of Li, therefore, the Al has a significant contribution in the volume of hydrogen produced. Consequently, the compound (AlLi)-water reaction is a promising method for hydrogen generation in a simple way and in relatively short times compared with other hydrogen production methods.

Keywords: AlLi compound, mechanical milling, hydrolysis, hydrogen generation

1. Introduction

The energy economy based on fossil fuels is considered unsustainable due to air pollution caused by the emission of large amounts of greenhouse gases (GHGs). The global energy system main inputs used as oil, coal and natural gas [1]. However, when fossil fuels are used as well as some of their derivatives or coal in ground, marine or air transport, large amounts of CO_2 are emitted that affect the environment. Therefore, it is essential to incorporate new fuels that do not generate greenhouse gases, which should be beneficial to health and the environment. This is the main reason why scientists around the world are trying to get mainly by burning fuels that avoid emitting greenhouse gases and can meet current and future global energy requirements and mitigate environmental degradation. The search for new energy sources is focused on the so-called hydrogen technology. This element is a renewable and environmentally friendly fuel with high calorific value [2,3] and an important energy carrier could play a fundamental role in reducing GHG emissions (see Table 1).

Table 1. Calorific value of various fuels [3].

Fuel	HHV (MJ/kg)
Hydrogen	141.9
Methane	55.5
Ethane	51.9
Gasoline	47.5
Diesel	44.8
Methanol	20

Today, the best known technologies for hydrogen production are natural gas reforming, bio-derived liquid reforming, coal gasification, water electrolysis and thermochemical, photoelectrochemical and biological processes, among others [4]. Another promising way to generate hydrogen is through the metal-water reaction, which can also be applied in energy storage, besides the metal oxides can be deoxidized and reused, this process can be considered as effective, safe and easy to use [5-7]. Current research has used metals such as Al, Zn and Mg to generate hydrogen and of these one, Al has been considered as the most viable candidate for this purpose [8] with Al being the most abundant metal in the earth's crust, with a high performance and that presents the advantage of being recycled [4]. Under normal conditions of pressure and temperature, it is possible to obtain 1245mL of H_2 per gram of aluminum by reacting completely [9]. However, one disadvantage of aluminum is the formation of an oxide layer on its surface, which limits the direct contact with water and thus difficult the reaction to obtain hydrogen efficiently. Other studies have focused on minimizing the oxide and proposed several effective methods for hydrogen production by forming Al alloys by mechanical alloying using fine particles and adding additives (alkalis, metal oxides, salts, hydrides, etc.) [10-13]. Mechanical alloying has the advantage of avoiding the loss by evaporation of molecules from metals with low melting during the preparation of alloys [7]. On the other hand, lithium is an

active metal that can react with water to produce hydrogen, it can also be added to obtain AlLi alloys and promote the activity of aluminum. It has been reported that the Li content has a considerable effect: when the concentration of Li is increased, the formation of lithium hydroxide LiOH is also higher which accelerates the hydrolysis of aluminum with water, thereby improving the reaction yield [14]. The Li content contributes considerably in the formation of the AlLi alloy by changing the AlLi compound to Al_2Li_3 and Al_4Li_9 when the lithium increases from 10 to 30 and 40% by weight respectively [15]. However, Chen et al. (2014) showed that this parameter not only affects the production of hydrogen, but also in the mechanical alloying with low concentration of Li causes agglomeration of particles and when the amount of Li decreases, these effects are more frequent. Consequently, when materials are prepared by mechanical alloying method it is common to add small amounts of process control agents or some additives to reduce the agglomerates, although the composition of the alloy becomes more complex, which causes some difficulties when the metal is recycled [16]. In the present work the elements of Al and Li with 20% by weight of Li were used, which were activated by mechanical milling at different milling times and without adding any process control agent, the reaction with water was carried out under normal conditions of pressure and temperature to generate hydrogen. The volume of H_2 obtained for each sample was compared according to the milling time and by X-ray diffraction the phases involved in hydrogen production were identified.

2. Materials and Methods

The metals used in the preparation of Al-Li compound were Al (Aldrich Chemistry) in granular form with particle sizes of approximately one mm and purity of 99.7%, and Li (Alfa Aesar) granular with particle sizes of 1-6 mm and purity of 99.4%. The content of metals was with a percentage ratio of 80:20 by weight for Al and Li respectively. The preparation of the AlLi phases was carried out by mechanical alloying with a spex high energy mill, the container and the milling media are made of stainless steel. Manipulating metals before milling was performed under Ar atmosphere. In each experiment were prepared approximately 5 g of compound with a ball/powder ratio of 5:1 using three milling media of 12 mm in diameter. The AlLi compounds were obtained with milling times of 30 minutes up to 3 hours. Hydrogen production was carried out in a glass vial of 100 mL sealed with a rubber stopper so that has a device with a hose through which the gas passes. The AlLi compound in powder form were placed from 20 to 200 mg, the reactions were carried out by adding a certain volume of distilled water in a gradual and slow manner because the reaction is exothermic. The volume of hydrogen was quantitated by liquid displacement using a graduated cylinder. The by-product after finishing the reaction was dried on a grill at controlled temperature. The samples before and after milling as well as the by-product obtained were characterized by X-ray diffraction technique using a Discover D8 Diffractometer. The scanning electron microscope (JEOL 5900 LV) equipped with a probe microanalysis energy dispersive X-ray (EDAX) were also used to determine the morphology and chemical composition of the samples.

3. Results and Discussion

Figure 1A shows a micrograph of aluminum pellets used in the preparation of the AlLi compound. The image shows particles with abnormal morphology since at naked eye are seen circularly and silver colored, however in a microscopic view as shown in the image are irregular, the form of this material may be due to the preparation method since it does not have a specific shape, on the image and according to the scale its size is greater than one mm, the particles have irregularities since at most one of its ends are narrower and the opposite side are wider, on the surface a series of overlapping plates with irregularities in all the granules is noted. The shape of these particles may be due to the preparation method as in some cases these metals are synthesized by electrolysis of some of their molten salt. The micrograph was obtained at a magnification of 50 enough to appreciate in detail these particles, these increases depend on their size because larger they are, less increases are required to visualize them. On this occasion, the electron beam with a power of 20 kV was used. Generally, these particles show a pattern in the thinnest part are folded.

Figure 1B represents an image of a metallic lithium granule in which a series of lines is observed on its surface as if the particle had undergone a cross section, the front is flat and the rest with cumulus. This material is very difficult to handle since it is a very reactive element to the environment especially reacts rapidly with humidity. Handling for its analysis by scanning electron microscopy was carefully carried out in an inert atmosphere in a glove box with argon atmosphere. Before analysis was quickly coated with a gold layer to prevent electric charge on while avoiding contact with the environment especially water. This analysis was performed at 40X, enough to see surface details.

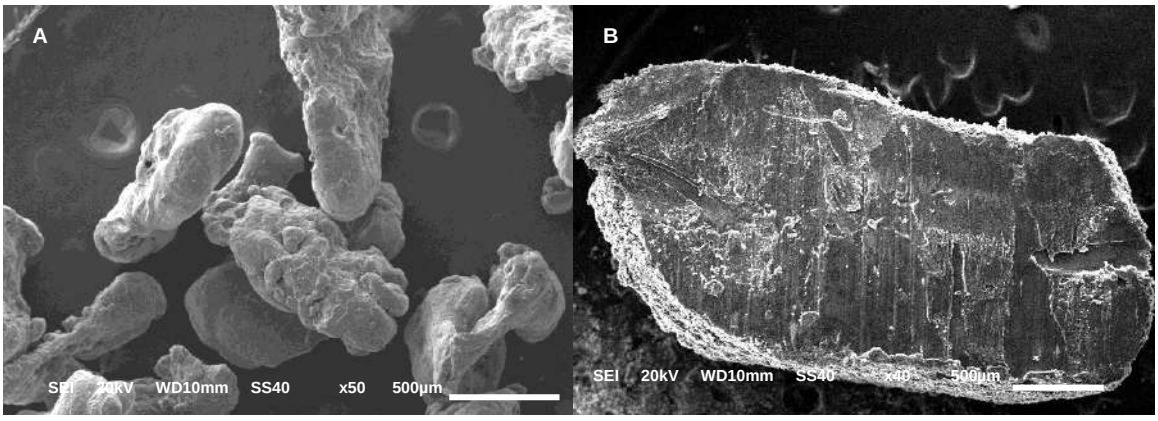

Fig. 1. Micrographs of aluminum and lithium A and B respectively used in the the preparation of the AlLi compound by mechanical alloying.

Figure 2 shows another image corresponding to the AlLi material which was obtained by mechanical alloying process for 3 hours with this milling time, clusters were obtained, which are formed by small particles. The analysis was obtained at 100X, is an overview of the powders which shows clearly the physical change of the material, the particle sizes are completely different from the original metals which are shown in previous images (Figs. 1A and 1B). The metal processing is performed depending on the milling time due to the high impact between the container walls and the milling media produced by the movement of the engine which is transmitted to the system where the container is placed. Another important factor that affects the transformation process of the material is due to the size of the milling media. In these experiments (12 mm), the metals are exposed to high pressures at each instant within the system causing the change in their morphology. During this process there is the phenomenon of fusion between these two metals due to their physicochemical characteristics which are considered soft metals and the fusion takes place much easier and in short milling times.

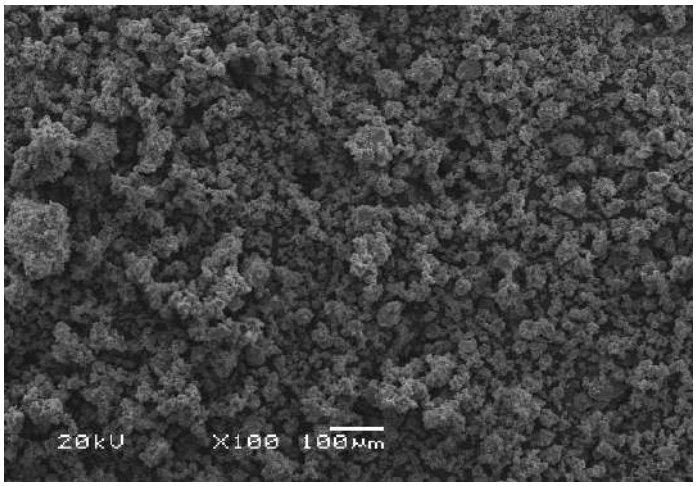

Fig. 2. Micrograph of AlLi powders milled for 3 h.

Figure 3 shows five diffraction patterns which correspond to the aluminum and the compounds obtained according to different milling times. It should be mentioned with respect to Li that this element can not be observed by the diffraction technique due to its low atomic number. The spectrum a) corresponds to the aluminum where five characteristic peaks of this metal appear which are in the range of 35 to 85 degrees in 2θ. The identification of their intensities was carried out with the JPDS card 04-07-87. The following spectra, b), c), d) and e) correspond to samples whose milling times were 30 minutes, 1, 2 and 3 hours, where two phases were obtained, which correspond to $Al_{8.9}Li_{1.1}$ and AlLi identified according to cards 65-49-05 and 65-75-33 respectively. In this sequence it is observed how the aluminum and lithium metals are transformed as a function of the milling time in both phases (AlLi and $Al_{8.9}Li_{1.1}$). The intensities of the phase $Al_{8.9}Li_{1.1}$ resemble those of the Al which can be differentiated with JPDS cards according to their respective reported values. The AlLi phase presents deflections completely different from those

of aluminum as seen in the different spectra where the peaks are well separated from one another throughout the spectrum. The angle 2θ of 38.473 corresponds to the main peak of aluminum, while the value of the main peak of phase $Al_{8.9}Li_{1.1}$ in angle 2θ is 38,506, that is, there is a difference in these values of 0.033. The displacement of the peaks indicates that the AlLi alloy was formed from 30 min of milling. To verify the formation of the phases, they were analyzed in detail comparing each aluminum peak with those of the $Al_{8.9}Li_{1.1}$ and AlLi phases, for which the extension of each intensity of the different spectra was carried out.

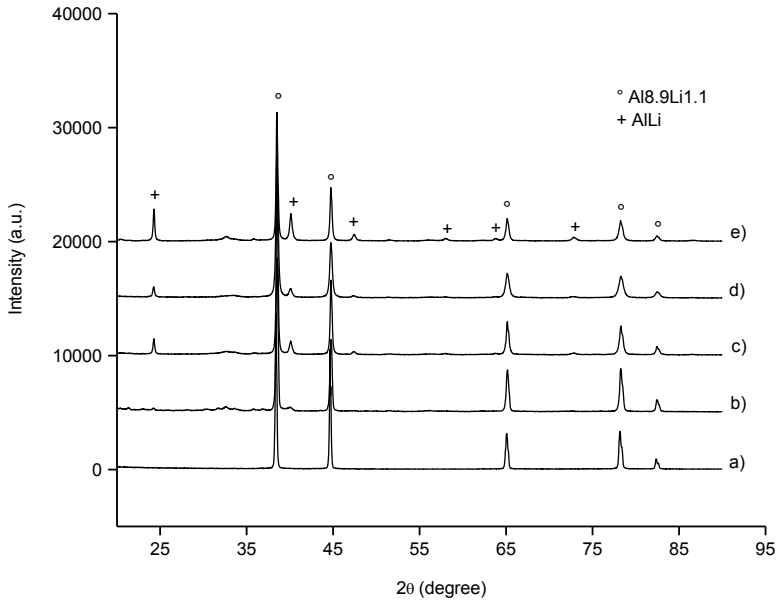

Fig. 3. Al-diffractograms and phases of $Al_{8.9}Li_{1.1}$ and AlLi as a function of milling time.

Figure 4 shows the main peak of both aluminum and $Al_{8.9}Li_{1.1}$ and AlLi phases amplified depending on the milling time, this comparison could be better appreciated in detail on the figure where the interval between the values of 33 to 44 degrees in 2θ was considered. As can be seen in the spectra, there is great similarity between the aluminum intensities and those of the $Al_{8.9}Li_{1.1}$ phase, therefore the comparison was performed in the five peaks of both compounds. Expanding each one, all presented displacements which were corroborated with their respective values reported for each of them. In the spectra, the main aluminum peak (fig a) was considered, which was compared with the angle value of the $Al_{8.9}Li_{1.1}$ phase. According to their respective values there is clearly a displacement of the aluminum peak with respect to the $Al_{8.9}Li_{1.1}$ phase. It is also observed that when the milling times pass, the peaks are wider in both phases AlLi and $Al_{8.9}Li_{1.1}$, because the size of the particles are smaller. This is one of the characteristics of the mechanical alloying technique because when using long times, the materials tend to become amorphous. On the other hand, the displacement value (0.033) indicates that the alloy has been

formed in the two mentioned phases. It is important to mention that the milling time was short (30 min) in the formation of the alloy considering the metals of Al and Li used in this work.

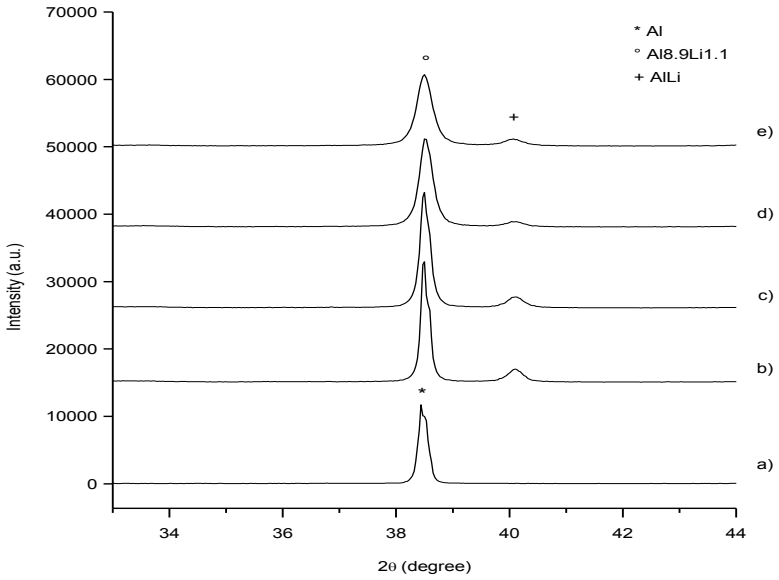

Fig. 4. Amplification and comparison of the main peak of the Al and the phases $Al_{8.9}Li_{1.1}$ and AlLi depending of the milling time.

In all experiments, after the mechanical alloying process, the material was allowed to passivate inside the container for 18 h to avoid spontaneous oxidation of the alloy. The Al 80 and Li 20% by weight ratio in all preparations was maintained. The alloys obtained were considered to perform the reaction with water to generate hydrogen.

Figure 5A shows the generation of hydrogen as a function of milling time, various time periods were considered to determine the optimal and programmed shorter time was 30 min milling under these conditions the hydrogen volume produced was 400 mL/g, it is assumed that at this time the formation of phases AlLi and $Al_{8.9}Li_{1.1}$ begins, which are the ones that react with water to produce hydrogen. On the other hand, also influences the particle size of the aluminum since according to the results of scanning electron microscopy even relatively large particles of Al were observed. This indicates that there is a limit of size to react with lithium and water and thus obtain the maximum volume of hydrogen. Another milling was programmed to 40 min, the volume value of hydrogen is clearly seen in the curve produced in only 10 min of difference from the previous milling. The volume of hydrogen obtained this time was 1500 mL/g. As the milling time was longer the volume of hydrogen produced also increased reaching the plateau which was obtained after 3 h of milling. The maximum volume of hydrogen obtained with this milling time was 1700 mL/g of material. Under these conditions, the particle size was uniform resulting

reaction throughout the material to produce the maximum volume of hydrogen. Other milling times of 5 and 10 h were programmed, however the volume of hydrogen remained almost constant which was obtained at 3 h of milling being the most suitable to produce the largest volume of hydrogen. It is assumed that after 3 h of milling the phases of AlLi and $Al_{8.9}Li_{1.1}$ were completely obtained which react with water to produce hydrogen.

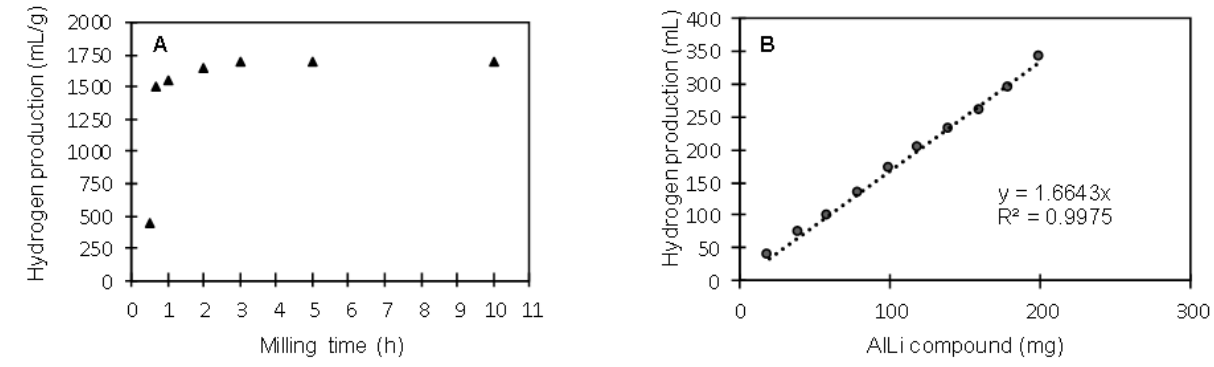

Fig. 5. Hydrogen production as a function of milling time (A) and volume of hydrogen depending on the amount of material used in the reaction with water (B).

Figure 5B shows the volume of hydrogen with respect to the amount of the alloy considered. Each point represents a value of the material which reacts with water. The amounts of the powders were from 20 to 200 mg. The quantities considered were small because the reaction between the AlLi material and the water was carried out quickly and vigorously. However, it is seen in the curve for a linear trend in the production of hydrogen according to the amount of material used. This is an important point since in principle any amount of material can be reacted with water and obtain large volumes of hydrogen. Under these experimental conditions, the reactions between the alloy (AlLi and $Al_{8.9}Li_{1.1}$) and the water were carried out under ambient conditions without adding catalysts to initiate the hydrogen production process. In this work, using the method of mechanical milling to produce alloy proved to be very favorable since the synthesis of the material was performed in only 3 h to obtain powders of nanometric size where the reaction with water was carried out in a simple way and fast.

The different events produced during the alloying process make it possible to quickly carry out the fusion of Al and Li metals without the need to use energy to reach their respective melting points and transform them into liquid phases. Mechanical alloying technique avoids these conditions besides the metals used in this work are considered soft metals which facilitates the preparation of the alloy. Throughout the process of production of hydrogen, no greenhouse gases are generated. Metals Al and Li should be handled in a controlled atmosphere to avoid during mechanical milling oxide formation since these two metals react rapidly with oxygen and humidity.

4. Conclusion

In this work AlLi and $Al_{8.9}Li_{1.1}$ phases were prepared from a ratio of 80% Al and lithium 20% in weight by mechanically alloying. Al and Li metals were easily melted with short milling times by using 12 mm diameter milling media causing greater impact with the container walls. Alloy formation began after 30 min of milling time with maximum 3 h. Likewise, the phases that reacted with water to produce hydrogen were identified. The reaction between AlLi and $Al_{8.9}Li_{1.1}$ phases and water were very fast which was controlled by the volume of water through drip. The volume of hydrogen obtained was 1700 mL/g of material. Alloy synthesis from Al and Li by mechanical alloying technique opens a possibility of obtaining a larger scale hydrogen. Throughout the process used in this work to produce hydrogen, unlike traditional methods, does not cause emission of greenhouse gases.

Acknowledgements

The authors thank the staff of XRD and SEM for their valuable support in carrying out the corresponding analyzes.

References

[1] Da Silva Veras T, Simonato Mozer T, da Costa Rubim Messeder dos Santos D, da Silva César A. Hydrogen: Trends, production and characterization of the main process worldwide. International Journal of Hydrogen Energy 2017; 42:2018-2033.

[2] Dincer I. Green methods for hydrogen production. International of Hydrogen Energy 2012; 37:1954-1971.

[3] Nikolaidis P, Poullikkas A. A comparative overview of hydrogen production processes. Renewable and Sustainable Energy Reviews 2017; 67:597–611.

[4] Franzoni F, Milani M, Montorsi L, Golovitchev V. Combined hydrogen production and power generation from aluminum combustion with water: Analysis of the concept. International Journal of Hydrogen Energy 2010; 35:1548–1559.

[5] Dincer I, Acar C. Review and evaluation of hydrogen production methods for better sustainability. International Journal of Hydrogen Energy 2015; 40(34): 11094-11111.

[6] Yavor Y, Goroshin S, Bergthorson JM, Frost DL, Stowe R, Ringuette S. Enhanced hydrogen generation from aluminum water reactions. International Journal of Hydrogen Energy 2013; 38(35): 14992-15002.

[7] Wang HZ, Leung DYC, Leung MKH. A review on hydrogen production using aluminum and aluminum alloys. Renewable and Sustainable Energy Reviews 2009; 13: 845-853

[8] Kravchenko OV, Semenenko KN, Bulychev BM, Kalmykov KB. Activation of aluminum metal and its reaction with water. J Alloys Compd 2005; 397: 58–62.

[9] Huang X, Gao T, Pan X, Wei D, Lv C, Qin L, Huang Y. A review: Feasibility of hydrogen generation from the reaction between aluminum and water for fuel cell applications. Journal of Power Sources 2013; 229: 133-140.

[10] Tousi SSR, Szpunar JA. Effect of addition of water-soluble salts on the hydrogen generation of aluminum in reaction with hot water. Journal of Alloys and Compounds 2016; 679: 364-374.

[11] Liu Y, Wang X, Liu H, Dong Z, Li S, Ge H, Yan M. Effect of salts addition on the hydrogen generation of Al-LiH composite elaborated by ball milling. Energy 2015; 89: 907-913.

[12] Shu LI, De-yu GAN, Yun-feng ZHU, Ya-na LIU, Ge ZHANG, Li-quan LI. Influence of chloride salts on hydrogen generation via hydrolysis of MgH2 prepared by hydriding combustion synthesis and mechanical milling. Trans. Nonferrous Met. Soc. China 2017; 27: 562−568.

[13] López-Miranda JL, Rosas G. Hydrogen generation by aluminum hydrolysis using the Fe2Al5 intermetallic compound. International Journal of Hydrogen Energy 2016; 41: 4054-4059.

[14] Chen X, Zhao Z, Hao M, Wang D. Hydrogen generation by splitting water with Al-Li alloys International Journal of Energy Research 2013; 37(13): 1624-1634.

[15] Fa M, Sun LX, Xu F, Mei D, Chen D, Chai W, Huang FL, Zhang QM. Microstructure of AlLi alloy and its hydrolysis as portable hydrogen source for proton-exchange membrane fuel cells. International Journal of Hydrogen Energy 2011; 36: 9791-9798.

[16] Chen X, Zhao Z, Liu X, Hao M, Chen A, Tang Z. Hydrogen generation by the hydrolysis reaction of ball-milled aluminium-lithium alloys. Journal of Power Sources 2014; 254: 345-352.

XVIII International Congress
of the Mexican Hydrogen Society

Design of an oxy-hydrogen system to be implemented in internal combustion engines of motorcycle

U. Maza-Nájera[1*], J. M. Sandoval-Pineda[1], R. González-Huerta[2], M. Rico-Cortez[3]

[1]Instituto Politécnico Nacional, ESIME-Azc., SEPI, Av. de las Granjas 682, Col. Santa Catarina, CP 02250, CDMX
[21]Instituto Politécnico Nacional, ESIQIE, Laboratorio de Electroquímica y Corrosión, UPALM, CP 07738, CDMX
[31]Instituto Politécnico Nacional, ESIME, SEPI, Edificio 5 tercer piso, UPALM, CP 07738, CDMX
* 5564107134 ulisesmaza94@gmail.com

ABSTRACT

The oxy-hydrogen production capacity of an electrolyzer (NL/min) is an important parameter for judging the performance of an electrolyzer. According to the need of energy or hydrogen, electrolyzers of different scales are designed to meet the varying needs of the end users. An electrolyzer can vary from the several W to several kW in terms of power consumption. Considering the volume of the electrolyzer (L_E) and the H_2 production rate, the unit of NL_{H2}/(L_E kWh min) symbolizes the mobility, energy consumed and capacity of the electrolyzer. From the safety point of view, the wide range of the flammability limits of H_2/O_2 mixture demands careful design of the system configurations. Leakage of the electrolyte is also a safety issue. Due to the corrosive nature of the electrolyte, the leakage is more likely to occur at the connections and the seals.
The present research work shows the design of an Oxy-hydrogen system to be implemented in internal combustion engines of motorcycle. The Quality Function Deployment (QFD) methodology was used in order to design of the electrolyzer and its components. The durability is also an important criterion for electrolyzers. Materials for system construction determine the electrolyzer lifetime, the selection of materials was carried out through the CES Edupack® software and the Ashby methodology. Based on the results obtained from the application of the QFD methodology, three design alternatives are proposed, which were modeled with the help of the SOLIDWORKS® Software. The virtual final design is presented, which consists of a deposit for four electrolysis cells, with square spirals electrodes connected in series. The operating condition will be 10 A-12 V to obtain an Oxyhydrogen production of 0.546 NL/min.

Keywords: Alkaline Electrolysis; Automotive Vehicles; Electrolyzer Design

1. Introduction

Currently we are living in a time of constant change, one of the most important is in the energy sector, because there is a migration from the use of fossil resources to resources derived from renewable sources, in our country about 46% of energy is consumed in the transport sector, such as air, rail and automotive. This is one reason because the use of various alternative fuels has been considered to reduce environmental pollution and respond to energy demand in the sector. There are several alternative fuels, such as ethanol, biodiesel, LP gas, hydrogen, among others. Of these options, hydrogen is considered one of the best because it can be used as a fortifier of traditional fuels gonzalez [1]. Hydrogen is often seen as the fuel of the future, because it can store intermittent energies such as solar and wind power uleberg [2].

One of the disadvantages of using hydrogen is that it is not free in nature, it is necessary to use some process to obtain it, such as: -Reforming of natural gas, -Gasification of coal, -Petroleum casting, -Gasification and reforming of heavy crude and finally -Electrolysis of water Tolentino [3]. Most of these methods are still pollutants and have high costs, except for the electrolysis of water, this is a simple and flexible method that can also be complemented as mentioned above with renewable energies such as the sun or wind, obtaining hydrogen is carried out by separating the molecules of water (H_2O) into hydrogen and oxygen, this with the help of a current passage through the electrodes, PEM and alkaline electrolysis exist, this work focuses on alkaline electrolysis, alkaline electrolysis cells consist of a pair of electrodes, positive and negative, a source of electrical current, the electrolytic substance normally NaOH or KOH, and a deposit or structure containing the above.

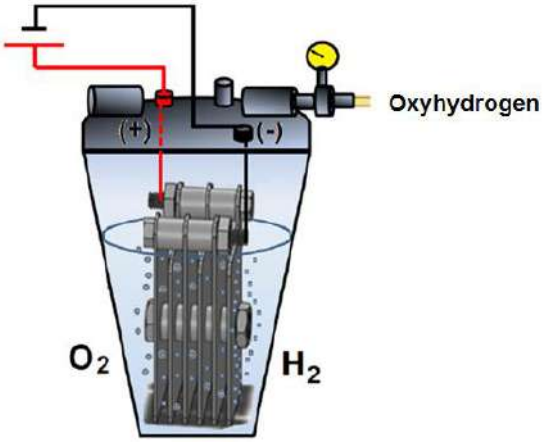

Fig. 1 Alkaline wet cell electrolyzer

Alkaline electrolysis produces an Oxy-Hydrogen gas mixture in a ratio of 2 hydrogen molecules to 1 oxygen molecule, there are two types of cells, wet and dry, the dry cell can be connected in series, parallel or a combination of both, while the wet cell is connected only in series, and the electrodes are always immersed in the electrolyte, each one offering different advantages over the other.

1.1 Background

One of the most important and used applications of hydrogen is as an enricher in internal combustion engines or burners, so there are several studies where hydrogen production systems are implemented in automobiles to inject hydrogen oxide gas to internal combustion engines.

Saravanan et al [4] In an investigation in which a dual fuel engine, hydrogen and diesel was used as the main fuel, the experiments focused on determining the optimal injection times, injection duration and hydrogen flow rate, it was found that varying these parameters reduces NOx emissions by 2% and CO emissions by up to 50%. Horcasitas et al [5] investigated the effects of injecting an Oxyhydrogen gas mixture into an internal combustion gasoline engine, adapted an electronically controlled injection system, the Oxy-hydrogen gas was produced by two alkaline electrolysers in a combination of parallel series arrays, the engine working under typical driving conditions in the city from 1000 to 2000 rpm, the experiments were carried out in two stages, the first stage was tested only with gasoline, in the second stage was worked with an Oxy-hydrogen gas flow injection of 903 smL/min, as a result of which the mixture of Oxy-hydrogen gas allowed a reduction in gasoline consumption as well as a reduction in CO_2 emissions. Shi et al [6] Focused on investigating the effects of spark on the combustion and emissions of a gasoline engine with direct injection of hydrogen, the engine operated at 1500 rpm experiments showed that thermal efficiency increased with increasing volume fraction of hydrogen injected, slowing down spark timing caused emissions of NOx, HC and CO to decrease, as well as when volume fraction of hydrogen injected increased emissions decreased.

Similarly, there are some patents on alkaline electrolysers such as these: US09361138: describes an internal combustion engine to which an electrolysis cell kit is attached, the cell consists of a sealed plastic body, with an inlet and an outlet, with the electrodes immersed in the solution from which the gases decompose. US09440192: has an autoelectric hydrogen generator, consisting of a plurality of similar cells, having the anode plates of aluminum and magnesium, and the cathode of stainless steel, sea water as electrolyte, applying an electric current through the terminals has the production of hydrogen in situ and low demand. US13225362: shows a hydrogen generation system to be injected as a fuel supplement into the internal combustion engines, the hydrogen is

generated in an electrolysis cell powered by the car battery, the hydrogen is injected into the engine air intake, while the oxygen is released into the environment, it has an engine sensor, which activates the system only when the vehicle is started.

As shown above, an area of opportunity has been found for the development of electrolysers to be implemented as auxiliary systems to the internal combustion engines and thus be able to enrich them with the mixture of Oxy-hydrogen gas. In this case, this work deals with the design of an alkaline electrolyzer to be implemented in an internal combustion engine of a motorcycle

2. Materials and Methods

2.1 Alkaline electrolyzer design methodology

Due to what was observed in the search for alkaline electrolyzers patents implemented in automotive vehicles, it was decided to apply a design methodology in order to have more accurate designs and oriented to our needs, in this work we used the QFD (Quality Function Deployment) methodology, this design methodology focuses on the voice of the customer, being a proactive method of decision making, considering the economic aspects, Martian [7], consists of a sequence of matrixes that join some areas of interest in order to have numerical and graphical indicators that help us to identify and prioritize customer requirements clearly and quickly. Figure 2 presents a general diagram of how the results obtained with this methodology are organized.

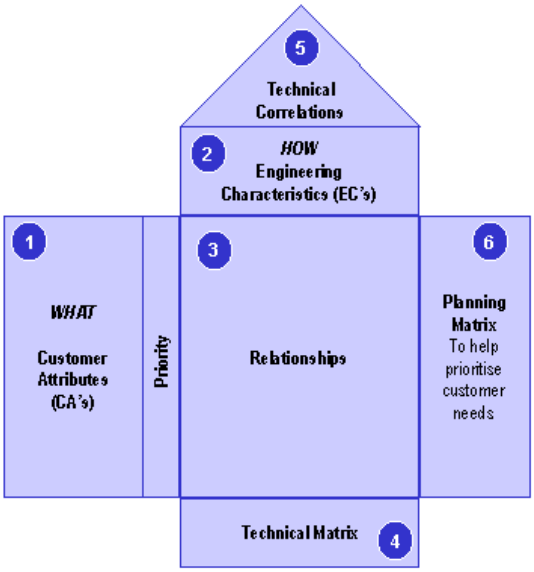

Fig. 2 House of Quality QFD

An analysis was made of the characteristics and the necessary requirements to be considered in the design of the alkaline electrolyzer, in order to obtain each of the matrices necessary to carry out the QFD methodology, in the following order:

- Requirements Matrix
- Requirements classification matrix, the classification was according to its Form, Functionality, or Manufacturing
- Desirable requirements matrix
- Weighting matrix
- Comparative Benchmarking Matrix
- Matrix of engineering requirements
- What with the Como" Relationship Matrix

All these matrices are concentrated in the diagram known as the QFD quality house. Figure 3 shows the house of quality of our design

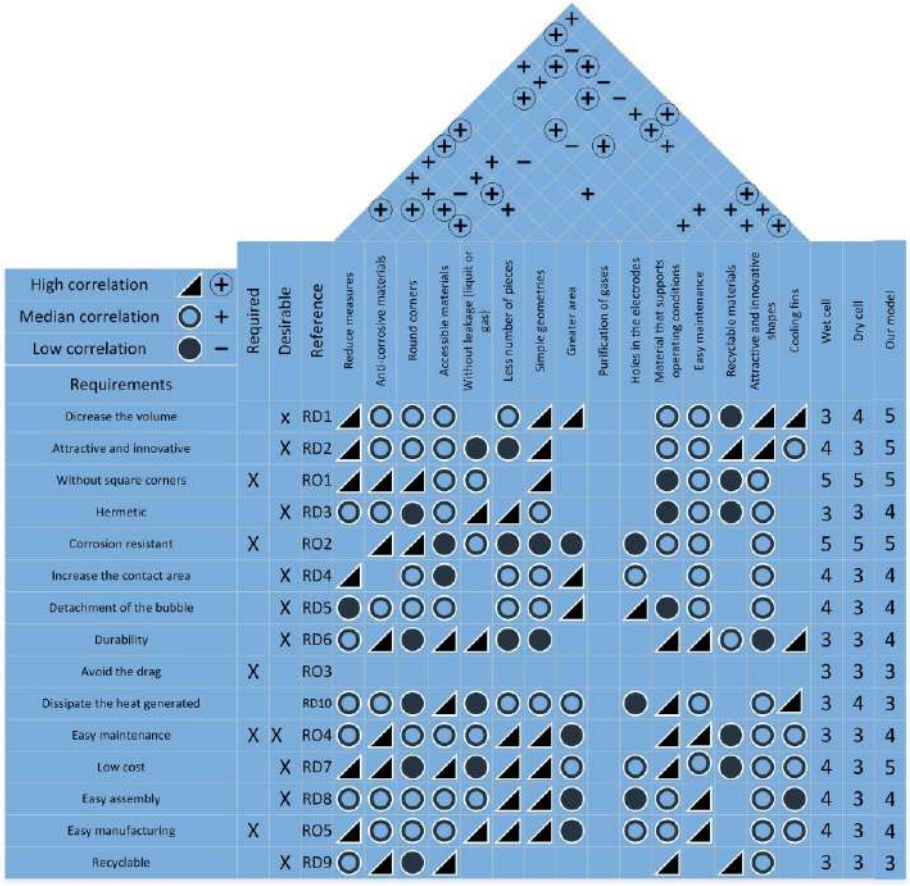

Fig. 3 Quality house for the design of an alkaline electrolyzer

Once we understand the existing requirements for the design of the electrolysis cell, with the help of the Ashby methodology we make the selection of materials, this methodology helps us to an adequate selection of the materials since it focuses on choosing the most suitable ones according to our application. The methodology is developed as shown in the flowchart shown in Figure 4.

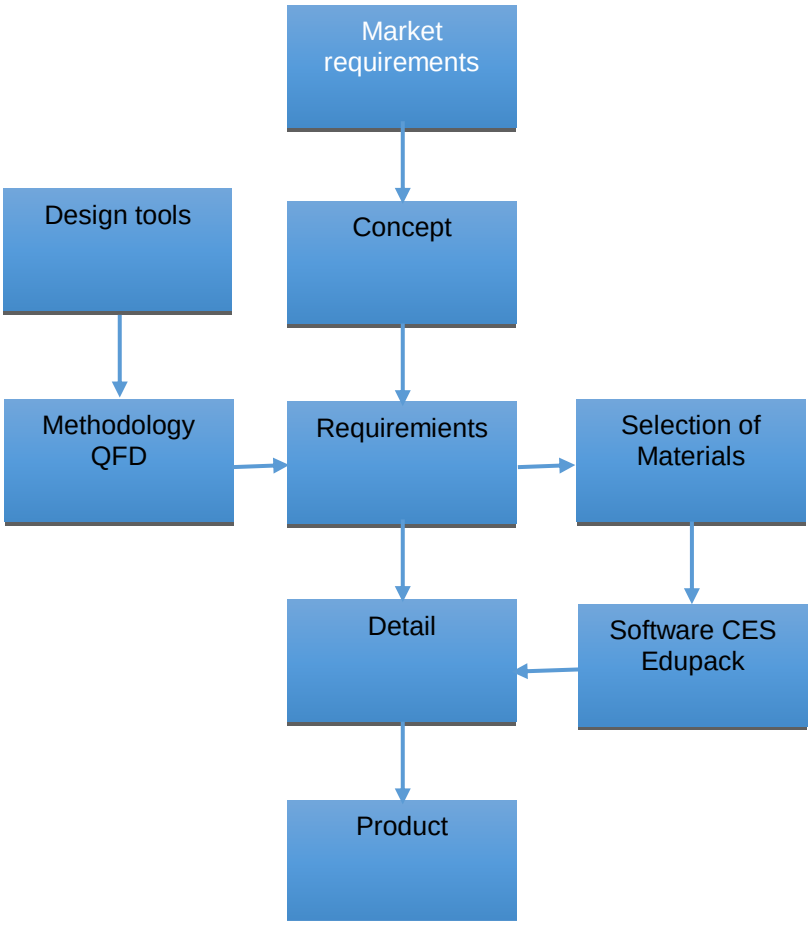

Fig. 4 Ashby methodology flow chart

According to the methodology, we already have the need, the concept, the requirements with the help of the QFD methodology, we proceed to the selection of the materials with the help of the CES Edupack® software, this program gives us a very wide perspective about the universe of available engineering materials, the possibilities of the materials are diminishing as the characteristics required for the components of the electrolysis cell are applied such as resistance to alkaline substances, temperature, density and flammability, the software provided a list of 8 possible materials, from which it was chosen to use epoxy resin for the manufacture of the tank body and the lid, for the manufacture of the electrodes AISI 304 stainless steel was chosen for its resistance to corrosion.

3. Results and Discussion

Having developed the QFD methodology for the design of the alkaline electrolyser, it was possible to understand the requirements needed to design the components of the alkaline electrolysis cell that are functional and comply with the standards. The designs were made using SOLIDWORKS® software. By representing the requirements in the design, three different possible solutions were obtained, which were evaluated to see which best met the design requirements. The possible solutions were those shown in Figure 5.

Each design was proposed considering the requirements obtained with the QFD methodology, these comply with them as far as possible, by making a comparative analysis between each design, taking into account that they comply so well with the desirable and mandatory requirements. Table 1 shows the comparison of the designs by assigning a rating to it, 5 being fully satisfactory and 1 not satisfactory.

Table 1. Comparison of designs based on compliance with requirements

Requiremient	**Design 1**	**Design 2**	**Design 3**
	Compliance (5,4,3,2,1)		
1	2	3	5
2	4	4	4
3	4	3	3
4	3	3	3
5	3	4	4
6	3	4	4
7	4	4	4
8	3	3	4
9	3	3	3
10	3	3	3
11	3	3	3
12	3	3	4
13	2	2	2
14	2	3	4
15	2	3	3
Total	44	48	53

With the help of the table you can define which of the three designs is more practical to manufacture, in an easier and more understandable way, therefore it is determined that the third design is the one that mostly complies with the requirements established by the methodology.

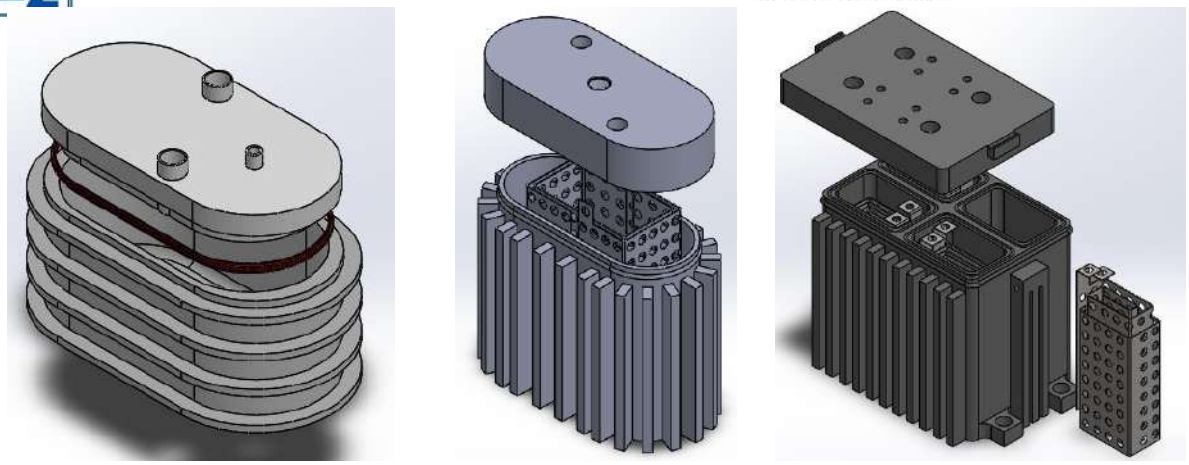

a) First design b) Second design c) Third design

Fig. 5 Proposed designs

The third design is a tank that groups four electrolysis cells, with cooling fins on its sides, 4 supports for holding the tank, in the lid has the holes for the electrical connections and the outlets for the gases, two tabs for closing it, in the upper side has 4 grooves for the placement of gaskets and thus obtain an airtight seal to prevent leakage of the electrolyte solution and gases (oxygen and hydrogen), the proposed electrodes have the shape of a square spiral interlaced between the cathode inside and the anode outside, will have a connection in series, with sodium hydroxide solution (NaOH) as electrolyte and is expected to work at 10 A-12 V to obtain an Oxi-hydrogen production of 0.546 NL/min.

4. Conclusion

Alkaline electrolysis offers many advantages over other methods of hydrogen generation, yet it requires improvements in energy efficiency, safety, operability, portability and cost. As it was observed in the patents shown there is a great tendency towards the implementation of hydrogen generator systems in automotive vehicles, whether they are diesel or gasoline engines, therefore the designs also need improvements in the systems offering greater portability and safety, given that in the vehicles there are reduced spaces for the auxiliary systems, the proposed design is intended to obtain improvements to respond to these needs, considering the volume occupied by the electrolyser and the hydrogen production rate, it symbolizes the mobility, energy consumed and the capacity of the electrolyzer, given that our design is more compact and occupies less volume but without neglecting the production of hydrogen it can be concluded that the proposed design is more efficient for this consideration, in addition to meeting the safety standards in terms of the high flammability range of the gases produced (Oxy-hydrogen).

In addition to the fact that the use of Ces Edupack® software helped us to make a better choice of material for the manufacture of alkaline electrolysis cell components and thus can support the operating conditions, thus giving a longer life cycle for the system, the use of QFD design methodology helped us significantly to obtain the design proposals for our application, in order to translate into improvements in the manufacture of alkaline electrolysers.

Acknowledgements

We thank the Instituto Politécnio Nacional for providing the necessary resources to carry out the research, as well as Doctors Juan Manuel Sandoval Pineda and Rosa de Guadalupe González Huerta for their support and guidance.

References

[1] R. González. Producción de oxi-hidrógeno para el enriquecimiento y ahorro de hidrocarburos: usos y retos, 2009, 1- 10.
[2] Ø. Ulleberg, Modeling of advanced alkaline electrolyzers: a system simulation approach, International Journal of Hydrogen Energy, 2003, 28, 21–33.
[3] González R., Oliver M., Rodríguez F., Hidrógeno producción y almacenamiento: Retos hacia su uso como vector energético sustentable, Editorial: CreateSpace (USA), ISBN: 978098099XXX, 1ra edición 2013.
[4] N. Saravanan, G. Nagarajan. Experimental investigation in optimizing the hydrogen fuel on a hydrogen Diesel dual-fuel engine, *Energy & Fuels* 2009, *23,* 2646–2657
[5] M. Horcasitas-Verdiguel, J. M. Sandoval-Pineda, B. A. Grunstein-Ramírez, L. F. Terán-Balaguer, R. de G. González-Huerta. Design and manufacture of ICE test module to reduce gasoline comsumption using oxy-hydrogen gas from an alkaline electrolyzer, Energy & Fuels 2016, 30, 6640−6645
[6] Shi W, Yu X., Zhang H, Li H, Effect of spark timing on combustion and emissions of a hydrogen direct injection stratified gasoline engine, International Journal of Hydrogen Energy 2016, 1-8.
[7] Martian D., “Practical Manual of Quality Function Deployment”, 2015.
[8] P. R. Bossard, US09440192.
[9] B. Ross, US09361138.
[10] D. Owens, US13225362.

XVIII International Congress
of the Mexican Hydrogen Society

Computational Design of an Oxyhydrogen Gas Burner

R. Moreno Soriano[1], R. de G. González-Huerta[2], J. M. Sandoval-Pineda[1], F. Soriano-Moranchel[1]

[1]Instituto Politécnico Nacional – ESIME – Azc, SEPI, Av. De las Granjas, No 682, Azcapotzalco, CP 02250, México
[2]Instituto Politécnico Nacional – ESIQIE, Laboratorio de Electroquímica y Corrosión, UPALM, CP 07738, México
* Corresponding author: 5568780642, beto.mec@outlook.es

ABSTRACT

The energy stored in hydrogen can be converted to useful energy through either fuel cells to directly produce electricity or combustion to produce power. The use of H_2 in combustion systems is attractive because it has a very wide flammability range, it is easy to ignite, and has a large flame propagation velocity and small quenching distance. The flame propagation velocity in a mixture of hydrogen and air is very large in comparison to that of hydrocarbons. This is due primarily to the faster reaction rates of the H_2/O_2 system. The large diffusion coefficient of H_2 also plays a role in the large flame speed because of the enhanced transport of radicals and heat ahead of the flame. Hydrogen also has a higher heat of combustion relative to hydrocarbon fuels on a per unit mass basis. At 298K and 1 atm the heat of combustion (lower heating value) of H_2 is about 120 MJ/kg while that of methane is 45 MJ/kg, however, that on a per unit volume basis the lower heating value for H_2 is about a factor of four less than CH_4.

The design of a pre-mixed burner for a gas flow of 2 (L/ min) is presented, using oxy-hydrogen as fuel gas. The design was based on a methodology available in the literature from hydrocarbons, p. e. CH_4. The flow velocity and pressure drop in the main areas of the burner were evaluated. Dimensions and geometry of the injector was varied, according to the operating conditions and considering the phenomena of takeoff and flashback of the flame. Primary air intake ports, some diameter, orientation and location of the same along the mixer were analyzed. The modeling of the obtained geometry was performed by means of computational tools, evaluating the mixing of the gases (hydrogen-oxygen) and the distribution of pressures of the gas flow through the different zones of the burner, emphasizing the pressures developed in the burner output ports, comparing the theoretical values of the laminar combustion speed for the hydrogen-oxygen and hydrogen -air mixtures according to the percentage of primary aeration.

Keywords (Maximum 4 words): Burner, oxy-hydrogen, combustion, flame speed

September 18th to 21st, 2018 in Mexico City, Mexico.

1. Introduction

In recent years, mixtures of hydrogen and hydrocarbons have been widely studied for use as alternative fuels. Hydrogen has a high combustibility, a high combustion speed with wide flammability limits, this allows to improve performance, extend operating ranges and reduce pollutant emissions from poor combustion, both in stationary and mobile systems. While the effects of adding water electrolysis products (hydrogen and oxygen) to gasoline and diesel engines to improve their performance have been widely studied, the effects of adding water electrolysis products to hydrocarbon gases have been studied to a limited extent. One possibility is to add oxygen (O2) to an oxidant (air) stream, oxygen enrichment to air, has been shown to significantly improve the combustibility of hydrocarbons, reducing ignition energy, increasing combustion speed and the temperature of the adiabatic flame. The addition of hydrogen (H2) to mixtures of hydrocarbon gases (methane, ethane and propane) allows the speed of laminar flame propagation to be increased, reducing the thickness of the flame surface itself. Enrichment in mixtures of hydrocarbon gases with hydrogen allows greater control of flame stability. Therefore, the simultaneous addition of H2 and O2 in hydrocarbon gas mixtures improves the reactivity of the mixture, providing greater flame stability, increasing combustion efficiency and reducing greenhouse gas emissions for flammability limits well below conventional limits.

As the use of gas burners has expanded, they have become the most important appliances and have changed their character to become the main heat supply for the residential kitchen. The global use of cooking burners today has reached millions and, although the amount of gas consumed by each burner is minimal, it has had a cumulative and significant impact on global fossil fuel consumption and environmental degradation. In recent years, with the growing concern of the general public for indoor air pollution, domestic burners have been forced to produce lower pollutant emissions, which has led to increased study and development of new equipment with better energy efficiency and better characteristics in the emission of pollutant gases. The effects of the addition of hydrogen and oxygen, either separately or together with a mixture of hydrocarbon gases (mainly methane), have been studied by different authors. These studies have evaluated the changes produced, both in the laminar combustion speed and in the stability of the flame in gas mixtures, varying the percentage of H2 and H2/O2 in the mixture.

[1].They carried out a numerical and experimental analysis of the effect of the addition of electrolysis products (H2 and O2) on the laminar combustion rate and the stability of the pre-mixed methane/air flames at atmospheric pressures. The study was conducted for methane/air mixtures with H2/O2 percentages between 10 and 25 % for a poor combustion regime. The results obtained show that the addition of H2/O2 to the methane in the proportions studied (10 - 25%) increases the laminar combustion speed with respect to the speed of the methane/air mixture. For a ϕ = 0.75, the intrinsic instabilities are observed for mixtures with a percentage of

25 % of H2/O2, causing the instability of the flame due to the hydrodynamic effects, however there was an increase of 14.8% in the combustion speed, increasing the flammability range in the methane/air mixture with the addition of H2/O2 in a volume ratio of 2:1. [2]. I perform a numerical analysis of the effect of the addition of 10-20% H2 and 10% H2/O2 (ratio 2/1) to methane. It was found that the same increase obtained in the laminar combustion rate is obtained by adding 20% of H2 or 10% of H2/O2 to the methane. In addition to this, it was found that the addition of 10- 20% H2 to methane does not significantly improve the flammability limits of methane, while the addition of 10% H2/O2 slightly improves this property. [3].I study the effect of the addition of hydrogen in pre-mixed methane/hydrogen/air flames at a pressure of 0.1 MPa and a temperature of 350 K. The results obtained indicate that hydrogen flames are more stable (wrinkled) compared to methane flames.

[1].Experimental measurements of the combustion rate in hydrogen-air mixtures were carried out, obtaining a speed of 296 cm/sec for a 50 % mixture, obtaining an important improvement with respect to the values reported by Dixon and Lewis. [5].Determined the laminar and turbulent combustion rates for hydrogen-air and hydrogen-oxygen mixtures for a hydrogen concentration range of 9 to 70% by volume. The accuracy of the measurements varies according to the percentage of hydrogen, for mixtures in the range of 20 - 50% hydrogen, the flames are thin and well defined, and the accuracy of the measurements made is ± 2%. Outside this range the accuracy for measurements at 10% hydrogen is ± 30% of the measured value and for 70% hydrogen the accuracy is ± 20%. For hydrogen-air mixtures at 42% by volume, combustion rates were determined using nozzles of 2, 3, 5 and 7 mm diameter, obtaining speeds of 3.8, 3.5, 3.3 and 3.2 m/s respectively. This concludes that the effect of nozzle diameter on combustion rates is minimal for nozzle diameters greater than 5 mm. The measurements obtained were compared with the results presented by different researchers and found to be consistent with the results obtained.

Self-priming or self-priming burners, designed to be powered by liquefied petroleum gas (LPG) are very popular for cooking in the domestic sector. These represent the main choice for the gaseous fuel available for this sector. Therefore, the higher the efficiency of self-priming burners, the greater the amount of energy that can be saved in this sector. Much research has been done on self-priming burners to improve thermal efficiency and reduce pollutant emissions by developing the geometry of the burner port and combustion system.

[6].A mid-20th century review of the studies carried out on atmospheric burners for LPG and natural gas, establishing the optimum parameters and design conditions for the sizing of the different burner components, which are based on the experience and research carried out to date. On the other hand. [7] Developed a methodology for the design of biogas burners, based on experimentation but without specific recommendations. [8].He found by experimentation that the distance from the throat inlet to the injector should be 2 to 2½ times the diameter of the throat, and that the length of the mixing tube should be about 10 to 12 times the diameter of the throat for atmospheric burners. 8], experimentally analyzed the effects on flame stability due to geometry, spacing, depth and load at the outlet port, using ports with diameters of 1 to 3 mm

and 1.2 mm depth, using methane gas as the main fuel, evaluating different mechanisms for flame retention and stability in multiport burners. [9].Conducted experimental and theoretical research on the characteristics of primary air entrainment for cold (non-combustion) and hot (combustion) conditions in an LP gas burner, developing a theoretical model for predicting the entrainment of primary air, according to the flow rate of the combustible gas.

Research on atmospheric burners designed to be powered by oxyhydrogen gas is less extensive compared to that conducted for hydrocarbon gases. This work takes advantage of the research carried out on self-priming burners for hydrocarbon gases, taking as a base the design methodologies developed for such equipment, with the aim of designing an atmospheric burner for the combustion of the H2/O2 mixture, for a volume ratio of 2/1. Enabling the development of oxyhydrogen gas burners, with the aim of reducing the consumption of hydrocarbon derived gases and the reduction of pollutant gas emissions in combustion systems for domestic applications, mainly in the following areas

2. Materials and Methods

The laminar combustion speeds of hydrogen-air-hydrogen-oxygen mixtures are important for the design and performance estimation of combustion systems, in which hydrogen is used as a fuel. For a one-dimensional laminar flame, the combustion rate is defined as the speed of the unburned gases normal to the flame, referred to a coordinate system in which the flame front is stationary. Figure 1 shows the values of the laminar combustion rate for hydrogen/oxygen and hydrogen/air mixture, the combustion rate varies according to the hydrogen/oxygen ratio and the percentage of primary aeration respectively. [5] y [6]

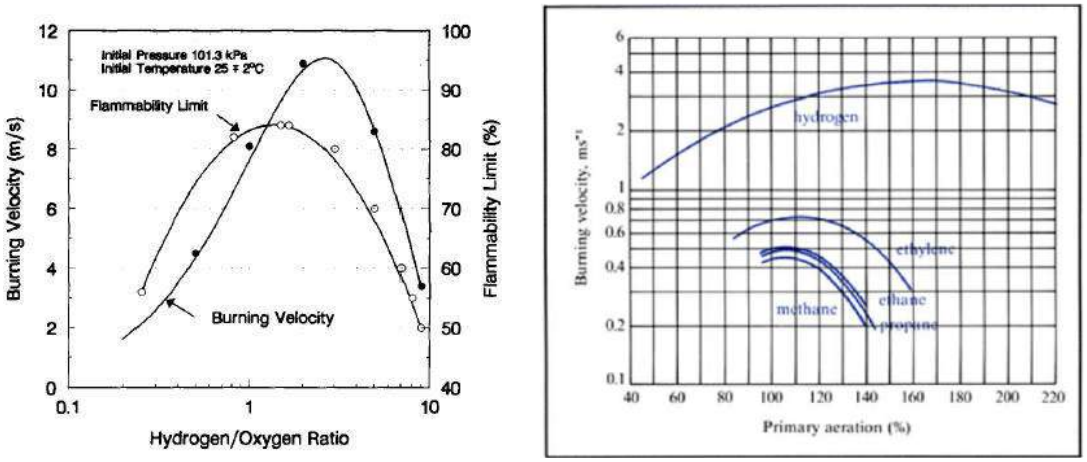

Fig. 1. Burning Velocities of hydrogen – oxigen and hydrogen – air mixtures.

2.1 Design methodology.

For the burner sizing, it is necessary to know the particular properties of the combustible gas, the pressure and flow conditions to which the gas is supplied as well as the theoretical air requirement necessary for the combustion of the gas. In this case, the Oxyhydrogen is supplied through an alkaline electrolyzer, which does not have a compression mechanism for the gas itself. Therefore, the gas supply pressure will vary throughout the burner operation. The design of the burner is based on the fundamental aspects of the main components of the burner, i.e. the injector, the air entrainment, the mixing tube and the geometry of the flame ports.

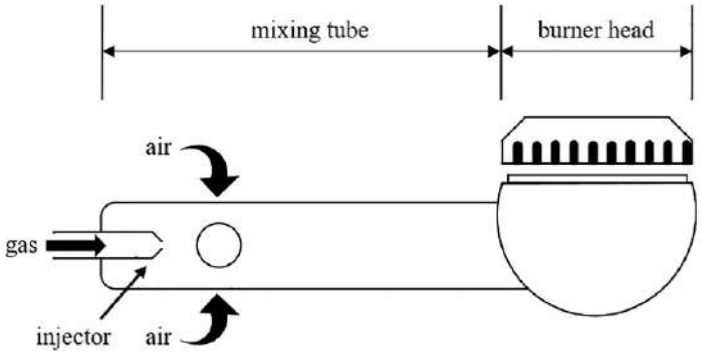

Fig. 2. Common Burner Configuration.

2.1.1. Injector configuration

In the design of the injector, the optimum area of the fuel outlet must be determined, ensuring the correct supply of gas and air to the burner. The size and shape of the injector controls the speed of the gas, converting the potential energy of the high-pressure gas into the kinetic energy of an emerging gas stream. By applying the equations of mass and energy conservation, the maximum heat input (q) through the injector is determined by equation (1).

$$q = 12.78 A_i W C_d \sqrt{P_i} \qquad (1)$$

and one obtains

$$A_i = \frac{q}{12.78 W C_d \sqrt{P_i}} \qquad (2)$$

As shown in equation (2), the area of the injector outlet orifice (Ai) depends on the heat input (q) required, the Wobbe number (W), the fuel gas supply pressure (Pi) and the discharge coefficient (Cd) in the injector. The Cd value depends on the configuration and the number of Reynolds through the injector port.

2.1.2. Primary air entrainment model.

Considering the jet of gas emitted from the injector outlet to the throat of the mixing tube as a jet of confined gas, which experiences a pressure drop, causing the entrainment and mixing of the primary air with the jet of combustible gas in the mixing tube. Assuming a balance of momentum and energy through equation (3). [9]

$$(P_t - P_o)A_t = \frac{\rho_g \dot{Q}_g^{\,2}}{A_i} - \frac{\rho_m \dot{Q}_m^{\,2}}{A_t} \quad (3)$$

For the section from the throat to the burner head.

$$P_c - P_t = \left(\frac{\rho_m \dot{Q}_m^{\,2}}{2A_t^{\,2}}\right)(1 - C_L) \quad (4)$$

Where CL is a loss coefficient for the mixing tube. This represents the sum of the individual losses in the throat and diffuser sections of the mixing tube, depending directly on the length of the tube, the diameter of the throat and the angle of narrowing of the diffuser.

For the discharge section between the burner outlet ports and the environment.

$$P_p - P_o = \frac{\rho_m \dot{Q}_m^{\,2}}{2A_p^{\,2}C_d^{\,2}} \quad (5)$$

2.1.3 Area ratios in burner sections:

The area ratios between the different sections of the burner allow them to be calculated with respect to the primary air entrainment. These relate the optimum ratio between the injector outlet area, throat and mixing tube outlet to the properties of the gas and gas/air mixture, based on the entrained primary air volume ratio. From the review carried out[6] on research on atmospheric burners for natural gas and LPG, the optimum efficiency in atmospheric burners is obtained from the maximum value of the Ai/At ratio by means of equation (6).

$$\frac{A_i}{A_t} = \frac{\rho_g \dot{Q}_g^{\,2}}{\rho_m Q_m^{\,2}(1 + C_L)} \quad (6)$$

Defining R as the entrainment ratio (air/fuel) in volume, from equation (7).

$$R = \frac{\dot{Q}_a}{\dot{Q}_g} \quad (7)$$

The density of the gas mixture (air/fuel), is determined from equation (8)

$$\rho_m = \frac{\rho_g \dot{Q}_g + \rho_a \dot{Q}_a}{\dot{Q}_m} \quad (8)$$

Equation (6) can be written as a function of R.

$$\frac{A_i}{A_t} = \frac{\sigma}{(\sigma + R)(1 + R)(1 + C_L)} \quad (9)$$

By combining equations (3) and (4) and substituting equation (9) in the resulting equation, equation (10) is obtained.

$$(P_p - P_o) = \left(\frac{\rho_g \dot{Q}_g{}^2}{A_t{}^2}\right) * \left(\frac{(\sigma + R)(1 + R)(1 + C_L)}{2\sigma}\right) \qquad (10)$$

By substituting equation (5) in (10), the A_t/A_c ratio is obtained for optimum burner efficiency.

$$\frac{A_t}{A_C} = C_d\sqrt{1 + C_L} \qquad (11)$$

Equations (9) and (11) represent the area ratios for the injector outlet (Ai), diffuser throat (At) and burner head area (Ac), relative to the loss coefficient (Cd), drag ratio (R), loss coefficient (CL) at the diffuser and relative density (σ) of the fuel gas.

2.1.4. Configuration of the flame ports

The flame port investigations for oxyhydrogen burners are less complete compared to those for hydrocarbon gases. The review submitted by [6], recommends a port spacing of less than 6 mm and more than 1.5 mm, a depth/diameter ratio greater than two for circular ports and a length/width ratio greater than two for rectangular ports. An increase in the spacing between ports increases the tendency for the flame to rise. This can be attributed to a reduction in the interaction of neighboring flames as ports become more widely spaced. The number of ports (np) in the burner head is determined from equation (12), which depends on the flow, speed and density of the gas mixture, as well as the area of the outlet port.

$$n_p = \frac{\dot{m}_m}{(\rho_m A_p V_p)} \qquad (12)$$

For a particular gas/air mixture, there is a critical port diameter known as the cooling diameter, below which the phenomenon of flame recoil through the burner does not develop. For circular ports, an increase in diameter reduces the tendency for the flame to rise, increasing the tendency for the flame to recede (for hydrogen) and decreasing the effective load in the port itself. From the investigations conducted by [12], critical diameters for combustible gases were determined under standard conditions, proposing a critical diameter of 0.8 mm for hydrogen/air mixtures and 3.5 mm for methane/air mixtures.

3. Results and Discussion

With the methodology and considerations presented above, the design of the main components of an atmospheric burner for oxyhydrogen gas that operates with a primary aeration of 60% is carried out. Producing a thermal power of 200 watts for a continuous flow of oxyhydrogen gas of 2 LPM. The geometric configurations of the different sections of the burner, obtained from the methodology and considerations mentioned above, are described below.

3.1 Injector design.

For the sizing of the burner components, the diameter of the injector must be known, which must be determined from equation (2) and knowing the properties of the gas, the power required and its geometric configuration.

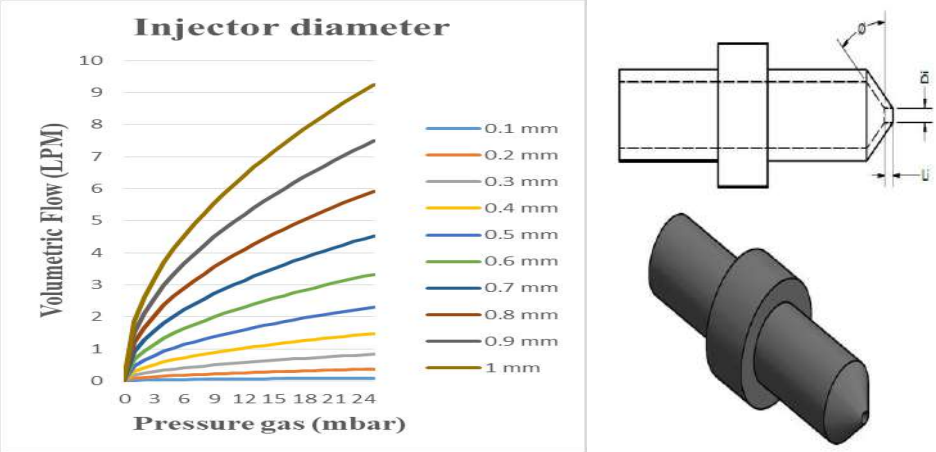

Fig. 3. (a) Variation of the volumetric flow rate of the hydrogen oxide gas through the injector, (b) injector configuration.

Figure 3 (a), shows the variation of gas flow through the injector, which is evaluated in a range of 0 to 1 mm in diameter and 0 to 25 mbar in gas supply pressure, considering the experiences reported by [13],[14] and[15]. For the design of the injector, the experiences reported by Jones were considered, considering a convergence angle (θ) of 45° and a Di/Li ratio of 0.58 for an area (Ai) in the injector outlet hole of 0.19635 mm2, with which the Cd loss coefficient will have a theoretical value of 0.81. The true value for Cd will be obtained from the characterization of the gas flow in the injector, using an empirical version of Bernoulli's theorem by means of equation (13). [7]

$$\dot{Q}_g = 0.0467 * C_d * A_t * \sqrt{\frac{P_i}{\sigma}} \qquad (13)$$

3.2. Design of the mixing tube.

The sizing of the convergence and divergence zones, as well as the throat of the mixing tube, are carried out from equations (9) and (11), knowing the properties of the Oxyhydrogen gas and selecting a drag ratio (R) according to the theoretical air volume necessary for the combustion of the hydrogen/air mixture.

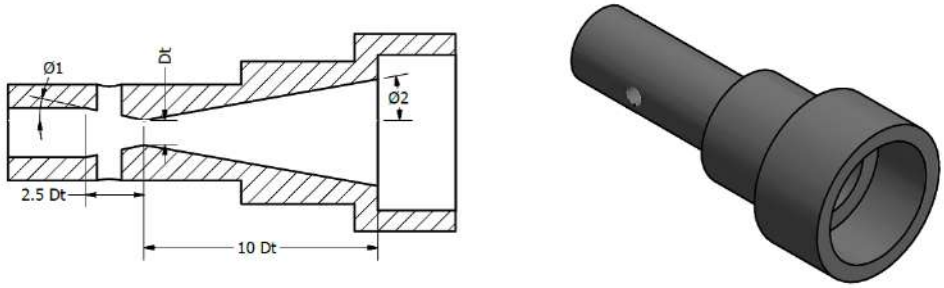

Fig. 4. Mixing tube configuration.

The design of the mixing tube was based on the research presented by [6] and [16]. The area of the mixer throat (At) was determined from the selection of the optimum diameter in the injector, which resulted in an area (At) of 7.0686 mm2 in the throat of the mixer. For the convergence zone, an angle (θ_1) of 10° and a length of 2.5 (D_t) was selected, and for the divergence zone, an angle (θ_2) of 10° and a diffuser length of 10 (Dt) were selected, the design was made considering a primary aeration percentage of 60% for the given flow conditions. According to the dimensions selected for the mixing zone in the burner, the loss coefficient (C_L) will be 0.35.

3.3 Burner head design.

The design of the burner head is based on the calculation of the number of flame ports required for the flow of the gas mixture provided. The calculation of the number of flame ports is made from equation (12) and knowing the combustion rate of the hydrogen/oxygen mixture, as well as the critical diameter in the flame port, considering the stability of the flame at all times. For the selection of the combustion rate, the results presented by [6] were taken as a reference considering the volume ratio of the hydrogen/oxygen mixture, as well as the percentage of primary aeration in the mixture itself. Similarly, for the sizing (Dp) of the flame ports, the results presented by[12] were used, maintaining an aspect ratio (Dp/Di) equal to 1 in the burner**.**

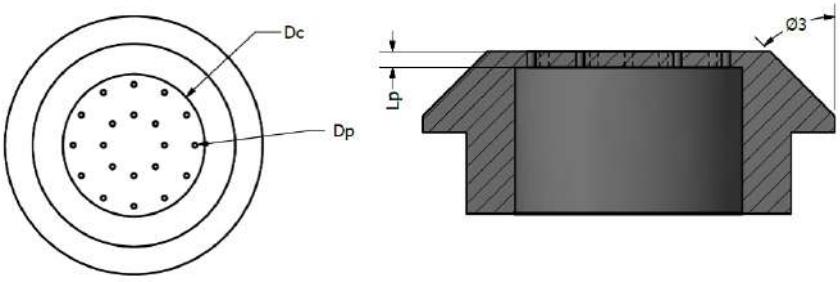

Fig. 5. Burner head configuration.

According to the volume of the gas mixture and the results presented by [5] and [6] for the combustion speed of the hydrogen/oxygen and hydrogen/air mixture, a total area in the burner

head (Ac) equal to 201.0624 (mm2) was obtained for a total of 20 flame ports, considering a separation between ports of 3 mm and an area in each port (Ap) of 0.19635 mm2.

Using the primary air entrainment model developed by[9], the development of the gas mixture pressure for the sections between the throat inlet and the burner outlet ports was evaluated. The change in the pressures of the gas mixture depends on the volumetric flow of the gas mixture and the cross-sectional area in the different sections, which are a function of the entrainment ratio and the pulse rate of the fuel gas, these are a function of the gas supply pressure at the injector outlet.

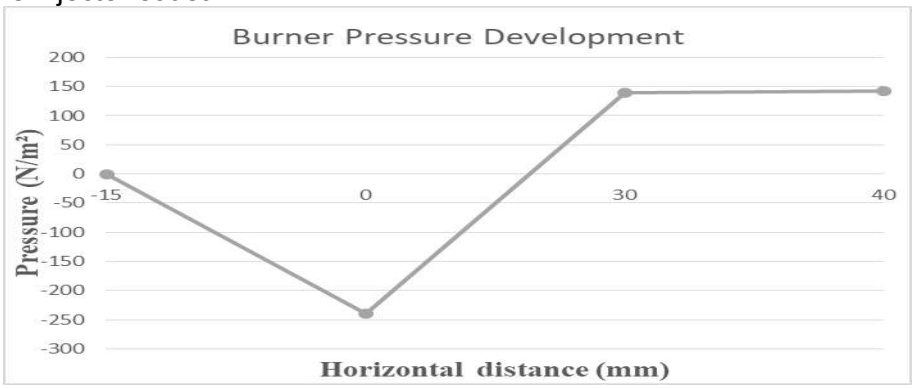

Fig. 6. Development of the pressure of the gas mixture along the burner.

4. Conclusion

Domestic gas burners are partially pre-mixed devices, designed to operate in atmospheric conditions, where the formation and homogenization of the gas mixture is due solely to the drag force of the gas stream emerging from the injector and the geometric characteristics of the different sections of the burner. Due to this, a poor correlation between the geometry of the injector, the mixing tube and the burner head will result in low primary air entrainment, causing incomplete combustion in the device, increasing the levels of pollutant gas emissions.

The design of the injector is based on balancing two contradictory considerations: On the one hand, a small diameter is desirable to obtain a high velocity in the gas jet at the outlet of the injector, with which an increase in the drag ratio is obtained, in the impulse of the fuel gas and in the entrainment of the primary air. On the other hand, a very small diameter will cause a high pressure drop in the jet of combustible gas, affecting the flow of gas through the injector. The dimensions of the burner elements depend directly on the diameter of the injector, as well as on the conditions of the gas at the outlet, which determine the impulse of the fuel gas and the entrainment ratio. The geometrical configuration of these elements is based mainly on results reported in the literature, which have been obtained under controlled conditions, because of this, the behavior and performance of the burner may vary under real conditions.

The rate of combustion depends on the type of combustible gas and the percentage of primary aeration. This is a key factor in the design of the burner ports, which must be designed to balance the flame front itself, the combustion speed and the speed of the gas mixture at the exit of the port, avoiding the phenomena of rising and falling of the flame. Although it is theoretically possible to obtain an approximate value for this variable, the experiences reported in the literature have revealed that the best predictive models for this variable are only approximations, so that experimental determination provides the best source of data for this variable.

References

[1] C. Echeverri-Uribe, A. A. Amell, L. M. Rubio-Gaviria, A. Colorado, and V. McDonell, "Numerical and experimental analysis of the effect of adding water electrolysis products on the laminar burning velocity and stability of lean premixed methane/air flames at sub-atmospheric pressures," *Fuel*, vol. 180, pp. 565–573, 2016.

[2] C. Uykur, P. P. Henshaw, D. S. K. Ting, and R. M. Barron, "Effects of addition of electrolysis products on methane/air premixed laminar combustion," *Int. J. Hydrogen Energy*, vol. 26, no. 3, pp. 265–273, 2001.

[3] E. C. Okafor, A. Hayakawa, Y. Nagano, and T. Kitagawa, "Effects of hydrogen concentration on premixed laminar flames of hydrogen-methane-air," *Int. J. Hydrogen Energy*, vol. 39, no. 5, pp. 2409–2417, 2014.

[4] H. Edmondson and M. P. Heap, "The burning velocity of hydrogen-air flames," *Combust. Flame*, vol. 16, no. 2, pp. 161–165, 1971.

[5] G. W. Koroll, R. K. Kumar, and E. M. Bowles, "Burning velocities of hydrogen-air mixtures," *Combust. Flame*, vol. 94, no. 3, pp. 330–340, 1993.

[6] *Jones, H.R.N., The application of combustion principles to domestic gas burner design, Taylor & Francis, vol 1, pp 0- 200, (1989).*

[7] D. Fulford, "Biogas Stove Design," *Biomass*, no. August, pp. 1–21, 1996.

[8] Berry, W.M., Brumbaugh, I.V., Moulton, G.F. and Shawn, G.B., US Bur. Stds., Techn. Paper 193 (1921).

[9] A. Namkhat and S. Jugjai, "Primary air entrainment characteristics for a self-aspirating burner: Model and experiments," *Energy*, vol. 35, no. 4, pp. 1701–1708, 2010.

[10] M. H. Saberi Moghaddam, M. Saei Moghaddam, and M. Khorramdel, "Numerical study of geometric parameters effecting temperature and thermal efficiency in a premix multi-hole flat flame burner," *Energy*, vol. 125, pp. 654–662, 2017.

[10] V. V. Gubernov, V. Bykov, and U. Maas, "Hydrogen/air burner-stabilized flames at elevated pressures," *Combust. Flame*, vol. 185, pp. 44–52, 2017.

[11] A. Namkhat and S. Jugjai, "Prediction of Total Equivalence Ratio for a Self-Aspirating Burner," *First TSME Int. Conf. Mech. Eng.*, no. March, 2011.

[12] Harris, J.A. and South, R., Gas Eng. Manag . no.18, pp 153. (1978).

[13] Harris, J.A. and Prigg, J.A., J. Inst Gas Eng. no.5, pp 203 (1965).

[14] Pritchard, R., Guy, J.J. and Connor, N.E., Industrial Gas Utilisation , Bowker.

[15] Griffiths, J.C. and Weber, E.J., Amer. Gas Assoc. Res. Bull. pp 77. (1958).

XVIII International Congress
of the Mexican Hydrogen Society

Evaluation of $NiWO_4$ as an oxygen carrier for the hydrogen storage by chemical looping.

P.E. González-Vargas; M.J. Meléndez-Zaragoza; J.M. Salinas-Gutiérrez; V. Collins-Martínez; A. López-Ortiz *

Centro de Investigación en Materiales Avanzados, S.C., Miguel de Cervantes 120, Complejo Industrial Chihuahua Chihuahua, Chih. México. C.P. 31136
* Tel: +52 6144394815; e-mail: alejandro.lopez@cimav.edu.mx

ABSTRACT

Chemical looping process (CL) have recently been used for various purposes, one of which is the hydrogen storage using metal oxides (MeO) as the only source of oxygen (oxygen carriers) to produce water ($MeO + H_2 = Me + H_2O$) and regenerating the metal oxide with a steam oxidizing atmosphere for the hydrogen release ($Me + H_2O = MeO + H_2$). It is important that these oxygen carriers have certain characteristics to be used for this purpose, such as thermal stability and the ability to store and release the lattice oxygen to the cyclic reaction conditions. In order to evaluate the nickel tungstate ($NiWO_4$) for this purpose, it was thermogravimetrically tested (TGA) in three accelerated redox cycles using a mixture of 5 v% of H_2/Ar as a reducing atmosphere and a mixture of 5 v% H_2O/Ar gas stream as the oxidizing atmosphere. Characterization made to the material before and after the redox cycles were performed by XRD, BET surface area, and SEM and have shown its favorable potential as an oxygen carrier when testing its thermal and reactive stability after three consecutive redox cycles. TGA tests revealed an oxidation mechanism of the reduced metals (Ni + W) that follows a reaction path, which consists in the formation of WO_3 by the oxidation of W with steam, followed by the formation of $NiWO_4$. This reaction path was confirmed by thermodynamic calculations that indicate that the oxidation of Ni, WO_3 and steam is presumably the rate-determining step.

Keywords: $NiWO_4$; redox reaction; chemical hydrogen storage; chemical looping.

1. Introduction

Although it is difficult to determine energy consumption in a precise way in the future, it is a fact that it will increase significantly in the coming decades. This is mainly due to the constant growth of the human population, which in turn demands the consumption of diverse natural

resources to satisfy basic needs. Such is the case of the use of fossil fuels, mainly used to obtain electricity, transport and for artificial air conditioning of buildings. It is due to the decrease of these fuels and the environmental impacts that they generate that a large number of researchers around the world find themselves searching for alternative energy sources and sustainable raw materials [1].

In recent times, hydrogen (H_2) has been of great interest, since it is considered as raw material for a wide variety of processes. For example, with nitrogen in the synthesis of ammonia, with CO and CO_2 to produce methanol, in the manufacture of medicines, production of hydrogen peroxide, in the electronics and petrochemical industries and to produce numerous chemical products in various syntheses [1-3]. Moreover, hydrogen is considered a clean source of energy because it has been reported to be a key element in the generation of clean and sustainable energy systems. Virtually any source of fuel, whether renewable or non-renewable, containing in its molecular structure hydrogen atoms (H) can be used for the generation of hydrogen as a gas (H_2). Due to its high energy efficiency (122 kJ/g), hydrogen has great potential to reduce dependence on oil and reduce GHG emissions, with an energy yield 2.75 times higher than that of hydrocarbons. Currently, hydrogen production accounts for around 2% of primary energy demand [4].

Nowadays, various physical and chemical methods for hydrogen storage have been proposed. Such as high-pressure and cryogenic-liquid storage, adsorptive storage on high-surface-area adsorbents, chemical storage in metal hydrides and complex hydrides, storage in boranes, carbon materials, and metal organic frameworks [5, 6]. However, each storage method has its advantages and difficulties due to safety, size, weight, cost and efficiency requirements [7].

To overcome the difficulties presented by many methods of hydrogen storage, recently, the use of redox reactions with metal oxides (MeO) under a chemical looping (CL) reaction scheme has been proposed. This principle of hydrogen storage is based on reactions (1) and (2) [5].

$$Me_xO_y + yH_2 \rightarrow xMe + yH_2O \qquad (1)$$

$$xMe + yH_2O \rightarrow Me_xO_y + yH_2 \qquad (2)$$

In order to be used in CL process, MeO species must be thermally stable to withstand the temperature gradients which are subjected during the process, to be able to store and release lattice oxygen at reaction conditions, and have good availability and affordable costs [8]. The most common MeO reported is iron oxide in its different oxidation states (Fe_3O_4, Fe_2O_3) and this process is commonly known as the steam-iron process. This process consists in the reduction of the iron oxide with H_2 for the H_2 storage, and the subsequent liberation of the H_2 when oxidizing the Fe with steam [9-11]. The theoretical maximum storage capacity of H_2 in this process is 4.8 wt% of Fe [5], i.e., based on the Fe as the only reactive solid. However, most of the processes suggested in various research works propose the impregnation and/or support on different materials of the iron oxide to improve the storage capacity and to avoid the material sintering [5, 9, 11-14], which causes generation of an additional inert load to the reactors, which in turn causes the reduction of up to 3 times the storage capacity of H_2 based on the total solids in the reactive species (including Fe).

In other studies related to the chemical looping partial oxidation of methane (CLPO), it has been reported that some mixed metal oxides used as oxygen carriers (OC), such as perovskites

and ilmenites (ABO_3), are resistant to high temperatures [15, 16]. These investigations attribute the thermal resistance of the material to the cation A, while high valence B cations would contribute to the catalytic action. An example of these materials is ilmenite ($FeTiO_3$) that is reported by Schwebel et al. [17] as an OC for H_2, CO and CH_4 as reducing gases, finding kinetics similar to previously reported, with the exception of the reaction with CH_4, which was lower due to limitations in the surface area. These materials are reported without the addition of inert solid species for their operation, a feature that may be of advantage in CL storage of H_2.

The cobalt tungstate ($CoWO_4$) proposed by De Los Ríos et al. [8, 18], doped with nickel (Ni) as a catalyst, reported that is highly stable before cyclic redox tests. In subsequent work, it is reported that this same material is capable of carrying out redox cycles at temperatures below 800°C and thermal efficiencies comparable to the literature [19]. This type of materials present a high thermal resistance, are stable to cyclic redox conditions due to the phenomenon of the solid diffusional reactive barrier [20] and theoretically, are capable of requiring lower temperatures compared to other mixed metal oxides.

Based on the principles and features of mixed metal oxides in CLPO processes, the nickel tungstate ($NiWO_4$) was selected in the present work to evaluate its thermal stability and its ability to store and release lattice oxygen through redox cycles using H_2 as the reductive and steam as oxidative atmospheres to study its performance as a H_2 storage material. The involved CL redox reactions of $NiWO_4$ with H_2 and H_2O are the following:

$$NiWO_4 + 4H_2 \rightarrow Ni + W + 4H_2O \quad (3)$$
$$Ni + W + 4H_2O \rightarrow NiWO_4 + 4H_2 \quad (4)$$

2. Materials and Methods

2.1 Synthesis

The $NiWO_4$ was synthesized by the precipitation method at room temperature with constant stirring, as reported by Song et al. [21]. Solutions of 100 mL 0.7 M of $Na_2WO_4 \cdot 2H_2O$ and $Ni(NO_3)_2 \cdot 6H_2O$ were mixed. Once the precipitate was obtained, it was filtered and washed repeatedly with deionized water and then dried at 100°C for 2 hours. After dried, it was calcined at 600°C for 5 hours and allowed to cool at room temperature.

2.2 Characterization

Characterization of the calcined sample was examined to study its crystalline structure, surface area, morphology and micoanalysis composition by X-ray diffraction analysis (XRD), BET surface area, scanning electron microscopy (SEM), and energy dispersive X-ray spectroscopy (EDS), respectively.

The XRD, SEM and EDS analyzes were performed on the sample before and after three redox cycles, in order to establish the stability of the material.

2.3 TGA Evaluation of Redox Cycles

The redox behavior of the $NiWO_4$ powder was followed by a conventional thermogravimetric analysis (TGA) system. All redox experiments were carried out at atmospheric pressure, the total reactive gas flowrate was 100 mL/min and the amount of $NiWO_4$ sample was

26 mg. Prior to the reaction, the sample was heated up in an inert atmosphere (Ar) to the desired temperature (700°C) and then isothermally treated under reducing/oxidizing flow. Before switching from reduction to oxidation atmosphere and vice versa, the reactive gases that remained were removed by an argon flow for approximately 5 min.

For the reduction process, a flow composed of 5 v% of H_2 and 95 v% Ar was used. The duration of this step was determined in order to achieve complete reduction of $NiWO_4$ to Ni and W, i.e., approximately 20.9% of weight loss.

For the reoxidation of the reduced sample, a mixture of water vapor and argon was supplied by water saturation of an argon flow of 60 mL/min at room temperature. The duration of this step was determined in order to complete de reoxidation of Ni and W to $NiWO_4$ (until no mass change could be detected).

3. Results and Discussion

Figure 1a shows the XRD pattern of the synthesized material. The obtained crystallographic phase was indexed with the Match! Software, which is in agreement with the nickel tungstate diffractogram ICSD collection code 015852 [22].

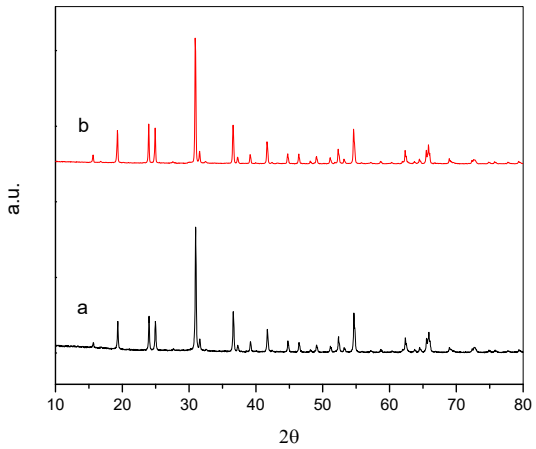

Fig. 1. X-Ray diffraction pattern of the fresh sample (a) and after the three redox cycles (b).

Figure 1b shows the XRD pattern from the sample after being exposed to three redox cycles in a TGA. The obtained crystallographic phase was indexed (as in Figure 1a) with the nickel tungstate diffractogram ICSD collection code 015852, i.e., the same crystallographic phase was present at the beginning and at the end of the redox cycles. This thermal stability can be explained based on what was reported by De Los Ríos et al. [23] that established that when the $CoTiO_3$ is exposed to H_2/Air redox cycles, during the reoxidation process, the cobalt returns to form the perovskite phase of titanate and cobalt, which inhibits the nucleation and migration of Co particles, thus considerably reducing the sintering process.

Table 1 shows results of BET surface area analysis and crystallite sizes of the $NiWO_4$ before and after of being exposed to three redox cycles. The crystallite size was determined through the characteristic signal from the samples crystalline structures and the Scherrer equation [24]:

$$\beta = \frac{0.95\lambda}{L\text{Cos}\theta}$$

Where, β is the width of the peak at half maximum intensity of a specific phase (hkl) in radians, K is a constant (0.95), λ is the wavelength of incident x-rays (0.1541 nm), θ is the center angle of the peak and finally L is the crystallite length (nm).

Table 1. BET surface area and crystallite size of the sample.

Sample	BET (m^2/g)	Fresh crystallite size (nm)	Crystallite Size – Three redox cycles (nm)
$NiWO_4$	4.25	47.2	56.6

According to Table 1, BET analysis results indicate a surface area within the range of other mixed metal oxides. As the mixed Fe-CeZr oxides doped with Ni reported by Sosa et al. [25] that report surface areas between 1.8 and 8.2 m^2/g.

The fresh crystallite size matches the size reported by De Los Rios et al. [20] for the $CoWO_4$ doped with Ni of 47.6 nm. This change in the size of the sample was expected, due to its exposure to the redox cycles at high temperatures as also reported by De Los Rios et al. [8] for the $CoWO_4$ after four redox cycles.

Figure 2 presents the SEM images and the EDS analysis results of the sample before and after the redox cycles. In these images, it can be observed that the fresh $NiWO_4$ sample is composed of sphere like particles whose sizes vary between 0.1 and 0.4 μm and forming agglomerates. In the sample after the redox cycles, it can be observed sphere like polygonal particles with an increase in particle size that ranges between 0.2 and 0.6 μm and also forming agglomerates with slight signs of sintering.

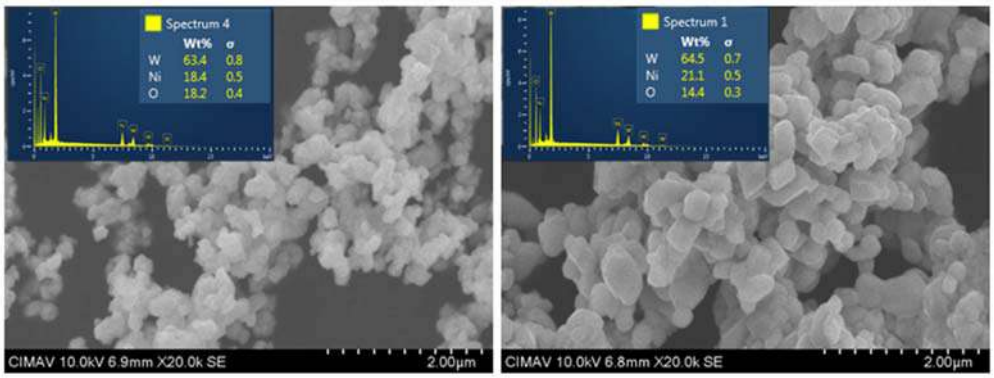

Fig. 2. SEM micrographs and EDS analysis of the fresh $NiWO_4$ (left) and after the redox cycles (right).

This change in morphology is due to the exposure of the material to the constant temperature of 700°C during the redox cycles. However, the signs of sintering of the material agree well with those reported by De Los Rios et al. [8], where these changes are reported to be considered not significant compared to other processes where the particle size can exceed up to one thousand times the original size after redox cycles [26]. In addition, this can be confirmed by observing that the cyclic behavior (Figure 4) and the weight composition (EDS results in Figure 3) of the material are not importantly affected within the performed cycles.

Evaluation of the storage and release of H_2 performance by TGA during three redox cycles can be observed in Figure 3. This test provides the behavior of the $NiWO_4$ during reduction using 5 v% H_2/Ar and reoxidation with ca. 5 v% H_2O/Ar at a constant temperature of 700°C. In this figure the weight change percentage is plotted as a function of time. The corresponding theoretical weight changes (%) from $NiWO_4$ (100%), the reduced metals W and Ni (79.1%), and the possible intermediate species NiO*WO_2 and Ni*WO_3 (94.8%) are represented by horizontal dotted lines. In this figure it can be observed that the material presents a high thermal stability during the redox cycles. It is also possible to observe that $NiWO_4$ is progessively adapting to each cycle since the reduction and oxidation times are decreasing as the number of cycles is increased. For example, in the case of the first cycle compared to the third, there is a time decrease during reduction from 85 to 60 minutes; and a decrease time during oxidation from 132 to 123 minutes. Moreover, there is a close agreement of the sample weight loss of 20.7% with respect to the theoretical value of 20.9% corresponding to the reduction of $NiWO_4$ to Ni and W according to reaction (3). Whereas, the experimental weight gain by oxidation was of approximately 20.7% compared to the theoretical 20.9%, corresponding to the reoxidation of Ni and W to $NiWO_4$ in agreement with reaction (4).

These results obtained also revealed a presumable oxidation mechanism of the reduced metals (Ni + W) that follows two oxidation stages, first W is either oxidized to WO_3 or WO_2 and secondly, Ni is oxidized by any of the previous tungsten oxide forms. The latter is because it is thermodynamically impossible to oxidize Ni with steam (see reaction 5, Gibbs free energy). Therefore, the only source of oxygen capable of regenerating the oxide must be through two reaction paths that involved the formation of WO_2 or WO_3 as intermediate species. The first path deals with the formation of WO_2 by the oxidation of W with steam and followed by the reaction of WO_2 with Ni and H_2O to form $NiWO_4$ according to reactions (6) and (7), respectively.

$$Ni + H_2O \rightarrow NiO + 2H_2 \qquad \Delta G_{700°C} = 43.3\ kJ/mol \qquad (5)$$
$$W + 2H_2O \rightarrow WO_2 + 2H_2 \qquad \Delta G_{700°C} = -23.93\ kJ/mol \qquad (6)$$
$$Ni + WO_2 + 2H_2O \rightarrow NiWO_4 + 2H_2 \qquad \Delta G_{700°C} = 6.92\ k/mo \qquad (7)$$
$$WO_2 + H_2O \rightarrow WO_3 + 2H_2 \qquad \Delta G_{700°C} = 14.25\ kJ/mol \qquad (8)$$
$$W + 3H_2O \rightarrow WO_3 + 3H_2 \qquad \Delta G_{700°C} = -9.68\ kJ/mol \qquad (9)$$
$$Ni + WO_3 + H_2O \rightarrow NiWO_4 + H_2 \qquad \Delta G_{700°C} = -7.33\ kJ/mol \qquad (10)$$

It is clear that this reaction path is not feasible, due to the fact that the reaction (7) will not thermodynamically occur because its ΔG is positive at reaction conditions (700°C). Furthermore, the formation of WO_3 from WO_2 and H_2O through reaction (8) is also not feasible ($\Delta G_{700°C}$ = 14.25kJ/mol). Therefore, the second reaction path, which consists in the formation of WO_3 by the reaction (9) followed by the formation of $NiWO_4$ through reaction (10) is presumably the most likely

reaction path to obtain the desired original oxide. Therefore, according to the kinetics behavior of the oxidation step it can be presumably inferred that reaction (10) should be the rate-determining step.

Furthermore, a thermodynamic equilibrium diagram shown in Figure 4 confirms that initial conditions of 1 kmol of Ni, 1 kmol of W and an excess of steam as the oxidizing atmosphere will insure the formation of $NiWO_4$ at equilibrium conditions.

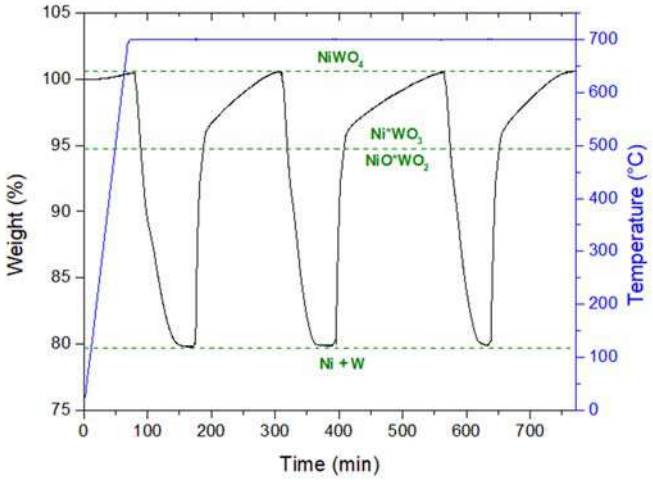

Fig. 3. TGA monitoring results of redox cycles for the sample of $NiWO_4$ at 700°C.

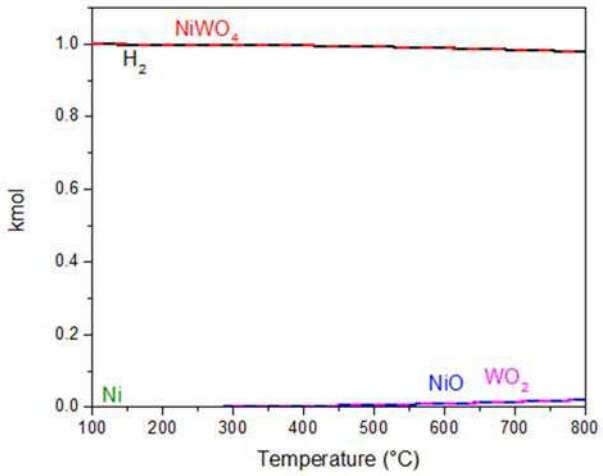

Fig. 4. Thermodynamic analysis of equilibrium composition between Ni, W, and H_2O.

A comparative H_2 storage capacity based on the total reduced solids between different previous research works can be observed in Table 2. The theoretical maximum H_2 storage capacity of $NiWO_4$ is 3.3 W% corresponding to a Ni/W stoichiometric ratio, which is a low capacity compared to iron oxides (4.8 W% maximum theoretical). However, it is worth to notice that this

proposed material is not mixed with any inert materials such as supports or dopants to improve the redox reactions and/or to prevent sintering, which makes the net loading of solids to the reactor totally reactive and the storage capacity of H_2 with respect to total solids is higher than several other Fe-based materials reported in the literature, where their capacity is reduced up to 1.4 W%.

Table 2. Comparative H_2 storage capacity of various metal oxydes.

Sample	H_2 storage capacity based on Total solids (W%)	Reference
$NiWO_4$	3.3	-
$Fe_2O_3/Al_2O_3/SiO_2$	3.4	[5]
Cu-Fe/Ce/Zr	1.8	[11]
Cu/Fe/YSZ	1.8	[12]
Fe_2O_3/YSZ-GDC-Zr-Ce	1.4	[27]
Fe_2O_3/Mo/Al	4.6	[28]

4. Conclusion

Hydrogen storage and release characteristics of pure $NiWO_4$ using TGA redox cycles were studied. Characterization of the material (XRD, BET surface area and SEM) before and after the redox cycles shown slight signs of sintering. However, TGA evaluation indicates that these changes do not significantly affect the performance of $NiWO_4$ as a hydrogen storage material. The isothermal redox test yielded a hydrogen storage capacity of 3.3 wt% based on Ni/W reduced metals, which competitive with current materials reporter in the literature. Furthermore, TGA tests revealed an oxidation mechanism of the reduced metals (Ni + W) that follows a reaction path, which consists in the formation of WO_3 by the oxidation of W with steam, followed by the formation of $NiWO_4$. This reaction path was confirmed by thermodynamic calculations that indicate that the oxidation of Ni, WO_3 and steam is presumably the rate-determining step.

Acknowledgments

The authors of this paper wish to thank the Mexican Society of Hydrogen for accepting the proposed research for dissemination and discussion during its XVIII International Congress, as well as the scholarship. We thank equally to CONACYT for the scholarship awarded to the student involved in the project.

References

1. Sunny, A., P.A. Solomon, and K. Aparna, *Syngas production from regasified liquefied natural gas and its simulation using Aspen HYSYS.* Journal of Natural Gas Science and Engineering, 2016. **30**: p. 176-181.

2. De Los Ríos, T., et al., *Synthesis, characterization and stability performance of CoWO4 as an oxygen carrier under redox cycles towards syngas production.* International Journal of Chemical Reactor Engineering, 2007. **5**(1).
3. Collins-Martinez, V., et al., *Absorption enhanced reforming of light alcohols (methanol and ethanol) for the production of hydrogen: Thermodynamic modeling.* International Journal of Hydrogen Energy, 2013. **38**(28): p. 12539-12553.
4. da Silva Veras, T., et al., *Hydrogen: Trends, production and characterization of the main process worldwide.* International Journal of Hydrogen Energy, 2017. **42**(4): p. 2018-2033.
5. Zhong, M., X. Rui, and Z. Huiyan, *Montmorillonite-Supported Iron Oxide for Hydrogen Storage by Chemical Looping.* Energy Technology, 2017. **5**(8): p. 1399-1406.
6. Eberle, U., M. Felderhoff, and F. Schueth, *Chemical and physical solutions for hydrogen storage.* Angewandte Chemie International Edition, 2009. **48**(36): p. 6608-6630.
7. Niaz, S., T. Manzoor, and A.H. Pandith, *Hydrogen storage: Materials, methods and perspectives.* Renewable and Sustainable Energy Reviews, 2015. **50**: p. 457-469.
8. De los Ríos Castillo, T., *Óxidos Metálicos Mixtos como Portadores de Oxígeno para Procesos REDOX a partir de Metano* in *Química de Materiales*. 2010, CIMAV: Chihuahua, México. p. 19, 21, 71, 121.
9. Hacker, V., R. Vallant, and M. Thaler, *Thermogravimetric investigations of modified iron ore pellets for hydrogen storage and purification: the first charge and discharge cycle.* Industrial & engineering chemistry research, 2007. **46**(26): p. 8993-8999.
10. Hui, W., S. Takenaka, and K. Otsuka, *Hydrogen storage properties of modified fumed-Fe-dust generated from a revolving furnace at a steel industry.* International journal of hydrogen energy, 2006. **31**(12): p. 1732-1746.
11. Kim, H.-S., et al., *Chemical hydrogen storage and release properties using redox reaction over the Cu-added Fe/Ce/Zr mixed oxide medium.* Journal of Industrial and Engineering Chemistry, 2010. **16**(1): p. 81-86.
12. Kim, H.-S., et al., *Hydrogen storage and release properties of a Cu-added Fe/YSZ redox system.* Journal of Nanomaterials, 2013. **2013**: p. 8.
13. Kim, Y.H., et al. *Hydrogen storage and release by redox reaction of iron oxide medium with Mo and Zr additives*. in *Advanced Materials Research*. 2012. Trans Tech Publ.
14. Kim, Y.H., et al. *Effect of Mo and Ce additives on redox behavior for hydrogen storage and release of iron oxide mediums*. in *Advanced Materials Research*. 2012. Trans Tech Publ.
15. Mihai, O., D. Chen, and A. Holmen, *Catalytic consequence of oxygen of lanthanum ferrite perovskite in chemical looping reforming of methane.* Industrial & Engineering Chemistry Research, 2010. **50**(5): p. 2613-2621.
16. Rydén, M., et al., *Combined oxides as oxygen-carrier material for chemical-looping with oxygen uncoupling.* Applied Energy, 2014. **113**: p. 1924-1932.
17. Schwebel, G.L., et al., *Apparent kinetics derived from fluidized bed experiments for Norwegian ilmenite as oxygen carrier.* Journal of Environmental Chemical Engineering, 2014. **2**(2): p. 1131-1141.
18. De los Ríos Castillo, T., et al., *Global kinetic evaluation during the reduction of CoWO4 with methane for the production of hydrogen.* International Journal of Hydrogen Energy, 2013. **38**(28): p. 12519-12526.

19. López-Ortiz, A., et al., *Thermodynamic analysis and process simulation of syngas production from methane using CoWO 4 as oxygen carrier.* International Journal of Hydrogen Energy, 2017.
20. De Los Ríos-Castillo, T., et al., *Study of CoWO4 as an Oxygen Carrier for the Production of Hydrogen from Methane.* Journal of New Materials for Electrochemical Systems, 2009. **12**(1): p. 55-61.
21. Song, Z., et al., *Synthesis of NiWO4 nano-particles in low-temperature molten salt medium.* Ceramics International, 2009. **35**(7): p. 2675-2678.
22. Match!©, *Calculated from ICSD using POWD-12++* 1997. p. 238
23. De los Rios, T., et al., *Redox Stabilization Effect of TiO2 in Co3O4 as Oxygen Carrier for the Production of Hydrogen through POX and Chemical Looping Processes*, in *International Journal of Chemical Reactor Engineering*. 2005.
24. Patterson, A., *The Scherrer formula for X-ray particle size determination.* Physical review, 1939. **56**(10): p. 978.
25. Vázquez, M.S., et al., *Synthesis gas production through redox cycles of bimetallic oxides and methane.* Journal of New Materials for Electrochemical Systems, 2009. **12**: p. 029-034.
26. S., T., S. V., and O. K., *Stotage and supply of pure Hydrogen from methane mediated by modified Iron Oxides* Energy & Fuels, 2004. **18**: p. 820-829.
27. Kosaka, F., et al., *Iron oxide redox reaction with oxide ion conducting supports for hydrogen production and storage systems.* Chemical Engineering Science, 2015. **123**: p. 380-387.
28. Hui, W., et al., *Hydrogen production by redox of bimetal cation-modified iron oxide.* international journal of hydrogen energy, 2008. **33**(23): p. 7122-7128.

XVIII International Congress
of the Mexican Hydrogen Society

Thermodynamic Evaluation and process simulation of the production of Hydrogen-Syngas Using Mixed Fe-based oxides with Methane

J.F. Cazares-Marroquin[1,2], J. M. Salinas-Gutierrez[2], M. J. Melendez-Zaragoza[2], V. Collins-Martinez[2], A. Lopez-Ortiz[2*]

[1]ESIQIE-Instituto Politécnico Nacional, Unidad Profesional Adolfo López Mateos, Edificio 8, Ciudad de México
[2]Departamentode Ingeniería y Química de Materiales, Centro de Investigación en Materiales Avanzados, S.C. Miguel de Cervantes 120, Chihuahua, Chih., 31136, México
*Alejandro López Ortiz: 6144394815, alejandro.lopez@cimav.edu.mx

ABSTRACT

Hydrogen-syngas production is one of the actual and continuous problem in the petrochemical and refining industry, whereas a process that exhibits an optimal industrial efficiency and usage is needed. The use of mixed metal oxides ($FeMO_4$, $FeMoO_4$, $Fe2ZnO_4$, Fe_2MnO_4) as oxygen carriers is proposed to minimize the disadvantages of the current partial oxidation of methane. The objective of the present work is to identify oxides that help the production of syn-gas and are able to regenerate through favorable conditions. This is accomplished by simulating an arrangement of two reactors. The main reduction reaction is carried out in the first reactor: $CH_4 + Fe_2MO_4 = H_2 + CO + Fe + M$. While in the second reactor the following reaction is carried out: $Fe + M + H_2O = Fe_2MO_4 + H_2$. Results indicate that It is possible for the oxide to be completely regenerated, while optimal reaction parameters were obtained for each reactor observing that the material were completely regenerated while not affecting the hydrogen. $FeMoO_4$ produced syn-gas at 750 ° C. However, it was possible not regenerate at favorable conditions. Otherwise, Fe_2ZnO_4 produced syn-gas at 730 ° C and regeneration was feasible at 440 °C. Finally, Fe_2MnO_4 produced syn-gas at 640 °C with regeneration at 600 °C, being the one with the best operating conditions among the studied materials. Simulation results of the different oxides are presented using Aspen-Plus©.

Keywords: Fe2MnO4; syn-gas; Hydrogen; reduction

1. Introduction

Currently about 80% of the energy demand is supplied by fossil fuels (natural gas and oil), 14% of different renewable energies and 6% by nuclear energy. These proportions need to be changed so that there is less dependence on fossil fuels as the global energy demand increases. It is necessary that the renewable energy and the nuclear energy increase considerably and consequently the energy of fossil fuels will eventually decrease. Hydrogen itself is not a source of energy, but if it is an energy vector, it can serve as a transition for the industry between the use of energy provided by hydrocarbons and energy from renewable sources [1].

Hydrogen is a fundamental raw material for the petrochemical and refining industries, it can be produced by various sources of energy from fossil fuels to renewable energy sources via electricity. The most economical route to produce hydrogen is from hydrocarbons, such as natural gas and methanol, through the methane reformation process (SMR) [1,6].

$$CH_4 + H_2O \rightarrow CO + 3H_2 \quad (1)$$

Currently, there are large capacity hydrogen generating plants, due to the great demand of the refining industry, due to the new regulations that restrict fuels with a very low content of sulfur and aromatics, since the hydrodesulphurization process requires a large amount of hydrogen [6]

The main disadvantage for this process is the hydrogen yield that occurs. With SMR it is possible to achieve energy efficiencies of 13.1-14.6 GJ / 1000 Nm^3 giving a yield of 2.4-2.7 mol H_2 for each mole of CH_4 [3].

An even more notable disadvantage is the significant amount of CO_2 that is released during the process. Other processes have been investigated, such as the reforming of methane with CO_2 with the use of metal catalysts [2-5]. The process consists in the reaction of reforming a greenhouse gas as would CH_4 + CO_2 to syn-gas (CO + H_2). The problem that occurs with these catalysts is the sintering that they suffer from the operating conditions and their deactivation by the formation of carbon (in the case of nickel-based catalysts) [4].

The current focus on hydrogen production is to find a way to obtain hydrogen from a renewable source of energy, for example; the electrolysis of water, the gasification of biomass or even nuclear energy. Currently the production of hydrogen by the above methods is not viable. The solution will continue to be to obtain hydrogen from natural gas, since a greater quantity is obtained despite its high CO_2 emissions. Therefore, it becomes necessary to find new ways to obtain hydrogen from hydrocarbons that reduce production costs, CO_2 emissions and increase their performance. [3]

It has been reported that the process of partial oxidation of methane (reaction 2, POX) has a better performance for the production of syn-gas and also has other advantages such as

being an exothermic reaction requiring less energy than the SMR and in addition to needing the use of small reactors because the residence time is short due to rapid kinetics (compared to the SMR). The reaction has been studied using catalysts of different compositions and natures. However, this presents some disadvantages as for example; the operating temperature is very high (900-1000 ° C) and the need for an oxygen plant, which increases the initial investment of the process, making it more expensive.

$$2CH_4 + O_2 = 4H_2 + 2CO \quad (2)$$

Recently, an improvement to the POX process has been reported, which consists in the partial oxidation through a chemical loop process (Chemical Looping Partial Oxidation, CLPO) which is a technology for the production of syn-gas, from natural gas and light hydrocarbons [7], this process was proposed by Ryden and Lyngfelt [9] and continued by Mattisson and Lyngfelt [8]. The most important advantage of this process is that from the produced syn-gas, the production of pure H2 is also feasible in a second stage of the process. Because heat transfer occurs directly between the gas and the oxygen carrier, it is convenient to reduce the size of the reactor, these factors make the CLPO a cheaper technology than the conventional one [7,9].

Use of metal oxides as carriers of oxygen is a strategy that avoids the expense of an oxygen plant to carry out the reaction 2. Since in the fuel reactor a reduction reaction is carried out to the metal oxide (MeO) providing the necessary oxygen (reaction 3) so that the partial oxidation of the methane is carried out and thus obtain syn-gas, in addition to the reduced metal as a reaction product. In the next step, the reduced metal is fed to the second reactor where it will be oxidized with water vapor (reaction 4). In Figure 1 you can see a basic outline of the CLPO process. It can also be seen that the final product of the first reactor is syn-gas and of the second, pure hydrogen is obtained.

$$CH_4 + MeO = 2H_2 + CO + Me \quad (3)$$

$$H_2O + Me = MeO + H_2 \quad (4)$$

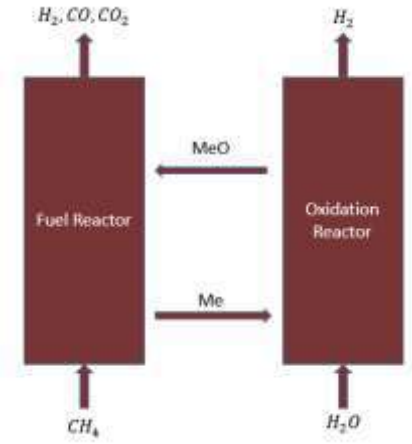

Fig. 1 CLPO process scheme

The MeO is used again in the fuel reactor, thus completing the cycle. This process has also been termed as POX-MeO. The performance of this process is determined by the performance of the oxygen carrier. Therefore, an ideal oxygen carrier must remain reactive after extensive redox cycles, in addition to its capacity as an oxygen carrier and its structural stability must be high [13].

The metal oxides that have been used have been studied for their performance as carriers of oxygen. In 2014 there were more than 700 oxygen carriers that had been synthesized and studied to improve this process [14]. The carriers are composed of two parts; the primary oxide and the inert support. In the study of primary oxides, the oxides of Fe, Ni, Cu, Mn, Co, Ti, etc. have been proposed as candidates. [7] Several processes have used the concept of CLPO as an example can be found; Ni-and Co-based carriers for pure hydrogen production developed by Svoboda et. to the. [18] the fluidized bed reactor using NiO on α-Al2O3 as oxygen carrier proposed by Diego et al. to the. [19] the three-reactor scheme (TRCL) projected by Kang et. to the. [20]. Examining recent CLPO studies, you can find the syngas chemical looping process by Fan et. to the. [21] using OCs based on Fe, Ni, and Ce. The results show a purity obtained from syn-gas of> 90% with Ni- and Fe-based OCs but to these conditions the deposition of carbon and the formation of carbon are shown. carbides (Fe_3C). Other proposed metals have avoided the deposition of carbon but have limited the conversion of methane, reducing the production of syngas.

There are many limitations with the single metals oxides, like thermodynamics and reaction kinetics, in order to solve these limitations, the binary metal oxides were proposed to enhance the kinetics and thermodynamics of the process, as well as the selectivity of the OCs for syngas production. Several examples can be found like the mixed metal ferrites studied by Aston et. al [22] with the 99% yield towards H_2 and the re-oxidation of the OC was confirmed. Results were compared with a single Fe-oxide and the mixed metal spinnels and showed a higher extent of reduction under the same reaction conditions, which

produced more H_2 than the Fe-based material (Fe_2O_3). The Fe-Mn oxides were studied by Lambert et. al. [16] for the chemical looping combustion process, showing a fast reduction of $(Mn,Fe)_2O_3$ to ($MnO + Fe^o$) proving that the Fe-based binary oxides are an excellent proposal for the POX-MeO process for their re-oxidation feasibility and low-cost material. Due to these important features it was decided to study Fe-based binary oxides ($FeMO_4$, M = Mn, Mo, Zn) that will provide high methane conversions towards syngas production, while providing chemical reactivity and high temperature stability of the OC's. Furthermore, the proposed Fe-based OCs ($FeMO_4$) are expected to follow the next reactions scheme:

$$4CH_4 + FeMO_4 \rightarrow 8H_{2(g)} + 4CO_{(g)} + Fe + M \quad (5)$$

$$CH_{4(g)} + FeMO_4 \rightarrow 2H_2O_{(g)} + CO_{2(g)} + Fe + M \quad (6)$$

$$CH_{4(g)} \rightarrow C + 2H_{2(g)} \quad (7a)$$

$$2CO_{(g)} \rightarrow C + CO_{2(g)} \quad (7b)$$

$$4H_2O_{(g)} + Fe + M \rightarrow FeMO_4 + 4H_{2(g)} \quad (8)$$

$$C + H_2O_{(g)} \rightarrow H_{2(g)} + CO_{(g)} \quad (9a)$$

$$C + 2H_2O_{(g)} \rightarrow 2H_{2(g)} + CO_{2(g)} \quad (9b)$$

The POX-MeO-1 (reaction 5) produces syngas (H_2 + CO) along with the reduced metallic species (Fe + M), while POX-MeO-2 (reaction 6) shows the complete oxidation of methane to produce (CO_2 + H_2O). Under these conditions other reactions may arise such as the methane decomposition and the Boudard reactions (reactions 7a and 7b, respectively), these reactions produce coal which is an undesirable product. The re-oxidation of the reduced metallic species is described by reaction 8 to produce the original $FeMO_4$ and H_2. Coal gasification may simultaneously occur in the re-oxidation stage (reactions 9a and 9b) leading to hydrogen production and carbon oxide species (CO and CO_2). Due to the reported reaction behavior of Ni and Co ferrites as OCs in the syngas production and the re-oxidation of its reduced species (Fe and Mn) make this reaction concept very attractive to be evaluated using similar metallic oxides, such as; Fe_2MnO_4, $FeMoO_4$ and Fe_2ZnO_4 under a CLPO reaction scheme.

The aim of the present work is to evaluate the theoretical feasibility of these metal oxides on a CLPO scheme, through the use of thermodynamic analyses and process simulation for the production of syngas. These will consist in the thermodynamic calculations of every reaction involved in the process to determine feasible operating conditions being; temperature, $CH_4/FeMO_4$ molar feed ratio in the fuel reactor and temperature and steam/Fe-M molar ratio in the oxidation reactor. Process simulations using Aspen Plus© will focus in determining process material and energy balances as well as optimal operating conditions in both reactors and in the entire process. The simulation results will be used to evaluate the

thermal efficiency H_2 and syngas yields of the process and compare them with current similar CLPO processes previously reported in the literature to estimate the potential of this technology.

2. Methodology

2.1. Thermodynamic analysis

Each reaction will be studied in terms of the Gibbs free energy as a function of temperature. Calculations of equilibrium concentrations in the CLPO for Fe_xMO4 oxygen carriers (M = Mn, Mo, Zn) were performed using the RGIBBS reactor model of Aspen Plus ©. Since this reactor makes use of a method based on the technique of minimization of Gibbs free energy and that includes all possible reactions that may have an effect according to the possible compounds and phases in the reaction system. For this method it is necessary to define all the compounds that will be involved in the reaction. Therefore, the following gaseous compounds were defined: CH_4 (g), CO, CO_2, H_2, Zn and H_2O, while for the solid compounds were included: C, Fe_2MnO_4, $Fe2ZnO_4$, $FeMoO_4$, MnO_2, MnO, Mn, ZnO, Zn, MoO_3, MoO_2, MoO, Mo and Fe. The aim of this thermodynamic analysis is to evaluate the feasibility of the binary metal oxides in the reaction scheme, using the flowsheet shown in Fig. 2.

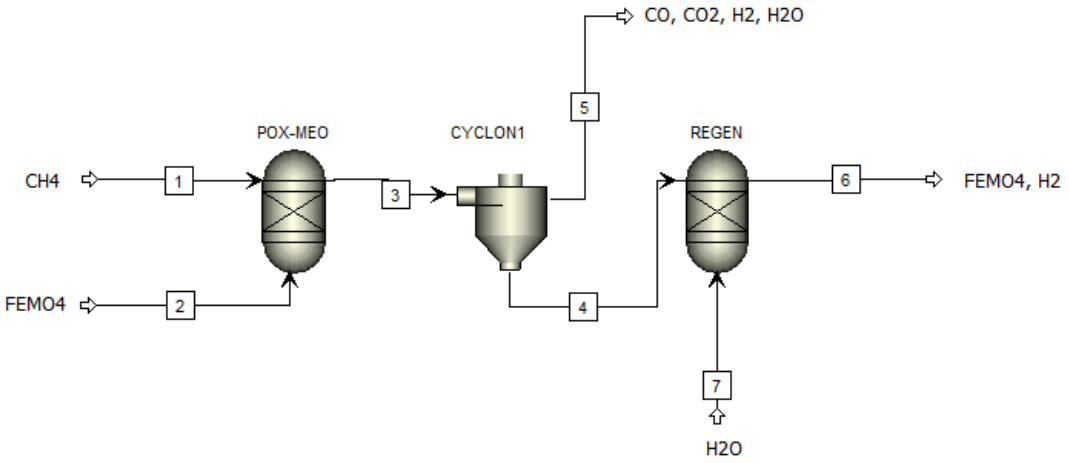

Fig. 2. Flowsheet for the thermodynamic analysis

2.2. Process Simulation

The simulation using Aspen Plus© concentrated on determining the material and energy balance of the process and finding the optimal operating conditions for each reactor. In the thermodynamic evaluation, the process variables studied were: reactor temperature, which varied from 100-1000 °C to 1 atm, the $FeMO_4$ molar feed which varied from 1 to 3 kmol/h.

Likewise, in the oxidation reactor the molar flow of H_2O was studied from 2 to 9 kmol/h in a temperature range of 100-1000 °C.

Simulation conditions used were: a thermodynamic system based on the Redlich-Kwong-Aspen (EOS) state equation to calculate the physical properties of the chemical compounds involved. The molar flow of CH_4 was fixed at 4 kmol/h, in addition to search for the conditions where coal formation is not possible.

Once the process units were established several sensitivity analyses were performed to obtain the optimal operating conditions for the process, while finding the highest yield towards syngas (fuel reactor) and hydrogen (oxidation reactor) and simultaneously avoiding carbon formation in the fuel reactor. The first sensitivity analysis was performed in the fuel reactor aiming to find the molar feed ratio $CH_4/FeMO_4$ and the operating temperature where the highest yield towards syngas and no carbon formation were obtained. The second sensitivity analysis was performed in the oxidation reactor aiming the complete regeneration of $FeMO_4$ and the highest yield of pure hydrogen production.

2.3. Syngas yield and thermal efficiency

The energy efficiency will be evaluated using equation (10) proposed by Abbott et al. [23], which is based on the first law of thermodynamics and is defined as the ratio between the energy produced (H_2 + CO) and the energy required (CH_4).

$$\eta = \frac{\dot{m}_i \times LHV_i}{\dot{m}_i \times LHV_i + W_i + q_i} \quad (10)$$

where m_i and LHV_i are the mass flow and the lower heating value of the "i" species, respectively, while W_i and q_i are the mechanical work and the required heat of the components "i", respectively. This latter refers mainly to the mechanical work and energy requirements of the equipment involved in the process to be evaluated. The mechanical work were not taken into account because it is out of the scope of the present work and the energy requirements are automatically calculated. Fuerthermore, the thermal effienciency was calculated according to the following expression:

$$\eta = \frac{\dot{m}_{H_2} \times LHV_{H_2} + \dot{m}_{CO} \times LHV_{CO}}{\dot{m}_{CH_4} \times LHV_{CH_4} + q_i} \quad (11)$$

The thermal efficiency can be calculated with the high caloric value (HHV) to obtain an suitable range of thermal efficiency. Table 1 shows the LHV and HHV of the species of interest involved in the process.

Table 1. HHV and LHV of process species

Fuel	HHV(MJ/kg)	LHV(MJ/kg)
Hydrogen	142.2	121.2
Carbon monoxide	10.1	10.1
Methane	55.5	50.0

Moreover, the yield to syngas was calculated from simulation results as a the mean yield of H_2 and CO, according to the following expression:

$$Y_{syngas} = \frac{Y_{H_2} + Y_{CO}}{2} * 100 \quad (12)$$

Besides, to reduce energy costs a Pinch Analysis was performed using heat exchangers from Aspen Plus, in order to exploit the temperature gradients between products and reactants involved in the process.

The CLPO process for the OC´s scheme is shown in Fig. 3. The aim of the pinch analysis was to optimize the thermal efficiency of the process. To achieve this, heat exghangers were strategically placed where product streams (GAS-1 and GAS-2) were able to exchange heat with feed streams (methane) to be preheated and to generate steam (STEAM and CH4-PRH streams). Also, in Figure 3 details of the entire process streams, recirculations and heat generation by burners to provide energy to reactors, stream splits and separation of gases from solids (cyclone separators) are presented.

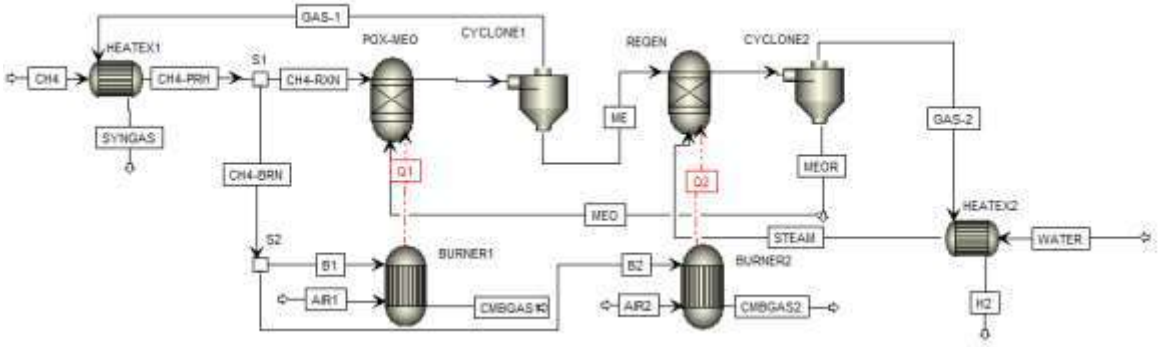

Fig. 3. Process Simulation Flowsheet

3. Results and Discussion

3.1. Thermodynamic analysis

Fig. 4 presents the thermodynamic analysis of the process variables, showing the operation area where the target conditions are achieved (No carbon formation and full OC regeneration).

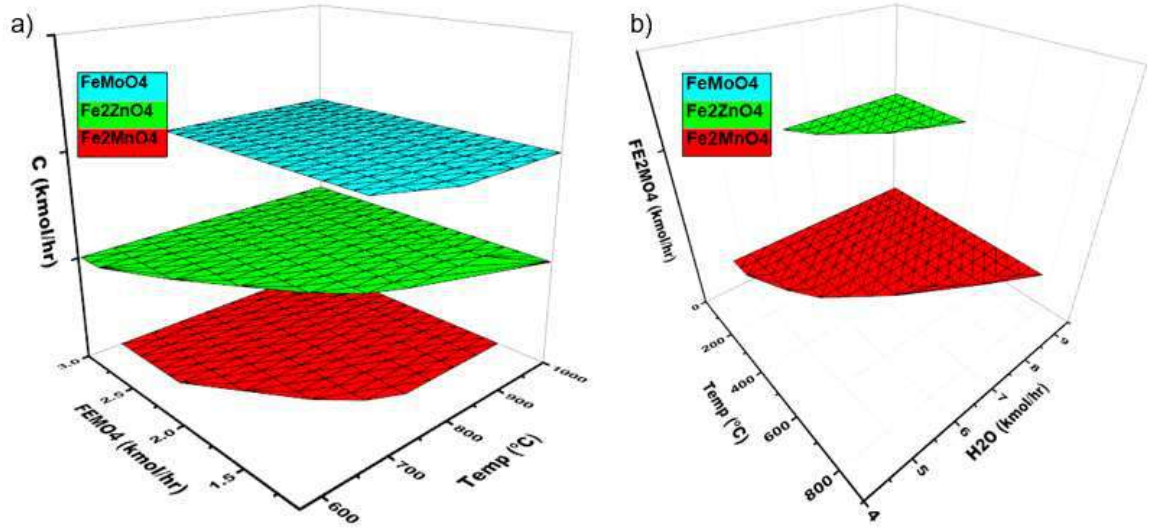

Fig. 4. Free-carbon operation area in fuel reactor (a) and full OC´s oxidation area in oxidation reactor (b).

Results of the thermodynamic analyzes indicate that the widest area belongs to Fe_2ZnO_4 followed by $FeMoO_4$ and Fe_2MnO_4. In the case of the regeneration area, the largest one belongs to Fe_2MnO_4, then to Fe_2ZnO_4, while complete oxidation is not possible when using $FeMoO_4$ as OC for the process. Therefore, $FeMoO_4$ can be discarded as a possible OC for the process, since it cannot be completely oxidized under the studied conditions. Although, Fe_2ZnO_4 presents the largest area of operation without carbon generation, its regeneration area is very small, thus limiting the conditions of the oxidation reactor $T < 400$ °C and $H_2O \leq 9$ kmol/h. However, this temperature is too low for a relatively fast desired reaction kinetics, whereas, a high amount of water used increases energy costs. On the other hand, Fe_2MnO_4 shows a good carbon-free operating area, with conditions of $T > 620$ °C and $Fe_2MnO_4 > 1.4$ kmol/h, which comply with a presumably fast desired reaction kinetics. For the case of the oxidation reactor, there is a good range of temperature and molar flowrate of H_2O where a complete regeneration can be obtained, making it possible to achieve suitable conditions for the entire process.

As a result of the thermodynamic analysis it can be deduced that the only OC that can satisfy with the previously stated requirements for the CLPO of methane process is Fe_2MnO_4, hence the process simulation was performed only for Fe_2MnO_4, which is presented in the following section.

3.2. Process Simulation

Simulation of the process was performed in two stages. In the first stage, the optimal parameters of each reactor were found by sensitivity analyses and results of the previous thermodynamic analysis. In the second stage, an optimal energy balance was achieved through an energy sensitivity analysis (Pinch Analysis) by adding heat exchangers between the input and output streams, thus obtaining the final simulation scheme presented in Figure 3.

Since, the avoidance of carbon formation in the fuel reactor is one of the main objectives of the simulation, a sensitivity analysis was carried out to study the variations presented as a function of the operating temperature and the molar feed to the POX-MeO reactor (fuel reactor).

Fig.5b shows results of this sensitivity analysis on carbon, where the stoichiometric methane feed (4 kmol/h) was fixed (according to the stoichiometric value in reaction 5). In this figure it can be seen that within the POX-MeO reactor carbon free operation can be achieved at conditions of T > 620°C and molar flowrates of Fe_2MnO_4 > 1.4 kmol/h. Fig. 5a presents other results of the sensitivity analysis on the production of hydrogen, which show a greater production of hydrogen at T > 600°C, and a trend to generate more hydrogen by feeding less Fe_2MnO_4, while the point of greatest hydrogen production (H_2 = 7.89 kmol/h) occurs at conditions of T = 1000 ºC and Fe_2MnO_4 = 1 kmol/h.

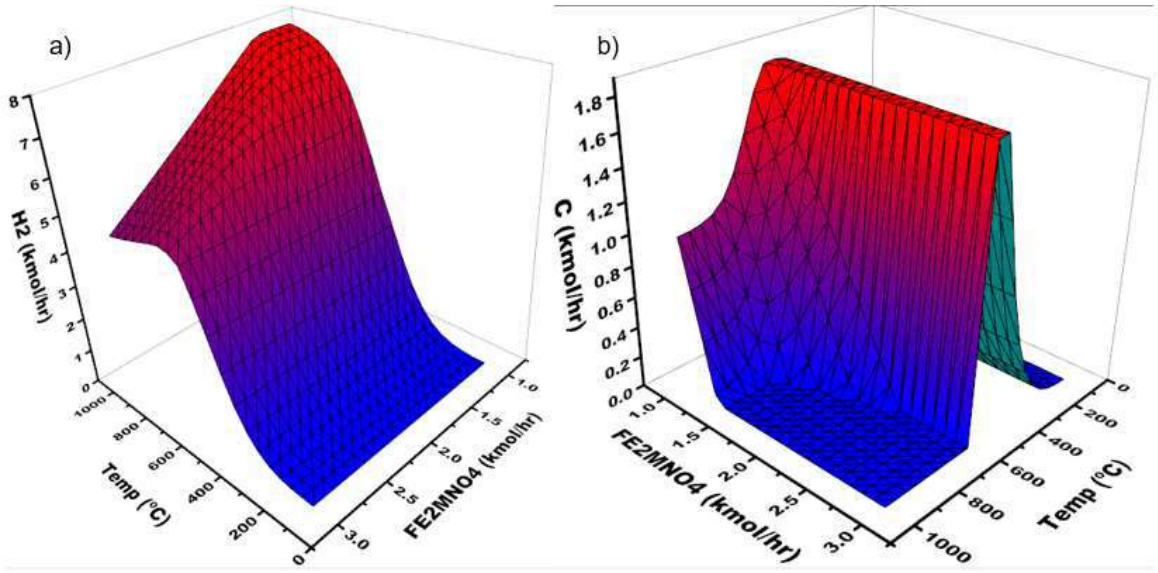

Fig. 5. Surface response of H_2(a) and C (b) formation in POX-MeO reactor

In Fig 6a it can be observed that the formation of CO has a similar behavior to the production of hydrogen, it is desirable that the molar H_2/CO ratio to be equal or greater than 2, which can be achieved at temperatures higher than 620 ºC and molar flowrates greater than 1.4 kmol/h. Results presented in Fig. 6b also show that reaction 6 is promoted at conditions of T = 620 °C and at higher OC molar flowrates, while at higher temperatures the CO_2

generation decreases. Even though it is not one of the main objectives of the present simulation, low CO_2 production is encouraged.

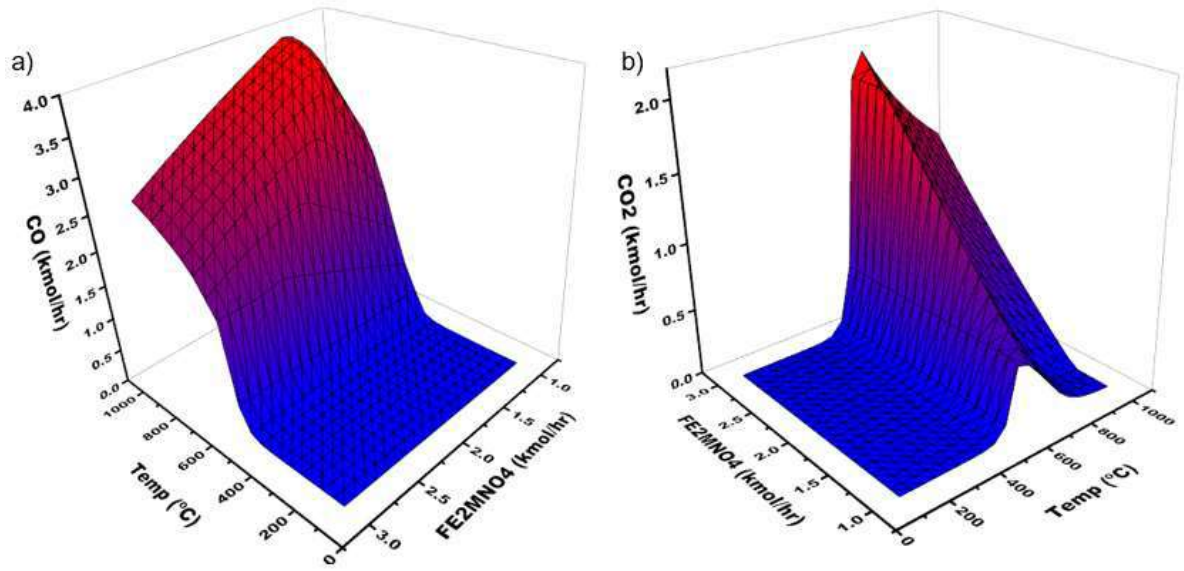

Fig. 6. Surface response of CO(a) and CO_2 (b) formation in POX-MeO reactor

Fig. 7a shows the production of reduced Fe, where it is promoted at the same conditions where no carbon formation is allowed, thus confirming that the operating conditions for the reaction 5 to be carried out at temperatures higher than 620 °C. Also, in Fig. 7b the production of MnO is shown, which is a product that does not agree with reaction 5, since at the thermodynamic conditions studied here the reduction of the MnO_4 ion was limited to

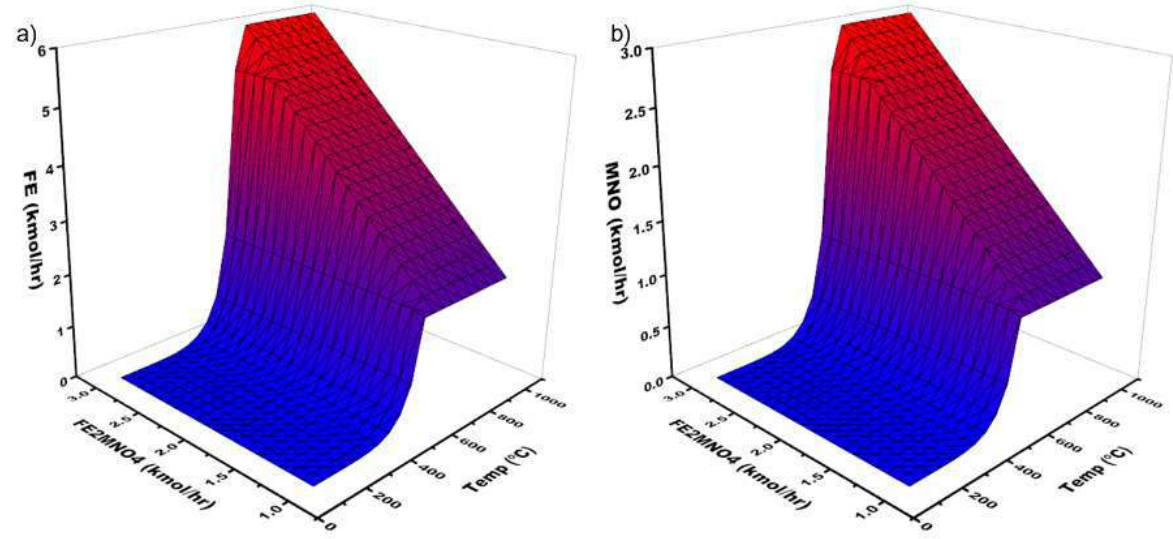

Fig. 7. Surface response of Fe(a) and MnO (b) formation in POX-MeO reactor

the formation of MnO because Mn generation was not favored. Here in this Figure it is also evident that the behavior of MnO production is very similar to Fe generation.

In order to find optimal operating conditions, a comparision of different syngas production scenarios is presented in Table 2. In this Table the production of H_2, CO, Fe and MnO at temperatures of 650ºC, 700ºC, 750ºC, 800ºC, 850ºC and 900ºC were obtained at a fixed molar flowrate of 1.63 kmol/h of Fe_2MnO_4. Likewise, this molar flowrate is proposed for an operating window, where no carbon formation is possibile.

Table 2. H_2, CO, Fe, MnO Production in function of temperature

Temperature (ºC)	H_2 (kmol/hr)	CO (kmol/hr)	Fe (kmol/hr)	MnO (kmol/hr)
650	5.31	1.61	3.2	1.6
700	6.17	2.54	3.2	1.6
750	6.84	3.33	3.2	1.6
800	7.21	3.62	3.2	1.6
850	7.36	3.69	3.2	1.6
900	7.39	3.75	3.2	1.6

When analyzing the production of hydrogen with respect to temperature it can be noted that from 800ºC there is no considerable variation in terms of syngas generation since only a marginal increase is presented. These extreme conditions (T > 800 °C) will ultilmately impact in the associated energy costs of the entire process. Therefore, a temperature within the range of 750ºC-800ºC is very appropriate for the present study. When evaluating this temperature range the temperature of 775ºC was considered suitable due to the fact that the syngas gemerated shows a H_2/CO molar ratio of 2.03, which is very convenient for further processsing of theis gas, for example towards the Fischer Tropsch process. Also, at these conditions Fe_2MnO_4 is completely reduced to Fe and MnO according to reaction 5.

Fuerthermore, Fig. 8 shows the contour plot of methane conversion as a function of reactor temperature (ºC) and Fe_2MnO_4 molar feed (kmol/h). By analyzing these results under the proposed required conditions, a methane conversion of 95.9% can be obtained. The 99% of methane conversion can be obtained at higher temperatures than 800 °C and higher Fe_2MnO_4 molar flowrates of 2.0, but this results in a minimal increase in conversion, compared with higher temperatures that would have to be reached at these conditions.

Consequently, the optimal operating conditions for the fuel reactor (POX-MeO) can be considered as T = 775 °C and Fe_2MnO_4 = 1.6 kmol/h feed. Finally, this is an important result since these are the conditions where there is no carbon deposition is feasible and a complete reduction of Fe_2MnO_4 also occurs, along with a high conversion of methane (95.9%) and a high production of syngas (CO + H_2 = 10.52 kmol/h) that has a H_2/CO molar ratio of 2.03, which is very convenient as described above.

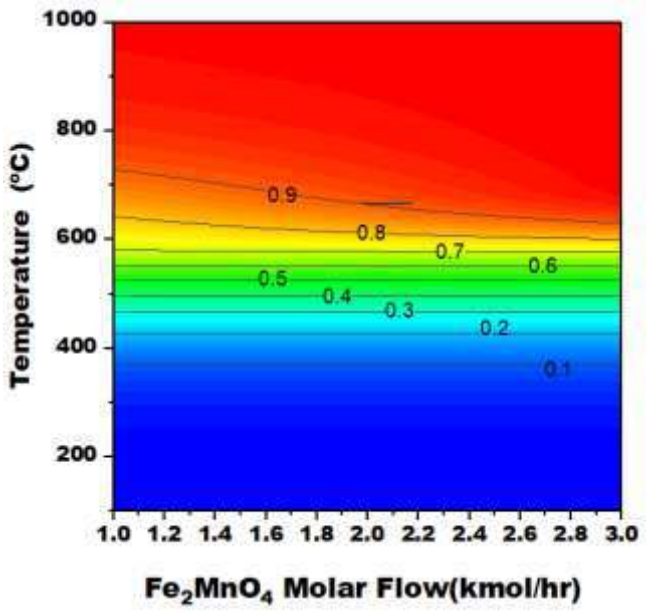

d

Fig. 8. Contour plot of methane conversion as function of temperature and Fe_2MnO_4

Moreover, Fig 9a and 9b show the production of pure hydrogen and the regeneration of the OC, respectively, with respect to the molar steam feed and the temperature of the oxidation reactor (REGEN) for the selection of the more favorable operating conditions in the process.

In Fig. 9b it is shown that the oxidation of Fe and MnO is feasible at very low temperatures (i.e. 100 °C) and a maximum H_2 production of 5.19 kmol/h can be obtained. However, in order to favor the kinetics of reaction (8), it is convenient to use temperatures above 500 °C, according to the results reported by Voldsund et. al. [24]. Thus, the optimum operating condition for the oxidation reactor can be established at T = 500 ºC and a steam molar flowrate of 6.8 kmol/h resulting in a production of Fe_2MnO_4 = 1.6 kmol/h and H_2 = 5.19 kmol/h.

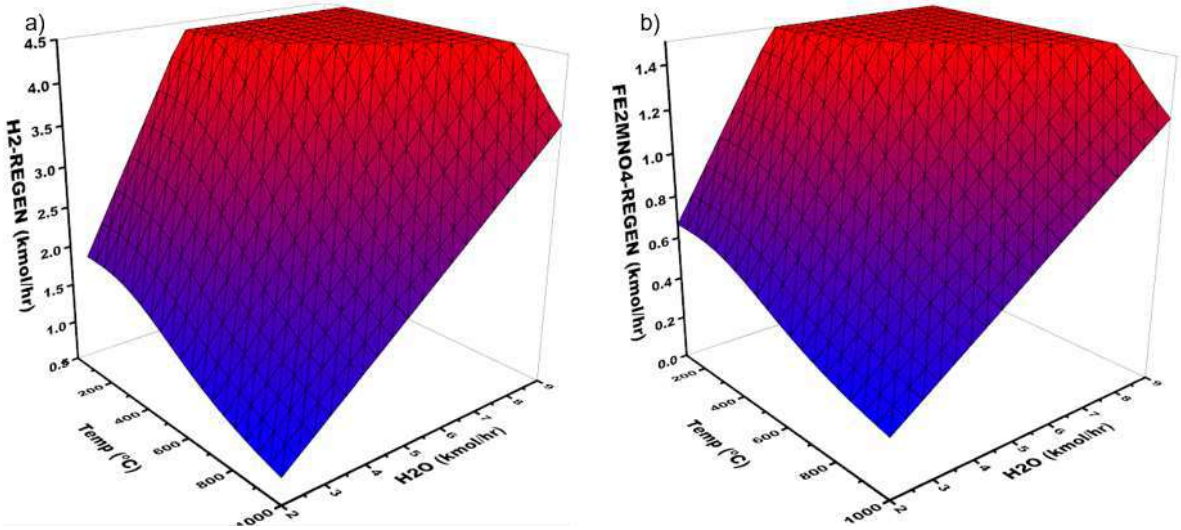

Fig. 9. Surface response of H_2(a) and Fe_2MnO_4 (b) formation in REGEN reactor

Furthermore, Table 3 presents the material and energy balance of the process simulation where two methane burners (BURNER1 and BURNER2) and two heat exchangers (HEATX1 and HEATEX2) were used according to the process scheme of Figure 3. The heat exchangers were used to preheat the methane and water fed to the process using the product gas streams of each reactor (GAS-1 and GAS-2). Methane is preheated and reaches a separator (S1) where it is divided into two streams, one for the reactor feed of 4 kmol/h (CH4-RXN stream) and the other stream for the burners, which will reach another separator (S2) to feed each burner (streams B1 and B2).

In order to achieve a temperature of approximately 775 °C in the POX-MeO reactor, it is necessary that the BURNER1 generates a heat of 987.73 MJ/h (Q1). Likewise, for the REGEN reactor to reach a temperature of approximately 500 °C, the BURNER2 is required to generate a heat of 192.35 MJ/h (Q2).

Furthermore, methane used as fuel combined with air to reach the required temperature in both reactors, these parameters were established by sensitivity analysis, once obtained for optimum parameters the results of the mass balance was obtained and results are reported in Table 3.

Table 3 shows the products of the POX-MeO reactor, with H_2 production of 7.05 kmol/h, together with 3.47 kmol/h, 0.38 kmol/h and 0.65 kmol/h of CO, CO_2 and H_2O, respectively. Finally, it is observed that 0.15 kmol/h of unreacted methane in the final syngas product stream. On the other hand, in the solids stream, a complete reduction of Fe_2MnO_4 is observed where 1.63 kmol/h of MnO and 3.2 kmol/h of Fe were achieved.

Otherwise, results of the REGEN reactor consisted of a complete regeneration of Fe_2MnO_4, with a flowrate of 1.63 kmol/h, which was recirculated to the POX-MeO reactor. In the case of hydrogen, 4.89 kmol/h was obtained, together with 1.91 kmol/h of H_2O (GAS-2).

Reported results of a typical steam methane reforming process (SMR) are approximately 75% H_2, 12% CO, 6% CO_2, and 7% CH_4, while results obtained by the POX-MeO process are 60% H_2, 30 % CO, 6% H_2O, 3% CO_2 and 1% CH_4. Although, the POX-MeO achieves a lower mole fraction of H_2 compared with steam reforming. However, POX-MeO generates a greater conversion of methane and syngas with less impurities than SMR. These results can also be compared with a similar CLPO processes, but with Ni-based OCs which obtained a dry gas product composition of 65% H_2, 25% CO, 9% CO_2 and 1% CH_4 [19]. These results are similar, but it can be noted that the H_2/CO molar ratio is less than 2, which is not a convenient feature for a syngas.

Table 3. Simulation results for the production of syngas from CH_4 and Fe_2MnO_4

STREAM	CH4	CH4-PRH	CH4-RXN	MEO	POX-MEO	GAS-1	SYNGAS	ME	WATER	GAS-2	STEAM	REGEN	H2
Temperature (ºC)	25.00	750.00	750.00	501.21	775.63	775.63	191.70	775.63	25.00	501.21	102.43	501.21	287.95
Pressure (atm)	1.00	1.00	1.00	1.00	1.00	1.00	1.00	1.00	1.00	1.00	1.00	1.00	1.00
Mole Flows (kmol / hr)	5.40	5.40	4.00	1.63	16.59	11.70	11.70	4.89	6.80	6.80	6.80	8.43	6.80
CH4	5.40	5.40	4.00	0.00	0.15	0.15	0.15	--	--	--	--	--	--
CO	--	--	--	--	3.47	3.47	3.47	--	--	--	--	--	--
CO2	--	--	--	--	0.38	0.38	0.38	--	--	--	--	--	--
H2	--	--	--	--	7.05	7.05	7.05	--	--	4.89	--	4.89	4.89
H2O	--	--	--	--	0.65	0.65	0.65	--	6.80	1.91	6.80	1.91	1.91
FE2MNO4	--	--	--	1.63	--	--	--	--	--	--	--	1.63	--
MNO	--	--	--	--	1.63	--	--	1.63	--	--	--	--	--
FE	--	--	--	--	3.26	--	--	3.26	--	--	--	--	--

3.3. Thermal Efficiency

Comparing with other reported studies, the use of a binary oxide as an oxygen carrier greatly helps to reduce temperature operating conditions, since reported operating temperature for the POX-MeO reactor using Fe_3O_4 can reach temperatures equal or greater than 1500ºC [21]. Therefore, results reported in the present work represent an important improvement for this process.

The thermal efficiency was calculated as previously indicated in the methodology section using the equation (10), resulting in a theoretical thermal efficiency that varied between 88.7% (using LHV) and 92.8% (using HHV).

In direct comparison with the efficiency of the SMR process (70-85%), the current process of CLPO (POX-MeO using Fe_2MnO_4 as OC), the efficiency of the process is between 3.7-22.8% higher, attributed entirely to the hydrogen generated in the regeneration stage, which makes the H_2/fuel molar ratio higher than 2.0, hence meaning a higher thermal efficiency.

3.4. Process Yield

According to the results of the mass balance, shown in Table 3. The theoretical yield obtained towards synthesis gas was calculated by the procedure described above. In addition, the molar ratio of H_2/fuel and H_2/CO were calculated and compared with other chemical looping processes already reported in literature. This comparison is shown in Table 4.

Table 4. Thermal Efficiency of the POX-MeO with other processes

Process	Thermal efficiency
SMR [25]	70-85%
ATR [26]	60-75%
POX [19]	60-75%
POX-MeO (Fe_2MnO_4)	88.7-92.8%

Furthermore, Table 5 presents a comparison of the obtained results of the POX-MeO process using Fe_2MnO_4 as OC with respect to other processes for syngas production reported in the literature. Here, in this Table it is evident that the present CLPO (POX-MeO) compared to a SMR process [25] produced twice more H_2 for each mole of CH_4 being fed. This is mainly attributed to the H_2 produced in the regeneration of Fe_2MnO_4 with steam. Additionally, Fe_2MnO_4 has proven to be a convenient OC since, compared to the results reported by de Diego [19], Fe_2MnO_4 obtains a 20% yield and a H_2/fuel molar ratio of 0.5, which is higher than that reported for Ni-based OCs. The H_2/fuel ratio is close to that reported for the autothermal methane process (ATR) by De Souza [26] with only 0.07 difference, but the POX-MeO process reports a greater methane conversion.

Table 5. Comparison of the POX-MeO process with respect other similar CL processes

Process	H_2/Fuel molar ratio	Y_{Syngas} (%)	H_2/CO molar ratio
SMR [25]	1.47	86.7	3.0-5.0
ATR [26]	2.91	61	1.6-2.6
POX [19]	2.5	67	2.6
POX-MeO (Fe_2MnO_4)	2.98	87.4	2.03-3.44

4. Conclusion

Different types of Fe_xMO_4 ($FeMoO_4$, Fe_2ZnO_4, Fe_2MnO_4) were evaluated by thermodynamic analyses and process simulation for the production of hydrogen-synthesis gas (syngas) using Aspen Plus. According to the thermodynamic analysis, it can be concluded that Fe_2MnO_4 is the best oxygen carrier among the Fe-based studied materials for the production of H_2 and syngas. Simulation results found optimal reaction conditions to carry out the POX-MeO process. The optimum temperature in the fuel reactor was 775ºC, obtaining a methane conversion of 95.9% without carbon formation, while the temperature of the oxidation reactor was established at 501ºC for a complete regeneration of the OC, in addition to a stream of pure hydrogen. Furthermore, these results show a syngas stream with a H_2/CO molar ratio of 2.03 from the POX-MeO reactor and high purity hydrogen stream from the REGEN

reactor. The thermal efficiency (88.7-92.8%) and yield (87.4%) obtained are higher compared to other conventional syngas production processes. Finally, an experimental evaluation of the present process is recommended, to assess the results obtained and the viability of this process.

Acknowledgements

The authors are thankful to Centro de Investigacion en Materiales Avanzados, S. C., and Instituto Politecnico Nacional, ESIQIE for their support in the use of the facilities. Furthermore, to the SMH and XVIII International Congress of the Mexican Hydrogen Society for the fellowship to present this research.

References

[1] Hydrogen Tools. Hydrogen production in Northamerica, https://h2tools.org/hyarc/data/hydrogen-production ;2017[accesed 06/07/2018]

[2] Kai Tao, Lei Shi, Qingxiang Ma, Ding wang, Chunyang Zeng, Chunlong Kong, Mingbo Wu, Liang Chen, Shenghu Zhou, Yibo Hu, Noritatsu Tsubaki. Methane reforming with carbon dioxide over mesoporous nickel–alumina composite catalyst, Chemical Engineering Journal, Volume 221, 2013, Pages 25-31.

[3] Bamidele V. Ayodele, Maksudur R. Khan, Su Shiung Lam, Chin Kui Cheng. Production of CO-rich hydrogen from methane dry reforming over lanthania-supported cobalt catalyst: Kinetic and mechanistic studies, International Journal of Hydrogen Energy, Volume 41, Issue 8, 2016, Pages 4603-4615.

[4] Guojie Zhang, Lanxia Hao, Yong Jia, Yannian du, Yongfa Zhang, CO2 reforming of CH4 over efficient bimetallic Co–Zr/AC catalyst for H2 production, International Journal of Hydrogen Energy, Volume 40, Issue 37, 2015, Pages 12868-12879.

[5] Amin R, Liu B, Huang ZB, Zhao YC. Hydrogen and syn gas production via CO2 dry reforming of methane over Mg/La promoted Co–Ni/MSU-S catalyst. International Journal of Hydrogen Energy. 2016;41(2):807-19.

[6] Rostrup-Nielsen T. Manufacture of hydrogen. Catalysis Today. 2005;106(1):293-6.

[7] Forutan HR, Karimi E, Hafizi A, Rahimpour MR, Keshavarz P. Expert representation chemical looping reforming: A comparative study of Fe, Mn, Co and Cu as oxygen carriers supported on Al2O3. Journal of Industrial and Engineering Chemistry. 2015;21:900-11.

[8] Mattisson T., Lyngfelt A., Leion H. Chemical-looping with oxygen uncoupling for combustion of solid fuels. Int J Greenhouse Gas Control. 2009. 3: p. 11-19.

[9] López-Ortiz A, González-Vargas PE, Meléndez-Zaragoza MJ, Collins-Martínez V. Thermodynamic analysis and process simulation of syngas production from methane using CoWO4 as oxygen carrier. International Journal of Hydrogen Energy. 2017;42(51):30223-36.

[10] Jaber O, Naterer GF, Dincer I. Natural gas usage as a heat source for integrated SMR and thermochemical hydrogen production technologies. International Journal of Hydrogen Energy. 2010;35(16):8569-79.

[11] Golmakani A, Fatemi S, Tamnanloo J. Investigating PSA, VSA, and TSA methods in SMR unit of refineries for hydrogen production with fuel cell specification. Separation and Purification Technology. 2017;176:73-91.
[12] Yinka S. Sanusi, Esmail M.A. Mokheimer, Mohamed A. Habib,Thermo-economic analysis of integrated membrane-SMR ITM-oxy-combustion hydrogen and power production plant,Applied Energy,Volume 204,2017,Pages 626-640.
[13] Chen Y, Galinsky N, Wang Z, Li F. Investigation of perovskite supported composite oxides for chemical looping conversion of syngas. Fuel. 2014;134:521-30.
[14] Adanez J, Abad A, Garcia-Labiano F, Gayan P, de Diego LF. Progress in Chemical-Looping Combustion and Reforming technologies. Progress in Energy and Combustion Science. 2012;38(2):215-82.
[15] Azimi G, Rydén M, Leion H, Mattisson T, Lyngfelt A, Institutionen för energi och miljö, Energiteknik, et al. (MnzFe1—z)yOx combined oxides as oxygen carrier for chemical-looping with oxygen uncoupling. AIChE Journal. 2013;59(2):582-8.
[16] Arnold Lambert, Céline Delquié, I. Clémeneçon, Elodie Comte, Véronique Lefebvre, J. Rousseau, B. Durand, Synthesis and characterization of bimetallic Fe/Mn oxides for chemical looping combustion, Energy Procedia, Volume 1, Issue 1, 2009, Pages 375-381.
[17] Schwebel GL, Leion H, Krumm W, Chalmers University of Technology, Chalmers tekniska högskola, Institutionen för kemi- och bioteknik, Oorganisk miljökemi, et al. Comparison of natural ilmenites as oxygen carriers in chemical-looping combustion and influence of water gas shift reaction on gas composition. Chemical Engineering Research and Design. 2012;90(9):1351-60.
[18] Svoboda K, Siewiorek A, Baxter D, Rogut J, Pohořelý M. Thermodynamic possibilities and constraints for pure hydrogen production by a nickel and cobalt-based chemical looping process at lower temperatures. Energy Conversion and Management. 2008;49(2):221-31.
[19] de Diego LF, Ortiz M, García-Labiano F, Adánez J, Abad A, Gayán P. Hydrogen production by chemical-looping reforming in a circulating fluidized bed reactor using Ni-based oxygen carriers. Journal of Power Sources. 2009;192(1):27-34.
[20] Kang K, Kim S, Kim C, Bae K, Cho W, Park C. Oxygen-carrier selection and thermal analysis of the chemical-looping process for hydrogen production. International Journal of Hydrogen Energy. 2010;35(22):12246-54.
[21] Fan L-S. Chemical looping systems for fossil energy conversions. Hoboken, NJ: John Wiley and Sons; 2010.
[22] Aston V, Evanko B, Weimer A. Investigation of novel mixed metal ferrites for pure H-2 and CO2 production using chemical looping. INTERNATIONAL JOURNAL OF HYDROGEN ENERGY. 2013;38(22):9085-96.
[23] Abbott MM, Smith JM, Van Ness HC. Introduction to chemical engineering thermodynamics. Boston: McGraw-Hill; 2001.
p. 619-26.
[24] Voldsund M, Jordal K, Anantharaman R. Hydrogen production with CO2 capture. Int J Hydrogen Energy 2016;41(9):4969-92.
[25] Sunny A, Solomon PA, Aparna K. Syngas production from regasified liquefied natural gas and its simulation using Aspen HYSYS. J Nat Gas Sci Eng 2016;30:176-81.

[26] De Souza Aeam, Maciel LJL, Filho NM, Moraes de Abreu CA. Catalytic activity evaluation for hydrogen production via autothermal reforming of methane. Catal Today 2010;149(3-4):413-7.

XVIII International Congress
of the Mexican Hydrogen Society

SYNTHESIS, CHARACTERIZATION AND PHOTOCATALYTIC EVALUATION OF $NiWO_4$ FOR THE PRODUCTION OF H_2 BY WATER SPLITTING

Ma. G. Joaquín-Morales[1], A. F. Fuentes[1], S. M. Montemayor[2], W.J. Pech-Rodríguez[3], M. J. Meléndez Zaragoza[4], J. M. Salinas Gutiérrez[4], A. López Ortiz[4], V. Collins-Martínez[4]*

[1]CINVESTAV, Unidad Saltillo, C.P. 25900, Ramos Arizpe, Coah. México, [2]Centro de Investigación en Química Aplicada, Blvd. Enrique Reyna No. 140, Col. San José de los Cerritos, 25294 Saltillo, Coah. México, [3]Universidad Politécnica de Victoria, departamento de Ingeniería Mecatrónica. Av. Nuevas Tecnologías 5902, Parque Científico y Tecnológico de Tamaulipas, C. P. 87138 Ciudad Victoria, Tamps. Mexico.[4]Centro de Investigación en Materiales Avanzados S. C., Miguel de Cervantes 120, C. P. 31136, Chihuahua, Chih. México.
virginia.martinez@cimav.edu.mx

ABSTRACT

This work describes the synthesis through precipitation, characterization and photocatalytic evaluation of nickel tungstate ($NiWO_4$) under visible light irradiation for the production of H_2 by the water splitting reaction. This photocatalyst was obtained at room temperature by a dissolution-precipitation reaction between the corresponding Ni^{+2} and $(WO_4)^{-2}$ ions. The precipitation reaction was carried out with the addition of oleic acid (AO, 0.1 and 1%V) using two stirring methods: magnetic (AM) and shear stress (TU) stirring, each performed separately. Characterization was carried out by TGA, XRD, BET, SEM and UV-Vis spectroscopy. Photocatalytic evaluation under visible light irradiation was followed by GC analysis. The thermal behavior of the samples (TGA) revealed the physical and chemical absorption of the OA on the surface of $NiWO_4$, reflected in the increase of the weight loss as a consequence of the increase in AO content. XRD patterns confirmed the crystalline phase of the wolframite structure, with a crystallite size around 22 nm for AM and 22-25 nm for UT for 0.1 and 1% AO. The BET surface area of the samples were 22.43, 24.25 m^2/g and 27 and 18 m^2/g for AM and UT in both percentages of AO, respectively. UV-Vis diffuse reflectance characterization of the samples revealed that these materials present an indirect transition of Eg ~ 2 eV, which is favorable for their photoactivation under visible irradiation of the electromagnetic spectrum. The photocatalytic evaluation for sample 1% AO under UT resulted in a production of 6.5 µmol $H_2/g*h$, resulting in a sevenfold increase compared to WO_3.

Keywords: Photocatalysis, N_iWO_4, water splitting, visible light.

1. Introduction

The growing interest in the use of hydrogen (H_2) as an energy carrier has been a consequence of today´s need of sustainable technologies. However, the routes to obtain this energy vector still have a dependence on traditional fuels, either electricity or fossil fuels [1], which does not contribute to reduce emissions of pollutants into the environment [2].

Solar energy has been taken as a reference in the use of an alternative and sustainable energy, because it is a renewable and accessible energy resource. The use of light or photons, has given rise to various investigations, which according to the thermodynamic reaction associated, can be divided into different areas such as photoelectrolysis, electrochemical photovoltaics and photocatalysis [3]. In general, the photocatalytic process material starts with the absorption of a photon over the surface of a semiconductor that induces the formation of an exciton, that is, an electron-hole pair (e^-/h^+), where the electrons of the valence band (BV) are promoted to the conduction band (BC), this energetic separation is called the band gap energy (Eg). In this photocatalysis process, with the use of semiconductor materials, reactions are carried out by the photons promoting oxidation and reduction reactions within the limits of interaction of the semiconductor and the water molecule, thus achieving its dissociation for the generation of H_2.

The interest in obtaining the optimal properties of a photocatalytic semiconductor consists mainly in the efficiently conversion of solar energy, that is why the search for materials that meet characteristics such as photoactivity under the visible light spectrum is a desirable property. Since, by the use of these materials some portion of solar radiation that reaches the earth can be the utilized, which accounts for around 44% [4].

Otherwise, transition metal tungstates are versatile materials that are used, for their chemical stability and optical properties [5], in many industrial applications such as humidity sensors, optical fibers, ceramic pigments, catalysis [6], photoluminescent devices, capacitors [7], dielectric materials and as photocatalytic materials for the degradation of organic compounds in aqueous phase [8]. Although there is a great interest in these materials as photocatalysts, there are few studies on their use towards the photocatalysis for the generation of hydrogen by water-splitting [9, 10].

These tungstate materials can be synthesized following different synthesis routes that include: electrochemical methods [11], hydrothermal processes [12, 13], mechanochemical synthesis [14], the molten salt technique and chemical methods in aqueous phase (co-precipitation, sol- gel and precipitation [15, 16]). However, many of these routes require sophisticated equipment and conditions that limit their synthesis on a larger scale. On the other hand, the precipitation route is a simple method that allows the incorporation of physical devices as a source of stirring, or even the use of surfactants in order to control the size and dispersion of the synthesized materials to obtain particles at the nanoscale [17].

Under the precipitation route, the stirring process is crucial for obtaining powders by the appropriate mixing of reagents in aqueous phase. Different stirring devices are used in order to homogenize the dispersion and to avoid the agglomeration of particles to obtain fine particles [18]. The movement of the components in the mixture can be carried out by different basic mechanisms. In the laboratory, one of the conventional methods is to use a rotating field of magnetic force, which is used to induce a constant mechanical stirring [19], which is commonly known as magnetic agitation (AM). On the other hand, the mixture can also be homogenized by shear stress stirring [20]. In this type of stirring technique, a device employs the rotor/stator principle, where the mixture is driven axially through interstices at high speed, causing small turbulences within the mixture. This phenomenon allows an enhanced dispersion of the mixtures, as well as the incorporation of powders in liquids, as a consequence of the wet milling process that continuously occurs in the interstices of the rotor.

In this paper a dissolution-precipitation route for the synthesis of nickel tungstate is proposed by the combined use of oleic acid as a surfactant and two different stirring techniques. These stirring methods consist in magnetic and shear stress, which were independently used during the precipitation process. Therefore, the aim of the present research is to synthesize, characterize and evaluate $NiWO_4$ under a visible light radiation and to find appropriate synthesis conditions that allow obtaining a material that is suitable for the production of H_2 by water-splitting.

2. Materials and Methods

Synthesis

$NiCl_2 \cdot 6H_2O$, $Na_2WO_4 \cdot 2H_2O$ and oleic acid as surfactant were used, all of these analytical grade materials purchased from Sigma-Aldrich. $NiWO_4$ was prepared via dissolution-precipitation directly in aqueous medium. The concentrations used were both 0.3 M, in a 1: 1 ratio for the Ni^{2+} and $(WO_4)^{2-}$ ions, under two independent stirring sources: magnetic using a Thermolyne Cimarec 2, Model SP46925 and by shear stress by a Ultra-Turrax equipment model T18, IKA brand. Each of these devices were used separately. When the mixing process took place, oleic acid (AO) was added at 0.1 and 1% by volume. Later, when the mixing process ended, the precipitate was left under stirring for five additional minutes. The formed precipitate was filtered and washed with hexane, deionized water and ethanol. Then, the materials were kept at 80 ° C for 24 hours in a drying oven, and finally were heat-treated at 400 °C, for four hours.

Characterization

The thermal and stability behavior of the materials were analyzed by TGA in a TA Instruments model SDT Q600 V20.9. The crystalline structure of the materials was examined by the X-ray diffraction technique (XRD) using a Philips Xpert diffractometer, and employing a Cu-Kα radiation (λ = 0.15406 nm). The diffraction data were recorded for 2θ values between 10 and 80°. The crystallite size was calculated from the data of the obtained XRD patterns by using the Scherrer´s equation. While, the morphological characterization was performed using a scanning electron microscope (SEM) (Philips brand model XL 30 ESEM). The surface area was studied by N_2 physisorption using the BET (Brunauer-Emmett-Teller) technique in a AUTOSORB-1C of

Quantachrome. For the band gap studies, a UV-Vis spectrophotometer equipped with an integration sphere (Perkin Elmer Lambda 25 brand) and the diffuse reflectance technique (DRS) were employed.

Photocatalytic Evaluation

Evaluation of the photocatalytic activity towards hydrogen production was performed using a 250 W Phillips metal halide lamp and a 2% V solution of methanol as a sacrifice agent. 0.2 grams of the synthesized $NiWO_4$ photocatalyst was suspended in distilled water and placed in a laboratory scale reactor. The monitoring of the reaction was carried out using a gas chromatograph (Perkin Elmer Clarus 580 brand) for a period of 8 hours, with sampling at 1 hour intervals. Figure 1, presents a general scheme of the photocatalytic evaluation system employed in this research.

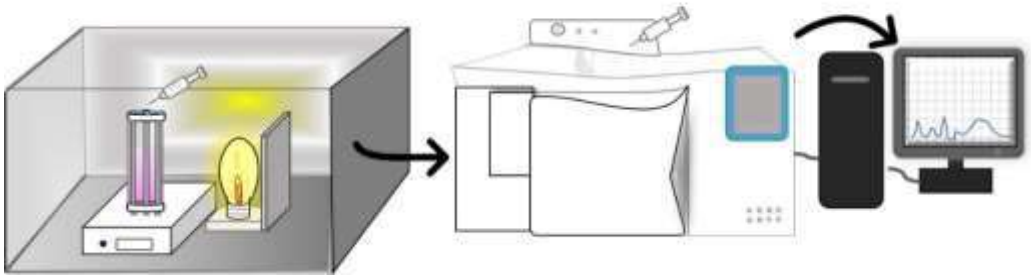

Figure 1. Photocatalytic evaluation system

3. Results and Discussion

Thermal Analysis

The thermal stability of the precipitated materials was determined through thermogravimetric analysis (TGA) experiments. Figure 2 presents results of TGA experiments performed on 0.1% V OA using magnetic stirring (AM) and 1% OA employing shear stress stirring (UT) samples and named 0.1%-AM, 0.1%-UT and 1%-AM, 1%-UT, respectively. In this Figure it can be seen that the synthesized materials present common characteristics. Below 100 °C, they present a weight loss that can be attributed to the elimination of water adsorbed on the surface of the material, consecutively the continuous loss of weight is attributed to chemically bound water up to a temperature of 100-250 °C. Furthermore, materials with 0.1% of AO have a weight loss of 8.5% by weight that is associated with the loss of 1.5 molecules of H_2O. For the samples with 1%, in the same interval, the loss was 7 and 7.5 H_2O molecules for AM and UT, respectively. The subsequent weight loss of these samples is associated with the temperature at which the decomposition of the AO occurs, according to reports in the literature [21, 22]. This decomposition can occur in stages or even in a single step due to the type of OA adsorption on the surface of the material [23]. For samples with 0.1% AO, a weight loss of 3% occurs in two stages, suggesting that the AO is adsorbed on the surface in a physical and chemical manner, being this last in a lower extent

[22]. For the case of samples with 1% OA the weight loss is greater, therefore, the interaction between the material and the AO is expected to be stronger.

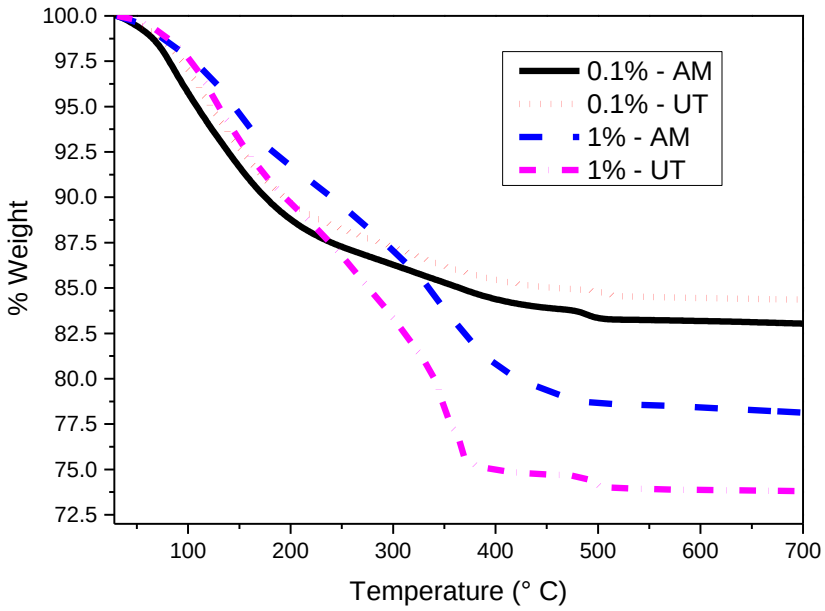

Figure 2. Thermogravimetric analysis curves of precipitated samples

X-Ray Diffraction

The X-ray diffraction analysis of the thermally treated samples at 400 °C is presented in Figure 3. Based on these XRD patterns, it can be seen that identified signals present in the samples belong to a monoclinic phase of $NiWO_4$ that matches with the standard of the Joint Committee for Powder Diffraction (JCPDS) with number 00-015-0755 [24-26]. Using the Scherrer´s equation, where half of the maximum width (FWHM) of the individual diffraction peak was taken as reference at ° 2θ = 19, crystallite sizes of 22 and 19 nm were calculated for samples with 0.1%, for AM and UT, respectively. While, samples with AO at 1% the for AM and UT presented crystallite values of 22 and 28 nm, respectively.

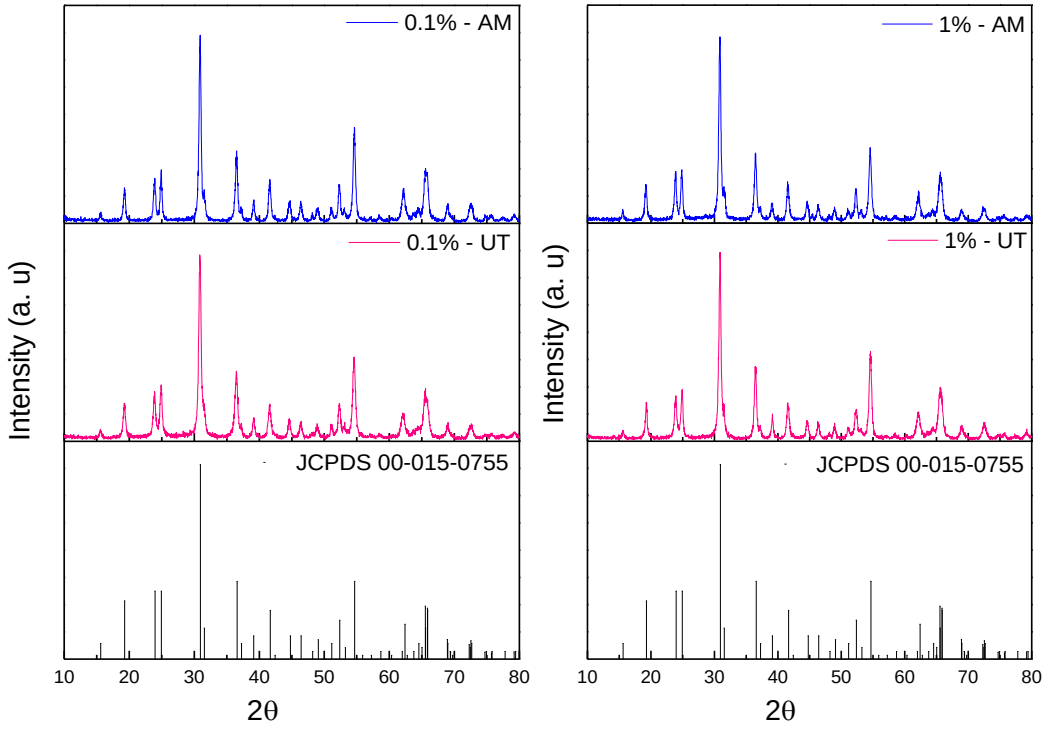

Fig. 3. Diffraction patterns of samples with 0.1 and 1% of AO using Am and UT stirring.

Morphology

Morphology of the samples was examined by SEM. Figure 4 show micrographs of thermally treated NiWO4 samples at different magnifications such as 20000 and 25000x. In this Figure, it is possible to notice that there are a series of lines corresponding to the sample holder and another region where a particle cluster is observed. The particles present a spherical type morphology with an average size of 75 and 65 nm for AM, with 0.1 and 1% AO, respectively. For samples stirred by UT the average size observed was 83 and 132 nm for UT with 0.1 and 1%, respectively.

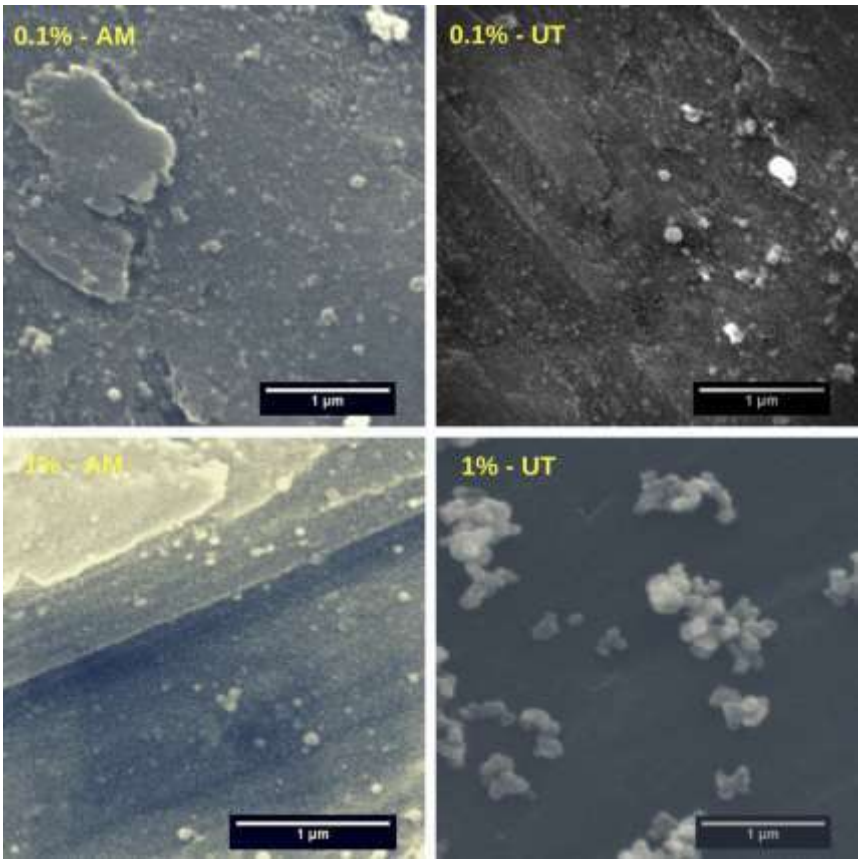

Fig 4. SEM images of the heat-treated $NiWO_4$ samples.

BET surface area

In order to determine the specific surface area and the pore size of the materials, BET tests were carried out. According to the results presented in Figure 5, the adsorption isotherms for the samples prepared by AM and UT (0.1 and 1% of AO) belong to a type IV with a H4 hysteresis curve, due to the range of P/Po (0.6-0.98) where the hysteresis occurs [27, 28], which is an indication that the material presents mesoporosity. Surface area of the AM samples were 22.4, and 27.7 m^2/g, while for UT were 26.9 and 18.5 m^2 g for 0.1 and 1% of AO, respectively. These values agree well with those reported in the literature for this material [29-32].

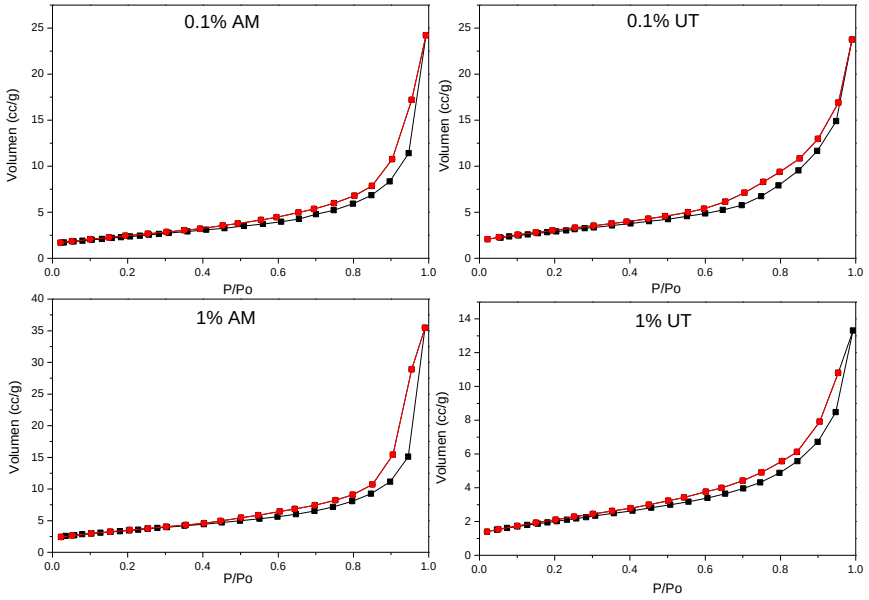

Fig 5. N_2 physisorption isotherms for $NiWO_4$

Optical Properties

For the study of the optical properties of $NiWO_4$, UV-Vis spectroscopy using the diffuse reflectance technique was used. The band gap energy (Eg) of the materials was calculated using the Kubelka-Munk function (K-M or F (R)) that is presented in Eq. 1.

$$F(R_\infty) = \frac{(1-R)^n}{2R} \qquad (1)$$

Figure 6 presents the values obtained from the F(R) function that were plotted versus *hv* and this representation is known as the Tauc method [33]. Furthermore, an Eg value is obtained by extrapolating a tangent line to the generated curve (with a positive slope) and the intersect value to the *hv* axis where F(R) is zero (see Fig. 6). The estimated values for the direct (n=½) and indirect (n=2) transitions were 2.27 and 3 eV for 0.1% OA and 2.2 ~ 2.4 and 3 eV for 1% OA, respectively for both AM and UT materials. According to the obtained Eg values from Figure 6, the values for the direct and indirect transitions fall within values reported in the literature (see Table 1). However, there are still no reports on a more accurate Eg for these materials. This is due to the fact that the material may contain structural defects that may change its optical properties, as Joy concluded [34]. In addition, considering the fact that the Eg value may vary according to an inverse relationship between the particle size and Eg, there is no significant difference in the Eg values obtained between agitation methods (AM and UT) and the amount of AO used.

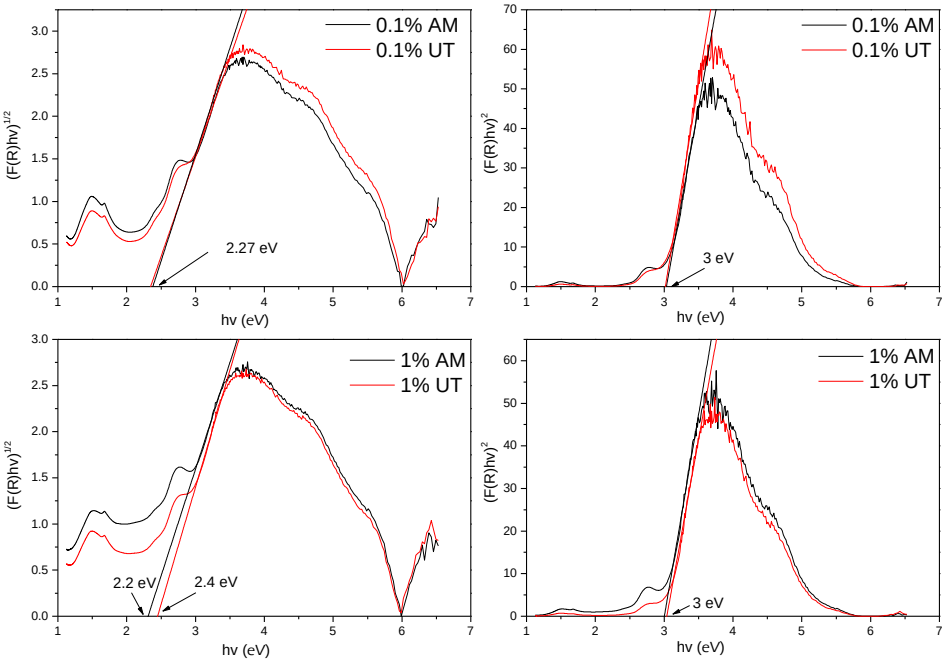

Fig. 6. Tauc plots for $NiWO_4$

Table 1. Band gap values reported for $NiWO_4$ using direct and indirect transition

This Work		Reported in the literature		
(n= ½) eV	(n=2) eV	(n=1/2) eV	(n=2) eV	"n" non-specified
2.27 (0.1%-AM) 2.27 (0.1%-UT) 2.2 (1%-AM) 2.4 (1%-UT)	3.0 (0.1%-AM) 3.0 (0.1%-UT) 3.0 (1%-AM) 3.0 (1%-UT)	2.28 [35] 2.25 [36] 1.35 [36] 2.95 [37]	2.0 [35] 3.2 [38] 1.82 [37]	2.23 [39] 2.10 [40] 2.2 [41]

Photocatalytic evaluation

The photocatalytic evaluation for the generation of hydrogen was carried out for 8 continuous hours with sampling intervals of one hour for each of the synthesized materials. The comparison of H_2 production was made taking WO_3 as reference material during the corresponding evaluation.

Figure 7 presents the photocatalytic evaluation of the $NiWO_4$ samples in comparison with WO_3 as a reference material. In this figure, the amount of H_2 produced per mas of catalyst ($\mu mH_2/g$) is

plotted as a function of time for each photocatalyst evaluated. In this plot it can be seen that the AM samples with 0.1 and 1% OA show a similar behavior to WO_3, exhibiting a production of 5 and 10 µmol H_2/g·h. Despite the fact that these samples presented a larger BET area and a similar Eg compared to the 0.1%-UT and 1%-UT samples, the production of the latter were 30 and 50 µmol H_2/g·h, respectively. That is, the double and triple compared to AM and with respect to materials reported by López X. et al. [30]. The factors that are involved in the photocatalytic activity of each of these materials mainly consist of the recombination velocity of the excitons and on the position of the VB and CB valances according to Montini et. at [37]. It is important to note that the research reported in the literature for the generation of H_2 by water splitting under the same conditions of these materials is scarce.

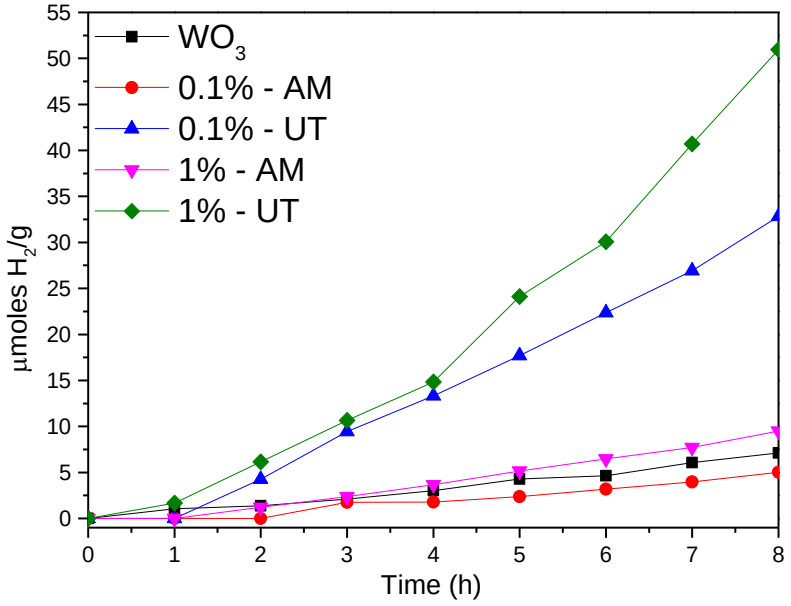

Fig. 7 Photocatalytic evaluation of the $NiWO_4$ samples compared to WO_3 as reference

4. Conclusion

The synthesis of $NiWO_4$ powders using different stirring methods and the incorporation of AO as a surfactant was successfully carried out. The characterization of the materials indicates that with a thermal treatment at 400 °C the materials present crystalline phases corresponding to the wolframite structure. Results of the photocatalytic evaluation for the generation of H_2 indicate that, it is possible to determine that the samples that were “shaken” under a UT stirring technique present a greater photocatalytic activity than those prepared by the conventional stirring method (AM. Furthermore, as part of the optical properties evaluated, in these materials no significant

differences were observed regarding the stirring method and the amount of surfactant (AO). However, from BET surface area results, it was possible to identify that an increase in the AO content in the samples did not contribute to a significant difference in the surface area values of the samples prepared by AM. On the other hand, the increase of 10% of AO in the UT sample is indicative of the limit values of the AO content that can be used for this material, if the purpose is to increase the sample surface area.

Acknowledgements
The authors acknowledge, Eng. Francisco Botello Rionda, M.Sc. Felix Ortega Celaya, M.Sc. Sergio Rodriguez Arias, Eng. Felipe de Jesus Marquez Torres, Eng. Wilber Antúnez Flores and Eng. Luis de la Torre Sáenz for their contributions to the results of TGA, DRX, SEM and BET. Special thanks are given to the National Nanotechnology Laboratory at the Advanced Materials Research Center, S.C. (CIMAV) and CINVESTAV Saltillo, for their support in the use of the facilities. In addition, thanks are given to CONACyT for the financial support provided to carry out the present research.

References

[1] Olah GA. Beyond Oil and Gas: The Methanol Economy. Angewandte Chemie International Edition. 2005;44:2636-9.
[2] Ahmad H, Kamarudin SK, Minggu LJ, Kassim M. Hydrogen from photo-catalytic water splitting process: A review. Renewable and Sustainable Energy Reviews. 2015;43:599-610.
[3] Pawar RC, Lee CS. Chapter 1 - Basics of Photocatalysis. In: Pawar RC, Lee CS, editors. Heterogeneous Nanocomposite-Photocatalysis for Water Purification. Boston: William Andrew Publishing; 2015. p. 1-23.
[4] James Martin D. Investigation into High Efficiency Visible Light Photocatalysts for Water Reduction and Oxidation. London, United Kingdom: University College London; 2015.
[5] Taneja P, Sharma S, Umar A, Mehta SK, Ibhadon AO, Kansal SK. Visible-light driven photocatalytic degradation of brilliant green dye based on cobalt tungstate ($CoWO_4$) nanoparticles. Materials Chemistry and Physics. 2018;211:335-42.
[6] Pourmortazavi SM, Rahimi-Nasrabadi M, Khalilian-Shalamzari M, Zahedi MM, Hajimirsadeghi SS, Omrani I. Synthesis, structure characterization and catalytic activity of nickel tungstate nanoparticles. Applied Surface Science. 2012;263:745-52.
[7] Xing X, Gui Y, Zhang G, Song C. $CoWO_4$ nanoparticles prepared by two methods displaying different structures and supercapacitive performances. Electrochimica Acta. 2015;157:15-22.
[8] Ahmadi F, Rahimi-Nasrabadi M, Fosooni A, Daneshmand M. Synthesis and application of CoWO4 nanoparticles for degradation of methyl orange. Journal of Materials Science: Materials in Electronics. 2016;27:9514-9.
[9] Chen P, He HY. H2 evolution from $H_2O/H_2O_2/MWO_4$ (M = Fe^{2+}, Co^{2+}, Ni^{2+}) systems by photocatalytic reaction. Research on Chemical Intermediates. 2014;40:1947-56.

[10] Jothivenkatachalam K, Prabhu S, Nithya A, Chandra Mohan S, Jeganathan K. Solar, visible and UV light photocatalytic activity of $CoWO_4$ for the decolourization of methyl orange. Desalination and Water Treatment. 2015;54:3134-45.
[11] Pourmortazavi SM, Rahimi-Nasrabadi M, Fazli Y, Mohammad-Zadeh M. Taguchi method assisted optimization of electrochemical synthesis and structural characterization of copper tungstate nanoparticles. International Journal of Refractory Metals and Hard Materials. 2015;51:29-34.
[12] Fu H, Lin J, Zhang L, Zhu Y. Photocatalytic activities of a novel $ZnWO_4$ catalyst prepared by a hydrothermal process. Applied Catalysis A: General. 2006;306:58-67.
[13] Deng J, Chang L, Wang P, Zhang E, Ma J, Wang T. Preparation and magnetic properties of $CoWO_4$ nanocrystals. Crystal Research and Technology. 2012;47:1004-7.
[14] Mancheva M, Iordanova R, Dimitriev Y. Mechanochemical synthesis of nanocrystalline $ZnWO_4$ at room temperature. Journal of Alloys and Compounds. 2011;509:15-20.
[15] Pourmortazavi SM, Rahimi-Nasrabadi M, Khalilian-Shalamzari M, Ghaeni HR, Hajimirsadeghi SS. Facile Chemical Synthesis and Characterization of Copper Tungstate Nanoparticles. Journal of Inorganic and Organometallic Polymers and Materials. 2014;24:333-9.
[16] Montemayor SM, Fuentes AF. Electrochemical characteristics of lithium insertion in several 3D metal tungstates (MWO_4, M=Mn, Co, Ni and Cu) prepared by aqueous reactions. Ceramics International. 2004;30:393-400.
[17] El-Shazly AN, Rashad MM, Abdel-Aal EA, Ibrahim IA, El-Shahat MF, Shalan AE. Nanostructured ZnO photocatalysts prepared via surfactant assisted Co-Precipitation method achieving enhanced photocatalytic activity for the degradation of methylene blue dyes. Journal of Environmental Chemical Engineering. 2016;4:3177-84.
[18] Yoruç ABH, Koca Y. DOUBLE STEP STIRRING: A NOVEL METHOD FOR PRECIPITATION OF NANO-SIZED HYDROXYAPATITE POWDER. Digest Journal of Nanomaterials & Biostructures (DJNB). 2009;4:73-81.
[19] Carrà S. FUNDAMENTALS OF CHEMISTRY - Volume I2009.
[20] Wilkinson JB, Moore RJ, Navarro MAR, Devesa DR. Cosmetología de Harry: Díaz de Santos; 1990.
[21] Baharuddin AA, Ang BC, Abu Hussein NA, Andriyana A, Wong YH. Mechanisms of highly stabilized ex-situ oleic acid-modified iron oxide nanoparticles functionalized with 4-pentynoic acid. Materials Chemistry and Physics. 2018;203:212-22.
[22] Zhao SY, Lee D-G, Kim C-W, Cha H-G, Kim Y-H, Kang Y-S. Synthesis of magnetic nanoparticles of Fe_3O_4 and $CoFe_2O_4$ and their surface modification by surfactant adsorption. Bulletin of the Korean Chemical Society. 2006;27:237-42.
[23] Shen L, Laibinis PE, Hatton TA. Bilayer Surfactant Stabilized Magnetic Fluids: Synthesis and Interactions at Interfaces. Langmuir. 1999;15:447-53.
[24] Nithiyanantham U, Ede SR, Anantharaj S, Kundu S. Self-Assembled NiWO4 Nanoparticles into Chain-like Aggregates on DNA Scaffold with Pronounced Catalytic and Supercapacitor Activities. Crystal Growth & Design. 2015;15:673-86.
[25] Mohamed MM, Ahmed SA, Khairou KS. Unprecedented high photocatalytic activity of nanocrystalline WO3/NiWO4 hetero-junction towards dye degradation: Effect of template and synthesis conditions. Applied Catalysis B: Environmental. 2014;150-151:63-73.

[26] Song Z, Ma J, Sun H, Wang W, Sun Y, Sun L, et al. Synthesis of $NiWO_4$ nano-particles in low-temperature molten salt medium. Ceram Int. 2009;35.
[27] Wang Y, Liping L, Li G. Solvothermal synthesis, characterization and photocatalytic performance of Zn-rich ZnWO4 nanocrystals. Applied Surface Science. 2017;393:159-67.
[28] Wang J, Zhou Y, Hu Y, O'Hayre R, Shao Z. Facile Synthesis of Nanocrystalline TiO_2 Mesoporous Microspheres for Lithium-Ion Batteries. The Journal of Physical Chemistry C. 2011;115:2529-36.
[29] M Zawawi SM, Yahya R, Hassan A, Mahmud HNME, Daud MN. Structural and optical characterization of metal tungstates (MWO_4; M=Ni, Ba, Bi) synthesized by a sucrose-templated method. Chemistry Central Journal. 2013;7:80.
[30] López XA, Fuentes AF, Zaragoza MM, Díaz Guillén JA, Gutiérrez JS, Ortiz AL, et al. Synthesis, characterization and photocatalytic evaluation of MWO_4 (M = Ni, Co, Cu and Mn) tungstates. International Journal of Hydrogen Energy. 2016;41:23312-7.
[31] Mohamed MM, Ahmed SA, Khairou KS. Unprecedented high photocatalytic activity of nanocrystalline WO3/NiWO4 hetero-junction towards dye degradation: Effect of template and synthesis conditions. Applied Catalysis B: Environmental. 2014;150-151:63-73.
[32] AlShehri SM, Ahmed J, Alzahrani AM, Ahamad T. Synthesis, characterization, and enhanced photocatalytic properties of $NiWO_4$ nanobricks. New Journal of Chemistry. 2017;41:8178-86.
[33] López R, Gómez R. Band-gap energy estimation from diffuse reflectance measurements on sol–gel and commercial TiO_2: a comparative study. Journal of Sol-Gel Science and Technology. 2012;61:1-7.
[34] Joy J. Doping Effect an Optical Band Gap and Luminescence of Pure and Nd-Doped $CoWO_4$ Wolframite Nanostructure Synthesized by Chemical Precipitation. Int J Chem Concepts. 2015;1:44-56.
[35] Pandey PK, Bhave NS, Kharat RB. Structural, optical, electrical and photovoltaic electrochemical characterization of spray deposited $NiWO_4$ thin films. Electrochimica Acta. 2006;51:4659-64.
[36] Karthiga R, Kavitha B, Rajarajan M, Suganthi A. Photocatalytic and antimicrobial activity of $NiWO_4$ nanoparticles stabilized by the plant extract. Materials Science in Semiconductor Processing. 2015;40:123-9.
[37] Montini T, Gombac V, Hameed A, Felisari L, Adami G, Fornasiero P. Synthesis, characterization and photocatalytic performance of transition metal tungstates. Chemical Physics Letters. 2010;498:113-9.
[38] Parhi P, Karthik TN, Manivannan V. Synthesis and characterization of metal tungstates by novel solid-state metathetic approach. Journal of Alloys and Compounds. 2008;465:380-6.
[39] Farsi H, Hosseini SA. The electrochemical behaviors of methylene blue on the surface of nanostructured $NiWO_4$ prepared by coprecipitation method. Journal of Solid State Electrochemistry. 2013;17:2079-86.
[40] Bharati R, Singh RA, Wanklyn BM. Electrical conductivity of single crystal nickel tungstate. Journal of Materials Science. 1983;18:1540-2.
[41] Ahmed MI, Adam A, Khan A, Siddiqui MN, Yamani ZH, Qamar M. Synthesis of mesoporous $NiWO_4$ nanocrystals for enhanced photoelectrochemical water oxidation. Materials Letters. 2016;177:135-8.

XVIII International Congress
of the Mexican Hydrogen Society

Photo-Assisted Synthesis of GO/ZnO Nanocomposites for the Production of Photocatalytic Hydrogen

B. C. Hernández-Majalca[1], E.J. Núñez-Murillo[2], S.A. Victor-Chavéz[3], J. L. Dominguez-Arvizu[1], J. Jiménez-Miramontes[1], J. C. Pantoja-Espinoza[1], M.J. Melendez-Zaragoza[1], J.M. Salinas-Gutiérrez[1], A. López-Ortiz[1], V. Collins-Martínez[1]*

[1] Departamento de Ingeniería y Química de Materiales, Centro de Investigación en Materiales Avanzados, S.C., Miguel de Cervantes 120, Chihuahua, Chih., 31136, México.
[2] Universidad Autónoma de Chihuahua, Facultad de Ingeniería, Circuito Número I s/n, Nuevo Campus Universitario II, 31100 Chihuahua, Chih.
[3] Instituto Tecnológico de Chihuahua, Avenida Tecnológico 2909, Colonia 10 de Mayo Chihuahua, Chihuahua, México
*virginia.collins@cimav.edu.mx

ABSTRACT

In this study, zinc oxide was synthesized by the precipitation method. Graphene oxide (GO) was prepared by oxidation of graphite powder using a microwave pretreatment. This GO was used for the modification of the photocatalytic properties of ZnO. Fixation of particles was carried out using a photoassisting technique by visible light irradiation. Characterization of the material consisted in morphology, crystalline structure and optical properties and these were performed by XRD, SEM, BET and UV-Vis spectrometry, respectively. Photocatalytic evaluation of the material towards the water splitting reaction was followed by gas chromatography, using a metal halide lamp of 250W as a light source in a quartz-sealed photocatalytic reactor, obtaining a production of 1,200 μmolH_2/g, showing an enhanced photocatalytic activity compared to ZnO.

Keywords: *graphene oxide, photo-anchoring, hydrogen production, ZnO/graphene oxide*

1. Introduction

In recent decades, world population has doubled, which has led to an increased energy consumption. The current lifestyle of humanity depends on energy coming from fossil fuels such as natural gas, methane and coal. Therefore, in order to alleviate the problem of future energy demand, renewable energies, such as solar energy, biofuels and nuclear energy, must be implemented, because fossil fuels are finite [1].

From today´s alternative energy options, hydrogen is considered a promising energy carrier derived from solar energy, and the use of hydrogen as an energy vector, especially in the automotive sector, has awaken the interest of hydrogen in the world´s energy arena, because it is clean, renewable, is abundant in nature and in combination with fuel cells are highly efficient for power generation systems. These are the reasons why several alternatives have been proposed for their production in an environmentally responsible way using green technologies [2–5]. Since the dissociation of the water molecule by photoelectrochemistry was reported, the production of H_2 by photocatalysis has been of great scientific interest [6] and the study of semiconductor materials with photocatalytic properties is nowadays a very active area of research. Examples of photocatalytic materials aiming the water splitting reaction for the production of hydrogen include $BiVO_4$ [7], TiO_2 [7,8], WO_3 [9], CdS [8], C_3N_4 [10], and ZnO [11,12].

ZnO is, like TiO_2, one of the most studied photocatalysts due to its low toxicity, thermal stability and high efficiency. However, one of its most important limitations lie in the photo-corrosion that this material presents. Furthermore, generally speaking, oxides exhibit a low charge mobility and ZnO is not the exemption. Therefore, it is necessary to develop a material or a combination of materials that will extend recombination times to compensate for the low density of ZnO carriers. Recently, different research aiming to improve photocatalytic properties of ZnO has emerged and proposed several strategies in an attempt to solve this problematic, such as the synthesis of ZnO nanorods [13], heterojunctions with other semiconductors [14], doping and inclusion of carbonaceous materials [3,15], including graphene.

Graphene, is a two-dimensional flat monolayer of carbon atoms bonded in a honeycomb structure, which exhibits very interesting electronic properties, such as zero band gap and high conductivity [16]. Recently, the incorporation of metal oxides in graphene sheets has been reported to obtain composite photocatalysts [3,17,18].

Based on the methodology proposed by Williams et al. in 2008 [19] for the assisted photo anchoring, this work proposes the use of visible light irradiation to anchor ZnO particles on the surface of GO, which according to the literature, the combination of GO with an appropriate photocatalyst such as ZnO may result in a significant improvement of the material photocatalytic activity. Furthermore, it is worth to mention that up to date, studies conducted on this material have been mainly focused on the photocatalytic degradation of pollutants in water.

2. Methodology

2.1. Synthesis of graphite oxide

Graphite oxide was synthesized from graphite powder using a modification of Hummers method [20,21]. 1 g of graphite was exposed to a microwave pretreatment [22] during 15 s, immediately after, a concentrated solution of H_2SO_4 /H_3PO_4 with a 9:1 ratio was added (43.2 mL and 4.8 mL, respectively). This mixture was kept under magnetic stirring and in an ice bath (4°C) for 4.5 h. After this time 6 g of $KMnO_4$ were added under constant stirring for 3 h, finally a solution of H_2O_2 (12 mL) and 10% HCl (13 mL) was added

by drip irrigation while keeping the mixture under stirring for 0.5 h and under an ice bath due to the exothermic nature of the reaction [20]. Next step was washing and filtering with three distillated water, assisted by a vacuum pump until the residuals of acid and potassium permanganate present in the mixture have been removed, once completed this step GO was dried in a muffle furnace at 65°C.

2.2. ZnO Synthesis

In order to prepare ZnO particles, the precursor solution was first prepared by a precipitation method. 100 mL of 1.5 M $Zn(NO_3)_2 \bullet 6H_2O$ solution was added dropwise into 126 mL of 2.5 M NH_4HCO_3 solution under vigorous stirring at 45 °C in a water bath for 30 min to produce $Zn(HCO_3)_2$. The product was filtered, washed, and rinsed with deionized water and 95% ethanol. In the last stage, the $Zn(HCO_3)_2$ product was dried in an oven at 100 °C for 24 h, followed by calcination at 600 °C for an additional 1 h.

2.3. ZnO anchoring in graphene oxide

In order to synthesize the GO/ZnO composite, a certain amount of GO and ZnO (as required to obtain 10 % by weight of graphene oxide (GO) was suspended in an aqueous solution at 30% ethanol and using an ultrasonic bath (Branson 2510) at a frequency of 40 kHz for 15 min, separately and simultaneously, the ZnO was also exposed to ultrasound vibrations to obtain a homogeneous suspension. After 15 min the GO suspension was poured into the ZnO suspension, while keeping a continuous exposure to sonication until 40 min. The sample was placed within a photoreaction system under visible light radiation of a metal halide lamp (250 W) and under constant stirring for 24 h, the resulting solution was dried on a hot plate at 80°C for 12h.

2.4. Characterization

In this study the crystalline phase present in each of the synthesized materials was determined by the x-ray diffraction technique using a Phillips Xpert Pro diffractometer, equipped with a Cu-kα radiation (λ = 1.54056 Å). Diffraction patterns were obtained with a 2θ sweep angle of 5° to 90°, with a step size of 0.05. The absorption and diffuse reflectance spectrum of the materials were obtained with a UV Visible Evolution 220 Thermo-spectrophotometer equipped with integration sphere. The BET surface area was determined with an Autosorb-1 brand Quantachrome using the N_2 adsorption technique from 0.05 to 0.3 relative pressure (P/P_0). Morphology of the samples were examined by field emission scanning electron microscopy (SEM) in a JEM-2200FS, where the sample was eposed to a beam of electrons generated from a tungsten filament, to minimize energy losses or deviations of the beam, the column must have an ultra-high vacuum of 10^{-8} Torr [21].

2.4.1. Photocatalytic Evaluation

The photocatalytic activity was evaluated based on the performance of the material towards the production of hydrogen for the dissociation of the water molecule, using as a

250W metal halide lamp as a source of energy and 2% methanol as a sacrifice agent. The reaction was monitored by gas chromatography using a Perking Elmer Clarus 580 gas chromatograph, taking samples at time intervals of 1h with 8 repetitions.

3. Results and discussion

3.1. X-ray diffraction

The crystalline structure of the samples was analyzed by X-ray diffraction. Figure 1 shows the diffraction patterns of ZnO, the synthesized graphene oxide (GO) and the GO/ZnO nanocomposite. The diffraction pattern of GO presents a signal at $2\theta = 10° = 10° \cong 8.842$Å, which corresponds to graphene oxide. The diffraction pattern of ZnO shows characteristic peaks of the Wurtzite phase with a crystallographic record of 00-080-0075, in which an average crystallite size of 16.31 nm was estimated by means of the Scherrer's equation [23]. In the GO/ZnO nanocomposite diffractogram it can be clearly observed the fading of the signal corresponding to graphene oxide showing mainly the characteristic peaks of ZnO, while maintaining the amorphous phase associated with graphene oxide, which shows that the presence of GO does not promote the formation of new crystals or changes in the preferential orientation of ZnO

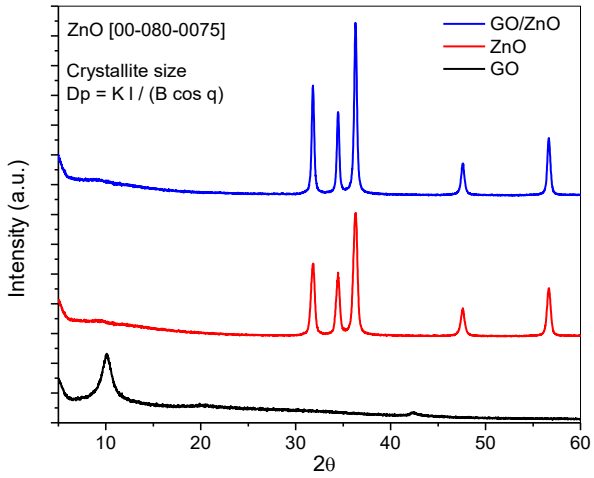

Fig. 1 X-ray diffraction patterns of GO, ZnO and GO/ZnO samples

3.2. Scanning electronic microscopy

Fig. 2 a, b and c show images of scanning electron microscopy for the GO/ZnO sample, where it can be seen that ZnO anchoring occurred only in certain places of GO, particularly on the edges, as well as a possible sintering of ZnO particles as shown in Fig. 2d, which probably be the cause of a poor distribution of these particles over leaves of GO. Furthermore, a scaly morphology can also be seen on some portions of GO, which was presumably caused by the exfoliation process.

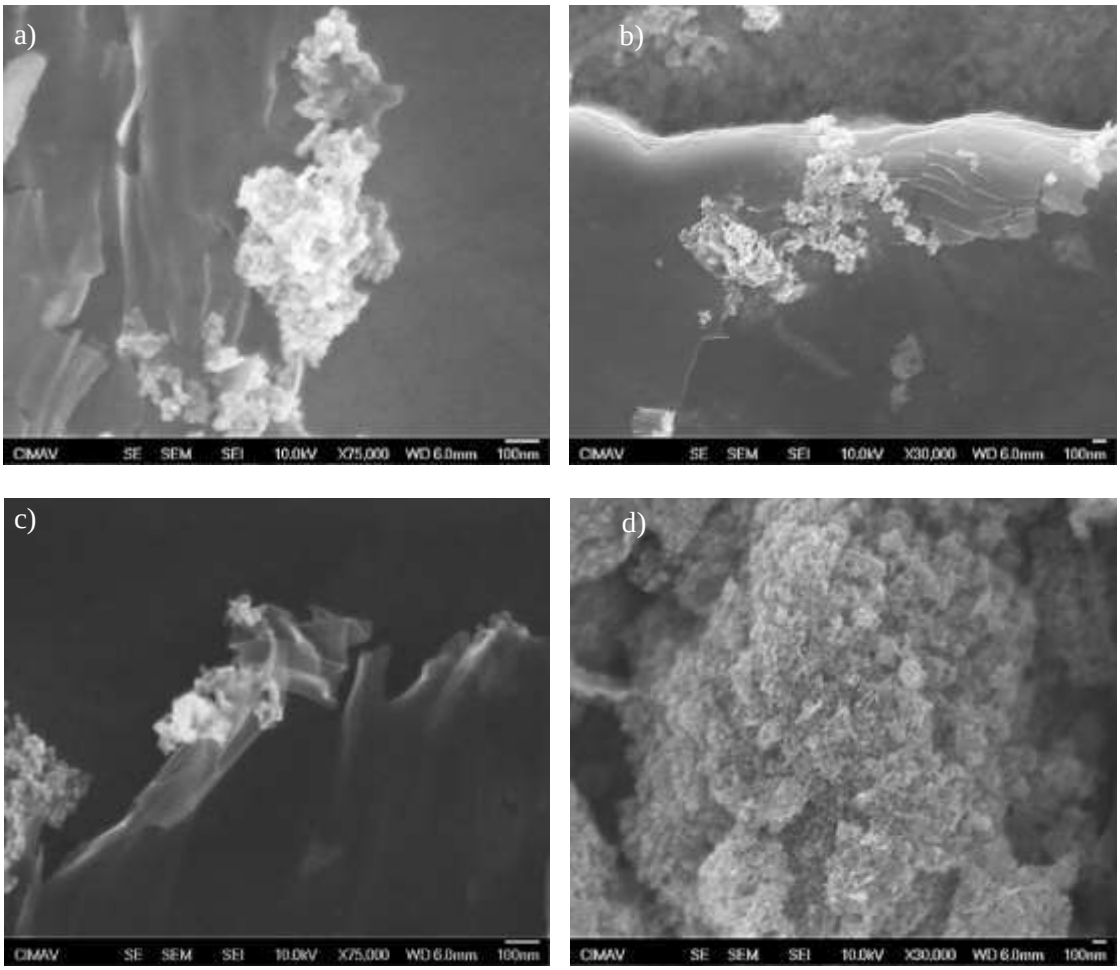

Fig. 2 SEM micrographs of the GO/ZnO composite.

3.3. UV-Vis Spectroscopy diffuse reflectance

Figure 3 presents the absorption spectrum of ZnO, GO and GO/ZnO samples obtained by the diffuse reflectance technique where ZnO shows a maximum absorption within the UV range at approximately 400nm. While, GO shows absorption in almost all the evaluated spectrum, so it can be assumed that the level of oxidation of the material is low [24]. On the other hand, the GO/ZnO behavior shows the limit of its absorption spectrum at 460 nm within the visible range. These results agree well with those reported in the literature for GO and ZnO nanocomposites under a similar composition of the nanocomposite under study [25].

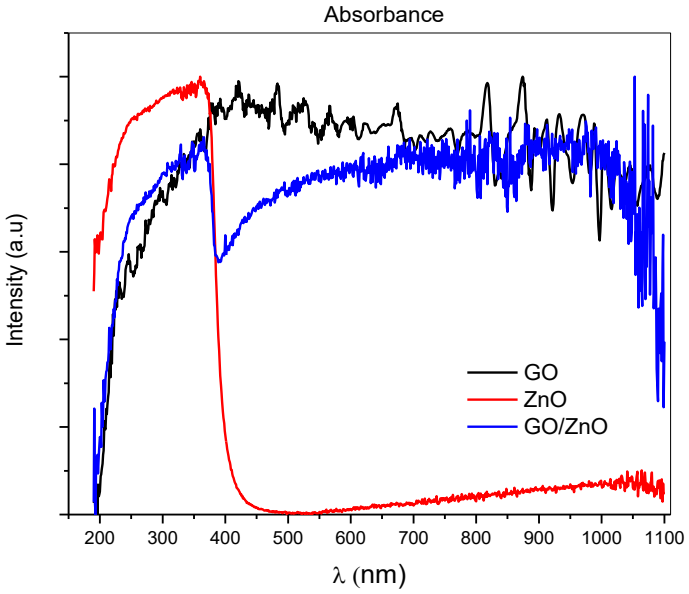

Fig. 3 UV-vis absorption spectra of GO, ZnO and GO/ZnO samples.

Estimation of the band gap energy was performed using the Tauc plot by means of the Kubelka-Munk function and this is presented in Figure 4. In this figure the numerical value of the band gap energy for ZnO and GO/ZnO is shown in Figure 4a) where the direct transition of both materials is presented. Here, ZnO shows an Eg of 3.22 eV [26] that agrees values found in the literature, where an Eg value similar to that of TiO_2 is considered. Otherwise, in plot 4b) the determination of Eg by indirect transition of ZnO and GO/ZnO composite samples presented values of 2.77 and 3.11 eV, respectively. This reduction in the band gap, according to the literature can be attributed to the inherent properties of the GO for its character of electron trap [14].

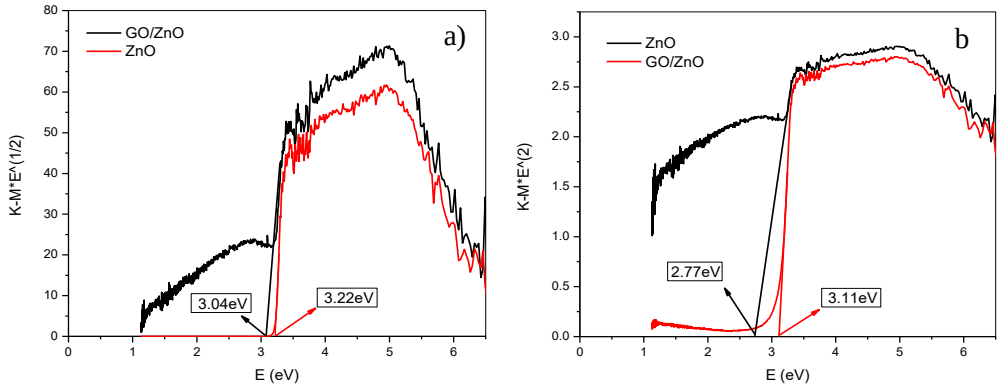

Fig. 4 Estimation of the direct and indirect Eg by the Kubelka-Munk method.

3.4. BET Surface Area

Figure 5 shows the adsorption isotherms of the GO/ZnO composite, where a surface area of 31 m^2/g was determined and presenting a type III isotherm, without porosity.

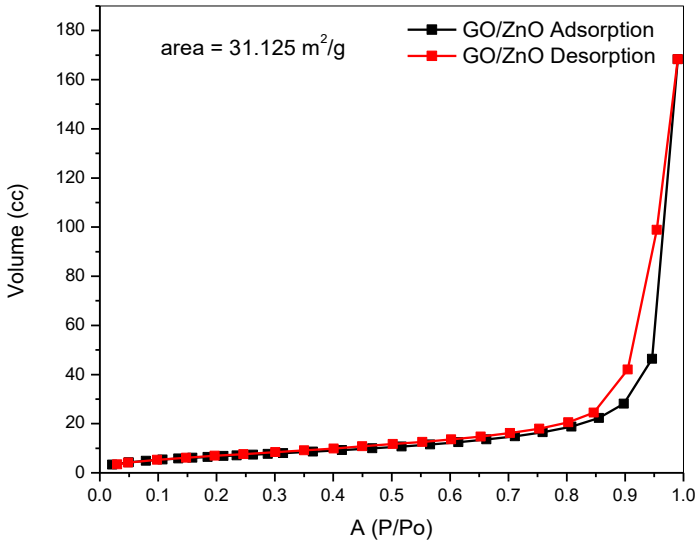

Fig. 5 BET Adsorption isotherms for samples GO, ZnO and GO/ZnO.

3.5. Photocatalytic Evaluation.

The incorporation of GO to ZnO generates interesting benefits in terms of photocatalytic properties. This is shown in Figure 6 where the performance towards the hydrogen production of each material (GO, ZnO and GO/ZnO) is presented in terms of $\mu molH_2$ as a function of time. Results indicate a hydrogen production of of 127, 50 and 156 μmol/g·h for GO, ZnO and GO/ZnO samples, respectively.

Furthermore, ZnO generates small amounts of hydrogen because its range of absorption of photons is in the UV range, due to this the density of charge carriers, is poor which results in a low photocatalytic activity. Regarding the performance of the GO/ZnO composite in the dissociation of the water molecule, it shows a significant improvement compared to its precursors, which can be associated to the surface interaction between the ZnO and the GO sheets. According to the literature, GO acts as an electron collector and presents a high charge mobility, a characteristic that is attributed to its two-dimensional profile, coupled with the conjugation of the π bond [27].

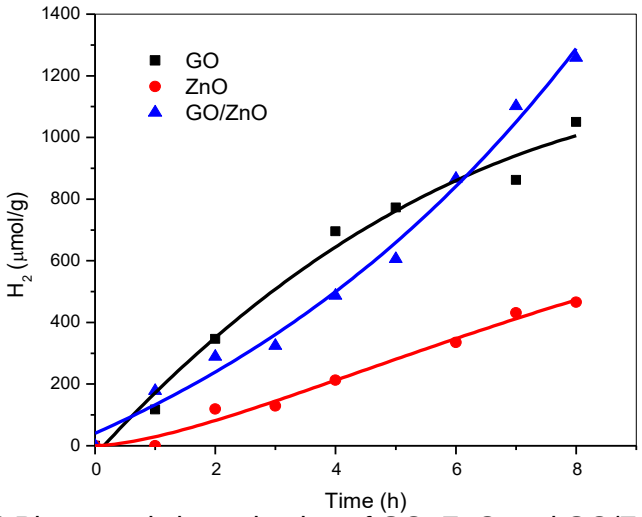

Fig. 6 Photocatalytic evaluation of GO, ZnO and GO/ZnO samples.

4. Conclusions

- It was possible to synthesize ZnO particles with a crystallite size of 16.31 nm by the precipitation method.
- GO was obtained by ultrasonic exfoliation.
- A GO/ZnO composite was produced by photo-assisted anchoring by visible light.
- The 400nm to 460nm shift from the absorption range in the GO/ZnO composite to the visible was achieved.
- A bandgap decrease was obtained at a less energetic level of 3.22 to 2.7 eV.
- The photocatalytic properties of ZnO in the production of hydrogen were improved by the addition of 10% by weight of GO, obtaining a production of 1250 µmol/g of hydrogen after 8 hours.

Las propiedades fotocatalíticas del ZnO en la producción de hidrógeno se mejoraron mediante la adición del 10% en peso de GO, obteniendo una producción de 1250 µmol/g de hidrogeno en 8 horas.

.

5. References

[1] Paracchino A, Laporte V, Sivula K, Grätzel M, Thimsen E. Highly active oxide photocathode for photoelectrochemical water reduction. Nat Mater 2011;10:456–61. doi:10.1038/nmat3017.

[2] Turner JA. A Realizable Renewable Energy Future. Science (80-) 1999;285.

[3] Akhavan O. Graphene Nanomesh by ZnO Nanorod Photocatalysts. ACS Nano

2010;4:4174–80. doi:10.1021/nn1007429.
[4] Millet P. Design and performance of a solid polymer electrolyte water electrolyzer. Int J Hydrogen Energy 1996;21:87–93. doi:10.1016/0360-3199(95)00005-4.
[5] Kreuter W. Electrolysis: The important energy transformer in a world of sustainable energy. Int J Hydrogen Energy 1998;23:661–6. doi:10.1016/S0360-3199(97)00109-2.
[6] Fujishima A, Honda K. Electrochemical photolysis of water at a semiconductor electrode. Nature 1972;238:37–8.
[7] Jia Q, Iwashina K, Kudo A. Facile fabrication of an efficient BiVO4 thin film electrode for water splitting under visible light irradiation. Proc Natl Acad Sci U S A 2012;109:11564–9. doi:10.1073/pnas.1204623109.
[8] Li Y, Hu Y, Peng S, Lu G, Li S. Synthesis of CdS Nanorods by an Ethylenediamine Assisted Hydrothermal Method for Photocatalytic Hydrogen Evolution. J Phys Chem C 2009;113:9352–8. doi:10.1021/jp901505j.
[9] Higashi M, Abe R, Takata T, Domen K. Photocatalytic Overall Water Splitting under Visible Light Using ATaO $_2$ N (A = Ca, Sr, Ba) and WO $_3$ in a IO $_3$ $^-$ /I $^-$ Shuttle Redox Mediated System. Chem Mater 2009;21:1543–9. doi:10.1021/cm803145n.
[10] Wang X, Maeda K, Thomas A, Takanabe K, Xin G, Carlsson JM, et al. A metal-free polymeric photocatalyst for hydrogen production from water under visible light. Nat Mater 2009;8:76–80. doi:10.1038/nmat2317.
[11] Fujishima A, Zhang X, Tryk DA. Heterogeneous photocatalysis: From water photolysis to applications in environmental cleanup. Int J Hydrogen Energy 2007;32:2664–72. doi:10.1016/j.ijhydene.2006.09.009.
[12] Amir M, Kurtan U, Baykal A. Rapid color degradation of organic dyes by Fe3O4@His@Ag recyclable magnetic nanocatalyst. J Ind Eng Chem 2015;27:347–53. doi:10.1016/j.jiec.2015.01.013.
[13] Cheng Y, Chan RC, Wong P. Disinfection of legionella pneu- mophila by photocatalytic oxidation. . 98. Water Res 2007:842 – 852.
[14] Yeh T-F, Cihlář J, Chang C-Y, Cheng C, Teng H. Roles of graphene oxide in photocatalytic water splitting. Mater Today 2013;16:78–84. doi:10.1016/j.mattod.2013.03.006.
[15] Gadipelli S, Guo ZX. Graphene-based materials: Synthesis and gas sorption, storage and separation. Prog Mater Sci 2015;69:1–60. doi:10.1016/j.pmatsci.2014.10.004.
[16] Xiang Q, Yu J. Graphene-based photocatalysts for hydrogen generation. J Phys Chem Lett 2013;4:753–9. doi:10.1021/jz302048d.
[17] Zhang H, Lv X, Li Y, Wang Y, Li J. P25-Graphene Composite as a High Performance Photocatalyst. ACS Nano 2010;4:380–6. doi:10.1021/nn901221k.
[18] Dreyer DR, Park S, Bielawski CW, Ruoff RS, Geim AK, Novoselov KS, et al. The chemistry of graphene oxide. Chem Soc Rev 2010;39:228–40. doi:10.1039/B917103G.
[19] Williams G, Seger B, Kamt P V. TiO2-graphene nanocomposites. UV-assisted photocatalytic reduction of graphene oxide. ACS Nano 2008;2:1487–91. doi:10.1021/nn800251f.
[20] Dehghanzad B, Razavi Aghjeh MK, Rafeie O, Tavakoli A, Jameie Oskooie A. Synthesis and characterization of graphene and functionalized graphene via chemical and thermal treatment methods. RSC Adv 2016;6:3578–85.

doi:10.1039/C5RA19954A.
[21] Goldstein JI, Yakowitz H. Practical Scanning Electron Microscopy : Electron and Ion Microprobe Analysis. Springer US; 1975.
[22] Liu X, Zhan D, Chao D, Cao B, Yin J, Zhao J, et al. Microwave-assisted production of giant graphene sheets for high performance energy storage applications. J Mater Chem A 2014;2:12166–70. doi:10.1039/c4ta01979b.
[23] Yang GCC, Chan S-W. Photocatalytic reduction of chromium(VI) in aqueous solution using dye-sensitized nanoscale ZnO under visible light irradiation. J Nanoparticle Res 2009;11:221–30. doi:10.1007/s11051-008-9423-y.
[24] Lian KY, Ji YF, Li XF, Jin MX, Ding DJ, Luo Y. Big bandgap in highly reduced graphene oxides. J Phys Chem C 2013;117:6049–54. doi:10.1021/jp3118067.
[25] Liu X, Pan L, Zhao Q, Lv T, Zhu G, Chen T, et al. UV-assisted photocatalytic synthesis of ZnO-reduced graphene oxide composites with enhanced photocatalytic activity in reduction of Cr(VI). Chem Eng J 2012;183:238–43. doi:10.1016/j.cej.2011.12.068.
[26] Kumar R, Singh RK, Singh DP, Savu R, Moshkalev SA. Microwave heating time dependent synthesis of various dimensional graphene oxide supported hierarchical ZnO nanostructures and its photoluminescence studies. Mater Des 2016;111:291–300. doi:10.1016/j.matdes.2016.09.018.
[27] Allen MJ, Tung VC, Kaner RB. Honeycomb carbon: A review of graphene. Chem Rev 2010;110:132–45. doi:10.1021/cr900070d.

XVIII International Congress
of the Mexican Hydrogen Society

SYNTHESIS OF CARBON-BASED SUPPORT FOR RUTHENIUM ELECTROCATALYST FOR ORR FORMED BY GRAPHITE AND ASPHALT CARBON PYROLYZED

A. Legarreta-Mendoza, J.M. Salinas-Gutiérrez, M.J. Meléndez-Zaragoza, A. López-Ortiz, V. Collins-Martínez, D. Lardizabal-Gutiérrez*

CIMAV, S.C., Miguel de Cervantes 120, Complejo Industrial Chihuahua, 31136, Chihuahua, Chih. México.
* 52(614) 439 1100, daniel.lardizabal@cimav.edu.mx

ABSTRACT

The oxygen reduction reaction (ORR) that takes place in the cathode of PEM fuel cells has been an object of study of great interest in the electrocatalysis field, due to its low reaction kinetics, compared to the hydrogen oxidation reaction (HOR) that occurs at the anode of the cell. Several research groups have focused on developing economic alternatives that can approximate the intrinsic kinetic values of these two reactions. Platinum (Pt) is the most efficient electrocatalyst for ORR, followed by other transition metals (Ru, Ir, Fe). The synthesis of metallic catalysts using different kinds of supports have improved their performance and helped to reduce their cost in the past. These supports are aimed to increase the dispersion of the active phase and reduce the metal loading without affecting the catalytic activity. Carbon black is a common used support, due to its high surface area, pore size distribution, and high electrical conduction properties. This study offers an alternative carbon-based support, which is obtained by pyrolysis of asphalt/graphite at 600°C (S-AG) under a nitrogen atmosphere (N_2). Through the combination of the physical and chemical properties of the two different carbon sources (asphalt and graphite) an improvement effect on the performance of the support is expected with respect to commercial carbon Vulcan®. For their performance evaluation, Ruthenium (Ru) at 20% W was used as an active phase. Ruthenium(III) chloride hydrate ($RuCl_3 \cdot XH_20$) was used as a precursor, which was reduced in two steps, the first one by $NaHB_4$ and the second in a reducing atmosphere (Ar/H_2) at 420°C for 1h. The obtained material was characterized by elemental analysis (ICP), XRD, BET Area and SEM. For the electrochemical evaluation, cyclic (CV) and linear sweep (LV) voltammetry were used. In a first stage of the study, results indicate a better electrocatalytic activity of the ruthenium (Ru) impregnated on the S-AG synthesized support.

Key words: ORR, electrocatalysis, carbon-base support, heteroatoms.

1. Introduction

The lifestyle of our modern society has caused a constant increase in the world energy consumption [1]. The consequences of fulfilling the demand, mainly through the combustion of fossil fuels, have brought a negative impact on the environment. Fuel cells are electrochemical devices that generate an electric current from chemical reactions. These devices allow a better use of energy vectors such as hydrogen and/or methanol, for the production of electricity, since they are more efficient compared to traditional fuel-burning electric generation, as well as being environment-friendly, because water and heat are their main reaction products. For this reason, they continue to be a viable option in combination with other renewable energy sources to contribute in the reduction of the carbon footprint generated by the power electricity industry.

One of the technical barriers that have prevented the establishment of this technology is the slow kinetics of the oxygen reduction reaction (ORR) in the cathode of the cell. The effectiveness of Platinum (Pt) as a catalyst for this reaction It is well documented. However, its high cost associated with its scarcity and wide field of applications, has triggered a large number of researches, seeking to obtain a material with adequate electrocatalytic properties at reasonable price. For this purpose, supported catalysts have been of special interest, since they allow a better dispersion and stability of the metallic particles, provide access to a greater amount of atoms of the active phase, thus reducing the amount of metal loading and decreasing their cost [2].

The use of different types of supports for this purpose has been widely studied [3][4][5][6]. Carbon-based supports are the most commonly used due to their chemical stability in acidic and basic environments and their ease to recover the metal by just burning the support [2]. Within ideal characteristics of an electrocatalyst support for PEM fuel cells include: must be a good electrical conductor, avoid agglomeration of the active phase, present high surface area, present adequate pore size distribution that allows interaction between the polymeric electrolyte and the catalyst, be resistant to corrosion, chemically inert and do not contain impurities that may inhibit target chemical reactions [7]. The most used carbon material support is carbon black; this material has good conductive properties, corrosion resistance and low cost [6]. However, there are alternate available materials that may contribute to the desired ideal characteristics of an electrocatalyst support such as graphite and asphalt.

Graphite is a blackish gray substance made of crystallized carbon. Carbon atoms are arranged in hexagonal ring planes stacked one on top of the other [9]. Only three of the four valence electrons of each carbon atom are involved in the formation of hybrid sp2 bonds with three other atoms of the same plane, this means that the fourth electron forms a π bond. These last electrons are mobile, so graphite has good electrical conduction properties [2] [10]. A situation to be highlighted is that although the carbons that contain sp^2 hybridization present a large number of free electrons for their π bonds, these electrons are partially inert to be used in the ORR. In the case of nanostructures doped with heteroatoms such as nitrogen (N) and sulfur (S), the π electrons of the carbon can be activated by conjugation with the pair of free electrons of the dopants, obtaining

better results [11][12][13][14]. Besides, according to the above mentioned ideal properties of a support, graphite has a better resistance to corrosion than amorphous carbon, which is an important feature for its application in fuel cells.

Furthermore, asphalt is classified as a set of macromolecules of polycyclic aromatic rings of carbon and hydrogen with heteroatoms such as nitrogen (N), sulfur (S) and oxygen (O) and metals (V and Ni), with chains of alkanes at their ends [15]. It is one of the main precursors of sludge and sediments in the process of extraction and treatment of crude oil. Although it has some commercial uses, it is mainly considered a waste product. In addition, asphalt is considered a rich material in carbon and heteroatoms.

Moreover, an additional consideration in the catalytic phenomena deals with the presence of active sites. Therefore, during the synthesis of a catalyst it is always sought to generate the largest possible number of these. According to the literature, within an electrocatalyst the simultaneous presence of a transition metal, carbon and heteroatoms are important components for the creation of active sites [8]. For this reason, in the present research it is proposed that the combination of graphite and asphalt, as raw materials, could provide improved physical and chemical characteristics during the synthesis of a carbon-based support than the black carbon support commonly used in today´s metal electrocatalysts for the ORR of a PEM fuel cell at the cathode. Furthermore, this work presents the synthesis, characterization and electrochemical evaluation of a support material obtained by the pyrolysis of asphalt-graphite at 600°C (S-AG) and its comparison against the most used carbon support, the Vulcan XC72R (Cabot), using Ruthenium (Ru) at 20% as the electrocatalyst active phase.

2. Materials and Methods

Synthesis

For the support preparation, a commercial solid asphalt bar and graphite powder (Meyer) were used as raw materials. The graphite was subjected to a milling process in high energy ball mill Spex 8000 M in a 7:1 ratio for 8 hours. 20% W ruthenium (Ru) was used as an active phase, by employing $RuCl_3xH_2O$ (Sigma-Aldrich) as the metal precursor, while $NaBH_4$ (Sigma-Aldrich) was used as a reducing agent. For the synthesis of the support (S-AG) by pyrolysis a Barnstead-Thermolyne model 21100 tubular furnace was used in combination with a stainless steel reactor equipped with an inner quartz tube to hold the sample. The initial mass in the pyrolysis reactor contained a mixture of 70% asphalt and 30% graphite. The first stage consisted of a pretreatment in air, with a flowrate of 100 ml/min, at a heating rate of 5°C/min to reach 250°C, for 60 minutes, this with the purpose of increasing the yield of the pyrolysis product up to 4%. Subsequently, a N_2 flowrate of 100 ml/min was introduced to the reactor and this further heated using a heating rate of 5°C/min, up to a temperature of 600°C, for 120 minutes. The obtained material was manually grounded in an agate mortar. For the synthesis of the electrocatalyst, the impregnation method was used. In a 125 ml Erlenmeyer flask, 1 g of $NaBH_4$ and 45 ml of water were mixed and stirred until complete dissolution of the sodium borohydride at room temperature (25°C). Then a 0.1 M solution of $RuCl_3$ was added dropwise, with the help of a hypodermic syringe, while keeping a

moderate stirring at a temperature between 55-60°C for one hour. Then the synthesized support (S-AG) was added to this resulting liquid and it was kept under continuous stirring for two hours at the same temperature, filtered and rinsed several times with warm water (60°C). The resulting sample was exposed to a second reduction process in the tubular furnace, under a reducing atmosphere of 95% argon (Ar) and 5% hydrogen (H_2), using a gas flowrate of 100 ml/min at a heating rate of 5°C/min up to a temperature of 420°C for 60 minutes. For the reference carbon support (Vulcan-XC72R, Cabot) the same former described impregnation procedure of Ruthenium (Ru) was employed.

Characterization

For the characterization of the synthesized electrocatalyst, a FlashSmart Elemental Analyzer of the Thermo Fisher Scientific brand was used to determined C, H, N, S, and O. For the crystal structure of the samples X-ray diffraction characterization (XRD) was achieved using a PANalytical diffractometer model XPert PRO, with X Celerator detector and a monochromatic radiation emitted by Cu Kα (λ = 1.5406 Å). The diffraction angle 2θ was varied from 5° to 90°, with a step size of 0.05°and time of 150 seconds. The Scherrer´s equation was used to determine the crystallite size. To determine the BET surface area, volume and pore distribution of the sample, a Quantachrome Instruments equipment model Autosorb-1C was used. The test was carried out in nitrogen at 77K for physisorption. Morphology characterization of the samples was made by scanning electron microscopy (SEM) using a Jeol JSM-7401F field emission microscope, the sample was prepared by adding methanol and placing it in a brass, copper, and zinc sample holder. The micrographs were taken with different working distances (WD).

Electrochemical evaluation

Cyclic (CV) and linear sweep voltammetry (LVL) were performed for the electrochemical evaluation of the catalyst. The equipment used was a Princeton brand potentiostat model VersaSTAT 3 and a rotary disc with a rotor speed regulator (PINE Instruments). An arrangement of three electrodes were employed, using a working electrode, a platinum electrode as a counter electrode (CE) and an Ag/AgCl electrode as a reference electrode (ER). The evaluation was performed in acid medium, using a solution of H_2SO_4 (JT Baker) 0.5 M as an electrolyte. Catalytic inks were prepared with 20 mg of catalyst sample, 1 ml of ethanol (JTBaker 99.6%) as a solvent and 30 µl of Nafion ® as an adhesive. This mixture was sonicated for 40 minutes. The inks obtained were deposited with the help of a micropipette, placing 30 µl of ink on a glassy carbon electrode of 5 mm in diameter, they were allowed to dry at room temperature for one day. The H_2SO_4 electrolyte was bubbled with nitrogen (N_2) for 20 minutes to displace any oxygen present in the solution. The material was activated by VC with a potential window of -0.2 to 1 V at 50 mV/s during 40 cycles while keeping N_2 bubbling. After activation, the electrolyte was left bubbling with N_2 for 15 minutes. Three VC cycles were run, at 20 mV/s, with the same potential window. Under the flow of N_2, a VL, from1 to 0.2 V was run at 5 mV/s at a rotation speed of 2000 RPM. To check material activity for the ORR, the electrolyte was bubbled with O_2 for 20 minutes. A VL was performed at 5 mV/s, at the same potential window at 5 mV/s with a rotation speed of 2000 RPM, while keeping the O_2 bubbling during the test.

3. Results and Discussion

Characterization

Table 1 present results obtained for the composition of the raw asphalt material determined by elemental analysis. It is observed that the elements of interest (C, N, and S) are present in the sample. The compositions in which these elements are found, agree well with those of asphalt reported by S. Akmaz et al. [16].

Table 1. Elemental Analysis CHNS/O of asphalt.

	C %	N %	H %	S %	O %
Asphalt	81.088	0.443	8.899	3.788	5.782

Moreover, sample S-AG synthesized by the pyrolysis process preserves the elements of interest in the amounts shown in Table 2. Here, there is an increase of 10% of carbon with respect to the asphalt sample and this is presumably due to the integration of the graphite within the material, while keeping the heteroatoms of interest.

Table 2. Elemental analysis CHNS/O of asphalt/graphite pyrolyzed at 600 ° C (S-AG).

	C %	N %	H %	S %	O %
S-AG	91.939	0.721	1.127	2.755	3.458

Figure 1 shows the XRD diffractogram for sample S-AG RuM. The diffraction peaks at 2θ = 38.2, 42.0 and 43.8° are assigned to the planes (100), (002) and (101), which are characteristic signals of hexagonal ruthenium according to the literature [17]. For the signals that do not correspond to the ruthenium, a literature review of articles related to the type of expected materials was carried out. According to this review L. Liu et al [18] reported a diffraction signal observed in 2θ between 24.5-26º which corresponds to semicrystalline carbon. The expected signals assigned to the graphitic structure are located around 2θ = 43º [19] [20]. However, they are not easily distinguishable by their concurrence with ruthenium (Ru) signals, which are more intense. In order to estimate the average crystallite size, the XPowder software was used, by the method of Scherrer, resulting in an average size of 6 nm.

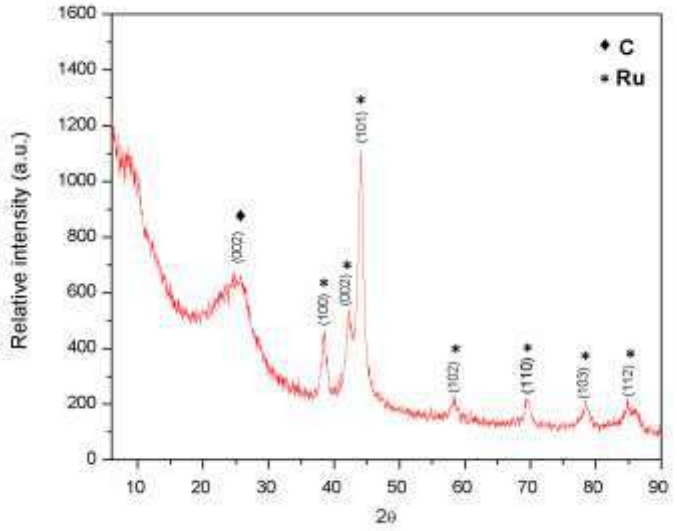

Figure 1. Diffractogram of the S-AG RuM electrocatalyst.

Figure 2 shows the adsorption/desorption N_2 isotherm obtained from the S-AG RuM sample. Here, it can be observed a type II isotherm, which is characteristic of non-porous solids or containing macropores, agreeing with results found in the literature [21]. The hysteresis loop of the isotherm does not completely close at low relative pressures (P/P0 < 0.4). This effect can be explained by the desorption mechanism, which is the end of the capillary condensation. In these cases, this fall is insufficient to connect the desorption to the adsorption lines. Furthermore, the material presented a BET su

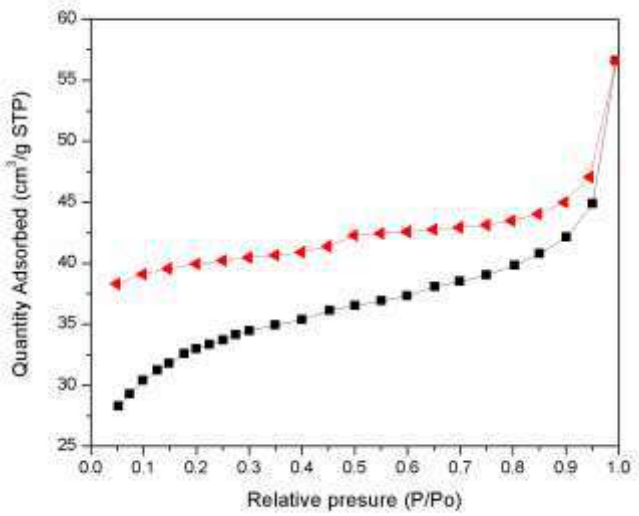

Figure 2. adsorption/desorption N_2 Isotherm for sample S-AG RuM.

82.202	1.372	2.815	6.351	7.26
84.952	N.D.	1.377	4.73	8.941
80.883	N.D.	0.785	4.694	13.638
86.421	N.D.	0.119	5.878	7.582

Figure 3 presents scanning electron microscope (SEM) micrographs taken at different magnifications by secondary electrons of the S-AG RuM sample. The carbon support (S-AG) exhibits irregular morphology, variable in each particle with different sizes among particles. Here in these micrographs the expected components in the electrocatalyst can be identified. The carbonaceous composition of the electrocatalyst is distinguished by presenting a dark color, and the presence of ruthenium metal active phase (Ru) can be distinguished by a lighter color. Also, ruthenium particles present agglomerations, which is undesirable for the purpose of this material.

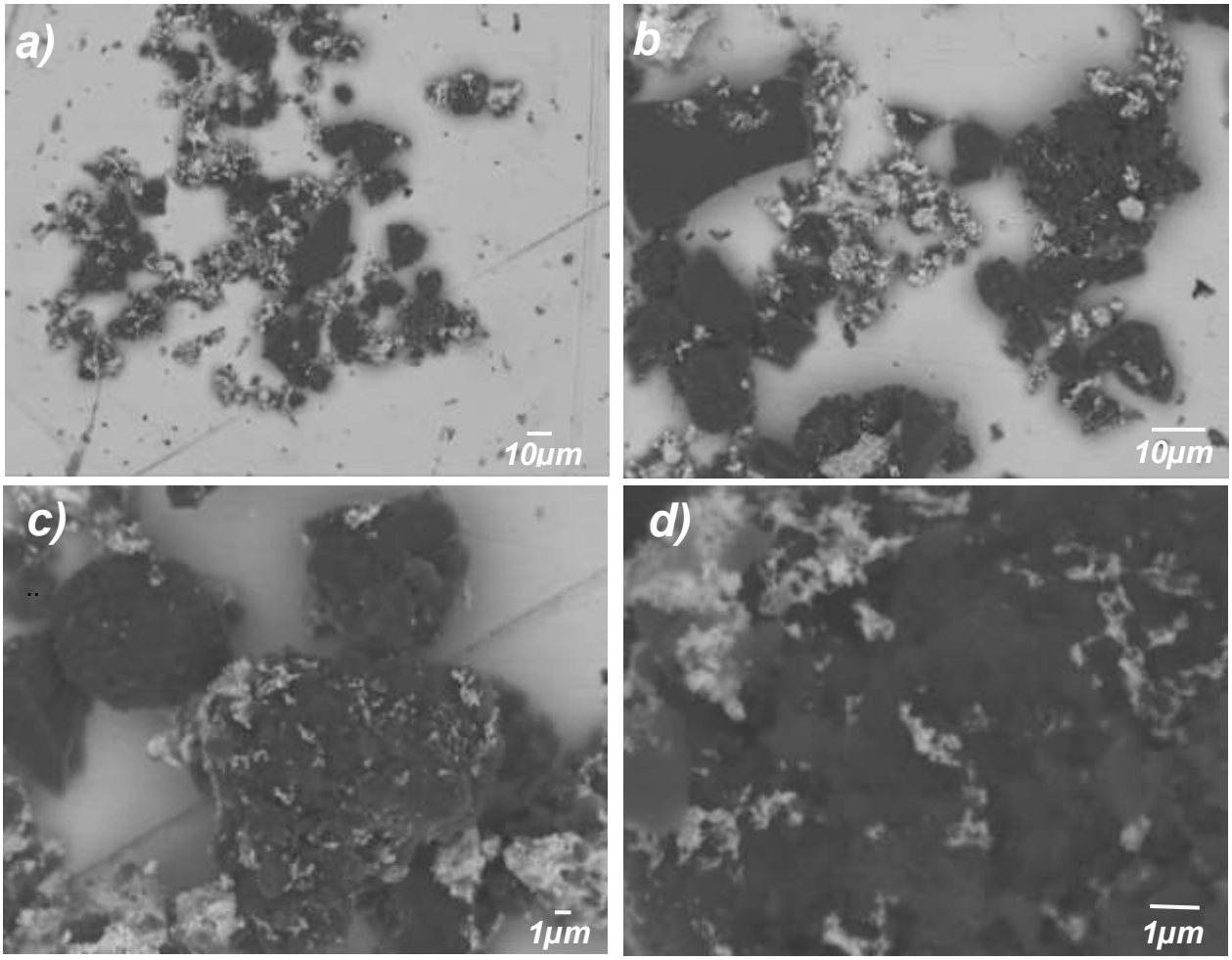

Figure 3. SEM images of S-AG RuM Electrocatalyst, taken at different magnifications: a) 500, b) 1,000 c) 3,000 and d) 10,000.

Electrochemical evaluation

The capacitive activity of the material was evaluated by cyclic voltammetry (CV) in N_2. Figure 4 shows the CV curves in N_2 of the materials. Both S-AG RuM and the Vulcan RuM, present good energy storage capacitance, according to the supercapacitance properties associated with carbon materials as reported in the literature [22].

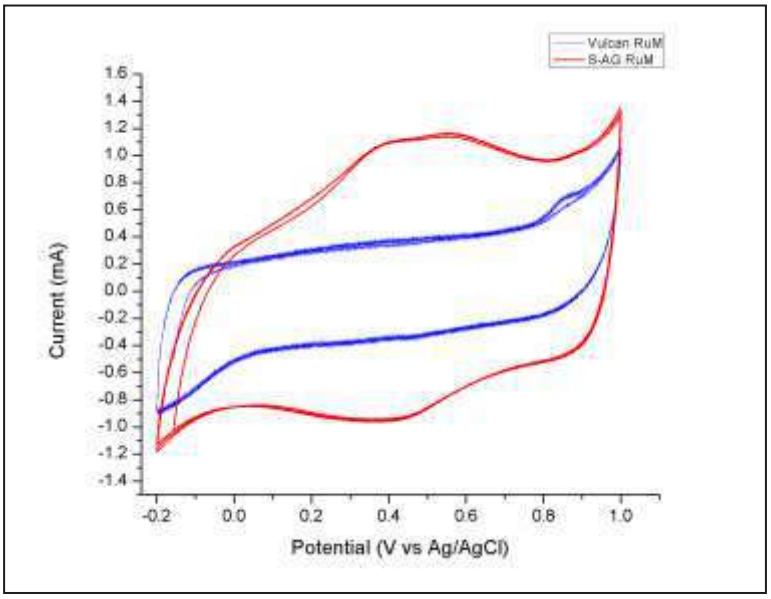

Figure 4. VC of the S-AG RuM and Vulcan RuM electrocatalyst.

Figure 5 shows the linear voltammetry of the S-AG Ru in N_2 and O_2, which verify its electrocatalytic activity. The first significant signal occurs approximately at 0.7 V. it presents a slight-pronounced drop compared to the characteristic behavior observed in Pt/C materials under the ORR [23]. Furthermore, Figure 6 shows an electrocatalyst activity comparison of ruthenium (Ru) supported in S-AG and carbon Vulcan in O_2 at 2000 RPM based on their linear voltammetry response. It can be deduced that while being the same ruthenium material, the synthesized S-AG carbon support helps to improve the activity of the electrocatalyst, even though the difference between this and Carbon Vulcan is approximately of 30 mA, which is a significant amount.

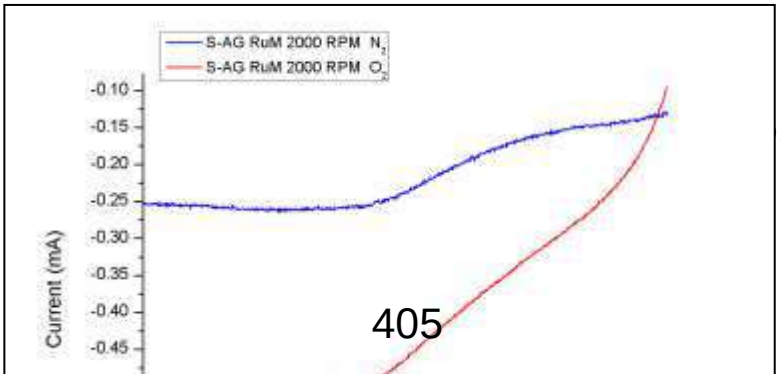

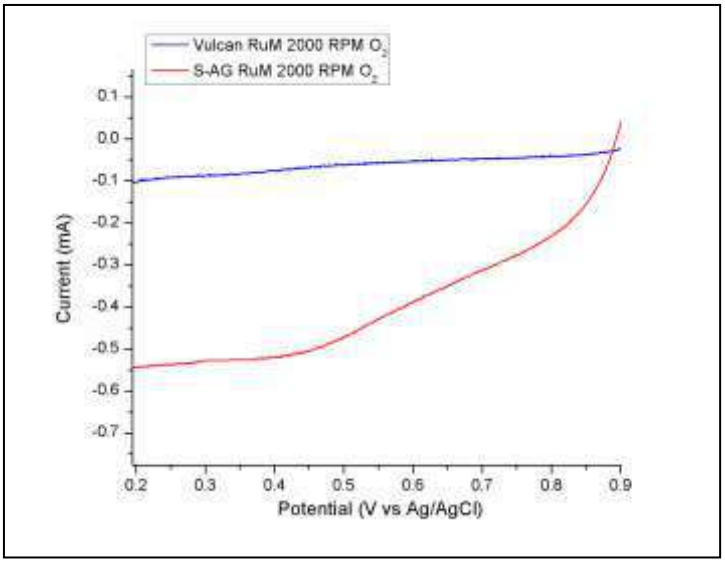

Figure 6. Linear Sweep Voltammetry of Electrocatalyst S-AG RuM Vs Vulcan RuM at 2000 RPM in O_2.

4. Conclusion

The carbon-based support obtained by the pyrolysis of asphalt and graphite (S-AG) exhibit some important characteristics that make possible to be used as an electrocatalyst support. This S-AG combines the good conductivity and superficial area of graphite with the increase of active sites due to the presence of asphalt's heteroatoms, since this is a self-doped carbonaceous material containing elements of interest such as nitrogen (N) and sulfur (S). The free electrons of these atoms, presumably modify the electronic distribution in the material, thus helping the electron donation by the neighboring carbon. The methodology employed to synthesize the support by pyrolysis is a simple route, which does not require the use of specialized equipment, while employing easily available raw materials, doing this procedure an inexpensive process. The electrochemical evaluation showed a good performance of the S-AG support compared to the conventional Vulcan XC72R, working with ruthenium (Ru) as the active phase of the electrocatalyst, in acid medium. Results presented here, will follow with the study of this material in order to determine its functionality and corrosion resistance under specific conditions of PEM fuel cells, which are more aggressive over extended periods of time.

References

[1] RENEWABLES 2017 GLOBAL STATUS REPORT n.d.

[2] Auer E, Freund A, Pietsch J, Tacke T. Carbons as supports for industrial precious metal catalysts n.d.

[3] Seger B, Kongkanand A, Vinodgopal K, Kamat P V. Platinum dispersed on silica nanoparticle as electrocatalyst for PEM fuel cell. J Electroanal Chem 2008;621:198–204. doi:10.1016/j.jelechem.2007.09.037.

[4] Huang SY, Ganesan P, Popov BN. Titania supported platinum catalyst with high electrocatalytic activity and stability for polymer electrolyte membrane fuel cell. Appl Catal B Environ 2011;102:171–7. doi:10.1016/j.apcatb.2010.11.026.

[5] Seger B, Kamat P V. Electrocatalytically active graphene-platinum nanocomposites. role of 2-D carbon support in pem fuel cells. J Phys Chem C 2009;113:7990–5. doi:10.1021/jp900360k.

[6] Bayrakçeken A, Smirnova A, Kitkamthorn U, Aindow M, Ays¸ A, Bayrakç Eken A, et al. Vulcan-Supported Pt Electrocatalysts for PEMFCs Prepared using Supercritical Carbon Dioxide Deposition. Chem Eng Commun 2008;196:194–203. doi:10.1080/00986440802290110org/10.1080/00986440802290110.

[7] Dicks AL. The role of carbon in fuel cells. J Power Sources 2006;156:128–41. doi:10.1016/j.jpowsour.2006.02.054.

[8] Popov BN, Li X, Liu G, Lee J-W. Power source research at USC: Development of advanced electrocatalysts for polymer electrolyte membrane fuel cells. Int J Hydrogen Energy 2011;36:1794–802. doi:10.1016/J.IJHYDENE.2009.12.050.

[9] Speight JG. Handbook of petroleum product analysis (2nd edition). J Chem Inf Model 2013;53:1689–99. doi:10.1017/CBO9781107415324.004.

[10] Yan Z, He G, Shen PK, Luo Z, Xie J, Chen M. MoC-graphite composite as a Pt electrocatalyst support for

highly active methanol oxidation and oxygen reduction reaction. J Mater Chem A 2014;2:4014–22. doi:10.1039/c3ta14251e.

[11] Awan Z, Zahoor A, Christy M, Hwang YJ, Lim YR, Kim P, et al. Improved electrocatalytic activity of carbon materials by nitrogen doping Evaluation of electrocatalytic properties of various nanostructured manganese oxides for nonaqueous lithium-air batteries View project Improved electrocatalytic activity of carbon m. Appl Catal B Environ 2014;147:633–41. doi:10.1016/j.apcatb.2013.09.043.

[12] Maldonado S, Stevenson KJ. Influence of nitrogen doping on oxygen reduction electrocatalysis at carbon nanofiber electrodes. J Phys Chem B 2005;109:4707–16. doi:10.1021/jp044442z.

[13] Sahoo M, Ramaprabhu S. Nitrogen and sulfur co-doped porous carbon – is an efficient electrocatalyst as platinum or a hoax for oxygen reduction reaction in acidic environment PEM fuel cell? Energy 2017;119:1075–83. doi:10.1016/j.energy.2016.11.066.

[14] Bhange SN, Unni SM, Kurungot S. Nitrogen and sulphur co-doped crumbled graphene for the oxygen reduction reaction with improved activity and stability in acidic medium. J Mater Chem A 2016;4:6014–20. doi:10.1039/c6ta00073h.

[15] Delgado JG. ASFALTENOS composición, agregación, precipitación, LABORATORIO DE FORMULACIÓN, INTERFASES REOLOGÍA Y PROCESOS UNIVERSIDAD DE LOS ANDES FACULTAD DE INGENIERIA ESCUELA DE INGENIERIA QUIMICA. n.d.

[16] Akmaz S, Gurkaynak MA, Yasar M. The effect of temperature on the molecular structure of Raman asphaltenes during pyrolysis. J Anal Appl Pyrolysis 2012;96:139–45. doi:10.1016/j.jaap.2012.03.015.

[17] Durón S, Rivera-Noriega R, Nkeng P, Poillerat G, Solorza-Feria O. Kinetic study of oxygen reduction on nanoparticles of ruthenium synthesized by pyrolysis of Ru3(CO)12. J Electroanal Chem 2004;566:281–9. doi:10.1016/J.JELECHEM.2003.11.065.

[18] Liu L, Kim H, Lee JW, Popov BN. Development of ruthenium-based catalysts for oxygen reduction reaction. J Electrochem Soc 2007;154:A123–8. doi:10.1149/1.2402108.

[19] Liu XY, Huang M, Ma HL, Zhang ZQ, Gao JM, Zhu YL, et al. Preparation of a carbon-based solid acid catalyst by sulfonating activated carbon in a chemical reduction process. Molecules 2010;15:7188–96. doi:10.3390/molecules15107188.

[20] Paraknowitsch BJP, Zhang J, Su D, Thomas A, Antonietti M. Ionic liquids as precursors for nitrogen-doped graphitic carbon. Adv Mater 2010;22:87–92. doi:10.1002/adma.200900965.

[21] Keller JU, Staudt R. Gas adsorption equilibria : experimental methods and adsorptive isotherms. Springer; 2005.

[22] Zhang LL, Zhao XS. Carbon-based materials as supercapacitor electrodes. Chem Soc Rev 2009;38:2520–31. doi:10.1039/b813846j.

[23] Wang S, Jiang SP, White TJ, Wang X. Synthesis of Pt and Pd nanosheaths on multi-walled carbon nanotubes as potential electrocatalysts of low temperature fuel cells. Electrochim Acta 2010;55:7652–8. doi:10.1016/j.electacta.2009.09.003.

Electrocatalyst and Fuel Cells

September 18 to 21, 2018 in Mexico City, Mexico

XVIII International Congress
of the Mexican Hydrogen Society

Synthesis and characterization of $IrRuO_x/TiO_2$ electrocatalysts for the oxygen evolution reaction in acidic médium

A. Martínez-Séptimo[1, 2], M.A.Valenzuela Zapata[1], R. de G. González Huerta[2*]

[1]Lab.Catálisis y Materiales, ESIQIE-Instituto Politècnico Nacional. Zacatenco, 07738, CDMX
[2]Lab. de Electroquímica y Corrosión, ESIQIE-Instituto Politècnico Nacional, Ed. Z-5, 3er piso, UPALM, C.P. 07738, México DF
Mail: abissaid@hotmail.com

ABSTRACT

Currently hydrogen is proposed as a viable energy vector considering its high energy density per unit mass and the by-products of its combustion do not generate an environmental impact. The most efficient and clean method for producing high purity hydrogen is the PEM electrolysers, however, it involves very high costs because the catalytic layer of the cathode and anode where the evolution of hydrogen and oxygen is carried out, respectively is made up of scarce and high cost metals, such as Pt, Ru and Ir. Therefore, there is a need to obtain electrocatalysts with a lower charge of precious metals or, in contrast, with other noble metal-free compounds. In this research work $IrRuO_x$ supported on TiO_2 ($IrRuO_x/TiO_2$) was obtained by the impregnation method followed by an oxidative heat treatment using of $RuCl_3$, $IrCl_3$ as Ru and Ir sources. The studied electrocatalysts contained nominal 50% mixed metallic phase (Ru 40% wt. and Ir 10% wt) supported on 50% wt of TiO_2 (Degussa P25). The prepared electrocatalysts were chemical and structurally characterized by means of XRF, XRD and SEM analyses. A typical cyclical and linear voltammetry was carried out by anodic scanning in a potential range of 0 to 1 V(NHE) and 1 to 1.68 V (ENH) in acid medium, respectively. $IrRuO_x/TiO_2$ electrocatalyst showed electrochemical stability practically equal to that of the commercial RuO_2-IrO_2 (3:1). Mass activities were obtained at E= 1.6 V(NHE), showing values of 89 mA/mg_{metal} for $IrRuO_x/TiO_2$, which was higher than commercial electrocatalyst, 60 mA mg_{metal}. These results were explained in terms of a higher and homogeneous dispersion of Ir and Ru oxides onto TiO_2 support.

Keywords: oxygen evolution reaction; ruthenium oxide; iridium oxide, anodic electrocatalysts

1. Introduction

Since the industrial revolution, humanity has been using fossil fuels such as oil and its derivatives, as well as natural gas and coal. These energy sources produce a high pollution index and are non-renewable. Therefore, there is an immediate need to develop alternative sources of energy that are renewable and that do not generate pollution or that are minimal. A viable alternative is hydrogen since it has a huge advantage over fossil fuels because it has a higher energy density (33 kW-h kg^{-1}), and its combustion process has as chemical byproducts water vapor and a small amount of nitrogen oxides that do not impact the environment considerably due to their low concentrations. [1-3]

Electrochemical process to hydrogen generation are viable for industrial and domestic application using renewable energy sources. Currently, there are three types of electrolysers: alkaline, proton exchange membrane (PEM) and solid oxide. PEM electrolyser (PEME) is more compact than alkaline and solid oxide electrolysers because they can work with a higher current density (~2A cm^{-2}) as well as, its solid electrolyte (polymeric membrane) gives a response time of less than one second and the hydrogen produced is of high purity (~99.99% w). [4-6] The catalysts used commercially for this type of electrolyser consist of compounds based on noble metals such as IrO_2-RuO_2 for the oxygen evolution reaction (OER) at the anode, since these noble metals have the best catalytic activity and electrochemical stability in acid medium in which the reaction takes place because the proton exchange membrane is generally composed of sulphonated polymers which gives it an acidic character, and Pt/C for the reaction of evolution of hydrogen (REH) at the cathode. [7-10]

As a result of the above, the economical price of PEM electrolysers is higher than alkaline electrolysers and consequently, the need arises to develop new electrocatalytic materials that are not based on noble metals or, failing that, reduce considerably the amount of these. [11,12] For the OER, several alternative catalytic materials have been synthesized, for example $IrRuCoO_x$ [1] and $IrSnO_2$ [2] to reduce the amount of noble metals by adding a transition metal or in contrast, catalysts have also been developed IrO_2/ATO [3] and IrO_2/SnO_2 [4] wherein the metal phase was dispersed on a support with a high specific area to increase the active area with respect to the metal load. In this work, the performance of $IrRuO_x/TiO_2$ obtained by impregnation is exposed. [5]

2. Materials and Methods

2.1 Electrocatalysts Synthesis of $IrRuO_x/TiO_2$

A range of catalysts was synthesized with weight percent of Ru and Ir in relation to the TiO_2, these materials are identified in Table 1, this table also includes the label of the mechanical mixtures of commercial catalysts that were evaluated for comparative purposes.

The amount of TiO_2 present in all the syntheses was 200 mg while the amount of precursors of $RuCl_3$ and $IrCl_3$ was varied to obtain a nominal weight of Ru in a range of 25% to 75% and 10% the Ir in relation to TiO_2. This precursors were dispersed by ultrasound for 5 min in 200 ml of deionized water; this dispersion was transferred to a rotavapor flask (1000 mL) in which the impregnation was carried out at vacuum, the temperature was controlled at 70 ° C for 3 hours. After impregnation, the resulting solid was subjected to oxidative thermal treatment in an air atmosphere saturated at 450 ° C for 4 hours in order to obtain the $IrRuO_x/TiO_2$. After, deionized water is added to the solid and dispersed by ultrasound for 5 minutes 5 times in order to dilute and separate $RuCl_3$ and $IrCl_3$ remnants.

Table 1. Composition and key of the range of synthesized catalysts

Key	%wRu	%wIr
I25	25	0
I50	50	0
I75	75	0
I4010	40	10
Comercial Electrocatalyst Sigma Aldrich®		
C100	100	0
C100	0	100
C7525	75	25

2.2 Pysicochemical caracterization

The crystalline structure type and the average particle size was obtained by X-ray diffraction (XRD), the Scherrer equation was utilized for this purpose. A Bruker D8 Diffractometer equipment was used, which has a high speed detector mark Lynx Eye with a monochromatic X-ray source of Cu-K_α with a wavelength λ = 1.54 Å and a photonic energy of 35 kV @ 25 mA, a scanning speed of 4°/min, in an angle range of Bragg from 20 ° to 100 ° with discrete increments of 0.02 °. The elemental analysis of the electrocatalysts with better electrocatalytic performance was carried out by X-ray fluorescence to establish the elemental species presents in the surface of the material, for this we used a Rigaku Supermini 200 equipment equipped with a 200 W Pd anode coupled to RX25 and LiF crystals with a Zr filter and proportional P-10 gas flow counter.
The electrocatalyst morphology, with better electrocatalytic performance, was obtained with a scanning electron microscope (SEM) Hitach SU3500, in addition, with the same equipment a surface quantitative mapping was performed, the elemental composition was obtained by X-ray dispersive energy spectroscopy (EDS) to compare with nominal composition and the composition obtained with X-ray fluorescence (XRF).

2.3 Electrochemical caracterization

The electrochemical tests were carried out in a potentiostat/galvanostat Autolab Diferentia Electrometer Amplifier PGSTAT12/30/302, the software used was the Nova version 1.11. For the cyclic voltammetry and linear scanning were performed in a double-walled glass cell in a three-electrode arrangement. 10 μL of a dispersion composed of 10 mg of the catalyst, 400 μL of ethyl alcohol, 100μL of deionized water and 30 μL of Nafion® was deposited on a glassy carbon electrode to generate thin layer, this is the working electrode, the reference electrode was sulfate Hg/ Hg_2SO_4 (E = + 0.68 V/NHE) and as a counter electrode was used a Pt mesh. The electrolyte was 0.5 M H_2SO_4 previously saturated with Ar. The cyclic sweeping voltammetry was carried out in a potential range from 0 V to 1 V/NHE and the linear scanning voltammetry was carried out in a potential range from 1.0 V to 1.68 V vs NHE.

3. Results and Discussion

3.1 Pysicochemical characterization

Figure 1 showed the X-ray diffraction pattern of I50 electrocatalyst wich had good experimental performance, we can see the characteristic signals of the RuO_2 and TiO_2, it is a proof that the Ru is present as oxide in the material, the average particle size is in the range between 13 nm to 17 nm according the Scherrer equation and a predominant tetragonal structure. It is a qualitative analysis, not quantitative and only confirms the presence or absence of RuO_2, not the relative amount of this over TiO_2.

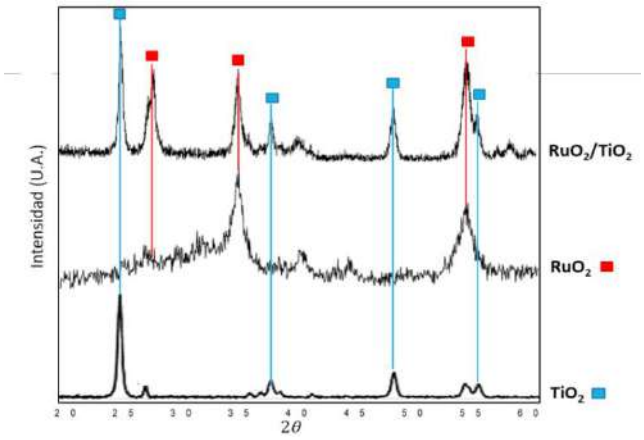

Figure 1. XRD pattern of I50

Figure 2 shows the elemental analysis of X-ray fluorescence for the electrocatalyst I4010, which presents the characteristic signals of Ir are underlinde in green and for Ru in red. In Table 2 we can see the mass concentration. There is a slight deviation between the nominal amount of Ti, Ir and Ru, for the Ir this difference is significant, the analysis shows lower concentration (2%) than

nominal concentration (10%), this loss is attributed to the synthesis process, The Ir fraction remains on the surface of the rotavapor flask because it is not completely reduced due to temperature, rotation speed and impregnation time. In future work, these variables will be optimized to avoid the high loss of Ir.

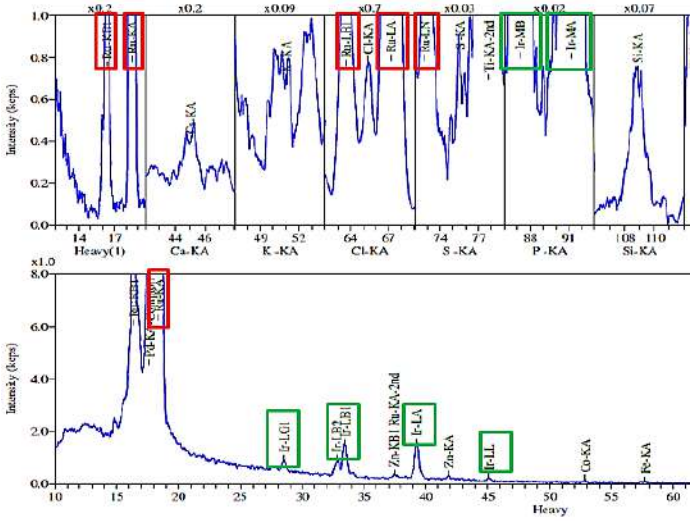

Figure 2. XRF pattern of I4010

Table 2. Elemental composition of I4010 (without O) determinated by XRF

Element	Intensity	%Weight
Ti	9.132	46.416
Ru	0.382	50.511
Ir	0.062	2.574
K	0.108	0.123
Co	0.026	0.1719
Si	0.087	0.1994
Total		99.996

The scanning electron microscopy (SEM) technique was used to obtain the morphology of the I4010 electrocatalyst, it is a little porous with some agglomerations of material that form macroparticles and microparticles, due to the resolution of the equipment (~ 125 nm per pixel), You can appreciate details such as the particle size as shown in Figure 3. From dispersive energy spectroscopy of secondary electrons (EDS) was obtained a mapping of the elemental composition of the electrocatalyst, the composition is homogeneous, but this is not accordance with the nominal and from XRF composition as is shown in Table 3, data were obtained from the Figure 4, EDS is punctual qualitative technique while XRF is a bulk compositional analysis, so we used composition from XRF technique.

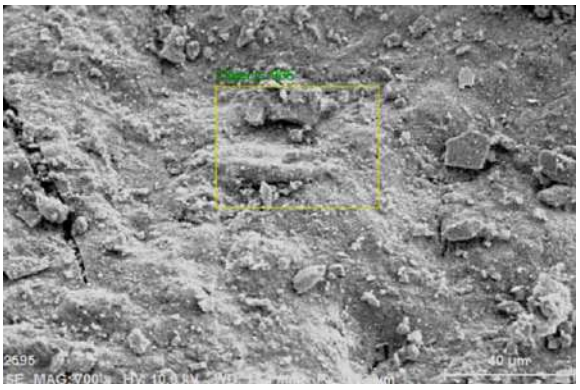

Figure 3. SEM micrography of I4010

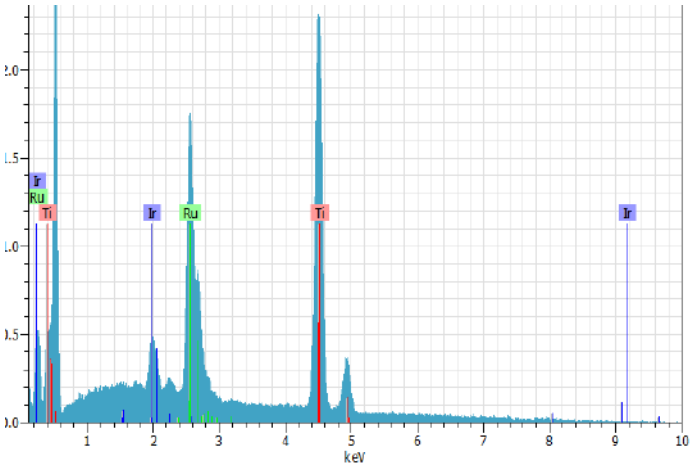

Figure 4. EDS pattern of I4010

Table 3. Elemental composition of I4010 (without O) determinated by EDS

Element	AN	Series	%Weight
Ti	22	K-series	70.76
Ru	44	L-series	25.17
Ir	77	M-series	4.07
Total			100.00

3.2 Elecrochemical characterization

Figure 5 corresponds to the cyclic voltammetry of the electrocatalyst I4010 in which it is observed that there are no oxidation processes with a sufficiently high current intensity in a potential range of 0.4 V(NHE) to 1 V(NHE) that could subsequently influence the performance of

the electrocatalyst in the potential range where the oxygen evolution reaction takes place (> 1.48 V @ 25°C), at lower potentials, between 0.0 V(NHE) and 0.4 V(NHE), we can see a reduction process, this is attributed to the start of the hydrogen evolution reaction, but it process is outside of the reaction under study. Figure 6 reports the mass activity of several electrocatalysts, this figure compares the performance of synthetized electrocatalysts and the commercial materials, where it is evident that the I50 and I4010 synthetized electrocatalysts have higher mass activity than commercial material C7525.

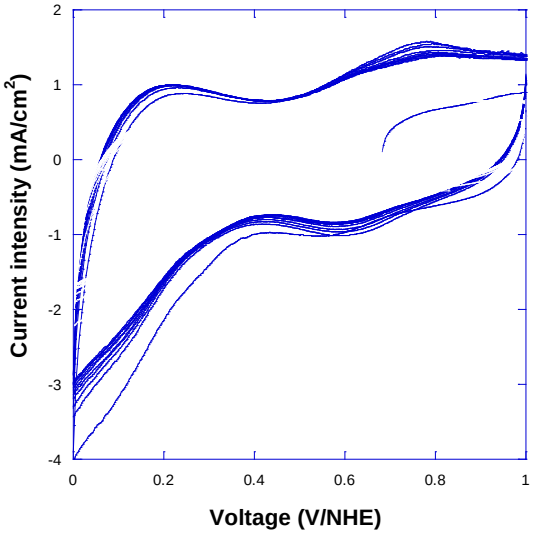

Figure 5. Cyclic voltammetry of I4010

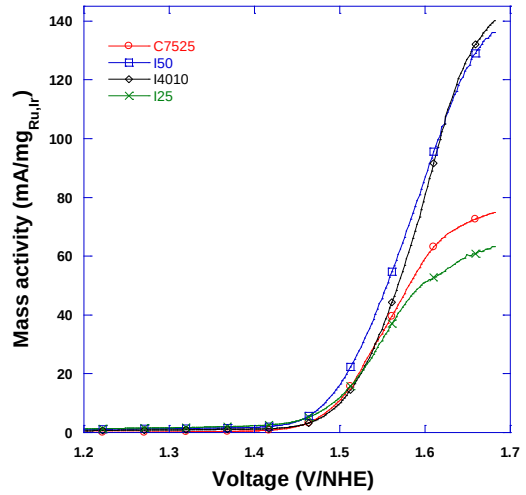

Figure 6. Linear sweep voltammetry of a range of electrocatalysts

Finally, the Figure 7 exposes the reduction of activity of the I4010 per cycle at 1.6 V where is clear that this reduction is bigger in first 20 cycles (0.06 mA/cm^2), after the 20th cycle activity slightly decreases (0.1 mA/cm^2). That means a high performance of the electrocatalyst, since it will has a constant activity in further cycles.

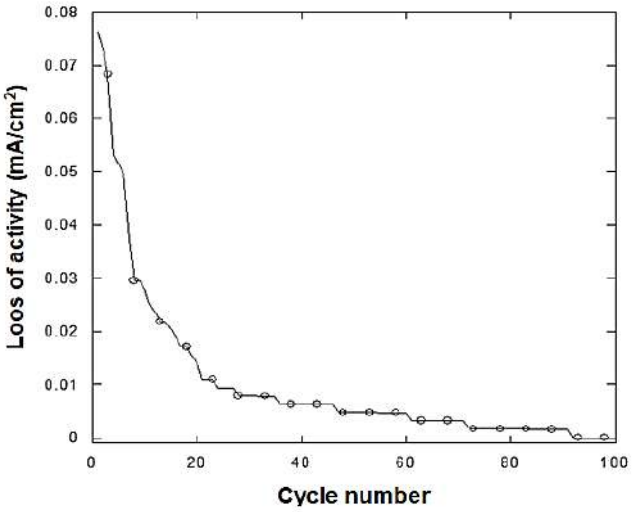

Figure 7. Stability of I4010 in 100 reaction cycles at acid medium

4. Conclusion

RuO_2/TiO_2 50% wRu (I50) and IrO_2RuO_2/TiO_2 10.40%w Ir, Ru (I4010) obtained by impregnation have better mass activity (89 mA mg_{metal}) than commercial material (C7525) of IrO_2-RuO_2 (60 mA mg_{metal}) both at 1.6 V/NHE. This is attributed to a high dispersion of Ir, Ru over TiO_2, which implies a greater electrocatalytically active area. The $RuIrO_x/TiO_2$ has electrocatalytic stability in acid medium, a potential range from 1.23 V to 1.68 V/NHE, similar to that of the commercial materials ($75RuO_2$-$25IrO_2$), it is considered that the addition of Ir modulates the energy of the Ru-OH bonds, avoiding that this intermediate compound is transformed into others, such as gaseous RuO_4 that cause a gradual deactivation of the electrocatalyst [6] [7]

Acknowledgements

The authors would like to acknowledge to the Instituto Politecnico Nacional for the financial support received through the Multidisciplinary Project 1820 and the CONACYT project CEMIE-Ocean-249795: Transversal Line I-LT1.

References

[1] J. L. Corona-Guinto, „Performance of a PEM electrolyzer using RuIrCoOx electrocatalysts for the oxygen evolution electrode," *International Journal of Hydrogen Energy,* Nr. 38, pp. 12667-12673, 2013.

[2] E. Mayousse, „Synthesis and characterization of electrocatalysts for the oxygen evolution in PEM water electrolysis.," *International Journal of Hydrogen Energy,* Nr. 36, pp. 10474-10481, 2011.

[3] K. Puthiyapuram-Vinod, „Physical and electrochemical evaluation of ATO supported IrO2," *Journal of Power Sources,* Nr. 269, pp. 451-460, 2014.

[4] J. Xu, „The electrocatalytic properties of an IrO2/SnO2 catalyst using SnO2 as a support and assisting reagent for the oxygen evolution reaction," *Electrochemical Acta,* Nr. 59, pp. 105-112, 2012.

[5] A. Mills, „A simple, novel method for preparing an effective water oxidation catalyst," *Chemical Communication,* Nr. 46, p. 2397–2398, 2010.

[6] M. Carmo, „A comprehensive rewiew on PEM water electrolysis," *International Journal of Hydrogen Energy,* Nr. 38, p. 4906, 2013.

[7] T. Reier, „Electrocatalytic Oxygen Evolution Reaction in Acidic Environments-Reaction Mechanisms and Catalysts," *Advance Energy Materials,* pp. 1601275-, 2017.

[8] W. Vielstich, Handbook of fuel cells: Fundameltals, technology and applications, Chichester, England; New York: Wiley, 2003.

[9] P. Strasser, „Lattice strain control of the activity in dealloyed core shell fuel cell catalysts," *Nature Chemistry,* Nr. 6, p. 454, 2010.

[10] S. Siracusano, „Electrochemical characterization of single cell and shrot stack PEM electrolyzers based on a naonsized IrO2 anode electrocatalyst," *International Journal of Hydrogen Energy,* Nr. 35, p. 5558, 2010.

[11] J. Russell, „Hydrogen generation by solid plymer electrolyte water electrolysis," *American Chemical Society Division of Fuel Chemistry,* Nr. 18, pp. 24-40, 1973.

[12] J. Polonsky, „Tantalum carbide as a novel support material for anode electrocatalysts in ploymer electrolyte membrane water electrolysers," *International Journal of Hydrogen Energy,* Nr. 37, p. 2173, 2012.

[13] M. Miles, „Periodic variations of overvoltages for water electrolysis in acid solutions from cyclic voltametric studies.," *Journal of the Electrochemical Society,* Nr. 123, p. 1459, 1976.

[14] D. R. Lide, Handbook of Chemistry and Physics, 87 Hrsg., Florida: CRC Press, 2006.

[15] R. Kotz, „XPS studies of oxygen evolution on Ru and RuO2 anodes," *Journal of the Electrochemical Society,* Nr. 130, p. 825, 1983.

[16] R. González-Huerta, „Producción de hidrógeno por electrólisis," in *Hidrógeno, producción y almacenamiento. Retos hacia su uso como vector energético.*, Ciudad de México, Create Space (USA), 2013, p. 66.

XVIII International Congress
of the Mexican Hydrogen Society

Oxygen reduction reaction on PtBi and PdBi alloys for PEMFC

O. X. Guerrero-Gutiérrez[1,*], M. A. Padilla-Islas[1], O. Solorza-Feria[1], P. B. Balbuena[2]

[1] Departamento de Química. Centro de Investigación y de Estudios avanzados, CINVESTAV-IPN. Av. IPN 2508, Zacatenco. México D.F.
[2] Artie McFerrin Department of Chemical Engineering, Texas A&M University, College Station, TX, USA
* Corresponding author: xguerrero@cinvestav.mx

ABSTRACT

Fuel Cells are a very promising alternative for clean energy production but commercializing them has been slowed down in great part by the high cost and instability of the catalysts. Pt is among the best catalyst for fuel cells because of its high activity towards the oxygen reduction reaction (ORR) and high stability. Preparing materials with less Pt content by alloying with different transition metals has shown to increase the electrocatalytic activity in some cases. This work focuses on evaluating the effect of Bi on Pt and Pd catalysts. Since Mexico is one of the largest Bi producers, it is also our objective to add value to this metallic national product. In this work, BiPt and BiPd nanoparticles were synthesized via chemical reduction and supported on a mesoporous carbon to evaluate their catalytic activities. The structure of the materials was characterized by XRD and TEM. Catalytic activities were measured via a thin film on a rotating disk electrode, getting the kinetic current generated at 0.9 V in acidic media and then compared with commercially available Pt nanoparticles. Cyclic voltammograms results show a non-Pt-like behavior. The results were also compared with theoretical density functional theory (DFT) calculations to examine the geometric and electronic structure to further explain the electrochemical behavior. Calculations were based on a slab model were adsorption energies for oxygen and density of states (DOS) analysis were performed for all adsorption sites. We show the changes in the descriptors of catalytic behavior d-band center and adsorption energy in respect to the Bi content.

Keywords (Maximum 4 words): electrocatalyst; ORR; fuel cell; DFT

1. Introduction

Fuel cells are electrochemical generators that convert the chemical energy of fuels into electricity directly, this allows them to have a more efficient energy transformation than other devices (e.g. internal combustion engines) [1]. The first application of fuel cells was in the US space program in the 60's. Presently, they are used in a variety of applications as stable and reliable energy sources in various industries like transportation, power supply, telecommunications, processing, space, military, etc. [2]. The use of this technology has not taken off due to several factors among which are the lack of infrastructure to handle hydrogen as a commercial fuel and the high cost of the technology. The high cost is due in part to the use of Pt (> $ 25,000 USD / kg [3]) as a catalyst. Most research on catalysts for fuel cells focuses on the cathode, where the slower reaction of oxygen reduction reaction (ORR) occurs.

It's been a keen interest to develop intermetallic catalytic materials that reduce the amount of noble metals without reducing the catalytic activity. It has been showed that by alloying Pt the catalytic activity can be increased [4-7]. Palladium alloys have also been shown to have a better catalytic activity than their pure counterpart [8]. Bismuth has been used to form intermetallic nanomaterials with Pt and Pd that work as catalysts [9-11]. It is an objective of this work to evaluate the influence of bismuth on PtBi and PdBi materials on the catalytic activity and performance towards the ORR. Since Mexico is the second largest producer of bismuth in the world [9], there's interest to use bismuth to add value to the national metal product.

We have combined experimental and theoretical results to study the ORR catalytic activity of alloys of Pt and Pd with Bi. Using adsorption energies and d-band center as descriptors of catalytic activity we have studied the influence of Bi in these well-known catalysts. These descriptors have been used extensively to model catalytic activity of materials and it has been predicted theoretically that optimal materials would have an O adsorption energy of 0.2 eV lower than that of Pt [12,13].

2. Materials and Methods

2.1 Chemical Synthesis

All materials were synthesized via chemical reduction. Two methodologies were followed to prepare the catalysts, they differ on the solvents used: one with ethylene glycol and the other one with a mixture of oleylamine and oleic acid (in a 8/2 v/v ratio). The two methodologies follow the same general procedure.

The precursors ($Pt(acac)_2$, $Pd(acac)_2$ and $Bi(NO_3)_3$; acac: acetylacetone C_5H_7O) were mixed in the solvent mixture. This mixture was stirred while saturating with $N_{2(g)}$ and then refluxed for 2 h. The resulting powder was obtained by centrifugation and was washed six times with H_2O (18 µS/cm) and then 2 times with ethanol. Finally, it was dried at 120°C for 2 h in a N_2 atmosphere.

2.2 Characterization

2.2.1 Electrochemical characterization

The electrochemical measurements were performed with a potenciostat/galvanostat (Autolab PGSTAT302N, Metrohm) in a conventional three-electrode cell. A platinum mesh was used as

counter electrode (CE), a normal hydrogen electrode (NHE) as the reference electrode (RE) and a glassy carbon electrode (5mm diameter) as the working electrode (WE) mounted on a rotor to use as a rotating disk electrode (RDE). $HClO_4$ 0.1M was used as electrolyte. The WE was coated with 10 µL of catalyst ink and mounted on the rotor upside-down to dry at 900 rpm. The catalyst ink was prepared by dispersing the catalyst on an aqueous solution with 20% isopropyl alcohol and 0.02% Nafion. The amount of catalyst dispersed was for 20 $\mu g_{Pt,Pd}/cm^2$.

As an activation or "cleaning" procedure a cyclic voltammetry with several (>20) cyclic sweeps between 0.05 V and 1.2 V at a scan rate of 100 mV/s was performed. This procedure allows us to observe the characteristic electrochemical profiles of the species present in the system. Then for higher resolution in the electrochemical profile (> 2) sweeps in the same range of potential were performed at 50 mV/s.

The electrochemically active surface area (ECSA) was calculated by CO stripping. $CO_{(g)}$ is bubbled into the electrolyte for 600 seconds for saturation, maintaining a 0.1 V polarization over the working electrode to adsorb CO over the catalyst surface. Subsequently $N_{2(g)}$ is bubbled for 600 seconds to remove the CO from the electrolyte. A cyclic voltammetry between 0.05 V and 1.2 V is performed at 20 mV/s and, in the first cycle, the adsorbed CO is oxidized. We then calculate the ECSA with:

$$ECSA\ (m^2 \cdot {g_{Pt}}^{-1}) = \left(\frac{Q_{CO}\,(\mathrm{C})}{420\ \mu\mathrm{C\ cm^{-2}} \cdot L_{Pt,Pd}(\mathrm{mg_{Pt,Pd}cm^{-2}}) \cdot A_{geo}(\mathrm{cm^2})}\right) \cdot 10^5 \qquad (1)$$

where Q_{CO} is the charge transferred in the CO electro-oxidation, L_{Pt} is the platinum/palladium loading on the WE and A_{geo} is the geometric area of the WE. The conversion factor (410 µC/cm^2) is taken from literature [14].

To determine the ORR catalytic activity the electrolyte is saturated with $O_{2(g)}$ and a linear sweep from 0.3 V to 1.0 V at 20 mV/s and 1600 rpm is performed. The kinetic current is calculated by correcting for the mass transport current [15]:

$$i_k = \frac{i_d \cdot i}{i_d - i} \qquad (2)$$

where i_k is the kinetic current, i_d is the diffusion limited current and i is the current. The kinetic current at 0.9 V is normalized with respect to the ECSA to obtain the specific activity (i_s) and with respect to the amount of Pt and Pd used to obtain the mass activity (i_m).

2.2.2 Physical characterization

X-ray diffraction (XRD), scanning transmission electron microscopy (STEM) and energy dispersive X-ray spectroscopy (EDX-SEM) were used for the physical characterization. XRD patterns were taken in a Bruker D8 Advance Eco diffractometer using Cu Kα radiation at room temperature. XRD patterns were used for phase identification. XRD data was analyzed with the Match! Software using the ICSD database. STEM images were taken in an ARM200F-JEOL

microscope operated at 200 keV. STEM was used to determine the morphology and particle size of the electrocatalysts and their dispersion on C.

2.3 Computational Details

A slab model was used as a representation of the surface the catalysts, the bottom layers were fixed to represent the effect of the bulk. The slabs were constructed from the bulk structures that were optimized from the Crystallography Open Database [16-20]. The construction of slab models was done with the Atomic Simulation Environment (ASE) python package [21]. The slabs were created by cleaving the optimized bulk structure at the (111) miller plane with a 15 Å vacuum spacing. The two bottom layers were kept fixed and the top layers were relaxed via DFT optimizations.

The O and OH adsorptions were investigated on the adsorption sites (shown in Fig. X) with a coverage of 0.25 monolayers. This coverage is the ratio of the number of adsorbates to the number of surface atoms. The adsorbates along with the top layers were allowed to relax to their lowest energy configuration. The adsorption energy, E_{ads}, is defined as follows:

$$E_{ads}=E_{adsorbate/slab}-(E_{slab}+nE_{adsorbate}) \quad (3)$$

where $E_{adsorbate/slab}$ is the total energy of adsorbate and the slab, E_{slab} is the total energy of the slab, n is the number of adsorbed species and $E_{adsorbate}$ is the total energy of the adsorbate.

The d-band center was obtained from the DOS of the surface atoms. It was calculated as the weighted average of the d contribution to the DOS using the following equation:

$$dbc=\frac{\sum_{i=0}^{n} w_i x_i}{\sum_{i=0}^{n} w_i} \quad (4)$$

where *dbc* is the d-band center, *x* represents the energy relative to the Fermi level and *w* represents the d contribution to the DOS.

The surface segregation energies, E_{seg}, were calculated by the difference in total free energy between the segregated and non-segregated slabs. The segregated structures were constructed by exchanging the positions of atoms of one element in the subsurface with the positions of atoms of the other element in the surface. A negative segregation energy indicates the segregated structure is more stable than the non-segregated one, suggesting that the specific atom is thermodynamically favored to segregate to the surface **¡Error! No se encuentra el origen de la referencia.**.

3. Results and Discussion

3.1 Experimental results

Figure 1 shows the TEM micrographs for the alloys. They all have the same morphology and particle agglomeration. The chemical composition determined by EDS confirms the presence of

Bi in the materials (results not shown). It can also be seen that the metals do not disperse well in the carbon support, this is result of the agglomeration they present.

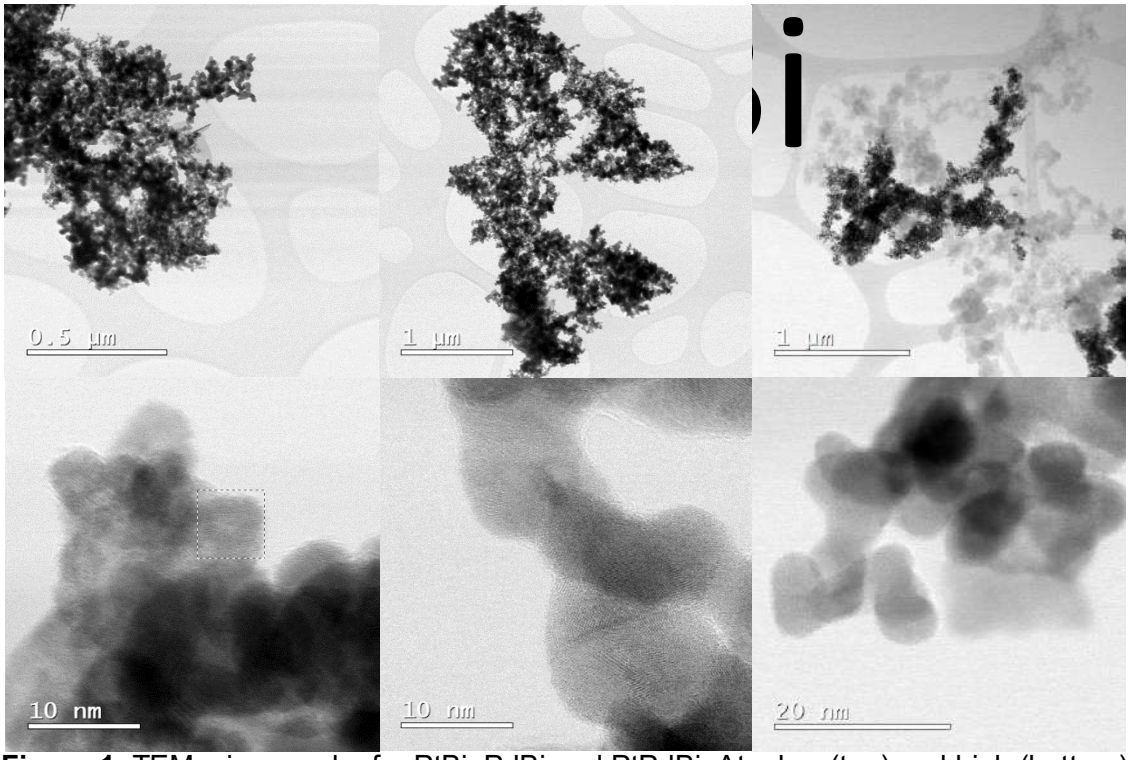

Figure 1. TEM micrographs for PtBi, PdBi and PtPdBi. At a low (top) and high (bottom) magnification.

Voltammograms from which the electrochemical results were obtained for $Pt_{45}Pd_{45}Bi_{10}/C$ are presented in Figure 2. The CV profile, CO-stripping, ORR-RDE and Tafel plots are presented. In the CV profile, we can see at low potentials hydrogen adsorption/desorption currents characteristic of Pt and near zero we can see an increased current characteristic of the interaction of protons with Pd. We can also observe the peak at around 0.8 V similar to the one Pd presents. In the CO-stripping measurement the electrooxidation peaks at 0.8 V, consistent with what we would expect for CO adsorbed on Pt. The area of this peak is converted to ECSA with the conversion factor 210 $\mu C/m^2$. The Tafel plot was calculated using the data from the RDE-ORR at 1600 rpm corrected by mass transport.

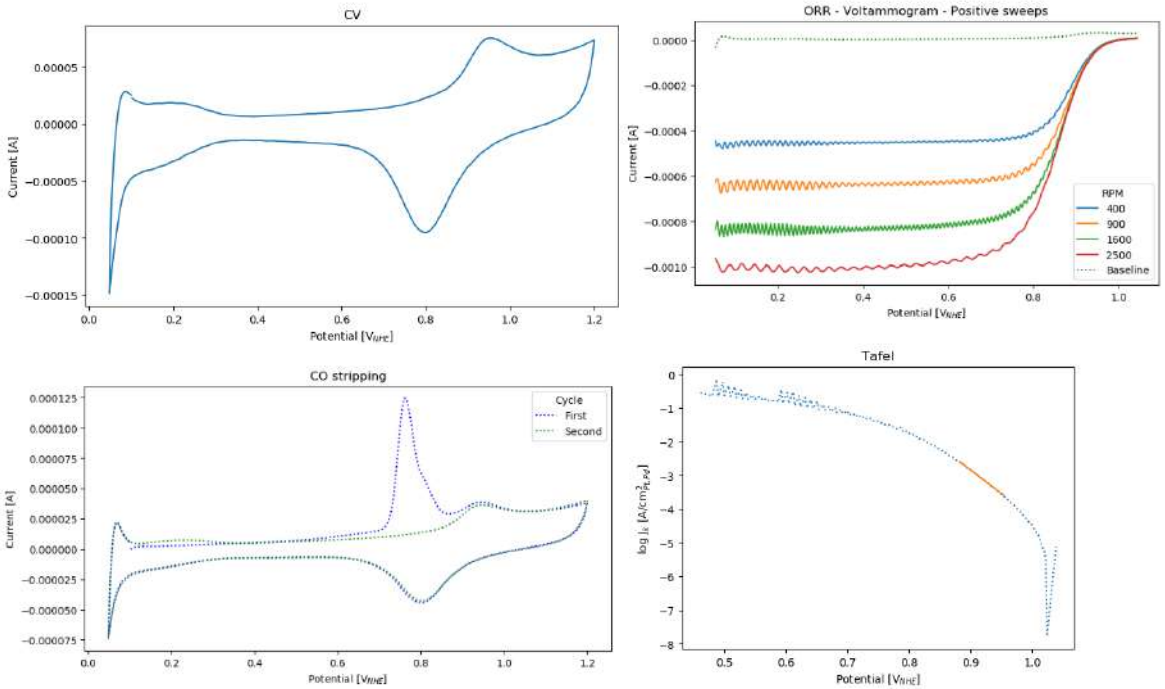

Figure 2. The CV profile (top left; 50 mV/s), CO stripping (bottom left; 20 mV/s), RDE-ORR (top right; 20 mV/s) and Tafel (bottom right) plots for $Pt_{45}Pd_{45}Bi_{10}$/C. In 0.1 M $HClO_4$.

Table 1 shows a summary of the ORR catalytic activities and the ECSA of the various catalysts prepared. We are more interested in the mass activity because it is the one that can be related directly to the cost of the catalyst. Specific activity is higher for the alloys because of the low ECSA values, this is result of the agglomeration they present (Fig. 1). Because of this, we will only focus on the mass activities. When alloyed with Bi, the catalytic activity of Pt is reduced but in Pd it increases. The trimetallic catalyst however, has a better catalytic activity then even pure Pt.

Table 1. Electrochemical results. Electrochemical Surface Area (ECSA), mass current (im) and specific current (is). Activities calculated at 0.9 V.

Sample	ECSA $cm^2_{Pt,Pd}$	i_m $mA/\mu g_{Pt,Pd}$	i_s $\mu A/cm^2_{Pt,Pd}$
Pt	112	50	45
Pd	33	6	6
$Pt_{90}Bi_{10}$	13	32	250
$Pd_{90}Bi_{10}$	16	26	160
$Pt_{45}Pd_{45}Bi_{10}$	24	69	282

3.2 Computational results

Figure 3 shows the structure of FCC (111) $Pt_{45}Pd_{45}Bi_{10}$ and the sites where atomic oxygen was adsorbed for the calculation of the adsorption energies. As shown, the slabs consist of 4 layers where the bottom 2 layers are fixed to represent binding to the bulk structure. All structures were built with no Bi on the surface layer.

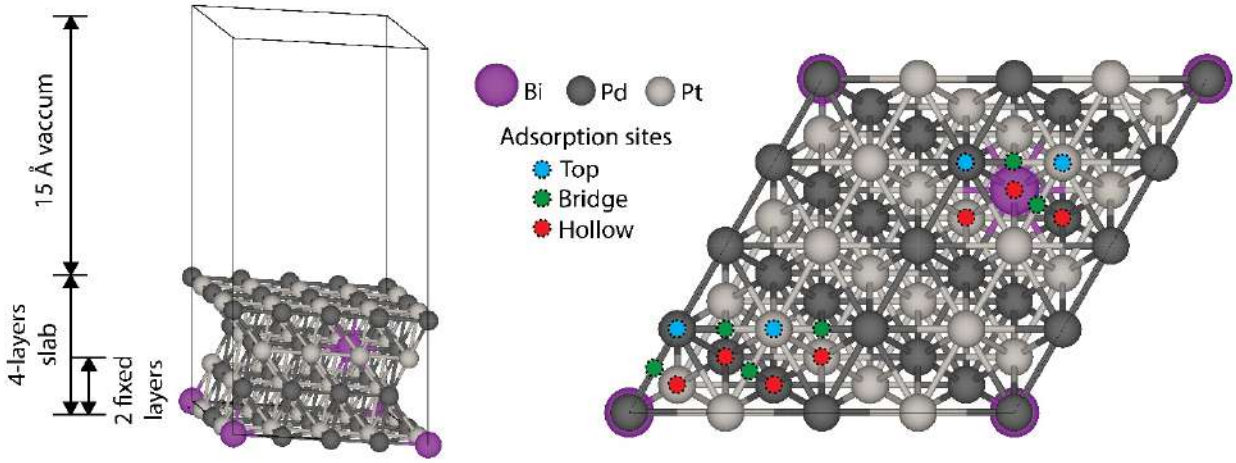

Figure 2. Slab structure of $Pt_{32}Pd_{30}Bi_2$ (left) and a top view showing the adsorption sites.

Table 2 shows the O adsorption energies and d-band center for the different materials. The O adsorption energies on Pt (-6.0 eV) and Pd (-6.2 eV) are practically the same when compared to their corresponding Bi alloy (-6.0 and -6.2 eV, respectively), however, the d-band center does change. When compared with their Bi alloy, the d-band center is more positive for Pt (from -2.38 to -2.25 eV) and more negative for Pd (from -1.79 to -2.25 eV). Even though the O adsorption energies are not changed the d-band center does change. It would be interesting to see the change in adsorption energies in different coverages and in the presence of water. Also, to have a better understanding of how Bi is affecting the catalytic activity, we should investigate the adsorption energies of other intermediates of the ORR to corroborate that they follow the same trend as O. It is important to note that, in a PdBi alloy, Bi is thermodynamically favored to segregate to the surface [23]. Because of this, it would be also interesting to investigate these systems with Bi on the surface and the energies of its interaction with the ORR intermediates.

Table 2. d-band center and O adsorption energies for the different materials studied. Energies are in eV.

Catalyst	d-band center	E_{ads}
Pt	-2.38	-6.04
Pd	-1.79	-6.25
$Pt_{31}Bi_1$	-2.25	-6.09
$Pd_{31}Bi_1$	-2.25	-6.26
PtPd	-2.00	-6.20

4. Conclusion

We prepared Pt, Pd, $Pt_{90}Bi_{10}$, $Pd_{90}Bi_{10}$ and $Pt_{45}Pd_{45}Bi_{10}$ and evaluated their ORR catalytic activity. The prepared alloys presented a high level of agglomeration which hinders the catalytic activity. The experimental results show that the small amount of Bi added on the Pt electrocatalyst decreases its catalytic activity, whereas in Pd it increases it. The $Pt_{45}Pd_{45}Bi_{10}$/C trimetallic electrocatalyst presents a higher catalytic activity than the mono or bimetallic electrocatalysts. The trimetallic is a better catalyst for the ORR than the separate components, even with the high agglomeration it presented. By modifying the synthesis method, we expect to be able to produce a better electrocatalyst.

We also studied these materials with DFT using atomic oxygen adsorption energy and d-band center as descriptors for ORR catalytic activity. When Bi is added to the Pt and Pd structures, we observe a change in the d-band center but not in the atomic oxygen adsorption energies. This could be because the Bi near the surface changes the electronic structure but is not concentrated enough to affect the adsorption energy. To resolve this, we should investigate the effect of adding more Bi to Pt and Pd and with more adsorption coverages.

Acknowledgements

To CONACYT and CINVESTAV for the grant and facilities without whom this work would have not been possible. To Laboratorio Avanzado de Nanoscopía Electrónica for the TEM images. To the Texas A&M University Supercomputer Facility for providing the computational resources.

References

[1] F.J. Rodríguez Varela, O. Solorza Feria, E. Hernández Pecheco; CELDAS DE COMBUSTIBLE; 2010
[2] Fuel Cell Technologies Market Report, Fuel Cell Technologies Office, U.S. Department of Energy, November 2014
[3] Kitco Metals Inc. http://www.kitco.com/charts/liveplatinum.html

[4] Y. Choi, K.A. Kuttiyiel, J.P. Labis, K. Sasaki, G.G. Park, T.H. Yang, R.R. Adzic. Enhanced oxygen reduction activity of IrCu core platinum monolayer shell nano-electrocatalysts. Top. Catal 2013; 56(12), 1059–1064.
[5] K.A. Kuttiyiel, K. Sasaki, Y. Choi, D. Su, P. Liua, R.R. Adzic. Bimetallic IrNi core platinum monolayer shell electrocatalysts for the oxygen reduction reaction. Energy Environ. Sci 2012; 5(1), 5297–5304.
[6] K. Gong, W. Chen, K. Sasaki, D. Su, M.B. Vukmirovic, W. Zhou, E.L. Izzo, C. Perez-Acosta, P. Hirunsit, P.B. Balbuena, R.R. Adzic, Platinum-monolayer electrocatalysts: palladium interlayer on IrCo alloy core improves activity in oxygen-reduction reaction. J. Electroanal. Chem 2010; 649(1-2), 232–237.
[7] T. Cochell, A. Manthiram. Pt@PdxCuy/C core–shell electrocatalysts for oxygen reduction reaction in fuel cells. Langmuir 2012; 28(2), 1579–1587.
[8] F. Fouda-Onana, S. Bah, O. Savadogo. Palladium–copper alloys as catalysts for the oxygen reduction reaction in an acidic media I: Correlation between the ORR kinetic parameters and intrinsic physical properties of the alloys. Journal of Electrocatalytical Chemistry 2009; 636, 1-9.
[9] C.-C. Chen, C.-L. Lin and L.-C. Chen. A binary palladium-bismuth nanocatalyst with high activity and stability for alkaline glucose electrooxidation. J. Pow. Sour 2015; 287,223-233.
[10] Xiulei et al. Nanocrystalline intermetallics on mesoporous carbon for direct formic acid fuel cell anodes. Nat. Chem 2010; 3, 286-293.
[11] Faisal et. al. Hydrogen Evolution and Hydrogen Oxidation on Palladium Bismuth Alloys. Top. Catal 2011; 54, 77-82.
[12] J. Greeley et al. Alloys of platinum and early transition metals as oxygen reduction Electrocatalysts. Nat. Chem 2009; 1, 552-556.
[13] J.K. Nørskov et. al. Origin of the overpotential for oxygen reduction at a fuel cell Cathode. J. Phys. Chem. B 2004; 108, 17886-17892.
[14] Mayrhofer KJJ, Strmcnik D, Blizanac BB, Stamenkovic V, Arenz M, Markovic NM. Measurement of oxygen reduction activities via the rotating disc electrode method: From Pt model surfaces to carbon-supported high surface area catalysts. Electrochimica acta 2007; 53:3181-3188.
[15] V. Stamenkovic et al.. Changing the activity of electrocatalysts for oxygen reduction by tuning the surface electronic structure. Angew. Chem. Int. Ed. 2006, 45, 2897-2901.
[16] Merkys, A., Vaitkus, A., Butkus, J., Okulič-Kazarinas, M., Kairys, V., Gražulis. COD: CIF: Parser: an error-correcting CIF parser for the Perl language. *Journal of Applied Crystallography* 2016; 49.
[17] S. Gražulis, A. Merkys, A. Vaitkus, M. Okulič-Kazarinas. Computing stoichiometric molecular composition from crystal structures. *Journal of Applied Crystallography 2015;* 48, 85-91.
[18] S. Gražulis et al., A. Crystallography Open Database (COD): an open-access collection of crystal structures and platform for world-wide collaboration. *Nucleic Acids Research* 2012; 40, D420-D427.
[19] Grazulis, S., Chateigner, D., Downs, R. T., Yokochi, A. T., Quiros, M., Lutterotti, L., Manakova, E., Butkus, J., Moeck, P., Le Bail, A. Crystallography Open Database – an open-access collection of crystal structures. *J. Appl. Cryst.* 2009; 42, 726-729.

[20] R.T. Downs, M. Hall-Wallace. The American Mineralogist Crystal Structure Database. *American Mineralogist* 2003; 88, 247-250.
[21] S.R. Bahn, K.W. Jacobsen. An Object-Oriented Scripting Interface to a Legacy Electronic Structure Code. Computing in Science & Eng 2002; 3, 56–66.
[22] Y. Ma, P.B. Balbuena. Pt Surface segregation in bimetallic Pt3M alloys: A density functional theory study. Surface Science 2008; 602, 107-113.
[23] O.X. Guerrero-Gutiérrez, O. Solorza-Feria, P.B. Balbuena. First-principles investigation of Pd3Bi as a catalyst for the oxygen reduction reaction. International Journal of Hydrogen Energy 2017; 42, 30359-30363.

XVIII International Congress
of the Mexican Hydrogen Society

Effect of nitrogen precursors on graphene-doping and electrochemical evaluation as an active electrocatalyst for oxygen reduction reaction

N.M. Sánchez-Padilla[1], R. Benavides[1]*, E. De-Casas[2], J.A. Mercado[2], S. Fernández[2], D. Morales-Acosta[1,*]

[1]Departamento de Procesos de Transformación de Plásticos, Centro de Investigación de Química Aplicada
[2]Laboratorio Nacional de Materiales Grafénicos, Centro de Investigación de Química Aplicada
Blvd. Enrique Reyna No. 140, Col. San José de los Cerritos, Saltillo, 25290; Coahuila, México.
*E-mail: roberto.benavides@ciqa.edu.mx, diana.morales@ciqa.edu.mx

ABSTRACT

Metal-free oxygen reduction reaction (ORR) catalysts are needed to have more available alkaline fuel cell technologies. In this study nitrogen-doped reduced graphene oxides (N-rGO) were obtained by hydrothermal reaction of graphene oxide with urea or amitrole. Graphene oxide (GO) was synthetized by Tour's method and simultaneously doped and reduced under hydrothermal process. N-rGO$_{urea}$ and N-rGO$_{amitrole}$ were characterized by XRD, TGA, Raman and FT-IR techniques. The electrocatalytic activity toward the ORR was evaluated in alkaline media by rotating disk electrode linear sweep voltammetry (RDE-LSV) at different rotating speeds. XRD, TGA and FT-IR results confirm the reduction of GO (rGO) while Raman spectra for N-rGO$_{amitrole}$ and N-rGO$_{urea}$ show a displacement of the G band located in ~1590 cm^{-1} confirming the successful doping of rGO. The LSV curves show a higher onset potential for N-rGO$_{amitrole}$ than N-rGO$_{urea}$ with (0.9 V vs 0.85 V) and a higher current density (4.6 mA cm^{-2}). Koutecky-Levich analysis indicated that N-rGO$_{amitrole}$ catalyze the ORR by a 4-electron pathway while N-rGO$_{urea}$ follows a 2-electron pathway.

Keywords: N-doped graphene, oxygen reduction reaction, fuel cells.

1. Introduction

Climate change and energy consumption are two of the main subjects in global outlook[1]. With the aim to supply the higher energy demand, an accelerated development of alternative energy devices are needed. Fuel cells are promising devices for energy conversion that can be

used. However, high prices and scarcity of Pt used as catalysts limit its commercialization[2]. The development of non-precious metal catalysts is needed for a rapid promotion of fuel cells technologies.

Graphene derivative materials have been recently studied, not only as catalyst support material, but as promising direct catalysts for fuel cells reactions. Carbonaceous materials as graphene can catalyze the oxygen reduction reaction (ORR) without precious metals, but proceeds by a 2-electron pathway, which is not a desired mechanism due to generation of overpotentials. However, the heteroatom doping of this materials with nitrogen atoms can lead to a highly desired 4-electron pathway[3].

Many methods are available to carry out the doping of graphene. One of them is the hydrothermal process due to the simplicity of the process and successful results [4]. Urea is the most studied nitrogen precursor for doping [5,6]. Recently, Grzyb and coworkers [7,8] employed new nitrogen precursors as guanidine and amitrole for higher nitrogen content in doped graphenes. Since then, few reports about the use of amitrole has been developed. In this work, two N-doped graphene catalyst with two different nitrogen precursors were synthesized. The results show that there is a significant difference between the use of amitrole or urea and the election of the precursor has an effect in the material's catalytic activity for ORR.

2. Materials and Methods

Graphene oxide (GO) was synthetized by Tour's method, where graphite powder was dispersed in concentrated mixture H_2SO_4:H_3PO_4 (9:1 volume ratio) and sonicated for 30 minutes. Then, the dispersion was placed in an ice bath and $KMnO_4$ (3:1 mass ratio with respect to graphite) was slowly added. The temperature was raised to 69 °C for 30 minutes. The reaction was cooled down to room temperature and water added (1.5:1 volume ratio with respect to volume of the acid mixture) and continuous stirring for 48 hours. A solution of 3 % H_2O_2 solution was added, in order to stop the reaction. The resulting solution was centrifuged, successively washed with water and ethanol to neutral pH and dried.

A mixture that contains GO and urea or amitrole (as N source) in a 1:15 mass ratio was hydrothermally treated in an autoclave at 180 °C for 5 h. At the end of the reaction time, the autoclave was allowed to cool down to room temperature. The product was washed and dried at 80 °C for 24 h. The resulting materials were labeled as N-rGO$_{urea}$ and N-rGO$_{amitrole}$.

The electrode was prepared as a catalytic ink as follows: the catalyst powder was dispersed in isopropanol and Nafion (5 μL) by ultrasound to form an ink with catalyst loading of 10 mg mL^{-1}. Then, an aliquot of 20 μL of the catalytic ink was deposited onto a glassy carbon disk (0.196 cm^2

as geometrical area), previously polished until mirror-finished surface. After drying, the working electrodes were obtained.

The catalytic activity was measured in a SP-300 (Biologic) bipotenciostat connected to an RDE (Pine Inst.) in an electrochemical cell. A Pt wire was used as counter electrode, while Ag/AgCl served as reference. All experiments were carried out in alkaline media (0.1 KOH) N_2-saturated. After 40 cycles at 50 mV s^{-1} cyclic voltammetry (CV) activation and CV profile at 20 mV s^{-1}, the ORR activity was measured at different rotation rates (400 until 2000 rpm) in a O_2-saturated electrolyte. CV was carried out to test the activity at 5 mV s^{-1}.

3. Results and Discussion

Fig. 1a show the experimental diffraction patterns from the graphite precursor GO, N-rGO$_{urea}$ and N-rGO$_{amitrole}$. GO sample shows a peak at 10.65° of 2θ scale related to the plane (001) and indicate an exfoliation of the graphite's sheets due to incorporation of functional groups after oxidation process[9]. The experimental pattern of N-rGO$_{urea}$ and N-rGO$_{amitrole}$ shows disappearance of the (001) plane and the appearance of a broad peak near to 25° related to the plane (002) of graphite. The later indicate that after hydrothermal treatment a reduction process occurs and cause a rehybridization $sp^3 \rightarrow sp^2$ from GO to its reduced form rGO. Fig. 1b shows the FT-IR spectra for GO, N-rGO$_{urea}$ and N-rGO$_{amitrole}$. For GO four bands are observed, corresponding to the functional groups incorporated due to the oxidation process: the stretching vibration of carbonyl group (1750 cm^{-1}); stretching modes for C=C (1630 cm^{-1}); C-O stretching vibration (at 1070 cm^{-1}) and stretching vibrations in epoxides (C-O-C at 850 cm^{-1})[10]. For N-rGO$_{urea}$ and N-rGO$_{amitrole}$ the displacement of the band related with C=C (from 1630 to 1590 cm^{-1}), suggests the incorporation of N in the carbon lattice due the overlapping of the vibrations of C=C and C=N[6]. Also, the appearance of a broad band at 1200 cm^{-1} related to the C-N bond suggests that the N atoms were covalently bonded to graphene lattice.

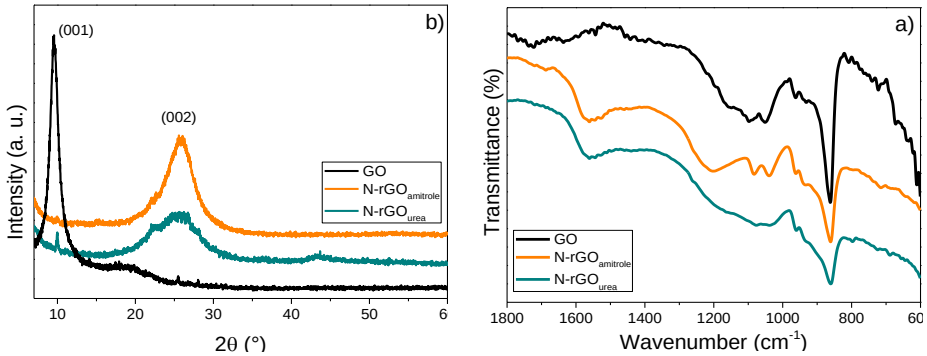

Fig. 1. Diffraction patterns (a) and FT-IR spectra (b) of GO, N-rGO$_{urea}$ and N-rGO$_{amitrole}$ samples.

TGA curves are depicted in Fig. 2a. For GO three main weight loses are observed; the first of them starts at room temperature and ends at 100 °C and is related to water desorption. The second one, and major weight loss is around ~150 °C corresponds to the release of labile functional groups incorporated into GO[11]; and the third one, between 220 and 600 °C is related with the pyrolysis of more stable oxygen containing groups. For N-rGO$_{amitrole}$ a loss due to water desorption is also observed, not seen for N-rGO$_{urea}$. Both doped materials show a slight progressive weight loss at high range temperature (between 200 and 600 °C). The later indicate an improved thermal stability due to the hydrothermal treatment and the doping process, suggesting a successful covalent functionalization with N [12]. Fig. 2b shows the Raman spectra for GO, N-rGO$_{urea}$ and N-rGO$_{amitrole}$. Two bands are observed for the three materials: at 1350 cm-1 the D-band, which is related to disorder induced in the graphene lattice and G-band at ~1588 cm-1, related to the vibration in plane of the sp^2 domains in graphene lattice [13]. Raman spectroscopy also give evidence about the introduction of heteroatoms in a carbon sp^2 lattice and could confirm the N-doping. Due to the dispersive behavior of D-band, shifts of its maxima are common, but any shift in G-band suggests the introduction of dopants or charge carriers in the lattice [14]. Meanwhile for GO the G-band located at 1588 cm^{-1}, for both doped materials a upshifting to 1600 cm^{-1} is observed, which strongly suggests the successfully doping with nitrogen atoms [5].

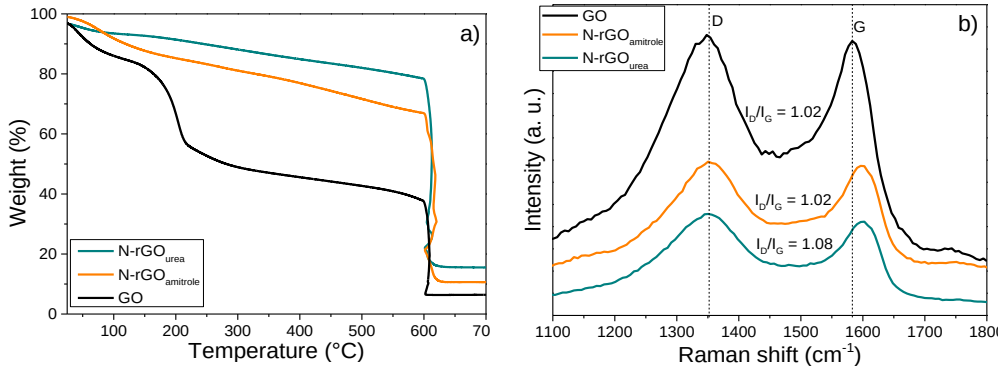

Fig. 2. TGA curves (a) and Raman spectra (b) of GO, N-rGO$_{urea}$ and N-rGO$_{amitrole}$ samples.

Fig. 3 shows the cyclic voltammograms of N-rGO$_{urea}$ and N-rGO$_{amitrole}$. Both materials show a near-rectangular shape voltammogram. Since N atoms in a carbon lattice improve the wettability of the material, an enhancement of the electrochemical performance for redox reactions can occur [8]. However, the current density of N-rGO$_{amitrole}$ is higher than N-rGO$_{urea}$ suggesting an increased surface area. Moreover, N-rGO$_{amitrole}$ shows a reversible hump at ~0.4 V, related to the contribution of remaining oxygen groups in the surface of the material. The later means that

faradaic processes are prone to occur in this material and suggests that the charge transfer process is more efficient comparing with N-rGO$_{urea}$.

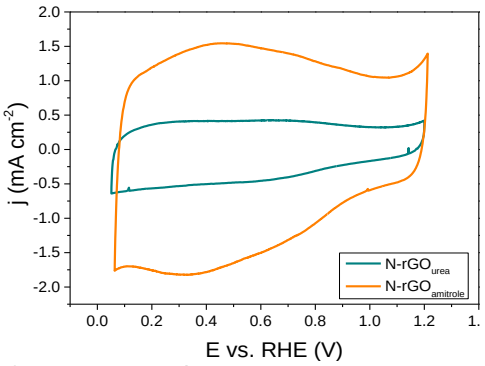

Fig. 3. Cyclic voltammetry of N-rGO$_{urea}$ and N-rGO$_{amitrole}$. 0.1 M KOH N_2-saturated at 20 mV s^{-1}.

The polarization curves for ORR are shown in Fig. 4. The capability of both materials for ORR is confirmed and three distinguished potential regions are revealed: kinetic (E > 0.8 V), mixed (0.6 < E < 0.8) and diffusion controlled (E < 0.6 V). For N-rGO$_{urea}$ the onset potential (E_{ORR}) is 0.83 V, and the current density (*j*) is 4.4 mA cm^{-2}; while for N-rGO$_{amitrole}$ the E_{ORR} is 0.88 V with a *j* of 4.7 mA cm^{-2}. The higher values of N-rGO$_{amitrole}$ are in good agreement with the results observed in cyclic voltammograms: a higher surface area and the capacity to carry out faradaic processes lead to a higher activity for the oxygen reduction reaction. The electrochemical behavior of N-rGO$_{urea}$ and N-rGO$_{amitrole}$ for RRO is comparable with materials previously reported for cathodes based on Pt [15], indicating: 1) the successfully incorporation of N-atoms in the graphene lattice and 2) that they are potential candidates for the replacement of catalysts based on noble metals.

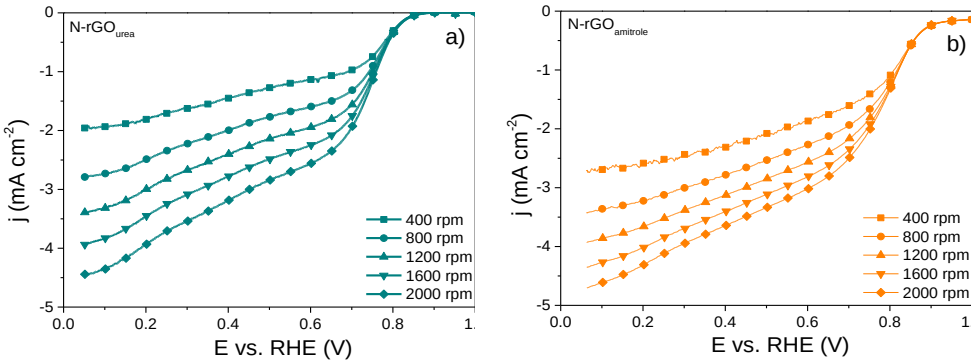

Fig. 4. ORR curves for N-rGO$_{urea}$ (a) and N-rGO$_{amitrole}$ (b). 0.1 M KOH O_2-saturated at 5 mV s^{-1}.

4. Conclusion

Two N-doped graphene catalysts were successfully synthesized through a hydrothermal route. A high current density was observed for both materials. Nevertheless, N-rGO$_{amitrole}$ shows a higher value of onset potential (0.88 V) and higher current density (4.7 mA cm^{-2}), which suggests that the nitrogen precursor play a big role in the doping process.

Acknowledgements

The authors are grateful to the National Council of Science and Technology (Conacyt) through the 259010, 270214. NMSP is thankful to Conacyt for the PhD scholarship. Authors also are grateful to Graphene Materials National Laboratory (LNMG) facilities provided for the use of some of its installations.

References

[1] S. Teske, T. Pregger, S. Simon, T. Naegler, W. Graus, C. Lins, Energy [R]evolution 2010—a sustainable world energy outlook, Energy Effic. 4 (2010) 409–433. doi:10.1007/s12053-010-9098-y.

[2] Z. Chen, D. Higgins, A. Yu, L. Zhang, J. Zhang, A review on non-precious metal electrocatalysts for PEM fuel cells, Energy Environ. Sci. 4 (2011) 3167. doi:10.1039/c0ee00558d.

[3] L. Yu, X. Pan, X. Cao, P. Hu, X. Bao, Oxygen reduction reaction mechanism on nitrogen-doped graphene: A density functional theory study, J. Catal. 282 (2011) 183–190. doi:10.1016/j.jcat.2011.06.015.

[4] Z. Xing, Z. Ju, Y. Zhao, J. Wan, Y. Zhu, Y. Qiang, et al., One-pot hydrothermal synthesis of Nitrogen-doped graphene as high-performance anode materials for lithium ion batteries., Sci. Rep. 6 (2016) 26146. doi:10.1038/srep26146.

[5] Z. Lin, G. Waller, Y. Liu, M. Liu, C.P. Wong, Facile synthesis of nitrogen-doped graphene via pyrolysis of graphene oxide and urea, and its electrocatalytic activity toward the oxygen-reduction reaction, Adv. Energy Mater. 2 (2012) 884–888. doi:10.1002/aenm.201200038.

[6] Y.K. Zhang, Z. Sun, H. Wang, Y.D. Wang, M. Liang, S. Xue, Nitrogen-doped graphene as a cathode material for dye-sensitized solar cells: effects of hydrothermal reaction and annealing on electrocatalytic performance, RSC Adv. 5 (2015) 10430–10439. doi:10.1039/c4ra13224f.

[7] B. Grzyb, S. Gryglewicz, A. Sliwak, N. Diez, J. Machnikowski, G. Gryglewicz, Guanidine, amitrole and imidazole as nitrogen dopants for the synthesis of N-graphenes, RSC Adv. 6 (2016) 15782–15787. doi:10.1039/C5RA24624E.

[8] A. Śliwak, B. Grzyb, N. Díez, G. Gryglewicz, Nitrogen-doped reduced graphene oxide as electrode material for high rate supercapacitors, Appl. Surf. Sci. 399 (2017) 265–271. doi:10.1016/j.apsusc.2016.12.060.

[9] C. Botas, P. ??Lvarez, P. Blanco, M. Granda, C. Blanco, R. Santamar??a, et al.,

Graphene materials with different structures prepared from the same graphite by the Hummers and Brodie methods, Carbon N. Y. 65 (2013) 156–164. doi:10.1016/j.carbon.2013.08.009.

[10] J. Chen, B. Yao, C. Li, G. Shi, An improved Hummers method for eco-friendly synthesis of graphene oxide, Carbon N. Y. 64 (2013) 225–229. doi:10.1016/j.carbon.2013.07.055.

[11] M. Fan, C. Zhu, J. Yang, D. Sun, Facile self-assembly N-doped graphene quantum dots/graphene for oxygen reduction reaction, Electrochim. Acta. 216 (2016) 102–109. doi:10.1016/j.electacta.2016.09.014.

[12] M. Barrejón, A. Primo, M.J. Gómez-Escalonilla, J.L.G. Fierro, H. García, F. Langa, Covalent functionalization of N-doped graphene by N-alkylation, Chem. Commun. 51 (2015) 16916–16919. doi:10.1039/C5CC06285C.

[13] A. Jorio, R. Saito, G. Dresselhaus, M.S. Dresselhaus, Raman Spectroscopy in Graphene Related Systems, 2011. doi:10.1002/9783527632695.

[14] L.M. Malard, M.A. Pimenta, G. Dresselhaus, M.S. Dresselhaus, Raman spectroscopy in graphene, Phys. Rep. 473 (2009) 51–87. doi:10.1016/j.physrep.2009.02.003.

[15] C.L. Lee, C.C. Yang, C.R. Liu, Z.T. Liu, J.S. Ye, Pt-coated Pd nanocubes as catalysts for alkaline oxygen reduction activity, J. Power Sources. 268 (2014) 712–717. doi:10.1016/j.jpowsour.2014.06.112.

VIII International Congress
the Mexican Hydrogen Society

Platinum sulfides: Synthesis, characterization and performance towards ORR

A. Sigüenza Orozco[1*], G. Alonso-Núñez[2], M. T. Oropeza-Guzmán, Y. Gochi-Ponce[3]

[1]Tecnológico Nacional de México. Instituto Tecnológico de Oaxaca, 68030, Oaxaca, Oax., México
[2]Centro de Nanociencias y Nanotecnología-UNAM, 22800, Ensenada, B.C., México
[3] Tecnológico Nacional de México. Instituto Tecnológico de Tijuana, 22000, Tijuana, B.C., México
* adriana.siguenza@gmail.com (+52) 951-119-1530

ABSTRACT

The cathodic electrocatalyst in proton exchange fuel cells (PEMFC) is a key component to these devices since the oxygen reduction reaction (ORR) rate is a limitative factor for the PEMFC performance. Platinum is the most used electrocatalyst for this aim, however due to its high cost it is desirable to decrease its content in catalytic materials by combining it with another element, for instance, platinum chalcogenides have been reported to be efficient catalysts towards ORR.
This work presents the synthesis of platinum sulfides supported on nitrogen doped carbon nanotubes (N-CNT) by three different methods: Solvothermal (PtS/N-CNT O), sulfuration (PtS/N-CNT U) and chemical reduction at two mole ratios (PtS1:1/N-CNT and PtS1:3/N-CNT).
The physical characterization was made by X-Ray diffraction (XRD), scanning electron microscopy (SEM) and transmission electron microscopy (TEM), the cooperite phase of platinum sulfur and crystalline platinum were identified. In addition, particle dispersion of catalyst synthesized by solvothermal method (PtS/N-CNT O) was optimal.
The electrochemical behavior of materials was analyzed in acidic media by cyclic voltammetry (CV) and linear sweep voltammetry (LSV). The analysis was carried out under inert atmosphere and oxygen saturated atmosphere, respectively. CV indicates that PtS/N-CNT O material is the best electrocatalyst for ORR. LSV analysis showed a lower response of PtS/N-CNT U when compared to other materials. It was also found that by varying the stoichiometric ratio of Pt and S in materials PtS1:1/N-CNT and PtS1:3/N-CNT the electrocatalytic behavior was affected. Finally, it was confirmed that PtS/N-CNT O showed the best electrocatalytical behavior towards ORR.

Keywords: Catalyst, ORR, PEMFC.

1. Introduction

Clean energy generation by means of chemical reaction can be performed by the use of Proton Exchange Fuel Cells (PEMFC) at a relatively low temperature. In these devices ORR takes place at the cathode of the cell and since this reaction is slow it acts as a limitative to the global reaction rate, hence the use of a catalyst is necessary [1, 2]. For decades platinum has been the best electrocatalyst used to this aim, however its high price, scarcity and degradation in fuel cell directs the investigation to the search of materials that allows to decrease Pt loading by combining it with

other elements and at the same time improves its performance and durability as cathode for ORR [3, 4].
Different types of combinations have been studied in order to decrease Pt content, for example transition metal chalcogenides. These materials can be synthesized at relatively low temperature by simple reaction mechanisms and have showed improved characteristics towards ORR [5], especially those of Pt, such as PtS or PtSe [6, 7]. However, it is widely known that the synthesis method of a material can affect its properties [8, 9, 10], in this context, nanometric size, high dispersion on carbon support, high electrocatalytic activity and thermal stability are desirable characteristics for a cathodic electrocatalyst.
In this work platinum sulfides were synthesized by 3 different methodologies: Solvothermal (PtS/N-CNT O), Sulfuration (PtS/N-CNT U) and Chemical Reduction at two mole ratios (PtS1:1/N-CNT and PtS1:3/N-CNT), and their physical and electrochemical properties were analyzed in order to evaluate their responses towards ORR. The results of this study reveal that the solvothermal method showed a prominent performance for this application.

2. Materials and Methods

2.1. Chemicals
Ammonium hexachloroplatinate (99.995%), ethylene glycol (99.8%), sodium borohydride (<99%), ethanol (99.8%) and nafion 117 (5%) were purchased from Sigma-Aldrich, sublimated sulfur U.S.P. (99%) were purchased from Fermont and sodium citrate (99%) was purchased from Faga-lab, whereas H_2S/H_2 gas (15% H_2), argon gas (99.9%) and oxygen gas (99%) were supplied by industrial gases Infra. All chemicals were used as received.
N-CNT were synthesized by modified spray pyrolysis [11, 12] and pre-treated with concentrated HNO_3 (70%, Sigma Aldrich) in a reflux system at 90 ºC during 6 h, after acid treatment N-CNT were washed and dried.

2.2. Preparation of PtS/N-CNT
Solvothermal reaction was made from a mixture of ammonium hexachloroplatinate ($(NH_4)_2PtCl_6$) and sodium citrate 1:2 mole ratio in 10 mL of ethylene glycol. The solution was stirred until the citrate was dissolved. Right after sulfur was added to the mixture in 10:1 mole ratio related to ammonium hexachloroplatinate, N-CNT's were added to the mixture (20% Pt metal loading). The solution was placed into a Teflon lined autoclave and heated to 195 ºC for 6 h. The material obtained was recovered by filtration, washed, dried overnight and sulfured in H_2S/H_2 atmosphere at 400 ºC for 2 h [6].
Sulfuration of PtS/N-CNT was carried out from a mixture of ammonium hexachloroplatinate and N-CNT, using as solvents water and isopropyl alcohol. The mixture was placed in an ultrasonic bath for 0.5 h, afterwards a solution of sodium borohydride 0.1 M was added to the mixture [8], the obtained material was filtered, washed, dried overnight and sulfured under H_2S/H_2 atmosphere at 400 ºC for 2 h.
The preparation process of chemical reduction of platinum sulfides supported on N-CNT's is described as follows: two mixtures were prepared, 1:1 and 1:3 mole ratio of ammonium hexachloroplatinate and sulfur respectively in water. Both mixtures were stirred for 72 h until sulfur was solubilized, afterwards N-CNT's were added to the mixture and placed in ultrasonic bath for

0.5 h. Finally, a solution 0.1 M of sodium borohydride was added to the mixture. The product was filtered, washed, dried overnight and thermally treated under inert atmosphere for 1 h [7, 8].

2.3. Materials characterization

The characterization of catalysts was made in a Phillips X´Pert MPD X-Ray diffractometer (XRD) using a Cu Kα (λ=0.154 nm) radiation source, in the region between 20º and 90º, meanwhile the SEM analysis was carried out in a JEOL JMS-5300, and TEM analysis was realized in a JEOL JEM-2100F.

2.4. Electrochemical measurements

The catalysts were evaluated by cyclic voltammery (CV) and Linear Sweep Voltammetry (LSV) using an Autolab PGSTAT302N potentiostat in a typical three electrode cell at room temperature, using 0.5 M H_2SO_4 as electrolyte under either argon or oxygen atmosphere. A glassy carbon rotating disk electrode (3 mm diameter) was used as a working electrode, at the same time saturated Ag/AgCl and a platinum coil were used as reference and counter electrodes respectively.

The inks were prepared as follows: 5 mg of the catalyst, 0.5 mL of ethanol and 30 μL of 1:3 Nafion-water solution were sonicated for 1 h, then 20 μL of ink was dropped on the glassy carbon electrode and dried at room temperature for 0.5 h.

3. Results and Discussion

3.1. Catalyst morphology

Figure 1 shows the powder XRD patterns of the catalysts, all them showed the characteristic reflections of the face centered cubic (fcc) crystalline Pt, the peaks at 39.7º, 46.2º, 67.4º, 81.2º and 85.7º were reflected from the (111), (200), (220), (311), (222) planes respectively. The characteristic reflections of the PtS (cooperite) were also seen, the peaks at 29.5º, 47.5º, and 61.5º were reflected from the (101), (112), (211) planes respectively while the peak located at 26.2º was due to the carbon support.

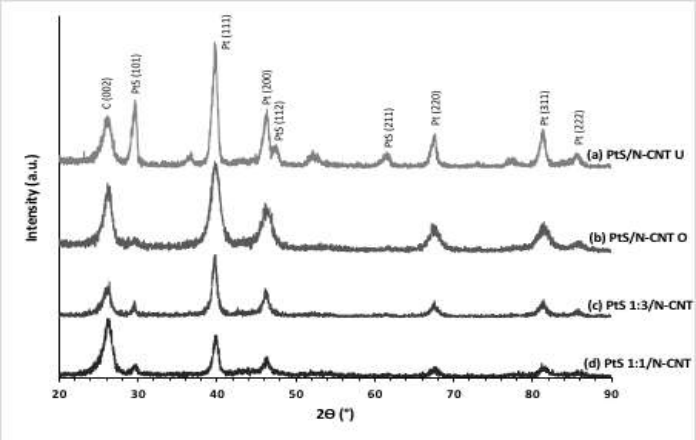

Figure 1. X-ray diffraction patterns of (a) PtS/N-CNT U, (b) PtS/N-CNT O, (c) PtS 1:3/N-CNT O and (d) PtS 1:1/N-CNT O

Figure 2a) shows the micrographs corresponding to the PtS/N-CNT U. Bright zones can be attributed to clusters formed by platinum nanoparticles on the surface of the carbon support. Although the particle sizes are in nanometric scale, they appear agglomerated on the carbon surface as it will be seen later. Figure 2b) shows the micrograph of the PtS/N-CNT O, N-CNT's are clearly visible with micrometrical length and the brightest areas on N-CNT's are attributed to groups of particles of the material on the N-CNT's surface, however these are minimal, which suggests a uniform distribution with particle sizes in the nanometric scale, as it is desirable. It is important to mention that according to Valenzuela's report, the thermal reduction of Pt results in smaller particle sizes [8]. When analyzing this material by means of EDS, the presence of sulfur was identified, which confirms that PtS was formed. Figure 2 c) and d) shows the micrographs corresponding to PtS 1:1/N-CNT and PtS 1:3/N-CNT respectively, it can be seen good dispersion of the material on the N-CNT's, however a few brighter areas of the micrographs show agglomerated particles in the micrometric scale despite this, PtS 1:3/N-CNT showed a greater agglomeration, which suggests that the change on the molar ratio affected the dispersion of the material on the support as well.

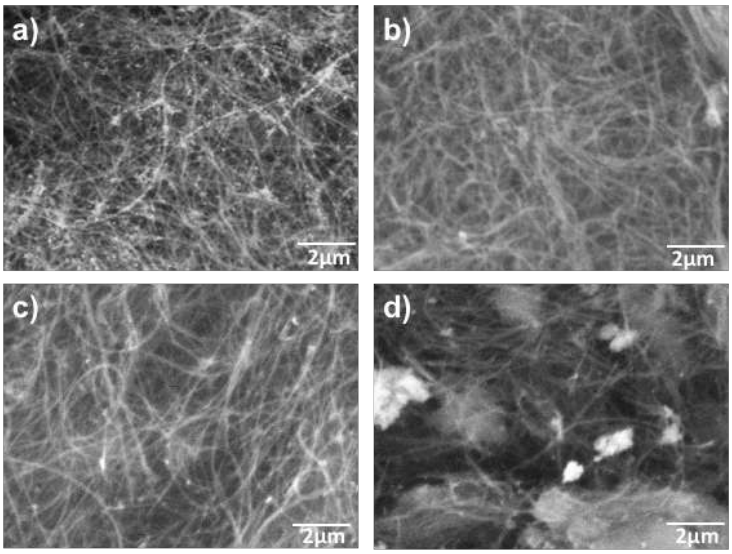

Figure 2. SEM images of a) PtS/N-CNT U, b) PtS/N-CNT O, c) PtS 1:1/N-CNT and d) PtS 1:3/N-CNT

Figure 3 a) and b) show the TEM micrographs of PtS/N-CNT O. Highly dispersed particles on a nanometric scale were observed over the entire surface of the nanotubes, as expected when thermal reduction synthesis is used [8]. These characteristics are desirable for the material since they increase the catalytic surface area causing a better performance unlike those materials with agglomeration of particles. Figure 3. C) and d) show TEM micrographs of chemically reduced material PtS1:1/N-CNT wich presented a higher agglomeration of the Pt particles. This results are consistent with that reported by Valenzuela [8] when comparing the synthesis methodologies by chemical and thermal reduction, although the material showed good dispersion, it did not exceed

PtS/N-CNT O. Agglomeration of particles is not a desirable feature for an electrocatalyst, which as will be seen decreases the electrocatalytic activity.

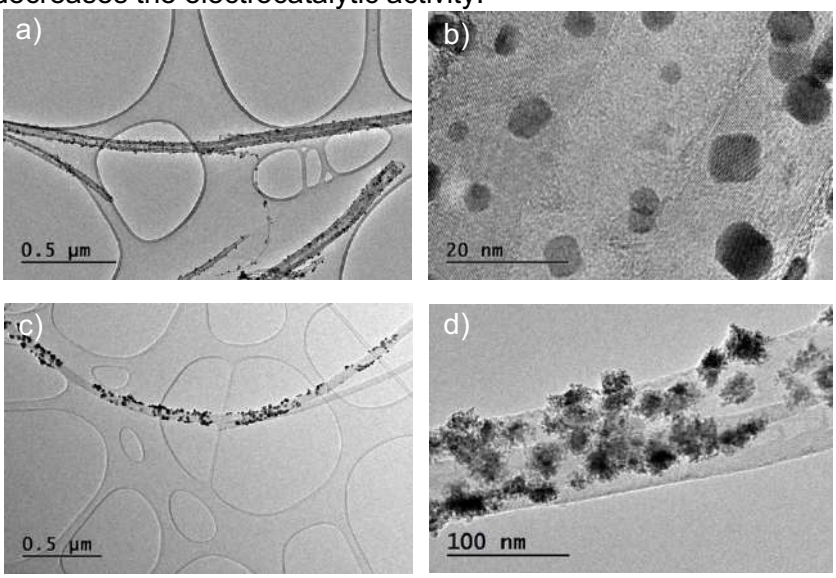

Figure 3. TEM images of a) PtS/N-CNT O and b) PtS1:1/N-CNT

3.2. Electrochemical measurements

Figure 4. shows the cyclic voltammograms of catalysts, PtS/N-CNT U presents a reduction peak potential in a range of 0.25 V-0.48 V; however, the current density response of this material is an order of magnitude smaller than the other catalysts, PtS1:1/N-CNT, PtS1:3/N-CNT and PtS/N-CNT O present reduction peaks in potential ranges of 0.2 V-0.6 V, 0.3 V-0.7 V and 0.2 V-0.7 V respectively. The current density response achieved in the reduction peak potential by PtS/N-CNT O is remarkable since it is higher than those observed in the other catalysts.

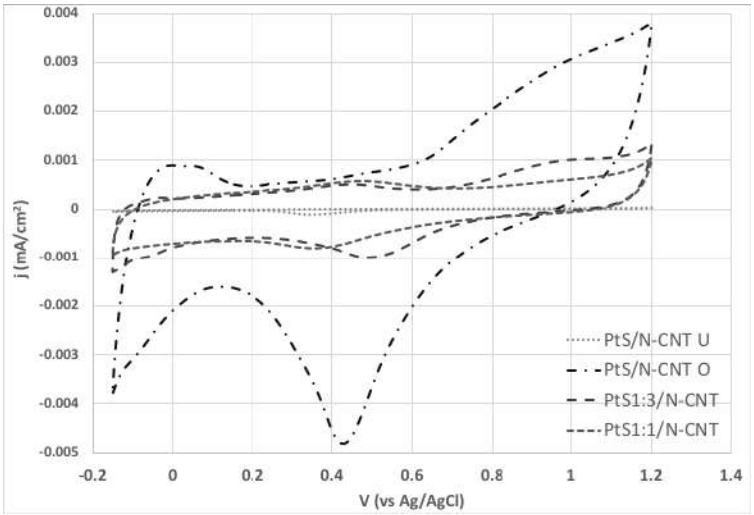

Figure 4. Cyclic voltammograms of catalysts in 0.5 M H_2SO_4 at a scan rate of 20mV/s

The electrocatalytic activity of the PtS catalysts was also examined by the LSV analysis. The rotation dependent polarization curves for ORR of all the materials as measured at 2500 RPM are shown in Figure 5a). The limiting current density analysis shows that material PtS/N-CNT O exhibited the highest ORR activity at 0.1 V compared with the other materials, as summarized in Table 1. The ORR onset potential for PtS/N-CNT O is 0.592 V vs Ag/AgCl, 0.134 V higher than PtS/N-CNT U. The difference between PtS1:1/N-CNT and PtS1:3/N-CNT onset potential is smaller, however the values of limit current of these two materials shows a significative difference as a function of the mole ratio used in the synthesis.

In order to further explore the ORR mechanism quantitatively, I-V curves were generated at different electrode rotation speeds. According to the theory of the rotating disk electrode (or the Koutecky-Levich theory) [13], the current density (i_d) at the disk electrode can be expressed as:

$$\frac{1}{i_d} = \frac{1}{i_k} + \frac{1}{i_{dl}} \qquad (1)$$

where i_k is the kinetic current density for the ORR and i_{dl} is the diffusion limiting current density. The diffusion limiting current density (i_{dl}) can be expressed as:

$$i_{dl} = 0.62nF C_{O_2} D_{O_2}^{2/3} \nu^{-1/6} \omega^{1/2} \qquad (2)$$

where n is the number of electrons transferred in the general reduction process, F is the Faraday constant, C_{O_2} is the concentration of oxygen, D_{O_2} is the diffusion coefficient of oxygen, ν is the kinematic viscosity of the electrolyte and ω is the rotation speed of the electrode.

Figure 5b) shows the slopes KL calculated for the electrocatalysts from the measurements with the rotating disc electrode at 0.15V. The analysis of the data showed that the materials PtS 1:1/N-CNT and PtS 1:3/N-CNT have a slope very close to that of the 2 electrons mechanism, obtaining a calculated value of 2.20 e^- and 2.59 e^- transferred respectively, whereas material PtS/N-CNT U presented a slope whose calculated value indicates an electron transfer of 2.99 e^- and material PtS/N-CNT O presents a slope closer to that of the 4 electrons mechanism. The value calculated for this material is 3.97e^-.

Figure 5c) shows the polarization curves at different rotation speeds of the PTS/N-CNT O in oxygen saturated 0.5M H_2SO_4. The magnitude of the current density increases steadily as a function of rotation speed between 400 and 2500 rpm, revealing the ORR. K-L plots generated for PtS/N-CNT O are shown in Figure 5d). Here all plots display a linear, parallel behavior in the mixed control polarization region indicating a first order ORR kinetics towards oxygen.

Table 1. Comparation of electrochemical properties of catalysts

Material	E_{onset} (V vs Ag/AgCl)	n @0.15 V K-L plot
PtS/N-CNT U	0.458	2.99
PtS/N-CNT O	0.592	3.97
PtS 1:3/N-CNT	0.555	2.59
PtS 1:1/N-CNT	0.511	2.20

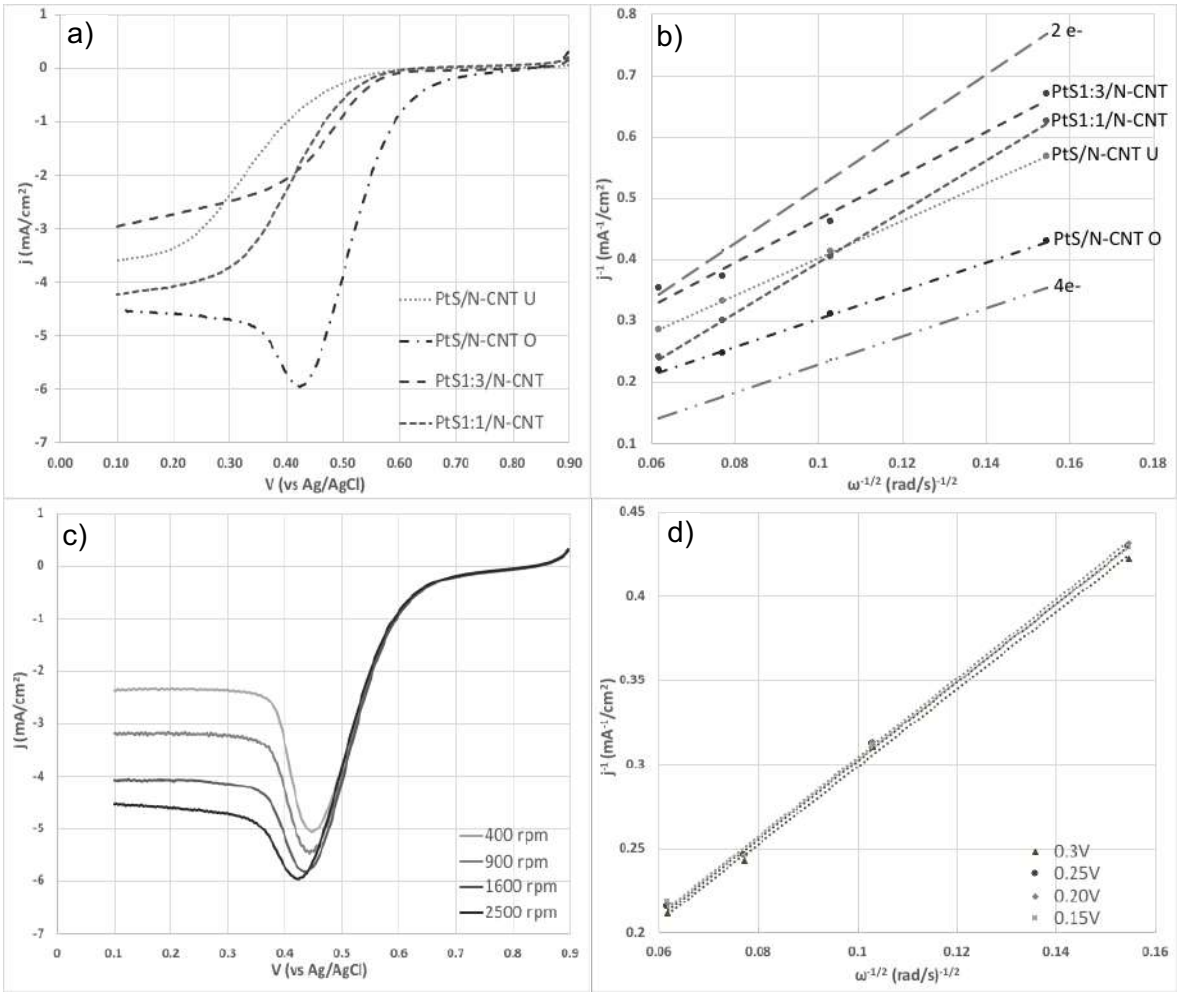

Figure 5. Linear sweep voltammograms at 5 mV/s for ORR in O2 saturated 0.5 M H2SO4 of a) PtS/N-CNT U, PtS/N-CNT O, PtS 1:3/N-CNT and PtS 1:1/N-CNT at 2500 RPM and d) PtS/N-CNT at 400-2500 RPM; K-L plots for PtS/N-CNT U, PtS/N-CNT O, PtS 1:3/N-CNT and PtS 1:1/N-CNT at 0.15 V vs Ag/AgCl and d) K-L plot for PtS/N-CNT O at different potentials.

4. Conclusion

Platinum Sulfides dispersed in N-CNT's were synthesized by three different methodologies. Solvothermal reaction followed by a thermal reduction showed the best results when analyzed by LSV to determine its performance towards ORR. Physical analysis of PtS/N-CNT O showed the formation of nanometric particles of PtS highly dispersed on the N-CNT support while electrochemical analysis indicates that this material presents 4 electron mechanism leading to the formation of H_2O in ORR which makes it a suitable alternative to its application as a cathodic electrocatalyst in PEMFC.

Acknowledgements

To CONACYT for the student grant 455275, to Eloisa Aparicio Ceja, Jaime Mendoza López, Israel Gradilla Martínez and Francisco Ruiz Medina for technical support.

References

[1] S. T. Revankard, P. Majundar, Fuel Cells: Principles, design and analysis, Boca Ratón: CRC Press, 2014.

[2] Srinivasan, Supramaniam, Fuel Cells: From fundamentals to applications, Springer, 2006, p. 691.

[3] A. Morozan, B. Jousselme, S. Palancin, "Low-Platinum and platinum-free cactalysts for the oxygen reduction reaction at fuel cell cathodes," *Energy & Enviromental Science,* vol. 4, pp. 1238-1254, 2011.

[4] A. Brouzgou, S.Q. Song, P. Tsiakaras; "Low and non-platinum electrocatalysts for PEMFCs: Current status, challenges and prospects," *Applied Catalysis B: Environmental,* vol. 127, pp. 371-388, 2012.

[5] D. Cao, A. Wieckowski, J. Inukai, N. Alonso-Vante, "Oxygen reduction reaction on rutenium and rodium nanoparticles modified with selenium and sulfur," *Journal of the electrochemical society,* vol. 153, pp. A869-A874, 2006

[6] Rong-Fang Wang, Shi-Jun Liao, Hai-Yang Liu, "Synthesis and characterization of Pt-Se/C electrocatalyst for oxygen reduction and its tolerance to metanol," *Journal of Power Sources ,* vol. 171, pp. 471-476, 2007.

[7] Y. Gochi-Ponce, G. Alonso-Nuñez, N. Alonso Vante, "Synthesis and electrochemical characterization of a novel platinum chalcogenide electrocatalyst with an enhenced tolerance to methanol in the oxygen reduction reaction," *Electrochemistry communications ,* vol. 8, no. 9, pp. 1405-1522, 2006.

[8] A. M. Valenzuela-Muñiz, G. Alonso-Nuñez, M. Miki-Yoshida, G. G. Botte, Y. Verde, "High electroactivity performance in Pt/MWCNT and PtNi/MWCNT electrocatalysts," *International Journal of Hydrogen Energy,* vol. 38, pp. 12640-12647, 2013.

[9] A. Esmaeilifar, S. Rowshanzamir, M. H. Eikani, E. Ghazanfari, "Synthesis methods of low-Pt-Loading electrocatalyst for proton exchange membrane fuel cell systems," *Energy,* vol. 35, pp. 3941-3957, 2010.

[10] M. Rajamathi, R. Seshadri, "Oxide and chalcogenide nanoparticles from hydrothermal/solvothermal reactions," *Current opinion in solid state & materials science,* vol. 6, pp. 337-345, 2002.

[11] I. Zeferino, A. M. Valenzuela-Muñiz, G. Alonso-Nuñez, "Influence of the synthesis parameters in carbon nanotubes doped with nitrogen for oxygen electroreduction," *Journal of Solid State Science and Technology,* vol. 6, pp. M3135-M3139, 2017.

[12] A. Aguilar, W. Antúnez, G. Alonso, F. Paraguay Delgado, F. Espinosa, M. Miki-Yoshida, "Study of carbon nanotubes synthesis by spray pyrolysis and model of growth," *Diamond and related materials,* vol. 15, no. 9, pp. 1329-1335, 2006.

[13] N. Job, M. Chatenet, F. Maillard, Basics of PEMFC Including the Use of Carbon-Supported Nanoparticles, Elsevier, 2013, pp. 401-423.

[14] H. Yang, J. Wu, "Platinum-based oxygen reduction electrocatalysts," *Accounts of chemical research,* vol. 46, no. 8, pp. 1848-1857, 2013.

XVIII International Congress
of the Mexican Hydrogen Society

Preparation of Pt and Pt-Ag nanostructured catalysts for alcohol oxidation reaction

Cano – Reséndiz O.[1*], Ruíz – Camacho B.[1], Fuentes – Ramírez R.[1], Galindo – Esquivel R. I.[1]

[1]Department of Chemical Engineering, Division of Natural and Exact Sciences, University of Guanajuato
Noria Alta S/N, Guanajuato, Guanajuato, CP 36000, México
* Phone: 4731443870, e – mail: o_cano_resendiz@hotmail.com

ABSTRACT

The search for new catalytic materials for direct alcohol fuel cells is the aim of this work. One of the main challenges presented by fuel cells is to have adequate catalytic material dispersed on a substrate to enhance its catalytic activity. We have synthesized by the ultrasound technique nanostructured electrocatalysts of Pt and Pt – Ag supported on Vulcan carbon (CV) and carbon nanotubes (NTC) with the goal of studying the effect of the properties of the substrate as electrical conductivity for the oxidation of methanol (MeOH). Particle size and metal dispersion were evaluated by transmission electron microscopy (TEM) and X-ray diffractometer (XRD) technique was used to determine the crystalline structure. Cyclic voltammetry (VC) and chronoamperometry (CA) were performed in acid medium. Preliminary results show the Pt and Pt – Ag nanoparticles were successfully synthesized by the ultrasound method. The method is simple, economical and easy to control, and the time spent is relatively little. Greater dispersion of the metallic phase was observed in monometallic catalysts compared with bimetallic catalysts due to the tendency of the Ag to agglomerate. The synthesized materials catalyze the oxidation reaction of methanol (MOR), however, the presence of Ag and the substrate used play a key role in the oxidation of methanol. When using Vulcan carbon as a substrate, the Pt-Ag / C shows the highest oxidation peak of methanol (5.1 mA cm^{-2}) with respect to Pt / C (4.4 mA cm^{-2}). When using NTC, it was observed that the bimetallic material Pt-Ag / NTC presents a lower intensity of the peaks of oxidation and electro-oxidation of methanol.

Keywords: Fuel cells, Catalysts, ultrasound

1. Introduction

Fuel cells are electrochemical devices that convert the chemical energy of reactions directly into electrical energy. A fuel cell consists basically of two electrodes, an anode and a cathode, separated by an electrolyte, in addition to a diffusion zone formed by a porous material that is generally carbon and that allows the passage of the substances that feed the cell (fuel and oxidant) helping to distribute them evenly. Figure 1 shows a general outline of a fuel cell.

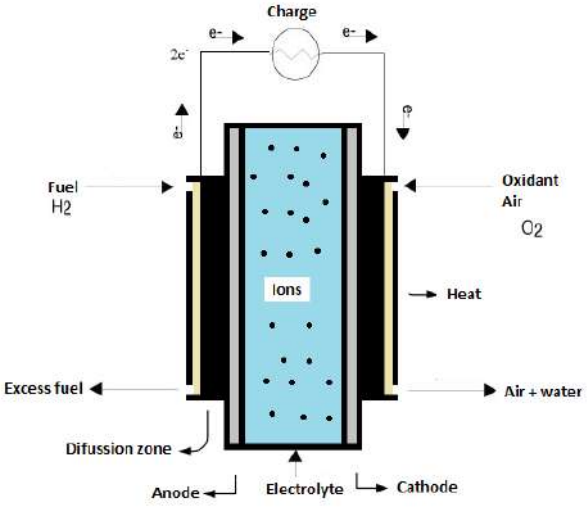

Figure 1. General outline of a fuel cell

Direct methanol fuel cells (DMFC's) are a relatively new technology and have a great potential in portable applications thanks to their operation at low temperatures, low emission of pollutants, high density of power and energy, as well as a compact design [1]. In low temperature fuel cells, it is necessary to use electrocatalysts, which are mainly based on high cost metals such as Pt, Pd, Au, among others. Currently, the main challenges presented by fuel cells are to have a suitable catalytic material and its distribution on a substrate that favors its function [2]. Although sometimes the catalytic material can be prepared to have a high surface area, sometimes it does not possess it, so it requires a support that contains high porosity and therefore a high surface area where it is dispersed [3]. Researchers have aimed to find new supports for the dispersion of the catalytic material with the aim of increasing the electrocatalytic activity of the cells. [4-6]. It is known that the electrocatalytic activity of Pt particles depends on factors such as the surface area, nature of the substrate and the catalyst preparation process [7]. In this work, the effect of the substrate was investigated using carbon Vulcan (CV) and carbon nanotubes CNTs in the catalytic activity of supported Pt and Pt-Ag.

2. Materials and Methods

2.1 Preparation of mono-metallic catalysts Pt / C, Pt / NTC and bimetallic Pt-Ag / C, Pt-Ag / NTC

The synthesis method used for the Pt / C and Pt / NTC catalysts was the previously reported ultrasound method [8]. 150 mL of precursor solution was used, to this solution the substrate was added and placed in ultrasound at room temperature for 4 h. Finally, the solvent was removed by evaporation at 100 °C for 12 h recovering the precipitate. For bimetallic catalysts Pt-Ag / C and Pt-Ag / NTC 150 mL of solution and $AgNO_3$ were used 1:1 by volume using the same methodology.

2.2 Physical characterization

The particle size and metal dispersion were evaluated by transmission electron microscopy (TEM) using a JEOL 1010 transmission electron microscope operated at 80 kV.

The crystalline phases presented on the supports and electrocatalysts were identified by XRD using a PANalytical Model Empyrean diffractometer.

2.3 Electrochemical characterization

Cyclic voltammetry (VC) and chronoamperometry (CA) were performed with a potentiostat / galvanostat Gamry Instruments (Warminster, PA, USA) 1000T and a RDE710 rotation speed controller. VC and CA were carried out in acid medium (0.5 M H_2SO_4) with a concentration of 0.5 M MeOH. The VC curves were measured with a scanning speed of 50 mV s^{-1} during 20 cycles. The chronoamperometry was carried out with a constant potential of 0.55 V and for 3600 s. The catalytic ink was prepared with 2 mg of catalyst, 50 µL of Nafion® and 250 µL of distilled water, sonicated for 1 h and finally 10 µL of the ink were deposited in the working electrode.

3. Results and Discussion

3.1 Results of physical characterization

Fig. 2 shows the morphology and dispersion of Pt and Pt-Ag nanoparticles on CV and NTC characterized by TEM. For Pt/C a good dispersion of the Pt particles can be observed. However, for the bimetallic catalyst Pt-Ag/C the particles present agglomeration. In the case of the mono and bimetallic materials supported in NTC, a similar behavior in the dispersion and size of the metallic particles is observed.

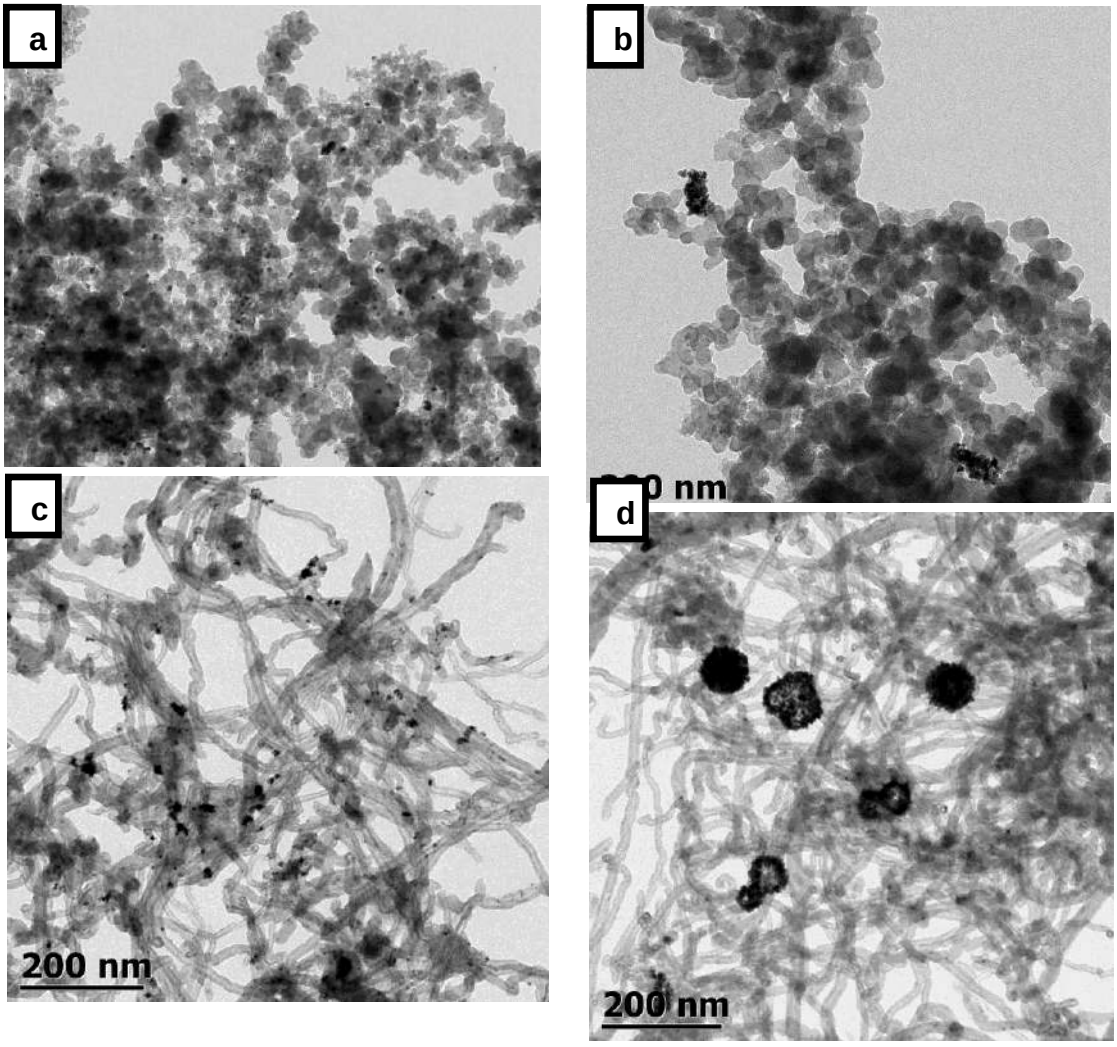

Fig. 2. TEM graphs for (a) Pt/C, (b) Pt-Ag/C, (c) Pt/NTC y (d) Pt-Ag/NTC electrocatalysts synthesized by sonication.

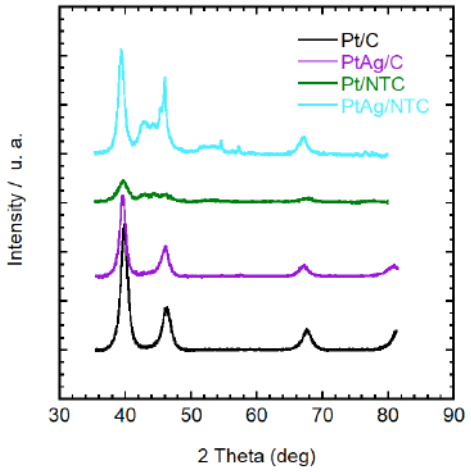

Fig. 3. XRD of Pt/C, Pt-Ag/C, Pt/NTC and Pt-Ag/NTC samples

The X-ray diffraction of Pt/C, Pt-Ag/C, Pt/NTC and Pt-Ag/NTC are shown in Fig. 3. The crystalline face-centered cubic structure (fcc) of platinum at 2θ values of 39.75°, 46.27° and 67.46° corresponds to the (200), (220) and (311) planes, and these were identified in all samples. However, the diffraction peaks of silver in the Pt-Ag/C and Pt-Ag/NTC catalysts were not detected, which can be due to the low percentage of Ag in the sample.

3.2 Results of methanol oxidation

Fig. 4 shows the voltammograms of the synthesized materials Pt and Pt-Ag supported in a) NTC and b) Carbon Vulcan in acidic medium, H_2SO_4 0.5 M. 20 cycles of CV were carried out to stabilize the surface of the electrode, after the cycle number 20 there were no visible changes in the CV profile of the catalysts, figures 4a and 4b, the curves show the typical characteristic of the platinum nanoparticles in the four study samples, however no information of the silver indicating an apparent dissolution of this in acid medium. A region of 0.05 to 0.3 V proton adsorption-desorption (NHE). It is evident that the mono metallic commercial sample presents higher current density in the entire range of study potential with respect to the samples containing silver.

Figure 5 illustrates the voltammograms of the synthesized materials Pt and Pt-Ag supported in a) NTC and b) carbon Vulcan in acid medium with methanol, 0.5 M H_2SO_4 and 0.5 M CH_3OH. In acid medium, two typical oxidation peaks appeared in the curves of CV, figures 5a and 5b. The peak of methanol oxidation is located between 0.84 and 0.87 V, however, it is important to note that for the Pt-Ag / NTC sample these peaks are very weak (figure 5a) compared with the other samples. The peak located around 0.7 V corresponds to the electro-oxidation of the adsorbed species when the oxidation of methanol takes place.

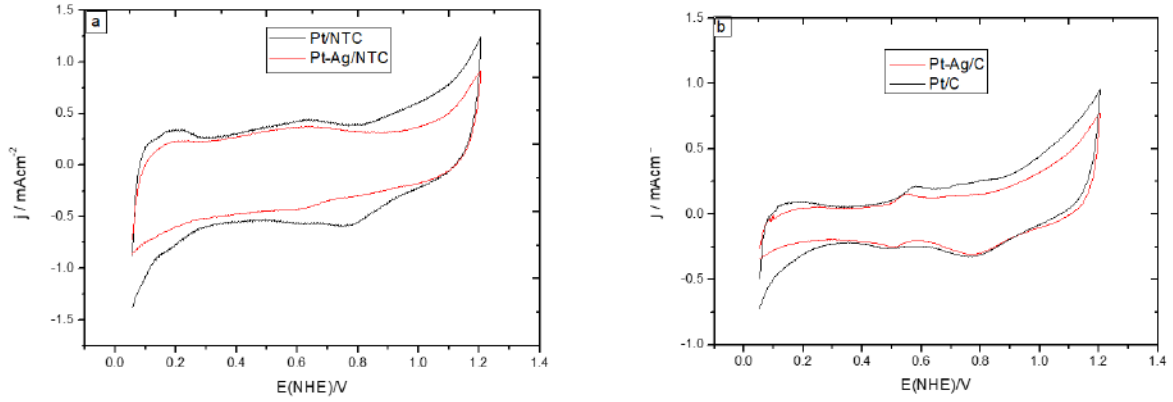

Fig. 4. Cyclic voltammetry of the synthesized materials Pt and Pt-Ag supported in a) NTC and b) carbon Vulcan in acid medium (0.5 M H_2SO_4), a 50 mV s^{-1}, nitrogen atmosphere at room temperature (RT).

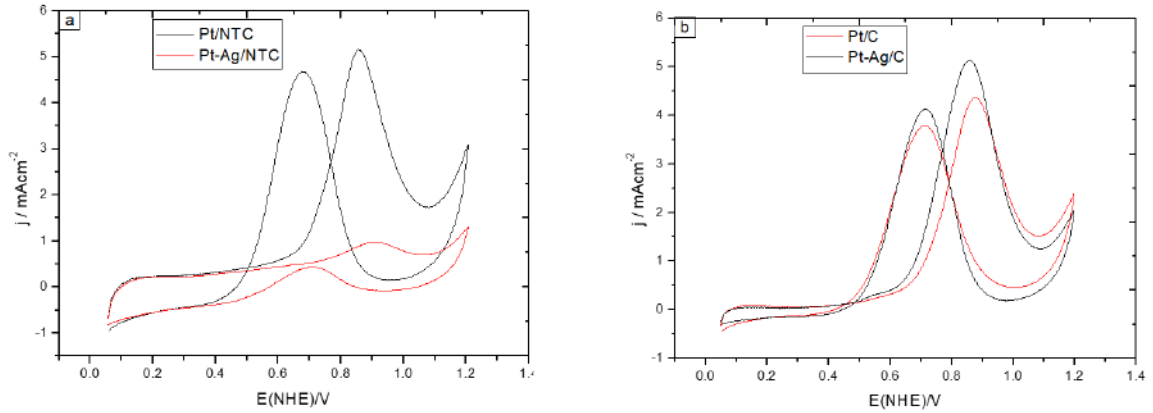

Fig. 5. Cyclic voltammetry of the Pt and Pt-Ag synthesized materials supported in a) NTC and b) Vulcan carbon in acid medium + methanol (0.5 M H_2SO_4 + 0.5 M CH_3OH) at 50 mV s^{-1}. N_2 atmosphere at RT.

Table 1 shows the relationship between the current density of the oxidation peak (j_f / mA cm^{-2}) and the electro-oxidation current density peak (j_b / mA cm^{-2}), which according to the literature reflects the ability of a catalyst material to remove CO after dehydrogenation of methanol, that is, high values of j_f / j_b indicate high efficiency of methanol oxidation [9]. The highest j_f / j_b ratio obtained in acid medium was for Pt-Ag / NTC (2.28), indicating that said material is more efficient for the oxidation of methanol.

Table 1. Electrochemical parameters of Pt and Pt-Ag catalysts supported on different carbon substrates for the methanol oxidation reaction.

Sample	Oxidation current density (j_f)	Electro-oxidation current density (j_b)	j_f/j_b
Pt/NTC	5.05	4.67	1.08
Pt-Ag/NTC	0.98	0.43	2.28
Pt/C	4.40	3.80	1.16
Pt-Ag/C	5.10	4.10	1.24

4. Conclusion

According to the results obtained, we can conclude that the Pt and Pt-Ag nanoparticles were successfully synthesized by the ultrasound method. The method is simple, economical and easy to control, and the time spent is relatively little. By means of TEM, a greater dispersion of the metallic phase was observed in the mono metal catalysts compared with the bimetallic catalysts due to the tendency of the Ag to agglomerate. The synthesized materials catalyze the oxidation reaction of methanol; however, the presence of Ag and the substrate used play an important role in the oxidation of methanol. When using Vulcan carbon as a substrate, the Pt-Ag / C shows the highest oxidation peak of methanol (5.1 mA cm^{-2}) with respect to Pt / C (4.4 mA cm^{-2}). When using NTC, it was observed that the bimetallic material Pt-Ag / NTC presents a lower intensity of the peaks of oxidation and electro-oxidation of methanol.

Acknowledgements

The authors thank the University of Guanajuato for the financial support of the present research. Omar Cano Reséndiz thanks to CONACyT for the scholarship (228383/208900).

References

[1] Zhang Y, Li F, Liu X, Lu J, Zhang G. Promoting Influence of Activated Carbon used in Carbon Paste Electrode on Platinum Nanoparticles Efficiency in Methanol Electrooxidation. Electrochim Acta 2017; 242:165–172.
[2] Sistiaga M., Pierna A.R. Application of amorphous materials for fuel cells. Journal of Non-Crystalline Solids 2003; 329:184–187.
[3] Smith J.M. Chemical Engineering Kinetics. 6th ed. McGraw Hill Book Company. 1991.

[4] Salgado J.R.C, Duarte R.G, Ilharco L.M, Botelho do Rego A.M, Ferraria A.M, Ferreira M.G.S. Effect of functionalized carbon as Pt electrocatalyst support on the methanol oxidation reaction. Applied Catalysis B: Environmental 2011; 102:496–504.
[5] Rajesha B, Ravindranathan Thampi K, Bonard J.-M., Mathieu H.J, Xanthopoulos N,Viswanathan B. Electronically conducting hybrid material as high-performance catalyst support for electrocatalytic application. Journal of Power Sources 2005; 141:35–38.
[6] Zhou L, Wang Y, Tang J, Li J, Wang S, Wang Y. Facile synthesis of holey graphene-supported Pt catalysts for direct methanol electro-oxidation. Microporous and Mesoporous Materials, 2017; 247:116-123.
[7] Gloaguen F, Lea Ger J.-M, Lamyc. Electrocatalytic oxidation of methanol on platinum nanoparticles electrodeposited onto porous carbon substrates. Journal of Applied Electrochemistry 1997; 27:1052-1060.
[8] B. Ruiz-Camacho, A. Medina-Ramírez, R. Fuentes-Ramírez, Claudia M. Gómez. Simple synthesis of Pt-Ag/SnO2-C for use as a catalyst of methanol oxidation in alkaline media, Journal of Solid State Electrochemistry 2017; 21: 2449-2456.
[9] Ruiz Camacho B, Rodríguez Santoyo HH, Medina Flores JM, Alvarez Martinez O. Platinum deposited on TiO2-C and SnO2-C composites for methanol oxidation and oxygen reduction. Electrochim Acta 2014; 120:344-9.

Fuel Cells components and stacks

September 18 to 21, 2018 in Mexico City, Mexico

XVIII International Congress
of the Mexican Hydrogen Society

Design of polymer nanocomposites based on polypropylene, carbon nanotubes and carbon nanofibers for application in bipolar plates

C. A. Ramírez-Herrera[a,*]; J. Pérez-González[b]; O. Solorza-Feria[c]; H. Martínez-Gutiérrez[d]; A. Flores-Vela[e]; J. G. Cabañas-Moreno[a]

[a]Programa de Doctorado en Nanociencias y Nanotecnología, CINVESTAV, Av. Instituto Politécnico Nacional 2508, Cd. de México, C.P. 07360, Mexico.
[b]Departamento de Física, Escuela Superior de Física y Matemáticas, Instituto Politécnico Nacional, Av. Instituto Politécnico Nacional s/n, Cd. de México, C.P. 07738, Mexico.
[c]Departamento de Química, CINVESTAV, Av. Instituto Politécnico Nacional 2508, Cd. de México, C.P. 07360, Mexico.
[d]Centro de Nanociencias y Micro y Nanotecnologías, Instituto Politécnico Nacional, Av. Luis Enrique Erro s/n, Ciudad de México, C.P. 07738, Mexico.
[e]Centro Mexicano para la Producción más Limpia, Instituto Politécnico Nacional, Av. Acueducto s/n, Cd. de México, C.P. 07340, Mexico.

* Corresponding author: Tel. +528331289066. E-mail: caramirezh@cinvestav.mx

---

ABSTRACT

Proton exchange membrane fuel cells (PEMFCs) have attracted particular attention as alternative power devices in transportation applications due to their high efficiency, low operating temperature, and zero emissions; however, the manufacturing costs of fuel cell stacks are relatively high and limit their current commercial viability. Bipolar plates constitute a key component of PEMFCs concerning their cost and weight; therefore, one of the major challenges in the production of economical PEMFCs is the development of materials for bipolar plates which can be readily manufactured and have high electrical conductivity and adequate mechanical strength. In this sense, polymer nanocomposites with carbon-based nanofillers have shown several advantages as suitable materials for bipolar plates. In this work, polypropylene (PP) nanocomposites using multi-wall carbon nanotubes (MWCNT) alone or in combination with carbon nanofibers (CNF) have been prepared by melt mixing using different loadings of MWCNT and CNF. The nanocomposites obtained were molded by compression for subsequent characterization. The maximum in-plane electrical conductivity for nanocomposites with a MWCNT content of 20 wt.% was close to 3 $S \cdot cm^{-1}$, whereas for nanocomposites combining 15 wt.% MWCNT and 15 wt.% CNF was about 8 $S \cdot cm^{-1}$. The addition of CNF to form hybrid PP/MWCNT/CNF nanocomposites allowed to increase to 30 wt.% the total content of nanofiller incorporated in the PP matrix and higher conductivities could be thus obtained. Moreover, the incorporation of 20 wt.% MWCNT in the PP matrix enhanced the tensile strength of the nanocomposites by 56% compared to the unfilled polymer, while the combined additions of 15

wt.% MWCNT and 15 wt.% CNF yielded an improvement of 63%. Similarly, the microhardness and elastic modulus of the nanocomposite with 20 wt.% MWCNT increased by about 71% and 44%, respectively, whereas in the hybrid nanocomposite the increases were around 83 and 67%, respectively, compared to the PP matrix. In general, the results show a positive effect of the combination of both nanofillers on the electrical conductivity, strength, and stiffness of the nanocomposites.

Keywords: bipolar plates; polymer nanocomposites; multi-wall carbon nanotubes; carbon nanofibers

---

1. Introduction

In the last decades, the high costs and harmful effects on the environment caused by the excessive consumption of fossil fuels have prompted research for new energy conversion and storage systems. Proton exchange membrane fuel cells (PEMFCs) have attracted particular attention as alternative power devices, in transportation applications due to their high efficiency, low operating temperature (<100°C), and zero emissions [1-4]. However, the manufacturing costs of fuel cell stacks are relatively high and limit their current commercial viability. In this context, bipolar plates are strongly related to these issues because they constitute a key component of PEMFCs, accounting for 30 to 45% of the stack costs and, in terms of weight and volume, they represent about 80% of the stack [3-6]. Therefore, one of the major challenges in the production of economical PEMFCs is the development of materials for bipolar plates which can be readily and economically manufactured and are able to comply with technical requirements related to their mechanical, electrical, thermal and chemical properties. Some of the technical requirements on which the development of bipolar plates is based are issued by the US Department of Energy (DOE) [7] and several companies [8], as shown in Table 1.

Traditionally, graphite has been used in the manufacturing of bipolar plates because this material possesses high electrical conductivity, good corrosion resistance, and a low density. However, graphite plates have a relatively high cost associated with the required machining operations as well as a low mechanical strength [9,10]. Bipolar plates made from metals such as aluminum [11], stainless steel [12], titanium and nickel [13] have good electrical conductivity, excellent mechanical properties, low cost and negligible gas permeability, and they can be stamped to form the flow channels required on the inner surfaces of bipolar plates. Nevertheless, compared to graphite, metals possess a higher susceptibility to corrosion and dissolution in the fuel cell operating environment of 80°C and a pH of 2-3 [14]. Alternatively, carbon-polymer composites have been investigated as materials to fabricate bipolar plates. Thermoplastic matrices and thermosetting resins in combination with carbon fillers like graphite, carbon black (CB), carbon fibers (CF) and, more recently, carbon nanomaterials, such as multi-walled (MWCNT) and single-walled carbon nanotubes, carbon nanofibers (CNF), graphene and graphite nanoplatelets (GNP), have been used for this purpose [15-17]. Carbon-polymer

composites offer the advantages of a lower cost, relatively high mechanical strength, good corrosion resistance and lighter weight. Bipolar plates are also easier to fabricate with these materials because the gas flow channels can be molded directly into the plate, eliminating expensive machining procedures [18]. However, carbon-polymer composites still exhibit problems related to their low electrical conductivity; thus, to satisfy the requirements of electrical conductivity, an excessive amount of conducting filler (ca. 70 wt.% CB) has to be added to the composite, promoting brittleness, poor processability, high porosity and gas permeability [19,20].

Table 1. US Department of Energy targets for bipolar plates [7,8].

Property	Unit	Target 2020
Cost[a]	$\$\cdot kW^{-1}$	3
H_2 permeability coefficient	$cm^3(scm^2Pa)^{-1}$	$<1.3\times10^{-14}$
Corrosion resistance at anode/cathode	$\mu A\cdot cm^{-2}$	<1
Bulk (in-plane) electrical conductivity	$S\cdot cm^{-1}$	>100
Area specific resistance	$\Omega\cdot cm^2$	0.01
Flexural strength	MPa	>25
Tensile strength[b]	MPa	>41
Thermal conductivity[b]	$W(mK)^{-1}$	>10
Thermal stability	°C	−40 to 120

[a]Cost projected to high volume production (500.000 stacks per year), assuming MEA meets performance target of 1000 $mW\cdot cm^{-2}$.
[b]Targets of Plug Power Co. for bipolar plates [9]

Many studies have focused on the incorporation of carbon nanomaterials into polymer matrices [e.g., 17,21,22]. These additions usually lead to significant improvements in the mechanical and electrical properties of the polymer nanocomposites [e.g., 21,23]. Such improvements often require relatively low filler loadings (< 5 wt.%) which facilitate the processing and molding of the composite. There are also some studies focused on the preparation of hybrid polymeric nanocomposites based on MWCNT and CNF, most of which dealing with applications in electrostatic discharge protection and electromagnetic interference shielding, for which electrical conductivities between 10^{-6} - 10^{2} $S\cdot cm^{-1}$ are required [24,25]. Both MWCNT and CNF are ideal filler candidates for polymer nanocomposites due to their extremely high stiffness, high electrical and thermal conductivities, and the capability to form conductive networks [26,27]. Therefore, the incorporation of MWCNT and CNF as nanofillers into a polymer matrix is a promising approach to design nanocomposites with improved electrical and mechanical properties suitable for use as bipolar plates. Nevertheless, to produce a high-performance multifunctional hybrid composite, a preferential distribution of well-dispersed nanofillers which form conductive 3D networks is required.

In this work, polypropylene (PP) based nanocomposites, using MWCNT alone or in combination with CNF, have been prepared by melt mixing using different loadings of MWCNT and CNF. The nanocomposites obtained were molded by compression for subsequent

characterization. The main emphasis is on the resulting electrical and mechanical properties of the nanocomposites to evaluate their performance as suitable materials for bipolar plates.

2. Materials and Methods

2.1 Materials

Commercial grade polypropylene, PP 4280W Impact copolymer (supplied by Total Petrochemicals) was used as the polymer matrix. As electrically conductive fillers, the materials used were (i) MWCNT (cat. number 773840 from Sigma-Aldrich) purity ≥ 98%, average outside diameter of 10 nm, length of 3-6 μm, and (ii) Pyrograf®-III CNF (cat. number 719781 from Sigma-Aldrich) with outside diameters and lengths ranging from 125 to 150 nm and 20 to 200 μm, respectively.

2.2 Preparation of PP nanocomposites

PP nanocomposites were prepared by melt mixing using up to 21.5 wt.% MWCNT alone and up to 20 wt.% CNF. The resulting composites were molded by compression at 200 °C into plates of thicknesses between 0.1 to 0.2 mm for further characterization. The procedure details were previously described elsewhere [28].

2.3 Characterization

The in-plane electrical conductivity of the nanocomposites was measured by the four-point probe (FPP) method at room temperature on specimens having dimensions of 10 x 10 x 0.15 mm and using a Four Probe Set-up DFP-02 (SES Instruments Pvt. Ltd., India). The average value of five readings at different locations for each sample was taken as the resistance (R, in Ω) of the nanocomposite. The resistivity (ρ, in Ω·cm) was calculated according to the FPP method [29], and the electrical conductivity (σ, in $S \cdot cm^{-1}$) was obtained by inverting the corresponding values of the resistivity. The tensile properties of the nanocomposites were measured in a tensile tester (Com-Ten Industries, USA) using extruded filaments with a length of 400 mm and a diameter of about 0.85 mm. The gauge length of the specimens was set at 88.5 mm, and a constant crosshead speed of 5 mm/min was maintained during the test. All tests were conducted at room temperature. The reported values were averages of eight to ten tests for each composite composition. Measurements of microhardness and elastic modulus were performed by indentation tests in a nanoindentation tester (TTX-NHT, CSM Instruments, USA) using a Berkovich diamond indenter. A loading rate of 10 mN/min was maintained until the indenter reached a maximum load of 5 mN which was held constant for 10 s before the indenter was unloaded. At least 25 indentations were made for each sample on randomly selected locations to obtain average values of indentation microhardness, H_{IT}, and elastic modulus, E_{IT}.

3. Results and Discussion

3.1 Electrical properties

The in-plane electrical conductivity of the PP/MWCNT and PP/MWCN/CNF nanocomposites as a function of nanofiller content is presented in Fig. 1. According to the supplier, the electrical conductivity of the PP matrix used in this study is about 1 x 10^{-16} S·cm^{-1}. For nanocomposites containing MWCNT alone, the conductivity is raised more than 15 orders of magnitude, to 9 x 10^{-1} S cm^{-1}, for the PP/10MWCNT nanocomposite, and 2.8 x 10^{0} S·cm^{-1}, for the PP/20MWCNT nanocomposite (Fig. 1a). On the other hand, the nanocomposite filled with 20 wt.% of CNF showed an electrical conductivity about one order of magnitude below than the PP/20MWCNT nanocomposite, which demonstrates that CNF by themselves exhibit lower ability to form conductive networks than MWCNT. The combination of MWCNT and CNF in the PP/10MWCNT/10CNF nanocomposite reached almost the same in-plane electrical conductivity than the PP/20MWCNT nanocomposite. In turn, the PP/15MWCNT/15CNF nanocomposite displayed the highest in-plane electrical conductivity of all specimens produced in the present work: 8.2 S·cm^{-1}, as shown in the zooming view on a linear scale in Fig. 1b. From these results, the addition of CNF in combination with MWCNT allowed the use of a larger content of total nanofiller content (and thus, a higher electrical conductivity) than the use of MWCNT alone, as previously reported elsewhere [28]. However, the highest value of in-plane electrical conductivity obtained in this work is still below the DOE target of 100 S·cm^{-1}.

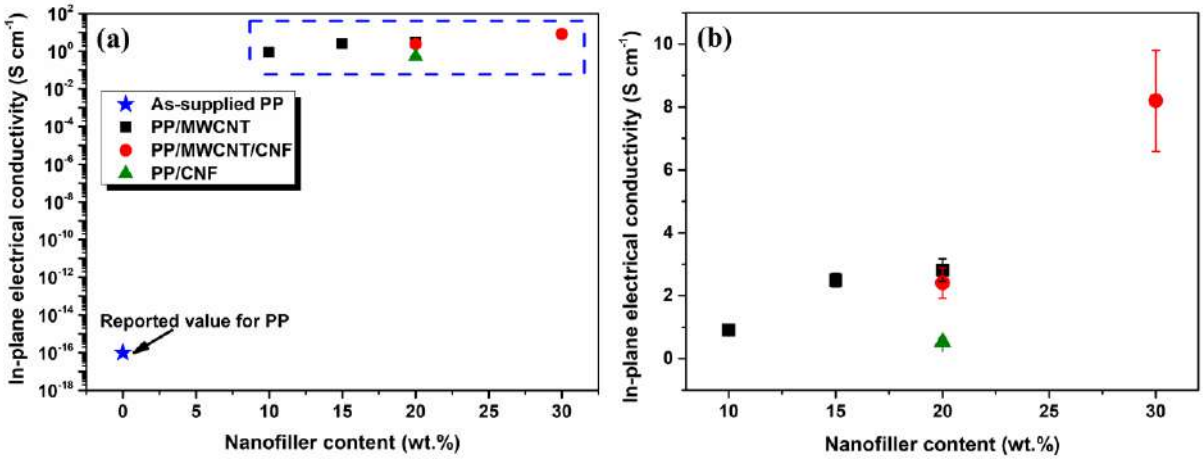

Fig. 1. (a) In-plane electrical conductivity of PP/MWCNT and PP/MWCNT/CNF nanocomposites. (b) Zooming view on a linear scale of the box area of (a).

3.2 Mechanical properties

3.2.1 Tensile properties

Fig. 2 shows representative tensile stress-deformation curves obtained from as-supplied PP, and PP/MWCNT and PP/MWCNT/CNF nanocomposites. It is evident that the incorporation of MWCNT in the PP matrix has significantly enhanced the tensile strength of the nanocomposites; compared to the unfilled polymer, it shows an increase of up to 56% with the addition of 20 wt.% of MWCNT. In contrast, most of the published reports indicate that high MWCNT contents produce a detriment of the tensile strength in PP/MWCNT nanocomposites [30-32].

Nevertheless, continuous increments of the tensile strength with MWCNT content have also been reported by Al-Saleh [33] in PP/MWCNT nanocomposites. Contrary to the observed effect of MWCNT, the PP/20CNF material showed a decreased mechanical strength, which is probably due to the poor interfacial adhesion between the CNF and the PP matrix, as previously reported [28]. In the case of the hybrid nanocomposites, the combined additions of 15 wt.% MWCNT and 15 wt.% CNF yielded the highest value of tensile strength (29.5 MPa) among all our samples, which represents an improvement of 63% compared to the unfilled PP; whereas the PP/10MWCNT/10CNF nanocomposite showed a slightly lower strength level, but comparable to the effect found for the PP/20MWCNT samples. This confirms the efficient effect of reinforcement of the MWCNT and CNF in the hybrid materials, even using higher contents than most of the previous studies, without degrading the tensile strength.

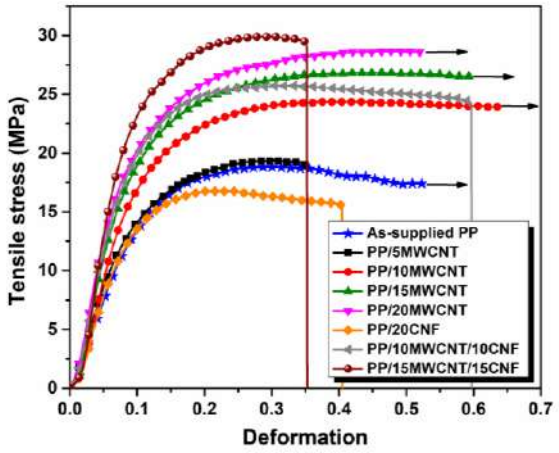

Fig. 2. Representative tensile stress-deformation curves of as-supplied PP, PP/MWCNT, and PP/MWCNT/CNF nanocomposites.

3.2.2 Microhardness, H_{IT}, and elastic modulus, E_{IT}.

Fig. 3 displays the values of microhardness and elastic modulus obtained for the as-supplied PP and the PP/MWCNT and PP/MWCNT/CNF nanocomposites. As can be observed in Fig. 3a, with the addition of MWCNT, the microhardness monotonically augmented over the value of the PP matrix (66.7 MPa) to reach 114 MPa for the PP/20MWCNT nanocomposite. On the other hand, the addition of CNF at the same nanofiller content (20 wt.%) produced a much lower increase of only about 10% with respect to unfilled PP. In the nanocomposites loaded with both MWCNT and CNF, an increase to 122 MPa was recorded for the PP/15MWCNT/15CNF nanocomposite. These results show a positive effect of the combination of both nanofillers to increase the strength of the materials, which may be related to the formation of an optimized microstructure, as previously reported [28].

Fig. 3b shows the values of elastic modulus obtained for the PP nanocomposites. For the PP/MWCNT nanocomposites, the additions of 15 and 20 wt.% led to significant increases of about 46% in the elastic modulus as compared to the as-supplied PP. Similarly, in the hybrid

nanocomposites, continuous increments in the elastic modulus were obtained with nanofiller additions, reaching an enhancement of 67% for the PP/15MWCNT/15CNF. In general, these results confirm the higher stiffness of the nanocomposites, which is required for its application as materials for bipolar plates.

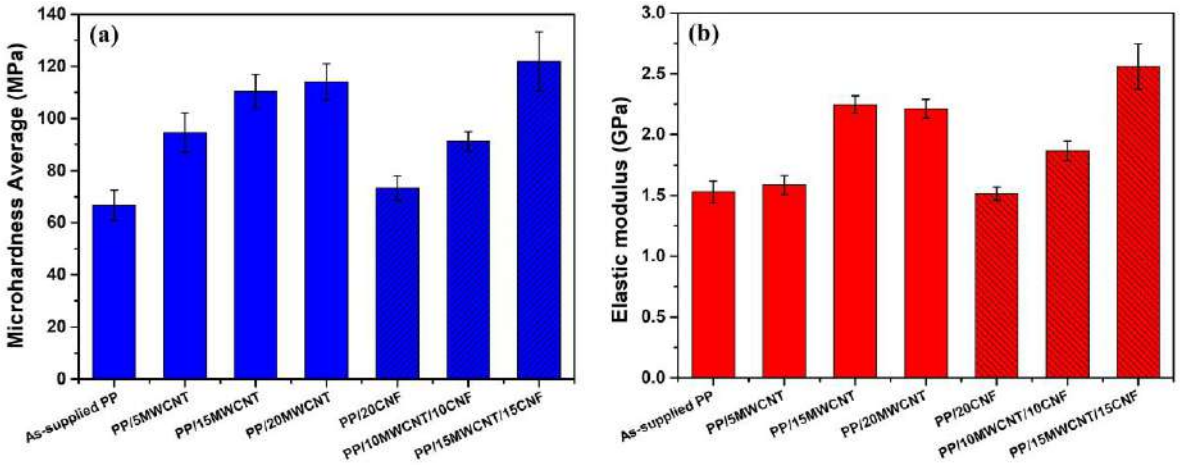

Fig. 3. Values of microhardness, H_{IT} and elastic modulus, E_{IT}, of as-supplied PP and PP/MWCNT and PP/MWCNT/CNF nanocomposites.

4. Conclusion

PP nanocomposites containing MWCNT alone or in combination with CNF have been prepared by melt mixing using different nanofiller loadings. The combination of MWCNT and CNF to form hybrid PP/MWCNT/CNF nanocomposites allowed to increase to 30 wt.% the total amount of nanofiller incorporated in the PP matrix, which led to the highest recorded values of electrical conductivity for PP/MWCNT/CNF composites. Further, it was found that the produced nanocomposites display an improvement in its mechanical performance (tensile strength, hardness, and elastic modulus), which reflects good perspectives for its application as materials for bipolar plates of PEM fuel cells.

Acknowledgements
C. A. Ramírez-Herrera is grateful to CONACYT for a graduate fellowship (registration number 258940). The authors acknowledge the financial support provided by grant 221795 SEP-CONACYT and CINVESTAV-IPN. CNMN-IPN, LANE-CINVESTAV, ESIQIE-IPN, and ESFM-IPN are recognized for technical and experimental support.

References

[1] Couture G, Alaaeddine A, Boschet F, Ameduri B. Polymeric materials as anion-exchange membranes for alkaline fuel cells. Prog Polym Sci 2011;36:1521-57.

[2] Thiam HS, Daud WRW, Kamarudin SK, Mohammad AB, Kadhum AAH, Loh KS, et al. Overview on nanostructured membrane in fuel cell applications. Int J Hydrogen Energy 2011;36:3187-205.
[3] Kim DJ, Jo MJ, Nam SY. A review of polymer–nanocomposite electrolyte membranes for fuel cell application. J Ind Eng Chem Res 2015;21:36-52.
[4] Hermann A, Chaudhuri T, Spagnol P. Bipolar plates for PEM fuel cells: A review. Int J Hydrogen Energy 2005;30:1297-302.
[5] de Oliveira MCL, Ett G, Antunes RA. Materials selection for bipolar plates for polymer electrolyte membrane fuel cells using the Ashby approach. J Power Sources 2012;206:3-13.
[6] Boyaci San FG, Tekin G. A review of thermoplastic composites for bipolar plate applications. Int J Energy Res 2013;37:283-309.
[7] U. S. D. o. Energy, Hydrogen, Fuel Cells & Technologies Program. In: Multi-year research, development and demonstration Plan. D.O. Energy, http://www1.eere.energy.gov/hydrogenandfuelcells/mypp/; 2012, p. 29.
[8] Kuo JK, Chen CK. A novel Nylon-6-S316L fiber compound material for injection molded PEM fuel cell bipolar plates. J Power Sources 2006;162:207-14.
[9] Mehta V, Cooper JS. Review and analysis of PEM fuel cell design and manufacturing. J Power Sources 2003;114:32-53.
[10] Cunningham BD, Huang J, Baird DG. Development of bipolar plates for fuel cells from graphite filled wet-lay material and a thermoplastic laminate skin layer. J Power Sources 2007;165:764-73.
[11] Mawdsley JR, Carter JD, Wang X, Niyogi S, Fan CQ, Koc R, et al. Composite-coated aluminum bipolar plates for PEM fuel cells. J Power Sources 2013;231:106-12.
[12] Wang H, Sweikart MA, Turner JA. Stainless steel as bipolar plate material for polymer electrolyte membrane fuel cells. J. Power Sources 2003;115:243-51.
[13] Hodgson DR, May B, Adcock PL, Davies DP. New lightweight bipolar plate system for polymer electrolyte membrane fuel cells. J. Power Sources 2001;96:233-5.
[14] Yeetsorn R, Fowler MW, Tzoganakis C. A review of thermoplastic composites for bipolar plate materials in PEM fuel cells. In: Cuppoletti J, editor. Nanocomposites with unique properties and applications in medicine and industry, London: InTech; 2011, p. 317-44.
[15] Liao SH, Yen CY, Weng CC, Lin YF, Ma CCM, Yang CH, et al. Preparation and properties of carbon nanotube/polypropylene nanocomposite bipolar plates for polymer electrolyte membrane fuel cells. J Power Sources 2008;185:1225-32.
[16] Mighri F, Huneault MA, Champagne MF. Electrically conductive thermoplastic blends for injection and compression molding of bipolar plates in the fuel cell application. Poly Eng Sci 2004;44:1755-65.
[17] Kakati BK, Ghosh A, Verma A. Efficient composite bipolar plate reinforced with carbon fiber and graphene for proton exchange membrane fuel cell. Int J Hydrogen Energy 2013;38:9362-9.
[18] Lee HE, Han SH, Song SA, Kim SS. Novel fabrication process for carbon fiber composite bipolar plates using sol gel and the double percolation effect for PEMFC. Compos Struct 2015;134:44-51.

[19] Heo SI, Yun JC, Oh KS, Han KS. Influence of particle size and shape on electrical and mechanical properties of graphite reinforced conductive polymer composites for the bipolar plate of PEM fuel cells. Adv Compos Mater 2006;15:115-26.
[20] Blunk R, Zhong F, Owens J. Automotive composite fuel cell bipolar plates: Hydrogen permeation concerns. J Power Sources 2006;159:533-42.
[21] Adloo A, Sadeghi M, Masoomi M, Pazhooh HN. High performance polymeric bipolar plate based on polypropylene/graphite/graphene/nano-carbon black composites for PEM fuel cells. Renew Energy 2016;99:867-74.
[22] Bairan A, Selamat MZ, Sahadan SN, Malingam SD, Mohamad N. Effect of carbon nanotubes loading in multifiller polymer composite as bipolar plate for PEM fuel cell. Procedia Chem 2016;19:91-7.
[23] Tjong SC. Polymer nanocomposite bipolar plates reinforced with carbon nanotubes and graphite nanosheets. Energy Environ Sci 2011;4:605-26.
[24] Al-Saleh MH, Saadeh WH. Hybrids of conductive polymer nanocomposites. Mater Des 2013;52:1071-6.
[25] Al-Saleh MH, Sundararaj U. A review of vapor grown carbon nanofiber/polymer conductive composites. Carbon 2009;47:2-22.
[26] Grundler M, Derieth T, Beckhaus P, Heinzel A. CarbonNanoTubes (CNT) in bipolar plates for PEM fuel cell applications. In: Stolten D, Grube T, editors. Fuel Cell Basics/Fuel Infrastructures. Proceedings of the WHEC, Verlag; 2010, p. 147-52.
[27] Tibbetts GG, Lake ML, Strong KL, Rice BP. A review of the fabrication and properties of vapor-grown carbon nanofiber/polymer composites. Compos Sci Technol 2007;67:1709-18.
[28] Ramírez-Herrera CA, Pérez-González J, Solorza-Feria O, Romero-Partida N, Flores-Vela A, Cabañas-Moreno JG. Highest recorded electrical conductivity and microstructure in polypropylene-carbon nanotubes composites and the effect of carbon nanofibers addition. Appl Nanosci 2018;8:1221-32.
[29] Schroeder DK. Semiconductor material and device characterization. New York: Wiley; 1990.
[30] Hemmati M, Rahimi GH, Kaganj AB, Sepehri S, Rashidi AM. Rheological and mechanical characterization of multi-walled carbon nanotubes/polypropylene nanocomposites. J Macromol Sci B Phys 2008;47:1176-87.
[31] Liu YH, Gao JL. Mechanical properties and wear behavior of polypropylene/carbon nanotube nanocomposites. Adv Mater Res 2011;299-300:798-801.
[32] Prashantha K, Soulestin J, Lacrampe MF, Krawczak P, Dupin G, Claes M. Masterbatch-based multi-walled carbon nanotube filled polypropylene nanocomposites: Assessment of rheological and mechanical properties. Compos Sci Technol 2009;69:1756-63.
[33] Al-Saleh MH. Electrically conductive carbon nanotube/polypropylene nanocomposite with improved mechanical properties. Mater Des 2015;85:76-81.

XVIII International Congress
of the Mexican Hydrogen Society

The effect of the sulfonation in the properties of poly(styrene-co-butyl acrylate) for proton exchange membrane fuel cells

L. Francisco-Vieira, D. Morales-Acosta*, E. Cuara-Diaz, R. Benavides*

Centro de Investigación en Química Aplicada, Blvd Enrique Reyna No. 140, Col. San José de los Cerritos, 25294. Saltillo, Coahuila, México
*Tel: +52844-4389830 E-mail: roberto.benavides@ciqa.edu.mx; diana.morales@ciqa.edu.mx

ABSTRACT

Proton exchange (PEMFC) and direct methanol (DMFC) electrolytic membranes for fuel cells are focused for portable and transport devices and this work is relates with the development of novel sulfonated aromatic hydrocarbon polymers for PEMs as alternatives to conventional perfluorinated polymers. Styrene-butyl acrylate (St:BuA) copolymer with 90:10 (St:BuA) comonomer composition was obtained by mass copolymerization via free radical reaction, using BPO as initiator. St:BuA copolymers with different degree of sulfonation (50, 100 and 150%) were considered in order to evaluate their potential for fuel cell application. The sulfonated copolymers presented good solubility in common solvents. Membranes were prepared from sSt-BuA copolymers through casting method. NMR ^{1}H and GPC were used for characterization of the prepared copolymers. The sSt-BuA degree of sulfonation (DS) and the ion-exchange capacity (IEC) were determinated by titration, while thermal properties were evaluated by thermogravimetric analysis (TGA). NMR ^{1}H spectroscopy confirmed the chemical composition of St-BuA copolymer, the molecular weight by GPC was Mw = 215,308 g·mol^{-1}. FT-IR and TGA results confirmed the successful sulfonation as well as a good thermal stability under 350 °C. The IEC of sSt-BuA membranes was found to be in the range of 0.55 to 1.09 meq·g^{-1}, depending of the concentration of the sulfonic groups. Degree of sulfonation varied from 12 to 27%. Results demonstrated that these copolymers are promising materials to be used as low cost membranes in fuel cells applications.

Keywords: Proton exchange membranes, styrene-co-butyl acrylate, fuel cells

1. Introduction

Polymer electrolyte membrane fuel cells (PEMFCs) are considered as one of the promising energy conversion devices, because of their high efficiencies and wide range of applications, such as power stations, electric vehicles and electronic applications [1]. The important requirements for PEMFC commercialization are: high performance and lifetime of their

multiple components that could reduce the fuel cell cost. The primary component within the PEMFC is the membrane electrode assembly (MEA) which consists of the proton exchange membrane (PEM), and the anode and cathode catalyst layers [1, 2]. Among them, PEM is the key part, which conducts H^+ ions from the anode to the cathode [3].

PEM materials used nowadays perfluorinated membranes, such as Nafion or Flemion, which have a good physical and chemical stability together with proton conductivity under a wide range of relative humidity conditions at moderate operation temperatures. However, they suffer from some disadvantages, as limited operation temperature (0–80 ^{o}C), high cost, insufficient durability and high methanol permeability [4, 5]. Thus, the improvement of Nafion properties as well as finding its alternative materials, based on non-fluorinated ionomers, has been the key issues of research during the past decade.

Sulfonation is a well-known process to increase the hydrophilicity and proton conductivity of polymer by attaching sulfonic groups to the polymer chains. The attached sulfonic groups can offer and retain relatively higher water due to the enhanced antifouling capacity and favorable hydrodynamic environment of the membrane, which is also a very important mechanism for proton conducting. However, in order to achieve sufficient proton conductivity, the sulfonated aromatic polymer membranes should possess a high sulfonation level [6].

In this context, the sulfonation of hydrocarbon polymers is a common alternative for preparation of the membranes. They are usually prepared by either direct sulfonation of polymer matrix with different sulfonating agents or synthetized from the sulfonated monomers by polymerization reactions [3, 7]. Polystyrene is a high performance polymer with good thermal and mechanical properties; additionally the copolymers based on polystyrene (Ps) are attractive due to its low cost and easy processability [5]. In this present work, the copolymer poly(styrene-co-butyl acrylate) (St:BuA) was synthetized by free radical mass copolymerization and further sulfonated, with the main idea of improving the thermal properties and to obtain membranes with convenient sulfonation degree (DS) to maintain high ion exchange conductivity (IEC) values.

2. Materials and Methods

2.1. Synthesis of poly (styrene-co-butyl acrylate)

Styrene and butyl acrylate were synthetized by free radical mass polymerization, using benzoyl peroxide (BPO) as initiator of the reaction. The copolymer was synthesized with a molar ratio of 90:10, the most being the styrene monomer. The copolymerization reaction was carried out in a two-neck ball flask, with a reflux condenser and magnetic stirring, at a constant temperature of 100 °C during 3 hours under a nitrogen atmosphere. The final product was dissolved in acetone and precipitated in methanol for several times. The copolymer St-BuA was dried in a vacuum oven at 50°C during 24 h.

2.2. Sulfonation of poly(styrene-co-butyl acrylate)

The sulfonation of poly(styrene-co-butyl acrylate) (St:BuA) was carried out in concentrated sulfuric acid (H_2SO_4, 98%), with the St:BuA previously dissolved in chloroform. Once the corresponding amount of sulfuric acid was added, the solution was heated and kept at 60 °C during 2 h under a nitrogen atmosphere. The reaction was stopped by pouring the sulfonated copolymer solution into a beaker with distilled water immersed in an ice bath. The solid sulfonated copolymer was washed several times with distilled water until neutral pH was reached; the solid was taken to a vacuum oven at 50 ^{o}C for 48 h, to remove residual water. The sulfonating agent (H_2SO_4) was added at different quantities (50, 100 and 150 % mol) relative to the theoretical molar amount of benzene rings. The sulfonated copolymers were labeled as sSt-BuA 50%, sSt-BuA 100% and sSt-BuA 150%. The synthetic and sulfonation route is decipted in **Scheme 1.**

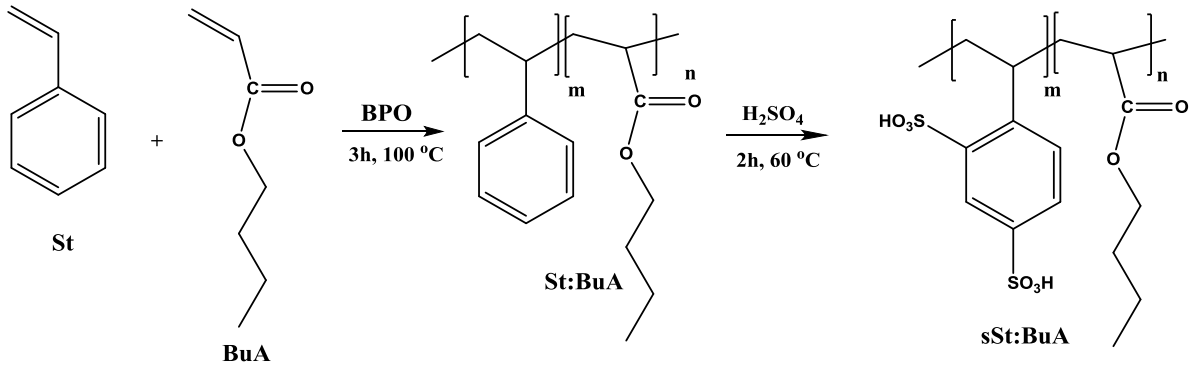

Scheme 1. Synthesis and sulfonation of poly (styrene-*co*-butyl acrylate).

2.4. Preparation of the membranes

The sulfonated styrene-co-butyl acrylate membranes (sSt-BuA) were prepared by the casting method using toluene as solvent. The copolymer mass/solvent ratio was prepared with 0.2 g·mL^{-1} and the dissolved copolymers were poured into a glass container. The casted membranes were put in a vacuum oven at 50 ^{o}C for 24 h, to remove residual solvent.

2.5. Characterization of membranes

The copolymer St:BuA 90:10 was characterized from NMR ^{1}H, using a Bruker Avance 3 spectrometer with 500 MHz of frequency; the copolymer sample was dissolved in $CDCl_3$. FTIR measurements were performed with an instrument Nicolet Magna – IR^{TM} Spectrometer 550, the conditions used: 32 scans, resolution de 4 cm^{-1} in the 4000-400 cm^{-1} region. The molecular

weight was obtained by GPC analysis operated at room temperature, using a GPC Waters Alliance 2695, tetrahydrofuran was used as solvent and a UV detector; calibrated with standards of the polystyrene.
Thermal stability was determined by TGA analysis, using an equipment TA Instruments model Q500 under nitrogen atmosphere and a heating rate of 10 $^{o}C \cdot min^{-1}$, from 30 ^{o}C to 600 ^{o}C.
Water uptake (WU) measurements of the sSt-BuA membranes were conducted by immersing the membrane samples into distilled water at room temperature for 24h for full equilibrium. Then, the membrane surface was wiped off with a tissue paper and weighed immediately in order to obtain the wet weight (W_{wet}). Membranes were dried in an oven at 80 ^{o}C under vacuum for 2h and weighed to determine the dry weight (W_{dry}). The percentage of water uptake is calculated by differences between dry/wet weights (in gr), according to the equation [8]:

$$WU(\%) = \frac{W_{wet} - W_{dry}}{W_{dry}} \quad (1)$$

The ion exchange capacity (IEC) of the sulfonated copolymers was evaluated by a titration method. The dried membrane was immersed into a 1M HCl solution for 24h; then, they were rinsed and submerged into a solution of 1M NaCl for 24h. Finally, the membrane was rinsed with deionizer water. The number of protons shifted of the membrane was determined using a pHmeter to detect the equivalent point during the titration on the solution of NaCl with a solution 0.005M of NaOH. The IEC was calculated using the following equation:

$$IEC = \frac{V_{NaOH} \cdot N_{NaOH}}{W_{dry}} \quad (2)$$

where V_{NaOH} (mL) is the volume of the 0.005 M NaOH (mL), N_{NaOH} is the concentration of NaOH ($mmol \cdot mL^{-1} \sim meq \cdot mL^{-1}$) and W_{dry} is the dry weight of the copolymer membrane [8].
The sulfonation degree of St:BuA is an important parameter, due to its effect on the physicochemical properties of the membranes based St:BuA. The sulfonation degree (DS) was calculated considering the values of IEC previously obtained, through the equation:

$$DS\ (\%) = \frac{IEC.M_{w(St:BuA)}}{1 - (IEC.M_{w(SO_3H)})} \quad (3)$$

where $M_{w\ St:BuA}$ ($gr \cdot mol^{-1}$) is the molecular weight of the copolymer (St:BuA) and $M_{w\ SO3H}$ ($gr \cdot mol^{-1}$) is the molecular weight of the sulfonic group [9].

3. Results and Discussion

The real copolymer composition was obtained by ^{1}H NMR analysis. Copolymer composition was calculated by comparison of the integrals from signals at 4 - 3.5 ppm, assigned to the two protons of the -OCH_2- group from butyl acrylate, and the broad signals at 7.5 - 6.3 ppm, due to the protons (5H per mole) from the aromatic ring of styrene (Figure 1) [10]. Figure 1 also shows the spectrum of polystyrene as a reference, allowing to see changes in the signals to confirm the presence of butyl acrylate. The real composition calculated was 89:11 (St:BuA), very close to the theoretical pretended composition (90:10).

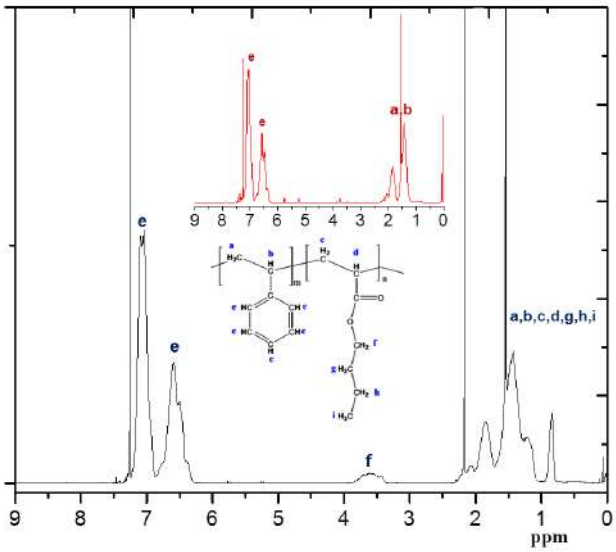

Fig. 1. ^{1}H NMR spectrum of St:BuA copolymer and polystyrene.

The FTIR analysis was carried out to corroborate the St-BuA copolymer formation, as well as the existence of sulfonic acid groups after the sulfonation process. In Figure 2 shows the spectra of the copolymers sulfonated at different levels aside the non-sulfonated St: BuA 90:10 copolymer. The copolymer shows the characteristics absorption bands located between 3100-3000 cm^{-1} from the C-H stretching mode in the aromatic ring; while the bands at 2962-2850 cm^{-1} are attributed to the asymmetric and symmetrical deformation, corresponding to the CH_2 and CH_3 groups present in the styrene aliphatic side. The characteristic signal of the ester group in the BuA monomer is also observed as an intense absorption band at 1722 cm^{-1}, corresponding to the C=O group. Then at 1140 cm^{-1} the absorption band corresponds to the stretching vibration of O-C (O)-C [11].

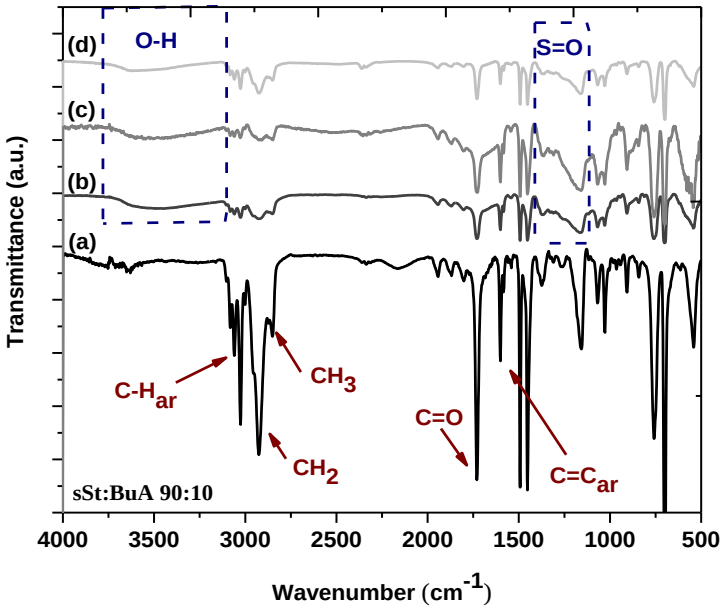

Fig. 2. FTIR copolymers: (a) St:BuA 90:10 (b) sSt:BuA 50%, (c) sSt:BuA 100%, (d) sSt:BuA 150%.

GPC analysis indicated the formation of a copolymer with mass molecular weight (Mw) of the 215,308 g mol^{-1} which is a very convenient size, since over 100,000 gr·mol^{-1} similar copolymers are able to form films useful for preparing membranes [12].

Sulfonation is also confirmed by the identification of the absorption bands at 1377-1300 cm^{-1}, characteristics of the asymmetric stretching of the S=O bond. It is noteworthy that with the increase of the concentration of sulfonic groups (50, 100 and 150%) in the polymer chain, there is a sequenced expansion of these bands in spectra along with sulfonation level, suggesting sulfonation reaction effectiveness. These bands originate due to the asymmetric and symmetrical SO_2 elongation found in the absorption bands at 1200 and 1168 cm^{-1}, respectively [13].

The thermal properties of non-sulfonated and sulfonated St-BuA copolymers are presented in Figure 3. Through the thermograms it was possible to confirm that the copolymer show a useful thermal stability for our application purpose, since it stable over 350 °C; after that it undergoes main chain degradation. Sulfonated sSt-BuA copolymers show weight loss in three steps. The first (100 – 110 °C) is due to the loss of water molecules, which may come from the process of the neutralization after the sulfonating reaction, or due to the absorption of ambient moisture in our highly hygroscopic sulfonated copolymers. The second loss (150 - 250 ^{o}C) is assigned to the decomposition or loss of pendant sulfonic acid groups (-SO_3H); this step is particular of sulfonated materials. Finally, the third loss weight (350 - 380 ^{o}C) is assigned to the degradation

of the main chain or polymer backbone [14]. Increasing sulfonation level, the loss weight is higher and the peak onset, from the corresponding sulfonic acid group loss, is shifted to lower temperature. From these results, it is clear that all the copolymers presented good thermal stability at temperatures of 150 ^{o}C, which is superior to fuel cell operation temperature.

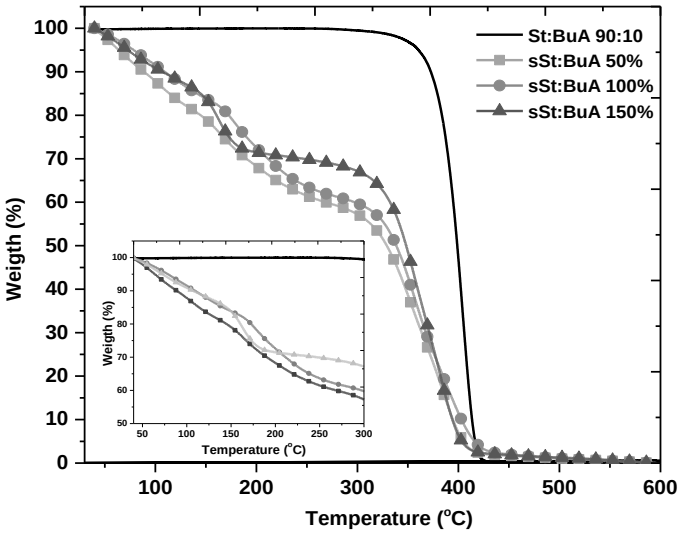

Fig 3. TGA curves of St:BuA and sSt-BuA (50, 100 and 150 %) copolymers.

Ion exchange capacity (IEC) and sulfonation degree (DS) are important parameters to provide information on the ability to exchange ionic groups in the membrane and a direct indication for proton conduction. Both parameters are also highly linked with the membrane's capacity to adsorb water, known as water uptake (WU), since water is needed to exchange ions inside the membrane of a fuel cell. IEC, DS and WU values obtained for the sulfonated St-BuA copolymers are presented in the table 1.

Table 1. Properties of sSt-BuA copolymers.

Sample	IEC (meq·g^{-1})	DS (%)	WU (%)
sSt-BuA 50%	0.55	12	6
sSt-BuA 100%	0.77	19	16
sSt-BuA 150%	1.09	27	23

It is clear to observe that along increment of DS, an increase of IEC and WU occurs. For the highly sulfonated copolymer sSt:BuA 150%, the material presented a IEC of 1.09 meq·g^{-1} with

DS of 27%; such values are high comparing with Nafion membranes (IEC = 0.91 meq·g^{-1}). Such results indicate that this membrane has favorable properties and makes it as a promising material for membranes to use in electrolytic applications.

4. Conclusion

The copolymers of sSt:BuA were successfully synthetized and sulfonated, as confirmed by NMR ^{1}H and FTIR, they also presented good molecular weight for to prepare membranes. Thermal stability was also obtained and indicated weight loss temperatures up to 300 ^{o}C by TGA. The copolymer had good physicochemical characteristics as proton exchange membranes, as confirmed by DS, WU and IEC results (IEC = 1.09 meq·g^{-1}).

Acknowledgements

This work has been supported by the Mexican Council of Science and Technology (CONACyT) through grants 174689. LFV thanks CONACyT for the support through the MSc scholarship. The authors also grateful to the SMH and XVII International Congress of the Mexican Hydrogen Society for accepting the presentation of this work.

References

[1] K. Oh, K. Ketpang, H. Kim, S. Shanmugam. Synthesis of sulfonated poly(arylene ether ketone) block copolymers for proton exchange membrane fuel cells. J. Memb. Sci. 2016; 507: 135–142.

[2] M. J. Parnian, S. Rowshanzamir, A. K. Prasad, and S. G. Advani. High durability sulfonated poly (ether ether ketone)-ceria nanocomposite membranes for proton exchange membrane fuel cell applications. *J. Memb. Sci.* 2018; 556: 12–22.

[3] F. Ahmed *et al.* Comparative study of sulfonated branched and linear poly(phenylene)s polymer electrolyte membranes for fuel cells. *Int. J. Hydrogen Energy.* 2018; 43: 5374–5385.

[4] T. Higashihara, K. Matsumoto, and M. Ueda. Sulfonated aromatic hydrocarbon polymers as proton exchange membranes for fuel cells. *Polymer (Guildf).* 2009; 50: 5341–5357.

[5] S. L. Chen, L. Krishnan, S. Srinivasan, J. Benziger, and A. B. Bocarsly. Ion exchange resin/polystyrene sulfonate composite membranes for PEM fuel cells. *J. Memb. Sci.* 2004; 243: 327–333.

[6] S. Mulijani, K. Dahlan, and A. Wulanawati. Sulfonated Polystyrene Copolymer : Synthesis, Characterization and Its Application of Membrane for Direct Methanol Fuel Cell (DMFC). 2014; 2: 36–40.

[7] S. Banerjee and K. K. Kar. Impact of degree of sulfonation on microstructure, thermal, thermomechanical and physicochemical properties of sulfonated poly ether ether ketone.

Polymer (Guildf). 2017; 109: 176–186.

[8] T. A. Sherazi, S. Ahmad, M. A. Kashmiri, D. S. Kim, and M. D. Guiver. Radiation-induced grafting of styrene onto ultra-high molecular weight polyethylene powder for polymer electrolyte fuel cell application. *J. Memb. Sci.* 2009; 333: 59–67.

[9] A. Basile, L. Paturzo, A. Iulianelli, I. Gatto, and E. Passalacqua. Sulfonated PEEK-WC membranes for proton-exchange membrane fuel cell: Effect of the increasing level of sulfonation on electrochemical performances. *J. Memb. Sci.* 2006; 281: 377–385.

[10] N. T. McManus, A. Penlidis, and M. A. Dube. Copolymerization of alpha-methyl styrene with butyl acrylate in bulk. *Polymer (Guildf).* 2002; 43: 1607–1614.

[11] D. J. K. Robert M. Silverstein, Francis X. Webster, *Spectrometric identification of organic compounds*, 7th ed. New York: Jonh Wiley & Sons, Inc, 2005.

[12] L. Melo, R. Benavides, G. Martínez, L. Da Silva, and M. M. S. Paula. Degradation reactions during sulphonation of poly(styrene-co-acrylic acid) used as membranes. *Polym. Degrad. Stab.* 2014; 109: 343–352.

[13] M. J. Parnian, S. Rowshanzamir, and F. Gashoul. Comprehensive investigation of physicochemical and electrochemical properties of sulfonated poly (ether ether ketone) membranes with different degrees of sulfonation for proton exchange membrane fuel cell applications. *Energy*. 2017; 125: 614–628.

[14] P. Knauth, H. Hou, E. Bloch, E. Sgreccia, and M. L. Di Vona. Thermogravimetric analysis of SPEEK membranes: Thermal stability, degree of sulfonation and cross-linking reaction. *J. Anal. Appl. Pyrolysis*. 2011; 92: 361–365.

XVIII International Congress
of the Mexican Hydrogen Society

Effect of the calcination temperature on the purity of $GdBaCo_2O_{5+\delta}$ synthesized by a sol-gel method

C. I. Ramos Villegas[1], R. Guzmán Salinas[1], D. A. Jurado Ferral[1], P. Castillo Ocampo[2], A. Tejeda Cruz[3], H. J. Ávila Paredes[1]*

[1]Departamento de Ingeniería de Procesos e Hidráulica, Universidad Autónoma Metropolitana, Unidad Iztapalapa, Av. San Rafael Atlixco186, Col. Vicentina, C.P. 09340, Ciudad de México, México.
[2]Laboratorio de Microscopía Electrónica, Universidad Autónoma Metropolitana, Unidad Iztapalapa, Av. San Rafael Atlixco186, Col. Vicentina, C.P. 09340, Ciudad de México, México.
[3]Laboratorio de Difracción de Rayos X, Instituto de Investigaciones en Materiales, Universidad Nacional Autónoma de México, Circuito Exterior, Ciudad Universitaria, C.P. 04510, Ciudad de México, México.
*(52) 55 5804 4600 ext. 1243; hjap@xanum.uam.mx

ABSTRACT

Solid oxide fuel cells (SOFC's) are energy conversion devices that can operate with hydrogen as a fuel, with efficiencies higher than those for the thermo-power generation systems. In order to prevent the issues that conventional SOFC's present due to the high operating temperatures, Intermediate Temperature (500-700 °) SOFC's are under development. When the operating temperature is below 800 °C, the catalytic activity of conventional cathodic materials is reduced, so that new materials need to be developed or found. Recently $GdBaCo_2O_{5+\delta}$ has been proposed as a promising cathodic material for SOFC's based on its high mixed conductivity values at intermediate temperatures. The most commonly used synthesis method for $GdBaCo_2O_{5+\delta}$ is solid state reaction, however this method offers disadvantages such as high temperature synthesis (> 500 °C), non-uniform particle sizes and formation of secondary phases. On the other hand, the sol-gel method allows obtaining uniform and small particle sizes, and a lower synthesis temperature (< 300 °C). The present work focuses on determining the effect of the calcination temperature on the purity of $GdBaCo_2O_{5+\delta}$ synthesized by a sol-gel method. The synthesized materials were characterized by x-ray diffraction, scanning electron microscopy coupled with energy dispersive x-ray spectroscopy. Chemical analyses of samples allowed determining the right amounts of precursors needed to obtain the pure $GdBaCo_2O_{5+\delta}$. The calcination temperature is a crucial factor in the synthesis: a higher temperature leads to a material of higher purity and a larger average crystallite size.

Keywords: Solid Oxide Fuel Cells; cathodic materials; sol-gel method; $GdBaCo_2O_{5+\delta}$.

September 18th to 21st, 2018 in Mexico City, Mexico.

1. Introduction

Solid oxide fuel cells (SOFC´s) are widely considered as a high efficient and low environmental impact technology for power generation. Currently, attention has been paid to lowering the operation temperature to the intermediate range (500 - 700 °C), to reduce the cost and improve the components compatibility. Decreasing the operation temperature, however has the drawbacks of increasing the ohmic resistance and reducing the electrode kinetics (mainly the cathodic).

Mixed conductors with a perovskite crystalline structure have been proposed as potential candidates for cathodes of intermediate temperature solid oxide fuel cells (IT-SOFC´s) [1, 2, 3, 4, 5]. In recent years, certain materials with a double perovskite structure have aroused great interest due to their higher electrical conductivity, compared with simple perovskites. These materials have a general chemical formula$AA'B_2O_{5+\delta}$ (Figure 1); some systems for IT-SOFC´s applications are summarized in the formulae $LnBaCo_2O_{5+\delta}$ and $LnBaCuFeO_{5+\delta}$, where Ln = La, Pr, Nd, Y, Sm and Gd [3]. The oxides with double perovskite structure consist of consecutive layers of $[BO_2]$ - [AO] - $[BO_2]$ - [A'O] arranged along the c-axis. Such a layered structure reduces the resistance of the oxygen bond with the layer [AO] and provides a free space for the movement of the oxygen ions, which improves their diffusivity within the crystal lattice [6]. Relatively rapid oxygen ion diffusion and high surface exchange kinetics have been confirmed in $GdBaCo_2O_{5+\delta}$ (GBCO) and $PrBaCo_2O_{5+\delta}$ (PBCO) compounds, which are significantly faster than in corresponding simple perovskite materials (e.g. $La_{0.5}Sr_{0.5}CoO_{3-\delta}$).

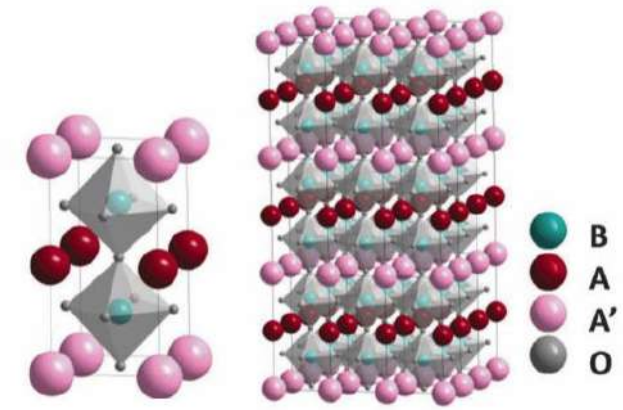

Fig. 1. Double perovskite $AA'B_2O_{5+\delta}$ crystalline structure [7].

GBCO has an average conductivity of 620 S * cm^{-1} in the range of 500 - 700 °C and its thermal expansion coefficient (TEC) values are between (16 – 20) x 10^{-6} K^{-1}, in addition to being compatible with GDC, an electrolyte material commonly used in IT-SOFC´s [8, 9]. The mostly used and reported method of synthesis for GBCO is the solid state reaction, although there are some others based on sol-gel and the nitrate-glycine methods. However, the sol-gel method has the advantages of allowing the synthesis of high purity materials with small and uniform particle sizes. In the above described context, the present work focuses on determining the effect of the calcination temperature on the purity of GBCO synthesized by a sol-gel method. The synthesized materials were characterized by x-ray diffraction, scanning electron microscopy coupled with energy dispersive x-ray spectroscopy.

2. Materials and Methods

GBCO samples were synthesized by a sol-gel method: stoichiometric amounts of $Gd(NO_3)_3 \cdot 6H_2O$ (Sigma Aldrich, 99.99 %), $Ba(NO_3)_2$ (Sigma Aldrich, 99.99 %) and $Co(NO_3)_2 \cdot 6H_2O$ (Sigma Aldrich, 99.99%) were dissolved in distilled water, then citric acid was added with a molar ratio of total metal ions: citric acid of 1:1.5. Subsequently the pH was adjusted around ~ 7 with an aqueous solution of 0.6 M ammonium hydroxide (J. T. Baker, 98 %). Then the solution was heated to 70 °C for 1 h with constant stirring to form a sol. The temperature was raised to 100 °C for 1 h with constant stirring to evaporate the solvent. Finally the samples were left at 300 °C for 12 h. The final product was ground in an agate mortar until a fine powder was obtained. The powders were conformed into cylindrical pellets via a cold isostatic pressing (7 MPa for 10 min). Pellets were calcined (800, 900, 1000 ° C for 4 h) in an air atmosphere.

Samples were characterized by X-ray diffraction (XRD), using a Bruker AXS Advance8 diffractometer with Cu Kα radiation (λ = 1.5406 °A) with an energy of 30 kV and the current of 30 mA, with a step of 1 ° per second, in a range of $20° \leq 2\theta \leq 80°$. The chemical composition of samples was estimated using X-ray energy dispersive analysis (EDS), using a scanning electron microscope (Jeol 7600 F) with a voltage of 15 kV and with a working distance of ~ 11 mm.

3. Results and Discussion

Figure 2 shows the XRD patterns of GBCO samples calcined at 900 °C for 4 h in air atmosphere. The difference of samples GBCO-1, GBCO-2 and GBCO-3 resides in the stoichiometric atomic ratio of the cations. The XRD patterns indicated a high crystallinity of the samples, there are peaks that correspond to the diffractogram of the cobaltite of barium and gadolinium in its orthorhombic crystalline phase. However, in the case of the XRD pattern of GBCO-1 there is an indication of a secondary phase: peaks corresponding to Gd_2O_3 are also observed.

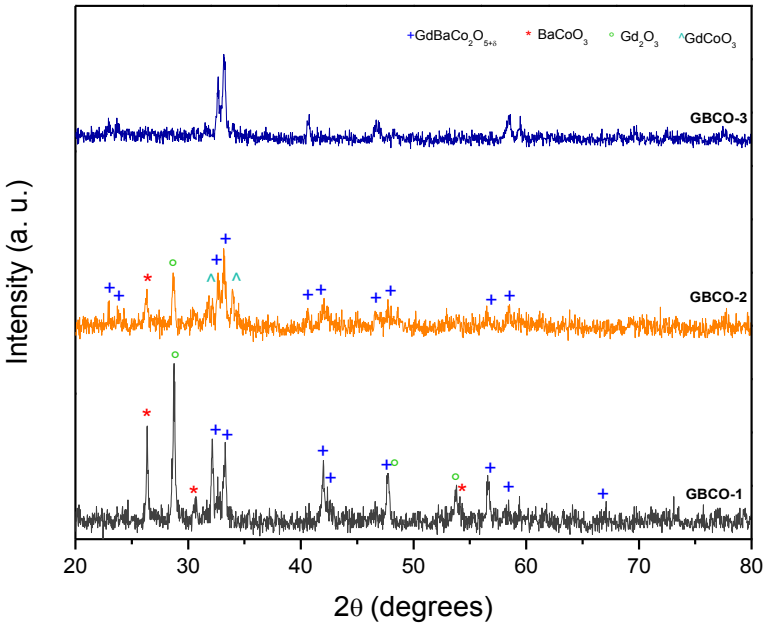

Fig. 2. XRD pattern for samples calcined at 900 °C for 4 hours in air atmosphere.

EDS results of sample GBCO-1 before and after calcination (Table 1) confirmed that the chemical composition was similar, which rules out a possible loss of any of the cations by evaporation. However, the analysis showed that the nominal stoichiometric ratio was not met. It is important to note that precursors are highly hygroscopic, so that water content could be cause of an error to the estimation of the amounts of cations. Based on the EDS results of samples GBCO-1 after calcination, the amounts of precursors were corrected and a new synthesis was carried out (GBCO-2). The XRD pattern ofGBCO-2 (Figure 2) still shows peaks of the undesired phase; the main peak of Gd_2O_3 decreased by~ 62 % in comparison to the peak of the GBCO-1 pattern. EDS analysis was performed on this sample; results indicated that the stoichiometry was not fulfilled (Table 1). Then the amounts of precursors were corrected with these results and sample GBCO-3 was synthesized. The XRD pattern of this sample showed a pure phase (Figure 2). The phase obtained in the present work agrees well with those reported by Myeong-Hee Ko et al., and Bo Wei et al. [2, 10; ICDD card 00-053-0135]. However, a study by Yan-Kun Tang et al., in which they used the sol-gel method, reported obtaining the perovskite structure with the tetragonal crystalline phase [11]. It is important to note thatthe crystalline structure adopted by GBCO (i.e. orthorhombic or tetragonal) depends on the oxygen stoichiometry [9].

Table 1. Stoichiometric atomic ratio (element: Gd ratio) of samples GBCO-1 and GBCO-2, calculated from EDS results.

Element	Gd	Ba	Co
Nominal atomic ratio	1	1	2
GBCO-1 before calcination	1 ± 0.095	1.143 ± 0.132	1.119 ± 0.141
GBCO-1 after calcination	1 ± 0.073	1.068 ± 0.101	0.0934 ± 0.098
GBCO-2 after calcination	1 ± 0.096	0.982 ± 0.039	1.479 ± 0.046

Once the right amounts of precursors were estimated, in order to determine the effect of the calcination temperature on the purity of the material, GBCO samples were synthesized with calcinations carried out at 800, 900 and 1000 °C for 4 h in air atmosphere. Figure 3 shows the corresponding XRD patterns. In the case of the sample calcined at 800 °C, the presence of a mixture of oxides corresponding to the formation of GBCO, $BaCoO_3$, Gd_2O_3 and $GdCoO_3$ was found, this confirms that at this temperature it is not possible to obtain the formation of pure GBCO perovskite. In the case of the sample calcined at 900 °C, the typical peaks of the GBCO perovskite with an orthorhombic structure (desired phase) are observed, however it can also be observed that low intensity peaks corresponding to $BaCoO_3$ and $GdCoO_3$ are present.

On the other hand, in the sample calcined at 1000 °C, the absence of impurities was determined, under the detection limit of the analytical technique, and this sample exhibited high crystallinity. The diffraction patterns can be indexed to an orthorhombic structure (*pmmm* symmetry: ICDD card 00-053-0135), it was also possible to identify the peaks of the planes (100), (002), (120), (102), (122), (040), (200), (004), (142), (124), (240) and (204) at ~ 23, ~ 24, ~ 32, ~ 33, ~ 41, ~ 46.5, ~ 47, ~ 48 , ~ 58.5, ~ 59.5, ~ 68 and ~ 69.5 ° respectively. The crystallite size estimated by Scherrer equation was ~ 185 and ~ 190 nm for samples calcined at 900 and 1000 °C, respectively.

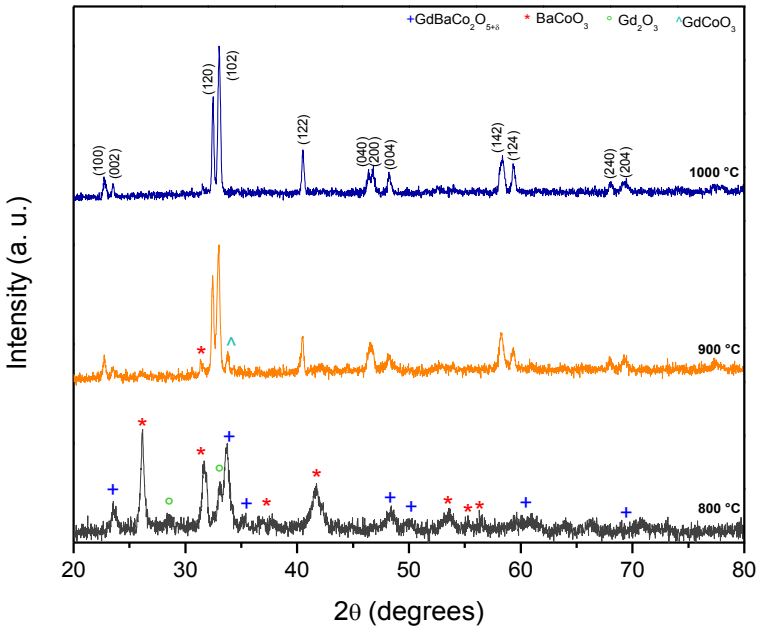

Fig. 3. XRD patterns for samples calcined at 800, 900 and 1000 °C for 4 hours in air atmosphere.

4. Conclusion

In summary, it was possible to synthesize GBCO by a sol-gel method. The stoichiometric ratio of the precursors determines the formation of the desired phase and plays a fundamental role in the purity of the final product. On the other hand, it was clearly observed that a higher calcination temperature in the 800-1000 °C range leads to a material of higher purity and a larger average crystallite size.

Acknowledgements

Funding for this research was provided by Universidad Autónoma Metropolitana. C.I. Ramos Villegas is thankful to Consejo Nacional de Ciencia y Tecnología for the scholarship received to pursue his Ph.D. studies.

References

[1] Na Li , Zhe Lu, Bo Wei, Xiqiang Huang, Kongfa Chen, Yaohui Zhang, Wenhui Su. Characterization of $GdBaCo_2O_{5+\delta}$ cathode for IT-SOFCs. Journal of Alloys and Compounds 454 (2008) 274–279.
[2] Bo Wei, Zhe Lu, Dechang Jia, Xiqiang Huang, Yaohui Zhang, Wenhui Su. Thermal expansion and electrochemical properties of Ni-doped $GdBaCo_2O_{5+\delta}$ double-perovskite type oxides. International Journal of Hydrogen Energy 35 (2010) 3775-3782.
[3] J. A. Flores y L.A. Rodríguez, Materiales para ánodos, cátodos y electrolitos utilizados en celdas de combustible de óxido sólido, Rev. Mex. Fis. 59 (2013), 66-87.
[4] Aiming Chang, Stephen. J. Skinner, and John. A. Kilner, "Electrical properties of $GdBaCo_2O_{5+\delta}$ for ITSOFC applications" Solid State Ionics, 177 (2006), 2009–2011.
[5] John A. Kilner and Monica Burriel, "Materials for Intermediate-Temperature Solid-Oxide Fuel Cells" Annu. Rev. Mater. Res. 44 (2014), 365–93.
[6] J. Alvarado- Flores, J. Espino-Valencia y L. Ávalos-Rodríguez, Análisis de materiales catódicos de estructura Perovskita para celdas de combustible de óxido sólido, SOFC´s, Revista Mexicana de Física 61 (2015), 32-57.
[7] Zhan Gao, Liliana V. Mogni, Elizabeth C. Miller, Justin G. Railsback and Scott A. Barnett. A perspective on low-temperature solid oxide fuel cells. Energy Environ. Sci., 9 (2016), 1602-1644.
[8] John A. Kilner and Monica Burriel. Materials for Intermediate-Temperature Solid-Oxide Fuel Cells. Annu. Rev. Mater. Res. 44 (2014), 365–93.
[9] Albert Tarancón, Alejandro Morata, Guilhem Dezanneau, Stephen. J. Skinner, John A. Kilner, Sonia Estradé, F. Hernández-Ramírez, F. Peiró, J.R. Morante. $GdBaCo_2O_{5+x}$ layered perovskite as an intermediate temperature solid oxide fuel cell cathode. Journal of Power Sources 174 (2007) 255–263.
[10] Myeong-Hee Ko, Young-Sung Yoo, Jin-Ha Hwang. Electrochemical estimation of GBCO ($GdBaCoO_{5+\delta}$) / GDC (Gd2O3 – doped CeO2) cathode composites designed for intermediate – temperature solid oxide electrochemical cells. Ceramics International 41 (2015), 4616 – 4620.
[11] Yan-kun Tang, Qian Yang, Xiao-fei Si, Jin-kang Han, Wei-wei Cao,Ya-fei Li, Fang Liu, Xiaoyan Yao, Ya Zhai. Effect of Sintering Temperature on Magnetic and Electrical Properties of $GdBaCo_2O_{5+\delta}$. J Supercond Nov Magn (2017) 30:1527–1531.

XVIII International Congress
of the Mexican Hydrogen Society

Construction and electrochemical characterization of a microtubular solid oxide fuel cell at intermediate temperatures

C. I. Ramos Villegas[1], R. Guzmán Salinas[1], D. A. Jurado Ferral[1], P. Castillo Ocampo[2], H. J. Ávila Paredes[1]*

[1]Departamento de Ingeniería de Procesos e Hidráulica, Universidad Autónoma Metropolitana, Unidad Iztapalapa, Av. San Rafael Atlixco186, Col. Vicentina, C.P. 09340, Ciudad de México, México.
[2]Laboratorio de Microscopía Electrónica, Universidad Autónoma Metropolitana, Unidad Iztapalapa, Av. San Rafael Atlixco186, Col. Vicentina, C.P. 09340, Ciudad de México, México.
*(52) 55 5804 4600 ext. 1243; hjap@xanum.uam.mx

ABSTRACT

Solid oxide fuel cells (SOFC´s) traditionally operate at high temperatures (800 - 1000 °C) at which they exhibit a high efficiency. However in recent years SOFC´s operating at significantly lower temperatures (500 - 700 ° C) have been developed in order to reduce manufacturing costs, but trying to conserve the high efficiency. The frequently used cathodic material for conventional SOFC´s is $La_{1-x}Sr_xMnO_{3-\delta}$ (LSM), which has high electronic conductivity and high catalytic activity for the reduction of oxygen at elevated temperatures. In addition, the LSM has a coefficient of thermal expansion close to zirconia stabilized with yttria (YSZ), the commonly used electrolyte at high temperatures. However, at intermediate temperatures, the catalytic activity of the LSM decreases and YSZ is no longer a good electrolyte. Currently, one of the cathodic materials that provides the highest performance for IT-SOFC´s is $La_{0.8}Sr_{0.2}Co_{0.2}Fe_{0.8}O_3$ (LSCF), due to its high conductivity (250 S / cm at 500 °C), and it has a good stability and compatibility $Ce_{0.8}Gd_{0.2}O_{2-\delta}$ (GDC), a good electrolyte for IT-SOFC´s [7]. On the other hand, the microtubular architecture allows using SOFC´s in portable applications. In the present work the results of the performance evaluation of an IT-SOFC prototype (Ni-GDC / GDC / LSCF) with a microtubular architecture are presented. The prototype was constructed based on a dip coating technique. The electrical characterization was performed by linear voltammetry and the performance of the cell was evaluated from polarization curves in the 500 - 700 ° C range; the cell was operated with air and water saturated hydrogen. Power density values were ~ 160 and ~ 225 mW / cm^2 at 500 and 600 °C, respectively..

Keywords: Energy Conversion; Solid Oxide Fuel Cells.

1. Introduction

Solid oxide fuel cells (SOFC´s) are energy conversion devices formed by two electrodes and a ceramic electrolyte, the latter being an ionic conductor (e.g. of oxygen) that is placed between the electrodes, isolates them electrically but forms an ionic bridge between them (Figure 1) [1, 2]. In the case of oxygen ion conductor electrolytes, oxygen is reduced on the cathode, so that oxygen ions are formed. Those oxygen ions migrate from cathode to anode through the electrolyte. At the anode, the fuel reacts with the oxygen ions (i.e. it is oxidized). The electrons produced by the oxidation reaction are conducted to an external circuit, forming the electric current.
SOFC´s are classified within the fuel cells of high operating temperature (> 500 °C) because they traditionally operate in the range of 800 - 1000 °C, at which they exhibit greater efficiency (60 % and 85 % in cogeneration) and electrical power (1-500 MW) [3]. Another characteristic of SOCF´s is that they can operate with different fuels (H_2, CH_4, CO_2). The high operating temperature of the SOFC´s causes inconveniences related to the degradation of cell components and the restriction of the type of materials to be used as interconnectors and supports (it is only possible to use ceramics), which increases the cost of these devices [4]. There has been an effort to reduce the operating temperature to the 500 - 700 °C range and thus develop Intermediate Temperature SOFC´s (IT-SOFC´s), with the aim of reducing manufacturing costs while maintaining high efficiency of these devices [5].

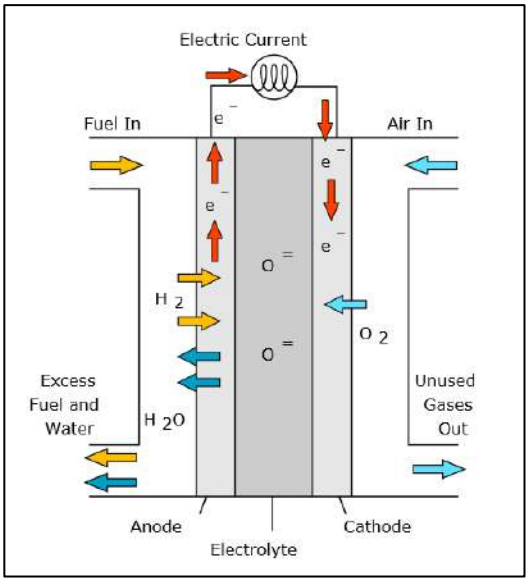

Figure 1. Schematic of a fuel cell [6].

The most commonly used cathodic material for conventional SOFC´s is $La_{1-x}Sr_xMnO_{3-\delta}$ (LSM), which has high electric conductivity (~ 300 S / cm at 900 °C) and high catalytic activity for the oxygen reduction at elevated temperatures [7, 8]. However, at intermediate temperatures the

catalytic activity of LSM decreases, and the conductivity too (~ 180 S /cm at 500 °C), and LSM is no longer an adequate cathode for IT-SOFC´s. Similarly, the conventional electrolyte $Zr_{0.84}Y_{0.16}O_{2-\delta}$ has to be replaced; at IT doped ceria can be used as an electrolyte (e.g. $Ce_{0.8}Gd_{0.2}O_{2-\delta}$, GDC). Currently, one of the cathodic materials that provides the highest performance for IT-SOFC´s is $La_{0.8}Sr_{0.2}Co_{0.2}Fe_{0.8}O_3$ (LSCF), due to its high conductivity (250 S / cm at 500 °C), and its stability and compatibility with GDC [7]. Traditional SOFC applications are in stationary power generation systems, but there are researches to develop micro-cells for portable applications. Micro-tubular SOFC´s (μSOFC´s; with length < 10 cm and diameter < 5 mm) have recently attracted great attention because of their lower operating temperature, higher tolerance to thermal cycling, faster start-up capacity and higher volumetric power density compared to conventional tubular SOFC´s [9,10]. In the present work the results of the performance evaluation, in terms of the electric power density, of a Ni-GDC ($Ce_{0.8}Gd_{0.2}O_{2-\delta}$) / GDC / LSCF ($La_{0.8}Sr_{0.2}Co_{0.2}Fe_{0.8}O_3$) microtubular IT-SOFC prototype are presented.

2. Materials and Methods

The fabrication of the μSOFC´s prototypes was carried out based on a dip coating process. The composition of the anodic, electrolytic and cathodic suspensions are shown in Table 1. Each suspension was homogenized in a cylinder mill, in jars with zirconia spheres, for 24 h. The coatings were made on polymethylmethacrylate bars (PMMA; ~1.10 mm diameter, Goodfellow) of 3 cm in length. First coatings of the anodic layer were made with subsequent drying (at 70 °C - 1 h, then at 100 °C - 1 h) until thickness close to 0.5 mm was reached, then two coatings of the electrolytic layer were made with subsequent drying (at 70 °C - 1 h, then at 100 °C - 1 h). Then the co-sintering of the semi-cell was carried out at 1420 °C for 8 h at a heating rate of 5 °C / min in air. Finally, two coatings of the cathodic layer were made by painting with subsequent drying at room temperature for 24 h. The final sintering of the cell was carried out at 1200 °C for 2 h at a heating rate of 5 °C / min in air. Silver wires were wound around the exposed cathodic (at the center) and anodic (extremes) parts and silver paint was applied, thus forming the current collectors.

Table 1. Composition of the anodic, electrolytic and cathodic suspensions.

Materials	Cathode (wt %)	Anode (wt %)	Electrolyte (wt %)
LSCF (LSCF-P, fuelcellmaterials)	41	-	-
GDC (fuelcellmaterials, 6.0 m^2 / g and *36.0 m^2 / g)	-	25	*20
PMMA (TechPolymer, 99 %)	5	12	-
NiO (fuelcellmaterials, 3.6 m^2 / g)	-	25	-
Ethyl-cellulose (Sigma Aldrich, 99 %)	-	0.5	-
Ink vehicle (fuelcellmaterials)	30	16	80
Bis-(2-ethylhexy) phthalate ((Alfa Aesar, 98 %)	-	5	-
2-butanone (Alfa Aesar, 99 %).	23	15.5	-

The cells were then connected into alumina tubes and a cement sealant was applied (Ceremabond 885). A thermal treatment at 260 and 370 °C for 2 h was carried out. Reduction of anode was performed at 500 °C for 2 h with a 5 mL / min H_2 (saturated with water at room temperature). The characterization of the cells was performed by Scanning Electron Microscopy (SEM), Linear Sweep Voltammetry (LSV) and Electrochemical Impedance Spectroscopy (EIS). Electrochemical measurements were performed with a PARSTAT Model 2273 potentiostat at 500 and 600 °C and a flow rate of 5 mL / min H_2 (3 % H_2O). Characterization by LSV was performed from the open circuit potential down to 0 V. EIS measurements were performed in the frequency range of 0.008 Hz - 1 MHz and an amplitude of 10 mV.

3. Results and Discussion

Figure 2a shows a scanning electron microscopy image, at 60 X, of the cross-sectional surface of a µSOFC manufactured in the present project. Dimensions of the µSOFC´s were: length ~ 1.8 cm and outer diameter ~ 0.8 mm. Figure 2b presents a micrograph at 750 X of the cross section of a prototype; the anodic, electrolytic and cathodic layers could be identified. No open porosity within the electrolyte was observed, which is a requirement to avoid direct contact of the gases supplied to the anodic and cathodic chambers. In contrast, open porosity of the anodic and cathodic sections was also clearly observed. Figure 2c shows a prototype with current collector, in which the cathodic layer is visualized in black, the anode in light green and the electrolytic layer is almost transparent white. Based on SEM images, the estimated thickness of the anode is ~ 290 µm, while the thickness of the electrolyte and cathode was ~ 11 µm and ~ 30 µm, respectively. Based on SEM images obtained from the prototypes and using the Image-J program in its online version for students, the average pore sizes of the anodic and cathodic layer respectively were estimated. An average pore size of ~ 3.92 ± 5.53 µm and ~ 6.58 ± 3.00 µm were obtained for anode and cathode respectively, while the porosity was ~ 27.70 % for anode and ~ 28.01 % for cathode.

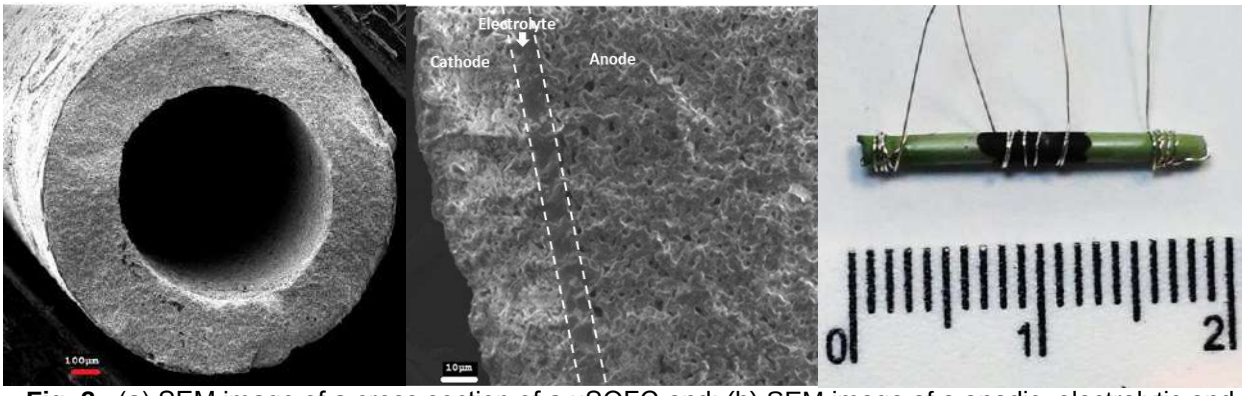

Fig. 2. (a) SEM image of a cross section of a µSOFC and; (b) SEM image of a anodic, electrolytic and cathodic layers of a µSOFC; (c) photograph of a µSOFC prototype.

Figure 3 shows the variation of the voltage and power density as function of current density for the Ni – GDC / GDC / LSCF prototype at 500 and 600 °C. The open circuit voltage (OCV) is ~ 0.98 and ~ 0.99 V at 500 and 600 °C, respectively; these results are close to the theoretical value (~ 1.2 V). The power density of μSOFC prototype increases with increasing the operating temperature. As the current density increases, the potential decreases; this behavior is typical of this type of systems. The maximum power densities are ~ 160 and ~ 225 mW / cm^2 at 500 °C and 600 °C, respectively. These power densities are in the range reported by T. Susuki et al. [11], they report power densities of 140 and 350 mW / cm^2 at 500 and 600 ° C respectively, for a prototype (Ni - GDC / GDC / LSCF) of 10 mm in length. Figure 4 shows EIS results of the Ni – GDC / GDC / LSCF prototype at 500 and 600 °C. The total resistance evaluated by EIS was ~ 600 and ~ 250 Ω at 600 and 500 °C, respectively. The estimated theoretical resistance of the electrolyte ~ 160 and ~ 192 Ω at 500 and 600 °C, respectively, these values agree well with those obtained from the intercepts of the Nyquist plots with the horizontal axis, so that the part of the Nyquist diagram shown in Figure 4 represents the impedance contributions of the anode and cathode in the μSOFC prototype. Unfortunately it was not possible to perform impedance measurements at lower frequency values due to equipment limitations, nor at higher temperatures due to cell degradation, which resulted in fractures occurring in the prototype after these measurements.

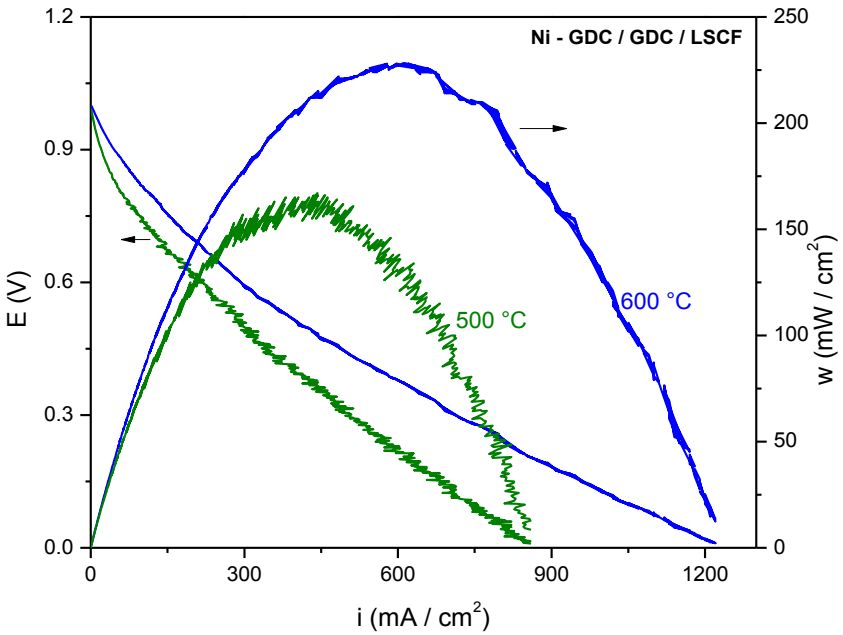

Fig. 3. Polarization curves of a μSOFC at 500 and 600 °C.

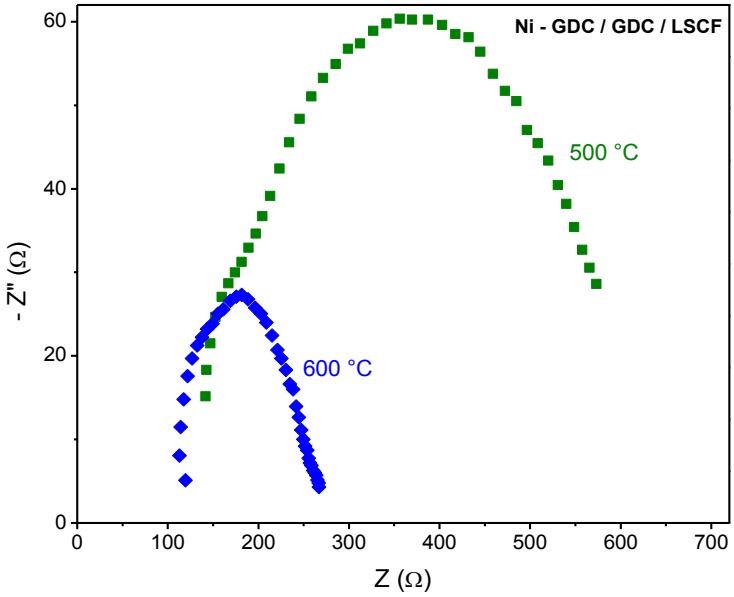

Fig. 4. Nyquist plots of a μSOFC at 500 and 600 °C.

Fabrication conditions of μSOFC prototypes are in the process of optimization, so that degradation of cells during measurements could be reduced and reproducibility of them could be reached.

4. Conclusion

It was possible to construct μSOFC prototypes of using a dip coating technique. The obtained prototypes present a null open porosity in the electrolyte, but the electrodes have adequate porosities. The electrochemically characterized μSOFC had an open circuit potential of ~ 0.98 and V and a power density of ~ 160 and ~ 225 mW / cm^2 at 500 °C and 600 °C, respectively with hydrogen as fuel. The results show to be promising, since the fabrication process could be further optimized.

Acknowledgements

Funding for this research was provided by Universidad Autónoma Metropolitana. C.I. Ramos Villegas is thankful to Consejo Nacional de Ciencia y Tecnología for the scholarship received to pursue his Ph.D. studies.

References

[1] Chandran P. R. and Arjunan. T. V. A Review of materials used for solid oxide fuel cell, International Journal of Chemical Technology Research. Res. 07(01), (2014), 488-497.
[2] Ramírez E. B., Huanosta A., Sebastian J. P., Huerta L., Ortiz A. and Alonso J. C. Structure, composition and electrical properties of YSZ films deposited by ultrasonic spray pyrolysis, Journal Materials Science. 42 (2007), 901-907.
[3] Minh N. Q. and Takahashi T. Science and technology of ceramic fuel cells. Elsevier, 1995.
[4] Wincewicz K. C. Cooper J. S. Journal of Power Sources. 140 (2005), 280-296.
[5] Miriam K. Riess I. Tannhauser D. S. Langpape R. Rohr F. J. Journal of Solis State Chemistry. 42 (1982), 125-129.
[6] www.sureste1558.blogspot.mx , April 2015.
[7] McEvoy A. J. Journal of Materials Science. Materials for high-temperature oxygen reduction in solid oxide fuel cells. 36 (2001), 1087-1091.
[8] Alvarado-Flores J. Espino-Valencia J. Ávalos-Rodríguez L. A. Análisis de materiales catódicos de estructura Perovskita para celdas de combustible de óxido sólido, SOFC´s. Revista Mexicana de Física. 61 (2015), 32-57.
[9] Yang C. Jin C. Cheng F. Micro-tubular solid oxide fuel cells fabricated by phase-inversion method. Electrochemistry Communications. 12 (2001), 657-660.
[10] Yamaguchi T., Galloway K. V., Yoon J., Sammes N.M. Electrochemical characterization of microtubular solid oxide fuel cells under a long-term testing at intermediate temperature operation. Journal of Power Sources. 196 (2011), 2627-2630.
[11] Susuki T., Funahashi Y., Yamaguchi T., Fujishiro Y., Awano M. Fabrication and characterization of micro tubular SOFCs for advanced ceramic reactors. Journal of Alloys and Compounds. 451 (2008), 632-635.

XVIII International Congress
of the Mexican Hydrogen Society

Environmentally friendly low-cost membranes for micro and meso-scale bioelectrochemical systems

MJ González-Pabón[1], F Figueredo[1], DC Martínez-Casillas[2], E Cortón[1*]

[1] Laboratory of Biosensors and Bioanalysis (LABB), Departamento de Química Biológica (IQUIBICEN-CONICET), Facultad de Ciencias Exactas y Naturales, Universidad de Buenos Aires, Ciudad Autónoma de Buenos Aires 1428, Argentina.
[2] Instituto de Energías Renovables, Universidad Nacional Autónoma de México, Priv. Xochicalco s/n, Col. Centro, 62580 Temixco, Morelos, México.
* eduardo@qb.fcen.uba.ar. TEL/FAX: INT + 54-11-4576-3342.

ABSTRACT

Microbial fuel cells (MFCs) and microbial electrolysis cells (MECs) are well known bio-electrochemical systems (BESs) that can be used to produce electricity, and hydrogen respectively, by means of microbial metabolic activity. Nonetheless, new strategies for constructions, start up, operation and maintenance are required to improve BESs efficiency and commercial feasibility. At that point, BESs manufacturing materials (electrodes and membranes) represent the main bottleneck for industrial use and scalable real-world applications. Then, one of the challenges to make MFCs and MECs a viable technology is to obtain low cost and environmentally sound materials to fabricate them. In this work we synthesized membranes by a simple procedure: using solution casting and solvent evaporation technique, involving low price and biodegradable materials such as poly (vinyl alcohol) (PVA), chitosan (CS) and PVA:CS, all cross-linked with sulfuric acid. The synthesized membranes were characterized by SEM and EIS, as well as their water uptake, oxygen diffusion and MFC performance, and compared to Nafion® 117, as our reference/control membrane. Conductivity values of the three synthesized membranes were lower than Nafion®. However, PVA and PVA:CS show lower oxygen permeability in comparison to Nafion® membranes, a strong advantage in order to maintain anaerobic conditions in the anodic compartment of MFCs. Membranes were first studied in a typical meso-scale H-Type MFCs with LB medium containing *E. coli* (OD = 1). Our results show that CS membrane has the best current output performance (76.1 ± 11.9 mA/m^2). On the other hand, PVA:CS membranes outperform Nafion® being more economic and performing better at MFC set up (power production). Furthermore, the best membrane in terms of power generation (PVA:CS) were used to made disposables paper-based micro-scale devices (16 µL), were power production was 6.95 ± 0.7 µW/cm^3. PVA:CS membranes presented here can be useful to fabricate miniaturized and biodegradable MFC, for analytical uses as biosensors, and meso-systems capable to produce energy in a sustainable mode.

Keywords: green technology; low cost membrane; oxygen permeability; micro-scale MFC; meso-scale MFC; PEM substitute.

1. Introduction

Bio-electrochemical systems (BESs) as microbial electrolysis cells (MECs) and microbial fuel cells (MFCs), can be used in different application. While MECs can produce hydrogen gas by metabolic microbial activity helped by an external supply of electricity [1-2], MFCs can be used for energy production and bio sensing applications [3]. MECs and MFCs (known as MXCs) are classify of many ways i.e. according architecture, scale, construction aspects and operation modes. Scaling up BESs make possible their use as power source, hydrogen production and wastewater treatment. Scaling down BESs enable their use as sensor and implantable power systems [4-5]. According total volume (V_t), MXCs can categorize as macro (V_t > 500 mL), meso (500 mL>= V_t >= 0.2 µL) and micro-scale MFCs (V_t <200 µL) [6]. Scaling of MXCs technology and massive production have to consider the use of materials and components with industrial characteristics as being easy to fabricate and dispose, use readily available low-cost materials, and have low environmental impact; moreover, the overall cost must be related to the price level that the product can find in the market.

MXCs mainly components are the electrodes and separation membranes. Electrodes are needed for the oxidation-reduction reactions. Membranes in MFCs allow a selective transport of protons from the anode to the cathode, avoiding the homogenization of the MFC compartments; also prevent the oxygen transport into the anode chamber [7]. Membranes in MECs systems improve the purity of the collected hydrogen, and prevent the consumption of this gas by some members of the microbial community [8]. In this study, we focused our work on the synthesis of alternatives membranes to Nafion, the commonly used polymeric exchange membrane (PEM) used in fuel cells and MXCs [9-10]. Some of the Nafion disadvantages are: i) high cost (about 1767 USD m^{-2}), ii) requires several activation steps [10], iii) present high oxygen permeability, that allows oxygen leakage from cathode to anode [11], iv) Nafion properties as extraordinary chemical and thermal stability become a problem when it needs to be disposed as waste.

Composite materials formed by polymers as chitosan (CS) have been previously investigated for MXCs membranes with promising good results in terms of low cost, reduced biofouling and oxygen diffusion [12-13]. Chitosan (CS) have been proposed for membrane fabrication since it is an abundant and natural polymer [14-15]. Free amine and hydroxyl groups (potential reactive sites) on the CS's backbone [16] make possible further CS modifications by cross-linking with sulphonic groups. Furthermore, CS can be blended with either hydrophilic or hydrophobic polymers (e.g. PVA) to enhance mechanical and thermal stability [17].

This work shows the synthesis of three economic and environmentally friendly (biodegradable) alternative membranes for MFCs devices, based on PVA, CS and PVA:CS. Features such as morphology, water uptake, conductivity, thickness, oxygen mass transfer and MFC-performance were assayed for all membranes prepared and compared with a Nafion (a well-known commercial membrane, used as a control). After MFC performance was assayed in a classical two-compartment H-type cell, the best membrane was further coupled with paper-based low cost electrodes in a meso-scale and micro-scale MFC system.

2. Materials and Methods

2.1 Reagents and Nafion® commercial membranes

Poly (vinyl alcohol), degree of polymerization ~1600, degree of hydrolysis 97.5-99.5 mol % and chitosan (poly-(1,4)-β-N-acetyl-D-glucosamine) low molecular weight with around 50% deacetylation degree were supplied by Sigma Aldrich. Analytical grade acetic and sulfuric acids were obtained from the same company. Dextrose anhydrous, sodium sulphite, methylene blue, NaCl, KCl, K_2HPO_4 were also used. Nafion® 117 membrane was obtained from DuPont Co. (Wilmington, DE, USA), and named in the text simply as Nafion.

2.2 Membrane synthesis

CS, PVA and PVA:CS membrane were synthesized by using solution casting and solvent evaporation technique, based on reported methodologies [18-21] used mainly for fuel cell membrane synthesis. After the synthesis procedure, all membranes were washed with Milli-Q water and stored at room temperature in a Falcon tube containing Milli-Q water.

2.3 Membrane activation procedure

The Nafion membrane was activated before to use by procedure describe by Hernandez-Flórez [10]. The three membranes synthesized in this work (CS, PVA and PVA:CS) were used without any activation procedure.

2.4 Surface topography study

Morphology of the synthesized membranes was observed with a field emission scanning electron microscope (FE-SEM Carl Zeiss NTS SUPRA 40, USA). The samples were dehydrated by immersion in alcohol solutions of 25-100 % v/v followed by sputter-coating with a thin layer of gold (20 nm) using a current of 30 mA for 30 s.

2.5 Water uptake capacity

The water uptake capacity of membranes was calculated by measuring membrane weight changes before and after hydration process. The membranes were first dried in an oven at 30°C for 15 h and then weighed (W_{dry}). Once dried, membranes were immersed in Milli-Q water during control times periods. By removing the excess water and weighing the membrane in a precision balance the wet weight (W_{wet}) of the membrane was determined. This measurement was conducted in triplicate. The water uptake (%W) was calculated with the following equation [22-23].

$$\%W = (W_{wet} - W_{dry}) / W_{dry})_{x} 100 \quad (1)$$

2.6 Conductivity determination

Electrochemical impedance (EIS) technique was used to determine proton conductivity of the synthesized and Nafion membranes. Range of frequency used for EIS analysis was 10^{-1} and 10^{6} Hz at open circuit potential with amplitude of 5 mV, using a commercial potentiostat (Interface 1000, Gamry, PA, USA). A four electrode cell was constructed in the laboratory, by using Teflon blocks and Pd wires [18, 24]. The analysis was performed at room temperature under 100 % RH

(relative humidity), achieved by immersing the membranes in Milli-Q water before each measurement (n = 3). Gamry Echem Analyst software was used to simulate equivalent circuits and data tuning to extract the ohmic or bulk resistance of the membrane. The conductivity was calculated with the following equation: $\sigma = l / (RS)$ (2). Where σ is conductivity (S cm^{-1}), *l* is the distance between the electrodes (cm), *R* is the ohmic resistance (Ω) of the membrane sample and *S* is the cross-sectional area of the membrane (cm^2) [18].

2.7 Dissolved oxygen crossover determination

Oxygen transport was measured with an oxygen probe (oxygen meter Model DO-5510 by Lutron Electronic Enterprise Co., Ltd., Taipei, Taiwan). A small diffusion cell was used, made it by replacing the original oxygen diffusion membrane of the oxygen electrode (as provided by the company) by the fabricated membranes (or Nafion) to be assayed. N_2 was bubbled to equilibrate the receptor (electrode chamber) and donor chambers. After that, the N_2 stream was stopped and air was bubbled at the donor chamber. DO was monitored in the receptor chamber. The oxygen transfer coefficient (k_{O_2}) was determined using the mass balance equation:

$$k_{O_2} = -\frac{V}{At}\ln\left[\left(\frac{C_{O_2}-C}{C_{O_2}}\right)\right] \quad (3)$$

Where *V* is the receptor chamber volume (50 µL), *A* is the membrane cross-sectional area, C_{O2} is the saturated oxygen concentration in the donor chamber, *C* is the DO concentration in the receptor chambers at time *t* [23, 24-25]. The oxygen diffusion coefficient (Do, cm^2 s^{-1}) was calculated replacing the membrane thickness (L_t) in the follow equation:

$$D_O = k_{O_2} L_t \quad (4)$$

2.8 H-type MFC architecture and operation

The performance of membranes (1.3 cm^2) was evaluated by polarization studies, by placing each membrane as separator of an H-Type MFC; anodic and cathodic compartments. All membranes used were disposed after each experiment (5 h of operation approximately). Toray paper was used as anode and cathode electrodes. The cathode compartment was filled with 16 mL a solution containing potassium ferricyanide (50 mM) and phosphate buffered (0.1 M, pH 6.2), whereas the anode compartment was filled with LB medium containing *E. coli* (OD = 1) and methylene blue (100 µM). Before MFC measurements, the anode compartment was bubbled with N_2 during 5 min to reach anoxic conditions. MFCs were maintained in a thermostatic chamber at 30º C during all the experiments. Potential measurements were done after 1 h at open circuit (OCV) and recorded with a data acquisition board (NI-USB 6210, National Instruments, USA) connected to a personal computer. Current (I, ampere) was calculated as I = E/R (5), where R was the external circuit resistor. Power (P, watt) was calculated as P = IE (6). These values were normalized by using the electrode geometrical area (4 cm^2 when H-type MFC was assayed), to obtain the current (*j*, A m^{-2}) and power (*p*, W m^{-2}) densities.

2.9 Meso and micro-scale, full assembled with low cost materials

The membrane that showed the best performance at H-type MFC experiments (Section 2.8) was also coupled in a fully low cost MFC system, that included our low-cost carbon nanotube-based (CNT) electrodes [26] in a meso-scale systems (H-type, section 2.8) as well micro-scale paper based MFC. Anodic and cathodic reservoirs in micro-scale paper based MFC were made of filter paper (Whatman N° 1). The volume of each compartment was chosen to be 1000-folds smaller than the H-Type MFC used, of 16 µL. The cathodic compartment solution was the same previously used (Section 2.8), whereas the anode compartment was filled with a solution containing *E. coli* (1.0×10^9 CFU mL^{-1}) in a minimal medium constituted by phosphate buffer (0.1 M, pH 6.2), glucose (20 g L^{-1}), sodium sulfite (0.1 g L^{-1}) and methylene blue (100 µM).

3. Results and Discussion

3.1 Surface topography study

FE-SEM pictures of CS membranes show a rough surface and porous structure, with pores of different diameters as can be seen in Fig. 1 (a-b) indicated by open arrows. PVA:CS and PVA membranes show a non-porous structure, with a mostly smooth surface and the presence of crystals indicated with solid arrows, Fig. 1 (c-d) and Fig. 1 (e-f), respectively. Surface topology is linked with fouling tendency of membranes, as well other properties. Rough surfaces foul more easily than smooth surfaces, due to the increase of surface area [13].

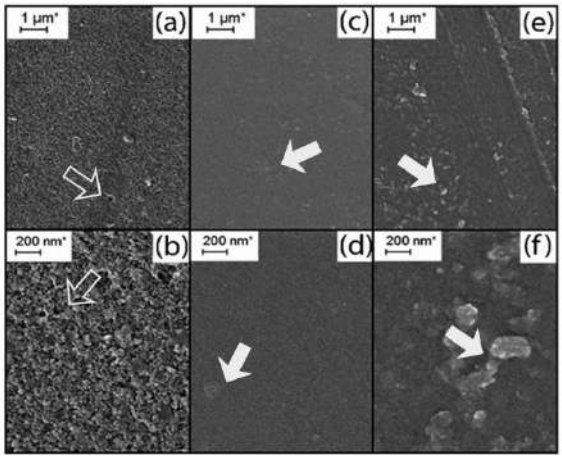

Figure 1. FE-SEM micrograph of the synthesized membranes. (a-b) CS, (c-d) PVA:CS and (e-f) PVA membranes. Open arrows indicates the pores, and solid arrows the PVA crystals.

3.2 Water uptake capacity

All membranes, including Nafion were quickly full hydrated in less than 20 min. Nafion water uptake value obtained was (23.32 ± 0.77) %, whereas synthesized membranes achieved more than 100% of their dry weight. Water uptake values obtained were (111.47 ± 3.28) % for CS, (105.18 ± 4.86) % for PVA and (108.73 ± 1.72) % for PVA:CS. The higher water uptake showed

by our synthesized membranes (when compared with Nafion) could be a great advantage when considering hydrated proton transport in water, which can considerably increase the proton mobility [23].

3.3 Membrane conductivity

Internal resistance of membranes were obtained by EIS technique (Fig. 2) and used to calculated proton conductivity (equation 2). The proton conductivities obtained were 11.9, 3.9, 11.3 and 81.0 mS cm^{-1} for CS, PVA, PVA:CS and Nafion, respectively. The chitosan based membranes displayed higher conductivity values than PVA membranes. Membrane conductivity is an important aspect when parameters such as voltage and current of a MFC are analyzed.

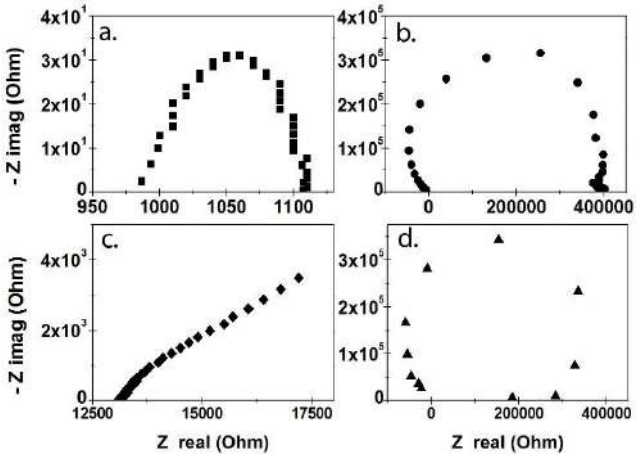

Figure 1. Nyquist plot for membranes tested. 1MHz-100 Hz of frequency. a. Nafion. b. PVA:CS. c. CS. and d. PVA.

3.4 Membrane dissolved oxygen crossover

Anoxic conditions in anodic compartment must be guaranteed in MFC operations. Anoxic conditions are necessary in the anodic chambers to avoid competition between the electrode and oxygen as electron acceptors; also, oxygen can be toxic for anaerobic bacteria [11]. For these reasons is important evaluate the oxygen crossover of the membranes. CS membrane shows the higher oxygen mass transfer (k_{O_2}), of 6.67 × 10^{-4} ± 9.8% cm s^{-1}. This can be related to it porous structure, as revealed in SEM pictures (Fig. 1a-b), which can allow easy oxygen permeation. PVA and PVA:CS membranes were very similar in their behavior (k_{O_2}), 1.70 × 10^{-4} ± 5.6% and 1.50 × 10^{-4} ± 1.5%, respectively, their oxygen permeability was approximately 4 times lower than CS membranes. These are the two membranes with better characteristic with respect to this parameter, to be used as MFC membranes. Nafion shows an intermediate oxygen mass transfer coefficient (2.71× 10^{-4} ± 10.8%), lower than CS and higher than PVA and PVA:CS.

3.5 MFCs performance in H-type cells

Synthetized membranes were assessment in H-type MFC in order to evaluate the membrane's effects under practical operational conditions. We used Nafion membrane as reference membrane for made our results stronger and comparable with respect to other published works. First, the MFC's OCV was measured for 1 hour and after 30 min, we obtained a stable OCV value. Then, the performance of each MFC was studied after the polarization experiments were made; adjusting the external load on the circuit, and measuring the stabilized potential (at 20 min). Maximum power densities are presented in Fig. 3. Among the membranes tested, MFCs with the Nafion and PVA membranes showed the lowest maximum power density (p_{max}), of about 5.6 ± 0.1 and 5.7 ± 0.9 mW m^{-2} respectively. On the other hand, CS containing membranes showed higher values of current (at their maximum power values, J_{max}) of 70.8 ± 6.3 and 76.1 ± 11.9 mA m^{-2} for PVA:CS and CS, respectively, and maximum power, p_{max} of 20.8 ± 2.9 and 11.5 ± 2.7 mW m^{-2} for PVA:CS and CS.

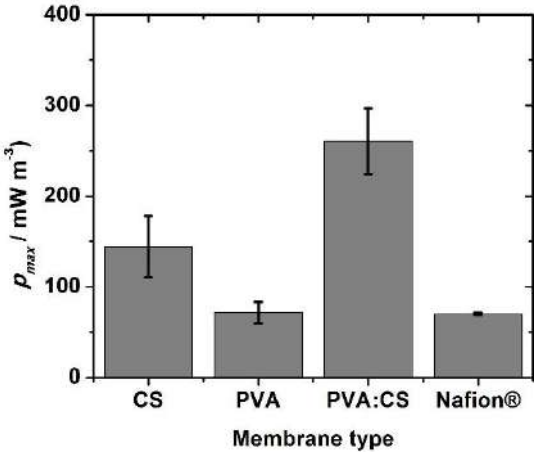

Fig. 3. H-Type MFC performance. Maximum power densities archived by CS, PVA, PVA:CS and Nafion® membranes. Standard deviations are presented at all data points.

PVA:CS membranes showed great characteristics related to the oxygen permeability, conductivity, and fourfolds more efficient than Nafion, when p_{max} is compared. These results indicate that this membrane has the potential to be employed as alternative to Nafion. Moreover, the MFCs assembled with the CS membranes, showed the highest J_{max} values and achieves the second-best power density. This reduction in power density performance of MFCs assembled with the CS membranes could be attributed to the high oxygen permeability of this membrane (section 3.4) due to its porous structure. Hence, oxygen reach the anodic compartment and acts as final electron acceptor instead of the electrode. As consequence, there are energy losses, and in general the MFC's efficiency is low.

On other side, cost analyst of PVA:CS membrane disclose a calculated cost of around 8.9 USD m^{-2}, meaning that PVA:CS copolymer is not only more efficient when used in a MFC, but also cost-effective, about 75 times cheaper.

3.6 Meso and micro-scale, full assembled with low cost materials

The membrane that showed the best performance at H-type MFC experiments (PVA:CS membrane, section 3.5) was assembled using low-cost materials, as CNT electrodes in a meso-scale systems (H-type MFC) as well in a micro-scale paper based MFC. Polarizations studies could be seem in Fig 4.

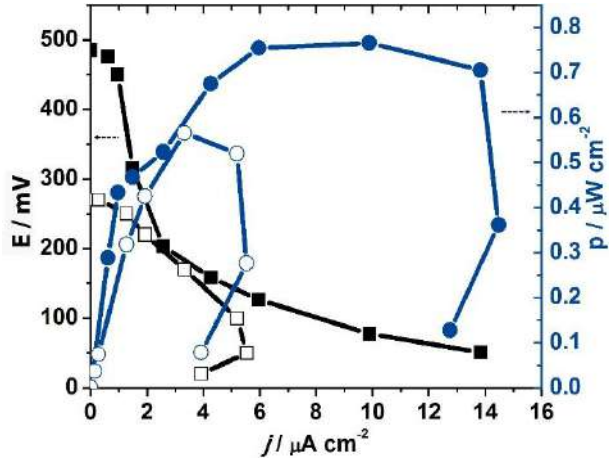

Fig. 4. Representative polarization and power curves of meso and micro-scale MFC. Meso-scale (H-type) system performance (solid symbol) and micro-scale (paper-based MFC) system performance (open symbol).

4. Conclusion

PVA, CS and PVA:CS based membranes were fabricated and characterized for meso-scale MFC and micro-scale MFC. Performance of PVA:CS membrane (MFC assayed) was higher compared with Nafion, PVA or CS membranes. One of the mainly advantages of PVA:CS membrane is that the oxygen permeability measured was lower than Nafion. However, conductivity values of PVA:CS membrane was lower than Nafion, we found very good performance of the PVA:CS membrane when it was incorporated to an H-Type MFC and into a paper-based micro-scale MFC. In this study, we described a high performance, biodegradable and cost-effective PVA:CS membrane capable of outperforming Nafion at least in the conditions we assayed, related with low-density power systems, as MFC. This behavior could be related to the interactions of all the characteristics of each membrane type.

Acknowledgements

The work presented here was funded by the National Agency of Scientific and Technological Promotion (ANPCyT) and CONICET.

References

[1] Li Z, Fu Q, Kobayashi H, Xiao S. Biofuel Production from Bioelectrochemical Systems. In: Liao Q, Chang J, Herrmann C, Xia A. (Eds) Bioreactors for Microbial Biomass and Energy Conversion. Green Energy and Technology. Springer, Singapore 2018. https://doi.org/10.1007/978-981-10-7677-0_11

[2] Kumar G, Saratale RG, Kadier A, Sivagurunathan P, Zhen G, Kim SH, et al. A review on bio-electrochemical systems (BESs) for the syngas and value added biochemicals production. Chemosphere 2017;177:84-92.https://doi.org/10.1016/j.chemosphere.2017.02.135

[3] Jiang Y, Yang X, Liang P, Liu P, Huang X. Microbial fuel cell sensors for water quality early warning systems: Fundamentals, signal resolution, optimization and future challenges. Renew. Sustain. Energy Rev 2018;81:292–305. https://doi.org/10.1016/j.rser.2017.06.099.

[4] Abrevaya XC, Sacco NJ, Bonetto MC, Hilding-Ohlsson A, Cortón E. Analytical applications of microbial fuel cells. Part I: Biochemical oxygen demand. Biosens Bioelectron 2015;63:580–90. https://doi.org/10.1016/j.bios.2014.04.034.

[5] Abrevaya XC, Sacco NJ, Bonetto MC, Hilding-Ohlsson A, Cortón E. Analytical applications of microbial fuel cells. Part II: Toxicity, microbial activity and quantification, single analyte detection and other uses. Biosens Bioelectron 2015;63:591–601. https://doi.org/10.1016/j.bios.2014.04.053.

[6] Ren H, Lee HS, Chae J, 2012. Miniaturizing microbial fuel cells for potential portable power sources: promises and challenges. Microfluid. Nanofluidics 2012;13:353–81. https://doi.org/10.1007/s10404-012-0986-7

[7] Christgen B, Scott K, Dolfing J, Head IM, Curtis TP. An evaluation of the performance and economics of membranes and separators in single chamber microbial fuel cells treating domestic wastewater. PloS One 2015. https://doi.org/10.1371/journal.pone.0136108.

[8] Kadier A, Simayi Y, Abdeshahian P, Azman NF, Chandrasekhar K, Kalil, MS, 2016. A comprehensive review of microbial electrolysis cells (MEC) reactor designs and configurations for sustainable hydrogen gas production. Alexandria Eng. J 2016;55:427–43. https://doi.org/10.1016/j.aej.2015.10.008

[9] Mauritz KA, Moore RB. State of understanding of Nafion. Chem Rev 2004;104:4535–86. https://doi.org/10.1021/cr0207123.

[10]Hernández-Flores G, Poggi-Varaldo HM, Solorza-Feria O. Comparison of alternative membranes to replace high cost Nafion ones in microbial fuel cells. Int. J. Hydrogen Energy. 2016;41: 23354-62. https://doi.org/10.1016/j.ijhydene.2016.08.206

[11]Chae KJ, Choi M, Ajayi FF, Park W, Chang IS, Kim IS. Mass transport through a proton exchange membrane (Nafion) in microbial fuel cells. Energ Fuels 2008; 22:169–76. https://doi.org/10.1021/ef700308u.

[12]Wu H, Fu Y, Guo C, Li Y, Jiang N, Yin C. Electricity generation and removal performance of a microbial fuel cell using sulfonated poly (ether ether ketone) as proton exchange membrane to treat phenol/acetone wastewater. Bioresource Technol 2018;260:130-4. https://doi.org/10.1016/j.biortech.2018.03.133.

[13]Antolini E. Composite materials for polymer electrolyte membrane microbial fuel cells. Biosens Bioelectron 2015; 69:54–70. https://doi.org/10.1016/j.bios.2015.02.013.

[14]Kalaiselvimary J, Sundararajan M, Prabhu MR. Preparation and characterization of chitosan-based nanocomposite hybrid polymer electrolyte membranes for fuel cell application, Ionics 2018;1-17. https://doi.org/10.1007/s11581-018-2485-7
[15]Witt MA, Barra GMO, Bertolino JR, Pires ATN. Crosslinked chitosan/poly (vinyl alcohol) blends with proton conductivity characteristic. J Braz Chem Soc. 2010;21:1692–8. http://dx.doi.org/10.1590/S0103-50532010000900014.
[16]Ye YS, Rick J, Hwang BJ. Water soluble polymers as proton exchange membranes for fuel cells. Polymers 2012; 4:913–63. https://doi.org/10.3390/polym4020913.
[17]Rhim J, Park H, Lee C, Jun J, Kim D, Lee Y. Crosslinked poly (vinyl alcohol) membranes containing sulfonic acid group: Proton and methanol transport through membranes, J Memb Sci 2004;238:143–51. https://doi.org/10.1016/j.memsci.2004.03.030.
[18]Mukoma P, Jooste BR, Vosloo HCM. Synthesis and characterization of cross-linked chitosan membranes for application as alternative proton exchange membrane materials in fuel cells, J Power Sources 2004;136:16–23. https://doi.org/10.1016/j.jpowsour.2004.05.027.
[19]Mukoma P, Jooste BR, Vosloo HCM. A comparison of methanol permeability in Chitosan and Nafion 117 membranes at high to medium methanol concentrations, J Memb Sci 2004;243: 293–9. https://doi.org/10.1016/j.memsci.2004.06.032.
[20]Papancea A, Valente AJM, Patachia S. PVA cryogel membranes as a promising tool for the retention and separation of metal ions from aqueous solutions, J Appl Polym Sci 2010;118:1567–73. https://doi.org/10.1002/app.32514.
[21]Darbari ZM, Mungray AA. Synthesis of an electrically cleanable forward osmosis membrane, Desalin Water Treat 2016;57:1634–46. https://doi.org/10.1080/19443994.2014.978390.
[22]Srinophakun P, Thanapimmetha A, Plangsri S, Vetchayakunchai S, Saisriyoot M. Application of modified chitosan membrane for microbial fuel cell: Roles of proton carrier site and positive charge. J Clean Prod 2017; 142: 1274–82. https://doi.org/10.1016/j.jclepro.2016.06.153.
[23]Kim Y, Shin SH, Chang IS, Moon SH. Characterization of uncharged and sulfonated porous poly (vinylidene fluoride) membranes and their performance in microbial fuel cells. J Memb Sci 2014; 463: 205–14. https://doi.org/10.1016/j.memsci.2014.03.061.
[24]Lee CH, Park HB, Lee YM, Lee RD. Importance of proton conductivity measurement in polymer electrolyte membrane for fuel cell application. Ind Eng Chem Res 2005;44:7617–26. https://doi.org/10.1021/ie0501172.
[25]Zinadini S, Zinatizadeh AA, Rahimi M, Vatanpour V, Rahimi Z. High power generation and COD removal in a microbial fuel cell operated by a novel sulfonated PES/PES blend proton exchange membrane, Energy 2017;125;427–38. https://doi.org/10.1016/j.energy.2017.02.146.
[26]Figueredo F, Gonzalez-Pabon MJ, Corton E. Low cost layer by layer construction of CNT/chitosan flexible paper-based electrodes: a versatile electrochemical platform for point of care and point of need testing. Electroanalysis 2018;30; 497-508.
[27]Day TJ, Schmitt UW, Voth GA, The mechanism of hydrated proton transport in water, J Am Chem Soc 2000;122:12027-8. https://doi.org/10.1021/ja002506n.

XVIII International Congress
of the Mexican Hydrogen Society

FUEL CELL DESIGN UP TO 50 W

A. T. Rodríguez-Victoria[1]; J. M. Sandoval Pineda[1], R de G. González-Huerta[2], M. Rico-Cortez[3]

[1]Instituto Politécnico Nacional, ESIME-Azc., SEPI, Av. de las Granjas 682, Col. Santa Catarina, CP 02250, CDMX
[2]Instituto Politécnico Nacional, ESIQIE, Laboratorio de Electroquímica y Corrosión, UPALM, CP 07738, CDMX
[3]Instituto Politécnico Nacional, ESIME, SEPI, Edificio 5 tercer piso, UPALM, CP 07738, CDMX
*Mail: ale_tona@icloud.com

RESUMEN

The concept of H2 as an energy carrier is often discussed. This concept can best be described in the context of H2 produced directly from water by electrolysis. While this process is not economically attractive at current costs, if the electricity required to convert H2O to H2 is provided by wind, ocean or solar energy, then H2 is produced without creating any CO2. Given the intermittent nature of renewable energy sources, the excess energy produced during large windy waves or sunny days could be used to produce H2 that is stored for later use. The energy stored in the hydrogen can be converted into useful energy (electricity) through the fuel cells.
In this research work we present the design of a fuel cell stack based on the APQP methodology, a virtual prototype was developed with the capacity to generate up to 50 W of power for lighting applications. The virtual design of the flow fields of the bipolar plates, which are a key component in this device, was performed. The bipolar plates connect each cell electrically, while the flow fields supply reactive gases to the anode and the cathode, and remove the reaction products from the cell. The novel promise that is proposed in this work, is the design and mechanization of the flow fields of radial type, 2 design alternatives are proposed based on the Fibonacci sequence, the objective is to observe the effect of orientation of the flow through the radial configuration, to understand and evaluate the effects of these configurations on the behavior of the fuel cell. As a result, a comparative analysis of these configurations was obtained evaluating the dispersion of the gases in the entire active area. It has been found that the uniformity of the dispersion of the gases depends to a large extent on the design of the flow channels.

palabras clave: *pila, celda de combustible, campos de flujo, hidrógeno, Fibonacci.*

1. Introduction

At present, the generation of energy with conventional sources and their excessive consumption are part of global warming. Experts' predictions indicate that greenhouse gas emissions will continue to rise in this century. Based on the foregoing, there are economic and

environmental reasons to encourage the use of alternative sources of energy. A variety of fuels have been proposed, including reformulated gasoline, ethanol, methanol and hydrogen. Of all these alternatives, hydrogen offers the greatest potential to reduce environmental pollution and the greatest benefits to complement the demand for energy.

The term "Hydrogen economy" is used in order to describe a different scenario, where pollution problems will be solved and our energy needs will be covered permanently and safely, without damaging the environment. The transition to a hydrogen economy can end the dependence on oil. It is important to free the world from the energy economy of fossil fuels to limit CO2 emissions and thus mitigate the effects of global warming on the already damaged biosphere of the earth [1].

In this sense, in recent years, great efforts have been made to reduce the impact of human activity on the environment and reduce the amount of pollutants in the atmosphere. The efforts have covered several scientific and technological aspects, including the development of new energy generating systems, which do not constitute a risk to the environment. These systems must comply with the requirements of zero or very low emissions of polluting waste into the atmosphere and present high conversion efficiencies. One of the most studied and most technologically advanced alternative technologies is that of fuel cells [2].

Fuel cells are a very promising energy technology with countless possible applications, fuel cells have many properties that make them attractive compared to conventional energy conversion technologies. These properties include the following: High efficiency, national security problems, simplicity and promise of low cost, size and weight [3].

2. Theoretical fundament

A fuel cell is an electrochemical energy converter that converts the chemical energy of the fuel into a process of generating electricity. A fuel cell generates electricity in a single step without the participation of moving parts, such device must be simpler therefore less expensive and much more efficient than four-step processes (internal or external combustion engines).

One of the main components of the PEM cells are bipolar plates, which fulfill several functions: carry the current in the cells, distribute heat and water flow in the assembly, allowing the flow of reagents in the device and providing structural integrity to the pile. To optimize the manufacturing process of the cells, different approaches have been implemented, from the use of different materials, to structural changes in the different flow fields [2].

The general principles of engineering can be applied to all types of fuel cells, this work deals with the PEM fuel cells its operation and design. PEM means polymer electrolyte membrane or proton exchange membrane, this technology has attracted attention for its simplicity, feasibility and quick start, as well as for the fact that it has been demonstrated in any conceivable application. At the heart of a PEM fuel cell is a polymer membrane that has unique capabilities, is gas-impermeable, but is proton-conducting. The membrane that acts as an electrolyte is compressed between the two electrically conductive porous electrodes. These electrodes are usually made of carbon cloth or carbon fiber paper. At the interface between the porous electrode and the support is a layer with catalyst particles, which typically works with carbon, the electrochemical reactions occur at the surface of the catalyst at the interface between the electrolyte and the membrane.

Hydrogen, which is fed on one side of the membrane, is divided into its primary components: protons and electrons. Each hydrogen atom consists of an electron and a proton. Protons travel through the membrane, while electrons travel through electrically conductive electrodes, through current collectors, and through the outer circuit where they perform useful work and return to the other side of the membrane. of catalyst between the membrane and the other electrode meets the protons that traversed the membrane and the oxygen that is fed on this side of the membrane. Water is created in the electrochemical reaction and then expelled from the cell with excess oxygen flow. The net result of these simultaneous reactions is a current of electrons through a direct electric current from an external circuit. The hydrogen side is negative and is called the anode, while the oxygen side of the fuel cell is positive and is called the cathode [3].

3. Fuel cell design

In the present work we describe the design of a fuel cell with the capacity to generate 50 W of power, with a radial type geometry for the flow channels. following the methodologies applied to it, thus explaining the design, It was decided to use the APQP methodology (advanced planning of product quality) to ensure as a result a reliable product for experimental purposes.

3.1 Phases of the APQP

a) Planning and definition of the program.
b) Design and development of the product.
c) Design and development of the process.
d) Production and validation of the process.
e) Launch, feedback, achievements and corrective measures.

3.1.1 Planning and definition of the program

In the case of the prototype to be developed, it is necessary to comply with the requirements for a fuel cell. The operation and structure of the components of the PEM fuel cells make it possible to understand their operation, whether in a stationary or dynamic state; having as base the kinetics of the electrochemical reactions, the physical and chemical properties of the membrane and the transport capacity of the internal layers.

The structure and components of a PEM cell are schematically presented in Figures 1A and 1B: The gas conducting channels of the anode, the gas diffusing layer of the anode, the anode catalyst layer, the proton exchange membrane, the catalytic layer of the cathode, its respective gas diffusing layer and finally the gas conduits of the cathode. Note the presence of nanocarbon particles as a support for platinum in the catalyst layers [6].

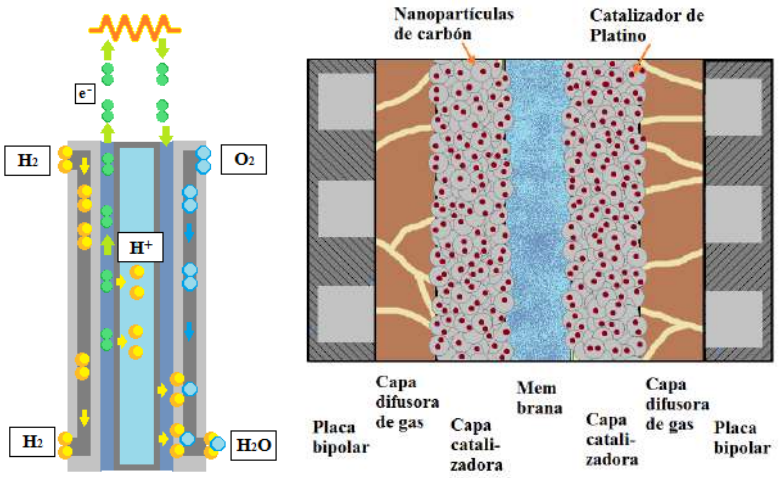

Fig. 1. (A) Diagram of the PEM cells. (B) MEA internal schema (Membrane Electrode Assembly, Membrane Electrode Assembly).

It has been recognized that both performance and operational stability of the proton exchange membrane fuel cells (PEMFC) are closely related to water transport and accumulation behaviors in the membrane electrode array. Therefore, optimal water management is highly desired.

In addition to the conventional parallel flow fields, serpentine flow fields, interdigitated flow fields, and other novel flow fields have also been proposed, such as mesh flow fields, cascading flow fields, fractal flow fields, fields of bionic flow and combined designs, Figure 2 shows some of the different types of commercial flow fields for PEM type fuel cells.

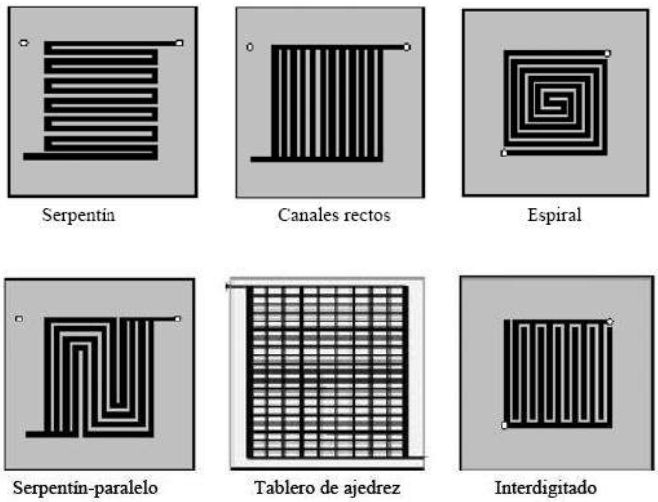

Fig. 2. Types of flow fields for bipolar plates of PEM type fuel cells

Although the aforementioned designs show their corresponding advantages, serpentine flow fields are still considered the most popular choice because of their high performance, reliability and acceptable pressure drop [4].

The water generated by the electrochemical reactions and the humidification of the reagents goes to the cathode side of the PEM fuel cell due to the gradient of temperature, local pressure and electro-osmotic resistance. The accumulation of water droplets on the cathode side in the PEM fuel cell occurs at high current densities and low temperatures. The accumulation of liquid water on the surface of the gas diffusion layer (GDL) reduces the efficiency of the PEM fuel cells. On the other hand, channel blockage increases pressure drop and pressure fluctuations, but on the other side, the polymer membrane must be humidified to preserve its ionic conductivity. Therefore, the flow fields must be designed and manufactured in such a way that there is neither flooding nor dehydration in the PEM fuel cell [5].

One of the main components of the PEM cells are the bipolar plates, which fulfill diverse functions: to carry the current in the cells, to distribute the heat and the water flow in the assembly, allowing the flow of reagents in the device and providing structural integrity to the pile. To optimize the manufacturing process of the cells, there are different approaches, from the use of different materials, such as graphite compounds or metal alloys; to structural changes in the different flow fields as can be seen in the commercial field [6].

In the present work the design of the 2-channel geometry is done, inspired by the Fibonacci sequence, the Fibonacci sequence is the succession of numbers that, starting from the unit, each of its terms is the sum of the previous ones (1,1,2,3,5,8,13). Surprisingly, such a mathematical construction appears recurrently in nature. The distribution of the leaves around the stem, the reproduction of the rabbits, or the arrangement of the seeds in numerous flowers and fruits is produced following sequences based exclusively on these numbers. In the case of radial type flow channels, designs are studied to improve cell performance, as well as to observe the effect of orienting the flow through the type of radial configuration.

Through a series of sketches the main idea is silvered, in figure 3 a flow field is described for the distribution of reagents inside a PEM type fuel cell. The objective of this flow field design is to guarantee the distribution uniform of reactive gases and the elimination of water.

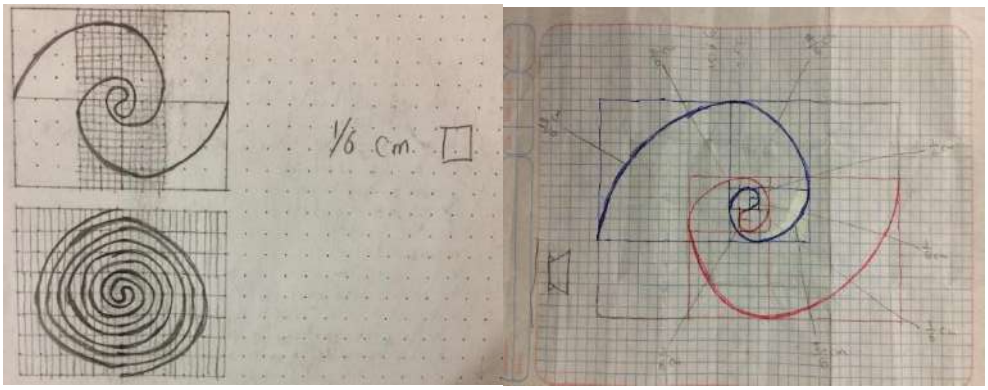

Fig. 3. Conceptual design of radial type flow channels.

3.1.2 *Design and product development*

Current collector plates are another key point in the construction of a PEM fuel cell. These dishes are the part with the greatest economic impact in the cells. There have been many economic studies on the subject, including mathematical models that help in the decision to use some material especially in accordance with different needs. These plates must have the following characteristics: Highly electrical and thermal conductors, very stable in acid media, not permeable to gases, light, thin, strong and easy to handle for the machining of flow fields. New forms in the synthesis of graphite-polymer compounds are studied, where it is demonstrated that it is possible to mold the material with stamping or with phenolic polypropylene injection [9].

The bipolar plates are the primary element of the distribution system of the flow of reactant gases in PEM fuel cells. These elements represent almost 90% of the total weight of a single cell and about 45% of that of a Stack, where the individual cells that make up the stack are mounted in series. Plates perform different functions within a stack, which can be summarized as follows:

- Homogeneous distribution of the gas flow over the electrodes.
- They help to evacuate the water that is generated in the cathode.
- They are the electric conduction bridges of the battery.
- They make up the mono cells in the Stack.
- Help extract heat from active areas (in the absence of cooling plates)

In this stage, the most suitable materials for the manufacture of the fuel cell are reviewed. In the market there are a great variety of designs in bipolar plates, however, this component is a prominent object in research projects that are carried out internationally, because depending on their geometry and manufacturing materials, so will the results to be achieved, where requires a low weight material, good conductor of electricity, resistant to wear and corrosion; together with the need for the lowest possible cost, to achieve efficiency and commercial competitiveness [11].

3.1.3 Design and development of the process

In the design of the bipolar plates the NX 8.5 design software was used, the different radial configurations for the flow channels are modeled, for a cell of 25 cm ^ 2 of active area.

The length of the channel is one of the main geometric elements to consider in the design of the flow fields of the bipolar plates since it directly affects the pressure, the transport in the system. Based on fluid mechanics, the change in pressure is due to three direct and indirect effects of the length: speed ratio along the channel, the effect of friction in the fluid and geometric variations.

On the other hand, it has been found that increasing the length of the channel will also directly increase the flow in the cell. In addition, slightly increasing the length of the channel improves hydration of the membrane by decreasing the vapor saturation pressure in the channels, resulting in a better distribution of density and temperature, and, therefore, an improvement in performance local of the PEM cell.

The cross-sectional relationship of the channel has a great influence on the performance of the PEMFC. For example, the effect of increasing the height of the channel in the operation of the cell: as the height of the channel increases, an increase in pressure loss occurs due to an increase in the cross-sectional area, which generates the formation of water inside it and reduces the performance of the cell in the parts near the exit due to the accumulation.

While increasing the width of the channel, two problems arise: dehydration of the membrane due to the insufficient presence of water flow and the deflection of the membrane in the channel.

The cross section of the channels most used has been the rectangular, although studies have been carried out in different types of geometries such as triangles or trapezoids and their effect on cell performance focusing mainly on the distribution of reagents in dead spots and also as a better distribution and circulation of the water generated inside the channels. The results obtained show that rectangular configurations have greater potential while the trapezoidal areas have a more homogeneous distribution of current.

For the first channel design based on the geometry of the Fibonacci spiral: an approximation of the golden spiral generated by drawing circular arcs connecting the opposite corners of the squares adjusted to the values of the sequence; successively attaching side squares 0, 1, 1, 2, 3, 5, 8, 13, 21 and 34. This geometry has 6 input channels and 5 output channels of 1 mm in width and 1 mm in height. It was designed in such a way that the channels cover the largest active area of the catalysts, in figure 4 the modeling of the geometry in the Nx software is shown.

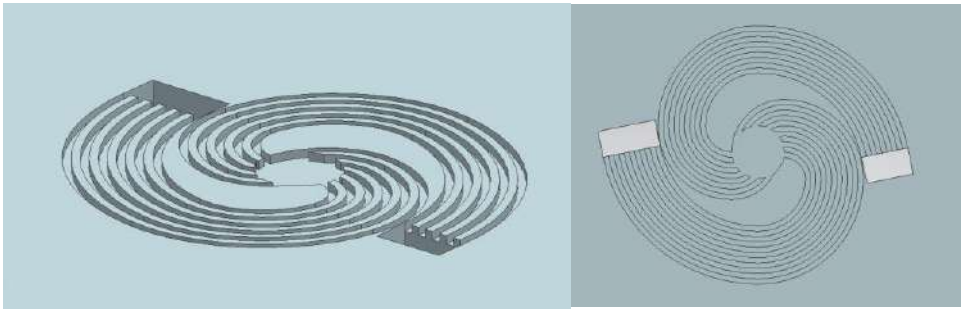

Fig. 4. Design of flow channels based on the Fibonacci spiral.

The second design was based on the golden spiral (also called golden spiral) is a logarithmic spiral associated with the geometric properties of the golden rectangle. The geometry has 3 input channels 1 mm wide and 1 mm high, 3 output channels 0.5 mm wide and 1 mm high, the aim of decreasing the width of the output channels is due to the fact that this way we would have less pressure drops increasing the efficiency of the cell. The outlet channels are designed to be smaller in size to partially block the gas flow so that the gases can be forced and penetrate through the gas diffusion layer and then reach the catalyst for the electrochemical reaction. As the sizes of the outlet channels are designed to be smaller than those of the inlet channels, the removal of water in the catalyst layers can also be improved. As discussed above, in spiral

channels, fluid movements, especially secondary flows, are significantly influenced by centrifugal force. [7] Figure 5 shows the modeling of the golden spiral geometry.

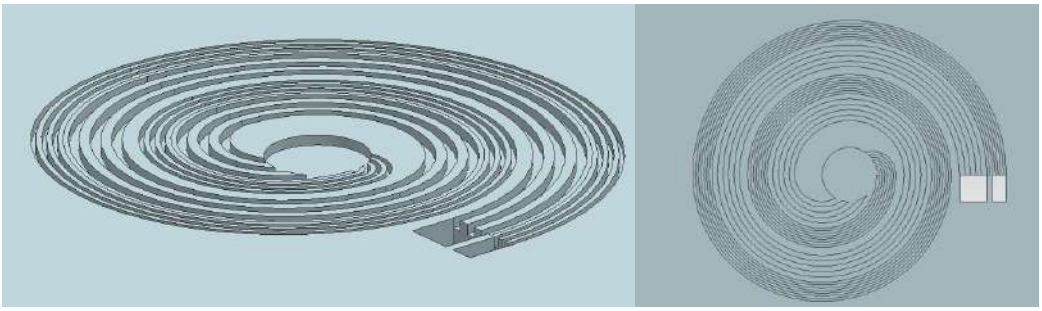

Fig. 5. Design of flow channels based on the golden spiral.

Figure 6 shows the design of a mono cell fuel cell stack for 50 W. An array or stack is a set of mono cells connected to each other, the arrangement can meet the needs of current, voltage and power required for the operation of a low power device. In the arrangements, the bipolar plates are the electrical contact between the anode of an MEA and the cathode of the next assembly.

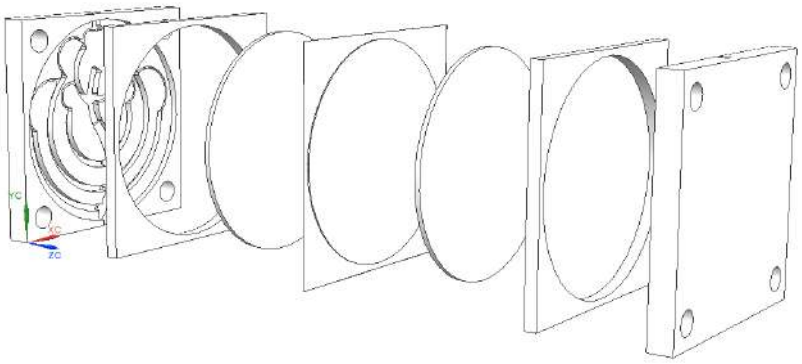

Fig. 6. Mono cell type PEM.

4. Results

With conventional channel patterns, such as parallel, serpentine and interdigitated channels, there are many abrupt turns that cause flow flows in the corners and produce large pressure drops in the flow fields. To improve the drawbacks, spiral or curved channels can be an alternative to replace conventional channels.

After several studies, it was found that the centrifugal force produced in the flow current by the curvature of the pipe caused a pair of vortices to evolve. It can be recognized that the secondary flow that take place in the curved channels can certainly improve heat and mass transfer [7].

According to the results obtained in the aforementioned reports, a spiral channel pattern presented in the present study is an attempt to increase heat and mass transfer and reduce pressure drop in fuel cell channels.

5. Conclusions

This paper presents the design and modeling of the flow fields for a fuel cell of up to 50 W of proton exchange membrane type (PEMFC). The study also presents the methodology for the design, where it was reached until the third phase of this.

The results of this flow field design allow the gases to mix at each turn to minimize the effect of blockage of the channel, preventing the accumulation of water. This configuration guarantees the uniform distribution of the reactive gases and the control of the loss of water from the fuel cell. This assumption is based on the analysis of different fields of flow developed in various research articles compiled for this work.

The actual results will be determined from a simulation and an analysis in the ANSYS fluent software in a later work.

6. References

[1] R. Gonzáles Huerta, O. Solorza Feria, M. Valenzuela Z. Tecnologías de hidrogeno y celdas de combustible de fuentes renovables, editorial académica española.

[2] F. J. Rodríguez Vera, O. Solorza Feria, E. Hernández Pacheco, Celdas de combustible.

[3] Frano Barbir, PEM: Theory and practice, Elservier, USA, 2013.

[4] W. Li, Q. Zhang, C. Wang, X. Yan, S. Shen, G. Xia, F. Zhu, J. Zhang, 2017. Applied Energy 195 (2017) 278–288, “Análisis numérico y experimental en 3d de campos de flujo para PEMFC”.

[5] M. Ashrafi, M. Shams 2017. Applied Energy 208 (2017) 1083–1096, ”Los efectos de la orientación del campo de flujo en la gestión del agua en las pilas de combustible PEM con canales serpentinos”.

[6] D. G. Huérfano Delgado, H. R. Morano Okuno, XVI International Congress of the Hydrogen Society, “Computational analysis of the machining and design parameters in the flow conditions of the electrodes in the PEM cells”.

[7] J. Jang, C. Cheng, W. Liao, Y. Huang, Y. Tsai 2012. Applied Energy 99 (2012) 67–79, “Estudio experimental y numérico de célula de combustible de membrana de intercambio de protones con canales de flujo en espiral”.

[8] I.B. Pérez Raya, A. Hernández Guerrero, D. Juárez Robles, J.C. Rubio Arana, 2009. Memorias del xv congreso internacional anual de la SOMIM, “Estudio de 3 configuraciones radiales para los campos de flujo de una celda de combustible tipo PEM”.

[9] A. B. Del Valle, S. J. Pathiyamattom, G. Alonzo Nuñez, S. Sánchez Gamboa, M. Macebo Gutiérrez, A. Chavez Alday, C. Acevedo Romano, A. García Pitoll, R. E. Olea Zavaleta, 2009. 8º Congreso Nacional de Mecatrónica, “fabricación de una celda de combustible tipo PEM por control numérico, para la industria automotriz”.

[10] S. Shimpalee, S. Greenway, J.W. Van Zee, 2006. Journal of Power Sources 160 (2006) 398–406, “El impacto de la longitud del camino del canal en el diseño del campo de flujo PEMFC”.

[11] E. T. Lincheta Mesa, Universidad de Matanzas “Camilo Cienfuegos” Cuba, Pilas de combustible, una alternativa importante en el desarrollo energético”.

Modelling and design

September 18 to 21, 2018 in Mexico City, Mexico

XVIII International Congress
of the Mexican Hydrogen Society

A suitable designed-cell for testing the catalyst performance applied towards hydrogen evolution reaction

R. Zenteno-López*,[1], A. Martínez-Séptimo[1], L. A. Estudillo-Wong[2], R. de G. González-Huerta[1]

[1]ESIQIE-IPN, Laboratorio de Electroquímica y Corrosión, UPALM, 07738, México, Ciudad de México.
[2]Departamento de Sociedad y Política Ambiental, CIIEMAD, Instituto Politécnico Nacional, Calle 30 de Junio de 1520, C.P. 07340, Ciudad de México, México.
*Corresponding author: 5537167728 and e-mail: zenteno_ricardo@outlook.com

ABSTRACT

Nowadays, it is possible to produce energy from different sources such as coal, natural gas, wood, wind and solar. However, some of these technologies have contributed with the greenhouse. In this context, fuel cells devices have more developed in order to generate less polluting gases. This device use hydrogen and oxygen gas in order to produce energy. Instead of oxygen gas, hydrogen has received an increasing attention due to its high contained energy. Nevertheless, we need to produce hydrogen gas through different technologies. One of the most promising technologies for approaching this challenge, is the electrolysis of water into the proton exchange membrane electrolyzer (PEME). Therefore, the efficiency and stability have to be improved, based on the design such as gas diffuser (porous titanium plate), plates (titanium current collector) and the material used as anode in the electrolyzer. For this propose, a new PEME design was developed. Thus, different loadings of iridium and ruthenium oxides were tested and compered with preliminary PEME. Chronoamperometry was used as electrochemical method for testing the performance. We observed a better performance with the new PEME design.

Keywords: Design PEME, porous titanium plate, titanium current collector.

1. Introduction

Currently, the increasing demand for energy by humans to carry out their activities has caused a strong impact on their environment. To meet this energy requirement, it has been necessary to extract more fuel from various sources, its main origin those obtained from non-

renewable sources, fossil fuels is the most important source with 81% of the total energy generated [1].

To eliminate this dependence on fossil fuels, several technologies have been proposed to satisfy the increasing energy demand [2], one of the options the use of hydrogen as an energy vector [3]. This because hydrogen can be obtained through several sources and processes such as chemical conversion, thermolysis, electrolysis, etc. [4].

In electrolysis, electrical energy is supplied to an electrolyzer to extract hydrogen from water, decomposing it into oxygen and hydrogen. This method is very efficient due to the high performance of the electrolyzer; but currently, due to the cost of electric power, its cost is high, compared to other methods of hydrogen production, so it is not economically viable. Its massive application will only be achieved when renewable sources are integrated into electrolysis systems [5]. An advantage of these systems is that they can provide hydrogen in a simple, scalable and easy to implement for relatively low consumption and close to the point of consumption [6].

Therefore, to support the development of electrolysis hydrogen production, several research groups focus on [7]:

- The use of new technologies that increase the lifespan of the equipment and reduce the manufacturing costs.

Through the synthesis of low-cost materials and alternative materials, including electrocatalysts, electrolytes for fuel cells, catalysts for hydrogen production from renewable organic inputs, bipolar plates, etc. [3].

- Development of prototypes for the hydrogen production.

The development of prototypes aims to take the developments of laboratories to a higher level, to test concepts and particularly to attract industry [3]. This is the focus of this work, in which an improved proton exchange membrane electrolyzer (PEME) prototype was developed as a test cell for different anodic catalysts, based on a design previously used in the group of ESIQIE, whose performance was very low, even using commercial materials.

2. Materials and Methods

2.1. Materials

The PEMEs are constituted by several components; the central structure of which is the electrocatalyst membrane assembly (MEA) which is the main component since this is where the oxygen and molecular hydrogen are electrochemically formed from water and an electrical power. The MEA consists of a five-layer structure; in the center of which is a proton exchange membrane that acts as an electrolyte, which separates the structure of the anode and cathode electrodes, preventing the gases from mixing. Each electrode consists of a gas diffuser with a layer of electrocatalyst that is located between the membrane and the diffuser. The MEA is supported in a pair of current distributing meshes, which in addition to draw on all the active area of the electrolyzer, helps to an effective detachment of the gases that occur along the electrodes surface. The seals serve to confine the water to the reactive area, and together with the

periphery of the exchange membrane, avoid any type of leakage. In this case, the materials used for the construction of the new design of the PEME were:

- Acrylic cases 'A1' and 'A2', 5x5 cm, 6 mm (15/64 ") thick with nozzles for liquid inlet and gas outlet.
- Seals of EPDM rubber 'B1' and 'B2', 5x5 cm of 0.94 mm (1/32 "), with holes of 3 mm in diameter to allow the entry of the liquid and exit of gases.
- Titanium current collector plates 'C1' and 'C2', with an area of 5x5 cm and a thickness of 0.75 mm, in addition, it must have a designated space to place alligators of 1x2 cm of area and holes of 3 mm of diameter to allow the entry of the liquid and gas outlet.
- Seals of EPDM rubber 'D1' and 'D2' of 5x5 cm, 1.5 mm (1/16 ") thick, with a space of 2x2 cm in the center of this to provide support to the diffusers of gases, with holes of 3 mm in diameter that are communicated to this space to allow the entry of the liquid and gas outlet to the diffuser.
- Porous titanium meshes gas diffusers 'E1' and 'E2', with an area of 2x2 cm and a thickness of 1.55 mm.
- A membrane of Nafion® 115 of a 3x3 cm area, previously activated, with the active area of the membrane of 4 cm2 (2x2 cm).
    - The catalytic ink used for the anode is iridium and ruthenium, using different proportions (25% IrO_2 - 75% RuO_2, 50% IrO_2 - 50% RuO_2 and 75% IrO_2 - 25% RuO_2), always being prepared for a concentration of 3 mg of catalysts (Ir-Ru) per unit active area.
    - For the cathode a commercial catalyst was used, that is, platinum supported on 40% carbon (Pt_{40}/C). This catalyst is already on a carbon mesh.

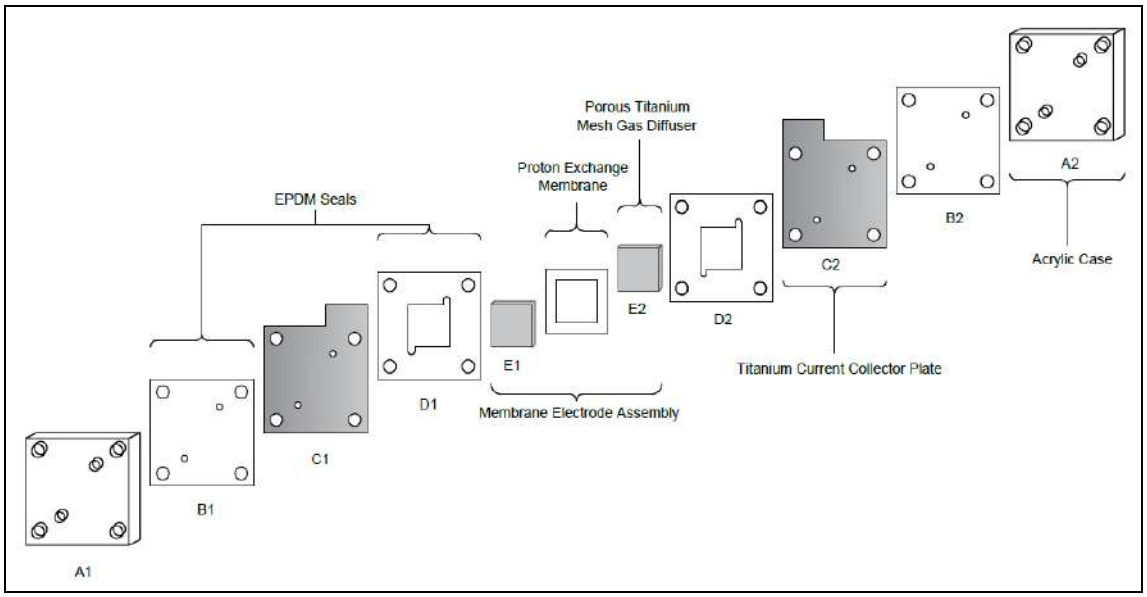

Fig. 1. Electrolyzer diagram

2.2. Method

2.2.1. MEAs preparation

To characterize a PEME, it is required to obtain its performance curve (current vs. voltage), which is generated by applying current pulses for a time until a constant voltage is observed. Different MEAs prepared with commercial catalysts, shown in Table 1, were tested to determine the performance curves of the new test electrolyzer and compare the performance curves with those obtained with the first design.

Table 1. Tested MEAs

MEA 1	MEA 2	MEA 3
25% IrO_2-75% RuO_2	50% IrO_2-50% RuO_2	75% IrO_2-25% RuO_2

For the preparation of MEAs, the membrane is activated as described in the literature [8], while the membrane is dried, the anodic catalytic ink is prepared in a 15 ml centrifuge tube with the following composition: catalyst (mixture of oxides of Iridium-Ruthenium) 3 mg per cm^2, 240 µL of ethyl alcohol, 60 µL of deionized water and 18 µL solution of Nafion® 5%w, this solution is placed on ultrasound for 30 minutes to form a homogeneous phase. Once the membrane is dry, the anode is painted on it using a dosing system with a model 781S valve with a VALVEMATE NP 7022120 controller, with regulating pedal, Figure 2, which was operated with the following operating conditions: a) input air pressure of 80 psig, b) input ink supply tank pressure at 20 psig, c) inpout actuating air pressure at 100 KPa, d) valve opening of 20%, e) time of atomization of 0.013 seconds, f) delay time of 4.5 seconds and g) height of the valve with respect to the MEA of 7 cm.

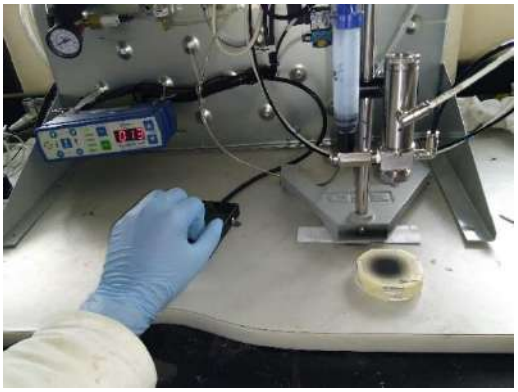

Fig. 2. Dosing system with a valve model 781S.

Once the anode has been painted, the MEA is integrated by a sintering process, placing commercial cathodes of carbon fabric impregnated with catalytic ink with 40% Pt. A hydraulic

press, Figure 3a, is used at a temperature of 120 ° C and a pressure of 5 tons is applied for 30 seconds, the MEA is cooled, Figure 3b, and is integrated into the test electrolyzer, Figure 3c.

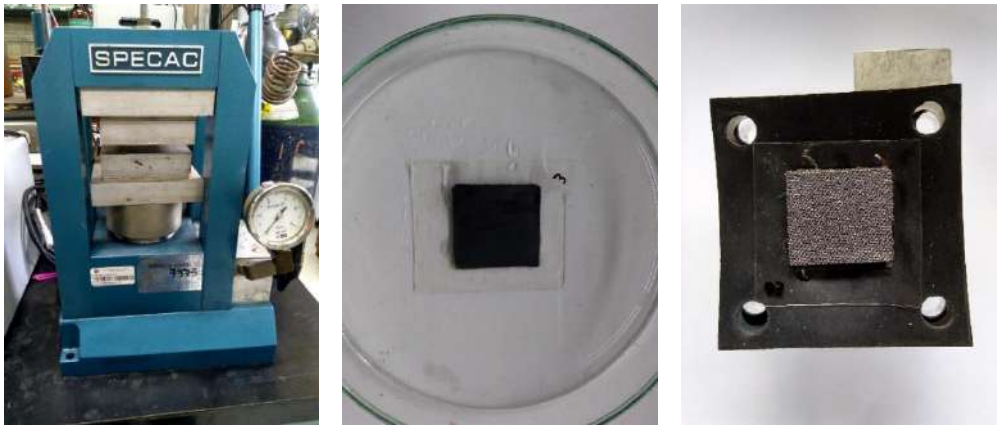

Fig. 3. (a) Sintering hydraulic press; (b) Sintered MEA; (c) MEA integrated to the test electrolyzer.

2.2.2 Integration and characterization of the electrolyzer

The following procedure is followed to assemble the new test electrolyser: The electrolyser is mounted by placing on the acrylic case 'A1' the EPDM seal 'B1', the distributor plate 'C1', the EPDM seal 'D1' and the diffuser 'E1', the membrane is placed with the anode ink on the diffuser 'E1' and on top of it the commercial catalyst of the cathode. Subsequently, the EPDM seal 'D2' and the diffuser 'E2' are placed on the commercial catalyst and finally the distributor plate 'C2', the EPDM seal 'B1' and the 'A2' case. They are fastened by screw studs, insulated by Teflon, plastic plugs, washer bolts, and nuts.

The electrolyzer is connected to the water supply tanks and to the model source MATRIX MPS-3003LK-3 by means of alligator clips.

For the characterization the intensity is increased from 0 to 0.1 A by means of variations of 0.01 A and once the value of 0.1 A is reached, the intensity is varied in 0.1 to 2 A. In each intensity value the voltage value is taken that is supplied to the electrolyser, allowing the equipment to stabilize for a minute and a half.

The results obtained were compared with those obtained in the previous design of electrolyzer.

To obtain the comparative data of the former electrolyzer design, it is necessary to connect in the same way as reported in literature [8].

It is necessary to emphasize that the former design consisted of graphite cases with a pool for the water, current collector plates of stainless steel and a gas diffuser of carbon mesh in the anode.

3. Results and Discussion

The test prototypes are shown in Figure 4. Figure 4a shows the existing test electrolyzer and Figure 4b shows the improved test electrolyzer.

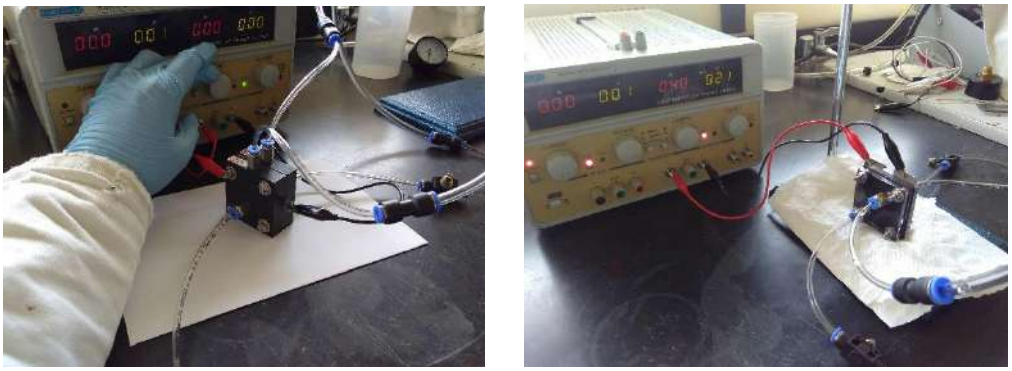

Fig. 4. (a) Initial test electrolyzer; (b) New test electrolyzer.

The values obtained in the demanded voltage to the different currents applied to the PEME from the experimentation are reported in Table 2. The performance curves of the two prototypes, the original and the improved design, are shown in Figure 5.

Table 2. Results of voltage demanded to the different flows applied to the PEME.

	Initial test electrolyzer			**New test electrolyzer**		
	25% IrO_2-75% RuO_2	**50% IrO_2-50% RuO_2**	**75% IrO_2-25% RuO_2**	**25% IrO_2-75% RuO_2**	**50% IrO_2-50% RuO_2**	**75% IrO_2-25% RuO_2**
Current (A)	**Voltage (V)**	**Voltage (V)**	**Voltage (V)**	**Voltage (V)**	**Voltage (V)**	**Voltage (V)**
0.01	1.6	1.5	1.6	1.5	1.4	1.4
0.02	1.7	1.6	1.6	1.5	1.5	1.5
0.03	1.8	1.7	1.8	1.5	1.5	1.5
0.04	1.9	1.8	1.8	1.6	1.6	1.5
0.05	2	1.8	1.9	1.6	1.6	1.5
0.06	2.1	1.8	2	1.6	1.7	1.5
0.07	2.3	1.9	2.1	1.6	1.6	1.5
0.08	2.4	1.9	2.1	1.7	1.6	1.6
0.09	2.6	2	2.2	1.7	1.7	1.6
0.1	2.9	2	2.2	1.7	1.7	1.6
0.2	4	2.3	2.8	1.9	1.8	1.7
0.3	-	2.8	3.3	2	2	1.8

Table 2. Results of voltage demanded to the different flows applied to the PEME (continuation)

	Initial test electrolyzer			New test electrolyzer		
Current (Amperes)	**25% IrO_2-75% RuO_2 (Volts)**	**50% IrO_2-50% RuO_2 (Volts)**	**75% IrO_2-25% RuO_2 (Volts)**	**25% IrO_2-75% RuO_2 (Volts)**	**50% IrO_2-50% RuO_2 (Volts)**	**75% IrO_2-25% RuO_2 (Volts)**
0.4	-	3.1	-	2.2	2.2	1.9
0.5	-	-	-	2.3	2.2	1.9
0.6	-	-	-	2.4	2.3	2
0.7	-	-	-	2.6	2.3	2.1
0.8	-	-	-	2.5	2.3	2.2
0.9	-	-	-	2.6	2.4	2.3
1	-	-	-	2.8	2.5	2.3
1.1	-	-	-	2.9	2.5	2.4
1.2	-	-	-	3	2.6	2.5
1.3	-	-	-	3.1	2.7	2.6
1.4	-	-	-	3.2	2.7	2.6
1.5	-	-	-	3.2	2.8	2.7
1.6	-	-	-	3.3	2.8	2.7
1.7	-	-	-	3.4	2.9	2.8
1.8	-	-	-	3.5	2.9	2.9
1.9	-	-	-	3.5	3	3
2	-	-	-	3.5	3	3

According to what is observed in Figure 5, the performance curves of the new test electrolyzer show better performance since for all the MEAs at an applied current the demanded voltage is lower. The MEA that obtained the best performance was the 75% IrO_2-25% RuO_2 (MEA 3) since at 1.5 A demanded 2.7 V, while the MEAs 1 and 2 at that same current required 2.8 and 3.2 V respectively. Regarding the initial test prototype, this presented a low performance, since at a current of 0.2 A MEAs 1, 2 and 3 demanded a high voltage of 4 V, 2.3 V, and 2.8 V respectively which is outside the parameters reported in the literature [9]. This is attributed to the fact that the steel mesh generates considerable resistance in the performance of the electrolyzer, since it does not have a good contact with the MEA; due the inclusion of a pool in the case design a hydrostatic pressure is generated on the active area that prevents the correct desorption of the gases generated in both electrodes, which causes an increase in the resistance of the system; with respect to the carbon mesh gas diffusers, this endures a low potential, around 2 V before decomposing in the form of CO and gaseous CO_2, and due to the resistance of the original design, these decompose at low values of intensity.

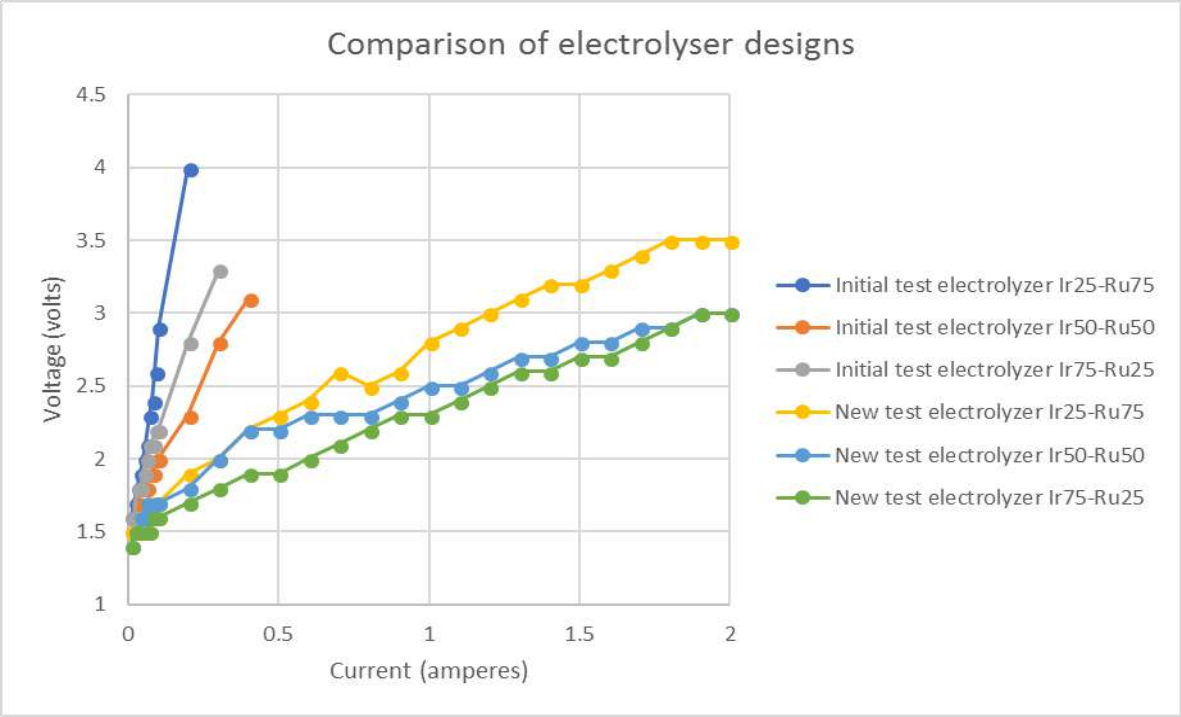

Fig. 5. Performance curves of the test electrolyzers.

4. Conclusion

A new design of a PEM cell prototype was developed that significantly improved the performance of the system by requiring a lower power to generate hydrogen. The performance curves of the new test electrolyzer show a better performance for all the MEAs, at an applied current the demanded voltage was lower.

Acknowledgements

Thanks for the financial support granted: to the IPN proyecto multidisciplinario SIP-1820 (2017-2018) and to the CONACYT project of the CEMIE-Ocean 249795: Línea Transversal I-LT1 Tecnologías y estrategias de interconexión eléctrica de energías del océano para el mar Territorial Mexicano.

References

[1] Prieto, P. Encrucijadas entre las energías fósiles y las energías renovables. In: Moreno, J. A.; Alonso, L. E.; Callejón, M. E.; De la Cuesta, M.; García de la Cruz, J. M.; Gimeno, J. A.;

Valor, C., editors. La energía. Retos y problemas, Madrid: Economistas sin fronteras; 2017, p. 10-14.
[2] Ogden, J. M. Hydrogen as an Energy Carrier: Outlook for 2010, 2030, and 2050. UC Davis: Institute of Transportation Studies (UCD). https://escholarship.org/uc/item/9563t9tc; 2004 [accessed 01.07.2018].
[3] Instituto Nacional de Electricidad y Energías Limpias. Hidrógeno como almacén de energía. https://www2.ineel.mx/taller_almacenamientoenergia/documentos/pdf/mesa3panelb_recopilacion.pdf; 2010 [accessed 01.07.2018]
[4] Linares Hurtado, J. I. & Moratilla Soria, B. Y. El hidrógeno como vector energético (I/II). https://www.icai.es/contenidos/publicaciones/anales_get.php?id=1412; [accessed 01.07.2018].
[5] Estrada Gasca, C. A. & Islas Samperio, J. Energías alternas: Propuestas de desarrollo tecnológico para México. Academia Mexicana de Ciencias. http://www.coniunctus.amc.edu.mx/libros/energias_alternas.pdf; 2010 [accessed 01.07.2018].
[6] U.S. Departament of Energy. Electrolytic Hydrogen Production Workshop Summary Report. https://www.energy.gov/sites/prod/files/2014/08/f18/fcto_2014_electrolytic_hydrogen_production_workshop_summary_report.pdf; 2014 [accessed 01.07.2018].
[7] Hinkley, J.; Hayward J.; McNaughton, R.; Gillespie, R.; Matsumoto, A.; Watt, M. & Lovegrove, K. Cost assessment of hydrogen production from PV and electrolysis. https://arena.gov.au/assets/2016/05/Assessment-of-the-cost-of-hydrogen-from-PV.pdf; 2016 [accessed 01.07.2018].
[8] Santillán Aragón, G. Diseño y construcción de un banco de pruebas para caracterizar nanomateriales en un electrolizador de membrana de intercambio protónico. Bachelor thesis. México, México city, 2010.
[9] Marcelo Carmo, Dvaid L. Fritz, Jürgen Margel, Detlef Stolten, A comprehensive review on PEM water electrolysis, International Journal of Hydrogen Energy 38 (2013) 4901-4934.

XVIII International Congress
of the Mexican Hydrogen Society

Model of a fixed bed catalytic reactor to produce H_2 by Ethanol steam reforming with a Ni-Co-Hydrotalcite catalyst

I.F. Martínez[a], J. L. Contreras[a]*, G. Pérez[a], J. Salmones[b] B. Zeifert[b], L. Nuño[a]

[a] Universidad Autónoma Metropolitana-Azcapotzalco, México, D.F.,02200, México
[b] Instituto Politécnico Nacional, ESIQIE, Ciudad de México, U.P. López Mateos, Zacatenco, México
* Corresponding author: 5591911047 and e-mail: jlcl@correo.azc.uam.mx

ABSTRACT

A mathematical model has been developed to predict the conversion profiles and temperature in axial and radial form of a fixed-bed catalytic reactor using a spherical catalyst of Ni-Co / Al_2O_3 with a particle diameter of 1/8 in. A reactor tubular with a diameter of ¾ in and with a length of 5.11 in was used. The operating conditions of the reactor were: operating pressure of 1 atm, water / ethanol mole ratio of 4, feed temperatures of 450, 480, 510 and 540 °C, the construction material of the reactor was stainless steel 316. After applying a differential balance of mass and energy, the solution of the differential equations were discretized by a variant of the implicit methodology of Crank-Nicholson. The values of the transport properties were obtained from the literature such as: the effective diffusivity and the effective thermal conductivity, as well as the reaction rate equation. For the numerical solution, physically reasonable conditions have been introduced in the model and, in this way, establish initial and border conditions that delimit the problem. The Wolfram Mathematica® software has been applied to calculate the conversion and temperature along the reactor. For the validation of the model, the conversions and the calculated temperatures were compared with the experimental ones. This study shows that the implemented program was reliable to simulate an integral fixed bed catalytic reactor.

Keywords: Model, Hydrogen, Integral Reactor, Reform-Ethanol-Water

1. Introduction

Hydrogen is an ideal energy vector, since it can be transformed into heat, mechanical energy, or electrical energy [1]. The clean and innovative technology of hydrogen is obtained from renewable sources such as bioethanol in the presence of metal catalysts [2]. Currently we

have developed a catalyst for the process of reforming ethanol with water vapor (ESR) based on Ni-Co-Hidrotalcita-WOx catalyst that has shown high selectivity to H_2 using a ratio H_2O / ethanol = 4, with low selectivity to CO and that it has been shown to be stable for times of more than 3 h at high temperature of 550 °C [3].

2. Materials and Methods

This catalyst was prepared and acquired a cylindrical shape by compaction at 205 kg/cm^2 giving dimensions of 1/8x1/8 in, in diameter and length respectively, to be evaluated later in a reactor with 13 cm (5.11 in) length of packed bed with 3/4 in diameter in 316 stainless steel.

The reaction of ethanol steam reforming is endothermic which makes it extremely demanding of energy [4], the heating was carried out externally by means of an electric furnace so that the reaction is carried out in a fixed bed. In order to determine the mathematical model of the conversion profile (mass balance) and temperature (energy balance) along the packed reactor, we start from the conservation equations applied to a control volume as shown in the Figure 1.

By realizing the material balance with respect to the limiting reagent through the control element, and according to the flux in the axial direction z, diffusion in the radial direction and losses by reaction, the two-dimensional model of mass balance [5] is obtained. Equation 1.

$$\partial x/\partial z - D_e/u\ ((\partial^2 x)/\partial r^2 + 1/r\ \partial x/\partial r) - (\rho_B\ r_P)/(G/PM\ y_{A0}) = 0 \qquad (1)$$

The equation of energy is obtained analogously. (Equation 2)

$$\partial T/\partial z - K_e/(G\ C_p)\ ((\partial^2 T)/\partial r^2 + 1/r\ \partial T/\partial r) + (\rho_B)\ \Delta H\ r_P)/(G\ C_p) = 0 \qquad (2)$$

Where the transport properties such as, the effective diffusivity was calculated according to the model proposed by Brokaw [6] for binary mixtures with participation of polar components. In the case of effective thermal conductivity, the two phases involved in the reactor were used. The first belongs to the gaseous phase fed and the second one based on the catalytic bed belonging to the solid phase [5,6].

For the resolution of partial differential equations the finite difference method was used. Within the latter are both explicit and implicit methods, where the problem was addressed by the Crank-Nicholson method as a variant of the implicit methodology [7]. The above increase accuracy and precision in the calculations, since it requires a higher number of nodes with respect to the explicit ie a more complex meshing. Finally, the series of equations that are generated must be solved simultaneously for each node [8]. The physical interpretation of the reactor provided the boundary conditions and initial values. The Wolfram Mathematica® software has been applied to calculate the phenomena present in the reactor of ethanol steam reforming towards the production of hydrogen.

Among the considerations made was to simulate the reactor symmetrically giving way to a short list of boundary conditions, or three geographical zones in the reactor: reactor center or the middle, reactor wall and intermediate points between these two borders [9].

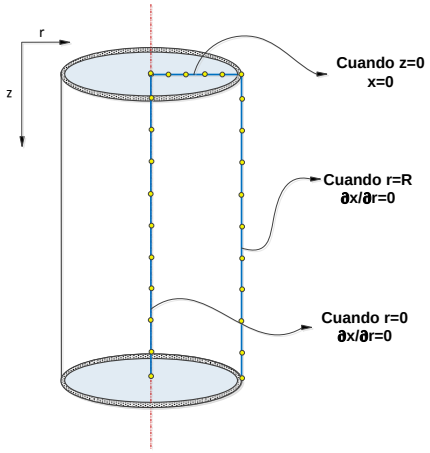

Fig. 1. Border conditions, material balance

Several parts of the fundamental section and in the simulation are: the operating conditions, the thermodynamic values of the reaction, the kinetic expression [10], effective dimensions of the reactor (internal diameter), physical properties of the catalyst, as well as the distribution and number of increases of the radial and axial axis. Table 1 show the operating conditions used in the simulation.

Table 1. Operating conditions used in the reactor for reforming Ethanol under pressure of 1 atm and temperature of 500 ° C in the feed. (See the units at the end of the manuscript)

Operating condition Values	**Value**
Surface speed (G)	100
Volumetric flow (V_o)	1
Feed Temperature (°C)	500
Wall Temperture (°C)	510
Effective Diffusivity (D_E)	$5.08x10^{-7}$
Effective Thermal Conductivity (K_E)	0.955765
Density of the catalytic bed (ρ_B)	580
Linear feed speed (u)	0.1
Number of points on the radial axis	18
Number of points on the axial axis	100
Initial composition of the limiting reagent	0.2

The method of preparation of the catalysts was by coprecipitation of the precursors $Ni(NO_3)_2$, $Co(NO_3)_2$, Ammonium tungstate, for the hydrotalcite (HT) was precipitated from $Mg(NO_3)_2$ and $Al(NO_3)_3$ in aqueous solution. The precipitate was left at rest to crystallize. The suspension was left at 70°C at a pH of 11 with stirring for 18 h, and the solid was washed several times with demineralized water and then dried at 110°C for 18 h, finally calcined at 450°C for 5 h . The catalyst was mixed with 10% boehmite as a binder and again dried at 110 ° C for 12 h to form 1/8 x 1/8 in cylinders using a stainless steel mold and pressing the compactor material up to 250 lb/in^2.

The evaluation of the bimetallic catalyst was carried out under a flow of 1 ml/s in a micro-reaction installation with two water and ethanol saturators driving the molar ratio of 4 moles of water to one of ethanol. The temperatures that were handled during the reaction were: 450, 480, 510 and 540 ° C.

3. Results and Discussion

It was observed in Figure 2, that the conversion in the reactor increases by 91% during the first 6 cm of the catalytic bed, and only by 8% in the next second half section of the reactor. It is probable that in the first section of the reactor the greater amount of H_2 is generated because in the feed of the reactor the highest molar ratio of water vapor / ethanol is due to the reaction.

$$CH_3CH_2OH + 3H_2O \rightarrow 6\ H_2 + 2\ CO_2 \qquad (3)$$

A decrease in temperature was observed in the center of the reactor using the Eley Rideal kinetic equation (Figure 3) and a minimum temperature value of 468°C was calculated. In the case of using a kinetic equation of power law, the minimum value calculated was 523° C.

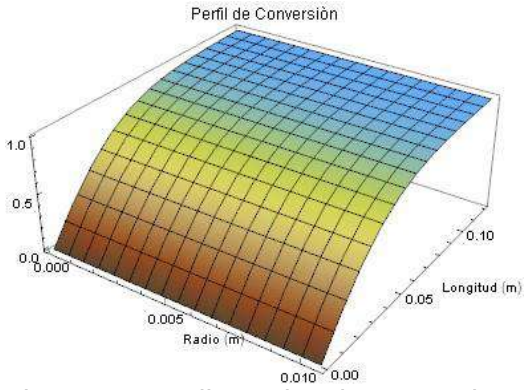

Fig. 2. Two-dimensional conversion profile using Eley Rideal reaction rate [10] at 550 ° C.

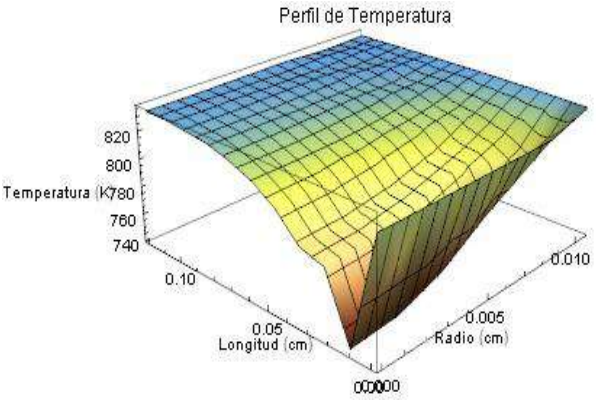

Fig. 3. Two-dimensional temperature profile using Eley Rideal reaction rate [10] at 550 ° C.

The calculation of the average conversion (Figure 4) was observed as the catalytic reaction temperature increases to 550°C and the difference in conversion of the calculated and experimental results decreases compared to the conversions calculated at a lower temperature (450°C) using the same kinetic equation.

The average temperature calculated of the catalytic bed, in the center (Figure 5) was observed from 2 cm a percentage of error very small in comparison to the experimental temperature, having its better coincidence to 9.5 cm of catalytic bed which was very similar to the values analyzed at 500 ° C.

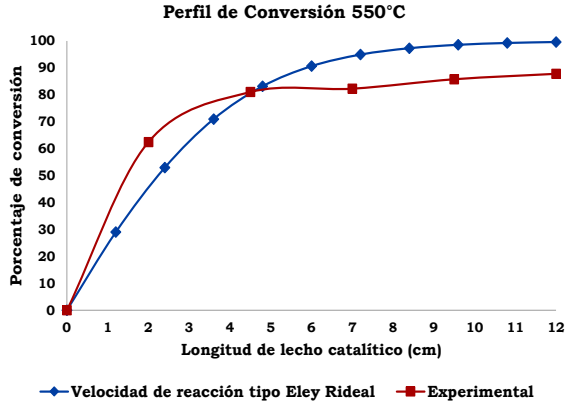

Fig. 4 Average conversion profile using reaction rate of the Eley Rideal type [10] at 550 ° C.

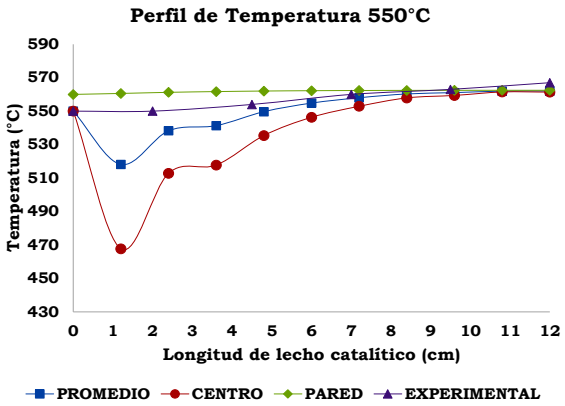

Fig. 5 One-dimensional temperature profile using Eley Rideal reaction rate [10] at 550 ° C.

The analysis on the conversion profiles and temperature according to the reaction rate equation was carried out with constant operating values, such as: density of the catalytic bed, flow and surface feed and initial composition, as well as the respective temperature-dependent transport properties, using the finite difference method to solve the pair of partial differential equations generated from the mass and energy balance.

The methodology implemented in our case study and developed by Crank-Nicolson (CN), defines that the stability is not altered by the existing relationship by the radial and axial step size, that is to say when performing the iterations of the equations algebraic it is possible to find simultaneous solution of each internal node.

In order to obtain percentages of average absolute error less than 15% for the conversion profile and temperature respectively, the step size in the radial and axial axis was reduced.It was observed that the conversion and temperature profiles exhibited similar behaviors as the temperature and mathematical simulation were increased to 450, 500 and 550 °C, showing better coincidence of the numerical and experimental results with an reaction equation of the type Eley Rideal, so it was selected to make changes in radial and axial pitch size.

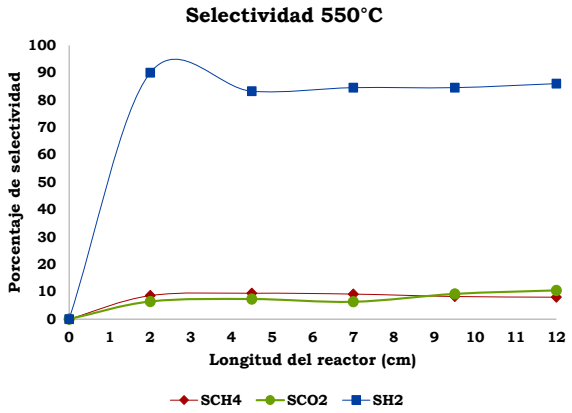

Fig. 6 Hydrogen selectivdy along its reactor length.

Table 2. Average error between experimental and calculated Temperatures.

		Absolute error %		
Port	*L (cm)*	*Conversion*	*Temperature*	
			Average	*Middle*
-	0.0	0	0	0
1	2.0	31.02	3.09	9.01
2	4.5	6.73	1.30	4.55
3	7.0	11.91	0.64	1.73
4	9.5	13.23	0.51	0.89
5	12.0	12.72	0.96	1.08
% average error		12.60	1.08	2.88

3. Conclusions

A mathematical model of a fixed-bed catalytic reactor for the ethanol steam reforming reaction to H_2 was developed describing the conversion and temperature profiles along the fixed-bed reactor of ¾ in internal diameter by 5.11 in of lenght using a Ni-Co-Hydrotalcites catalyst in the form of tablets of 1/8 x 1/8 in. The transport properties such as diffusivity and effective conductivity were calculated while the reaction rate equations were taken from the literature.
It was observed, that the conversion in the reactor, increases by 91% during the first 6 cm of the catalytic bed, and only increases again in the 8% of the next second half section of the reactor. The radial difference of the conversion in three axial sections of the reactor (1.2, 6 and 12 cm) was relatively small since it was not greater than 0.56% of the conversion, when 1080 algebraic equations were solved. The Eley Rideal rate equation is best adjusted, after analyzing the numerical and experimental results at 450, 500 and 550°C. The highest percentage of error was observed in the conversion results and the lowest error value in conversion (11.35%) was determined at a reaction temperature of 500°C. The greatest radial difference in temperature was located 1.2 cm from the length of the catalytic bed and decreases as a smaller step size is used. The presence of CO, CH_3CHO and $CH_2 = CH_2$ were not observed through the catalytic bed. There were very low deviations in the validation of the model because low values of temperature errors (1.3%), were found especially from 4 to 12 cm in length.

Acknowledgements

The authors are grateful for the financial support of this research to the Universidad Autónoma Metropolitana-Azcapotzalco. The M. in C. Iván F Martinez is grateful for the CONACYT scholarship for his master in Process Engineering and support for a stay with the Dr. Hugo de Lasa, of the Chemical Reactor Engineering Center (CREC) of the University of Western Ontario, Canada.

References

[1] M. N. Barroso, Manuel F. Gomez, Luis Arrúa, M. Cristina Abello, “Hydrogen production by etanol Reforming over NiZnAl catalysts” Appl. Catal. A: General, 2006,304, 116-123,.

[2] J. L. Contreras, M. A. Ortiz, G. A. Fuentes, M. Ortega, “Catalysts for H_2 production using the ethanol steam reforming (A review)”, Int. Journal of Hydrogen Energy, 2014,39,1835-1853.

[3] A. Figueroa A., “Síntesis de catalizadores Ni-Co/Hidrotalcitas para la producción de hidrógeno a partir de bio-etanol”, Tesis de Licenciatura. Universidad Autónoma Metropolitana, México, 2014.

[4] Alessia Santucci, Maria A., Fabio B., Luigi M., Martina R., Silvano T., “Oxidative steam reforming over a Pt/Al2O3 catalyst in a Pd-based membrane reactor”, Int. Journal of Hydrogen Energy, ,2011, 36,1503-1511.

[5]J. M. Smith, “Chemical Engineering Kinetics”, Mc Graw-Hill, México,1991.

[6] Bruce E. Poling, John M. Prausnitz, John P. O´Connell, “The Properties of Gases and Liquids”, Mc Graw-Hill, Mexico,2001.

[7] John H. Mathews, Kurtis D. Fink, “Numerical Methods using MATLAB”, Prentice Hall, Mexico,2002.

[8] V. G. Jensen, G. V. Jeffreys, “Mathematical Methods in Chemical Engineering”, Mc Graw-Hill, Mexico,2001.

[9] Stanley M. Walas, “Modelling with Differential Equations in Chemical Engineering (Butterworth-Heinemann Series in Chemical Engineering)”, Prentice Hall, Mexico, 2002.

[10] Abayomi A., Ahmed A., Raphael I., Ajay D., “Kinetic modelling of hydrogen production by the catalytic reforming of crude ethanol over a co-precipitated Ni-Al2O3 catalyst in a packed bed tubular reactor”, Int. Journal of Hydrogen Energy,2006, 31,1707-1715.

NOMENCLATURE

D_e Effective diffusivity, $\frac{m^2}{s}$

u Lineal feed speed, $\frac{m}{s}$

ρ_B	Density of the catalytic bed, $\frac{Kg}{m^3}$
r_p	Reaction rate, $\frac{Kmol}{h \cdot Kg\ cat.}$
G	Surface speed, $\frac{Kg}{h \cdot m^2}$
P.M.	Average molecular weight of the mixture fed, $\frac{Kg}{Kmol}$
y_{Ao}	Percentage fraction of limiting reagent in the feed, Adimensional
K_e	Effective thermal conductivity, $\frac{W}{m \cdot K}$
K_m	316 stainless steel thermal conductivity, $\frac{W}{m \cdot K}$
C_p	Heat capacity of the mixture fed, $\frac{KJ}{Kg \cdot K}$
ΔH	Reaction Enthalpy, $\frac{KJ}{Kmol}$
m	Number of points on the radial axis, where it starts from 0 and must be an integer value.
n	Number of points on the axial axis, where it starts from 0 and must be an integer value.
Δz	Value of the increase in the axial axis,
Δr	Value of the increase in the radial axis,
r_{ext}	External reactor radio, m
r_{int}	Radio interno del reactor, m
V_o	Volumetric flow in the feed $\frac{ml}{s}$

Renewable energy systems

September 18 to 21, 2018 in Mexico City, Mexico

XVIII International Congress
of the Mexican Hydrogen Society

Dilute phosphoric acid hydrolysis of stem of faba bean for reducing sugar production

J. C. Gómora-Hernández[1,2], M. del C. Carreño de León[1], S. M. Fernández-Valverde[2,*]

[1]Depto. de Química, ININ, A.P. 18-1027, México D.F. C.P.11801, Mexico. Tel. 5553297200 ext 12277
[2]ITT, Avenida Tecnológico s/n, Fracc. La Virgen, Metepec, Edo Mex., México. C.P. 52149. Tel. 7222087200
* Corresponding author: 5553297200 ext. 12277, suilma.fernandez@inin.gob.mx

ABSTRACT

One of the most important agricultural harvests in Mexico State is faba bean; this harvest reaches an annual production of 32,033 tons. After harvesting, residues such as stems, leaves and husks are generated, among all these, stems are not metabolized by cattle and usually are disposed in open dumps contributing to soil erosion and environmental damage. Due to the high amount of carbohydrates, stem of faba bean has a great potential for its transformation by biological methods into many value add products such as hydrogen, however, a previous depolymerization of these carbohydrates into monomeric sugars is needed. The objective of the present work was to evaluate the efficiency of dilute phosphoric acid hydrolysis in sugars production from stems of faba bean. These were obtained from local crops located at Mexico State, and treated at different temperatures and phosphoric acid concentrations The sugar production increased with the increases in acid concentration and temperature, the maximum obtained yield was 21.20 g of sugar / 100 g of stem of faba bean obtained at 110 ºC, 1.34 M and 270 minutes reaction time, at longer reaction times the amount of sugars diminished due to thermal saccharides decomposition. FTIR analysis showed a diminishing in intensity of the main vibrational bands of cellulose and the increasing of amplitude and intensity of lignin vibrations after hydrolysis. Sugar production data was well fitted to Saeman model and according to thermodynamic parameters sugar production by dilute acid hydrolysis of stem of faba bean was an endothermic and nonspontaneous reaction. Sugars obtained from stem of faba bean are a potential substrate for fermentative biohydrogen production however is necessary to increase cellulose degradation.

Keywords: Fermentative biohydrogen; Agricultural waste; fermentable sugars; acid treatment

1. Introduction

The depletion of petroleum and the climate change attributed to fossil fuels burning have increased the energetic and the environmental crisis, thus, a new source of sustainable, clean and efficient energy is required [1]. Hydrogen has the highest calorific power and after energy production, the main products are energy and water. In the last decades the production of this fuel employing biological routes has been studied and dark fermentation has been reported as the most efficient technology due to the high yield and hydrogen production rate [2]. Fermentative bacteria uses a wide range of substrates like hexoses, pentoses, wastewater or lignocelluloses to produce hydrogen, thus the use of lignocellulosic biomass is associated with the reduction in hydrogen producing cost; since this biomaterial is the most abundant around the world and it can be obtained from agro-industrial, forestry, agricultural and even municipal wastes. The high amount of carbohydrates in lignocellulosic matrix is another advantage of this natural resource, however in order to increase the fermentability and the performance of biohydrogen production is necessary to transform these carbohydrates (cellulose and hemicellulose) into monomeric sugars [1,3]. One of the most efficient methods to do that is acid hydrolysis; in contrast with enzymatic hydrolysis this method is economic, rapid and has the capability to produce fertilizers and food nutrimental after hydrolysis [4]. Some organic and inorganic acids have been employed for sugar production, not only sulfuric but phosphoric acid have been reported as viable options to increase sugar recovery, this last one has the advantage to be less toxic and corrosive than sulfuric acid, in recent years hydrolysis with phosphoric acid at low and high concentrations has been reported [4,5].

The aim of the present work was to evaluate the potential of stem of faba bean for reducing sugar production by dilute phosphoric acid hydrolysis and to determine the kinetic and thermodynamic parameters of the process. Stem of faba bean is a lignocellulosic material which has not been extensively studied and is one of the most abundant agricultural wastes in Mexico State. Also the estimation of biohydrogen production from reducing sugars employing yields previously reported is also discussed.

2. Materials and Methods

2.1 Raw material

Samples of stem of faba bean without pesticides were collected from a local crops located in Xalatlaco, Mexico State, Mexico. Stems were air-dried at room temperature, milled in an agricultural mill, particles inferior to 250 µm were recovered, to eliminate intermediates as chlorophyll, terpenes and resins, an extraction with ethanol-toluene (1:2) in a soxhlet extractor was carried out. After the solid fraction was characterized according to Standard Methods [6] to quantify the amount of ashes and total of volatile solids, holocellulose was determined by chlorite method [7] and acid insoluble lignin by sulfuric acid digestion.

2.2 Dilute acid hydrolysis

For acid hydrolysis, 1 g of milled and dried stem of faba bean was mixed into 30 mL glass flasks, with 15 mL of phosphoric acid solutions at two concentrations 0.58 and 1.34 M, the mixtures were slowly homogenized and heated at 90, 100 and 110 ºC. 2 samples were taken every 30 minutes until 300 minutes, and then cooled at room temperature during 10 minutes. The liquid and solid phases were separated by filtration; the solid phases were washed with hot distilled water until neutrality. The hydrolysate (liquid phase) was used to determine the amount of reducing sugars.

The reducing sugars were quantified by dinitrosalicylic acid (DNS) method [8]. 300 µL of each hydrolysate were diluted with deionized water until a final volume of 3 mL and sodium hydroxide was added until reaching a pH 8, then they were centrifuged at 10,000 rpm for 5 minutes. 500 µL of the liquid phase were taken and mixed with 500 µL of DNS reagent in a 12 mL test tube, which were subsequently placed in a water bath at 92 ºC for 5 minutes. Tubes were cooled at room temperature and deionized water was added 10 mL. Absorbance was read in a Perkin Elmer Spectrophotometer λXLS at 540 nm; the calibration curve was made using glucose as reference.

2.3 Kinetic and thermodynamic analysis

For acid hydrolysis, the first and the most employed kinetic model was proposed by Saeman [9]. This is based on two consecutive first order reactions; the first associated with sugar production while the second corresponds to thermal sugars degradation. Sugar production data was fitted adequately to Saeman model (Ec. 1). All the fittings were performed in Origin 8.6 software using a non-linear regression analysis.

$$M = \frac{P_o \cdot k_1}{k_2 - k_1}\left[e^{-k_1 \cdot t} - e^{-k_2 \cdot t}\right] \qquad \text{(Ec. 1)}$$

Where M is the amount of reducing sugars produced, P_o the initial amount of cellulose and hemicellulose; both given in g / 100 g of stem of faba bean, t is the reaction time in minutes, k_1 and k_2 correspond respectively to production and decomposition of sugars rate constants given in min^{-1}.

Arrhenius equation (Ec. 2) was used to determine the Activation Energy (*Ea*) and the Frequency factor (*A*)

$$\ln(k) = lnA - \frac{E_a}{RT} \qquad \text{(Ec. 2)}$$

In this equation k is the rate constant given in min^{-1}, T the temperature in K, R the ideal gas constant (8.3144 J mol^{-1} K^{-1}), *Ea* in KJ mol^{-1} and A in min^{-1}.

The change on Enthalpy (*ΔH*) and Entropy (*ΔS*) was quantified by Eyring equation (Ec. 3).

$$\ln\left(\frac{k}{T}\right) = ln\frac{k_B}{h_p} + \frac{\Delta S}{R} - \frac{\Delta H}{RT} \qquad \text{(Ec. 3)}$$

k is the rate constant given in sec^{-1}, k_B the Boltzmann constant ($1.3807X10^{-23}$ J K^{-1}) h_p the Planck constant ($6.6261X10^{-34}$ J s), *ΔH* given in KJ mol^{-1} and *ΔS* in J mol^{-1} K^{-1}.

Free Gibbs energy (*ΔG* in KJ mol^{-1}) was calculated by thermodynamic relationship shown in Ec. 4.

$$\Delta G = \Delta H - T\Delta S \qquad \text{(Ec. 4)}$$

2.4 Characterization of stem of faba bean by FTIR

After hydrolysis and neutralization, the remainder solid phase was dried overnight at 45ºC and milled. FTIR was used to evaluate the structural changes due to acid hydrolysis. Raw and hydrolyzed stem of faba bean were analyzed in a "Varian 640" spectrometer employing a spectral range of 400 to 4000 cm^{-1} with a resolution of 4 cm^{-1} and 16 scans.

2.5 Estimation of biohydrogen production from reducing sugars

The highest yield of sugar production obtained in dilute acid hydrolysis was used to estimate the expected biohydrogen production by dark fermentation. For this, some biohydrogen production yields using acid hydrolysates as substrate given in mol H_2 / mol hexose reported previously were considered to estimate the volume of biohydrogen expected at different fermentative conditions.

3. Results and Discussion

3.1 Raw material composition

The amount of moisture determined for stem of faba bean particles was 3.27 ± 0.11%. Holocellulose is defined as the sum of cellulose and hemicellulose fraction, and for stem of faba bean the percentage of holocellulose was 61.48 ± 0.30%, while the acid insoluble lignin reached a value of 12.16 ± 0.66%. Total volatile solids is a measure of organic matter that microorganisms can metabolize, in contrast, ashes are associated with the amount of inorganic material and minerals. The amount of total volatile solids and ashes were 92.18 ± 0.18% and 7.82 ± 0.18% respectively. The percentage of ashes and lignin resulted similar to that obtained by Petersson *et al.* [10], who characterizing faba bean from Denmark determined percentages of 7.9 and 14.4% for ashes and lignin respectively. The amount of holocellulose calculated by them was lower (48.8%) to that obtained in present work, the difference can be associated to the nature of the faba bean, the growth conditions and the nature of the cultivation soil.

3.2 Reducing sugar production by phosphoric acid hydrolysis

Sugar production units in present work are given in g of sugar / 100 g of faba bean stem. As can be seen in **Fig. 1** in all experiments the maximum sugar production yield was achieved after 300 minutes, however, the experiment carried out at 110 ºC and 1.34 M H_3PO_4 showed the maximum sugar production after 270 minutes of 21.20 g of sugar / 100 g stem of faba bean, this value corresponds to a holocellulose-sugar conversion of 29.19%. One possible explanation for the decreasing in sugar production is that: the velocity of sugars decomposition to furfural and hydroximethyl furfural (inhibitory compounds at very low concentrations) was higher compared to sugars production rate. The lowest sugar production yield and the lowest holocellulose-sugar conversion were 5.11 g of sugar / 100 g of faba bean stem and 7.47% respectively, determined for the experiment at 0.58 M H_3PO_4, 90°C and 300 minutes reaction time.

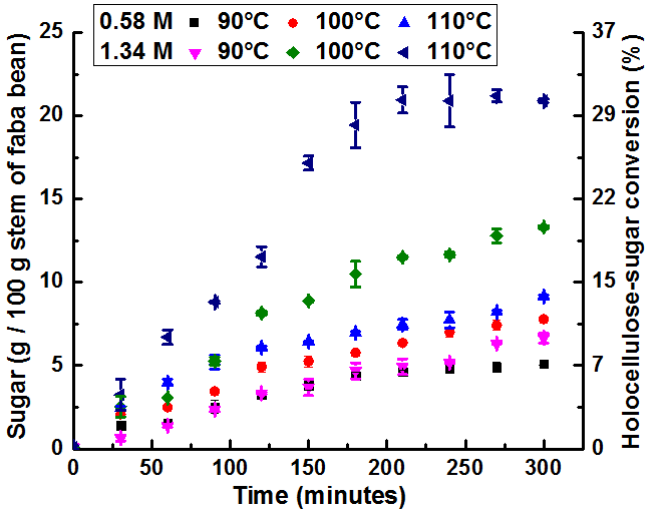

Fig. 1 Reducing sugars production from stem of faba bean at different hydrolysis conditions

In **Fig. 1** is observed the influence of acid concentration, temperature and reaction time in sugar production, at the same reaction time 270 min and temperature 110°C for 0.58 M and 1.34 M phosphoric acid concentrations, the sugars yields changed from 8.21 to 21.2 g of sugar / 100 g of stem of faba bean respectively. In contrast, at the same phosphoric acid concentrations 0.58 M or 1.34 M sugar production yields increased as a function of temperature, the maximum yields was achieved at 110 °C; 9.16 at 300 min reaction time and 21.2 g at 270 min reaction time respectively.

The production yield of 21.20 g of sugar / 100 g stem of faba bean obtained at 110°C in 1.34 M H_3PO_4 and after 270 minutes, is higher compared to that of 16.57 g of sugar / 100 g stem of faba bean obtained by our research team in a previous hydrolysis with 1.34 M H_3PO_4, 130°C and 120 minutes reaction time [11]. López-Linares *et al.* [4] in an acid hydrolysis of rapeseed straw with phosphoric acid 0.036 M reached an optimal sugar production of 12.9 g of sugar / 100 g raw material; this yield was similar to that obtained in present work with 1.34 M, 100°C and

300 minutes. Moreover, the maximum yield is comparable but slightly lower to that reported by Guerra-Rodríguez [12] who evaluated sugar production from wheat straw. The differences in sugar production can be attributed to the kind and amount of carbohydrates in lignocellulosic matrix, hydrolysis temperature and acid concentration.

3.3 Kinetic and thermodynamic parameters for acid hydrolysis of stem of faba bean

In order to determine the kinetic parameters for dilute acid hydrolysis of stem of faba bean, Saeman model (Ec. 1) was employed. As can be seen in **Fig. 2** the non-linear fitting of this model was adequately. **Table 1** summarizes the kinetic and statistical parameters for this model.

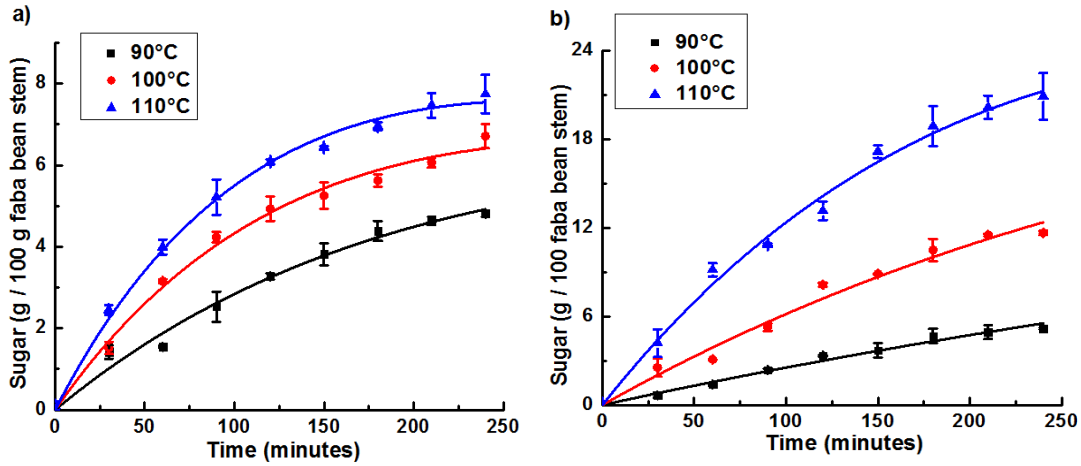

Fig. 2 Experimental sugar production data and Saeman model fitting in H_3PO_4 hydrolysis carried out with a) 0.58 M and b) 1.34 M

Table 1 Kinetic and statistical parameters for acid hydrolysis of stem of faba bean

Model	**Saeman**		
Test	k_1 (min^{-1})	k_2 (min^{-1})	R^2
0.58 M and 90°C	$5.93X10^{-4}$	$4.51X10^{-3}$	0.982
0.58 M and 100°C	$1.03X10^{-3}$	$6.79X10^{-3}$	0.991
0.58 M and 110°C	$1.39X10^{-3}$	$7.72X10^{-3}$	0.995
1.34 M and 90°C	$4.39X10^{-4}$	$8.96X10^{-4}$	0.987
1.34 M and 100°C	$1.14X10^{-3}$	$1.41X10^{-3}$	0.987
1.34 M and 110°C	$2.55X10^{-3}$	$2.22X10^{-3}$	0.996

Kinetic constants shown in **Table 1** were considered to determine thermodynamic parameters by Arrhenius and Eyring equations. **Fig. 3** shows the linear fittings of Arrhenius equation using the rate constants calculated with Saeman model.

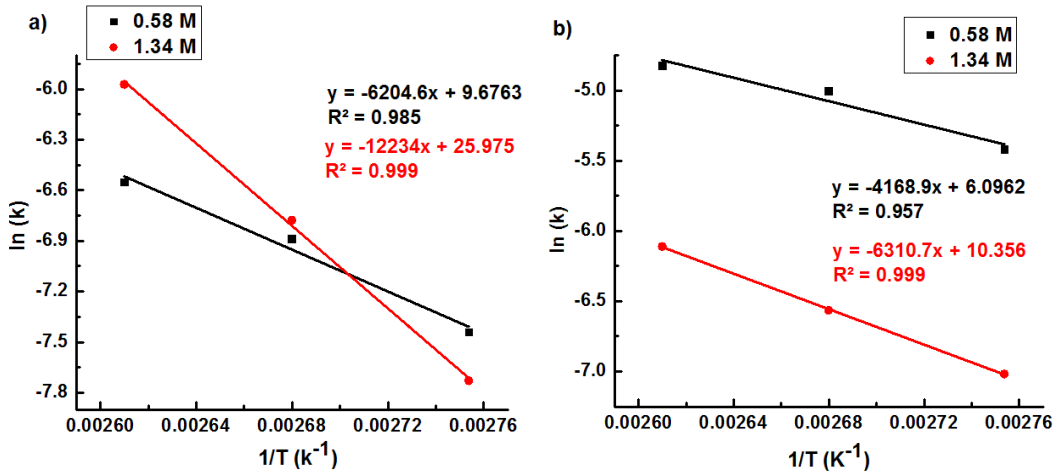

Fig. 3 Linear fittings of Arrhenius equation using a) k_1 and b) k_2 rate constants calculated with Saeman model

Table 2 Thermodynamic parameters for phosphoric acid hydrolysis of stem of faba bean

H_3PO_4 (M)	Ea (KJ mol^{-1})	A (min^{-1})	ΔH (KJ mol^{-1})	ΔS ($Jmol^{-1}K^{-1}$)	K	ΔG (KJ mol^{-1})
For k_1						
0.58	51.59	$7.9X10^3$	48.49	-208.69	363.15	124.28
					373.15	126.36
					383.15	128.45
1.34	96.01	$3.21X10^{10}$	98.62	-73.18	363.15	125.19
					373.15	125.93
					383.15	126.66
For k_2						
0.58	31.23	$1.46X10^2$	31.56	-238.46	363.15	118.16
					373.15	120.54
					383.15	122.93
1.34	78.98	$1.21X10^8$	49.37	-203.04	363.15	123.10
					373.15	125.13
					383.15	127.16

The slope and the intersection with Y axis were used to determine thermodynamic parameters. As can be seen in **Table 2**, the parameters *Ea, A, ΔH* and *ΔG* resulted in positive values while *ΔS* were negative. In agreement with collisions and activated complex theory sugar production by acid hydrolysis of stem of faba bean is an endothermic and non-spontaneous reaction with the maximum amount of energy on reactants. The *Ea* and *ΔH* calculated in this work with 0.58 M

resulted similar to that reported previously by Tizazu *et al.* [13], who evaluated the xylose production in an acid hydrolysis of sugarcane bagasse with 0.2 M sulfuric acid in a temperature range of 100-130 °C. A direct comparison results difficult due to the differences in the nature of biomass, kind and concentration of acid and the analyzed sugar. Kinetic and thermodynamics of dilute acid hydrolysis has been studied fewer and more researches are needed.

3.4 Characterization of stem of faba bean by FTIR

Normalized FTIR spectra of the samples taken before and after acid hydrolysis with 1.34 M H_3PO_4, 110°C and after 180 and 300 minutes are shown in **Fig 4**. The acronyms C, H and L correspond to cellulose, hemicellulose and lignin respectively, and the symbol β is associated to the beta 1-4 glycosidic linkage, characteristic of cellulose and hemicellulose. The main characteristic vibrations of cellulose appear between 1200 and 1000 cm^{-1}. Hemicellulose has their main characteristic bands at 1240 cm^{-1} and 1732 cm^{-1} [14], this last vibration has been attributed to the C=O linkage of acetyl group and has not been observed in any spectra of the **Fig 4a**, this fact suggests that the amount of hemicellulose present in stem of faba bean was low. The vibration located at 1054 cm^{-1} corresponds to C-O-C bond of hemicellulose and cellulose, however, it also has been associated to the primary and secondary alcohols of lignin. This vibrational band increased their amplitude and became more defined after 300 minutes of acid hydrolysis, this fact that can be attributed to the depolymerization of cellulosic fraction, since the characteristic region of this polysaccharide overlapped the vibration at 1054 cm^{-1}. In **Fig. 4b** a vibrational band located at 1422 cm^{-1} is observed, this band corresponding to the characteristic CH_3-O functional group of lignin increased it amplitude after hydrolysis, in contrast; the vibrations at 1373 and 1366 cm^{-1} associated to the C-H bond of cellulose and hemicellulose decreased their intensity as a function of sugar production.

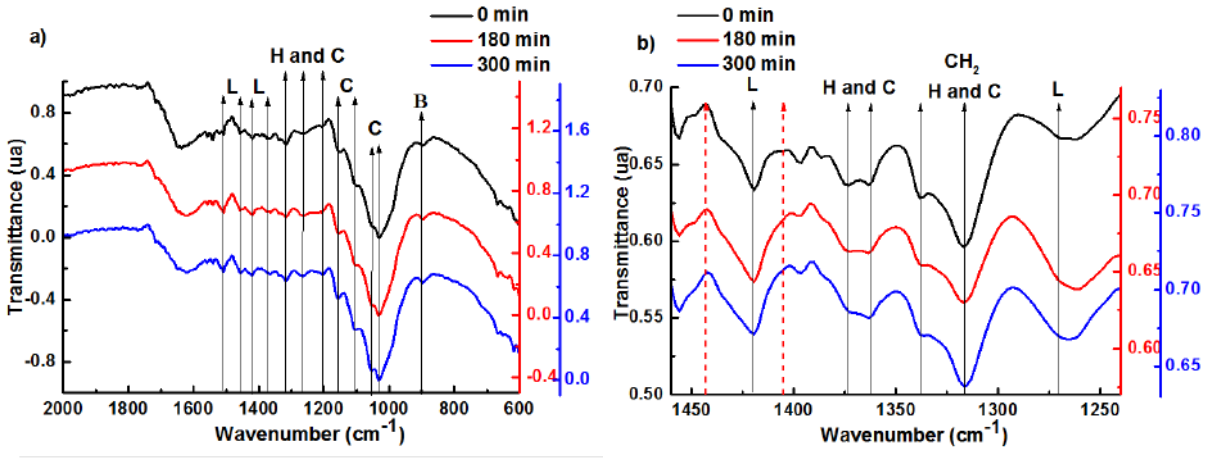

Fig. 4 FTIR spectra of corn stover before and after acid hydrolysis at 130°C and 1.34 M H_3PO_4 in spectra ranges of a) 2000–600 cm^{-1} and b) 1460-1240 cm^{-1}

3.5 Estimation of biohydrogen production from reducing sugars

The maximum sugar production yield obtained in present work (21.20 g of sugar / 100 g of stem of faba bean) was used as basis to estimate biohydrogen production by anaerobic digestion employing different fermentative conditions. A previous work reported by Gómora *et al.* [11], studied the production of biohydrogen with a consortia made by *Clostridium butyricum* and *Enterobacter cloacae* using stem of faba bean hydrolysates as substrate, the maximum hydrogen production yield obtained by them was 0.33 mol H_2 / mol hexose. Taking into account this hydrogen yield and glucose as reducing sugars, the volume of hydrogen expected is 0.87 liters. Sagnak *et al.* [15]. obtained a hydrogen yield of 1.46 mol H_2 / mol hexose in mesophilic fermentation of waste ground wheat hydrolysate using anaerobic sludge as substrate, with this yield the expected maximum volume of hydrogen is 3.85 liters. Cao *et al.* [16] and Ozmihci *et al.* [17] evaluated the potential of corn stover and wheat starch hydrolysates for biohydrogen production using thermophilic fermentation, the maximum yields obtained by them were 2.24 and 2.70 mol H_2 / mol hexose respectively. Considering these yields, the maximum volume of hydrogen that can be produced from the maximum reducing sugars yield obtained in present work is 5.91 and 7.13 liters respectively. These values show the potential of hydrolysates for biohydrogen production.

Detoxification of hydrolysates prior to fermentation allows to increase biohydrogen production, and one of the most employed detoxification methods is neutralization, this method not only partially eliminate inhibitors but can produce salts of commercial interest. From this point of view, biohydrogen production from acid hydrolysates has a great potential and seems to be economically viable and scalable, however, is necessary to deepen knowledge of lignocellulose composition of faba bean to increase sugar production and to reduce the operational costs for hydrogen production.

Conclusion

The maximum sugar production yield was 21.20 g of sugar / 100 g of stem of faba bean. An increase in sugar production is associated with an increase in acid concentration and temperature before the formation of inhibitory compounds. Sugar production data was fitted adequately with Saeman model. According to thermodynamic parameters, sugar production by dilute phosphoric acid hydrolysis of stem of faba bean is an endothermic and non-spontaneous process with maximum amount of energy on reactants. The maximum calculated yield of hydrogen production was 6.5 ± 0.5 liters/100 g of stem of faba bean. In order to evaluate the real potential of stem of faba bean hydrolysates as substrate for fermentative purposes, is necessary to obtain experimental data of biohydrogen production.

Acknowledgements

Julio César Gómora Hernández thanks CONACYT for his Doctorate scholarship. ITT and ININ sponsored this work.

References

[1] Gokfiliz-Yildiz P., Karapinar I. Optimization of particle number, substrate concentration and temperature of batch inmobilized reactor system for biohydrogen prodcution by dark fermentation. *International Journal of Hydrogen Energy.* 2018; 43: 10655-10665.

[2] Lukajtis R., Holowacz I., Kucharska K., Glinka M., Rybarczik P., Przyjazny A., Kaminski M. Hydrogen production from biomass using dark fermentation. *Renewable and Sustainable Energy Reviews*. 2018; 91: 665-694.

[3] Behera S., Arora R., Nandhagopal N., Kumar S. Importance of chemical pretreatment for bioconversion of lignocellulosic biomass. *Renewable and Sustainable Energy Reviews*. 2014; 36: 91-106.

[4] López-Linares J. C., Cara C., Moya M., Ruiz E., Castro E., Romero I. Fermentable sugar production from rapeseed straw by dilute phosphoric acid pretreatment. *Industrial Crops and Products*. 2013; 50: 525-531.

[5] Siripong P., Duangporn P., Takata E., Tsutsumi Y. Phosphoric acid pretreatment of *Achyrantes aspera* and *Sida acuta* weed biomass to improve enzymatic hydrolysis. *Bioresource technology,* 2016; 203: 303-308.

[6] APHA. 2005. Standard Methods for Water and Wastewater Examination, 21 st ed. American Public Health Association-American Water Works Association, *Water Environment Federation Publication*, Washington, DC. USA.

[7] Wise L. E., Murphy M., D'Adieco A. Chlorite holocellulose, its fractionation and beating on summative wood analysis and on studies on the hemicelluloses. *PaperTradeJournal*. 1946; 122:35-45.

[8] M. G. Lorenz. Use of dinitrosalicylic acid reagent for determination of reducing sugars. *Analytical Chemistry.* 1959; 31: 426-428.

[9] J. F. Saeman, Kinetics of wood saccharification: Hydrolysis of cellulose and decomposition of sugars in dilute acid at high temperature, *Industrial and Engineering Chemistry*, 1945; 37: 43-52.

[10] Petersson A., Thomsen M. H., Hauggaard-Nielsen H., Thomsen A. B. Potential bioethanol and biogas production using lignocellulosic biomass from winter rye, oilseed rape and faba bean. *Biomass & Bioenergy,* 2007; 31: 812-819.

[11] Gómora-Hernández J. C., Alcántara-Díaz D., Fernández-Valverde S. M., Hernández-Berriel M. C. Biohydrogen production by anaerobic digestion of corn cob and stem of faba bean hydrolysates. *2016 XVI International Congress of the Mexican Hydrogen Society.* 2017:1-6.doi: 10.1109/CSMH.2016.7947659.

[12] Guerra-Rodríguez E., Portilla-Rivera O. M., Jarquín-Enríquez L., Ramírez J. A., Vázquez M. Acid hydrolysis of wheat straw: A kinetic study. *Biomass & Bioenergy*. 2012; 36: 346-355.

[13] Tizazu B. Z., Moholkar V. S. Kinetic and thermodynamic analysis of dilute acid hydrolysis of sugarcane bagasse. *Bioresource technology,* 2018; 250: 197-203.

[14] Li P., Cai D., Luo Z., Qin P., Chen C., Wang Y., Zhang C., Wang Z., Tan T. Effect of acid pretreatment on different parts of corn stalk for second generation ethanol production. *Bioresource technology,* 2016; 206: 86-92..

[15] Sagnak R., Kargi F., Kapdan I. K. Biohydrogen production from acid hydrolyzed waste ground wheat by dark fermentation. International Journal of Hydrogen Energy, 2011; 36: 12803-12809.

[16] Cao G., Ren N., Wang A., Lee D. J., Guo W., Liu B., Feng Y., Zhao Q. Acid hydrolysis of corn stover for biohydrogen production using *Thermoanaerobacterium thermosaccharolyticum W16. International Journal of Hydrogen Energy,* 2009; 34: 7182-7188.

[17] Ozmihci S., Kargi F., Cakir A. Thermophilic dark fermentation of acid hydrolyzed waste ground wheat for hydrogen gas production. International Journal of Hydrogen Energy, 2011; 36: 2111-2117.

XVIII International Congress
of the Mexican Hydrogen Society

Hydrogen Production by Anaerobic Digestion from *Agave lechuguilla* Hydrolysates

Leopoldo J. Rios-González[1,*], Thelma K. Morales-Martínez[1], Gabriela G. Hernández-Enríquez[1], José A. Rodríguez-De la Garza[1], and Mayela Moreno-Dávila[1].

[1] Departament of Biotechnology, Faculty of Chemistry, Autonomous University of Coahuila.
Boulevard V. Carranza y José Cárdenas Valdez, col. Republica Oriente. C.P.25280. Saltillo, Coahuila, México.
Tel: +52 844 4155752, ext. 5. Fax: +52 844 4159234
* Corresponding author: leopoldo.rios@uadec.edu.mx

ABSTRACT

This work assessed the hydrogen production from enzymatic hydrolysates of *Agave lechuguilla* pretreated by autohydrolysis. The pretreatment was carried out in a high-pressure reactor using a solid/liquid ratio of 1:6 (w/v) at 190 °C over 30 min at 200 rpm. The pretreated solids were enzymatically hydrolyzed and then digested with a treated mixed consortium under different conditions using a Taguchi ($L_9(3^4)$) experimental array. The results showed that the xylan was 65.17% solubilized during pretreatment, and the glucan preserved was 77.52% hydrolyzed, obtaining a hydrolysate with 55 g/L of glucose. The production of hydrogen after anaerobic digestion of hydrolysates was significantly influenced mainly by the temperature (80.6%) and glucose concentration (15.1%). The best conditions were 40 ºC, glucose 20 g/L, inoculum 5% (v/v), and initial pH 7. Under optimal conditions, the hydrogen yield achieved was 3.48 mol H_2/mol glucose consumed at 120 h.

Keywords: *Agave lechuguilla; Autohydrolysis pretreatment; Anaerobic digestion; Hydrogen*

1. Introduction

Energy plays a major role in world economic and social development; however, today's energy is produced mainly from non-renewable sources that are considered pollutants. Therefore, continuous diversification of energy sources is of crucial importance to every nation, and Mexico is no exception [1]. Hydrogen is one of the most promising energy carriers due to its high energy-yield efficiency and low generation of pollutants [2]. Natural gas reforming is a well-established technology used in many refineries and chemical industries in Mexico for large-scale H_2 production [3]. However, the production of hydrogen *via* this process generates large

quantities of carbon dioxide (CO_2), one of the main causes of global warming [4]. The biological process of anaerobic digestion is an environmental friendly process and can utilize a wide range of substrates [5], including different lignocellulosic feedstocks such as forest and agricultural residues or crops not used for food or feed [6]. However, due to the complex plant cell wall structures, lignocellulosic materials are not capable of undergoing fermentation without previous pretreatment and hydrolysis [7].

There is abundant research on hydrogen production from lignocellulosic hydrolysates [1,2,4,5,7,8,9,10,11,12,13]. However, only a few studies from agave biomass are available in the current literature [1,14,15]. *Agave lechuguilla* (lechuguilla) is a common plant of northern Mexico, occupying the largest range of all agaves with almost 20 million hectares of the arid and semiarid lands of México [16].*A. lechuguilla* traditionally has been exploited for extracting fibers used in the manufacture of metal polishing brushes, furniture and car seat fillings, carpets and cleaning brushes, as a construction material in combination with thermoplastic resins, and as a concrete reinforcement [17]. *A. lechuguilla* cogollos (the heart or pulpy central stem with attached leaf bases) can be harvested many times without sacrificing the whole plant. The annual productivity, with 427 mm of average rainfall, is 4 tons per hectare [18], making it an attractive energy crop. Moreover, *A. lechuguilla* has potential as a feedstock for ethanol production [19,20,21]

During anaerobic digestion, the sludge contains different microorganism groups. Hydrogen consumers like methanogens are present and are strongly subjected to deactivation *via* different methods (high temperature, UV radiation, extremely low or high pH) to obtain an enriched mixed consortium of *Clostridium*-like microorganisms that are known to produce hydrogen [5]. Several factors affect hydrogen production in addition to the nature and treatment of the mixed consortia, such as temperature, pH, mineral medium formulation, type of inoculum, the profile of organic acids produced, and the type and concentration of substrate [12].

The present work assesses the effects of temperature, substrate concentration, initial pH, and inoculum on hydrogen production from *A. lechuguilla* hydrolysates in batch reactors to optimize the process *via* a Taguchi ($L_9(3^4)$) experimental array.

2. Materials and Methods

2.1 *Feedstock*

All cogollos (*A. lechuguilla*) were harvested from Ramos Arizpe, Coahuila, Mexico (latitude 25° 55' 47" North, longitude 101° 55' 47" West). For storage purposes, the cladodes of the cogollos were completely separated and dried for 24 to 30 h at 45 °C in a tray dehydrator (model KL10, Queretaro, Mexico). The dried material was milled to obtain a particle size of 2 mm in a cutting mill (Retsch SM100, Retsch, Haan, Germany). After milling, the material was stored in plastic containers at room temperature until further use.

2.2 Determination of feedstock composition and pretreatment

Before chemical composition determination, the moisture content was determined with a moisture analyzer (Moisture Analyzer OHAUS; Parsippany, NJ). Cellulose (glucan), hemicellulose (xylan), and lignin were quantified according to Rios *et al*. [20] using *A. lechuguilla*

extractives free, which was removed and determined using the analytical method NREL/TP-510-42619 [22]. Finally, ashes and proteins were determined using the analytical method NREL/TP-510-42622 [23] and Kjeldahl method, respectively.

The autohydrolysis pretreatment of *A. lechuguilla* was carried out in a 5-gallon high-pressure stainless-steel reactor (Parr Instruments Company, Moline, IL, USA). The dried and milled material (2.192 kg of *A. lechuguilla*) was suspended in 13.15 L of distilled water (resulting in a 1:6 w/v solid/liquid ratio) at 190 °C and 200 rpm for 30 min, corresponding to a severity factor (SF) of 4.127; the heating up and cooling down time was not considered in SF calculations. These conditions were established previously by Ortíz-Méndez *et al*. [24]

The reactor was opened when the temperature decreased to 50 °C. Subsequently, the pretreated material was washed with water and the glucan, xylan, and lignin content were determined. The enzymatic loading calculations were established according to the glucan content present in the pretreated material.

2.3 Enzymatic hydrolysis of the pretreated solids

The pretreated solid fraction was hydrolyzed using Cellic® CTec3 (kindly provided by Novozymes A/S, Kalundborg, Denmark), with a cellulase activity of 217 FPU/mL. FPU is the activity unit of cellulase when filter paper is used as the enzymatic hydrolysis substrate, according to Ghose [25]. The enzymatic hydrolysis was carried out at a solids loading of 25% (w/w) in the presence of 0.05 M sodium citrate buffer at a pH of 4.8, using an enzyme loading of 15 FPU per gram of glucan in a 15 L glass reactor with mechanical stirring and controlled with an eZ Applikon® module (Schiedam, Netherlands). The reactor was maintained at 50 °C and 200 rpm for 72 h. The slurry obtained was withdrawn from the reactor and centrifuged at 10000 × *g* for 15 min. The liquid fraction (hydrolysate) was filtered and analyzed by HPLC to determine the glucose concentration.

The enzymatic hydrolysis yield was expressed as the relationship between the amount of glucose released during saccharification and the initial amount of glucan present in the pretreated material. The enzymatic hydrolysis yield was calculated as described by Fang *et al*. [26]

2.4 Inoculum and treatment

The anaerobic granular sludge used in the present work was obtained from a large-scale up-flow anaerobic sludge blanket (UASB) reactor provided by the Modelo S. De R. L. De C. V. brewery located in Torreon, Coahuila, Mexico. To eliminate hydrogen-consuming microorganisms, the sludge was heated in a boiling water bath at 105 °C for 30 min, then cooled down and followed by an acid treatment that involved decreasing the pH of the sludge to 3.0 using 0.1 N HCl solution for 24 h. After this period, the pH was adjusted to 7.0 with a 0.1 N NaOH solution [27]. The sludge obtained was separated by filtration and used as an inoculum in the hydrogen production assays.

2.5 Optimization of hydrogen production from enzymatic hydrolysate

An orthogonal experimental array ($L_9(3^4)$) was applied to optimize the hydrogen production from enzymatic hydrolysates of *A. lechuguilla* biomass. Nine experiments were

carried out at the temperatures 30, 40, and 50 °C; glucose concentrations 20, 37.5, and 55 g/L; inocula of 5, 10, and 15% (v/v); and initial pH values 5, 6, and 7. The hydrogen fermentation conditions and the orthogonal experiment array are shown in the Tables 1 and 2, respectively.

Table 1. Factors and Levels in the Orthogonal Experiments

Factors	Levels		
	1	2	3
A, Temperature (°C)	30(A1)	40(A2)	50(A3)
B, Glucose concentration (g/L)	20(B1)	37.5(B2)	55(B3)
C, Inoculum (v/v, %)	5(C1)	10(C2)	15(C3)
D, Initial pH	5(D1)	6(D2)	7(D3)

Each experiment was carried out in a 25 mL glass bottle that contained 10 mL of hydrolysate. The hydrolysate was previously supplemented with a mineral medium described by Contreras-Dávila *et al*. [15], in g/L: $NH_4H_2PO_4$, 4.5; Na_2HPO_4, 0.635; K_2HPO_4, 0.125; $MgCl_2{\cdot}6H_2O$, 0.1; $ZnCl_2$, 0.075; $FeSO_4{\cdot}7H_2O$, 0.025; $MnSO_4{\cdot}H_2O$, 0.009; and $CuSO_4{\cdot}5H_2O$, 0.005. The glucose concentration and pH of the hydrolysates were adjusted as described in the experimental design. The amount of anaerobic treated sludge (inoculum) added for each experiment is described in Table 2.

Table 2. Orthogonal Experiment Array

Experiment No.	Factors/Levels			
	A, Temperature (°C)	B, Glucose Concentration (g/L)	C, Inoculum (v/v, %)	D, Initial pH
1	A1	B1	C1	D1
2	A1	B2	C2	D2
3	A1	B3	C3	D3
4	A2	B1	C2	D3
5	A2	B2	C3	D1
6	A2	B3	C1	D2
7	A3	B1	C3	D2
8	A3	B2	C1	D3
9	A3	B3	C2	D1

After adding the inoculum, the reactors were sealed with butyl rubber stoppers and aluminum caps to avoid gas leakage and flushed with N_2 (100%) gas for 15 min to promote an anaerobic environment. Hydrogen and methane production were determined by gas chromatography and measured at 20, 44, 68, and 92 h. After every measurement, the reactors were flushed with N_2 (100%) as described above. The initial and final glucose concentration were determined by High Performance Liquid Chromatography

(HPLC). The hydrogen production yield (mol H_2/mol of consumed glucose) was considered the dependent variable. The experimental data was analyzed statistically by the ANOVA method using Qualitek-4® software (Nutek, Inc., Bloomfield Hills, MI, USA). To validate the results, a set of experiments were further performed using the obtained optimized conditions with a 50.5 mL of hydrolysates.

2.6 Analytical Methods

The hydrogen and methane produced were measured by gas chromatography (Varian 3400, Palo Alto, USA) equipped with a TCD detector at 200 °C and a Molecular Sieve 5A packed column at 30 °C, using argon as the carrier gas with a flow rate of 6 mL/min. The sugars (glucose, xylose, cellobiose, and arabinose) were determined by HPLC (Agilent 1260 Infinity, CA, USA) equipped with a refractive index detector at 45 °C, using an Agilent Hi-Plex H column at 35 °C (7.7 x 300 mm, CA, USA) and 5 mM H_2SO_4 as the mobile phase at a flow rate of 0.5 mL/min. All experiments were carried out in triplicate, and the average values are reported.

3. Results and Discussion

3.1 Composition of A. Lechuguilla and Autohydrolysis Pretreatment

The extractives were the main component in *A. lechuguilla* cogollos in dry base w/w (29.84%). The glucan, xylan, and lignin contents were 18.21%, 7.71%, and 21.67%, respectively. The ashes and protein contents were 8% and 5.5%, respectively and a 9.07% corresponded to non-detected components.

The solids composition of *A. lechuguilla* pretreated by autohydrolysis is summarized in Table 3. The glucan content was increased after pretreatment compared with untreated biomass (increasing from 18.21% to 28.19%). From the initial glucan content present in the untreated material, 86.42% remained in the solid phase. The hydrolysis of xylan is one of the main effects of the autohydrolysis process, and its degradation products are dissolved in the liquid phase during pretreatment, while glucan and most of the insoluble lignin are retained completely in the solid phase [28,29]. As expected, autohydrolysis mainly affected the hemicellulosic components, and under these conditions 65.17% of the original xylan content was solubilized. The solids recovered after pretreatment were 55.82% from the raw material, mainly due to the solubilization of extractives and xylan during the process. The lignin was not solubilized during the pretreatment process, and these results are similar to previous reports with other materials pretreated with the same method, in which the lignin content increased by over 100% relative to the initial lignin content in the raw material [30,31].

Delignification is not the only factor to decrease lignocellulose recalcitrance; in a previous study on ethanol production from *Agave tequilana* bagasse pretreated by autohydrolysis [20],the hemicellulose (xylan) removal improved the enzymatic hydrolysis (obtaining an 81.5% hydrolysis yield).

3.2 Enzymatic hydrolysis of the pretreated solids

Table 3 also shows the enzymatic hydrolysis of pretreated *A. lechuguilla*, reaching a

glucose concentration of 55 g/L at 72 h, corresponding to a hydrolysis yield of 77.52%. However, no significant increase in the glucose concentration was observed after 24 h of enzymatic hydrolysis (data not shown), and it is likely that in this period, the cellulases started to present inhibition. This result can be attributed to an increase in the diffusional limitation of cellulases by a high solid loading, or to lignin's effect on the action of enzymes *via* the blocking of access to the cellulose [32].

The sugar (glucose) concentrations used (55 g/L, 37.5 g/L, and 20 g/L) are similar to other reports of H_2 production using hydrolysates obtained from *A. tequilana* bagasse. [1] assessed the H_2 production using hydrolysates, with total sugar concentrations of 27.9 and 18.9 g/L from cooked and uncooked bagasse, respectively, obtained by acid hydrolysis with HCl. Using the same raw material, Arreola-Vargas *et al*. [14] assessed H_2 production using acid and enzymatic hydrolysates, with total sugar concentrations of 17.3 g/L and 8.9 g/L, respectively. Contreras-Dávila *et al*.[15], assessed this same process (H_2 production) using two enzymatic hydrolysates with a total sugar concentration that ranged from 11 to 12.5 g/L.

Table 3. *A. lechuguilla* Composition after Autohydrolysis Pretreatment and Performance of Enzymatic Hydrolysis of Pretreated Solids.

Pretreatment (% w/w)		**Enzymatic Hydrolysis (72 h)**
Glucan	28.19 ± 0.94	Glucose (g/L)
Xylan	4.81 ± 0.36	55 ± 0.51
Lignin	48.50 ± 0.72	Hydrolysis Yield (%)
Solids Recovery	55.82 ± 1.6	77.52 ± 0.72

3.3 Optimization of hydrogen production from enzymatic hydrolysate

Table 4 shows that maximum H_2 production was obtained at 40 °C (3.58 to 4.09 × 10^{-3} mol), with a significant decrease at 50 °C (0.733 to 0.936 × 10^{-3} mol). The optimal temperature for H_2 production varies widely based on the nature of the biocatalyst and the type of substrate used. For mixed consortia, diverse optimum temperatures have been reported [32]. Glucose consumption was observed in all cases; however, higher hydrogen yields were observed in the cases where the initial glucose concentration was lower (20 g/L), while the maximum hydrogen yield (3.3 mol H_2/mol glucose consumed) was observed in the case of an experiment carried out at 30 °C, 10% (v/v) of inoculum and initial pH of 7.0. The decrease in the hydrogen yield can be attributed to an inhibition caused by high initial substrate concentration or to the presence of a higher concentration of inhibitory by-products present in the hydrolysate, such as furfural and HMF [20]. In addition, a high substrate concentration can cause a buildup of cell concentration and volatile fatty acids (VFAs) in the system, leading to a decline of pH in the reactor that could inhibit hydrogen production [33].

Table 4. Hydrogen Production and Glucose Consumption from *A. lechuguilla* Hydrolysate at 92 h of Fermentation.

Experiment No.	**H_2 (mol x 10^{-3})**	**Glucose Consumed**	**Final pH**	**mol H_2/mol Glucose**

		(mol x 10^{-3})		Consumed
1	2.4 ± 0.12	1.1 ± 0.05	5.1 ± 0.01	2.2 ± 0.08
2	1.6 ± 0.08	1.6 ± 0.14	4.9 ± 0.03	1.0 ± 0.11
3	3.37 ± 0.13	2.3 ± 0.12	5.0 ± 0.01	1.4 ± 0.12
4	3.58 ± 0.07	1.1 ± 0.08	4.8 ± 0.04	3.3 ± 0.07
5	4.53 ± 0.28	1.7 ± 0.11	5.2 ± 0.08	2.7 ± 0.19
6	4.09 ± 0.43	1.7 ± 0.19	5.0 ± 0.03	2.4 ± 0.31
7	0.799 ± 0.09	0.8 ± 0.06	5.1 ± 0.15	0.9 ± 0.07
8	0.936 ± 0.08	1.4 ± 0.15	5.0 ± 0.09	0.7 ± 0.11
9	0.733 ± 0.05	1.9 ± 0.11	5.2 ± 0.18	0.4 ± 0.08
*Methane not detected in all cases.				

As mentioned above, an inhibitory effect of high substrate concentration generally occurs in anaerobic digestion processes, depending on the type of substrates and microorganisms. The initial substrate concentration plays an important role on the yield and production rate of hydrogen [12,34] observed a decrease in H_2 production at a sugar concentration of 30 g/L present in the hydrolysate of sugar cane bagasse that was previously subjected to acidic hydrolysis. Chen *et al*. [35] reported that H_2 production from sucrose by *Clostridium butyricum* CGS5 was higher at an initial sucrose concentration of 20 g-COD (Chemical Oxygen Demand)/L, while the fermentation process was inhibited at an initial sucrose concentration of 30 g-COD/L. Similar behavior was mentioned by Oh *et al*. [36], who reported the H_2 production by *Citrobacter* sp. Y19 with glucose as a carbon source and mentioned that hydrogen yield gradually decreased with the increase of glucose concentration at levels higher than 20 g/L.

Table 4 shows that pH values were similar for all cases (4.8 to 5.2). The pH, as mentioned before, is an important factor in anaerobic biological processes, due to its effects on Fe-hydrogenase activity, metabolic pathways, and the duration of the lag phase [37]. Carbohydrate-rich substrates have a greater potential to acidify the media during anaerobic fermentation, and as a result, in some situations system stability is hard to maintain. In hydrogen fermentation, reactors tend to acidify readily, and a reduction in the pH may take place. Low initial pH values below 5.0 inhibit hydrogen production. On the other hand, high initial pH values such as 9.0 decrease the lag phase time but tend to produce less hydrogen [12].

Table 5 shows the average effect of the factors at the assigned levels on the hydrogen yield. Both the lowest (0.4) and the highest (3.3) hydrogen yield were attributed to Factor A (Temperature) at level 2 (40 ºC) and level 3 (50 ºC), respectively. In the present study, three levels for each factor were selected, and the R values (Range extreme difference) were calculated based on the difference between the highest and lowest hydrogen yield. The highest R value was considered the most influential factor. As seen in the Table 5, the influence of these four factors on hydrogen yield was in the order A, B, D, C, based on R values.

Table 5. Main Effects of Selected Factors

Factor	Level 1	Level 2	Level 3	R
(A) Temperature (ºC)	1.60	2.78	0.67	2.12
(B) Glucose (g/L)	2.22	1.42	1.42	0.80
(C) Inoculum (% v/v)	1.75	1.63	1.67	0.12
(D) pH	1.78	1.45	1.82	0.37

Figure 1 shows the influence of each individual factor. The increase in the glucose concentration resulted in a decrease in hydrogen yield. For the temperature, the hydrogen yield was higher in level 2, increasing the temperature over 40 °C led to a reduction in hydrogen yield. The pH and inoculum were the factors with less influence over hydrogen yield, obtaining similar results for all levels. Taking into account the optimization process for the four factors, the optimum conditions were A2 (40 °C); B1 (20 g/L glucose); C1 (5 % v/v inoculum); D3 (initial pH 7).

Table 6 shows the ANOVA for hydrogen yield. According to Fisher test (F), the temperature is a more significant factor than the hydrogen yield. After the temperature, the glucose concentration was more significant than hydrogen yield, and pH and inoculum were the factors with the least significance.

Fig. 1. Individual factors performance at different levels

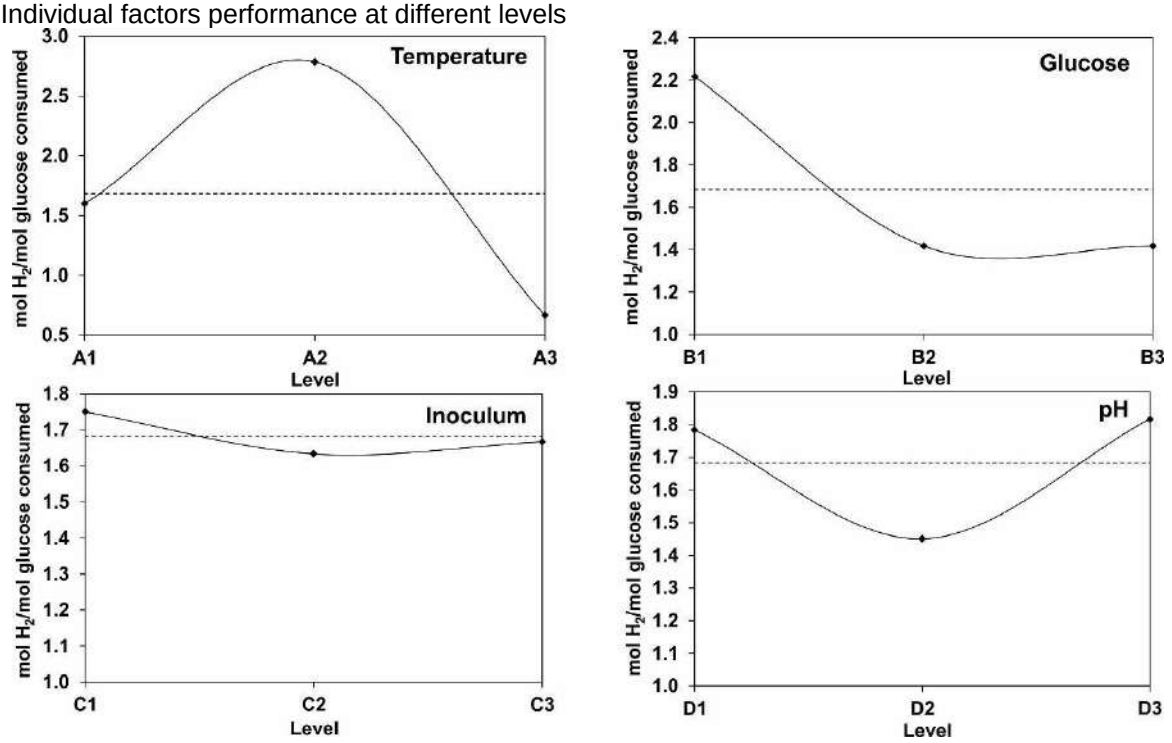

Fig. 1. Individual factors performance at different levels

Table 6. Analysis of Variance (ANOVA)

Factors	DOF	Sums of Squares	Variance	F-Ratio	Pure Sum	Percentage
Temperature	2	13.50	6.75	578.72	13.48	80.6
Glucose	2	2.56	1.28	109.71	2.54	15.185
Inoculum	2	0.04	0.02	1.86	0.02	0.119
pH	2	0.49	0.25	21.14	0.47	2.813
Other/Error	9	0.10	0.01			1.189
Total	17	16.71				

Figure 2 shows the relative influence of the four factors over the hydrogen yield. The temperature showed the highest impact over hydrogen yield (80.6%). Controlling each factor individually or as a whole can lead to a major increase in hydrogen yield. By studying the main effects of each factor, the general trends of the influence of the factors towards the process can be characterized. The characteristics can be controlled such that a lower or a higher value in a particular influencing factor can produce the preferred result. Therefore, the levels of factors to produce the best results can be predicted, so that the higher levels of hydrogen yield can be achieved with optimized conditions obtained: temperature of 40 ºC, glucose of 20 g/L, inoculum of 5% (v/v), and pH of 7. The expected result under optimum conditions was 3.515 mol H_2/mol glucose consumed.

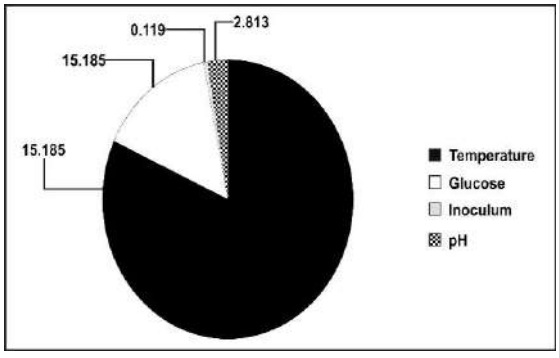

Fig. 2. Relative influence of factors

The final experimental stage consisted in applying the optimum conditions obtained to confirm or validate the results of the previous stage. Figure 3 shows the experimental results using optimum conditions predicted by the Taguchi L9 orthogonal array, from which it can be seen that hydrogen yield is greatly improved at the selected levels, resulting in a value of 3.48 mol H_2/mol glucose consumed at 120 h, very similar to the previously mentioned expected value. The hydrogen yield in the present work was greater than that reported by Arreola-Vargas *et al*

[38] and Contreras-Dávila *et al*. [15] in which they used an enzymatic hydrolysate from *Agave tequilana* bagasse, obtaining a hydrogen yield of 3.4 mol H_2/mol hexose (in batch mode) and 1.53 mol H_2/mol substrate (in continuous mode), respectively.

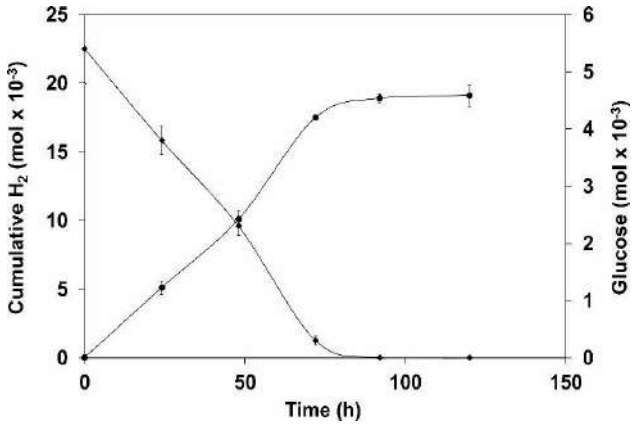

Fig. 3. Hydrogen production (circle mark) and glucose consumption (diamond shape mark) from *A. lechuguilla* hydrolysate during validation of results under optimum conditions

Conclusions

1. The results demonstrated the potential of hydrogen production from the enzymatic hydrolysates of *A. lechuguilla* pretreated by autohydrolysis.
2. The hydrogen production was significantly influenced by the operational conditions, mainly by the temperature and the initial glucose concentration. The hydrogen yield achieved (3.48 mol H_2/mol glucose consumed) was greater compared to early reports using hydrolysates of agaves.
3. Future research will be focused on assessing the production of hydrogen during continuous mode operation at different organic loading rates to study the economic feasibility of this process on a large-scale.

Acknowledgements

The authors are grateful to Innovation Promotion Program (Programa de Estímulos a la Innovación PEI-2016) from the National Council of Science and Technology of Mexico (CONACyT) for financial support.

References cited

[1] Arreola-Vargas, J., Ojeda-Castillo, V., Snell-Castro, R., Corona-González, R. I., Alatriste-Mondragón, F., and Méndez-Acosta, H. O. Methane production from acid hydrolysates of Agave tequilana bagasse: Evaluation of hydrolysis conditions and methane yield. Bioresource Technol. 181, 191-199. DOI: 10.1016/j.biortech.2015.01.036

[2] Han, W., Hu, Y., Li, S., Li, F., and Tang, J. Biohydrogen production in the suspended and attached microbial growth systems from waste pastry hydrolysate.Bioresource Technol.

2016; 218:589-594.
[3] Ortiz, A. L., Zaragoza, M. J. M., and Collins-Martínez, V. Hydrogen production research in Mexico: A review.Int. J. Hydrogen Energ. 2016;41:23363-79
[4] Arriaga, S., Rosas, I., Alatriste-Mondragón, F., and Razo-Flores, E. Continuous production of hydrogen from oat straw hydrolysate in a biotrickling filter.Int. J. Hydrogen Energy 2011;36: 3442-9.
[5] Sattar, A., Arslan, C., Ji, C., Sattar, S., Umair, M., Sattar, S., and Bakht, M. Z. Quantification of temperature effect on batch production of bio-hydrogen from rice crop wastes in an anaerobic bio reactor. Int. J. Hydrogen Energ.2016;41:11050-61.
[6] Liu, C.-M., Wu, S.-Y., Chu, C.-Y., and Chou, Y.-P. Biohydrogen production from rice straw hydrolyzate in a continuously external circulating bioreactor, Int. J. Hydrogen Energ. 2014;39: 19317-22.
[7] Zhao, L., Cao, G.-L., Wang, A.-J., Ren, H.-Y., and Ren, N.-Q. Evaluation of continuous biohydrogen production from enzymatically treated cornstalk hydrolysate.Int. J. Hydrogen Energ. 2013; 38:15100-04.
[8] Baêta, B. E. L., Lima, D. R. S., Filho, J. G. B., Adarme, O. F. H., Gurgel, L. V. A., and de Aquino, S. F. Evaluation of hydrogen and methane production from sugarcane bagasse hemicellulose hydrolysates by two-stage anaerobic digestion process. Bioresource Technol. 2016; 218:436-46.
[9] Ding, L., Cheng, J., Yue, L., Liu, J., Zhang, L., Zhou, J., and Cen, K. Fermentative hydrogen and methane co-production from pretreated Spartina anglica biomass with optimal saccharification effect under acid/alkali-assisted steam/microwave heating and enzymolysis. Energ. Convers. Manage.2016; 127: 554-60.
[10] Gonzales, R. R., Sivagurunathan, P., Parthiban, A., and Kim, S.-H. Optimization of substrate concentration of dilute acid hydrolyzate of lignocellulosic biomass in batch hydrogen production. Int. Biodeterior. Biodegradation 2016; 113:22-7.
[11] Rorke, D., and Kana, E. B.G. Biohydrogen process development on waste sorghum (Sorghum bicolor) leaves: Optimization of saccharification, hydrogen production and preliminary scale up.Int. J. Hydrogen Energy 2016; 12941-12952.
[12] Sangyoka, S., Reungsang, A., and Lin, C.-Y. Optimization of biohydrogen production from sugarcane bagasse by mixed cultures using a statistical method.Sustainable Environment Research 2016; 26,:235-42.
[13] Kumar, K., Sivagurunathan, P., Sen, B., Kim, S.-H., and Lin, C.-Y. Mesophilic continuous fermentative hydrogen production from acid pretreated de-oiled jatropha waste hydrolysate using immobilized microorganisms. Bioresource Technol. 2017.
[14] Arreola-Vargas, J., Flores-Larios, A., González-Álvarez, V., Corona-González, R. I., and Méndez-Acosta, H. O. (2016). Single and two-stage anaerobic digestion for hydrogen and methane production from acid and enzymatic hydrolysates of Agave tequilana bagasse 2016; Int. J. Hydrogen Energ. 41:897-904.
[15] Contreras-Dávila, C. A., Méndez-Acosta, H. O., Arellano-García, L., Alatriste-Mondragón, F., and Razo-Flores, E. Continuous hydrogen production from enzymatic hydrolysate of Agave tequilana bagasse: Effect of the organic loading rate and reactor configuration.Chem. Eng. J. 2017; 313:671-9.

[16] Castillo, Q. D., Mares, A. O., and Villavicencio, G. E. E. Lechuguilla (Agave lechuguilla Torr.) planta suculenta de importancia económica y social de las zonas áridas y semiáridas de México. Boletín de la Sociedad Latinoamericana y del Caribe de Cactáceas y otras Suculentas 2011; 8:6-9.
[17] Pando-Moreno, M., Pulido, R., Castillo, D., Jurado, E., and Jiménez, J. Estimating fiber for lechuguilla (Agave lechuguilla Torr., Agavaceae), a traditional non-timber forest product in Mexico. Forest. Ecol. Manag. 2008; 255:3686-90.
[18] Escamilla-Treviño, L. L. Potential of plants from the genus agave as bioenergy crops. Bioenerg. Res.2012; 5:1-9.
[19] Morales-Martínez, T. K., Díaz-Blanco, D. I., Rodríguez-de la Garza, J. A., Morlett-Chávez, J., Castro-Montoya, A. J., Quintero, J., Aroca, G., and Rios-González, L. J. Assessment of different saccharification and fermentation configurations for ethanol production from Agave lechuguilla,. BioResources 2017; 12: 8093-8105.
[20] Rios-González, L. J., Morales Martínez, T. K., Rodríguez Flores, M. F., Rodríguez de la Garza, J. A., Castillo Quiroz, D., Castro Montoya, A. J., and Martínez, A. Autohydrolysis pretreatment assessment in ethanol production from agave bagasse. Bioresource Technol. 2017; 242: 184-190.
[21] Díaz-Blanco, D. I., de La Cruz, J. R., López-Linares, J. C., Morales-Martínez, T. K., Ruiz, E., Rios-González, L. J., Romero, I., and Castro, E.Optimization of dilute acid pretreatment of Agave lechuguilla and ethanol production by co-fermentation with Escherichia coli MM16. Ind. Crop. Prod. 2018; 114:154-163.
[22] Sluiter, A., Ruiz, R., Scarlata, C., Sluiter, J., and Templeton, D.Determination of Extractives in Biomass (Report No. TP-510-42619) 2005, National Renewable Energy Laboratory, Golden, CO.
[23] Sluiter, A., Hames, B., Ruiz, R., Scarlata, C., Sluiter, J., and Templeton, D. Determination of Ash in Biomass (Report No. TP-510-42622) 2008, National Renewable Energy Laboratory, Golden, CO.
[24] Ortíz-Méndez, O. H., Morales-Martínez, T. K., Rios-González, L. J., Rodríguez-de la Garza, J. A., Quintero, J., and Aroca, G. Bioethanol production from Agave lechuguilla biomass pretreated by autohydrolysis. Rev. Mex. Ing. Quim. 2017;16:467-476.
[25] Ghose, T. K. (1987). Measurement of cellulase activities. *Pure and applied Chemistry*, *59*(2), 257-268.
[26] Fang, H., Zhao, C., and Song, X.-Y. Optimization of enzymatic hydrolysis of steam-exploded corn stover by two approaches: Response surface methodology or using cellulase from mixed cultures of Trichoderma reesei RUT-C30 and Aspergillus niger NL02. Bioresource Technol. 2010; 101:4111-19.
[27] Hu, B., and Chen, S. Pretreatment of methanogenic granules for immobilized hydrogen fermentation. Int. J. Hydrogen Energ. 2007;32:3266-73.
[28] Amiri, H., and Karimi, K. A promising pretreatment for the improvement of acetone, butanol, and ethanol production from woody materials. Chem. Eng. Sci. 2015; 137:722-9.
[29] Zhuang, X., Wang, W., Xu, Q., Qi, W., Wan, Q., Tan, X., Zhou, G., and Yuan, Z. Liquid hot water pretreatment of lignocellulosic biomass for bioethanol production accompanying with high valuable products. Bioresource Technol.2016; 199: 68-75.
[30] Moniz, P., Pereira, H., Quilhó, T., and Carvalheiro, F. Characterization and hydrothermal

processing of corn straw towards the selective fraction of hemicelluloses. Ind. Crop. Prod.2013; 50:145-153.
[31] Bharathiraja, B., Sudharsanaa, T., Bharghavi, A., Jayamuthunagai, J., and Praveenkumar, R. Biohydrogen and biogas – An overview on feedstocks and enhancement process. Fuel 2016; 185: 810-28.
[32] López-Linares, J. C., Romero, I., Cara, C., Ruiz, E., Moya, M., and Castro, E. Bioethanol production from rapeseed straw at high solids loading with different process configurations. Fuel 2014;122:112-8.
[33] Fan, Y. T., Li, C. L., Lay, J. J., Hou, H. W., and Zhang, G. S. Optimization of initial substrate and pH levels for germination of sporing hydrogen-producing anaerobes in cow dung compost. Bioresource Technol. 2004; 91:189-193.
[34] Fabiano, B., and Perego, P.Thermodynamic study and optimization of hydrogen production by Enterobacter aerogenes. Int. J. Hydrogen Energ. 2012; 27:149-156.
[35] Chen, W. M., Tseng, Z. J., Lee, K. S., and Chang, J. S.Fermentative hydrogen production with Clostridium butyricum CGS5 isolated from anaerobic sewage sludge. Int. J. Hydrogen Energ. 2005; 30:1063-70.
[36] Oh, Y. K., Seol, E. H., Kim, J. R., and Park, S. Fermentative biohydrogen production by a new chemoheterotrophic bacterium Citrobacter sp. Y19. Int. J. Hydrogen Energ.2013; 28: 1353-9.
[37] Lay, J. J. Modeling and optimization of anaerobic digested sludge converting starch to hydrogen.Biotechnol. Bioeng. 2000; 68:269-78.
[38] Arreola-Vargas, J., Alatriste-Mondragón, F., Celis, L. B., Razo-Flores, J., López-López, A., and Méndez-Acosta, H. O. Continuous hydrogen production in a trickling bed reactor by using triticale silage as inoculum: Effect of simple and complex substrates. J. Chem. Technol. Biotechnol. 2014;90:1062-9

XVIII International Congress
of the Mexican Hydrogen Society

Effect of fermentation time/hidraulic retention time in a UASB reactor for hydrogen production using surface response methodology.

Ileana Mayela María Moreno Dávila[1*], Emma Berenice Herrera Ramírez[1], José Antonio Rodríguez de la Garza[1], Leopoldo Javier Ríos González[1], Yolanda Garza García[1].

[1] Departament of Biotechnology, Faculty of Chemistry, Autonomous University of Coahuila. Saltillo, Coahuila, México.
* Corresponding author: phone number +52 1 8443819485
email: imayelamorenod@hotmail.com

ABSTRACT

The aim of the present work was to study the fermentation time and also the hydraulic retention time effect using surface response methodology for hydrogen production using a synthetic media as sustrate. The inoculum used for biofilms was previously pretreated, the anaerobic sludge was heat (100°C, 30 min.) and after was subject to acid-basic procedures to selectively enrich the hydrogen producing mixed consortia. The reactor used 44 spheres with anaerobic biofilms developed in fiber ixtle for immobilization of anaerobic sludge and was operated at mesophilic temperatures and initial pH of 5.0. A factorial arrangement of 2^3 was carry out on MINITAB statistical program, the statistical analysis of the surface response methodology of the hydrogen production process during the development and growth of biofilms was carried out at 3 different hydraulic retention times (1,3,6 h), as well as three fermentation times, as response variables (40, 140 and 280 h). The analysis of variance given by the statistical program with respect to the two factors studied: hydraulic retention time and fermentation time showed that they are highly significant, but in the interaction between variables no significance was detected. A longer time of hydraulic retention (TRH = 6) as well as a longer fermentation time (280h) the hydrogen production is favored obtaining 4.34 moles, and no methane was detected.

Keywords: hydrogen, anaerobic biofilms, surface response methodology, hydraulic retention time***.***

---

1. Introduction

Global energy consumption increased 17 times in the last century because of industrial development and population growth [1]. However, conventional energy sources such as fossil fuels, which solve almost all of the energy requirements currently, doesn´t solve the growing demand for energy.Faced with this problem, it is vital to the urgent search for new energy sources to sustainable development and a higher operating efficiency of the industry in modern societies without affecting the environment [2]. The production of hydrogen through biotechnological processes has emerged as one of the most attractive and promising alternatives for obtaining renewable and ecological energy [3]. Using the fermentative method, hydrogen can be produced continuously and can use several kinds of substrates, including organic waste [4].

The use of lignocellulosic biomass for the production of biofuels has attracted the attention of researchers in recent years [5]. The pulp and paper industry in Mexico generates approximately 110,000 tons of dry weight per year of waste paper and other solid waste, this industry is the second industry that contributes the most to pollution in Mexico.

Hydrogen production based on lignocellulosic biomass by means of the enzymatic method is more efficient and is obtained under environmental conditions in which no toxic residue is generated. Regardless of the type of lignocellulosic substrate, the cost and hydrolytic efficiency of the enzymes are the main factors that limit the commercialization of biomass bioconversion processes [6].

In this research, microorganisms were used to form biofilm systems, which have gained great importance in recent years due to the advantages they offer compared with free cell systems [7]. Among the potential advantages include: protection against toxic compounds and antimicrobials such as biocides or antibiotics; lower growth rate; high operational stability to sudden changes in pH, temperature and substrate concentration; higher yield due to a higher concentration of active biomass [8]. In the formation of the biofilm some researchers have used materials of natural origin for the development of biofilms such as activated carbon, sand, straw, jute, stone, etc., and in this case the support used in this investigation was the trunk of a Cactacea found in Northeast Mexico and called Opuntia imbricata.

Materials and Methods

2.1 Manufacture and conditioning of the support.

Natural ixtle fiber cord with an approximate diameter of 2.24 mm was used as a natural support. Two meters of ixtle string were used to cover a plastic sphere with an approximate diameter of 25.54 mm. Sixty spheres covered with ixtle cord were hydrated with water for a period of 18-24 h in order to register their wet weights.

2.2 Physical pretreatment to the waste of the paper industry.

The solid waste from the paper industry was collected from a paper processing industry located in Ramos Arizpe, Coahuila. The residue was cut, dried in an oven, crushed and sieved to a particle size of 710 µ.

2.3 Characterization of waste from the paper industry.

Waste from the paper industry with physical pre-treatment was used for the chemical characterization, in order to know the content of cellulose, hemicellulose and lignin according to the methodologies described by Van Soest [9]

2.4 Pretreatment to the mixed anaerobic microbial inoculum.

The mixed anaerobic microbial consortium was obtained from a RAFA reactor of a wastewater treatment plant of the brewing industry located in Coahuila, Mexico. 0.5 L of granular slurry was prepared and macerated and subsequently pretreated by combining two pretreatments described by Chen et al. [2] and modified by Moreno-Dávila et al. [10].The thermal-acid pretreatment was carried out by placing the microbial consortium in a water bath at a temperature higher than 90 ° C for a minimum period of 30 min, shaking vigorously during this time and finally submitting the container container of the consortium to thermal shock in water with ice. Subsequently, the consortium at room temperature was subjected to acid pretreatment in which the pH was reduced to 3.0 with a 3N HCl solution for a period of 24 h and finally the pH was readjusted to 7.0 with a 3N NaOH solution.

3. Results and Discussion

3.1 Statistical analysis of the hydrogen production process during the development and growth of biofilms in natural support using synthetic medium.

It was performed in statistical analysis of the continuous flow process at 3 different times of hydraulic retention (1,3,6 h), establishing three fermentation times as response variables (40, 140 and 280 h).

Table 1. Factorial experiment design 3^2

No. Experiment	HRT	Time (h)	Repetition	Hydrogen (mol)	Sugar reducers(mg/L)
1	1	40	1	0.326	6421.5
2	1	140	1	1.667	6660.3
3	1	280	1	3.744	3090.7
4	3	40	1	0.531	2129.1
5	3	140	1	2.106	304.4
6	3	280	1	4.146	102.8
7	6	40	1	0.697	6421.5
8	6	140	1	1.932	6660.3
9	6	280	1	4.341	3090.7
10	1	40	2	0.326	6394.7

11	1	140	2	1.816	6650.0
12	1	280	2	3.729	3103.4
13	3	40	2	0.531	2128.8
14	3	140	2	2.088	303.3
15	3	280	2	4.146	102.9
16	6	40	2	0.695	6394.7
17	6	140	2	1.932	6650.0
18	6	280	2	4.341	3103.4

A factorial arrangement of 3^2 was established with the MINITAB program (GRAPH), shown in Table 1, and hydrogen and reducing sugars were obtained for each experiment as the response variable during the course of kinetics of hydrogen for the development of biofilms.
The analysis of variance (Table 2) that the statistical program showed with respect to the two factors studied: hydraulic retention time and fermentation time showed that they are highly significant, but the interaction between variables does not detect significance, which can be observe in the interaction graph (1).

Table 2. Analysis of variance for the production of hydrogen during the development of biofilms in a UASB reactor at different HRT's using a synthetic medium

Fuente	**GL**	**SC Sec**	**SC Ajust.**	**CM Ajust.**	**F**	**p**
Flujo	2	0.5192	0.5192	0.2596	206.21	0.000
Tiempo	2	38.5043	38.5043	19.2522	15294.08	0.000
Flujo*Tiempo	4	0.1253	0.1253	0.0313	24.88	0.000
Error	9	0.0113	0.0113	0.0013		
Total	17	39.1601				

S = 0.0354795 R-cuad. = 99.97% R-cuad.(ajustado) = 99.95%

For the hydrogen it is concluded that the 2 factors (retention time and time) are highly significant but the interaction between them does not influence their production as observed in the interaction graph (Figure 1).

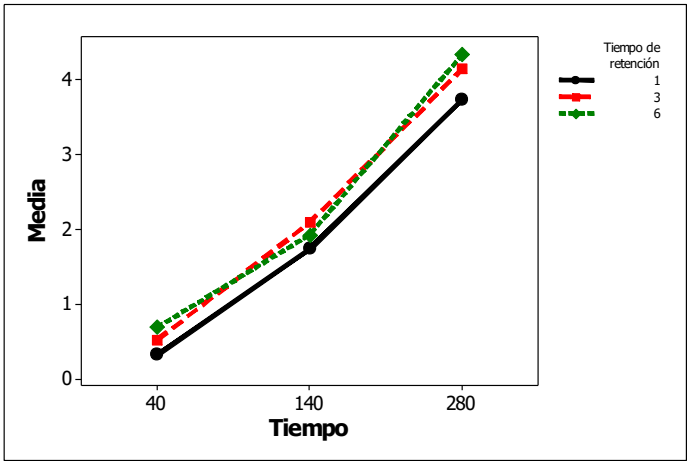

Figure 1. Interaction of factors (hydraulic retention time-fermentation time) on the production of H2 during the development of the biofilms.

The HRT flow of 6 h favors the production of hydrogen more than the HRT of 3 and being less favorable to the HRT of 1 h, as well as Chun-Feng et al. [11] in their study of the influence of the hydraulic retention time in the production of Hydrogen and Clostridium in the fermentation from glucose found a HRT of 6-8 h as optimal. The longer hydraulic retention time (HRT = 6) and the longer fermentation time (280h) the hydrogen production is favored (Figure 2).

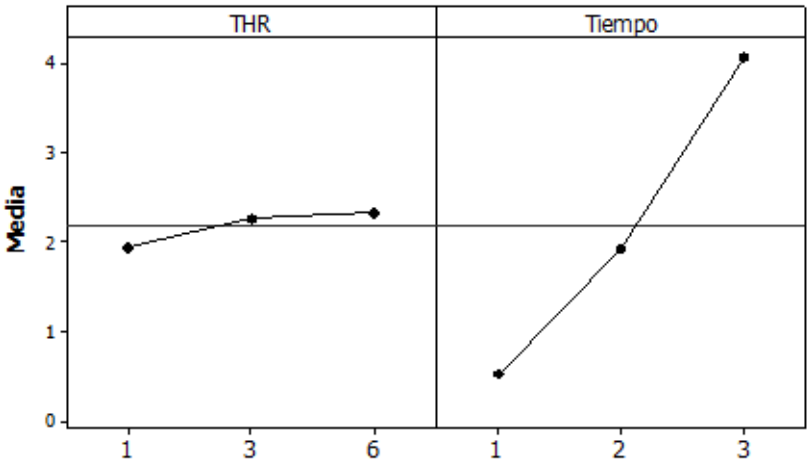

Figure 2. Main effect graphs (MINITAB GRAPH),
a) Effect of hydraulic retention time and
b) Effect of fermentation time.

The graph of main effects gives the optimum conditions of operation for the greater production of hydrogen, as it is observed the retention time of 3 or 6 h are optimal for being above the average. As can be seen in Figure 1, the optimal condition is the hydraulic retention time of 6 h and the longer fermentation time, which resulted in 280 h.

3.2 Interactions of surface graphics.
Figure 3 shows the graphic representation of response surface in which we can observe that at higher TRH and higher fermentation times the production of hydrogen increases.

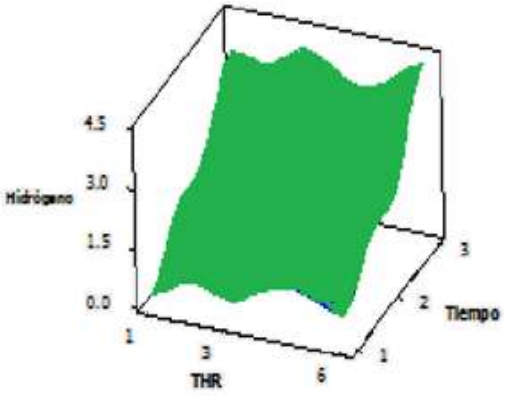

Figure 3. Surface graph of response of TRH factors and fermentation time of hydrogen production during the development of biofilms

.

4. Conclusion

Through the statistical analysis of the continuous flow process that was carried out at 3 different times of hydraulic retention (1, 3 and 6 h), as well as three fermentation times were established as response variables (40, 140 and 280 h), a factorial arrangement of 32 was determined, and thus hydrogen and reducing sugars for each experiment were obtained as a response variable during the course of the hydrogen production kinetics for the development of biofilms in an UASB reactor. The analysis of variance that the statistical program showed with respect to the two factors studied: hydraulic retention time and fermentation time showed that they are highly significant, but the interaction between variables is not detected significance; so it is concluded

that the higher hydraulic retention time (HRT = 6) and greater fermentation time (280h), the hydrogen production is promoted.

Acknowledgements

The authors are grateful to the National Council of Science and Technology of Mexico (CONACyT) for financial support

References

[1] Nikolic S., Mojovic L., Rakin M., Pejin D. Bioethanol production from corn meal by simultaneous enzymatic saccharification and fermentation with immobilized cells of Saccharomyces cerevisiae var. ellipsoideus. Fuel.2009;88(9):1602–07.
[2] Chen S., Hu B. Pretreatment of methanogenic granules for immobilized hydrogen fermentation. Int J Hydrogen Energ.2007; 32 (15): 3266-73.
[3] Hwang S-J, Lee M-J, Song J-H.Effects of acid pre-treatment on bio-hydrogen production and microbial communities during dark fermentation. Biores Technol. 2009;100: 1491-1493.
[4] Wang J., Wan W. Experimental design methods for fermentative hydrogen production: A review. Int J Hydrogen Energ. 2008:1-10.
[5] Pandey A., Sukumaran R.K., Singhania R.R., Mathew G.M.Cellulase production using biomass feed stock and its application in lignocellulose saccharification for bio-ethanol production. Renew Energ. 2009; 34:421-424.
[6] Kurabi A., Berlin A., Gilkes N., Kilburn D., Bura R., Robinson J., Markov A., Skomarovsky A., Gusakov A., Okunev O., Sinitsyn A., Gregg D., Xie D., Saddler J. Enzymatic hydrolysis of steam-exploded and ethanol organosolv-pretreated Douglas-fir by novel and commercial fungal cellulases. Appl Biochem Biotechnol. 2005; 121-124: 219-230.
[7] Kim Y.H., Kim J.O., Ryu J.Y., Song B.K., Kim I.H., Yeom S.H. Immobilization methods for continuous hydrogen gas production biofilm formation versus granulation. Process Biochem. 2005; 40: (3-4): 1331-7.
[8] Show K-Y., Zhang Z-P., Tay J-H., Yan R., Liang D.T., Lee D.J., Jiang W.J. Biohydrogen production in a granular activated carbon anaerobic fluidized bed reactor. Int J Hydrogen Energ. 2007;32 (2): 185-191.
[9] Van Soest, P. J. Use of detergents in the analysis of fibrous feeds. 2. A rapid method for the determination of fiber and lignin. Journal of the Association of Official Agricultural Chemists 1963; 46*:* 829-835.
[10] Moreno-Dávila I.M.M., Ríos-González L.J., Garza-García Y., Rodríguez-de la Garza J.A. and Rodríguez-Martínez J. Biohydrogen production from diary processing wastewater by anaerobic biofilm reactors. African Journal of Biotechnology 2011; 10(27):5320-6.
[11] Chu, C. F., Li, Y. Y., Xu, K. Q., Ebie, Y., Inamori, Y., & Kong, H. N. A pH-and temperature-phased two-stage process for hydrogen and methane production from food waste. International Journal of Hydrogen Energy 2008; 33(18): 4739-46.

Policies, economy and market strategies

September 18 to 21, 2018 in Mexico City, Mexico

XVIII International Congress
of the Mexican Hydrogen Society

The need for a strategic plan for the effective use of hydrogen as an alternative energy in Mexico

María Liliana Ávalos Rodríguez[1]*, José Juan Alvarado Flores[2], Armonía Borrego[1], Jorge Víctor Alcaraz Vera[3]

[1]Centro de Investigaciones en Geografía Ambiental (CIGA), campus Morelia, perteneciente a la Universidad Nacional Autónoma de México. Antigua carretera a Pátzcuaro 8701, sin nombre, INDECO, la Huerta. Morelia, Michoacán.
[2]Instituto Tecnológico del Valle de Morelia (ITVA). Carretera Morelia-Salamanca, km. 6.5, Morelia, Michoacán.
[3]Instituto de Investigaciones Económicas y Empresariales (ININEE), Universidad Michoacana de San Nicolás de Hidalgo, Francisco J. Mújica S/N, Col. Felicitas del Rio, C.P. 58040, Morelia, Michoacán, México.
* Corresponding author: 4434 09 59 44, lic.ambientalista@gmial.com

ABSTRACT

In Mexico, alternative sources of energy from hydrogen, taking care of their legal right that makes their extraction, storage, commercialization and use feasible; therefore, the objective of the current research is to provide the methodological and legal basis through which the guidelines for the formulation of a hydrogen strategic plan as a management tool that promote viable and feasible strategies for energy needs, in Consideration of the limitations and strengths of public policies and the regulatory framework. In this sense, through a deductive, inductive, exploratory, descriptive, correlational, comparative and explanatory analysis, the reality of hydrogen in current public policies and legal systems will be known in order to highlight that the guidelines of the hydrogen strategic plan must include the economic line, environmental, social, legal, technological, political and educational, where objectives, goals and precise strategies are recognized around the progress of the hydrogen economy and the Mexican reality, this will lead to responsibility shared and joint participation of all social sectors in order to promote conditions of sustainable development. It is also appreciated that there is feasibility of the hydrogen strategic plan because to date the existence of a document that integrates the social needs in the field of energy, the scope of public policies and legal issues, the benefits of using the hydrogen, the promotion of scientific research and the environmental benefits that it represents in the short, medium and long term in order to promote sustainable development conditions through precise and feasible strategies.

Key words: *legal framework, public policies, hydrogen strategic plan, sustainable development*

1. Introduction

The global energy landscape reflects the need for viable alternatives that make it possible to use elements other than fossils to supply energy demand. It is known that, for some countries, this problem has had priority in the public agenda and has the legal backing to make it a reality, for example, countries such as the United States, Holland, Germany, Sweden, Japan, Australia, Canada, etc., have incorporated hydrogen (H_2) into political, economic, technological and legal actions to close the economic gap of the H_2 [1], [2] y [3], however, in Mexico there are great challenges to be overcome in order to think about the possibility of starting this energy transition gap [4], in addition, not only the technological and economic challenges slow down the energy transition, there are social, cultural, academic, political and legal challenges that hinder the effectiveness of H_2 as a real energetic alternative.

It should be noted that Mexico has one of the few natural resources recognized worldwide that should be a priority in its public agenda, a situation that has been recognized in the information bases of public dependencies, stating that it is a priority government commitment to have for 2024 with the lowest 35% share in the generation of energy from non-fossil sources [5], however, six years after this deadline is met, 92% is still dependent [6] of fossil fuels and according to official reports, there is only a reserve level that will allow a hydrocarbon production to be maintained in a period of less than 10 years [5].

Another limiting factor that has been rescued from the situation of H_2 in Mexico, is the limited existing legal support, because Mexican legislation promotes wind energy renewable by 2%; the thermoelectric plant by 69%; thermoelectric geo by 6%; the hydroelectric plant by 1%; the photovoltaic one in 0%; the dual by 12%; the coal-fired by 7% and the nuclear power by 6% [6], leaving aside the alternative from the H_2, this according to the provisions of the Mexican legal energy framework, which is made up of the Political Constitution of the United Mexican States (PCUMS); by fourteen laws of the federal order; two regulations of article 27 of the PCUMS; ten Regulations to the laws of the federal order and an internal regulation of the Secretariat of Energy. Another type of public actions is located in the National Development Plan 2013-2018; the Fund for the Energy Transition and the Sustainable Use of Energy; the Sectoral Energy Program; the National Inventory of Renewable Energies and the National Energy Balance.

Under this context, in Mexico H_2 alternatives have been sought from the academy to the government, a situation that should start in reverse, for example, a National Hydrogen Plan has been proposed in 2016: Alternative Energy, whose main objective will be uniting the individual efforts of researchers, institutions and companies in order to position the H_2 as an energy vector for Mexico, through the objective evaluation of the research lines, human resources, infrastructure and training programs for specialized personnel, as well as Research, development and application of H_2 technologies for the benefit of society [7], the main achievement of this proposal is that to date, an association has been created that encourages H_2 research and promotes spaces for rapprochement with the different social sectors.

In this sense and considering all these antecedents that serve as a basis for believing in the feasibility and viability of an H_2 Strategic Plan, it is convenient to think that this should be a management tool that not only promotes research and rapprochement of social sectors, must motivate with precise strategies the use of H_2 from its legal and political recognition. The

strategies must necessarily be directed to the environmental, economic, social, political, technological, legal and academic aspects.
That is why, to address the proposal, it begins by outlining the position of H_2 in the global energy problem, to later know the reality of the H_2 in the current public policies and legal systems, and the proposal of the Strategic Plan of the H_2 as an environmental management tool precursor of sustainable development.

2. Materials and Methods

The article is based on a deductive, inductive, exploratory, descriptive, correlational, comparative and explanatory analysis of the reality of hydrogen in current public policies and legal systems in Mexico in order to emphasize that the guidelines of the hydrogen strategic plan must include the economic line, environmental, social, legal, technological, political and educational.

3. Results and Discussion

- *The position of H_2 in the global energy problem*

The accelerated population growth, the excessive consumerism and the globalization of natural elements, has brought as a consequence a constant concern for the limits of fossil fuels, especially when appreciating that they emit large amounts of CO_2 and thereby reduce the quality of life. In addition, it adds to this fact that the volume of vehicles is seven orders of magnitude higher than the current population rate [8]. That is why, it is imperative to promote viable technologies with environmental limits and according to social needs. Therefore, it has been specified that techniques that reduce CO_2 emissions are required, that renewable energies are used extensively, that motor efficiency is promoted through the improvement of design, that the industry and the economic services sector are made more efficient. The above should be promoted from the so-called Economy of the H_2 that replaces the current economy of fossil fuels, and that countries like the United States, Holland, Germany, Sweden, Japan, Australia, Canada, among others, are already promoting and that They aim to reduce energy dependence, increase energy efficiency and, in the near future, absent themselves from CO_2 emissions.
However, at present, there are still barriers that must be overcome, such as the difficulty of storage of H_2, safety regulations and social recognition of their efficiency. For example, it is known that fuel cells are the leading mechanism that, through the H_2, offers alternatives that go from the micros to the macros and are nowadays in some countries, a tangible reality of energy efficiency, but for that, the society that benefits from the research of the academy, recognizes, accepts and promotes the use of H_2 from these cells. Then, then, social recognition is crucial so that the results of the energy sources from the H_2 are feasible.
Regarding these technological advances that seek to meet the energy demand, countries such as the United States have generated from scientific knowledge, a Fuel Cell Program, which aims to balance the technological, economic and institutional aspects to promote the commercialization of Cells made out of fuel. For this, there is a group made up of academia,

industry, institutions and national laboratories that, in coordination with other programs, have managed to reduce the production costs of H_2; identify new materials that offer a 50% improvement in the storage capacity of H_2 in cars and, validate the H_2 technologies with the addition of 1400 vehicles equipped with fuel cells and the creation of H_2 spouts.
On the other hand, they have bet on projects that promote I+D activities in production, storage, manufacturing, technological validation, security, H_2 education, market transformation, system analysis and financing.
Other actions that stand out worldwide, the energy strategies of Japan that have promoted the generation of batteries for use in the automotive industry, development of fuel cells and building infrastructure, clean fuels and low consumption automotive, expansion of safe biotechnology second generation and advanced motorized society concepts.
For its part in Europe, highlights the CUTE project (Clean Urban Transport for Europe) which aims to nine cities (Amsterdam, Barcelona, Stockholm, Hamburg, London, Luxembourg, Madrid, Porto and Stuttgart) have public transport buses equipped with a fuel cell powered by H_2 [9].
The H_2 to fuel the fuel cell was produced by electrolysis of water or by reforming natural gas. Each vehicle had an approximate power of 250 kW contributed by the fuel cell. The vehicles were equipped with H_2 cylinders at a pressure of 350 bar. In this way the vehicle had an estimated range of 200 km. In addition, it is noted that no major security incidents were recorded.
There are other similar projects, such as ECTOS and HyWays, the latter aimed to develop a roadmap for the introduction of H_2 in the European energy system with emphasis on the transport sector, in addition to the one promoted by France that seeks the production of H_2 in wind energy: EolHY.
On the other hand, the initiatives of the Brazilian Government for the development of the H_2 economy focused on the Science, Technology and Innovation Program for the H_2 Economy (Pro H_2) stand out; the networks of the PRO H_2; H_2 Production and storage network; Network of Polymeric Electrolyte Fuel Cells (PEFC); Network of Solid Oxide Fuel Cells (SOFC) (RedPaCOS) [8].

- *The above, leads to rethink the proposals carried out so far and think about the conditions and realities of Mexico.*

In Mexico it has been sought to move towards alternative energies, however, there have been no concrete actions that exceed sexennial proposals and that propitiate the economy of the H_2, because the energy sector continues to be based on sources of fossil origin despite political speeches energy transition based on environmental constraints such as programs that limit vehicular circulation, mandatory reports of atmospheric emissions and forums on climate change; the economic benefits that would be achieved in the transition to renewable energies and, the need to reduce risks in energy facilities, this in the face of possible attacks or failures.
These conditions have left aside the main mechanism of clean development promoted in the Kyoto Protocol signed by Mexico in June 1998 and ratified in September 2000. This mechanism seeks to enable projects that benefit developing economies, such as Mexico, through the use of clean sources; however, Mexico has participated only as a mechanism that receives investment in wind and hydroelectric projects [10], although the natural elements of Mexico facilitate these

mechanisms and do not really offer an energy alternative, they only encourage foreign direct investments.

Another international event that influenced the ideology of energy mechanisms in Mexico was, was the Bonn Conference of 2004 that sought to promote the global participation of renewable energies as substantial for sustainable development by promoting access to energy especially to those with scarce resources, mitigate greenhouse gas emissions and thereby reduce pollution.

To achieve this, it was thought that developing countries such as Mexico would improve their markets, financing, technologies and policies, all under a scheme of international cooperation. However, a political, educational and technological co-participation is required [11]. This last factor has been affected due to the reduction of the budget to scientific research in Mexico in less than 1% of the Gross Domestic Product.

Mexico, the energy sector has faced an organic transition, in the sense that until 2013 all the processes related to the management of hydrocarbons and electricity were centralized in Petróleos Mexicanos (PEMEX), in the Federal Electricity Commission (FEC) and in Luz y Fuerza del Centro (LFC). It was until the end of 2013 that the energy reform in Mexico is sought, which aims to implement a new contracting model in the exploration and extraction of hydrocarbons through private investment [12].

There are other precedents that have contributed elements in this phase of transition, such as international agreements and legal systems, in the first item highlight IPCC: Intergovernmental Panel on Climate Change (2007); International Energy Agency (2009); the Conference on Climate Change (2015); etc., in the second item, the Law of Energy for the Field (2002) stands out; the Law of Promotion and Development of Bioenergetics (2008); the Law of the Energy Regulatory Commission and the Electricity Public Service Law (2014) and its Regulations (which are currently repealed), the Geothermal Energy Law (2014); the Law of the Coordinated Regulatory Bodies on Energy Matters (2014); the Hydrocarbons Law (2014); the Law on the National Agency for Industrial Safety and Environmental Protection of the Hydrocarbons Sector (2014) and the Income on Hydrocarbons Law (2014), all of which are still in force.

In 2015, the Law for the Use of Renewable Energy and the Financing of the Energy Transition and its Regulations was published, as well as the Law for the Sustainable Use of Energy and its Regulation (currently abrogated), however, in the same 2015 other laws that are still in force are published, such as the Energy Transition Law; In 2016, the Federal Law to Prevent and Punish the Crimes Committed in the Field of Hydrocarbons was published and in 2017, Mexico launched the 2017-2021 Strategic Program with the support of the National Center for Energy Control.

As you can see, the actions in energy matters are generally translated into strategic programs that seek to meet specific needs, few countries have pushed laws that coercively make the energy transition possible, Mexico has not been the exception, however, it is recognized that the actions he has undertaken have recently been highlighted and all of them emphasize renewable energies and not alternate energies, which is why it is price to start carrying out studies on the feasibility of H_2 storage, which should start from the infrastructure starting of an analysis of the supply chain through different sources of energy to supply the nearby market niches.

1.3. Scope and limitations of the Mexican legal framework in energy matters.

As already mentioned, the Mexican legal framework on energy matters is made up of the PCUMS; by fourteen laws of the federal order; two regulations of article 27 of the PCUMS; ten Regulations to the laws of the federal order and an internal regulation of the Secretariat of Energy. Another type of public actions is located in the National Development Plan 2013-2018; the Fund for the Energy Transition and the Sustainable Use of Energy; the Sectoral Energy Program; the National Inventory of Renewable Energies and the National Balance of Energy and to know the role played by H_2 in these legal systems it is convenient to analyze them.

It is observed that, 29% of the laws of the federal order including in these the PCUMS, make superficial reference of the H_2, without specifying in their forms of use and advantage, for example, the PCUMS in its article 27 indicates that it corresponds to the Nation the domain of the carbides of solid, liquid and gaseous hydrogen; The Law of PEMEX indicates in article 5 of a general form about the exploration and extraction of solid, liquid or gaseous hydrogen carbides. The Organic Law of the Federal Public Administration states in article 33 that the Ministry of Energy will have the function of regulating and promoting the development and use of alternate energy sources to hydrocarbons and, the Energy Transition Law indicates in the sixteenth of Transitaros that will be understood as clean energy "The minimum efficiency so that the use of hydrogen is considered a Clean Energy will not be less than 70% of the lower calorific value of the fuels used in the production of said hydrogen".

The rest of the laws and regulations that are derived from these as the Regulations, do not emphasize the use and utilization of H_2 or alternative forms of energy, focusing on renewable energy and based on fossils.

In this context it is feasible to argue that the legal basis for H_2 in Mexico has as its main weakness the legal support, although there are national programs and plans that seek to promote the use of alternative energies, it is not enough that they exist due to their scope limited that transcend presidential presidential terms. That is why the weakness lies in the fact that there is no legal backing that promotes the use and exploitation of H_2 and that thereby actually consolidates the energy transition gradually away from oil.

A strong strength is in the Mexican legal framework is the viability of placing through a legal reform, the figure of the H_2 and raise it to a viable and sustainable alternative energy. Based on scientific research that although it is scarce, has been developed by researchers in Mexico, as is the case of the proposal of the National Hydrogen Plan, which seeks to offer a vision of the use of it as an energy vector, through the incentive in infrastructure and specialized personnel training programs that Mexico has, as well as opportunities for research, development and application of H_2 technologies for the benefit of society. In addition, it is necessary to promote hydrogen technologies that offer solutions according to Mexican needs and based on current environmental conditions, considering that the storage potential of H_2 could reach 118,560 GEh per year of renewable energy. [12].

Additionally, it is convenient to think about the need to bring the current energy programs closer: The Sectorial Energy Program 2013-2018 [13], the Fund for Energy Transition and the Sustainable Use of Energy [14], the National Strategy of Energy Transition and Sustainable Use

of Energy 2013-2027 [15], the Special Program of the Energy Transition (2017) [16], with Mexican society, in order to achieve its effectiveness.

1.4. Proposal of the H_2 Strategic Plan as an environmental management tool that is a precursor of sustainable development

The reinforcement of the legal framework is elementary to legitimize the actions that incorporate the H_2 in decision-making at an economic, technological, social and political level; therefore, it should also be thought about, strengthening citizen participation mechanisms in the environmental management of the state; in the strengthening of competitiveness taking into consideration the criteria of the ecological footprint of companies; promote the competitive advantages of biological diversity and the configuration of the territory; promote alliances between the governmental, business and academic sectors and promote scientific and technological capacities to face risks, problems, conflicts [17]; Once these criteria are considered, the H_2 Strategic Plan should start with the incorporation of three bases: sustainability, security and competitiveness, forming a program of action supported by the consensus of governmental, economic, social and academic agents and in relation to legal and political legitimation.

In this sense, the H_2 Strategic Plan should start from:

a) A diagnosis that identifies the potential elements for obtaining H_2, in addition this diagnosis will gather the necessary information to determine the limits of production, storage and distribution, considering the existing technological, economic and social scope.
b) Subsequently, it will be necessary to plan and formulate goals and objectives, agree policies, define priorities, establish programs and projects, seek co-financing actions and formulate plans to execute them.
c) Once the planning and formulation has been carried out, the execution phase will be followed, which will seek the implementation, training and tripartite cooperation between government agents, economic agents (companies, industries and services) and the academic sector. Once the planning and formulation has been carried out, the execution phase will be followed, which will seek the implementation, training and tripartite cooperation between government agents, economic agents (companies, industries and services) and the academic sector.
d) The next phase will be the monitoring and evaluation that will seek the monitoring of activities, constant feedback, the review of the scope, goals and objectives and, if necessary, the corrective redirection of the actions.

The foregoing should be based on continuous and constant actions of communication, participation and coordination between the sectors involved once the legal and political scope has been contextualized in order to legitimize the actions to be followed.

As it has been observed, the implementation of the H_2 Strategic Plan is feasible in Mexico, since the negotiation conditions can be given in order to diagnose, plan, execute and evaluate the possibilities for the incorporation of this element in the legal and regulatory frameworks. political,

giving substantial weight to carry out actions of procurement, storage and distribution as an alternative source of energy and thus be in the possibilities of initiating the energy transition to the H_2 economy, generating opportunities for sustainable development.

4. Conclusion

The use of H_2 is a reality that must be addressed from the legal and political, in the sense that it is unlikely to think about its use without having a legal backing that legitimizes all procurement, storage and distribution. Therefore, starting from a legal and political contextualization of current actions, allows us to have the guidelines to formulate a H_2 Strategic Plan according to real and feasible needs, involving all social sectors, such as government, economic, political and academic to diagnose, plan and formulate, execute and evaluate the efficiency of the actions foreseen in said Strategic Plan.
For this, it should be considered that in Mexico it is elementary to reform the legal framework that promotes efficient public policies, as well as to generate scientific advances that promote feasible technologies and generate lines of educational action that motivate social sectors to become involved in the actions of the H_2Strategic Plan.

References

[1] Jeremy, R. (2002). La economía del hidrógeno. editorial Paidós, Buenos aires.
[2] Botas, J. A., Calles, J. A., Dufour, J., y San Miguel, G. (2005). La economía del hidrógeno–Una visión global sobre la revolución energética del siglo XXI. Revista de la Asociación Española de Científicos, 9.
[3] Alvarado F. J. J., Valencia, J. E., y Rodríguez, M. L. Á. (2015). La necesidad de incorporar el hidrógeno como potencial fuente alterna de energía en la legislación mexicana. *Revista Catalana de Dret Ambiental*, *6*(1).
[4] Morales Ramos, A. C., Pérez Figueroa, M., Pérez Gallardo, J. R., & De León Almaraz, S. (2017). Energías renovables y el hidrógeno: un par prometedor en la transición energética de México. Investigación y Ciencia, 25(70).
[5] Secretaría de Energía. Prospectiva de Energías Renovables 2012-2026. Recuperado en julio del 2017 a través de https://www.gob.mx/sener/documentos/prospectivas-del-sector-energetico
[6] Vázquez, A. L. (2015). Desarrollo y prospectivas de energía renovable en México. Economía Informa, 390, 132-135
[7] Sánchez, B. F, (2016) Plan Nacional de Hidrógeno Hidrógeno: Alternativa Energética, recuperado en julio del 2018 a través de https://petroquimex.com/PDF/SepOct16/Plan_Nacional_de_Hidrogeno.pdf
[8] Laborde, M. A., Lombardo, E. A., Noronha, F. B., & Boaventura Filho, J. S. (2010). Potencialidades del hidrogeno como vector de energía en Iberoamérica. *Buenos Aires: Ediciones CYTED*.
[9] Laborde M., Rubiera González F. La energía del hidrógeno. Ediciones CYTED

2010 http://redhidrogenocyted.
com.ar/
[10] CDM Watch (2017). Recuperado en julio del 2018 a través de: http://www.cdmwatch.org/project
[11] Internacionale Konferenz für Erneuenbare Energien (2004). Alemania URL: http://www.renewables2004.de, consultado en julio del 2018.
[12] Ramos, A. C. M., Figueroa, M. P., Gallardo, J. R. P., & Almaraz, S. D. L. (2017). Energías renovables y el hidrógeno: un par prometedor en la transición energética de México. *Investigación y Ciencia: de la Universidad Autónoma de Aguascalientes*, (70), 92-101.
[13] Secretaría de Energía. Programa Sectorial de Energía (PROSENER) (2013-2018). Gobierno de la República. Recuperado en julio del 2018 en https://www.gob.mx/sener/acciones-y-programas/programa-sectorial-de-energia-2013-2018
[14] Secretaría de Energía. Fondo para la Transición Energética y el Aprovechamiento Sustentable de la Energía (FOTEASE), 2009-2015. Informe 0, consultado en julio del 2018 a través de https://www.gob.mx/sener/articulos/el-fondo-para-la-transicion-energetica-y-el-aprovechamiento-sustentable-de-la-energia-es-un-instrumento-de-politica-publica-de-la-secretaria
[15] Secretaría de Energía. Estrategia Nacional de Transición Energética y Aprovechamiento Sustentable de la Energía 2013-2027 (ENTEASE) 2013-2027. Recuperado en julio del 2018 a través de https://www.gob.mx/sener/documentos/estrategia-nacional-de-transicion-energetica-y-aprovechamiento-sustentable-de-la-energia
[16] Secretaría de Energía. Programa Especial de la Transición Energética (2017-2018), recuperado en https://www.gob.mx/sener/documentos/programa-especial-de-la-transicion-energetica-2017-2018 en julio del 2018.
[17] Aita, p. g. lineamientos para un plan estratégico en energías renovables.

Codes, standards and safety issues

September 18 to 21, 2018 in Mexico City, Mexico

XVIII International Congress
the Mexican Society of Hydrogen

Measurement of pollutant Emissions for an internal combustion engine gasoline Enriched System with oxyhydrogen

Santos Fernández M.1 *, Hernandez M. Hernandez 1, Lopez Contreras LF 1 Cortés Escobedo CA 1

[1] Instituto Politécnico Nacional, CIITEC
* marianna.sf@hotmail.com, Phone number: +9221991228

ABSTRACT

Description and analysis of a validation protocol for analytical methods applied to the measurement of emissions for combustion engine system enriched gasoline-oxyhydrogen reactor based on the EURACHEM Guide (The Fitness for Purpose of Analytical Methods – A Laboratory Guide to Method Validation and Related Topics) is presented.

The validation of the methodologies, together with other activities included in the control of quality assurance, allows to demonstrate to the laboratories that their analytical methods provide reliable results. However, there are no validated methodologies to determine the specifications of maximum permissible limits or analytical techniques with adequate detection limits for the measurement of polluting emissions in oxyhydrogen coupled systems.

The objective of this research is to analyze requirements for the validation of analytical methods satisfying the requirements of conformity assessment of measuring emissions oxyhydrogen coupled system, based on the EURACHEM guide.

The precision and robustness indicators suggested by the NMX-EC-17025-IMNC-2006 were studied, as well as the application criteria implemented by the Entidad Mexicana de Acreditación (EMA) AC.

Measurements were made in accordance with national and international standards corresponding to vehicle emissions internal combustion engine-oxyhydrogen coupled systems:

- Emissions of Vehicle Gases, Test FTP-75, Cold phase, Test HOT 505, carried out in the Vehicle Emissions Laboratory referenced in the NMX-AA-11-1993-SCFI standard.
- Vehicle emissions speciation, based on the method: Standard Test Method for Determination of Gaseous Organic Compounds by Direct Interface Gas Chromatography-Mass 1 ASTM D 6420- Spectrometry 99.
- Measurements of polluting emissions by infrared sensors or probes.

Results of concentration of total hydrocarbons, CO_2, O_2, CO and NOx for a combustion engine coupled to an oxyhydrogen reactor, as well as without it. A slight decrease in the total hydrocarbons (0.065%) was found between the chromatographic results and the results of infrared spectrometry.

Keywords: validation methods, oxyhydrogen coupled systems, vehicular Emissions.

September 18th to 21st, 2018 in Mexico City, Mexico.

1. Introduction

Air pollution in Mexico is a serious problem in large urban areas. Nevertheless, in recent years the large population and industrial growth, together with the increase in vehicle fleet and consequently on fuel consumption, has brought the extent of this problem to other parts of the country, which means that each more people live in cities where they are exposed to poor air quality. This becomes important when you take into account that several studies conducted in Mexico have identified an association between air pollution, especially particulate matter and ozone, and increased visits to emergency rooms for asthma attacks, the incidence of respiratory infections, cases of chronic bronchitis, truancy, the presence of respiratory symptoms, and decreased lung function in children, reduced heart rate variability, and increased mortality in adults and infants. [1]

Therefore, in recent years it has sought ways to reduce pollutant emissions emanating from vehicles, in addition to the reduction in energy consumption, *ie* increase energy efficiency. This can be achieved through the implementation of various measures and investments in technology, management and cultural habits in the community. [2]

Alkaline electrolysers (EA) have a mature technology development is handled commercially in various industries for the production of hydrogen at low and medium scale not using noble materials in its electrodes and hydrogen is obtained in 99.2% of purity.

It is possible to implement a process of generating hydrogen and oxygen by alkaline electrolysis, where the working range of voltage and current are determined by the design and manufacture of the electrolyser, so that the gas feed generated an internal combustion engine, in order to save gas, or may be enriched with hydrogen gas line, which is fed to a boiler, burner, etc. Thus this type of device may extend the use of fossil fuels and reduce pollutant emissions into the atmosphere.

In the last decade, alkaline electrolysers have been used to enrich the oil, either by coupling to an internal combustion engine to increase fuel efficiency (gasoline, diesel, etc.) or a natural gas line for an open combustion and save this gas, see Figure 1. The current is used and the potential generated in the own car battery or photovoltaic system for electrolysis of water and generate the oxyhydrogen gas which is fed into the engine or natural gas line. In systems like this, the alkaline electrolyser is called "oxyhydrogen reactor". Records show fuel savings ranging from 10 to 30%. [3]

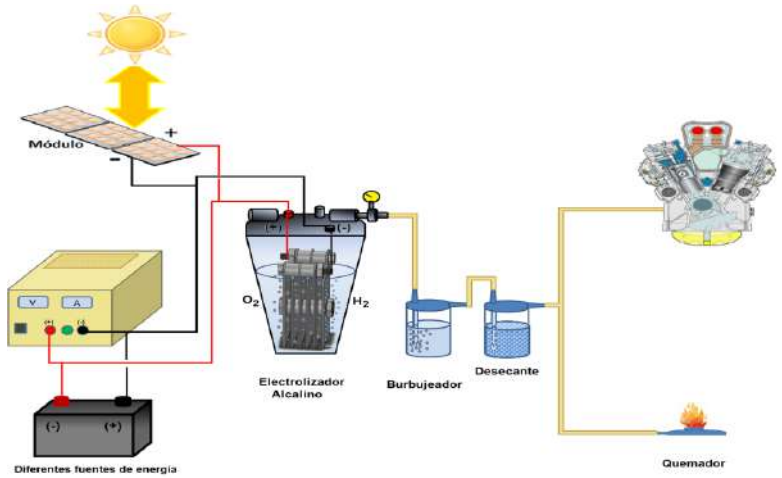

Figure 1Hydrocarbon enrichment coupling a oxyhydrogen reactor. [3]

Validation is based on systematic laboratory studies process by which it is apparent that a particular analytical method has performance characteristics appropriate to the application that you want to give. These characteristics are specified in quality parameters such as accuracy, precision, detection limits and quantification, the dynamic range, sensitivity, selectivity and robustness.

From the above point of view, all methods need to be known by laboratories that use them to establish their application limits and parameters to be used for control. This implies not only validation of equipment (instruments and equipment), software and results, but can also include validation of the sampling procedure, handling and transportation of the sample, whereby the representativeness of the results is guaranteed. However, this work has been excluded validation stage sampling, handling and transportation of the sample consider that often the testing laboratory is not responsible for these tasks, such as commercial laboratories.

This work has primarily need for suitable for determining the specifications of maximum permissible limits or analytical techniques with limits of detection for the measurement of pollutant emissions in analytical methodology coupled systems

A method must be validated when necessary to verify that their performance parameters are suitable for use in a specific analytical problem. For example:
• A new method developed for a specific problem;
• An established method and revised to incorporate improvements or extend it to a new problem;
• When quality control indicates that a method already established is changing over time;
• An established method used in a different or different analysts or different instrumentation laboratory;

• To demonstrate equivalence between two methods, for example, between a new method and a reference. [4]

The validation process is in fact an application known as the Deming cycle or PDCA (Plan, Do, Check, Adjust) cycle is also interpreted as an application of the scientific method. Following this cycle, plans for the characteristics of analytical methods meet the requirements are, it is experienced. experiment results are compared, *ie* the characteristics of the method, the requirements, and if the method is adjusted as appropriate with the intention that new results with the modified method satisfying the requirements [5].

Within the criteria of implementation of the ISO / IEC 17025 [6] standard indicates that trials involving physical measurements the minimum parameters to validate the analytical methods are:

1. Verification equipment performance against the requirements set in the method.
2. Using reference materials required by the method, when applicable.
3. Compliance of facilities and environmental conditions in the laboratory with the provisions of the method.
4. Study repeatability and reproducibility in compliance with the acceptance criteria as specified by the method, or, if the criteria established by the laboratory by performance data.
5. Evidence of assessing the accuracy and precision of the measurement method by experiment to assess the bias and repeatability of the method in the laboratory, either using reference materials or by interlaboratory comparison, see the series of NMX-CH-5725-IMNC standards.

This paper presents the results of analysis of the analytical methods and validation parameters are presented to satisfy the requirements of conformity assessment of a measuring system emissions oxyhydrogen coupled to an internal combustion system, based on the EURACHEM guide. [4]

2. Materials and Methods

The validation protocol must contain the following specifications according Castillo Aguilar, B., & Gonzalez Hernandez, R. (1996) in its validation protocol analytical methods: [7]

1. *Identify analytical requirements.* First establish the analytical requirement that defines the performance characteristics of the method must meet to solve a need: the type of parameters or measurements to be made and its range or margin for the method have to be useful.
2. *Description of the characteristics of the method.* In response to the requirements standardized methods to be modified are identified, they must be aware that there are legal rules requiring follow certain methods. The method should be designed by the laboratory from scratch, or gathering information from all possible sources
3. *Verification, calibration and control equipment.* Currently most producers develop the validation of analytical equipment to meet international requirements allowing use in quality

control in different industries and even though user manuals specifications of precision and accuracy of the equipment appear for typically, the user must develop its own procedure for checking the proper functioning of the instrument or follow the manufacturer's recommendations. When the computer is verified, a simple control routine is performed.

4. *Staff training.* The staff responsible for conducting analytical testing will be training specifically in this type of work and training him will be rigorously documented.
5. *Standard Operating Procedure method*. It reflects the exact procedure for implementing the analytical method and be annexed to protocol validation.
   On the one hand, validation will be determined by the technical possibilities available to the laboratory, such as availability of reliable reference patterns, technical difficulties in conducting the test, required accuracy, etc., and on the other hand, validation must take into account factors related to the risk associated with the performance of the assay, so that the severity of the consequences of a failure in carrying out the method shall be taken into account when allocating resources for validation.
   Sometimes the validation process or calibration test methods, such as some analytical methods are available only to laboratories or research centers equipped with the best and most advanced resources. This paper has been excluded validation stage sampling, handling and transportation of the sample consider that often the testing laboratory is not responsible for these tasks, such as commercial laboratories. [8]

2.2 Equipment and accessories

For purposes of valuation methods, analysis of pollutant emissions was performed using different techniques, in order to have reliable results-based regulations. Below are listed:

- Gas Emissions Vehicle, Hot 505 test (cold phase) of the FTP-75 test was conducted at the Laboratory of Vehicular emissions of Mexican Petroleum Institute according to the NMX-AA-11-1993-SCFI standard. [9]
- Speciation of hydrocarbons from vehicle emissions conducted at the Laboratory of Vehicular Emissions of Mexican Petroleum Institute, based method, Standard Test Method for Determination of Gaseous Organic Compounds by Direct Interface Gas Chromatography-Mass Spectrometry1 ASTM D 6420-99. [10]
- Measurements of emissions by Gas Analyzer AGS-688 BRAINBEE, by a static test based on the NOM-047-SEMARNAT-2014 standard paragraph 6 [11] conducted at the Laboratory of Clean Energy Research Center and Technological Innovation -IPN.

3. Results and Discussion

3.1 Measurement analysis.

Table 1 shows the average results of pollutant emissions in the car with the probe shown, it is possible to observe a reduction in emissions mainly in total and carbon monoxide hydrocarbons, this reduction is mostly visible in idle running, this directly influences in increased emissions of carbon dioxide, the result of improved combustion of hydrocarbons.

Table 1 Testing probe light car BRAINBEE. compared emissions reduction.

PROTOTYPE WITHOUT AUTOMOVIL						AUTOMOVIL prototyped					REDUCTION IN %			
	HC	CO_2	CO	O_2	λ	HC	CO_2	CO	O_2	λ	%HC	CO_2	CO	O_2
	% vol	% vol	% vol	% vol		% vol	% vol	% vol	% vol		% vol	% vol	% vol	% vol
Idling	0.108	10.700	5.533	6.103	1.063	0.045	14.000	0.660	6.200	1.255	0.063	-3.300	4.873	-0.097
2000 rpm	0.004	14.600	0.033	4.237	1.201	0.002	14.300	0.010	6.877	1.197	0.002	0.300	0.023	2640
3000 rpm	0.002	14.500	0.010	3.413	1.164	0.001	14.533	0.010	2.030	1.104	0.001	-0.033	0.000	1.383

Table 2 Testing motorcycle BRAINBEE probe compared emissions reduction.

MOTORCYCLE WITHOUT PROTOTYPE						MOTORCYCLE WITH PROTOTYPE					REDUCTION IN%			
	HC	CO_2	CO	O_2	λ	HC	CO_2	CO	O_2	λ	HC	CO_2	CO	O_2
	% vol	% vol	% vol	% vol		% vol	% vol	% vol	% vol		% vol	% vol	% vol	% vol
Idling	0.046	1.733	2.417	16.85	3.382	0.031	1400	2.487	17.28	3.631	0.015	0.333	-0.070	-0.423
500 rpm	0.031	1.667	3.050	16.710	3.040	0.030	1.500	3.043	16.590	3.104	0.002	0.167	0.007	0.120
1000 rpm	0.034	1.767	3.447	16.010	2.716	0.026	1.867	3.947	15.927	2.504	0.007	-0.100	-0.500	0.083

In table 2 the average emissions results are shown in the motorcycle with the probe, one can see a reduction in carbon dioxide mainly; this reduction is mostly visible in idle running.

Table 3 minimally reduced non-methane hydrocarbons and total hydrocarbons, conversely, the values of CO and CO_2 have a slight increase is observed. This slight increase in the carbon

monoxide may indicate inefficient combustion, however, can not be said reducing or increasing concentrations because the percentage is below the uncertainty value Hot 505 test.

Table 3 Average pollutant emissions test prototype Hot 505 with no prototype (3.6).

	THC ppm	LCO ppm	NOx ppm	CO_2 %	NMHC ppm
prototyped	5.826	38.024	1.117	0.695	5.826
No prototype	6.779	17.769	0.950	0.693	6.779
Reduction in%	0.0001	-0.0020	0.0000	-0.0020	0.0001

NOTE: The negative sign in Tables 1, 2 and 3 represents a percentage increase in emissions. For testing Hot 505 was calculated from the difference of the average of the results with prototype without prototype (Table 4), then the relevant conversion units ppm to % was made, and thus the effect of injection of oxyhydrogen gas compared. For other groups it is calculated with a direct difference between their average values.

In Table 4 the results of the chromatographic speciation which shows that differences between the concentration of total hydrocarbons (THC) from vehicle emissions before and after installation of the prototype, are less than 0.01g shown, although there is a minimal reduction, this value does not represent a significant or important difference.

Result of this chromatographic analysis, it has to total hydrocarbon concentrations are reduced 0.065% that while it is low, confirming the results obtained with the probe.

Table 5 is a detailed extract speciation chromatography, which shows how hydrocarbons are found in greater concentration in future testing an analysis of why the majority presence of such components in the mixture could be performed, and causes modification or reducing some of them with the use of oxyhydrogen gas.

Table 4 Speciation chromatographic results.

Proof	Cell NMTHC in g / Km	Chromatography NMTHC g / Km	NMTHC identified g / Km	NH4 g / km	THC in cell	THC Chromatography	THC identified g / km
No prototype	0.061	0.051	0.048	0.007	0.068	0.058	.0550
No prototype	0.069	0.068	0.060	0,005	0.074	0.074	0.0650
Average	0.065	.0597	.0537	0.006	0.071	0.066	0.0600
prototyped	0.062	0.057	0.050	0.006	0.068	0.063	.0562
prototyped	0.048	0.053	.0470	0,005	0.053	0.058	.0522
Average	0.055	.0548	0.0486	0.006	0.061	0.060	.0542

Table 5 Hydrocarbon concentration increased presence
Chromatographic result of speciation (g / Km)

	W/O prototype		W/O prototype	Average
HC Totals	0.051	**HC Totals**	0.068	0.060
2-methylpentane	0.004054	**2-methylpentane**	0.004995	
toluene	0.003588	**isopentane**	0.004808	
224-trimethylpentane	0.003380	**224-trimethylpentane**	0.004635	
isopentane	0.003232	**toluene**	0.003987	

	With prototype		With prototype	Average
HCtotales	0.057	**HCtotales**	0.053	0.055
2-methylpentane	0.003932	**isopentane**	0.003409	
toluene	0.003629	**224-trimethylpentane**	0.003400	
224-trimethylpentane	0.003590	**2-methylpentane**	0.003354	
isopentane	0.002784	**toluene**	0.003330	

3.2 Statistic analysis

3.2.1 Statistical analysis for testing HOT 505

The standard deviation of the results for each population data is determined.

Table 6 **Repeatability standard deviation for Hot 505 without prototype test**

THC	LCO	Nox	CO_2
0.550129076	0.519723484	0.189504617	0.000707107

Table 7 **Repeatability standard deviation for testing with prototype Hot 505**

THC	LCO	NOx	CO_2
1.065609919	7.307241477	0.044547727	0.000707107

According to the results of the standard deviation of the test HOT 505 without prototype and prototype it shows that the population data of NOx, carbon dioxide (CO_2) acceptable variation exists in the data set, in other words, their samples are representatively equal. However, for the case of total hydrocarbons (THC) and carbon monoxide (LCO) changes if they are present, meaning that if there are significant differences in the data set, it is noteworthy that these analyzes should corroborated more data each family, which could not be performed by the laboratory responsible disposal.

3.2.2 Test statistical analysis to test measuring emissions for motorcycle and automobile using a gas analyzer. Static method.

"Null hypothesis" referring to a null significant variation in the samples, and "alternative hypothesis" referring to a significant variation in the samples: one F statistical test where two hypotheses are were performed.

According to the test F In the case of car it shows that at all three levels applied gear (Idling, 2000 RMP and 3000 RPM) the data set groups of total hydrocarbons (THC), carbon dioxide (CO_2) and carbon monoxide (CO) accept the null hypothesis that the population means that data no statistically significant changes between their own groups, however in the case of oxygen (O_2) exists influence among all its subsets; analysis prototype without prototype analysis; *ie* there are significant differences between them.

In the case of data obtained in the analysis motorcycle there are different variations in population data set and there is no consistency in the F test performed. Since for all test data Idling it is observed that there are significant variations for groups Carbon dioxide (CO_2) and oxygen (O_2) but for groups of total hydrocarbons (THC) and carbon monoxide (CO) there are no significant variations; It is indicating that the implementation of the prototype in the latter two groups have no direct influence.

On the other hand during the test of 500 revolutions per minute it was found that there are significant variations for the data groups of THC (total hydrocarbons), carbon dioxide (CO_2) and carbon monoxide (CO) and in the case of oxygen (O_2) there were no changes, this effect occurs under the mechanical characteristics of the motorcycle and small variations in rpm; then it can be said that the above inconsistency is attributed to the instability rpm during operation. Therefore any attachment applied to the bike has influence on data from pollutant emissions.

4. Conclusion

A simple and straightforward analysis was to describe the methodology that represents the measuring emissions for internal combustion engine fuel system enriched with oxyhydrogen. The proposals described have advantages in aspects such as sensitivity offering methods allowing the determination and quantification of pollutant emissions generated by an internal combustion engine fuel enriched with oxyhydrogen, inexpensive analysis only for the case of the probe system , low consumption of organic solvents and minimal waste generation.

In the analysis results with the probe it was obtained up to 0063% reduction in total hydrocarbons and up to 4.9% CO, both idle mode in case the car. In the case of motorcycle analysis results with the probe it was obtained up to 0015% reduction in total hydrocarbons and an increase of 0.0070% CO, at idle.

The test results Hot 505, there is a decrease of .0001% and .0020% increase CO and CO_2, however, both values are below uncertainty values they are therefore not significant. With the results of the chromatographic speciation of hydrocarbons, which is thinner, it is obtuvor 0065% reduction in total hydrocarbons, which although less confirms the results obtained with the probe.

Acknowledgments

The authors thank the National Council for Science and Technology for funding for PEI 242633 project and Dr. Juan Manuel Sandoval Pineda and ESIME for the facilities for the development of the project.

References

[1] Castillo Aguilar, B., & Gonzalez Hernandez, R. Validation protocol analytical methods for quantitation of drugs. Revista Cubana de Farmacia; 1996.
[2] Gonzalez, NE (n). Aspects of the instantaneous dynamic measurement of engine emissions. Application to the development of a laptop and a methodology for studies of pollution vehicles in real traffic.
[3] González Huerta RG, Cortés Escobedo C., Sandoval Pineda J.M. Multidisciplinary scientific research project and technology-design and manufacture of oxyhydrogen reactors for saving fossil fuel development; 2015.
[4] Morillas, PP al Eurachem Guide: The fitness for use of analytical methods A Laboratory Guide for validation of methods and related subjects. 1st Edition; 2016.
[5] R., & Hernandez I. Method validation: a practical approach. Symposium metrology; 2004.
[6] ISO, B. IEC 17025: 2005 General requirements for the competence of testing and calibration laboratories. In ICS; 2005.
[7] Castillo Aguilar, B., & Gonzalez Hernandez, R. validation protocol analytical methods for quantitation of drugs. Revista Cubana de Farmacia 30 (1); 1996.
[8] quality engineering and metrology. ISO 17025 method validation testing and calibration; 2013 ,http://www.icm-calidad.com/Articulos/acreditacion/validacion. [Accessed 07/26/2018]
[9] NMX-AA-11-1993-SCFI, test method for evaluating exhaust gas emissions from new motor vehicles using gasoline ground as fuel, Secretary of Commerce and Industrial Development International Standard; December 27, 1993.
[10] ASTM D6420-99 (2004) Standard Test Method for Determination of Gaseous Organic Compounds by Gas Chromatography-Interface Direct Mass Spectrometry, ASTM International, West Conshohocken, PA; 2004.
[11] NOM-047-SEMARNAT-2014, which sets the equipment characteristics and the measurement procedure for the verification of the limits of emission of pollutants from motor vehicles in circulation that use gasoline, liquefied petroleum gas, gas Natural or other alternative fuels, Secretariat of Environment and Natural Resources; December 2014.

XVIII International Congress
of the Mexican Hydrogen Society

Immobilization of Glucose oxidase on glutathione capped Carbon or CdTe Quantum Dots for use in biosensors and biofuel cells

Jairo Daniel Lozano-López[1], Marisol Galván-Valencia[1], Ricardo Escalona-Villalpando[2], Sergio M. Durón-Torres[1*]

[1]Unidad Académica de Ciencias Químicas, Universidad Autónoma de Zacatecas, Campus Siglo XXI, Carretera a Guadalajara Km. 6.0, Ejido la Escondida, Zacatecas, Zac. México, 98160.
[2]Centro de Investigación y Desarrollo Tecnológicoen Electroquímica S.C. Sanfandila, Santiago de Querétaro, México, 76703.
* Tel: +524929256690 Ext. 4655; e-mail: serduro@yahoo.com

ABSTRACT

The enzyme immobilization on conductive materials is a topic research for the development of biosensors and biofuel cells. The most common anchoring methods (covalent binding, cross-linking or inclusion in gels and membranes), often interfere with enzymatic catalysis due to active sites occlusion, enzyme denaturation or substrate diffusion problems. The use of quantum dots as support matrix for the enzyme immobilization, has been reported as a viable alternative for the macromolecules anchoring, diminishing to a great extent the most well-known problems.

In this work, a comparison between Graphene QD´s (GSH-CQD) and CdTe QD´s (GSH-CdTeQD) coated with glutathione is presented for the immobilization of the enzyme Glucose oxidase (GOx). The surface of graphite electrodes was modified, with 5,10,15,20-Tetrakis (1-methyl-4-pyridinium) Porphyrin, a layer of QD was deposited to finally anchor GOx. The modified electrodes were evaluated by cyclic voltammetry (CV) in PBS 0.1 M pH 7.4 at 50 mVs-1. The results obtained show that “QD´s modified electrodes” have a greater immobilization capacity than graphite electrode. This suggests that the use of GSH-CQD could be exploited in the design of enzymatic electrodes for glucose biofuels anodes.

Keywords: biofuel cell, enzyme immobilization, quantum dots, glucose

1. Introduction

Focusing on the need to decrease the usage of fossil fuels for energy generation, biofuel cells development has become a very promising research field [1] this is how enzymatic biofuel cells have been developed. Enzymatic biofuel cells are devices capable of obtaining energy from oxidation-reduction reactions, catalyzed by different enzymes anchored to conductive supports that function as anodes and cathodes [2].

For this purpose Glucose Oxidase (GOx) is one of the most studied enzymes, since anchored to an electrode, catalyzes the glucose to gluconolactone oxidation ,and this process allows obtaining electrons that can be used to generate an electric current [3]. However, one of the main challenges on this enzyme usage is its immobilization, since most of the anchoring methods intervene with protein active sites, so decreasing the enzyme catalytic activity [4]. One of the most recommended methods for enzymatic immobilization is adsorption, since produces very low enzyme denaturation, and may generate an optimal microenvironment that keeps properly the three-dimensional protein structure [5]. On this basis, ionic nanoparticles capable to bind proteic structures on their surface are needed, it opens the way for the use of quantum dots.

Quantum dots (QD's) are semicrystalline nanoparticles smaller than 10 nm that have size dependent conduction and photoluminescence properties. According to their surface modifications, QD´s may also have ionic behavior [6]. Glutathione capped cadmium telluride QD´s (GSH-CdTeQD) has been reported to have good affinity for GOx, and due to their shape, size and surface, could provide an optimal anchor site for this enzyme, improving its orientation, and keeping the occlusion of its active sites to a minimum [7]. Also, GSH-CdTeQD, possess high affinity for tetracationic porphyrins, as 5,10,15,20-Tetrakis (1-methyl-4-pyridinium) porphyrin, to which they bind strongly [8].

The synthesis of glutathione capped carbon QD's (GSH-CQD) has also been published. These QD's have great luminescence and have been described as good electronic conductors [9], so they could be another viable option for enzymatic immobilization.

In this work, we report the synthesis and characterization of GSH-CQD and GSH-CdTeQD, as well as their use as enzymatic immobilizers in a layer-by-layer arrangement of Porphyrin/QD's/GOx. It´s shown a comparison between both QD´s types, considering their performance in the construction of glucose-sensitive enzymatic electrodes. The possible application of these electrodes in the development of an enzymatic biofuel cell that uses glucose as a substrate is also explored.

2. Materials and Methods

2.1 Chemicals, reagents, solutions and pretreatments

Glucose oxidase (GOx 225283 units g^{-1}), 5,10,15,20-Tetrakis (1-methyl-4-pyridinium) porphyrin tetra(p-toluenesulfonate) $C_6H_8O_7$, Ferrocene-methanol (Fc-MeOH), glucose and graphite rods (3 mm diameter x 75 mm length) was purchased from Sigma-Aldrich and used with no additional purification. $CdCl_2$ * $2.5H_2O$, Na_2TeO_3, Glutathione (GSH), and $NaH_2(C_3H_5O(COO)_3)$ was purchased from Merck. For to carry out the analyzes, 5 mg of GOx was dissolved in a PBS 0.1 M pH 7.4, and a 0.1 mM solution of porphyrin was prepared in a 0.1 M Tris 8% methanol buffer solution. QD´s was used as obtained from synthesis. Graphite rods were vertically immersed in epoxy resin, and polished to obtain a 3mm diameter electrode surface. For electrochemical glucose detection a 0.5 mM FcMeOH solution was prepared using 0.1 M pH 7.4 PBS as solvent.

2.2 Synthesis of Quantum dots

Both types of QD´s were synthesized according to previously reported methodologies [9] [10]. GSH-CQD's were prepared by pyrolysis of citric acid at 240 ° C in the presence of GSH for 10 minutes until the formation of a brown liquid that was subsequently dissolved in deionized water. GSH-CdTeQD's were synthesized by reflux of $CdCl_2$ * $2.5H_2O$ and Na_2TeO_3 in the presence of GSH and NaH_2 $(C_3H_5O$ $(COO)_3)$ * $2H_2O$.

2.3 Optical and physicochemical characterization of materials

Firstly, both types of QD's were irradiated under a UV_{360} lamp to confirm photoluminescence. Subsequently QD´s spectrophotometric characterization was performed in a Jenway UV-Vis spectrophotometer Model 6405. For interactions between used materials, IR spectra was measured for Graphite, Graphite/Porphyrin, Graphite/GSH-CdTeQD, Graphite/Porphyrin/GSH-CdTeQD and Graphite/Porphyrin/GSH-CdTeQD/GOx in a FT-IR Spectrum Two spectrometer. Size particle of GSH-CdTeQD determined by DLS and surface charge of Porphyrin, GSH-CdTeQD, and Porphyrin/GSH-CdTeQD complex were measured by Zeta potential in a Malvern Zetasizer Nano range.

2.4 Electrode modification

Graphite electrodes were polished on sandpaper and bond paper. All materials were drop coated over polished clean graphite surfaces, first individually for each material characterization, and then in a layer by layer arrangement, dropping 3 μl of Porphyrin solution, then 3 mL of respective QD's suspension, and finally 3 mL of GOx solution.

2.5 Electrochemical measurements

All electrochemical measurements were performed in a Gamry 600 Potentiostat/Galvanostat. Cyclic voltammetry (CV) was used as electrochemical characterization tool employing a conventional three electrodes cell, with a saturated calomel electrode (SCE) as reference, and a Pt wire as counter. A 0.1M pH 7.4 PBS solution was used as support electrolyte for

electrochemical characterizations; for glucose detection, a 0.5 mM FcMeOH was dissolved on same electrolyte. Scan rate was 50 mVs^{-1} in electrochemical fingerprint determination, while for glucose detection a 5 mVs^{-1} scan rate was applied. Chronoamperometric analyzes were carried out at a 0.245 V vs SCE potential.

2.6 Biofuel cell and microfluidic biofuel cell measurements

Porphyrin/GSH-CdTeQD/GOx and Porphyrin/GSH-CQD/GOx graphite anodes were evaluated by linear sweep voltammetry in a single compartment fuel cell using a Pt wire as cathode, in a "FcMeOH-PBS" solution as electrolyte, containing 20 mM of glucose. For the microfluidic biofuel cell (μBFC) measurements, graphite was replaced by Toray carbon paper. All materials were dropped as described above. Same microfluidic arrangement, and enzymatic Laccase/An-MWCNT cathode reported by Escalona-Villalpando [11] was used in this work.

3. Results and Discussion

3.1 Synthesis and characterization of the QD's

High-fluorescence QD's were obtained, as shown in Fig. 1. The photoelectric behavior of the GSH-CdTeQD is widely described, and its growth as a function of the synthesis time could be monitored over different times (Fig. 1a). The GSH-CQD, on the other hand, show a greater blue photoluminscence than "glutathioneless" CQD, a behavior also previously described in the literature [9]. An increase of approximately 20.4% in the photoluminescence of the GSH-CQD´s was calculated with respect to the CQD (Fig.1 b and c), using the *ImageJ* image analyzer. The spectrophotometric analysis of both types of QD´s showed the characteristic absorbance spectrum of each one (data not shown). According to the consulted literature, which relates the wavelength with higher absorbance to the particle size range, the absorbance peak of the GSH-CQD indicates a particle size around 3 nm [9], while the GSH-CdTeQD possess a particle size around 7 nm obtained by the equation of Yu for this type of QD's [12].

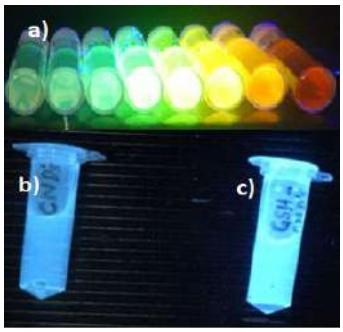

Fig. 1. QD's observed under UV360 light. In the upper part, aliquots of the GSH-CdTeQD obtained at different synthesis times **(a)** are shown. Down, a comparison between the "glutathioneless" CQD **(b)** and the GSH-CQD **(c)** is presented.

3.2 Voltammetric evaluation of Porphyrin/QD´s complexes

The voltammetric analysis of 5,10,15,20-Tetrakis (1-methyl-4-pyridinium) porphyrin deposited over graphite, shows a trend similar to that reported on literature. As shown in Fig. 2, this molecule exhibits a pair of redox processes at potentials of 25 and 255 mV vs SCE at anodic direction, and -410 and -690 mV in the cathode direction, which are associated with the formation of a dication and a dianion of nitrogens in the macrocycle center. It is also possible to distinguish a signal that appears at 620 mV in the anodic sense, which has also been reported as characteristic for the oxidation of two electrons, responsible for the aromatic character of the porphyrin ring [13]. This allows us to suggest that Porphyrin is indeed bound to graphite.

The deposit of both QD's types, caused a significant change in the voltammetric signal of the Porphyrin. In the first case, the presence of GSH-CdTeQD, produced a considerable increase in the reduction currents associated with the porphyrin dianion, and an apparent decrease in the oxygen evolution overpotential. The signal of the dication diminishes considerably, but the peak associated with the aromaticity of the macrocycle is conserved. Conversely, with the presence of GSH-CQD over Porphyrin, the dianionic signal remains almost intact, and the peaks attributed to the porphyrin dicatión take a plateau-like shape, while the signal associated with the aromaticity of the macrocycle, fades almost completely.

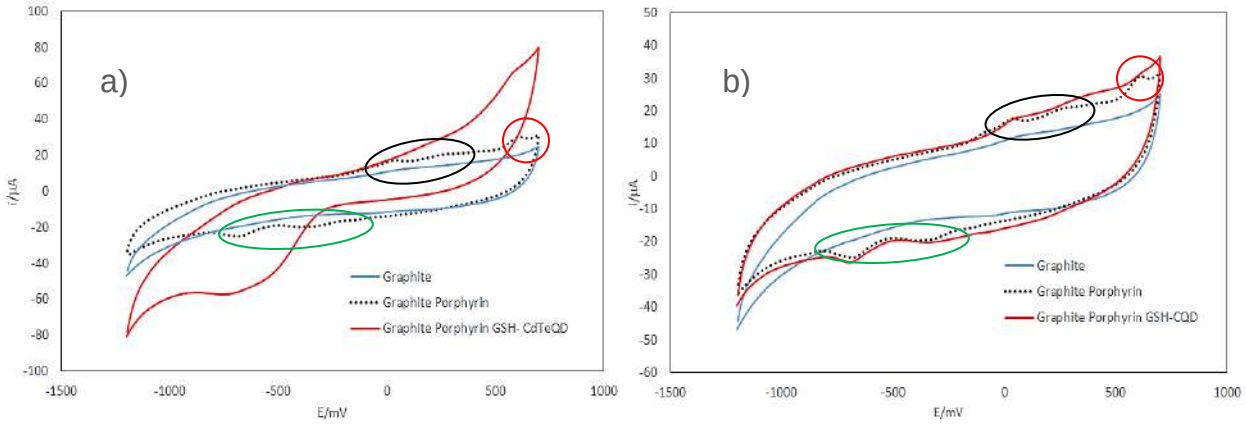

Fig. 2. Voltammetric fingerprint for graphite electrodes (blue) modified with Porphyrin (black) and Porphyrin/QD (red) using GSH-CdTeQD (a) or GSH-CQD (b). Dication and dianion signals are circled in black and green respectively, while aromaticity peak is circled in red for both graphs.

3.3 GOx adsorption voltammetric evaluation

GOx adsorption was evaluated by monitoring FAD/$FADH_2$ group, since this cofactor exhibits a characteristic redox pair between -400 and -500 mV vs SCE. By subtracting the baseline to the FAD oxidation peak in each voltammogram (Fig. 3, inside), considerable variations in the current may be observed. As shown, higher current values were obtained in QD´s modified electrodes than in Graphite/GOx electrode.

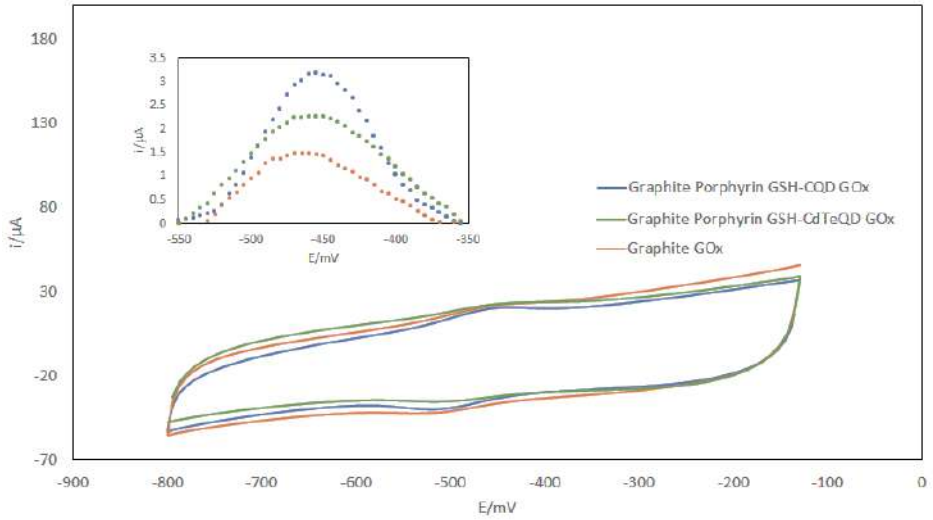

Fig. 3. Voltammetric response of GOx (orange), Porphyrin/GSH-CdTe/GOx (green) and Porphyrin/GSH-CQD/GOx (blue) modified graphite electrodes. The inside graph shows the FAD oxidation peak for each voltammogram, after subtracting their baselines.

3.4 Porphyrin/QD´s/GOx electrodes glucose sensitivity

The sensitivity to glucose of the modified electrodes was evaluated as an indirect measure of the enzymatic activity, taking as reference the increase in the oxidation current of the FcMeOH mediator. The obtained results suggest that the electrode modified with GSH-CQD has low sensitivity to glucose (0.187 mA/mM). On the other hand, electrode that uses GSH-CdTeQD as a support for GOx showed a major response to glucose additions giving a 0.671 mA/mM sensitivity, which seems to indicate that these QD's keep better the GOx activity. On this basis, only Porphyrin/GSH-CdTe/GOx electrodes were chosen for biofuel cell assays.

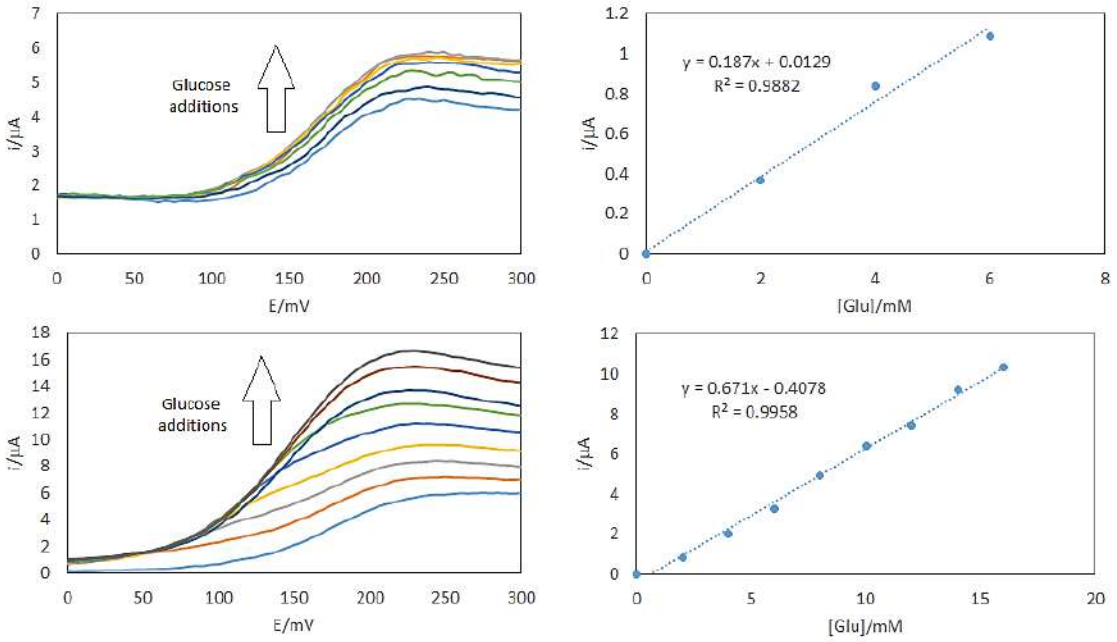

Fig. 4. Linear increase in the oxidation current of FcMeOH as a function of the glucose additions for a GSH-CQD modified electrode **(a)** and **(b)**, and one using GSH-CdTeQD **(c)** and **(d)**.

3.5 Enzymatic anodes evaluation in a single-compartment cell and microfluidic biofuel cell.

Graphite enzymatic electrodes were evaluated in a single-compartment cell against a platinum cathode in presence of 20 mM glucose, using FcMeOH as a mediator. The obtained OCP was 0.145 V, Imax = 8.26 μA and a Wmax = 2.9 μW. The Porphyrin / GSH-CdTeQD / GOx system was deposited on Toray paper and evaluated using a Laccase/AnMWCNT cathode in a previously described microfluidic array [11]. The flow rate was 3mLh^{-1} using 0.1 M PBS pH7.4 for anode and pH 5.7 for cathode. OCP obtained in this arrangement was 0.63 V, Imax = 11.2 mA and Wmax = 3.4 mW.

3.6 Physicochemical and infrared analyzes

In order to know the properties of the assembled system, as well as to explore the possible interactions between Porphyrin, GSH-CdTeQD and enzyme, the approximate size of the QD's, and the surface charge of the Porphyrin/GSH-CdTeQD complex was determined by DLS. The results of this analysis are shown in Table 1, in which it is observed that the approximate size of the QDs determined by DLS, coincides with that obtained mathematically in the spectrophotometric analysis. In addition, the Porphyrin/GSH-CdTeQD complex appears to generate "particles" of around 400 nm diameter. This could be due to the formation of conglomerates by interaction between QD's and Porphyrins. For its part, the surface charge of

both components is added, giving a more negative net charge when both materials are in contact.

Table 1. Zetasizer results for size (DLS) and surface charge (Zeta potential) analyzes.

Sample	Theoretical size (nm)	Surface charge (mV)
Porphyrin	-	-4.3
GSH-CdTeQD	7.3	-29.3
Porf/GSH-CdTeQD	453.6	-33.86

The materials deposited on graphite were also characterized by FT-IR. In Fig. 5 the spectra obtained for each sample are shown, starting with clean graphite, then Porphyrin, GSH-CdTe, Porphyrin/GSHCdTe complex, and finally Porphyrin/GSH-CdTe/GOx all on graphite. An apparent combination between the bands at 3400 cm -1 could be noted when Porphyrin and GSH-CdTeQD were combined. In addition in 400-1600 region, the signals seem to be combined when layer-on-layer materials are deposited. A better IR analysis is being done in order to determine the formation of links or interactions between the component systems.

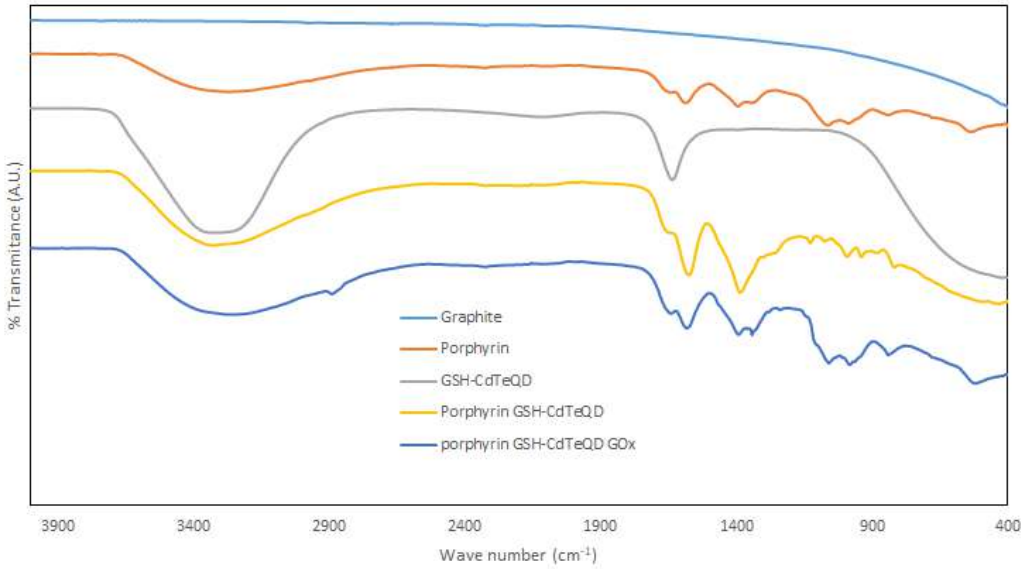

Fig. 5. FT-IR spectra for the materials evaluated. From top to bottom appears graphite, Porphyrin, GSH-CdTeQD, Porphyrin/QD's complex, and Porphyrin/GSH-QD/GOx assembly.

4. Conclusion

From these results it can be concluded that Quantum dots (either carbon or CdTe) coated with glutathione are useful to increase the amount of GOx deposited on graphite electrodes modified with Porphyrin. However, regardless of the observed FAD/$FADH_2$ signal, the GSH-CdTeQD seem to better preserve the catalytic activity of GOx compared to the GSH-CQD, since the electrodes modified with this material are more sensitive to the presence of glucose. Also, the electrodes modified with Porphyrin/GSH-CdTeQD/GOx show good values of current and power in a microfluidic array, so they could be implemented in a biofuel cell construction.

Acknowledgements

The authors thank the Mexican Council of Science and Technology CONACYT and Secretary of Energy SENER for financial support provided through the MCyTQ Program.

References

[1] Christwardana M, Kim D-H, Chung Y, Kwon Y. A hybrid biocatalyst consisting of silver nanoparticle and naphthalenethiol self-assembled monolayer prepared for anchoring glucose oxidase and its use for an enzymatic biofuel cell. Applied Surface Science. 2017;429:180-6.
[2] Rasmussen M, Abdellaoui S, Minteer SD. Enzymatic biofuel cells: 30 years of critical advancements. Biosensors & bioelectronics. 2016;76:91-102
[3] Zhao M, Gao Y, Sun J, Gao F. Mediatorless glucose biosensor and direct electron transfer type glucose/air biofuel cell enabled with carbon nanodots. Analytical chemistry. 2015;87(5):2615-22.
[4] Zhou Z, Hartmann M. Progress in enzyme immobilization in ordered mesoporous materials and related applications. Chemical Society reviews. 2013;42(9):3894-912.
[5] Jesionowski T, Zdarta J, Krajewska B. Enzyme immobilization by adsorption: a review. Adsorption. 2014;20(5-6):801-21.
[6] García C, Fuenzalida F, Ruiz D, Aguirre J. Electrochemical, spectroscopic and morphological characterization of electrostatic self-assembled hybrids of tetracationic phosphonium porphyrins and CdTe quantum dots. J Appl Electrochem. 2014;44(1):1345-1353.
[7] Cao, L., Ye, J., Tong, L., & Tang, B.. A new route to the considerable enhancement of glucose oxidase (GOx) activity: the simple assembly of a complex from CdTe quantum dots and GOx, and its glucose sensing. Chemistry. 2008;14(31), 9633-9640.
[8] O.F. Mohammed, G. Ahmed, S. Aly, A. Usman, M. Eita and V. MelnikovQuantum confinement-tunable intersystem crossing and triplet state lifetime of cationic porphyrin-CdTe quantum dot nano-assemblies Chem. Comm. 2015;51, 8010-8013.
[9] Liu JJ, Zhang XL, Cong ZX, Chen ZT, Yang HH, Chen GN. Glutathione-functionalized graphene quantum dots as selective fluorescent probes for phosphate-containing metabolites. Nanoscale. 2013;5(5):1810-5.

[10] Sheng Z, Han H, Hu X, Chi C. One-step growth of high luminescence CdTe quantum dots with low cytotoxicity in ambient atmospheric conditions. Dalton transactions. 2010;39(30):7017-20.
[11] Escalona-Villalpando RA, Reid RC, Milton RD, Arriaga LG, Minteer SD, Ledesma-García J. Improving the performance of lactate/oxygen biofuel cells using a microfluidic design. Journal of Power Sources. 2017;342:546-52.
[12] Liu YF, Yu JS. In situ synthesis of highly luminescent glutathione-capped CdTe/ZnS quantum dots with biocompatibility. Journal of colloid and interface science. 2010;351(1):1-9.
[13] Van Caemelbecke E, Derbin A, Hambright P, Garcia R, Doukkali A, Saoiabi A, et al. Electrochemistry of [(TMpyP)M(II)]4+ (X-)4 (X- = Cl- or BPh4-) and [(TMpyP)M(III)Cl]4+ (Cl-)4 in N,N-dimethylformamide where M is one of 15 different metal ions. Inorganic chemistry. 2005;44(11):3789-98.

Nanostructured materials

September 18 to 21, 2018 in Mexico City, Mexico

XVIII International Congress
of the Mexican Hydrogen Society

Methanol oxidation using Pt /oxide graphene-carbon as electrocatalyst in acid medium

J. A. Palafox Segoviano[1], B. Ruiz Camacho[1]*, A. Medina Ramírez[1], C. Martínez Gómez[1], C. M. López Badillo[2]

[1]Deparment of Chemical Engineering, Division of Natural and Exact Sciences, University of Guanajuato Noria Alta S/N, Guanajuato, Guanajuato, CP 36000, México

[2]Facultad de Ciencias Químicas, Universidad Autónoma de Coahuila, Blvd. V. Carranza y José Cárdenas, 25280, Saltillo, Coahuila, México

* Corresponding author: 473-73200-06, beatriz.ruiz@ugto.mx

ABSTRACT

Pt and Pd supported on carbon Vulcan are the most commonly catalysts used for methanol oxidation reaction. However, new support with more stability and higher dispersion are required in fuel cells systems. Recently, various studies has been focused in improved the stability of carbon support researching with different materials as carbon nanospheres, graphene, carbon nanotubes, ordered mesoporous carbon and graphene, graphene oxide and graphene reduced. In this work, Pt nanoparticles supported on graphene oxide (GO), carbon (C) and graphene oxide-carbon (1:1) (GO-C) were synthesized as electrocatalysts for methanol oxidation reaction (MOR) in order to investigate the effect of the support. The materials Pt/oxide graphene, Pt/oxide graphene-carbon and Pt/carbon were synthesized by ultrasound method and characterized by X-Ray diffraction (XRD). Samples synthesized were electrochemically evaluated by cyclic voltammetry (CV) and chronoamperometry (CA) techniques in acid media in presence and absence of methanol. Significates differences in the current intensity peak of methanol oxidation reaction were found it CV curves. The sample Pt/graphene-carbon (1:1) showed the higher electrochemical activity for MOR. The half-wave potential ($E_{1/2}$ = 0.77 V) and onset potential (E_{onset} = 0.6 V) indicated that the Pt/oxide graphene-C had the higher electrochemical activity for MOR compare to Pt/carbon and Pt/oxide graphene. The test of stability indicated that materials synthesized are more stables than on carbon Vulcan. Last results are associated at the formation of fewer intermediaries (formaldehyde and formic acid) during the methanol oxidation reaction. The materials synthesized using graphene oxide exhibits electrochemical activity for MOR.

Keywords: fuel cell, electrocatalysts, graphene, Pt nanoparticles

September 18th to 21st, 2018 in Mexico City, Mexico.

1. Introduction

The demand for energy and the excessive use of fossil fuels have caused an increase in environmental pollution. For this, it is necessary new ways of obtaining energy, one of these alternatives are the fuel cells (CC), as they are characterized by zero or low emission of pollutants during operation [1]. A CC is a device that converts the chemical energy to electric energy. Proton exchange membrane fuel cells (PEMFC) and direct alcohol fuel cells (DAFCs), which use hydrogen and alcohol as fuel, respectively, have emerged as promising renewable power devices.

DAFC have the advantage of using a liquid fuel (methanol, ethanol, etc.) that can be stored and handled more easily than other fuels in gaseous state (hydrogen, for example). The DAFCs are mainly used to supply electric power in portable electronic devices. Specifically, at the anode of a DAFC it is necessary to have highly active electrodes to catalyze the oxidation reaction of alcohols (methanol, ethanol, etc.) in an efficient and selective manner, reducing the formation of intermediates (carbon monoxide or formaldehyde). The first CC developments of methanol and direct ethanol were carried out in the 1950s and 1960s by Shell Co. and later by Exxon [2]. The reactions that occur in a direct methanol CC are as follows AT Anode, the expression 1, the Reduction at Cathode expression 2 and the Global Reaction, expression 3.

$$CH_3OH + H_2O \rightarrow CO_2 + 6H^+ + 6e^- \quad (1)$$

$$\frac{3}{2}O_2 + 6H^+ + 6e^- \rightarrow 3H_2O \quad (2)$$

$$CH_3OH + \frac{3}{2}O_2 \rightarrow CO_2 + 2H_2O \quad (3)$$

The use of an alcohol as fuel for the fuel cells has several advantages as a compound: its low toxicity, easy handling and storage, and cheap due to can be easily synthesized by biomass. However, in the complete methanol oxidation reaction is complexes and several intermediates can be formed when platinum is used as electrocatalysts [3].

Pt-based materials have been employed efficiently as catalysts of the two electrochemical reactions (oxidation and reduction) for direct alcohol fuel cells (DAFCs). However, Pt/C has drawbacks such as high cost and vulnerability toward poisoning by CO or carbonaceous intermediates [4,5]. In this way one of the major efforts in alcohol fuel cell catalysts research is to improve the electrocatalytic activity for alcohol oxidation and alcohol tolerance, as well as reducing its cost. Pt supported on carbon, is one of the best electrocatalysts for both anode and cathode electrodes in DAFCs. However, is necessary to investigated new supports alternatives to carbon Vulcan due to the carbon corrosion process during the performance of the fuel cells. According to Habibi [6], graphene and reduce graphene oxide (RGO) is characterized by its high mechanical stiffness, ultrahigh electron conductivity and extremely large surface area as well as

superior thermal/ chemical stability. Graphene can be an alternative as catalysts support for fuel cells application.

Graphene oxide can be defined as a sheet of graphene functionalized with different oxygenated groups. Graphene oxide can be synthesized in a simple way by a process of oxidation of graphite, known as the Hummers method [7]. By this method, graphite is reacted with a mixture of potassium permanganate, sodium nitrate and concentrated sulfuric acid.The interest of this material is that it can be used as a precursor to produce graphene or as a graphene material itself, due to the wide range of applications it presents. This wide range of applications is based mainly on its good electrical properties, high flexibility and high resistance to breakage.

Therefore the aim of this work was to evaluate the electrochemical activity of Pt supported on graphene oxide compare to the typical carbon Vulcan. Three supports of Pt were evaluated in methanol oxidation reaction, graphene oxide, carbon Vulcan and the combination of graphene oxide-carbon (1:1). Pt was incorporated to the supports by reduction method. The electrochemical activity was investigated by using cyclic voltammetry (CV) and chronoamperometry (CA) techniques.

2. Materials and Methods

2.1 Synthesis for the electrocatalyst

For the synthesis was taken 50 mL of Chloroplatinic acid ($1x10^{-3}$ M) and 60 mL Isopropyl alcohol was added into with 0.80 mg substrate (carbon, graphene oxide or graphene oxide-carbon). After that, the mixture was put into ultrasound Elmasonic P at 37 KHz for two hours at room temperature. Finally, the liquid was evaporated and the solid was recovered.

2.2 Physical characterization

The crystalline phases presented on the supports and electrocatalysts were identified by XRD using a PANalytical Model EMpyrean diffractometer.

2.3 Electrochemical characterization

The electrocatalyst were investigated by Cyclic voltammetry (CV) in acid media and methanol and by Chronoamperometry (CA) in a conventional tree electrode cell. For the preparation for the working was necessary dissolve electrocatalyst into ink. The ink was prepared using 6 mg for the electrocatalyst, 500 μL Isopropoyl alcohol and 50μL Of Nafion®. The solution was put into ultrasound Elmasonic P at 37 KHz for two hours at room temperature. After that, was taken 11μL for the ink over a vitreous carbon electrode (geometrical surface area

0.196 cm^2). The reference electrode was a Saturated Calomel Electrode (SCE) and the counter electrode was used a graphite bare.

The methanol oxidation test was performed by employing as electrolyte: 0.5M H2SO4 plus 0.5M CH_3OH. The CV curves were measured at a scanning rate of 50 mV s^{-1} in a nitrogen atmosphere; the potential applied was between 0.05 and 1.2 V/NHE; 20 cycles were necessary to stabilize the system. To evaluate the lifetime performance of catalysts, the CA test was carried out under constant potentials of 0.55 V during 3000s.

3. Results and Discussion

3.1 X ray diffraction measurements

The X-ray diffraction results (Fig. 1) shows the crystalline face-centered cubic structure (fcc) of platinum at 2 Theta values of 39.76°, 46.24°, 67.45° and 81.28° corresponds to the (111), (200), (220) and (311) planes in both samples (Pt/VC and Pt/GO). Additionally in the Pt/GO electrocatalyst, the peaks at 2theta values of 26.96° and 55° in XRD patterns correspond to the supporting carbonic material (graphite powder) (002) and (004), respectively. The signal around 46° corresponds to GO (100) of graphene oxide was interfered by Pt peak.

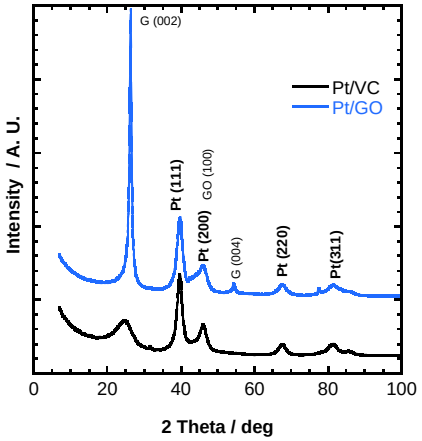

Fig. 1. XRD results of Pt/VC and Pt/GO synthesized by ultrasound.

3.2 CV measurements

Fig. 2 displays the CV curves for Pt in acid medium supported on Vulcan carbon (VC), graphene oxide (GO) and graphene oxide-carbon (GO-C) in nitrogen saturated 0.5M H_2SO_4. The CV of Pt in acid medium should be characterized by three regions: (I) the hydrogen

adsorption/desorption on the Pt surface between 0.05 and 0.3V, (II) the oxide region takes place at 0.7–0.8V and III) the double layer region in the range 0.3 to 0.4V. However, a larger capacitive current is obtained in the Pt electrocatalysts supported on graphene oxide.

3.3 Methanol electrooxidation reaction

Fig. 3a shows the methanol oxidation curves of Pt supported on Vulcan Carbon (VC), Graphene Oxide (GO) and Graphene Oxide-Carbon (GO-C). CV curves present a typical profile characteristics of MOR in acid medium, two oxidation peaks were observed, an anodic peak around 0.86V/NHE obtained during the forward scan (j_f / mAcm^{-2}) is associated with the catalytic activity for the MOR and a backward peak around 0.65–0.7 V/NHE (j_b / mA cm^{-2}) is mainly related to the electro-oxidation of methanol and removal of CO species [8]. A dramatic increase of methanol oxidation current peak of Pt supported on graphene oxide-carbon compared to carbon and grahene oxide was obtained. The maximum oxidation peak was observed for Pt/OG-C (16.9 mA cm^{-2}) which is about 1.5 times higher than Pt/C and Pt/OG, showing both samples a current density of 10.7 mAcm^{-2}. The onset potential (Eo) and the current of methanol oxidation are always considered as the indicators for evaluating the catalytic properties. Pt/oxide grahene-C shows the lowest E_{onset} and the highest current density indicating that the mixed of GO-VC could significantly improve the catalytic activity of Pt.

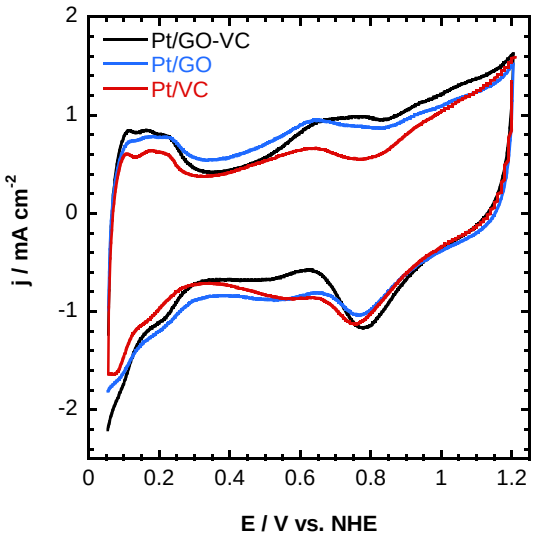

Fig. 2. Cyclic voltammetry of Pt/VC, Pt/GO and Pt/GO-VC electrocatalysts in N_2 saturated H_2SO_4. Scan rate 50 mV s^{-1} 0.5 M.

Fig. 3b shows the current-time response was monitored during 3000s in 0.5M H_2SO_4 containing 0.5 M CH_3OH in order to further investigate the durability of materials synthesized. The Pt/VC, Pt/OG and Pt/OG-VC catalysts showed CA curves with similar slopes, a rapid initial current density decrease is observed due to the surface poisoning by the CO adsorbed as intermediate species. The current density at 3000 s on the Pt/OG-VC was 2.9 $mAcm^{-2}$ Pt, which is higher than Pt/OG (0.66 mA cm^{-2} Pt) and Pt/VC (0.44 mA cm^{-2} Pt) this result is related to the stability and activity of the electrocatalyst.

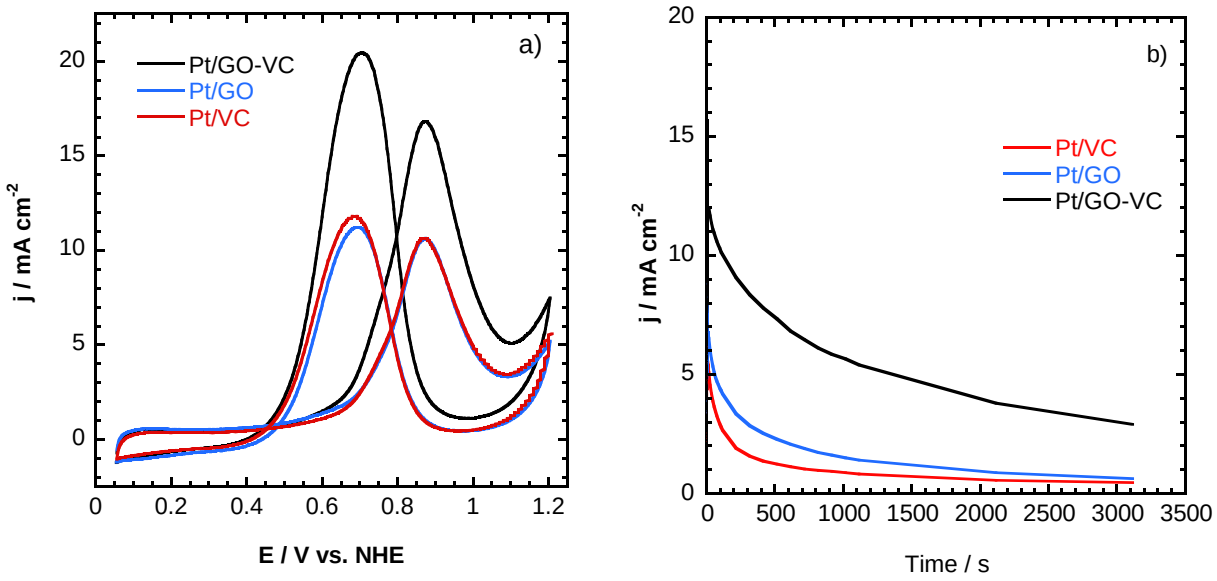

Fig. 3. a) CV curves and b) Chronoamperometry curves of Pt supported on Vulcan Carbon (VC), Graphene Oxide (GO) and graphene oxide-carbon (GO-C) in nitrogen saturated 0.5M H_2SO_4 plus 0.5M CH_3OH. Scan rate of 50 mV s^{-1}. RT.

4. Conclusion

The synthesis of Pt nanoparticles by ultrasound is simple, effective and reproducible.
The mixture of OG with CV in ratio (1:1) achieves a synergy effect by improving the catalytic activity of the Pt compared with the use of the graphe oxide and carbon substrates used separately.
DRX allows identify the crystalline structure of Pt successful.
Pt/GO-VC exhibits the highest electrochemical activity for MOR compared to Pt/GO and Pt/VC. According to chronoamperometry results Pt/GO-VC shows more stability and density current at 3000 s.

This work opens new possibilities on reference to electrocatalysts to be tested with different substrates and relationships for future application in fuel cells.

Acknowledgements

The authors are grateful for a University of Guanajuato through the DAIP office for providing financial support for the present research.

References

[1] U.S. Environmental Protection Agency. Combined Heat and Power Partnership. Section 6. Technology Characterization – Fuel Cell. CHP Technologies 2015:1-21.
[2] Hoyos, Bibian. El mecanismo de electro-oxidación de Metanol y Etanol. Una revisión bibliográfica; Dyna; 2002:69: 9-22.
[3] S. Baranton, C. Coutanceau, C. Roux, F. Hahn, J.-M. Le´ger. Oxygen reduction reaction in acid medium at iron phthalocyanine dispersed on high surface area carbon substrate: tolerance to methanol, stability and kinetics. Journal of Electroanalytical Chemistry 2005:577:223–234.
[4] Velázquez-Palenzuela, Centellas F, Brillas JA, P.-L- Cabot, Sn-modified carbon-supported Pt nanoparticles synthesized using spontaneous deposition as electrocatalysts for direct alcohol fuel cells. International Journal of Hydrogen Energy 38 (2013) 16418-16426.
[5] M. Amani, M. Kazemeini, M. Hamedanian, H. Pahlavanzadeh, H. Gharibi, Investigation of methanol oxidation on a highly active and stable Pt–Sn electrocatalyst supported on carbon–polyaniline composite for application in a passive direct methanol fuel cell, Materials Research Bulletin 68 (2015) 166-178.
[6] Habibi B, Delnavas N. Pt-CeO2/reduced graphene oxide nanocomposite for the electrooxidation of formic acid and formaldehyde. RCS Advances 2015;5-73639-50.
[7] N.I. Zaaba, K.L.Foo, U.Hashim, S.J.Tan, Wei-Wen Liu, C.H.Voon. Synthesis of Graphene Oxide using Modified Hummers Method: Solvent Influence, Procedia Engineering, 2017:184:469-477.
[8] Medina Ramírez A, Ruiz Camacho B, Villicaña Aguilera M, Galindo Esquivel IR, Ramírez-Mánguela JJ. Effect of different zeolite as Pt supports for methanol oxidation reaction. Appl Surf Sci 2018;456:204-14.

XVIII International Congress
of the Mexican Hydrogen Society

Synthesis of Pt/nanozeolite–graphene oxide composite and its electrochemical evaluation for formic acid electrooxidation

V.K. González Rodríguez[1], A. Medina Ramirez[1,*] L.K. Arellano Ariza[1], B. Ruiz Camacho[1]

[1]Universidad de Guanajuato, Departamento de Ingeniería Química, División de Ciencias Naturales y Exactas. Noria Alta s/n Z.P. 36050, Guanajuato, Guanajuato, Mexico
* Corresponding author: phone number: +55 (01) 473732006 adriana.medina@ugto.mx

ABSTRACT

The properties of the catalyst support in the direct formic acid fuel cells (DFAFC) influence the electrochemical response and the efficiency of the oxidation reactions of the formic acid. Particularly, the surface and structure of the support affect the size and morphology of the active specie and therefore its electrochemical performance. For these reasons in the present work the effect of distribution of the platinum nanoparticles on the nanozeolite-graphene oxide (GO) composite on the electrochemical evaluation was studied. EMC-2–type nanozeolite was synthesized by hydrothermal treatment and then the GO was incorporated to nanozeolite by ultrasound method. The electrocatalyts were obtained by incorporation of platinum to the supports using the ultrasound method. The nanozeolite and composite were characterized by X Ray Difracttion and Transmission Electronic Microscopy. The electrochemical activity of the nanomaterials was performed as electrocatalyst for formic acid electrooxidation in acid media using cyclic voltammetry and choronoamperometry. The results indicate that the EMC-2 nanozeolite was identified as crystalline phase of hexagonal morphology with a size of 20 nm. For nanozeolite-GO composite the nanocrystals of EMC-2 were located onto and between the graphene oxide sheets. The electrochemical behavior of the electrocatalysts evaluated indicated that the structure and dispersion of platinum affect the formic acid electro-oxidation reactions. The pathways of the electrical conductivity of the supports are enhanced by the hydrogen spillover through zeolite channels, the nature of the acid sites and the electrical conductivity of the graphene oxide.

Keywords: nanozeolite; graphene oxide; formic acid; electrooxidation

1. Introduction

The fuel cells are considered as more promising energy-conversion strategies for the sustainable energy development because of their low greenhouse emission compared to technologies which use fossil combustible [1]. Particularly the Direct Formic Acid Fuel Cells (DFAFCs) are characterized by use formic acid that is liquid at room temperature which makes

its storage and transportation safe. Additionally the formic acid is a strong electrolyte which improves the transport of protons to the anode. However the formic acid oxidation efficiency is influence by the catalyst.

Direct formic acid fuel cells that react with platinum (Pt) have dual path mechanism of reaction which are dehydrogenation and dehydration. Dehydrogenation process does not produce carbon monoxide (CO) as intermediate reaction which is poisonous. The dehydrogenation reaction produces carbon dioxide, (CO_2) directly:

$HCOOH \rightarrow CO_2 + 2H+ + 2e-$

The reaction shows the direct oxidation of formic acid to CO_2, at the same time as dehydration producing the poisoning intermediate CO [2]:

$HCOOH + Pt° \rightarrow Pt\text{-}CO + CO + H_2O$ (1)
$Pt° + H_2O \rightarrow Pt\text{-}OH + H^+ e^-$ (2)
$Pt\text{-}CO + Pt\text{-}OH \rightarrow CO_2 + H^+ e^-$ (3)
Total reaction: $HCOOH \rightarrow CO_2 + 2H^+ + 2e^-$ (4)

The Pt supported on carbon exhibits a high catalytic activity nevertheless the poisoning by CO and the degradation of the catalyst-support has triggered the development of Pt supported on carbon-based nanomaterials. These kinds of nanomaterials are more durable, stable and have a higher specific surface area for homogeneous dispersion of platinum [3].
Among carbon-based nanomaterials graphene has attracted broad interests at the energy community due to the promising advantages of high conductivity, mechanical flexibility, adjustable energy levels and long-term stability. [4]. These good characteristics make it a good nanomaterial to be used in fuel cells to be used as electrodes or charge transport materials. Unfortunately graphene is easy to self-aggregate due to interaction between the graphene sheets, this behavior generates a loss of catalytic activity of the support catalysts [5]. For these reasons several researches have been focused on incorporate nanoparticles to minimize or suppress the aggregation enhancing improved properties for different applications.

Nanozeolites have been reported that are efficient for use as electrocatalyst supports such as zeolite Ni-ZSM-5 that has a high surface area, its preparation is easy and low cost [6], the faujasite zeolite with carbon (FAU-C) [7], that improves the catalytic activity of methanol oxidation, the Ni-SOD-CS / CPE zeolite that presents resistance, easy preparation, stable response and very low ohmic resistance [8] among others.

In this work, we proposed the used of one composite of nanozeolite-graphene oxide as support of platinum as alternative electrocatalyst for formic acid oxidation. Pt/ nanozeolite-graphene oxide was electrochemical characterized by cyclic voltammetry and chronoamperometry in acid medium at room temperature.

2. Materials and Methods

2.1 Nanozeolite synthesis

For nanozeolite EMC-2 synthesis the procedure reported by Ng et al [9] was followed. Briefly two solutions were prepared, the alumina precursor was obtained by dissolution of sodium aluminate and sodium hydroxide in deionized water, the molar composition of the solution was $0.0071Al_2O_3$:$0.080Na_2O$:$0.8055H_2O$. A second solution corresponding to silica precursor was prepared by dissolution of colloidal silica (LUDOX 40HS) and sodium hydroxide in deionized water, to obtain a solution of molar composition of 0.0398 SiO_2:$0.0470Na_2O$:$0.75H_2O$. The alumina solution was added drop by drop to silica solution. The gel obtained was transferred to reactor Teflon-lined stainless steel autoclave and submitted to hydrothermal treatment at 30°C for 36 h. Afterwards the product was recovered by centrifugation and washed with deionized water. The solid was dried at 60°C for 12 h.

2.2 Composite nanozeolite-graphene oxide (NZ-OG)

For the composite synthesis commercial graphene oxide (Sigmaaldrich) was used. The preparation was according to Kathamian et al [10]. One hundred and twenty five milligrams of graphene oxide were added to 15 mL of ethanol, the suspension was sonicated for 3 h. Then the nanozeolite (0.125 g) was added, the slurry was keeping under stirring. Subsequently the temperature was increased to evaporate the solvent. The solid was recovered and dried at 60°C for 12 h.

2.3 Preparation of the electrocatalyst Pt/nanozeolite-graphene oxide

The Pt nanoparticles were obtained by reduction method as reported previously [11]. Briefly, fifty milliliters of 1 mM solution of platinum (H_2PtCl_6) were mixed with 60 mL of isopropyl alcohol as reducing agent. After that, the Composite nanozeolite-graphene oxide was mixed with the platinum nanoparticles in solution to obtain a metal load of 10wt.% Pt. This alcoholic solution was maintained under sonication in an ultrasonic bath (42 kHz) for 4h. The pH and temperature of the system were monitored each hour, indicating that temperature increased from 25 to 60°C and a pH of 6.9 was maintained. Finally, the solvent was removed by evaporation in an oven at 150°C for 4 h.

2.4 Physicochemical and electrochemical evaluation

The nanozeolite and composite were characterized by XRD using a PANalytical Model Empyrean difractometer with a CuK α (λ=1.5604Å) radiation source in the 7-60° 2θ range. The morphology was examined by TEM using a JEOL 1010 field emission microscope.

The electrochemical evaluation was performed by Cyclic voltammetry (CV) in acid media and methanol and by Chronoamperometry (CA) in a conventional three electrode cell. For the

preparation for the working electrode was necessary dissolve electrocatalyst into the ink. The ink was prepared using 6 mg of the electrocatalyst, 500 µL Isopropoyl alcohol and 50L of Nafion®. The solution was put into ultrasound Elmasonic P at 37 KHz for two hours at room temperature. After that, 11µL of the ink were put on a vitreous carbon electrode (geometrical surface area 0.196 cm^2). The reference electrode was a Saturated Calomel Electrode (SCE) and the counter electrode was a Pt wire.
The formic acid oxidation test was performed by employing as electrolyte: 0.5 M H_2SO_4 plus 0.5 M HCOOH. The CV curves were measured at a scanning rate of 50 mV s^{-1} in a nitrogen atmosphere; the potential applied was between 0.05 and 1.2 V/NHE; 20 cycles were necessary to stabilize the system. To evaluate the lifetime performance of catalysts, the CA test was carried out under constant potentials of 0.65 V/NHE during 3000 s.

3. Results and Discussion

3.1 Physcochemical characterization

In Figure 1(a) are shown the XRD patterns of the nanozeolite and composite. It can be observed that the nanozeolite exhibits the characteristic peaks corresponding to EMT zeolitic phase which is a polymorph of faujasite. This zeolite presents a hexagonal framework with tridimensional channels system. In case of the composite pattern is observed that the peaks intensity of the zeolite phase are diminished, moreover new peaks are detected which corresponding to presence carbon-base nanomaterial. According to literature [12] the peaks associated to graphite and oxidation grade of graphene are located at 26.3°, particularly the decreasing in the intensity indicate a higher oxidation grade, and a peak close to 10° is associated to oxidation when this peak is increasing the oxidation grade is favored. Additionally a peak of low intensity is detected at 43.3° of 2θ which corresponding to graphene oxide assigned to the (100) plane [13]. Therefore in the composite evaluated the graphene oxide is mainly constituted by graphitic domains rather than oxidized domains.
By TEM were analyzed the morphology and distribution of the zeolite nanoparticles and graphene oxide (Fig. 1b) where were observed the characteristic sheets of graphene oxide while the nanozeolite particles were distributed between the graphene oxide layers. It is noticeable some regions with high density of nanozeolite particles.

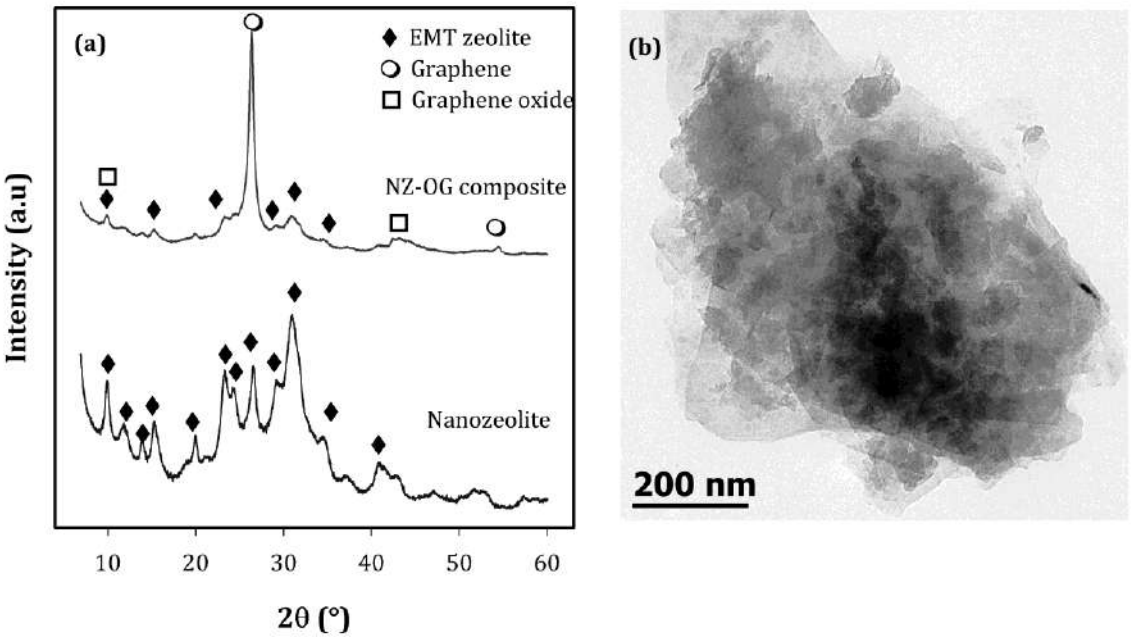

Fig. 1 (a) XRD patterns of nanozeolite EMC-2 and EMC-2-OG composite; (b) TEM micrograph of the EMC-2-OG composite.

3.2 Electrochemical Characterization

In Figure 2(a) depicts the cyclic voltammogram of Pt/EMC-2-OG in acid medium. The curves clearly reveal the characteristic of platinum nanoparticles: a) the hydrogen adsorption and desorption are located around between 0.05 and 0.3 V and b) the platinum oxide region of oxidation and reduction is observed at 0.75 V.

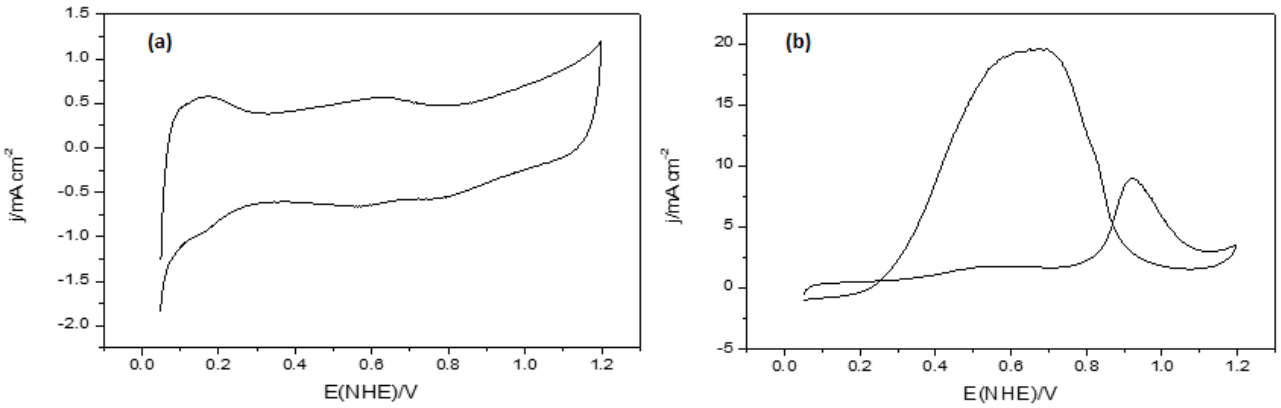

Fig. 2 CV of Pt/EMC-2-OG at scan rate of 50 mV/s. (a) CV of 0.5 M H_2SO_4. (b) CV of 0.5 M formic acid plus 0.5 M H_2SO_4

The electrocatalytic activity of the Pt/EMC-2-OG toward the oxidation of formic acid was evaluated by cyclic voltammetry in Fig. 2(b). Results show Pt/EMC-2-OG exhibits a small peak almost negligible around 0.6 V, which can be attributed to the formic acid oxidation via the dehydrogenation pathway. The second anodic peak at 0.95 V correspond to oxidation of (CO_{ads}) generated by the dehydration of formic acid [14]. Finally, during the backward scan, some CO remain adsorbed until they are oxidized, producing the highest current peak at 0.6 V. This anodic peak in the reverse scan is attributed to the removal of the incompletely oxidized carbonaceous species formed in the forward scan [15]. The large difference in the peaks in 0.7V and 0.96 V indicates that the oxidation of formic acid is not efficient.

The long-term activity and durability of electrocatalyst was evaluated using the chronoamperometry technique. Figure 3 shows the typical chronoamperometric curve of 0.5 M formic acid in 0.5 M H_2SO_4 on the Pt/EMC-2-OG electrocatalyst under a constant potential of 0.65 V. The material synthesized exhibit a significant stability toward formic acid.

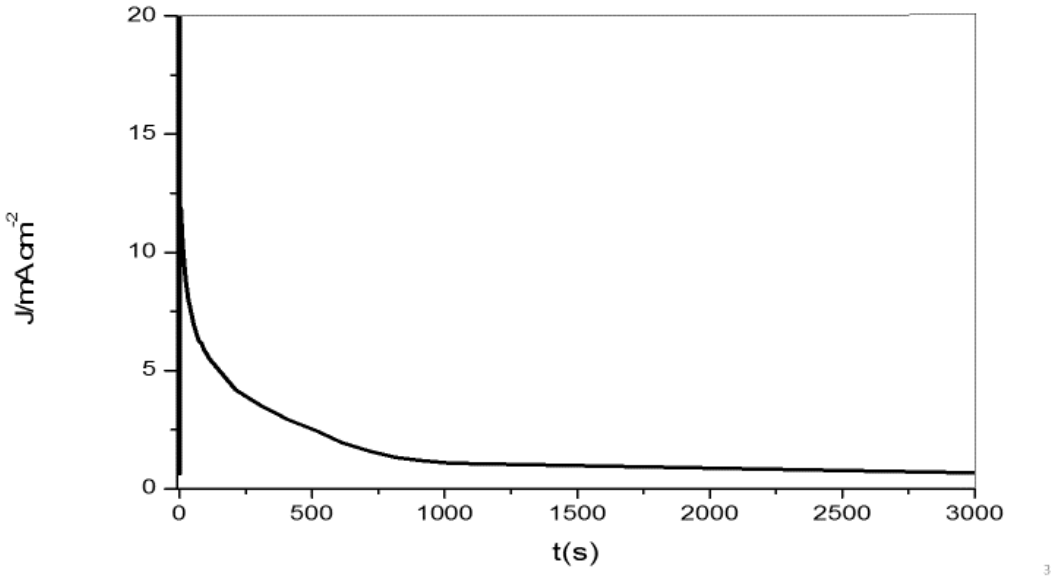

Fig. 3 Chronoamperometric curve of 0.5 M formic acid electrooxidation in 0.5 M H_2SO_4 at the Pt/EMC-2-OG

4. Conclusion

In the present work the nanozeolite –graphene oxide composite was synthesized by ultrasound method and it was evaluated as support for acid formic electrooxidation. According to TEM the zeolite nanocrystals were located onto and between the graphene oxide sheets. The voltametric response of the platinum catalyst supported on the composite (Pt/EMC2-OG) shown a low oxidation efficiency for carbonaceous species which allow to infer that the oxidation take place mainly by dehydration pathway. On the other hand the chronoamperometric evaluation indicated that the Pt/EMC-2-OG electrocatalyst exhibited a structure stable for formic acid.

Acknowledgements

The authors are grateful for a University of Guanajuato through the DAIP office for providing financial support for the present research.

References

[1] Wang S, Jiang SP, Prospects of fuel cell technologies, Natl Sci Rev, 2017, 4(2), 163-166.

[2] Aslam N, Masdar M, Kamarudin S, Daud W, Overview on Direct Formic Acid Fuel Cells (DFAFCs) as an Energy Sourses, APCBEE Procedia, 2012, 33-39.
[3] Julkapli NM, Bagheri S, Graphene supported heterogeneous catalysts: An overview, Int. J. Hydrogen Energy, 2015, 40, 948-979.
[4] Xuemei F, Limin X, Jiaxin L, Xuemei S, Huishen P, Flexible solar cells based on carbon nanomaterials, Carbon, 2018.
[5] Lili C, Tao P, Ying L, Xingquan H. Layer-by-layer construction of graphene/cobalt phthalocyanine composite film on activated GCE for application as a nitrite sensor. Electrochim Acta 2013;88:559-564.
[6] Rahimnejad M, Hassaninijad-Darzi S, Organic template-free synthesis of Ni-ZSM-5 nanozeolite: a novel catalyst for formaldehyde electrooxidation onto modified Ni-ZSM-5/CPE, Bio-Inorganic Hybrid Nanomaterials (2015); 4, 141-153.
[7] Medina A, Villicaña M, López C, Ruiz B, Synthesis of FAU zeolite-C composite as catalyst support for methanol electro-oxidation, Hydrogen Energy (2017); 42, 30291-30300.
[8] Rahimnejad M, Hassaninijad-Darzi S, Masoomeh S, Preparation of template-free sodalite nanozeolite– chitosan-modified carbon paste electrode for electrocatalytic oxidation of ethanol, Iranian Chemical Society; 12, 413-425.
[9] Ng E-P, Chateigner D, Bein T, Valtchev V, Mintova S, Capturing Ultrasmall EMT Zeolite from Template-Free Systems, Science, 2012, 35,70-73.
[10] Kathamian M, Khodakarampoor N, Saket-Oskoui M, Efficient removal of arsenic using graphene-zeolite based composites, Journal of Colloid and Interface Science 498 (2017) 433–441.
[11] Medina A, Ruiz B, Villicaña M, Galindo Esquivel IR, Ramírez- Minguela JJ. Effect of different zeolite as Pt supports for methanol oxidation reaction. Appl Surf Sci 2018;456:204-14.
[12] Krishnamoorthy K, Veerapandian M, Yun K, Kim S-J. The chemical and structural analysis of graphene oxide with different degrees of oxidation, Carbon,2013, 53, 38-49.
[13] Guerrero-Contreras J, Caballero-Briones F, Graphene oxide powders with different oxidation degree, prepared by synthesis variations of the Hummers method, Materials Chemistry and Physics 153 (2015) 209-220.
[14] Timperaman L, Gago AS, Alonso-Vante N. Oxygen reduction reaction increased tolerance and fuel cell performanc of Pt and RuxSey onto oxide-carbon composites. J. Power Sources 2011;196:4290-97.
[15] Habibi B, Delnavas N. Pt-CeO2/reduced graphene oxide nanocomposite for the electrooxidation of fromic acod and formalheyde. RCS Advances 2015;5-73639-50.

XVIII International Congress
of the Mexican Hydrogen Society

Photocatalytic behaviour of TiO_2, ZnO and CuO modified SBA-15 in hydrogen production

J. A. Colín-Luna[1*], J. C. Espinoza Tapia[1], A. K. Medina-Mendoza[2], E. Barrera-Calva[3], J.L. Contreras-Larios[1], I. Hernández-Pérez[3], J. García-Martínez[1]

[1]UAM-Azc, Departamento de Energía, [2]Departamento de Ciencias Básicas, Av. San Pablo 180, Col. Reynosa-Tamaulipas, 02200, CDMX, México.
[3]Universidad Autónoma Metropolitana Iztapalapa, Departamento de Química, Av. San Rafael Atlixco 186, Col. Vicentina, CP. 09340, CDMX, México.
* Corresponding author: 015553189044 and jacl@azc.uam.mx

ABSTRACT

Photocatalytic water splitting is one of the cleanest and economic methods employed to produce hydrogen. In the literature is have reported TiO_2 can be used as photocatalysts in the photodegradation of many organic molecules as colorants. Although semiconductors show limitations due to the recombination of the electron-hole pair, the photocatalysts also have high bandgap and require the use of a source luminescent within the UV region. For this reason, it is important to implement materials with photocatalytic properties that improve efficiency in a heterogeneous photocatalysis process, suppressing the limitations in the production of hydrogen. Some recent researches have shown that other metal oxides such as ZnO or CuO, also present excellent properties as photocatalyst materials

Keywords: hydrogen; alternative energies; SBA-15, nanoparticles; water splitting

1. Introduction

The production of H_2 using photocatalysis where the cost of energy and the emissions of pollutants are reduced compared to the catalytic reformation or electrolysis of water, has awakened the interest of the scientific community for the substitution of conventional energy sources such as that come from oil [1-5]. The photocatalyst commonly used is TiO_2, it is stable, non-toxic, environmentally friendly, cheap and can be synthesized at low temperatures. However, its wide band gap energy (3.2 eV) limits its use to the UV region so it could not be used with sunlight [2,3]. Therefore, despite of the extensive efforts made by the scientific community, some complications still need to be overcome for the full use of this technology. Perhaps one of the most important challenges is that catalysts sensitive to sunlight have not yet been developed, which would favor the replacement of UV radiation, further decreasing the cost of H_2 production [3-5].

The other challenge to be overcome is the backward reaction, in other words, the conversion of hydrogen and oxygen to water, which is carried out quickly, decreasing the production of fuel. Finally, the rapid recombination of the electron-hole photogenerated pair decreases the photocatalytic dissociation of water [3]. Overcoming these deficiencies in order to obtain a cheap and sustainable fuel represents an academic and scientific challenge. However, many advances have been made to meet these challenges. On the one hand, TiO_2 photocatalysts have been synthesized with particles of the size of the order of nanometers, apparently small particles reduce the hollow-electron recombination because the transfer distance is shorter [6-9]. On the other hand, the presence of organic molecules in the water, to become oxidized by the holes in the valence band, would donate electrons, while the remaining electrons in the conduction band can strongly reduce the protons to hydrogen molecules. It is evident that in this process the organic molecules, also known as sacrificial molecules or hole scavenger, are degraded as in the treatment of contaminated water, so that the elimination of contaminating molecules and the production of hydrogen can be carried out simultaneously , making the photocatalytic process more advantageous [10,11]. Another way to develop more efficient catalysts in the photolysis of water to produce hydrogen, is the use of mesostructured materials type SBA-15 because they have a high specific area (> 600 m^2/g), a large pore diameter (ca. 3.0 nm) and simple incorporating of cations in its silica matrix [12-17]. Additionally, the incorporation of the Ti to the silica matrix can favor the dispersion of the Ti as well as to supply the electrons that maintain the formation of the electron-hole pair and avoid the recombination of hydrogen and oxygen [13]. The confining of Ti particles to the well-ordered pores of the SBA-15 would help the distribution of pores of narrow sizes (<10 nm) by increasing the photocatalytic properties.
Therefore, in this work, is proposed to use semiconductors of TiO_2, ZnO, and CuO which improve their photocatalytic properties when incorporated into a mesoporous SBA-15 materials. By increasing the number of possible reaction sites, an improvement in the photocatalytic production of hydrogen will be obtained with the synthesized materials (supported); this in comparison with the metal oxides outside the support in the presence of a sacrificial molecule (glycerol) [18,19].

2. Materials and Methods

2.1 Synthesis of SBA-15 and chemical grafting

In a typical synthesis, 16 g of Pluronic were added to 474mL of 2M HCl solution (previously prepared from the HCl reactant at 37% vol., Sigma-Aldrich) and 26 mL of deionized water. After stirring for a few hours, a clear solution was obtained. The resulting white suspension was transferred to a Teflon lined stainless steel autoclave and heated to 310 K for 1 h. Then, 32 g of TEOS (tetraethylorthosilicate) solution was quickly added to the surfactant solution and stirred for 24 h at 310 K and after for 72h at 370 K. The solid product was recovered by filtration, washed several times with water and dried overnight at 370 K. Finally, the material was heated in air at a heating rate of 0.8 K/min to 390 K for 2 h and after 0.9 /min at 820 K maintained at this temperature for 6 h. Incorporation of Ti, Zn and Cu in this pure silica SBA-15 material was carried out by chemical grafting method to a molar ratio SiO_2/M^+O^- = 0.5,1 and 2 using as metal sources titanium isopropoxide, zinc acetate and copper acetate, respectively. The metal salts were dissolved in absolute alcohol and were added to the pure silica, keeping it in agitation for 8 h at 298 K. The product was recovered by filtration, washed with alcohol, dried overnight at 370 K and calcined a

820 K, using the same heating speeds as pure silica. The materials thus synthesized were denominated as SBAY(X), where Y is Ti, Zn and Cu and X the ratio SiO_2/M^+O^- of 0.5,1 and 2

2.2 Characterization

2.2.1 Structural analysis

XRD patterns were recorded on DRX Phillips Xpert, coupled to an X-ray generating tube with a copper radiation filament (λ = 0.15409 nm, with Cu anode), the equipment worked with a scanning speed of 0.02 º/s, operated at 45 kV and 40 mA; a range of 0.5 to 3.5 ° and within the range of 10 to 80 in the 2θ domain to obtain the porous ordering and the structural and crystallographic information of the metal oxides (Ti, Zn, Cu) incorporated in the mesoporous structure of SBA-15. Acccording to each case; the crystal size was also determined using the expression of Debye – Scherrer (ecn. 1):

$$\mathcal{D}_p = \frac{K\lambda}{\beta \cos\theta} \qquad (1)$$

where D_p corresponds to crystal particle size, θ is the diffraction angle, λ is the wave radiation length, K is a correction factor equal to 0.9, and finally the term β corresponds to the average width of the peak to median height [20].

2.2.2 Physisorption analysis

The textural properties of the samples were analyzed by recording N_2 adsorption isotherms at 77 K, using a Micromeritics TriStar II. Before gas sorption analysis, the powder was pretreated for 16 h at 410 K under vacuum (~10^{-6} kPa). The specific surface area was determined using the Brunauer–Emmett–Teller (BET) model. Pore size distribution was estimated by applying BJH method to the desorption branch of isotherms. Finally, the pore volume was calculated at P/P_0 near to 1.

2.2.3 UV-vis spectroscopy

The band gap energy (*Eg*) of each sample was calculated by converting percent reflectance spectrum attained from an Frontier UV Visible Spectrophotometer to Perkin-Elmer, which was equipped with a diffuse reflectance accessory. A given amount of material powder was uniformly pressed in the tablet and placed in the sample holder on integrated sphere for the reflectance measurements. The reflectance data was converted to the absorption coefficient values according to the Kubelka–Munk .

2.2.4 Raman Spectroscopy

The phase composition of the samples was also determined by Raman spectroscopy through a inVia Qontor brand Renishaw using a He-Ne laser (532 nm) as the light source, 20 mW to 50% was used, the study process was carried out with 5 accumulations of 10 s/accum. to reduce the noise.

2.2.5 Scanning Electron Microscopy

For morphological characterization of the samples, top and cross-sectional views were recorded by scanning electron microscopy (SEM) using a JEOL MEB JSM-6701F with an electron beam of 15 kV, a secondary electron detector (SEI) and a X-ray energy dispersion detector (EDS) to determine the elemental chemical analysis of the samples.

2.3 Photocatalytic evaluation

Photocatalytic hydrogen production test were carried out in a 500 mL double wall quartz vessel equipped with a commercial lamp of Philips as photon source (10 W and λ = 365 nm) located in the center of the vessel and thermocouple in the sidewise of the vessel. In a typical test the reactor vessel was put inside a reflector box equipped with a magnetic stirrer to mix 275 mL of a glycerol (10% vol.) –water solution, 0.25 g of photocatalyst and 0.25 mL of hydrogen peroxide as a radical initiating agent. Prior to irradiation, reactor was purged by N_2 to eliminate air during activity test for not affecting the process. Two pH values reaction medium were evaluated (pH= 7 y 12.5) by means of a solution 1 M of NaOH. The reactions were carried out for 3 h irradiation. The scavenger molecule was followed during 3 h of irradiation by means of UV-vis spectroscopy to maxim wave length. The gas product was analyzed using a flame test.

3. Results and Discussion

3.1 Structural and textural analysis

Figure 1 shows the diffractograms at low angle of the original SBA-15 and those modified with the incorporation of Ti, Zn and Cu. In these images the corresponding basal reflections at 0.9, 1.5 and 1.8 of 2θ correspond to planes (100), (110) and (200) characteristics to mesoporous materials with mesoporous arrange. As can be seen to increase the ratio SiO_2/M^+O^- of 0.5,1 and 2 the peaks of the characteristic planes are still present but a lateral displacement in the position 2θ is shown due to the interactions (microtensions) generated by the incorporation of the metal in the silica structure.

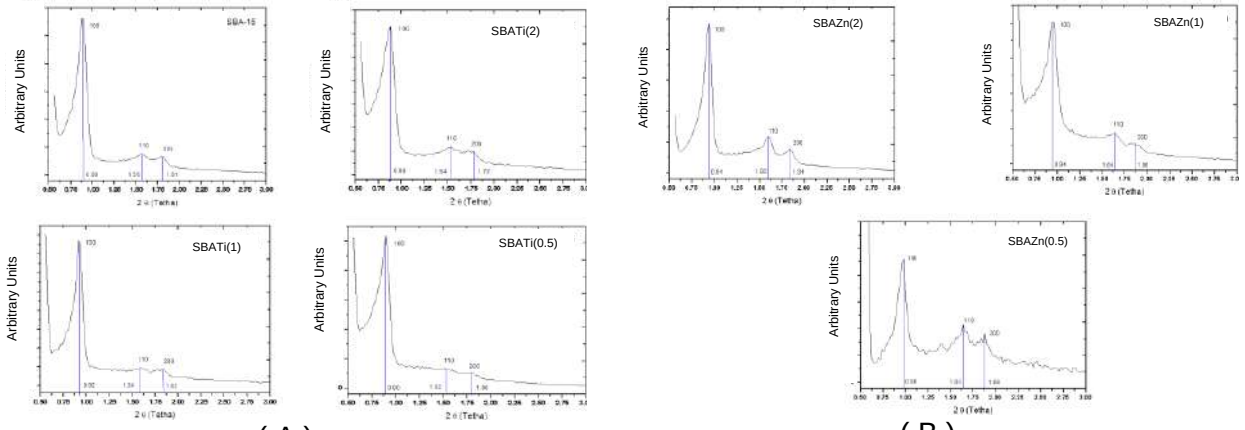

(A) (B)

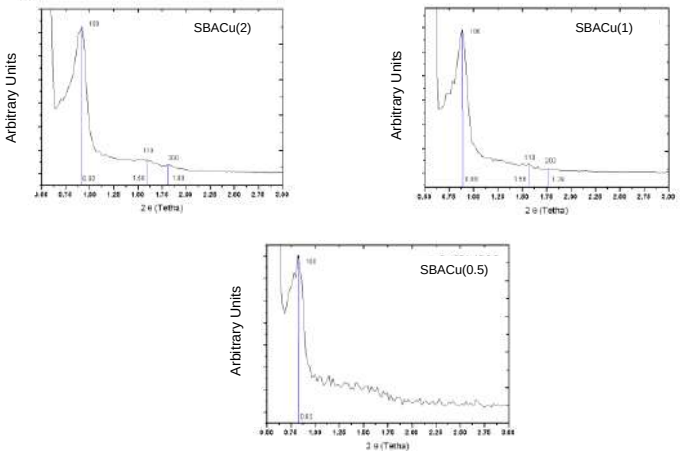

(C)

Figure 1. Patterns diffractions of modified SBA with cations A) TiO_2, B) ZnO_2 and C) CuO_2

The physisorption analyses shown that the isotherms of the SBA - 15 presents a typical behavior of Type IV according to IUPAC with hysteresis loops of the H1 type characteristic of cylindrical pores. For the case of those modified with Ti, Zn and Cu, changes in the shape of the isotherm were observed, a consequence of the type of the cation and the SiO_2/M^+O^- ratio (no shown here). Table 1 shows the surface area and pore diameter of the supports. Such as expected a decreased was observed in surface area to introduce de cation. A drastic decrease was observed in the SBAZn(X) compared with modified SBA with Ti and Zn.

Table 1. Particle sizes, textural analyses and band gap energy of the photocatalysts.

SAMPLE	Particle size (nm)	Surface Area (m^2/g)	Pore diameter (nm)	Band gap energy (eV)
SBA	-	614.2	4.0	6.1
SBATi(2)	34.5	492.3	3.4	3.3
SBATi(1)	51.9	335.0	2.8	3.0
SBATi(0.5)	60.2	297.4	2.3	2.9
TiO_2	58.9	12.1	2.5	3.2
SBAZn(2)	35.4	336.4	3.6	3.1
SBAZn(1)	40.6	217.1	3.5	3.1
SBAZn(0.5)	42.4	136.3	3.0	2.9
ZnO	53.2	1.6	1.8	3.2
SBACu(2)	30.2	469.3	3.6	1.4
SBACu(1)	32.6	336.6	3.2	1.4
SBACu(0.5)	35.3	240.8	2.9	1.4
CuO	39.1	0.6	1.5	1.5

3.2 UVDRS of SBA modified Ti, Cu and Zn.

Figure 2 show the UVDRS spectra of the semiconductors. As was expected SBA-15 presents an *Eg* higher than 6 eV, which places it outside the range of a material (<4 eV); while the reference

TiO_2 has an *Eg* of 3.2 eV (typical of the anatase phase). Table 1 show that photocatalysts SBACu(X) have the least band gap energy (ca. 1.4 eV).

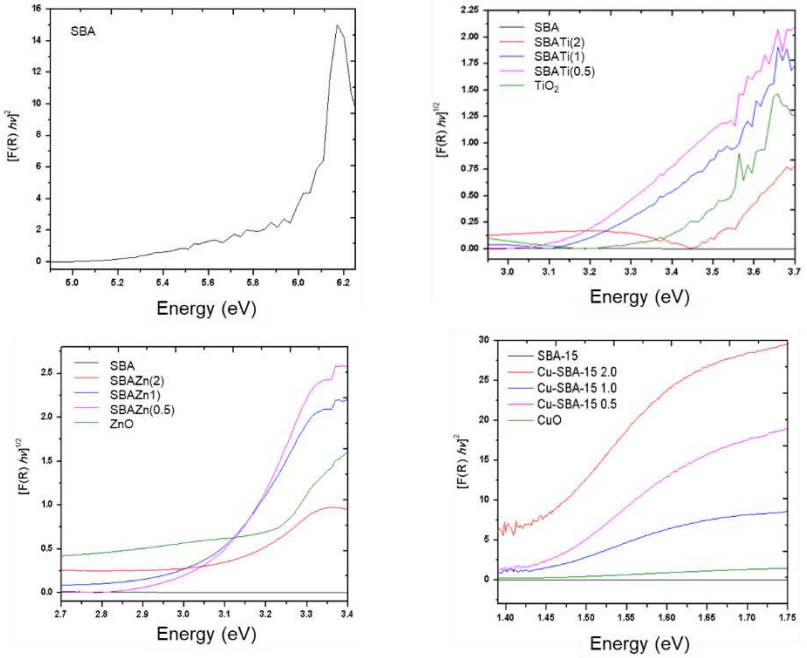

Figure 2. Band gap energy of the semiconductors employed

3.3 IR spectra of SBA modified Ti, Cu and Zn.

The results obtained (not shown here) confirm the presence of the characteristic interactions of mesoporous material type SBA, such as the stretching of the Si - OH molecules (silanol group) around 3448 cm^{-1}, in this region the bands are also located of the vibrations of extension of the hydrogens of the group O - H. In the same way the bands located around the 1636 cm^{-1} are response of the splitting vibrations of the silanol group, signals that overlap with the bands of vibration of stretching of the C - O - C bonds. Around 1230 cm^{-1} and 1096 cm^{-1} we find the signs of symmetrical and asymmetric vibration of characteristic extension of Si - O - Si; also in this region we find the vibration signals of Si - O - C, C - O - C and Si - C overlapped. Also the vibrations that are close to 956 cm^{-1} refer to the stretching vibrations of the free silanol group in the amorphous surface of the solid and overlapped are the bands of the stretching vibrations; the band located at 799 cm^{-1} and up to 790 cm^{-1} corresponds to the signal of symmetrical vibrations of the structure formed by Si-O-Si groups; and finally, between 480 cm^{-1} at 455 cm^{-1}, are associated to signals of the flexion vibrations of the Si-O-Si group.

3.4 Raman spectra of SBA modified Ti, Cu and Zn.

Figure 4 show the signals at 485, 538, 790, 810 and 977 cm^{-1}, the spectrum observed is similar to a pure silica with the exception of the signal at 977 cm^{-1} which is relevant for a mesoporous system; the signals at 790 and 810 cm^{-1} correspond to the vibration of the siloxane groups (R_1 -

Si - R_2), while the ring vibrations of siloxane groups (R - Si - R) and finally the signal corresponding to the 977 cm^{-1} is attributed to the surface vibrations of the silanol groups (Si-OH), characteristic of the surface of an SBA-15. With this technique it is possible to identify the different crystalline structures of TiO_2, the anatase phase for example is identified by maintaining a tetragonal space centered on faces belonging to the space group D4h (I41 / *amd*) maintains six active vibrational modes for raman located between the region of 100 - 650 cm^{-1}, which are located in a monocrystal material at 144 (Eg), 197 (Eg), 399 (B1g), 513 (A1g), 519 (B1g) and 639 (Eg) cm^{-1}, while the rutile structure that maintains a simple tetragonal structure and belongs to the group D4h (P42 / mnm), for this compound only four normal vibration modes active for raman are counted which are 143 (B1g), 447 (Eg), 612 (A1g) and 826 (B2g) cm^{-1}. The samples of ZnO has various crystalline structures, the wurtzite (hexagonal) and the zinc blende (cubic). For the case of the wurtzite structure belongs to the space group P63mc, so the ZnO has four characteristic signals that are generated by the corresponding vibrational modes that are 330 (2E2), 379 (A1), 410 (E1) and 439 (E2)) cm^{-1} for the case of a bulk; but in the case of ZnO nanocrystals, due to phenomena of quantum confinement the frequency of the phonon in the vibrational modes is stimulated, which generates the formation of three characteristic signals that are 330 (E2), 436 (A1) and 582 (E1) cm^{-1}, therefore the characteristic bands are located between the interval of 300 - 600 cm^{-1} for the wurtzite phase and depend on the crystal size. For the zinc-blended structure there are three typical vibration modes for raman that are at 410 (E1), 480 (E2) and 840 (A1) cm-1 for bulk materials, so for those structures whose analysis results are in the range between 400 - 850 cm^{-1} will be considered a zinc blended

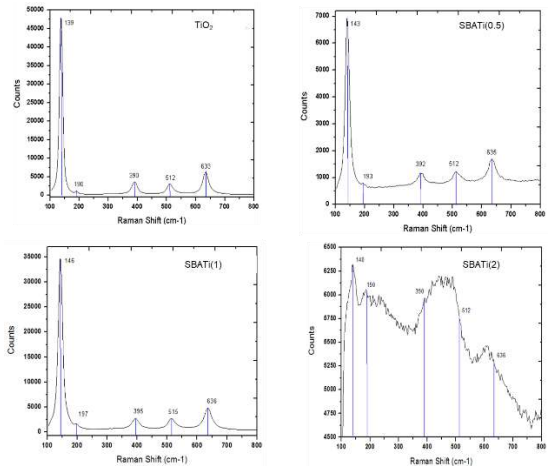

(A)

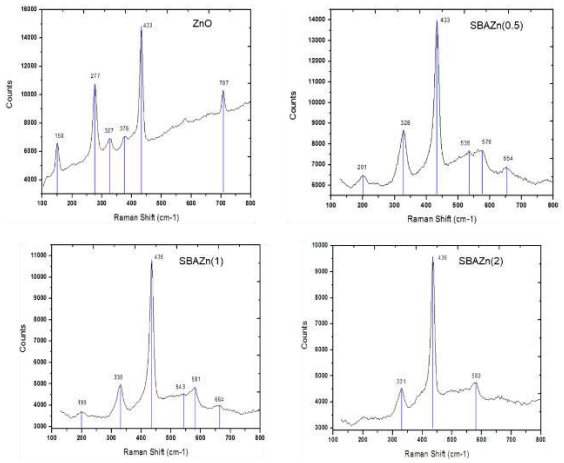

(B)

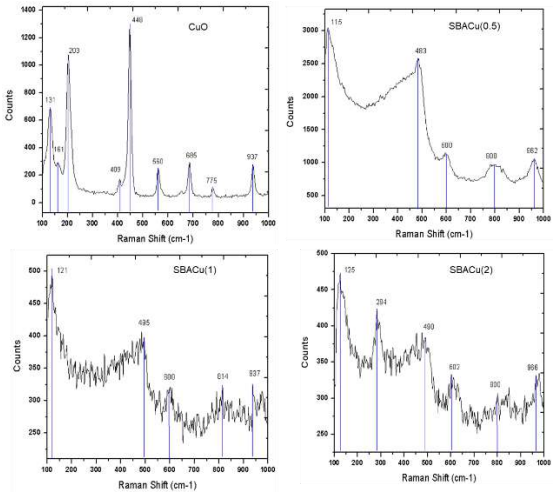

(C)

Figure 3. Raman spectra of the semiconductors employed A) TiO2, B) ZnO and C) CuO.

3.5 SEM analysis of the modified SBA with Ti, Zn and Cu

Figure 4, show the morphology of the original SBA and the cations incorporated. According with this images all the samples show an amorphous morphology and agglomerates of the metal particles were not observed. Likely this is due to the metal particles being housed in the mesoporos of the SBA.

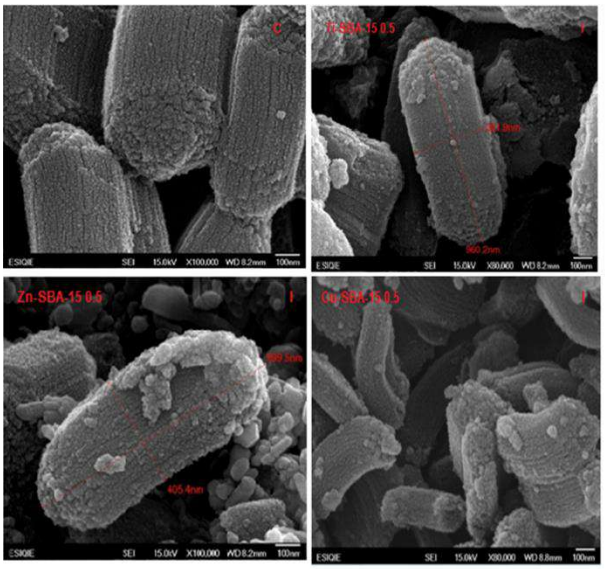

Figure 4. SEM micrographs of modify SBA with TiO_2, ZnO and CuO.

3.6 Photocatalytic evaluation

Finally, photocataytic evaluation was followed by means to the maximum signal of the UV band corresponding to glycerol. In particular, the SBACu photocatalyst (5) showed widened and more pronounced bands than those found for those of SBAZn (X) and SBATi (X) inclusive. According to the results obtained by the characterization of UVDRS, textural and particles sizes, it is probable that this photocatalyst presents a greater resistance to the recombination electron hollow.

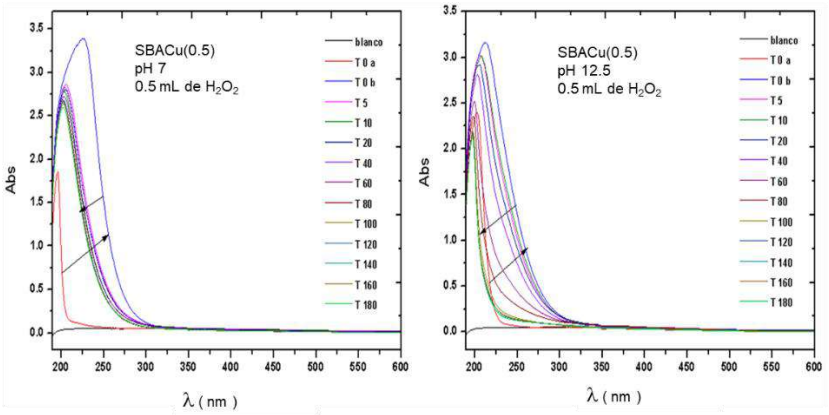

Figure 5. UV spectra of glycerol photodegradation of SBACu(0.5).

4. Conclusion

It was verified through the development of evaluations that the molecule used (glycerol) plays an important role in obtaining hydrogen; and thanks to this compound it is possible to obtain different products. For the semiconductors of Ti and Zn, a total mineralization of the initial molecule is not achieved, which results in the formation of derivative by-products and although in the formation of these derivative products there is the liberation of hydrogen. For the particular case of Cu materials, the total mineralization of the compound was achieved in an alkaline medium and the three different materials and only in one of the cases was it obtained in a neutral medium in less than 120 min.

Acknowledgements

J. C. Espinoza Tapia thanks CONACYT for the scholarship awarded for graduate studies.

References

[1] Holladay J.D., Hu J., D.L. King, Y. Wang. An overview of hydrogen production technologies. Catalysis Today 2009; 139:244–260.
[2] Dincer I.. Green methods for hydrogen production. Int. J. of Hydrogen Energy 2012; 37: 1954-1971.
[3] Ni M., Leung M.K.H., Leung D.Y.C., Sumathy K. A review and recent developments in photocatalytic water-splitting using TiO2 for hydrogen production. Ren. and Sust. Energy Reviews 2007; 11: 401–425.
[4] Chen X., Shen S., L. Guo, Mao S.S. Semiconductor-based Photocatalytic Hydrogen Generation. Chem. Rev. 2010;110: 6503–6570.

[5] Lopez Ortiz A., Melendez- Zaragoza M.J., Collins-Martínez V. Hydrogen production research in Mexico: A review. Int. J. of Hydrogen Energy 2016; 41: 23363 – 23379.
[6] Subramanian V., Wolf E. E., Kamat P. V., Catalysis with TiO2/Gold Nanocomposites. Effect of Metal Particle Size on the Fermi Level Equilibration, J. Am. Chem. Soc. 2004; 126: 4943-4950.
[7] Zhu J., Zäch M., Nanostructured materials for photocatalytic hydrogen production, Current Opinion in Colloid & Interface Science 2009;14: 260–269.
[8] Jiang Ch., Lee K. Y., Parlett Ch. M.A., Bayazit M. K.,. Lau Ch. Ch, Ruana Q., Moniz S. J.A., Lee A.F., Tanga J., Size-controlled TiO_2 nanoparticles on porous hosts for enhanced photocatalytic hydrogen production, Applied Catalysis A: General 2016; 521: 133–139.
[9] Liu Y., Li Z., Green M., Just M., Li Y., Chen X., Titanium dioxide nanomaterials for photocatalysis, J. Phys. D: Appl. Phys. 2017; 50:193003 (15pp)
[10] Patsoura A., Kondarides D. I., Verykios X. E., Photocatalytic degradation of organic pollutants with simultaneous production of hydrogen, Catalysis Today 2007;124:94–102.
[11] Jing D., Guo L., Zhao L., Zhang X., Liu H., Li M., Shen S., Liu G., Hu X., Zhang X., Zhang K., Ma L., Guo P., Efficient solar hydrogen production by photocatalytic water splitting: From fundamental study to pilot demonstration, Inter. National J of Hydrogen Energy 2010; 35: 7087 – 7097.
[12] Guimaraes Sanches S., Huertas Flores J., Pais da Silva M. I., Ti dispersion on SBA-15 porous host to enhance photocatalytic hydrogen production, Journal of Molecular Structure 2018;1170:9-17.
[13] Zhuang Y., Song H.-Y., Li G., Xu Y.-J., Ti-HMS as a single-site photocatalyst for the gas-phase degradation of benzene, Mater. Lett. 2010; 64: 2491-2493.
[14] López-Muñoz M.-J., Van Grieken R., Aguado J., Marugan J., Role of the support on the activity of silica-supported TiO2 photocatalysts: structure of the TiO_2/SBA-15 photocatalysts, Catal. Today 2005;101: 307-314.
[15] Jun S., Joo S.H., Ryoo R., Kruk M., Jaroniec M.,. Liu Z, Ohsuna T., Terasaki O., Synthesis of new, nanoporous carbon with hexagonally ordered mesostructure, J. Am. Chem. Soc. 2000;122: 10712-10713.
[16] Salameh C.,. Nogier J.-P, Launay F., Boutros M., Dispersion of colloidal TiO_2 nanoparticles on mesoporous materials targeting photocatalysis applications, Catal. Today 2015; 257: 35-40.
[17] Busuioc A.M., Meynen V., Beyers E., Mertens M., Cool P., Bilba N., Vansant E. F. Structural features and photocatalytic behaviour of titania deposited within the pores of SBA-15, Applied Catalysis A: General 2006;312: 153–164.
[18] Amorós-Pérez A., Cano-Casanova L., Lillo-Ródenas M.A., Román-Martínez M. C., Cu/TiO_2 photocatalysts for the conversion of acetic acid into biogás and hydrogen, Catalysis Today 2017; 287: 78–84.
[19] Panagiotopoulou P., Karamerou E. E., Kondarides D. I., Kinetics and mechanism of glycerol photo-oxidation and photo-reforming reactions in aqueous TiO_2 and Pt/TiO_2 suspensions, Catalysis Today 2013;209: 91–98.
[20] Hammond C., The Basics of Crystallography and Diffraction, International Union of Crystallography, 3rd Edition, 2009,Oxford University Press.

XVIII International Congress
of the Mexican Hydrogen Society

Green synthesis of Ni-Co nanoparticles for their use as anodic catalyst in urea fuel cells

Beatriz Ivone Rojas-de Soto[1], Marisol Galván-Valencia[1], Ricardo A. Escalona-Villalpando[2], Sergio M. Durón-Torres[1,*]

[1]Autonomous University of Zacatecas, Zacatecas, México, 98160

[2] Center for Research and Technological Development in Electrochemistry, Pedro Escobedo, Sanfandila, Santiago de Querétaro, México, 76703

* Corresponding author: 492 106 29 33, serduro@yahoo.com

ABSTRACT

Nickel metallic nanoparticles exhibit electrochemical activity to oxidize biological substances such as urea and producing electrical energy in fuel cells (FC). The FC are used as an alternative in energy production with an associated decrease in environmental pollution. Additional advantages are achieved, if the synthesis of catalytic materials is obtained by "green chemistry" by exploiting the reducing properties of plant extracts to generate metallic nanoparticles from inorganic precursors.

In this study are presented the results of the electrochemical evaluation of Ni-Co bimetallic nanoparticles synthesized from the use of *Punica granatum* and *Eucalyptus globulus* reducing extracts that avoids the utilization of inorganic harmful compounds such as NaBH4. The synthesis was based on the reduction of a $NiCl_2.6H_2O$ / $CoCl_2.6H_2O$ solution by using aqueous extracts of the plants. The synthesis consisted in the addition of the extract to a 1% $NiCl_2$-$CoCl_2$ solution at an alkaline pH. Glassy carbon electrodes modified with catalytic inks were used to evaluate the presence of the Ni redox pair in 1M KOH solution by cyclic voltammetry (VC). Using the same technique the urea oxidation capacity was determined in a 0.33M / KOH 1M solution.

It was found that the reduced particles showed catalytic activity for the urea oxidation reaction (UOR). The electrochemical response for UOR obtained with the nanoparticles synthesized with green chemistry can be compared with those synthesized by conventional methods that use NaBH4 as reducing agent, so the NiCo nanoparticles thus obtained were evaluated in urea microfluidic fuel cell, where a maximum of 1.3 mW cm^{-2} and 5.2mA cm^{-2} were obtained.

Keywords (Maximum 4 words): green chemistry; anodic catalysts

September 18th to 21st, 2018 in Mexico City, Mexico.

1. Introduction

Recently, and due to the problem of pollution that occurs throughout the world, scientific community has shown interest in the use of renewable energy to reduce the dependence on fossil fuels. A lot of research is focused on the use of fuel cells, where different type of molecule are used that can be oxidized, obtaining energy during the process. Urea, as an example, is considered a virtually inexhaustible (1) resource because it comes from organic wastes of living organisms. Urea also comes into contact with the environment due to its agricultural use as fertilizer, so that urea is one of the most abundant molecules in the world. In order of take advantage of the availability of the molecule and its high energy density (16.9 MJ/L) (2,3), have been developed urea fuel cells (UFC), where in addition of produce energy from the use of wasted or residual materials.

For the purpose of to achieve the urea oxidation reaction (UOR), the use of an anodic catalyst is crucial. Usually, noble metal catalysts are the first choice due their great catalytic activity, however, the use of noble metal could increase the cost of the fuel cells and energy generation and the global process would not be profitable. So, other metal catalysts have been assayed, such as nickel, a cheap metal that shown high activity in the UOR but a high overpotential near of 0.45 V vs SHE compared to the thermodynamic potential of -0.46 V for UOR (4).

In order to reduce the overpotential, bimetallic nanoparticles with cobalt (Co) have been synthetized to improve their catalytic activity. Several authors report that the ideal ratio for the catalyst is Ni (40%), Co (10%) and C (50%). Although some researchers affirm that the addition of Co could be decrease the current density of anodic peaks and displace the potential toward positive potentials, this effect could be due to the amount of Co added and the synthesis methods (2). This means that additional studies are required, in order to achieve an efficient synthesis, that produce stable and economical electrocatalysts that reduce the overpotential of the UOR and optimize the performance of the cell.

Although the underlying concept is to obtain energy starting of waste products, an additional advantage can be obtained from green chemistry that can be used for the synthesis of the anodic catalyst by exploiting the chemical reduction properties of various extracts plants, eradicating the use of harmful agents such as $NaBH_4$ which is widely used as a reducing agent (5). In this way, overall energy can obtained of waste, and the synthesis of the catalyst is carried out with leaves extracts of plants that are not given any suitable use, but are also considered waste.

Based on the great antioxidant potential and reported phenolic content of the *Eucalyptus globulus* and *Punica granatum,* extract leaves have been proposed as reducing agents for the synthesis of Ni and NiCo nanoparticles (6), with the aim of obtain metallic catalysts which promote the electrochemical reaction of UOR, seeking to reach high efficiency and adequate performance to justify its use in low power generation devices such as microfluidic fuel cells (7).

2. Materials and Methods

To obtain Ni and NiCo bimetallic nanoparticles, were used synthesis methods employing natural extracts of the leaves of *P. granatum* and *E. globulus,* for the reduction of inorganic precursors $NiCl_2 \cdot 6H_2O$ and $CoCl_2 \cdot 6H_2O$.

2.1 Extract preparation

For the extracts of *P. granatum* and *E. globulus* the leaves were collected in April 2018 in local areas of Zacatecas, Mexico. The choice was of branches leaves "tender" and good condition, which were artificially dried in an oven at 40ºC for 12 hours those *P. granatum* and 24 of *E. globulus.* The dry materials were crushed and an aqueous maceration was carried out with 3.15 g of leaves in 100 ml of deionized water at 80ºC. The contact time was 60 minutes for *P. granatum* leaves, and 40 for *E. globulus* [8]. After time elapsed, the mash was filtered and centrifuged at 10000rpm for 10 minutes and the supernatant was stored for synthesis.

2.2. Green synthesis of Ni and NiCo nanoparticles

A solution of $NiCl_2 \cdot 6H_2O$ 1% and $NiCl_2 \cdot 6H_2O$ / $CoCl_2 \cdot 6H_2O$ (4:1) 1% was prepared. Then, 5 ml of extract leaves was added to 1.5 ml of inorganic precursors, holding the temperature at 30ºC under vigorous stirring. The pH was increased with NaOH addition.
The material synthetized were centrifuged at 13000 rpm/10 minutes and washed with hot water and ethanol in triplicate. Ethanol was evaporated in an oven at 25ºC for 12 hours and materials were ground in a quartz ball mill for 20 minutes each one [9-12].

2.3. Electrode preparation

Catalytic inks were prepared with 2 mg of material, Vulcan carbon, Nafion and ethanol. Then 2 µl of ink was dropped onto glassy carbon electrodes (A = 0.07 cm^2) previously polished with alumina, and 4 µl on Toray paper electrodes (A = 0.032 cm^2).

2.4. Electrochemical measurements

For electrochemical measurements were used a Pt counter electrode, an Hg/HgO electrode ,0.09V (SHE), was used as reference electrode. The support electrolyte, KOH 1M, was bubbled by nitrogen gas for 15 minutes before the test, and was used urea 0.33M as fuel.
Electrochemical measurements were performed with and without urea solution in a three-electrode system connecting to an electrochemical workstation. Cyclic voltammetries were make exploring the potential of 0.2 to 0.8V. The polarization curves of cells were obtained by potentiostatic current measurement from OCV to 0V in a flow-through microfluidic cell with dimensions of 3 x 4 cm and using the Toray paper electrodes.

3. Results and Discussion

The two types of nanoparticles, Ni and Ni-Co, were synthesized to verify the effect of the o cobalt addition on the reduction of UOR overpotential. Both plant extracts were used as reducing agents in order to choose the most appropriate to obtain the metallic nanoparticles. The voltammetric profile of the materials was obtained with the modified glassy carbon electrodes in

KOH 1M to evaluate the presence of the Ni redox pair, and the catalytic activity was evaluated by adding urea at 0.33M. The figure 1 shows the cyclic voltammetries (CV) of Ni and NiCo nanoparticles synthesized with *P. granatum* extract leaves (Fig.1a,1b) where can be observed that the current density increased 0.6 mA cm^{-2} at 0.43 V, and 5.4 mA cm^{-2} at 0.41 V respectively after the urea addition. Similarly, can be observed (Fig. 1c and 1d) that on Ni and NiCo materials synthesized with *E. globulus* extract leaves, a higher current density was obtained with the bimetallic material, where it increased 10.9 mA cm^{-2} at 0.43 V. Thus, Co addition in both syntheses favored the overpotential reduction and apparently have better catalytic activity [2]. Besides, the NiCo (*P. granatum*) has more reversible peaks than the rest, with a difference of 0.12 V, unlike the NiCo (*E. globulus*) material that has 0.22 V difference between the anodic and cathodic peak.

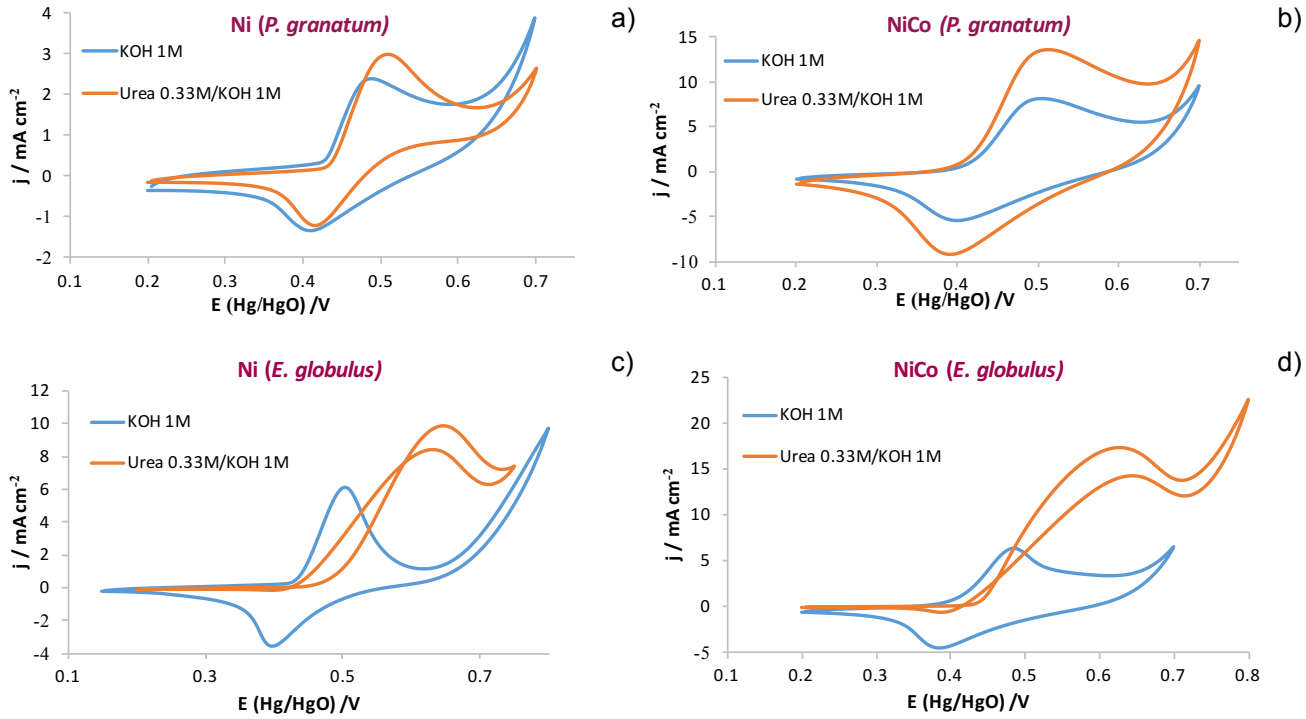

Fig. 1. Cyclic voltammograms of materials synthesized in 1M KOH with and without 0.33M urea addition at 20ºC. The CVs were conducted on (a) Ni, (b) NiCo *P. granatum,* and (c) Ni, (d) NiCo *E. globulus* coated GCE at a scan rate of 50 mV s^{-1}.

In order to study the performance of the best catalyst in a fuel cell system, bimetallic nanoparticles NiCo (*P. granatum)* deposited on Toray paper were evaluated in a microfluidic fuel cell. As a cathode was used a Toray electrode with Pt/C (20%) load of 1 mg cm^{-2}. As anolyte 1M KOH/Urea 0.33M, catholyte H_2SO_4 1.5M were used and flow rate of 3 ml/h, obtaining a potential

maximum of 1.3 mW cm^{-2} and 5.2 mA cm^{-2} as density current maximum an open circuit voltage of 0.68 V (Fig. 2). These results can be compared with those already reported by other authors, where they obtain 0.98 mW cm^{-2} and 2.2 mA cm^{-2} even whenthey use a 3M KOH concentration as anolyte [7,13], so the results in this work can be improved by increasing the concentrations of both fuel and anolyte. Nevertheless, although the results are promising, there are still parameters to improve because the theoretical open circuit voltage in a double electrolyte cell is 1.9 V [2,7,13], so a large gap exists between the theoretical value and the measured value in a cell. The energy loss comes from electrochemical limitations at the electrodes caused by activation overpotentials and slow reaction rates [13]. Another energy loss aspect is the heat loss resulting from the interfacial acid-base neautralization that is an exothermic reaction, independently from the electrochemical reaction.

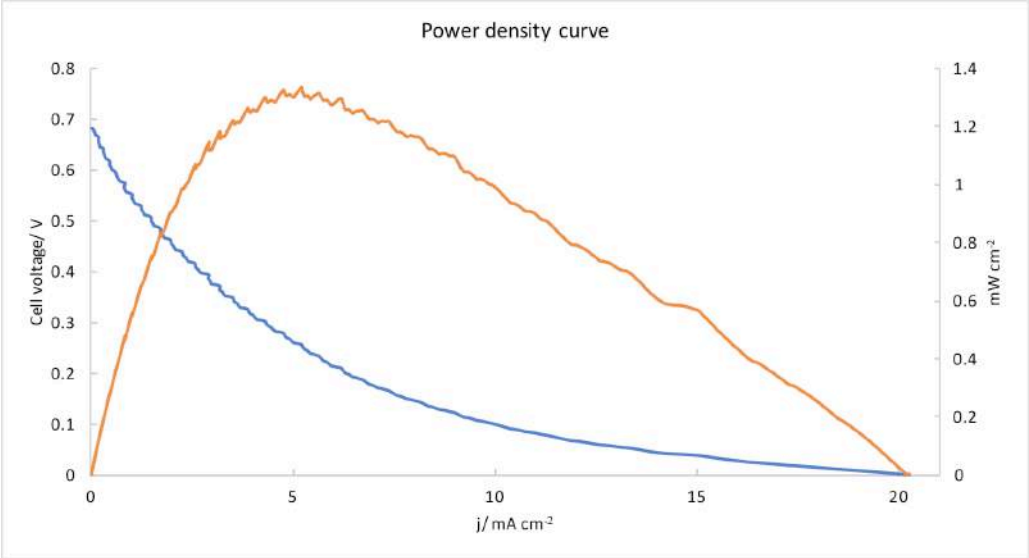

Fig. 2. Power density curve of urea microfluidic fuel cell using NiCo/C catalyst synthesized with *P. granatum* extract leaves

4. Conclusion

The use of extract plants seems to be a viable alternative for the synthesis of nanoparticles that can be used as catalysts in different systems, besides in energy production it is an advantage because waste products are used and expensive materials are not [14]. The results of cyclic voltammetry show a reversible process, therefore, in this study the convenience of using extracts of *P. granatum* and *E. globulus* as reducing agents for catalysts synthesis was demonstrated, because the results are comparable with those catalysts obtained bases on harmful reagents such $NaBH_4$.

The results of microfluidic fuel cell, although efficient, can be improved with strategies that involve variation in fuel and the electrolyte concentration differential, flow rate and temperature. By obtaining better results, the system can get to feed on industrial waste and municipal wastewater to have a low-cost wastewater treatment and have a viable alternative of production energy [7,13].

Acknowledgements

We appreciate the Mexican Council for Science and Technology and Energy Secretary for scholarship CONACYT-SENER, as well as Center for Research and Technological Development in Electrochemistry for the facilities provided.

References

[1] Alemán-Nava GS, Casiano-Flores VH, Cárdenas-Chávez DL, Díaz-Chavez R, Scarlat N, Mahlknecht J, et al. Renewable energy research progress in Mexico: A review. Renewable and Sustainable Energy Reviews. 2014;32(Supplement C):140-53

[2] Xu W, Zhang H, Li G, Wu Z. Nickel-cobalt bimetallic anode catalysts for direct urea fuel cell. Scientific reports. 2014;4:5863

[3] Munnings C, Kulkarni A, Giddey S, Badwal SPS. Biomass to power conversion in a direct carbon fuel cell. International Journal of Hydrogen Energy. 2014;39(23):12377-85

[4] Dan W., Wei Y., Gerardine G., Botte, Exfoliated nickel hydroxide nanosheets for urea electrolysis, Electrochemistry Communications, (2011) 13:10

[5] Mariam A, Kashif M, Selvaraj A, Bououdina M, G. V. Sankaracharyulu M, Muthurulandi, et al. Bio-synthesis of NiO and Ni nanoparticles and their characterization (2014) 1007-19

[6] Ting W., Xiaoying J., Zuliang C., Mallavarapu M., Ravendra N., Green synthesis of Fe nanoparticles using eucalyptus leaf extracts for treatment of eutrophic wastewater, Science of The Total Environment, (2014) 466–467;210-213

[7] Zhang, H., Wang, Y., Wu, Z. A direct urea microfluidic fuel cell with flow-trough Ni supported carbon nanotube coated sponge as porous electrode. Journal of Power Sources, (2018) 363; 61-69

[8] S. Machado, S.L. Pinto, J.P. Grosso, H.P.A. Nouws, J.T. Albergaria, C. Delerue-Matos,Green production of zero-valent iron nanoparticles using tree leaf extracts, Science of The Total Environment, (2013) 445–446;1-8

[9] Constable, D. Principles of Green Chemistry and Green Engineering, American Chemical Society, 2018

[10] Mariam A, Kashif M, Selvaraj A, Bououdina M, G. V. Sankaracharyulu M, Muthurulandi, et al. Bio-synthesis of NiO and Ni nanoparticles and their characterization2014. 1007-19 p

[11] Shakeel, A., Saifullah, MA., Babu LS., Saiqa I., Green synthesis of silver nanoparticles using Azadirachta indica aqueous leaf extract, Journal of Radiation Research and Applied Sciences, (2016) 9:1;1-7

[12] Ting W., Xiaoying J., Zuliang C., Mallavarapu M., Ravendra N., Green synthesis of Fe nanoparticles using eucalyptus leaf extracts for treatment of eutrophic wastewater, Science of

The Total Environment, (2014) 466–467;210-213
[13] Chino I, Muneeb O, Do E, Ho V, Haan JL, A paper microfluidic fuel cell powered by urea, Journal of Power Sources, Volume 396, 2018, 710-714
[14] Lan R, Tao S, Irvine JTS, A direct urea fuel cell – power from fertiliser and waste, *Energy Environ. Sci*., (2010) 3, 438-441

XVIII International Congress
of the Mexican Hydrogen Society

One step synthesis of Ru, Sn and Sb based catalyst for Oxygen Evolution Reaction

[a]N. J. Pérez-Viramontes, [a]I. L. Escalante-García, [a]M. Galván-Valencia, [b]V. Collins-Martínez, [a]S. M. Durón-Torres*

[a]Unidad Académica de Ciencias Químicas, Universidad Autónoma de Zacatecas, Campus Siglo XXI, Carretera a Guadalajara Km. 6.0, Ejido la Escondida, Zacatecas, Zac. México, 98160.

[b]Departamento de Ingeniería y Química de Materiales, Centro de Investigación en Materiales Avanzados, S.C., Miguel de Cervantes 120, Chihuahua, Chih., 31136, México

Tel: +524929256690 Ext. 4655; e-mail: duronsm@prodigy.net.

ABSTRACT

Multimetallic oxide of Ru, Sn, and Sb was synthetized by simple thermal decomposition method of the chloride precursor $RuCl_3xH_2O$, $SnCl_4x5H_2O$, and $SbCl_3$ in ethanol. This material functions as electrocatalyst and support for the oxygen evolution reaction (OER) in Solid Polymer Electrolyte Water Electrolyzer (SPEWEs). Four different proportions of $RuCl_3$ was used in the synthesis (10, 20, 30 and 40 at. %) of the catalyst support material. The effect of the ruthenium amount was evaluated on the electrocatalytic activity for OER by cyclic voltammetry (CV) and linear sweep voltammetry (LSV). Cyclic voltammetry shows the presence of ruthenium oxide, this is more evident as the increase of ruthenium amount in the catalyst. The onset potential for OER was found close to 1.4 V vs NHE, which is less than Ir based catalyst synthetized by the same technique (previously reported). From the linear sweep voltammetry analysis was possible to obtain the Tafel slope which is close to 60 mV dec^{-1}. The obtained parameters for the metallic oxides make it attractive as electrocatalyst for OER in SPEWE.

Keywords: Ruthenium oxide, Electrocatalyst, Support, SPEWEs

1. Introduction

Water electrolysis is one of the most viable technique for obtaining pure hydrogen and oxygen, without the production of greenhouse gases.[1,2] There are some technologies already established for this process as alkaline water electrolyzers (AWE) and solid polymer electrolyte water electrolyzers (SPEWE). AWE has some advantages as that it is a well stablished technology, use of non-noble metal catalyst and relative low cost. It also has some

disadvantages such as low current densities, low purity in the gases, the electrolytic medium is highly corrosive[3]. Advantages offered by SPEWE are high current densities, high voltage efficiency, compact system design and high gas purity. High cost of the components, possibly low durability and use of noble metal based catalyst are some of this technologies disadvantages,.

Due to its advantages SPEWE is considered as one of the most important technologies for hydrogen production. However, there are some problems that must be solved for its commercialization, one of the main is the high energy consumption at the anode, due to the oxygen evolution reaction (OER).[4,5]

Ruthenium oxide has been considered as one of the most electroactive material for oxygen evolution reaction, however, its use has some drawbacks, such as its low abundance in the earth´s crust, high cost and instability at high overpotentials.[6–8] Therefore, it is necessary to combine this catalyst with more stable, resistant and cheap materials, known as supports. There are different types of catalytic supports, as black carbon, carbon nanotubes, graphene,[9,10] aluminates, silicates, metal carbides, metal nitrides[11] and metal oxides.[12–14] Antimony Doped Tin Oxide (ATO) is one of the most used due to its high electrical conductivity, high corrosion resistance and low cost.

The dispersion technique of the catalyst on the surface support is one of the considered topics in order to avoid the particles agglomeration and to obtain the maximum performance catalyst-support mixture.

The present work focuses on synthesis of the catalyst-support material by one step method. The technique consist on the simple thermal decomposition of a ethanolic solution of Ru, Sn and Sb ,metal precursor to obtain Ru-Sn-Sb-O material varying metal percent on the catalyst. So also in the obtention of some of its electrocatalytic properties for the oxygen evolution reaction by cyclic voltammetry, linear sweep voltammetry and Tafel plots construction.

2. Materials and Methods

2.1.Preparation of the multimetallic catalyst

Multimetal catalyst were prepared by simple thermal decomposition method. Four solutions 0.25 M of $RuCl_3xH_2O$, $SnCl_4x5H_2O$, and $SbCl_3$ (Aldrich) in absolute ethanol were prepared. Each one varying the atomic ration of metal in the solution. (1) 10 at.% Ir, 85 at.% Sn and 5 at.% Sb, (2) 20 at.% Ir, 76 at.% Sn and 4 at.% Sb, (3) 30 at.% Ir, 67 at.% Sn and 3 at.% Sb and (4) 40 at.% Ir, 60 at.% Sn and 3 at.% Sb. The ethanolic solution was then heated at 50 °C under N_2-atmosphere for 2 h. After this time the solutions were calcinated at 450 °C for 30 min. The synthesized powder were three times washed with deionized water and one with ethanol, then dried for 8 h at 80 °C. The metallic catalyst are denoted Ru-Sn-Sb-O (x), where the x represents the theoretical at.% of Ru in the oxide (10, 20, 30 and 40).

2.2 Electrochemical characterization

A catalytic ink for each catalyst was prepared using 3 mg of the powder, 10 μL of Nafion® (5% wt%, Aldrich) and 60 μL of ethanol. Each ink was then placed in an ultrasonic bath for 30 min in order to get a homogeneous and well dispersed particles in suspension. Afterwards, 1.5

mL of ink was deposited on a clean polished glassy carbon electrode (GCE, 3 mm diameter). The prepared electrode was dried at 60 °C for 30 min.

All the electrochemical measurements were conducted in a typical three electrode cell. A sulfate electrode (0.68 V vs NHE) was used as reference electrode and platinum mesh as counter electrode. An aqueous solution 0.5 M of H_2SO_4 N_2 saturated was employed as electrolytic medium for all electrochemical studies. Cyclic voltammetry (CV) was done to obtain the electrochemical profile of the synthesized Ru-Sn-Sb-O materials from 0.68 to 1.5 V vs NHE at a scan rate of 50 mVs^{-1}. To evaluate the oxygen evolution reaction kinetics on the catalyst, Linear Scan Voltammetry (LSV) was performed an a scan rate of 3 mV s^{-1} in the anodic direction from 0.5 to 1.0 V. All the electrochemical measurements were performed using a potentiostat/galvanostat (EG&G, PAR Versastat 3). A precision rotor (PINE MSRX) was used to support the GCE. All electrode potentials in this work and the current density was normalized to the electrodes geometric area.

3. Results and Discussion

Fig. 1 shows the cyclic voltammograms (CVs) for the synthesized catalysts. The Ru-Sn-Sb-O (10) (dotted line), Ru-Sn-Sb-O (20) (continuous line), Ru-Sn-Sb-O (30) (dashed dotted line) and Ru-Sn-Sb-O (40) (dashed line) in N_2 saturated H_2SO_4 0.5 M. The voltammograms curves for the Ru-Sn-Sb-O materials show an electrochemical behavior that is comparable to ruthenium oxide deposited on a titanium substrate in acidic media synthesized by thermal decomposition[15].

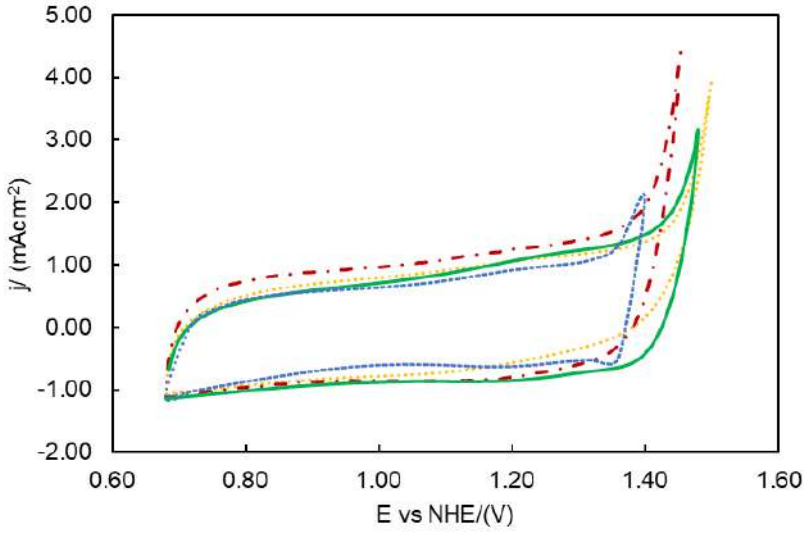

Fig. 1 Cyclic voltammogram of a. Ru-Sn-Sb-O (10) (····), b. Ru-Sn-Sb-O (20) (——), c. Ru-Sn-Sb-O (30) (− · −) and d. Ru-Sn-Sb-O (40) (− − −).

In the voltammograms curves, is observed a potential wave between 0.7 V to 1.0 V, which is associated with the Ru(III) to Ru (IV) conversion. Likewise, an oxidation wave is observed among 1.1 V to 1.28 V, associated with the Ru(V) to Ru(VI) transition. Besides there is an observable reduction peak close to 1.3 V vs NHE.[15] Oxidation and reduction peaks were more evident with the increase of ruthenium atm %.The differences between voltammograms of the different catalyst were associated with the different composition of metal oxides due to the difference in ruthenium atomic percent. The materials present similar pseudo-capacitance, this effect is attributed to the well dispersed nanoparticles, providing a reproducible catalytic film on the surface of the GCE. The cyclic voltammograms allowed estimate the electrochemical properties of the materials. The onset potential for the oxygen evolution reaction (E_{OER}) were evaluated at 1.42, 1.41. 1.40 and 1.39 V for Ru-Sn-Sb-O (10), Ru-Sn-Sb-O (20), Ru-Sn-Sb-O (30) and Ru-Sn-Sb-O (40) respectively. The onset potential values for OER for the synthesized catalyst are consistent with previously reported values.[16]

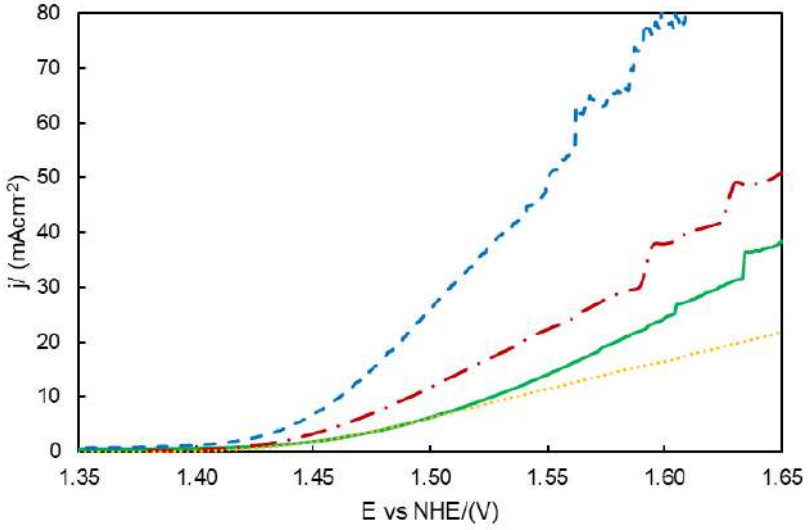

Fig. 2. Linear Scan Voltammograms of a. Ru-Sn-Sb-O (10) (····), b. Ru-Sn-Sb-O (20) (——), c. Ru-Sn-Sb-O (30) (− · −) and d. Ru-Sn-Sb-O (40) (− − −).

The electrocatalytic properties of the Ru-Sn-Sb-O materials were obtained by LSV measurements as show in Fig. 2. LSV results indicated that the OER is favored with the increase of ruthenium content, this results are consistent with previously discussed in CVs results. The onset potential for Ir-Sn-Sb-O materials are similar for that obtained by CVs. Ru-Sn-Sb-O (10) material presents the higher onset potential for OER with at 1.44 V, Ru-Sn-Sb-O (20) presents 10 mV less in the onset potential for OER, as Ru-Sn-Sb-O (30), Ru-Sn-Sb-O (40) presents the lowest overpotential for OER at 1.39 V. Current density is evident higher for Ru-Sn-

Sb-O (40)> Ru-Sn-Sb-O (30)> Ru-Sn-Sb-O (20)> Ru-Sn-Sb-O (10). At 1.60 V vs NHE the current density for the prepared electrodes were 16.5 $mAcm^{-2}$ for Ru-Sn-Sb-O (10), 25.15 $mAcm^{-2}$ for Ru-Sn-Sb-O (20), 38.50 $mAcm^{-2}$ for Ru-Sn-Sb-O (30) and 77.95 $mAcm^{-2}$ for Ru-Sn-Sb-O (40). The slope of the LSV are similar for all synthesized materials, suggesting that the water reaction mechanism is the same.

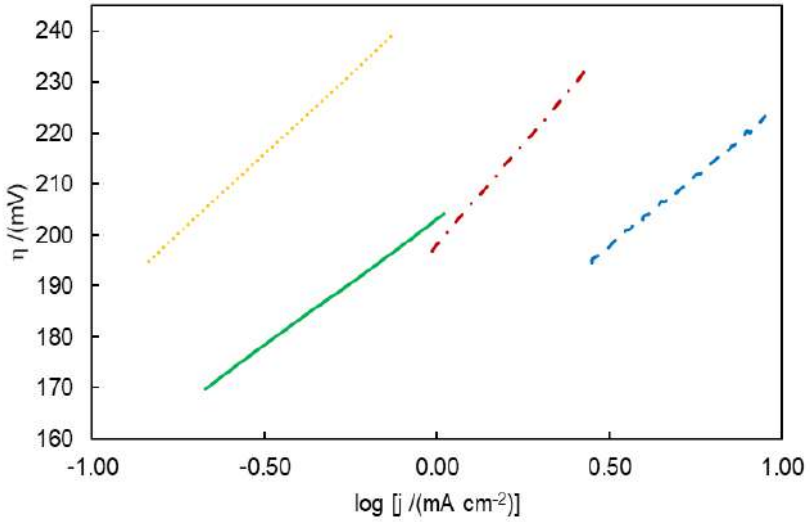

Fig. 3 Tafel plots for OER on a. Ru-Sn-Sb-O (10) (····), b. Ru-Sn-Sb-O (20) (——), c. Ru-Sn-Sb-O (30) (− · −) and d. Ru-Sn-Sb-O (40) (− − −) after IRs correction.

Tafel plots were obtained after ohmic drop correction of the LSV curves to elucidate the rate-determining step (rds) for the OER, this is show in Fig. 3. The Tafel slopes were 63.35, 51.72, 80.67, 55.91 mVdec-1 for Ru-Sn-Sb-O (10), for Ru-Sn-Sb-O (20), for Ru-Sn-Sb-O (30) and for Ru-Sn-Sb-O (40) respectively. These values are similar to those previously reported[5,17,18] Tafel slopes close to 60 $mVdec^{-1}$ suggest that the rate determinate step is (2) according to the mechanism proposed for the OER on active oxide electrodes in acidic media as shown below.[19–22]

$$S + H_2O \rightarrow S - OH + H^+ + e^- \quad (1)$$

$$S - OH \rightarrow S - O^- + H^+ \quad (2)$$

$$S - O^- \rightarrow S - O + e^- \quad (3)$$

$$2S - O \rightarrow 2S + O_2 \quad (4)$$

S represents the active sites on the catalyst surface, S-OH and $S\text{-}O^-$ are the adsorbed intermediates. The Tafel slope for Ru-Sn-Sb-O materials suggest that the rds for the OER is a chemical step after the transfer of the first electron, corresponding to the dissociation of the S-

OH complex. The oxygen evolution on the catalyst surface is carried out by a electrochemical-chemical mechanism (EC).

Table 1 Summary of OER parameters obtained by LSV and Tafel plots.

Electrode	E_{OER} /(V)	b/ (mVdec^{-1})	α	j_0 /(μA cm^{-2})	r^2
Ru-Sn-Sb-O (10)	1.40	63.35	0.4507	0.1232	0.9998
Ru-Sn-Sb-O (20)	1.39	51.72	0.5521	0.1171	0.9983
Ru-Sn-Sb-O (30)	1.38	80.67	0.3540	0.6380	0.9995
Ru-Sn-Sb-O (40)	1.36	55.91	0.5107	0.9207	0.9999

Conclusion

Ru-Sn-Sb-O powder materials synthesized by simple thermal decomposition show an electrochemical behavior similar to ruthenium oxide deposited on a titanium substrate. The voltammetric results show that the amount of ruthenium in the catalyst is a determining factor in the current obtained at high overpotential, however, the onset potential for the oxygen evolution reaction is similar for all the synthesized catalysts. The Tafel slopes obtained for the Ru-Sn-Sb-O electrodes indicate that in these materials, the catalytic center is the ruthenium oxide, because the calculated slopes are similar to obtained in other metallic oxides. It will be necessary to perform the physicochemical characterization in order to know the composition, particle size, electrical conductivity and surface area in the material. The electrochemical results in the present study suggest that the Ru, Sn and Sb based catalyst are a promising materials for it use as anode for the oxygen evolution reaction.

Acknowledgements

The authors acknowledge to the Mexican Council for Science and Technology (CONACyT) for the financial support, and for the graduate fellowship granted to N.J. Pérez.

References

[1] Carmo M, Fritz DL, Mergel J, Stolten D. A comprehensive review on PEM water electrolysis. International Journal of Hydrogen Energy 2013;38:4901–34. doi:10.1016/j.ijhydene.2013.01.151.

[2] Chaubey R, Sahu S, James OO, Maity S. A review on development of industrial processes and emerging techniques for production of hydrogen from renewable and sustainable sources. Renewable and Sustainable Energy Reviews 2013;23:443–62. doi:10.1016/j.rser.2013.02.019.

[3] Stiller C, Hochrinner H. Use of Conventional and Green Hydrogen in the Chemical Industry. In: Töpler J, Lehmann J, editors. Hydrogen and Fuel Cell, Springer Berlin Heidelberg; 2016, p. 173–86. doi:10.1007/978-3-662-44972-1_10.
[4] Giordano L, Han B, Risch M, Hong WT, Rao RR, Stoerzinger KA, et al. pH dependence of OER activity of oxides: Current and future perspectives. Catalysis Today 2016;262:2–10. doi:10.1016/j.cattod.2015.10.006.
[5] Reier T, Oezaslan M, Strasser P. Electrocatalytic Oxygen Evolution Reaction (OER) on Ru, Ir, and Pt Catalysts: A Comparative Study of Nanoparticles and Bulk Materials. ACS Catal 2012;2:1765–72. doi:10.1021/cs3003098.
[6] Audichon T, Mayousse E, Napporn TW, Morais C, Comminges C, Kokoh KB. Elaboration and characterization of ruthenium nano-oxides for the oxygen evolution reaction in a Proton Exchange Membrane Water Electrolyzer supplied by a solar profile. Electrochimica Acta 2014;132:284–91. doi:10.1016/j.electacta.2014.03.141.
[7] García-Peña NG, Redón R, Herrera-Gomez A, Fernández-Osorio AL, Bravo-Sanchez M, Gomez-Sosa G. Solventless synthesis of ruthenium nanoparticles. Applied Surface Science 2015;340:25–34. doi:10.1016/j.apsusc.2015.02.186.
[8] Cornell A, Håkansson1 B, Lindbergh1 G. Ruthenium based DSA® in chlorate electrolysis—critical anode potential and reaction kinetics. Electrochimica Acta 2003;48:473–81. doi:10.1016/S0013-4686(02)00679-5.
[9] Espinola A, Miguel PM, Salles MR, Pinto AR. Electrical properties of carbons—resistance of powder materials. Carbon 1986;24:337–41. doi:10.1016/0008-6223(86)90235-6.
[10] Takamura T, Brodd RJ. CARBONACEOUS MATERIALS FOR BATTERIES. Springer Netherlands; 2006.
[11] Lavacchi A, Miller H, Vizza F. Nanotechnology in electrocatalysis for energy. n.d.
[12] Ávila-Vázquez V, Cruz JC, GalvÁn-Valencia M, Ledesma-García J, Arriaga LG, GuzmÁn C, et al. Electrochemical study of sb-doped SnO2 supports on the oxygen evolution reaction: Effect of synthesis annealing time. International Journal of Electrochemical Science 2013;8:10586–600.
[13] Chhina H, Campbell S, Kesler O. An oxidation-resistant indium tin oxide catalyst support for proton exchange membrane fuel cells. Journal of Power Sources 2006;161:893–900. doi:10.1016/j.jpowsour.2006.05.014.
[14] Dimitrov M, Guncheva M, Zhiryakova D, Lazarova T, Lalev G, Tsoncheva T. Nanostructured tin dioxide – a promising multipurpose support material for catalytic and biocatalytic applications. Chemical Engineering Journal 2014;252:55–63. doi:10.1016/j.cej.2014.04.052.
[15] Chalupczok S, Kurzweil P, Hartmann H, Schell C. The Redox Chemistry of Ruthenium Dioxide: A Cyclic Voltammetry Study—Review and Revision. International Journal of Electrochemistry 2018. doi:10.1155/2018/1273768.
[16] Reier T, Teschner D, Lunkenbein T, Bergmann A, Selve S, Kraehnert R, et al. Electrocatalytic Oxygen Evolution on Iridium Oxide: Uncovering Catalyst-Substrate Interactions and Active Iridium Oxide Species. J Electrochem Soc 2014;161:F876–82. doi:10.1149/2.0411409jes.

[17] Thuv H. The Oxygen Evolution Reaction at Iridium-Ruthenium Oxide Catalysts for PEM Water Electrolysis. 142 2015.
[18] Cherevko S, Geiger S, Kasian O, Mingers A, Mayrhofer KJJ. Oxygen evolution activity and stability of iridium in acidic media. Part 1. – Metallic iridium. Journal of Electroanalytical Chemistry 2016;773:69–78. doi:10.1016/j.jelechem.2016.04.033.
[19] Doyle R, Lyons M. The Oxygen Evolution Reaction: Mechanistic Concepts and Catalyst Design, 2016, p. 41–104. doi:10.1007/978-3-319-29641-8_2.
[20] De Pauli CP, Trasatti S. Composite materials for electrocatalysis of O2 evolution: IrO2+SnO2 in acid solution. Journal of Electroanalytical Chemistry 2002;538–539:145–51. doi:10.1016/S0022-0728(02)01055-0.
[21] Faria LAD, Boodts JFC, Trasatti S. Electrocatalytic properties of ternary oxide mixtures of composition Ru0.3Ti(0.7−x)CexO2: oxygen evolution from acidic solution. J Appl Electrochem 1996;26:1195–9. doi:10.1007/BF00243745.
[22] Lodi G, Sivieri E, Battisti AD, Trasatti S. Ruthenium dioxide-based film electrodes. J Appl Electrochem 1978;8:135–43. doi:10.1007/BF00617671.

Environmental aspects

September 18 to 21, 2018 in Mexico City, Mexico

XVIII International Congress
of the Mexican Hydrogen Society

Photocatalytic Activity of Layered Perovskite Oxides $Sr_{2.7-x}Ca_xLn_{0.3}Fe_2O_{7-\delta}$ for MB Degradation

L.E. Verduzco[1], R. Garcia-Diaz[2], J. Oliva[3], A.I Martinez[1], C. Gomez-Solis[4], C.R. Garcia[2], A. F. Fuentes[1] and K. P. Padmasree[1*]

[1]Cinvestav Unidad Saltillo, Parque Industrial, Ramos Arizpe, Coahuila, 25900, México
[2]CONACYT-Facultad de Ciencias Físico-Matemáticas, Universidad Autónoma de Coahuila, 25000, Saltillo, México
[3]CONACYT-Facultad de Ciencias Químicas, Universidad Autónoma de Coahuila, 25280, Saltillo, México
[4]Universidad de Guanajuato, Campus León, División de Ciencias e Ingenierías, 37150 León, Guanajuato, México
* Corresponding author: phone number: 8444389600 (8521), e-mail: padmasree@cinvestav.edu.mx

ABSTRACT

The semiconductor photocatalyst such as TiO_2, ZnO etc. are very efficient for the photocatalytic degradation of organic pollutants from water because of their excellent photocatalytic activity, ultraviolet absorbency, low cost and photochemical stability. However, these oxides absorb only a small portion of solar spectrum in the ultraviolet region which limits their practical applications. Therefore, the development of photosensitized degradation process by utilizing visible light has recently received much attention. Perovskite oxides have received significant attention because of their unique properties such as oxygen vacancy order, high conductivity, intrinsic oxygen reduction reaction activity etc. Many perovskite and perovskite-type oxides have been found to be suitable for photocatalytic degradation reaction. In this work we analyzed the photocatalytic activity of the layered perovskites belonging to n = 2 series of Ruddlesden – Popper oxides $Sr_{2.7-x}Ca_xLn_{0.3}FeO_{7-\delta}$ where x = 0 and 0.3 and Ln = La and Nd. The samples were synthesized by solid-state reaction method and characterized by X-ray diffraction, scanning electron micrograph, diffuse reflectance UV-visible spectroscopy etc. As the lanthanide size decreases, the absorption band in the US-VIS-NIR region increases. Similarly, the Ca-substituted sample exhibited a small decrease in absorption band. The band gap energy (E_g) value was obtained from the Kubelka-Munk plot. The photocatalytic activity of the samples was analyzed by the degradation of MB at room temperature under solar and UV irradiation. An increased degradation of MB was shown by Nd samples compared to La samples because of the increased absorbance and low band gap values shown by Nd samples. Under solar irradiation degradation was faster (180 min) compared to UV irradiation (300 min).

Keywords: Photocatalyst; layered perovskite; methylene blue; solar and UV irradiation

September 18th to 21st, 2018 in Mexico City, Mexico.

1. Introduction

Solar photocatalysis has been used for alleviating environmental pollutants, waste water treatment, generating solar fuels from the photocatalytic splitting of water, fixing nitrogen etc. [1,2]. Photocatalysis is a significant method for the degradation of organic waste in water into harmless substances. The photocatalytic activity depends on the ability of a catalyst to create electron-hole pairs, which generate free radicals capable of undergoing secondary reactions. Numerous catalysts has been developed for solar photocatalysis in the recent years. Among them the most widely used catalyst is TiO_2 because it is relatively easy and inexpensive to synthesize, non-toxic and can totally degrade different type of pollutants [2]. However, the wide band-gap (3.2 eV) and the recombination of photogenerated electron-hole pairs limit its use. The large band-gap requires the use of UV light for the photogeneration of electrons and holes. UV light compose of less than 5% of solar irradiation and this limits the effective use of the visible portion of the solar energy. Methylene blue (MB) is a blue, organic cationic thiazine dye that has been commonly used in the textile industry and is normally degraded using materials such as sulfides, non-semiconducting oxides, and persistent phosphors [2]. The total degradation time reported for MB is in the range of 100-200 min. Consequently, materials with stronger solar absorbance in the VIS-NIR region and appropriate band gap are still an important subject of research for solar photocatalysis. Therefore, several new catalysts were developed with increased efficiency for the degradation of organic waste through photocatalysis [3].

Numerous perovskites and other complex oxide such as $SrTiO_3$, $LaCoO_3$, $BiVO_4$, Bi_2WO_6 have been exhibited promising photocatalytic activity because of their strong visible light absorption [4-6]. These complex oxides have better photocatalytic activity than TiO_2 under sunlight [5]. The catalytic activity of these complex oxide can be improved by the partial substitution on A- and/or B-site with a cation of different valence state which changes the electronic structure and correspondingly their electrical and optical properties [6]. Recently, the layered perovskites belonging to Ruddlesden-Popper (R-P) family with the general formula $A_{n+1}B_nO_{3n+1}$ (A = alkali, alkaline earth or rare earth; B = transition metal) have been found to exhibit higher photocatalytic activity [7,8]. These R-P oxides have rock salt layers alternating with a single (n = 1), double (n = 2) or triple (n = 3) perovskite layers along the *c*-axis [9]. It was reported that the layered perovskites use their interlayer space as reaction sites where the electron-hole recombination process could be retarded by physical separation of the electron-hole pairs generated by photo-absorption [8]. The R-P oxides shows an enhancement in the structural stability compared to simple perovskites and can accept a large oxygen non-stoichiometry without structural transformation [9]. Photocatalytic activity of the layered perovskites is highly dependent on the electronic band structure as well as bulk crystal structure. The semiconducting properties like electronic conductivity and band gap at room temperature of the layered perovskites suggest that they can be effective for the degradation of dyes [10].

The perovskite oxides based on $LaFeO_{3-\delta}$ and $LaCoO_{3-\delta}$ are studied widely as cathodes for the electrochemical reduction of oxygen in solid oxide fuel cells (SOFCs) and recently many

groups investigated their photocatalytic activity [11,12]. Similarly, we have reported earlier an enhanced photocatalytic activity and an increased absorbance with Ca substitution in the layered perovskites oxides of n = 3 series $Sr_{3.2-x}Ca_xLa_{0.8}Fe_{1.5}Co_{1.5}O_{10-\delta}$ [13]. The layered perovskites belonging to R-P oxides of n = 2 series $(Sr,La)_3Fe_2O_{7-\delta}$ has been studied widely as cathode material for SOFCs and oxygen separation membranes due to its mixed oxide-ion and electronic conducting properties [23]. The crystal structure of $(Sr,La)_3Fe_2O_{7-\delta}$ having (Sr,La)O rock-salt layers alternating with two $(Sr,La)FeO_3$ perovskite layers along the *c*-axis. Neutron diffraction studies of then = 2 series have shown that oxygen vacancies are localized on the vertex shared by two FeO_6 octahedra in the perovskite layer [14]. Though $(Sr,Ln)_3Fe_2O_7$ oxides have been reported for SOFC applications, there is no report of this oxide on the photocatalytic studies. In this work, R-P oxide of n = 2 series $Sr_{2.7-x}Ca_xLn_{0.3}Fe_2O_{7-\delta}$ with x = 0 and 0.3, and Ln = La and Nd were synthesized, and investigated the photocatalytic activity by monitoring the degradation of MB dye under solar and UV exposure.

2. Materials and Methods

$Sr_{2.7-x}Ca_xLn_{0.3}FeO_{7-\delta}$ oxides were synthesized by the conventional solid-state reaction. Appropriate amounts of La_2O_3, Nd_2O_3, $SrCO_3$, $CaCO_3$ and Fe_2O_3 (Sigma Aldrich) were weighed and thoroughly mixed with ethanol in an agate mortar and pestle and calcined in air at 1000 °C for 12 h. The calcined powders were then ground and pressed into pellets and sintered in air at 1300 °C for 24 h. The sintered pellets were ground into fine powder for further characterizations. Four $Sr_{2.7-x}Ca_xLn_{0.3}FeO_{7-\delta}$ samples were synthesized with different lanthanides (Ln = La and Nd) with and without Ca substitution: SLFO (x = 0 and Ln = La), SNFO (x = 0 and Ln = Nd), SCLFO (x= 0.3 and Ln = La) and SCNFO (x = 0.3 and Ln = Nd).

The synthesized $Sr_{2.7-x}Ca_xLn_{0.3}FeO_{7-\delta}$ oxides were characterized by X-ray diffraction (XRD) with a Philips X'pert diffractometer using Cu K_α radiation in the 2θ range 10 – 80° with a step of 0.02°. The morphology of the sample powder was analyzed by scanning electron microscopy (SEM) with a Philips XL30 ESEM microscope. The absorbance spectra of the powders were acquired with a Perkin-Elmer Lambda 365 spectrophotometer with an integrating sphere of Spectralon in the range of 200 nm-1100 nm.

The samples were prepared by mixing 0.3 g of $Sr_{2.7-x}Ca_xLn_{0.3}FeO_{7-\delta}$ powder with the 100 mL MB solution. Before visible light irradiation, the mixture of MB dye and $Sr_{2.7-x}Ca_xLn_{0.3}FeO_{7-\delta}$ solutions were magnetically stirred for 60 min in the dark. This permits the formation of the adsorption-desorption equilibrium between the interface of the photocatalyst and the dye molecules under ambient conditions. After that, the beakers with the solutions and the photocatalysts were irradiated with sunlight up to 180 min in a sunny day. The photocatalytic degradation of methylene blue was monitored by withdrawing 200 µL of the MB solution at regular intervals during solar irradiation and immediately centrifuged at 15000 rpm for 20 min to separate the photocatalyst from the water.

For UV measurements, the photocatalytic process was carried out using a reactor fabricated with three 4 W UV lamps. Those lamps emitted UV light centered at centered at 254 nm, with a FWHM around 12 nm. The samples were prepared by mixing 70 mL of 25 ppm

methylene blue solution and 0.3 g of the $Sr_{2.7-x}Ca_xLn_{0.3}FeO_{7-\delta}$ powders. Afterwards the UV lamps were turned on and the samples of 1 mL were extracted every 30 min and the powders were separated from the liquid by centrifugation at 15000 rpm. The absorbance measurements were recorded by using a Cary-60 UV-Vis spectrophotometer in the range of 200-700 nm. Subsequently, the absorbance of each sample was measured to observe a decrease in the intensity of the main absorption band of the methylene blue centered at 665 nm. The absorbance spectrum of MB liquid was determined with a UV-Vis UNICO SQ-4802 spectrophotometer in the range of 300 nm – 800 nm.

3. Results and Discussion

The XRD pattern of SCLFO sample is shown in Fig. 1a as a representative of all the synthesized R-P oxides. The rest of the samples presented the same diffraction peaks and crystalline planes and corresponds to a single phase having the tetragonal crystal structure of space group I4/mmm of the *n* = 2 member of the R–P series. The main observed planes are (105), (110), (116), (0010), (200) and (215). The X-ray diffraction peaks shifted towards higher angles as the lanthanide size decrease and also with Ca substitution on the Sr site. A zoom of the XRD pattern of all the samples showing the peak shift in the 2θ range 30-35° is shown in Fig. 1b. The lattice parameters (a) and (c), and unit cell volume (V) decreases with Ca substitution

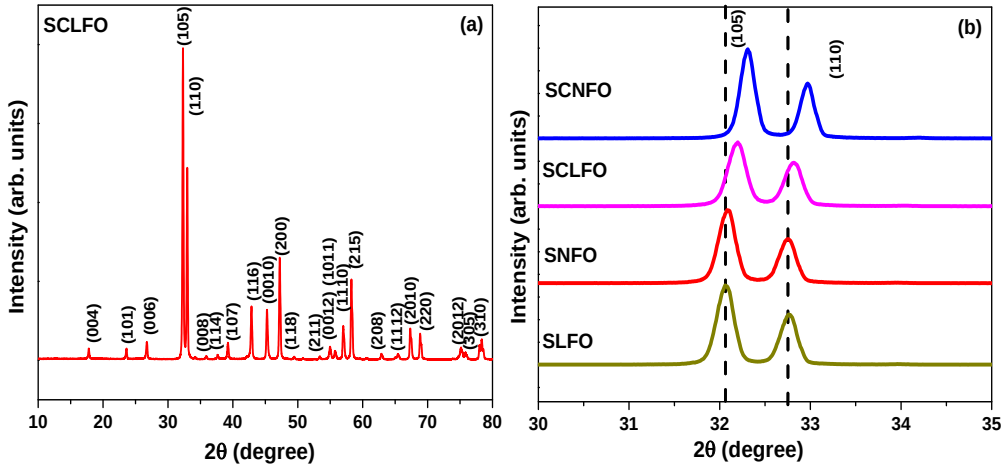

Fig. 1. (a) XRD pattern of SCLFO sample as a representative of all the synthesized R-P oxides (b) A zoom of the XRD pattern of all the samples showing the peak shift in the 2θ range 30-35°

and with the decrease in the lanthanide size. This is due to the decreasing ionic size of lanthanides from Ln = La to Nd and also the ionic size of Ca is smaller than that of Sr. SEM images of SLFO and SCLFO samples are shown in Fig. 2. The microparticles are highly agglomerated and the Ca substitution for Sr in La and Nd samples does not show any change in the morphology. The smaller microparticles are obtained for the Nd based samples compared to La based samples (Figure not shown here). The Ca doped and undoped lanthanides exhibit a mixture of small and large grains of irregular size in the range 0.1-3.9 μm.

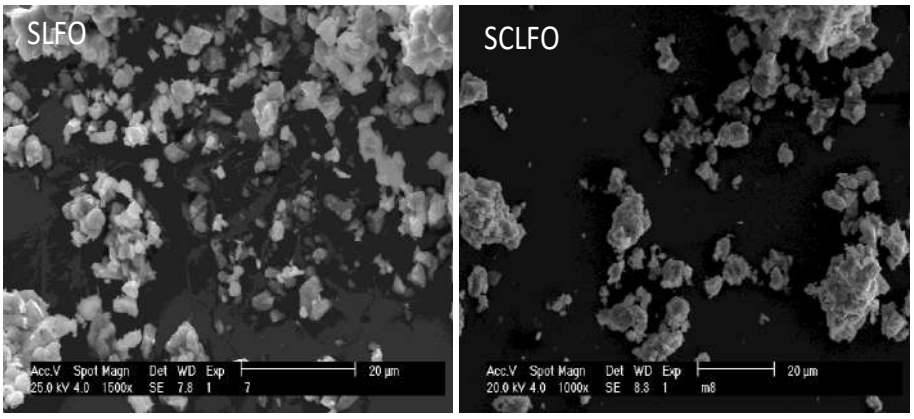

Fig. 2. SEM images of SLFO and SCLFO samples

The UV-vis-NIR absorbance spectra shows the samples absorb light in the UV-VIS-NIR region, which is an advantage over the popular TiO_2 photocatalyst that only absorbs in the UV region. The optical absorption in the near UV range and VIS-NIR region slightly improved in the Nd samples compared to La based samples. In addition, the samples doped with Ca presented a lower absorption intensity compared to the samples without Ca. The band gap energy values obtained are 1.6, 1.74, 1.4 and 1.55 eV, respectively for the SLFO, SCLFO, SNFO and SCNFO samples. The lower energy band gap values obtained for the Nd based samples compared to La based samples suggest that the presence of Nd contributed to slight increase in the electrical conductivity and optical absorbance of the samples, which is beneficial for the photocatalytic degradation of MB as explained in the next section. Furthermore, Ca doped samples have a slightly higher band gap values compared to that of the samples without Ca. This could be due the presence of large number of oxygen vacancies in the Nd and Ca doped samples in comparison with those with La and Ca doped samples. In Nd and Ca doped samples, higher content of oxygen vacancies would be expected because of stronger crystalline distortions, due to the small ionic radii of Nd compared to La.

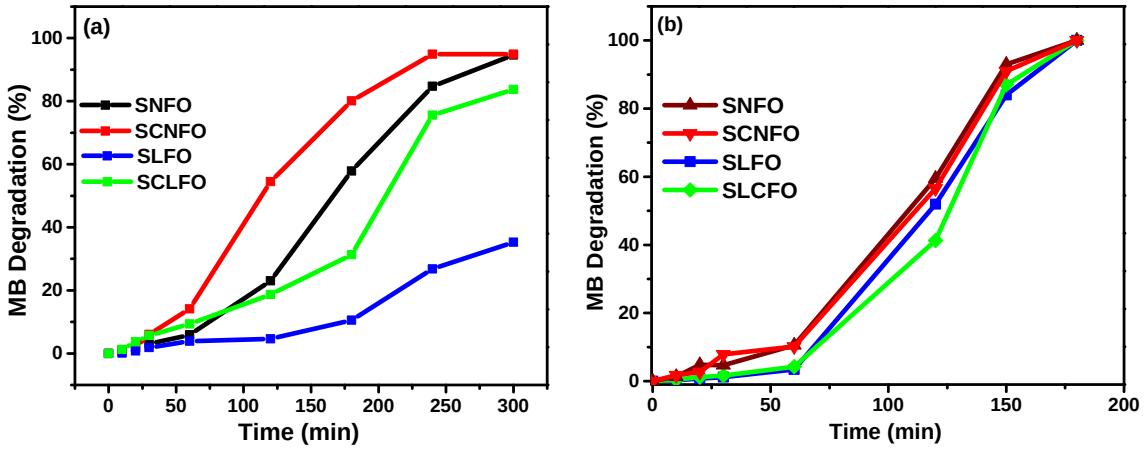

Fig. 3. MB degradation percentage as a function of time for $Sr_{2.7-x}Ca_xLn_{0.3}FeO_{7-\delta}$ samples under (a) UV irradiation and (b) solar irradiation.

The photocatalytic activity of the $Sr_{2.7-x}Ca_xLn_{0.3}FeO_{7-\delta}$ layered perovskite oxides was assessed by monitoring the degradation of the methylene blue dye, which is a common organic pollutant rom the textile industry. Fig.3 (a) and (b) show the degradation of MB dye using the $Sr_{2.7-x}Ca_xLn_{0.3}FeO_{7-\delta}$ oxides under UV and solar radiation, respectively. All the samples could totally degrade the MB dye after 180 min under solar irradiation. Under solar irradiation the degradation rates obtained were higher than that of UV irradiation, suggesting that the photocatalytic activity is more efficient under solar light. Similarly, there is no obvious difference in the MB degradation rate under solar irradiation, indicating that any of the studied samples could be a feasible for solar photocatalytic degradation of dyes.

In this study, the Nd-doped samples exhibited the best degradation efficiency because they have the smallest band gap [12] and exhibited the highest absorbance, which is due to the oxygen vacancy formation in Nd doped samples. The formation of oxygen vacancies is due to the lattice distortion caused by the incorporation of the Nd and La ions (with smaller ionic radii than that of Sr) in the Sr sites. It is expected a higher concentration of oxygen vacancies in Nd doped samples because the ionic radii of Nd are less than that of La [13]. The absorption spectrum of the MB solution as a function of time obtained during the photocatalytic activity of SCNFO sample under UV and solar irradiation are shown in Fig. 4 (a) and (b). The absorption curves of MB are characterized by strong overlapping bands around 600 and 665 nm. The figure shows the intensity of the characteristic absorption peaks of MB decreases with the irradiation time, which specifies a progressive degradation of MB dye by the destruction of its

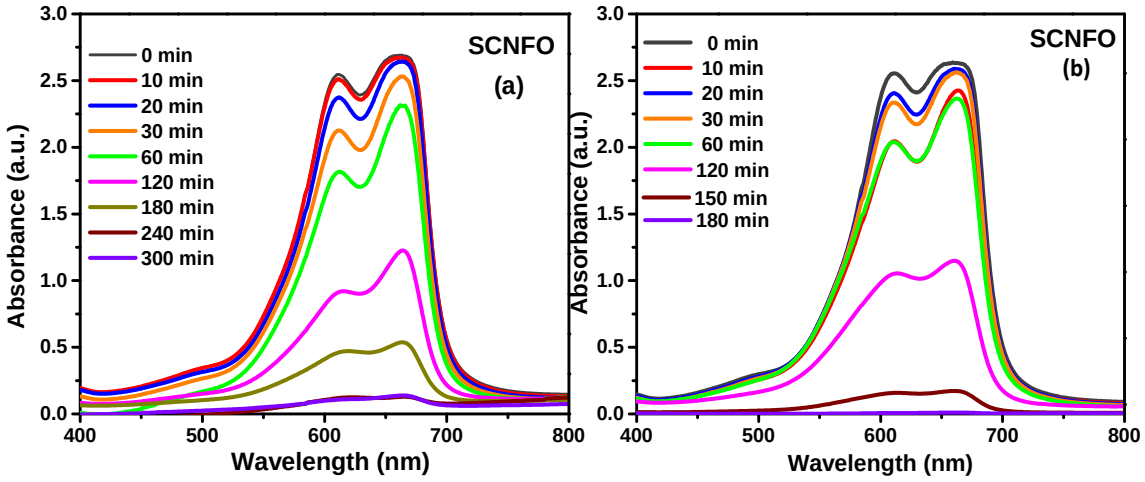

Fig. 4. Absorbance spectra of MB solution obtained SCNFO samples at different times under (a) UV irradiation and (b) solar irradiation

aromatic ring [12]. The figure shows the photocatalytic activity is more efficient under solar light. In the two-layer R-P oxides, oxygen vacancies are mainly localized on the vertex shared by two FeO_6 octahedra in the perovskite layer [14]. The oxygen vacancies in the R-P structure increases the oxygen adsorption ability since oxygen vacancy is the absorption center for active oxygen [11]. In the photocatalytic reaction, the absorbed oxygen is the active oxygen that prevents the electron-hole recombination and accelerate the photocatalytic reaction by creating the high activity ·OH radicals [12]. The degradation of MB was due to the generation of oxidizing radicals by the photocatalyst. During the experiment, the pH in the MB aqueous solution increased from 7.2 (t =10) to 9.4 (t = 180 to 300 min), which indicates the formation of ·OH radicals. Similarly, the blank solutions without photocatalyst maintained a constant pH of 7.6 during the experiment which indicates the there is no formation of oxidizing radicals.

4. Conclusion

The two-layer R-P oxides $Sr_{2.7-x}Ca_xLn_{0.3}Fe_2O_{7-\delta}$ has been prepared and studied the effect of Ca and lanthanides substitution. A slightly increased absorption in the UV-VIS-NIR region and less band gap exhibited by Nd doped samples compared to the La samples. Similarly, a slightly

increased MB dye degradation under both UV and solar irradiation is exhibited by Nd samples. Under solar irradiation the MB degradation rate was faster compared to UV irradiation. The results obtained shows that $Sr_{2.7-x}Ca_xLn_{0.3}Fe_2O_{7-\delta}$ oxides could be a feasible choice for the degradation of pollutant dyes under solar irradiation under water treatment plants.

Acknowledgements

The authors acknowledge the support from CONACYT Mexico for the grant C/2607/15/261205.

References

[1] Hoffmann MR, Martin ST, Choi W, Bahnemann DW. Applications of semiconductor photocatalysis. Chem Rev 1995;95:69 – 96.
[2] Weber AS, Grady AM, Koodali RT. Lanthanide modified semiconductor photocatalyst. Catal S Technol 2012;2:683-693.
[3] Wang W, Tade MO, Shao Z. Research progress of perovskite materials in photocatalysis- and photovoltaic-related energy conversion and environmental treatment. Chem Soc Rev 2015;44 5371-5408.
[4] Fu S, Niu H, Tao Z, Song J, Mao C, Zhang S, Chen C, Wang D. Low temperature synthesis and photocatalytic property of perovskite-type $LaCoO_3$ hollow spheres. J Alloy Compd 2013;576:5-12.
[5] Geng Y, Zhnag P, Kuang S. Fabrication and enhanced visible-light photocatalytic activities of $BiVO_4/Bi_2WO_6$ composites, RSC Adv. 2014;4:46054-46059.
[6] Ghaffari M, Shannon M, Hui H, Tan OK, Irannejad A. Preparation, surface state and band structure studies of $SrTi_{(1-x)}Fe_xO_{(3-\delta)}$ (x=0-1) perovskite-type nano structure by X-ray and ultraviolet photoelectron spectroscopy. Surf. Sci 2012;606:670-677.
[7] Huang Y, Wu J, Wei Y, Hao S, Huang M, Lin J. Synthesis and photocatalytic activity of hydrated layered perovskite $K_{2-x}La_2Ti_{3-x}NbxO_{10}$ ($0 \leqslant x \leqslant 1$) and protonated derivatives. Scripta Mater 2007;57:437–440.
[8] Liang Z, Tang K, Shao Q, Li G, Zheng S, Zheng H. Synthesis, crystal-structure, and photocatalytic activity of a new two-layer Ruddlesden-Popper phase, $Li_2CaTa_2O_7$. J Solid State Chemistry 2008;181964-970.
[9] Padmasree KP, Lai Ke-Yu, Kaveevivitchai W, Manthiram A. Effect of Ca substitution on the electrochemical properties of the Ruddlesden-Popper oxides $Sr_{3.2-x}Ca_xLn_{0.8}Fe_{1.5}Co_{1.5}O_{10-\delta}$. J Power Sources 2018;374:249-256.
[10] Huang Y, Wei Y, Cheng S, Fan L, Li Y, Lin J, Wu J, Photocatalytic property of nitrogen-doped layered perovskite $K_2La_2Ti_3O_{10}$. Sol Energy Mater Sol cells 2010;94:761-766.
[11] Taylor FH, Buckeridge J, Catlow CRA. Defects and oxide ion migration in the solid oxide fuel cell cathode material $LaFeO_3$. Chem Mater 2016;28:8210-8220.
[12] Shen H, Xue T, Wang Y, Cao G, Lu Y, Fang G. Photocatalytic property of perovskite $LaFeO_3$ synthesized by sol-gel process and vacuum microwave calcination. Mater Res Bull 2016;84:15-24.

[13] Oliva J, Garcia CR, Verduzco E, Martinez AI, Manthiram A, Padmasree KP. Enhancing the photocatalytic activity of the perovskite-based intergrowth oxide $Sr_{3.2}La_{0.8}Fe_{1.5}Co_{1.5}O_{10-\delta}$ with Ca substitution. Ceram Int 2017;43:14074-14081.
[14] Tomkiewicz AC, Tamimi M, Huq A, McIntosh S. Oxygen transport pathways in Ruddlesden-Popper structured oxides revealed via in situ neutron diffraction. J Mater Chem A 2015;3:21864–21874.

XVIII International Congress
of the Mexican Hydrogen Society

Residual power in portable energy storage electrochemical devices: an experimental collection approach.

C. M. Bautista-Rodríguez[1*], A. Horta-Mendez[2], M. Maldonado-Santoyo[1], B. Ruiz-Camacho[3], Richard R. Lindeke[4].

[1] Centro de Innovación Aplicada en Tecnologías Competitivas (CIATEC). Dirección de Investigación y Posgrado, Omega 201, Fraccionamiento Industrial Delta, P.O. Box 37545, León, Guanajuato, México.
[2] Universidad Politécnica del Bicentenario. Ingeniería en Agrotecnología. Carretera Estatal Silao – Romita Km 2. Col. San Juan de los Durán, CP. 36283. Silao, Guanajuato, México.
[3] Departamento de Ingeniería Química, División de Ciencias Naturales y Exactas, Universidad de Guanajuato, Campus Guanajuato, Noria alta S/N, CP. 36050, Guanajuato, Gto. México.
[4] Professor Emeritus University of Minnesota Duluth, Volunteer Peace Corps Mexico at CIATEC.
[*] Corresponding author: + 52 (477) 710 0011, ext. 13003 ; cbautista@ciatec.mx

ABSTRACT

This document presents the results of an experimental program for appropriate handling of discarded domestic batteries (single-cells), including the next procedures: (1) collection, (2) classification, (3) parametric records, (4) temporal storage and (5) sending to recycle processes. A statistical study was designed later at the collect, classification and record battery parameters, including residual voltage and residual current, present in discarded domestic single-cell batteries. The results showed that 55% of discarded batteries registered more than 70% of their nominal voltage and only 19% contained indicators of exhaustion, representing a significant energy waste by consumers. Of the collected AA cell batteries, more than 57% had residual voltage up of 1.0 V, and 29.5% more than 1.3 V, when compared to their nominal 1.5 V starting voltage. In other hand, measures of residual electrical current was recorded for new and discarded cell-batteries. Power curves was obtained for new and discarded cell batteries to know the contained energy inside the cells. The values of contained energy was calculated by power area integration using 1/3 Simpson´s rule. This measures confirms high values of residual energy presents in cell-batteries discarded versus energy values recorded on new cell batteries. After comparing energy parameters (voltage and electrical current) between discarded and new batteries, we concluded that the incomplete use of stored energy is significant. We conclude then that measures of electrical current would be a better indicator of the energy level present in the domestic batteries rather than voltage, which is a characteristic of battery size, but not of the available energy.

Keywords. Energy, Cells, batteries, residual power, alkaline batteries.

1. Introduction.

Many new systems have emerged in our society for power consumption, particularly in personal electronics, where devices like portable audio and video equipment, mobile and stationary electronic clocks, electronic data managers, calculators and laptop computers, notebooks and the ever-present cellular phone, seem to be everywhere. These 'technical' and social phenomena have generated a significant increase in energy demands of society. A characteristic of this energy demand is the increased use of "domestic batteries" to power these portable electronic devices. Usually, when the electronic device that employs the battery bank stops working, the user assumes that the batteries' energy has been exhausted, so they simply discard these batteries and replace them with new ones. This is even true for those batteries that are considered rechargeable. Seldom does the battery user verify the level of residual energy in the discarded batteries or consider any further impact they may have on the environment.

The global market of batteries was approximately $50 billion USD in 2006, by 2015 it had grown to $65 billion USD with projections to $100 billion USD by 2025. In 2006, approximately $5.5 billion USD are destined for rechargeable batteries a market that had reached $49 billion USD by 2014 with projections to over $100 billion USD by 2025 [1-5]. This implies a current global market value of approximately 100 billion dollars in 2017. On the other hand, The Freedonia Group, a Cleveland-based industry research firm, expects the global demand for primary and secondary batteries to grow by 7.7% annual, reaching 120 billion dollars in 2019. The real growth resides in secondary batteries (rechargeable) and secondary batteries represent 76.4% of the global market, and the remaining 23.6%, for primary (single use) batteries, is equivalent to 28.32 billion dollars. Specifically, the global market for primary alkaline batteries represents 4.25 billion dollars, suggesting that 15% of the global market corresponds to this class of primary (chemical) cell batteries [1-5].

A cell battery is an electrochemical device with the capacity to convert chemical energy stored in its internal components into electrical energy. These devices consist of one or several primary elements (that are chemically irreversible, and called "non-rechargeable") or one or more secondary elements (chemically reversible, and called "rechargeable") [6]. The basic elements of a household battery are the anode, the cathode and the electrolyte (acid or alkaline). Each of these are compacted and sealed with a cover to shape the electro-chemical pile and facilitate handling. For a battery to generate electrical energy, these components interact in a process called oxide-reduction (REDOX) reactions; here one of the electrodes is oxidized, losing electrons, and the other is reduced through gaining electrons. Once an electrode is completely oxidized (or reduced), the REDOX process ends and so does the battery operation [6]. In the case of rechargeable batteries, the REDOX process is reversible, making it possible to reverse this electron flow action and prepare the batteries for continued cycles of this natural REDOX action. Hence, the criterion for classifying batteries as either 'rechargeable' or 'single-use' is the ease of accomplishing the reversibility of the REDOX processes [7]. Additionally, the concept of battery or cell should not be confused, a battery (single cell) is an electrical or electronic circuit formed by two or more cells (electro-chemical piles) in series or parallel configuration [8, 16].

Discarded domestic cells/batteries have been legislated as hazardous wastes by several countries, giving rise to the international regulations for the management and handling of discarded electronic devices. Comparing the regulation of the European Union, Canada, the United States, Brazil and Japan, we observe that all their handling standards prohibit the use of mercury if it exceeds the established permissible limits and observe similarly detailed labeling system [8, 9-15]. However, the draft Mexican regulation PROY-NOM-212-SCFI-2016 is not the same as the standards of the aforementioned countries. In fact, in requires the collection and treatment of said batteries and imposes, on battery manufacturers, all the financial costs for collection, treatment and recycling processes. Unfortunately, while this official Mexican draft standard moves in a very positive direction for the environment, there is no domestic production of cell batteries in Mexico, all are imported from other countries. And thus it will be nearly impossible to force this regulation onto manufacturers unless consumption in Mexico is otherwise regulated [14].

In this document, the authors present a study on the residual energy present in discarded AA alkaline domestic batteries, which were collected by the GAE-CELLBAT-05 program on the campus of the Benemerita Universidad Autonoma de Puebla (BUAP) in the city of Puebla Mexico. After their collection, the team performed a statistical analysis of the remaining power in the collected batteries. The average resident electric power in the batteries was estimated by P = i*E, after the electrical variables had been measured: electric current (i, mA) and voltage (E, V). The team, finally compared power estimates from the discarded battery measurements against power estimates taken from samples taken using batteries fresh from the original packaging.

2. Materials and Methods

The GAE-Cellbatt-05 program was a pilot collection and recycling project for discarded domestic batteries that followed five recommended procedures. These are: (1) Collection (PGAE-RCL-01), (2) Classification (PGAE-CLS- 01), (3) Measurement of Residual Variables (PGAE-MDC-01), (4) Temporary Storage (PGAE-ALM-01) and (5) Distribution to recycling projects (PGAE-DTR-01) of discarded household batteries [16]. Campus BUAP applied the five procedures 8 weeks and used MINITAB 17 software to perform a statistical analysis of the findings. During the recycling project, the team purchased a package of 6 alkaline "AA" domestic cell batteries, with lot number 6J25CH16, for comparison. Each of the 6 purchased cells was individually identified and simultaneous measurements of voltage and ‘residual current’ were recorded as a function of time for both new and discarded batteries. Using the measured values the electric power available for each cell was computed. A one minute sampling interval was chosen and they were obtained using the electric circuit presented in Figure 1.

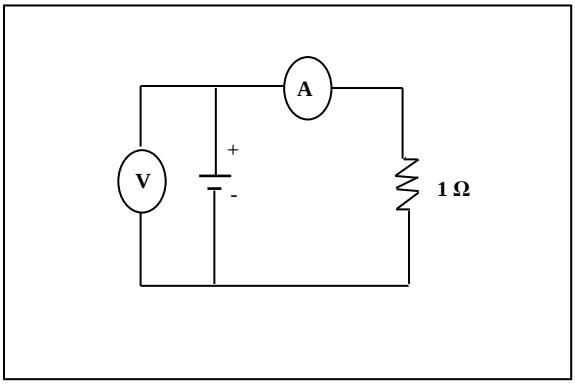

Figure 1. Sketch of electric circuit used for measure and record resident variables in discarded and new domestic cell batteries

Figure 2. Measurement and record system physical setup.

The equipment used for the electrical measurements were: (1) a BK Model 390A Precision Multimeter and (2) a Steren model MUL-600 Multimeter. Both multimeters were connected to a personal computer to record the current and voltage values at the specified one minute intervals. Figure 2 is a photograph of the actual electrical measurement system. Resident power of the cells/batteries, was computed using Ohm's power law, eqn. 1:

$$P = I * E \quad \ldots\ldots\ldots\ldots (1)$$

where: I = electrical current in Amperes (A) and E is cell potential in Volt (V).

Graphing the electrical power as a function of time it is possible to obtain the adjustment function, later integrated with Simpson's 1/3 Method to obtain the estimated value of the residual power in any domestic cell/battery. The integration calculation was performed using a Fortran 77 (v. 6.2) program.

3. Results and Discussion

The total number of individual cells/batteries collected during the 8 week program was 3171 and the percentage classification, by size, is shown in Fig. 3a (left). We found that 69.3% of the batteries collected were "AA" size and 21.3% size "AAA". We found, then, that 90.4% of the total collected sample was the smaller energy storage devices with the remaining 9.6% corresponded to larger and/or rechargeable batteries. These results confirm the high demand for single-use (and cheap) energy storage units used in the typical portable electronic device.

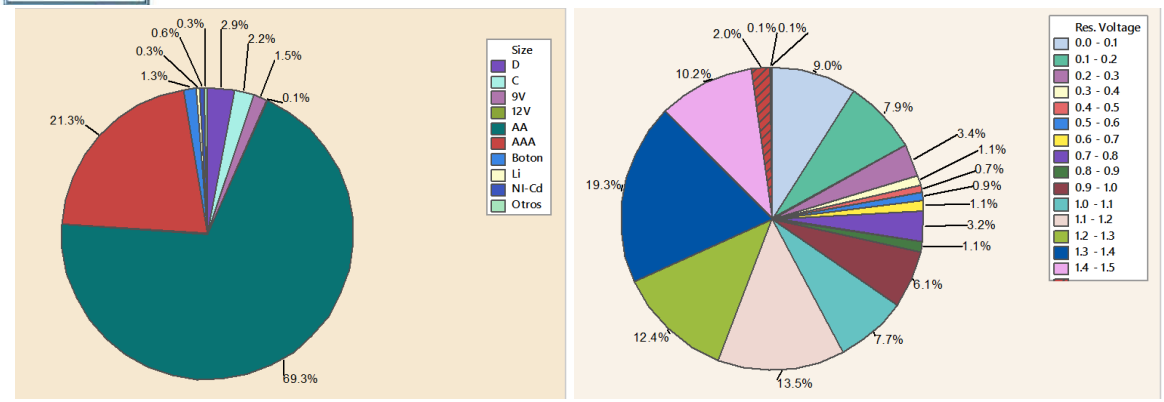

Figure 3. Statistics for collection and classification of discarded domestic cell batteries by size (left), and residual voltage measured in "AA" sized batteries (right).

The right graph in Fig. 3 shows a percentage classification according to the voltage level recorded for samples of the discarded "AA" batteries. As with nearly all of the small domestic cell batteries, the nominal voltage of size “AA” is 1.5 V for new batteries. The team points out that of the samples of discarded batteries, 55.4% displayed a voltage higher than 1.1 V, or approximately 73% of its as manufactured nominal value. Even more surprising were the resuts of measurement showing values about the “New Nominal” up to 1.9 V in the discarded samples. Additionally, only 16.9% of the sample exhibited voltage values of 0 - 0.2 V, which one would normally expect from an exhausted cell/battery.

The observed behavior can, likely, be attributed to the type of modern electronic device and its extreme sensitivity to micro current during operation. Most modern micro-electronic circuits, used in these devices, are designed for use over a very narrow voltage range, and hence current draw, to limit flash over within their transistors, diodes and semiconductor based components due to excessive, or potentially, insufficient, current flow as the available voltage departs from the designed nominal voltages of the electro-chemical piles. The need to maintaining consistent voltage, over very narrow ranges, therefore, reduces the operating time of a battery as the flow of electrons, and hence available current is a strictly limited amount due to the REDOX reactions. Thus, users often are forced to discard most batteries long before completely exhausting their stored energy. In a sense, then, society should reevaluate this general waste from the discarded batteries tossed away while still having a significant level of stored residual energy.

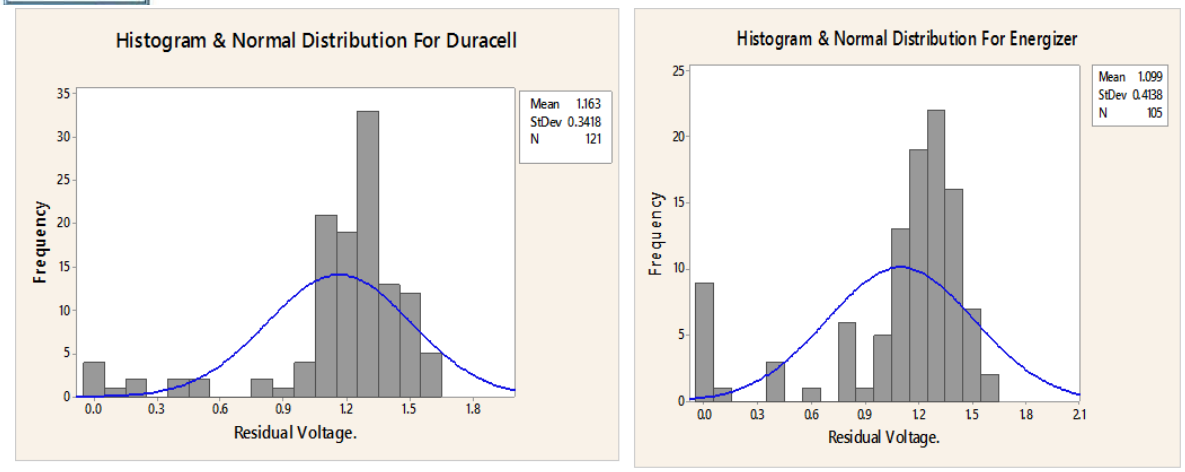

Figure 4. Histogram graphs and normal distribution for the most representative discarded cell batteries brands according to the registered voltage classification.

The results and the discussion that follows focus on alkaline domestic cell batteries. Figure 4 presents a histogram and normal distribution graphs for the registered voltage in discarded alkaline domestic cell/batteries, of the most popular brands found in the collected sample (brand names: Duracell and Energizer). These brands exhibited the highest concentration of batteries exhibiting residual voltage greater than 1.0 V. We wish to point out, however, that similar behavior was found in all the battery brands that were collected, so high values of residual voltage is not particular to the either of the brands used in the data of figure 4, it is, rather, a characteristic of this portable electronic technology in general.

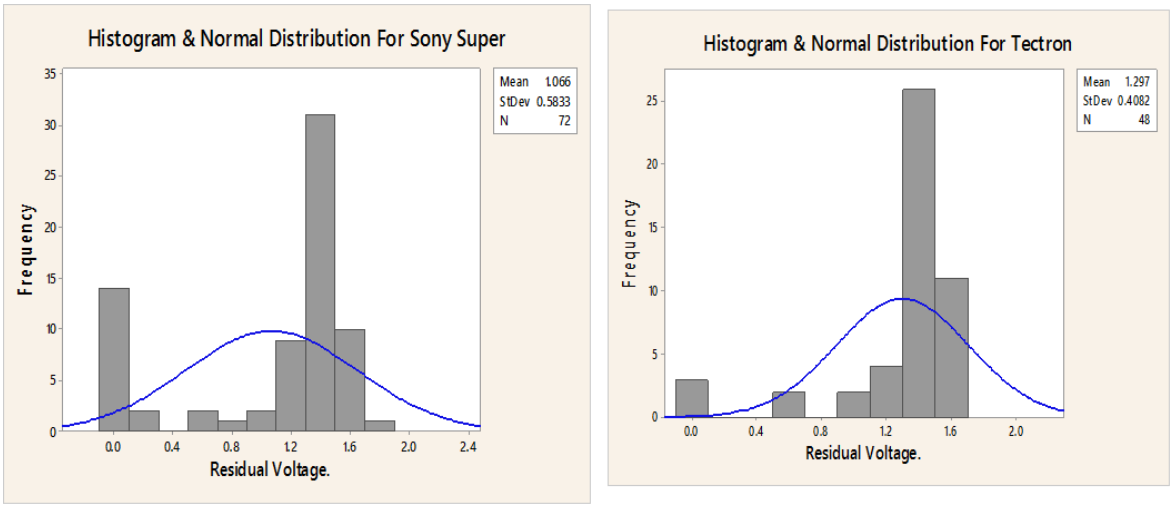

Figure 5. Histogram graphs and normal distribution for the most representative discarded Zn-C cell batteries brands (acid electrolyte) according to the registered voltage classification.

Figure 5 confirms the same behavior noted in alkaline discarded cell-batteries, now for Zn-C and acid electrolyte. Where high frequency values of residual voltage for these discarded batteries are concentered between 1.2 and 1.6 Volt, here, we can suppose the same discussions for cell-batteries of acid electrolyte.

In other way, the voltage and current values for new "AA" alkaline cell batteries were recorded, shown in Table 1. The six brand new batteries had an average voltage of 1.552 V and an average electric current of 0.2578 A. It is also interesting to observe that each of them had voltage higher than the nominal value (1.5 V) expected for this classification, with two having voltages more than 7% above the nominal value.

Table 1. Specific Measurements recorded in new Duracell batteries "AA"

ID	*Current (A)*	*Voltage (V)*
MDCD-A	0.2689	1.502
MDCD-B	0.2656	1.547
MDCD-C	0.2150	1.610
MDCD-D	0.2801	1.606
MDCD-E	0.2406	1.542
MDCD-F	0.2765	1.506

Using the methodology described earlier for measuring and recording voltage and current over time enabled charting of the devices power behavior. Here Fig. 6 shows the behavior for two new "AA" alkaline batteries, the left one was from the group listed in Table 1 and the right graph plots the power behavior from a different lot obtained one year later. The initial cell was sampled, following the described methodology and electrical circuit, over a period of 183.3 minutes (3.06 h). Here electric power displayed a very inconsistent behavior as can be seen.

In the new battery case (right), which came from a lot produced later in time, one observes stable and consistent power profile over a much longer time frame (1000 minutes -- 16.66 h). In the second case, the power curve follows a consistent (nearly exponential) depletion to about 600 minutes (10 h) of continuous work. At this time it was “depleted” (zero watts) which was unchanged over the rest of the testing time (400 minutes). The differences in behavior surely must be attributable to the composition and characteristics of each battery lot (manufacturing), as well as the individual characteristics of their assembly. However, in the first case, the inconsistency in the work of the device could determine the useful life of the device when operating in a battery electro-chemical pile, so if only one of the individual cells followed this behavior pattern the functionality and efficiency of the whole electro-chemical piles would be compromised. Under these conditions, the user could consider that the set of elements of the

battery electro-chemical piles are exhausted, replacing all and discarding that bank of batteries that the user erroneously considers to be without power.

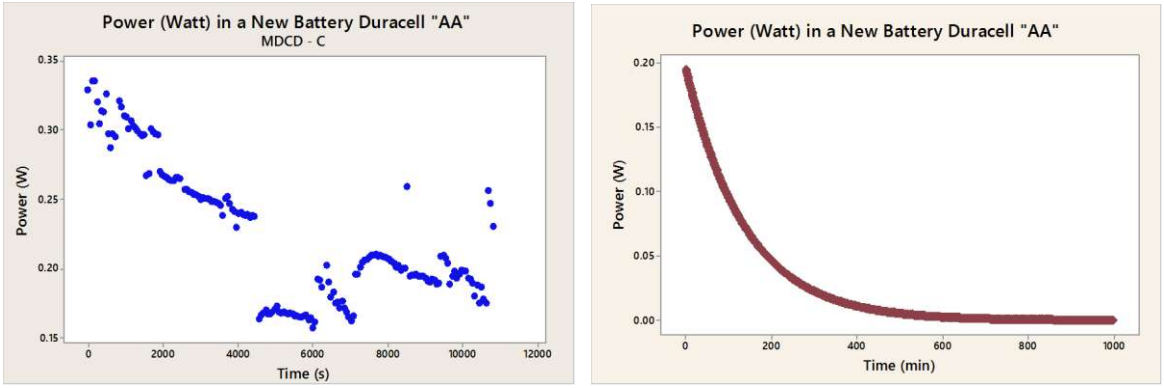

Figure 6. Behaviors of the power developed by new "AA" alkaline cell batteries as a function of time, at left the cell battery referenced in table 1 and at right, other new cell battery acquired one year later.

Table 2 presents individual “point values” recorded on discarded domestic "AA" batteries chosen at random from the discard bin. The measured current seemed to be a function of voltage, as would be expected in these electro-chemical devices. It is notable to observe that some of the discarded cell batteries had voltages close to their nominal value (1.5 V) and current readings similar to the average values recorded in new batteries.

Table 2. Point measurements recorded in discarded "AA" cell batteries.

ID	*Brand*	*Current (A)*	*Voltage (V)*
MDCSA-01	Sony Alcalina	0.1625	0.836
MDCDU-02	Duracell Ultra	0.2416	1.543
MDCDU-03	Duracell Ultra	0.2013	1.419
MDCRM-04	Rayovac Maximum	0.0450	0.741

Figure 6 presents the power graphs generated for these discarded devices. The similarity of behavior between MDCSA-01 and MDCRM-04 (in the right graph) batteries is remarkable, After a short sampling period, both of these devices displayed low power values (less than 0.02 W). Hence, internal residual energy dramatically falls when residual voltage reaches about 0.8 V. Our team, then, suggests that a device (truly) reaches the end of its life cycle when voltage falls below 0.8V. On the other hand, the curves of residual power presented for MDCDU-02 and MDCDU-03 cells, the left graph in Fig. 7, show different energy levels. For MDCDU-02 power was measured to be between 0.39 and 0.29 W with an initial voltage of 1.543 V, while MDCDU-03 power ranged between 0.29 and 0.23 W with an initial voltage of 1.419 V. This significant difference in electrical power (about 25%) between these cells with a voltage difference of 0.124

V (about 8%), shows the apparent sensitivity of the electric power to the cell voltage, a measurement of the electrical potential for driving electrons (the electrical current) through the measurement circuit.

These observations suggest that the highest energy capability for AA domestic alkaline batteries, would be available above 1 V. It is probable, with properly developed electrical systems, that these “spent” devices could, most probably, be able to supply power in less demanding electrical environments.

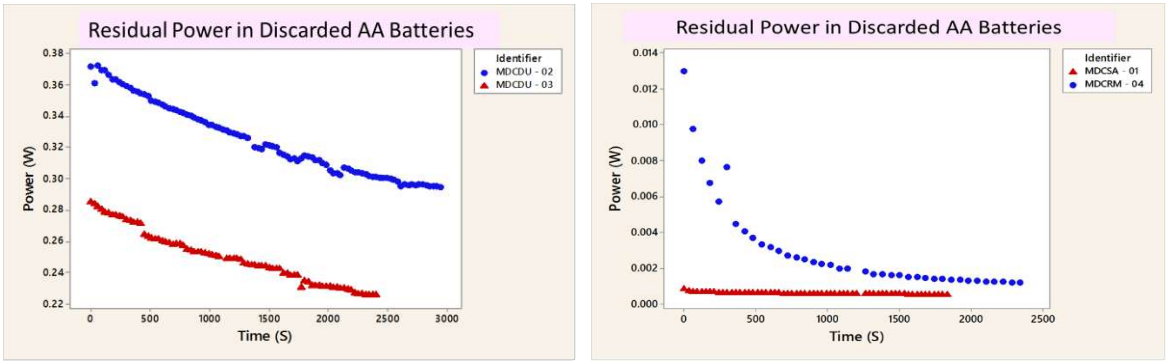

Figure 7. Behavior of the residual power curves in the group of discarded domestic cell batteries presented in table 2.

The curves of Fig. 8, tracking discarded battery voltage over the sampling period, mirror, to some extent, the corresponding residual power curves of Fig. 7. Note, however, that the drop offs in residual currents, as presented in Fig. 9 are much closer in shape to the residual power curves. These observations suggest that in the computation of residual power the rapid decay in residual current, corresponding to fewer available REDOX sites in a “spent” battery device, have a very strong influence on the residual power of discarded AA alkaline domestic cell batteries.

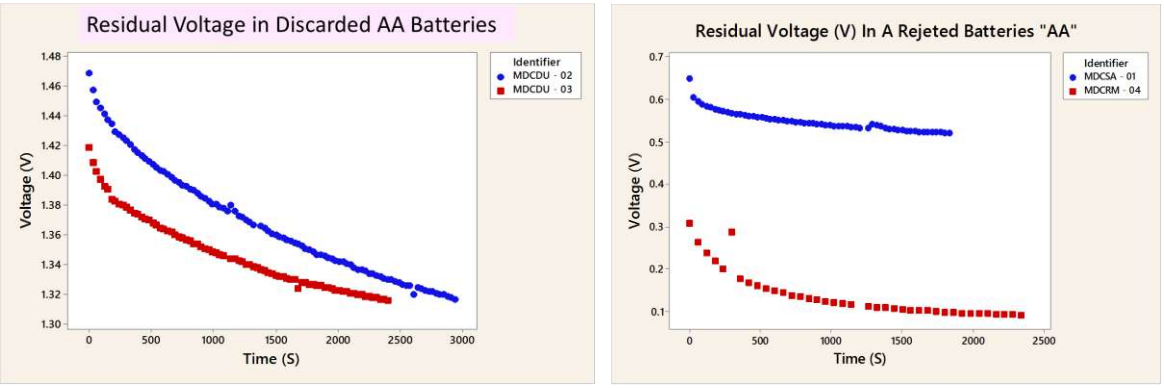

Figure 8. Residual voltage behavior in the group of discarded domestic cell batteries presented in table 2.

Finally, the results of the calculated area under the residual power curve for the discarded alkaline batteries was completed. These calculations for the four discarded batteries were computed using a Fortran 77 program that implemented Simpson's 1/3 rule.

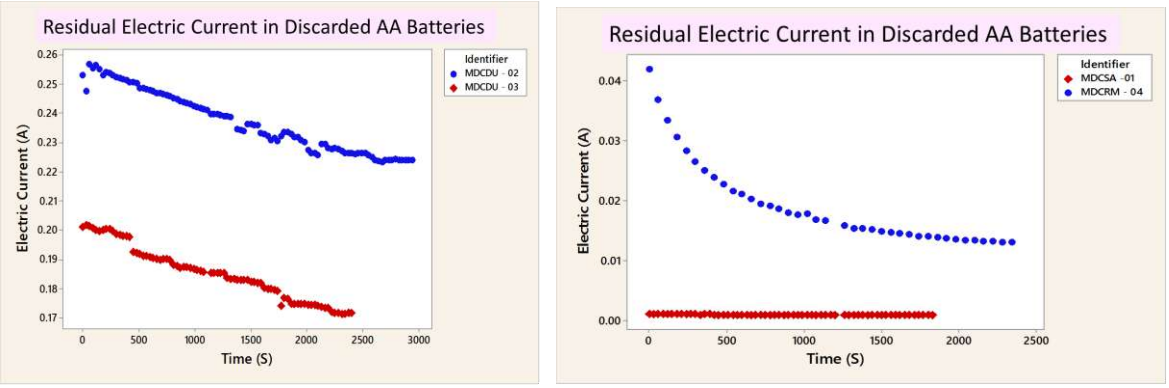

Figure 9. Behavior of the residual current in the group of discarded cell batteries presented in table 2.

The results obtained are presented in Table 3. Here we report the the potential resident power in the cell batteries in Watts (W), the estimated available operating life in hours (h) and the estimated energy for doing useful work from these discarded cells in Watt-hour (W-h) over their lifetime.

Table 3. Results obtained by the integration of the measured electric power function in "AA" domestic batteries.

ID	Resident Power (W)	Estimated Life (h)	Estimated Work (W-h)
MDCSA-01	5.333	9.950	0.536
MDCDU-02	4562.792	24.950	182.880
MDCDU-03	3105.310	29.125	106.620
MDCRM-04	9.140	3.250	2.810
MDCD-C	5098.658	40.650	125.430

Note here that for the discarded batteries numbered MDCDU-02 and MDCDU-03 that their residual power values are of the same order of magnitude as the nominal power in new a battery (MDCD-C). Discarded battery DU-02 offered 89.49% of the resident power of the new battery, while DU-03 retained 60.9%. One result to highlight is that the estimated energy (available work) value measured is higher in the discarded battery (DU-02) compared to the new battery, however, its expected life was only 61% of a new one. These observations confirm the uncertainty of setting a standard energy quantity, as a function of the nominal voltage, in

new and discarded AA alkaline batteries. It seems, then, that nominal and residual energy is a function of the intrinsic characteristics of each device, and its prediction will display significant uncertainty whether based on initial, nominal or residual voltage. Which conditions the users energetically to manufacturing conditions, but not to an energy load standardized in these devices, consequently, it is possible to consider energetic and economic disadvantages for consumers.

4. Conclusion.

Electric power developed by AA alkaline domestic batteries seems to rely more on generated current than the voltage developed by any individual cell. Voltages for these devices appears to be a function of battery size and not a well-defined measurement of available energy. Additionally, the the energy generation continuity seems to be a function of manufacturing characteristics, so that a malfunction in a individual cell can affect the efficiency of all batteries in a bank. Thus even if a single misbehaving cell is present, a user would likely replace and dispose of the entire bank, mistakenly, thinking that whole set is exhausted. On the other hand, it is important to consider that the portable electrical devices that employ domestic batteries are being designed with higher energy requirements than the generation capabilities that are possible from regular batteries. Consequently, after operating for only a short time the batteries are unable to meet the power demands. The battery banks are then removed, and erroneously, considered to be exhausted of all power. Thus oftentimes batteries are discarded inappropriately due to poorly designed portable device circuits throughout much of the world. These societal losses lead to economic and environmental wastes. Therefore, their solution offers a dual opportunity for sustainable advancement through (1) real and timely regulation applicable throughout the world and (2) design and development of more tolerant electric circuit schemes for employment in the portable electronic marketplace.

5. Acknowledgments

The main author thanks to the Faculty of Chemical Engineering of the Benemérita Universidad de Puebla for providing facilities and operations for the program GAE-CELLBATT-05.

6. References

[1] Battery University. *"Battery Statistics".*
http://batteryuniversity.com/learn/article/primary_batteries (Consulted in 11/02/2017)

[2] Battery University. "*BU-103: Global Battery Markets".*
http://batteryuniversity.com/learn/article/global_battery_markets (Consulted in 11/02/2017)

[3] https://www.weforum.org/projects/global-battery-alliance. (Consulted in 29/03/2018)

[4] http://www.rechargebatteries.org/knowledge-base/market/ (Consulted in 29/03/2018)
[5] https://www.energyandcapital.com/articles/can-lithium-batteries-cope-without-cobalt/6032 (Consulted in 29/03/2018)
[6] D. Linden and T. B. Reddy. *"Handbook of Batteries"*, McGraw-Hill, New York, 2001
[7] J. S. Newman., *"Electrochemical Systems"*, Prentice Hall, Englewood Cliffs NJ, 1991
[8] Castillo V. J. I., Bolaños B. J. L. *"Technology for the treatment of discarded batteries and batteries from portable electronic equipment". International Journal for Environmental Pollution*, vol. 21, sup. 1, pp. 1159-1164 (2005), ISSN: 0187-4999.

[9] Directiva del parlamento europeo, Recuperado de: Boletín oficial del estado del gobierno de España. "pilas y acumuladores y la gestión ambiental de sus residuos". Año 2015 Disponible en: https://www.boe.es/buscar/doc.php?id=BOE-A-2015-8340 (Consulted in 10/20/2017)
[10] Gaceta de Canada: Battery Legislation, policies and Management disponible en: https://www.ec.gc.ca/nopp/docs/rpt/battery/en/c6.cfm (Consulted in 10/20/2017)
[12] Primary Battery Stewardship Law (Act 139) Summary Sheet Disponible en: http://dec.vermont.gov/sites/dec/files/wmp/SolidWaste/Documents/ANR-primary-battery-summary-sheet.pdf (Consulted in 10/20/2017)
https://www.epa.gov/eg/battery-manufacturing-effluent-guidelines-documents (Consulted in 10/20/2017)
[13] RESOLUCIÓN CONAMA N ° 401, de 4 de noviembre de 2008 Publicada en el DOU nº 215, de 5 de noviembre de 2008, Sección 1, página 108-109 Correlación: • modificado por la Resolución N ° 424 de 2010. • revoca la Resolución CONAMA Nº 257/99 Disponible en http://www.mma.gov.br/port/conama/legislacao/CONAMA_RES_CONS_2008_401.pdf (Consulted in 10/20/2017)
[14] PROYECTO de Norma Oficial Mexicana PROY-NOM-212-SCFI-2016, Pilas y baterías primarias-Límites máximos permisibles de mercurio y cadmio-Especificaciones, métodos de prueba y etiquetado. Disponible en: *dof.gob.mx/nota_to_doc.php?codnota=5465033* (Consulted in 10/20/2017)
[15] Battery Association Japan Disponible en: http://www.baj.or.jp/e/ (Consulted in 10/20/2017)
[16] M. Mercedes Galicia Pineda. *"Manual de procedimientos GAE-CellBatt-05 aplicado en la BUAP para la gestión de pilas domesticas desechadas".* Tesis como requisito parcial para recibir el grado de Ingeniero Ambiental. Benemérita Universidad Autónoma de Puebla. Noviembre 2007.

XVIII International Congress
of the Mexican Hydrogen Society

Synthesis and characterization of Bi_2O_3:Gd for hydrogen production under visible light.

Durvel de la Cruz Romero[1], David Salazar Marín[1*], V. Collins-Martinez[2]. M. J. Melendez-Zaragoza[2], Srinivas Godavarthi[1].

[1]Universidad Juárez Autónoma de Tabasco, División Académica de Ciencias Básicas, Carretera Cunduacán-Jalpa KM. 1 Col. La Esmeralda, Cunduacán, Tabasco, 86690, México.

[2]Departamento de Ingeniería y Química de Materiales, Centro de Investigación en Materiales Avanzados, S.C. Miguel de Cervantes 120, Chihuahua, Chih., 31136, México

*David Salazar Marín: 9371217446, xd_smd160991@hotmail.com

ABSTRACT

Photocatalytic water splitting is one of the cleaner processes for molecular hydrogen and oxygen production using semiconductor. For better utilization of solar spectrum and complete redox for water splitting applications, it is required to have a semiconductor which is photoactive in visible region. The Bi_2O_3:Gd photocatalyst was successfully synthesized by Pechini method. The physical and chemical properties of as-prepared samples were characterized based on XRD, SEM, BET and UV-vis. Bi_2O_3 is an important inorganic functional material. It has got much attention due to its unique electrical and optical properties, which lead to its extensive usage in catalysis. Also, it is a promising visible-light-driven photocatalyst whit a narrow bandgap (2.6-2.9 eV). It has been proved that β-Bi_2O_3 had the higher photocatalytic activity than α-Bi_2O_3 but only a few researches on β-Bi_2O_3 have been reported due to the difficulty of synthesizing the metastable β-phase [3]. The β-phase was confirmed using DRX.

Keywords: Bi_2O_3; Photoelectrolysis; Hydrogen; Photocatalyst

1. Introduction

Production of cleaner energy using renewable resources and non-energy intensive process are in great demand to cater the present and future energy supply. Hydrogen gas served as low density and high energy content cleaner fuel, demonstrated as best alternative to fossil fuels for sustainable energy developments. Hydrogen as an important energy carrier in the future has a number of advantages. For example, a large volume of hydrogen can be easily

stored in several different ways. Hydrogen is also considered as a high efficiency, low polluting fuel that can be used for transportation, heating, and power generation in places where it is difficult to use electricity. In some instances, it is cheaper to ship hydrogen by pipeline than sending electricity over long distances by wire. However, the large-scale H_2 production is mainly based on fossil fuels splitting or water electrolysis, which has led to high energy consumption and severe environmental pollution. Since the pioneering work of Fujishima and Honda on semiconductor photocatalysis, the direct H_2 production via water splitting using solar energy has been extensively investigated as a promising way to meet the ever-growing global energy demands. Bi_2O_3 semiconductor photocatalyst has gained considerable attention due to its good absorption capacity (band gap of 2.8 eV) and found to be very good catalyst for environmental application as well as photocatalytic water splitting.

2. Material and methods

Reagents		
$Bi(NO_3)_3 \cdot 5H_2O$	Aldrich	98%
$Gd(NO_3)_3 \cdot 5H_2O$	Aldrich	98%
Ethylene glycol	Aldrich	>99%
Tartaric acid	E. Merck	99.5%
HNO_3	J.T. Baker	69-70%
Water	---	Deionized
NaOH	J.T. Baker	89%

To obtain Bi_2O_3 by the Pechini method, we used $Bi(NO_3)_3 \bullet 5H_2O$ and $Gd(NO_3)_3 \bullet 5H_2O$ as a precursor, tartaric acid as a chelating agent and ethylene glycol as a polymeric agent, $Bi(NO_3)_3 \bullet 5H_2O$ was dissolved in a 5% HNO_3 solution, with moderate agitation for 30 minutes to obtain a transparent solution of Bi^{+3}. On the other hand, a solution of tartaric acid was prepared, this solution was added dropwise to the Bi^{+3} solution to carry out the chelation of the metal in a 1: 1 molar ratio. To this mixture was added ethylene glycol in a 1:1 molar ratio (tartaric acid: ethylene glycol), the addition was made drop by drop to polymerize the previously formed complex. The mixture stirred for a period of 24 h and subsequently adjusted to pH 0.5 with NaOH at 25% with a potentiometer, until forming a dense sun. Through a reflux system, the formed sun was heated at 80 °C for 2 h and then at 105 °C for 2 h to achieve condensation and finally kept in slow agitation for 24 h. Later we proceeded to eliminate the remaining solvent using a rotaevaporator with a water bath at 90 °C to get the xerogel. The xerogel was dried at 95 °C for 2 h and subsequently the white solid has been pulverized and calcined in a muffle at 390 °C for 3 h, with a heating ramp of 2 °C min^{-1}.

3. Results and discussion

3.1. XRD

The diffractogram of figure 1 shows that the phase obtained from undoped Bi_2O_3 by the Pechini method is the monoclinic alpha phase, in the figure 2 when the Bi_2O_3 was doped with the gadolinium, we obtain a mixture of phases due to a transition in the crystalline structure of the material. Phase transition occurs from the monoclinic alpha phase to a tetragonal beta phase, as we can see in figure 2 this probably due to the rearrangement of the atoms when gadolinium is added to the catalyst, finally, in figure 3 we can see that we only have present the beta phase of the material, which has been reported as the most photoactive crystalline phase.

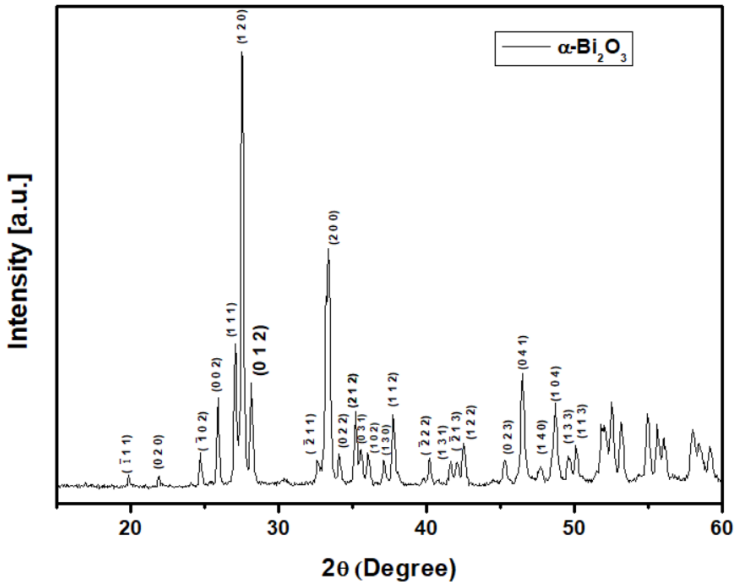

Figure 1. Diffractogram obtained by XRD of pure Bi_2O_3 without doping.

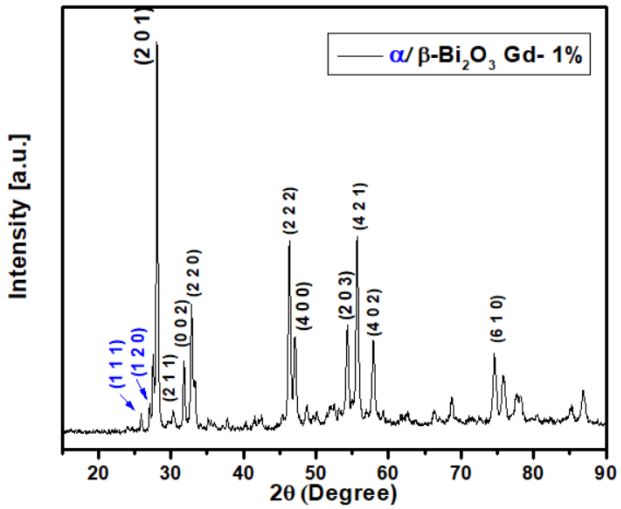

Figure 2. Diffractogram obtained by DRX of Bi_2O_3 doped with 1% gadolinium.

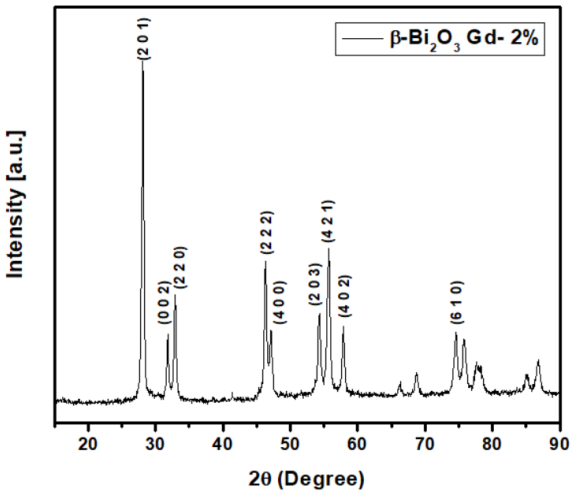

Figure 3. Diffractogram obtained by DRX of Bi_2O_3 doped with 2% gadolinium.

3.2. DRS Uv-Vis

It can be observed in figure 4 that when doping the material with gadolinium a change is obtained in the optical Bandgap of the material, the Bandgap obtained with the pure Bi_2O_3 is 2.95 and it is possible to reduce it to a value of 2.53 when doping with gadolinium.

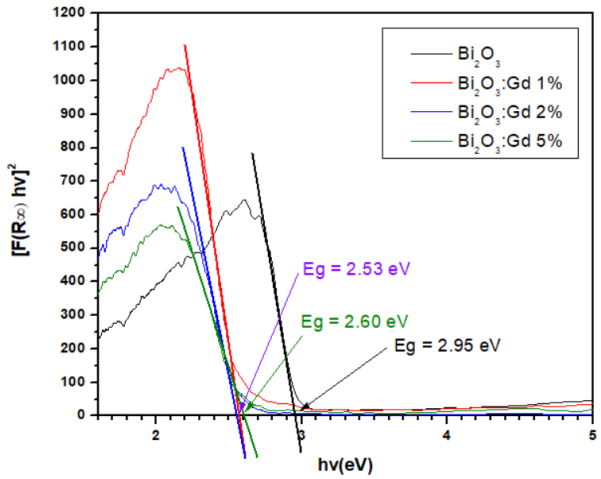

Figure 4. Calculation of optical Bandgap using the diffuse reflectance method Uv-Vis.

3.3. Scanning Electron Microscopy (SEM)- Energy Dispersive Spectroscopy (EDS).

In figure 5 we can observe the formation of bars and flakes of Bi_2O_3, the formation of these structures are characteristic of the synthesis method and the material, which have been previously reported. In the Energy Dispersive Spectroscopy results the presence of bismuth oxide was confirmed

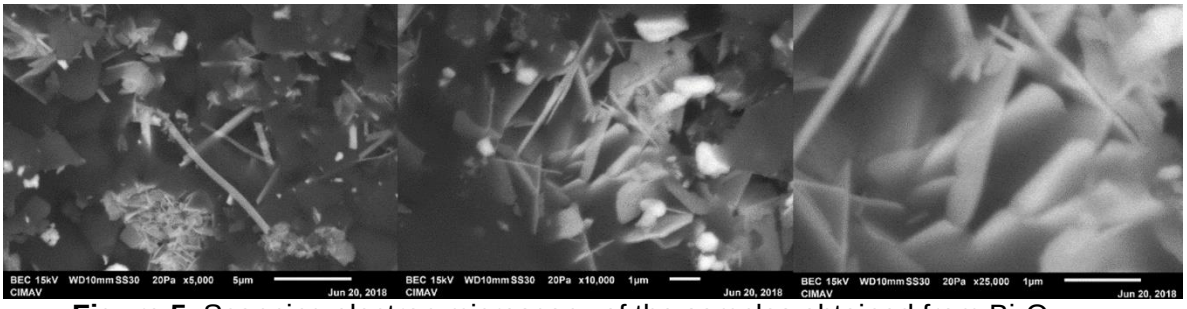

Figure 5. Scanning electron microscopy of the samples obtained from Bi_2O_3.

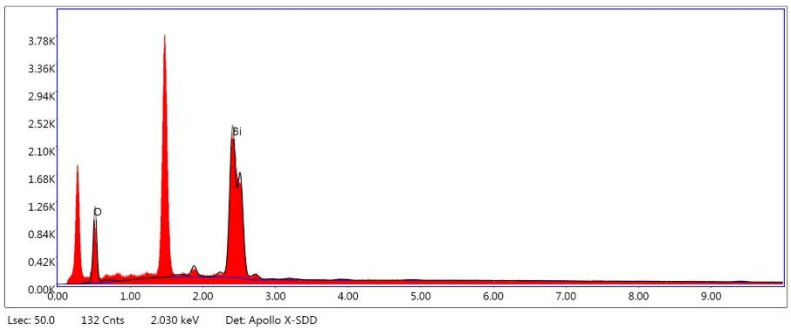

Element	Weight %	Atomic %
O K	38.89	89.26
BiM	61.11	10.74

Figure 6. Energy Dispersive Spectroscopy of the samples obtained from Bi_2O_3.

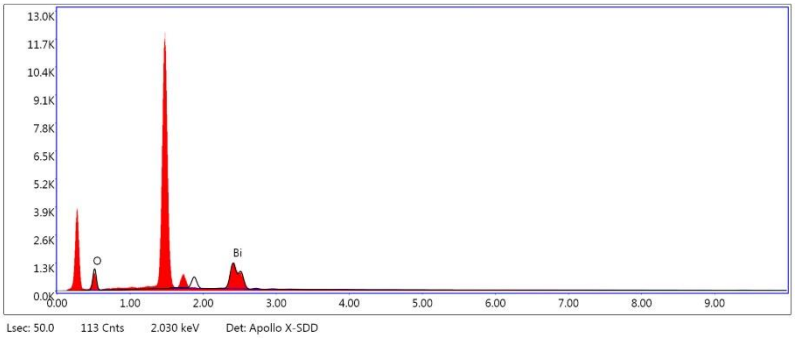

Element	Weight %	Atomic %
O K	26.89	82.77
BiM	73.11	17.23

Figure 7. Energy Dispersive Spectroscopy of the samples obtained from Bi_2O_3 with 1% Gd.

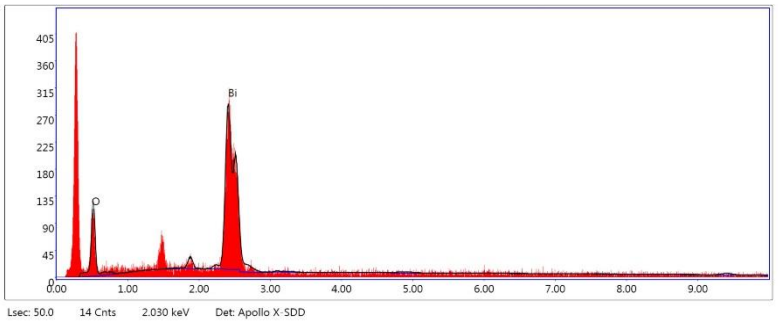

Figure 8. Energy Dispersive Spectroscopy of the samples obtained from

Bi_2O_3 with 2% Gd.

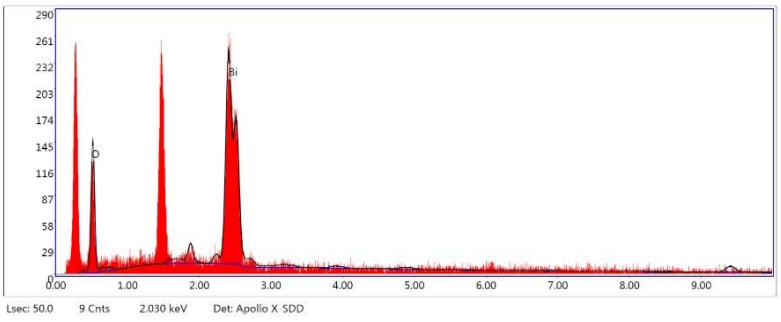

Element	Weight %	Atomic %
O K	29.86	84.15
BiM	70.14	15.24

Figure 9. Energy Dispersive Spectroscopy of the samples obtained from Bi_2O_3 with 2% Gd

3.4. N_2-fisisortion (BET)

Type IV isotherms were obtained which are characteristic of the mesoporous solids, this hysteresis cycle is due to the mesoporous filling process which is governed by capillary condensation phenomena, the hysteresis loops are type 3, which are obtained when working with pore agglomerates of parallel plates, which agrees with the micrographs obtained in MEB where the formation of flakes in the material can be seen, the Bi_2O_3 catalysts had a low specific area, they did not present a significant change in the pore radius, and an increase in the specific area was observed in the Bi_2O_3:Gd 5% samples.

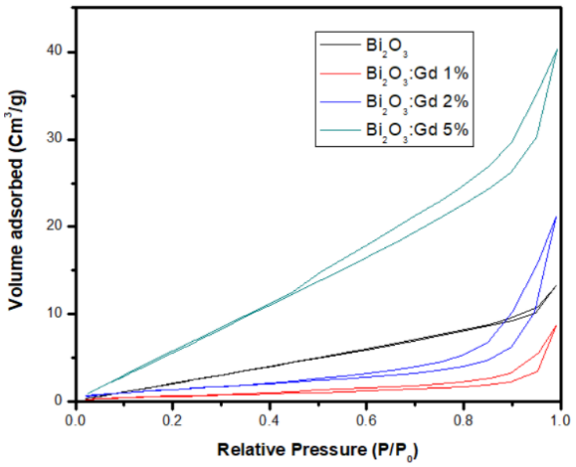

Figure 10. Nitrogen fisisorption isotherms of catalysts based on Bi_2O_3.

Element	Weight %	Atomic %
O K	32.87	86.48
BiM	67.13	13.52

	Bi_2O_3	Bi_2O_3:Gd 1%	Bi_2O_3:Gd 2%	Bi_2O_3:Gd 5%
Surface Area (m^2/g)	9.983	2.037	5.092	28.279
Pore Volume (Cm^3/g)	0.020	0.013	0.032	0.061
Pore Radius Å	15.441	15.440	15.291	15.243

3.5. Photocatalytic evaluation of hydrogen production.

It can be seen in the graphs that the material with the best performance with respect to hydrogen production was Bi_2O_3: Gd 2%, obtaining a considerably better performance than

that obtained with Bi_2O_3: Gd 1% and Bi2O3: Gd 5%, the doping of the gadolinium material favored the production of hydrogen. Hydrogen production was not obtained with the pure Bi_2O_3 catalysts.

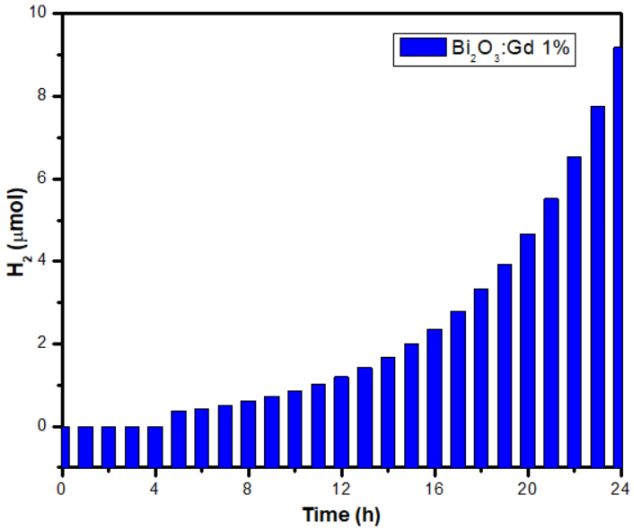

Figure 11. Photocatalytic evaluation of hydrogen production with Bi_2O_3 catalyst:Gd 1%.

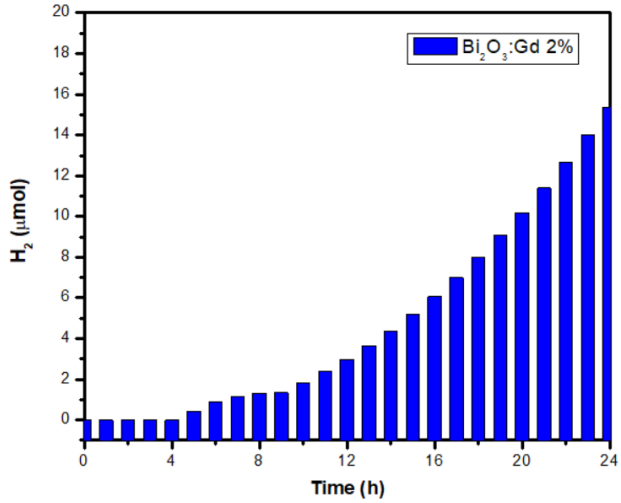

Figure 12. Photocatalytic evaluation of hydrogen production with Bi_2O_3 catalyst:Gd 2%.

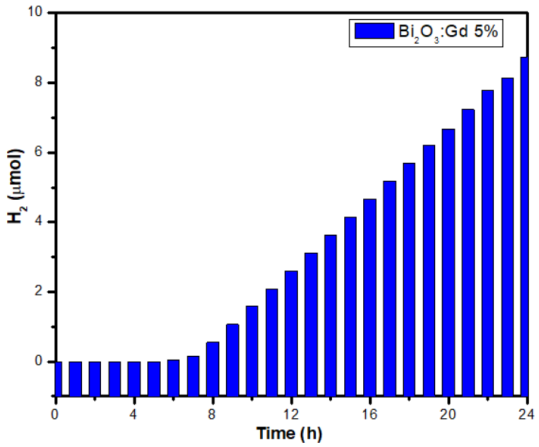

Figure 13. Photocatalytic evaluation of hydrogen production with Bi_2O_3 catalyst:Gd 5%.

3.6. Discussion

The addition of gadolinium at different percentages in the catalyst affects its optical and structural properties, causing a phase change due to a transition in the crystalline structure of the material. The phase transition occurs from the monoclinic alpha phase to a tetragonal beta phase, due to the rearrangement of the atoms as gadolinium is added to the catalyst. A reduction of the Bandgap in the doped materials was also obtained, since the Bi_2O_3 presents an optical Bandgap of 2.95 eV and when adding the gadolinium to the material, a reduction of the optical Bandgap is obtained up to a value of 2.53 eV and therefore a better photocatalytic activity in the visible light spectrum. The isotherms obtained by nitrogen fisisorción are type IV which are characteristic of the mesoporous solids, in addition to presenting hysteresis loops of type 3 which agree with pores of parallel plates type, these results agree with the micrographs obtained in the MEB, in which the formation of bars and flakes characteristic of the synthesis method can be observed. Finally of the synthesized materials, the best was the Bi_2O_3:Gd 2%, which presented a crystalline structure in the tetragonal beta phase, which has been reported as the most photoactive phase.

4. Conclusions

The doping of Bi2O3 materials in different percentages could allow to improve their optical and structural properties, alpha and beta crystalline structure of the material was obtained, the beta phase showed the greatest photocatalytic activity, a transition between the crystalline phases was achieved by changing the percentage of gadolinium in $B_{i2}O_3$, materials with a Bandgap between 2.95 eV - 2.53 eV were also obtained, which allows a better photocatalytic activity of the material in the visible spectrum, the micrographs achieved the characteristic morphology of the synthesis method, finally the results obtained in Photocatalytic evaluation of hydrogen production showed that the

material with the best photocatalytic activity is Bi_2O_3: Gd 2%, probably due to the fact that it has the lowest Bandgap and a tetragonal beta crystalline structure, which has been reported as the most photoactive phase of Bi_2O_3.

5. Acknowledgments

The authors are thankful to Universidad Juárez Autónoma de Tabasco and Centro de Investigacion en Materiales Avanzados, S. C. Furthermore, and XVIII International Congress of the Mexican Hydrogen Society for the fellowship to present this research.

6. References

K.Gurunathan. (2004). Photocatalytic hydrogen production using transition metal ions-doped γ-Bi_2O_3 semiconductor particles. International Journal of Hydrogen Energy, 29, 933–940.

S. H. Hsieh, G. J. Lee. (2012). Synthesis of Pt Doped Bi_2O_3/RuO_2 Photocatalysts for Hydrogen Production from Water Splitting Using Visible Light. Journal of Nanoscience and Nanotechnology, 12, 5930–5936.

Jingrun Ran, Jun Zhang. (2013). Earth-abundant cocatalysts for semiconductor based photocatalytic water splitting. Chem. Soc. Rev., 43, 7787-7812.

Brundabana Naik, Satyabadi Martha, K.M. Parida. (2011). Facile fabrication of $B_{i2}O_3$/TiO_2-xNx nanocomposites for excellent visible light driven photocatalytic hydrogen evolution. International journal of hydrogen energy, 36, 2794-2802.

N. Lakshmana Reddy, G. Krishna Reddy. (2016). Highly Efficient Hydrogen Production using Bi_2O_3/TiO_2 Nanostructured Photocatalysts Under Led Light Irradiation. Materials Today: Proceedings, 3, 1351–1358.
Kazuhiko Maedaa. (2011). Photocatalytic water splitting using semiconductor particles: History and recent developments. Journal of Photochemistry and Photobiology C: Photochemistry Reviews, 12, 237-268.

Hankwon Lim, Sher Bahadur Rawal. (2017). Integrated Bi_2O_3 nanostructure modified with Au nanoparticles for enhanced photocatalytic activity under visible light irradiation. Progress in Natural Science: Materials International, 27, 289-296.

S. H. Hsieh, G. J. Lee. (2012). Synthesis of Pt Doped Bi_2O_3/RuO_2 Photocatalysts for Hydrogen Production from Water Splitting Using Visible Light. Journal of Nanoscience and Nanotechnology, 12, 5930-5936.

K.Gurunathan. (2004). Photocatalytic hydrogen production using transition metal ions-doped γ-Bi_2O_3 semiconductor particles. International Journal of Hydrogen Energy , 29, 933-940.

Rishabh Sharma a, Manika Khanuja. (2017). Reduced band gap & charge recombination rate in Se doped α-Bi_2O_3 leads to enhanced photoelectrochemical and photocatalytic performance: Theoretical & experimental insight. International Journal of Hydrogen Energy, 42, 20638-20648.